



TalentDetector

**TalentDetector2024\_Summer  
INTERNATIONAL STUDENTS SCIENTIFIC  
CONFERENCE**

**Scientific editor:  
Mirosław Bonek**

Department of Engineering Materials and Biomaterials,  
Faculty of Mechanical Engineering,  
Silesian University of Technology  
17<sup>th</sup>-19<sup>th</sup> June 2024  
Gliwice, Poland



**Katedra Materiałów**  
Inżynierskich i Biomedycznych



**Katedra Materiałów Inżynierskich i Biomedycznych****Wydział Mechaniczny Technologiczny****Politechnika Śląska**

ul. Konarskiego 18a, 44-100 Gliwice tel. +48 (32) 2371322

**Redakcja techniczna i skład komputerowy:**

dr hab. inż. Mirosław Bonek, prof. PŚ

**Recenzenci:**

M. Bonek, A. Czupryński, A. Drygała, K. Gołombek, A. Kania, M. Kciuk, A. Kloc-Ptaszna, M. Kremzer, M. Król, B. Krupińska, L. Kuchariková, S. Lesz, G. Matula, C. Meran, M. Musztyfaga-Staszuk, J. Nowak, D. Pakuła, O. Polishchuk, M. Polok-Rubinić, M. Spilka, M. Sroka, M. Staszuk, M. Szindler, A. Śliwa, T. Tański, E. Tillová, M. Uhrčík, A. Włodarczyk-Fligier

Materiały są opublikowane na podstawie oryginałów dostarczonych przez Autorów, zaopiniowanych przez Zespół Recenzentów.

**Wydano za zgodą:**

Kierownika Katedry Materiałów Inżynierskich i Biomedycznych

Wydziału Mechanicznego Technologicznego

Politechniki Śląskiej

**Wydawca:**

Katedra Materiałów Inżynierskich i Biomedycznych

Wydział Mechaniczny Technologiczny

Politechnika Śląska

Gliwice 2024

Wszystkie opublikowane materiały stanowią utwór podlegający ochronie na mocy prawa autorskiego. Utwór ten w całości ani we fragmentach nie może być powielany ani rozpowszechniany za pomocą urządzeń elektronicznych, mechanicznych, kopiujących, nagrywających i innych. Ponadto utwór ten nie może być umieszczany ani rozpowszechniany w postaci cyfrowej zarówno w Internecie, jak i w sieciach lokalnych, bez pisemnej zgody posiadacza praw autorskich.

**Seria wydawnicza:**

Prace Katedry Materiałów Inżynierskich i Biomedycznych

Wydział Mechaniczny technologiczny

Politechnika Śląska

Publikacja: czerwiec 2024

ISBN 978-83-65138-41-5



**INTERNATIONAL STUDENTS SCIENTIFIC CONFERENCE**  
**TALENTDETECTOR2024\_SUMMER**  
**SILESIA UNIVERSITY OF TECHNOLOGY, GLIWICE, POLAND**  
**17<sup>TH</sup>-19<sup>TH</sup> JUNE 2024**

The International Student Scientific Conference TalentDetector2024\_Summer aims to integrate the student and scientific community dealing with topics related to material technologies. It is a place that gives the opportunity to exchange experiences, knowledge, skills and present current scientific achievements, developing and expanding students' interests in the field of materials engineering, surface engineering, biomaterials and biomedical engineering, nanotechnology, pro-ecological technologies and computer materials science. The conference allows for the presentation of projects conducted with the industry as part of the activities of Student Scientific Circles, doctorates, projects implemented in the form of PBL - Project Based Learning as part of the Excellence Initiative - Research University at the Silesian University of Technology, projects in the framework of EURECA PRO/European University in Responsible Consumption and Production and international bilateral cooperation between Universities.

**CONFERENCE ORGANIZER**

Materials Science Circle of the Association of Alumni of the  
Silesian University of Technology, Gliwice, Poland



**CONFERENCE CO-ORGANIZER**

Department of Engineering Materials and Biomaterials, Faculty  
of Mechanical Engineering, Silesian University of Technology,  
Gliwice, Poland



**INTERNATIONAL SCIENTIFIC COMMITTEE**

prof. Mirosław Bonek, Silesian University of Technology, Gliwice, Poland - *President of the International Scientific Committee*

prof. Marcin Adamiak, Silesian University of Technology, Gliwice, Poland  
prof. Sedat Alkoy, Gebze Technical University, Gebze, Turkey  
prof. Rafał Babilas, Silesian University of Technology, Gliwice, Poland  
prof. Ahmet Durgutlu, Gazi University, Ankara, Turkey  
prof. Boris Gitolendia, Georgian Technical University, Tbilisi, Georgia  
prof. Afrim Gjellaj, University of Pristina, Pristina, Kosovo  
prof. Adam Grajcar, Silesian University of Technology, Gliwice, Poland  
prof. Alexander Horn, Laserinstitut Hochschule Mittweida, Mittweida, Germany  
prof. Volkan Kılıçlı, Gazi University, Ankara, Turkey  
doc. Lenka Kuchariková, University of Zilina, Zilina, Slovakia  
prof. Martin Kusy, Slovak Technical University in Bratislava, Trnava, Slovakia  
prof. Grzegorz Matula, Silesian University of Technology, Gliwice, Poland  
prof. Janusz Mazurkiewicz, Silesian University of Technology, Gliwice, Poland  
prof. Serhii Matiukh, Khmelnytskyi National University, Khmelnytskyi, Ukraine  
prof. Cemal Meran, Pamukkale University, Denizli, Turkey  
prof. Oleh Polishchuk, Khmelnytskyi National University, Khmelnytskyi, Ukraine  
prof. Mykola Skyba, Khmelnytskyi National University, Khmelnytskyi, Ukraine  
prof. Tomasz Tański, Silesian University of Technology, Gliwice, Poland  
doc. Miroslava Tavodova, Technical University in Zvolen, Zvolen, Slovakia  
prof. Eva Tillova, University of Zilina, Zilina, Slovakia

**ORGANIZING COMMITTEE***Chairman*

prof. Mirosław Bonek

prof. Klaudiusz Gołombek	dr. Anna Kloc-Ptaszna
prof. Sabina Lesz	dr. Mariusz Król
prof. Janusz Mazurkiewicz	dr. Beata Krupińska
prof. Małgorzata Musztyfaga-Staszuk	dr. Agnieszka J. Nowak
prof. Daniel Pakuła	dr. Magdalena Polok-Rubiniec
prof. Marek Sroka	dr. Weronika Smok
prof. Marcin Staszuk	dr. Magdalena Szindler
prof. Agata Śliwa	dr. Marek Szindler
prof. Tomasz Tański	dr. Anna Włodarczyk-Fligier
prof. Adam Zarychta	dr. Anna Woźniak
dr. Aleksandra Drygała	Ksenia Czardyban MSc
dr. Rafał Honysz	Amadeusz Dziwis MSc
dr. Aneta Kania	Wojciech Mikołajko MSc
dr. Monika Kciuk	Sichale Worku Fita MSc
dr. Marek Kremzer	Marta Zaborowska MSc

## **TalentDetector HISTORY**

The International Student Scientific Conferences TalentDetector from 9 edition (since 2018) have been a place for the exchange of experience, knowledge, skills and presentation of students' current scientific achievements in the field of materials engineering, surface engineering, biomaterials and biomedical engineering since the 8th edition. As part of the conference, two international scientific monographs, TalentDetector\_Summer and TalentDetector\_Winter, are published annually, which already contain over 500 scientific articles resulting from the implementation of PBL, EURECA PRO, Students Scientific Cycles projects and projects with secondary school students with international authors. Participation in the form of presentations and posters in TalentDetector International Student Scientific Conferences allows members of the project teams to integrate the student and scientific community of the Silesian University of Technology as well as young staff from foreign research centres in Austria, the Czech Republic, Ethiopia, Ghana, Georgia, Iran, Slovakia, Ukraine and Turkey, dealing with topics related to materials technologies.

Scientific monographs are prepared based on articles, mostly with international authors, reviewed by an international scientific committee.

The initiative of the cyclical organization of the International Student Scientific Conference TalentDetector significantly expands activities in the field of student education, organizational and popularization activities for the scientific community related to materials engineering at the national and international level.

Thanks to extensive international cooperation, over 160 articles were published free of charge.

The history of TalentDetector in numbers:

### **2018**

TalentDetector 2019 (Gliwice)

Number of articles: 59

Number of authors: 206

Number of countries: 1

### **2021**

TalentDetector2021\_Winter (Gliwice)

Number of articles: 37

Number of authors: 134

Number of countries: 2

TalentDetector2021\_Summer (Zawiercie)

Number of articles: 57

Number of authors: 173

Number of countries: 3

**2022**

TalentDetector2022\_Winter (Gliwice)

Number of articles: 79

Number of authors: 179

Number of countries: 4

TalentDetector2022\_Summer (Wisła)

Number of articles: 79

Number of authors: 176

Number of countries: 4

**2023**

TalentDetector2023\_Winter (Gliwice)

Number of articles: 73

Number of authors: 143

Number of countries: 6

TalentDetector2023\_Summer (Brenna)

Number of articles: 105

Number of authors: 173

Number of countries: 9

**2024**

TalentDetector2024\_Winter (Gliwice)

Number of articles: 82

Number of authors: 135

Number of countries: 7

TalentDetector2024\_Winter (Gliwice-Zilina)

Number of articles: 84

Number of authors: 147

Number of countries: 8

Number of cooperating universities: **11**

Gazi University, Ankara, Turkey

Gebze Technical University, Gebze, Turkey

Georgian Technical University, Tbilisi, Georgia

Khmelnitskyi National University, Khmelnytskyi, Ukraine

Laserinstitut Hochschule Mittweida, Mittweida, Germany

Pamukkale University, Denizli, Turkey

Silesian University of Technology, Gliwice, Poland

Slovak Technical University in Bratislava, Trnava, Slovakia

Technical University in Zvolen, Zvolen, Slovakia

University of Pristina, Pristina, Kosovo

University of Zilina, Zilina, Slovakia

Activity supported by  
**International Visegrad Fund's**  
**V4 Generation Mobility Mini-Grant No 12410044**

The project has access to the possibility for participants to use the analysis of available literature and the results of innovative material testing in order to apply technological parameters, including laser treatments of functional elements in ecological technologies. The aim of the scientific project is the impact of the use of a laser in the operation of laser thermal power and melting of the surface layers of metal materials on the structure and substances on the surface. Scientific research undertaken to optimize laser technological conditions in order to provide a fine-grained structure of the surface layers, ensuring a specialized increase in the operational level of the surface. The aim of the project is to strengthen cooperation between young people who want to develop scientifically. The activities will involve encouraging contact with authorities who share their life experiences. Maintaining and constantly deepening bonds of friendship, cultivating the tradition of self-education and the principles of professional ethics at the international level.

Organizer:

**Association of Alumni of the Silesian University of Technology, Gliwice, Poland.** Cooperation on a Master & Apprentice basis. Encouraging contact with Authorities who share their life experiences. Maintaining and constantly deepening the bond of friendship, cultivating the tradition of the profession and the principles of professional ethics at the international level (Poland, Slovakia). Organizing self-education assistance for youth and university graduates. Development of various forms of care for the youngest pupils and students starting their professional careers. Action to increase the prestige and importance of the idea of lifelong learning. Organization of the TalentDetector International Scientific Seminar twice a year (talentdetector.polsl.pl), which is a place for the exchange of experience, knowledge, skills and presentation of the current scientific achievements of students and graduates in the field of materials engineering and surface engineering.

Partner:

**University of Žilina, Department of Materials Science and Engineering, Zilina, Slovakia** completed the comprehensive accreditation process, which included the restructuring of activities. A series of seminars was planned based on interdisciplinary teams with the strong involvement of foreign scientists and external university institutions, as well as establishing procedures for expanding activities in cooperation with the Interdepartmental Research Center. The main emphasis will be on promoting modern methods of teaching materials and technologies among pupils and students. The University of Žilina actively participates in various coordination activities of new European technology platforms. The University of Žilina has scientific staff, experience and laboratories that fully justify its choice as a place for joint seminars.

**Direct target groups:**

Participants: 15 people from Slovakia and 15 people from Poland (high school students, university students, PhD students - age 17-26) and 6 international supervisors from Poland and Slovakia (professors and PhD):. 30

**Event 1**

**TalentDetector Seminary Zilina, 5<sup>th</sup>-7<sup>th</sup> June 2024, Zilina, Slovakia**

Visit to the University of Zilina, Department of Materials Science and Engineering, (several faculties of the University, the area of the city of Zilina, Rajecské Teplice) - Groups of several participants will

participate in 3-day workshops at the University and the surrounding area - visits to historical places and meetings with regional history experts.

The project has access to the possibility for participants to use the analysis of available literature and the results of innovative material testing in order to apply technological parameters, including laser treatments of functional elements in ecological technologies.

Participants will be divided into 6-person international teams. The partner has unique research equipment allowing to determine the mechanisms of material consumption and scientific staff guaranteeing a high level of the seminar. During the visit, the students will gain knowledge enabling them to explain the structural mechanism of improving the properties of the surface layer by increasing the hardness and resistance to abrasion and tribocorrosion using modern lasers in the laser surface treatment process. Classes will be held in laboratories, lecture halls and production companies related to the Zilina region. The meetings will be held in accordance with the approved program consisting of meetings at the University, shared meals, sightseeing around Zilina and meetings with people who cherish the history of the region and materials engineering graduates.

## Event 2

### **TalentDetector2024\_Summer, 17<sup>th</sup>-19<sup>th</sup> June 2024, Gliwice, Poland**

The International Seminary TalentDetector2024\_Summer – 3-day meeting at a laboratories, science centres and in hotel in Gliwice. Presentations of common interests, knowledge competitions, integration meetings, learning about the history of Poland and Slovakia on expeditions around the old city. Discussion on social and cross-border issues with invited international guests. The seminar will include lectures and discussion panels with scientific authorities. Participants will be able to present their scientific and social projects at the oral and poster sessions. There will be an integration meeting devoted to the history of the regions the participants come from and a joint miner feast. During the afternoon classes, there will be a visit to nearby attractions such as the silver mine in Tarnowskie Góry and the museum of history of industry on Silesian region. Materials from the seminar in the form of concise studies by individual teams will be published in a monograph (each participant will receive a book with a monograph) and transferred to the publicly available library system. During the seminar, proposals for further cooperation within the established teams will be prepared and forms of broad promotion of international Visegrad Fund projects among candidates, students and graduates of fields related to materials engineering will be developed. Information about the tasks carried out in the project will be disseminated by youth and accompanying persons via social media and at seminars organized online.

[www.talentedetector.polsl.pl](http://www.talentedetector.polsl.pl)

The project is co-financed by the Governments of Czechia, Hungary, Poland and Slovakia through Visegrad Grants from the International Visegrad Fund. The mission of the fund is to advance ideas for sustainable regional cooperation in Central Europe.





## INTERNATIONAL STUDENTS SCIENTIFIC CONFERENCE

### Contents

Analytical Modelling of the Effects of Etchant Concentration on Adhesion Energy and Contact Length Between FTO and Glass Substrates Addae Elizabeth Adzo, Wojciech Sitek, Marek Szindler .....	1
Influence of LST (Laser Surface Texturing) on the Microstructure and Hardness of Magnesium RZ5 Alloy John Ampah-Essel, Augustine N.S Appiah, Oktawian Bialas, Beatrice N.A. Ardayfio, Marcin Adamiak .....	8
Influence of CWJ (Continuous Water Jet) Pressure on the Surface Structure of Peened SLM AISi10Mg Alloy Beatrice N.A Ardayfio, Augustine N.S Appiah, Przemysław Snopiński, Anna Woźniak, John Ampah-Essel, Benjamin Agyei-Tuffour .....	16
Laser welding Jennifer Badora, Justyna Janoszka, Julia Muszyńska, Magdalena Szindler, Mirosław Bonek .....	22
Literature Review on Additive Manufacturing Drilon Beqiri, Afrim Gjellaj, Vladimir Dukovski, Bejtë Çela .....	27
Effect of niobium content on corrosion resistance and hardness of CoCrFeNiNb <sub>x</sub> high entropy alloys Jakub Bicz, Wojciech Łoński, Katarzyna Młynarek-Żak, Rafał Babilas .....	41
Degradation of thermoplastic based composite materials reinforced with natural particals Konrad Bogdał, Agnieszka J. Nowak.....	50
Thrust stand for measuring static thrust of brushless electric motors Wojciech Cofalik, Patryk Mondry, Dariusz Myszor .....	59
Laser technology in the production of silicon solar cells (part II) Aleksandra Drygała, Jakub Budzynowski, Kamil Dziendzioł, Adrian Marusiński, Mateusz Magiera, Małgorzata Muszyfaga-Staszuk, Marcin Staszuk .....	67

---

Characterization of dye-sensitized solar cells Judyta Drygała, Bartosz Drygała, Janusz Wyrwał, Sabina Lesz, Aleksandra Drygała .....	75
Plant-based synthesis of SnO <sub>2</sub> nanoparticles using aqueous extract from <i>Aglaonema commutatum</i> leaves Alicja Duda, Bartosz Kopyciński, Krzysztof Pęczak .....	82
Symulator samolotu Cessna 172 bazujący na platformie ruchu Anna Dyrda, Karolina Kempa, Paweł Ledwoń, Alan Pawleta, Bartosz Pokorski, Nikodem Wspaniały, Wojciech Cofalik, Patryk Mondry, Kacper Matys .....	89
Computer simulation of the strength properties of a hammer with a metal and wooden head made using FEM Aleksander R. Dziwis, Pascal Bzdon, Wojciech Mikołajko, Agata Śliwa, Marek Sroka .....	97
Comparison of the impact of the laser beam in various industrial processes using the finite element method Amadeusz Dziwis, Bartłomiej Józwiak, Nikodem Juszczyk, Stanisław Kiełkowski, Mirosław Bonek .....	104
Computer analysis of the transmission cushion of a passenger car Amadeusz Dziwis, Wojciech Mikołajko, Mirosław Bonek, Agata Śliwa, Eva Tillova .....	112
Application of 3D printing in medicine Aleksandra Dzwonek, Karolina Malon, Maja Święcicka, Magdalena Szindler, Mirosław Bonek .....	118
Analysis of Group Technology and surface roughness for cutting processes Arlinda Elezi, Afrim Gjelaj, Besart Berisha .....	126
Supporting 3D Printing with 3D scanners Miłosz Ferdyn, Michał Podgórski, Max Żukowski, Magdalena Szindler, Mirosław Bonek .....	133
Optimization of a selected production process using the DOE method Katarzyna Furman, Dominik Towarnicki, Ewa Jonda .....	138
Analysis of management systems frequently used in the automotive industry Katarzyna Furman, Dominik Towarnicki, Hubert Przybyszewski .....	147
Observations of the microstructure of sintered gradient materials using various microscopic methods Aleksandra Gałęska, Emilia Młócek, Oleksandra Nikolaieva, Anna Kloc-Ptaszna, Daniel Pakuła, Konrad Adamczyk, Marcin Staszuk .....	153



---

Kompozyty polimerowe modyfikowane nanorurkami haloizytowymi Michał Głogowski, Julia Pindur, Karolina Romberg, Klaudiusz Gołombek, Mateusz Lis.....	161
The properties of glass fiber polymer composites Magdalena Gorlicka, Magdalena Polok-Rubiniec .....	167
Comparison of the structure of PVD+ALD hybrid coatings applied to austenitic stainless steel Karolina Grzesikiewicz, Lena Trzewiczek, Agata Zarzycka, Marcin Staszuk, Daniel Pakuła .....	171
Korózia horčíka a jeho zliatin Ľuboš Halimovič, Milan Uhrčík, Mirosław Bonek.....	177
Long-Term Effects of Autonomous Vehicles Mohammed Hesham, Givi Sanadze .....	183
Konštrukčný návrh kempingovej platformy na spanie do kufra osobného automobilu Edita Illichmanová, Lenka Kuchariková, Mirosław Bonek.....	187
Project of the personalized knee joint orthosis intended for manufacturing using additive technologies Jakub Jabłoński, Agnieszka J. Nowak .....	194
Wpływ obróbki plastycznej na mikrostrukturę i własności stopu Cu-Cr Marcin Jaroszek, Beata Krupińska.....	206
Corrosion behaviour of passivated 304 stainless steel Justyna Jaworska, Monika Kciuk .....	213
Unconventional applications of additive technologies Alicja Kłapsia, Emilia Krajewska, Jakub Kuta, Magdalena Szindler, Mirosław Bonek .....	218
Selected properties of perlite concrete also with waste lightweight aggregate Nicole Kocierz, Barbara Słomka-Słupik .....	226
Flammability behavior of UV-curable varnishes for protection of wood-based substrates Bartosz Kopyciński, Sebastian Jurczyk, Izabela Gajlewicz, Alicja Duda, Ewa Langer .....	234
Steel hardness Mateusz Kozłowski, Maja Kubacka, Julia Popis, Sabina Lesz .....	242

---

Design of wrist orthosis made by 3d printing technique using reverse engineering methods Mariusz Król, Szymon Jędrzejewski, Daniel Tatar, Adam Woszczak, Branislav Hadzima .....	250
Proecological aspects of laser cutting of metals and their alloys Mateusz Król, Jakub Kukuczka, Anna Woźniak, Mirosław Bonek, Wojciech Pakieła.....	256
Analysis of the possibilities of using BMS technology in network analysis – on the example of the Nazca environment Kacper Krysiak, Bartosz Nikiel, Kamil Oleksy, Szymon Szeja, Mirosław Bonek .....	261
Stal nierdzewna do zastosowań w sztukach Natalia Łonczek, Agata Majnusz, Miłosz Kuźniak, Barbara Grzegorzczak.....	270
The microstructure and properties of the nitrided layer with a compound zone after laser modification Anna Mękarska, Karolina Rogalewska .....	278
Deburring Tool Design for Copper Wire Drawing Cemal Meran, Cihan Atik, Batuhan Gölcük, Atike Oskay, Orhan Akyuz, Gizem Ordu .....	287
Investigation of Changes in Mechanical Properties of Nickel Plated Copper Wires at Drawing Stages Cemal Meran, Recep Tufan Celik, Emre Guzel, Arda Sengul, Orhan Akyuz, Ismail Kiyici .....	292
Investigation of the Effect of Silicon Dioxide Nanoparticle on Carbon and Basalt Composites Cemal Meran, Batuhan Şenkaya .....	299
Aplikácia DLC povlakov na valivé ložiská Matúš Murín, Martin Vicen, Mirosław Bonek .....	307
Identification and assessment of the employee's mental load at a selected production workplace Klaudia Niedziela, Monika Spilka .....	316
Microprocessor color recognition and replication system Bartosz Nikiel, Mirosław Bonek .....	320
The resistance to abrasive wear of internal oesophagus prosthesis Agnieszka J. Nowak .....	326

---

Polymer composite materials Anna Nowak, Anna Włodarczyk-Fligier .....	334
The impact of cerium oxide nanoparticle addition on the morphology of electrospun PVP nanofibers used in the medical industry Antonina Olszewska, Wiktoria Wanczura, Wiktor Matysiak .....	338
Modern 3D Printing Technologies in Space Industry Emil Pająk, Błażej Tomiczek .....	347
Schlieren Optics: Unveiling the Invisible Emil Pająk, Alicja Jankiewicz, Błażej Tomiczek .....	355
3D Printing Applications in Manufacturing Patryk Pająk, Mateusz Zapiór, Michał Ledwoń, Magdalena Szindler, Mirosław Bonek ...	363
Analysis of the structure and thickness of the nitrided layer in 1.2343 steel depending on the furnace used for thermochemical treatment Mateusz Paluch, Szymon Jędrzejewski, Janusz Mazurkiewicz .....	368
Influence of sintering time on the composition and properties of sinters obtained from elemental powder mixture of refractory metals Krzysztof Pęczak, Piotr Tomczyk, Alicja Duda, Monika Czerny .....	376
Using laser and 3D printing in fashion Michał Pietruszka, Olaf Sobek, Magdalena Szindler, Mirosław Bonek .....	383
Computer simulation of hip joint loading Jakub Polis, Jakub Bicz, Zuzanna Buchaj, Rafał Szymik, Zuzanna Zielińska, Mateusz Szojda, Agata Śliwa, Marek Sroka, Amadeusz Dziwis, Wojciech Mikołajko .....	389
Computer simulation of crankshaft loading Jakub Polis, Jakub Bicz, Agata Śliwa .....	496
Computer simulation of gear wheel loading Jakub Polis, Jakub Bicz, Agata Śliwa .....	403
Brain-Computer-Interface Numeric Keyboard Designs Maja Rudnicka, Michał Lasak, Igor Puchała, Piotr Bartosz, Dominik Bereta, Dariusz Myszor .....	410
Wireless communication between a flight simulation and its controllers Maja Rudnicka, Michał Lasak, Igor Puchała, Piotr Bartosz, Dominik Bereta, Dariusz Myszor, Maria Ochman, Jakub Wieczorek .....	417

---

Sample collection and containment system for a compact planetary exploration rover Maja Rudnicka, Michał Lasak, Igor Puchała, Piotr Bartosz, Dominik Bereta, Dariusz Myszor .....	423
Advanced Surface Engineering and characterization Techniques for Enhancing and Understanding Charge Injection Processes in Metal/Organic Interfaces of Optoelectronic Devices Sakineh Akbari Nia, Mirosław Bonek .....	431
The micro-laser texturing process of stainless steel Jan Sędkak, Jakub Gawek, Wojciech Pakieła, Mirosław Bonek, Anna Woźniak.....	439
Wykorzystanie termowizji w kontroli przebiegu laserowej obróbki powierzchniowej Tymoteusz Setnik, Jan Płocica, Mirosław Bonek .....	445
Computer simulation of the mechanical properties of the piston of a passenger car internal combustion engine Agata Śliwa, Martin Kusy .....	450
Thin films of PNDI(2HD)2T conductive polymer for use in photovoltaics Michał Śladek, Patryk Radek, Jarosław Tłołka, Magdalena Monika Szindler, Marek Szindler, Grzegorz Nowak.....	459
Description of the process of preparing ceramic bas-reliefs cast from slips using 3D scanning and printing and making plaster molds Barbara Słomka-Słupik, Marek Kremzer, Wojciech Zieliński, Julia Franosz, Anna Słupik, Władysława Buriak, Daniel Kostyra .....	463
Analysis of corrosion changes in geopolymer binders. Carbonation Barbara Słomka-Słupik, Paulina Wiśniewska .....	469
Deep Convolutional GAN for realistic sky image generation Katarzyna Słowiak, Dariusz Myszor.....	475
Interactive diagram of transformations of subcooled austenite Tomasz Sokoła, Łukasz Soja, Marek Romanowski, Rafał Honysz .....	482
Enhancing Osteointegration of Dental and Orthopedic Implants Through Advanced Surface Engineering Techniques Maryam Soleimani .....	487
Process mapping on a selected example Magdalena Stanik, Aneta Kania .....	494

---

Methodology for EEG signal comparison in virtual and real-life flight scenarios Michał Sujkowski, Dariusz Myszor, Piotr Bartosz, Jakub Sarno, Wojciech Cofalik, Patryk Mondry .....	498
Development of an active vibration protection system Tornike Tetunashvili, Amkoladze Khatuni, Givi Sanadze .....	503
Optimization of the electrospinning process of PVP nanofibers used in the production of dressings Wiktoria Wanczura, Antonina Olszewska, Wiktor Matysiak .....	507
Corrosion mapping with the use of ultrasonic testing Edyta Wójtowicz, Santina Topolska, Andrzej Wójtowicz .....	515
Modelling and Simulation of gyroid structure-based bone scaffold using TiZrNb titanium alloy for bone scaffold; state-of-the-art and evaluation of deformation Sichale Worku Fita, Mirosław Bonek, Sebastian Sławski, Anna Woźniak .....	522
Strategic Site Selection for the Expansion of the University of Prishtina's Faculty of Mechanical Engineering laboratory: Developing a Production Center for Research and Education Samet Xhemajli, Besart Berisha, Afrim Gjellaj .....	530
UWB objects positioning system with the ability to change the ranging method dynamically Tomasz Zawadzki, Krzysztof Paszek .....	537
Laser technology in the production of silicon solar cells (part I) Dominik Żebrowski, Olaf Humeniuk, Mikołaj Guzek, Małgorzata Muszyfaga-Staszuk, Aleksandra Drygała, Krzysztof Wiśniewski, Marcin Staszuk .....	543
Leveraging the CARLA Simulator for Realistic Image Generation to Train and Evaluate AI Methods for Autonomous Vehicles Michał Zieliński, Dariusz Myszor, Marcin Paszkuta, Tomasz Kukuczka, Eryk Szmyt, Daniel Sobieraj, Kacper Matys, Michał Wieczorek, Paweł Michalski, Krzysztof Pawełczyk, Michał Polończyk .....	551
Development of LMD surfacing technology and evaluation of the properties of surface layers produced on components of oil and gas extraction tools Julia Żuławska, Michał Wnętrzak, Mateusz Dziergas, Bartosz Siedlaczek, Artur Czupryński .....	558
Modeling of a screw extruder 3D printer Oleh Polishchuk, Andrii Polishchuk, Volodymyr Misiats, Svitlana Lisevych, Mirosław Bonek .....	567



17th-19th June 2024  
Gliwice, Poland

DEPARTMENT OF ENGINEERING MATERIALS AND BIOMATERIALS  
FACULTY OF MECHANICAL ENGINEERING  
SILESIA UNIVERSITY OF TECHNOLOGY

## INTERNATIONAL STUDENTS SCIENTIFIC CONFERENCE

### **Analytical Modelling of the Effects of Etchant Concentration on Adhesion Energy and Contact Length Between FTO and Glass Substrates**

Addae Elizabeth Adzo<sup>a</sup>, Wojciech Sitek<sup>b</sup>, Marek Szindler<sup>c</sup>

<sup>a</sup> Silesian University of Technology, Faculty of Mechanical Engineering, Scientific and Didactic Laboratory of Nanotechnology and Material Technologies, email: eaddae@polsl.pl

<sup>b</sup> Silesian University of Technology, Faculty of Mechanical Engineering, Scientific and Didactic Laboratory of Nanotechnology and Material Technologies, email: Wojciech.Sitek@polsl.pl

<sup>c</sup> Silesian University of Technology, Faculty of Mechanical Engineering, Scientific and Didactic Laboratory of Nanotechnology and Material Technologies, email: Marek.Szindler@polsl.pl

**Abstract:** Electrically conducting substances with a comparatively limited capacity for light absorption are known as transparent conducting oxides, (TCOs). These materials are primarily used in opto-electronic devices and are more frequently manufactured using thin film processes. FTO was the preferred TCO in this work, after depositing it onto a glass substrate at (~ 3000 rpm for 15-30 seconds) the etchant concentration and time and other conditions for fabrication were used to make an analytical modeling. The highest adhesion energy obtained was  $2.5 \times 10^{-13} \text{ J/m}^2$  -  $2.7 \times 10^{-13} \text{ J/m}^2$  using an etchant concentration of  $\text{FeCl}_3$  (~1 M) and  $\text{HCl}$  (~1 M). It was also obtained that the allowable particle size between the FTO layer and glass substrate was  $0.04 \times 10^{-13} \text{ m}$  –  $0.07 \times 10^{-13} \text{ m}$ . The stronger the concentration of the etchant, the more particles would be removed which can inherently affect the adhesion.

**Keywords:** Etchant concentration, Fluorine Doped Tin Oxide, Adhesion energy, Contact length

## 1. INTRODUCTION

Before the invention of Transparent Conducting Oxides (TCOs), silicon was heavily used as a semiconductor in integrated circuit and device fabrication. Apart from silicon being expensive it is only applicable in the visible region; it reflects about one third of light that can be converted in solar cells to electricity. It is difficult to integrate it with other semiconductors in devices and needs to be doped before it can be used to perform its desired purpose. All these defects and disadvantages made device fabrication difficult and expensive to acquire[1].

Transparent conducting oxides (TCOs) are electrically conducting materials that possess a relatively low ability to absorb light. These materials are more often prepared with thin film

technologies and mostly applied in opto-electronic devices. Their conductivity can be manipulated from insulating through to conducting as well as their transparency. TCOs are semiconductor compound where the non-metallic part is made of oxygen. TCOs are electrically conducting materials with relatively low absorption of light ability. They are used in opto-electrical devices. Examples of these materials are doped ZnO, SnO<sub>2</sub> and In<sub>2</sub>O<sub>3</sub> and are very resourceful in the transparent electrodes in optoelectronic applications. Optoelectronics is the research and implementation of electronic devices and systems, that detects the sources and stimulates the control of light, usually known to be a subfield of photonics [2].

In this project, the relationship between the adhesion energy, etchant concentration and size particles in the patterning of a Fluorine Doped Tin Oxide (FTO) will be investigated.

This would help to determine whether TCOs with high surface and elastic energy would need a higher concentration of etchant and a high etching time or not. In patterning of a TCO a process called etching is used to remove all forms of debris or impurity and to dissolve the surface of the substrate. Patterning of TCOs is also termed as photolithography where desired pattern is masked with a photoresist and the parts to be etched are exposed so they can dissolve after etching [3].

## 2. MATERIALS AND METHODOLOGY

Even though specific optical properties are required and crucial, additional important criteria should be met and by the method used for the deposition. Before deposition of the TCO layer, the glass substrates were submerged in acetone within an ultrasonic cleaner and sonicated for 15-20 minutes. The glass substrates were thoroughly rinsed with isopropanol to remove acetone residues. The glass substrates were placed in deionized water within the ultrasonic cleaner and sonicated for another 15-20 minutes. The rinsed glass substrates were placed in a drying oven. . A precursor solution containing Tin(IV) chloride (SnCl<sub>4</sub>), hydrofluoric acid (HF) and acetic acid stirred for 5 hours at 50<sup>0</sup>C and then forms FTO gel through sol-gel.

The glass substrate was held on a spinner chuck by vacuum and FTO is coated to uniform thickness by spin coating (~ 3000 rpm for 15-30 seconds) and the FTO thickness is set by primarily FTO viscosity, secondarily spinner rotational speed. The FTO thickness is given by equation 3 as:

$$t = \frac{kp^2}{w^{1/2}} \quad (1)$$

where k is the spinner constant, typically 80 -100– p is the Resist solids content in percent (%) and w is the spinner rotational speed in rpm/1000.

The samples are then dried in an oxygen rich oven at 400<sup>0</sup>C for 30 minutes.

Since FTO does not react with acid, its etching is not possible by an acid. Therefore, a unique method was used to etch FTO in which Zn powder is spread on FTO then concentrated HCl is added. Zn reduces H<sup>+</sup> to H atom that penetrates into FTO network and reduces Sn<sup>4+</sup> to metallic Sn [4,5]. This reduction of Sn<sup>4+</sup> slowly breaks down FTO structure, which eventually causes the detachment of the FTO layer from the glass substrate [6]. Since H atom can penetrate reduced Sn, there is no control of etching unless all the Zn is used up or substrate is taken out from the etching bath [7]. Thus, the etching of masked area is frequently observed, which produces undercut or side etching. To overcome this problem, FeCl<sub>3</sub> (~1 M) is used as a penetration controlling and oxidizing agent with Zn and HCl Zn reduces Fe<sup>3+</sup> to Fe<sup>2+</sup> along with H<sup>+</sup> ions, and these Fe<sup>2+</sup> ions are involved in producing the shiny film of Sn on the FTO that acts as barrier to

further reduction. Moreover,  $Fe^{3+}$  ions can dissolve metallic Sn. Thus,  $FeCl_3$  along with Zn and HCl is used to fine line the etching process [8].

## RESULTS AND DISCUSSION

### Analytical modelling

Using the thickness of the FTO layer obtained, annealing temperature, etching concentrations and environmental conditions analytical models were done to investigate the adhesion energy and contact length between the FTO layer and the glass substrate to understand how effective the layer deposition is at a microscopic level.

#### Adhesion

Adhesion energy is the attractive energy between two unlike molecules. They are caused by forces acting between two materials, that is mechanical forces (sticking together) and electrostatic forces (attraction due to opposite charges) [9].

The relation between the contact profile and adhesion energy can be represented by:

$$\gamma = \frac{2Et^2h^2}{3(1-\nu^2)a^4} \quad (2)$$

E= Young's modulus

V=Poisson ratio

t=thickness

h=height of the blister under the beam

Adhesion energies are required in modelling of the role of adhesion during contact between two surfaces. In a recent study the relation between stiff materials such as glass and other interlayers of the devices are represented using the Derjaguin, Muller and Toporov (DMT) model. It gives

$$\gamma_{DMT} = -\frac{F_{adhesion}}{2\pi R} \quad \gamma_{JKR} = \frac{2F_{adhesion}}{3\pi R} \quad (3)$$

$F_{adhesion}$  is the adhesion force and R is the effective contact radius, which is given by

$$R = \left( \frac{1}{R_{tip}} + \frac{1}{R_{rms}} \right) \quad (4)$$

Where  $R_{tip}$  and  $R_{rms}$  are radius of the atomic force microscopy (AFM) tip and root mean square roughness of the substrate.

$$U_e = \frac{6EIH^2}{5^3} \quad (5)$$

E= young's modulus

I= second moment area of the beam

h =height of the dust particle

$U_s$  = surface energy due to adhesion at the region where there is a contact given by

$$U_s = -\gamma A_c \quad (6)$$

$A_c$  =contact

$\gamma$  = adhesion energy



$A_c$  is given by

$$\begin{aligned} A_c &= W \times L_c \\ &= W \times (L-s) \end{aligned} \quad (7)$$

$L_c$  =contact length

$$U_s = - \gamma w(L-s) \quad (8)$$

The total energy of the system is the sum of  $U_e$  and  $U_s$

$$U_T = \frac{6EIh^2}{s^3} - \gamma w(L-s) \quad (9)$$

The total energy will be least (minimum) at an equilibrium value of  $s$ . Therefore, by differentiating.

$$\frac{dU_T}{ds} = \frac{18EIh^2}{s^4} + \gamma w \quad (10)$$

$\frac{dU_T}{ds} = 0$ , hence the Adhesion energy

$$\gamma = \frac{18EIh^2}{s^4 w} \quad (11)$$

where the analytical form of the second moment of area  $I$ , is given by

$$I = \frac{wt^3}{12} \quad (12)$$

In terms of the adhesion energy and the void lengths

$$\gamma = \frac{3Et^3h^2}{2s^4} \quad (13)$$

$$s^4 = \left( \frac{3Et^3h^2}{2\gamma} \right)^{1/4} \quad (14)$$

Since the length of the void is in relation to the entire beam length and the contact region of the two layers ( $L_c$ ), the nominal contact length is related by

$$s = \left( \frac{3Et^3h^2}{2\gamma} \right)^{1/4} = L - L_c \quad (15)$$

$$\text{The nominal length of the contact is } \frac{L_c}{L} = 1 - \left( \frac{3Et^3h^2}{2\gamma} \right)^{1/4} \quad (16)$$

Surface roughness often causes adhesion energy to rise. Stronger interactions between particles and surfaces result from rough surfaces because they offer more places of contact for adherence [10]. However, results from the graph shows that adhesion energy between the FTO layer and the Glass substrate decreases with the increase in the size of the particle and vice versa, meaning the smaller the size of the particle the higher the adhesion energy. For a thin layer of FTO to adhere appropriately on a glass surface after etching, the particle sizes must be between  $0.04 \times 10^{-13} \text{ m} - 0.07 \times 10^{-13} \text{ m}$  to obtain adhesion range from  $2.5 \times 10^{-13} \text{ J/m}^2 - 2.7 \times 10^{-13} \text{ J/m}^2$ . These values correspond with literature where the average allowable particle size in a thin film is 0.1 to 0.6  $\mu\text{m}$  with a median diameter [11]. Therefore, from these findings it can be concluded that there is a limit to the theory that roughness of a surface increases adhesion energy. In this case  $\text{FeCl}_3$  ( $\sim 1 \text{ M}$ ) and  $\text{HCl}$  ( $\sim 1 \text{ M}$ ) were able to achieve this adhesion energy values. It can also be deduced that in order to get more surface roughness the etchant concentration must be reduced and vice versa.

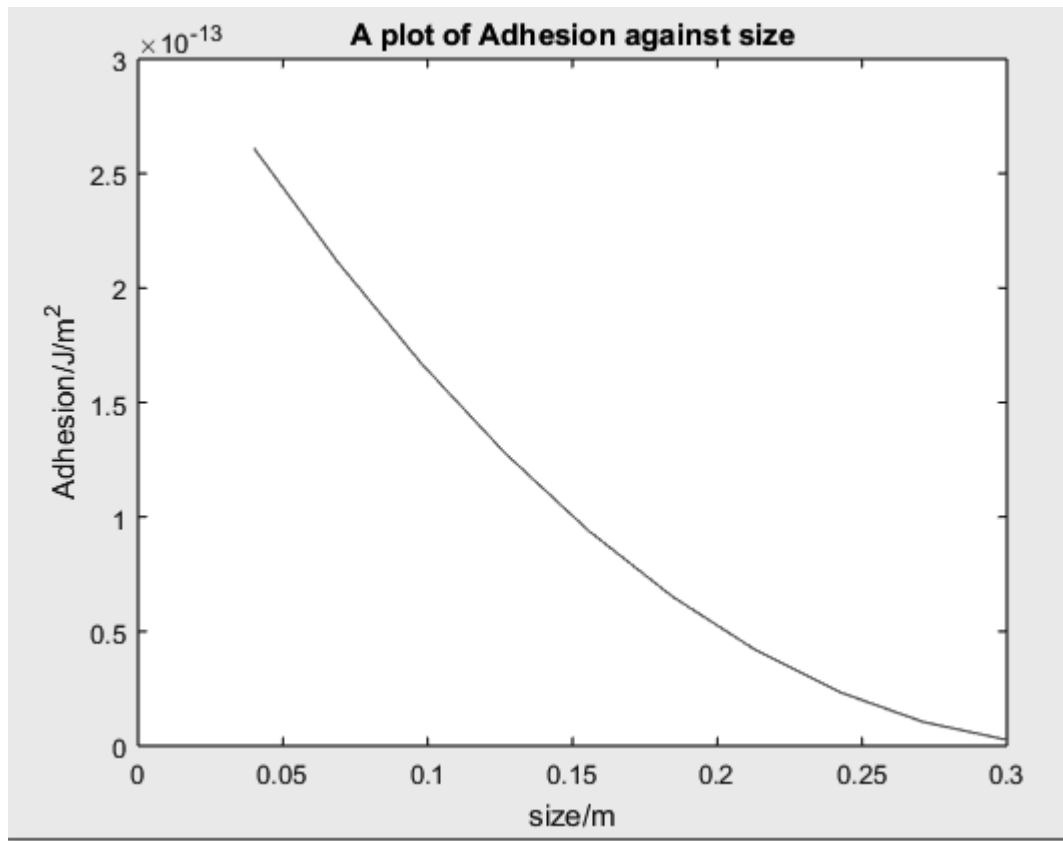


Figure 1. shows a schematic graph of the analytical modelling of the FTO on Glass plotting the adhesion energy against size of the particle.

In materials science, the contact length between particles can influence properties such as mechanical strength, electrical conductivity, and thermal conductivity of materials. The contact length is often related to the particle size and shape distribution within a material [12]. Results from the graph shows that the contact length between the FTO layer and the Glass substrate increases with the size of the particle. Between particle size ranges  $0.04\text{--}0.07 \times 10^{-13}$  m shows minimal contact length which is required for adequate adhesion between the layers. Large contact length means little to no adhesion, therefore the particles on the glass substrate must not exceed  $0.07 \times 10^{-13}$  m after etching.

### 3. CONCLUSION

This work proved the limitation to the claim that stronger interactions between particles and surfaces result from rough surfaces because they offer more places of contact for adherence. The analytical modelling proved that when particle sizes are too huge, the contact length between the FTO layer and glass substrate surface increase which can affect the adherence between the layers. This could be true for particles measured in micrometres or nanometres but not large particle sizes. Additionally, it may be inferred that decreasing the etchant concentration is necessary to increase surface roughness and vice versa.

However, it would be recommended if the etchant concentrations were varied and also analytical methods like UV-Vis analysis and X-Ray Diffractometry (XRD) analysis are done to support the Analytical Modelling results.

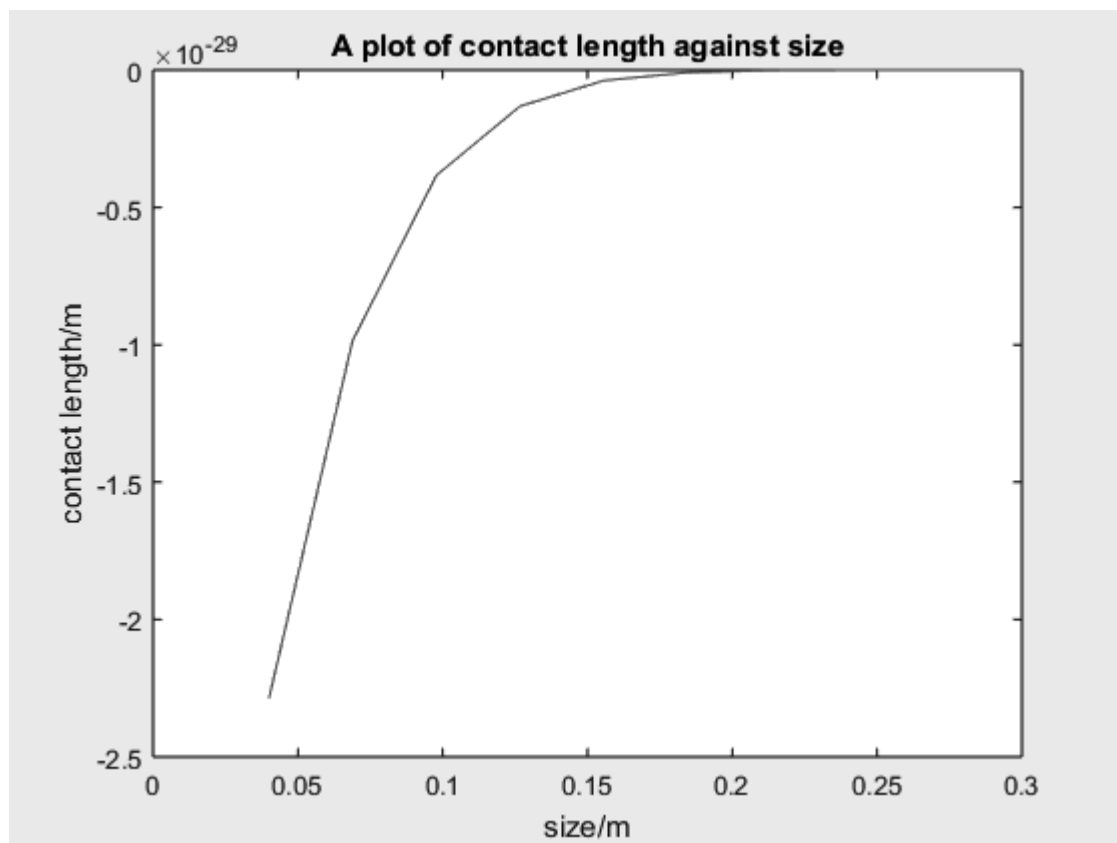


Figure 2. shows a schematic graph of the analytical modelling of the FTO on Glass plotting the contact length against size of the particle.

## BIBLIOGRAPHY

1. J. Brittan and C. Ferekides, Appl. Phys. Lett. 62, 2851 (1993). Google Scholar Scitation
2. S. K. Das and G. C. Morris, J. Appl. Phys. 73, 782 (1992). Google Scholar Scitation
3. J. Watson, K. Ikohura, and G. S. V. Coles, Meas. Sci. Technol. 4, 711 (1993). Google Scholar Crossref
4. D. J. Yoo, J. Tamaki, S. J. Pank, N. Miura, and N. Yamazoe, J. Mater. Sci. Lett. 14, 1391 (1995). Google Scholar Crossref
6. T. Arai J. Phys. Soc. Jpn., 15 (1960), p. 916 CrossRefView Record in Scopus
7. H. Kawazoe, M. Yasukawa, H. Hyodo, M. Kurita, H. Yanagi, H. Hosono Nature, 389 (1997), p. 939. View Record in Scopus
8. H. Yanagi, H. Kawazoe, A. Kudo, M. Yasukawa, H. Hosono J. Electroceram., 4 (2000), p. 427
9. A. Kudo, H. Yanagi, K. Ueda, H. Hosono, H. Kawazoe, Y. Yano Appl. Phys. Lett., 75 (1999), p. 285. CrossRefView Record in Scopus

10. Gao, Y., Yang, Y., & Crick, C. R. (2018). Adhesion energy between polymers and metals: Methods of measurement and influencing factors. *Progress in Organic Coatings*, 115, 93-105
11. D.S. RIMAI, D.J. QUESNEL (2002). *Adhesion Science and Engineering, Surfaces, Chemistry & Applications*.
12. Omidvar, M. N., & Hedayati, A. (2013). The effect of particle size distribution on the fracture behaviour of particulate composites. *Powder Technology*, 235, 1093-1099.



17th-19th June 2024  
Gliwice, Poland

DEPARTMENT OF ENGINEERING MATERIALS AND BIOMATERIALS  
FACULTY OF MECHANICAL ENGINEERING  
SILESIA UNIVERSITY OF TECHNOLOGY

## INTERNATIONAL STUDENTS SCIENTIFIC CONFERENCE

### **Influence of LST (Laser Surface Texturing) on the Microstructure and Hardness of Magnesium RZ5 Alloy**

John Ampah-Essel<sup>a, d</sup>, Augustine N.S Appiah<sup>b</sup>, Oktawian Bialas<sup>c</sup>, Beatrice N.A. Ardayfio<sup>a, d</sup>, Marcin Adamiak<sup>b</sup>

<sup>a</sup> Department of Materials Science and Engineering, School of Engineering Sciences, College of Basic and Applied Sciences, University of Ghana, Accra, Legon, Ghana

<sup>b</sup> Materials Research Laboratory, Faculty of Mechanical Engineering, Silesian University of Technology, 18A Konarskiego Street, 44-100 Gliwice, Poland

<sup>c</sup> Scientific and Didactic Laboratory of Nanotechnology and Material Technologies, Faculty of Mechanical Engineering, Silesian University of Technology, 18A Konarskiego Street, 44-100 Gliwice, Poland

<sup>d</sup> Faculty of Mechanical Engineering, Silesian University of Technology, 18A Konarskiego Street, 44-100 Gliwice, Poland

email: ja900646@student.polsl.pl; jeampah-essel@st.ug.edu.gh

**Abstract:** Magnesium alloys are emerging as materials of choice in high-performance applications due to their exceptional strength-to-weight ratio. This study focuses on the microstructural and mechanical properties of Magnesium RZ5 alloy, which contains zinc and rare earth elements, providing enhanced mechanical strength. We examine the alloy's microstructure and hardness before and after laser surface treatment. Laser surface treatment was performed on Mg RZ5 alloy in a wide range of parameters. Variability included both number of passes and laser texture patterns. Light optical microscopy, SEM, and hardness tests were performed to investigate the microstructure and hardness of the alloy. Results indicate significant microstructural changes and increased hardness in the heat-affected zones, particularly with multiple laser passes. These findings demonstrate the potential of LST to enhance the properties of Magnesium RZ5 alloy, making it suitable for more demanding engineering and medical applications.

**Keywords:** Magnesium RZ5, laser surface treatment, micro-texture, microstructure, hardness

## 1. INTRODUCTION

Magnesium alloys are dominant in engineering applications where strength-to-weight ratio is a critical factor in material selection. These alloys exhibit excellent damping capabilities and are non-toxic, making them suitable for medical applications. Though current research of these alloys in medical applications is limited, they are employed mostly as materials for specific components for aerospace and automobile applications. This stems from their ability to absorb

shock and vibrations, also making them suitable for cast components such as helicopter gearbox housings. Aside their low density of  $1.74 \text{ g/cm}^3$  compared to aluminium's of  $2.7 \text{ g/cm}^3$  and steel's of  $7.86 \text{ g/cm}^3$ , they also possess higher specific strength and specific stiffness with better casting properties [1][2]. However, commercially available magnesium alloys are designed to be useful in most general applications and for some specific applications, further modifications are required to enhance their desirability.

The tailoring of metallurgical characteristics of these alloys through purification, mechanical processing, and heat treatment methods can modify the microstructure and composition, thereby improving upon their mechanical characteristics and extending their usability in various high-performance applications. Surface modification has been proven to improve on the mechanical properties and corrosion resistance of magnesium alloys [3]. One of the effective methods of surface modification is laser surface texturing.

Laser surface texturing (LST) processes utilize intense thermal energy of laser beams for modification, alloying, deposition, and cladding the surface of substrate materials. LST processes proceed with advantages such as very high cooling rates, very narrow heat-affected zone (HAZ), etc. Laser surface treatment of materials is an important technique because it offers a possibility to enhance various properties such as the surface strength, hardness, roughness, coefficient of friction, chemical resistance, wear resistance, and corrosion of various materials by altering the structure of the materials [4]. The texture designs are inspired by crocodile, shark skins, fish scales, lobster, turtle shells, leading to square, circular, diamond, and hexagonal micro-texture patterns for engineering material design. The various micro-textures are displayed in **Figure 1**.

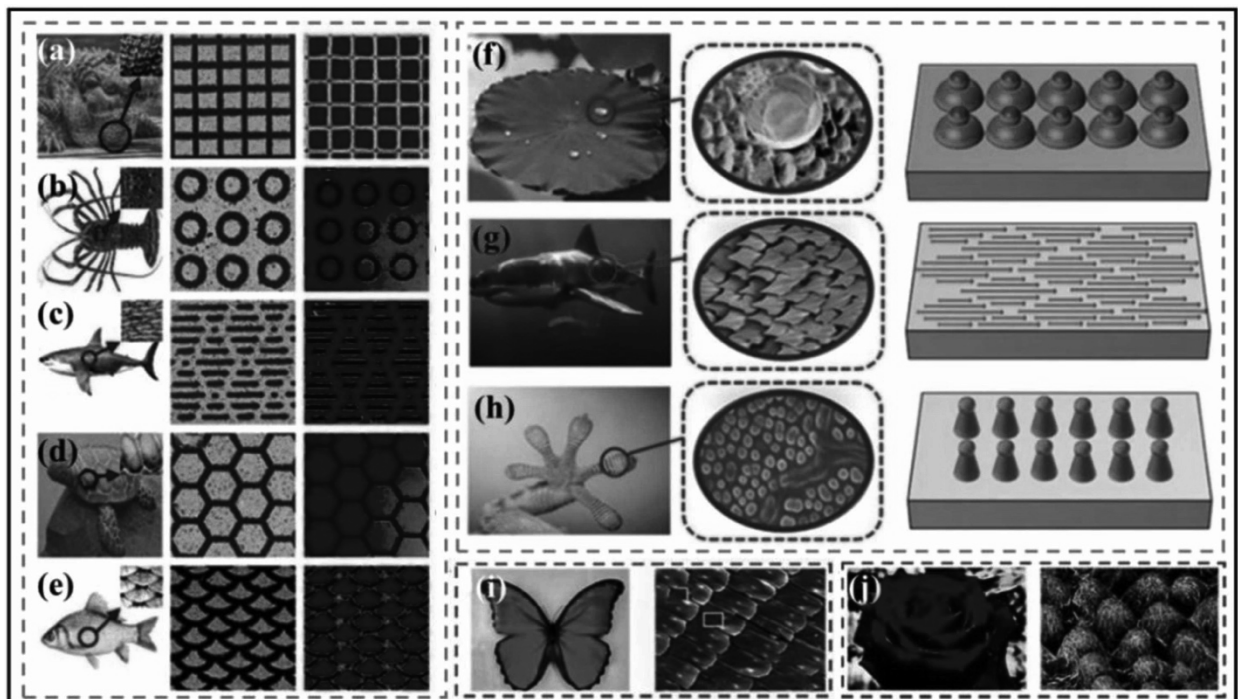


Figure 1 Biomimetic micro-textures and microstructures for laser surface treatment[5]

According to Amukarimi et al. [6], Magnesium RZ5, containing zinc and rare earth elements, offers improved mechanical properties and corrosion resistance. Despite its properties, the

possibility of improving upon its mechanical attributes using LST has yet to be explored. This study therefore aims to contribute to knowledge by investigating the evolution of microstructure and hardness properties of Magnesium RZ5 alloy after laser surface treatment to determine its suitability for various high-performance applications.

## 2. MATERIALS AND METHODS

To evaluate the microstructural and mechanical properties of Magnesium RZ5 alloy, samples sourced commercially were used, and cut with 15 mm x 15 mm x 15 mm thickness and mounted in resin for metallographic procedure. Samples were grinded using SiC paper with grit size 1200, followed by mechanical polishing following sequential order of: 9  $\mu\text{m}$ , 6  $\mu\text{m}$ , 3  $\mu\text{m}$ , 1  $\mu\text{m}$  diamond suspension, and finally 0.04  $\mu\text{m}$  colloidal silica to achieve a mirror finish. Laser surface treatment was performed using an A-355 laser micromachining system (Oxford Lasers, Didcot, UK) based on a 355 nm wavelength diode-pumped solid state picosecond laser, to induce surface textures using laser power of 21 mW at a speed of 1 mm/s. Three specimens were fabricated using two unique textures – honeycomb and square. A summary of the specimen identities and texturing conditions are summarized in **Table 1**.

Table 1. LST conditions for investigated samples.

Sample ID	Laser Texture	Number of Passes
Base	–	–
HC-SP	Honeycomb	1
HC-DP	Honeycomb	2
SQ	Square	1

Microstructural investigations were performed using optical microscopy (ZEIS, Jena, Germany) and scanning electron microscopy (SEM) using ZEIS Evo MA 15 series instrument. Hardness tests were conducted using a Vickers microhardness tester and diamond indenter with a load of ~1 Newton [N] and dwell time of 5 seconds. The average hardness was investigated for the heat-affected zone (HAZ), and melt pool after laser surface treatment, which is crucial in determining the strength and durability of the alloy.

## 3. RESULTS AND DISCUSSION

### 3.1 Microstructure

The microstructures of the alloy before and after LST are presented in **Figure 2**. The optical micrograph of the alloy prior to LST, as shown in **Figure 2(a)**, reveals that the conventional casting process produced a coarse dendritic structure with equiaxed grain morphology similar to those reported by Meher et al.[2], and Mehra et al.[7], with an estimated average grain size of approximately 122  $\mu\text{m}$ . Following the application of LST in a single pass, **Figure 2(b)** demonstrates that the laser tracks divide the surface melt pool into isolated hexagonal cells, each with an approximate surface area of  $4.53 \times 10^{-4} \text{ cm}^2$ , spaced about 18.7  $\mu\text{m}$  apart. After a second laser pass, the honeycomb structure in the HC-DP sample (**Figure 2(c)**) shows a slight reduction in cell area to approximately  $4.39 \times 10^{-4} \text{ cm}^2$ , accompanied by a marginal increase in the inter-

hexagonal spacing to approximately 19  $\mu\text{m}$ . In contrast, the square texture depicted in **Figure 2(d)** results in squared melt pool patterns with inter-square spacing of about 19.7  $\mu\text{m}$  and each square having a surface area of approximately  $5.29 \times 10^{-4} \text{ cm}^2$ . To further analyze the microstructural transformations and heat-affected zones induced by LST, detailed examinations of the textures were conducted using SEM.

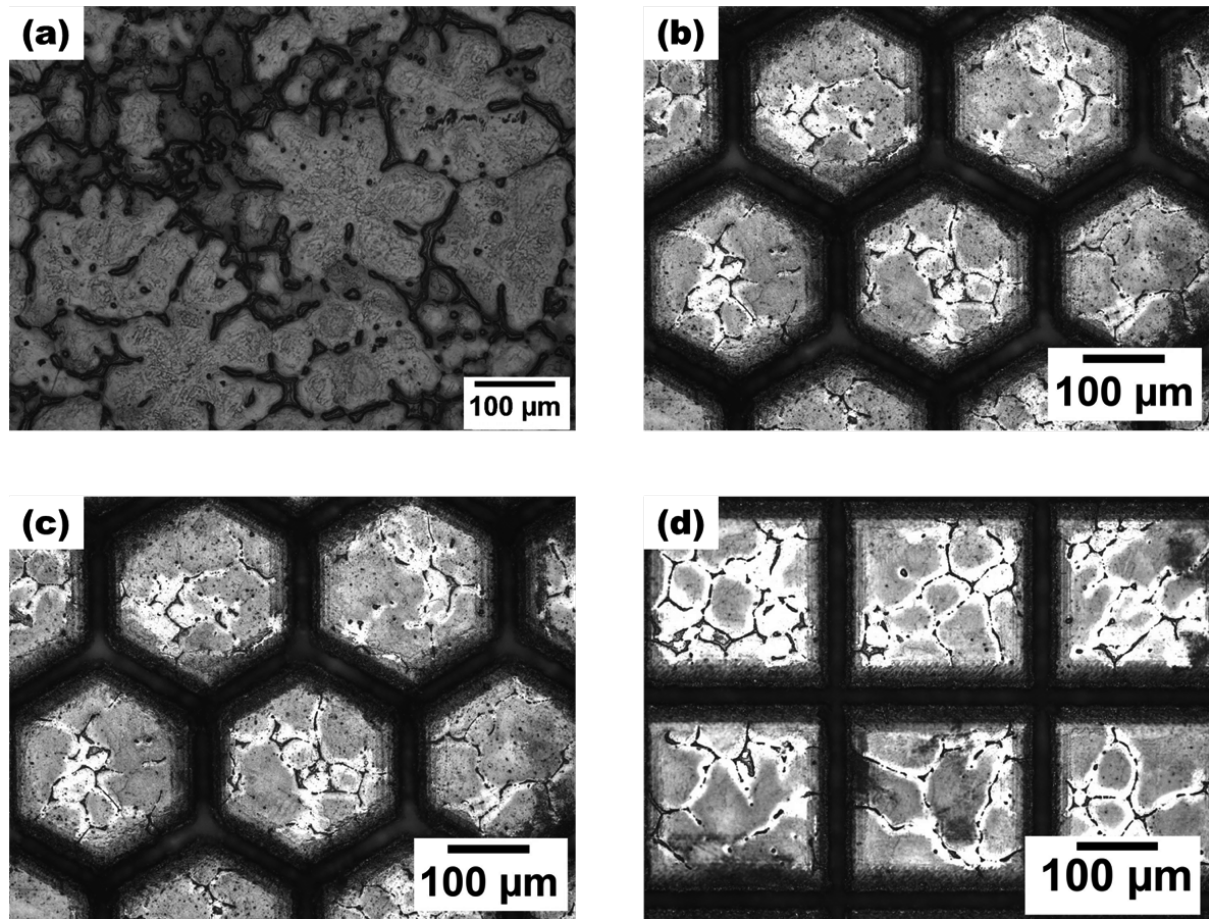


*Figure 2 Light Optical Microscopy of Magnesium RZ5 alloy (a) before LST, and after (b) HC-SP (c) HC-DP (d) SQ LST patterns*

The scanning electron microscopy (SEM) image presented in **Figure 3** illustrates the microstructural characteristics of the RZ5 alloy prior to laser surface treatment (LST). The micrograph reveals a significant presence of non-equilibrium eutectic phases, predominantly arising from the segregation of zinc (Zn) and silicon (Si) at the boundaries of the melt pool and within the interdendritic regions. This observation is corroborated by the energy dispersive x-ray spectroscopy (EDS) chemical composition maps, which highlight these segregations. The data strongly suggest the formation of the  $\text{Si}_2\text{Zn}$  binary intermetallic compound during the casting solidification process within the melt pool.



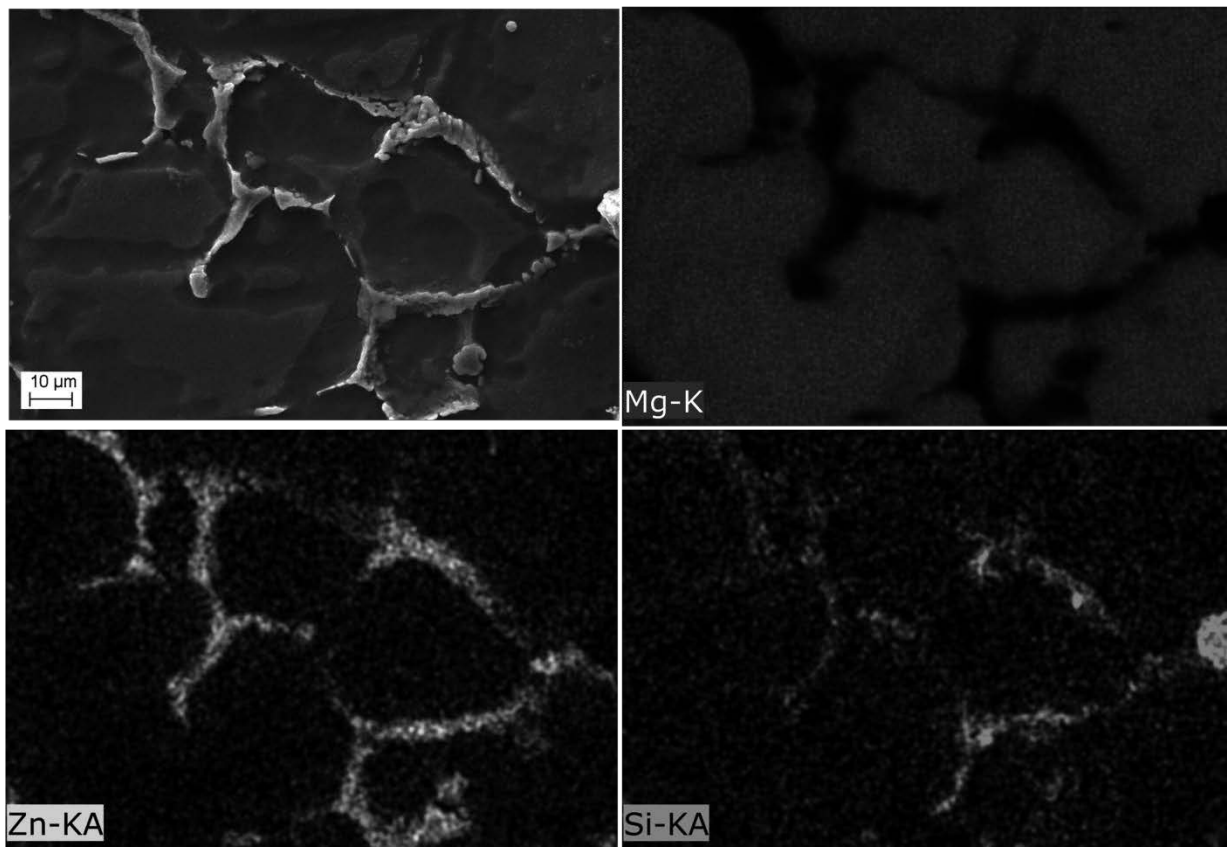


Figure 3 SEM image of the microstructure of Mg RZ5 before LST, with Energy dispersive X-ray spectroscopy (EDS) chemical composition maps.

The impact of number of passes and LST pattern are further observed in **Figure 4** which depicts the SEM micrographs of Magnesium RZ5 after laser surface treatment. A trend of increasing size of heat affected zone (HAZ) with increasing number of passes is observed for honeycomb single- and double-passes. The average size of the heat affected zone of HC-SP was found to be  $21.8 \mu\text{m} \pm 2 \mu\text{m}$  which is displayed in **Figure 4(b)**, while HC-DP recorded an average of  $25.5 \mu\text{m} \pm 3.7 \mu\text{m}$  displayed in **Figure 4(c)**. Laser surface treatment with square pattern (SQ) recorded an average HAZ size of  $24.4 \mu\text{m} \pm 3.3 \mu\text{m}$  as displayed in **Figure 4(d)**.

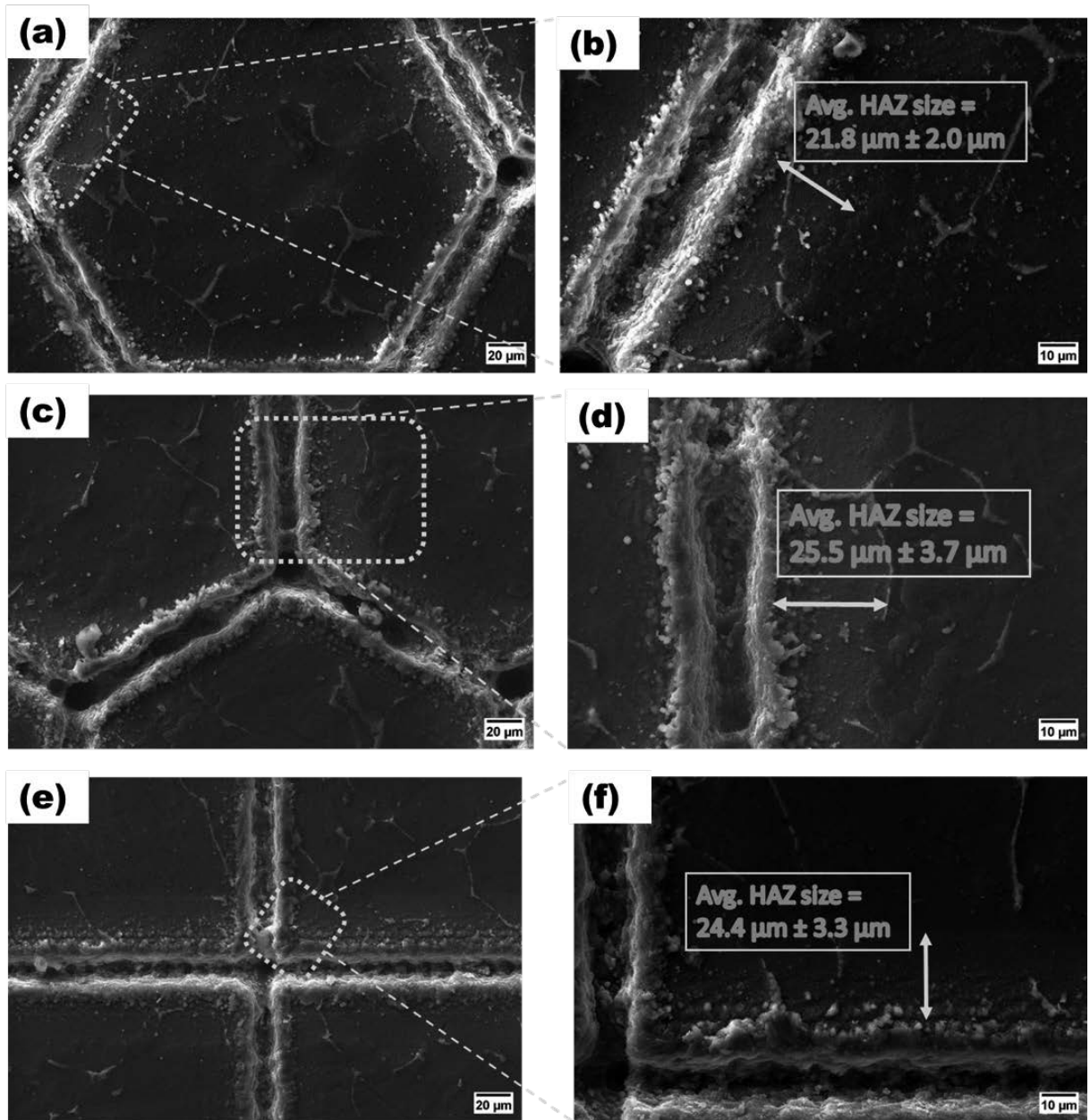


Figure 4 SEM images of the microstructure of Mg RZ5 after (a-b) HC-SP (c-d) HC-DP (e-f) SQ LST patterns

### 3.2 Hardness

The Vickers microhardness of the prepared samples was investigated at room temperature, to assess the mechanical performance before and after laser surface treatment. **Figure 5** displays the average microhardness results observed in the heat affected zone (HAZ) and melt pool of the samples, taking into account all surface conditions after metallographic polishing. The least microhardness of  $49.4 \text{ HV} \pm 2.7 \text{ HV}$  was recorded in the melt pool for the base metal. The highest average of  $93.5 \text{ HV} \pm 12.8 \text{ HV}$  was recorded in the HAZ for honeycomb double-pass (HC-DP) sample, while honeycomb single-pass recorded an average hardness of  $81.6 \text{ HV} \pm 4.2 \text{ HV}$ . There was a significant increase in hardness of the HAZ of  $\sim 15\%$  after honeycomb double-pass as

compared to honeycomb single-pass. The average hardness of the square pattern was found to be  $84.9 \text{ HV} \pm 8.7 \text{ HV}$ , which is 4% higher than honeycomb single-pass. Overall, the heat affected zones (HAZ) of the samples after laser surface texturing were higher than that of the corresponding melt pools, which is attributed to the change in microstructure due to the heat associated with the treatment process.

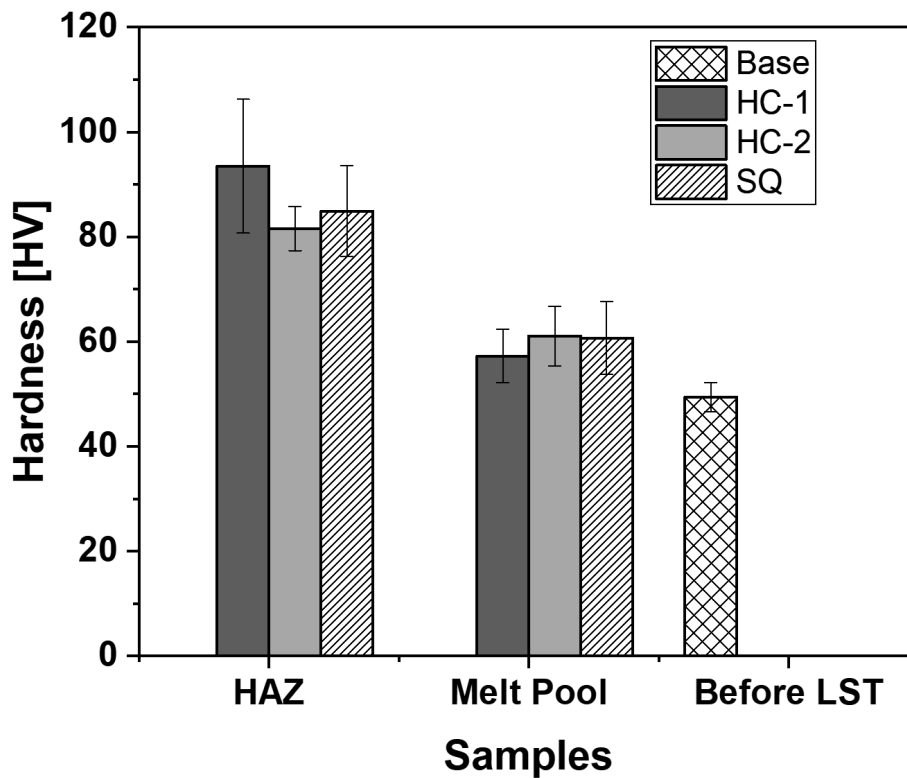


Figure 5 Hardness of Mg rz5 alloy before LST, and after LST in the HAZ and melt pool

This study has demonstrated the significant impact of laser surface treatment (LST) on the microstructural and mechanical properties of Magnesium RZ5 alloys. By applying various LST patterns, including honeycomb single-pass, honeycomb double-pass, and square patterns, we observed substantial changes in both the microstructure and hardness of the alloy. The light optical microscopy and SEM analyses revealed that the LST process induces a clear alteration in the microstructure, particularly in the heat-affected zone (HAZ). The size of the HAZ increased with the number of laser passes, indicating a correlation between the extent of surface treatment and the resulting microstructural modifications. Specifically, the honeycomb double-pass pattern resulted in the largest HAZ, followed by the square and honeycomb single-pass patterns. The Vickers microhardness test results further corroborated these observations. The hardness of the HAZ was significantly higher than that of the melt pool across all treated samples. Notably, the honeycomb double-pass pattern exhibited the highest hardness, demonstrating a marked improvement of approximately 15% over the single-pass pattern, followed by the square pattern with a 4% improvement over the honeycomb single pass pattern. This enhancement in hardness is attributed to the refined microstructure and increased density of dislocations induced by the LST process[8].

#### 4. CONCLUSION

The findings underscore the potential of LST as an effective technique for modifying the microstructure and enhancing the mechanical properties of Magnesium RZ5 alloys. The ability to tailor the microstructure and improve hardness through controlled laser surface texturing opens new avenues for extending the application of Mg RZ5 in high-performance and demanding environments. Future research could focus on optimizing the LST parameters further and exploring the long-term performance and durability of the treated alloys in various operational conditions.

#### BIBLIOGRAPHY

1. B. Liu, J. Yang, X. Zhang, Q. Yang, J. Zhang, and X. Li, "Development and application of magnesium alloy parts for automotive OEMs: A review," *J. Magnes. Alloy.*, vol. 11, no. 1, pp. 15–47, 2023, doi: 10.1016/j.jma.2022.12.015.
2. A. Meher, M. M. Mahapatra, P. Samal, and P. R. Vundavilli, "Study on effect of TiB<sub>2</sub> reinforcement on the microstructural and mechanical properties of magnesium RZ5 alloy based metal matrix composites," *J. Magnes. Alloy.*, vol. 8, no. 3, pp. 780–792, 2020, doi: 10.1016/j.jma.2020.04.003.
3. Z. E. Kennedy, Shivappa, B. Poorani, V. Hariram, and S. Mohan, "Laser Texturing on Magnesium Alloys for Bio-Implants," *Int. J. Veh. Struct. Syst.*, vol. 15, no. 6, pp. 848–851, 2023, doi: 10.4273/ijvss.15.6.22.
4. W. M. Steen and J. Powell, "Laser surface treatment," *Mater. Des.*, vol. 2, no. 3, pp. 157–162, 1981, doi: 10.1016/0261-3069(81)90056-X.
5. P. Lei *et al.*, "Research status of laser surface texturing on tribological and wetting properties of materials: A review," *Optik (Stuttg.)*, vol. 298, no. December 2023, p. 171581, 2024, doi: 10.1016/j.ijleo.2023.171581.
6. S. Amukarimi and M. Mozafari, "Biodegradable magnesium-based biomaterials: An overview of challenges and opportunities," *MedComm*, vol. 2, no. 2, pp. 123–144, 2021, doi: 10.1002/mco2.59.
7. D. Mehra, M. M. Mahapatra, and S. P. Harsha, "Processing of RZ5-10wt%TiC in-situ magnesium matrix composite," *J. Magnes. Alloy.*, vol. 6, no. 1, pp. 100–105, 2018, doi: 10.1016/j.jma.2018.01.002.
8. P. K. S, D. B. P, J. Gautam, A. K. Rai, and C. P. Paul, "Synergistic integration of laser shock peening and heat treatment for refined microstructure and enhanced mechanical properties in additively manufactured 17–4PH stainless steel," *J. Mater. Process. Technol.*, vol. 328, no. December 2023, p. 118395, 2024, doi: 10.1016/j.jmatprotec.2024.118395.



17th-19th June 2024  
Gliwice, Poland

DEPARTMENT OF ENGINEERING MATERIALS AND BIOMATERIALS  
FACULTY OF MECHANICAL ENGINEERING  
SILESIA UNIVERSITY OF TECHNOLOGY

## INTERNATIONAL STUDENTS SCIENTIFIC CONFERENCE

### **Influence of CWJ (Continuous Water Jet) Pressure on the Surface Structure of Peened SLM AlSi10Mg Alloy**

Beatrice N.A Ardayfio<sup>a</sup>, Augustine N.S Appiah<sup>b</sup>, Przemysław Snopiński<sup>c</sup>, Anna Woźniak<sup>b</sup>, John Ampah-Essel<sup>a</sup>, Benjamin Agyei-Tuffour<sup>a</sup>

<sup>a</sup> University of Ghana, CBAS, Department of Materials Science and Engineering

<sup>b</sup> Silesian University of Technology, Faculty of Mechanical Engineering, Materials Research Laboratory

<sup>c</sup> Silesian University of Technology, Faculty of Mechanical Engineering, Department of Engineering Materials and Biomaterials, email: bnaardayfio@st.ug.edu.gh

#### **Abstract**

Water jet peening serves as a surface modification method commonly used to introduce residual stresses at both surface and sub-surface levels, enhancing the strength of various materials, such as metals. Nonetheless, the resultant surface roughness post-peening can significantly impact its suitability for specific applications. This study delves into the effect of water jet pressure on the ensuing surface roughness, exploring pressures ranging from 140 MPa to 280 MPa. Through macro and micro examinations, along with surface profilometry, the study identifies an optimal pressure of 280 MPa for generating peened surfaces with the most pragmatic surface roughness.

**Keywords:** Water jet peening, AlSi10Mg alloy, Surface treatment, Selective laser melting.

#### **1. INTRODUCTION**

The transition from heavy to lightweight metals, such as aluminum and its alloys, in the automotive and aerospace industries is a crucial step in promoting sustainable engineering practices. Lightweight metals offer a balance of strength and reduced weight, leading to enhanced fuel efficiency, reduced emissions, and improved performance across various applications [1][2]. The use of lightweight materials aligns with sustainability objectives by promoting energy efficiency, decreasing environmental impact, and optimizing resource utilization. Research focusing on the development of high-performance, sustainable, lightweight, and thermally stable bulk materials underscores the importance of this shift for future structural applications [3].

Despite their benefits, lightweight materials face challenges that hinder their widespread adoption. For example, aluminum and its alloys, commonly used for lightweight structures, often exhibit a tradeoff between strength and ductility. To address these challenges, various forming processes have been explored, with additive manufacturing[4] being particularly noteworthy. Snopiński et al.[5] demonstrated the potential of selective laser melting (SLM) in fabricating AlSi10Mg alloy, highlighting its heterogeneous structure as a significant step towards

overcoming the strength-ductility tradeoff. This structure enables post-SLM operations to enhance the alloy's performance.

Among these post-processing operations, including heat treatment and plastic deformation, surface engineering techniques such as laser surface treatments, peening operations[6], and surface coatings deposition stand out. These techniques offer significant advantages by enhancing alloy properties through surface or sub-surface modifications without altering the material's bulk structure. In particular, water jet peening employs a high-pressure water jet to bombard the surface of the treated material. This bombardment introduces compressive residual stresses into the material, thereby strengthening it and improving its fatigue resistance[7]. Consequently, water jet peening is a crucial process for components subjected to repeated stresses, such as aircraft wings and engine components[8].

The degree of surface roughness in structural materials is a critical indicator of their susceptibility to failure phenomena such as corrosion and wear, which directly impacts their performance and lifespan[9][10]. Therefore, it is essential to meticulously monitor the surface condition and its roughness during water jet peening operations to produce surfaces capable of withstanding harsh environmental conditions. This study aims to contribute to this field by evaluating the influence of water jet pressure on the resulting surface morphology and roughness of AlSi10Mg alloys subjected to water jet peening surface treatment.

## 2. METHODOLOGY

### 2.1 Sample Preparation

The AlSi10Mg test specimens were fabricated using Selective Laser Melting (SLM) with commercially obtained gas atomized powders from Sigma Aldrich. The fabrication utilized the TruPrint 1000 system (Trumpf, Ditzingen, Germany) to create test pieces measuring 15 mm x 15 mm x 50 mm. The laser power was set to 175 W, with a layer thickness of 20  $\mu\text{m}$  and a focused beam diameter of 55  $\mu\text{m}$ . The laser scan speed was 1400 mm/s, with a rotation angle of 90°.

The surfaces of the as-built specimens were treated with peening using a continuous water jet (CWJ). The peening process was conducted at a travel speed of 1500 mm/s, with the water jet positioned 60 mm above the surface. The pressure was varied to produce four different peened surface conditions as shown in Table 1.

Sample ID	Continuous Water Jet Pressure [MPa]
CWJ140	140
CWJ180	180
CWJ230	230
CWJ280	280

Microscopic observations were carried out using the Leica DVM6 (Leica Microsystems, Heerbrugg, Switzerland) digital microscope. Surface roughness profiles were acquired using Surtronic 25 from Taylor Hobson.

### 3. RESULTS AND DISCUSSION

#### 3.1 Surface Morphology

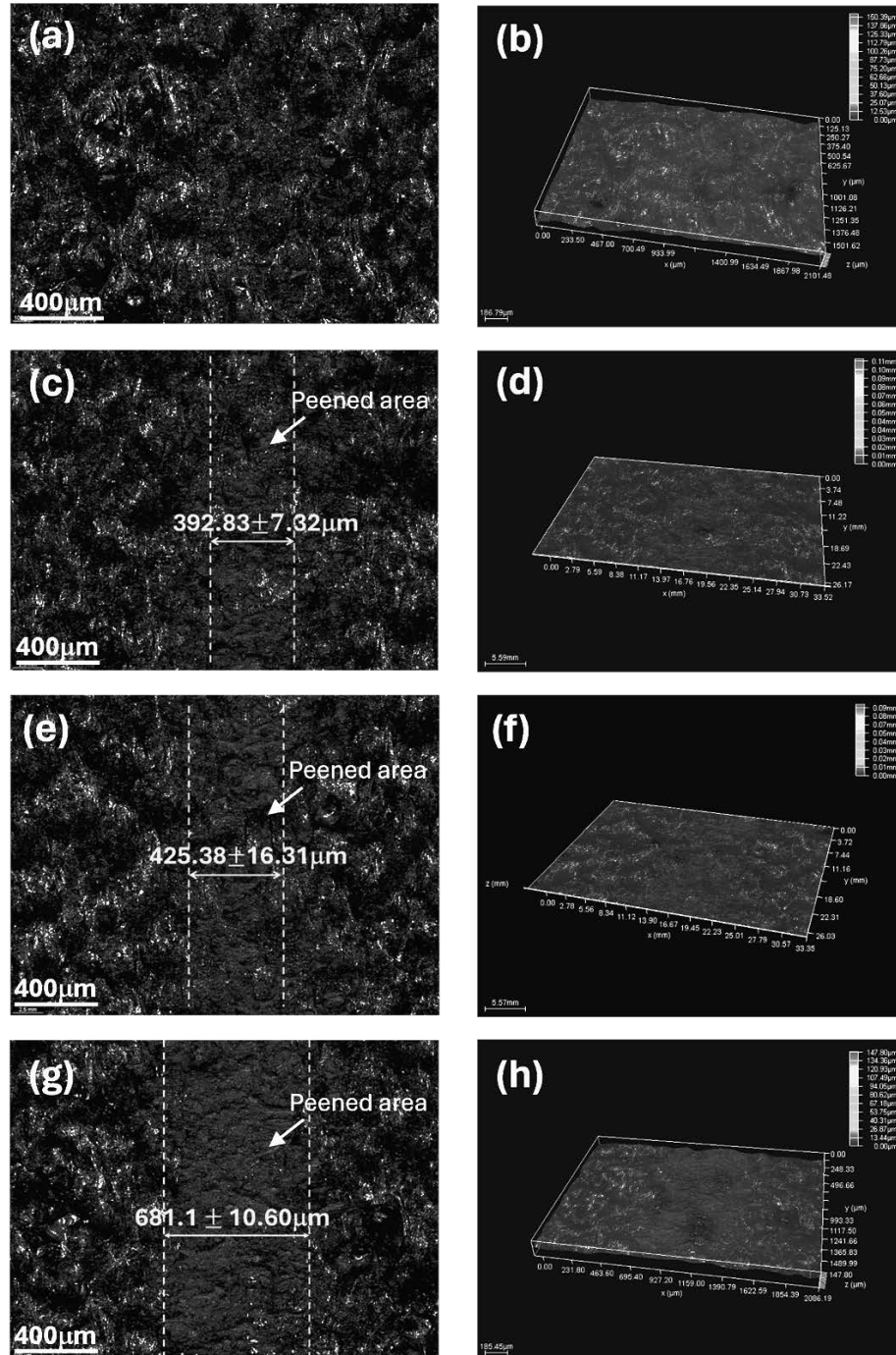


Figure 1. Digital micrographs of peened tracks (a) & (b) show the width of peened area and depth color contour map for CWJ1 sample, (c) & (d) show the width of peened area and depth color contour depth map for CWJ2 sample, (e) & (f) show the width of peened area and depth color contour depth map for CWJ3 sample, and (g) & (h) show the width of peened area and depth color contour depth map for CWJ4.

The post-peening surface morphologies of the peened tracks were analyzed using a digital microscope, and the results are presented in **Figure 1**. At a pressure of 140 MPa, the digital micrograph of CWJ1 in **Figure 1(a)** shows no discernible change in the morphology of the peened area compared to the unpeened surface of the as-built sample. The depth map of this specimen, shown in **Figure 1(b)**, corroborates this observation, indicating no visible difference in the depth of the peened area. Upon increasing the pressure to 180 MPa, the morphology of CWJ2's peened area displayed a notable distinction from the unpeened area, as seen in **Figure 1(c)**. The peened area appears relatively smoother than the unpeened zone, with a mean width of approximately 393  $\mu\text{m}$ . The corresponding depth map for this specimen in **Figure 1(d)** shows a distinct peened zone with a depth of approximately 0.11 mm. When the pressure was increased to 230 MPa, the width of the peened area in CWJ3 increased by about 8.4% to approximately 425  $\mu\text{m}$ , as depicted in **Figure 1(e)**. The depth map in **Figure 1(f)** indicates a decrease in the depth of the peened track by 18% to 0.09 mm. At a pressure of 280 MPa, the width of the peened area in CWJ4 further increased by 60% to approximately 681  $\mu\text{m}$ , as shown in **Figure 1(g)**. The corresponding depth of the peened area, as seen in **Figure 1(h)** decreased from the surface of the as-built specimen to 0.147 mm, representing an approximate decrease in depth of 84% compared to CWJ3.

The results indicate a trend of increasing the width of the peened area on the surface and a corresponding decrease in the depth of the peened area as the CWJ pressure increases. Additionally, the surface of the peened area exposed more subsurface structures as the CWJ pressure increased. CWJ4 demonstrated the most unique combination of peened surface structure and the lowest depth of the peened zone, making it desirable for CWJ peening operations that require effective treatment of a thin surface layer.

### 3.2 Surface roughness

The surface roughness profiles are shown in Figure 2. It is observed in Figure 2(a) that there are peaks which are below the mean line signifying that the surface of the CWJ1 sample is smooth and has no major irregularities on the surface. In Figure 2(b), the CWJ2 sample similarly shows a comparable level of smoothness since irregularities on the surface are equally not as pronounced. CWJ3 exhibits a rather lower level of roughness in Figure 2(c). The profiles above the mean line as not as pronounced as observed in CWJ1 and CWJ2 and the those below the mean line are similarly shallower. The CWJ4 sample shows the most significant variations in the profiles above and below the mean line in Figure 2(d), showcasing higher levels of surface irregularities and consequently, the highest surface roughness among the investigated samples.



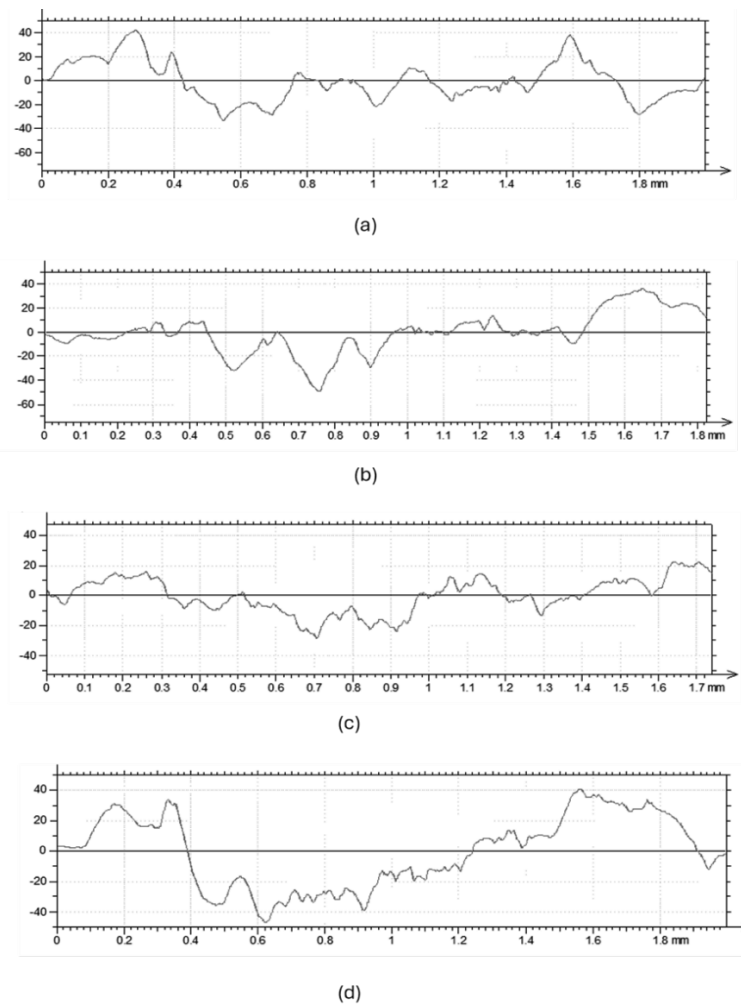


Figure 2. Surface roughness profiles (a) CWJ1, (b) CWJ2, (c) CWJ3, and (d) CWJ4.

#### 4. CONCLUSION

The results demonstrate a significant influence of CWJ pressure on the surface structure of the peened samples. As the pressure increases, the CWJ effectively exposes more subsurface structures, accompanied by an expansion in the size of the peened area. Conversely, an inverse relationship is observed with the depth of the peened area; higher CWJ pressure results in a reduction in the depth of the peened region. The pressure of 280 MPa was identified as optimal for water jet peening processing, as it efficiently treats the surface while confining modifications to a thin surface layer. Additionally, this pressure produced the highest surface roughness among the investigated CWJ pressures.

#### FUNDING

The research was funded by the National Science Centre, Poland based on the decision number 2021/43/D/ST8/1946. This research was completed in association with the project Innovative

and additive manufacturing technology—new technological solutions for 3D printing of metals and composite materials, reg. no. 319 CZ.02.1.01/0.0/0.0/17\_049/8 407, financed by Structural Funds of the European Union.

## BIBLIOGRAPHY

- [1] D. Labus Zlatanovic *et al.*, “Influence of rotational speed on the electrical and mechanical properties of the friction stir spot welded aluminium alloy sheets,” *Weld. World*, vol. 66, no. 6, pp. 1179–1190, 2022, doi: 10.1007/s40194-022-01267-8.
- [2] S. S. Lal, “FABRICATION OF ALUMINIUM 6061-SiC-Al<sub>2</sub>O<sub>3</sub> MMC AND HMMC BY STIR,” no. August, 2019.
- [3] X. Yan *et al.*, “Microstructure and mechanical properties of pure copper manufactured by selective laser melting,” *Mater. Sci. Eng. A*, vol. 789, p. 139615, 2020, doi: 10.1016/j.msea.2020.139615.
- [4] Y. Ding, J. A. Muñiz-Lerma, M. Trask, S. Chou, A. Walker, and M. Brochu, “Microstructure and mechanical property considerations in additive manufacturing of aluminum alloys,” *MRS Bull.*, vol. 41, no. 10, pp. 745–751, 2016, doi: 10.1557/mrs.2016.214.
- [5] P. Snopiński, A. N. S. Appiah, O. Hilšer, and M. Kotoul, “Investigation of microstructure and mechanical properties of SLM-fabricated AlSi10Mg alloy post-processed using equal channel angular pressing (ECAP),” *Materials (Basel)*, vol. 15, no. 22, p. 7940, 2022.
- [6] S. Qutaba, M. Asmelash, K. Saptaji, and A. Azhari, *A review on peening processes and its effect on surfaces*, vol. 120, no. 7–8. Springer London, 2022. doi: 10.1007/s00170-022-09021-6.
- [7] R. Muruganandhan, M. Mugilvalavan, K. Thirumavalavan, and N. Yuvaraj, “Investigation of water jet peening process parameters on AL6061-T6,” *Surf. Eng.*, vol. 34, no. 4, pp. 330–340, 2018, doi: 10.1080/02670844.2017.1394564.
- [8] A. H. Mahmoudi, F. Salahi, and A. Ghasemi, “Comparison Between Residual Stress Induced By Waterjet Peening and Shot Peening,” *Int. Conf. Surf. Modif. Technol. 29TH*, no. December 2017, 2016.
- [9] M. R. Stoudt, L. E. Levine, A. Creuziger, and J. B. Hubbard, “The fundamental relationships between grain orientation, deformation-induced surface roughness and strain localization in an aluminum alloy,” *Mater. Sci. Eng. A*, vol. 530, no. 1, pp. 107–116, 2011, doi: 10.1016/j.msea.2011.09.050.
- [10] A. Toloei, V. Stoilov, and D. Northwood, “The relationship between surface roughness and corrosion,” *ASME Int. Mech. Eng. Congr. Expo. Proc.*, vol. 2 B, pp. 1–10, 2013, doi: 10.1115/IMECE2013-65498.



17th-19th June 2024  
Gliwice, Poland

DEPARTMENT OF ENGINEERING MATERIALS AND BIOMATERIALS  
FACULTY OF MECHANICAL ENGINEERING  
SILESIA UNIVERSITY OF TECHNOLOGY

## INTERNATIONAL STUDENTS SCIENTIFIC CONFERENCE

### Laser welding

Jennifer Badora<sup>a</sup>, Justyna Janoszka<sup>a</sup>, Julia Muszyńska<sup>a</sup>, Magdalena Szindler<sup>b</sup>, Mirosław Bonek<sup>b</sup>

<sup>a</sup> Silesian University of Technology, Faculty of Mechanical Engineering, Student of Engineering Production and Management, Gliwice,

<sup>b</sup> Silesian University of Technology, Faculty of Mechanical Engineering, Department of Engineering Materials and Biomaterials

**Abstract:** The subject of consideration in the following article will be gas laser welding using CO<sub>2</sub> gas, which has found significant application in various industries such as aviation, automotive, and electronics. In the respective sections of the article, basic information about CO<sub>2</sub> laser welding, its parameters, comparison of various laser welding methods, as well as the advantages and disadvantages of the selected method - CO<sub>2</sub> laser welding, have been presented.

**Keywords:** welding technology, laser welding, gas laser, CO<sub>2</sub>

### 1. INTRODUCTION

Laser welding systems are divided into two groups: gas lasers and solid-state lasers. CO<sub>2</sub> lasers belong to the group of gas lasers, where CO<sub>2</sub> is a component of the active medium in the gas mixture CO<sub>2</sub>+N<sub>2</sub>+He. Laser radiation, also known as laser light, is a specific type of electromagnetic radiation that covers a range of wavelengths from 10.0 nm to 1.0 mm, including ultraviolet, infrared, and visible light. The laser light beam is generated in laser generators through energetic transitions of atoms between higher and lower energy states in the laser's active medium. Laser radiation is produced through stimulated emission of energy. It is characterized by high uniformity in time and space and a narrow range of wavelengths, meaning it is monochromatic. The main characteristics of laser light radiation include:

- Monochromaticity; for example, CO<sub>2</sub> gas lasers are characterized by a very narrow spectral line of output radiation, and the theoretical beam width is on the order of hundredths of nanometers.
- Collimation; in CO<sub>2</sub> lasers, the divergence of the laser beam remains below 2-5 milliradians.
- High radiation energy; the power density of continuous-wave lasers ranges from 10<sup>3</sup> to 10<sup>7</sup> [W/mm<sup>2</sup>], while the power density of pulsed and shockwave lasers ranges from 10<sup>9</sup> to 10<sup>11</sup> [W/mm<sup>2</sup>].
- Minimal divergence of the laser beam results from its coherence, spatial and temporal coherence, which means equality of phases and uniformity of amplitude on the surface of electromagnetic waves.

Table 1. Comparison of Lasers

Laser type	CO <sub>2</sub> Gas Laser	Nd: YAG Pumped with white Light	Nd: YAG Pumped with Diode Laser	Yb-Doped Multimode Fiber Laser	Nd: YAG Disk Laser
Laser Medium	Gas Mixture	Crystal Rod	Crystal Rod	Doped Fiber	Crystal Disk
Emitted Wavelength [μm]	10,6	1,06	1,06	1,07	1,03
Beam Transmission	Mirrors, lenses	Fiber, lenses	Fiber, lenses	Fiber, lenses	Fiber, lenses
Typical Transport Fiber Diameter [μm]	-	600	400	100-200	150-300
Output Power [kW]	Up to 50	4,0	Over 6	Up to 50	Up to 10
Beam Quality BPP at 1.0 kW Power - [mm x mrad]	3,7	25	12-25	12	7
Beam Quality BPP at 1.0 kW Power - [mm x mrad]	3,7	12	<12	1,8	4
Periodic Maintenance Interval [hours]	2000	800-1000	2000-5000	10000	2000-5000
Energy Efficiency [%]	5-8	1-5	10-20	20-30	10-20
Approximate Cost of Laser per 1.0 kW Power [1000 USD]	60	130-150	150-180	130-150	130-150
Device Footprint	Very large	Medium	Medium	Small	Medium
Laser Mobility	Low	Low	Low	High	Low

## 2. CONSTRUCTION OF A CO<sub>2</sub> GAS LASER WITH TRANSVERSE FLOW OF THE LASER GAS MIXTURE

Operating principle: The CO<sub>2</sub>+N<sub>2</sub>+He gas mixture is introduced and flows through discharge tubes made of quartz glass. For high-power lasers, additional unstable resonators (composed of segments of tubes arranged in a rectangular or triangular configuration) are used to limit the obtained laser radiation beam in the discharge tubes. This design allows for increasing power, improving cooling conditions, and extending the path of the radiation beam. An example of the above-described CO<sub>2</sub> gas laser with transverse flow of the laser gas mixture is shown in the picture of the Trumpf Model Tlf 3800 Turbo laser located at the Welding Center in Gliwice.

The mentioned model is used for cutting and welding sheets of various thicknesses.



Figure 1. Tlf 3800 Turbo Laser

### 3. ADVANTAGES AND DISADVANTAGES

Laser welding is a method of joining materials that offers several significant benefits in industry. One of the main advantages is the minimal amount of heat required to create the weld and the small heat-affected zone, ensuring precise and controlled connections with minimal risk of material distortion. Additionally, the short welding time allows for efficient joining of materials of considerable thickness in a single pass, even up to around 30 mm, resulting in time and cost savings in production. The ability to weld in a controlled atmosphere or in a vacuum adds versatility to this method, allowing for applications in various environmental conditions. Focusing the laser beam on a small area enables the joining of small, closely spaced objects, which is useful in the production of components with precise dimensions. Automation of the welding process through numerical and computer control contributes to increased efficiency and repeatability of welding operations. The absence of a magnetic field influence on the weld eliminates the risk of undesirable magnetic effects. Laser welding also enables the joining of diverse materials, making this method versatile. The narrow shape of the weld and the ability to precisely control the process guarantee high-quality connections. Additionally, the ability to transmit the laser beam to multiple workstations increases the flexibility of the welding process, allowing for simultaneous operations on multiple components or at different stages of production.

Despite its numerous advantages, this method has certain limitations. Firstly, the joint must

be accurately positioned under the laser beam, taking into account its focal point, which requires precision and proper preparation of materials. Additionally, the surfaces to be joined should be tightly pressed together, requiring similar accuracy to electron beam welding to ensure adequate joint quality. The maximum thickness of the joined elements is also limited, typically practically up to around 19 mm, although this may vary depending on the power of the device used. Finally, for some metals such as aluminum, copper, and their alloys, high light reflectivity and high conductivity can have an adverse effect on weldability, requiring additional attention during the welding process.

### **3.1 CO<sub>2</sub> Gas Laser with Longitudinal Flow of Laser Gas Mixture**

It is characterized by very high beam quality achieved at a comparably lower maximum output power compared to other types of lasers. Additionally, it allows for operation with both continuous and pulsed emission of laser radiation, with different pulse frequency ranges that can range from 100 Hz to 100 kHz. An important advantage is also the compact design of the resonator, which contributes to the stability and efficiency of operation of the CO<sub>2</sub> gas laser with longitudinal flow of laser gas mixture. These features make it an attractive solution for many applications in industry and other fields where high beam quality and operational flexibility are crucial.

The issue of electrode burnout arises, which results from the interaction between the electrode material and the molecules of the laser gas mixture, which can lead to the need for frequent electrode replacement. Additionally, the necessity of continuous replacement of the laser gas mixture is caused by contamination with electrode wear products, which can generate additional costs and make it difficult to maintain laser stability. Moreover, poorer heat dissipation conditions from the discharge area can lead to problems with effective cooling, which can affect laser stability. Finally, high electricity consumption is another significant drawback, which can be a significant factor in terms of operating costs and environmental impact. These factors may be important in evaluating the choice of CO<sub>2</sub> gas laser with longitudinal flow of laser gas mixture for specific applications, considering both the benefits and limitations of this technology.

### **3.2 CO<sub>2</sub> Gas Laser with Transverse Flow of Laser Gas Mixture.**

This method boasts high output power, a result of multiple beam reflections, translating into process efficiency and effectiveness. Additionally, its high operational reliability is a significant advantage, ensuring stable operation in various environmental and operational conditions. The long lifespan of electrodes contributes to reduced maintenance and operating costs, particularly in the long term. Furthermore, low gas mixture consumption and effective cooling contribute to resource efficiency and minimize overheating issues. Low electricity consumption is another significant benefit, impacting both operational costs and environmental benefits. Finally, the simplicity of the laser radiation generator's design facilitates its operation and maintenance, enhancing user convenience and reducing maintenance costs. These features make the CO<sub>2</sub> gas laser with transverse flow of laser gas mixture an attractive solution in many industrial and technological applications.

However, this laser has relatively low beam quality. This means that the beam may be less focused and coherent, which can affect the precision and efficiency of processes utilizing this laser. This characteristic may be significant in applications where high precision and quality are required, such as in the electronics or medical industries. Nevertheless, despite this drawback,

CO<sub>2</sub> gas lasers with transverse flow of laser gas mixture still find wide application in many fields, especially where slightly lower beam quality is acceptable in exchange for other benefits, such as high output power or low operating costs.

#### **4. APPLICATION**

Laser welding is a technological process closely related to the development of sciences such as mathematics, physics, and chemistry. The advancement of industrial technologies largely depends on achievements in these fields. This is an observable direction of development that concerns practically all sectors of industry, including electronics, electrical engineering, information technology, precision mechanics, and metallurgy. Modern welding technologies that utilize lasers provide an excellent example where the principles of laser radiation physics, material physics, and metallurgy play a crucial role.

CO<sub>2</sub> gas laser with longitudinal flow of laser gas mixture is used in industrial and technological processes. These include cutting, perforating, and grooving materials, where high precision and speed of execution are crucial. Additionally, this laser is also used in spot welding, allowing for the creation of durable and precise connections between elements. Other applications include cladding, soldering, and surface treatment, where the laser enables precise and controlled application of materials or modification of surface structure.

CO<sub>2</sub> gas laser with transverse flow of laser gas mixture encompasses surface processing, allowing for precise and controlled modifications of material structure and properties. Another significant application is laser welding with a keyhole technique, enabling the creation of durable and precise connections between elements, often without additional material. Moreover, hybrid laser-arc welding is increasingly being used, combining the advantages of both technologies to ensure high quality and process efficiency. Thanks to its effectiveness and versatility, CO<sub>2</sub> gas laser with transverse flow of laser gas mixture plays a significant role in industry, contributing to the efficient and precise execution of various production and machining operations.

#### **BIBLIOGRAPHY**

1. Klimpel, Andrzej Adam, *Technologie laserowe w spawalnictwie*, Gliwice, 2011
2. Marcelli Mazur, *Podstawy spawalnictwa, wydanie II*, Gliwice, 1999
3. Artur Czupryński, Agnieszka Rzeźnikiewicz, *Specjalne technologie spawalnicze w ćwiczeniach laboratoryjnych, cz.II*, Gliwice, 2020



17th-19th June 2024  
Gliwice, Poland

DEPARTMENT OF ENGINEERING MATERIALS AND BIOMATERIALS  
FACULTY OF MECHANICAL ENGINEERING  
SILESIA UNIVERSITY OF TECHNOLOGY

## INTERNATIONAL STUDENTS SCIENTIFIC CONFERENCE

### Literature Review on Additive Manufacturing

Drilon Beqiri<sup>a</sup>, Afrim Gjelaj<sup>b</sup>, Vladimir Dukovski<sup>c</sup>, Bejtë Çela<sup>d</sup>

<sup>a</sup> University of Mitrovica, Faculty of Mechanical and Computer Engineering, Department of Manufacturing Technology, email: drilon.beqiri@umib.net

<sup>b</sup> University of Prishtina, Faculty of Mechanical Engineering, Department of Manufacturing and Industrial Engineering with Management, email: afrim.gjelaj@uni-pr.edu

<sup>c</sup> Ss. Cyril and Methodius University in Skopje, Faculty of Mechanical Engineering, Department of Manufacturing and Industrial Engineering with Management, email: vladimir.dukovski@mf.edu.mk

<sup>d</sup> HIGH SCHOOL SHMLP, Kastriot, email: shmlp.idumoshi@gmail.com

**Abstract:** Additive manufacturing, commonly known as 3D printing, has revolutionized the manufacturing industry. It enables the production of intricate and customized objects with a level of detail and efficiency not possible with traditional production methods. This technology has catalyzed new approaches in design and the fabrication of complex geometries, fostering innovation in manufacturing techniques and processes. This technology stands in stark contrast to conventional manufacturing methods, providing unparalleled design flexibility, production speed, and efficiency.

**Keywords:** Additive Manufacturing, AM Technology, 3D Printing, Additive Manufacturing Materials, Material Extrusion Processes, Design for Additive Manufacturing (DfAM), Digital Design, AM Industry Impact, AM Sustainability

### 1. INTRODUCTION

The versatility of additive manufacturing extends across multiple sectors such as aerospace, automotive, healthcare, and consumer goods, demonstrating its influence on contemporary production modalities [1].

The scope of this seminar paper is a comprehensive literature review that delves into the breadth and depth of additive manufacturing. This review anchors its analysis in scholarly publications where authors have elucidated various aspects of additive manufacturing processes. We aim to draw from these academic discussions to identify the current consensus, breakthroughs, and prevailing challenges as reported by leading researchers in the field.

By examining scientific studies and technical reports, the paper will emphasize the transformative impact of additive manufacturing on product quality, material utilization, and cost efficiency. We will dissect the literature to understand how machine characteristics, material properties, and process technology contribute to the final outcome of printed products.



Additionally, we will explore the strategic implications of 3D printing technology on design thinking and operational management within the modern manufacturing paradigm. AM technology has enabled the tooling sector to eliminate environmentally damaging process enablers while also repairing and remanufacturing critical tools and dies [2].

### 1.1. Literature review Additive Manufacturing: Challenges, trends, and Applications

Additive manufacturing (AM), characterized by its layer-upon-layer material addition process, has become a cornerstone of modern industrial innovation. The ability to fabricate complex geometries with reduced material waste positions AM as a strategic technology that aligns with sustainable manufacturing goals and the drive toward customization and flexibility in production. As such, AM is not just transforming manufacturing processes but also setting new benchmarks for product design, supply chain management, and resource efficiency. This review will provide a critical assessment of the state-of-the-art in AM. Focus the technological and material advancements, process innovations, economic considerations, and sector-specific implementations that define the field's progress (3) This research provides a critical analysis of the current state of Additive Manufacturing (AM), focusing on key aspects shaping its development. This paper explores the technological advances, material developments, printing processes, post-processing techniques, quality control measures, and various applications of AM. By investigating these key components, we gain insight into how AM continues to evolve and impact different industrial sectors.

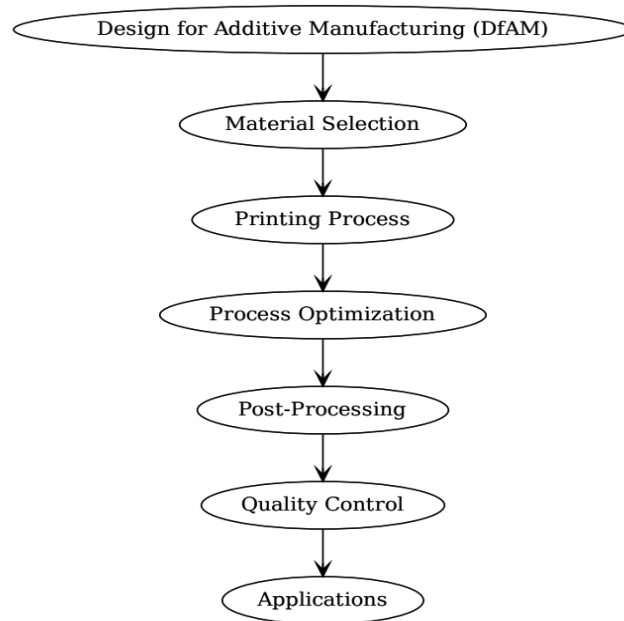


Figure 1. Additive Manufacturing Overview Flowchart

## 2. METHODOLOGY

In order to establish a robust scientific foundation for our methodology, we have conducted an extensive review and drawn upon existing scientific literature and research findings. This

chapter offers an in-depth exploration of additive manufacturing technologies, processes, and materials, integrating insights and knowledge derived from pertinent scientific works.

It comprehensively examines various 3D printing techniques and their applications, providing a detailed analysis of their strengths, limitations, and recent advancements. After three decades of development, additive manufacturing has evolved into a pivotal manufacturing process. Additive manufacturing, commonly referred to as AM, produces products by incrementally adding materials layer by layer, directly guided by a 3D model. This process involves the fabrication of objects through the meticulous addition of material layer by layer, guided by 3D models. Additive manufacturing empowers the creation of complex components and offers greater design flexibility compared to conventional manufacturing techniques. The primary objective of this paper is to gain a comprehensive understanding of the current state of advanced additive manufacturing technologies that incorporate machine learning in this field furthermore, it includes forward-looking discussions and perspectives on this topic. Additive manufacturing entails a layer-by-layer construction approach. Therefore, the most significant AM technologies typically employ a concentrated heat source to melt feedstock materials, such as powders or wires, which are subsequently consolidated through cooling to form a complete component.

### 3. ADDITIVE MANUFACTURING TECHNOLOGIES AND PROCESSES

Additive Manufacturing (AM) technologies and processes have revolutionized the way we create objects and products. As per the ASTM F2792-12a standard, AM encompasses seven main categories of processes, which are illustrated in Figure 2: These processes can be divided into three groups:

1. binder-based AM, including binder casting (BJ) and material extrusion (ME);
2. high-energy AM heat source, including direct energy deposition (DED),
3. powder bed fusion (PBF), and sheet lamination; and liquid-based AM, including material casting and vat photopolymerization. Metal parts can be fabricated using technologies based on binders and high-energy heat sources [4].

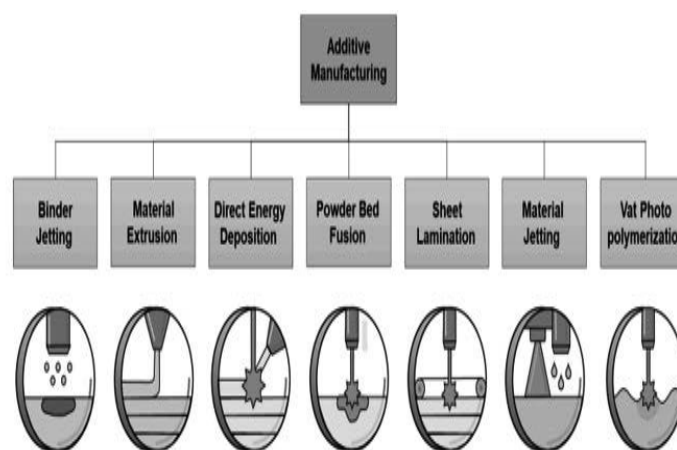


Figure 2. Main types of additive manufacturing (AM) processes according to ASTM F2792—12a

### 3.1 Exploring the Key 3D Printing Technologies Revolutionizing Additive Manufacturing

We are witnessing significant developments in the advancement of multifunctional materials through additive manufacturing techniques, enhanced by the Industry 4.0 revolution. Among the various existing techniques, the additive manufacturing (AM) process has gained much popularity over the last two decades and is one of the most revolutionary production techniques. The world of additive manufacturing, or 3D printing, has witnessed remarkable advancements in recent years, revolutionizing traditional manufacturing processes. This innovative technology has paved the way for the creation of complex and intricate objects, offering unprecedented design freedom and manufacturing possibilities. In this section, we will provide a brief introduction to some of the key 3D printing technologies that have played a pivotal role in shaping the field [5].

### 3.2 ME is a fascinating additive manufacturing (AM)

This process that uses a unique approach to create three-dimensional parts. Unlike other methods that rely on loose metal powder, ME machines use a flexible feedstock that resembles the media used in metal injection molding (MIM). This feedstock consists of metal powders bound together within a polymer matrix, creating a safer and more manageable material [6].

To visualize the process, let's look at a typical ME machine shown in Figure 3(a) his machine includes two essential components: the bonded powder raw material and a special coil containing the ceramic release material. Both are housed in a heated room to facilitate optimal printing conditions.

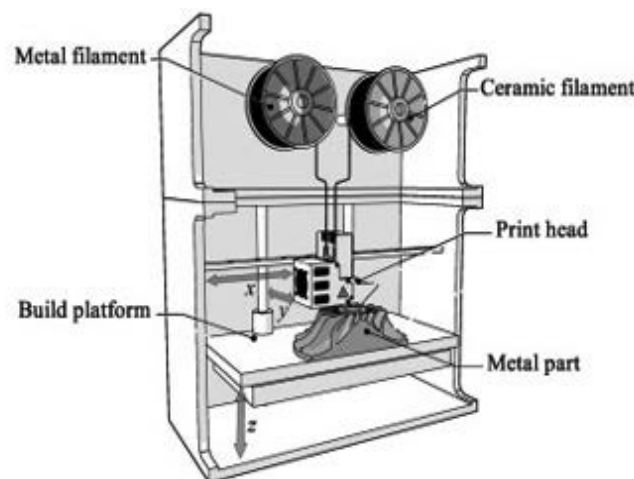


Figure 3. Schematic of a ME machine

During printing, the raw material is subjected to heat from the print head, which raises its temperature above the melting point of the polymer binders. Consequently, the softened material is extruded onto a hot build plate. As the build plate moves along the vertical z-axis, the material is deposited in successive layers, each equidistant from the previous layer. Simultaneously, the print head, attached to a gallery system, moves in the perpendicular (x, y) plane, forming the part into the desired shape [7].

This complicated process may seem strange at first glance, but it allows the creation of complex geometries and detailed structures. By carefully controlling the extraction and layering of the raw material, I enable the production of high-quality parts with exceptional precision and reliability.

### 3.3 BJ technology

Metal BJ can trace its origins to 1993 when the technology was developed by Sachs et al of MIT. and later patented as 'three-dimensional printing' (3DP), a universally accepted term for most AM technologies. The ExOne company obtained sole licensing of the MIT patent in 1996, however, it was revised in 2004, allowing Z Corporation the exclusive right to use it. Since then, and with the expiration of the patent, many companies have developed various BJ metal technologies [8]. Unlike other MAM machines that consume relatively large amounts of energy, BJ machines require much less resources, neither lasers nor electron beams are needed.

Although many variations of the original design have appeared since 1993, the ExOne and DM machines have been reviewed and mechanical properties compared [9].

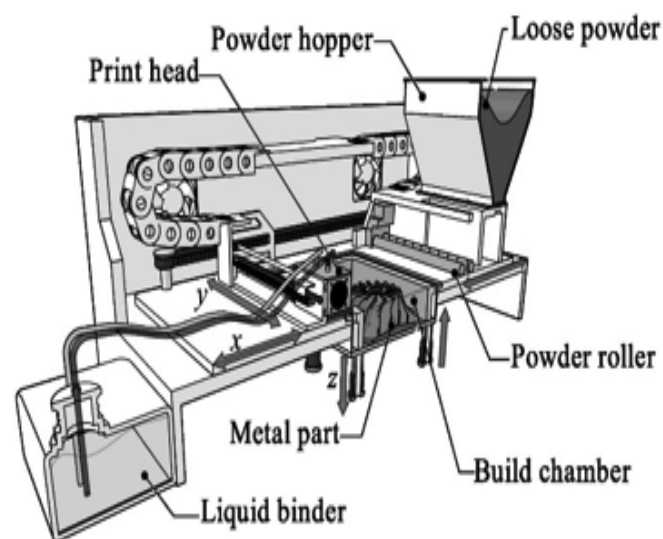


Figure 4. Schematic of a typical BJ machine

### 3.4. PBF technology

PBF involves fusing or fusing metal particles together using a thermal heat source. These include a build chamber with an inert atmosphere to reduce oxidation of the molten metal, a heat source for melting the metal powder particles, a mechanism to control melting, and a method for depositing and softening each layer of metal powder. The distinguishing feature of PBF systems is the energy source used, usually a laser or electron beam. Technologies that use electron beams are described as EBM processes [10].

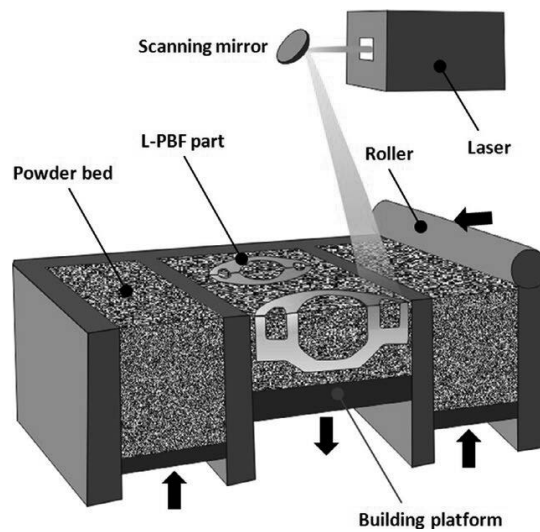


Figure 5. Schematic setup of L-PBF additive manufacturing technique

#### 4. ADDITIVE MANUFACTURING MATERIALS

In additive manufacturing (AM), the selection of materials is paramount for both understanding the manufacturing processes and leveraging the full capacity of this transformative technology. Initially, AM employed polymers, paper laminates, and waxes, which were instrumental in the developmental stages of the technology. Subsequently, the integration of plastics marked a significant progression, expanding the range of applicable materials to include metals, composites, and ceramics. These materials have continued to play a critical role in the advancement of AM. As the field evolves from rapid prototyping to rapid manufacturing, a comprehensive understanding of these materials—classified by their utility in AM—is essential. This analysis serves to illuminate the array of material options available to the industry and emphasizes the necessity for a meticulous assessment of their applications in various AM techniques.

This review elucidates the spectrum of materials accessible for industrial application within additive manufacturing (AM) and underscores the imperative for judicious analysis of their deployment across different AM methodologies. It emphasizes the breadth of material choices — spanning polymers, metals, composites, and ceramics — and their consequential role in AM's transition from prototyping to full-scale manufacturing. The pivotal role of materials is central to the innovation in additive manufacturing technology. The evolution and choice of materials — including metals, alloys, ceramics, polymers, composites, and biomaterials — are fundamental in defining the performance, capability, and quality of items created with this cutting-edge method [11]. The continuous progression of material science is a major underpinning that drives the advancement of this transformative tech.

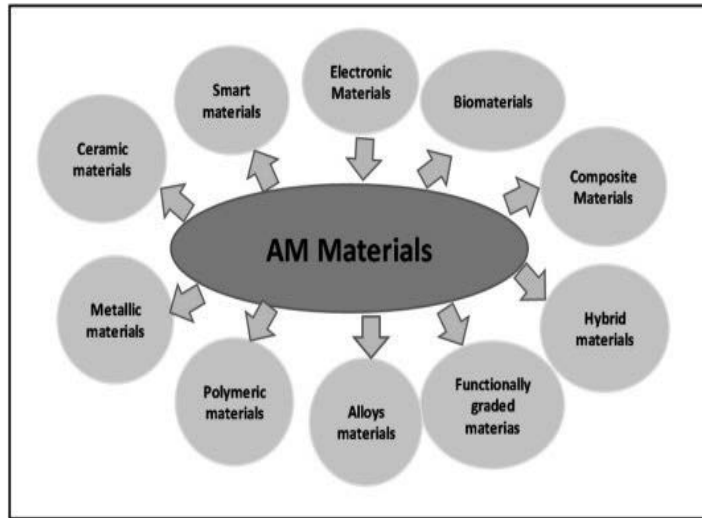


Figure 6. Illustrates the broad categorization of materials used in additive manufacturing (AM).

#### 4.1 Multi-materials for additive manufacturing

Each category represents a distinct group of materials with unique properties and characteristics. These materials contribute to the versatility and applicability of additive manufacturing across various industries [12].

According to the analyzed literature, the two most widely investigated categories of materials include polymers and metals, studied in 76 and 66 publications, respectively. Among polymers, the most commonly investigated MM include PLA, and PET to improve strength, stability, and functionality. For metals, the majority of research on MMs has been conducted on alloys of titanium, copper, aluminum, and steels for improving the functionality of designed components as well as enhancing characteristics such as hardness, conductivity, magnetic properties, wear resistance, strength, and thermal performance [13].

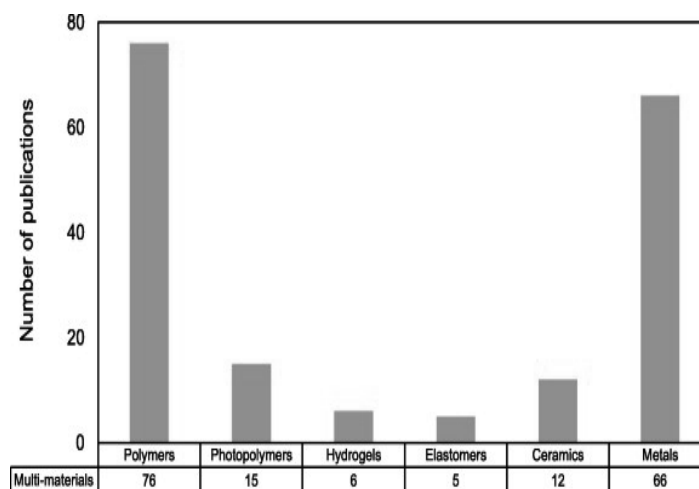


Figure 7. Materials combinations utilized in additive manufacturing of multi-materials literature.

The selection and advancement of materials are critical factors directly influencing the performance, responsiveness to different conditions, and overall quality of objects produced using 3D printing technology. Importance of Materials and Their Development in Additive Manufacturing:

- Standardization ensures quality and reliability.
- Regulatory compliance for critical applications.
- Material properties affect component performance.
- Unique materials enable complex designs and innovations.
- Customization for individual needs and medical applications.
- Compatibility with 3D printing technologies ensures efficiency.
- Material advances provide a competitive advantage.
- Cross-industry applications drive technology transfer.

#### 4.2 A Review of additive manufacturing processes

Additive manufacturing, also known as 3D printing, has transformed manufacturing by offering unprecedented opportunities for innovation and efficiency. The success of additive manufacturing heavily relies on understanding and optimizing various parameters throughout the process. These parameters play a pivotal role in determining the quality, functionality, and overall outcome of the printed parts. Here, we highlight the significance of these parameters in the additive manufacturing workflow [14]. Optimizing these parameters unleashes the full potential of additive manufacturing, enabling enhanced part quality, reduced production time, cost-effectiveness, and greater customization across industries. As AM technology continues to advance, a comprehensive understanding of these parameters will drive further innovation and integration of 3D printing into mainstream manufacturing practices [15].

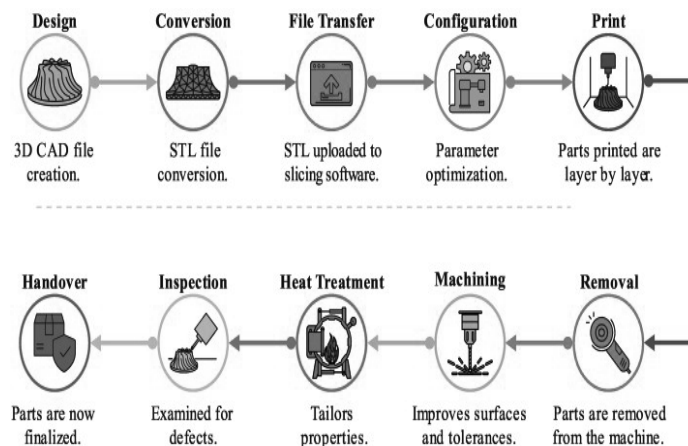


Figure 8. An example of a typical MAM process workflow

*Design:* Engineers and designers create a 3D model of the desired object using CAD software, leveraging the design freedom of AM for complex geometries and optimized designs. *File Conversion and Transfer:* The 3D model is converted to a suitable format (e.g., STL or AMF) and transferred to the AM machine via local connections or cloud-based platforms.

*Setup and Slicing:* AM machine parameters are set based on material and design requirements, and slicing software divides the 3D model into layers for printing [16].

*Additive Manufacturing (Printing):* The printing phase can vary greatly depending on the technology employed. Depending on the geometry and size,

*Post-Machining:* Some AM processes may require post-machining steps of support removal, cleaning, curing, or heat treatment to improve part properties slicing software divides the 3D model into layers for printing.

*Setup and Slicing:* AM machine parameters are set based on material and design requirements *Inspection:* Finished parts can also be subjected to external non-destructive tests (NDT) such as fluorescent liquid penetrant (PT), visual (VT), surface roughness, and dimensional accuracy. Internal radiography (RT), electromagnetic (ET), and ultrasonic (UT) to check for defects

*Delivery and Use:* Approved parts are ready to be delivered to end-users or integrated into the final product, reducing production time.

*File Conversion and Transfer:* The 3D model is converted to a suitable format (e.g., STL or AMF) and transferred to the AM machine via local connections or cloud-based platforms.

### 4.3 Investigating 3D Printer Parameters for Optimal Printing Quality

The realm of 3D printing has revolutionized traditional manufacturing methods by offering a dynamic approach to crafting objects with intricate designs and diverse materials. Achieving the finest printing quality necessitates a profound understanding of the various parameters that exert influence over the printing process. This study embarks on an exploration of these critical parameters, aiming to uncover their interplay and significance in achieving optimal 3D printing results.

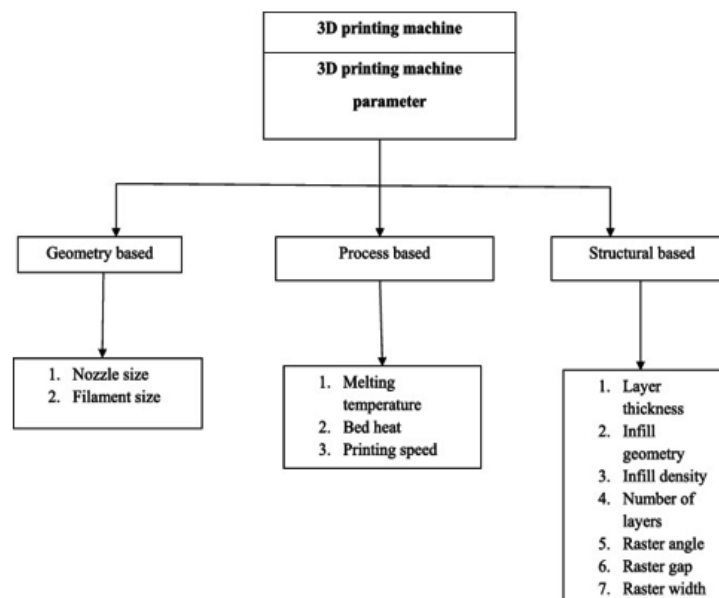


Figure 9. Printing Parameters

The diagram visually represents the three key parameters in 3D printing: Infill Density, Layer Height, and Printing Speed. Each parameter is depicted as follows:



- **Infill Density (%)**: Shown in red, this parameter indicates the percentage of the object's interior volume filled with material.
- **Layer Height (mm)**: Illustrated in blue, it represents the thickness of each layer that constitutes the object.
- **Printing Speed (mm/s)**: Displayed in green, this parameter reflects the speed at which the printing process occurs [17].

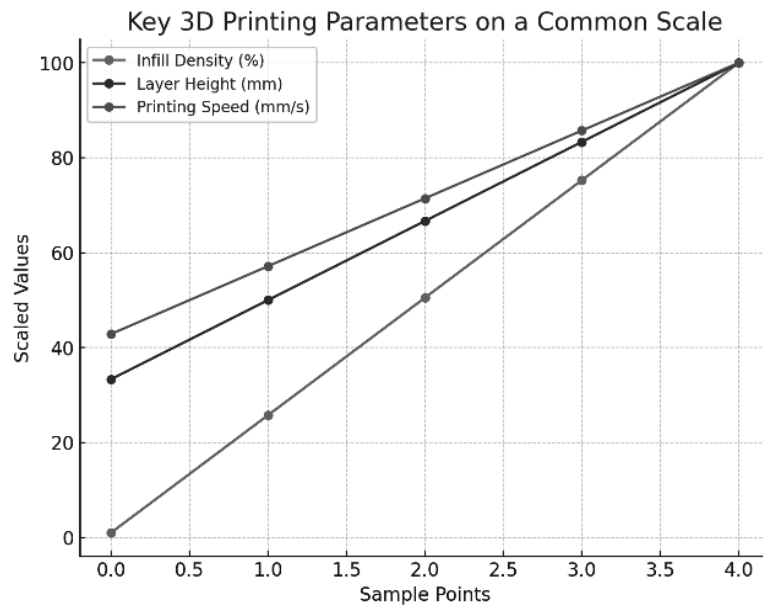


Figure10. Literature Review Summary: 3D Printing Trends

#### 4.4 Integrating CAD Modeling and 3D Scanning: Bridging Design and Reality in Additive Manufacturing

In recent years, there has been a significant improvement in additive manufacturing technologies and researchers have explored its applications in various fields of engineering and medicine. Additive manufacturing is a type of manufacturing technology in which materials such as powder, plastic or metal are deposited layer by layer to fabricate the 3D model from the Computer-Aided Design (CAD) model. This method is different from traditional manufacturing technology because instead of removing material; adds materials layer by layer. (18)

Computer-aided design (CAD) is a digital tool used in additive manufacturing to create detailed and precise 2D and 3D models. CAD software allows designers and engineers to design, modify, and visualize objects before they are physically manufactured. It provides the flexibility to manipulate shapes, dimensions, and materials, enabling the creation of intricate and customized designs. CAD plays a crucial role in translating creative concepts into printable models for additive manufacturing. Scanning involves capturing real-world objects or environments using specialized equipment such as 3D scanners. The scanned data is then converted into digital 3D models that can be used for various purposes, including additive manufacturing [19].

## **5. 3D PRINTING AND INDUSTRY 4.0**

Industry 4.0, the fourth industrial revolution, is characterized by the integration of advanced technologies, including the synergy of additive manufacturing (AM) with the digital interconnectivity of the Internet of Things (IoT), which facilitates unprecedented levels of automation and machine-to-machine communication. Keeping in view the technical aspects of 3D printing and the goals of Industry 4.0, 3D printing is an important component in the concept of Industry 4.0 [20]. Further, the recent advancements in the area of 4D Printing wherein the development of smart materials has become possible have further increased the role of additive manufacturing in Industry 4.0.

While the concept of Industry 4.0 also involves the digitalization of industries, 3D printing can play a vital role in the Industry 4.0 scenario. Industry 4.0 also aims to develop an industrial setup wherein, the systems are autonomous and there is sufficient interconnectivity amongst the employees, machines, suppliers, and end users. In the aforementioned discussion, we have included the different materials, processes, and technologies related to 3D Printing [21]. The various benefits of 3D Printing such as digital data transfer, remote access, need for minimum human intervention, ability to develop complex geometries and smart materials, less wastage, and fewer post-processing requirements shall help to achieve the goals of Industry 4.0.

### **5.1. Challenges and potential future applications**

In future systems, designers can generate complex multi-material objects simply by specifying design performance. Efficient and high-fidelity simulation algorithms will be required to analyze and synthesize complex forms, constraints, and specifications in physics, movement, and other functions [22].

Generating patterns that can have increasingly complex shapes and material composition is an open research question. Consequently, new methods for geometric calculation such as layers depth normal images using distance fields and adaptive strategies are being developed for 3D model renderings for AM. New geometric modeling and computational methods are necessary for future product components whose shapes and material composition would be orders of magnitude more complex than the current product designs [23]. Geometric representations are also necessary for optimizing material support during production, designing for specific physics properties, and AM-based repair/reproduction. The advantages that AM claims to differentiate it from traditional manufacturing need further research for it to become the more practical alternative. New research towards these developments is slow (especially at the interfaces of research laboratories and commercial machine manufacturers) due to the traditional gaps between academic and industrial settings. Industry-academic exchange faces further challenges as the industry has now developed the ability to produce machines that are complex, expensive, and not open architecture.

While AM continues to provide innovation in various industry sectors, there are also many new opportunities in research and development for the application of the technology [24].

Figure: 8 highlights four areas of interest, including innovation services, bio-inspired design, robotic fabrication, and machine learning, that are relevant to advancing AM using DfAM frameworks.

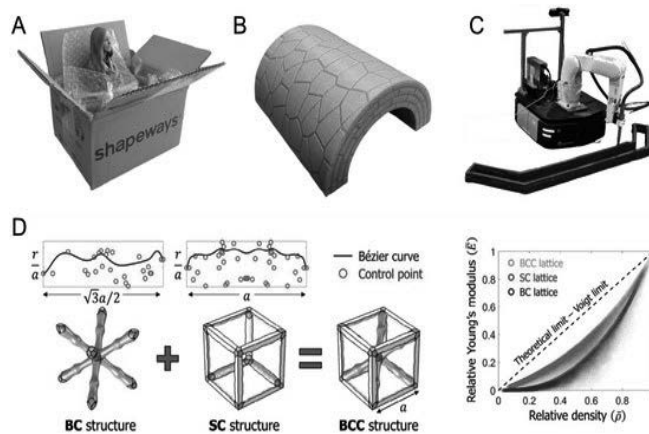


Figure 8. Future outlook in highlighted areas for DfAM, including emerging (A) innovation services, (B) bio-inspired design, (C) robotic fabrication, and (D) machine learning approaches.

## CONCLUSION

This paper provides a thorough examination of Additive Manufacturing (AM) and its transformative impact on modern manufacturing practices. It underscores the vital research in manufacturing processes, materials, and product design necessary as product complexity grows. Highlighting the ASTM F2792-12a standard, it delves into the categorization of AM processes into binder-based, high-energy heat source, and liquid-based methods, elucidating the diversity of technologies in the AM field. These categories underscore the capability of AM in producing metal parts and complex designs with groundbreaking techniques.

The importance of material selection and its progress is emphasized, affecting the functionality and excellence of 3D-printed objects. Considerations such as material properties, customization, technological compatibility, durability, cost, cross-industry applications, and regulatory adherence are discussed, demonstrating materials' crucial role in AM's success.

The workflow of additive manufacturing is elaborated, starting with CAD software, which empowers the creation of complex models, followed by detailed descriptions of conversion, transfer, setup, cutting, and printing stages. The significance of technology and software in the AM process is accentuated, along with post-processing, inspection, and delivery stages that guarantee the production of dependable, high-quality components suitable for final product incorporation.

As AM technology advances, it signals a significant shift from traditional manufacturing methods, providing innovative responses to current challenges. The paper's comprehensive literature review advances our understanding of AM and actively forecasts upcoming developments in the sector. Future advancements are expected to exploit AM's full potential for creating intricate multi-material items, tailored to specific design requirements. The creation of effective simulation algorithms is projected to be crucial for the evaluation and creation of complex forms and meeting precise physical specifications, which will influence AM's future direction in the manufacturing sector.

**BIBLIOGRAPHY**

1. "Additive manufacturing technologies: state of the art and trends." In *Additive Manufacturing Handbook: Product Development for the Defense Industry*. CRC Press, 2017.
2. Additive manufacturing: scientific and technological challenges, market uptake and opportunities." *Materials Today*, 21, 2018.
3. Thompson, M.K.; Moroni, G.; Vaneker, T.; Fadel, G.; Campbell, R.I.; Gibson, I.; Bernard, A.; Schulz, J.; Graf, P.; Ahuja, B.; et al. "Design for Additive Manufacturing: Trends, opportunities, considerations, and constraints." *CIRP Annals - Manufacturing Technology*, 2016, 65, pp. 737–760.
4. Technical Committee AMT/8. "BS EN ISO/ASTM 52900: additive manufacturing - general principles - terminology." International Standard, 2017, pp. 1-30.
5. Al-Dulimi, Z.; Wallis, M.; Tan, D.K.; Maniruzzaman, M.; Nokhodchi, A. "3D printing technology as innovative solutions for biomedical applications." *Drug Discovery Today*, 2020.
6. Characterization of 17-4 PH processed via bound metal deposition (BMD)." In *Minerals, Metals & Materials Series*, Springer, 2020.
7. Directed energy deposition processes." In *Additive Manufacturing Technologies*, Springer, New York, 2015, pp. 245-268, 10.1007/978-1-4939-2113-3\_10.
8. Hitzler, L.; Hirsch, J.; Heine, B.; Merkel, M.; Hall, W.; Öchsner, A. "On the anisotropic mechanical properties of selective laser-melted stainless steel.
9. Gibson, I.; Rosen, D.; Stucker, B. "Additive Manufacturing Technologies. 3D Printing, Rapid Prototyping, and Direct Digital Manufacturing," 2nd edition, Springer: New York, 2015.
10. Flexural, pull-out, and fractured surface characterization for multi-material 3D printed functionally graded prototype." *Journal of Composite Materials*, 54, 2019.
11. Zheng, X.; Williams, C.; Spadaccini, C.M.; Shea, C. "Perspectives on multi-material additive manufacturing." *Journal of Materials Research*, Volume 36, 2021, Pages 3549–3557.
12. Multi-material 3D printing: The relevance of materials affinity on the boundary interface performance." *Additive Manufacturing*, 23, 2018, pp. 45-52, 10.1016/J.ADDMA.2018.06.027.
13. Yin, J.; Li, M.; Dai, G.; Zhou, H.; Ma, L.; Zheng, Y. "3D printed multi-material medical phantoms for needle-tissue interaction modelling of heterogeneous structures." *Journal of Bionic Engineering*, 18, 2021, pp. 346-360, 10.1007/S42235-021-0031-1.
14. Hopkinson, N.; Hague, R.J.M.; Dickens, P.M. "Rapid manufacturing: an industrial revolution for the Digital Age," 2006, 10.1002/0470033991.
15. Sheoran, A.J.; Kumar, H. "Fused Deposition modeling process parameters optimization and effect on mechanical properties and part quality: Review and reflection on present research." *Materials Today: Proceedings*, 2020, 21, pp. 1659–1672.
16. Kam, M.; İpekçi, A.; Şengül, Ö. "Investigation of the effect of FDM process parameters on mechanical properties of 3D printed PA12 samples using Taguchi method." *Journal of Thermoplastic Composite Materials*, 2023, 36, pp. 307–325.
17. Bintara, R.D.; Lubis, D.Z.; Pradana, Y.R.A. "The effect of layer height on the surface roughness in 3D Printed Polylactic Acid (PLA) using FDM 3D printing." Published under license by IOP Publishing Ltd.

18. Diegel, O.; Singamneni, S.; Reay, S.; Withell, A. "Tools for Sustainable Product Design: Additive Manufacturing." *Journal of Sustainable Development*, 3(3), 2010, pp. 68-75.
19. Smith, J.; Doe, A. "The impact of 3D printing on the evolution of Industry 4.0." *Journal of Innovative Manufacturing Technologies*, 35(3), 2021, pp. 588-602.
20. Verner, I.; Merksamer, A. "Digital design and 3d printing in technology teacher education." *Procedia CIRP*, 2015, 36, pp. 182–186.
21. World manufacturing forum report, skills for the future of manufacturing: Technical report." *World Manufacturing Forum*, 2019.
22. Augmented reality tools for industrial applications: What are potential key performance indicators and who benefits?"
23. Kantaros, A.; Diegel, O.; Piromalis, D.; Tsaramirsis, G.; Khadidos, A.O.; Khadidos, A.O.; Khan, F.Q.; Jan, S. "3D printing: Making an innovative technology widely accessible through maker spaces and outsourced services." *Materials Today Proceedings*, 2022, 49, pp. 2712–2723.
24. Tran, P.; Ngo, T.D.; Ghazlan, A.; Hui, D. "Bimaterial 3D printing and numerical analysis of bio-inspired composite structures under in-plane and transverse loadings." *Composites Part B: Engineering*, 2017, 108, pp. 210–223.modeling



17th-19th June 2024  
Gliwice, Poland

DEPARTMENT OF ENGINEERING MATERIALS AND BIOMATERIALS  
FACULTY OF MECHANICAL ENGINEERING  
SILESIA UNIVERSITY OF TECHNOLOGY

## INTERNATIONAL STUDENTS SCIENTIFIC CONFERENCE

### Effect of niobium content on corrosion resistance and hardness of CoCrFeNiNb<sub>x</sub> high entropy alloys

Jakub Bicz<sup>a</sup>, Wojciech Łoński<sup>b</sup>, Katarzyna Młynarek-Żak<sup>c</sup>, Rafał Babilas<sup>b</sup>

<sup>a</sup> Student of Silesian University of Technology, Faculty of Mechanical Engineering  
e-mail: jakubic839@student.polsl.pl

<sup>b</sup> Silesian University of Technology, Faculty of Mechanical Engineering, Department of Engineering Materials and Biomaterials

<sup>c</sup> Silesian University of Technology, Faculty of Mechanical Engineering, Department of Engineering Processes Automation and Integrated Manufacturing Systems

**Abstract:** In this work, CoCrFeNiNb<sub>x</sub> high entropy alloys with variable niobium content ( $x = 0.25, 0.45$  and  $0.65$ ) were prepared using the induction melting method and then solidified with low cooling rate in Al<sub>2</sub>O<sub>3</sub> crucibles. The structure of the alloys studied was investigated with the use of light microscopy. The electrochemical measurements were performed using 2 and 5% NaCl solutions at a temperature 25°C to determine corrosion resistance of the prepared alloys. Mechanical properties were examined by the Vickers microhardness test. The increasing content of niobium caused an increase of corrosion resistance. Simultaneously, increase in niobium content correlated with higher hardness value.

**Keywords:** High entropy alloys, Microstructure, Hypoeutectic, Hypereutectic, Corrosion resistance, Electrochemical measurements

## 1. INTRODUCTION

High entropy alloys (HEAs) are being new concept of alloys design, introduced independently by the Yeh et al. [1] and Cantor et al. [2] in the year 2004. Differently from conventional alloys, usually based on one dominant element and alloying elements, these alloys are composed of five or more principal elements, in equimolar or near equimolar ratios – according to most commonly used definition, ranging between 5 and 35 at.%. These alloys can also contain alloying additions, with content less than 5 at.%. Novel composition lead to another feature, which distinguishes them from conventional alloys – which is the exceptionally high value of configurational entropy. This is due to the fact that configurational entropy of alloy reaches maximum when elements constituting these are in equimolar ratios, and increases with the number of alloy constituents. It was assumed, that as HEAs are classified alloys with value of configurational entropy exceeding  $1.5 R$  (where  $R$  represents the gas constant) [3-5].

HEAs attracted great attention due to their unique properties, in many cases outperforming those of conventional alloys. They exhibit enhanced mechanical properties, such as high strength and higher fracture toughness. HEAs open up new capabilities in the field of advanced structural materials showing enhanced resistance to corrosion and outstanding high-temperature resistance [6,7]. An example of a beneficial properties combination is AlCoCrFeNiSi<sub>0.75</sub> alloy connecting high hardness – exceeding 850 HV, with excellent corrosion resistance – evidenced by low value of corrosion current density recorded during potentiodynamic polarization measurements in 3.5% NaCl solution [8]. It is considered, that HEAs can meet demand for high-performance materials in areas such as energy generation and aviation, for example replacing the nickel superalloys in gas turbines [6].

The concept of high-entropy alloys is intrinsically connected with four “core effects”, which contributes to its exceptional properties. These effects include: high entropy effect, sluggish diffusion, severe lattice distortion, and the so-called cocktail effect [3].

Initial expectations imply that alloys with this composition may have a complex microstructure composed of numerous intermetallic phases, thus restricting possibilities for their practical use. However, observations proved that HEAs often exhibit much simpler microstructures due to formation of solid solution phases. High configurational entropy exhibited by these alloys contributes to enhancing the mutual solubility of constituent elements, allowing for the formation of solid solution phases, and simultaneously inhibiting the formation of intermetallic phases. Furthermore, many of the reported HEAs exhibit single phase solid solution with face-centered cubic (FCC), body-centered cubic (BCC) and hexagonal close-packed structures (HCP) [3,4].

Severe lattice distortion arises from the atomic size difference of atoms constituting the crystal lattice of high entropy alloys. This effect contributes to increase in hardness due to solution hardening effect. Lattice distortion, which causes electron scattering, also reduces electrical conductivity, and similarly, thermal conductivity by disrupting phonon flux [3,4,7].

The slow diffusion effect is connected with the diversification of atoms present in the crystal lattice of HEAs. Because of variability in arrangement of atoms, the lattice potential energy between the lattice sites significantly varies. Numerous sites with low potential energy present in the lattice serve as "traps" contributing to the low diffusion rate. Sluggish diffusion affects phase nucleation, growth, and distribution, thus influencing microstructure and properties. It also increases recrystallization temperature and improves creep resistance [3,7,9].

The cocktail effect is used to highlight the influence of synergistic interactions between the constituent elements on the properties of the alloy obtained. It implies that the effect of mutual interactions between the constituent elements and severe lattice distortion can result in the acquisition of specific properties, which can significantly differ from predictions based on the influence of individual elements [3,4].

HEAs can be classified into alloy families due to their constituent elements – among these, the most widely explored are alloys based on 3d transition metals and refractory metals. A typical example of the 3d transition metal HEA is the CoCrFeMnNi, also known as Cantor alloy – being the first reported 5-component alloy with a single-phase solid solution structure [1]. Based on the Cantor alloy, CoCrFeNi-X alloying system has been developed that is currently one of the most intensively studied [4,10].

The structure type is the most important factor determining the mechanical properties. High entropy alloys with single-phase face-centered cubic structure, such as CoCrFeNi alloy, exhibit high ductility and relatively low strength. On the contrary, those with body-centered cubic structure have superior strength, however, with simultaneously limited plasticity. One of the

methods to achieve a balance between strength and ductility is modification of alloys with FCC structure by introducing elements causing the formation of intermetallic phases. In the case of the CoCrFeNi alloy, this effect can be obtained through the addition of niobium. Due to the larger atomic radius, niobium increases lattice distortion, in larger amounts causing destabilization of the solid solution phase resulting in the formation of intermetallic phases. Niobium addition affects also the corrosion behavior of these alloys, contributing to the formation of a passive layer consisting of niobium oxides on their surface [5,11,12]. Accordingly, the aim of this paper is to investigate the corrosion behavior of hypoeutectic, near eutectic and hypereutectic CoCrFeNiNb<sub>x</sub> (where x = 0.25, 0.45 and 0.65) high entropy alloys prepared from the liquid state using induction melting method. In order to determine influence of niobium content on mechanical properties of the investigated alloys, the Vickers hardness measurements were also conducted.

## 2. MATERIALS AND METHODS

The alloys were prepared by the induction melting method using elements with the 99,99 wt.% purity. Process was conducted using a NG-40 induction generator under argon atmosphere. Ingots were solidified with low cooling rate, crucibles made of Al<sub>2</sub>O<sub>3</sub> were used. For microstructural investigations, a Zeiss Axio Observer light microscope was used. The hardness of the alloys was measured using a Future Tech FM-7000 Vickers hardness tester under a load of 1000 g for a 10 s dwell time. In order to evaluate the corrosion resistance, the samples were subjected to potentiodynamic polarization measurements, conducted in the 2 and 5% NaCl solution. An Autolab 302N potentiostat equipped with a three-electrode measuring system was used for the study. The saturated calomel electrode (SCE) was used as the reference electrode, a platinum wire was the counter electrode, and the studied sample was the working electrode. During the electrochemical measurements, changes in open-circuit potential ( $E_{OCP}$ ) were recorded in stabilization time of 3600 s, followingly with measurements of polarization in range of -400 mV to 400 mV, with a scan rate of 0.001 V/s. Based on the obtained results, the corrosion potential ( $E_{corr}$ ) and corrosion current density ( $j_{corr}$ ) were determined with the use of the Tafel extrapolation method.

## 3. RESULTS AND DISCUSSION

With the increasing content of niobium, evolution in the microstructure is clearly seen. In case of CoCrFeNiNb<sub>0.25</sub> alloy (Figure 1a) structure is mainly composed of bright dendrites, homogenously distributed in a dark matrix. Eutectic lamellar structures can be seen in interdendritic regions. For CoCrFeNiNb<sub>0.45</sub> alloy, refinement of microstructure can be observed resulting from significantly higher content of eutectic structures (Figure 1b). Microstructure is comprised of regions with fine eutectic lamellar structures located between larger dendrites. Contrastingly to alloys with lower content of niobium, in case of CoCrFeNiNb<sub>0.65</sub> dendrites are composed of darker phase, while matrix is brighter (Figure 1c). According to the publication of Chanda et al. [11] brighter phase can be identified as face-centered cubic solid solution of CoCrFeNi with small amount of Nb, while darker phase is intermetallic Laves phase with hexagonal close-packed structure. Consequently, dendritic structures in case of CoCrFeNiNb<sub>0.25</sub> and CoCrFeNiNb<sub>0.45</sub> alloys correspond to the solid



solution phase, while those of  $\text{CoCrFeNiNb}_{0.65}$  are constituted of Laves phase indicating that hypoeutectic structures was obtained for two first alloys compositions. Alloy with the highest content of niobium can be in this case described as hypereutectic. Significant content of eutectic lamellar structure in case of the  $\text{CoCrFeNiNb}_{0.45}$  alloy indicates that their composition is close to eutectic.

In order to evaluate the dependence between the content of niobium and corrosion behaviour of investigated alloys, electrochemical measurements in chloride solutions of different concentrations were conducted. In result of open-circuit potential measurement in the milder environment of 2% NaCl solution – significantly higher values of  $E_{\text{OCP}}$  are obtained for alloys with higher content of niobium, for both assuming near zero values (Figure 2). The parameters obtained as result of potentiodynamic polarization measurements (Figure 3), conducted in 2% NaCl solution, were summarized in Table 1. For  $\text{CoCrFeNiNb}_{0.45}$  and  $\text{CoCrFeNiNb}_{0.65}$  alloys, significant decrease in corrosion current density values can be noticed – exceeding two orders of magnitude, with simultaneously significantly higher polarization resistance values. The corrosion potential are shifted in the positive direction, comparing to the  $\text{CoCrFeNiNb}_{0.25}$  alloy. The lowest value of corrosion current density and the highest value of polarization resistance were obtained for  $\text{CoCrFeNiNb}_{0.65}$  indicating the highest corrosion resistance in this environment. The alloy with highest content of niobium exhibits ability to passivation indicated by stabilization of the corrosion current value in the anodic branch of the curve. However, the current density rapidly increases at the last stage of measurement, which can be linked to the breakage of the passivation layer. Breakage potential can be estimated to 0.39 V.

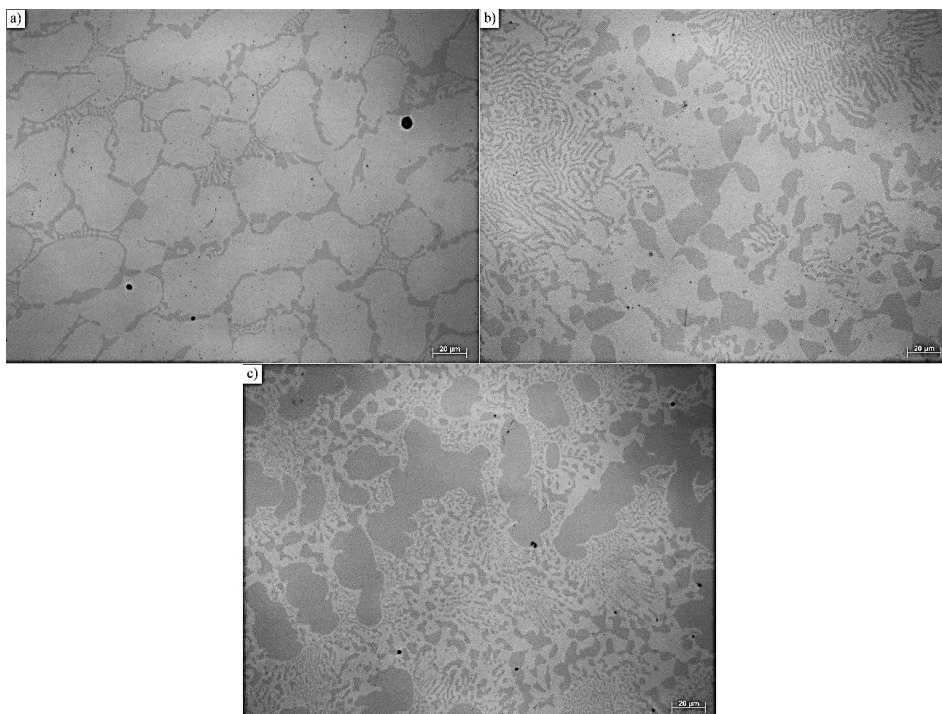


Figure 1. Microstructures of tested alloys: a)  $\text{CoCrFeNiNb}_{0.25}$ , b)  $\text{CoCrFeNiNb}_{0.45}$  and c)  $\text{CoCrFeNiNb}_{0.65}$ .

In case of measurements conducted in 5% NaCl solution, positive shifts of open-circuit potential with increasing content of niobium can be observed (Figure 4). Significant fluctuations of the potential values during measurement can be noticed for the CoCrFeNiNb<sub>0.65</sub> alloy. Characteristic parameters obtained as a result of potentiodynamic polarization measurements (Figure 5) are summarized in Table 2. A clear trend can be seen – increasing content of niobium lead to decrease of corrosion current density and increasing polarization resistance. Beneficial effect of the niobium addition is further evidenced by positive shift in corrosion potential values. It is worth noting that there is a significant difference in corrosion current density and polarization resistance for CoCrFeNiNb<sub>0.65</sub> alloy compared to CoCrFeNiNb<sub>0.25</sub> and CoCrFeNiNb<sub>0.45</sub> alloys. All of the samples evaluated in this environment exhibit ability to passivation, indicated by sustaining of nearly constant levels of current densities in the last stage of measurement. The most beneficial characteristics are obtained for CoCrFeNiNb<sub>0.65</sub>, exhibiting the lowest corrosion current density and the highest polarization resistance values.

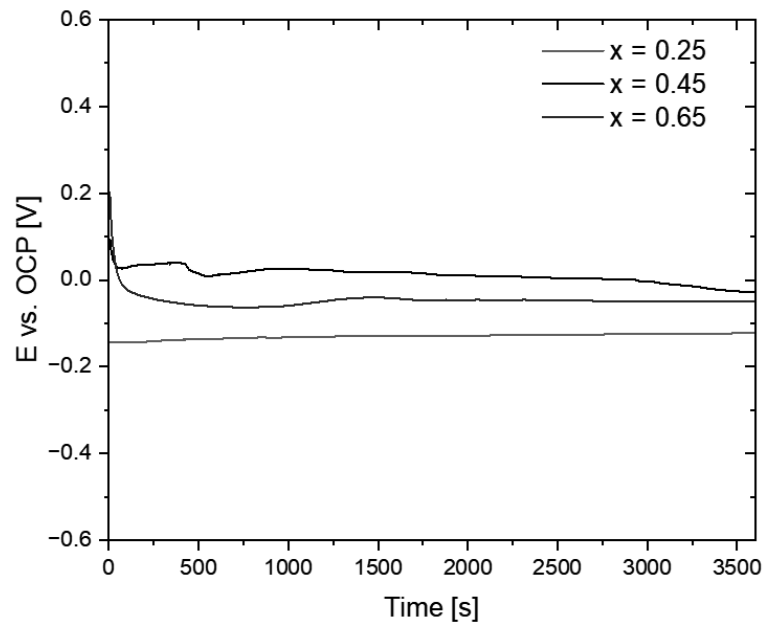


Figure 2. Open-circuit potential as a function of time for CoCrFeNiNb<sub>x</sub> ( $x = 0.25, 0.45$  and  $0.65$ ) alloys measured in 2% NaCl solution at 25°C.

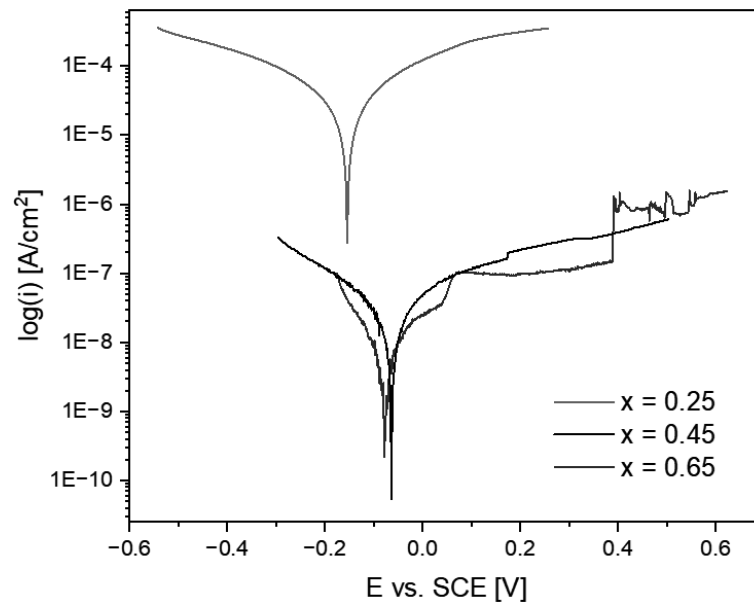


Figure 3. Potentiodynamic polarization curves for  $\text{CoCrFeNiNb}_x$  ( $x = 0.25, 0.45$  and  $0.65$ ) alloys measured in 2% NaCl solution at 25°C.

Table 1. Results of the electrochemical measurements conducted in 2% NaCl solution at 25°C.

Alloy	$E_{\text{corr}}$ [V]	$j_{\text{corr}}$ [ $\mu\text{A}/\text{cm}^2$ ]	$R_p$ [ $\text{k}\Omega\text{cm}^2$ ]
$\text{CoCrFeNiNb}_{0.25}$	-0.154	338	0.79
$\text{CoCrFeNiNb}_{0.45}$	-0.063	1.69	324
$\text{CoCrFeNiNb}_{0.65}$	-0.079	0.065	1 138

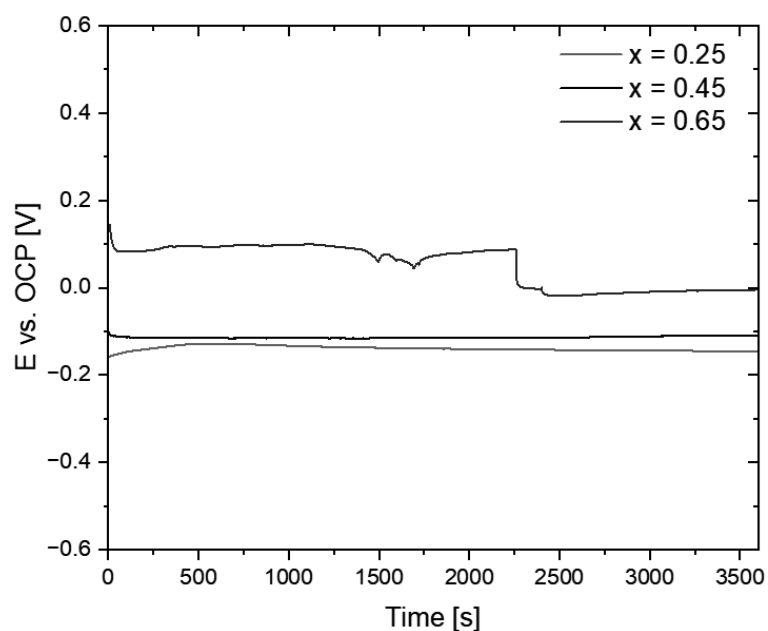


Fig. 4. Open-circuit potential as a function of time for  $\text{CoCrFeNiNb}_x$  ( $x = 0.25, 0.45$  and  $0.65$ ) alloys measured in 5% NaCl solution at 25°C.

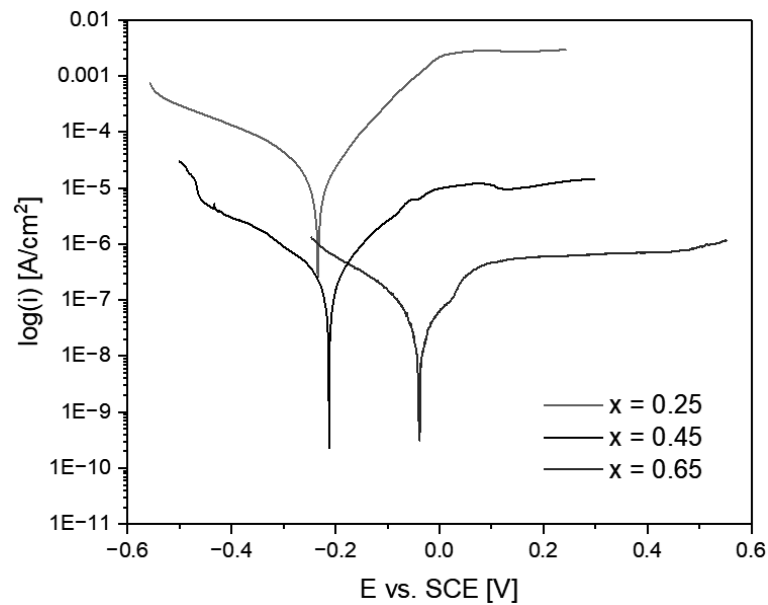


Figure 5. Potentiodynamic polarization curves for  $\text{CoCrFeNiNb}_x$  ( $x = 0.25, 0.45$  and  $0.65$ ) alloys measured in 5% NaCl solution at 25°C.

Table 2. Results of the electrochemical measurements conducted in 5% NaCl solution at 25°C.

Alloy	$E_{\text{corr}}$ [V]	$j_{\text{corr}}$ [ $\mu\text{A}/\text{cm}^2$ ]	$R_p$ [ $\text{k}\Omega\text{cm}^2$ ]
$\text{CoCrFeNiNb}_{0.25}$	-0.234	72.4	0.85
$\text{CoCrFeNiNb}_{0.45}$	-0.212	5.33	23.54
$\text{CoCrFeNiNb}_{0.65}$	-0.038	1.46	196.32

Significant effect of niobium content on the hardness of the investigated alloys can be also observed (Figure 6). An increase in niobium content, causing a rise in the volume content of hard intermetallic phases in the microstructure, contributes to significantly higher hardness values. In particular, substantial differences can be noticed comparing  $\text{CoCrFeNiNb}_{0.25}$  (301 HV) and  $\text{CoCrFeNiNb}_{0.45}$  (452 HV) alloys. The highest hardness was exhibited by the  $\text{CoCrFeNiNb}_{0.65}$  alloy (534 HV). In case of this alloy, it is worth noting that there is also a significant variation in the hardness values, probably connected to the larger size of Laves phases constituting the dendrites present in the microstructure and simultaneous occurrence of a soft solid solution matrix.

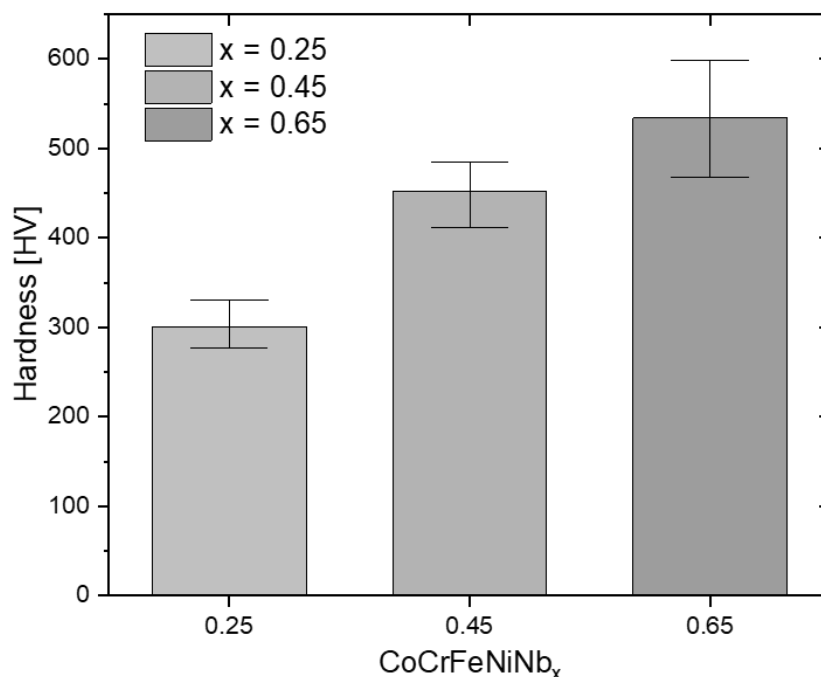


Figure 6. Vickers hardness of CoCrFeNiNb<sub>x</sub> ( $x = 0.25, 0.45$  and  $0.65$ ) alloys with increasing content of niobium.

#### 4. CONCLUSIONS

The addition of niobium has a significant effect on the microstructure of studied high entropy alloys. All of the investigated alloys exhibit dual-phase dendritic microstructures, with the presence of eutectic lamellae structures. The volume of eutectic structures is correlated to the niobium content – reaching a maximum in case of CoCrFeNiNb<sub>0.45</sub> ingot, among the alloys considered.

Based on conducted measurements, it can be stated that increase in the content of niobium contribute to improvement in the corrosion resistance of the investigated alloys. For measurements carried out in a milder environment of 2% NaCl solution, both CoCrFeNiNb<sub>0.45</sub> and CoCrFeNiNb<sub>0.65</sub> alloys exhibited low values of the corrosion current density and near-zero values of the corrosion potential, indicating excellent corrosion resistance in this environment. In more aggressive environment of 5% NaCl solution, the difference between studied alloys is more pronounced, emphasizing the effect of higher content of niobium on corrosion resistance.

Based on the obtained results, it can be stated that variance in the content of niobium substantially affects the mechanical properties of investigated alloys. Evolution of the microstructure caused by increasing content of niobium results in a substantial increase in its hardness.

#### 5. ACKNOWLEDGEMENTS

The work was supported by the National Science Centre of Poland under research project no. 2022/47/B/ST8/02465.

**BIBLIOGRAPHY**

1. B. Cantor, I. T. H. Chang, P. Knight, A. J. B. Vincent, Microstructural development in equiatomic multicomponent alloys, *Material Science and Engineering A* 375–377, 2004, p. 213–218.
2. J. W. Yeh, S. K. Chen, S. J. Lin, J. Y. Gan, T. S. Chin, T. T. Shun, Nanostructured high-entropy alloys with multiple principal elements: novel alloy design concepts and outcomes, *Advanced Engineering Materials* 6 (5), 2004, p. 299–303.
3. B.S. Murty, J.W. Yeh, S. Ranganathan, P.P. Bhattacharjee, *High Entropy Alloys – second edition*, Elsevier, Amsterdam, 2019.
4. D.B. Miracle, O.N. Senkov, A critical review of high entropy alloys and related concepts, *Acta Materialia* 122, 2017, p. 448–511.
5. Y. Zhang T.T. Zuo, Z. Tang, M.C. Gao, K.A. Dahmen, P.K. Liaw, Z.P. Lu, Microstructures and properties of high-entropy alloys, *Progress in Materials Science* 61, 2014, p. 1–93.
6. T. Sonar, M. Ivanov, E. Trofimov, A. Tingaev, I. Suleymanova, An overview of microstructure, mechanical properties and processing of high entropy alloys and its future perspectives in aeroengine applications, *Materials Science for Energy Technologies* 7, 2024, p. 35–60.
7. B. Yu, Y. Ren, Y. Zeng, W. Ma, K. Morita, S. Zhan, Y. Lei, G. Lv, S. Li, J. Wu, Recent progress in high-entropy alloys: A focused review of preparation processes and properties, *Journal of Materials Research and Technology* 29, 2024, p. 2689–2719.
8. W. Łoński, M. Spilka, M. Kaździółka-Gaweł, P. Gębara, A. Radoń, T. Warski, K. Młynarek-Żak, R. Babilas, The effect of cooling rate on the structure and selected properties of AlCoCrFeNiSi<sub>x</sub> (x = 0; 0.25; 0.5; 0.75) high entropy alloys, *Journal of Alloys and Compounds* 905, 2022, p. 1–10
9. S. Salifu, P. A. Olubambi, Effects of fabrication techniques on the mechanical properties of high entropy alloys: A review, *International Journal of Lightweight Materials and Manufacture* vol. 7, issue 1, 2024, p. 97–121.
10. An-Chen Fana, Jian-Hong Li, Ming-Hung Tsai, On the phase constituents of four CoCrFeNiX (X = Y, Ti, Zr, Hf) high-entropy alloys after prolonged annealing, *Journal of Materials Research and Technology* 9 (5), 2020, p. 11231–11243.
11. B. Chanda, J. Das, Composition Dependence on the evolution of nanoeutectic in CoCrFeNiNbx (0.45 ≤ x ≤ 0.65) high entropy alloys, *Advanced Engineering Materials*, 2017, 1700908.
12. W. Wang, S. Yuan, J. Chen, X. Li, Z. Niu, R. Wei, T. Wang, T. Zhang, S. Guan, F. Li, C. Chen, Corrosion in Cr-Fe-Co-Ni-Nb hypoeutectic and hypereutectic high entropy alloys, *Materials Today Communications* 31, 2022, 103612.



17th-19th June 2024  
Gliwice, Poland

DEPARTMENT OF ENGINEERING MATERIALS AND BIOMATERIALS  
FACULTY OF MECHANICAL ENGINEERING  
SILESIA UNIVERSITY OF TECHNOLOGY

## INTERNATIONAL STUDENTS SCIENTIFIC CONFERENCE

### Degradation of thermoplastic based composite materials reinforced with natural particulates

Konrad Bogdał<sup>a</sup>, Agnieszka J. Nowak<sup>b</sup>

<sup>a</sup> Absolwent Politechniki Śląskiej, Wydział Mechaniczno Technologiczny, Management and engineering production; e-mail: bogdalkonrad@gmail.com

<sup>b</sup> Politechnika Śląska Wydział Mechaniczny Technologiczny, Laboratorium Naukowo-Dydaktyczne Nanotechnologii i Technologii Materiałowych, ul Towarowa 7a, 44-100 Gliwice; e-mail: agnieszka.j.nowak@polsl.pl

**Abstract:** This paper addresses issues related to polymer-based composite materials reinforced with natural fibres. In addition, it describes the types of recycling used for polymers. A scientific investigation connected to this study area was conducted on bioplastic's water absorption and degradation with additions of eggshell and walnut shell at 10%, 20%, 30%, 50%, and 60% content. Microscopic observations of their structure were performed, and FTiR spectra were also analyzed in this paper. In the case of both bioplastics, the initiation of the biodegradation process was demonstrated after 96 hours, with a reduction in mass below the original value occurring within just a few weeks

**Keywords:** Thermoplastic materials, polymeric materials, polymeric composites, polymeric matrix, fillers, recycling of polymeric materials, plastic waste, microscopic observations, FTIR analysis, absorption test

## 1. INTRODUCTION

The present times are characterized by a focus on sustainable development and environmental protection, which is one of the main priorities. Biodegradable bioplastics are becoming an important alternative to traditional plastics. Bioplastics, being biodegradable materials, may provide a potential solution to the problems associated with excessive environmental pollution caused by traditional plastics. These materials, known as synthetic bioplastics, are produced from renewable biomass sources such as corn starch, sugarcane, or potatoes, making them more environmentally friendly. Additionally, despite the potential benefits of using bioplastics, there is a need to deepen our knowledge of bioplastic degradation processes, as this issue has significant implications for effective waste management. With the increasing popularity of bioplastics, understanding how environmental conditions affect their decomposition is crucial for developing effective recycling strategies and proper management of biodegradable waste. Various types of bioplastics, such as polylactic acid (PLA), polyhydroxyalkanoates (PHA), and others, have different properties and degradation rates. It is

also important to emphasize that research on bioplastics should encompass various aspects, such as the impact of their production on natural resource consumption and a life cycle analysis, to accurately assess their ecological benefits compared to traditional plastics. Furthermore, identifying potential applications of bioplastics in industries can contribute to sustainable development and reduce negative environmental impacts.

In the context of the discussed topic, the importance of analyzing and evaluating the degree of degradation of composite bioplastic materials is increasingly significant. To obtain a fuller picture of the degradation process, various research methods are used, such as composting tests, as well as thermal and chemical analyses. Understanding how quickly and effectively bioplastics decompose is a key element in establishing standards and guidelines directly related to proper management of biodegradable thermoplastic waste. Moreover, understanding plays a crucial role in promoting the sustainable use of bioplastics, contributing to more efficient and environmentally friendly management of these materials in environmental protection.

The main goal of the described engineering project was to conduct a detailed analysis and assessment of the degradation degree of selected composite materials (bioplastics). Produced in the Scientific and Didactic Laboratory of Nanotechnology and Material Technology as part of the activities of the student scientific circle "Plastics and Composites Processing HEAD TO HEAD". The obtained results were used to gather important information that will serve as the basis for developing recommendations for optimizing the composting and recycling processes of the aforementioned bioplastics. Additionally, the obtained research results can be used to develop practical guidelines that will contribute to the promotion and efficient use of bioplastics in various industries.

## **2. BIOPLASTICS**

The increase in global environmental awareness due to natural disasters caused by synthetic materials pollution and the pursuit of reducing dependence on fossil fuels has resulted in the need for the development of eco-friendly materials. Both society and scientists show significant interest and a need for the development of materials that could replace synthetic ones and potentially dethrone them. As a result of these efforts, there has been an increased demand for the use of composites containing natural fibers in various industrial sectors on a commercial scale in recent years. However, there is diversity in defining bioplastics, depending on the research context. Three dominant definitions are distinguished. The first defines bioplastics as polymers derived from renewable sources or synthesized by microorganisms, typically produced from biomass, referred to as biomass-based products. According to the second definition, bioplastics include all biodegradable polymers, regardless of their origin, including those derived from fossil fuels. The third definition is more restrictive and recognizes only those polymers as bioplastics that are both biomass-based and biodegradable, excluding both biomass-based polymers that are non-biodegradable and biodegradable polymers derived from petroleum-based sources. Natural fibers are an environmentally sustainable response to synthetic materials because they are readily available in nature, their mechanical properties are comparable to synthetic counterparts, and they possess advantages such as low cost, lightweight, renewability, and, importantly, biodegradability of polymers containing natural fibers. Meeting market demands by being a sustainable material, composites with natural fibers have been widely adopted in various manufacturing sectors. Since bioplastics originate from non-fossil sources, such as plants that absorb CO<sub>2</sub>, they have the advantage of potential carbon



neutrality, even if bioplastic waste is used for energy or undergoes incineration. However, energy recovery is not a preferred method of handling bioplastics as it does not leverage the biodegradability of various types of bioplastics.

### **3. THERMOPLASTIC STARCH**

A solution for traditional recycling is the biodegradation process of bioplastics, which involves the work of microorganisms that metabolically break down the material. Unlike, for example, incineration, which can leave behind toxic waste if the process is not conducted under appropriate conditions, the biodegradation process leaves behind carbon dioxide, methane, and various salts. A known characteristic of plastics is their resistance to environmental conditions and slow degradation, which means that they can remain in the natural environment for up to 1000 years. Assuming that one generation is 25 years, only after 40 generations would the plastic waste generated by a distant relative begin to degrade. The reason for these characteristics of plastics is the durability of the covalent bonds of polymers. All of this means that each piece of waste will accumulate, and we may not become its problem, but 40 generations into the future and thus millions of tons of waste later, we are faced with a huge environmental problem. That is why waste management and emphasis on research into biodegradable plastics are so important. Unfortunately, even breakthroughs in research on materials that perfectly replace current ones with their mechanical and biodegradable parameters do not solve the problem of existing waste because, despite many studies, an effective solution enabling the faster biodegradation of already produced plastics from fossil fuels has not yet been developed.

When considering the issue of biodegradation, we must categorize plastics derived from fossil fuels into three main groups because each of them undergoes a different type of degradation. The first group includes polymers with a carbon structure, such as PE, PS, PP, and PVC. The second group contains PET-type polymers characterized by an ester-linked backbone and side chains. The last one comprises polymers with hetero/carbonate bonds (urethane), such as polyurethane (PU).

### **4. MATERIALS**

The material selected for research was developed at the Silesian University of Technology, Faculty of Mechanical and Technological Engineering, Scientific and Didactic Laboratory of Nanotechnology and Material Technology (Polisl RMT L2). The composite material was developed as part of the activities of the student scientific circle (SSC) "Plastics and Composites Processing HEAD TO HEAD". The BIPLAST GS 2189 was chosen for the production of the composite. The chosen matrix was characterized by a relatively low melt flow temperature of 58°C and a high melt flow rate (MFR). This translates into the ability to homogenize and portion the material into standardized samples using injection molding. Moving on to the selection of natural fillers for the chosen composite material, ground waste in the form of walnut shells and eggshell powder was chosen. This choice was driven by their biodegradability, suitability for contact with food, and availability.

## 5. FTIR TEST

To illustrate the changes occurring in the analyzed samples and track the degradation process, Fourier transform infrared spectroscopy (FTIR) was employed (Fig. 1). This method allows us to examine the structure of individual molecules and their composition. The technique is based on the phenomenon where some of the infrared radiation is absorbed as it passes through the sample under investigation. The registered radiation that passes through the sample allows for the generation of spectra characteristic of various molecules, enabling their identification and differentiation. These spectra are unique, akin to human fingerprints or DNA. FTIR spectroscopy is chosen as the method in infrared studies for several significant reasons. Primarily, it does not cause destruction to the analyzed sample (Tab. 1-2).



*Fig. 1. Spectroscopy system "Thermo Scientific" with the "Gladi ATR"*

Additionally, it is characterized by significant speed compared to older methods. It is also more sensitive and precise. These advantages result from the use of an interferometer, which acts as the "source" of infrared radiation, allowing for faster operation, as well as the application of Fourier transformation. Fourier transformation is a mathematical procedure that decomposes waves and returns their frequency based on time. What we obtain from the interferometer is not directly a spectroscopic spectrum but a graph known as an "interferogram." Fourier transformation converts the interferogram into a recognizable and useful graph of the infrared spectroscopy spectrum. The study was conducted using a spectroscopy system from "Thermo Scientific" with the "Gladi ATR" extension from "Pike Technologies".

Tab. 1. The results of egg spectra comparisons with the library

First test	Second test	Thierd Test
<b>B/90/J/10</b>		
10%Trimethyl/9%ethanol water	46% Dibutyl tartrate	76% polyester/ 72% Poly
<b>B/80/J/20</b>		
14% Fluorocarbon	39% ethyl chlorothiolformate/ 39% Dibutyl tartate	72%/Polyester/ 68% Poly
<b>B/70/J/30</b>		
43% Fluorocarbon/ 40% Ground calcium carbonate	42% Dibutyl tartrate/ 41%Ethyl chiorothiolformate	61% Ground calcium carbonate
<b>B/50/J/50</b>		
43% Fluorocarbon	74%Polyethylene type f/ 73%Polyethylene high density	74% Ground calcium carbonate
<b>B/40/J/60</b>		
9%Trimethyl/9%Magnesium carbonate	45%Polyethylene high denisty/ 45%xt polymer	84% Ground calcium carbonate

Tab. 2 .The result of spectrum comparisons of walnut with the library

First test	Second test	Thierd Test
<b>B/90/O/10</b>		
72%Ethane homopolymer/72%Calcium stearate	42%a-Methoxyphenylacetic/41%Dibutyl tartrate	74% polyester/ 71% Poly
<b>B/90/O/20</b>		
45%Glyceryl tripropionate/45%Cellulose propionate	40% Dibutyl tartrate/ 38%Ethyl chiorothiolformate	73%/Polyester/ 67% Poly
<b>B/70/O/30</b>		
42%Calcium stearate/42%Oxidized clay	41% Dibutyl tartrate/37%fluorocarbon	80%/Polyester/ 75% Poly
<b>B/50/O/50</b>		
41%Polyethylene /41%Calcium stearate	45%Dibutyl tartrate/41%Octylene glycol	87%/Polyester/ 79% Poly
<b>B/40/O/60</b>		
40%Callulose propionate	41% Dibutyl tartrate/39%fluorocarbon	85%/Polyester/ 78% Poly

## 5.1. WATER ABSORPTION

To assess water absorption according to the PN-EN ISO 62 standard, the tested samples were placed in distilled water at a temperature of 75°C. Subsequently, measurements of their mass were to be taken at cyclical time intervals, but before this, the samples were removed from the water and dried. Measurements were taken after 1, 2, and 3 hours, as well as before

the start of the test. Subsequent measurements were planned at intervals of 1, 3, 7, 14, 21, 28, 35, 42, 49, 54, and 64 days. However, the intended testing period was not achieved due to changes in the physical parameters of the samples and their high brittleness, which prevented measurements from being taken after 7 days (Fig. 2-6).

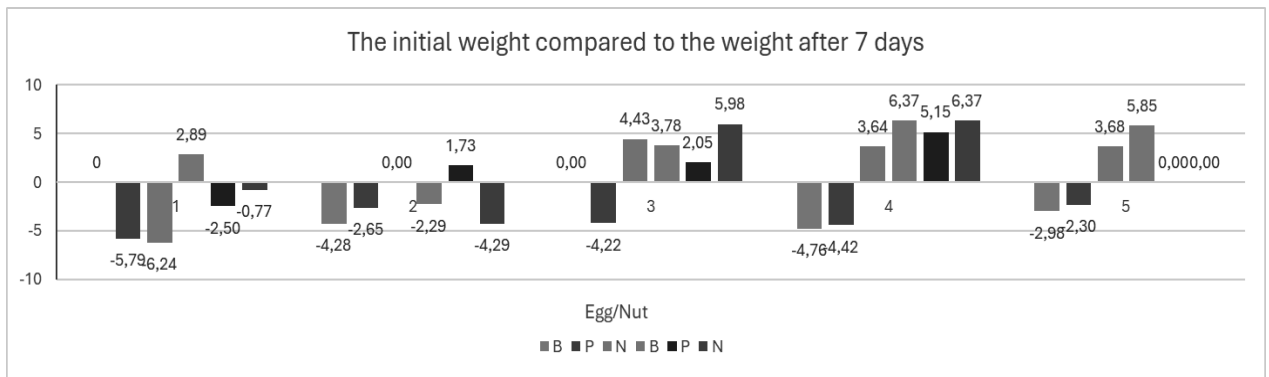


Fig. 2. Bar chart of sample mass changes over 7 days

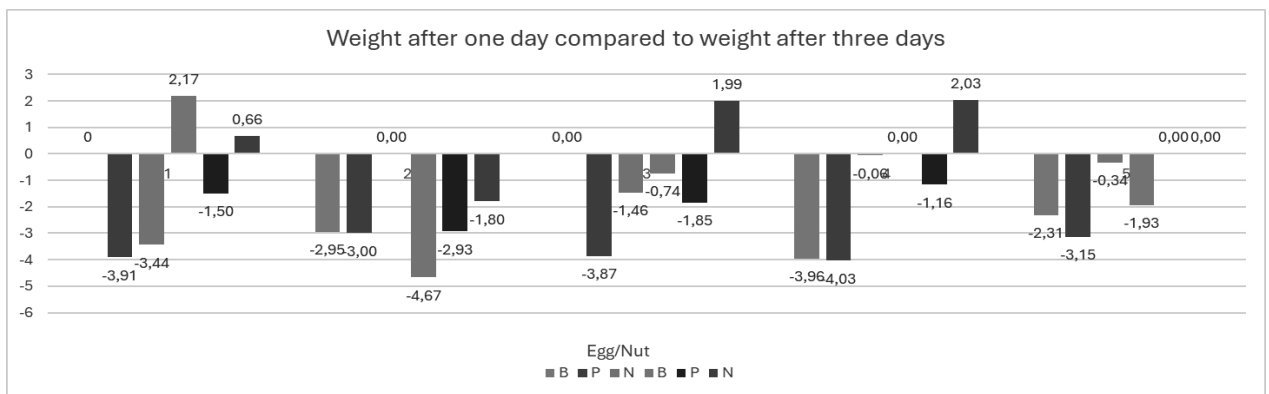


Fig. 3. Bar chart of sample mass changes between day 1 and day 3

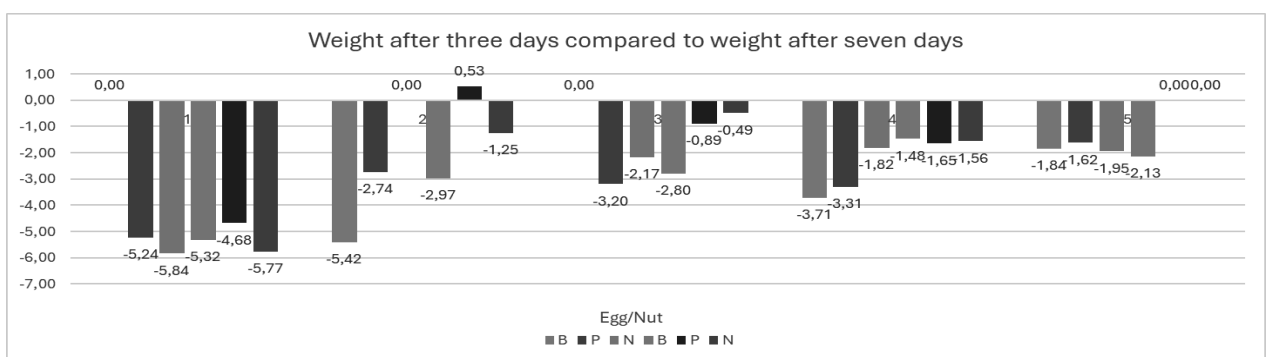


Fig. 4. Bar chart of sample mass changes between day 3 and day 7



Fig. 5. Photos example of containers containing samples of composites with the addition of egg meal



Fig. 6. Photos example of containers containing samples of composites with the addition of walnut flour

## 6. SUMMARY

Polymeric composites with a biodegradable thermoplastic matrix reinforced with natural fibers can serve as an alternative to conventional polymers and petrochemical-based composites. One of the areas of application is the food industry, where there is an increasing emphasis on the use of environmentally friendly packaging. However, natural fibers have drawbacks such as high hydrophilicity, low thermal resistance, and lack of compatibility with natural reinforcement, often requiring surface treatment of natural fibers or the addition of auxiliary agents. In the case of single-use items, it is important for them to be fully degradable.

In the course of this study, samples of composite materials based on the thermoplastic polymer BIOPLAST GS 2189 filled with walnut shell powder and eggshell powder at volumetric ratios of 10%, 20%, 30%, 50%, and 60% were selected for degradation testing. Microscopic images were taken and Fourier transform infrared spectroscopy (FTIR) was conducted. Subsequently, the mass of selected samples in the form of beams, pellets, and irregular shapes was measured. The weighed samples were placed in glass containers with a capacity of 120 ml, filled with distilled water. These containers were then placed in a dryer set to 75 degrees Celsius. Mass measurements of the samples were taken every hour for the next 3 hours. Mass measurements were also taken after 1 day, 3 days, and finally after a week. When mass measurement became impossible due to the high brittleness of the samples, photographic documentation was conducted weekly, with three photos taken of each sample. FTIR measurements were repeated on the 28th and 70th days. During the study, it was determined that the material underwent significant degradation, confirmed by the spectra obtained. This process likely began within 24 hours of the samples being placed in an environment conducive to degradation at 75 degrees Celsius. The study also showed that the addition of eggshell powder was a better additive in terms of degradation, as it statistically exhibited a faster onset

of degradation compared to the walnut shell powder additive. However, no significant influence was observed between the volume content of the bio additive in the composite and the degradation rate. During the experiment, three FTIR analyses were conducted, and the spectra obtained were compared with a library. The results of the first analysis were inconclusive, as each sample showed different convergences, indicating a significant influence of background noise on the spectra obtained. This could be due to improper preparation of the instrument and/or sample contamination. However, this changed in the second cycle of analyses, where the results largely overlapped. The most accurate results were obtained in the third cycle of analyses after 70 days, and the obtained spectra were consistent.

## 7. CONCLUSIONS

Analysis and interpretation of the research results on chemical, biological, moisture absorption, FTIR, and microscopic properties of composites based on BIOPLAST GS 2189 with 10%, 20%, 30%, 50%, and 60% volumetric content of eggshell powder and walnut shell powder particles allowed for the formulation of the following conclusions:

- BIOPLAST GS 2189 with 10%, 20%, 30%, 50%, and 60% volumetric content of eggshell powder and walnut shell powder particles exhibit biodegradable properties.
- 23 out of 29 samples show tendencies to initiate the biodegradation process within 24 hours.
- Samples initiate the biodegradation process at the latest after 96 hours.
- Samples containing eggshell additives show a more regular mass decrease.
- Samples containing walnut shell additives exhibit more irregular mass decreases.
- No significant influence was observed between the volume content of the bio additive in the composite and the degradation rate.
- FTIR analysis becomes precise in degradation studies only after a period of 70 days.
- After 7 days, the samples became very brittle, allowing for their fragmentation without the use of significant force; finer fractions would disintegrate even faster

## LITERATURE

- [1] Blicharski M., *Inżynieria materiałowa*, Wydawnictwa Naukowo-Techniczne, Warszawa 2012
- [2] Boczkowska A., Krześciński G., *Kompozyty i techniki ich wytwarzania*, Oficyna Wydawnicza Politechniki Warszawskiej, Warszawa 2016
- [3] Zwawi M., *A Review on Natura! Fiber Bio-Composites, Surface Modifications and Applications*, *Molecules*, vol. 26 (2), 2021
- [4] Mucha M., *Polimery a ekologia*, Wydawnictwo Politechniki Łódzkiej, Łódź 2002
- [5] Klepka T. (red.), *Nowoczesne materiały polimerowe i ich przetwórstwo. Część 3*, Politechnika Lubelska, Lublin 2017
- [6] Gurunathan T., Mohanty S., Nayak S. K., *A review of the recent developments in biocomposites based on natural fibres and their application perspectives*, *Composites: Part A*, vol. 77, 2015, pp. 1-25

- [7] Li X., Tabil L. G., Panigrahi S., Chemical Treatments of Natural Fiber for Use in Natural Fiber-Reinforced Composites: A Review, *Journal of Polymers and the Environment*, vol. 15 (1), 2007, pp. 25-33
- [8] Adekunle K. F., Surface Treatments of Natural Fibres — A Review: Part 1, *Open Journal of Polymer Chemistry*, vol. 5 (3), 2015, pp. 41-46
- [9] Chmielnicki B., Konieczny J., Flisiak J., Kompozyty WPC: wytwarzanie, przetwórstwo i możliwości zastosowania, *Przetwórstwo Tworzyw*, t. 23, nr 3 (177), 2017, str. 172-184
- [10] Matta A. K., Umamaheswara Rao R., Suman K. N. S., Rambabu V., Preparation and Characterization of Biodegradable PLA/PCL Polymeric Blends, *Procedia Materials Science*, vol. 6, 2014, pp. 1266-1270
- [11] Rudolph, Natalie Kiesel, Raphael Aumnate, Chuancom, *Understanding Plastics Recycling*, Druga edycja, Hanser, 2020
- [12] Błędzki Andrzej K., Regina Jeziórska, Jacek Kijeński, *Odzysk i recykling materiałów polimerowych*, PWN, 2023.



17th-19th June 2024  
Gliwice, Poland

DEPARTMENT OF ENGINEERING MATERIALS AND BIOMATERIALS  
FACULTY OF MECHANICAL ENGINEERING  
SILESIA UNIVERSITY OF TECHNOLOGY

## INTERNATIONAL STUDENTS SCIENTIFIC CONFERENCE

### Thrust stand for measuring static thrust of brushless electric motors

Wojciech Cofalik<sup>a</sup>, Patryk Mondry<sup>a</sup>, Dariusz Myszor<sup>b</sup>

<sup>a</sup> Silesian University of Technology, Student Scientific Circle of Virtual Flying.

<sup>b</sup> Silesian University of Technology, Faculty of Automatic Control, Electronics and Computer Science, Department of Algorithmics and Software, e-mail: [dariusz.myszor@polsl.pl](mailto:dariusz.myszor@polsl.pl)

**Abstract:** The article describes the key structural elements of the thrust stand, including mechanisms for measuring torque, thrust, rotational speed and power. Particular attention was paid to calibration methods, measurement system validation and drive system tests.

**Keywords:** thrust stand, propulsion systems, thrust, torque, measurement

### INTRODUCTION

Student Scientific Circle vFly conducted a project entitled "Thrust stand for measuring static thrust of brushless electric motors". Students designed and then built a station to collect data on thrust, torque, engine rpm, current, voltage and temperature obtained from brushless electric motors. The project aims to familiarize with the principle of operation of aircraft propulsion systems and to conduct detailed tests of various propulsion systems. Propeller drives are commonly used in drones and other UAVs (Unmanned Aerial Vehicles). Choosing the right propeller for a drive unit (that includes a brushless electric motor or a piston internal combustion engine) is important in terms of the efficiency of the drive system. Optimal selection of the propeller, i.e. propellers with the right diameter and pitch in relation to the engine parameters. The stand can also be used to test newly designed propeller geometries.

### CONSTRUCTION OF A THRUST STAND

The supporting structure of the measuring station is made of v-slot profiles, which ensure the required rigidity of the structure and facilitate the assembly of the modules. Bolts and nuts designed for v-slot profiles were used to ensure secure connections. Thrust and torque measurement is carried out using 3 loadcells. The loadcell located perpendicular to the engine axis is responsible for measuring the thrust. The remaining two loadcells parallel to the engine axis have been connected by a hinge to an element made of steel sheet, to which the engine bed is then attached. The use of a hinge prevents the accumulation of torsional torque on the loadcells, which would prevent correct measurement. To calculate the torque generated by the



motor, add the forces deposited on the beams and then multiply them by the force arm. The method of determining the length of the arm is presented in the further part of the article.

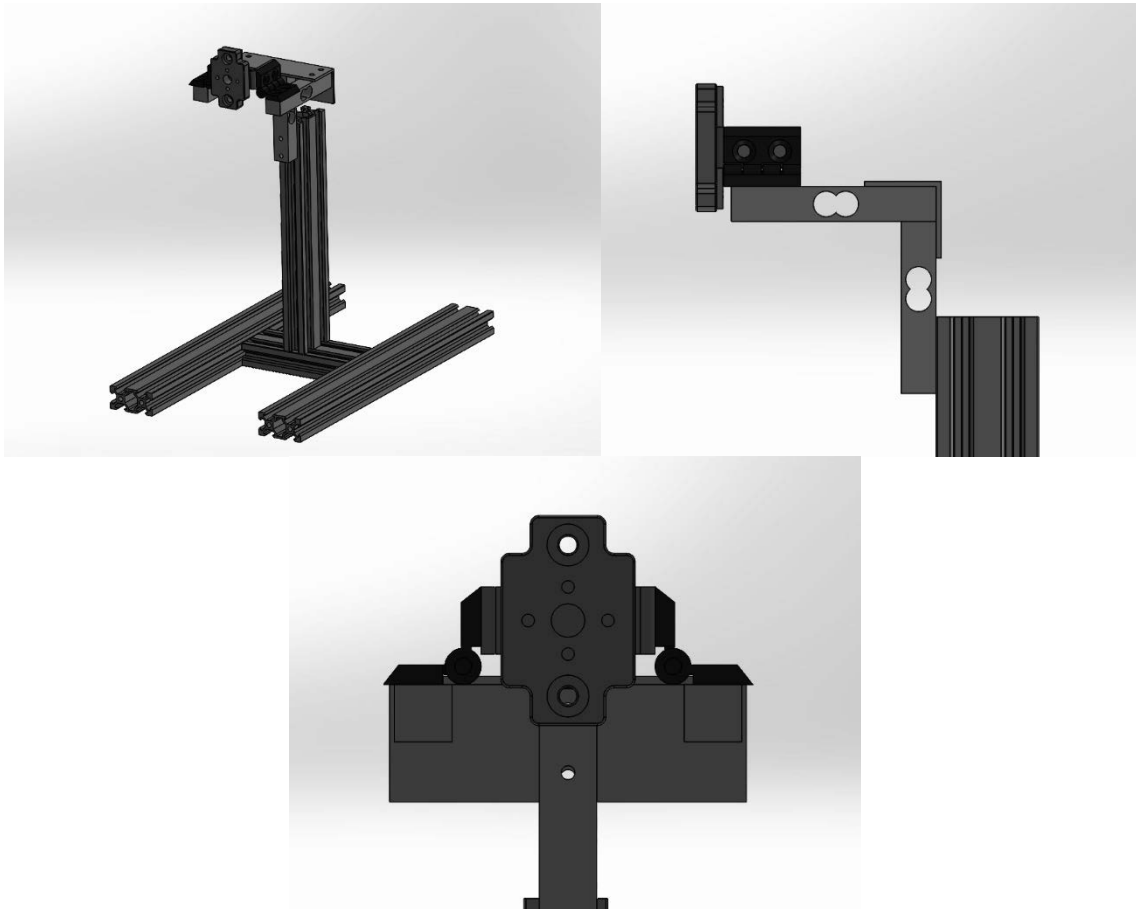


Figure 1. CAD Model of a Measurement Station

Resistance strain gauges allow to measure the deformations that occur on the surface of the material. Knowing the value of the deformation, it is possible to determine the value of the force acting on the object, e.g. a loadcell. [2] Loadcells used in the measuring station are capable of measuring forces up to 50N. The beam leads were connected to HX711 transducers, in which the calibration data of the loadcells are stored.

To measure the current consumed by the motor and the ESC (Electronic Speed Controller), the ACS758 Hall Effect sensor was used. Its use allows for accurate measurement of current up to 50A, drawn from the power source. However, it was not easy to measure the current in the BLDC motor circuit due to the fact that the current is not consumed linearly. The measurements obtained were distorted by interference and too low frequency of data downloads. In order to eliminate the phenomenon, an LC filter was used at the output of the sensor, which cleans the output signal of interference.

The RPM measurement was carried out with a reflective optical sensor consisting of an infrared light-emitting diode and a photo-transistor. On the bell of the engine, there is a white sticker reflecting the light emitted by the diode. The reflected light excites the phototransistor. Arduino

reads and counts the pulses generated by the sensor and records the time elapsed between pulses, the rotational speed can be calculated from the acquired values.

To measure the voltage on the battery, a simple voltage divider based on two resistors of known resistance was used. The use of the divider allowed to expand the measurement range of the analog-to-digital converter located in the Arduino board microprocessor. The output voltage of the divider is linearly proportional to the input voltage and is in the range of 0-5V, which is in a safe range for the microprocessor.

Arduino has been programmed in a way to effectively collect data from sensors and send it to a terminal on a computer. An automatic test has been created. When started, it increases the PWM signal filling in 10% increments, and hence the engine speed. At the same time, the readings from the sensors are transmitted to the computer every 200ms, after 60 readings the speed is increased again. The automatic test is designed to achieve the highest possible repeatability of the tests performed.

The prototype of the stand is shown (Figure 2). A special calibration instrument was prepared to determine the length of the arm between the beams and the engine shaft axis. The device was mounted in the place of the engine, and then a weight of known weight was hung on its 100 mm long arm. The torque value was experimentally determined according to the formula:

$$M = F_1 l_1 \quad (1)$$

$F_1$  – the value of the force applied to the arm

$l_1$  – arm length

Knowing the values of the forces that act on the strain gauge beams, it is possible to calculate the moment generated by the engine:

$$M = (F_2 + F_3)l_2 \quad (2)$$

$F_2$  – force acting on the loadcell 1

$F_3$  – force acting on loadcell 2

$l_2$  – force pair arm

Equating equation (1) to (2) we obtain the length of the arm between the motor shaft axis and the loadcell.

$$l_2 = \frac{F_1 l_1}{F_2 + F_3} \quad (3)$$

Knowing the values of the forces acting on the beams and the size of the arm calculated from equation (3), the engine torque can be calculated.



Figure 2. Prototype of the thrust stand

## PROPELLER PRINCIPLE OF OPERATION

The impulse theory involves a step change in flow parameters in the plane of propeller rotation. In order to apply this theory, a hypothetical channel should be created, the axis of which coincides with the axis of the propeller shaft, and the diameter of the propeller jet in the plane of rotation of the propeller is equal to its diameter. The propeller jet is limited by imaginable infinitely thin walls across which there is no airflow. An analogy can be drawn here to rotating machines such as compressors or turbines. Energy is supplied in the plane of the propeller's rotation, so the pressure increases abruptly. As for the parts that are located in front of and behind the propeller plane, the flow is lossless. [1,3]

The theory of the blade element is to calculate the aerodynamic forces that act on the blade profile (airfoil), add up the elementary forces along the blade, and multiply by the number of blades. The theory assumes a stationary flow around the propeller. The influence of swirl surfaces is ignored, as it is a small error. [1]

An important element of the propeller mechanics is its slippage.

$$p = \frac{(H-H_0)}{H_0} \quad (4)$$

p – slippage %

H – geometric jump

H<sub>0</sub> – Basic/aerodynamic jump

When the aircraft is stationary,  $V = 0$ , the aerodynamic pitch of the propeller  $H_0 = 0$ , and then the slip of the propeller strives for infinity. In conditions of operation with maximum efficiency, the propeller slip is about 10% for wooden and about 5% for metal/composite. This

difference results from the propeller manufacturing technology, and more specifically, the thickness of the profile. [1] Knowledge of this is important because in the case of static tests, the air inflow velocity is zero, so the propeller slip is infinite. Static measurements are sufficient to determine the efficiency of the motor and the ESC speed controller. However, it is not possible to determine the efficiency of the propeller due to the zero speed of air inflow to the propeller.

## MEASUREMENT DATA PROCESSING

Using the sensors described above, the station is capable of recording the following parameters:

- Thrust,  $T$  [N]
- Torque,  $M$  [Nm]
- RPM,  $IR$
- Voltage,  $U$  [V]
- Current,  $I$  [A]

Based on the data, characteristics describing the propeller-engine assembly will be determined:

Electrical power:

$$P_e = U I \quad (5)$$

Mechanical power:

$$P_m = \omega M \quad (6)$$

where:

$\omega$  – angular velocity [rad/s]

Motor efficiency:

$$\eta = \frac{P_m}{P_e} \quad (7)$$

## FIRST MOTOR TEST

A Kavan 2836-1050KV motor and an APC 11x7 propeller were mounted to the measuring station, and an automatic test was run. The results of the measurements obtained during the tests were developed and compared with the parameters included by the manufacturer in the engine data sheet. The values obtained during the test coincide with the drive's datasheet. The data are presented in the graphs below (Chart 1, 2, 3, 4):

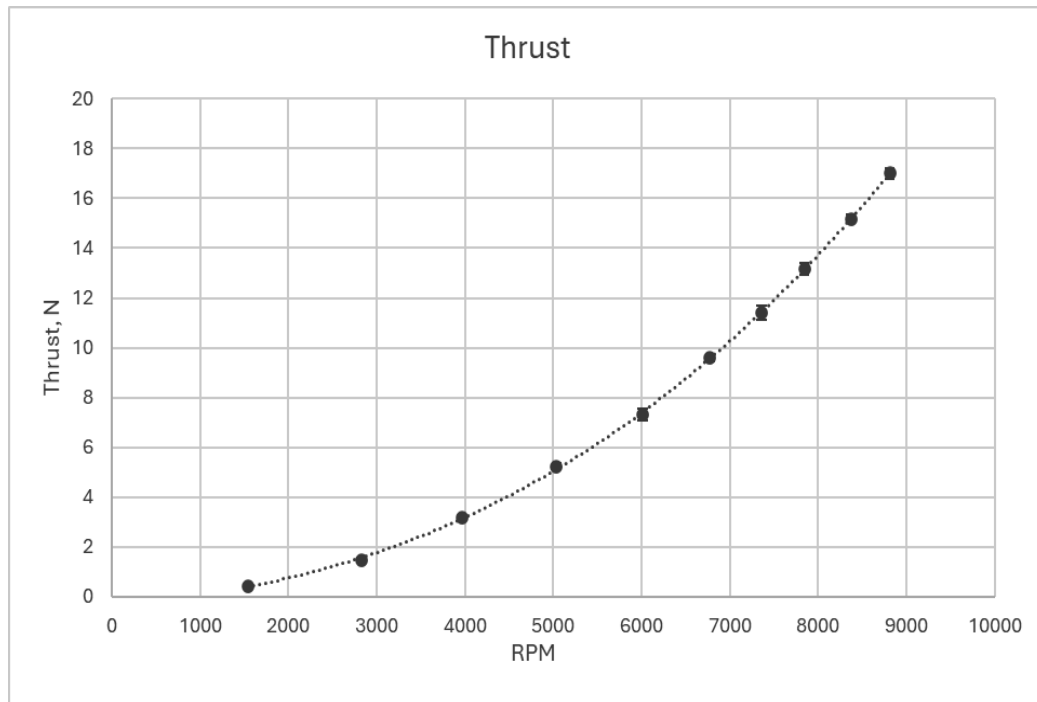


Chart 1. The thrust versus RPM dependency chart

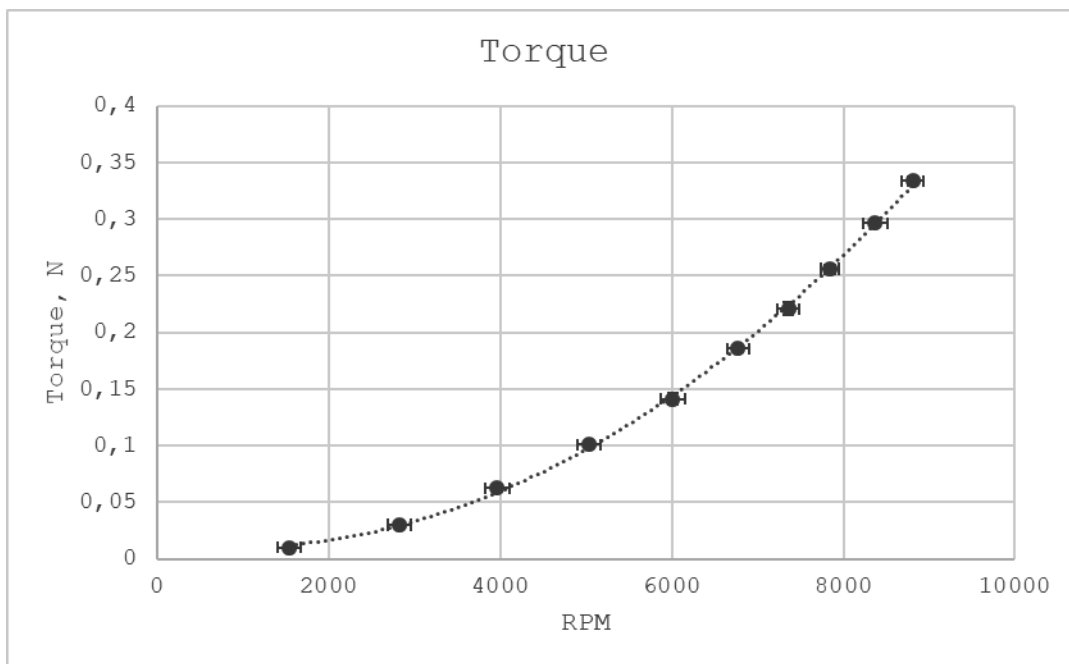


Chart 2. The torque versus RPM dependency chart

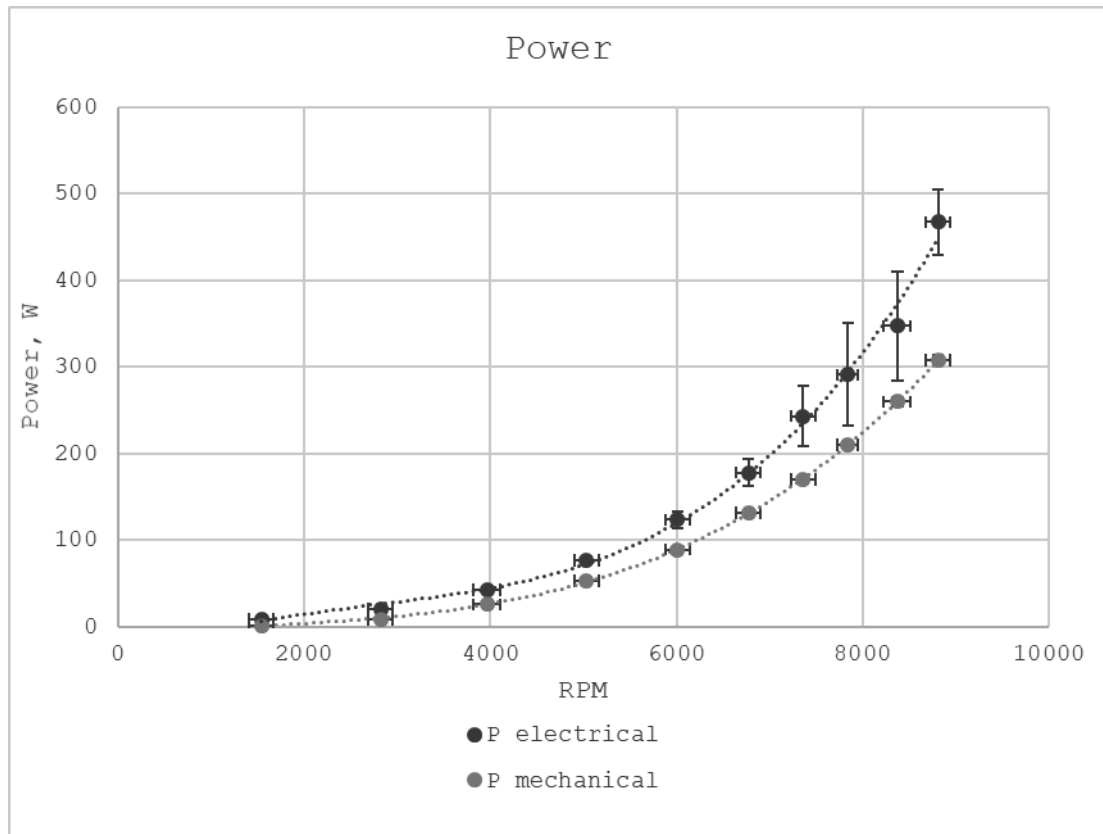


Chart 3. The power, electrical power versus RPM dependency chart

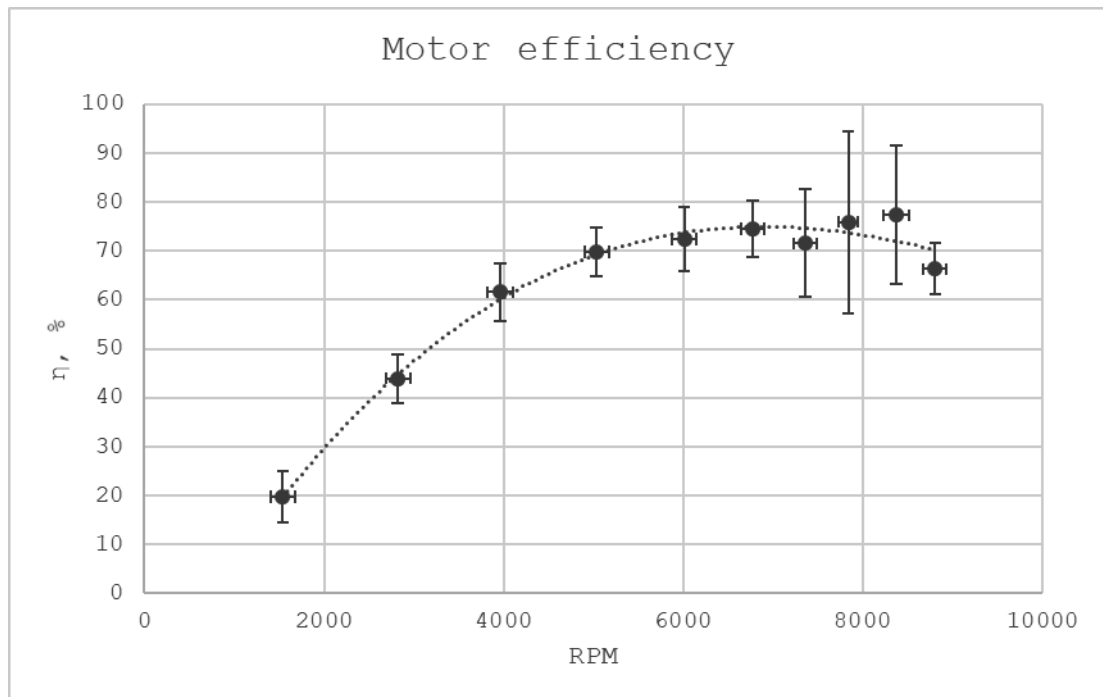


Chart 4. The motor efficiency versus RPM dependency chart

**SUMMARY**

The created thrust stand is a development-ready project that allows for the addition of new functionalities. Other ideas include the implementation of a vibration sensor in the form of an accelerometer to determine the frequency spectrum using FFT, the use of a Prandtl tube, and a differential pressure transducer to measure speed behind the propeller. A station can then be placed in the wind tunnel to determine the characteristics of the powertrain in conditions similar to those that occur during the flight of a flying model. Such a test will allow to check the efficiency of the propeller and measure the velocity field in the propeller stream. The tests carried out and the comparison of the results obtained with the engine documentation allowed to conclude that all sensors are working properly and the data processing method is correct.

**BIBLIOGRAPHY**

1. J. Bukowski, W. Łucjanek, Napęd Śmigłowy Teoria i Konstrukcja, Wydawnictwo Ministerstwa Obrony Narodowej.
2. J. Zakrzewski M. Kampik, Sensory i Przetworniki Pomiarowe, Wydawnictwo Politechniki Śląskiej, Gliwice 2013
3. Wilbur C. Nelson, Airplane Propeller Principles,



17th-19th June 2024  
Gliwice, Poland

DEPARTMENT OF ENGINEERING MATERIALS AND BIOMATERIALS  
FACULTY OF MECHANICAL ENGINEERING  
SILESIA UNIVERSITY OF TECHNOLOGY

## INTERNATIONAL STUDENTS SCIENTIFIC CONFERENCE

### Laser technology in the production of silicon solar cells (part II)

Aleksandra Drygala<sup>a</sup>, Jakub Budzynowski<sup>b</sup>, Kamil Dziendzioł<sup>c</sup>, Adrian Marusiński<sup>c</sup>,  
Mateusz Magiera<sup>c</sup>, Małgorzata Muszyfaga-Staszuk<sup>d</sup>, Marcin Staszuk<sup>a</sup>

<sup>a</sup> Silesian University of Technology, Faculty of Mechanical Engineering, Department of Engineering Materials and Biomaterials, Konarskiego 18a, 44-100 Gliwice, Poland

<sup>b</sup> Student, Silesian University of Technology, Faculty of Mechanical Engineering, Konarskiego 18a, 44-100 Gliwice, Poland

<sup>c</sup> Pupil, Complex of Communication Schools, Warszawska 35, 44-100 Gliwice, Poland

<sup>d</sup> Silesian University of Technology, Faculty of Mechanical Engineering, Welding Department, Konarskiego 18a, 44-100 Gliwice, Poland

email: [aleksandra.drygala@polsl.pl](mailto:aleksandra.drygala@polsl.pl)

**Abstract:** The laser technology in the manufacturing of solar cells has become an indispensable element of modern photovoltaics. In this work, the optical and electrical properties of multicrystalline silicon solar cells with textures made traditionally by chemical etching and using a laser beam were compared.

**Keywords:** photovoltaics, solar cell, multicrystalline silicon, texturization, laser processing

### 1. INTRODUCTION

Solar cell is the device that converts the energy of light into electricity. Silicon is the most common material used in the production of solar cells. This semiconductor is the second most abundant element on the Earth [1]. The photovoltaic device consists of p-type and n-type silicon. In the n-type layer, there is an abundance of electrons, and in the p-type layer, there is an excess of positively charged holes [2]. By joining these two types of semiconductors, an electric field is formed in the region of the p-n junction. Electrons move to the positive p-side and holes change position to the negative n-side. A depletion zone is created at the p-n junction where there are no more chances of any charge carrier transfer. These separated static positive and negative charges initiate an electric field across the depletion region which provide the force or voltage needed to push the current through an external circuit. When sun rays strike the semiconductor surface, a part of photons is absorbed into the material, thus giving rise to photogenerated electron-hole pairs. The electric field initiate movement of electrons to the n-type semiconductor and holes to the p-type layer. The carriers generated in the silicon are collected by metal electrodes formed on the front and back silicon surfaces. In addition solar cells are design with an antireflection coating on the surface of device to increase absorption of sunlight [3, 4, 5].



Silicon solar cells can be based on amorphous or crystalline silicon. The crystallised form is preferable and most commonly used due to the greater power conversion efficiency. Monocrystalline silicon has an ordered crystal structure, with each atom ideally lying in a pre-determined position but because of the careful and slow manufacturing processes required, it is also the most expensive type of silicon. Techniques for the production of multicrystalline silicon are simpler and cheaper but the material quality is lower than monocrystalline material due to the presence of grain boundaries which reduce the solar cell performance [3].

The laser technology in the manufacturing of solar cells has become an indispensable element of modern photovoltaic technology. It can be used for [6]:

- edge isolation,
- laser grooved buried contacts,
- laser beam doping for selective emitter formation,
- cutting wafer,
- laser fired contacts,
- drilling,
- wafer marking.

The properties of laser radiation, which enable precise processing of various materials with efficiency and accuracy significantly exceeding conventional methods, have a significant impact on the use of laser treatment in various technological operations. Coherent and monochromatic laser beam focused to small spot produces high power densities. The wide range of applied power and power densities available from lasers and the possibility of accurate laser beam control are features which contribute to its successful application in many different aspects of surface treatment [7]. In this study, the laser beam was applied for surface texturing of multicrystalline silicon. During the design process of solar cells, one of the main goals is to reduce all types of losses. Optical losses mainly affects the power produced from a photovoltaic device by reducing the short-circuit current. Optical losses include light which potentially could have generated an electron-hole pair, but actually does not generate any, because the light is reflected from the front surface [8]. Flat surface of silicon has 30% reflectivity, but this can be lowered by texturing the surface and antireflection coating (ARC) deposition [9].

*Table 1. Comparison of the effective reflection coefficients for the different method of the crystalline silicon surface texturing [5, 10, 11]*

Surface texturing method	Effective reflectance $R_{eff}$
Etching in alkaline solutions without masking	~24
Etching in alkaline solutions with masking	~20
Etching in acid solutions without masking	~9
Etching in acid solutions with masking	~3
Reactive ion etching	~6
Mechanical techniques	~5

Texturization of the silicon is one of the major techniques in decreasing the reflection loses. The conventional methods such as alkaline etching used for monocrystalline silicon texturization are ineffective when applied to multicrystalline silicon texturing. This is related to random distribution of grains of different crystallographic orientations on the surface of

multicrystalline silicon [12]. In multicrystalline silicon solar cells, this is achieved by various methods such as mechanical techniques, reactive ion etching, alkaline and acidic etching [13]. The comparison of different texturing silicon surfaces methods are shown Table 1. The paper presents results of the optical and electrical properties of multicrystalline silicon solar cells with textures made traditionally by chemical etching and using a laser beam.

## 2. MATERIALS AND METHODS

Material used as a substrate was p-type, boron-doped multicrystalline silicon with  $1\div 3 \Omega\text{cm}$  resistivity, area of  $50 \times 50 \text{ mm}$  and thickness of  $200\pm 30 \mu\text{m}$ . The tests were carried out on wafer after:

- alkaline texturing in KOH solution,
- laser texturing by means of Nd:YAG laser and removal of the damaged layer by etching.

The topography of laser textured surfaces consisting of grid of grooves were investigated using ZEISS SUPRA 25 scanning electron microscope (SEM). The reflectance of textures was measured by Thermo Scientific UV-Vis spectrophotometer. Electrical parameters of solar cells were characterized by measurements of I-V light characteristics under standard AM 1.5 radiation for irradiance  $1000 \text{ W/m}^2$  and temperature  $25^\circ\text{C}$ .

## 3. RESULTS

Alkaline solutions are usually used to produce textures in the form of random pyramids in (100) monocrystalline silicon to reduce the reflectivity from the front surface of silicon solar cells (Fig. 1). For multicrystalline silicon, this etching are less effective for texturing due to the different orientations of the crystallographic grains (Fig. 2).

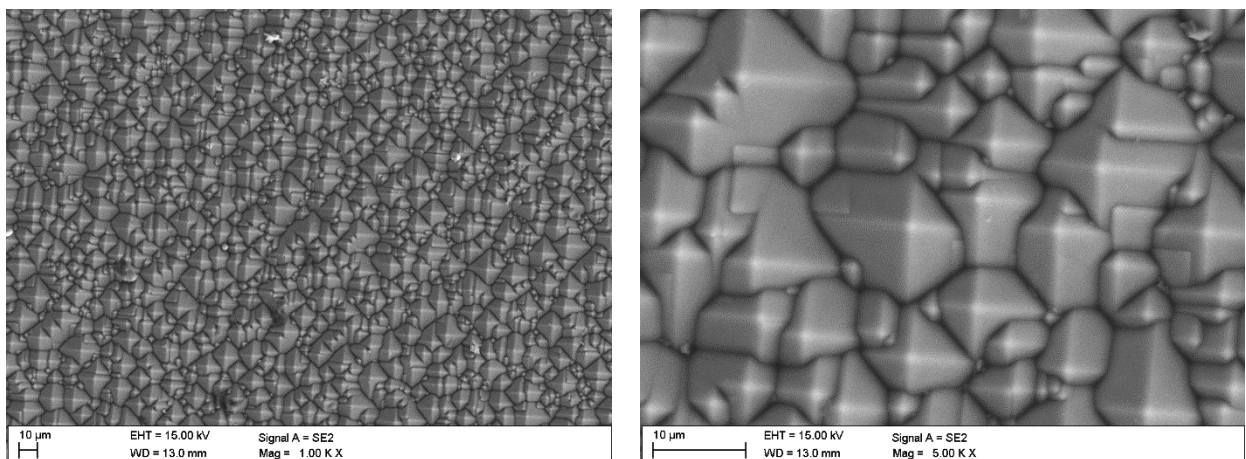


Figure 1. Topography of monocrystalline silicon surface after alkaline texturing

Figure 3 presents the surface of multicrystalline silicon wafer after laser texturization. Laser processing allowed for obtaining a uniform texture regardless of the random crystallographic orientation of various grains. Bottom and sidewalls of laser scribed grooves are covered with molten, not evaporated and resolidified material. A detailed inspection revealed crevices and microcracks on the laser textured surface of multicrystalline silicon.

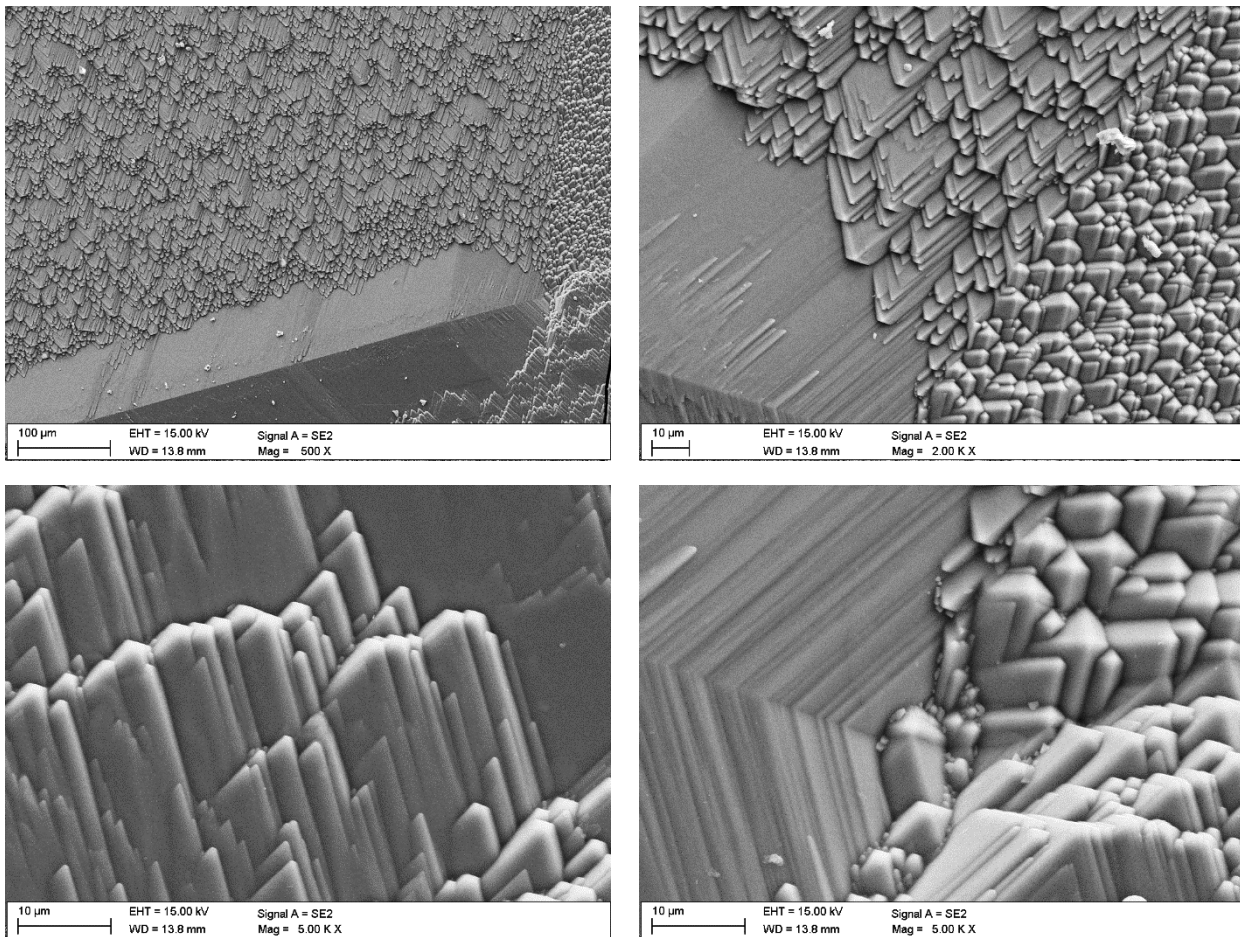


Figure 2. Topography of multicrystalline silicon surface after alkaline texturing

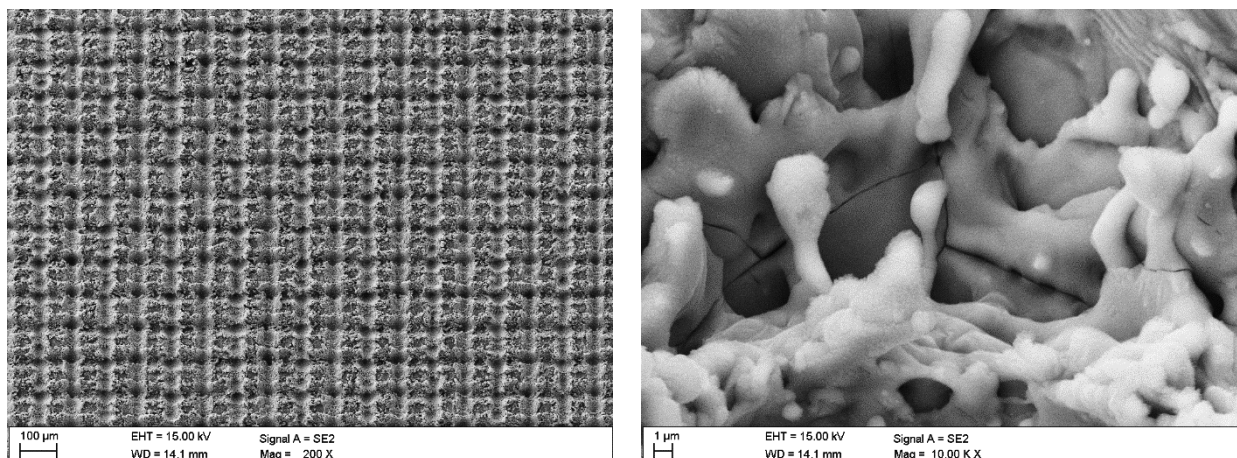


Figure 3. Topography of multicrystalline silicon surface after laser texturing

Post-laser processing etching was performed to remove laser damaged layer (Fig. 4). During etching, a layer of distorted material is eliminated. Moreover, in the places where the grooves intersect, hollows are created. They are repeatable on the entire textured surface.

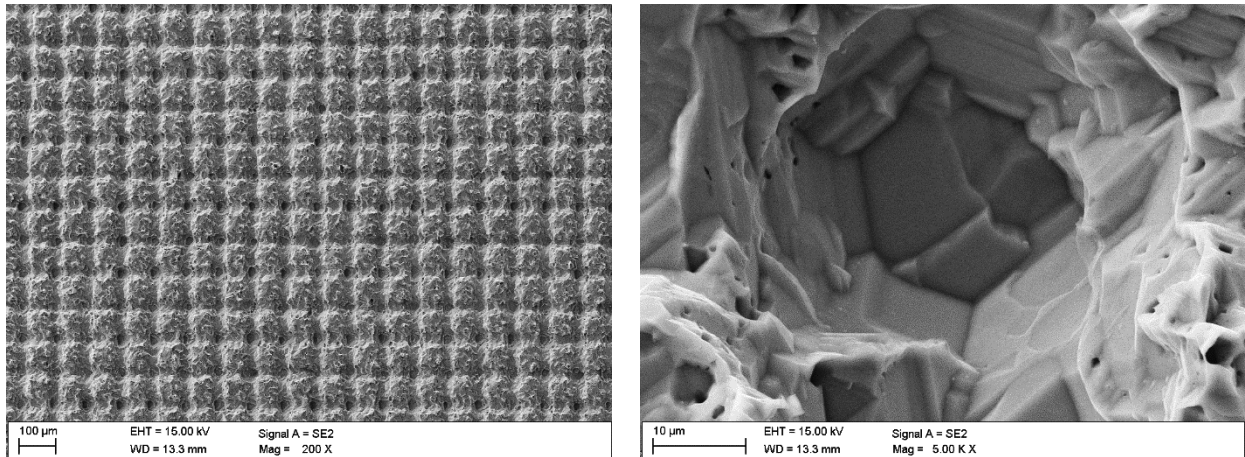


Figure 4. Topography of multicrystalline silicon surface after laser texturing and etching off laser induced damage layer

The texturing method significantly influences the optical properties of multicrystalline silicon wafers (Fig. 5). The reflectance of laser textured multicrystalline silicon is lower compared to alkaline textured wafers. Applied etching procedure causes the laser texturing surface to flatten out reducing its optical effectiveness. For a wavelength of 600 nm, the reflectance of laser-textured silicon and laser textured wafer after removal of laser induced damage layer is lower by about 9% and 4%, respectively, compared to alkaline-textured multicrystalline silicon. Additionally, decrease in the difference in reflection as the wavelength increases was noticed. Alkaline textured silicon exhibits the highest reflectance in whole range of wavelength.

Based on the measured current-voltage characteristics (Fig. 6), the electrical properties of solar cells manufactured from alkaline and laser textured wafers after removal of laser induced damage layer were determined. Open circuit voltage ( $V_{oc}$ ), short circuit current ( $I_{sc}$ ), efficiency ( $E_{ff}$ ), and fill factor (FF) was presented in Table 2. It was observed that laser textured solar cell exhibit better properties - short circuit current and open circuit voltage were higher by 9,1 mA and 8,8 mV respectively. Additionally, laser textured multicrystalline silicon solar cell shows higher efficiency by 0.4 percentage points.

Table 2. Electrical parameters of multicrystalline silicon solar cells manufactured from alkaline and laser textured wafers

Type of texturing	Electrical properties			
	$I_{sc}$ [mA]	$V_{oc}$ [mV]	FF [-]	Eff [%]
Alkaline	303.2	541.4	0.68	9.0
Laser	312.3	550.2	0.68	9.4

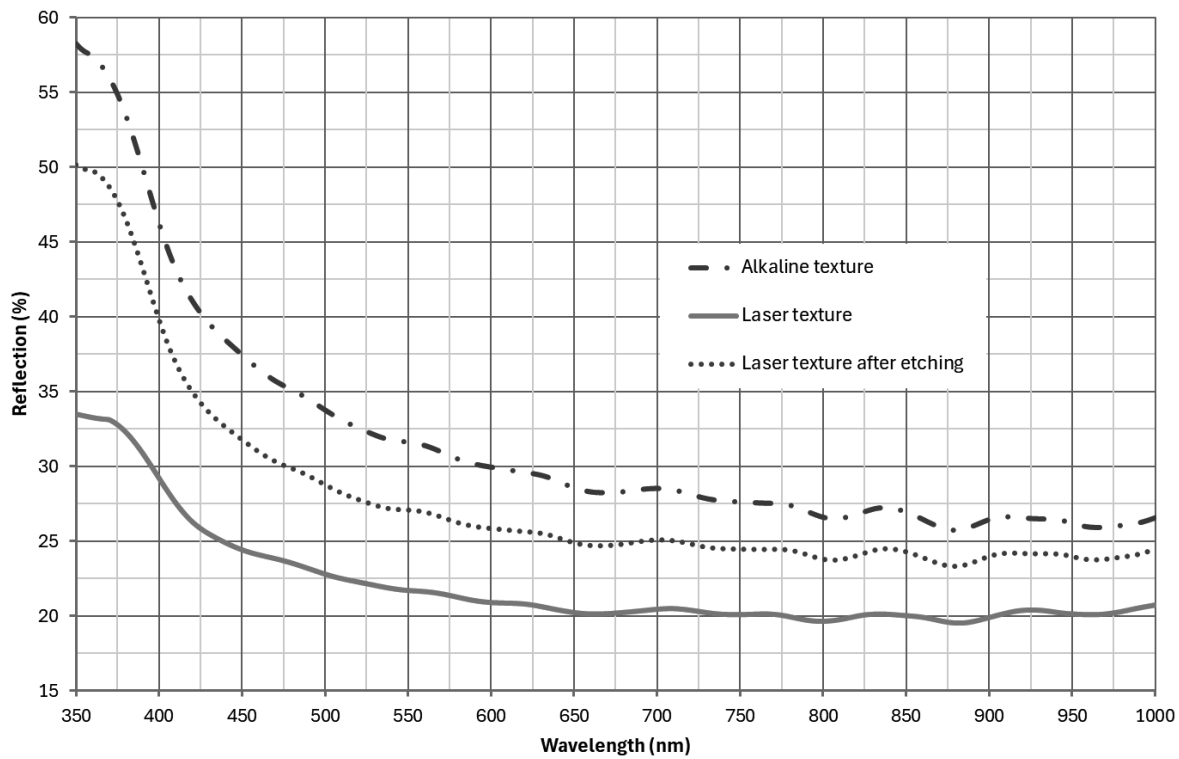


Figure 5. Reflectance for multicrystalline silicon wafer with alkaline and laser texture

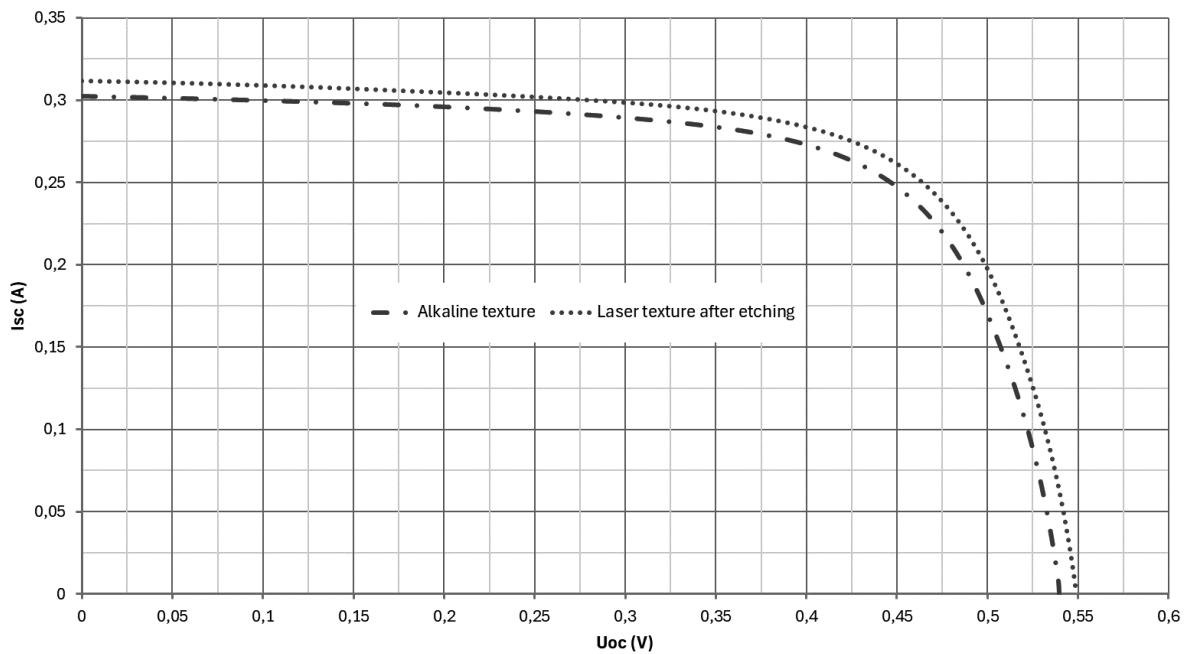


Figure 6. Current-voltage characteristics of multicrystalline silicon solar cells manufactured from alkaline and laser textured wafers

#### 4. CONCLUSIONS

Advances in photovoltaics manufacturing and technologies may drive further cost reductions and facilitate market growth going forward. Laser technology plays a key role in the economical production of high-quality solar cells. In this paper laser processing was applied for texturisation of multicrystalline silicon surface. Laser surface treatment introduce defects into the top layer of processed silicon but applied post-laser texturing etching step makes it possible to remove distorted layer. The texturing of multicrystalline silicon surface using laser makes it possible to increase absorption of the incident solar radiation. The efficiency of the laser textured multicrystalline silicon solar cell is 0.4 percentage points higher compared to the device based on alkaline textured silicon. Laser processing is very promising technique for texturing multicrystalline silicon independent on grains crystallographic orientation compared to alkaline texturing methods in technology of solar cells.

#### ACKNOWLEDGEMENTS

The work was created as a result of a project carried out with secondary school pupils as a part of the Excellence Initiative - Research University program, Silesian University of Technology.

#### BIBLIOGRAPHY

1. Pierwiastki w skorupie ziemskiej, PCC Group, 2023, <https://www.products.pcc.eu/pl/academy/pierwiastki-w-skorupie-ziemskiej>.
2. M. Macek, A. Drygała, Ogólna charakterystyka krzemowych ogniw fotowoltaicznych, *Prace Studenckich Kół Naukowych*, 26/2010 (2010) 13-24.
3. L.A. Dobrzański, A. Drygała, Surface texturing of multicrystalline silicon solar cells, *Journal of Achievements in Materials and Manufacturing Engineering*, 31/1 (2008) 77-82.
4. K. Siuzdak, M. Klein, M. Szkoda, Badania i rozwój technologii ogniw fotowoltaicznych, *Czysta Energia*, 12 (2014) 32-34.
5. L.A. Dobrzański, A. Drygała, Influence of laser processing on polycrystalline silicon surface, *Materials Science Forum*, 706-709 (2012) 829-834.
6. Kim H, Park S, et al., Influence of surface texturing conditions on crystalline silicon solar cell performance, *Current Applied Physics*, 13 (2013) S34–S40.
7. M. Gruszecka, J. Grudziński, A. Stępniewsk, Analiza metod teksturowania powierzchni krzemu krystalicznego stosowanego w fotowoltaice, *Motrol. Commission Of Motorization And Energetics In Agriculture – 2013*, 15/1 (2013) 41–46.
8. L.A. Dobrzański, A. Drygała, Wpływ obróbki laserowej na topografie powierzchni krzemu polikrystalicznego, *Elektronika: konstrukcje, technologie, zastosowania*, 52/4 (2011) 53-54
9. L.A. Dobrzański, A. Drygała, Laser application in photovoltaics for surface texturization of silicon and front electrode deposition, *Materials Performance and Characterization*, 8/6 (2019) 1136-1146.
10. L.A. Dobrzański, A. Drygała, Obróbka laserowa powierzchni krzemu polikrystalicznego, *Inżynieria materiałowa*, 34/6 (2013) 661—664.

11. Smets, K. Jaeger, et al., Solar Energy: The Physics and Engineering of Photovoltaic Conversion, Technologies and Systems, 462 (2016).
12. Soteris A. Kalogirou, Solar Energy Engineering: Processes and Systems, Third Edition, Elsevier, 2023.
13. K. Drabczyk, P. Panek, Silicon-based solar cells: Characteristics and production processes, Institute of Metallurgy and Material Science of Polish Academy of Sciences, 2012.



17th-19th June 2024  
Gliwice, Poland

DEPARTMENT OF ENGINEERING MATERIALS AND BIOMATERIALS  
FACULTY OF MECHANICAL ENGINEERING  
SILESIA UNIVERSITY OF TECHNOLOGY

## INTERNATIONAL STUDENTS SCIENTIFIC CONFERENCE

### Characterization of dye-sensitized solar cells

Judyta Drygała<sup>a</sup>, Bartosz Drygała<sup>b</sup>, Janusz Wyrwał<sup>c</sup>, Sabina Lesz<sup>d</sup>, Aleksandra Drygała<sup>d</sup>

<sup>a</sup> Student, Silesian University of Technology, Faculty of Architecture, Akademicka 7, 44-100 Gliwice, Poland

<sup>b</sup> Student, Silesian University of Technology, Faculty of Automatic Control, Electronics and Computer Science, Akademicka 16, 44-100 Gliwice, Poland

<sup>c</sup> Silesian University of Technology, Faculty of Automatic Control, Electronics and Computer Science, Department of Measurements and Control Systems, Akademicka 16 Str., 44-100 Gliwice, Poland

<sup>d</sup> Silesian University of Technology, Faculty of Mechanical Engineering, Department of Engineering Materials and Biomaterials, Konarskiego 18a, 44-100 Gliwice, Poland  
email:aleksandra.drygala@polsl.pl

**Abstract:** Dye-sensitized solar cells (DSSCs) have been recognized as promising candidates for next-generation solar cells mainly due to comparatively low manufacturing cost, ease of fabrication, and relatively good efficiency. In this paper, the topography of selected device elements, electrical and optical properties of DSSCs were analysed.

**Keywords:** photovoltaics, dye-sensitized solar cell, photoanode, counter electrode

### 1. INTRODUCTION

Recently, the global climate has been changing significantly, which poses an increasing threat to ecosystems, human health, and the economy. Moreover, the global electricity demand is constantly increasing. Renewable energy sources (RES) are the future of energy, hope for reducing environmental pollution, and becoming independent from traditional energy supplies. Renewable energy sources use the Earth's natural resources, which are not harmful to the environment, do not contribute to the increase in the average global temperature, and depletion of the Earth's resources [1].

Solar radiation is the most abundant source of energy available in the world. The amount of energy supplied in the form of solar radiation reaching the Earth significantly exceeds the energy needs of humanity, so it can be considered practically inexhaustible. In addition to the fact that it is safe for the natural environment, it can be described as infinite, completely free, and does not require transport. One way to use solar energy is to convert it into electricity using solar cells, without generating noise, pollution, and other factors that cause negative changes in the environment [2,3].



Dye-sensitized solar cells (DSSCs) are devices classified as third-generation solar cells, which are devoid of the classic semiconductor p-n junction and imitate processes occurring in nature, as they use chemical reactions similar to the phenomenon of photosynthesis [3]. Under the influence of incident solar radiation, the photon is absorbed by the dye molecules, causing the electron to be excited from the ground state. The electron is transferred to the conductive transparent conductive oxide (TCO) electrode through a porous semiconductor layer (usually  $\text{TiO}_2$ ) and flows through the external circuit to the counter electrode (cathode), where it is reduced. A layer of platinum applied to a conductive, transparent substrate constitutes the cathode of a dye-sensitized photovoltaic cell. It aims to catalyse the reduction reaction of  $\text{I}_3^-$  to  $\text{I}^-$ . The electrolyte, filling the space between the electrodes, regenerates the dye, allowing it to return from the excited state to the ground state [4-7].

Dye-sensitized solar cells are an alternative to traditional silicon-based photovoltaic cells. The advantages of DSSCs include their low weight, operation at a wide angle of light incidence and low radiation intensity, and lower production cost compared to traditional silicon-based photovoltaic cells. Transparency and the possibility of changing colour thanks to the use of different coloured dyes significantly increase the scope of their use [8-10]. In this paper, the topography of selected device elements, electrical and optical properties of DSSCs were analysed.

## 2. MATERIALS AND METHODS

In the present study, the following materials were used to produce the dye-sensitized solar cells:

- FTO (fluorine-doped tin oxide) coated glass with the resistivity of  $7 \Omega/\square$ , Sigma-Aldrich,
- 18NR-T titania paste, Greatcell Solar,
- platinum paste, Sigma-Aldrich,
- N719 (Di tetrabutylammonium cis-bis (isothiocyanato) bis (2,2'-bipyridyl-4,4'-dicarboxylato) ruthenium (II)), Greatcell Solar,
- EL-HPE electrolyte, Sigma-Aldrich.

The produced DSSCs consist of a photoanode (FTO coated glass/mesoporous  $\text{TiO}_2$ /N719 dye), an electrolyte, and a counter electrode (FTO coated glass/platinum). FTO coated glass with a size of 25 x 25 x 2.2 mm was used as a substrate in dye-sensitized solar cells. The substrate was cleaned by ultrasonication using isopropanol, detergent, and ethyl alcohol for 10 minutes for each solvent, and then dried with compressed air. Photoanode was prepared by applying  $\text{TiO}_2$  paste onto FTO covered glasses substrates. The layer was heated to the temperature of  $500^\circ\text{C}$  and after cooling, it was moved directly to N719 dye solution. The counter electrode was prepared by deposition of platinum paste by screen printing, which was then heated at  $500^\circ\text{C}$ . The working and counter electrodes were assembled into a sandwich type cell and the space between them was filled with iodine-based redox electrolyte.

Scanning Electron Microscope (SEM, Zeiss Supra 35) was applied to characterize the topography of selected DSSC elements. Scanning Electron Microscopic (SEM) images were taken with an accelerating voltage 5-7 kV. Thermo Scientific Evolution 220 UV-Vis spectrophotometer (Fig. 1) was used for recording the optical properties in the wavelength range of 300 - 800 nm. The electrical performance of the DSSC devices was investigated by Solar Cell I-V Tracer System (Fig. 2) and 2401 Keithley digital source meter under standard AM 1.5 illumination with light intensity of  $1000 \text{ W/m}^2$ .



Figure 1. Thermo Scientific Evolution 220 UV-Vis spectrophotometer



Figure 2. System for measuring current-voltage characteristics from PV Test Solutions Tadeusz Żdanowicz

### 3. RESULTS

Figures 3 and 4 show images of the FTO coated glass. The FTO thin layer is transparent, homogenous, compact, and pinhole free. The distribution of grains of various shapes was observed. The surface of the  $\text{TiO}_2$  layer is uniform, and as a result of dyeing it changes color from semi-transparent white to dark red (Fig. 5). As shown in Figure 6, the screen-printed  $\text{TiO}_2$  layer is porous without cracks. The pore distribution is homogeneous. The large internal surface area of the  $\text{TiO}_2$  layer ensures the adsorption of the sufficiently large number of dye molecules for efficient harvesting of solar radiation.

The Pt in the counter electrode helps in the regeneration of dyes by catalysing the  $I^-$  regeneration from the  $I_3^-$  in the redox couple. Figures 7 and 8 present the surface topography of screen printed Pt layer. Pt nanoparticles are well dispersed on the FTO surface and not agglomerated.

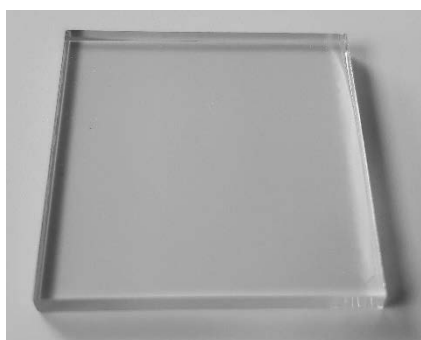


Figure 3. FTO coated glass on macroscopic scale

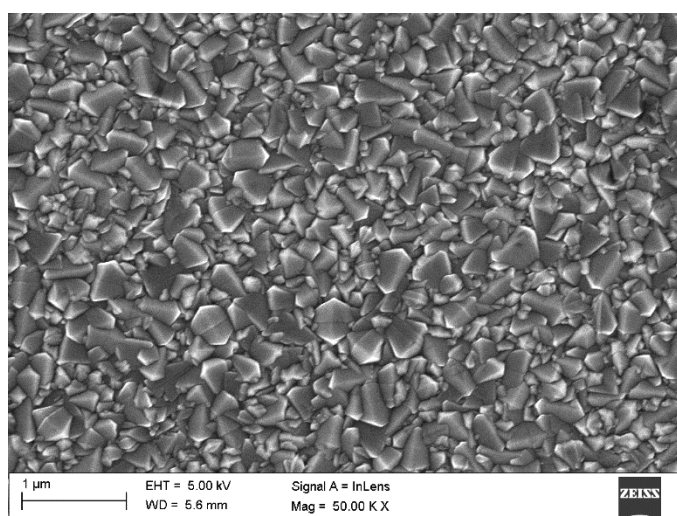


Figure 4. SEM topography of FTO coated glass

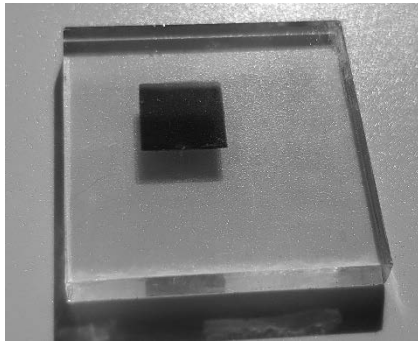


Figure 5. Photoanode of DSSC on macroscopic scale

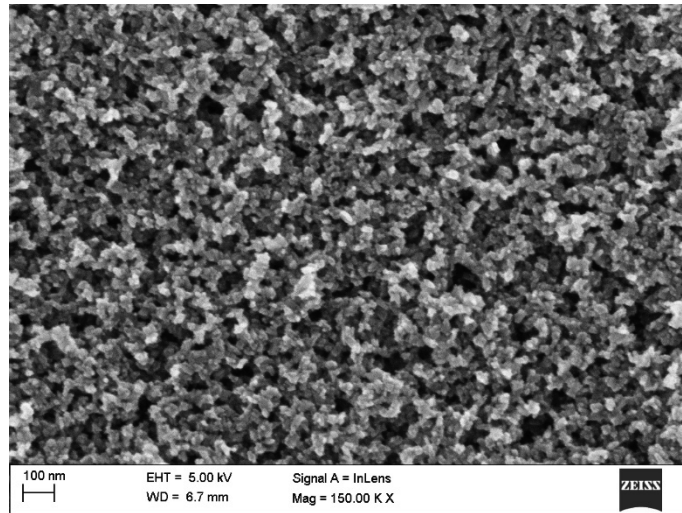


Figure 6. SEM topography of DSSC photoanode

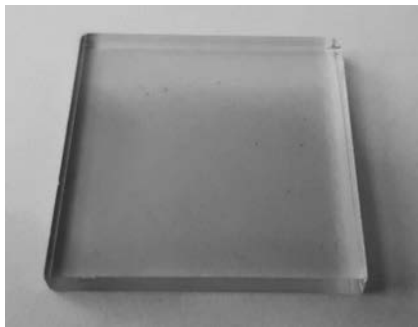


Figure 7. Counter electrode of DSSC on macroscopic scale

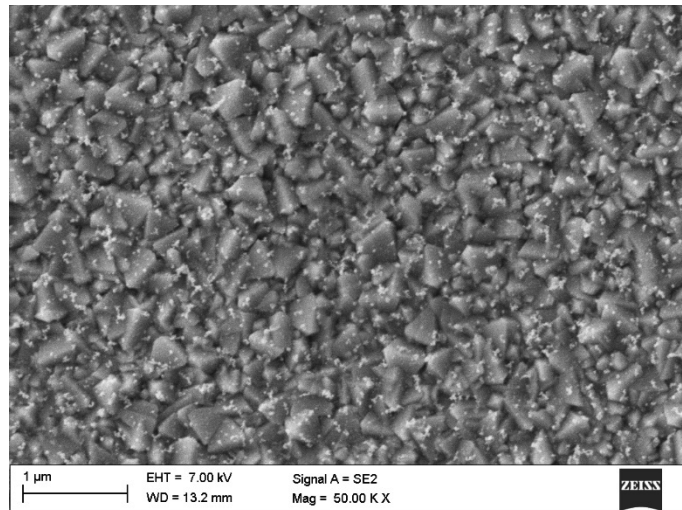


Figure 8. SEM topography of DSSC counter electrode

The results of the absorbance measurement tests for the layers constituting the DSSC photoanode are shown in Figure 9. The FTO coated glass has the lowest light absorption. It absorbs radiation below 340nm. The deposition of the mesoporous layer onto the substrate causes the absorption edge to shift towards longer wavelengths (by about 50 nm for absorbance 1.5 compared to FTO-coated glass). It was found that the photoanode dyeing significantly improves the absorption of visible radiation, and the absorption peaks were observed for wavelengths of approximately 400 and 535 nm.

Figure 10 presents the transmittance for DSSC counter electrode. The cathode has high transmission in the visible range. It was found that the transmittance was above 80% for the substrate:

- without a catalytic layer for wavelengths above 362 nm,
- with screen-printed platinum for wavelengths in the range of 530÷750 nm.

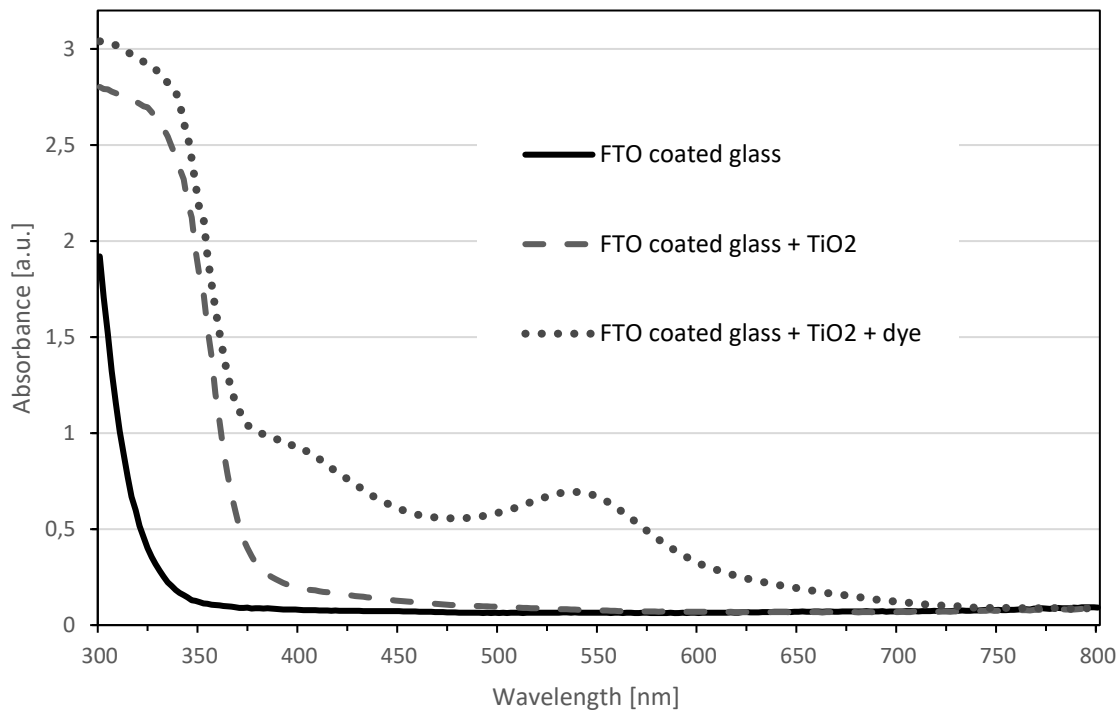


Figure 9. Absorbance for layers of DSSC photoanode

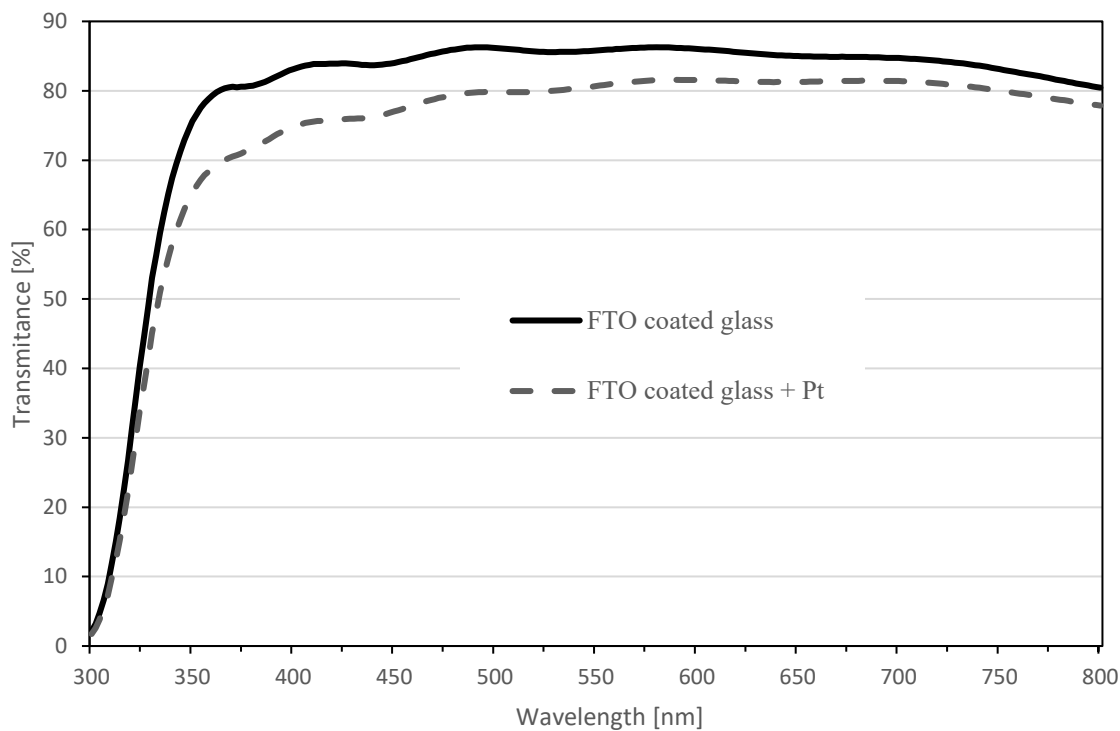


Figure 10. Transmittance for layers of DSSC counter electrode

Electrical parameters of three manufactured DSSCs were characterized by measurement of current-voltage characteristics at a light intensity of  $1000 \text{ W/m}^2$  and AM 1.5 radiation. The determined values of: open circuit voltage  $V_{oc}$ , short-circuit current  $I_{sc}$ , fill factor  $FF$ , maximum power  $P_m$ , and efficiency  $E_{ff}$  of DSSCs are listed in Table 1. It was found that the average efficiency of the produced DSSCs is 4.86 %, and the technology used allows to obtain devices with repeatable electrical properties.

Table 1. Electrical parameters of produced dye-sensitized solar cells

$I_{sc}$ [mA]	$V_{oc}$ [mV]	$P_m$ [mW]	$FF$ [-]	$E_{ff}$ [%]
5.09	680	2.04	0.59	4.84
4.97	676	2.03	0.60	4.86
5.34	672	2.10	0.59	4.88

#### 4. CONCLUSIONS

Dye-sensitized solar cells have lower efficiencies compared to commercially produced silicon photovoltaic cells. However, taking into account their advantages, such as a good price-efficiency ratio, transparency, operation at a wide angle of incidence of light, and low radiation intensity, make them competitive with first generation solar cells. The efficiency of photovoltaic cells depends on phenomena occurring at the interface between the semiconducting metal oxide, the dye, the catalytic layer and the electrolyte.

The photoanode of DSSCs plays important functions, namely governing the collection and transportation of photo-excited electrons from dye to external circuit as well as acting as a scaffold layer for adsorbed dye molecules. In this study, the  $\text{TiO}_2$  layer is uniformly deposited on the FTO coated glass. This semiconductor has a porous structure, and large specific surface area. Unfortunately, this material does not absorb visible light. Adsorbing the N719 dye on its surface significantly increases its absorption properties. The screen-printed platinum layer has a slight effect on reducing the transparency of the DSSC counter electrode. The technology used in this work allowed the production of DSSCs with an average efficiency of 4.86%.

#### BIBLIOGRAPHY

1. J. Yuan, R. Yang, Q. Fu, Aspects of renewable energy influenced by natural resources: How do the stock market and technology play a role?, *Resources Policy* 85 (2023) 103820
2. A.O.M. Maka, J.M. Alabid, Solar energy technology and its roles in sustainable development, *Clean Energy* 6/3 (2022) 476-483
3. J. Mohtasham, Renewable Energies, *Energy Procedia* 7 (2015) 1289-1297
4. B. Akinoglu, B. Tuncel, V. Badescu, Beyond 3rd generation solar cells and the full spectrum project. Recent advances and new emerging solar cells, *Sustainable Energy Technologies and Assessments* 46 (2021) 101287
5. A. Drygała, Influence of  $\text{TiO}_2$  film thickness on photovoltaic properties of dye-sensitized solar cells, *IOP Conf. Series: Earth and Environmental Science* 642 (2021) 012001

6. A. Agrawal, S.A. Siddiqui, A. Soni, G.D. Sharma, Advancements, frontiers and analysis of metal oxide semiconductor, dye, electrolyte and counter electrode of dye sensitized solar cell, *Solar Energy* 233 (2022) 378–407
7. J. Budzynowski, K. Tyczyński, S. Bielec, J. Sobolewski, A. Drygała, J. Wyrwał, S. Lesz, E, Tillová, P. Palček, Co-sensitization of titanium dioxide layers for photovoltaic applications with dyes, *Proceeding of TalentDetector2024\_Winter: International Students Scientific Conference, 26th January 2024, Prace Katedry Materiałów Inżynierskich i Biomedycznych, 2024, Gliwice, Katedra Materiałów Inżynierskich i Biomedycznych (2024) 55-61*
8. J. Romani, A. Ramos, J. Salom, Review of transparent and semi-transparent building-integrated photovoltaics for fenestration application modeling in building simulations, *Energies* 16/9 (2022) 3286
9. N.A. Karim, U. Mehmood, H.F. Zahid, T. Asif, Nanostructured photoanode and counter electrode materials for efficient Dye-Sensitized Solar Cells (DSSCs), *Solar Energy* 185 (2019)165–188
10. K. Barczak, K. Herka, D. Czulyt, J. Budzynowski, S. Lesz, A. Zarychta, A. Drygała, Wpływ grubości warstwy półprzewodnikowej na własności optoelektryczne barwnikowych ogniw fotowoltaicznych, *Proceeding of TalentDetector'2023 Summer. International Students Scientific Conference, Brenna, Poland, 26th June 2023. Red. Mirosław Bonek, Gliwice: Katedra Materiałów Inżynierskich i Biomedycznych. Wydział Mechaniczny Technologiczny. Politechnika Śląska (2023) 41-48*



17th-19th June 2024  
Gliwice, Poland

DEPARTMENT OF ENGINEERING MATERIALS AND BIOMATERIALS  
FACULTY OF MECHANICAL ENGINEERING  
SILESIA UNIVERSITY OF TECHNOLOGY

## INTERNATIONAL STUDENTS SCIENTIFIC CONFERENCE

### Plant-based synthesis of SnO<sub>2</sub> nanoparticles using aqueous extract from *Aglaonema commutatum* leaves

Alicja Duda<sup>a,c</sup>, Bartosz Kopyciński<sup>b,c</sup>, Krzysztof Pęczak<sup>a,c</sup>

<sup>a</sup> Łukasiewicz Research Network – Institute of Non-Ferrous Metals, Sowińskiego 5 St., 44-100, Gliwice, Poland

<sup>b</sup> Łukasiewicz Research Network – Institute for Engineering of Polymer Materials and Dyes, Marii Skłodowskiej-Curie 55 St., 87-100, Toruń, Poland

<sup>c</sup> Doctoral School, Silesian University of Technology, Akademicka 2A St., 44-100, Gliwice, Poland, email: alicja.duda@imn.lukasiewicz.gov.pl

**Abstract:** The use of plant extracts in the synthesis of metal and metal oxide nanoparticles has been gaining a lot of attention in the scientific world for the past few years. In this article, an attempt was made to obtain SnO<sub>2</sub> nanoparticles using an aqueous extract of *Aglaonema commutatum* leaves. The synthesis process involved two stages - preparation of the hydroxide intermediate product and then its thermal reduction. The obtained powder materials were subjected to phase composition analysis via X-ray powder diffraction. In addition, physical properties such as apparent density, specific surface area, and average particle size were determined. Color measurements of the intermediate product and the final reaction product were also performed, as well as the examination of the morphology of the obtained nanoparticles. The possibility of obtaining SnO<sub>2</sub> nanoparticles using the *Aglaonema commutatum* leaves extract was confirmed. The average size of particles was stated at 33 nm and various acicular-flake shapes were observed.

**Keywords:** plant-based synthesis, plant extracts, nanomaterials, powder metallurgy

## 1. INTRODUCTION

The development of metal and metal oxide nanoparticles (NPs) production has been the subject of numerous studies for at least the past 20 years and that is mainly because of their extraordinary properties such as small size, diverse structure, or great application potential in different scientific and industrial branches [1]. Recently, the search for eco-friendly strategies for their preparation has been particularly mentioned in the literature. One of the directions followed by the world of science is biological synthesis methods, in which often toxic and environmentally harmful chemicals are replaced by plant extracts. Such methods are characterized by safe nature, low production costs, and the opportunity to exploit a wide range of natural origin, fully renewable materials [2]. Biological syntheses are included in the *bottom-*

up routes of metallic NPs formation. The growing interest in this topic results primarily from the unique features of natural raw materials, which play the role of reducing and capping agents in the production of metals and metal oxides. Thanks to this, the final material can be obtained via chemical reduction, sometimes combined with the thermal decomposition of the intermediate product [3]. The first step, however, is the effective extraction of reducing compounds, i.e. polysaccharides, flavones, anthocyanidins, or phenolic acids. These can be easily obtained from various parts of plants, i.a. seeds, leaves, roots, fruits, or flowers [4]. Then, the actual synthesis path can be proceeded, which traditionally includes three main stages. Initially, as a result of the reaction with hydroxyl groups originating from plant extracts, metal ions from its salts are reduced. In the second stage, a so-called Ostwald ripening occurs. Here, the NPs are formed in a process of heterogeneous nucleation which leads to particle growth followed by further reduction of metal ions. This phenomenon is observed due to the strong bond energy between the atoms of the formed metal. In the last stage, thanks to the ability of compounds contained in plant extracts to stabilize metallic NPs, particles undergo conversion to the energetically favorable structure. In some cases, the formation of a desired product does not always occur directly in the reduction process. Hence, an additional step involving thermal reduction of the intermediate product formed during the reaction with the plant extract is often used [5]. Metal and metal oxide NPs are among the most frequently mentioned materials obtained from the use of plant extracts in the literature. This is due to their potential for application as antibacterial and antifouling agents, biosensors, fertilizers for plant cultivation purposes, and chemical tools in light-activated processes, pharmaceutical synthesis, or hydrogen production [2].

In this work, the biological synthesis of SnO<sub>2</sub> NPs was carried out on the example of the reaction of SnCl<sub>4</sub> with an aqueous extract of *Aglaonema commutatum* leaves. The obtained final product was characterized using the X-ray diffraction method (XRD). The physical properties of the powders, such as actual density (AD), specific surface area (SSA), and average particle size (AvPS) were determined. Additionally, color measurements were performed in the CIELab color space, as well as the imaging of SnO<sub>2</sub> NPs morphology with the use of scanning electron microscopy (SEM). The summary briefly discusses the potential of performed research and includes a critical look at the limitations related to plant-based synthesis methods.

## 2. EXPERIMENTAL

### 2.1. Preparation of extract

50 g of home-grown *Aglaonema commutatum* leaves were washed under running water and air dried. Leaves prepared this way were ground, added to 250 ml of DI water, and stirred at 45°C for 5 h. The resulting mixture was allowed to cool and filtered through cellulose filters. To reduce the probability of photodegradation, the extract was stored in the dark.



## 2.2. Tin (IV) oxide synthesis

SnO<sub>2</sub> NPs synthesis was based on a two-step method. First, 100 ml of 0.1 M tin chloride dihydrate (SnCl<sub>4</sub>·2H<sub>2</sub>O, PolAura) aqueous solution was added to 200 ml of previously prepared *Aglaonema commutatum* leaves extract and stirred at 60°C for 4 h. After this time, the mixture was allowed to cool to the room temperature while stirring for the next 2 h. The obtained precipitate was centrifuged at 3500 rpm for 10 minutes using a centrifuge (Eppendorf Centrifuge 5804), then washed twice with DI water and EtOH (Stanlab) and dried at 70°C for 2 h. In the second stage, the powder was thermally decomposed in a tube furnace at a temperature of 400°C for 4 hours in an air atmosphere.

## 2.3. Powder characterization

- X-ray powder diffraction (XRD)

Qualitative phase analysis was carried out on powders and coatings using diffractograms recorded with an XRD7 diffractometer made by Seifert-FPM. Characteristic X-ray radiation of Cu K $\alpha$  and nickel filter were used for the investigation. Analysis was carried out in the 2 $\theta$  range 10°÷100°. Identification of the phases was done using Seifert and Match! software, basing the results on the ICDD PDF-4+ catalog from 2023.

- Apparent density (AD)

AD was measured by the gas pycnometry method using the Micromeritics AccuPyc 1340 II pycnometer. Measurements were performed at room temperature in a sample chamber with a volume of 10 cm<sup>3</sup> and helium as an inert gas. Results for density were obtained for 15-cycle repetitions.

- Specific surface area (SSA)

The determination of SSA was carried out on a Micromeritics Gemini 2360 apparatus. The measuring range was 0.01 m<sup>2</sup>/g for the specific surface and 0.1÷300 m<sup>2</sup> for the total surface. Samples were dried overnight at 105°C under a nitrogen atmosphere. The measurements were performed in the P/P<sub>0</sub> range of 0.05÷0.30 (value taken before the measurements).

- Average particle size (AvPS)

On the basis of the AD and SSA measurements, AvPS of obtained powders was determined. Calculations were done with the use of the equation:

$$\bar{d} = \frac{6 \cdot 10^3}{\rho \cdot S}$$

where  $\rho$  – apparent density [g/cm<sup>3</sup>], S – specific surface area [m<sup>2</sup>/g].

- Color measurements

The color of the powders was determined using an SP62 X-rite portable, handheld sphere spectrophotometer with a measuring geometry of d/8 according to ISO 7724-2 *Paints and varnishes – Colorimetry – Part 2: Color measurement*. The color coordinates in CIELab color space were calculated (L\* – brightness, a\* – color from green to magenta, b\* – color from blue to yellow). The color difference  $\Delta E$  was determined in accordance with ISO 7724-3 *Paints and*

varnishes – Colorimetry – Part 3: Calculation of color differences. The calculations were made based on the following formula:

$$\Delta E = \sqrt{(\Delta L^*)^2 + (\Delta a^*)^2 + (\Delta b^*)^2}$$

- Scanning electron microscopy (SEM)

SEM observation was performed using LEO Gemini 1525 high-resolution scanning electron microscope with a resolution of 1.5 nm at a current voltage of 20 kV and equipped with an InLens detector. Before measurement, the sample was dried overnight at 50°C and then sputtered for 50 s with an Au conductive layer in an Ar protective atmosphere using SEI supplies sputter coater.

### 3. RESULTS AND DISCUSSION

As mentioned in the introduction, plant-based NPs synthesis usually involves the chemical reduction of metal salts using a plant extract. This research involved a reduction of SnCl<sub>4</sub> salt with the use of extract obtained from *Aglaonema commutatum* leaves, thanks to which an intermediate reaction product was obtained. In the next stage, a thermal reduction process was carried out to obtain nanometric SnO<sub>2</sub> powder. A fundamental scheme of the discussed synthesis is shown in Figure 1.

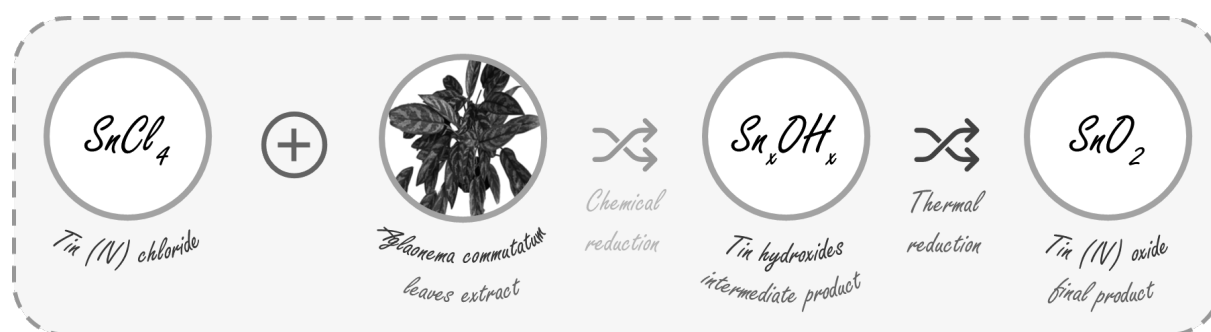


Figure 1. Scheme of plant-based SnO<sub>2</sub> NPs synthesis

#### 3.1. X-ray powder diffraction

XRD phase analysis was the fundamental method to confirm SnO<sub>2</sub> formation in the process of SnCl<sub>4</sub> reduction with the use of *Aglaonema commutatum* leaf extract. Figure 2 shows XRD patterns of the intermediate (SnHydOx\_Agm) and final (SnOx\_Agm) reaction products. As can be seen, the starting material – SnCl<sub>4</sub>·2H<sub>2</sub>O – has not been fully reduced to the desired oxide, and XRD analysis shows that the intermediate product consists of transitional phase Sn<sub>21</sub>Cl<sub>16</sub>O<sub>6</sub>(OH)<sub>14</sub> with a structure of mineral abhurite. The presence of SnO<sub>2</sub> was proved after the thermal reduction of Sn<sub>21</sub>Cl<sub>16</sub>O<sub>6</sub>(OH)<sub>14</sub> and it was shown that the obtained powder sample is single phase and consists of SnO<sub>2</sub> with a structure of mineral cassiterite.

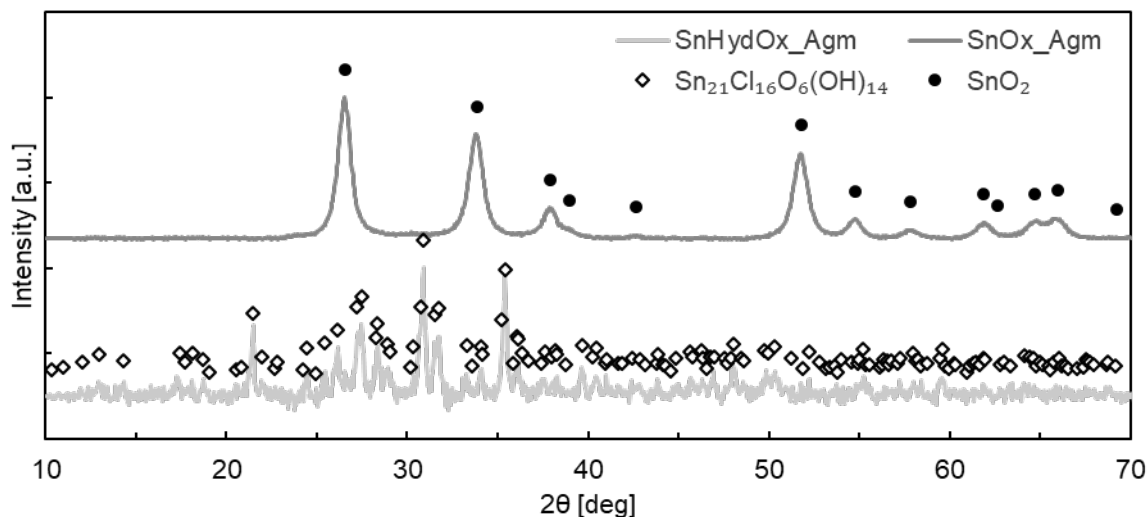


Figure 2. XRD patterns for SnHydOx\_Agm and SnOx\_Agm samples

### 3.2. Powders characterization – physical properties

The measured values of the AD and SSA of the powders were stated at 4.11 g/cm<sup>3</sup> and 7.06 m<sup>2</sup>/g for SnHydOx\_Agm and 6.70 g/cm<sup>3</sup> and 27.54 m<sup>2</sup>/g for SnOx\_Agm. The AvPS of the obtained materials was stated at around 207 and 33 nm for SnHydOx\_Agm and SnOx\_Agm, respectively. The results are summarized in Table 1. The AD value of the SnOx\_Agm sample confirms the formation of SnO<sub>2</sub> NPs and corresponds to the literature data dedicated to similar research [6]. Moreover, it was observed that the resulting SnO<sub>2</sub> powder is nanometric and the SSA value is relatively high.

Table 1. Powder samples physical properties

Sample	AD [g/cm <sup>3</sup> ]	SSA [m <sup>2</sup> /g]	AvPS [nm]
SnHydOx_Agm	4.1056 ± 0.0034	7.0580 ± 0.0197	207.06
SnOx_Agm	6.6982 ± 0.0051	27.5384 ± 0.0662	32.53

The AvPS analysis was complemented by SEM imaging performed for the SnOx\_Agm sample (Figure 3). It can be seen that the obtained powder formed micrometric flake-shaped agglomerates of spherical nanoparticles. It was observed that the morphology of the obtained material is diverse and is divided mainly into two forms - acicular (spicule-like) and flake shapes. During the synthesis, particles with sizes ranging from 20 to 150 nm were obtained.

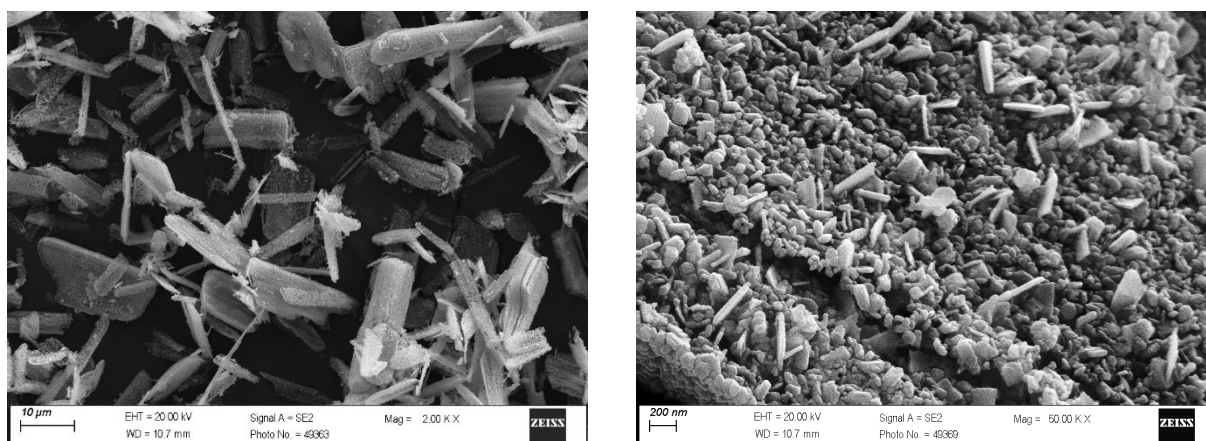


Figure 3. SEM images of the SnOx\_Agm sample

An additional feature for the confirmation of the correct reaction course is the color of both the intermediate and the final product (Figure 4). Tin hydroxides are usually white, whereas the SnO<sub>2</sub> color ranges from off-white/light gray to beige shades [7, 8]. In the case of the synthesis performed in this article, it was observed that the SnHydOx\_Agm sample turned slightly ecru. This was caused by the extract used in the synthesis process. The SnOx\_Agm sample was light taupe. In addition to the visual assessment of the color of the powders, colorimetric measurements were carried out to determine their actual shades (Table 2). Moreover, a significant change was observed in the color of powders and  $\Delta E$  was stated at 23.13.



Figure 4. Images of intermediate product SnHydOx\_Agm (left) and resulting nanopowder SnOx\_Agm (right)

Table 2. Color measurements of the intermediate product (SnHydOx\_Agm) and the resulting SnO<sub>2</sub> NPs (SnOx\_Agm)

Sample	L*	a*	b*	$\Delta E$
SnHydOx_Agm	87.11	0.01	23.42	23.13
SnOx_Agm	69.40	2.12	13.01	

#### 4. CONCLUSION

The results reviewed in this article are an introduction to broader research on the production of ceramic oxide nanopowders. The possibility of the SnO<sub>2</sub> NPs formation using extract obtained from *Aglonema commutatum* leaves was confirmed. The presence of a pure reaction

product was proved via XRD phase analysis. The average size of the formed NPs was stated at 33 nm, and their morphology was varied, with a predominance of acicular and flaky shapes.

Thanks to the relatively facile route and low costs of performed synthesis, there is a great potential for its further optimization. The first key aspect of improving the efficiency of the discussed processes is the emphasis on increasing the effectiveness of extraction of the necessary reducing compounds from plants. In addition to the possibility of using various plants and their different parts, extraction tests with low environmental impact solvents (i.a. ethyl or isopropyl alcohols, glycerin, or acetone), changes in the pH or temperature of the environment, and the method of mixing the solution should be taken into account [9]. Moreover, some steps related to changing the conditions of the metal salt reduction reaction itself will certainly also have a positive impact on the results. In this case, focus on the type of metal precursor, its concentration, and the temperature conditions of the reactions should be emphasized [2].

The methods for the replacement of harmful chemicals in the processes of NPs formation are undoubtedly worthy of further exploration. The main advantage of such an approach is reduction of waste that harms the environment and the application potential of green synthesized nanopowders will surely lead to their exploitation on a larger scale.

## BIBLIOGRAPHY

1. N. T. T. Nguyen, L. M. Nguyen, T. T. T. Nguyen, T. T. Nguyen, D. T. C. Nguyen, T. V. Tran, Formation, antimicrobial activity, and biomedical performance of plant-based nanoparticles: a review, *Environmental Chemistry Letters* (2022) 20:2531–2571.
2. A. Duda, B. Kopyciński, Overview of the plant-based synthesis of metal and metal oxide nanoparticles and their potential application in the formation of protective coatings, *Ochrona przed Korozją* (2023) 66(7):197-205.
3. M.Yadi, E. Mostafavi, B. Saleh, S. Davaran, I. Aliyeva, R. Khalilov, M. Nikzamir, N. Nikzamir, A. Akbarzadeh, Y. Panahi, M. Milani, Current developments in green synthesis of metallic nanoparticles using plant extracts: a review, *Artificial Cells, Nanomedicine, and Biotechnology* (2018) 46.
4. S.Ying, Z. Guan, P.C. Ofoegbu, P. Clubb, C. Rico, F. He, J. Hong, Green synthesis of nanoparticles: Current developments and limitations, *Environmental Technology & Innovation* (2022) 26.
5. W. M. Alarif, Y. A. Shaban, M. I. Orif, M. A. Ghandourah, A. J. Turki, H. S. Alorfi, H. R. Z. Tadros, Green synthesis of TiO<sub>2</sub> nanoparticles using natural marine extracts for antifouling activity, *Marine Drugs* (2023) 21(2):62.
6. S. Gorai, Bio-based synthesis and applications of SnO<sub>2</sub> nanoparticles - an overview, *Journal of Materials and Environmental Sciences* (2018) 9(10):2894-2903.
7. W. D. Honnick, J. J. Zuckerman. *Inorganic Chemistry* (1976) 15(12):3034–3037.
8. F. M. Santiago-Giraldo, A. A. Lugo-Ruiz, S. J. Bailón-Ruiz, Production and characterization of tin oxide (SnO<sub>2</sub>) nanostructures, *MRS Advances* (2022) 7:249–254.
9. B. Kopyciński, A. Duda, E. Langer, G. Kamińska-Bach, Color photostability assessment of ultrasound-assisted extracts from European blueberry (*Vaccinium Myrtillus* L.) obtained with the use of non-toxic solvents, *Wood. Research papers. Reports. Announcements* (2024) 67.



17th-19th June 2024  
Gliwice, Poland

DEPARTMENT OF ENGINEERING MATERIALS AND BIOMATERIALS  
FACULTY OF MECHANICAL ENGINEERING  
SILESIA UNIVERSITY OF TECHNOLOGY

## INTERNATIONAL STUDENTS SCIENTIFIC CONFERENCE

### Symulator samolotu Cessna 172 bazujący na platformie ruchu

Anna Dyrda<sup>a</sup>, Karolina Kempa<sup>a</sup>, Paweł Ledwoń<sup>a</sup>, Alan Pawleta<sup>a</sup>, Bartosz Pokorski<sup>a</sup>, Nikodem Wspaniały<sup>a</sup>, Wojciech Cofalik<sup>a</sup>, Patryk Mondry<sup>a</sup>, Kacper Matys

<sup>a</sup> Politechnika Śląska, Wydział Automatyki, Elektroniki i Informatyki, Studenckie Koło Naukowe Wirtualnego Latania vFly  
emai: ap302734@student.polsl.pl

**Streszczenie:** Artykuł przedstawia prace Studenckiego Koła Naukowego vFly nad symulatorem samolotu, który ma zagwarantować immersję operatora bazując na odczuciach haptycznych uzyskiwanych przy pomocy platformy ruchu oraz realistycznej grafice wyświetlanej na goglach rzeczywistości wirtualnej.

**Abstract:** The article presents the work of the vFly Student Scientific Association on a flight simulator designed to ensure operator immersion through haptic feedback obtained using a motion platform and realistic graphics displayed on virtual reality goggles.

**Keywords:** symulator lotu, unity, platforma ruchu

### 1. WSTĘP

Symulatory lotnicze odgrywają kluczową rolę w szkoleniu i rozwoju umiejętności pilotów oraz załóg lotniczych. Stanowią one realistyczne i kontrolowane środowisko, które pozwala na bezpieczne i efektywne przyswajanie wiedzy oraz doskonalenie procedur operacyjnych [1][2]. Dzięki zaawansowanym technologiom, symulatory mogą wiernie odtwarzać warunki lotu, w tym dynamikę lotu, reakcje na warunki pogodowe i awarie systemów pokładowych. Symulator samolotu to projekt łączący zaawansowaną część hardwarową, z możliwościami softwarowymi, udostępnionymi przez środowisko Unity 3D. Projekt jest realizowany przez studentów wydziału Automatyki, Elektroniki i Informatyki w ramach studenckiego koła naukowego vFly.

### 2. WARSTWA SPRZĘTOWA

Stanowisko symulatora prezentowane w artykule składa się z trzech elementów, gogli rzeczywistości wirtualnej, platformy ruchu oraz fizycznych kontrolerów odwzorowujących urządzenia kontrolne zainstalowane w samolocie.

- **Gogle VR HP Reverb G2**

Gogle są podstawowym elementem wpływającym na immersję użytkownika, dlatego dobranie odpowiedniego modelu jest kluczowe dla sukcesu projektu. Zdecydowano się na wybór modelu HP ReverbG2 ponieważ, zapewnia on wysoką rozdzielczość ekranu (4320x2160 pikseli dla obu oczu) oraz szerokie pole widzenia na poziomie 110 stopni. Urządzenie posiada dwa głośniki zapewniające wysoką jakość dźwięku. Gogle zapewniają także stabilne łącze przewodowe, bazujące na złączu DisplayPort, tym samym minimalizując obciążenie stacji roboczej. Gogle są wyposażone w precyzyjny akcelerometr i żyroskop, co pozytywnie wpływa na jakość śledzenia ruchów głowy użytkownika i tym samym na realizm symulacji.

- **Symulator ruchu YawVR standard edition**

Platforma Yaw VR to kompaktowy symulator ruchu dedykowany do wykorzystania w aplikacjach bazujących na rzeczywistości wirtualnej. Dzięki możliwości ruchu w trzech obszarach określanych jako **yaw** (obrót ciągły w zakresie 360 stopni w stosunku do osi pionowej), **pitch** oraz **roll** (oba w zakresie od +20 do -20 stopni względem osi poziomej), symulator dostarcza realistyczne wrażenie lotu samolotem. Dodatkowo parametry platformy w zakresie prędkości obrotowej (określane przez producenta na 360 stopni na sekundę dla yaw oraz 45 stopni na sekundę dla pitch oraz roll) umożliwiają na sprawne reagowanie na zmianę położenia oraz obrotu wirtualnego pojazdu. Samo urządzenie pozwala na łączność poprzez kabel RJ-45 z siecią lokalną, co umożliwi łatwe nawiązanie połączenia z YawVR poprzez stację roboczą (obsługującą aplikację symulacyjną) podłączoną do tej samej sieci. Platforma oferuje także możliwość połączenia bezprzewodowego z wykorzystaniem Wi-Fi, jednakże połączenie przewodowe redukuje możliwość utraty pakietów oraz opóźnień w dostarczaniu pakietów. Producent udostępnia oprogramowanie Yaw SDK, w efekcie możliwa jest integracja platformy ze środowiskiem Unity oraz Unreal Engine.

- **Kontroler LOGITECH G Saitek PRO Flight Yoke System**

G Saitek Pro Flight Yoke System to kontroler typu wolant produkowany przez firmę LOGITECH. Wolant pozwala na uzyskanie precyzyjnego sterowania akcjami samolotu. Zestaw wyposażony jest w pedały oraz przepustnice, które zwiększają immersję sterowania statkiem powietrznym. Komunikacja z kontrolerem odbywa się poprzez przewodowe połączenie USB, co wpływa korzystnie na prędkość przesyłania informacji w porównaniu do odpowiedników łączących się bezprzewodowo. Dodatkowo, wolant oraz pedały pozwalają na ruch w pięciu osiach oraz umożliwiają zaprogramowanie do 75 funkcji przy wykorzystaniu 25 przycisków. Funkcjonalność ta była niezmiernie istotna w realizowanym projekcie, ponieważ pozwoliła na rezygnację z przepustnicy. Osoby testujące zaimplementowany symulator zwracały uwagę na trudność znalezienia przepustnicy, w symulacji opartej o gogle VR, w takim przypadku operator nie widzi prawdziwego otoczenia, dlatego też znalezienie komponentów sterujących na których nie trzyma się rąk jest niezmiernie trudne. Powyższe elementy, zostały precyzyjnie skomponowane oraz skonfigurowane, aby jak najdokładniej odwzorować ruch

prawdziwego samolotu. (Rysunek 1) przedstawia skonfigurowany zestaw w trakcie testów integracyjnych platformy symulacyjnej z zaimplementowanym oprogramowaniem symulacyjnym.



Rysunek 1. Zdjęcie z realizacji testów w trakcie wykonywania manewru skrętu w lewo.  
*Figure 1. Photo from tests carried out during a left turn maneuver.*

### 3. SOFTWARE

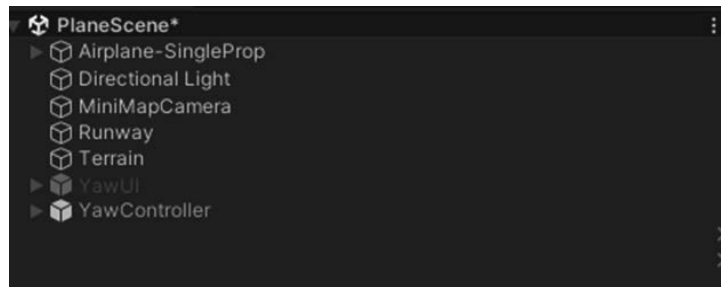
Wybór Unity jako głównego narzędzia projektowego był strategiczny z kilku kluczowych powodów, m.in.

- wszechstronność i elastyczność środowiska
- intuicyjny interfejs użytkownika oraz wsparcie dla początkujących użytkowników umożliwiające szybkie prototypowanie, nawet bez doświadczenia programistycznego
- wykorzystanie języka C#, umożliwiającego efektywne programowanie logiki symulacji.

Unity wspiera różne platformy oraz urządzenia VR i AR, co zapewniało elastyczność i możliwość dostosowania do różnych wymagań projektowych. Optymalizacja pod kątem wydajności gwarantowała płynne działanie aplikacji nawet na mniej wydajnych urządzeniach, co było kluczowe dla jakości użytkowej.

Hierarchia projektu w Unity stanowi kluczowy element organizacyjny, umożliwiający skuteczną strukturyzację elementów sceny oraz określenie ich wzajemnych powiązań. Poniżej przedstawiono skrócony opis każdego elementu hierarchii projektu (Rysunek 2.):



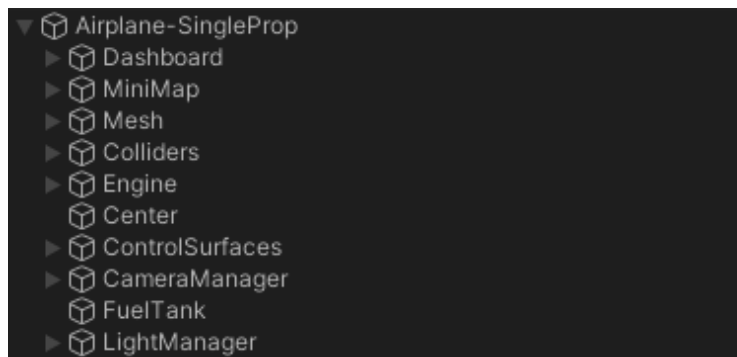


Rysunek 2. Hierarchia projektu.

Figure 2. Project hierarchy.

### 1. Airplane-SingleProp

Główny obiekt symulatora, reprezentujący model samolotu jednosilnikowego (Rysunek 3). Zawiera modele 3D samolotu, skrypty kontrolujące zachowanie, animacje, materiały i tekstury:



Rysunek 3. Hierarchia Airplane-SingleProp

Figure 3. Airplane-SingleProp Hierarchy

- a. Dashboard: panel kontrolny w kokpicie samolotu z przyrządami nawigacyjnymi i kontrolnymi.
  - b. MiniMap: panel w kokpicie przedstawiający mini-mapę dla orientacji przestrzennej.
  - c. Mesh: geometria 3D samolotu, obejmująca model kadłuba, skrzydeł, sterów i śmigła.
  - d. Colliders: komponenty fizyczne definiujące kolizje samolotu, np. collider kół, kadłuba i skrzydeł.
  - e. Engine: komponent odpowiedzialny za dźwięki samolotu, zapewniając realistyczne efekty dźwiękowe.
  - f. Center: punkt centralny samolotu, odpowiadający środkowi jego masy.
  - g. ControlSurfaces: Powierzchnie sterujące samolotu, np. ster wysokości, ster kierunku, lotki.
  - h. CameraManager: Zarządza kamerami w symulatorze, umożliwiając uzyskanie różnych widoków z kamery.
  - i. FuelTank: Zbiornik paliwa samolotu, monitorujący poziom paliwa i jego zużycie.
  - j. LightManager: Zarządza oświetleniem samolotu, kontrolując różne źródła światła.
2. Directional Light: Źródło światła kierunkowego symulujące naturalne światło słoneczne.
  3. Minimap Camera: Dodatkowa kamera wyświetlająca mini-mapę.

4. Runway: Reprezentacja pasa startowego na lotnisku, służącego do startów i lądowań.
5. Terrain: Obiekt terenu, przedstawiający krajobraz wokół lotniska.
6. YawUI: Element interfejsu użytkownika wyświetlający informacje o przechyleniu samolotu. Pozwala również podłączyć platformę YawVr.
7. YawController: Komponent zarządzający przechyleniem samolotu, kontrolujący jego ruch wzdłuż osi Yaw.

#### 4. PREZENTACJA SYMULACJI

Na zdjęciach (Rysunek 4,5,6), zaprezentowano różne etapy rozgrywki, kluczowe elementy interfejsu użytkownika i otoczenia symulacji.



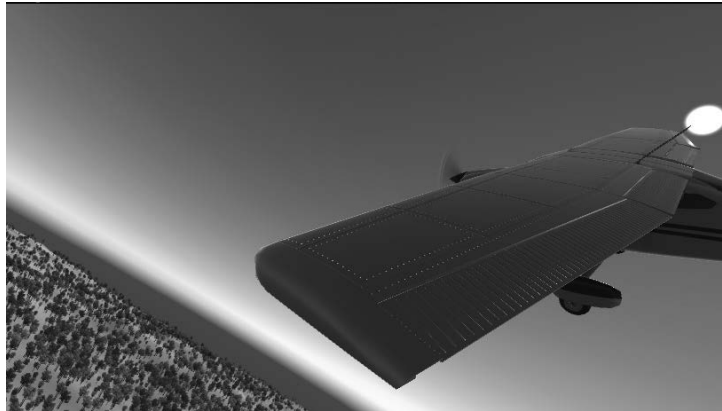
Rysunek 4. Widok ze środka samolotu, na pasie startowym.

*Figure 4. View from inside the plane, on the runway.*



Rysunek 5. Widok ze środka samolotu, podczas skrętu w prawo.

*Figure 5. View from inside the plane while turning right.*



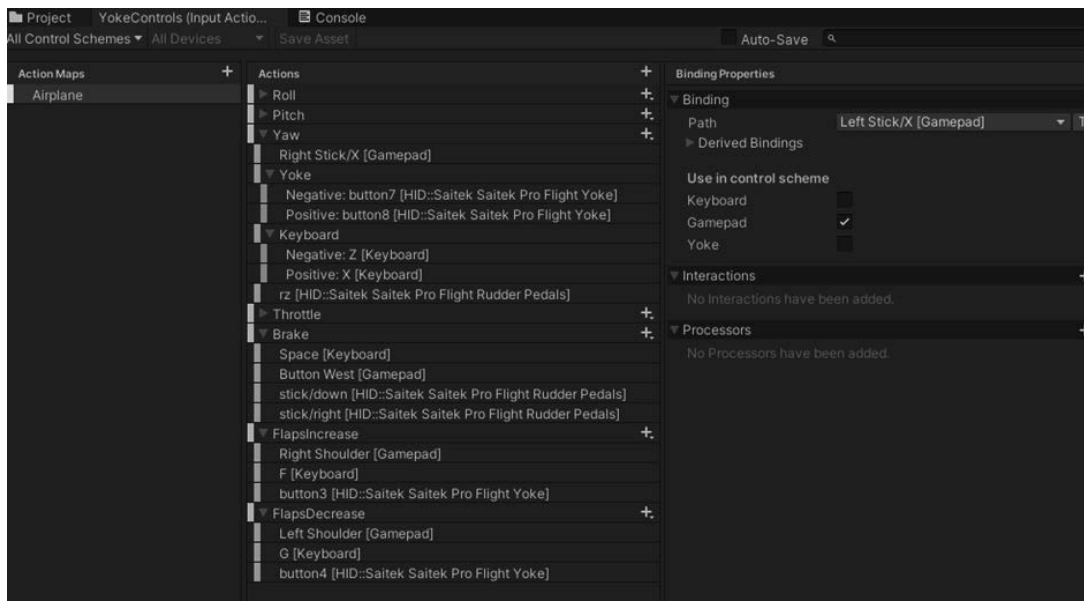
Rysunek 6. Widok ze skrzydła samolotu.

Figure 6. View from the wing of the plane.

## 5. KONFIGURACJA

### 5.1 Input System

Kontrola ruchu symulatora została opracowana za pomocą pakietu Unity Input System[5], (Rysunek 7). Przygotowane tam są definicje akcji, pod które zostały podpięte przyciski funkcyjne wolantu oraz alternatywne dla pada oraz klawiatury.



Rysunek 7. Input System

Figure 7. Input System

Taki system sterowania dodany został do komponentu Player Input, użytym w głównym modelu samolotu (Rysunek 8).



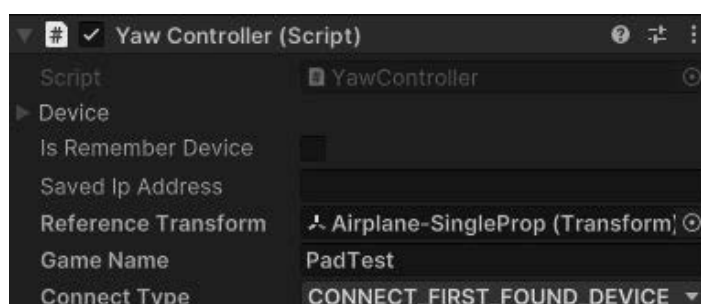
Rysunek 8. Player Input

*Figure 8. Player Input*

W projekcie skorzystano z prefabrykatu samolotu z zasobu Simple Airplane Physics Toolkit - Lift, Drag, Thrust [3] autorstwa Dylana Auty'ego, który zawiera model awionetki oraz implementacje fizyki samolotów.

## 5.2 YawVR

Pakiet Yaw VR [4], pozwala nam zarządzać i kontrolować symulator ruchu Yaw VR z poziomu projektu Unity. Kontroler YawController (Rysunek 9) wysyła orientację obiektu YawTracker do podłączonego urządzenia. Aby kontrolować symulator ruchu, wystarczy animować orientację obiektu YawTracker, a ta zostanie przesłana do fizycznego urządzenia.

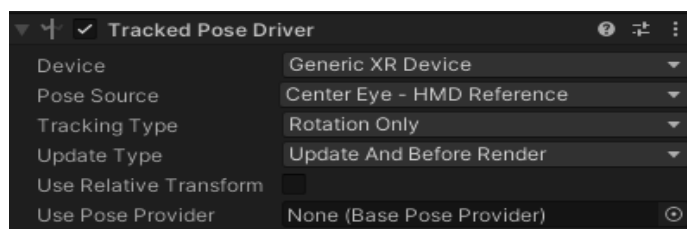


Rysunek 9. Yaw Controller

*Figure 9. Yaw Controller*

## 5.3 VR

W celu podłączenia gogli VR skonfigurowano projekt z użyciem wtyczek XR Plug-in Management i OpenXR (Rysunek 10). Następnie zainstalowano narzędzie Windows Mixed Reality Feature Tool, pozwalające na instalację wtyczki Mixed Reality OpenXR. Dodano profil kontrolera HP Reverb G2 do ustawień OpenXR. Na koniec przekonwertowano kamerę na XR Rig, umożliwiając śledzenie ruchu głowy.



Rysunek 10. Tracker Pose Driver

*Figure 10. Tracker Pose Driver*

## 6. PODSUMOWNIE

W niniejszym artykule skupiono się na analizie procesu tworzenia symulatora lotu w środowisku Unity, z uwzględnieniem jego zalet, możliwości oraz praktycznego wykorzystania. Istotnym aspektem projektu jest ciągle doskonalenie grafiki oraz planowane wprowadzenie nowych funkcji, takich jak edycja warunków symulacji, co pozwoli na jeszcze większą różnorodność i realizm doświadczeń użytkownika.

Perspektywa dalszego rozwoju projektu obejmuje planowaną implementację wielu lotnisk rozmieszczonych na różnych biomach, co dodatkowo zwiększy atrakcyjność i realizm symulacji. Ponadto, wprowadzenie edycji warunków symulacji, takich jak pogoda czy pora dnia, umożliwi użytkownikowi jeszcze większą kontrolę nad doświadczeniem symulacji oraz zapewni dodatkową różnorodność.

Warto podkreślić, że projekt ten stanowi istotny wkład w rozwój technologii symulacji lotu oraz wzbogaca zasób dostępnych aplikacji wirtualnej rzeczywistości. Dalsze badania i rozwój projektu mogą przyczynić się do jeszcze większego poszerzenia jego możliwości oraz zastosowań praktycznych.

Ostatecznie, tworzenie symulatora lotu w środowisku Unity stawia przed badaczami ciekawe wyzwania, wymagające zarówno zaangażowania technicznego, jak i kreatywności. Ten dynamicznie rozwijający się obszar oferuje wiele możliwości dla przyszłych badań i projektów, otwierając nowe perspektywy w dziedzinie symulacji lotu.

## LITERATURA

1. Myers III, Paul L., Arnold W. Starr, and Kadie Mullins. "Flight simulator fidelity, training transfer, and the role of instructors in optimizing learning." *International Journal of Aviation, Aeronautics, and Aerospace* 5.1 (2018): 6.
2. Allerton, D. J. "The impact of flight simulation in aerospace." *The Aeronautical Journal* 114.1162 (2010): 747-756.
3. D. Auty, Simple Airplane Physics Toolkit, <https://assetstore.unity.com/packages/tools/physics/simple-airplane-physics-toolkit-lift-drag-thrust-146915>, 2022
4. Yaw VR Unity SDK Documentation, <https://yaw.one/UnitySDK/Documentation/html/>, 2022
5. Unity Input System Documentation, <https://docs.unity3d.com/Packages/com.unity.inputsystem@1.8/manual/index.html>, 2024

## Computer simulation of the strength properties of a hammer with a metal and wooden head made using FEM

Amadeusz R. Dziwis<sup>a</sup>, Pascal Bzdon<sup>a</sup>, Wojciech Mikołajko<sup>b</sup>, Agata Śliwa<sup>b</sup>, Marek Sroka<sup>b</sup>

<sup>a</sup> II Liceum Ogólnokształcącym im. Romualda Traugutta w Częstochowie  
email: aleksanderdziwis@gmail.com, paszczal2@wp.pl,

<sup>b</sup> Silesian University of Technology, Faculty of Mechanical Engineering, Department of Engineering Materials and Biomaterials  
email: wojciech.mikolajko@polsl.pl, agata.sliwa@polsl.pl, marek.sroka@polsl.pl

**Abstract:** The objective of this thesis was to create a computer simulation of the material properties of hammers with metal and wooden obesity with included forces on them. Includes application of FEM in carrying out computer analysis of stress, displacement which occurred on the surface of hammers under three forces, and the appointment safety factor.

**Keywords:** hammer, Inventor, stress distribution, displacements, safety factor

### 1. INTRODUCTION

One of the oldest and most common types of hand tools are hammers. These tools are often used to hit the material to process it (chisel) and drive the material into another element (wedge, nail). A hammer as a hand tool works by accumulating kinetic energy in a heavy head during a relatively long swing and then transferring it to the struck object in a short time. The hammer consists of two essential elements: the head and the shaft. Figure 1 shows a locksmith's hammer with a wooden shaft and a metal head. Due to their structure and the ability to transfer kinetic energy, hammers are used in almost every construction work and other fields [1].

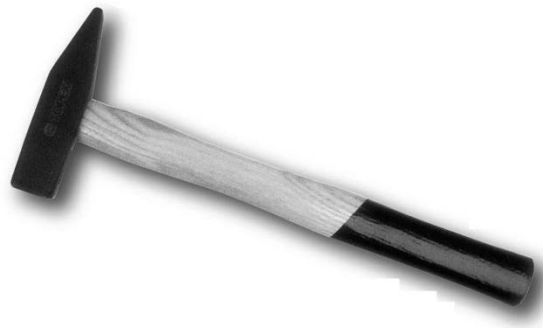


Figure 1. Locksmith's hammer [2]

The most frequently used material [3,4] for the hammer shaft is wood (birch).

In the case of blunt force, the most frequently used materials are [3,4] carbon steels:

- N6;
- N7;
- N7E.

The head has a shape similar to an elongated cuboid with one end bevelled on one or both sides. Generally, a wedge reinforces the connection between the shaft and the head, and the shaft has a structure similar to a cylinder. The basic quantity characterizing hammers is the head weight, approximately 150 g, and the total weight for the enormous two-handed hammers is up to 20 kg [3].

In addition to the traditional hammer for mechanical work (locksmith's hammer), there are also hammers for special applications. Hammers for special applications can be divided into [3]:

- Sheet metal hammers;
- Carpenter's hammers;
- Shoemaker's hammers;
- Mason's hammers;
- Kitchen hammers;
- Geological hammers;
- Judges' gavels;
- Stonemason's hammers;
- Carving hammers;
- Jewelry hammers.

## **2. ANALYSIS OF STRESS DISTRIBUTION FOR A HAMMER WITH A METAL AND WOODEN HEAD**

3D models of locksmith hammers were made, maintaining the actual dimensions, stresses, displacements, and safety factors, which were analyzed using the Autodesk Inventor Professional program.

The geometric model of a locksmith's hammer is shown in Figure 2. The properties of the material from which the head of the locksmith's hammer was made are listed in Table 1. The properties of the material from which the shaft of both hammers was made are shown in Table 3. Figure 3 shows the point of application of force.

Figures 4-9 show the distribution of Von Mises stresses occurring in a locksmith's hammer when forces of 1000N, 5000N and 10000N are applied. These stresses increase with increasing force and are most outstanding in the same places in both cases. A hammer with a wooden head has much greater stress than a steelhead.



Figure 2. Model of hammer



Figure 3. Point of application force

Table 1. Material properties of hammers with metal and wooden obesity

Properties	Carbon steel	Wood (birch)
<b>Mass density</b>	<b>7.85 g/cm<sup>3</sup></b>	<b>0.55 g/cm<sup>3</sup></b>
<b>Yield strength</b>	<b>350 MPa</b>	<b>56.3 MPa</b>
<b>Tensile strength</b>	<b>420 MPa</b>	<b>6.3 MPa</b>
<b>Young's modulus</b>	<b>200 GPa</b>	<b>10.3 GPa</b>
<b>Poisson's ratio</b>	<b>0.29 ul</b>	<b>0.0001 ul</b>
<b>Modulus of elasticity</b>	<b>77.5194 GPa</b>	<b>5.14949 GPa</b>

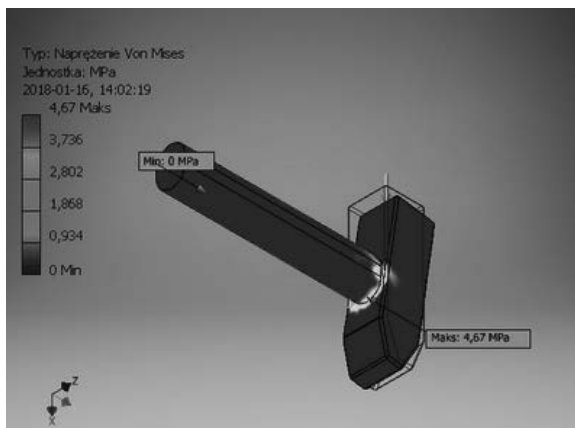


Figure 4. Von Mises Stress for wooden hammer 1000N force

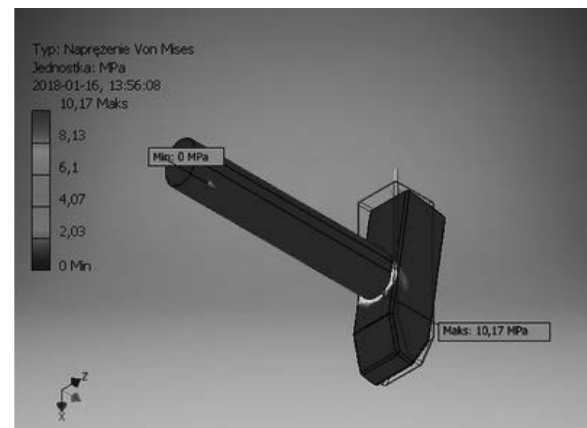


Figure 5. Von Mises Stress for steel hammer under 1000N force



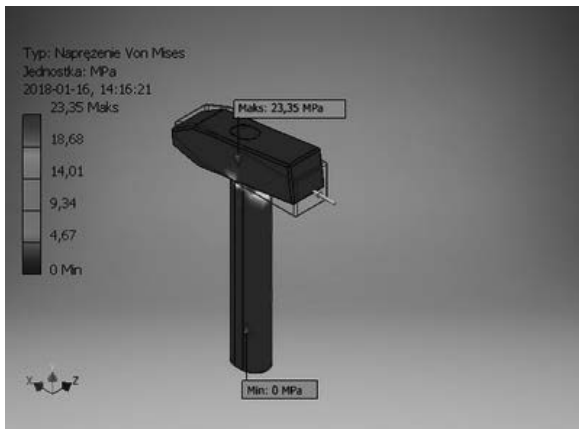


Figure 6. Von Mises Stress for wooden hammer 5000N force

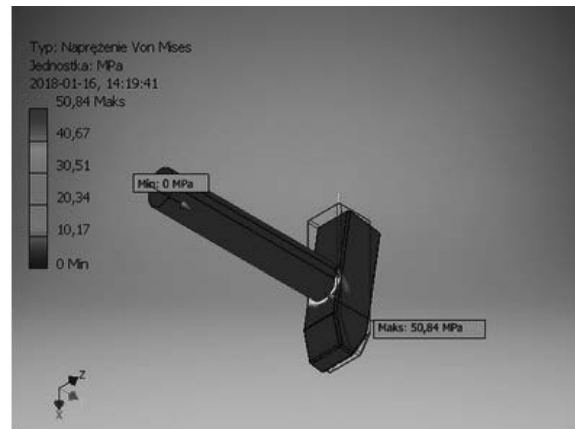


Figure 7. Von Mises Stress for steel hammer under 5000N force

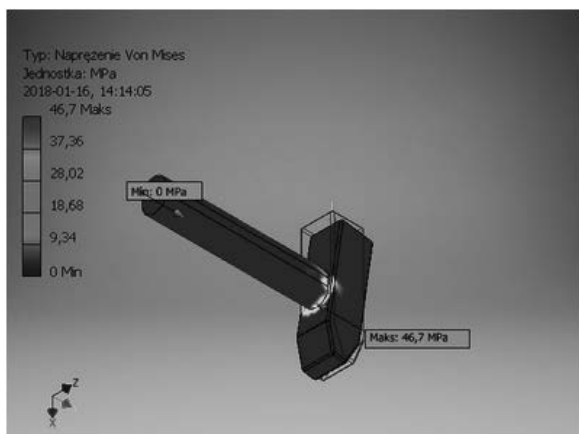


Figure 8. Von Mises Stress for wooden hammer 10000N force

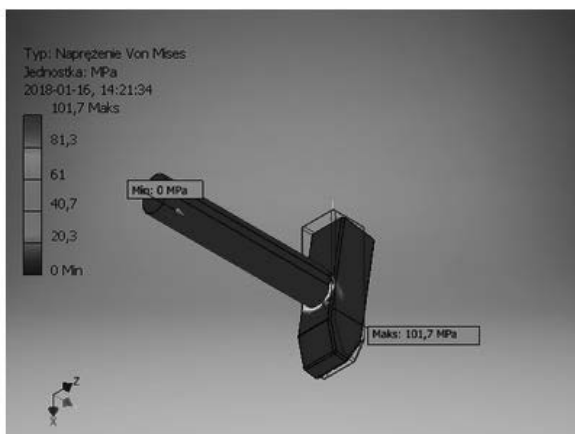


Figure 9. Von Mises Stress for steel hammer under 10000N force

### 3. ANALYSIS OF DISTRIBUTION DISTRIBUTION FOR A HAMMER WITH A METAL AND WOODEN HEAD

Figures 10-15 show the displacement of both hammers when forces of 1000N, 5000N, and 10000N are applied, respectively. The deformation value increases with increasing force, and both hammers deform in the same way. The displacement on a hammer with a wooden head is 0.34 mm, significantly exceeding that on a hammer with a metal head, while for the latter, it is only 0.08 mm.

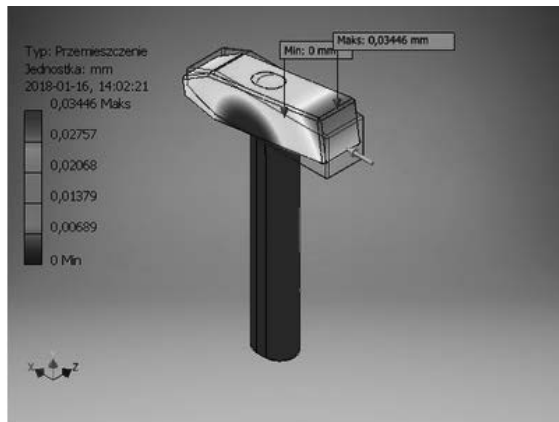


Figure 10. Displacements for wooden hammer under 1000N force

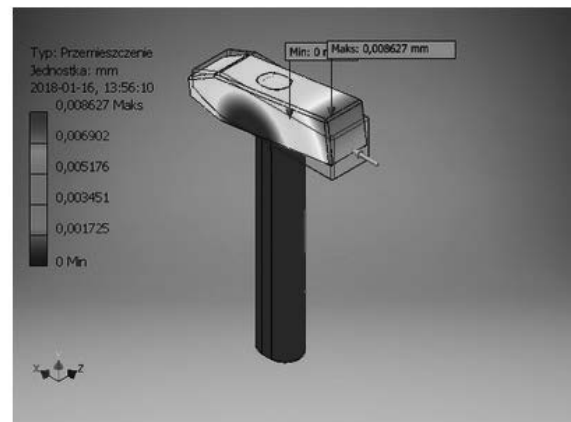


Figure 11. Displacements for steel hammer under 1000N force

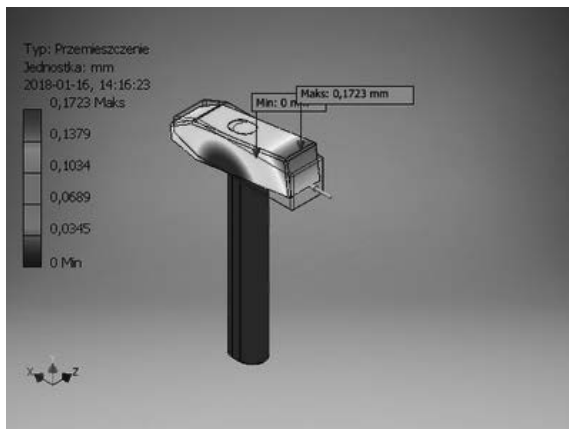


Figure 12. Displacements for wooden hammer 5000N force

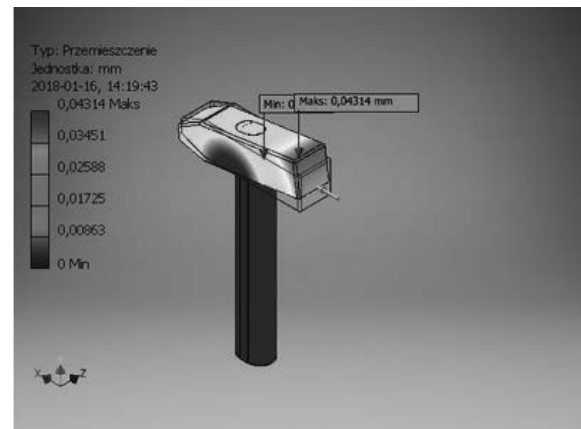


Figure 13. Displacements for steel hammer under 5000N force

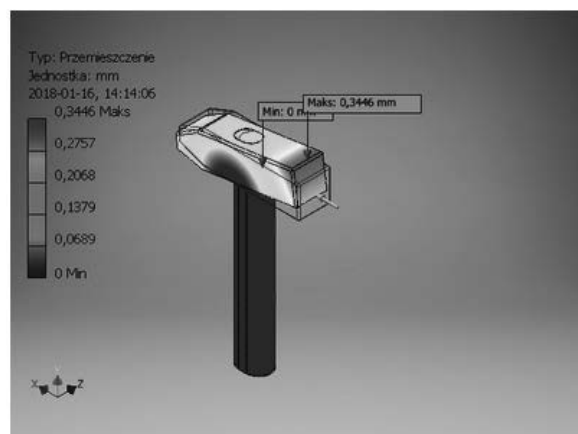


Figure 14. Displacements for wooden hammer 10000N force

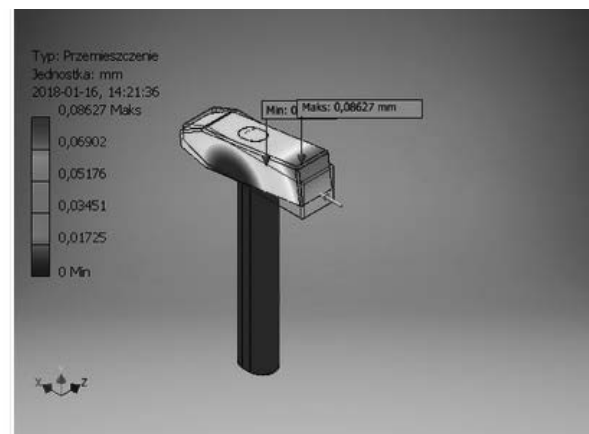


Figure 15. Displacements for steel hammer under 10000N force

#### 4. SAFETY FACTOR ANALYSIS FOR A HAMMER WITH A METAL AND WOODEN HEAD

Figures 16-21 show the safety factor for both hammers when forces of 1000N, 5000N and 10000N are applied, respectively. The value of the coefficient decreases as the force increases. The lowest values are achieved in places with the highest stresses.

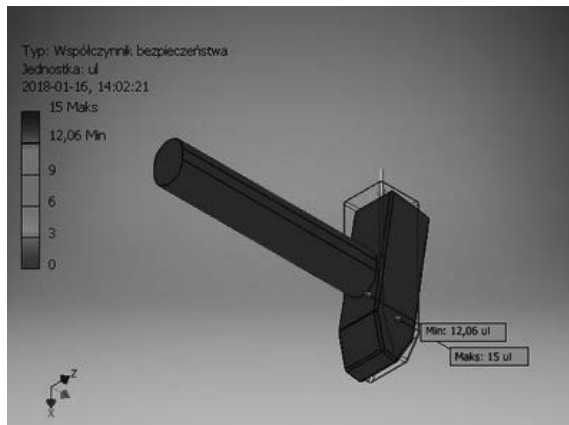


Figure 16. Safety factor for wooden hammer under 1000N force

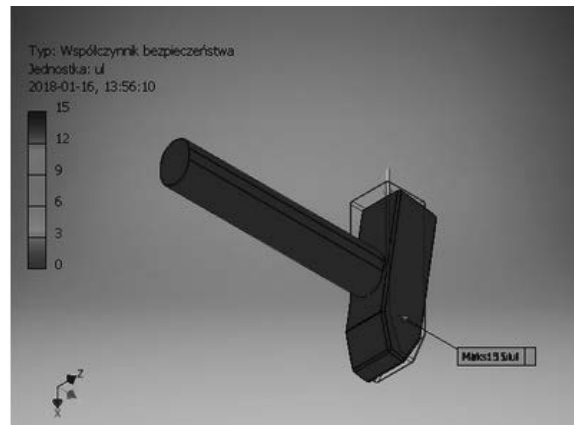


Figure 17. Safety factor for steel hammer under 1000N force

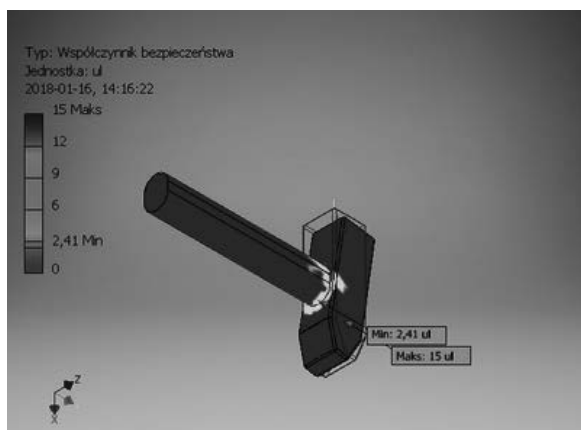


Figure 18. Safety factor for wooden hammer under 5000N force

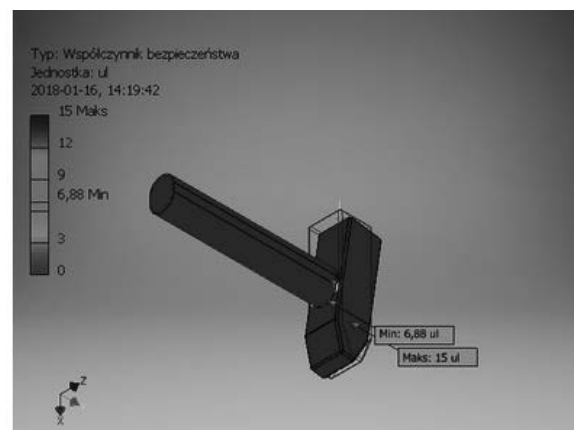


Figure 19. Safety factor for steel hammer under 5000N force

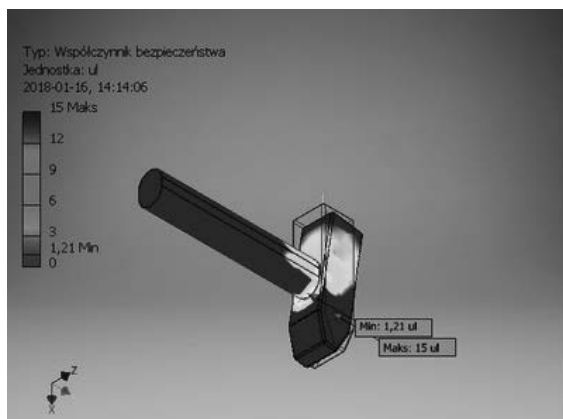


Figure 20. Safety factor for wooden hammer under 10000N force

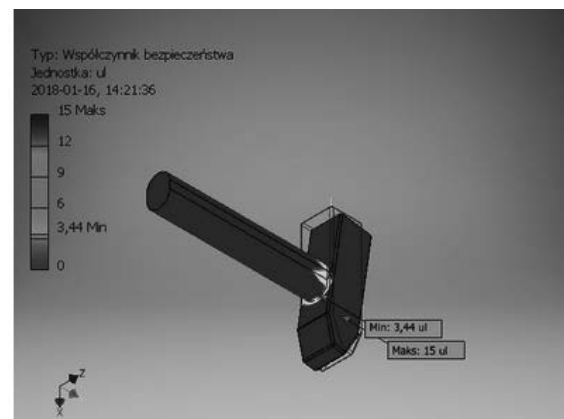


Figure 21. Safety factor for steel hammer under 10000N force

#### **4. RESULTS AND DISCUSSION**

In this work, a computer simulation of the material properties of a hammer with a steel head and a wooden head subjected to various loads was performed. Two models of hammers were created while maintaining their actual dimensions. Hammers were made of multiple materials. Then, using the Autodesk Inventor Professional program, the Finite Element Method was used to analyze stresses, displacements and the safety factor on the surface of two hammers loaded with three forces of 1000N, 5000N, and 10000N.

Based on the numerical analyses, the following conclusions can be drawn:

- When loaded with a force of 10000N, the hammer is likely to be damaged with a wooden head.
- A hammer with a metal head can withstand a force of 10000N.
- A hammer with a metal head has better resistance to deformation than one with a wooden head.
- Von Misses stresses increased with increasing force and turned out to be more than twice as high in the hammer with a metal head - as much as 101.7 MPa, while the one with a wooden head amounted to 46.7 MPa.
- The displacement increased with the increase in force and turned out to be more than four times greater for the hammer with a wooden head - it amounted to 0.34 mm and 0.08 mm for the one with a metal head.
- A hammer with a wooden head at the highest load showed a safety factor of 1.2, which is a condition in which it may be enough to deform the tool permanently.
- In both cases, the tool deformed in the same direction and the highest stresses occurred in the same places because they did not differ in shape but only in the material from which the hammerhead was made.

#### **ACKNOWLEDGEMENT**

The work was created as part of projects with secondary school students in the third competition as part of the Initiative of Excellence—Research University, Silesian University of Technology.

#### **LITERATURE**

1. Legutko S.: Podstawy eksploatacji maszyn i urządzeń. Wydawnictwo szkolne i pedagogiczne Warszawa 2013PN-M-65009:1988 Klucze do śrub i nakrętek ogólne wymagania i badania
2. [http://zrobiszsam.murator.com.pl/galeria/zdjecie\\_motek-slusarski,34\\_581\\_3736.html](http://zrobiszsam.murator.com.pl/galeria/zdjecie_motek-slusarski,34_581_3736.html)
3. <https://pl.wikipedia.org/wiki/Młotek>
4. Dobrzański L. A.: Podstawy nauki o materiałach i metaloznawstwo. Wydawnictwo Naukowo-Techniczne Warszawa 2002



17th-19th June 2024  
Gliwice, Poland

DEPARTMENT OF ENGINEERING MATERIALS AND BIOMATERIALS  
FACULTY OF MECHANICAL ENGINEERING  
SILESIA UNIVERSITY OF TECHNOLOGY

## INTERNATIONAL STUDENTS SCIENTIFIC CONFERENCE

### Comparison of the impact of the laser beam in various industrial processes using the finite element method

Amadeusz Dziwis<sup>a</sup>, Bartłomiej Józwiak<sup>b</sup>, Nikodem Juszczyk<sup>b</sup>, Stanisław Kiełkowski<sup>b</sup>,  
Mirosław Bonek<sup>b</sup>

<sup>a</sup> Silesian University of Technology, Faculty of Mechanical Engineering, Department of Engineering Materials and Biomaterials

<sup>b</sup> the 5th Andrzej Struga Secondary School with Bilingual Departments in Gliwice.

**Abstract:** The article presents a comparison of the action of the laser beam on the material during welding, cladding and laser hardening. To obtain data, the SolidWorks computer simulation program was used.

**Keywords:** surface engineering, laser processing, FEM

#### 1. INTRODUCTION

Laser radiation and the associated acronym LASER are one of the most important inventions of modern times, having the greatest impact on the technical and civilizational development of humanity. Already in 1917, Albert Einstein published his work on quantum mechanics, the photoelectric effect, the quantum structure of light and the possibility of stimulating the emission of coherent, monochromatic electromagnetic radiation, creating the basis for modern welding technologies: laser welding, surfacing, fusion, heat treatment, ablation and cutting. One of the first industrial applications of laser technology in welding took place in the early 1970s, and it was CO<sub>2</sub> gas laser cutting of steel sheets, ensuring higher quality and efficiency of cutting sheets up to 15 mm thick than in cutting processes. oxygen and plasma arc cutting. the latest solutions in the design of laser beam generators, especially solid-state, rod, fibre and disk lasers, ensure increasingly higher laser beam powers at lower device costs. modern laser welding devices enable precise adjustment of all parameters of the laser beam, i.e.: the type of continuous, pulsed or impact radiation, the shape and dimensions of the focus, power density, focal length, as well as tracking and control of the laser beam travel path. Laser welding of butt joints, T-joints, lap joints, corner joints, rebate joints, flange joints, i.e. basically all typical joints of welded structures made of weldable engineering materials, consists in fusing the joining area with the heat generated by introducing a concentrated laser beam of very high intensity to this area. power density of the order of  $10^2 \div 10^11$  W/mm<sup>2</sup>. Laser welding can be carried out using a welding technique without additional material, with a weld eye or with a weld pool, on one or both sides. In the case of joints of greater thickness, especially joints of structures made of difficult-to-weld steel with a high yield point, eyelet welding with additional

material or hybrid welding - LHW - laser welding + GMA welding - is increasingly carried out. Laser technologies for creating surface layers of machine and device parts have been developed for many years, bringing very tangible economic effects because of a significant increase in tribological properties, corrosion resistance, heat resistance, etc. Surface layers can be surfacing with basically all known metal and cermet materials, with a thickness ranging from tenths of a millimetre to even more than 10 mm using the multi-layer surfacing technique, while ensuring very accurate control of the share of the substrate material in the applied layer, from 2 to 90%. Such a low share of substrate material means that the required chemical composition of the surface layer can be obtained already in the first layer. If it is required to create a surface layer with a small thickness, even a few  $\mu\text{m}$ , but with higher functional properties than the base material, laser alloying, remelting or increasingly widely used heat treatment techniques are irreplaceable on the working surfaces of machine and device parts [1-3].

The industrial application of laser technologies takes place in several specific processes, they are based on the process of melting the processed material and, in some cases, also the batch material. They are based on the process of heating the processed material and, in some cases, also the input material to temperatures below the melting point or with remelting [2].

### Laser welding

In the construction of modern machines and devices, it is increasingly necessary to use sheets of dimensions that cannot be produced using rolling technology for a given thickness. Then it is necessary to connect the sheets butt-together to obtain the dimensions required by machine and device designers. Laser welding technology (Fig. 1) enables the creation of a very high-quality butt joint between sheets without additional material and the need for mechanical processing after welding. Moreover, the small amount of heat introduced during welding minimizes welding stresses and deformations [2,3].

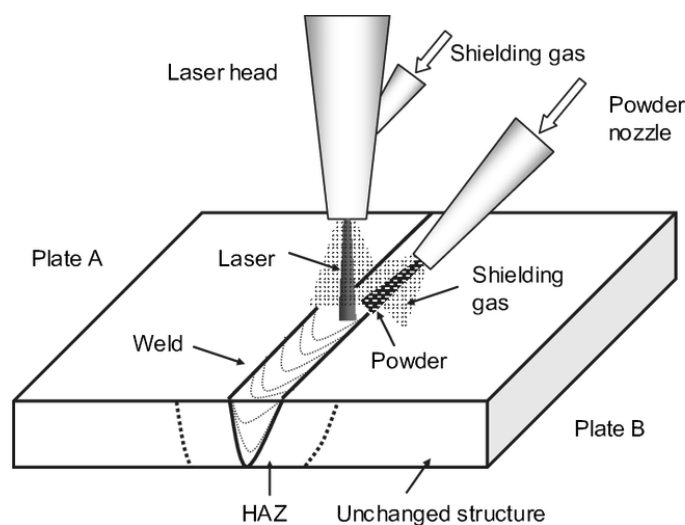


Figure. 1 Laser welding diagram [4]

### Laser cladding

Laser cladding (Fig. 2) technology enables the creation of a usable surface layer on new elements and the precise regeneration of parts of machines and devices. The precision and flexibility of the process enable the regeneration of parts whose repair has not been technologically possible or economically justified so far, and the replacement of conventional

regeneration technologies to increase the quality of the repair and shorten its time. This translates directly into reduced costs not only of regeneration itself, but also of machine downtime costs. Savings also result from the reduction of mechanical processing time after laser cladding compared to conventional cladding technologies, which results from the possibility of applying very even layers and reducing the machining allowance [2,5].

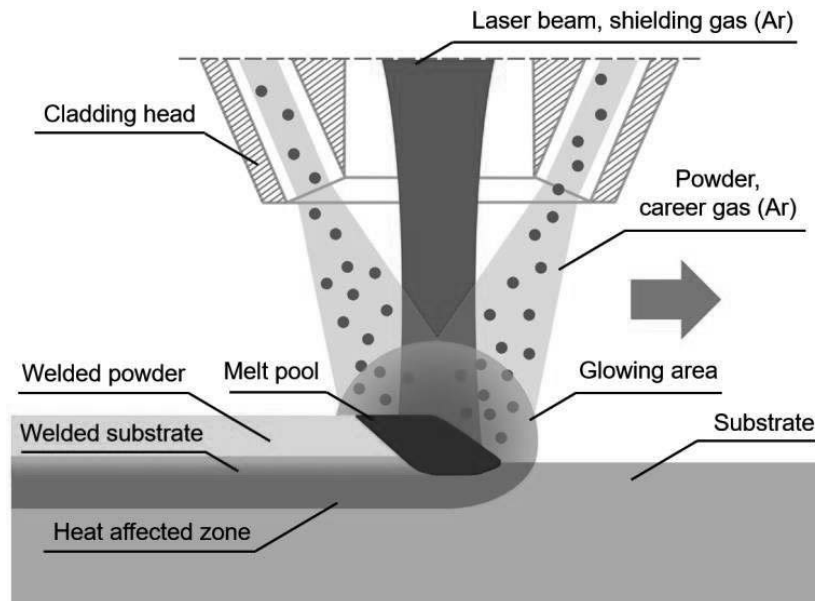


Figure. 2 Laser cladding diagram [6]

### Laser heat treatment

Laser hardening (Fig. 3) technology is much less energy-consuming than traditional furnace and induction hardening methods. The energy of the laser beam is absorbed only by the processed surface layer of the element intended for hardening, so its energy is used only for heating the surface layer at high speed, and the core of the element remains in the raw state. This ensures many times lower energy consumption compared to traditional hardening processes, especially furnace hardening, where the entire element is heated in the furnace to the hardening temperature. During laser hardening, much less heat is introduced into the element than in conventional hardening processes. This translates into a significant reduction in internal stresses, which significantly reduces the deformation of items heat treated with a laser beam. This results in the elimination of additional technological operations after the hardening process itself, such as finishing, straightening and stress relief. When designing and manufacturing a product, it is unnecessary to consider processing allowances, and therefore laser heat treatment can be easily integrated into the production process. Eliminating finishing machining of the already hardened hard surface of the element significantly reduces the time and energy consumption of the production process. Self-cooling of elements in laser hardening means that the use of water and oil in the process is eliminated [2,5].

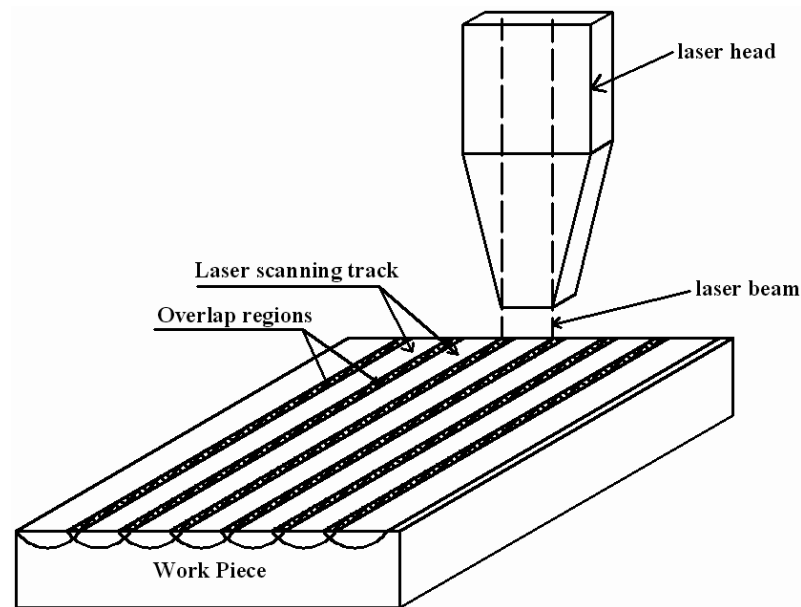


Figure. 3 Laser hardening diagram [7]

In most cases, the results of laser processing can only be obtained by destroying the weld deposit or the obtained surface layer. To determine the properties of the obtained products, the finite element method, a computer simulation technique, has become widely used. FEM allows you to carry out all the mentioned laser processing processes in a digital environment without the need to have the actual materials and machines needed to carry out the process, thus saving time and funds. In addition to these obvious advantages, the use of computer simulation allows for any modification of the model and parameters intended to reflect the machining process. This allows you to perform several completely different simulations on one and the same model, giving an approximate picture of the actual effect of these processes, allowing you to optimize even before starting the production process [8].

## 2. MATERIAL AND RESEARCH

As part of the work, models were created to reflect three types of laser processing. These were welding, cladding and laser hardening models. The simulation assumed that the processed material was S235JR steel from which the plates were made, in which the distribution of stresses, strains and displacements arising during the simulated processes were examined. To reproduce the laser processing conditions, boundary conditions were imposed on the models to reflect the energy applied through the heat released from the weld, the heat released from the padding formed on the surface of the plate and the direct heating of the plate during the hardening process. In order to carry out the simulation, the following three models were made:

- Model 1 with dimensions 20x20 cm and 0.5 cm thick
- Model 2 (Fig. 4) with dimensions of 20x20 cm and a thickness of 0.5 cm with a coating of 0.5 mm thick
- Model 3 (Fig. 5) two 10x10 cm plates connected by welding.

All 3 models were subjected to temperature and then static simulation aimed at determining the values of forces introduced into the material as a result of laser processing.



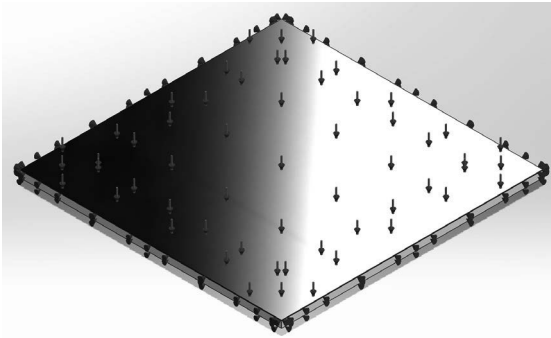


Figure 4. Model 2 with boundary conditions

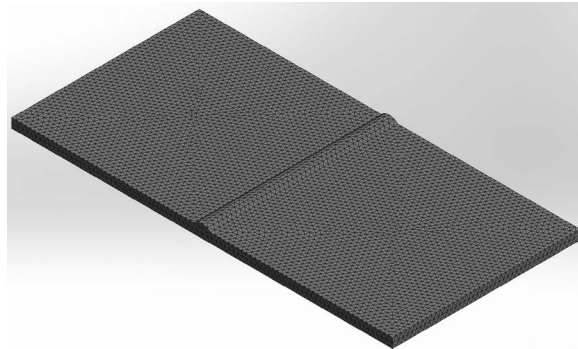


Figure 5. Model 3 with a finite element mesh

### 3. RESULTS AND CONCLUSION

The first simulations were carried out on model 1, in which the distribution of stresses was compared in the case of heating the entire surface of the material at the same time and in the case of spot heating using a laser beam. The temperature to which the processed material was heated was 900 C. The results of this simulation are presented in Figures 6 - 9 and summarized in Table 1.

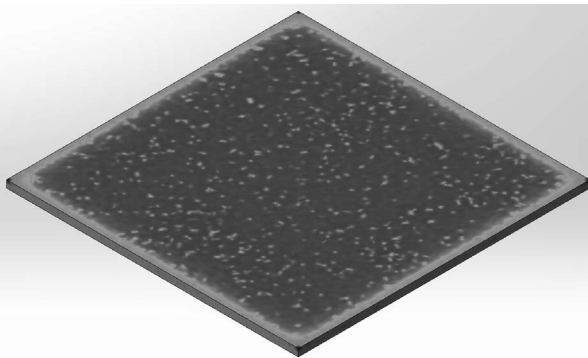


Figure 6. Stress results for the model with heating of the entire surface

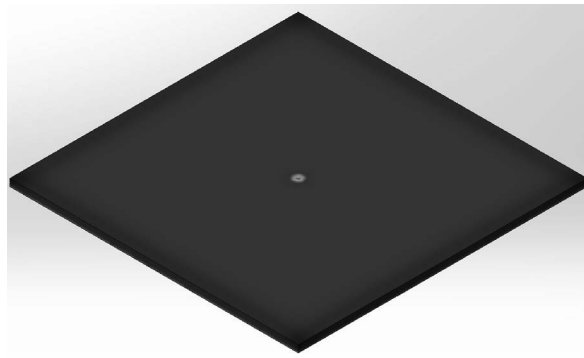


Figure 7. Stress results for the spot-heated model

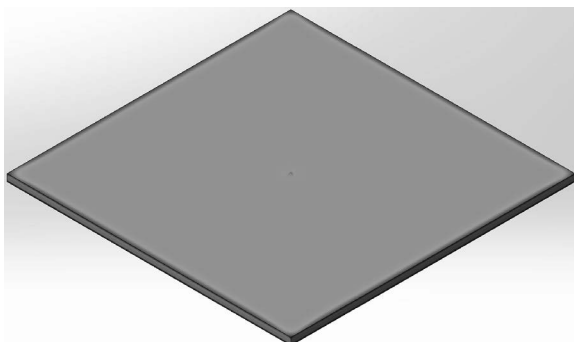


Figure 8. Displacements results for the spot-heated model

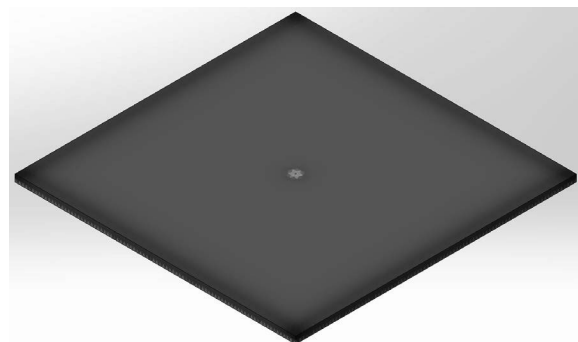


Figure 9. Deformations results for the spot-heated model

Table 1. Summary of results for model 1

Stress surface-heated model [MPa]	Stress spot-heated model [MPa]	Displacements spot-heated model [mm]	Deformations spot-heated model
>235	115,485	0,001	0

In the second simulation, the coating was applied to the plate using the cladding method. For this reason, two thermal simulations were performed, similarly to the first model, i.e. with heating of the entire coating (simultaneous heating of the entire coating) and a short linear one (laser cladding process). The results of this simulation are presented in Figures 10 to 13 and summarized in Table 2.

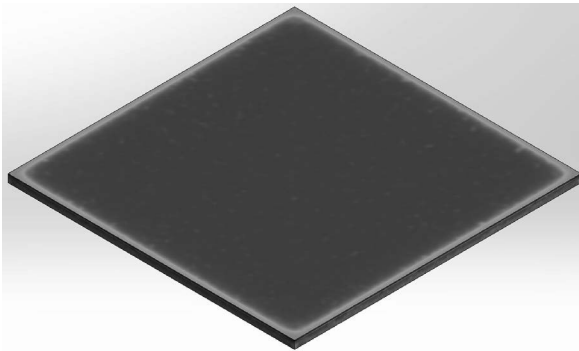


Figure 10. Stress results for the model with heating of the entire surface

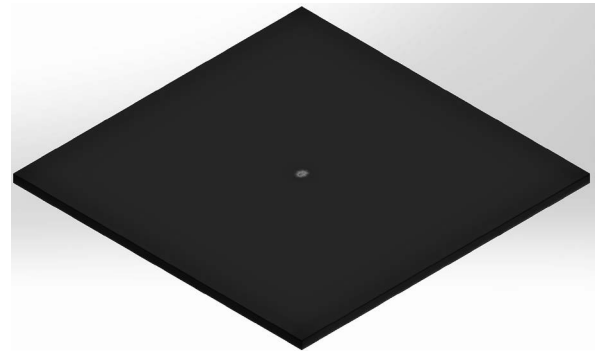


Figure 11. Stress results for the spot-heated model

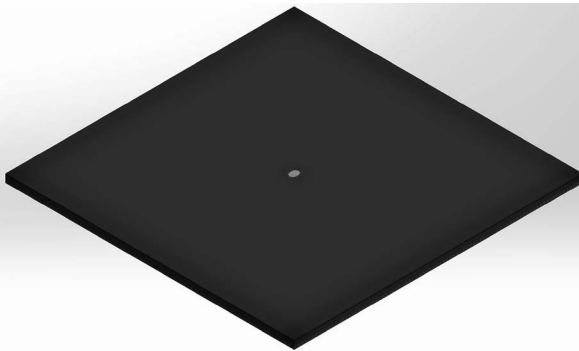


Figure 12. Displacements results for the spot-heated model

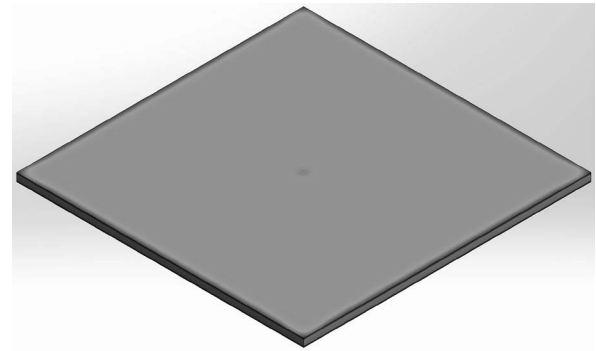


Figure 13. Deformations results for the spot-heated model

Table 2. Summary of results for model 2

Stress surface-heated model [MPa]	Stress spot-heated model [MPa]	Displacements spot-heated model [mm]	Deformations spot-heated model
246,225	184,892	0,001	0,001

The last simulations were performed on a model consisting of two butt-welded plates and a weld. In this simulation, the highest temperature value was used, resulting from the need to melt the welded material and the filler metal. In the case of this simulation, no point application of temperature was used, but it was distributed evenly over the entire weld. The welding simulation results are shown in Figures 14 to 17 and summarized in Table 3.

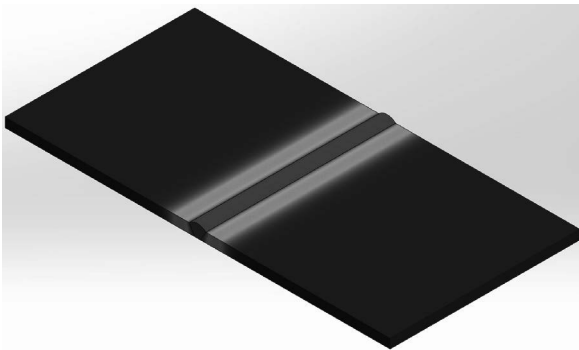


Figure 14. Model of temperature distribution in the initial phase of welding

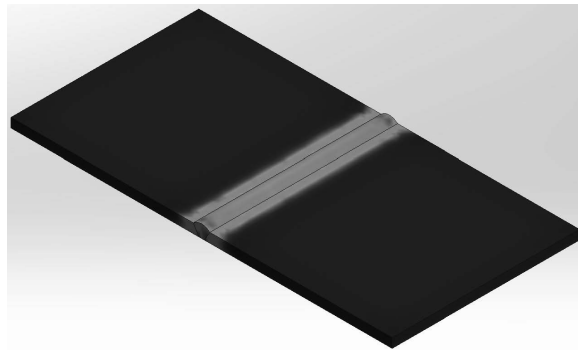


Figure 15. Stress simulation results

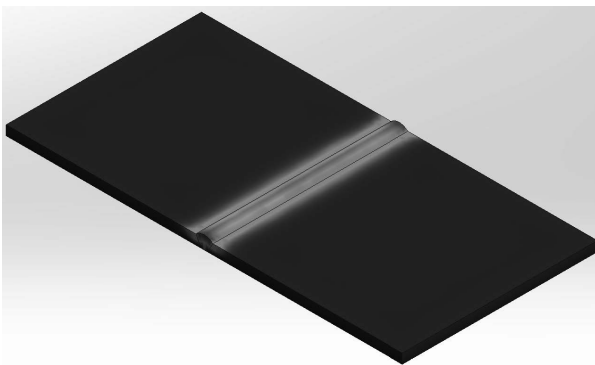


Figure 16. Displacements simulation results

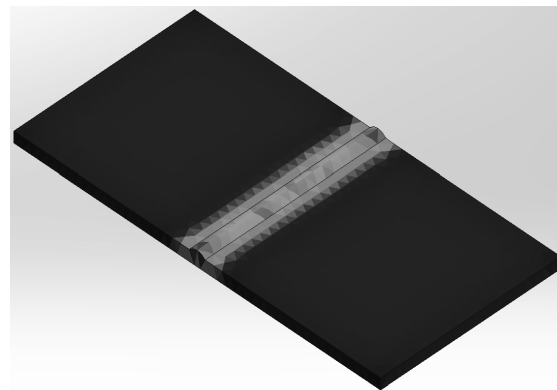


Figure 17. Deformations simulation results

Table 3. Summary of results for model 3

Stress [MPa]	Displacements [mm]	Deformations
299,807	0,009	0,001

The results of the computer simulation allowed to conclude that:

- The use of point heating, which can be obtained thanks to a laser beam, creates much smaller stresses in the material, thus allowing for a reduction in the costs and time of the hardening process due to the possibility of resigning from the tempering necessary to reduce the stresses in the material resulting from heating the entire surface at the same time.
- In the case of laser cladding, despite the use of much higher laser power (higher set temperature), the stresses created in the coating were lower than in the case of hardening, despite the entire surface of the material being subjected to the process at once.
- In the case of welding, stresses, deformations, and displacements are concentrated in areas of increased temperature (applied force), i.e. around the weld, unlike models 1 and 2. In the case of model 1, the displacements were concentrated on the boundaries of the model, similarly to the deformations in model 2.

## **ACKNOWLEDGEMENTS**

The work was created as a result of a project carried out with secondary school students as part of project-oriented education - PBL, as part of the Excellence Initiative - Research University, Silesian University of Technology program.

## **BIBLIOGRAPHY**

1. A. L. Dobrzański, Podstawy nauki o materiałach i metaloznawstwo, WNT, Warszawa, 2002
2. A. Borek, R. Grzelka, A. Kimpel, S. Mucha, S. Ścibisz, technologie laserowe spawania, wytwarzania i obróbki cieplnej warstw wierzchnich, Przegląd Spawalnictwa 10/2013
3. A. Klimpel, Technologie laserowe. Wyd. Politechniki Śląskiej. Gliwice 2012
4. X F. Czerwiński, Welding and Joining of Magnesium Alloys, Magnesium Alloys - Design, Processing and Properties, January 2011
5. J. F. Ready Industrial Applications of Lasers, Second Edition 1997
6. R. V. Chkalov, D. G. Chkalov, Laser Powder Cladding Complex: Principles of Advanced Automated Control, OP Conference Series Materials Science and Engineering 969(1):012093
7. P. Dinesh Babu, K. R. Balasubramanian, G. Naidu Buvanashkaren, Laser surface hardening: A review, International Journal of Surface Science and Engineering 5(2/3):131 – 151, July 2011
8. H. Xiaocong, Finite Element Analysis of Laser Welding: A State of Art Review, Materials and Manufacturing Processes Volume 27, 2012 - Issue 12



17th-19th June 2024  
Gliwice, Poland

DEPARTMENT OF ENGINEERING MATERIALS AND BIOMATERIALS  
FACULTY OF MECHANICAL ENGINEERING  
SILESIA UNIVERSITY OF TECHNOLOGY

## INTERNATIONAL STUDENTS SCIENTIFIC CONFERENCE

### Computer analysis of the transmission cushion of a passenger car

Amadeusz Dziwis<sup>a</sup>, Wojciech Mikolejko<sup>a</sup>, Mirosław Bonek<sup>a</sup>, Agata Śliwa<sup>a</sup>, Eva Tillova<sup>b</sup>

<sup>a</sup> Silesian University of Technology, Faculty of Mechanical Engineering, Department of Engineering Materials and Biomaterials

email: amadeusz.dziwis@polsl.pl, wojciech.mikolejko@polsl.pl, miroslaw.bonek@polsl.pl, agata.sliwa@polsl.pl

<sup>b</sup> Žilinská univerzita v Žiline, Strojnícka fakulta, Katedra materiálového inžinierstva, Univerzitná 8215/1, 01026 Žilina, Slovak Republic Žylinie

email: eva.tillova@fstroj.uniza.sk

**Abstract:** The article presents a computer simulation of the combustion engine gearbox mounting present in BMW cars, model E36. The analysis was performed on 3 values of the applied force.

**Keywords:** FEA, Automotive, Car Engine

### 1. INTRODUCTION

Computer simulation has its origins in the 1970s when it began to be used in the automotive and aero-space industries. Nowadays, we are seeing rapidly changing technology which also has an impact on computer simulation, which is now used in every field of industry from those that people encounter daily such as the industry that manufactures telephones, cars and everyday things around us, as well as in the very advanced aerospace and military industries. Computer simulations make it possible to answer many questions just before the final production of a component. It is possible to select the right material, the geometry of the component, add possible reinforcements. Advanced computer simulations also make it possible to answer many questions such as whether a given structure will withstand a given load, determine the thermal properties of the model, determine the system's own vibrations, generated noise or determine the life of the model. Thanks to such solutions, companies are able to save on production time, which is reduced by producing the required structures for, for example, strength tests, and already at the design stage determine many factors of the manufactured component. Thus, there is also a noticeable improvement in the economy of the company, which saves production materials as well as machinery exploitation [1,2].

Programs that allow you to perform these calculations belong to the group of CAE programs - Computer Aided Engineering. These programs use numerical methods in the main Finite Element Method, this method consists in discretizing the model into a finite number of elements connecting at nodes. The model is divided into very small elements, the quality of

which, i.e. the size of the elements as well as the shape, depends on the computational capability of the computer. The quality of the finite elements mainly determines the results that are obtained from the simulation, also the correct execution of the discretization of the model allows to obtain the most accurate results, approximating reality. CAx programs are a group of computer-aided engineering programs and can be divided into smaller modules such as [1,3]:

- CAE - Computer Aided Engineering,
- CAD - Computer Aided Design,
- CAM - Computer Aided Manufacturing,
- FEA - Finite Element Analysis,
- CFD - Computational Fluid Dynamics,
- MBD - Multibody Dynamics.

The work in FEA systems can be divided due to three stages, which can be classified into the software component from which they are built [4]:

- Preprocessor - is a program that allows you to specify the physical properties of the model such as shape, geometry, assign material. At this stage, the mesh of the model is also prepared, and boundary conditions are assigned to perform the desired simulation,
- Processor - this system uses the computing power of the workstation to carry out the calculations defined in the preprocessor, the time to solve the calculations depends on the computing power as well as how complex the element is, i.e. the number of finite elements.
- Postprocessor - at this stage, the user has at his disposal tools related to reading the results as well as the way they are presented. It is also possible to import the results into other programs.

CAE-type programs can include SolidWorks, Ansys, HyperWorks, Siemens NX. The transmission cushion, also known as the transmission mount, is a key mounting component in a car's drivetrain. Its main function is to connect the transmission to the vehicle's frame, while damping vibrations and oscillations that may be transmitted from the engine and transmission to the vehicle's body [4].

Key features of the transmission cushion (Fig. 1) [5]:

- Material: Transmission cushions are typically made of a rubber or elastomer compound (e.g., rubber, silicone) that provide flexibility and vibration-damping capability. They are often reinforced with steel elements for extra strength.
- Vibration damping function: Thanks to its flexibility, the cushion absorbs and dampens vibrations and oscillations generated by the operation of the engine and transmission, which increases driving comfort and reduces interior noise.
- Durability: Transmission cushions must be strong enough to withstand the dynamic and static loads that occur during driving, acceleration, braking and shifting.
- Safety: In the event of a crash, the transmission cushion helps protect the transmission and other drivetrain components, minimizing damage and protecting passengers.



Figure 1. StrongFlex gearbox mount [6]

## 2. RESEARCH

To perform the static analysis of the stress distribution, the gearbox cushion was first modeled in SolidWorks Figure 2. It was decided to design the steel geometry of the gearbox cushion. Then, according to the sequence of work in CAx systems, boundary conditions were prepared: the finite element mesh was applied, the static force ( purple arrows - Fig. 3. ) and model fixings ( green arrows - Fig. 3. ) were set. To study the effect of masses of 5, 10 and 15 [Kg], three forces of 50, 100 and 150 [N], respectively, were applied. Then three simulations were run, which gave solutions to the given boundary conditions.



Figure 2. Geometric model of the gearbox cushion

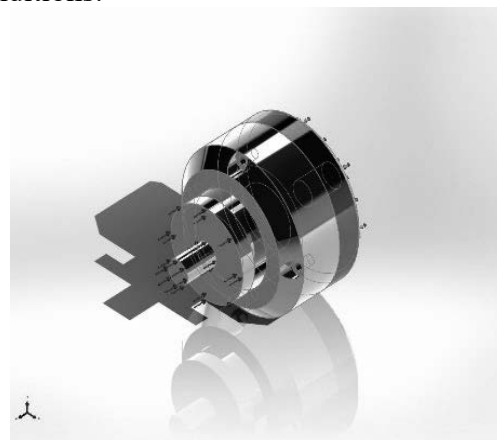
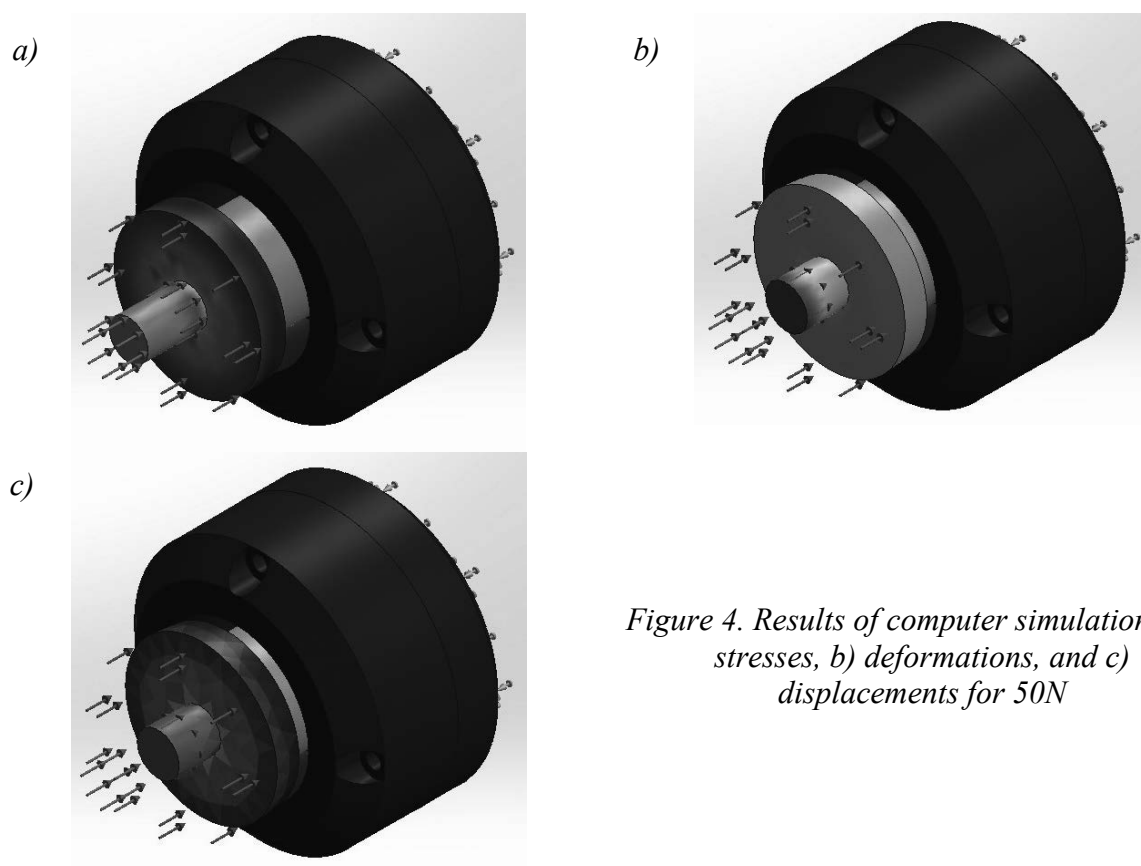


Figure 3. Geometric model of the gearbox cushion with boundary conditions applied

### 3. RESULTS

Figures 4 5 and 6 show the results of three different simulations with applied forces of 50, 100 and 150 [N], respectively. In turn, subfigures (a) (b) and (c) show the stresses, strains and displacements, respectively. From the results, we can see the accumulation of stresses in the vicinity of the force application point in subfigure a). From the results of the deformations, we can see that the largest ones are on the mandrel where the thread for attaching the actual gearbox cushion should originally be located. The displacement results show that the entire part at the point of force application has been driven into the center of the gearbox cushion.



*Figure 4. Results of computer simulation of a) stresses, b) deformations, and c) displacements for 50N*



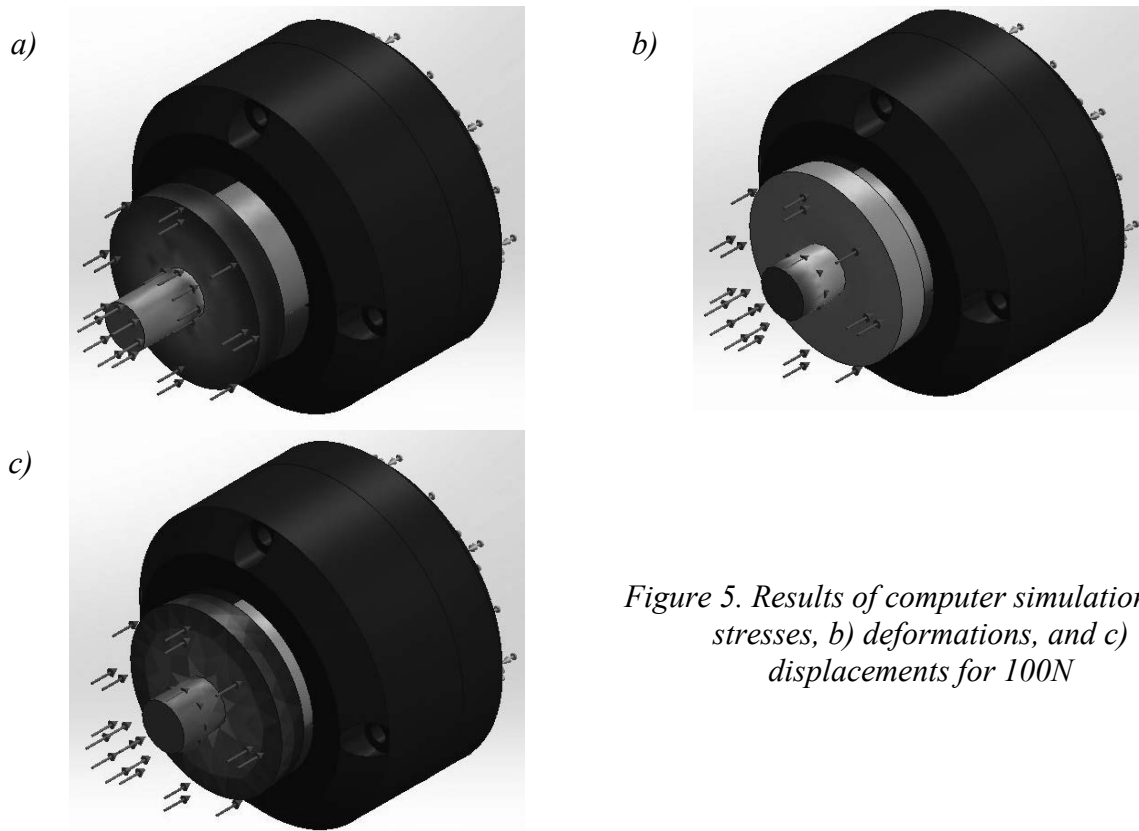


Figure 5. Results of computer simulation of a) stresses, b) deformations, and c) displacements for 100N

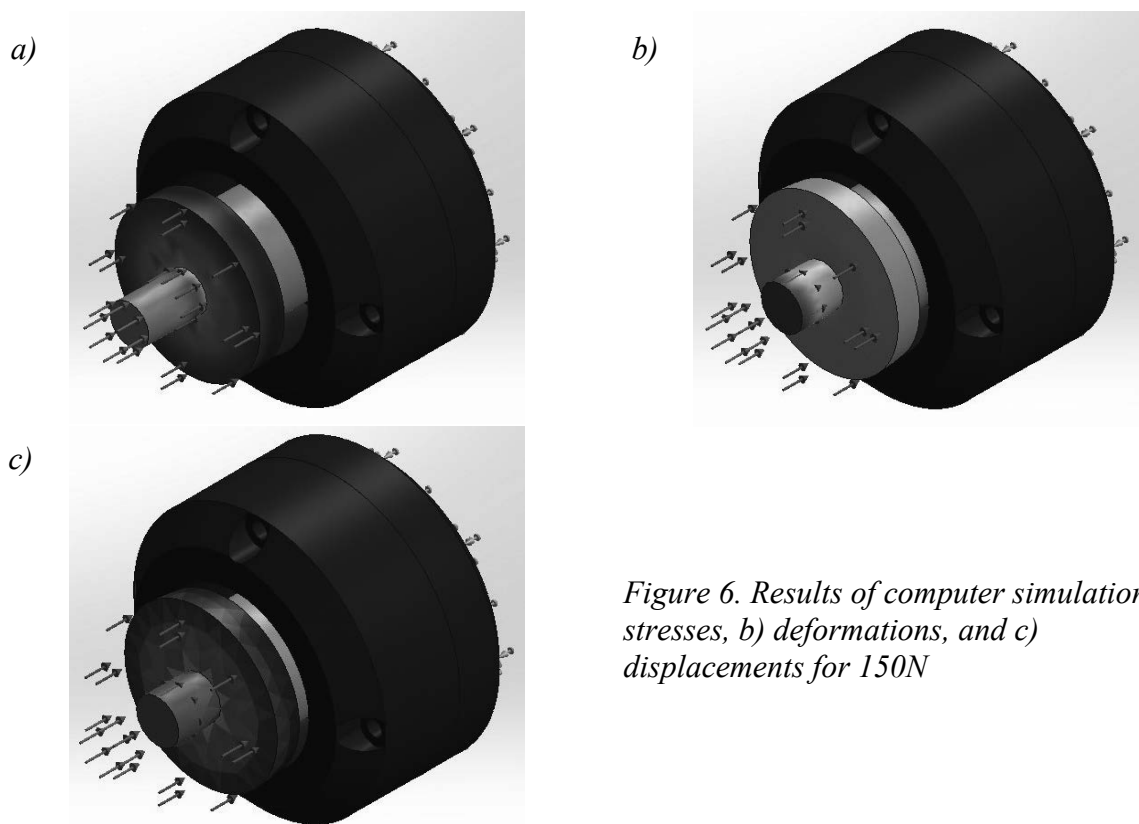


Figure 6. Results of computer simulation of a) stresses, b) deformations, and c) displacements for 150N

Table 1. Summary of simulation results

	50N	100N	150N
Stresses [MPa]	1,148	2,296	3,444

The simulation results showed that the mass of the BMW E36 gearbox will not damage or even destroy the cushion. This means that the material used, and the geometry of the element fulfill their purpose. For further work, it is possible to optimize the material and shape of the gearbox cushion mounting. Such optimization could allow for better results in the distribution of forces in the tested element, and the use of a different material could reduce material costs or, in the case of lighter materials, reduce weight.

## ACKNOWLEDGEMENTS

The publication was created within the framework of the joint Slovak-Polish project International Visegrad Fund's V4 Generation Mobility Mini-Grant No 12410044 as a result of cooperation between the Association of Alumni of the Silesian University of Technology, Gliwice, Poland and the University of Žilina, Slovakia.

The project is co-financed by the Governments of Czechia, Hungary, Poland and Slovakia through Visegrad Grants from the International Visegrad Fund. The mission of the fund is to advance ideas for sustainable regional cooperation in Central Europe.



## BIBLIOGRAPHY

- [1] C. Cichoń, Wprowadzenie do metody elementów skończonych, Kraków, Wydaw. PK 1994
- [2] M. Paszynski, Klasyczna i izogeometryczna metoda elementów skończonych, AGH, 2020
- [3] W. Rachowicz, Metoda elementów skończonych i brzegowych: podstawy kontroli błędów i adaptacji, Kraków, Wydaw. PK 2012
- [4] O. Zienkiewicz, C. Taylor, R. Leroy, J.Z. Zhu, The finite element method - Its basis and fundamentals, Butterworth-Heinemann (1990-2005).
- [5] W. Micknass, R. Popiol, A. Sprenger, Sprzęgła, skrzynki biegów, wały i półosie napędowe, Wydawnictwa Komunikacji i Łączności WKŁ, 2019
- [6] <https://www.strongflex.eu>



17th-19th June 2024  
Gliwice, Poland

DEPARTMENT OF ENGINEERING MATERIALS AND BIOMATERIALS  
FACULTY OF MECHANICAL ENGINEERING  
SILESIA UNIVERSITY OF TECHNOLOGY

## INTERNATIONAL STUDENTS SCIENTIFIC CONFERENCE

### Application of 3D printing in medicine

Aleksandra Dzwonek <sup>a</sup>, Karolina Malon <sup>a</sup>, Maja Świącicka <sup>a</sup>, Magdalena Szindler <sup>b</sup>,  
Mirosław Bonek <sup>b</sup>

<sup>a</sup> Silesian University of Technology, Faculty of Mechanical Engineering, Student of Engineering Production and Management, Gliwice

<sup>b</sup> Silesian University of Technology, Faculty of Mechanical Engineering, Department of Engineering Materials and Biomaterials

**Abstract:** The article discusses the various methods and applications of 3D printing in medicine. Presenting the latest developments and technologies that enable the printing of precise anatomical structures and organs. It also describes how 3D printing can be used to produce anatomical models for surgical planning, to create customised medical implants for patients and to print organs and tissues for transplantation. The article highlights the importance of 3D printing in the development of modern medical solutions and the potential to improve the quality of healthcare for patients.

**Keywords:** 3D printing, medicine, bioprinting, materials

### 1. INTRODUCTION

3D printing technology is rapidly expanding its applications within the healthcare sector, continuously broadening its scope of activity. This innovative method finds extensive use in medicine, offering numerous possibilities across various fields. The application of 3D printing techniques encompasses orthopedic, plastic, transplant, and vascular surgery, as well as otolaryngology, ophthalmology, urology, and oncology. 3D printing significantly impacts improving patients' quality of life, reducing treatment time and costs, and enhancing the rehabilitation process. The utilization of this technology translates into more effective and personalized therapy methods, crucial in modern medicine. Various materials are employed in this method, including titanium, plastic, natural and synthetic polymers such as PLA (polylactide), ABS (acrylonitrile butadiene styrene), photopolymers, and bioink. The proper 3D printing process varies depending on the initial material used in printing.

Among the various manufacturing processes currently utilized by the industry, 3D printing is an additive technique. It is a process through which a three-dimensional solid object, practically of any shape, is generated based on a digital model. Medical 3D printing was once an ambitious dream. However, time and investments have turned it into reality. Currently, 3D printing technology presents a significant opportunity to assist pharmaceutical and medical companies in creating more specific drugs, enabling the rapid production of medical implants,

and changing the way doctors and surgeons plan procedures. This technology has numerous applications, with the fastest-growing innovation in the field of medicine being 3D printing itself.

### 1.1 History of 3D printing

The history of 3D printing spans over fifty years, significantly impacting various industries. The technology's origins trace back to the 1970s, but a key development occurred in 1981 when Dr. Hideo Kodama described a layer-by-layer manufacturing method, a precursor to stereolithography (SLA), although he failed to patent it. In 1984, French engineers explored SLA but abandoned it due to lack of business prospects. The breakthrough came in 1986 when Charles "Chuck" Hull patented SLA and founded 3D Systems Corporation, which introduced the first commercial 3D printer in 1988.

The late 1980s saw the introduction of new methods: Carl Deckard patented selective laser sintering (SLS) in 1988, and Scott Crump patented Fused Deposition Modeling (FDM), laying the groundwork for modern 3D printing.

The 1990s saw rapid advancements in 3D printing and CAD tools. New manufacturers like EOS GmbH emerged, creating the first industrial prototyping system. Stratasys patented FDM in 1992, and ZCorp introduced binder jetting technology.

In the early 2000s, 3D printing gained media attention. The first kidney was printed in 2000, and in 2004, the RepRap project aimed to create a self-replicating 3D printer, popularizing FDM. ZCorp introduced a high-resolution color 3D printer in 2005, and the first 3D-printed limb prosthesis was created in 2008.

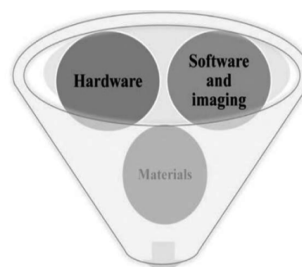
The expiration of the FDM patent made 3D printing more accessible, boosting its use in industries and households. In 2013, President Barack Obama highlighted 3D printing as a future key technology, increasing its popularity.

In the last decade, 3D printing has grown dynamically, with an annual market growth of about 45%. New materials, including biodegradable and food-grade filaments, and printers capable of creating large objects like buildings have emerged. This technology continues to evolve, impacting industries, medicine, and daily life, becoming integral to modern manufacturing and prototyping.

### 1.2 Basic components of 3D printing

The basic components of 3D printing can be divided into three groups:

- Hardware (the 3D printer itself),
- Software (used for communication with the hardware and for converting CAD images into SLA images recognized by the printers),
- Materials used for printing objects.



Components of 3D printing

Figure 1 Components of 3D printing [1].

The choice of printer depends on compatibility with materials intended for specific applications, which is why various materials for additive manufacturing of implants, prosthetics, and medical instruments are currently being researched. Currently, non-metallic biodegradable materials, especially titanium and its alloys, are preferred for printing medical implants due to their excellent corrosion resistance, high strength, and biocompatibility. Although metallic materials are considered almost inert and do not cause adverse reactions at the implantation site, their applications are limited.[1]

To obtain 3D-printed structures with the required shapes and dimensions, it is necessary to combine 3D printers with appropriate prototyping software, which provides 3D design files for reading and execution by the printer. High-resolution images or scans of the patient's body parts are needed for printing patient models, devices, implants, or organs. Techniques such as computer tomography (CT), cone-beam computer tomography (CBCT), and magnetic resonance imaging (MRI) are used to obtain specific anatomical information. CT and CBCT are mainly used for viewing bone structures, while MRI provides high-resolution images of soft tissues. CT uses X-rays to scan the body layer by layer from various angles, and detectors record two-dimensional images of each layer. During post-processing, these images are aligned together to create a detailed three-dimensional image of pathology. MRI uses magnetic and radio waves to scan and create cross-sectional images of soft tissues, differentiating between tissue types and detecting boundaries between them. However, both methods provide limited information about cell types and their distribution in tissue. Reconstructed histological sections are therefore used to obtain detailed information about tissue composition. Alternatively, a computer model of an organ or tissue can be created. Software available on the market can create precise anatomical models of organs. A combination of different imaging techniques, mathematical modeling, and computer simulation can provide comprehensive 3D models of complex organs.

The next step is the reconstruction of 3D tissue models using obtained 2D scans from CT or MRI. CAD software analyzes and processes each 2D scan individually, and then the contours are arranged together in three dimensions. The reconstructed CAD 3D model contains complete information about the geometry and structure of the patient's organ, and then it is converted to an STL format for printing.

### 1.3 Benefits of 3D printing in medicine

The benefits of 3D printing in medicine bring about many advantages that revolutionize traditional treatment methods and patient care. [3] The main benefits of its application include:

- High degree of treatment personalization:

3D printing enables the creation of personalized medical devices, such as implants and prosthetics, precisely tailored to the unique anatomical features of each patient. This not only makes treatment methods more comfortable for the patient but also increases therapy effectiveness, which is particularly important in cases of complex medical interventions.

- Application before, during, and after surgeries:

3D printing is used at various stages of the medical process. Before surgery, it allows for the production of anatomical models for better visualization and surgical planning. During surgery, surgeons can use tools and implants tailored to the individual needs of the patient. After surgery, this technology can be used to create devices to support rehabilitation.

- Shortening treatment stages:

3D printing accelerates many stages of treatment, from diagnosis to recovery. Faster adaptation of medical tools and devices reduces waiting times for surgeries and shortens hospitalization periods, directly leading to faster patient recovery.

- Minimizing the risk of complications and the need for repeat procedures:

The accuracy and personalization of devices produced by 3D printing minimize the risk of medical errors, leading to a reduction in complications and the need for repeat surgeries. Improved precision in surgery, for example, through the use of models for surgical planning, increases overall patient safety.

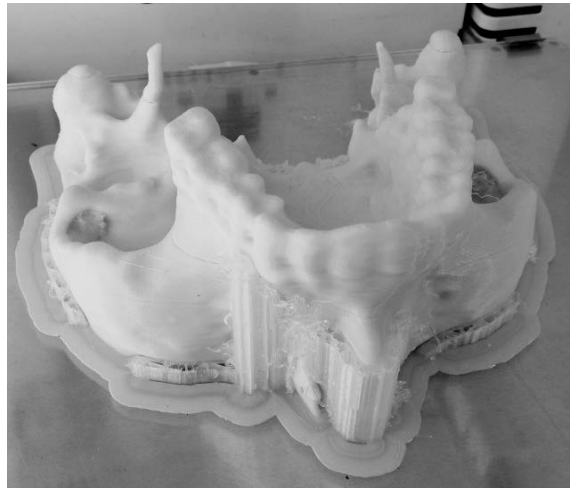


*Figure 2 Prototype of a jawbone implant [4].*

## 2. APPLICATIONS

The technology of 3D printing in medicine has broad and diverse applications, revolutionizing many aspects of healthcare.[5] The main benefits of its application include:

- Printing surgical templates and diagnostic tools:

One of the key applications of 3D printing in medicine is the creation of surgical templates and diagnostic tools. Surgical templates enable surgeons to precisely plan and perform procedures, which is crucial in operations requiring high accuracy, such as transplantations or bone tumor resections. Traditional methods of creating templates using computed tomography (CT) data have certain limitations – the models are rigid and difficult to fit to soft tissues. The use of 3D printing allows for the creation of more flexible and accurate models that can accurately replicate the structure of bones, nerves,

and blood vessels. This reduces the risk of improper implant placement, leading to faster patient recovery and fewer complications.

- Organ printing:

Organ printing is one of the most innovative and promising applications of 3D printing in medicine. This process, also known as bioprinting, involves creating living tissues and organs from patient cells. Special biocompatible materials and advanced engineering techniques are

used for this purpose. Bioprinting allows for precise placement of cells, which can develop and function like natural tissues. This is particularly important in transplantology, where there is a high demand for organs for transplantation. Organ printing has the potential to revolutionize this field in the future, eliminating the problem of a lack of available organs and the risk of transplant rejection.[6]

- Disease modeling:

3D printing is also used to create models of diseases, which are extremely useful in research into new therapies. An example is the creation of models of cancerous tissues using bioprinting. For example, models of ovarian tissues that mimic the tumor microenvironment can be used to study tumor development and test new drugs. These models allow for accurate replication of interactions between cancer cells and healthy tissues, enabling better understanding of disease mechanisms and development of more effective therapies. This allows researchers to test different combinations of drugs and treatment strategies in controlled laboratory conditions before they are applied in clinical trials.

- Personalized pharmaceuticals:

Another area where 3D printing plays a crucial role is the production of personalized pharmaceuticals. Traditional methods of drug production are often limited in terms of dosage precision and the ability to create individual combinations of active substances. 3D printing allows for the creation of tablets with precisely specified doses that can be tailored to the specific needs of patients. This is particularly important in the treatment of chronic and rare diseases, where standard drug doses may not be sufficiently effective or may cause adverse side effects. 3D printing also enables the creation of drugs with complex structures that release active substances at specific times or in specific locations in the body, increasing their effectiveness and safety.

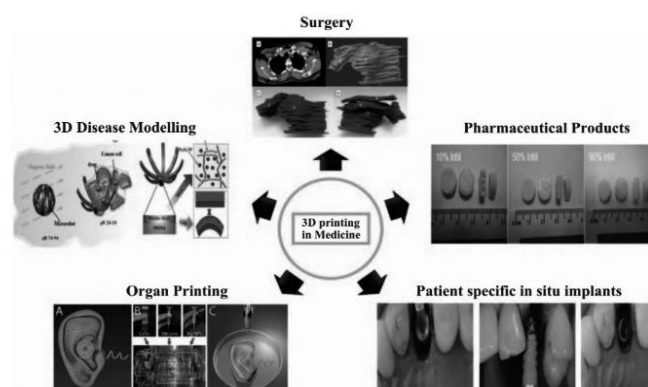
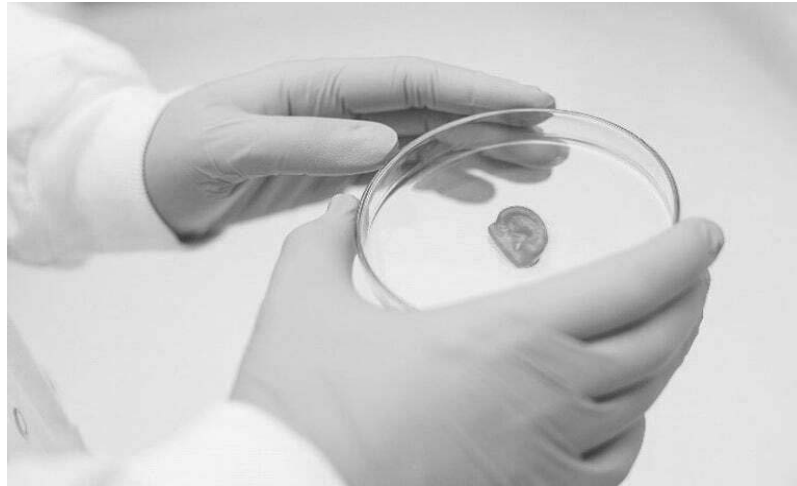


Figure 3. The use of 3D printers in medicine.

### 3. BIOPRINTING 3D

Bioprinting, also known as bio-printing, is an advanced biomedical engineering technique that enables the creation of three-dimensional biological structures, such as tissues and organs, using cells or other biological building materials. By precisely depositing these materials layer

by layer, bioprinting allows for the fabrication of functional biological structures, which have applications in regenerative medicine, scientific research, and drug testing. [7]



*Figure 5 3D bioprinted ear model [7].*

BIO X and BIO X6 are modern 3D bioprinters that stand out in the market due to their versatility and ease of adaptation to the dynamically evolving needs in the field of biological printing. A key feature highlighting their innovation is the intuitive mounting system for printing heads. With this solution, users can quickly and easily expand their equipment with new heads, which are regularly developed and introduced to the market in response to the latest discoveries and research needs.

- **The pneumatic printing head** is designed for extruding a wide range of materials with varying viscosities.
- **The thermoplastic head** can reach a temperature of 250°C, allowing for work with synthetic polymers such as PCL, PLA, and PLGA.
- **The temperature-regulated printing head** is used for printing temperature-sensitive materials that require cooling and heating. Designed for materials like GelMA or Collagen, it features a temperature range from 4°C to 65°C, enabling dynamic adaptation to almost any task.
- **The EMD printing head** is an electromagnetic droplet head for rapid on-demand printing, similar to inkjet printers.
- **The syringe pump printing head** for 3D bioprinting allows users to increase resolution even in small volumes. Using inkjet technology, this head can efficiently and quickly create spheroids or micro-patterns on constructs.
- **The UV printing head** was developed in response to customer needs. This technology allows users to deposit light in specific segments of the construct, creating effective biomechanical gradients.
- **The HD camera head** enables quality control of the print by capturing each stage of the printing process.



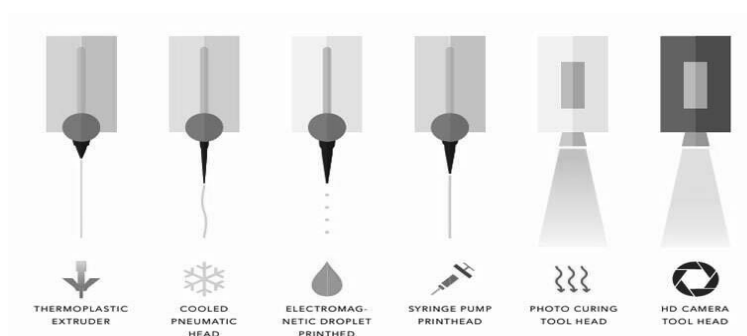


Figure 6 Bioprinting process on the BIO X6 [7]

This flexibility in device configuration allows for significantly expanding its functionality without the need to invest in entirely new printing systems. Users can tailor the bioprinter to specific applications, such as printing various biological materials, including soft tissues, bone structures, or even complex cell models from different types of biomaterials.

BIO X and BIO X6 are also equipped with advanced printing technologies that enable precise placement of cells and biomaterials, which is crucial for achieving optimal results in bioengineering and regenerative medicine. With their versatility, researchers and technicians can experiment with new protocols and optimize existing processes, contributing to faster progress in developing medical fields.

Additionally, the ease of exchanging and updating heads makes BIO X and BIO X6 ideal solutions for research institutions that need to quickly adapt to changing requirements of research and clinical projects. This, in turn, allows for shortening the time from conception to experiment execution, speeding up research processes and innovations in the field of bioengineering.

As a result, BIO X and BIO X6 not only increase efficiency in laboratory work but also open up new possibilities for scientists aiming for breakthroughs in personalized medicine and advanced therapeutic approaches. With their adaptability and upgradeability, they serve as valuable tools that can grow alongside the needs and ambitions of users.

#### 4. SUMMARY

The article reviews the advancements and applications of 3D printing in medicine, highlighting its role in improving patient care, reducing costs, and enhancing rehabilitation. It traces the technology's development from the 1970s to its widespread use today.

Key components of 3D printing—hardware, software, and materials—are discussed, emphasizing the need for compatibility. Benefits in medicine include treatment personalization, shortened treatment stages, reduced complication risks, and increased precision.

Applications such as surgical templates, diagnostic tools, organ printing, disease modeling, and personalized pharmaceuticals are explored, showcasing the technology's potential to revolutionize these areas.

Bioprinting, which creates three-dimensional biological structures using cells, is also introduced. Modern bioprinters like BIO X and BIO X6 are noted for their versatility. The article underscores the significance of these advancements in driving innovation in personalized medicine and advanced therapies, benefiting both patients and researchers.

**BIBLIOGRAPHY**

- [1] D.M. Kalaskar (ed.), 3D Printing in Medicine, Second Edition, Elsevier, Amsterdam, 2023, [access:16.05.2024 ].
- [2] A. Wieczorek, Historia druku 3D – od czego się zaczęło?, [https://botland.com.pl/blog/historia-druku-3d/?cd=19651600289&ad=148844894107&kd=&gad\\_source=1&gclid=CjwKCAjw9IayBhBJEiwAVuc3fhgrKc\\_v\\_I99CHjQ8IRWcg8g8GNws9gikk2dsj2HBQ9DCNshLrOgdxCsHAQAvD\\_BwE](https://botland.com.pl/blog/historia-druku-3d/?cd=19651600289&ad=148844894107&kd=&gad_source=1&gclid=CjwKCAjw9IayBhBJEiwAVuc3fhgrKc_v_I99CHjQ8IRWcg8g8GNws9gikk2dsj2HBQ9DCNshLrOgdxCsHAQAvD_BwE), 2022, [access:16.05.2024 ].
- [3] Eksperymentalne protezy 3D, <https://3dcad.pl/aktualnosci/9538/eksperymentalne-protezy-3d.html>, 2015, [access:16.05.2024 ].
- [4] <https://3dwpraktyce.pl/wp-content/uploads/2017/05/Prototyp-implantu-kosci-rzuchwy-01-600x450.jpg>, [access:16.05.2024 ].
- [5] Druk 3D w medycynie – wydruki do zadań specjalnych, Laser Trade, <https://lasertrade.pl/zastosowanie-druku-3d-w-medycynie>, 2021, [access:16.05.2024 ].
- [6] Likus, W., Nechoritis, K., Różycka-Nechoritis, A., Wilk, R., Hudecki, A., Gaweł, W. ... Markowski, J. (2020). Use of 3D printing in head and neck surgery. *Annales Academiae Medicae Silesiensis*, 74, 99-115. <https://doi.org/10.18794/aams/114163>, [access:16.05.2024 ].
- [7] Biodruk 3D - w kierunku medycyny przyszłości, Sygnis, <https://sygnis.pl/biodruk-3d-w-kierunku-medycyny-przyszlosci/>, 2021, [access:16.05.2024 ].



17th-19th June 2024  
Gliwice, Poland

DEPARTMENT OF ENGINEERING MATERIALS AND BIOMATERIALS  
FACULTY OF MECHANICAL ENGINEERING  
SILESIA UNIVERSITY OF TECHNOLOGY

## INTERNATIONAL STUDENTS SCIENTIFIC CONFERENCE

### Analysis of Group Technology and surface roughness for cutting processes

Arlinda Elezi<sup>a</sup>, Afrim Gjelaj<sup>b</sup>, Besart Berisha<sup>b</sup>

<sup>a</sup> University of Prishtina, Faculty of Mechanical Engineering, Department of Manufacturing and Industrial Engineering with Management, email: arlinda.elezi@student.uni-pr.edu

<sup>b</sup> University of Prishtina, Faculty of Mechanical Engineering, Department of Manufacturing and Industrial Engineering with Management, email: afrim.gjelaj@uni-pr.edu

University of Prishtina, Faculty of Mechanical Engineering, Department of Manufacturing and Industrial Engineering with Management, email: besart.berisha@uni-pr.edu

**Abstract:** For the successful implementation of workpiece machining, it is important to consider all stages of the manufacturing process, starting from the design phase and ending with workpiece machining. Depending on the type of product to be produced, different technologies are used, with lower production costs and many other advantages. "Group Technology" is often used, which means that parts with similar characteristics such as the geometry of the workpieces, material, destination, etc., which will be subjected to the same technological process. The parts of the group technology realized in practice will be subjected to surface roughness measurements. The results will be analysed with the Taguchi method or Minitab software.

**Keywords:** Group technology, machining, surface roughness, Taguchi Method.

## 1. INTRODUCTION

In this paper Opitz method are used to classify parts into "groups", which will be explained later in this paper. A clamping tool has been chosen for practical implementation, after choosing the part and the technology in which it will be processed, the part will be designed first in the Autodesk Inventor software, then the workshop drawings will be prepared, and the part will be worked practically. With the designed parts, some examples will be demonstrated to show how to classify parts according to the Opitz system, and then the part code will be formed according to this classification. Practically realized parts of the clamping tool will be subjected to measurements, these measurements will be mainly on surface roughness [1].

GROUP TECHNOLOGY (GT) is a management philosophy that attempts to group products with similar design and/or manufacturing characteristics. Group Technology (GT) has been recognized as a method for streamlining the production of small and medium-sized groups for some time. One of the first considerations to be made regarding this topic was put forward by Mitrofanov [2].

The identification of these parts [3], will be based on the following characteristics that result in processing in a type of machine:

- Shape characteristics
- Dimensional parameters
- Material group
- Work area
- Special equipment, etc.

An example of GT - Center can be seen below, where similar parts from a technical and economic point of view are processed by the same machine (left side milling machine, right side lathe machine).

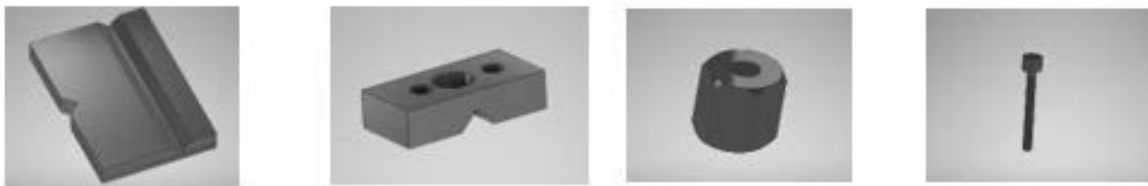


Figure 1. Processing of parts with similar characteristics in the respective machines.

## 2. OPITZ CLASSIFICATION SYSTEM

### 2.1. The basic form of the Opitz code classification

As mentioned above, the Opitz classification system is one of the parts classification systems that has found greater use compared to other classification and coding systems [4-7]. The Opitz classification system can be divided into three components which consist of digits or numbers in a certain order.

Table 1 shows the Opitz Code structure.

Geometric shape code	Additional code	Secondary code
1 2 3 4 5	6 7 8 9	ABCD

Clarification step by step:

1. The first five numbers indicate the code on the shape of the workpieces.
2. The following four numbers form a supplementary code that describes in more detail the features of the product, which are related to manufacturing.
3. Finally, there is a secondary code that fills it in, if necessary, with information about the work piece that is needed for the production cycle.

To demonstrate a case of how a designed part can be read and know the design specifications only by coding, we will take an example of a plate which is designed and practically realized in this paper, as a component part of whole (the clamping tool).

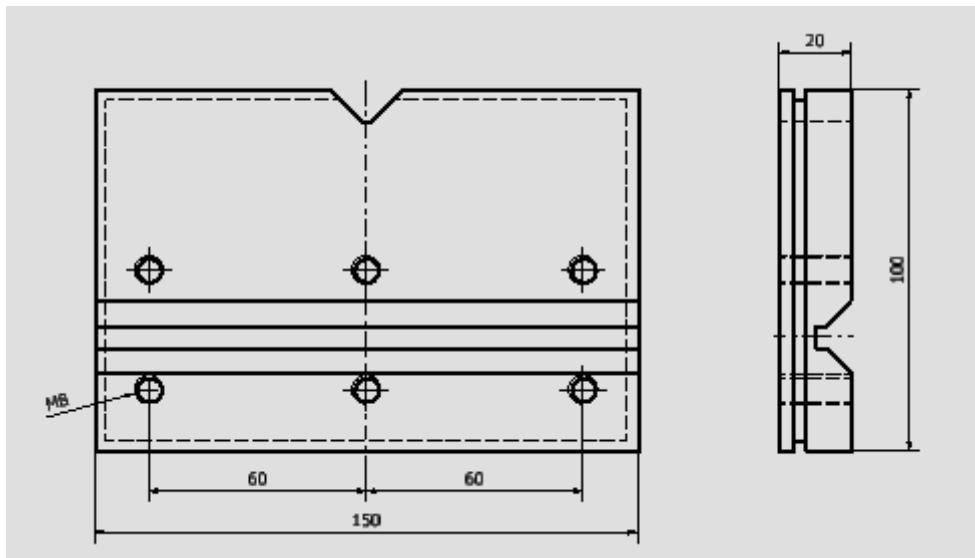


Figure 2. Flat plate with specifications

To form the code, the first digit is first determined, which determines the type of part, whether it is a rectangle, a cubic part, or another shape showed in table 2.

Table 2 General dimension of plate and their code

Dimension $A$ [mm]	Dimension $B$ [mm]	Dimension $C$ [mm]	Dimension $A/B$ [mm]	Dimension $A/C$ [mm]
150	100	20	$\leq 3$	$> 4$

So, from the equations of the calculations  $A/B=1.5$  mm and  $A/C=7.5$  mm, it is understood that the number 6 is chosen, which results in the part being in the group of non-rotating flat parts. Thus, for the realization of the coding of this part through the Opitz code, the table 1, from figure 1, is used, which corresponds to the main form of the part.

Digit 1: From the calculations above, the first digit will be 6 which is presented in the main Opitz classification table. Number 2: The number which has to do with the main shape and this shape corresponds to number 5. Where the part is in the shape of a rectangle and flat with small deviations. Number 3: Also, this number is 5, since here there are more than two parallel main holes. Number 4: In the surface treatment, the number must be chosen which in this case suits the shape of the surface treatment, which is the channel which is almost in the middle of the plate and also the channel around the plate which serves to position the plate in table. Number 5: 0 as it does not have any of the other features.

And the code for this plate according to the Opitz classification system is: **6 5 5 5 0**

### 3. ROUGHNESS MEASUREMENT WITH THE MITUTOYO DEVICE

The measurement of the roughness was done by means of the Mitutoyo device which is found in the laboratories of the Faculty of Mechanical Engineering, the roughness of the surface will be realized for the 3 plates cut on the milling cutter, i.e. for the base plate, the clamping plate, and the plate with a hole in the center for tightening [8].

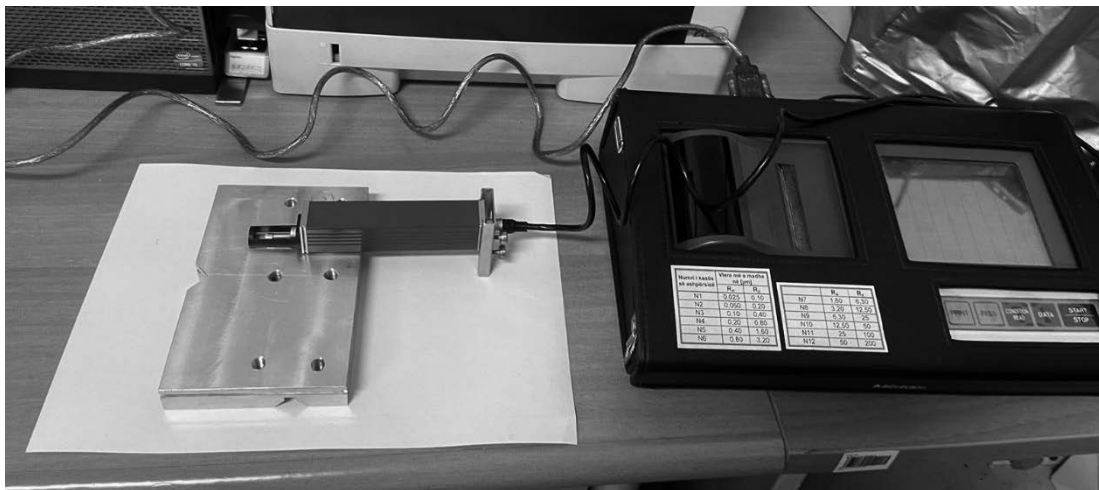


Figure 3. Measurement of surface roughness using the Mitutoyo device.

The diagram of probability plot for surface roughness Ra in percentage, is showed in figure 4.

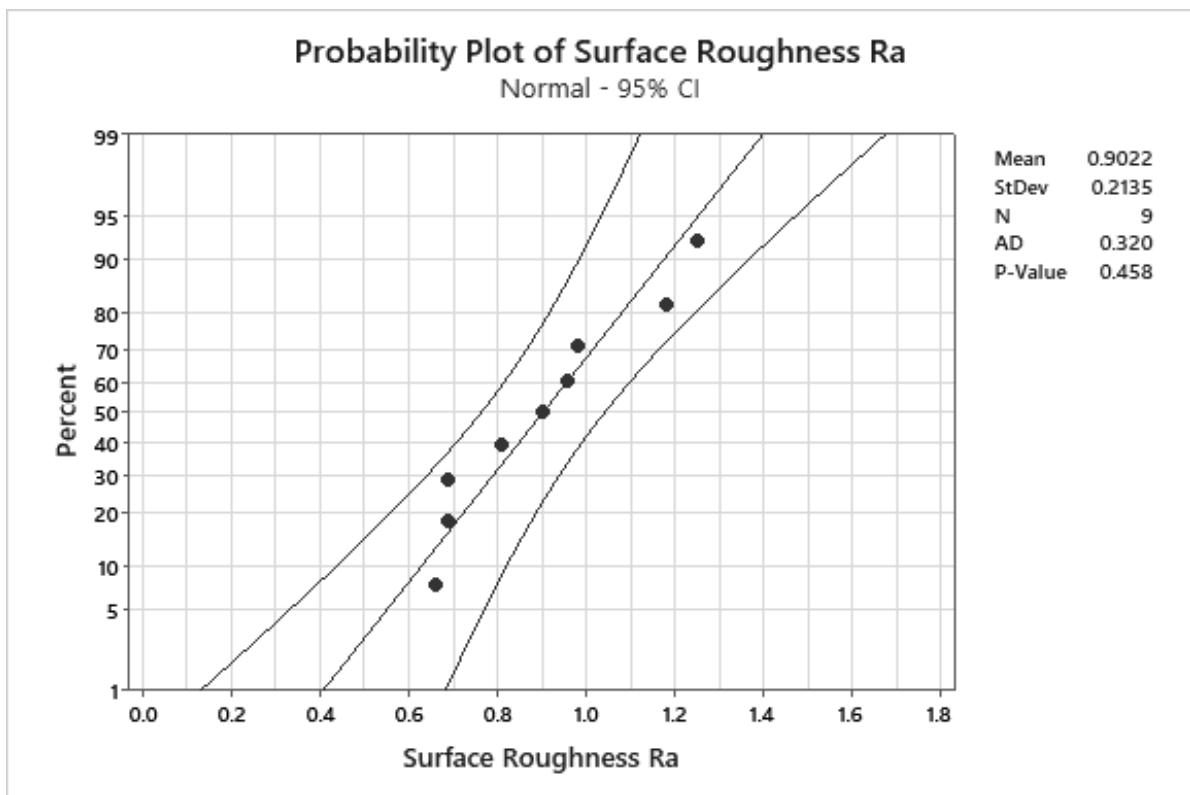


Figure 4. Probability plot of surface roughness Ra

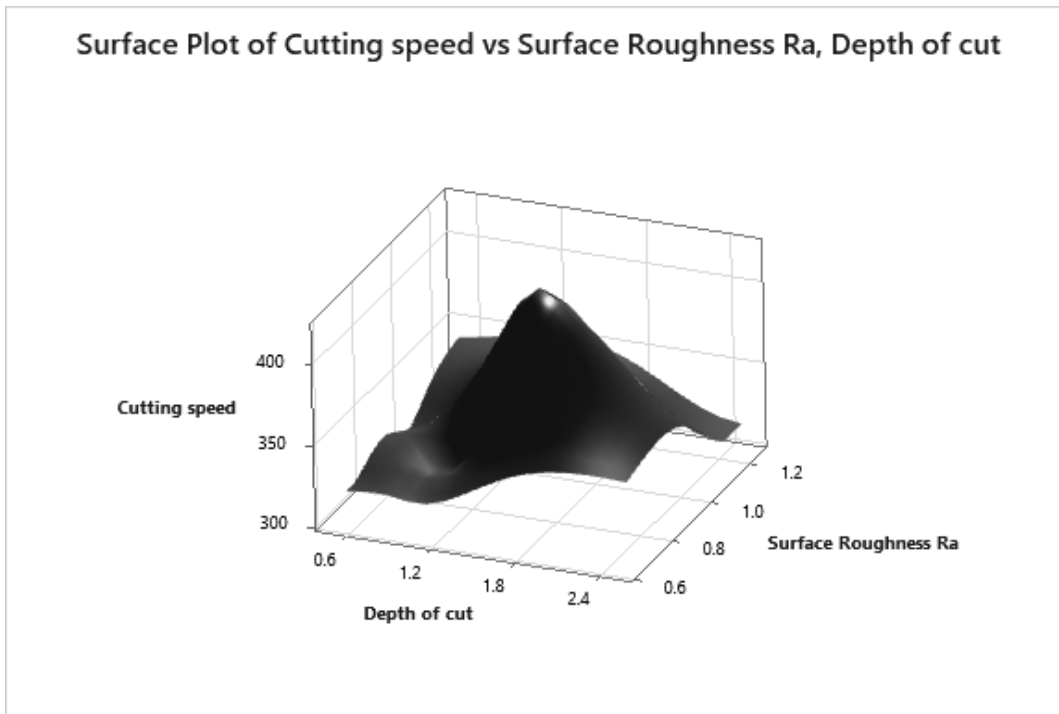


Figure 5. Regression Analysis: Cutting speed versus Surface Roughness Ra

The regression equation is showed as follow:  
 Cutting speed = 323.9 + 15.99 Surface Roughness Ra

Model Summary is showed in table 3.

S	R-sq	R-sq(adj)
49.3627	0.54%	0.00%

Analysis of Variance is showed in table 4.

Source	DF	SS	MS	F	P
Regression	1	93.3	93.29	0.04	0.850
Error	7	17056.7	2436.67		
Total	8	17150.0			

In figure 6, fitted line plot in function of cutting speed and Surface roughness Ra. 4.

### CONCLUSION

As a conclusion, the use of group technology based on the planned production process has been elaborated in this paper, from the beginning of the paper, i.e. the first chapter, the methods used in various manufacturing industries have been shown, where with a basis of planning and technological analysis, production can be realized with high productivity.

The surface roughness was analysed with using the Taguchi method, where you can see the diagrams, where the combinations of the feed rate, cutting speed, depth of cutting for the surface roughness Ra were obtained.

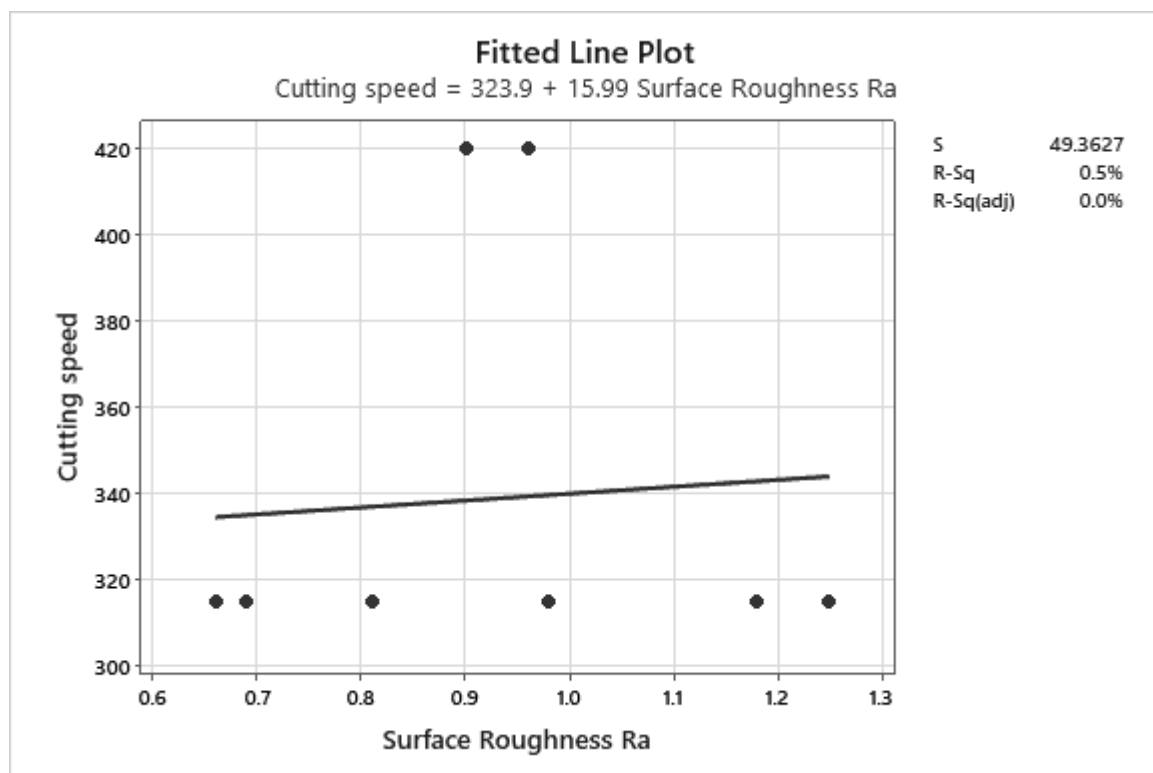


Figure 6. Diagram of fitted line plot in depend on cutting speed and surface roughness.

## BIBLIOGRAPHY

1. U. Wemmerlov and N. L. Hyer, "Procedures for the part-family/ machine group identification problem in cellular manufacturing," J. Op. Management, vol. 6, no. 2, pp. 125-147, 1986.
2. Mitrofanow, s.P.: Wissenschaftliche Grundlagen der Gruppentechnologie. VEB Verlag Technile Berlin 1960.
3. E. A. Arn - Group Technology - An Integrated Planning and Implementation Concept for Small and Medium Batch Production, Springer-Verlag Berlin. Heidelberg. New York 1975
4. A Group Technology Based Classification and Coding System for Reinforced Concrete Structures. (Joseph F. Sacchett, Victor E. Sanvidob\* & Soundar R. T. Kumaraa a Department of industrial and Management Systems Engineering. Department of Architectural Engineering, Pennsylvania State University, University Park, Pennsylvania 76802, USA.)
5. Heragu, S. S. (1994). Group technology and cellular manufacturing. IEEE Transactions on Systems, Man, and Cybernetics, 24(2), 203–215. doi:10.1109/21.281420
6. Knight, W. A. (1998). Group Technology, Concurrent Engineering and Design for Manufacture and Assembly. Group Technology and Cellular Manufacturing, 15–36. doi:10.1007/978-1-4615-5467-7\_2
7. Master Thesis Nr. 3374 "Implementation of an Optimized Distance Function for Retrieval and Similarity Comparison of Non-rotational Parts"- Javier Aguilera Díez.
8. Gjelaj, A., Berisha, B., Sitek, W. (2022). An Experimental Based Approach Using Artificial Intelligence Algorithm for Determining the Surface Roughness by Milling



Process. International Transaction Journal of Engineering, Management, & Applied Sciences & Technologies, 13(5), 13A5B, 1-11. <http://TUENGR.COM/V13/13A5B.pdf>  
DOI: 10.14456/ITJEMAST.2022.86



17th-19th June 2024  
Gliwice, Poland

DEPARTMENT OF ENGINEERING MATERIALS AND BIOMATERIALS  
FACULTY OF MECHANICAL ENGINEERING  
SILESIA UNIVERSITY OF TECHNOLOGY

## INTERNATIONAL STUDENTS SCIENTIFIC CONFERENCE

### Supporting 3D Printing with 3D scanners

Miłosz Ferdyn<sup>a</sup>, Michał Podgórski<sup>a</sup>, Max Żukowski<sup>a</sup>, Magdalena Szindler<sup>b</sup>, Mirosław Bonek<sup>b</sup>

<sup>a</sup> Silesian University of Technology, Faculty of Mechanical Engineering, Student of Engineering Production and Management, Gliwice

<sup>b</sup> Silesian University of Technology, Faculty of Mechanical Engineering, Department of Engineering Materials and Biomaterials

**Abstract:** The article discusses the growing role of 3D scanners in 3D printing. It presents various types of scanners, their functions, and how three-dimensional scanning technology contributes to improving the efficiency and precision of printing. The article also addresses the challenges and opportunities associated with this innovative technology.

**Keywords:** scanners, printing, three-dimensional

### 1. INTRODUCTION

In the last two decades, structured-light scanning research has gained considerable attention worldwide. Different types of scanners (e.g. hand-held scanner, stationary scanners) based on the structured-light scanning systems can be put under the classification of 3D scanning systems, where objects are bombarded with structured-light and the acquired patterns are analyzed to compute the 3D coordinates in the object coordinate space. Structured-light based scanning approach provides flexibility in data quality and acquisition time. It is mainly implemented to capture accurate dense data with simple hardware setup. Objects of certain sizes can affect the performance (due to lack of calibration, small fields of view, non-cosited/cosited/1°30' arrangements in projector-camera setups) and accuracy due to visibility or illumination issues (mostly in outdoor). [1] [2]

Three-dimensional (3D) scanning and 3D printing are becoming increasingly important for numerous applications. Over the last few years, 3D printing has opened new opportunities for various industries including pharmaceuticals, electronic engineering, automotive, industrial design, fashion design, and prototyping [3]. The elevated status of 3D printing can be attributed to its rapid production rates, reduced setup time, high flexibility, maintaining small production volume, 80% to 90% material waste reduction, economic production cost at large scale, development of complex geometry, and the ability to produce customized unique items with consistent quality [4]. On the other hand, 3D scanning is one of the most active research subjects in the research community and industry, and have been implemented in multiple application fields such as the cultural heritage, reverse engineering, digitalization of the physical objects, and medical applications [5].

## 1.1 Background of 3D Printing and 3D Scanning

Three-dimensional (3D) printing, or Additive Manufacturing (AM), allows the creation of three-dimensional models from computer-designed templates or medical imaging data using specialised 3D printers. The evolution of 3D printing techniques, from SLA to SLS and FDM, has expanded its applications beyond industries like automotive and aerospace to include medical fields like hand surgery, enabling the production of intricate anatomical forms and customised medical devices [6]. However, 3D printing continues to be under-utilised across a wide array of surgical subspecialties [7]. Three-dimensional (3D) scanning is the process of digitising physical objects to create mathematical representations in 3D space. Like 3D printing, 3D scanning was developed in the mid-1980s and has experienced considerable improvements in price and performance in the past decade. Combination of 3D printing with 3D scanning has the potential to enhance preoperative planning and drive the development of customised prosthesis in orthopaedics [8]. In this article, we discuss the potential applications of 3D scanning within orthopaedics, limitations, and potential solutions.

## 2. TYPES OF 3D SCANNERS

3D scanners provide a powerful way to capture geometric models into the digital world. In contrast to cameras, 3D scanners are designed to capture detailed shape information of the real-world entities instead of their aesthetics. For instance, 3D scanners can digitize complex world heritage, such as the stone carving clusters in Chartres cathedral, natural wonders, such as the delicate finely-formed sea shells, or simply human faces or sculptures. The power of 3D scanners has perfectly lifted such entities, and the solid digital representation can be accurate to the sub-millimeter level. A concrete scanner can be beneficial throughout the process of 3D modeling, as external shape information can be directly input into 3D modeling applications. [9][10]

There are various classifications of 3D scanners based on hardware technologies, working methodologies, and applications. Hardware technologies include laser scanners, structured-light scanners, parallel stereoscopic cameras, time-of-flight scanners, and ultrasound scanners. Each type of scanner digitizes 3D shapes using different principles, and they each have their unique advantages and adaptability. In terms of working methodologies, 3D scanners can be divided into coordinate-measuring scanners and depth image grabbers. Coordinate-measuring scanners are devices with built-in range detection capabilities, while depth image grabbers are able to produce depth information but are not specifically designed for 3D range detection. [9][11][12]

## 3. APPLICATIONS OF 3D SCANNING IN 3D PRINTING

3D scanning has been widely utilized for capturing existing artifacts in order to create printed replicas. Many artifacts that are not readily available in 3D modeling libraries can be scanned and then turned into 3D models. Subsequently, these 3D models can be used for 3D printing. Additionally, 3D scanning and 3D printing can work in conjunction for certain artifacts. For instance, three common preparatory steps involve scanning, repairing, and orienting artifacts before printing. Initially, 3D models of the artifacts are captured using real 3D scanning systems. Following this, the captured artifacts often require cleaning up and refining to be

suitable for printing. Finally, these repaired artifacts are positioned correctly for printing. As our focus is on 3D scanning to support 3D printing, readers are encouraged to explore additional resources for discussions on reducing costs, enhancing quality, and optimizing performance of 3D printers. Some advanced 3D printers not only have scanning capabilities but are also designed to be user-friendly, powerful, durable, cost-effective, and beneficial for small and medium enterprises transitioning into digital technologies. [13][14]

### 3.2. Prototyping and Rapid Manufacturing

With the maturity of 3D printing technology, an increasing number of products and spare parts can be made by 3D printers. However, we still need to compare fabricated objects with the physical world to check the correctness of objects, but violators may disappear in the coming age of digital manufacturing. As a result, we need to classify as many relics as possible for later generations before losing them. This need for digitization is so we can analyze, preserve, and exhibit them without exposure to the real artifacts. Highly efficient terrestrial laser scanners enable us to easily record forward-looking 3D models at the highest level of detail for large buildings, historical sites, and outdoor objects. 3D printing the scanned models can enable us to exhibit them in the form of plastic. There is an even more significant application in the fields of culture and education; people can get close to historical heritage by touching them rather than just looking at photos.

Accurate reproductions can be used for business purposes such as making costume parts for cosplay, props of movies, and non-standard spare parts for equipment. Appropriate sizes can be made when the original objects are too large or too small. Large-scale exhibits cannot be disassembled and transported but small-scale exhibits can. It is tough to be especially careful about the preservation of priceless artifacts such as relics and fossils during transport, so it is safer to place lightweight 3D replicas at the exhibition. Three-dimensional scanners and 3D printers are used in fields such as archaeology, mineralogy, and paleontology. Using a 3D scanner to capture instances in situ to create a 3D print of the object is widely appealing in Italy, where public access to Italian cultural heritage objects can increase the overall understanding of scarce or, in some cases, overexposed cultural heritage. Therefore, supporting 3D printing with 3D scanners is highly significant.

## 4. CHALLENGES AND LIMITATIONS

The initial hypothesis for the presented research is that a 3D scanner would support the use of a 3D printer. Around less than 5% of 3D printer owners have experience with 3D design. As already stated, with a 3D scanner, a user with non-advanced traditional CAD skills would be able to create or fix objects for 3D printing. This tool would facilitate usage of a 3D printer and its adoption, especially for non-technology expert individuals. Nevertheless, 3D scanning equipment seems either very expensive, not suitable for the required material or users have doubts on their potential based on professional and public reviews - these are inconsistencies between reviews that some sites reveal. [15]

In qualifying environments for the everyday use of digital fabrication tools, it is important to consider the practical limitations and measures of precision and accuracy in terms of geometric model acquisition. 3D scanning is a fast-growing area of research and technology, and is an enabling technology for a variety of applications in science, medicine, gaming, animation,

consumer entertainment and fashion. However, the various 3D scanning methods have different constraints imposed by numerous practical challenges such as: geometric limitations, computational cost, large amounts of data, limited accuracy and precision. These challenges are emphasized in the 3D scanning task specifically targeted by the presented work, which emphasizes their relevance to the need of the end-users.

## **5. FUTURE DEVELOPMENTS**

A number of research teams have been exploring the use of mobile phones to construct 3D models of the world. This offers an opportunity for 3D printer operators to trivially capture 3D models of objects for printing. In this paper, we explore the various limitations of these techniques and analyze where they can best be exploited for a 3D printing workflow.

During our exploration of capturing objects for 3D printing, we discovered that there is a severe lack of good comparisons of 3D scanner hardware or software. This paper contributes a thorough evaluation of six low-cost 3D scanners in comparison to thirty-eight 3D models and their ability to support parametric improvements to that model. This data can inform future research that traditionally aims to avoid these limitations.

Most 3D printers rely on designers to define the form and behavior of a 3D model by interacting with a modeling application. This is an obstacle for non-expert designers as it places a burden on them to be able to manipulate the modeling program. 3D scanners have been improving over time and are now capable of capturing objects of most organic forms. With 3D scanners, we are quickly approaching a point where point and click 3D scanning software can create models that are printable in seconds and with minimal effort. However, these models are often of low quality: they contain a great deal of noise and closed shapes.

### **5.1. Advancements in 3D Scanning Technologies**

The latest technological advancements in 3D scanning have introduced applications in complex fields, such as architecture, the analysis of historical artifacts, and applications in the medical and entertainment fields - video gaming. Researchers aim at improving their scanning system's capacity with capturing increasingly complex and larger scenarios with better accuracy. Wong and Chau achieved good results in scanning large objects by integrating a laser stripe with a motion control system. Laser stripe-based 3D scanning is a popular method for capturing information about the 3D surfaces of an object. This method, by projecting laser lines to the surface of the object and capturing the object from a different perspective through a camera, creates a triangulation after the image is acquired. This method embodies advantages and is becoming increasingly popular due to its portability, good capture ability, and high accuracy. Among many 3D scanners are the Artec Spider, a handheld 3D scanner with 3D reconstruction through an infrared line laser, and DOF Reality's 3D body scanner, which utilizes blue light technology to possess a patterning effect for high-efficiency scanning.

Moreover, the latest developments in smartphone technology, in the form of a personalized or integrated ToF camera, ensure portability and efficiency. The integrated ToF camera has a relatively poor capture distance and accuracy due to its relatively low resolution, compared to those equipped with the special-purpose PDA. However, cost-effective and more user-friendly approaches have seen an acceleration in 3D scanning applications. Yang et al. contributed to improvements and the algorithm of ToF cameras. Tengrouse et al. investigated a more user-friendly application of 3D scanning. They used a photographing platform equipped with

modified Fuhrmann FS30 3D scanners to accomplish a limited number of scans of sites of real complex surfaces, from which accurate 3D models of bastion fragments, large wall paintings, and 3D stone databases to be showcased in a virtual museum were successfully created. The results not only reduced the waiting time and task complexity but also significantly reduced the cost of specialized operators. Their work guides related professionals to think of applications in the context of cultural heritage scanning and contributes to future 3D scanners, creating better application platforms for traditional cultural applications or digital learning.

## BIBLIOGRAPHY

- [1] B. Cui, W. Tao, and H. Zhao, "High-precision 3D reconstruction for small-to-medium-sized objects utilizing line-structured light scanning: A review," *Remote Sensing*, 2021. [mdpi.com](https://doi.org/10.3390/rs13020202)
- [2] A. H. Dorrah and F. Capasso, "Tunable structured light with flat optics," *Science*, 2022. [nju.edu.cn](https://www.nyu.edu/cn)
- [3] M. Daneshmand, A. Helmi, E. Avots, F. Noroozi et al., "3D Scanning: A Comprehensive Survey," 2018. [PDF]
- [4] R. González-Merino, E. Sánchez-López, P. E. Romero, J. Rodero et al., "Low-Cost Prototype to Automate the 3D Digitization of Pieces: An Application Example and Comparison," 2021. [ncbi.nlm.nih.gov](https://www.ncbi.nlm.nih.gov)
- [5] Q. Gu, K. Herakleous, and C. Poullis, "3DUNDERWORLD-SLS: An Open-Source Structured-Light Scanning System for Rapid Geometry Acquisition," 2014. [PDF]
- [6] M. Keller, A. Guebeli, F. Thieringer, and P. Honigmann, "Overview of In-Hospital 3D Printing and Practical Applications in Hand Surgery," 2021. [ncbi.nlm.nih.gov](https://www.ncbi.nlm.nih.gov)
- [7] M. Kappanayil, N. Rao Koneti, R. R Kannan, B. P Kottayil et al., "Three-dimensional-printed cardiac prototypes aid surgical decision-making and preoperative planning in selected cases of complex congenital heart diseases: Early experience and proof of concept in a resource-limited environment," 2017. [ncbi.nlm.nih.gov](https://www.ncbi.nlm.nih.gov)
- [8] P. Giacomelli and A. Smedberg, "The Eve of 3D Printing in Telemedicine: State of the Art and Future Challenges," 2014. [PDF]
- [9] M. Javaid, A. Haleem, R. P. Singh, and R. Suman, "Industrial perspectives of 3D scanning: features, roles and it's analytical applications," *Sensors International*, 2021. [sciencedirect.com](https://www.sciencedirect.com)
- [10] A. Crisan, M. Pepe, D. Costantino, and S. Herban, "From 3D Point Cloud to an Intelligent Model Set for Cultural Heritage Conservation," *Heritage*, 2024. [mdpi.com](https://www.mdpi.com)
- [11] R. H. Helle and H. G. Lemu, "A case study on use of 3D scanning for reverse engineering and quality control," *Materials Today: Proceedings*, 2021. [sciencedirect.com](https://www.sciencedirect.com)
- [12] C. Gollob, T. Ritter, and A. Nothdurft, "Forest inventory with long range and high-speed personal laser scanning (PLS) and simultaneous localization and mapping (SLAM) technology," *Remote Sensing*, 2020. [mdpi.com](https://www.mdpi.com)
- [13] A. Kantaros, T. Ganetsos, and F. I. T. Petrescu, "Three-dimensional printing and 3d scanning: Emerging technologies exhibiting high potential in the field of cultural heritage," *Applied Sciences*, 2023. [mdpi.com](https://www.mdpi.com)
- [14] S. Hong and Y. H. Jo, "A Study on Three-Dimensional Printing Replication for Usability Of Artifacts," in *The International Archives of the ...*, 2021. [copernicus.org](https://www.copernicus.org)
- [15] A. Kantaros, O. Diegel, D. Piromalis, G. Tsaramirsis, "3D printing: Making an innovative technology widely accessible through makerspaces and outsourced services," *Materials Today*, Elsevier, 2022. [sciencedirect.com](https://www.sciencedirect.com)



17th-19th June 2024  
Gliwice, Poland

DEPARTMENT OF ENGINEERING MATERIALS AND BIOMATERIALS  
FACULTY OF MECHANICAL ENGINEERING  
SILESIA UNIVERSITY OF TECHNOLOGY

## INTERNATIONAL STUDENTS SCIENTIFIC CONFERENCE

### Optimization of a selected production process using the DOE method

Katarzyna Furman<sup>a</sup>, Dominik Towarnicki<sup>b</sup>, Ewa Jonda<sup>c</sup>

<sup>a</sup> Silesian University of Technology, Faculty of Mechanical Engineering, Department of Automation of Technological Processes and Integrated Manufacturing Systems  
email: katafur136@student.polsl.pl

<sup>b</sup> Silesian University of Technology, Faculty of Mechanical Engineering, Department of Automation of Technological Processes and Integrated Manufacturing Systems  
email: domitow239@student.polsl.pl

<sup>c</sup> Silesian University of Technology, Faculty of Mechanical Technology, Department of Materials Engineering and Biomedical, ul. Konarskiego 18a, 44-100 Gliwice

**Abstract:** This article presents the glass production process, describes the characteristics of glass and its processing methods. In the practical part, the samples were tempered, considering the parameters of the DOE experiment, such as heating time and tempering pressure. Two tests were then conducted: four-point bending and crack pattern analysis on 18 samples of reinforced float glass. The results of both tests were compared, and conclusions were drawn based on them.

**Keywords:** float glass, four-point bending, crack pattern, tempering process, process optimization

### 1. INTRODUCTION

This project concerns the optimization of the glass tempering process. In the current times, numerous technological solutions based on automation and robotics have been observed. Optimization plays a key role in the competitive market and the efficiency of enterprises. In the past few years, there has been a significant increase in the use of flat glass in construction. This material has been known for over 2000 years, and for the past centuries, it has been mainly used to fill window and door frames, primarily creating inconspicuous building elements. Nowadays, thanks to technological progress and increase of the knowledge, the glass is increasingly used to construct more responsible elements in buildings [1,2]. In Poland, industrial development and increased economic activity of industrial enterprises have been observed for last several years. However, the outbreak of the COVID-19 pandemic in 2020 led to a slight slowdown in industrial development.

The introduction of certain restrictions on economic activities resulted in a decrease in the activity of industrial enterprises in Poland, which was reflected in the decline of basic indicators characterizing the socio-economic situation of the industry: sold production, turnover, including non-domestic turnover and turnover within the eurozone, average

employment, investment outlays, initiated investments, and financial results. Poland fared relatively well despite the deteriorating situation of the Polish industry compared to other EU countries. Many sectors of the Polish industry, after a deep slump in the first quarter of 2020, recorded better results in the following months than EU countries [3]. In 2020, the production of float glass amounted to 104,000 m<sup>2</sup>. The dynamics of industrial product production indicators varied across different industries. In August 2021, compared to the same month in 2020, the production of float glass and polished surface glass increased by 42.5%, and multi-chambered insulating glass units by 20% (according to GUS data) [3].

## 2. MATERIALS AND METHODS

The aim of the study was to optimize the technological parameters of the glass tempering process, improve product quality, production efficiency, and ensure the glass met appropriate norms and quality standards. The research problem was the glass did not meet the required standards, including four-point bending and crack patterns, which were used to standardize testing procedures and determine evaluation criteria. This allows ensuring the production processes meet strength and quality requirements.

The glass melting process is a crucial stage in its production. During this process, raw materials are transformed into a molten, formable glass mass. The schematic of the glass melting process is shown in Figure 1. The melting process takes place in glass furnaces, where mixed raw materials are continuously poured from one side [A], and molten glass is discharged from the other side [E]. In the melting zone of the furnace [B], the glass batch loses moisture adsorbed on the raw material grains, the components heat up, and melting occurs. In the clarifying zone [C], degassing of the glass mass from excess gases and gas bubbles formed due to chemical reactions between raw material components, gases adsorbed on raw material grains, furnace atmosphere, and refractory materials of the glass tank occurs. The next step is the homogenization of the glass mass [D]; this is a process of uniformity - releasing the melt from visible streaks, leading to obtaining uniform properties of the mass throughout its volume. The final stage is the pouring of the glass mass onto a layer of molten tin and forming glass sheets [3].

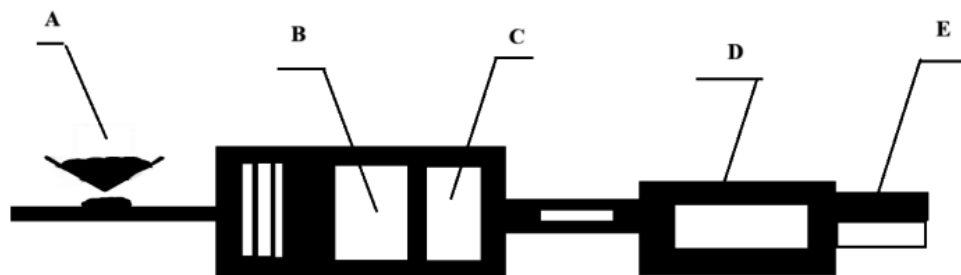


Fig. 1. Schematic diagram of the glass melting process in a glass tank (developed based on [3])

### 2.1 Glass Processing Methods

The processing method allows applying specific properties to a product, such as shape or dimension. It's employed for various reasons, with the type depending on the intended use of the glass product or customer preferences. There are two main types: mechanical and heat-based. Below are several primary glass processing methods:



**Mechanical:**

- Cutting
- Shaping
- Drilling
- Beveling
- Grinding
- Polishing
- Screen printing

**Heat-based:**

- Melting

**2.2 Float Glass**

Float glass is a flat, soda-calcium-silica glass, transparent, colorless, or tinted, with parallel and fire-polished surfaces, produced by the continuous pouring onto the surface of molten metal. In the contemporary architectural applications, float glass sheets (as it's called) form the basis for producing various types of façade glazing in modern buildings.

The raw materials for producing float glass consist of the following components:

Composition of glass mass:

- 60% quartz sand ( $\text{SiO}_2$ )
- 20% sodium carbonate ( $\text{NaCO}_3$ )
- 20% calcium carbonate ( $\text{CaCO}_3$ ), in accordance with the requirements of standard PN-EN 572-2,
- defined the requirements for soda-calcium-silica architectural glass.

**2.3 Physicochemical Properties of Float Glass**

Table No. 1 presents the properties of a float glass according to PN-EN 572-2, titled "Glass in construction - Basic products of soda-calcium-silica glass - Part 2: Float glass".

*Table 1. Physicochemical Properties of Flat Glass (compiled based on [3])*

Property	Symbol	Numerical Value and Unit
Density (at 18°C)	R	2500 kg/m <sup>3</sup>
Hardness		6 units (according to Mohs scale)
Young's Modulus (longitudinal elasticity modulus)	E	$7 \times 10^{10}$ Pa
Poisson's Ratio	V	$0.72 \times 10^{-3}$ (J/kg·K)
Specific Heat	C	$9 \times 10^{-6}$ K <sup>-1</sup>
Average Linear Coefficient of Thermal Expansion between 20°C and 300°C	$\alpha$	1 W/(m·K)
Thermal Conductivity	$\Lambda$	1.5

Average Refractive Index in the visible spectrum (from 380 to 780 nm)	N	$9.0 \times 10^{-6}K$
Linear Expansion Coefficient	$\alpha$	12-30 N/mm <sup>2</sup>
Flexural Strength		
Compressive Strength		400 N/mm <sup>2</sup>

The subject of the study is a tempered float glass. Figure 2 shows the tested sample of a float glass, while its specifications are provided in Table 2.

Table 2. Dimensions of the Sample (compiled by the author)

Name	Length (mm)	Width (mm)	Thickness (mm)
Tempered Float Glass	1100	360	4



Fig. 2. Float Glass Sample (author's compilation)

#### 2.4. Research Methodology

The project utilized the Design of Experiments (DOE) method, following the steps outlined below:

1. Selection of two key factors: heating time and tempering pressure.
2. Experimental design, conducting experiments based on several combinations as presented in Table 3.

Each experiment consists of two samples: one sample undergoes four-point bending, while the other undergoes a crack grid test.

Table 3. Experimental Plan (author's compilation)

Experiment Number	Heating Time (s)	Tempering Pressure (Pa)
1	135	4750
2	135	5250
3	135	5750
4	155	6250
5	155	6750
6	155	7250
7	175	7750
8	175	8250
9	175	8750

### 3. RESULTS OF THE STUDY

Based on the results obtained from the experiments conducted on 18 samples using the Design of Experiments (DOE) method, optimal tempering process parameters were defined. Subsequently, the influence of selected parameters on the product's strength was compared. The study consisted of 2 stages. In the first stage, the four-point bending method was used to examine the glass strength. In the second stage, crack grid tests of the product were performed.

#### 3.1 Four-Point Bending

Nine experiments of four-point bending were conducted on samples with a thickness of 4 mm. Table 4 presents a comparison of the parameters describing four-point bending.

Table 4. Comparison of Parameters Describing Four-Point Bending

Sample Number	Maximum Force, Fmax (N)	Bending Strength (MPa) or (N/mm <sup>2</sup> )
1	245	55
2	303	68
3	351	79
4	412	93
5	430	97
6	503	114
7	563	127
8	651	147
9	712	161

Based on the data provided in table no. 9, it can be concluded the samples 7, 8, and 9 comply with the standard because the bending strength value is higher than 120 N/mm<sup>2</sup>.

### 3.2 Crack Grid Test

Nine experiments of the crack grid test were conducted on samples with a thickness of 4 mm. Table 5 presents the results of parameters characterizing the crack grid. The value is expressed as either >40 (if the number of fragments is greater than 40) or <40 (if the number is less than 40).

Table 5. Comparison of Results of Fragments

Sample Number	Number of Fragments (>40 or <40)
1	<40
2	<40
3	<40
4	<40
5	<40
6	<40
7	>40
8	>40
9	>40

Based on Table 5, it can be concluded the samples 7, 8, and 9 comply with the standard because the number of fragments is higher than 40.

### 3.3 Comparison of Results of Furnace Parameters, Four-Point Bending Test, and Crack Grid Test

Based on the data from the DOE experiment presented in Table 3, the tempering process, four-point bending test, and the crack grid test were conducted to compare two samples: one compliant with the standard (sample 9) and one non-compliant with the standard (sample 1).

**Sample compliant with the standard - sample 9**

**Sample non-compliant with the standard - sample 1**

**• Furnace Parameters**

Comparison of the two samples based on the report generated from the tempering furnace showed significant differences in the values of heating time and tempering pressure. The sample compliant with the standard is characterized by significantly higher tempering pressure values compared to the sample non-compliant with the standard. Figures 3-4 depict the reports from the tempering furnace.

Receptury – wstępne ustawienia Hartowanie, 4mm, Wyczyść		Receptury – słowa kluczowe OGOLNA		Identyfikator recepty #1290 (Zmodyfikowany)	
Ustawienia załadunku	20 s	Czas nagrzewania	175 s	Poziom temperatury sekcji górnej	678 °C
Opóźnienie ładowania	1000 mm	Ustaw	175 s	Ustaw	681 °C
Etap ładowania	550 mm/s	Rzeczywista		Średnia	
Prędkość ładowania					
Poziom temperatury sekcji dolnej		Ustawienia prędkości przenoszenia		Schładzacz	
Ustaw	678 °C	Prędkość przenoszenia	550 mm/s	Odległość dysz	18 mm
Średnia	678 °C	Prędkość początkowa	80 mm/s	Ustaw	17 mm
		Prędkość środkowa	140 mm/s	Średnia	
		Prędkość końcowa	210 mm/s		
		Rozkład prędkości	60 %		
Schładzacz		Schładzacz		Ciśnienie hartowania	
Równowaga powietrza do hartowania		Równowaga powietrza do chłodzenia		Ustaw	8750 Pa
Ustaw	-15 %	Ustaw	-15 %	Średnia	8528 Pa
Średnia	-15 %	Średnia	-15 %		
Ciśnienie schładzania					
Ustaw	4500 Pa				
Średnia	4412 Pa				

Fig. 3. Report from the tempering furnace for sample 9

Receptury – wstępne ustawienia Hartowanie, 4mm, Wyczyść		Receptury – słowa kluczowe OGOLNA		Identyfikator recepty #1460 (Zmodyfikowany)	
Ustawienia załadunku		Czas nagrzewania		Poziom temperatury sekcji górnej	
Opóźnienie ładowania	30 s	Ustaw	135 s	Ustaw	675 °C
Etap ładowania	1800 mm	Rzeczywista	135 s	Średnia	676 °C
Prędkość ładowania	550 mm/s				
Poziom temperatury sekcji dolnej		Ustawienia prędkości przenoszenia		Schladzacz	
Ustaw	675 °C	Prędkość przenoszenia	550 mm/s	Odległość dysz	
Średnia	675 °C	Prędkość początkowa	40 mm/s	Ustaw	17 mm
		Prędkość środkowa	60 mm/s	Średnia	18 mm
		Prędkość końcowa	140 mm/s		
		Rozkład prędkości	75 %		
Schladzacz		Schladzacz		Ciśnienie hartowania	
Równowaga powietrza do hartowania		Równowaga powietrza do chłodzenia		Ustaw	5000 Pa
Ustaw	-22 %	Ustaw	-22 %	Średnia	5028 Pa
Średnia	-22 %	Średnia	-22 %		
Ciśnienie schładzania					
Ustaw	4500 Pa				
Średnia	4548 Pa				

Fig. 4. Report from the tempering furnace for sample 1

• Based on the Results of the Four-Point Bending Test

Comparison of the results of the two samples showed significant differences in the values of maximum force and bending strength. Figures 5 and 7 present the values of maximum forces. The highest value of destructive force for sample 9 was 0.712 kN, equivalent to 712 N. For sample 1, the maximum destructive force value was 0.430 kN, corresponding to 430 N.

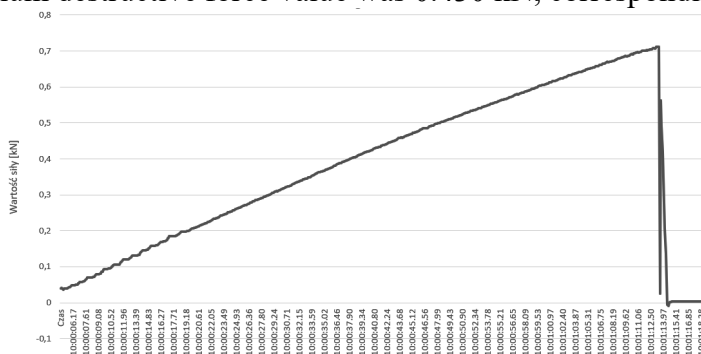


Fig. 5. Graph of maximum force values for sample 9

Parametry obliczeniowe i jednostki	Dane geometryczne	Formuły/ wyniki
szerokość próbki (pomiar), B [dokładność do 0,001m]		0,36
grubość próbki (pomiar), h [dokładność 0,00001m]		0,00384
siła maksymalna (pomiar), Fmax [dokładność 1N]		712
iloczyn obliczeniowy 2Bh <sup>2</sup>		1,06168E-05
różnica Ls-Lb, [m]		0,8
iloraz obliczeniowy 3(Ls-Lb)/2Bh <sup>2</sup>		226056,1343
<b>Wytrzymałość na zginanie <math>\sigma_{bB}</math> [MPa] lub [N/mm<sup>2</sup>]</b>		<b>161</b>
Rodzaj szkła		Float
Rodzaj obróbki krawędzi		Stępanie
Temperatura		20
Wilgotność		40%
Wynik spr. stanowiska wg PN-EN 1288-3 Zg/Ng*		Zg
Wynik badania**		Pozytywny

Fig. 6. Four-point bending form generated in Excel program

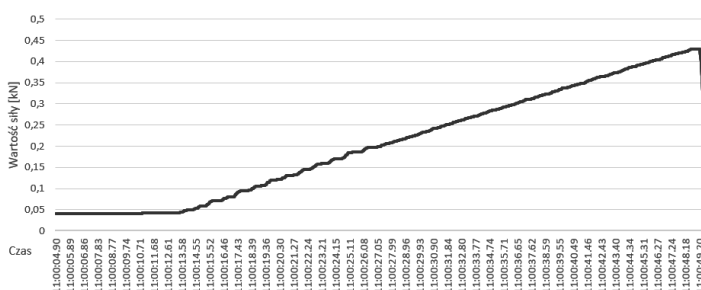


Fig. 7. Graph of maximum force values for sample 1

Parametry obliczeniowe i jednostki	Dane geometryczne	Formuły/ wyniki
szerokość próbki (pomiar), B [dokładność do 0,001m]	0,36	
grubość próbki (pomiar), h [dokładność 0,00001m]	0,00384	
siła maksymalna (pomiar), Fmax [dokładność 1N]		430
iloczyn obliczeniowy $2Bh^2$		1,06168E-05
różnica Ls-Lb, [m]		0,8
iloraz obliczeniowy $3(Ls-Lb)/2Bh^2$		226056,1343
<b>Wytrzymałość na zginanie <math>\sigma_{bB}</math> [MPa] lub [N/mm<sup>2</sup>]</b>		<b>97</b>
Rodzaj szkła		Float
Rodzaj obróbki krawędzi		Stępianie
Temperatura		20
Wilgotność		40%
Wynik spr. stanowiska wg PN-EN 1288-3 Zg/Ng*		Zg
Wynik badania**		Negatywny

Fig. 8. Four-point bending form generated in Excel program (author's compilation)

• **Based on the Crack Grid Test**

Comparison of the two samples based on the report obtained from the crack grid test showed significant differences in the counts of detected fragments. The maximum number of fragments in sample number 9 exceeds 40 because more were counted. Figure 9 depicts the entire glass sample after breakage, while Figure 10 shows the tested area (50x50 mm) displayed at significant magnification.

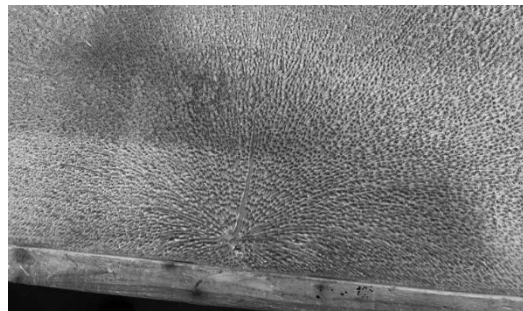


Fig. 9. Sample 9 after breakage

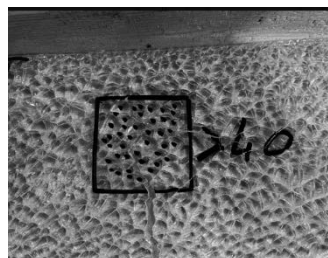


Fig. 10. Tested area (50x50 mm) displayed at significant magnification, sample 9

The number of fragments in sample number 1 reaches a maximum value of 25. Figure 11 shows the entire glass sample after breakage, while Figure 12 shows the tested area (50x50 mm) displayed at significant magnification.

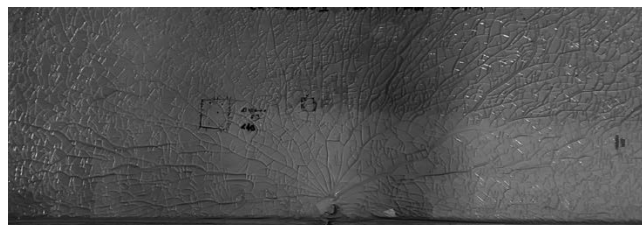


Fig. 11. Sample 1 after breakage

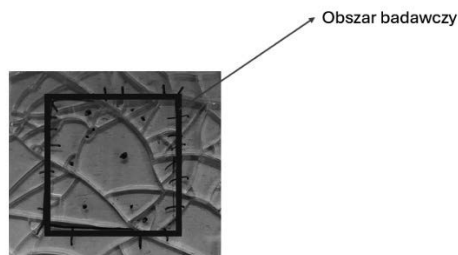


Fig. 12. Tested area (50x50 mm) displayed at significant magnification, sample 1

#### 4. CONCLUSIONS

Based on the conducted research and analysis, the following conclusions were formulated:

1. The results of experiments 7, 8, and 9 showed optimal parameter values, resulting in positive outcomes both in the four-point bending test and crack grid evaluation.
2. The DOE method proved to be an effective tool in identifying optimal process parameters.
3. Continuous monitoring of the process and possible further research are recommended to maintain and improve the quality of the produced material.

#### ACKNOWLEDGEMENTS

The publication was created within the framework of the joint Slovak-Polish project International Visegrad Fund's V4 Generation Mobility Mini-Grant No 12410044 as a result of cooperation between the Association of Alumni of the Silesian University of Technology, Gliwice, Poland and the University of Žilina, Slovakia.

The project is co-financed by the Governments of Czechia, Hungary, Poland and Slovakia through Visegrad Grants from the International Visegrad Fund. The mission of the fund is to advance ideas for sustainable regional cooperation in Central Europe.



#### BIBLIOGRAPHY

1. Struct E. , Structural Use of Glass in Buildings (2" edition), The Institution of Structural Engineers – IstructE, 2014
2. Lenk P. , Designing with Structural Glass, Challenging Glass 5 - Conference on Architectural and Structural Applications of Glass, Ghent University,2016
3. Kosmal M. , Kuśnierz A. , Kozłowski M. „Szkło budowlane”, Wydawnictwo Naukowe PWN, Warszawa 2022
4. <https://www.rkglass.pl/typy-szkla-i-rodzaje-obrobek-krawedzi/> (Data uzyskania 02.01.2024)
5. Kowalski D. „Materiały szklane w lekkiej obudowie Część 1”, Builder 62 styczeń 2017.



17th-19th June 2024  
Gliwice, Poland

DEPARTMENT OF ENGINEERING MATERIALS AND BIOMATERIALS  
FACULTY OF MECHANICAL ENGINEERING  
SILESIA UNIVERSITY OF TECHNOLOGY

## INTERNATIONAL STUDENTS SCIENTIFIC CONFERENCE

### **Analysis of management systems frequently used in the automotive industry**

Katarzyna Furman, Dominik Towarnicki, Hubert Przybyszewski

<sup>a</sup> Silesian University of Technology, Faculty of Mechanical Engineering, Department of Automation of Technological Processes and Integrated Manufacturing Systems  
email: katafur136@student.polsl.pl, domitow239@student.polsl.pl

**Abstract:** The development of the automotive industry requires effective management that considers the specific requirements of the industry. The introduction of integrated management systems, in line with industry standards, is becoming a key element in improving business operations. This article examines the importance and application of selected industry standards in the automotive industry.

**Keywords:** ISO 9001:2015, ISO 14001:2015, ISO26262, IATF 16949, ISO/IEC 27001, ISO 2231, management systems

### **1. INTRODUCTION**

The automotive industry, as one of the most dynamic and innovative sectors of industry, constantly challenges companies with regard to quality, safety and sustainability.

In an increasingly competitive market environment, companies in this sector must not only meet the high expectations of customers, but also comply with strict regulations and industry standards. The implementation of appropriate industry standards thus becomes a key element of effective management in the automotive industry. By complying with these standards, companies can not only ensure the high quality of their products and services, but also increase the safety of vehicle occupants and minimise the negative impact on the environment. The requirements of national and international standards describe a modern approach to process management and promote continuous improvement of organisations, the correct application of which can help to reduce the challenges posed by a radically changing internal and external environment [1].

This article aims to explain the relevance and application of selected industry standards in the automotive industry. Analysing these standards will help you better understand the demands placed on companies in the automotive industry and the benefits they can derive from their implementation, and why adherence to these standards is key to success in this dynamic industry.



## 2. ANALYSIS OF SELECTED MANAGEMENT SYSTEMS

### 2.1. ISO 9001:2015

Quality management systems based on PN-EN ISO 9001:2015 are based on an analysis of risks and opportunities, ensuring continuous improvement, elimination of non-conformities and guaranteeing the highest quality of products. Meeting expectations and verifying the organisation's objectives and strategy result from identifying stakeholders and analysing both the internal and external context of the organisation. Ensuring the highest quality in accordance with the requirements of the international standard ISO 9001:2015 has become a common standard that is applied by every organization, regardless of its type or size. Compliance with this standard must be confirmed by external certification [2].

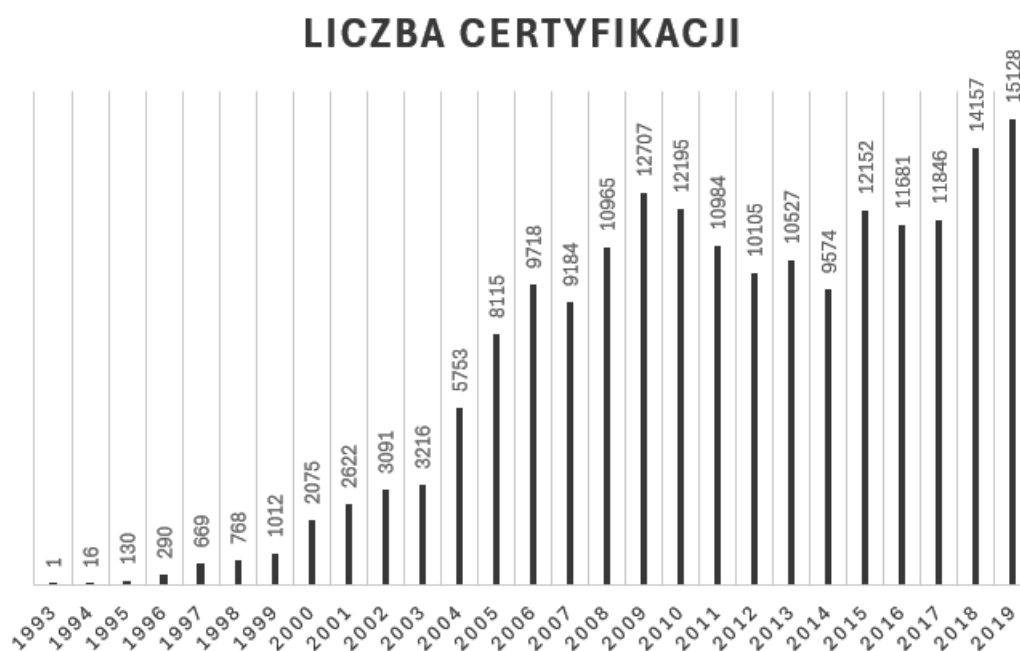


Figure 1 shows the number of ISO 9001 certifications per year [6]

On the basis of the submitted graph concerning the number of ISO 9001 certifications in Poland in the years 1993-2019 can be drawn the following conclusions:

After 2009, the number of certifications shows some stabilization with slight fluctuations. For example, after reaching 12,707 in 2009, the number of certifications fell to 10,527 in 2013, but then rose again, reaching 12,152 in 2015.

The increase in the number of certifications may be related to the growing importance of quality standards in global trade and increased awareness of the benefits of ISO 9001 certification among Polish companies.

## 2.2. ISO 14001:2015

Environmental management system according to PN-EN ISO 14001:2015 aims to protect the environment. It focuses mainly on the reduction of waste, the possibilities and methods of its utilization, the prevention of pollution and the reduction of the use of natural resources. In the context of the transport sector, the scheme aims to reduce emissions. Its idea is to continuously improve environmental protection activities by identifying hazards, assessing risks and encouraging companies to comply with environmental legislation [3].

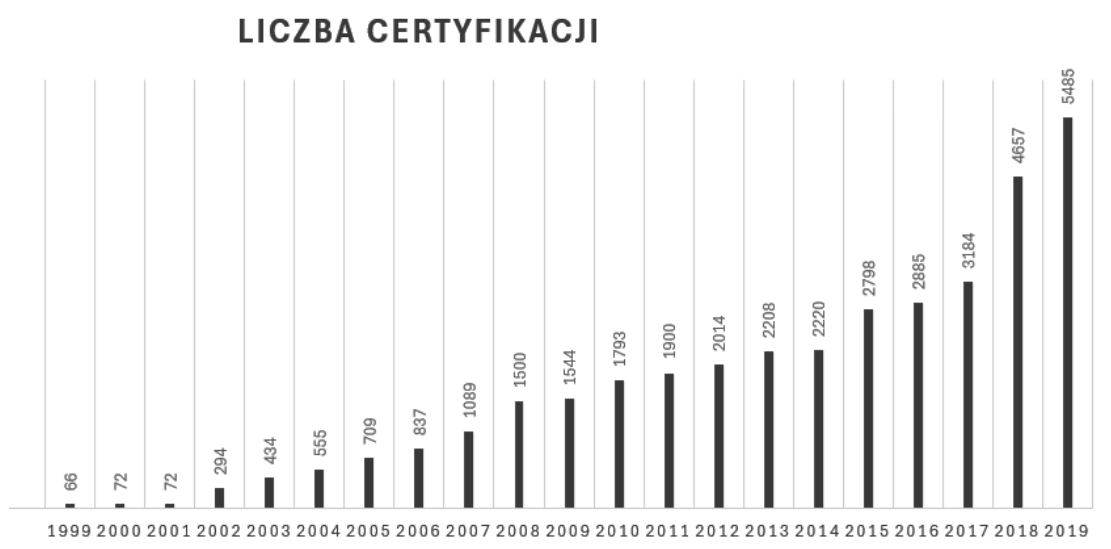


Figure 2 shows the number of ISO14001 certifications per year[6]

Based on the submitted graph of the number of ISO 14001:2015 certifications in Poland in the years 1999-2019, the following conclusions can be drawn:

The number of ISO 14001 certificates in Poland has steadily increased in the years 1999-2019.

Significant increases in recent years from 2015 to 2019 the number of certificates grew rapidly, which may indicate a growing awareness and commitment to environmental management in Poland.

## 2.3. ISO26262

ISO 26262 is a document defining the functional safety of electrical and electronic systems installed in vehicles. According to the concept of functional safety, the design, development, production, operation, servicing and decommissioning processes should be planned and implemented in such a way as to eliminate risks. The main objective is to achieve a state in which the failure of any of the system components would not pose a threat to the safety of persons and the vehicle would remain under control. Risks must be identified and appropriate remedial measures taken, taking into account the Automotive Safety Integrity Level (ASIL) classification. Components classified as ASIL-A have the least impact on the safety of persons [4].

## 2.4. IATF 16949

IATF 16949 is based on ISO 9001 and national automotive quality standards and can be easily integrated with other management system standards. While ISO 9001 focuses on customer satisfaction, IATF 16949 focuses on customer-specific requirements for continuous improvement, defect prevention, and reduction of supply chain volatility and waste. Enables a continuous process to help identify, report and improve management system areas and relevant business processes. This standard applies to any organisation producing components, assemblies, and parts for the automotive industry, covering the entire global supply chain [5].

## 2.5. ISO 22301

ISO 22301 is an international standard for business continuity management that is used in a variety of industries, including the automotive industry. Its aim is to ensure that organisations are prepared for possible business disruptions and can quickly return to normal operations. In the context of the automotive industry, ISO 22301 may be of relevance due to the complexity of the supply chain, quality requirements and product safety[7].

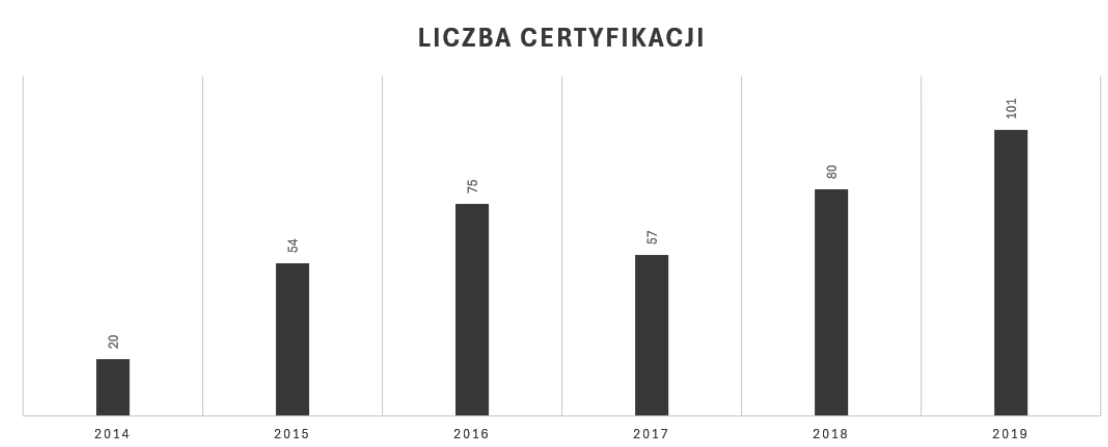


*Figure 3 shows the number of ISO 22301 certifications per year*

Based on the submitted graph of the number of ISO 22301 certifications in Poland in the years 2014-2019 the following conclusions can be drawn:

The increase in the number of ISO 22301 certifications indicates a growing awareness and need for companies to implement business continuity management systems.

The steady growth following a 2017 downturn may suggest that companies have understood the importance of certification and implementing business continuity procedures, which is crucial in the face of a variety of threats, both internal and external.

## 2.6 ISO/IEC 27001

ISO/IEC 27001 is an international information security management standard that is widely used in a variety of industries, including automotive. This standard specifies requirements for

the establishment, implementation, maintenance and continuous improvement of an Information Security Management System (ISMS). The implementation of ISO/IEC 27001 in the automotive industry helps companies effectively manage information security, which is critical in the face of increasing cyber threats and increasing regulatory requirements[8].

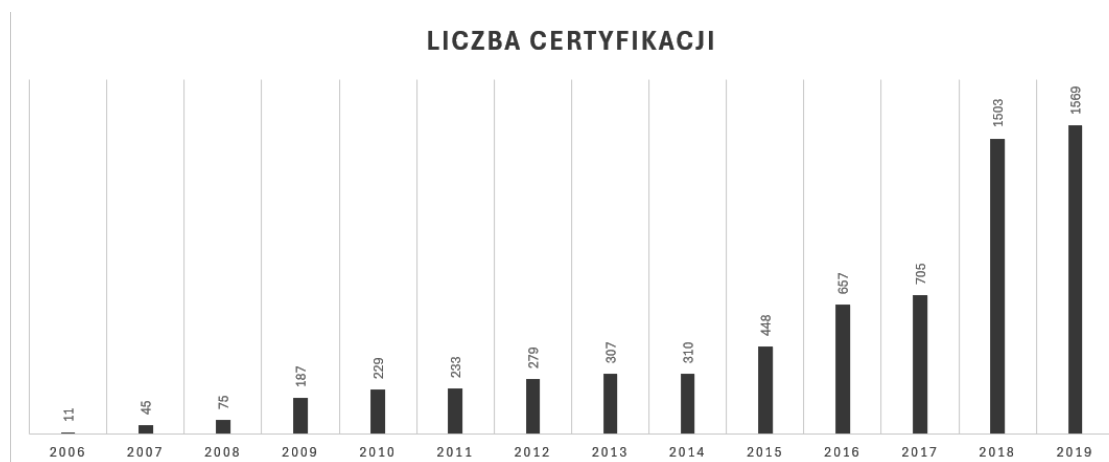


Figure 4 shows the number of ISO/IEC 27001 certifications per year

Based on submitted ISO/IEC 27001 certification number chart in Poland in the years 2006-2019 the following conclusion can be drawn:

The increase in the number of certifications may result from a growing number of cyber threats and legal and regulatory requirements that force organizations to implement information security management systems [8].

### 3. SUMMARY

The automotive industry faces quality, safety and sustainability challenges, requiring the implementation of standards such as ISO 9001:2015, ISO 14001:2015, ISO 26262, IATF 16949, ISO 22301 and ISO/IEC 27001. These standards ensure high quality products and services, increase the safety of vehicle occupants and minimise negative environmental impacts. Compliance with these standards helps companies meet market demands and industry regulations, promoting continuous organizational improvement and risk management in a rapidly changing environment.

### 4. CONCLUSIONS

The implementation of international standards in the automotive industry is key to ensuring high quality products and services, increasing user safety and minimising negative environmental impacts. Standards such as ISO 9001:2015, ISO 14001:2015, ISO 26262, IATF 16949, ISO 22301 and ISO/IEC 27001 promote a modern approach to process management,

enabling companies to effectively manage risk and continuously improve their operations. Adhering to these standards helps businesses meet the demands of the market and industry regulations that are essential to succeed in a rapidly changing environment. The long-term benefits of implementing these standards include increased competitiveness, better reputation and greater customer loyalty, which contributes to the sustainable development and innovation of the automotive sector.

## ACKNOWLEDGEMENTS

The publication was created within the framework of the joint Slovak-Polish project International Visegrad Fund's V4 Generation Mobility Mini-Grant No 12410044 as a result of cooperation between the Association of Alumni of the Silesian University of Technology, Gliwice, Poland and the University of Žilina, Slovakia.

The project is co-financed by the Governments of Czechia, Hungary, Poland and Slovakia through Visegrad Grants from the International Visegrad Fund. The mission of the fund is to advance ideas for sustainable regional cooperation in Central Europe.



## BIBLIOGRAPHY

1. N. Góra, Zintegrowane systemy zarządzania w ujęciu teoretyczno- praktycznym, Management and Quality- Zarządzanie i Jakość, Volume 3, No 2
2. M. Mazurek, System Zarządzania Jakością wg PN EN ISO 9001:2015, www.akademijakosci.com, Kraków, 2020
3. N. Jagodzińska, Wymagania standardu zarządzania środowiskowego ISO 14001 i spodziewane efekty jego wdrażania w przedsiębiorstwach transportowych, Autobusy, Volume 6, s.71, 2019
4. International Standards Organization, "ISO26262 – Road Vehicles Functional Safety" 2018 (ISO 26262:2018)
5. <https://www.dnv.pl/services/iatf-16949-zarzadzanie-jakoscia-w-przemysle-motoryzacyjnym-3284/>
6. The ISO Survey of Management System Standard Certifications – 2019
7. René St-GERMAIN, Faton ALIU, ISO 22301 BEZPIECZEŃSTWO ORGANIZACJI SYSTEMY ZARZĄDZANIA TRWAŁOŚCIĄ BIZNESOWĄ, [https://cts.com.pl/wp-content/uploads/2017/11/whitepaper\\_iso-22301.pdf](https://cts.com.pl/wp-content/uploads/2017/11/whitepaper_iso-22301.pdf)
8. J. Łuczak, M. Tyburski - SYSTEMOWE ZARZĄDZANIE BEZPIECZEŃSTWEM INFORMACJI wgISO/IEC27001,<https://jacekluczak.pl/images/download/Systemowe.pdf>



17th-19th June 2024  
Gliwice, Poland

DEPARTMENT OF ENGINEERING MATERIALS AND BIOMATERIALS  
FACULTY OF MECHANICAL ENGINEERING  
SILESIA UNIVERSITY OF TECHNOLOGY

## INTERNATIONAL STUDENTS SCIENTIFIC CONFERENCE

### Observations of the microstructure of sintered gradient materials using various microscopic methods

Aleksandra Gałaska <sup>a</sup>, Emilia Młoczek <sup>a</sup>, Oleksandra Nikolaieva <sup>a</sup>, Anna Kloc-Ptaszna <sup>b</sup>, Daniel Pakuła <sup>b</sup>, Konrad Adamczyk <sup>c</sup>, Marcin Staszuk <sup>b</sup>

<sup>a</sup> V Liceum Ogólnokształcące im. Andrzeja Struga w Gliwicach, Górnych Wałów 29, Gliwice, Poland

email: ola.galaska10@gmail.com; emilia.mlocek@gmail.com; sasha252924@gmail.com

<sup>b</sup> Silesian University of Technology, Faculty of Mechanical Engineering, Department of Engineering Materials and Biomaterials, Konarskiego 18A, Gliwice, Poland

email: anna.kloc@polsl.pl; daniel.pakuła@polsl.pl; marcin.staszuk@polsl.pl

<sup>c</sup> Capek sp. z o.o., ul. Powstańców Śląskich 236, Skrzyszów, Poland

email: konrad.adamczyk@capek.pl

**Abstract:** The work was carried out with high school students from Andrzej Strug V High School in Gliwice. The purpose of the work was to familiarize the participating students with the methodology of studying the microstructure of engineering materials using various microscopic methods. This article is devoted to analysing the structure of a gradient tool material using two commonly used microscopic techniques: light microscopy and scanning electron microscopy (SEM). The study investigated four-layer specimens, where each successive transition layer, starting from the surface layer, contained a progressively lower volume fraction of the WC carbide reinforcing phase until reaching the final layer of the high-speed steel. On the basis of the analysis of the test results, the gradient structure of the materials was confirmed.

**Keywords:** gradient materials; FGM; light microscopy; scanning electron microscopy (SEM)

## 1. INTRODUCTION

Structural studies by light and electron microscopy in materials engineering are of crucial importance. Their main purpose is the detailed analysis of the microstructure of materials, the identification of phases, the detection and analysis of defects, and the study of interfaces and grain boundaries. These studies allow quality control of materials, optimization of manufacturing processes and design of new materials with desired properties. In addition, they make it possible to understand the mechanisms of corrosion and degradation of materials and

verify theories and models with actual observations. With these techniques, technological innovations are possible, leading to the development of advanced materials and the continued advancement of technology in various industries.

In today's fast-paced industrial environment, continuous improvement of tool materials is essential to improve tool performance and durability in a variety of applications. In this context, the study and understanding of the microscopic structure of tool materials, especially those with a gradient structure, is becoming a key component of the materials engineering process.

Functionally graded materials (FGM) are characterized by a gradual change in properties in a specific direction, resulting from a controlled technological process. This variability in properties can relate to many aspects, such as density, strength, flexibility, or thermal conductivity [1]. Gradient materials can be classified according to various criteria. The most common classification of gradient materials is based on structural criteria, manufacturing methods and application [3-6].

In nature, many examples of materials with graded structures can be found. One of the most well-known examples is bamboo, which has a hard outer wall providing strength, while its inner core is soft and delicate, giving it flexibility. This gradual change in fibre density makes bamboo both lightweight, strong, and flexible.(Fig.1.). Other examples of gradient structures in nature include shells, which consist of layers of different hardness and flexibility, providing them with resistance to fractures. Teeth have hard enamel on the outside and more flexible dentin inside, allowing them to withstand significant mechanical loads. Plant tissues also exhibit varying density and flexibility, helping plants adapt to changing environmental conditions.

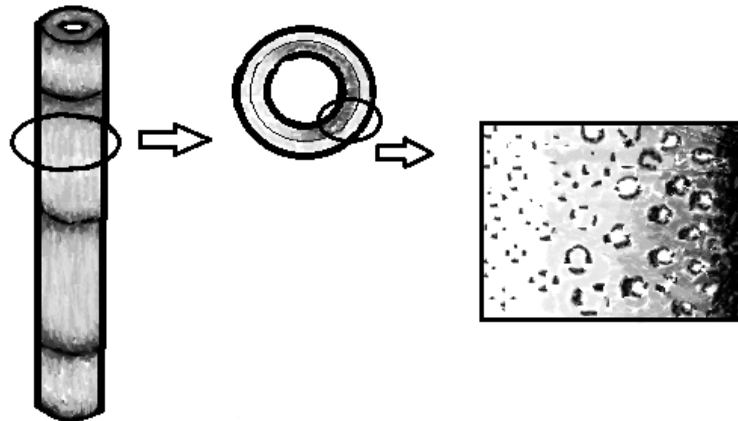


*Fig.1. Diagram of the cross-section of the bamboo internode [2]*

## **2. DESCRIPTION OF THE TEST MATERIAL**

This work focusses on examining the structure of gradient tool materials created using a conventional powder metallurgy process, which involves uniaxial pressing in a closed die followed by sintering. Materials were produced from a mixture of high-speed steel powder and

WC carbide. The study investigated four-layer specimens, where each successive transition layer, starting from the surface layer, contained a progressively lower volume fraction of the WC carbide reinforcing phase until reaching the final layer. A substrate containing only high-speed steel (Fig. 2.).

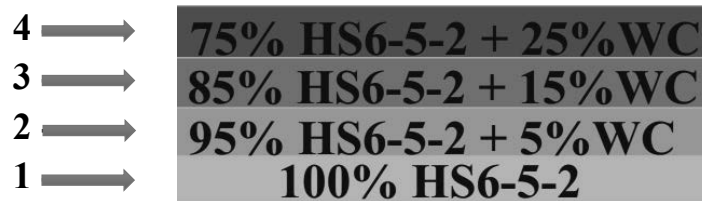


Fig. 2. Schematic of a gradient sample, in which successive transition layers were formed from a surface layer with an increasingly smaller volume proportion of tungsten carbide up to a high-speed steel layer substrate containing only high-speed steel

### 3. RESEARCH PROCESS

Structural studies were performed using a light microscope and a scanning electron microscope.

The first part of the research was conducted on a Supra 25 scanning electron microscope. The secondary electron detector was used with an acceleration voltage of 15 to 20 kV. A range 2000-5000 times magnification was used for the photographs.

The chemical composition of the undigested sample studied was also analysed. The chemical composition of samples can be analyzed using techniques such as energy dispersive X-ray spectroscopy (EDS), often integrated with SEM. This allows the identification and quantitative analysis of the chemical elements present in the sample, which is crucial for understanding material properties and potential applications.

The second part of the research was conducted on an Axio Observer metallographic light microscope (Zeiss). A 200-fold magnification was used. The light microscope, also known as an optical microscope, uses visible light to illuminate the sample and optical lenses to magnify the image. It is commonly used in metallographic studies to analyse the microstructure of metals and alloys. Light microscopes, such as the Axio Observer, enable high-quality imaging at moderate magnifications, which is useful for structural analysis and assessing the surface quality of the sample.

### 4. DISCUSSION OF RESEARCH RESULTS

Photos of the structure of the etched and un-etched sample taken with a scanning electron micrograph are shown in Fig. 3. Photos of the structure of the etched and un-etched sample



taken with the light microscope are shown in Fig. 4. The X-ray energy-dispersive spectrum of the area is shown in Fig. 5.

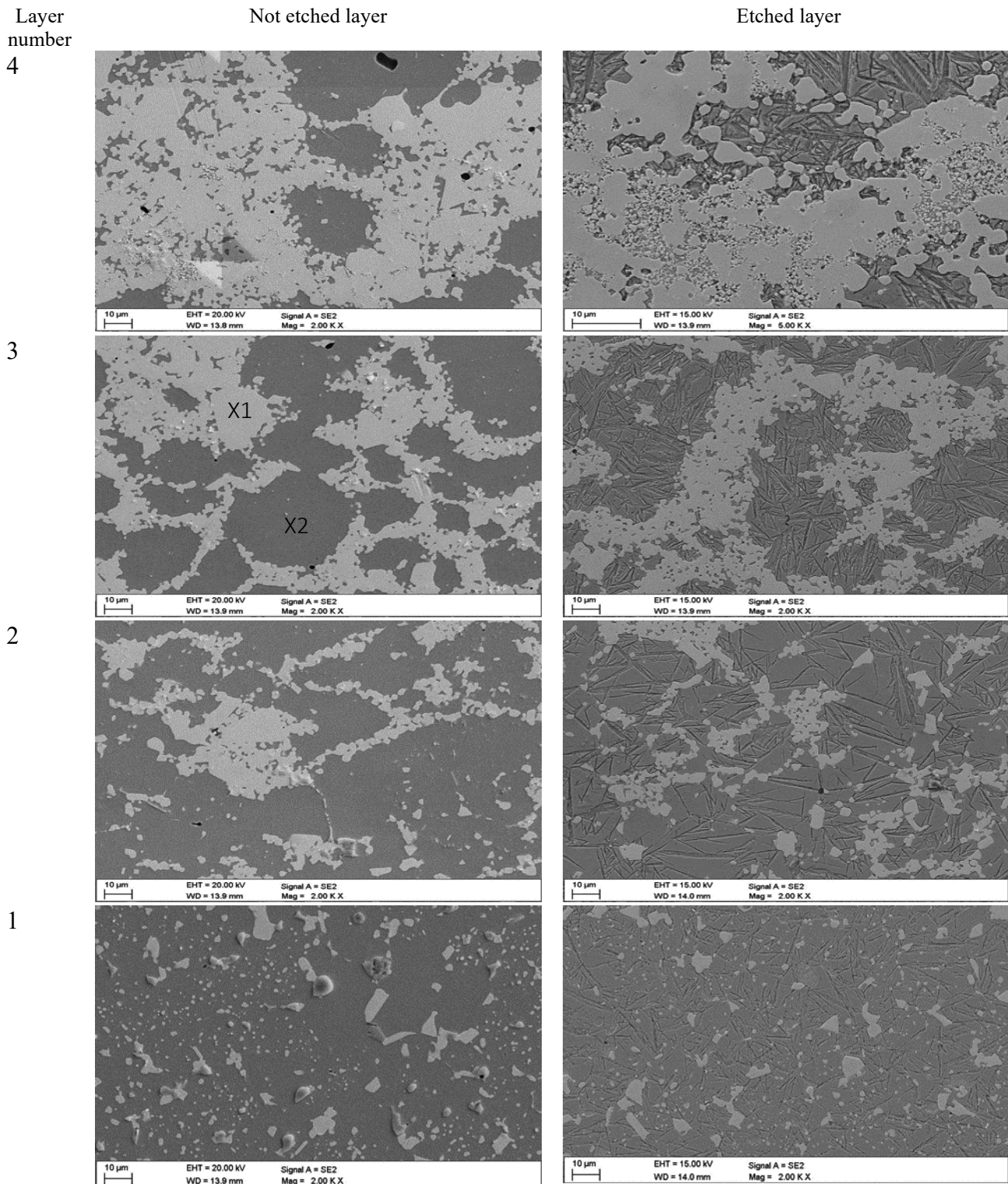


Fig. 3. Images of individual layers from scanning electron microscopy

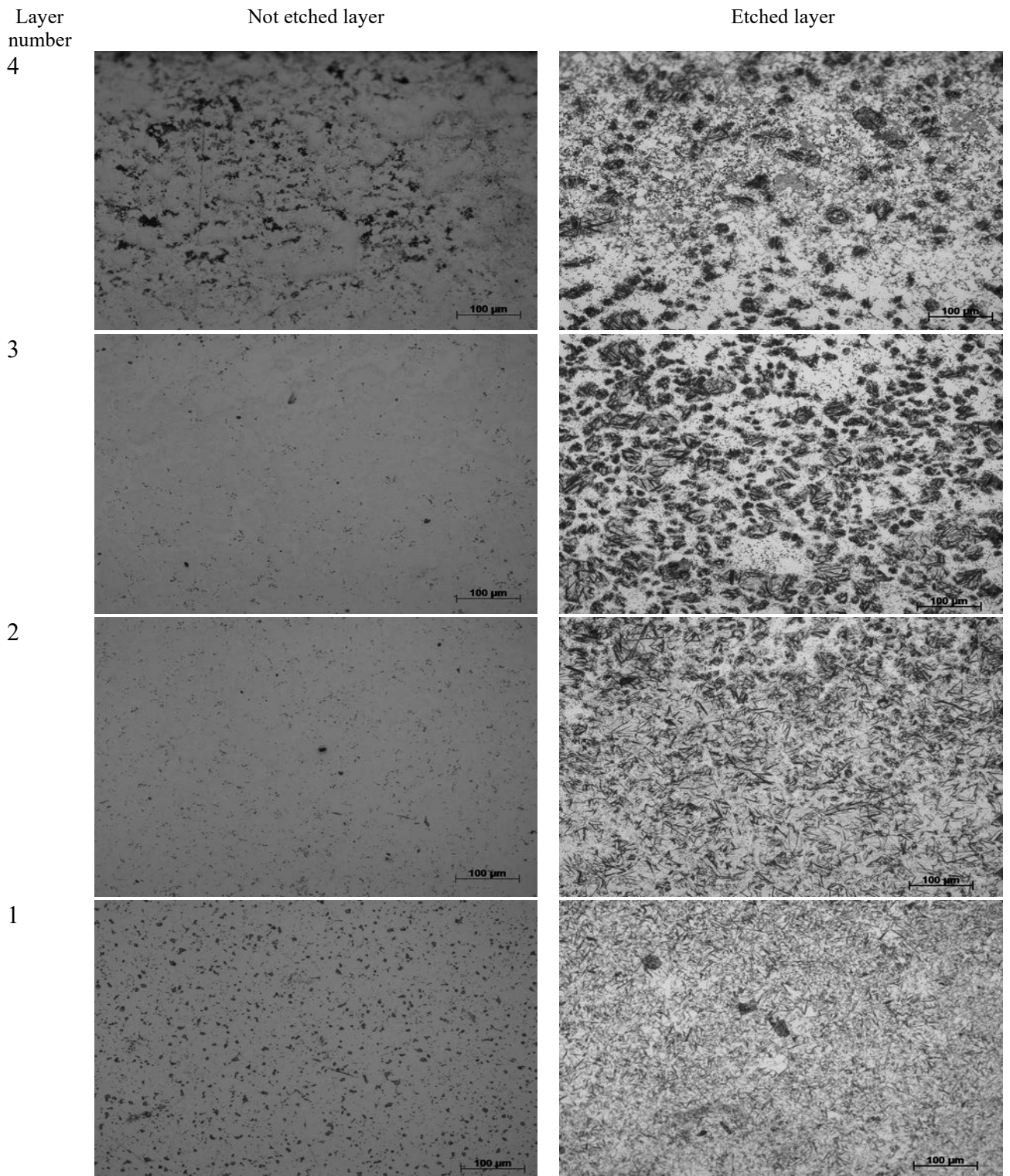


Fig. 4. Images of individual layers from light microscopy

On the basis of the obtained photographs, visible differences between the metallographic light microscope and the scanning electron microscope can be observed. The light microscope is the simplest, producing 2D images with a maximum magnification of 1000 times. It is widely used in metallography to analyze the microstructure of metals and alloys. The images produced by light microscopes, such as the Axio Observer, are high-quality but limited to moderate magnifications, making them useful for structural analysis and surface quality assessment of samples.

However, the electron microscope is sophisticated and advanced equipment that captures realistic 3D images, allowing for a more precise examination of the sample's structure. The maximum magnification of this microscope reaches up to 10 million times, providing an unprecedented level of detail. The scanning electron microscope (SEM), such as the Supra 25 used in this study, uses a beam of electrons to scan the surface of the sample. The secondary electron detector collects signals that create high-resolution images, revealing structural details at the micrometre and submicrometer levels.

On the basis of the analysis of the test results, the gradient structure of the materials was confirmed. It was shown that the developed sintered gradient carbides are characterized by a multiphase structure (Fig. 5.).

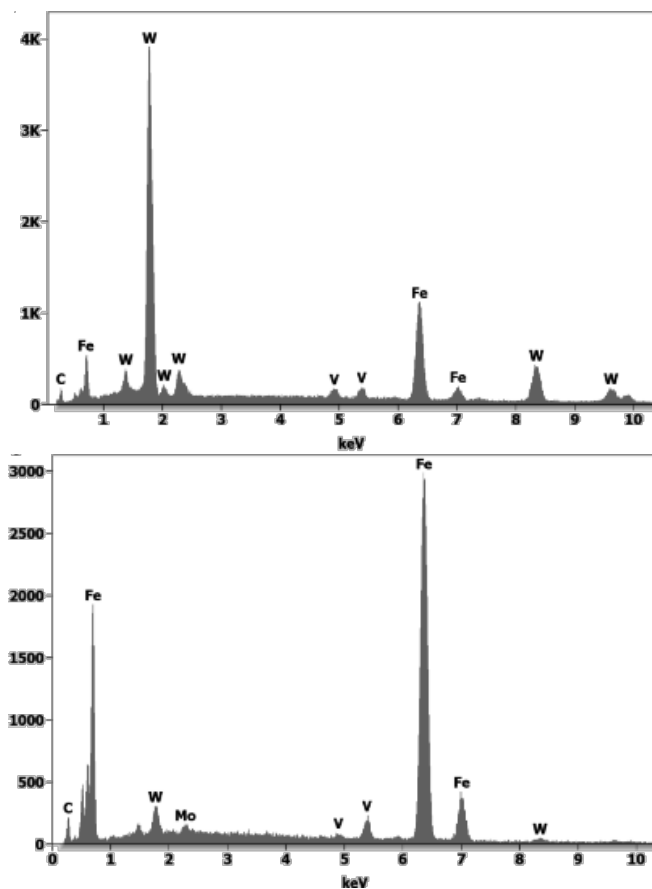


Fig. 5. X-ray energy-dispersive spectrum of the area shown in Fig 1 a) EDS plot of the area X1, b) EDS plot of the area X2

## 5. SUMMARY

Electron microscopes are often preferred to examine samples with high resolution. Unlike light microscopes, electron microscopes use electrons instead of light to create images, allowing for much higher magnification and resolution. This capability is crucial for analysing fine structures and surface features of samples that cannot be resolved with light microscopes.

Additionally, electron microscopes have the capability to analyse the surface composition of materials through techniques such as energy-dispersive X-ray spectroscopy (EDS). This technique is often integrated with SEMs and allows the identification and quantitative analysis of chemical elements present in the sample. This provides valuable information about the elemental composition of the sample, which is essential to understand the material's properties and potential applications.

These features make electron microscopes indispensable tools in various fields of scientific research. In materials science, they are used to study the microstructure and composition of metals, ceramics, and polymers. In biology, electron microscopes allow for the detailed examination of cellular structures, viruses, and tissues. In nanotechnology, they are essential for visualising and characterizing nanomaterials and nanostructures.

The combination of high magnification, resolution, and the ability to perform chemical analysis makes electron microscopes highly versatile and powerful instruments. They provide insights that are not possible with traditional light microscopy, thus playing a critical role in advancing scientific knowledge and technological innovation.

## ACKNOWLEDGEMENTS

This work was produced as part of the project implemented within the framework of project-oriented education - PBL project implemented with secondary school students, in the III competition under the Excellence Initiative - Research University program, at the Silesian University of Technology.

## BIBLIOGRAPHY

1. L.A. Dobrzański, A. Kloc-Ptaszna, M. Pawlyta, W. Pakieła: Fabrication methods and heat treatment conditions effect on structure and properties of the gradient tool materials; Instytut Inżynierii Materiałów i Biomateriałów Politechniki Śląskiej.
2. L.A. Dobrzański, A. Kloc-Ptaszna: Powder metallurgy fundamentals and case studies - rozdział 9: Fabrication, Structure, Properties and Application of Gradient Sintered Carbide-Steels with HS6-5-2 Matrix.
3. Bicz J, Kloc-Ptaszna A. Klasyfikacja funkcjonalnych materiałów gradientowych ze względu na materiały składowe, stan skupienia w trakcie przetwarzania oraz strukturę

- wewnętrzna. W: Bonek M, redaktor. TalentDetector2023\_Summer : International Students Scientific Conference, Brenna, Poland, 26th June 2023. 2023. p. 83–90.
4. Bicz J, Kloc-Ptaszna A. Klasyfikacja funkcjonalnych materiałów gradientowych ze względu na rodzaj, wielkość oraz rozkład gradientu. W: Bonek M, redaktor. TalentDetector2023\_Summer : International Students Scientific Conference, Brenna, Poland, 26th June 2023. 2023. p. 75–82.
  5. Polis J, Kloc-Ptaszna A. Klasyfikacja funkcjonalnych materiałów gradientowych ze względu na ich zastosowanie. W: Bonek M, redaktor. TalentDetector2023\_Summer : International Students Scientific Conference, Brenna, Poland, 26th June 2023. 2023. p. 542–547.
  6. Polis J, Kloc-Ptaszna A. Klasyfikacja funkcjonalnych materiałów gradientowych ze względu na wartość naprężeń szczątkowych oraz stopień kontroli gradientu. W: Bonek M, redaktor. TalentDetector2023\_Summer : International Students Scientific Conference, Brenna, Poland, 26th June 2023. 2023. p. 537–541.



17th-19th June 2024  
Gliwice, Poland

DEPARTMENT OF ENGINEERING MATERIALS AND BIOMATERIALS  
FACULTY OF MECHANICAL ENGINEERING  
SILESIA UNIVERSITY OF TECHNOLOGY

## INTERNATIONAL STUDENTS SCIENTIFIC CONFERENCE

### Kompozyty polimerowe modyfikowane nanorurkami haloizytowymi

Michał Głogowski<sup>a</sup>, Julia Pindur<sup>a</sup>, Karolina Romberg<sup>a</sup>, Klaudiusz Gołombek<sup>b</sup>, Mateusz Lis<sup>b</sup>

<sup>a</sup> IV Liceum Ogólnokształcące im. Bolesława Chrobrego w Bytomiu

<sup>b</sup> Politechnika Śląska, Wydział Mechaniczny Technologiczny, Laboratorium Badania Materiałów

email: klaudiusz.golombek@polsl.pl

email: mateusz.lis@polsl.pl

**Streszczenie:** W pracy przedstawiono wyniki badań oraz dokonano analizy wpływu napełniacza glinokrzemianowego – nanorurek haloizytowych na właściwości i strukturę kompozytów opartych na osnowie żywicy epoksydowej lub biodegradowalnego polimeru – polikaprolaktonu.

**Abstract:** In this study, the effect of aluminosilicate filler - halloysite nanotubes on the properties and structure of composites based on epoxy resin matrix or biodegradable polymer - polycaprolactone was investigated and analysed.

**Słowa kluczowe:** kompozyty, PCL, haloizyt, SEM

#### 1. WSTĘP

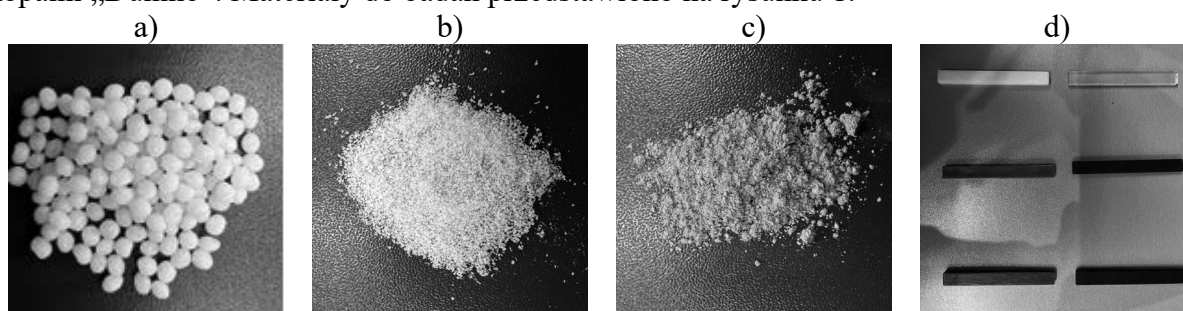
Dyamiczny rozwój techniki sprawia, że ciągle wzrasta zapotrzebowanie przemysłu na nowe materiały konstrukcyjne, które powinny charakteryzować się coraz to lepszymi właściwościami użytkowymi oraz trwałością, przy zachowaniu możliwie jak najmniejszej masy. Materiały kompozytowe o osnowie polimerowej wzmacniane cząstkami ceramicznymi mogą stać się odpowiedzią na to zapotrzebowanie. Dzięki zastosowaniu polimerów, jako materiału osnowy kompozytów, można uzyskać takie pożądane właściwości gotowych produktów, jak niską masę, zdolność tłumienia drgań, odporność na korozję, łatwość kształtowania oraz izolacyjność cieplną i elektryczną [1, 2]. Do surowców mineralnych, które ze względu na szerokie rozpowszechnienie w naturze są powszechnie wykorzystywane jako wypełnienie kompozytów zaliczyć można glinokrzemiany, takie jak haloizyt. Haloizyt to minerał o wzorze  $\text{Al}_2\text{Si}_2\text{O}_5(\text{OH})_4$ , charakteryzujący się budową warstwowo-rurkową, zbudowany jest z dwuwarstwowych pakietów o typie budowy 1:1 (z tetraedrycznej warstwy tlenku krzemu oraz oktaedrycznej warstwy uwodnionego tlenku glinu). Charakteryzuje się on również dużą powierzchnią właściwą, jonowymiennością oraz porowatością [3-5].

Celem badań było opracowanie i wytworzenie kompozytów polimerowych opartych na osnowie żywicy epoksydowej i biodegradowalnego polimeru – polikaprolaktonu oraz napełniacza mineralnego - nanorurek haloizytowych.

## 2. MATERIAŁ I METODYKA BADAŃ

### Materiał do badań

Do wytworzenia kompozytów polimerowo-ceramicznych wykorzystano jako osnowę epoksydową żywicę typu L + utwardzacz EPH 161, charakteryzującą się niskim napięciem powierzchniowym, dobrą adhezją i minimalnym skurczem i granulaty polikaprolaktonu (PCL), a jako napełniacz zastosowano modyfikowany haloizyt o granulacji poniżej 45 µm pochodzący z kopalni „Dunino”. Materiały do badań przedstawiono na rysunku 1.



Rys. 1. Materiały: a, b) granulaty PCL; c) surowy haloizyt; d) próbki do badań  
 Figure 1. Materials: a, b) PCL pellets; c) raw halloysite; d) samples for testing

W pierwszym etapie prac wysuszono polimer oraz proszek haloizytu w suszarce w temperaturze 50°C w celu usunięcia wilgoci, a żywicę połączono z utwardzaczem w proporcji wagowej 100:25 – żywica do utwardzacza. Następnie odważono składniki za pomocą wagi laboratoryjnej firmy Radwag i wykonano mieszaniny proszku haloizytu z żywicą lub PCL. (tablica 1).

Tablica 1. Oznaczenie próbek  
 Table 1. Sample designations

Oznaczenie	Osnowa	Zawartość haloizytu [%]
PCL0	PCL	0
PCL5		5
PCL10		10
Epox0	Żywica epoksydowa	0
Epox5		5
Epox10		10

W ramach pracy wykonano następujące badania:

- dobrano optymalny polimer jako osnowę, ze względu na zastosowanie – żywica chemoutwardzalna oraz biodegradowalny polikaprolakton PCL,
- dobrano udział masowy napełniacza glinokrzemianowego – haloizytu - w żywicy chemoutwardzalnej i PCL i przygotowano mieszaniny,

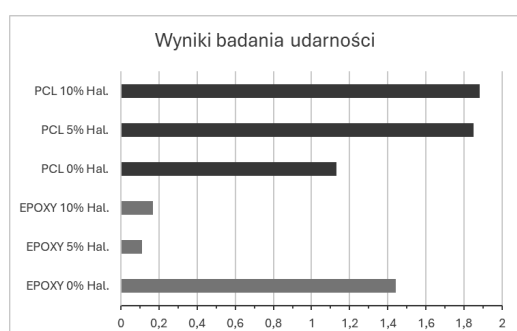
- wytworzono kompozyty polimerowe modyfikowane haloizytem metodą zalewania,
- zbadano strukturę z wykorzystaniem wysokorozdzielczego skaningowego mikroskopu elektronowego i mikroskopu świetlnego, wykonano analizy spektralne z wykorzystaniem detektora energii rozproszonego promieniowania rentgenowskiego,
- zbadano podstawowe własności fizyczne i mechaniczne – gęstość, porowatość, wytrzymałość na rozciąganie, udarność.

Badania udarności (pracy łamania) wykonano za pomocą młota wahadłowego typu Charpy o energii początkowej wynoszącej 5J. Badania wytrzymałości na rozciąganie kompozytów wykonano zgodnie z normą PN EN ISO 527-1 na maszynie wytrzymałościowej Zwick/Roell Z020. Wykonano po trzy pomiary udarności oraz wytrzymałości na rozciąganie dla każdej z próbek bez napełniacza oraz z napełniaczem haloizytowym.

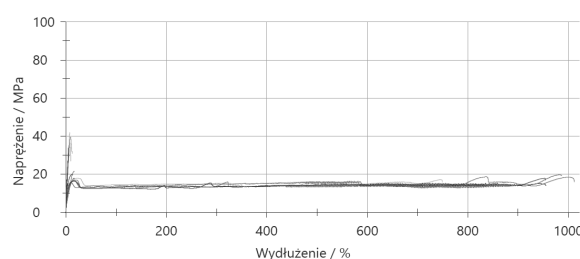
Obserwację struktury próbek wykonano wykorzystując mikroskop stereoskopowy ZEISS, model SteREO Discovery.V12, przy powiększeniu 10x-45x oraz w wysokorozdzielczym skaningowym mikroskopie elektronowym ZEISS SUPRA 35 wyposażonym w detektor EDS. Przed przystąpieniem do badań w SEM na powierzchnię nieprzewodzących próbek napyłano cienką przewodzącą powłokę ze złota w napyłarce próżniowej Bal-Tec SCD 050.

### 3. WYNIKI BADAŃ

Na rysunku 2 przedstawiono wyniki badań udarności, a na rysunku 3 i w tabelicy 2 wyniki wytrzymałości na rozciąganie.



Rys. 2. Wyniki badań udarności  
Figure 2. Results of the impact tests



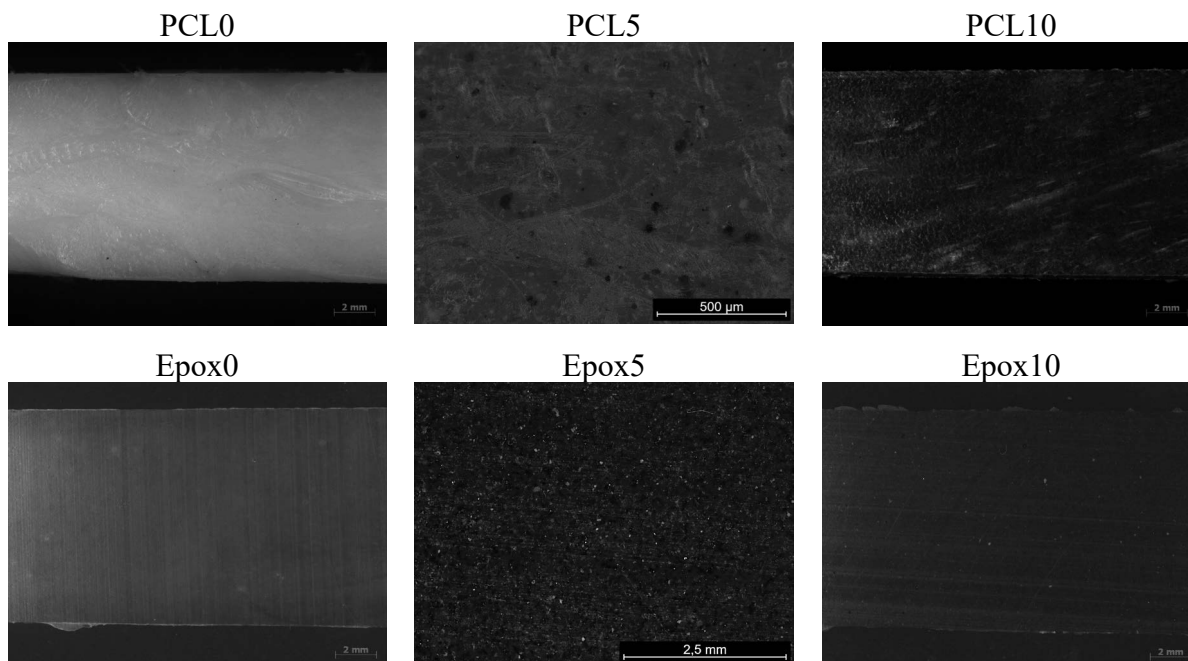
Rys. 3. Wyniki badań wytrzymałości na rozciąganie  
Figure 3. Results of tensile strength tests

Tablica 2. Średnie wyniki badań własności na rozciąganie badanych próbek  
Table 2. Average results of tensile strength of tested specimens

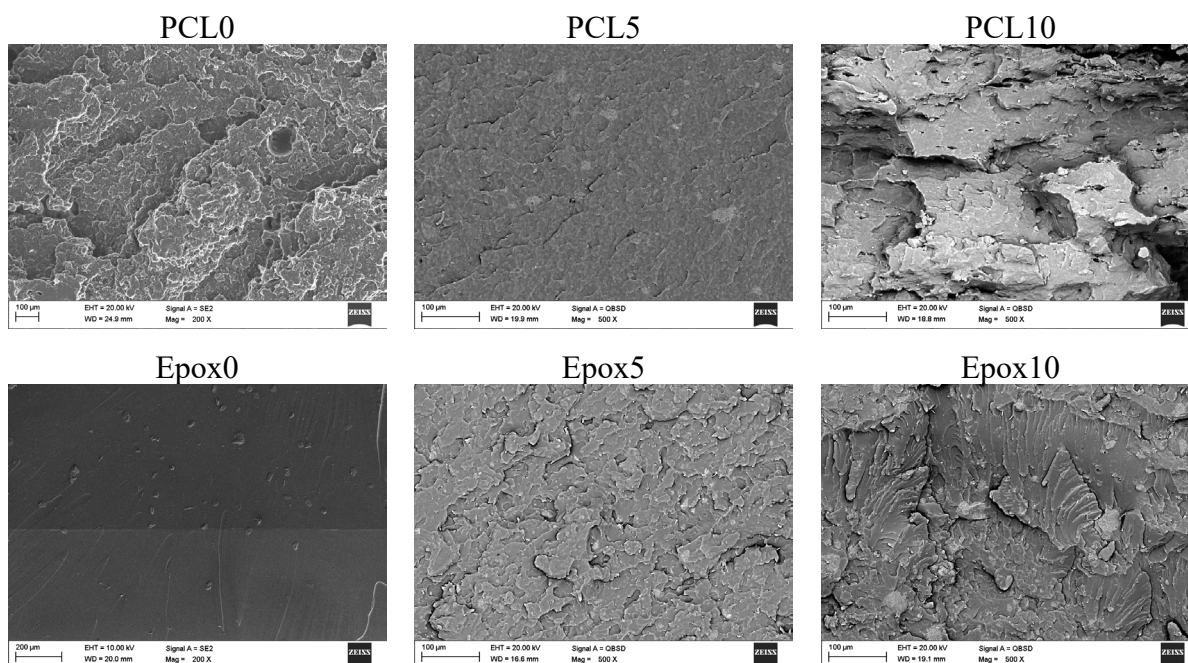
Próbka	Wytrzymałość na rozciąganie [MPa]
PCL0	16
PCL5	19
PCL10	17
Epoxy0	33
Epoxy5	39
Epoxy10	37



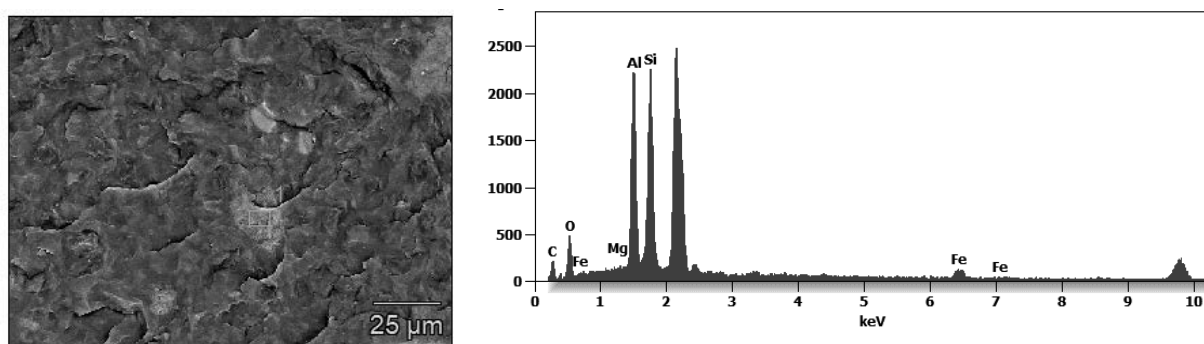
Badania struktury przelomów po próbie udarności i wytrzymałości na rozciąganie wykonano na mikroskopie stereoskopowym i w SEM. Mikrostruktury badanych kompozytów przedstawiono na rysunkach 4 i 5, a analizy składu chemicznego EDS na rys. 6, 7.



Rys. 4. Powierzchnia przelomu badanych próbek, mikroskop stereoskopowy  
*Figure 4. Fracture surface of tested specimens, stereoscopic microscope*



Rys. 5. Powierzchnia przelomu badanych próbek, SEM  
*Figure 5. Fracture surface of tested specimens, SEM*



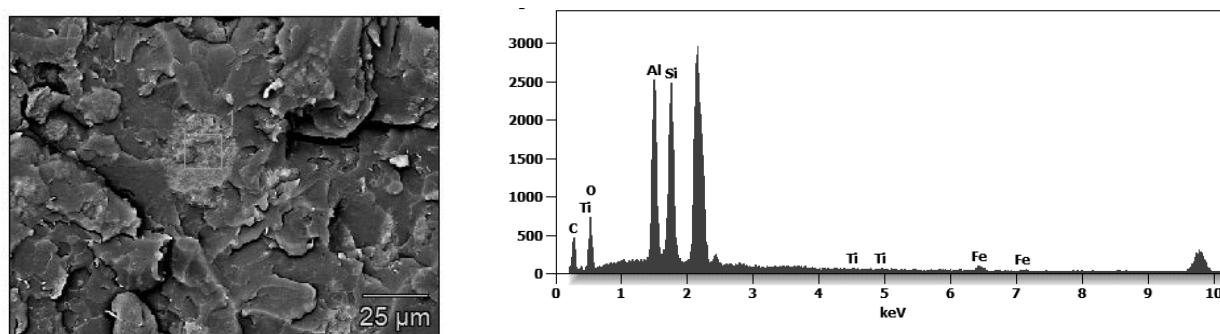
Masowo %

	<i>C</i>	<i>O</i>	<i>Mg</i>	<i>Al</i>	<i>Si</i>	<i>Fe</i>
<i>Obszar 1</i>	17.4	19.7	0.1	22.4	33.9	6.6

Atomowo %

	<i>C</i>	<i>O</i>	<i>Mg</i>	<i>Al</i>	<i>Si</i>	<i>Fe</i>
<i>Obszar 1</i>	29.9	25.4	0.1	17.2	24.9	2.4

Rys. 6. Wyniki analizy EDS z zaznaczonego obszaru dla próbki PCL5  
 Figure 6. Results of the EDS analysis from the marked area of specimen PCL5



Masowo %

	<i>C</i>	<i>O</i>	<i>Al</i>	<i>Si</i>	<i>Ti</i>	<i>Fe</i>
<i>Obszar 1</i>	25.7	24.2	18.7	28.7	0.2	2.6

Atomowo %

	<i>C</i>	<i>O</i>	<i>Al</i>	<i>Si</i>	<i>Ti</i>	<i>Fe</i>
<i>Obszar 1</i>	39.5	27.9	12.8	18.9	0.1	0.9

Rys. 7. Wyniki analizy EDS z zaznaczonego obszaru dla próbki Epox10  
 Figure 7. Results of the EDS analysis from the marked area of specimen Epox10

#### 4. PODSUMOWANIE I WNIOSKI

W ramach badań dokonano oceny wpływu haloizytu, o udziale masowym 5% i 10% na strukturę i własności wytrzymałościowe kompozytu o osnowie z żywicy epoksydowej lub polikaprolaktonu. Na podstawie badań gęstości stwierdzono, że polikaprolakton - PCL charakteryzuje się gęstością wynoszącą  $1,16 \text{ g/cm}^3$ , natomiast glinokrzemian w postaci nanorurek haloizytowych wykazuje gęstość równą  $2,73 \text{ g/cm}^3$ . Kompozyty modyfikowane

nanorurkami haloizytowymi, zarówno gdy osnową jest polikaprolakton, jak i żywica epoksydowa, wykazują wyższą wytrzymałość na rozciąganie, a w przypadku próbek PCL+H również wzrost udarności w porównaniu do kompozytów bez cząstek ceramicznych. W badaniach mikroskopowych LM i SEM materiałów kompozytowych potwierdzono równomierną w całej objętości obecność haloizytu i dobrą homogenizację tego napełniacza z PCL i żywicą jako osnową.

Na podstawie otrzymanych wyników badań można stwierdzić, że kompozyty polimerowe wzmocnione cząstkami ceramicznymi – nanorurkami haloizytowymi mogą mieć szerokie zastosowanie dzięki takim własnościom, jak: niska masa, gęstość, łatwość kształtowania i przede wszystkim możliwość recyklingu.

## PODZIĘKOWANE

Badania wykonano w ramach II edycji projektów badawczych zorientowanych projektowo – PBL (Project Base Learning), realizowanych na Politechnice Śląskiej z uczniami szkół ponadpodstawowych w programie Inicjatywa Doskonałości – Uczelnia Badawcza.

## LITERATURA

1. M. Madej, D. Ozimina, A. Wdowin, Tworzywa sztuczne i materiały kompozytowe, Politechnika Świętokrzyska, Kielce, 2010.
2. W. Królikowski, Polimerowe kompozyty konstrukcyjne, Wydawnictwo Naukowe PWN, Warszawa, 2012
3. E. Joussein and B. Delvaux, Halloysite clay minerals - A review, Clay Minerals, no. 40, (2005) 383-426.
4. P. Yuan, D. Tan and F. Annabi-Bergaya, Properties and applications of halloysite nanotubes: recent research advances and future prospects, Applied Clay Science, vols. 112-113 (2015) 75-93.
5. J. Matusik, „Naturalne i syntetyczne minerały o budowie warstwowej w nanotechnologiach”, Wydawnictwo AGH, Kraków, 2017.
6. M. Lis, J. Mścichecka, P. Sakiewicz, K. Gołombek, Wpływ silanizacji haloizytu na mikrostrukturę kompozytów na osnowie polietylenu, Konferencja Studenckich Kół Naukowych: TalentDetector’2018, t. 5, M. Bonek, Red. 2018, 28.
7. P. Sakiewicz, R. Nowosielski, W. Pilarczyk, K. Gołombek, M. Lutyński, Selected properties of the halloysite as a component of Geosynthetic Clay Liners (GCL), Journal of Achievements of Materials and Manufacturing Engineering, t. 48, nr 2 (2011) 177–191.



17th-19th June 2024  
Gliwice, Poland

DEPARTMENT OF ENGINEERING MATERIALS AND BIOMATERIALS  
FACULTY OF MECHANICAL ENGINEERING  
SILESIA UNIVERSITY OF TECHNOLOGY

## INTERNATIONAL STUDENTS SCIENTIFIC CONFERENCE

### The properties of glass fiber polymer composites

Magdalena Gorlicka<sup>a</sup>, Magdalena Polok-Rubinić<sup>b</sup>

<sup>a</sup> Students of Materials Engineering and Technologies, Faculty of Mechanical Engineering

<sup>b</sup> Silesian University of Technology, Faculty of Mechanical Engineering, Department of Engineering Materials and Biomaterials, email: magdalena.polok-rubinić@polsl.pl

**Abstract:** The article presents the results of impact tests and observations of the structure of a polyethylene-polypropylene blend reinforced with glass fiber 0.1 to 1 mm long. The impact strength test was performed on samples without notches at a load of 5J at room temperature and after immersion in liquid nitrogen. It was found that the tested composite was not damaged during the impact test at room temperature, but the samples broke during the test performed at a lower temperature. At room temperature, the tested composite is characterized by high flexibility. As a result of observing the structure of fractures after impact testing in liquid nitrogen, an uneven distribution of glass fibers in the polyethylene-polypropylene matrix was noticed.

**Keywords:** Polypropylene, polyethylene, glass fiber, impact test, structure

### 1. INTRODUCTION

The dynamic development of materials engineering, as well as the continuous development of the industry and the increase in interest in polymer materials towards new applications, necessitates research on improving the properties of materials through their modification. Composites based on polymeric materials with the addition of fillers in the form of powders, fibers and nanoadditives are becoming increasingly important among construction materials. The most commonly used powder fillers are: powdered mica, quartz sand, chalk, quartz flour, kaolin, graphite, dolomite flour, mica. Commonly used nanoadditives in polymer composites are silver nanoparticles and soot nanoparticles, as well as allotropic varieties of carbon - carbon nanotubes, graphene. The most commonly used fibers include carbon, glass and ceramic fibers. In recent years, carbon fillers have also been successfully used. Active fillers in the polymer matrix improve mechanical, tribological, rheological, thermal, dielectric, chemical and processing properties.

In recent years, in addition to the widely used carbon, aramid and ceramic fibers, glass fibers have become particularly important. These are one of the earliest fibers created, appearing on the market in 1931. Initially, they were used as reinforcement for mortar and concrete, and then as reinforcement for larger structures. Compared to the most famous carbon fibers, they are characterized by a greater ability to absorb energy and a lower price. Due to these properties,

they are mainly used in the automotive and construction industries. The continuous expansion of the applications of glass fiber on the industrial market is reflected in the upward trend in its production. In the years 2012-2019, the total global production of glass fiber increased from 5.3 million tons to 8 million tons, and the increasingly new possibilities of the processing industry and new market.

Scientific research presented in the literature has shown that the addition of glass fiber to the polypropylene matrix significantly improves its strength properties. The tensile strength of pure PP was 26.7 MPa, while the strength of the polypropylene composite with 30% glass fiber increased to 35.6 MPa. This is due to the high tensile strength of glass fibers, which therefore act as a reinforcer of the polypropylene composite (1700-2500 MPa). This material is used to produce prefabricated elements such as bars, sleeves and plates [1-4].

## 1. MATERIALS AND METHODOLOGY

The tests were carried out on samples in the form of type 1A paddles (in accordance with the ISO 527-2:2012 standards [5]) made of a polymer composite consisting of 85% by weight of polyethylene and 15% by weight of polypropylene granules with the addition of PP/GF glass fiber. (PE-PP/GF 85-15), in a proportion of 60/40%. Glass fiber with a length of 0.1 to 1 mm was used.

The impact strength of the polymer composites was tested at a load of 5J on samples without notches at room temperature and, for comparison, after immersion in liquid nitrogen. The test was performed on a 25P device from Zwick/Roell using the Charpy method in accordance with the PN-EN ISO 179-1:2010 standard [6].

The structure of fractures formed after the impact test were observed on a Zeiss SteREO Discovery.V12 stereoscopic microscope. and on a Leica DVM6 light microscope.

## 2. RESULTS

The samples made of the PE-PP/GF 85-15 composite were not damaged during the impact test at room temperature, and the test was then performed on samples immersed in liquid nitrogen. An impact strength of 2.99 J/cm<sup>2</sup> was obtained for the tested PE-PP/GF 85-15 composite. According to literature data, samples made of pure polyethylene did not break during the impact test at room temperature, while polypropylene samples tested under the same conditions did break [7]. The impact strength of polypropylene (3 J/cm<sup>2</sup>) is similar to the impact strength of the tested PE-PP/GF 85-15 composite (2.99 J/cm<sup>2</sup>) at reduced temperature. It can be concluded based on research and literature data that the addition of PP to PE and the presence of glass fibers did not strengthen the composite sufficiently [7].

Observations of the structure of fractures after impact tests in liquid nitrogen showed uneven distribution of glass fibers (Fig. 1a-d) in the polyethylene-polypropylene matrix. Larger fiber clusters were noticed (Fig. 1b,c) closer to the center of the sample than at the periphery. Dispersed glass fibers in the matrix of different lengths were also found and were partially broken (Fig. 2 a,b).

In the tested composites, the occurrence of regular holes was also observed (Fig. 1 c), which are remnants of fibers torn out from the matrix when samples were broken at a reduced temperature (Fig.1d). This phenomenon proves poor adhesion between the polymer matrix and

the fiber. Degradation of the structure of the tested polymer composite may be caused by the following changes in the structure: debonding, cracks in glass fibers and polymer matrix, or delamination [8].

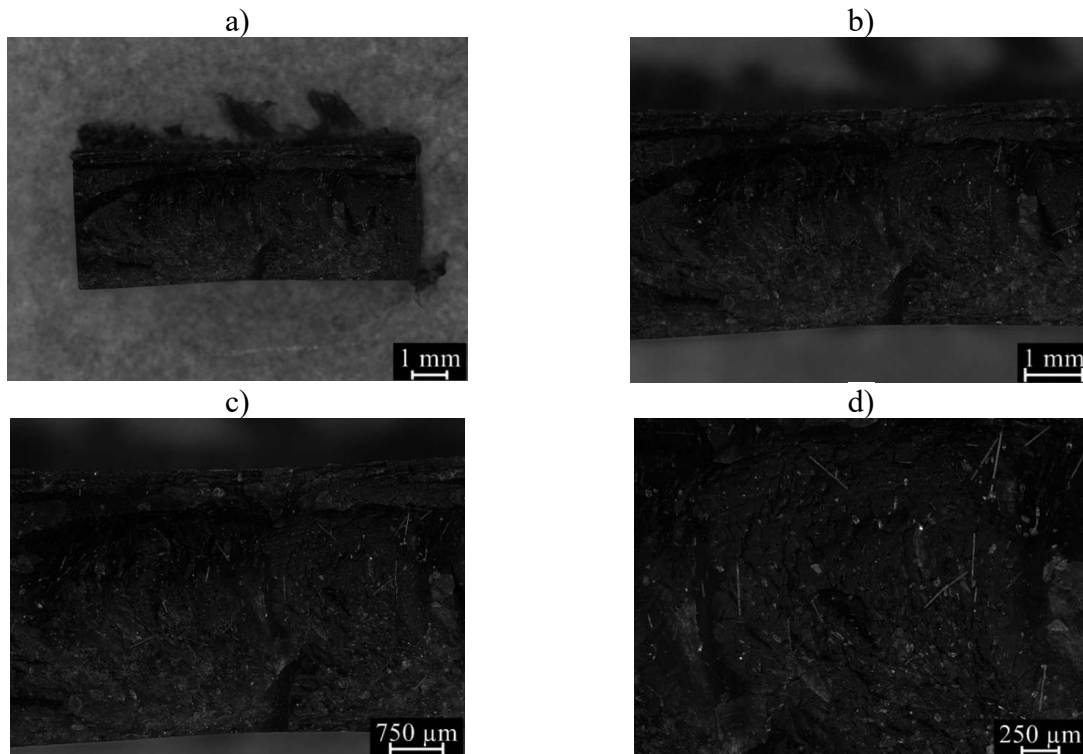


Figure 1. The structures of fractures of a mixture of 85% PE and 15% PP granules with 40% glass fiber content, made on a light microscope at magnifications: a) 16x, b) 27x, c) 34, d) 72x.

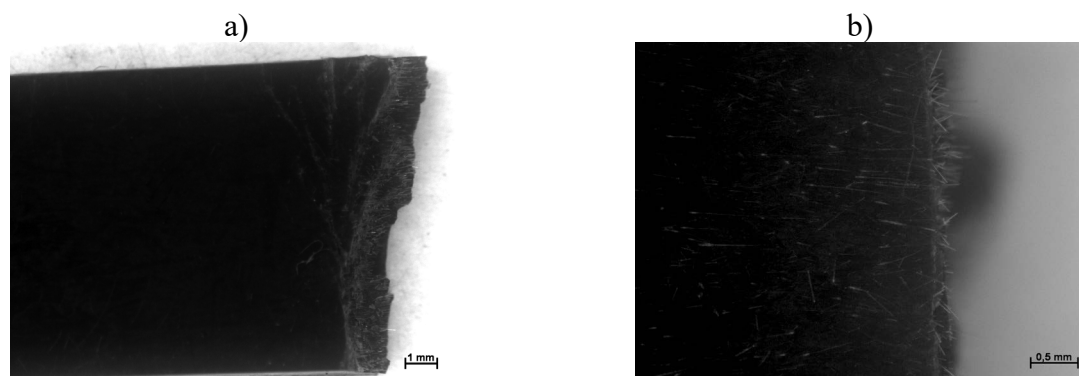


Figure 2. The structures of fractures of a mixture of 85% PE and 15% PP granules with 40% glass fiber content made on a stereoscopic microscope at magnification: a) 20x, e) 30x.

### 3. SUMMARY

The impact strength of the polyethylene-polypropylene composite with the addition of glass fiber is  $2.99 \text{ J/cm}^2$  after immersion in liquid nitrogen. Lowering the temperature causes the

polymer to lose its plastic properties and it is destroyed during the impact test, but it does not break at room temperature. Microscopic observations showed uneven distribution of glass fibers in the polymer matrix, characterized by different lengths at the fractures formed after impact testing in liquid nitrogen. There were also numerous holes resulting from torn fibers during the impact test, which is the result of poor adhesion between the fiber and the polymer.

## BIBLIOGRAPHY

1. T. Klepka (Ed.), Modern polymer materials and their processing, chap. 1, Lublin University of Technology, Lublin, (2014), 26-28, in polish
2. A. Boczkowska, G. Grzesiński, The composites and their production techniques, OWPW, Warsaw, (2016), 50-56, in polish
3. W.N. Ota, S.C. Amico, K.G. Satyanarayana, Studies on the combined effect of injection temperature and fiber content on the properties of polypropylene-glass fiber composites, Composites Science and Technology 65 (2004), 873-881
4. T. Sathishkumar, Satheeshkumar, J. Naveen, Glass fiber-reinforced polymer composites - a review, Journal of Reinforced Plastics and Composites, (2014), 1258-1275
5. PN-EN ISO 179-1:2010 Plastics - Determination of Charpy impact properties - Part Non-instrumented impact test
6. PN-EN ISO 527-1:2012 Plastics - Determination of tensile properties - Part 1: General principles
7. <https://www.plastem.pl/oferta/tworzywa-sztuczne/polietylen-pe>
8. <https://www.kipp.pl/pl/pl/Serwis/Przegl%C4%85dsurowc%C3%B3w/Thermoplast/Polyporylen.html>



17th-19th June 2024  
Gliwice, Poland

DEPARTMENT OF ENGINEERING MATERIALS AND BIOMATERIALS  
FACULTY OF MECHANICAL ENGINEERING  
SILESIA UNIVERSITY OF TECHNOLOGY

## INTERNATIONAL STUDENTS SCIENTIFIC CONFERENCE

### Comparison of the structure of PVD+ALD hybrid coatings applied to austenitic stainless steel

Karolina Grzesikiewicz<sup>a</sup>, Lena Trzewiczek<sup>a</sup>, Agata Zarzycka<sup>a</sup>, Marcin Staszuk<sup>b</sup>, Daniel Pakuła<sup>b</sup>

<sup>a</sup> Students of the 5<sup>th</sup> High School named after Andrzej Struga in Gliwice

<sup>b</sup> Silesian University of Technology, Faculty of Mechanical Engineering, Department of Engineering Materials and Biomaterials,  
email: marcin.staszuk@polsl.pl, daniel.pakula@polsl.pl

**Abstract:** The article was written as part of a PBL project (3<sup>rd</sup> edition) carried out with high school students entitled: "Electron microscopy? What is it for? Applications of microscopy in surface engineering." The purpose of this study was to investigate the structure of CrN+Cr<sub>2</sub>O<sub>3</sub>/TiO<sub>2</sub> and TiN/ZnO hybrid coatings deposited by physical vapour deposition (PVD) and atomic layer deposition (ALD) methods on 316L austenitic steel. The morphology of the coatings was studied using scanning electron microscopy (SEM) and atomic force microscopy (AFM) as well as chemical composition analysis using an X-ray energy dispersive spectrometer (EDS).

**Keywords:** SEM, AFM, PVD, ALD, Hybrid coatings

## 1. INTRODUCTION

For many years, 316L austenitic steel has been widely used in various industries and biomedical applications due to its excellent mechanical properties and corrosion resistance, which result from the presence of elements such as chromium and nickel. Because of its low manufacturing costs, 316L steel is widely used in biomedicine, for example, in bone screws and plates, or joint prostheses. However, the nickel contained in it can be released into the patient's body as a result of corrosion in the tissue environment, causing allergic reactions. To prevent this drawback, appropriate surface treatment is applied. The application of biocompatible coatings improves corrosion resistance and ensures osteointegrative or antibacterial properties, without deteriorating the mechanical properties of the coated material. Coatings with such properties can be produced, among others, by physical vapour deposition (PVD) or the latest method of chemical vapour deposition – atomic layer deposition (ALD), or in a hybrid process combining both techniques. Coatings obtained by the PVD method in engineering materials increase surface microhardness, reduce the coefficient of friction, improve aesthetic values, and enhance electrochemical properties. Unfortunately, these coatings are characterized by structural defects in the form of grain boundaries and



discontinuities in the form of craters, which are a side effect of the technological deposition process. In this case, the anticorrosive properties are not always satisfactory, and in some instances, they may even worsen the corrosion resistance of the materials they cover. To solve this problem, an additional ALD coating is applied to the PVD coatings, which aims to fill structural defects to effectively reduce the risk of damage to the used component and consequently extend its lifespan. Numerous research studies have proven that sealing a PVD coating with an ALD coating in a hybrid system on stainless austenitic steel significantly improves operational properties, particularly increasing corrosion resistance [1-10].

The purpose of this work is to present the results of structural studies of hybrid PVD+ALD coatings: CrN+Cr<sub>2</sub>O<sub>3</sub>/TiO<sub>2</sub> and TiN/ZnO deposited on 316L austenitic steel substrates.

## 2. MATERIALS AND METHODOLOGY

The material used for the study was AISI 316L austenitic steel, which was coated with hybrid PVD+ALD coatings. Appropriately prepared steel substrates were coated using the PVD method (layers of CrN+Cr<sub>2</sub>O<sub>3</sub> and TiN) as well as the ALD method (layers of TiO<sub>2</sub> and ZnO), resulting in the following combination of hybrid coatings:

1. CrN+Cr<sub>2</sub>O<sub>3</sub>/TiO<sub>2</sub>
2. TiN/ZnO

Scanning electron microscopy (SEM) was used to study the fracture structures and surface topography of the examined materials. Studies were carried out using an HRSEM SUPRA 35 microscope, with an SE mode voltage ranging from 10 to 20 kV and magnifications between 5000 and 70000 times. For the InLens mode, the voltage was 7 kV, and the magnifications were 100000 and 200000 times. Furthermore, chemical composition analysis (EDS) was performed in selected microareas.

Moreover, surface topography studies were conducted using an atomic force microscope in non-contact mode. The results obtained with the PARK SYSTEMS XE100 microscope are presented graphically. Additionally, the arithmetic average roughness parameters (Ra) were calculated using software.

## 3. RESULTS

Based on studies using a scanning electron microscope (SEM), it was found that the hybrid coatings CrN+Cr<sub>2</sub>O<sub>3</sub>/TiO<sub>2</sub> and TiN/ZnO are continuous and homogeneous, and the individual layers adhere closely to each other and to the substrate material. As reported in the literature [1] and confirmed by observations, the CrN+Cr<sub>2</sub>O<sub>3</sub> coating consists of alternating layers of CrN and Cr, with a Cr<sub>2</sub>O<sub>3</sub> layer on the surface. The research confirmed that the PVD layers, CrN + Cr<sub>2</sub>O<sub>3</sub> and TiN, exhibit a structure with columnar grains similar to the structure of the T zone according to Thornton's model [1,3]. Fractographic studies indicate that the ALD layers, TiO<sub>2</sub> and ZnO - adhere closely to the PVD coatings. The ALD layers of titanium oxide and zinc oxide uniformly cover the PVD coating, sealing it against structural discontinuities. This sealing of the PVD coating with an ALD layer is in line with the concept of hybrid PVD/ALD coatings, resulting in a significant improvement in the performance properties of the examined

materials, as shown in studies [1-3]. The thickness of the CrN+Cr<sub>2</sub>O<sub>3</sub>/TiO<sub>2</sub> coating is approximately 2.9 μm, while the thickness of the TiN/ZnO coating reaches 1.3 μm (Fig. 1).

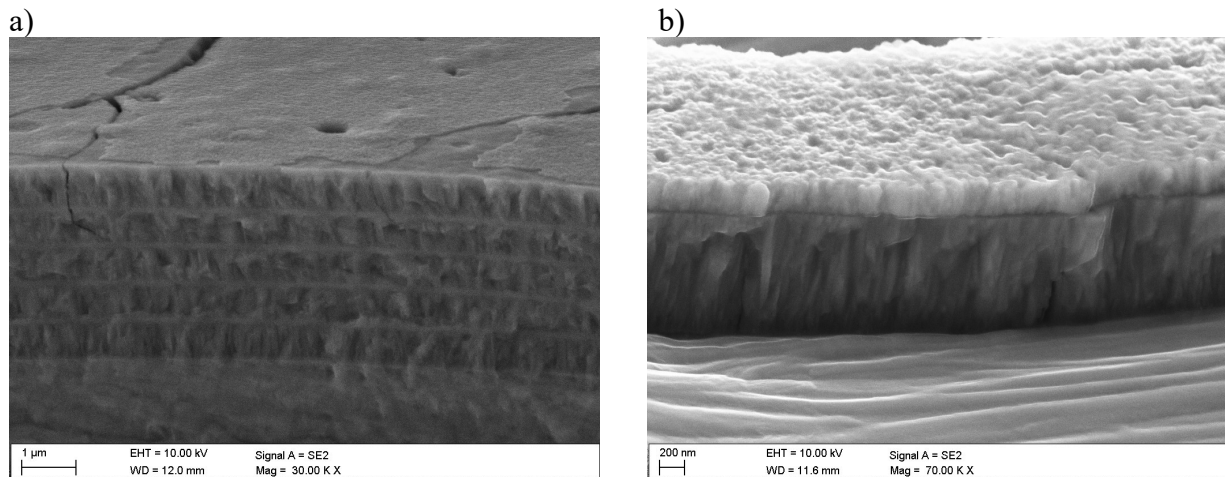


Fig. 1. Fracture of the: a) CrN+Cr<sub>2</sub>O<sub>3</sub>/TiO<sub>2</sub> coating, b) TiN/ZnO coating

Micro-scale surface analysis of the examined hybrid coatings confirms the presence of a topographical structure typical of coatings obtained by the PVD method. On the surface of the tested materials, fine scratches are visible, remnants of the substrate preparation process for coating. This confirms that these coatings precisely replicate the substrate's topography. The analyzed coatings are homogeneous, and their surface shows no discontinuities except for micropores or cracks. SEM studies revealed the presence of microcraters from coagulated droplets of the deposited metal (chromium or titanium). The size of these craters ranges from approximately 0.5 μm to 10 μm for the CrN+Cr<sub>2</sub>O<sub>3</sub>/TiO<sub>2</sub> coating, and from approximately 0.5 μm to several micrometers for the TiN/ZnO coating. This study indicates that the droplets fell after the coating deposition process was completed. As noted in the literature [1-3,9], this may indicate stresses developing in the coatings during the deposition process. Additionally, agglomerates of several coagulated droplets with sizes of a few micrometers were observed. The ALD layers, in turn, precisely replicate the morphology of the PVD layers, as confirmed by high magnification SEM and atomic force microscopy (AFM) studies. On the nanometric scale, the CrN+Cr<sub>2</sub>O<sub>3</sub>/TiO<sub>2</sub> coating exhibited a granular morphology across the entire examined surface, while the TiN/ZnO coating displayed a granular morphological structure with random orientation elongated grains, characteristic of the ZnO layer, as confirmed by previous research [3] (Fig. 2).

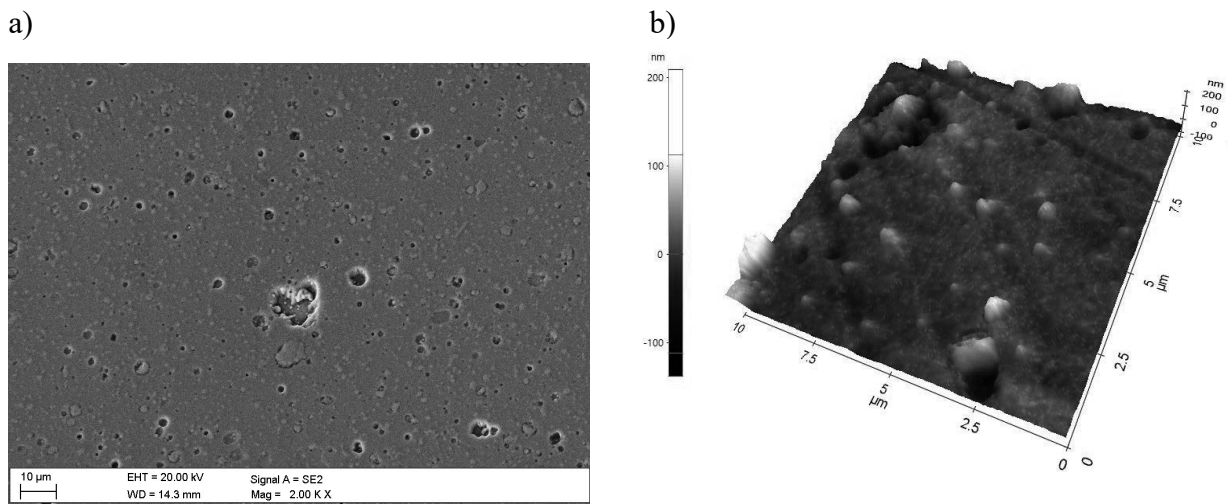


Fig. 2. Topography of the CrN+Cr<sub>2</sub>O<sub>3</sub>/TiO<sub>2</sub> coating, a) SEM b) AFM

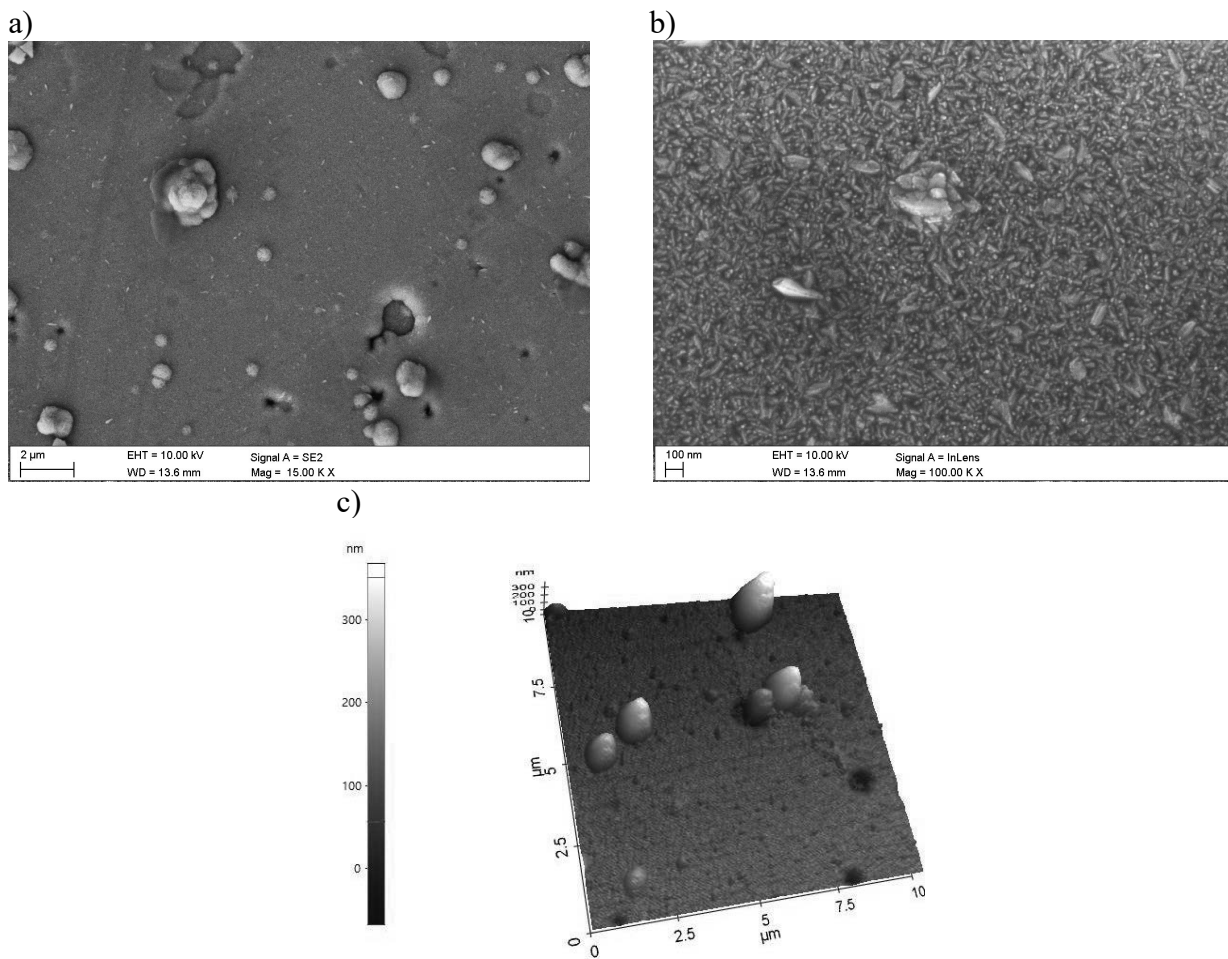


Fig. 2. Topography of the TiN/ZNO coating, a,b) SEM c) AFM

The chemical composition analysis of the surface using the EDS method confirms the presence of chemical elements corresponding to the examined coatings, specifically zinc, chromium, titanium, oxygen, and nitrogen (Fig. 3).

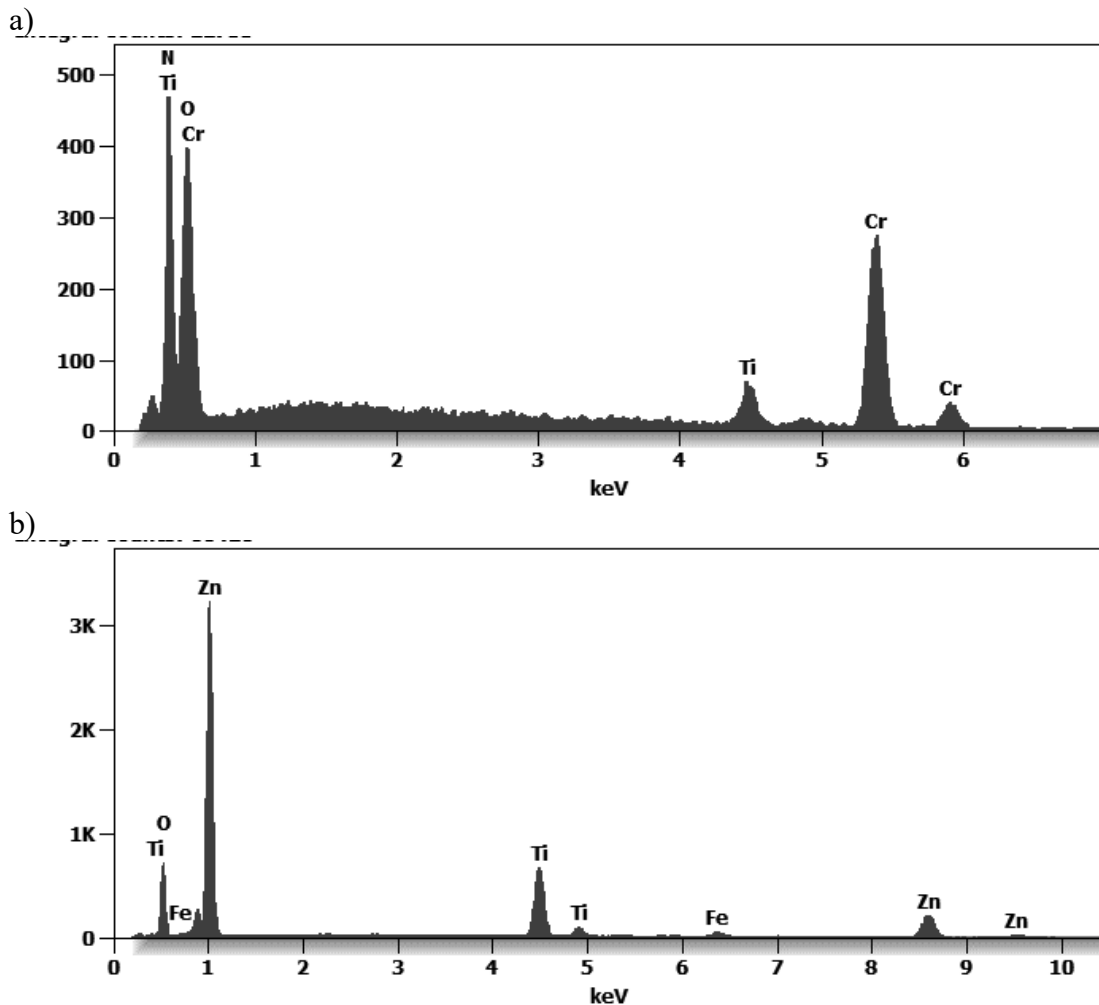


Fig. 3. EDS analysis from the: a) area  $\text{CrN}+\text{Cr}_2\text{O}_3/\text{TiO}_2$  coating, b) area  $\text{TiN}/\text{ZnO}$  coating

#### 4. CONCLUSIONS

Based on the conducted research, it has been determined that:

- The hybrid PVD/ALD coatings of  $\text{CrN}+\text{Cr}_2\text{O}_3/\text{TiO}_2$  and  $\text{TiN}/\text{ZnO}$  were evenly applied without discontinuities and delaminations, adhering closely to the substrate material as well as to each other.
- In both coating systems, the PVD coatings of  $\text{CrN}+\text{Cr}_2\text{O}_3$  and  $\text{TiN}$  exhibit a structure of equiaxed columnar grains resembling the T-zone according to Thornton's model.

- The surface topography of the tested coatings is characteristic of coatings obtained by the PVD technique. The surface mainly shows microcraters from dropping droplets of the deposited metal and the presence of agglomerates of several solidified droplets.
- The ALD layers of TiO<sub>2</sub> and ZnO with granular morphology precisely replicate the surface topography of the PVD coatings, effectively sealing the PVD coatings.

### ACKNOWLEDGEMENTS

This work was produced as part of the project implemented within the framework of project-oriented education - PBL project implemented with secondary school students, in the III competition under the Excellence Initiative - Research University program, at the Silesian University of Technology.

### BIBLIOGRAPHY

1. M. Staszuk Investigations of CrN+Cr<sub>2</sub>O<sub>3</sub>/TiO<sub>2</sub> coatings obtained in a PVD/ALD hybrid method on austenitic 316L steel substrate, *Vacuum* 207 (2023) 111653.
2. M. Staszuk, D. Pakuła, Ł. Reimann, A. Kloc-Ptaszna, M. Pawlyta, A. Kříž, Structure and Properties of TiO<sub>2</sub>/nanoTiO<sub>2</sub> Bimodal Coatings Obtained by a Hybrid PVD/ALD Method on 316L Steel Substrate. *Materials* 14 (2021) 4369.
3. M. Staszuk, D. Pakuła, Ł. Reimann, A. Kloc-Ptaszna, K. Lukaszewicz, Structure and properties of the TiN/ZnO coating obtained by the hybrid method combining PVD and ALD technologies on austenitic Cr-Ni-Mo steel substrate, *Surfaces and Interfaces* 37 (2023) 102693.
4. C.X. Shan, Xianghui Hou, Kwang-Leong Choy, Patrick Choquet, Improvement in corrosion resistance of CrN coated stainless steel by conformal TiO<sub>2</sub> deposition, *Surface and Coatings Technology* 202 (2008) 2147–2151.
5. E. Marin, L. Guzman, A. Lanzutti, L. Fedrizzi, M. Saikkonen, Chemical and electrochemical characterization of hybrid PVD+ALD hard coatings on tool steel, *Electrochemistry Communications* 11/10 (2009) 2060–2063.
6. M. Yazici, H. Kovacı, A.F. Yetim, A. Çelik, Structural, mechanical and tribological properties of Ti and TiN coatings on 316L stainless steel, *Ceramics International* 44/12 (2018) 14195-14201.
7. L. Shan, Y. Wang, J. Li. X. Jiang. J. Chen, Improving tribological performance of CrN coatings in seawater by structure design, *Tribology International* 82/A (2015) 78–88.
8. J. Leppäniemi, P. Sippola, M. Broas, J. Aromaa, H. Lipsanen, J. Koskinen, Corrosion protection of steel with multilayer coatings: Improving the sealing properties of physical vapor deposition CrN coatings with Al<sub>2</sub>O<sub>3</sub>/TiO<sub>2</sub> atomic layer deposition nanolaminates, *Thin Solid Films* 627 (2017) 59–68.
9. M. Staszuk, Ł. Reimann, D. Pakuła, M. Pawlyta, M. Musztyfaga-Staszuk, P. Czaja, P. Benes, Investigations of TiO<sub>2</sub>/nanoTiO<sub>2</sub> bimodal coatings obtained by a hybrid PVD/ALD method on Al-Si-Cu alloy substrate, *Coatings* 12 (2022) 338.
10. S. Jannat, H. Rashtchi, M. Atapour, M.A. Golozar, H. Elmkhah, M. Zhiani, Preparation and performance of nanometric Ti/TiN multi-layer physical vapor deposited coating on 316L stainless steel as bipolar plate for proton exchange membrane fuel cells, *J. Power Sources* 435 (2019) 226818.



17th-19th June 2024  
Gliwice, Poland

DEPARTMENT OF ENGINEERING MATERIALS AND BIOMATERIALS  
FACULTY OF MECHANICAL ENGINEERING  
SILESIA UNIVERSITY OF TECHNOLOGY

## INTERNATIONAL STUDENTS SCIENTIFIC CONFERENCE

### Korózia horčíka a jeho zliatin

Luboš. Halimovič<sup>a</sup>, Milan Uhrčík<sup>a</sup>, Mirosław Bonek<sup>b</sup>

<sup>a</sup> Žilinská univerzita v Žiline, Strojnícka fakulta, Katedra materiálového inžinierstva, Univerzitná 8215/1, 010 26 Žilina, Slovak Republic  
email: halimovic@stud.uniza.sk; milan.uhrčík@fstroj.uniza.sk

<sup>b</sup> Silesian University of Technology, Faculty of Mechanical Engineering, Department of Engineering Materials and Biomaterials, Gliwice, Poland

**Abstrakt:** Článok sa zaoberá základným popisom korózneho správania horčíka a jeho zliatin v podmienkach elektrochemickej korózie - teda za prítomnosti elektrolytu a elektrických veličín.

**Kľúčové slová:** horčík, zliatiny horčíka, korózia, elektrochemická korózia

**Abstract:** This article describes the corrosion behavior of magnesium and magnesium alloys in electrochemical corrosion conditions - in the presence of electrolyte and electrical quantities.

**Keywords:** magnesium, magnesium alloys, corrosion, electrochemical corrosion

### 1. ÚVOD

V technologickej praxi je možné sledovať trend ekologických požiadaviek a to nielen na recykláciu napr. polymérnych materiálov, ale práve aj na kovové materiály a ich zliatiny. Preto prichádzajú do úvahy materiály, ktoré svojimi vlastnosťami zodpovedajú súčasným požiadavkám ako ekologickým tak aj konštrukčným, či technologickým.

Práve kvôli požiadavkám na znižovanie ekologickej stopy je nutné znižovať hmotnosti vozidiel, ktoré spaľujú palivá na báze uhľovodíkov - čím nižšia hmotnosť vozidla, tým je potrebné menšie množstvo pohonných látok. Pre zníženie hmotnosti existuje niekoľko alternatív a to použitie hliníka a jeho zliatin, titánu a jeho zliatin a v neposlednom rade aj horčíka a jeho zliatin, po prípade použitie kompozitných materiálov, nakoľko tieto materiály majú nízku mernú hmotnosť a súčasne majú pomer pevnosti v ťahu k mernej hmotnosti veľmi priaznivý.

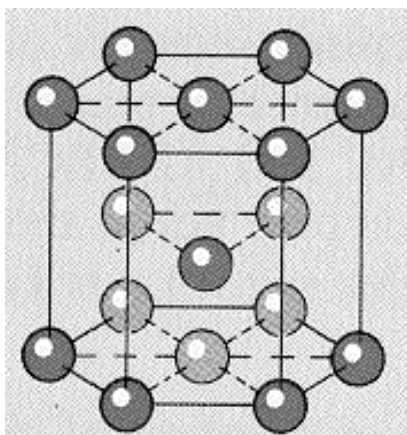
Horčík a jeho zliatiny nachádzajú uplatnenie nielen v automobilovom a leteckom priemysle, ale aj biomedicínskom prostredí. Zliatiny horčíka sa v súčasnosti používajú pre rôzne biomedicínske aplikácie, napr. ako dočasné implantáty v ľudskom tele. Keďže sa horčík nachádza v ľudskom tele ako minerál, je voľba horčíkových zliatin značne opodstatnená.

V prírode sa bežne vyskytuje v podobe rôznych zlúčenín, kde nadobúda formu dvojmocného iónu ( $Mg^{2+}$ ). Táto skutočnosť nie je priaznivá z pohľadu na jeho koróznou odolnosť. Nie je

termodynamicky ušľachtilý, čo znamená, že má vysokú reaktivitu s prostredím. Z tohto dôvodu sa mnohé výskumné tímy po celom svete venujú práve koróznemu správaniu sa horčíka a jeho zliatin a po prípade hľadaniu spôsobov ako predísť korodovaniu týchto materiálov.

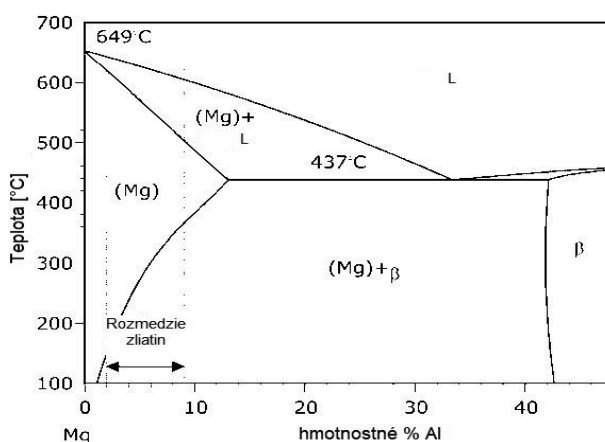
## 2. HORČÍK A JEHO ZLIATINY

Horčík (Mg) je kov kryštalizujúci v hexagonálnej tesne usporiadanej mriežke (Obr. 2). Je veľmi silne zastúpeným prvkom v zemskej kôre ako aj v morskej vode, čo ho činí veľmi dostupným a hlavne recyklovateľným [1].



Obr. 1 Hexagonálna tesne usporiadaná mriežka

Figure 1. Hexagonal close-packed lattice



Obr. 2 Časť binárneho diagramu Mg-Al [4]  
Figure 1. Part of Mg -Al binary diagram [4]

Horčík, tak ako väčšina kovov používaných v technickej praxi, sa ako čistý kov nepoužíva. Hlavnými dôvodmi sú jeho nepriaznivé mechanické vlastnosti, ako aj korózna odolnosť, ktorá je veľmi nízka. Jeho merná hmotnosť je  $1740 \text{ kg}\cdot\text{m}^{-3}$  a teplota tavenia  $650^\circ\text{C}$ . Veľmi zle sa tvárni, čo zhoršuje zvýšenie jeho pevnosti plastickým pretvorením [1,2]. Horčík je dobre elektricky aj tepelne vodivý a má dobrú zliateľnosť [1 - 3].

Horčík ako samostatný kov nevyhovuje požadovaným aplikáciám. Z tohto dôvodu sa zlieva s inými kovmi [1]. Horčíkové zliatiny sú prednostne používané na odliatky, avšak existujú aj zliatiny pre tvárnenie [2]. Medzi bežne dostupné zliatiny horčíka patria zliatiny na báze horčík - hliník [1]. Pre bežné zliatiny sa používa približne od 2 hm. % do 10 hm. % Al (Obr. 2) [4].

V súčasnosti sa do tejto bázy pridáva aj zinok (Zn). Takéto zliatiny sú podľa ASM normy označované ako AZXX (XX predstavujú orientačné hodnoty hm. % jednotlivých prvkov, kde prvá číslica označuje hm. % prvého prvku, druhá druhého). Hliník a zinok v týchto zliatinách zvyšujú pevnosť, tvrdosť ako aj koróznou odolnosť. Zinok je pridávaný v množstvách okolo 1 hm. %. So zvyšovaním hm. % Zn dochádza k poklesu zvariteľnosti a koróznej odolnosti [5].

Medzi ďalšie prvky s ktorými sa horčík zlieva sú kovy vzácnych zemín (ozn. RE). Tieto zliatiny nachádzajú uplatnenie predovšetkým v automobilovom priemysle, nakoľko sú žiarupevnejšie ako ostatné zliatiny. Používajú sa hlavne po tepelnom spracovaní, po ktorom nadobúdajú požadované vlastnosti. Nepriaznivou skutočnosťou je však ich cena [5,6].

V súčasnosti sa zliatiny horčíka zlievajú s rôznymi inými kovmi ako napr. Mg-Zn, Mg-Al-Zr, Mg-Zr-Y, Mg-Zn-Zr, Mg-Li, Mg-Ca-Zn, atď. V mnohých prípadoch sa jedná o vývojové zliatiny - teda o zliatiny, ktoré sú z hľadiska ich budúcej aplikácie veľmi perspektívne [2,3,6,7]. Vplyv vybraných prvkov na výslednú zliatinu je uvedený v Tab. 1.

Tab. 1 Vplyv vybraných prvkov v zliatinách horčíka [7]  
Table 1. Influence of selected elements on magnesium alloy [7]

Vplyv/prvok	Al	Ca	RE	Si	Zn
Tvrdosť	Zvyšuje	-	-	-	-
Pevnosť	Zvyšuje	-	-	Zvyšuje	-
Ťažnosť	Znižuje	-	-	-	-
Oxidácia	-	Znižuje	-	-	-
Korózna odolnosť	Zvyšuje	-	Zvyšuje	Zvyšuje	Zvyšuje
Odolnosť proti tečeniu	-	-	Zvyšuje	-	-

## 2. KORÓZIA HORČÍKOVÝCH ZLIATIN

Jedným z najrozhodujúcejších faktorov, prečo sa horčík v technickej praxi nevyužíva je jeho nízka termodynamická stabilita v bežných prostrediach. Jedným zo základných ukazovateľov termodynamické stability akéhokoľvek materiálu je štandardný elektródový potenciál  $E^0$ . Čím je jeho hodnota kladnejšia, tým je materiál stabilnejší.  $E^0$  horčíka je oproti iným materiálom veľmi záporný (Tab. 2) [1,3,6].

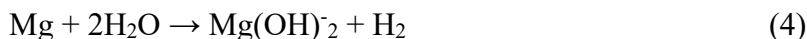
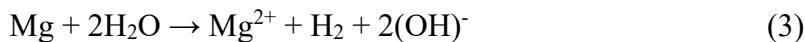
Tab. 2 Štandardné elektródové potenciály vybraných prvkov [8]  
Table 2. Standard electrode potentials of selected elements [8]

Tvorba katiónov	Štandardný elektródový potenciál $E^0$ [V]
$\text{Cu} \rightarrow \text{Cu}^{2+} + 2\text{e}^-$	+ 0,35
$2\text{H} \rightarrow 2\text{H} + 2\text{e}^-$	0
$\text{Fe} \rightarrow \text{Fe}^{2+} + 2\text{e}^-$	- 0,44
$\text{Zn} \rightarrow \text{Zn}^{2+} + 2\text{e}^-$	- 0,76
$\text{Mn} \rightarrow \text{Mn}^{2+} + 2\text{e}^-$	- 1,1
$\text{Zr} \rightarrow \text{Zr}^{4+} + 4\text{e}^-$	- 1,53
$\text{Al} \rightarrow \text{Al}^{3+} + 3\text{e}^-$	-1,69
$\text{Mg} \rightarrow \text{Mg}^{2+} + 2\text{e}^-$	- 2,37

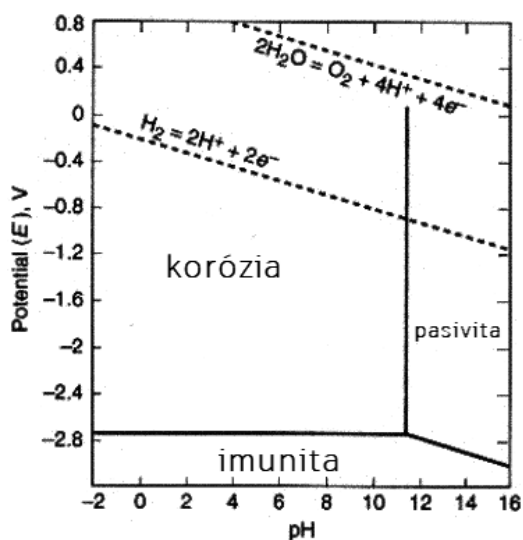
Z termodynamického hľadiska sa teda jedná o materiál, ktorý má vysokú reaktivitu a náchylnosť k odovzdávaniu elektrónov, teda k vytvoreniu kladne nabitého iónu -  $\text{Mg}^{2+}$  (1). Takto kladne nabitá častica na seba nabaľuje záporne nabité atómy zo vzduchu, alebo vody - prevažne kyslík, alebo skupiny (napr. hydroxidová skupina) (3). Následne vznikne korózný produkt (4) [9].







Dôležitú informáciu o koróznom správaní sa materiálu podávajú aj tzv. Pourbaixove diagramy. Vykresľujú závislosť medzi pH a potenciálom, ktorý vzniká medzi materiálom a prostredím s daným pH. Horčík koroduje takmer vo všetkých prostrediach, jedine pri nízkych potenciálových napätiach sa správa imúnne (teda nekoroduje) a pri vysokých pH sa správa pasívne (vytvorí sa vrstva ochranných oxidov) (Obr. 3).



Obr. 3 Pourbaixov diagram pre čistý horčík [4]

Figure 3. Pourbaix diagram for pure magnesium [4]

Z rovníc a z Pourbaixovho diagramu (Obr. 3) je zrejmé, že horčík sa vie nachádzať v rôznych stavoch. Každý tento stav má určitý chemický potenciál, ktorý vo všeobecnosti podáva informáciu o tom, ako veľmi je daný prvok, ión, či zlúčenina, stabilný. Najstabilnejšou zlúčeninou je hydroxid horečnatý (Tab. 3). Avšak táto zlúčenina nedokáže byť v bežných podmienkach stabilnou natoľko, aby povrch chránila.

Povrch takéhoto skorodovaného materiálu je porézny, čo umožňuje vznik rôznych kapilárnych efektov, v ktorých korózia môže prebiehať intenzívnejšie, ako pri nenapadnutom povrchu [1,3,11].

Tab. 3 Chemický potenciál rôznych stavov horčíka [1]

Table 3. Chemical potential of different states of magnesium [1]

Zložka	Chemický potenciál [kcal/kmol]
Mg	0
Mg <sup>2+</sup>	-109
MgO	-139
Mg(OH) <sub>2</sub>	-199

Avšak nakoľko v praxi sú využívané zliatiny horčíka je zrejmé, že významný vplyv na koróziu odolnosť majú aj prísadové prvky v zliatinách. Väčšina prvkov je ušľachtilejších, ako horčík. V matici zliatiny teda vznikajú mikrogalvanické účinky, ktoré majú za následok rozpad materiálu. Horčík ako menej ušľachtilý kov sa prirodzene stane anódou voči zložke, ktorá je s ním zliata [1,3,6,11].

Jednotlivý vplyv na koróziu odolnosť horčíkových zliatin je už pomerne známy a vo všeobecnosti každý legujúci prvok z časti aj koróziu odolnosť zlepšuje. Nie je však možné zabezpečiť dostatočnú koróziivzdornosť a to práve kvôli mikrogalvanickému účinku, ktorý spôsobuje vznik galvanických trhlín a následne koróziu (niekedy korózne-únarový) lom. Riešením sú prvky ako chróm, alebo titán - tieto prvky sú schopné vytvárať oxidy na povrchu, ktoré sú homogénne a zamedzujú tak ďalšiemu korodovaniu. Z dôvodu ich vysokej mernej hmotnosti sa ale stráca zmysel zlievať horčík s týmito prvkami, keďže hmotnosť takýchto odliatkov by sa pohybovala výrazne vyššie, ako sú napr. hmotnosť zliatin Al, ktorých korózia odolnosť je postačujúca [1,3,5,6].

Jedným z ďalších faktorov, ktoré sú perspektívne, sú povrchové úpravy horčíkových zliatin. Jedná sa buď o rôzne typy povlakovania, vrstvenia, alebo mechanického opracovania. Z rôznych výskumov je zrejmé, že niektoré úpravy povrchu ako napr. konvenčné brúsenie, alebo leštenie môže zvýšiť koróziu odolnosť oproti bežne frézovanému, alebo odliatemu povrchu [13,14]. Bežne dostupné metódy síce zlepšujú koróziu odolnosť horčíkových zliatin, avšak nie natoľko, aby to postačovalo pre konkrétne aplikácie. Jednou z ďalších možností sú laserové, poprípade shot peeningové možnosti opracovania povrchu.

Výsledky experimentov v súčasnosti však nie sú priaznivé - korózia odolnosť po ovplyvnení povrchov týmito metódami výrazne klesá [3,8]. Ďalšou možnosťou sú možnosti vytvárania vrstiev. Existuje už niekoľko spôsobov ako na povrchu vytvoriť vrstvu, ktorá je nevodivá, takže sa zníži možnosť prúdenia elektrónov a tým sa zamedzí elektrochemickej korózii.

Jeden z takýchto typov vrstiev sú vrstvy vytvorené plazmovou elektrolytickou oxidáciou (PEO). Tieto vrstvy dokážu zvýšiť odpor povrchu voči elektrickým veličinám aj o dvojnásobok [8,11].

### 3. ZÁVER

Predkladaný článok sa zaoberá základnými poznatkami v oblasti korózie horčíka a jeho zliatin. Na základe týchto poznatkov je možné vysloviť nasledovné závery:

- Horčík je ako čistý kov v praxi nevyužiteľný - je nutné ho zlievať s inými prvkami, pri čom v súčasnosti majú najavššie využitie zliatiny horčíka na báze Mg-Al-Zn
- Korózia odolnosť čistého horčíka je veľmi slabá. Najstabilnejší korózny produkt, ktorý by mohol materiál chrániť je hydroxid horečnatý ( $Mg(OH)_2$ ), ktorý však v bežných prostrediach nie je stály natoľko, aby zliatinu chránil.
- Zliatiny horčíka je možné korózne chrániť aj vplyvom legujúcich prvkov, ktoré by mali nie len vytvárať oxidy, ale taktiež dvíhať celkový štandardný elektródový potenciál zliatiny. Vo všeobecnosti je ale tento efekt často potlačený mikrogalvanickými účinkami, kedy horčík koroduje na úkor legujúceho prvku.
- Možnosťou zlepšenia korózne odolnosti horčíkových zliatin sú taktiež povrchové úpravy. Okrem konvenčných metód ako brúsenie a leštenie existujú nové progresívne metódy úprav povrchu, ktoré sú v súčasnosti predmetmi skúmania. Mnohé z nich ako napr. PEO majú na

koróznou odolnosť významný vplyv - odpor vrstiev vytvorených touto metódou vzrastá až o dvoj alebo trojnásobok.

## POĎAKOVANIE

Príspevok vznikol v rámci riešenia spoločného slovensko-poľského projektu International Visegrad Fund's V4 Generation Mobility Mini-Grant No 12410044 ako výsledok spolupráce medzi Politechnikou Slaskou (Poľsko) a Žilinskou univerzitou Žilina a projektov KEGA č. 004ŽU-4/2023 a KEGA č.009ŽU-4/2023.



## BIBLIOGRAPHY

1. G. L. Song. Corrosion of Magnesium Alloys. Elsevier, 2011, ISBN 978-0-85709-141-3.
2. P. Skočovský et al. Náuka o materiáli. EDIS, Žilina, 2014, ISBN 978-80-554-0871-2.
3. E. Halimovič. Vplyv nekonvenčných úprav povrchu na korózne charakteristiky horčíkových zliatin, Bakalárska práca. Žilinská univerzita v Žiline, 2023.
4. Part of Mg-Al binary diagram, [www.researchgate.net/publication/265168745\\_Design\\_with\\_Magnesium-Alloys\\_properties\\_and\\_casting\\_processes/figures?lo=1](http://www.researchgate.net/publication/265168745_Design_with_Magnesium-Alloys_properties_and_casting_processes/figures?lo=1)
5. E. Koç, et al. Influence of zinc on the microstructure, mechanical properties and in vitro corrosion behaviour of magnesium-zinc binary alloys, Journal of Alloys and Compounds, vol 648 (2015). ISSN 0925-8388. DOI: 10.1016/j.jallcom.2015.06.227.
6. B. Hadzima. Korózia zliatin Mg-Al-Zn. Dizertačná práca. Žilinská univerzita v Žiline, 2003.
7. D.S. Kumar, et al. Magnesium and Its Alloys in Automotive Applications - A Review, American Journal of Materials Science and Technology, vol 4. 2015. DOI: 10.7726/ajmst.2015.1002.
8. F. Pastorek, B. Hadzima, D. Kajánek. Preparation and corrosion properties of structural materials with refined grain structure. Person, 2019. ISBN 978-8396-1054-7.
9. A. Atrenset al. Review of Recent Developments in the Field of Magnesium Corrosion. In Advanced Engineering Materials, vol 17, 2015 DOI: 10.1002/adem.201400434.
10. Pourbaix diagram for pure magnesium [https://www.researchgate.net/figure/Magnesium-in-water-Pourbaix-diagram-at-25-C\\_fig4\\_289256819](https://www.researchgate.net/figure/Magnesium-in-water-Pourbaix-diagram-at-25-C_fig4_289256819).
11. D. Kajánek. Štúdium mechanizmov korózneho napadnutia povrchovo upravených horčíkových zliatin. Dizertačná práca. Žilinská univerzita v Žiline, 2019.
12. M.A.F Romzi, J. Alias, M.I.M. Ramli. Effect of Zinc (Zn) on the microstructure and corrosion behaviour of Magnesium (Mg). In. Materials Today: Proceedings, vol 48, part 6, 2022. ISSN 2214 - 7853. DOI: 10.1016/j.matpr.2021.09.261
13. U. Reddy et al. Effect of Surface Roughness Induced by Milling Operation on the Corrosion Behavior of Magnesium Alloys. In. Journal of Materials Engineering and Performance, vol 30, 2021. DOI: 10.1007/s11665-021-05933-8, 2021



17th-19th June 2024  
Gliwice, Poland

DEPARTMENT OF ENGINEERING MATERIALS AND BIOMATERIALS  
FACULTY OF MECHANICAL ENGINEERING  
SILESIA UNIVERSITY OF TECHNOLOGY

## INTERNATIONAL STUDENTS SCIENTIFIC CONFERENCE

### Long-Term Effects of Autonomous Vehicles

Mohammed Hesham, Givi Sanadze

Georgian Technical University, Faculty of Transport Systems and Mechanical Engineering,  
Department of Mechanical Engineering and Technology  
email: mohammed\_hesham@gtu.ge, sanadzegivi05@gtu.ge

**Abstract:** In recent years, we've had huge speculations about the so called self driving cars or as we like to scientifically term them as the autonomous vehicle. While we have observed their models from Tesla or even recently the Mercedes and realized that there still is a lot of technical and legal issues that are needed to be solved, but the days of complete adoption of these models are really inevitable. This revolutionary shift from dependence vehicle to autonomous vehicles sure do have their own outcomes, be it the positive and negative or direct and indirect or the length of their societal benefits and harm. It still doesn't seem to be clear on these aspects. Here in this article we shall identify several of these outcomes and we will also explore the conditions in the broader transportation system.

**Keywords:** autonomous vehicle, long-term Effect, self-driving car.

### 1. INTRODUCTION

Autonomous vehicles (AVs, often referred to as "self-driving cars" or "fully automated vehicles") have always been a point of discussion in the car industry since decades. They've played a huge role of creative imaginations in the film and animation industry, mainly in the Sci-Fi Genre. I remember as a child fantasizing my dad's car being driven without someone in the driving seat but I never expected I'd experience that in reality.

It sure is a fact that the expected benefits of this technology are numerous like it is predicted that the autonomous system can result in far safer operation and improved efficiency in the flow of traffic.

Furthermore, it is also believed that the subscribers to these vehicles are more prone to productive and pleasant use of their commuting time.

Our research and article aims to focus on some of the effects of vehicle automation at the major system level.

## 2. METHOD

Okay now the best way for us to understand the very potential effects of vehicle automation at the system level, we decided to build our work on a very informative base model in terms of transportation, here we tend to describe the known relations and connections between a constructive set of variables.

With that being said, we took a good note different productive interviews and workshops to investigate how our base model shall change and take different forms during the different scenarios of AV introduction. This particular section shall give a brief on the modelling and data collection of our base model.

As a creative way to investigate effects of vehicle automation on a systems level, we have decided to use system dynamics, which is an efficient way of approach approach used to analyze complex, dynamic systems (Forrester, 1958). At its core is a mapping process, which helps us to identify key variables and the relation among them.

Because of this our work is limited to the use of causal loop diagrams (CLDs). CLDs here really make our jobs easier to create a perceived system structures—and thus expand them for analysis, discussion, and opinion making.

Given the amount of various uncertainty in the potential effects of autonomous vehicles, we tend to apply scenario-analysis methods. Where rather than trying to determine the most likely outcomes, this approach aims to develop useful insights by exploring a range of different futures. It helps us to identify the main forces that will affect outcomes in question, and in the end followed by speculation about the development of these forces.

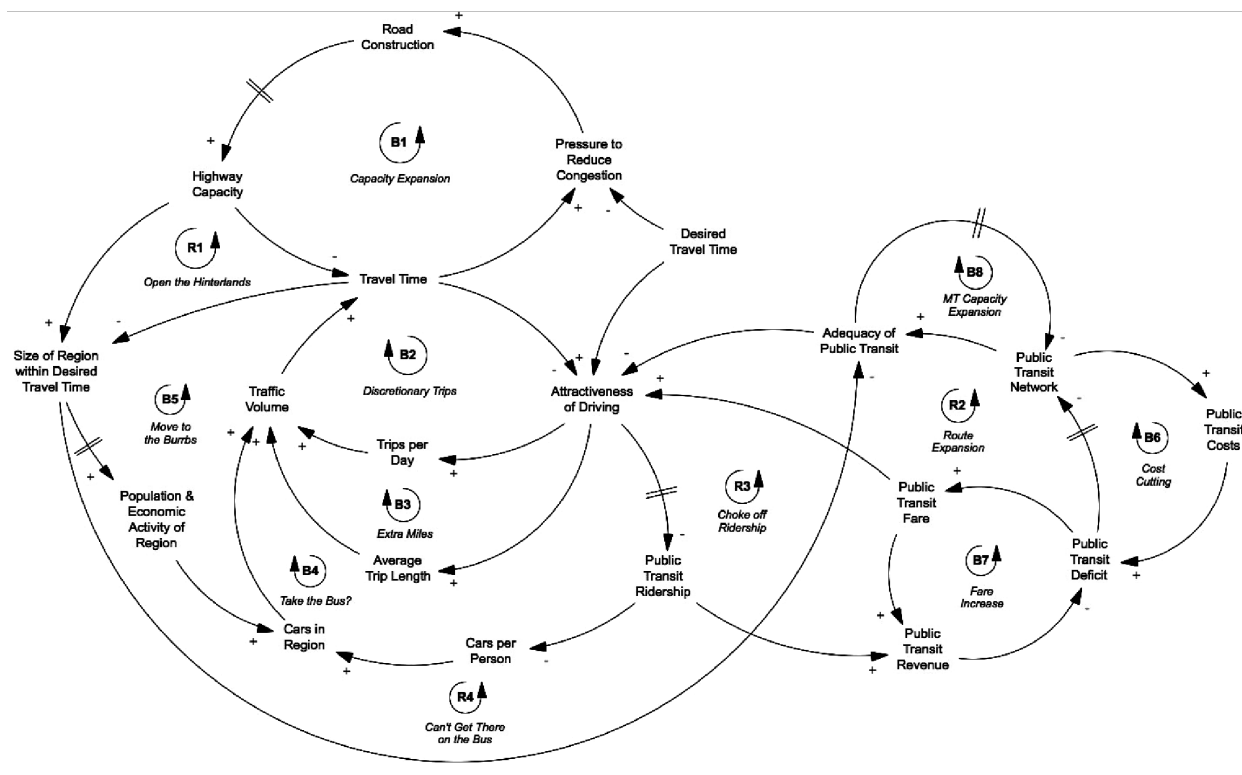


Figure 1. The Baseline Model

As the public discussion at the moment rarely questions if autonomous vehicles will become a reality which technically sure has become - we assumed in our scenarios that autonomous vehicles are successfully developed and fully adopted. Technological challenges, legal obstacles, or factors that may affect or hinder adoption, and the adoption process itself were not subjects of our study.

Okay the most awaited part is finally here, our baseline model or as we mentioned earlier, the base model. We made the most of our established CLD of traffic and congestion to indeed analyze and investigate the effects of vehicle automation. At the very deep core of this model like the question of how to reduce the road congestion.

With days and years and subsequently decades passing by the more number of people choose to head towards driving their own vehicles, this further more contributes to more number of roads/highway capacity to expand allowing the consumer to be able to travel farther in less time resulting in the Size of the Region that can be reached within a Desired Travel Time to increase, this eventually reduces the so called Adequacy of Public Transit followed by the increase in Attractiveness of Driving which means fewer people ride transit; fewer people riding transit means less revenue and poorer service. As a result, the number of people riding transit decreases even further, which in turn leads to more people driving.

We're glad to picturize this in the form of our Baseline Model below (Figure 1).

### **3. INTRODUCING AUTONOMOUS DRIVING IN TERMS OF A SCENARIO**

In this scenario let's assume no change in behavior or in ownership. AVs are going to be used in the same way as we use cars are today and vehicles are privately owned. Expected improvements (e.g., our interview subjects presumed that "driving will be so much safer," or "my commute will be so much more pleasant") do not lead to any kind of behavioural changes.

Alright so our main assumption here basically is going to be that general behaviour regarding choices of travel will remain the same and not change due to the introduction of AVs. But however we will surely allow the increase in trips per day and also vehicles per person, because of course due to the increase in Mobility for those Unable to Drive.

We definitely do consider autonomous vehicles to be a way to increase road efficiency. Which is why the Pressure to Increase Efficiency of Traffic Flow replaces Pressure to Reduce Congestion and Efficiency of Vehicle Operation replaces Road Construction.

In the case that autonomous vehicles do not cause a change in people's behaviour, a lot of benefits on a system level can be expected compared to our current mobility system. Travelling by car will be cheaper, safer, more environmentally friendly, less energy consuming, and a lot of time spent in the car can be used in a better way. Also, the situation of millions of people who currently have limited access to mobility would improve. Although these new traffic participants will increase traffic volumes, it can be assumed that this effect could be offset by the increased efficiency of vehicle operation and traffic flow.

### **4. CONCLUSION**

Finally into the conclusion I'll of course love to say that our scenario illustrated here express a variety of potential outcomes with the very soon normalisation of autonomous

vehicles. I mean ofcourse they are sure not describing a crisp image of the future for sure but rather it portrays a range of possible futures.

Autonomous vehicles shall sure enable driving to become a safer means of travel, the time spent in the vehicle can be utilized in a whole different perspective and ofcourse last but not the lease, the situation of general population with limited access to mobility would surely improve. And not forgetting that the per-mile cost and also the energy consumption would decrease significantly.

## **BIBLIOGRAPHY**

1. Abbas, K.A. The Use of System Dynamics in Modelling Transportation Systems with Respect to New Cities in Egypt. System Dynamics Society Conference Proceedings. 1990.
2. Anderson, J.M., Kalra, N., Stanley, K.D., Sorensen, P., Samaras, C., Oluwatola., O.A., 2014. Autonomous Vehicle Technology: A Guide for Policymakers. RAND Cooperation, Santa Monica, CA.
3. Babbie, E.R. The basics of social research. Wadsworth Publishing, Belmont, CA. 2014.
4. Brustein, J., Self-Driving Cars Will Mean More Traffic. Bloomberg. 2014. <http://www.bloomberg.com/bw/articles/2014-07-21/self-driving-carswill-mean-more-traffic>.
5. Burns, L., Jordan, W., Scarborough, B. Transforming Personal Mobility. Earth Institute, Columbia University. 2013.



17th-19th June 2024  
Gliwice, Poland

DEPARTMENT OF ENGINEERING MATERIALS AND BIOMATERIALS  
FACULTY OF MECHANICAL ENGINEERING  
SILESIA UNIVERSITY OF TECHNOLOGY

## INTERNATIONAL STUDENTS SCIENTIFIC CONFERENCE

### **Konštrukčný návrh kempingovej platformy na spanie do kufru osobného automobilu**

Edita Illichmanová<sup>a</sup>, Lenka Kuchariková<sup>a</sup>, Mirosław Bonek<sup>b</sup>

<sup>a</sup> Žilinská univerzita v Žiline, Strojnícka fakulta, Katedra materiálového inžinierstva, Univerzitná 8215/1, 010 26 Žilina, Slovak Republic

\*email: illichmanova@stud.uniza.sk

<sup>b</sup> Silesian University of Technology, Faculty of Mechanical Engineering, Department of Engineering Materials and Biomaterials, Gliwice, Poland

**Abstrakt:** Článok sa zaoberá konštrukčným návrhom lôžkovej konštrukcie do kufru osobného automobilu. Rozkladacia konštrukcia je využiteľná najmä pre kemping a navrhnutá s minimálnym zásahom do vozidla, jednoduchou obsluhou a s efektívnym využitím batožinového priestoru.

**Abstract:** This article deals with the construction design of a bed structure for the trunk of a passenger car. The folding structure is particularly useful for camping and designed with minimum interference to the car, easy operation and efficient use of the boot space.

**Kľúčové slová:** konštrukčný návrh, automobil, kempingová platforma

**Keywords:** construction design, automobile, camping platform

## 1. ÚVOD

Autokempy boli v minulosti veľmi obľúbenou možnosťou, ako stráviť dovolenku prakticky kdekoľvek v zahraničí bez toho, aby ste sa finančne zruinovali. Kempovanie nestráca na atraktivite ani dnes a veľa ľudí na pobyt v kempe nedá dopustiť. Pre nadšencov autokempingu je, v dnešnej dobe, možnosť nájsť na trhu veľké množstvo automobiliek, ktoré vyrábajú vozidlá prispôbené pre kemping, prípadne firmy, ktoré na trh dodávajú rôzne doplnky vyvinuté pre kempovanie. Hlavným cieľom tejto práce je vytvoriť konštrukčný návrh kempingovej platformy, na spanie pre dve osoby, do kufru automobilu VW Caddy. Dôvodom je, aby sa znížili náklady za ubytovanie pri cestovateľských výletoch a náklady za kúpu novej konštrukcie spacieho systému, navrhnutej firmami.

Čiastkové ciele potrebné na naplnenie hlavného cieľa:

- Vytvorenie zoznamu požiadaviek a spracovanie konštrukčného návrhu s využitím CAD systémov
- Vyhotovenie technickej dokumentácie a pevnostná analýza v softvéri ANSYS.



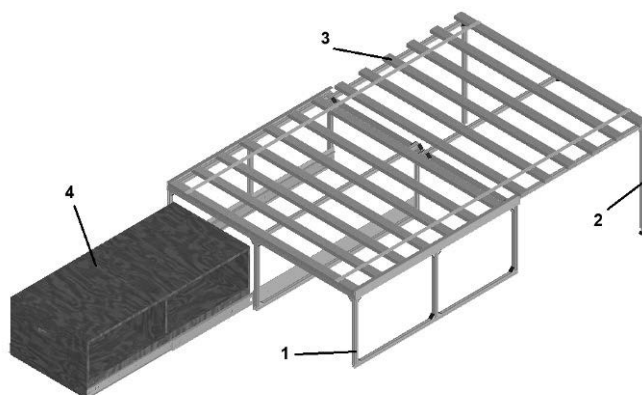
## 2. KONŠTRUKČNÝ NÁVRH

Pri tvorbe konštrukčného návrhu sme vychádzali z požiadavkového listu, zostaveného na základe požiadaviek zákazníka (tabuľka 1). Dbalo sa najmä na výber materiálov s nízkou hmotnosťou a vysokou pevnosťou, dobrou dostupnosťou a adaptivitou a na minimalizovanie zásahu do vozidla.

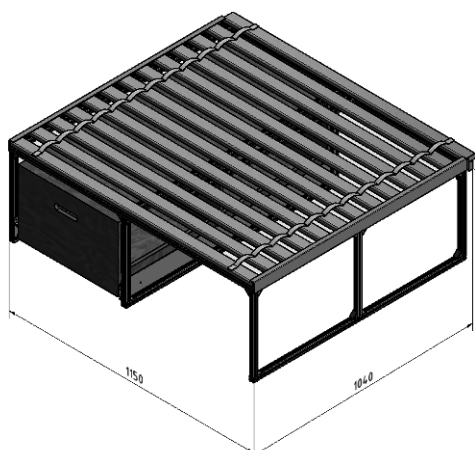
Tab. 1. Požiadavkový list  
Tabelle 1. Wish list

Č.	Požiadavka	Dôležitosť
<b>Funkčné požiadavky:</b>		
1	Minimálna nosnosť konštrukcie 160 kg	Priorita
2	Úložný priestor	Priorita
<b>Konštrukčné požiadavky:</b>		
1	Maximálne rozmery 1800 x 1160 x 600 mm	Priorita
2	Dostatočná tuhosť a pevnosť	Priorita
3	Minimálny zásah do vozidla	Priorita
4	Nízka hmotnosť	Prianie
<b>Výrobné požiadavky:</b>		
1	Jednoduchá vyrobiteľnosť - dielenské alebo domáce podmienky	Priorita
<b>Prevádzkové požiadavky:</b>		
1	Jednoduchá montáž a demontáž	Priorita
2	Prevádzka bez demontovania zadných sedadiel	Prianie
3	Jednoduchá údržba	Prianie
<b>Ekonomické požiadavky:</b>		
1	Cena nižšia ako podobné výrobky na trhu	Priorita
2	Použitie normalizovaných dielov	Prianie
<b>Bezpečnostné požiadavky:</b>		
1	Prvky konštrukcie zaistené proti pohybu pri jazde vozidla	Priorita

Platforma na spanie je zložená z troch základných častí (obr.1) - nosný rám konštrukcie - zložený z pevnej (1) a posuvnej (2) časti, pevný rošt (3) a matrac. Ďalej je možnosť prídania výsuvných úložných boxov (4), podľa preferencií a potrieb zákazníka. Rozmery sú dokumentované na obr. 2 a obr. 3.

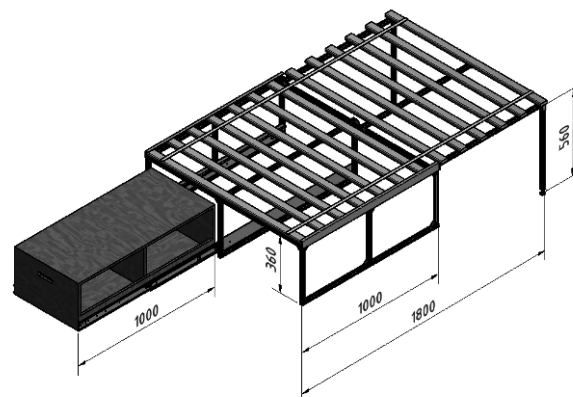


Obr.1 Základné časti konštrukcie  
Figure 1. Basic parts of the construction



Obr.2 Základné rozmery konštrukcie v zloženom stave

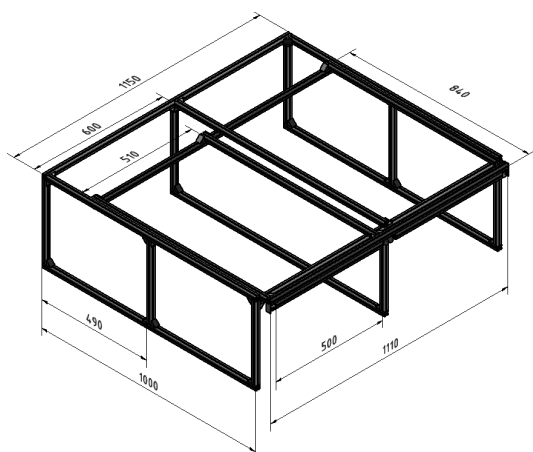
Figure 2. The main dimensions of the construction in the folded state



Obr.3 Základné rozmery konštrukcie v rozloženom stave

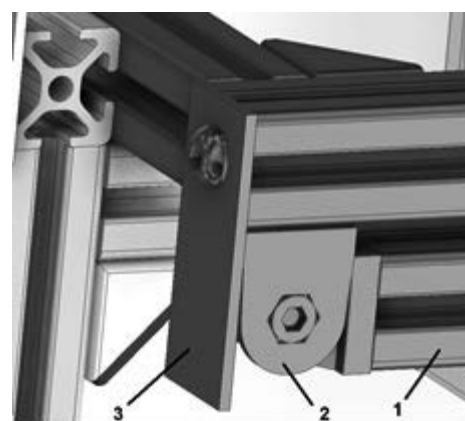
Figure 3. The main dimensions of the construction in unfolded state

Rám konštrukcie je navrhnutý z hliníkových profilov rady 5 s rozmermi 20 x 20 mm [2]. Skladá sa zo zadnej nosnej časti, ktorá je uložená v kufri vozidla (obr. 4). Tá je navrhnutá z troch priečok pod roštom, pre dostatočnú pevnosť. Nohy zadnej časti sú uložené na priečnom profile, ktorý tiež slúži na rozloženie tlaku do podlahy.



Obr.4 Rozmery nosnej časti rámu hliníkovej konštrukcie

Figure 4. Dimensions of the load-bearing part of the frame of the aluminium construction



Obr.5 Detail prednej časti rámu so sklopenou nohou

Figure 5. Detail of the front part of the frame with folded support

Predná časť rámu je užšia v porovnaní so zadnou časťou a vysúva sa v smere osi jazdy, ponad sklopené zadné sedadlá. Pre úplné rozloženie rámu, je potrebné posunúť predné sedadlá o pár centimetrov dopredu. Na prednej časti rámu sa nachádzajú sklopené nohy (1) s dĺžkou 500 mm uchytené pomocou kĺbov (2) a hliníkové lišty (3), ktoré zabezpečujú pretočenie kĺbov o viac ako 90 stupňov (obr. 5). Na spodnej časti nôh sú pripevnené stavacie nôžky s kruhovou podstavou. Tie umožňujú nastavenie správnej výšky nôh pomocou závitú a vyrovnanie sklonu

vďaka guľovému čapu. Počas zloženého stavu sú sklopené nohy ku rámu prichytené pásmi suchého zipsu alebo magnetovými blokmi vloženými v drážkach profilu.

Hliníkové profily zadnej aj prednej časti konštrukcie sú navzájom spojené pomocou uholníkovej sady, ktorá sa skladá z pozinkovaného odliatku uholníku 5 20 x 20 mm [2], z upínacích prvkov, podložiek a plastovej krytky. Uholníky zabezpečujú posilnenie spojov a spoje bez potrebného opracovania profilov.

V prípade návrhu je dôležité myslieť aj na dostatočnú ventiláciu pod matracom, vzhľadom na zamedzenie akumulácie nadbytočného tepla a rast mikroorganizmov. Z tohto dôvodu sa ako platforma pod matrac použijú drevené lamely namiesto plošných dosiek. Toto riešenie tiež prináša výhodu nižšej hmotnosti.

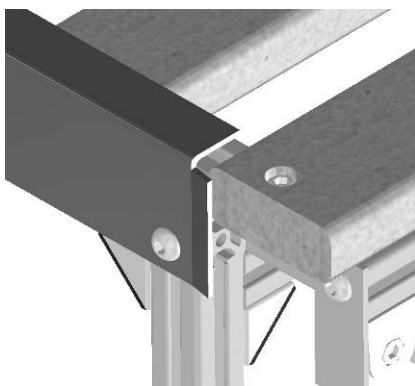
Pre konštrukciu sa zvolila kúpa latového roštu s rozmermi 1200 x 2000 mm z borovicového masívu. Nosnosť na jedno lôžko (pre každú polovicu postele), v prípade podopretia roštu aj v strednej časti, je uvádzaná 150 kg. Rošt sa skladá zo 14 ks latiek s rozmermi 50 x 20 mm [3].

Rošt je ku konštrukcii upevnený len na okrajoch prvej a poslednej latky pomocou skrutiek s valcovou hlavou a drážkovými maticami. Toto upevnenie umožňuje posuvný pohyb stredných latiek a rolovací systém pri zložení a rozložení konštrukcie.

Pre zamedzenie pohybu latiek do strán, sú k pevnej časti rámu pripevnené hliníkové lišty L - profilu s rozmermi 20 x 45 x 2 mm s dĺžkou 1000 mm (obr. 6). Hliníkové lišty sú na konci upravené s malým vyhnutím, ktoré slúži ako násypka pre správne zasúvanie latiek.

Podľa aktuálnych potrieb výjazdu je možné do zadnej časti konštrukcie primontovať výsuvný box s úložným priestorom. Jeho plný výsuv, s dĺžkou 1000 mm, v smere von z vozidla, zabezpečujú ložiskové plnovýsuvy bez tlmenia. Tie sú o rám konštrukcie uchytené pomocou hliníkových lišt s navítanými dierami podľa ložiskového výsuvu. Lišty sú o konštrukciu prichytené pomocou skrutiek s valcovou hlavou a drážkových matic bez potrebnej úpravy hliníkových profilov.

Výhodou úložných boxov (obr. 7) je zamedzenie voľného pohybu materiálu po vozidle počas jazdy, a tiež využitie horizontálnej plochy, ako pracovného stola, napríklad na prípravu jedla a uloženie variča.



Obr.6 Detail uloženia lišty L - profilu s vyhnutím  
Figure 6. Detail of the installation of the L - profile rail with avoidance



Obr.7 Varianty návrhov úložných boxov  
Figure 7. Variants of storage box designs

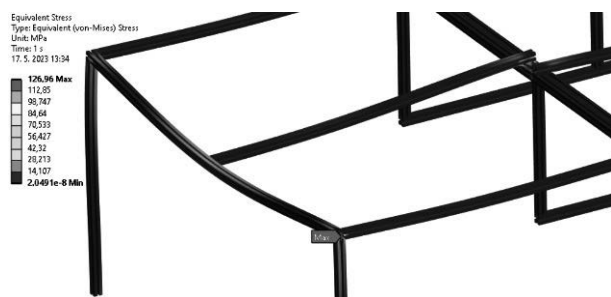
Finálny výkres kempingovej zostavy je dokumentovaný na obr. 8 a súpis jednotlivých položiek potrebných na jej vyhotovenie s predpisom materiálu je uvedený v tab. 2.



**Mechanické a fyzikálne vlastnosti materiálu EN AW-6063 T66:**

Medza pevnosti v ťahu $R_m$	min. 245 MPa
Medza klzu $R_p0,2$	min. 195 MPa
Hustota	2,7 kg/dm <sup>3</sup>
Ťažnosť $A_5$	min. 10%
Ťažnosť $A_{10}$	min. 8%
Koef. tepelnej rozťažnosti	23,6x10 <sup>-6</sup> 1/K
Modul pružnosti v ťahu E	cca 70 000 MPa
Modul pružnosti v šmyku	cca 25 000 MPa
Tvrdosť	cca 75 HB 2,5/187,5

Následne sa vytvorila sieť elementov a boli zadané okrajové podmienky. Konštrukcia je zaťažená na všetkých profiloch, ktoré sú v kontakte s dreveným roštom, so sústredením do stredu ťažiska rámu. Zaťaženie je zadané hmotnosťou 160 kg (1 600 N), pričom sa rátalo s priemernou hmotnosť človeka 80 kg a zaťažením pre dve osoby.



Obr.9 Ekvivalentné napätia v zostave  
Figure 9. Equivalent voltages in the assembly



Obr.10 Posunutia v smere osi Z  
Figure 10. Displacement in the Z-axis direction

Obr. 9 popisuje ekvivalentné napätia v zostave, pričom najväčšie napätia, o hodnote 127 MPa, vznikajú v oblastiach spojov a v strede dĺžok profilov. Maximálne napätie je relatívne vzdialené od medze klzu materiálu.

Ako reakcia na tieto napätia vznikli v jednotlivých profiloch priehyby. Na obr. 10 v smere osi Z je možné odčítať najväčší priehyb 0,18 mm, v smere osi X je najväčší priehyb 0,5 mm a v smere osi Y 4,3 mm.

Konštrukcia pri daných podmienkach zaťaženia z hľadiska pevnosti vyhovuje. Z výsledkov však vyplýva, že pri vyššom zaťažení by bolo potrebné posilniť najkritickejšiu oblasť výsuvnej časti pomocou podpery, alebo použitím silnejších profilov.

#### 4. ZÁVER

Účelom práce, bolo navrhnuť konštrukciu na spanie do kufru osobného automobilu, využiteľnú pre kemping. Medzi hlavné požiadavky patrila dostatočná povnosť, rozoberateľnosť, vytvorenie úložného priestoru a využiteľnosť pre dve osoby.

V práci je zahrnutý popis konštrukčného návrhu základnej časti zostavy, jej jednotlivých častí, ako je uloženie podzostáv, riešenie spojov, potrebné doplnenie hliníkových líš, či výber dreveného roštu. Článok zahŕňa tiež návrh pre využitie úložného priestoru a rôzne varianty

úložných boxov, podľa preferencií zákazníka. Posledná kapitola sa zaoberá pevnostnou analýzou namáhania konštrukcie s využitím metódy konečných prvkov. Pomocou pevnostnej analýzy, v softvéri Ansys Workbench, bolo zistené, že pri zadaných podmienkach, z hľadiska pevnosti, je rám konštrukcie vyhovujúci. Platforma bola navrhnutá pre dvoch ľudí, s priemernou hmotnosťou dospeléj osoby 80 kg, čo je pre zákazníka vyhovujúce. Navrhnutá konštrukcia spĺňa všetky požiadavky uvedené v požiadavkovom liste. V prípade budúcej zmeny požiadaviek na vyššiu hmotnosť zaťaženia, je možnosť ku rámu doplniť podperné kompatibilné hliníkové profily, prípadne zvážiť tento fakt pred výrobou a použiť hliníkové profily rady 6 s prierezom 30 x 30 mm.

## POĎAKOVANIE

Príspevok vznikol v rámci riešenia spoločného slovensko-poľského projektu International Visegrad Fund's V4 Generation Mobility Mini-Grant No 12410044 ako výsledok spolupráce medzi Politechnikou Slaskou (Poľsko) a Žilinskou univerzitou Žilina a projektov KEGA č. 004ŽU-4/2023 a KEGA č.009ŽU-4/2023.



## BIBLIOGRAPHY

1. ILLICHMANOVÁ, E. 2023 Konštrukčný návrh kempingovej platformy na spanie do kufra osobného automobilu pre dve osoby: bakalárska práca. [cit. 2024-4-20] Žilina: Žilinská univerzita v Žiline, 2023. 50s
2. Katalóg Stavebnicový systém MB, ITEM Industrietechnik GmbH [online] 2019 [cit. 2024-4-20] Dostupné z: <[https://www.haberkorn.cz/sk/data/uploads/Download/Katalog/ss-item-mb\\_9/book\\_cz\\_interaktivni/682/index.html](https://www.haberkorn.cz/sk/data/uploads/Download/Katalog/ss-item-mb_9/book_cz_interaktivni/682/index.html)>
3. Online produkt: Latový rošt 120x200 (150 kg/osoba) [online] [cit. 2024-4-20] Dostupné z: <<https://www.wilsondo.sk/masivny-rost-buk-120x200--150-kg-osoba/>>



17th-19th June 2024  
Gliwice, Poland

DEPARTMENT OF ENGINEERING MATERIALS AND BIOMATERIALS  
FACULTY OF MECHANICAL ENGINEERING  
SILESIA UNIVERSITY OF TECHNOLOGY

## INTERNATIONAL STUDENTS SCIENTIFIC CONFERENCE

### Project of the personalized knee joint orthosis intended for manufacturing using additive technologies

Jakub Jabłoński<sup>a</sup>, Agnieszka J. Nowak<sup>b</sup>

<sup>a</sup> Absolwent Politechniki Śląskiej, Wydział Mechaniczny Technologiczny, Automation and Robotics; e-mail: jakub.jablonski541@gmail.com

<sup>b</sup> Politechnika Śląska Wydział Mechaniczny Technologiczny, Laboratorium Naukowo-Dydaktyczne Nanotechnologii i Technologii Materiałowych, ul Towarowa 7a, 44-100 Gliwice; e-mail: agnieszka.j.nowak@polsl.pl

**Abstract:** This paper presents issues covering additive technologies, Computer-Aided Design (CAD) and knee orthoses. A personalized knee brace was designed. Single component parts were designed, assembled, and then additively manufactured using FDM/FFF 3D printing technology. The developed prototype uses a pneumatic actuator that protects against sudden changes in the bending angle. The completed orthosis design allowed for the formulation of conclusions necessary to undertake further research on the optimization of the proposed solution.

**Keywords:** Additive technologies, 3D printing, Computer-Aided Design (CAD), orthosis, manufacturing.

## 1. INTRODUCTION

The development of additive manufacturing technology is slowly becoming everydayness. Its impact on medicine is easily visible in sectors such as orthopedics, dentistry and cardiology. The use of 3D printing takes place in pre-operative diagnosis and planning of procedures as well as teaching aids for students.

In the history of manufacturing, an important factor limiting personalized production was the high costs of production preparation, sometimes too high to make one product. The new era based on additive technologies primarily shortens production time, reduces prototyping and implementation costs, minimizes material costs, and limits the amount of waste.

Computer-aided design CAD is used, among others, in mechanical, electrical and construction engineering. An important part of CAD design is digital geometric modeling aimed at developing a digital record of the product's structure by determining its geometric, dynamic and technological features. Computer support is a key element used and described in this work.

The aim of the work is to design and produce an innovative prototype of a personalized knee brace using a selected incremental method, using computer-aided CAD and an automation element - a pneumatic actuator.

The work consists of two parts. The literature review describes issues related to additive methods, selected technologies and their properties, basic information about orthoses with a broader presentation of knee joint orthoses, as well as information about computer-aided design and manufacturing systems, CAD systems in particular. The second part is of its own work describing the actions taken in the design and production processes. The developed prototype was manufactured using FDM additive technology - the components were made on the Prusa i3 MK3 model using the CarbonLook Carbon Black PLA filament.

The summary of the results described in the work allowed for the formulation of conclusions, as well as the physical assembly of a demonstration model enabling analysis of the correctness of the design assumptions and visualization of the need for possible design changes in further design proceedings.

## 2. FDM

FDM technology (Fused Deposition Modeling), also known as FFF (Fused Filament Fabrication), is the most common additive method. The genesis of its creation, similarly to other technologies, was the need to reduce the costs and time of creating prototypes. Over the years, finished products and their components began to be manufactured. In the case of FDM, the manufacturing process involves the use of a thermoplastic polymer, forming its geometry under the influence of high temperature. The models are printed by depositing successive layers of a semi-liquid material that is extruded from a heated nozzle at a specific pressure and temperature. The material used is has a constant diameter (1.75 mm or 2.85 mm). It is extruded continuously through the printer's nozzle. This is a simple mechanism consisting of a bearing pressed by a spring to a gear wheel, moved by a stepper motor, which is responsible for introducing the material to the print head. It looks like two rollers moving in opposite directions (Fig. 1) [3, 4].

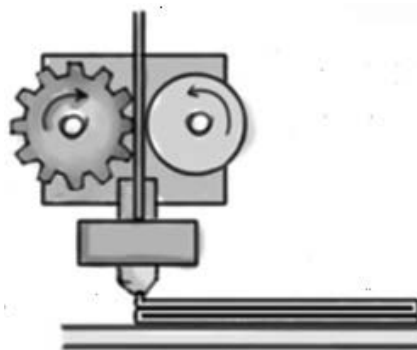


Fig. 1. Picture of FDM technology [4]

The most popular types of materials used in this additive method are [4]:

- ABS – thermoplastic used in industry,
- PLA – thermoplastic based on organic compounds,
- PA – highly durable, used e.g. for the production of ropes,
- PETG – used, among others, for the production of plastic bottles,



- TPU – flexible, rubber-like.

The materials are available in various colors. The material is most often hung on the printer's arm, but it can be placed in another place intended for this purpose. It is recommended to pay attention to feeding it to the extruder and print head so that it is uninterrupted. We can improve this process by feeding the material through a tube. The head is heated to the temperature that a given filament needs to be melted. These temperatures can reach up to 260°C. The exact value depends on the printer model. The filament is transformed into a semi-liquid state, which is sufficient to draw a shape on the worktable of the 3D printer. The material that is placed on the work table dries almost immediately. However, if we use a model with a heated table, it still remains plastic [3,4].

Printing takes place after importing the CAD model from the selected environment (such as Inventor, NX, Solid Edge), via a file with the STL extension to the printer software (for example Slicer), which is an input signal for the 3D printer, causing the printing nozzle to move in the desired arrangements. and paths based on G-code obtained from the software. The print head moves above the worktable in the XY axes and, like a plotter, places plastic on the surface of the worktable according to the previously created shape. If the printer is equipped with one print head, the color of the model is the same as the color of the filament. Manual replacement is possible by pausing the printout, but the differences will only be visible in the Z axis (Fig. 2) [3, 4].

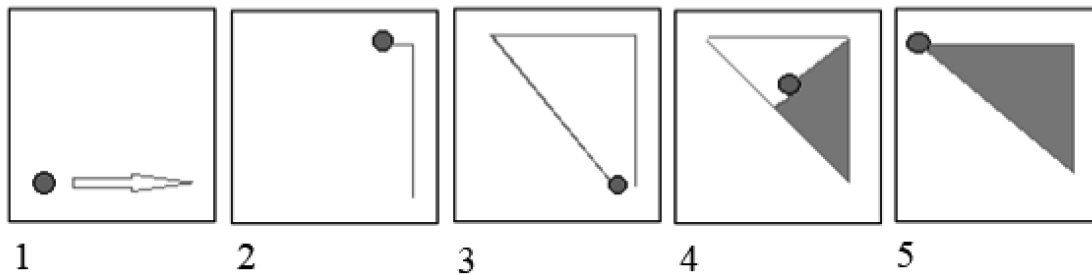


Fig. 2. Creating the first layer of a 3D printed element [4]

Then the worktable or head moves in the Z axis and the next layer is applied. In this way, a spatial model is created layer by layer. Simply remove the finished model from the work table and remove the "supports" - print support structures that can be generated by us. FDM is the only existing additive technology capable of printing models from pure ABS and other injection thermoplastics. It can be used both in the production of functional prototypes, final products and semi-finished products [4].

### 3. KNEE JOINT ORTHOSIS

The knee is the largest and most complex joint in the human body. It is characterized by a hinge structure and connects the femur with the lower leg. Due to its functions, location and structure, the knee joint may be subject to dislocations, sprains, contusions and fractures. Therefore, we want it to be both flexible and resistant to overload. Orthoses for this part of the body are popular among athletes due to their simple structure and low total weight. We can divide them into: clock, semi-rigid and flexible. The main criterion that we should follow when choosing the right orthosis is the type of injury. It is also important whether it will be

a preventive, corrective or therapeutic solution. In each of these situations, the attending physician should have a key influence on the decision. There are three types of knee orthoses [5, 6]:

- **Clock** (Fig. 3A) recommended for damage to the anterior and lateral cruciate ligaments, surgical treatment of ligaments, patella or meniscus. A physiotherapist or orthopedist is responsible for changing the bending angle and general adjustment; trying to adjust it yourself may aggravate the injury.
- **Semi-rigid** (Fig. 3B) which is a type of joint strengthening or to prevent the regeneration of an injury. It has the form of a sleeve with splints sewn in parallel to the joint to stabilize the knee during activity.
- **Flexible** (Fig. 3C) used mainly by athletes who are exposed to minor knee injuries. Also recommended in case of overload, moderate joint sprain and degeneration of its surface. The advantage of this type of orthosis is its versatility. It is also helpful in the treatment of rheumatoid arthritis, chronic knee pain and swelling. Unfortunately, it is not reinforced in any way.



Fig. 3. Knee joint braces: clock (A), semi-rigid (B), flexible (C) [7-9]

An important factor when choosing a knee brace is its size. Too large, it may slip and, consequently, it will not provide proper stabilization. Too little may cause pressure, leading to wounds. The material for the orthosis is also crucial. Stiffeners are made primarily of carbon and glass fibers due to their lightness. However, elastic elements are made of neoprene or knitted fabrics - breathable materials. They ensure the drainage of fluids, do not cause abrasions and improve movement [5, 6].

#### 4. CAD

The first computer-aided CAD systems were called Computer Aided Drafting. They were used only to create and modify drawings that were part of the construction documentation. Their development took place towards geometric and functional integration with CAP, CAM and PPC systems through network communication (CIM structure), and then into open multifunctional systems with a distributed data structure with full integration with the EDM (Engineering Data Management) system, engineering and the PDM (Product Data

Management) system for. CAD programs differ in their scope of support and degree of universality, and can be divided into three groups [10]:

- 1) used for drawing,
- 2) mid-level modelers,
- 3) top-level modelers.

Computer Aided Design (CAD) is the use of computer hardware and software to support technical design or digital geometric modeling. The latter is an intermediate stage between concept and production. The product information environment is shown in Figure 4 [10].

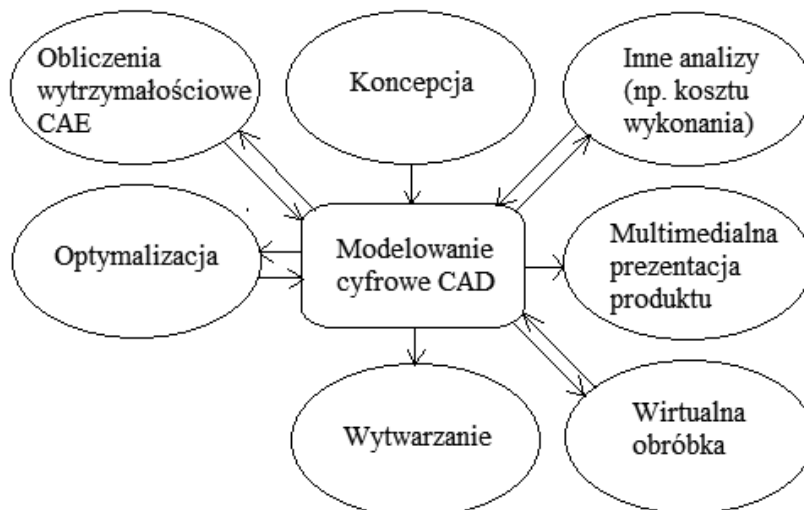


Fig. 4. Information environment of CAx digital modeling [10]

The basic components of CAD include the following [10]:

- computer representation of structures: digital modeling, preparation of drawing documentation from digital models, drawing using a computer for drawing - CADD (Computer Aided Design and Drafting);
- databases, e.g. of standardized elements or material properties;
- simulation, visualization and animation – CAID (Computer Aided Industrial Design), for the purpose of digitally presenting products.

In addition, other areas of engineering activities are connected with CAD, such as [10]:

- optimization of structures and processes,
- strength engineering calculations, e.g. using the FEM method,
- reverse engineering - obtaining digital models of objects by scanning their shapes and internal structure,
- neural networks (artificial intelligence algorithms, including expert systems, advisory systems),
- word processors and spreadsheets in technical design.

Digital geometric models created and saved using CAD systems are most often used in product design and manufacturing processes. We distinguish the following types of digital geometric models [10]:

- edge,
- surface,
- solid CSG (Constructive Solid Geometry),

- solid B-Rep (Boundary Representation),
- hybrid,
- fractal (using the self-similarity of objects),
- composed of voxels (voxel models).

In modern enterprises, an important factor is the archiving and central availability of information about descriptive product data. Full PDM documentation (Product Data Management) consists of the following items [10]:

- construction documentation - CAD geometric models, construction drawings, parts list, order sheets,
- technological documentation – digital CAM models, description of manufacturing technology, requirements for the finished product,
- normative documentation - reports confirming tests performed, use risk analyses, CE declarations of conformity, certificates and approvals,
- manuals and commercial documents - user manuals, warranty cards, price lists, lists of spare parts, labels, advertising brochures.

The above-mentioned data are most often stored in electronic form in databases, enabling their regular updating and also facilitating the keeping of a history of introduced changes [10].

## **5. MODELING, ASSEMBLE and 3D PRINTING**

The individual elements of the orthosis were designed in Autodesk Inventor 2024. The press-fit connection was chosen as the connection method. The geometry of the components was developed based on the anatomical dimensions of the author's leg. The measurements were carried out using a standard tailor's meter and a drawing ruler. A modular design was chosen due to its simplicity. 7 different parts were modeled, 4 of them (Upper Rim, Lower Rim, Left HingeInner, Right HingeInner) were printed individually. The remaining ones (Hinge, Connector 1, Connector 2) were produced in quantities of 2 pieces. The CAD models are shown in Figures 5.

Assemble: figure 6 shows the assembly of previously designed orthosis elements in the Siemens NX program. In this way, it was checked whether the dimensional accuracy was maintained enabling its assembly in real conditions (after production), and computer visualization was carried out.

3D printing: after assembly, the original CAD models allowed for test prints to be made for actual visualization, allowing for subsequent dimension corrections.

Each element was saved in the STL format and placed in the Prusa Slicer 2.7.1 environment, and then "cut" after setting the printing parameters, along with supports on the table - figures no. 7. The finished G-code was saved on a memory card, which, when placed in a 3D printer, enabled the element to be printed.

The initial elements were printed with only 15% infill to reduce material consumption and save time and energy, while maintaining the minimum strength needed for a real test assembly. Selected of them are shown in Figures 7. The test assembly is shown in Figure 8.

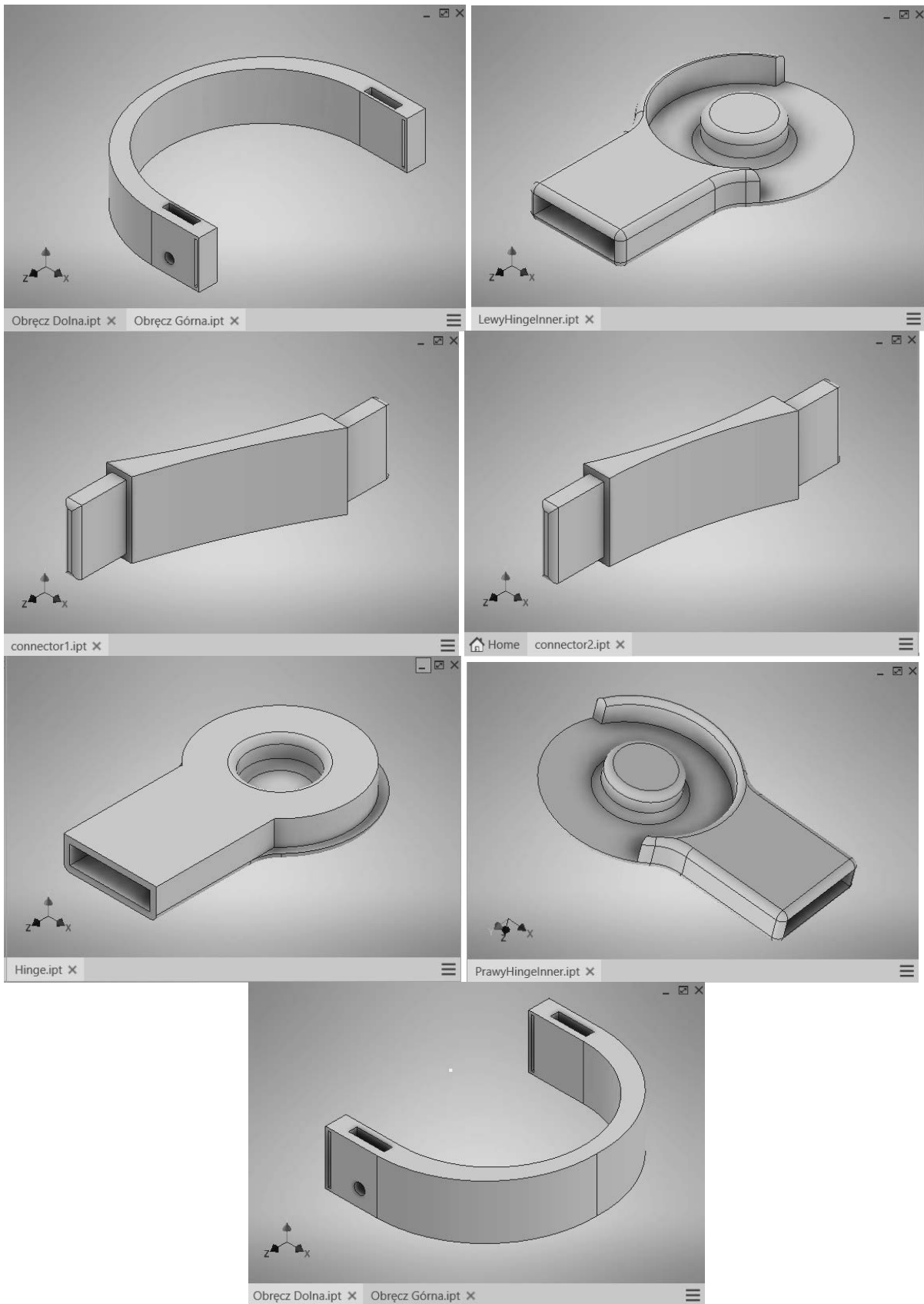


Fig. 5. Parts models designed in Autodesk Inventor 2024

In the case of test prints, the material used was a PLA (polylactide) filament, in various colors, characterized by good durability, low material shrinkage and visual attractiveness. It is widely used, among others, for making functional prototypes, figurines and large models [12]. All parts were manufactured on a Prusa i3 MK3 3D printer shown in Figure 7.

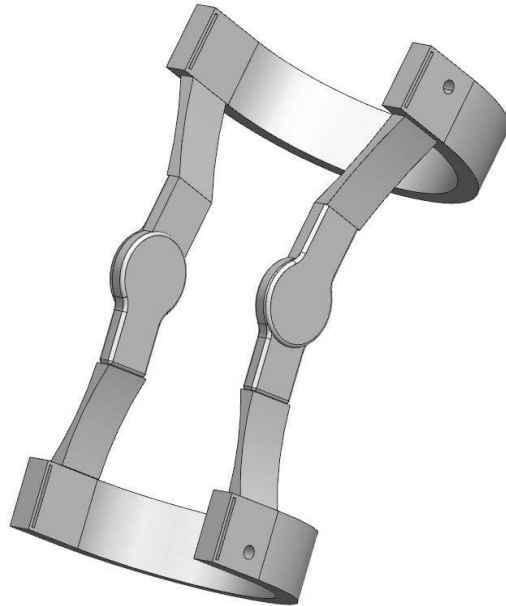


Fig. 6. View of the orthosis assembly in the Siemens NX program

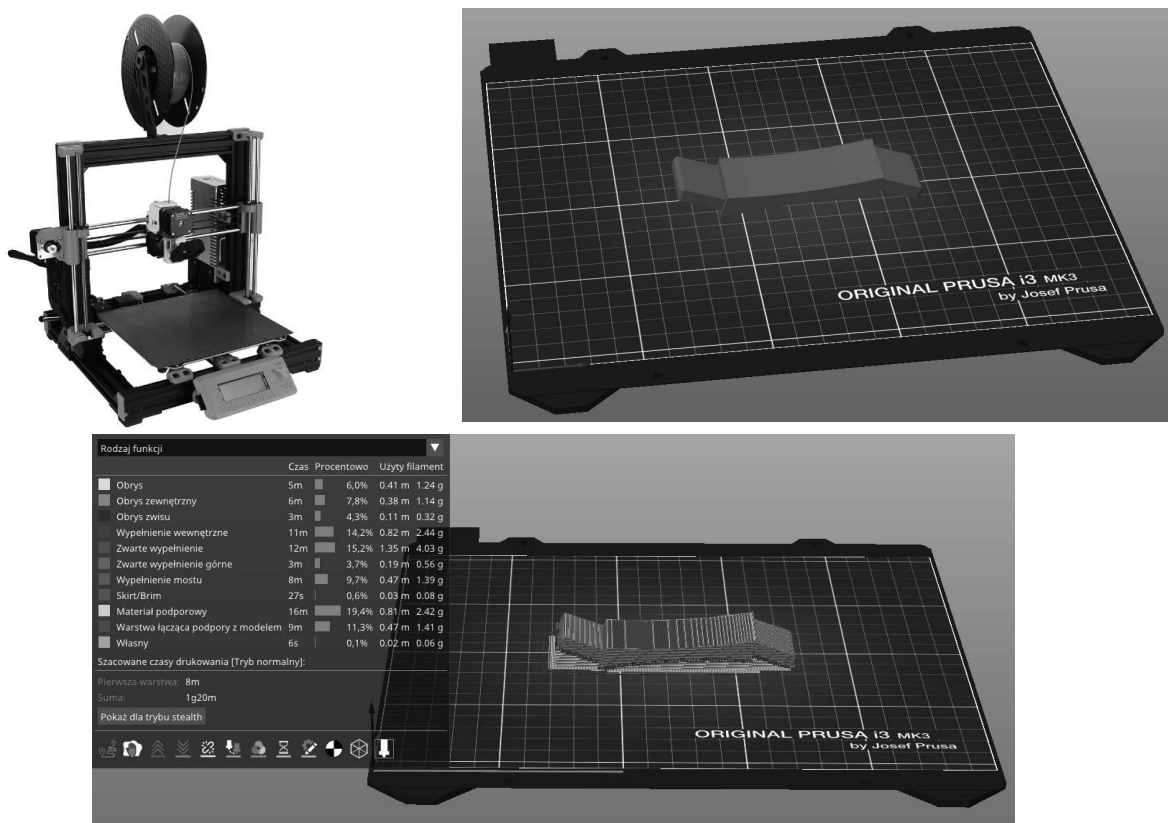


Fig. 7. Prusa i3 MK3 3D printer [11]; Element 3 "Connector1" in the base state; Element 3 being cut, along with generated supports

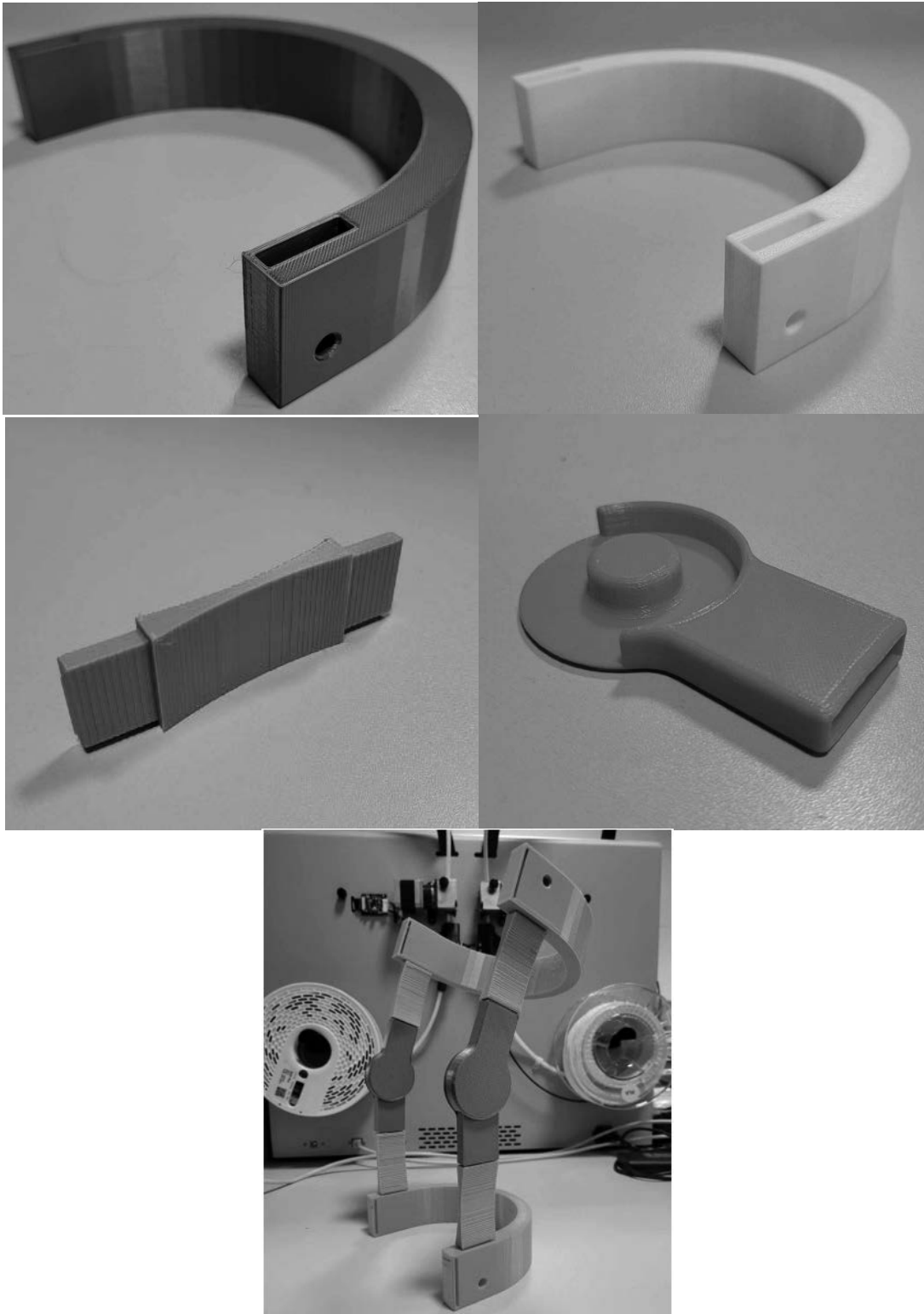


Fig. 8. Test prints and Test assemble.

The final prints were made with the CarbonBlack Carbon Look PLA filament (Fig. 9), containing the addition of carbon fibers, which enabled the printing of models with a satin surface and hardly visible layers [13]. The infill percentage was increased (70%) to balance the

strength properties, stiffness and weight of the structure. The internal filling method was also changed to a gyroidal pattern. It is one of the few structures that provide support in every direction, prints relatively quickly, and allows you to save material without crossing paths. An additional feature is the original appearance [14].

Technical specifications of the material:

- Diameter: 1.75 [mm]
- Net weight: 1 [kg]
- Printing temperature: 195 – 225 [°C]
- Table temperature: 40 – 60 [°C]
- Cooling: 50 – 100 [%]



Fig. 9. Filament PLA CarbonBlack [13]

A pneumatic actuator, specifically a gas spring, was used in the work. Its role is to prevent a sudden change in the assumed bending angle, which could cause the patient to develop a new injury or increase the current one. A gas spring with a force of 50N and a stroke of 100 mm was used. Angular ball joints on screws with M8 metric thread were used as mountings. The nominal dimensions of the spring and mountings are shown in Figures 10.

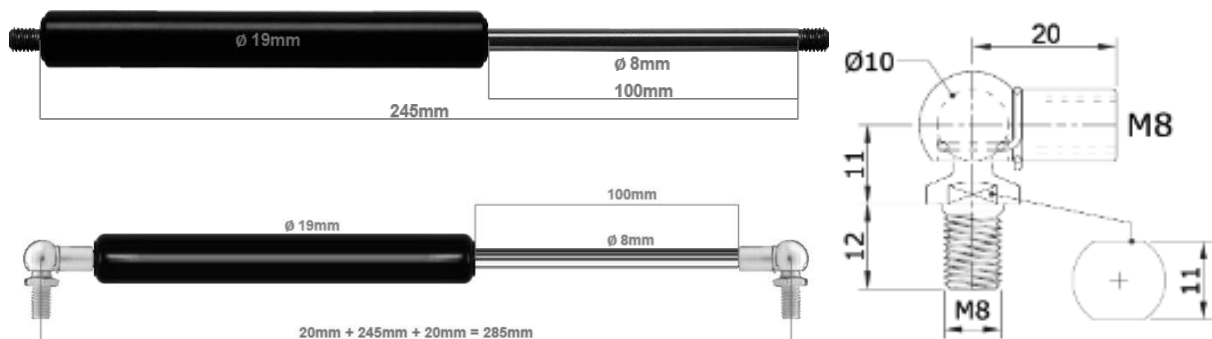


Fig. 10. Spring dimensions with joints.

Actual assemble: the personalized knee brace shown in Figures 11 was finally assembled from the printed elements together with the actuator.



Fig. 11. Views of the final assembly of the orthosis



## 6. SUMMARY

3D printing is the technology that increase its popularity rapidly in recent years. Products manufactured by using a 3D printer are useful both in everyday life and in industrial sectors dealing with commercial production. Using CAD design in the Autodesk Inventor 2024 and Siemens NX environments, the efficient development of the orthosis assembly model and the introduction of necessary corrections at the test printing stage were possible. Additive manufacturing using FDM technology with the appropriate selection of material is a relatively simple process. It requires only basic theoretical knowledge in the field of operating the control panel, basic printer maintenance and knowledge of computer software dedicated to a given device model. Treatment of knee joint problems requires the use of special stiffeners, which helps the joint to be kept in its proper position and not to exposed it to overload. By using appropriate orthoses, we are able to full recovery faster and more confidently. They are useful primarily in rehabilitation after fractures, surgeries, Achilles tendon damage and other similar problems. While developing the project, it was primal task to balance the comfort of use and functionality of the orthosis based solely on the anatomical dimensions of the lower limb of the author of the work. The greatest difficulty encountered was the external shape of the knee, which had to be taken into account in order to maintain the above-mentioned. features. The ideal solution would be to use a 3D scanner and combine the spatial visualization of the object for which the solution is being implemented with an assembly design in a virtual environment. This would reduce the consumption of time, energy and material for work related to verifying the design assumptions of the developed orthosis. Additionally, after determining the final geometry of the orthosis and the material from which it will be made, a strength analysis should be performed using, for example, the finite element method (FEM). The use of an actuator is a futuristic idea, aimed at, among others: considering the inclusion of automation elements in the designs of orthopedic appliances as various types of stabilizers, counters, or supporting parts. The next stage of design research should be to perform operational tests, including functional tests, and perform optimization or structural improvement of the described solution in order to obtain a more optimal one.

## 7. CONCLUSIONS

The analysis of the prints produced in the course of the work and the complete actual assembly of the developed orthosis allowed to formulate following conclusions:

- The developed prototype of a personalized knee orthosis fulfills the intended functions, it stabilizes and relieves the joint, and also keeps it in a given position, preventing from sudden movements.
- The use of a pneumatic actuator has executed the expected effect - it does not allow for a sudden change in the bending angle. Considering that this is only a prototype, it offers considerable scope for developing the idea of an orthopedic device using an automation element.
- The use of computer support in creating CAD models significantly speeds up the design process. The possibility of relatively simple dimensions change and other possible corrections is crucial in today's times which require for us to increase our use of computer support in our projects.

- The process of manufacturing elements using additive technologies is a process that requires much less time, energy and material use compared to other manufacturing methods, which makes it certainly one of the most developing technologies.

## BIBLIOGRAPHY

1. Kugaevskii Sergey, Pizhenkov Eugenius, Gamberg Alexey: „The effectiveness of additive SLM-technologies in the manufacture of cutting tools”; *Materials Today: Proceedings*; Volume 19, Part 5, Strony 1977-1981; 2019.
2. Blog internetowy B3D: „Technologie przyrostowe, podstawowe informacje”, 2021 [Online]. Available: [b3d.com.pl/technologie-przyrostowe-podstawowe-informacje/](http://b3d.com.pl/technologie-przyrostowe-podstawowe-informacje/) (dostęp dnia 14.12.2023).
3. Khan Saifuddin, Joshi Ketan, Deshmukh Samadhan: „A comprehensive review on effect of printing parameters on mechanical properties of FDM printed parts”; *Materials Today: Proceedings*; Volume 50, Part 5, Strony 2119-2127; 2022.
4. Ślusarczyk Paweł: „Technologia FDM – Co to jest i na czym polega?”, 2018 [Online]. Available: [centrumdruku3d.pl/technologia-fdm-rozdzial-1-co-to-jest-i-na-czym-polega/](http://centrumdruku3d.pl/technologia-fdm-rozdzial-1-co-to-jest-i-na-czym-polega/) (dostęp dnia 14.12.2023).
5. Blog internetowy ACUSMED: „Co to jest orteza i jakie ma zastosowanie?” [Online]. Available: [acusmed.pl/blog/co-to-jest-orteza-i-jakie-ma-zastosowanie/](http://acusmed.pl/blog/co-to-jest-orteza-i-jakie-ma-zastosowanie/) (dostęp dnia 22.12.2023).
6. Lek. Wańczyk-Dręczewska Beata, Wasilonek Monika: „Orteza - zastosowanie, rodzaje”, 2018 [Online]. Available: [www.medonet.pl/zdrowie,orteza---zastosowanie--rodzaje/](http://www.medonet.pl/zdrowie,orteza---zastosowanie--rodzaje/) (dostęp dnia 22.12.2023).
7. Rysunek 3A: „Zegarowa orteza stawu kolanowego” [Online]. Available: [www.orteo.pl/zegarowa-orteza-stawu-kolanowego-breg-komfort-i-stabilizacja-t-scope-knee](http://www.orteo.pl/zegarowa-orteza-stawu-kolanowego-breg-komfort-i-stabilizacja-t-scope-knee) (dostęp dnia 21.12.2023).
8. Rysunek 3B: „Półsztywna orteza stawu kolanowego” [Online]. Available: [www.orteo.pl/orteza-kolana-z-szynami-stabilizujaca-bocznie-i-odciazajaca-armor-ark2104](http://www.orteo.pl/orteza-kolana-z-szynami-stabilizujaca-bocznie-i-odciazajaca-armor-ark2104) (dostęp dnia 21.12.2023).
9. Rysunek 3C: „Elastyczna orteza stawu kolanowego” [Online]. Available: [www.medicaltradecenter.pl/pl/p/Orteza-kolana-GenuAction/693](http://www.medicaltradecenter.pl/pl/p/Orteza-kolana-GenuAction/693) (dostęp dnia 21.12.2023).
10. Capanidis Dymitry, Kowalewski Piotr: “Przegląd systemów wspomagania procesów konstruowania i wytwarzania”, Tom 1, Strony 25 – 42, Oficyna Wydawnicza Dolnośląskiej Wyższej Szkoły Przedsiębiorczości i Techniki im. Jana Wyżykowskiego, 2012.
11. Rysunek 23: „Drukarka Prusa i3 MK3” [Online]. Available: [pl.aliexpress.com/i/1005004753071285.html](http://pl.aliexpress.com/i/1005004753071285.html) (dostęp dnia 21.12.2023)
12. Strona Atmat.pl: „Te filament warto znać” [Online]. Available: [www.atmat.pl/te-filamenty-warto-znac.-dowiedz-sie-wiecej-o-ich-wlasciwosciach.](http://www.atmat.pl/te-filamenty-warto-znac.-dowiedz-sie-wiecej-o-ich-wlasciwosciach.) (dostęp dnia 21.12.2023)
13. Sklep botland.com.pl „Filament PLA CarbonLook” [Online]. Available: [botland.com.pl/filamenty-pla/22915-filament-rosa3d-pla-carbonlook-175mm-1kg-carbon-black](http://botland.com.pl/filamenty-pla/22915-filament-rosa3d-pla-carbonlook-175mm-1kg-carbon-black) (dostęp dnia 21.12.2023).
14. Blog Prusa 3D „Wypełnienie gyroidalne” [Online]. Available: [blog.prusa3d.com/pl/wszystko-co-musisz-wiedziec-o-wypelnieniu\\_43579/](http://blog.prusa3d.com/pl/wszystko-co-musisz-wiedziec-o-wypelnieniu_43579/) (dostęp dnia 21.12.2023).



17th-19th June 2024  
Gliwice, Poland

DEPARTMENT OF ENGINEERING MATERIALS AND BIOMATERIALS  
FACULTY OF MECHANICAL ENGINEERING  
SILESIA UNIVERSITY OF TECHNOLOGY

## INTERNATIONAL STUDENTS SCIENTIFIC CONFERENCE

### Wpływ obróbki plastycznej na mikrostrukturę i własności stopu Cu-Cr

Marcin Jaroszek<sup>a</sup>, Beata Krupińska<sup>b</sup>

<sup>a</sup> Politechnika Śląska, Wydział Mechaniczny Technologiczny, Mechatronika Przemysłowa

<sup>c</sup> Politechnika Śląska, Wydział Mechaniczny Technologiczny, Katedra Materiałów Inżynierskich i Biomedycznych, 44-100 Gliwice, ul. Konarskiego 18a, e-mail: beata.krupinska@polsl.pl

**Streszczenie:** Celem pracy było określenie wpływu odkształcenia plastycznego na wybrane własności mechaniczne i mikrostrukturę stopu miedzi CuCr. Materiał poddano odkształceniu plastycznemu, a następnie wyżarzono w różnych temperaturach. Wykonano badanie ścieralności metodą ball-on-plate o ruchu posuwisto-zwrotnym, które zostało zrealizowane przy użyciu trybometru firmy CSM Instruments do badań trybologicznych w trybie obrotowym, oscylacyjnym i posuwisto-zwrotnym, możliwość badań trybologicznych w cieczech i w temperaturze do 150 °C, wyposażony w profilometr Tylor-Hubson Sutronic 25 oraz zbadano wytarcie za pomocą mikroskopu elektronowego.

**Abstract:** The aim of the work was to determine the influence of plastic deformation on selected mechanical properties and microstructure of the CuCr copper alloy. The material was subjected to plastic deformation and then annealed at various temperatures. An abrasion test was carried out using the ball-on-plate method with reciprocating movement, which was carried out using a CSM Instruments tribometer for tribological tests in rotational, oscillating and reciprocating mode, possibility of tribological tests in liquids and at temperatures up to 150 °C, equipped with with a Tylor-Hubson Sutronic 25 profilometer and abrasion was examined using an electron microscope.

**Słowa kluczowe:** Cu-Cr, odkształcenie plastyczne, mikrostruktura, ścieralność

#### 1. WSTĘP

Miedź jest ważnym pierwiastkiem znanym już od starożytności. Należy do grupy metali nieżelaznych. Charakteryzuje się metalicznym połyskiem i czerwoną barwą. Zaletami czystej miedzi jest duża plastyczność, dobra przewodność cieplna i elektryczna oraz odporność na korozję. Miedź nie rdzewieje a także nie trzeba jej specjalnie konserwować co sprawia, że jest materiałem dobrze znoszącym wpływ czasu. Głównymi zastosowaniami między innymi są: przewody elektryczne, pokrycia dachów, rury i wymienniki ciepła [1, 2].

Stopy miedzi z cynkiem są nazywane mosiądzami, z niklem miedzioniklami, natomiast z cyną albo pozostałymi pierwiastkami - brązami. Własności mechaniczne miedzi można zwiększyć stosując niewielki dodatek pierwiastków stopowych. Taki materiał nazywa się

miedzią stopową. Dodatek pierwiastków ma wpływ na zmianę własności mechanicznych oraz mikrostruktury [3-5].

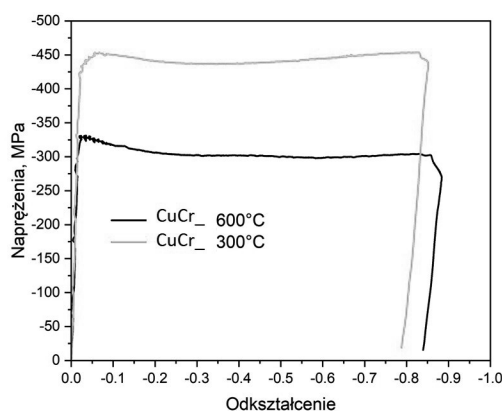
Chrom jest jednym z pierwiastków stopowych dodawanych do miedzi w celu zwiększenia jej wytrzymałości oraz zmiany konduktywności. W przypadku stopu CuCr, dodatek chromu może powodować zmiany struktury krystalicznej, co wpływa na zwiększenie ilości defektów w mikrostrukturze oraz zmianę przewodnictwa stopu. Przewodność materiału zależna od wielu czynników, w tym od struktury krystalicznej, rozkładu fazowego oraz obecności dodatków stopowych. Dodatek chromu do stopu CuCr może jednocześnie zwiększyć, jak i zmniejszyć przewodność w zależności od warunków procesu wytwórczego oraz zawartości chromu. Dodatek chromu do stopu CuCr ma wpływ na jego konduktywność poprzez strukturę krystaliczną, rozkład fazowy oraz wystąpienia defektów punktowych i granic ziaren, co powoduje zmiany właściwości fizycznych materiału [6].

Wiele przewodów ma żyły wykonane w technologii wielodrutowej tzn. kilka lub kilkanaście cieńszych drutów splecionych ze sobą. W przypadku gdy taki przewód pracuje, występuje tarcie pomiędzy poszczególnymi drutami co w ostateczności prowadzi do zużycia się przewodu.

## 2. MATERIAŁY I METODYKA BADAŃ

Badanym stopem jest znormalizowany stop CuCr gdzie około 0,85% to Cr, a 0,15% Zr. Do badań przygotowano stop w postaci cylindrycznej o średnicy  $\phi 12\text{mm}$  i wysokości 12mm. Przed rozpoczęciem badania materiał wyżarzano w temperaturze  $500^{\circ}\text{C}$  przez godzinę w ochronnej atmosferze argonu.

Badany stop poddano odkształceniu plastycznemu na zimno i gorąco. Miedź stopowa była poddana odkształceniu plastycznemu z wartością stopnia gniotu wynoszącym 60%. Na rysunku 1 przedstawiono krzywe naprężenia w funkcji odkształcenia stopu CuCr odkształconego plastycznie z wykorzystaniem symulatora obróbki cieplno-plastycznej Gleeble 3800 będącego na wyposażeniu Laboratorium Naukowo-Dydaktycznego Nanotechnologii i Technologii Materiałowych Politechniki Śląskiej. Na podstawie wykonanych testów stwierdzono, iż wraz ze wzrostem temperatur odkształcenia plastycznego z  $300$  do  $600^{\circ}\text{C}$  stwierdzono obniżenie wartości maksymalnych naprężeń uplastyczniających o około 130 MPa, a dokładniej odpowiednio z  $455\text{MPa}$  na  $325\text{MPa}$ .



Rysunek 1. Krzywe naprężenia w funkcji odkształcenia stopu CuCr odkształconego plastycznie w temperaturze  $600$  oraz  $300^{\circ}\text{C}$

Figure 1. Stress versus strain curves of a CuCr alloy plastically deformed at 600 and 300 °C

Wyżarzanie rekrystalizujące zostało zrealizowane dla materiału, który wcześniej był odkształcony plastycznie na zimno. Stop wyżarzono w temperaturach: 450°C, 500°C i 550°C, które były dobrane na podstawie analizy literatury [6-8]. Proces wykonano w piecu firmy Nabertherm w atmosferze ochronnej Ar. Czas trwania wyżarzania materiału wynosił 1h. Następnie materiał chłodzono swobodnie do temperatury pokojowej.

Tabela 1. Oznaczenia w zależności od zastosowanej obróbki cieplno-plastycznej.

Table 1. Markings depending on used type of thermoplastic treatment.

Oznaczenie stopu	Temperatura odkształcenia plastycznego, [°C]	Temperatura wyżarzania, [°C]
CuCr/300(OP)	300	-
CuCr/600(OP)	600	-
CuCr/300(OP)/450(W)	300	450
CuCr/300(OP)/500(W)	300	500
CuCr/300(OP)/550(W)	300	550

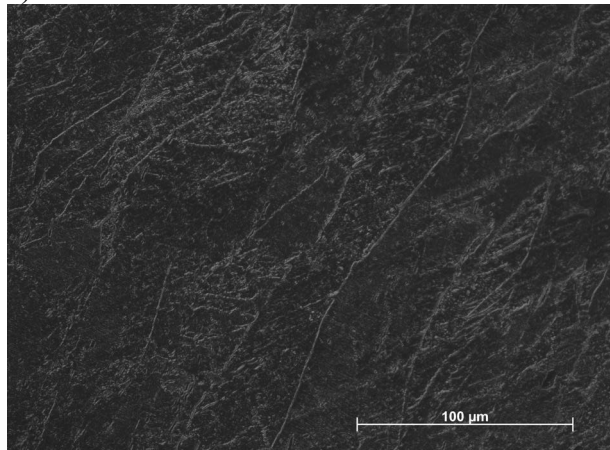
*OP – obróbka plastyczna; W - wyżarzanie*

### 3. WYNIKI BADAŃ

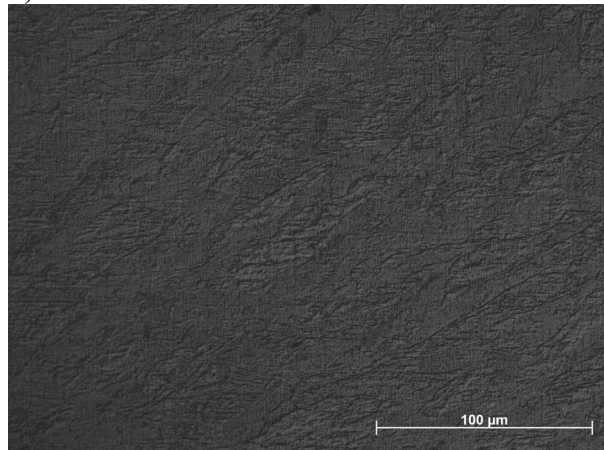
#### 3.1. 3.1. Badanie mikrostruktury

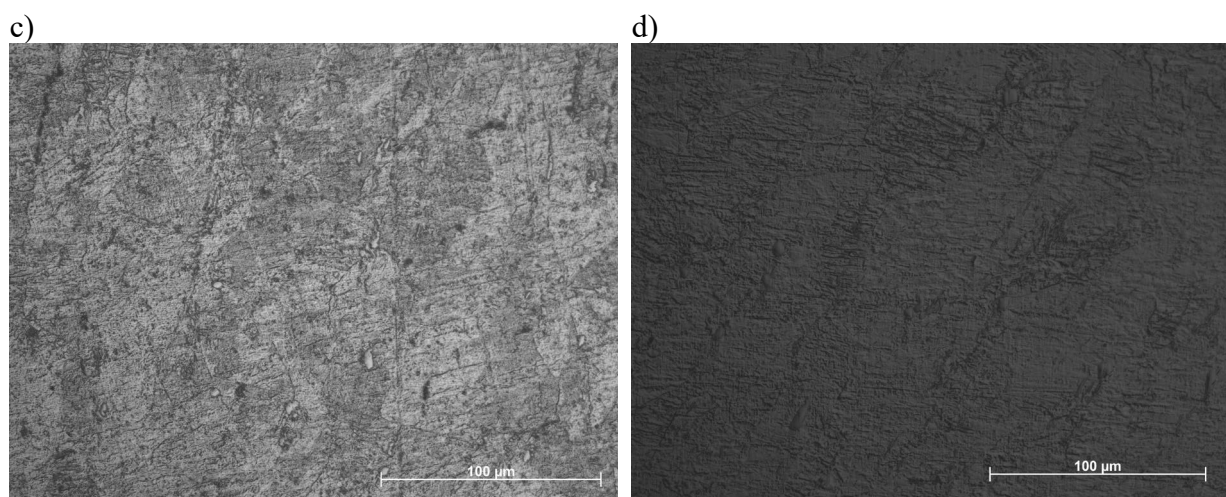
Badania mikrostruktury (Rysunek 2a-2d) zostały zrealizowane za pomocą mikroskopu świetlnego Axio Observer firmy Zeiss wraz z dedykowanym oprogramowaniem do analizy obrazu struktur metalograficznych. Do badań mikrostruktury zostały przygotowane zglądy metalograficzne przy użyciu: półautomatycznej szlifierko-polerki STRUERS LaboPol-5 z głowicą LaboForce-3, szlifierko-polerki STRUERS Tegramin-30 z głowicą automatyczną oraz dozownikiem wielokanałowej oraz urządzenia do elektro-polerowania i elektrotrawienia - automatycznej elektropolerki do zglądów inkludowanych wraz z bazą odczynników STRUERS LectroPol-5.

a)



b)





Rysunek 2. Mikrostruktura stopu a)CuCr/600(OP); b)CuCr/300(OP); c)CuCr/300(OP)/550(W); d) CuCr/300(OP)/450(W)

Figure 2. Microstructure of the alloy a) CuCr/600(OP); b)CuCr/300(OP); c)CuCr/300(OP)/550(W); d) CuCr/300(OP)/450(W)

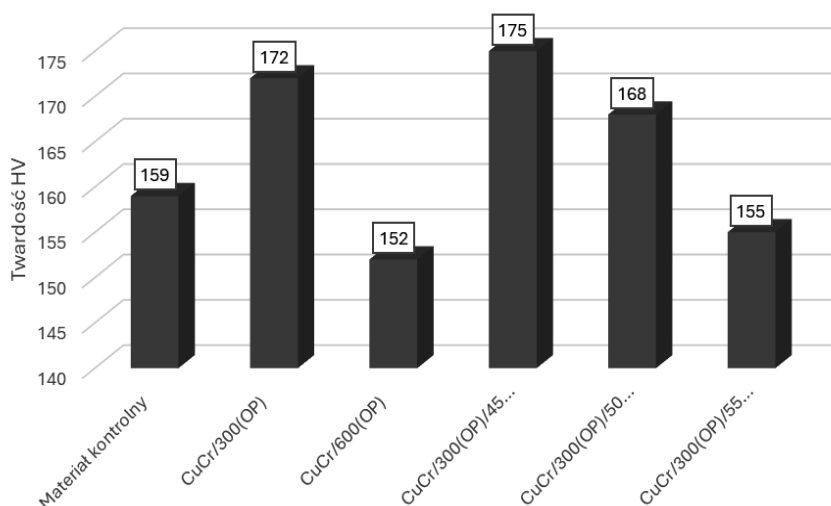
### 1.2. Badanie twardości

Badania twardości zrealizowano przy użyciu twardościomierza Vickersa (HV5) z automatycznym torem pomiarowym z wykorzystaniem analizy obrazu FUTURE-TECH FM-ARS 9000 (czas pom. 10 s).

Tabela 1. Wyniki pomiaru twardości stopów CuCr

Table 2. Hardness measurement results stopów CuCr

Twardość HV					
Materiał kontrolny	CuCr/300 (OP)	CuCr/600 (OP)	CuCr/300 (OP)/450(W)	CuCr/300 (OP)/500(W)	CuCr/300 (OP)/550(W)
159	172	152	175	168	155



Rysunek 3. Wyników badania twardości stopów CuCr

Figure 3. The hardness test results CuCr alloys

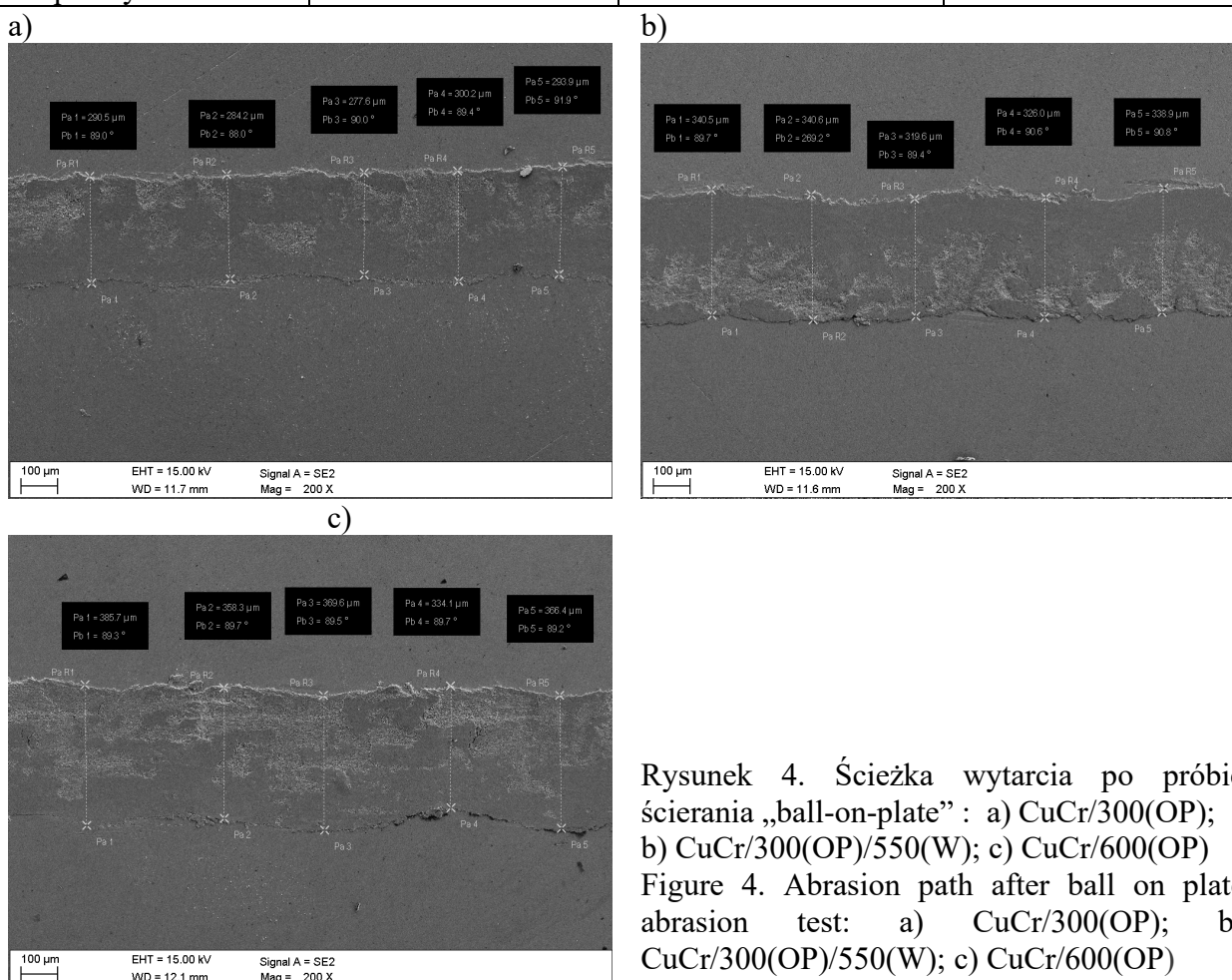
### 1.3. Badanie ścieralności

Pomiar odporności na ścieranie metodą ball-on-plate o ruchu posuwisto-zwrotnym zostało zrealizowane przy użyciu trybometru firmy CSM Instruments do badań trybologicznych w trybie obrotowym, oscylacyjnym i posuwisto-zwrotnym, możliwość badań trybologicznych w cieczach i w temperaturze do 150 °C, wyposażony w profilometr Tylor-Hubson Sutronic 25.

Materiałem ścierającym była kulka wykonana z  $Al_2O_3$  o średnicy 6mm. Badanie wykonano w temperaturze pokojowej. Siła docisku kulki do ścieranego materiału wynosiła 5N. Wytarcie było w formie linii, gdzie kulka poruszała się z maksymalną prędkością 5 cm/s wykonując łącznie 5000 cykli. Zarejestrowany wynik współczynnika tarcia dla badanych materiałów zamieszczono w tabeli 3. Szerokość wytarcia wyznaczono przy użyciu mikroskopu elektronowego Supra-35 (Rysunek 4, Tabela 4).

Tabela 3. Współczynnik tarcia stopów CuCr odkształconych plastycznie i wyżarzonych  
Table 3. Friction coefficient of plastically deformed and annealed alloys ( CuCr/300(OP) ; CuCr/300(OP)/550(W) ; CuCr/600(OP))

Badany materiał	CuCr/300(OP)	CuCr/300(OP)/550(W)	CuCr/600(OP)
Wartość współczynnika tarcia	0,52	0,53	0,54



Rysunek 4. Ścieżka wytarcia po próbie ścierania „ball-on-plate”: a) CuCr/300(OP); b) CuCr/300(OP)/550(W); c) CuCr/600(OP)  
Figure 4. Abrasion path after ball on plate abrasion test: a) CuCr/300(OP); b) CuCr/300(OP)/550(W); c) CuCr/600(OP)

Tabela 4. Wyniki pomiaru szerokości ścieżki wytarcia

Table 4. Results of measurement of abrasion width

	Szerokość wytarcia [ $\mu\text{m}$ ]					Wartość średnia
CuCr/300 (OP)	290,5	284,2	277,6	300,2	293,9	289,28
CuCr/300 (OP) /550(W)	340,5	340,6	319,6	326	338,9	333,12
CuCr/600 (OP)	385,7	358,3	269,6	334,1	366,4	342,82

## 2. PODSUMOWANIE

Zmiana własności zależy głównie od stopnia gniotu, temperatury, ale także od szybkości odkształcenia. Z rysunku 1 wynika, że stop miedzi w temperaturze 600°C wymagał najmniejszej siły odkształcenia. Oznacza to, że w materiale nie doszło do umocnienia. Dla temperatury 300°C potrzebna siła była znacznie większa, oznacza to, że doszło do umocnienia a zgniot został wykonany na zimno.

Podczas wyżarzania po zgniocie dochodzi do przemian w materiale. Dostarczona energia pozwala na powrót atomów do położenia o najmniejszej energii. W wyniku czego zachodzi stopniowy zanik defektów sieci. [4]

Oba materiały przedstawione na rysunku 2 c) i d) były poddane obróbce plastycznej i następnie wyżarzone. Jedyną różnicą tkwi w temperaturze wyżarzania 550 i 450 °C. W przypadku obróbki plastycznej z wyższą temperaturą można zauważyć po granicy ziaren, iż są one zauważalnie większe niż przypadku wyżarzania w temperaturze 450 °C. Świadczy to o wystąpieniu zjawiska rekrytalizacji wtórnej. Charakteryzuje się ona rozrostem ziaren i pochłanianiem tych mniejszych. Zjawisko to może wystąpić w górnych zakresach rekrytalizacji materiału. Dla badanego materiału zakres ten wynosi od około 400 do 600 °C. Analizując mikrostruktury przedstawione na rysunku 2 a) i b) możemy zaobserwować tworzenie się zarodków nowych ziaren. W materiale wyżarzonym w niższej temperaturze (450°C) zarodki nie rozrosły się do takiej wielkości jak w przypadku wyżarzania w temperaturze 500 °C. Widoczne zarodkowanie w obu przypadkach świadczy o wystąpieniu rekrytalizacji pierwotnej.

Odształcenie plastyczne to proces, w którym materiał ulega trwałej deformacji pod wpływem zewnętrznej siły. W przypadku stopów miedzi, odkształcenie plastyczne ma istotny wpływ na ich konduktywność elektryczną. Stopy miedzi są jednym z najważniejszych materiałów stosowanych w przemyśle elektrycznym i elektronicznym ze względu na swoją wysoką konduktywność.

Podczas odkształcenia plastycznego stopu poniżej temperatury rekrytalizacji, do sieci krystalicznej wprowadzane są dyslokacje. Dyslokacje te utrudniają ruch innych dyslokacji, prowadząc do wzrostu wytrzymałości i twardości materiału. Stopień zgniotu ma istotny wpływ na umocnienie materiału.

Wyżarzanie odkształconego plastycznie stopu prowadzi do rekrytalizacji i wzrostu ziaren, co może zmniejszyć gęstość dyslokacji, a w konsekwencji zmniejszyć twardość materiału. Widać to podczas zestawienia wyników pomiaru twardości (tabela 2) z współczynnikiem tarcia (tabela 3), szerokością ścieżki wytarcia (tabela 4). Zachodzi tu mocna korelacja pomiędzy dużą twardością materiału, a małą szerokością ścieżki wytarcia.



## PODZIĘKOWANIE

Praca powstała w wyniku realizacji projektu w ramach kształcenia zorientowanego projektowo - PBL, w konkursie X w ramach programu Inicjatywa Doskonałości – Uczelnia Badawcza, Wydział Mechaniczny Technologiczny, Politechnika Śląska.

## LITERATURA

1. Z. Celiński, Materiałoznawstwo elektrotechniczne, Oficyna Wydawnicza Politechniki Warszawskiej, Warszawa 1998.
2. L. Dobrzański, Podstawy nauki o materiałach i metaloznawstwo, Wydawnictwo Naukowo-Techniczne, Warszawa 2002.
3. M. Blicharski, Wstęp do inżynierii materiałowej, Wydawnictwo Naukowo-Techniczne, Warszawa 1998.
4. K. Przybyłowicz, Metaloznawstwo, Wydawnictwo Naukowo-Techniczne, Warszawa 1999
5. K. i J. Przybyłowicz, Materiałoznawstwo w pytaniach o odpowiedziach, Wydawnictwo Naukowo-Techniczne, Warszawa 2000.
6. Z. Rdzawski, Miedź stopowa, Wydawnictwo Politechniki Śląskiej Gliwice 2009.
7. Z. Rdzawski, Rapidly solidified strips of Cu-Cr alloys, Scripta materialia 34 (11), 1759-1763, 1996.



17th-19th June 2024  
Gliwice, Poland

DEPARTMENT OF ENGINEERING MATERIALS AND BIOMATERIALS  
FACULTY OF MECHANICAL ENGINEERING  
SILESIA UNIVERSITY OF TECHNOLOGY

## INTERNATIONAL STUDENTS SCIENTIFIC CONFERENCE

### Corrosion behaviour of passivated 304 stainless steel

Justyna Jaworska, Monika Kciuk<sup>a</sup>

<sup>a</sup> Silesian University of Technology, Faculty of Mechanical Engineering, Department of Engineering Materials and Biomaterials  
email: monika.kciuk@polsl.pl

**Abstract:** In this paper corrosion tests have been conducted on 304 steel, chemically passivated in 10% nitric acid, 10% and 20% citric acid. Corrosion behaviour have been investigated in 3.5% NaCl solution. The aim of this work was to compare corrosion resistance of examined material after passivation in different solutions. EIS measurements were performed in a conventional three-electrode cell at ambient temperature (25°C), after stabilization for approximately 1 h at open-circuit potential (OCP). The data obtained as a result of the study allowed for determination of the Bode and Nyquist plots.

**Keywords:** 304 austenitic stainless steel, corrosion resistance, EIS

### 1. INTRODUCTION

Modern technology places a number of different requirements on construction materials in terms of durability and reliability of the structure, low cost and availability of the materials used, good strength properties, corrosion resistance and low specific weight. There is a constant search for new materials and technologies that can meet the requirements. Issues related to corrosion currently deserve more and more attention due to the increased corrosive aggressiveness of the natural environment due to increasing air and water pollution [1].

The chemical resistance of a group of corrosion-resistant steels is based entirely on the phenomenon of passivation. The corrosion resistance results from the thin oxide film formed on the surface of the steel (Figure 1.) [2]. The most commonly used chemical method to passivate a stainless steel surface is to apply nitric acid [3]. Nitric is a strong mineral acid and will quickly dissolve all iron compounds and other trace metals on the surface. It is also a strong oxidizer and will simultaneously activate the chromium oxide layer. Even though nitric acid is a strong chemical, high temperatures and extended times are used to ensure the reaction is effective and complete [4-6].

Citric acid is sometimes used for passivating stainless steel. As well as being effective at removing iron and its compounds from surfaces, it is safer to use than nitric acid, is biodegradable, produces fewer effluent concerns and is also used as a food ingredient. But, it is not an oxidizer and will not achieve the second step of classic passivation and relies on natural air oxidation [7].

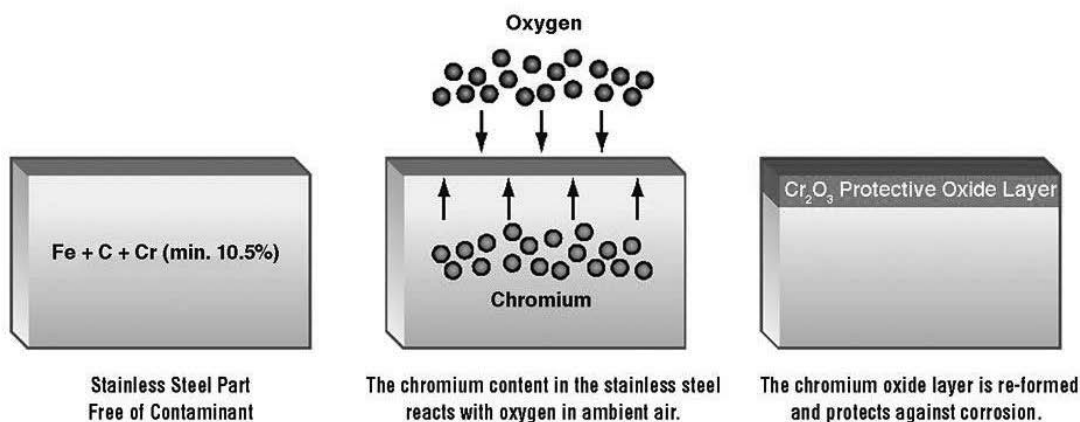


Figure 1. Stainless steel passivation process [2]

## 2. MATERIALS AND METHODS

304 austenitic stainless steel was used in this study with chemical composition in wt. 100% as follows:  $\text{C} \leq 0.07$ ;  $\text{Si} \leq 1.0$ ;  $\text{Mn} \leq 2.0$ ;  $\text{P} \leq 0.045$ ;  $\text{S} \leq 0.015$ ,  $\text{Cr} = 17.5\text{-}19.5$ ;  $\text{Ni} = 8.0\text{-}10.5$ ;  $\text{N} \leq 0.11$ . The metallographic examinations were performed using Zeiss Axio Observer Z1m optical microscope with 400 and 1000x magnification.

Before corrosion investigations the base steel was cut into 10mm x 10mm plates and surface of the material was grinded with SiC paper and polished with  $\text{Al}_2\text{O}_3$  solution in order to obtain the surface without roughness and scratches. All specimens were ultrasonically cleaned in ethanol for 10 minutes.

Chemical passivation was performed in 10% nitric acid, 10% and 20% citric acid solution. A citric acid solution is an environmentally friendly alternative to nitric acid, offering effective passivation while minimizing environmental impact.

Corrosion behaviour have been investigated using apparatus showed in Figure 2. The set consists of a steel wire as a counter-electrode (CE), the reference electrode Ag/AgCl (RE) and working electrode (WE) includes an examined material. To evaluate sample corrosion performance electrochemical impedance spectroscopy (EIS) was used. The electrolyte was 3.5% NaCl solution, naturally aerated at room temperature with an exposed sample area of 34.2  $\text{mm}^2$ .

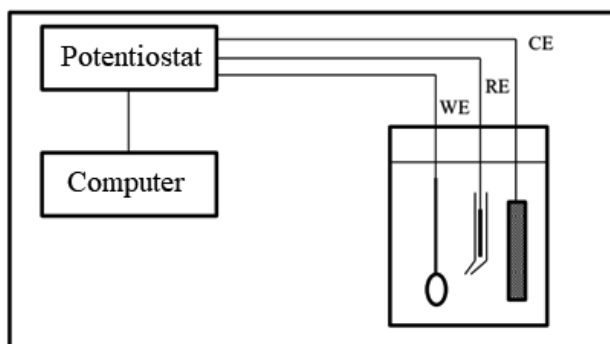


Figure 2. Experimental set-up of the corrosion investigations

### 3. EXPERIMENT RESULTS

Based on metallographic observations of austenitic steel 0H18N9 (1.4301) 304 in the initial state, it was found that the structure of the tested steel consisted of austenite grains with numerous slip lines and bands after plastic deformation (Figure 3).

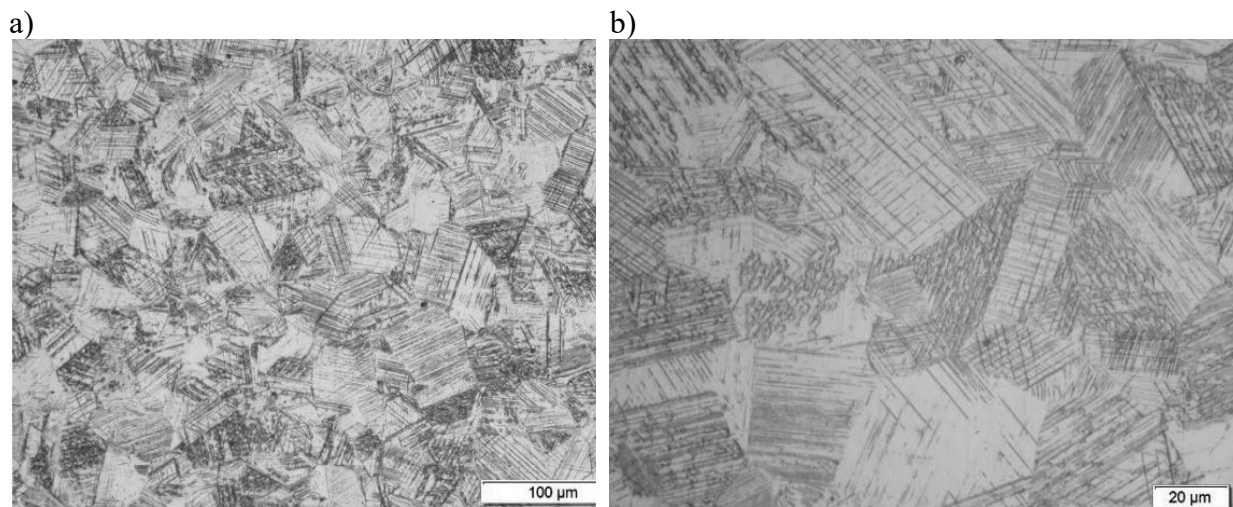


Figure 3. Optical micrographs of AISI 304 steel in initial state a) 400x, b) 1000x respectively

Table 1 shows the impedance results for the tested samples, Figure 4 shows Nyquist plots and Figure 5 show Bode plots in the coordinate system:  $\log(Z)$ ,  $\log(f)$ , phase shift angle.

Nyquist plots of the samples represent fragments large incomplete semicircles, which are a typical impedance response for thin films oxides. Analyzing Nyquist plots, it was observed that the highest value of  $\text{Im}Z_x$  (opposite imaginary impedance) and the largest semicircle radius was achieved in case sample passivated in 10% nitric acid ( $\text{Im}Z_x = -310 \text{ k}\Omega \cdot \text{cm}^2$  at impedance real equal to  $\text{Re}Z_x = 720 \text{ k}\Omega \cdot \text{cm}^2$ ), however, the effects are not significantly better than these obtained for steel in its initial state. The lowest value was shown for the sample passivated in 20% citric acid ( $\text{Im}Z_x = -320 \text{ k}\Omega \cdot \text{cm}^2$   $\text{Re}Z_x = 970 \text{ k}\Omega \cdot \text{cm}^2$ ).

The sample in its original state, without a chemically produced passive layer, showed higher  $\text{Im}Z_x$  value ( $\text{Im}Z_x = -340 \text{ k}\Omega \cdot \text{cm}^2$   $\text{Re}Z_x = 890 \text{ k}\Omega \cdot \text{cm}^2$ ) than the 10% passivated sample citric acid ( $\text{Im}Z_x = 330 \text{ k}\Omega \cdot \text{cm}^2$  at  $\text{Re}Z_x = 900 \text{ k}\Omega \cdot \text{cm}^2$ ). The Nyquist plot shows that passivation in citric acid decrease corrosion. Obtained values of the phase shift angle are very similar for all tested samples, and the curves are represents similar shape.

The highest value of  $R_1$ , i.e. the resistance of metal ions to solution, was found for the sample passivated in nitric acid and this value is much higher than those obtained for remaining samples. The next highest result was obtained for the reference sample ( $4623.76 \Omega \cdot \text{cm}^2$ ), however, this value is almost 5 times lower than for nitric acid ( $19021.93 \Omega \cdot \text{cm}^2$ ). The worst results were obtained for samples passivated in citric acid, of which the sample was the least resistant to corrosion processes passivated in a 20% solution. CPE is a parameter related to diffusion and imperfection surface. The highest values of electrical capacitance CPE1 were recorded for the sample passivated in nitric acid ( $41.165 \text{ S}/\text{cm}^2$ ), and the lowest for the one passivated in citric acid 10% ( $35.345 \text{ S}/\text{cm}^2$ ). Reducing electrical capacity is also associated with increasing the thickness of the passive layer.

Table 1. EIS results of examined samples

Sample	$R_s$ [ $\Omega \cdot \text{cm}^2$ ]	N1	CPE1 [ $\text{S}/\text{cm}^2$ ]	$R_1$ [ $\Omega \cdot \text{cm}^2$ ]
Citric acid 10%	2.734	0.884	35.345	3809.89
Nitric acid 10%	2.830	0.890	41.165	19021.93
Initial state	3.057	0.902	36.264	4623.76
Citric acid 20%	2.107	0.883	37.057	3541.89

The sample passivated in 20% citric acid showed a slightly higher value capacity of CPE1 than the sample in the initial state. Parameter "n" in most cases approaches 1, which indicates that the tested surface is smooth and there are quite passive layers compact and porosity-free.

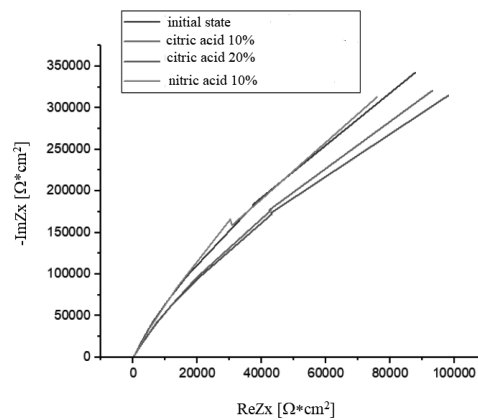


Figure 4. Nyquist plot of experimental data

The lowest value of the N1 parameter was obtained for the reference sample (0.902), on which no passive layer was chemically produced, however, all values are very close to each other. Based on the results obtained, the equivalent system shown in the following was adapted (Figure 6). It consists of two resistors,  $R_s$  and  $R_1$ , respectively, and also contains a capacitor designated CPE1. The beginning of the system is marked with the letter "a" and its end is marked as "a'".

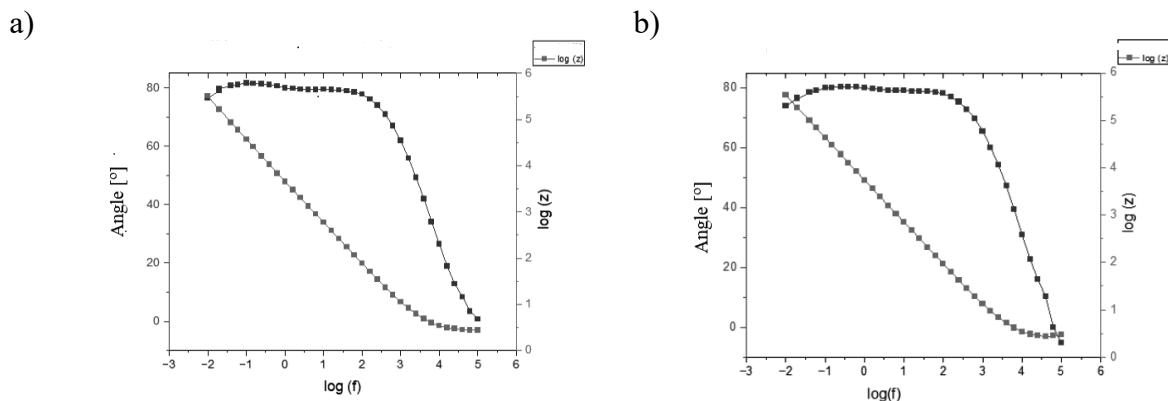


Figure 5. Bode plots a) sample passivated in 10% citric acid, b) sample passivated in 10% nitric acid

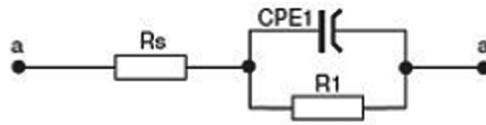


Figure 6. Equivalent Circuits

#### 4. CONCLUSIONS

Based on the analysis of the investigation results, the following conclusions were formulated:

1. Application of the nitric acid solution to the chemical passivation process results in better steel corrosion resistance than in the case of passivation with a citric acid solution of the same concentration.
2. Passivation in both acids, as well as a self-generated passive layer provide effective protection of austenitic steel against pitting corrosion in atmospheric conditions chloride ions.
3. Increasing the concentration of citric acid from 10 to 20% used for chemical passivation does not improve the corrosion resistance of austenitic steel.

#### BIBLIOGRAPHY

1. L. Ma, E.M. Pascalidou, F. Wiame, S. Zanna, V. Maurice, P. Marcu, Passivation mechanisms and pre-oxidation effects on model surfaces of FeCrNi austenitic stainless steel, *Corrosion Science* 167 (2020), s. 252-294
2. <https://www.thefabricator.com/thefabricator/article/testingmeasuring/passivation-basics-will-this-stainless-steel-rust>
3. N. Padhy, R. Paul, U.K. Mudali, B. Raj, Morphological and compositional analysis of passive film on austenitic stainless steel in nitric acid medium, *Applied Surface Science* 257/11 (2011) s. 5088-5097
4. S. Parsons, O. Poyntz-Wright, A. Kent, M.C. McManus, Green chemistry for stainless steel corrosion resistance: life cycle assessment of citric acid versus nitric acid passivation, *Materials Today Sustainability* 3-4 (2019), s. 250-275
5. B. F. Giannetti, P.T.A. Sumodjo, T. Rabockai, A.M. Souza, J. Barboza, Electrochemical dissolution and passivation of tin in citric acid solution using electron microscopy techniques, *Electrochimica Acta* 27/1 (1992) s. 143-148
6. <https://www.pfonline.com/articles/citric-acid-passivation-of-stainless-steel>
7. <https://www.csidesigns.com/blog/articles/passivation-of-stainless-steel-what-is-it-and-how-does-it-work>



17th-19th June 2024  
Gliwice, Poland

DEPARTMENT OF ENGINEERING MATERIALS AND BIOMATERIALS  
FACULTY OF MECHANICAL ENGINEERING  
SILESIA UNIVERSITY OF TECHNOLOGY

## INTERNATIONAL STUDENTS SCIENTIFIC CONFERENCE

### Unconventional applications of additive technologies

Alicja Kłapsia <sup>a</sup>, Emilia Krajewska <sup>a</sup>, Jakub Kuta <sup>a</sup>, Magdalena Szindler <sup>b</sup>, Mirosław Bonek <sup>b</sup>

<sup>a</sup> Silesian University of Technology, Faculty of Mechanical Engineering, Student of Engineering Production and Management, Gliwice

<sup>b</sup> Silesian University of Technology, Faculty of Mechanical Engineering, Department of Engineering Materials and Biomaterials

**Abstract:** The continuous development of additive technologies is beginning to play an increasingly important role in industrial and service industries. The following article presents three unusual uses of additive technologies in industries such as construction, culinary and clothing.

**Keywords:** additive technologies, 3D printing, FDM

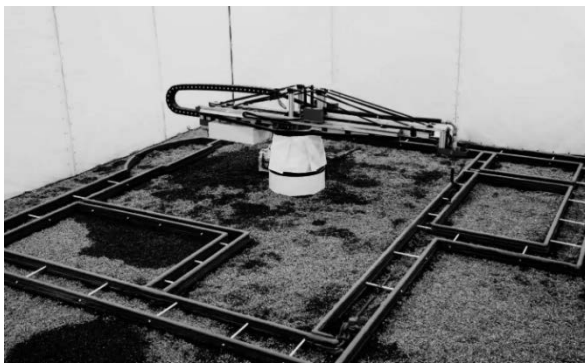
### 1. INTRODUCTION

Products can be manufactured in three different ways: subtractive, shaping, or additive technology. In recent years, additive technology has developed significantly. Initially used for rapid prototyping, additive manufacturing has become increasingly popular for creating finished objects and is now accessible to everyone. 3D printing is often used for producing toys and prosthetics, architectural model prototypes, car parts, and even complete components for aircraft engines or objects later sent into space. The market offers a wide selection of printers and materials. The process involves feeding material in the form of a filament or other into a special printing head, which melts and layers it, creating our product layer by layer. The printing head's operation is based on digital code, which is set after the modeling of the element in a program, followed by subtractive processing and the actual printing of the product. Common materials used in 3D printing are polymeric materials such as PLA (Polylactic Acid), ABS (Acrylonitrile Butadiene Styrene), PET-G, PVA (polyvinyl alcohol), PA 66 (Polyamide 66, more commonly called "nylon"), Laywood (a composite of polymeric materials and wood), and Laybrick (a composite of polymeric materials and gypsum). The dynamic development of this technology makes it an increasingly serious alternative to subtractive and shaping techniques. Furthermore, additive technologies can be increasingly seen in constructions, catering and even the clothing industry. [1]

## 2.1 ADDITIVE TECHNOLOGIES IN CONSTRUCTION

Additive technology is beginning to play a significant role in the construction industry. It offers an innovative approach to building design. Utilizing this technology allows for shorter construction times, reduced environmental pollution, streamlined house design, and, most importantly, lowered construction costs. [2-4]

This technology in construction utilizes robotic arms. Depending on the building's needs, they enable the arm to be placed at its center, allowing the head to move in a wheel-based motion, applying layers of cement (*Picture 1*). Alternatively, special scaffolding and rails can be set up over the construction site to enable the head to apply layers of material (*Picture 2*). [7,8]



*Picture 1 Central robotic arm*



*Picture 2 Different construction of robotic arm*

The process itself resembles classic additive technologies, layering the material according to the design. Special concrete mixtures are used for construction, characterized by a faster setting time.

This reduces the concrete setting time sufficiently for the entire building to be constructed in a single continuous process. The material must also meet other requirements such as high plasticity, allowing easy extrusion of material by the printer nozzle, resistance to weather conditions and mechanical loads to ensure the longevity of the building. Sometimes, reinforcing fibers and setting accelerators are added to the mix to enhance the material's mechanical properties. Furthermore, research also focuses on developing ecological concrete mixtures that could be produced from recyclable waste materials [6-9].

Automating the construction process and reducing waste materials significantly lower construction costs. Buildings constructed using additive technology can be cheaper than their conventional counterparts by 30-60%, depending on their design and location. The time needed to build such a house also decreases significantly, with continuous printer operation and a reduced number of required workers, construction can take from a few days to a few weeks [2-4].

Homes built using additive technology can already be seen in many countries around the world, for example, a 5-story building in China (*Picture 3*), military barracks of 350 m<sup>2</sup> in Texas, USA, and an entire neighbourhood in Mexico built solely using additive technology (*Picture 4*). [8,9]





*Picture 3 5-story building in China*



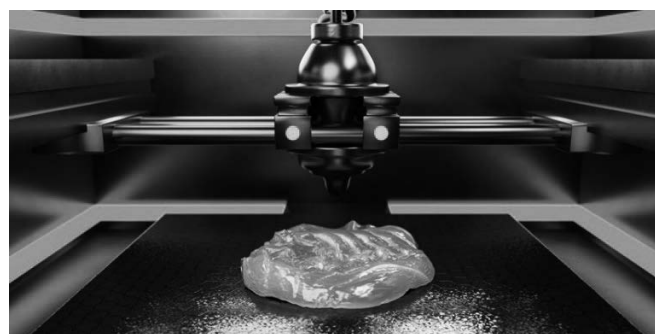
*Picture 4 Estate in Mexico*

Additive technologies in construction have the potential to revolutionize our approach to building design and construction. They not only offer cost and time savings but also provide solutions to various issues such as rapid and easily accessible social housing for the less fortunate, reconstruction of buildings affected by natural disasters, and even the construction of structures on other planets. [5]

## 2.2 ADDITIVE TECHNOLOGIES IN GASTRONOMY

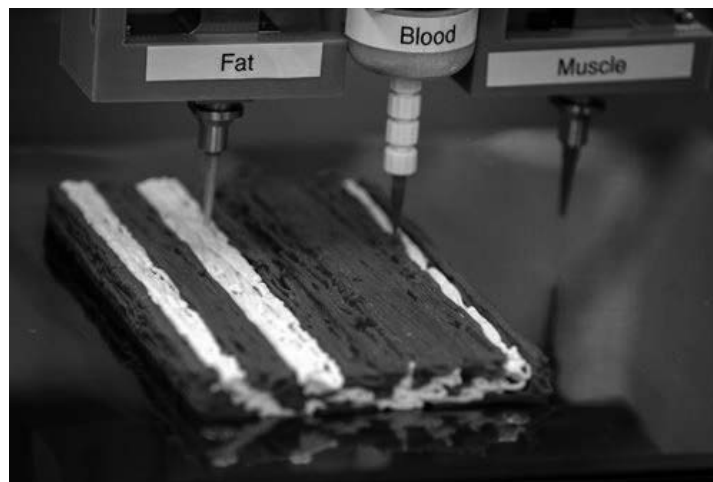
Over the last few years, additive technologies have become the mainstream of technological development to such an extent that a method of food printing has begun to be developed. The original idea was to enable astronauts in space to print food.

In 2007, researchers at Columbia University's Creative Machines Lab developed a personal fabrication system called Fab@Home that allows you to create edible objects for example using cake frosting, chocolate, processed cheese, and peanut butter. They devoted their further research to finding a way to cook food while printing it. Adding lasers to the 3D printer turned out to be the solution that allowed these activities to be performed on the same machine. To check the correctness of the printer, a test was carried out comparing the taste of 3D printed and laser-cooked chicken with traditionally cooked chicken. (Picture 5) The poultry from the machine was twice as juicy, did not shrink that much and, most importantly, tasted like regular chicken. The research team is constantly working on expanding the system's capabilities to include printing from materials in forms other than liquids, such as powders, solids, gels. [10]



*Picture 5 3D printed chicken*

Meat isn't the only thing that additive technology can revolutionize. Israeli company Redefine Meat uses 3D printing to create plant-based meat with the same structure, texture and taste as beef steaks. Among other things, the company analyzes the properties of meat using a standard compression test to see how it changes during chewing and recreates the way muscle fibers adhere to each other to carefully locate plant fibers. The idea is to imitate as closely as possible the various components of a steak bite, such as muscle fibers, fat inclusions and connective tissue, and to simulate the experience of eating it, including its aroma, flavor and juices. (Picture 6) Final plant-based steaks have more fiber and less fat than traditional steaks. Moreover, they have the same amount of protein but no cholesterol. [11]



*Picture 6 Vegetable meat similar to beef steak*

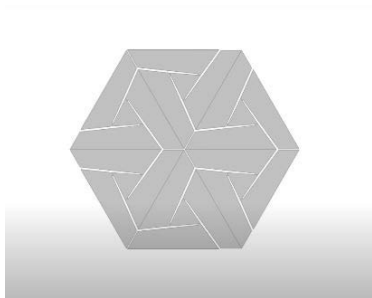
Printing our meals can help fight food waste, which is what the Netherlands-based company Uprising Foods does, which wants to turn discarded food into edible printing material. The increasing availability of consumer printers will likely make 3D printed food more common, and therefore food printing will significantly reduce the amount of carbon dioxide released into the atmosphere and contribute to reducing the amount of animal farming. In a special application it would be possible to select a menu that coincides with food materials with the appropriate viscosity. Advanced technology would help manipulate the amount of nutrients delivered according to demand, but some nutrients, such as vitamin C, are inherently unstable and may degrade under the heat of the printer. [10,11]

### **2.3 ADDITIVE TECHNOLOGIES IN CLOTHING AND FASHION**

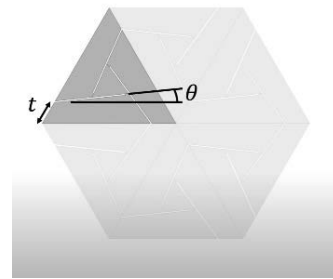
FDM technology (Fused Deposition Modeling) is currently the most used additive method. It has found its application even in fashion industry. FDM makes three-dimensional element by squeezing thread like liquid thermoplastic material throughout the jet. As every other additive technology, FDM applies subsequent layers to create the expected product. After appropriately matching the filaments and the geometry of printed object, it can be used to produce flexible products that will resemble textile materials. The most common materials used in 3D printing is thermoplastic polyurethane (TPU) and sometimes polyamide 66 colloquially known as nylon. Many fashion brands and fashion designers have used clothing printing in various ways. As all

of that methods used FDM technology the differences between them lie in the material geometry design techniques.

The most interesting and complicated method is using self-assembling material. The designer calls it a bistable auxetic structure, it can be called a material that has mechanism. Auxetic materials are the one with negative Poisson's ratio, by definition "these materials expand in all directions when a tensile force is applied in one direction." [12] They also contract laterally when compressed. Designing such a material involves applying special cuts to it, by which that material will be able to spread in different ways and sizes depending on adopted length  $t$  and angle  $\theta$  value (*Picture 8*). During stretching, the smaller elements move and rotate in two dimensions while still being connected (*Picture 7 and 9*). It is also possible to print auxetic material that will expand in three dimensions. Thanks to these properties and using TPU as a filament, printed material will be flexible and stretchy (*Picture 10*). Clothes made by this method are comfortable to wear and can adapt to every build. [13]



*Picture 7 Auxetic material before expanding*



*Picture 8 Length  $t$  and angle  $\theta$*



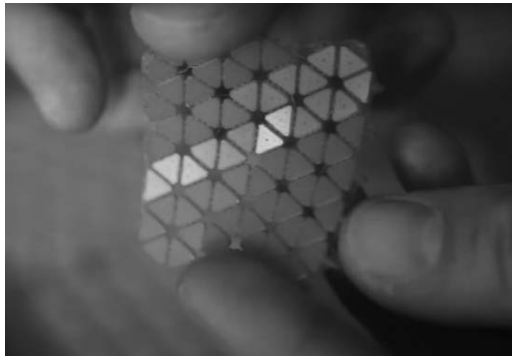
*Picture 9 Expanded auxetic material*



*Picture 10 Dress made of auxetic material*

The next method for printed clothes is to use old chainmail geometry (*Picture 11*). It is possible to print material that will resemble textile materials in its movement. The important thing is to select the appropriate size of printed elements, too small and thinner ones will be more susceptible to breakage. Larger elements, however, will affect the smoothness of material movement.

From the outside, printed garment looks like it is made of scales, but from the inside, the joints of each of the, are visible. The material is printed seam-side up and can bend freely (*Picture 12*). The direction of bending depends on the shape of the shell and connections.



*Picture 11 Chainmail-like material*



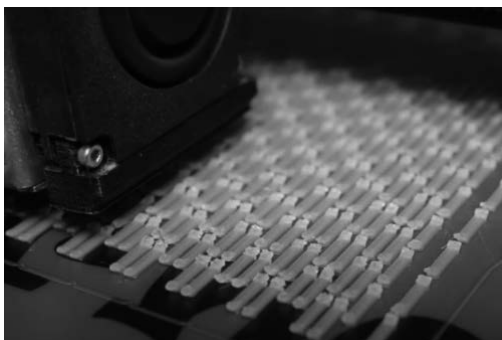
*Picture 12 Printed material*

DIY dress: Hex made of hexagons, which are printed separately and then assembled into the final product. (Picture 13)

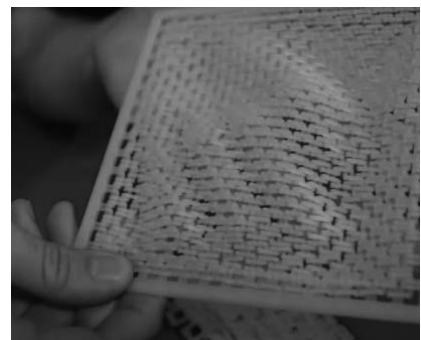


*Picture 13 Hex Dress*

Some also took inspirations from chains. In this case, the entire material is printed in one go. (Picture 14 and 15)



*Picture 14 PinteD chain-like material*



*Picture 15 Chain-like material*

This is how "Harmonograph Dress" was created, printed with the Object500 Connex3 3D Printer, by the New York fashion house ThreeASFOUR (*Picture 16*). The dresses of their design are created based on previously made silhouettes (pl. silhouettes) made of textile material, by scanning a model wearing a given design. Thanks to this, it is possible to continue working on the dress in the program. It is important for designers to maintain the ergonomics of creations, which is why geometry is developed. Parts of the dress that are to be more susceptible to bending (e.g. armholes) are made of smaller and thinner elements, while those that are to be more rigid are made of larger ones. The use of such a connection allows maintaining the ergonomics of the human body and free movement. [14]



*Picture 16 Harmonograph Dress*



*Picture 17 Harmonograph Dress by closer look*

The next example by ThreeASFOUR is "Oscillation Dress" done in a slightly different way. Unlike previous methods, the parts of the creation are connected through fabric linings that have been sewn together. Each part of the dress was printed separately and later lined with a thin layer of fabric. (*Picture 18 and 19*) [14]



*Picture 18 Oscillation Dress*



*Picture 19 Fabric on Oscillation Dress*

Currently, there are many brands working on garment printing using 3D printing methods. Some of them came up with the idea of returning clothes no longer wanted by the consumer to be able to melt them and reuse them, thanks to which the production of clothes from a printer can be ecological.

### 3. CONCLUSIONS

The use of additive technologies is still niche compared to subtractive technologies, but it provides many modern solutions and countless possibilities. The development of this industry branch can have a crucial impact on the future in many sectors, not only in construction, culinary, and clothing.

### BIBLIOGRAPHY

- [1] „Programowanie i obsługiwanie procesu druku 3D” M. Cader, K. Burzyński, E. Burzyńska
- [2] <https://www.youtube.com/watch?v=D19rhG5BPrM>
- [3] <https://www.youtube.com/watch?v=DradkrIHFUI>
- [4] <https://www.youtube.com/watch?v=kmSfAwGmouI>
- [5] <https://all3dp.com/2/first-3d-printed-house/>
- [6] <https://apis-cor.com>
- [7] <https://www.iconbuild.com/technology>
- [8] <https://www.iconbuild.com>
- [9] <https://www.winsun3d.com/En/>
- [10] [https://www.youtube.com/watch?v=2kCjSq\\_1-0s](https://www.youtube.com/watch?v=2kCjSq_1-0s)
- [11] <https://www.acs.org/education/resources/highschool/chemmatters/articles/3d-printed-foods.html>
- [12] “Handbook of Mechanics of Materials” Hsueh Chun-Hway – Reference work 2019
- [13] [https://www.youtube.com/watch?v=4AISkNqSW-8&list=PLg4Okiua3lc5jePwNf395SsZR0WU\\_qaXi&index=7&t=60s](https://www.youtube.com/watch?v=4AISkNqSW-8&list=PLg4Okiua3lc5jePwNf395SsZR0WU_qaXi&index=7&t=60s)
- [14] [https://www.youtube.com/watch?v=4j6iZDKpwTQ&list=PLg4Okiua3lc5jePwNf395SsZR0WU\\_qaXi&index=3&t=249s](https://www.youtube.com/watch?v=4j6iZDKpwTQ&list=PLg4Okiua3lc5jePwNf395SsZR0WU_qaXi&index=3&t=249s)



17th-19th June 2024  
Gliwice, Poland

DEPARTMENT OF ENGINEERING MATERIALS AND BIOMATERIALS  
FACULTY OF MECHANICAL ENGINEERING  
SILESIA UNIVERSITY OF TECHNOLOGY

## INTERNATIONAL STUDENTS SCIENTIFIC CONFERENCE

### Selected properties of perlite concrete also with waste lightweight aggregate

Nicole Kocierz, Barbara Słomka-Słupik<sup>a</sup>

<sup>a</sup> Silesian University of Technology, Faculty of Civil Engineering, Department of Building Structures

email: barbara.slomka-slupik@polsl.pl

**Abstract:** The article describes properties of ecological concrete with lightweight aggregate. Many lightweight concrete mixtures were designed, prepared and tested, the main aggregate of which was perlite. Waste lightweight aggregate was also added to the mixtures to check its effect on the properties of the perlite concrete. The compressive strength, density and water absorption of the designed mixtures of hardened concrete was tested. The greater the strength of the samples, the lower the water absorption and the higher the density of the concrete samples, similarly to conventional concrete.

**Keywords:** lightweight concrete, lightweight aggregate, perlite, circular economy, recycling

### 1. INTRODUCTION

Concrete in the simplest sense is a combination of aggregate, binder, water and possibly admixtures and additives. Traditional concrete is made of sand (fine aggregate), gravel (coarse aggregate), cement and water, and its strength increases with hardening time [1]. The division of concrete includes heavy concrete with an apparent density  $> 2600 \text{ kg/m}^3$  and ordinary concrete  $2000\text{-}2600 \text{ kg/m}^3$  and lightweight concrete  $< 2000 \text{ kg/m}^3$ . There are also special concretes and cementless concretes. Concrete can also be divided according to its purpose in construction - into structural, structural and insulating, insulating and architectural concrete [1]. Another example is ultra-light concrete, it is concrete with a density below  $800 \text{ kg/m}^3$ , composed mainly of light and ultra-light aggregates, air-entraining and shrinkage-reducing admixtures, dispersed reinforcement and composite meshes, cement or geopolymer binders and special additives [2]. They are characterized by low compressive strength, in the range of 1.5 - 15 MPa, low thermal conductivity and low bulk density, so they can be used for facades [2]. Currently, when creating concrete mixtures, ecological solutions are being sought, not only due to the lack of natural aggregates in the world or due to the large carbon footprint during the production of the binder (cement), but also due to the properties of the material itself. One of these properties, as already mentioned, is thermal conductivity [3]. To keep the heat transfer coefficient low, the material should be porous. Concrete porosity can be obtained, for example, by using porous aggregate, also known as lightweight aggregate.

Lightweight aggregates can be divided into natural and artificial, i.e. foamed and sintered or granulated.

Perlite is classified as sintered artificial aggregates because it is created in the process of swelling of metamorphosed volcanic rock at temperatures above 850-870°C [4]. Expanded perlite is a natural aggregate, and its production process does not produce waste, which is why it is also an ecological aggregate [5]. World literature extensively describes research on foam concrete and polystyrene concrete, but we know little about perlite concrete, expanded clay concrete, sawdust concrete and the like. Moreover, special attention is paid to them as thermal insulation materials, and less as construction materials [6].

The research work described here was carried out as part of the engineering project of the author (N. Kocierz) and as part of the work in the "Build Green" Student Scientific Club. The aim of the work was to show the influence of recycled lightweight aggregate on the properties of perlite concrete. The compressive strength, water absorption and bulk density of reference samples without and with recycled aggregate were tested. Therefore, the work contains elements of circular economy.

## 2. MATERIALS AND METHODS

Tap water and "CEM I 52.5R turbo" cement from the Holcim cement plant, formerly Lafarge, were used to prepare the concrete mixtures. The cement used declared a compressive strength after 28 days of no less than 52.5 MPa, and "R" means that it had a high dynamics of early strength development. The main aggregate used, marked "K-I", is horticultural perlite from NOVA MINERALS, a natural quartz mineral. However, the additional aggregate, marked "K-II", was individually prepared from construction waste and is currently covered by a patent application. Figure 1 shows perlite as the main aggregate (K-I) and additional lightweight aggregate (K-II).

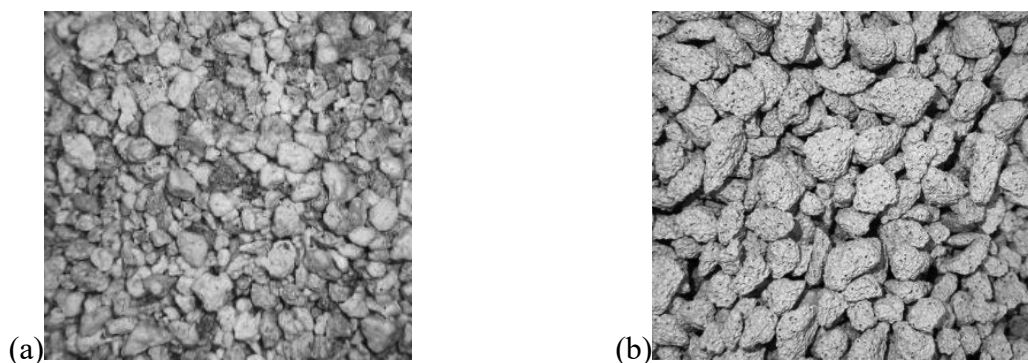


*Figure 1. Aggregate K-I (a) and K-II (b)*

Concrete mixtures were prepared mainly based on the rheological properties observed during mixing. Therefore, the mixtures were designed by observation, based on the consistency and properties of the fresh concrete mixture. This is also how subsequent modifications of the aggregate composition or cement content were determined. The goal was to obtain a workable mixture - it could not be too pourable, nor too thick or dry. First, a base mixture (PB1) was prepared, with cement as the binder and perlite as the aggregate. The PB2 mixture



contained half as much cement and the same amount of perlite as PB1, but its water demand increased. The following mixtures: B3, M1, M2 and M3 contained additional aggregate, which was also highly porous, just like perlite, but their porosity was open, unlike perlite grains. The compositions of the mixtures are given in Table 1, grain distribution - in Figure 2, and their consistency in Figure 3. Cross-sections of 10×10×10 cm cubes of hardened concrete are shown in Figure 4. The research methods were modified standard methods for preparing and testing concrete.

Table 1. Percentage content of concrete mixtures components

Name of mixture	PB1	PB2	B3	M1	M2	M3
Water	33.63	36.23	35.03	34.29	38.34	36.51
Cement CEM I 52.5R	53.81	43.48	19.77	20.00	18.77	21.16
Aggregate K-I	12.56	20.29	7.91	9.71	9.12	8.99
fractions, mm			Aggregate K-II			
0,063-0,125	-	-	2.94	-	-	-
0.125-0.25	-	-	5.88	6.86	5.36	5.29
0.25-0.5	-	-	5.88	6.86	5.36	5.29
0.5-1	-	-	5.88	5.71	4.83	4.76
1-2	-	-	5.88	5.71	4.83	4.76
2-4	-	-	2.94	2.29	2.68	2.65
4-8	-	-	7.91	2.86	4.29	4.23
8-16	-	-	-	5.71	6.43	6.35

According to the graph included in the standard [7], the area below curve A (Fig. 2) includes coarse-grained mixtures, between curves A and B - coarse-grained to medium-grained mixtures, while between B and C there are medium-grained to fine-grained mixtures. However, the grain size range proposed in the research classifies approximately all mixtures as fine-grained, because their aggregate grain curves are located in the area above the C curve.

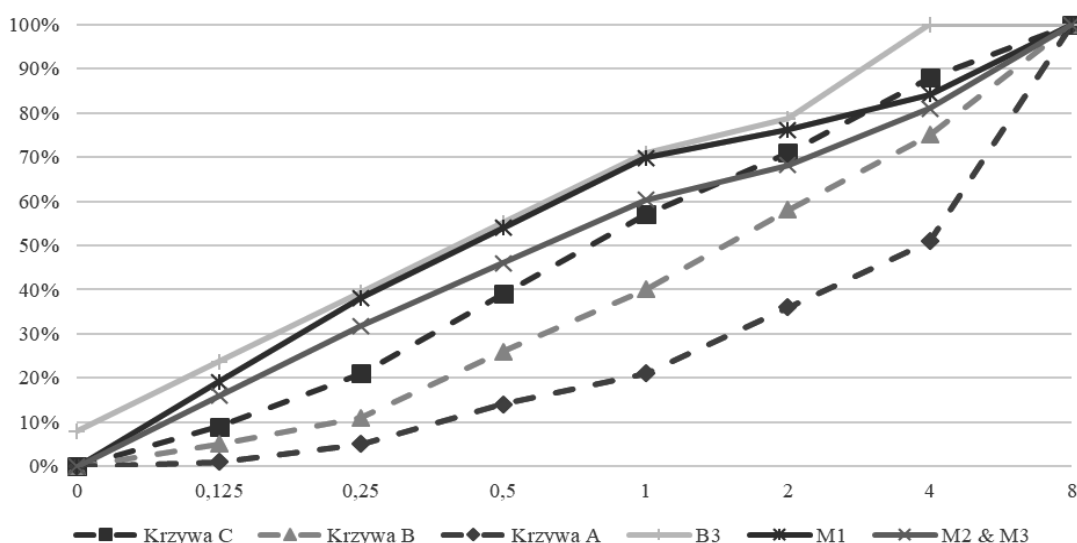


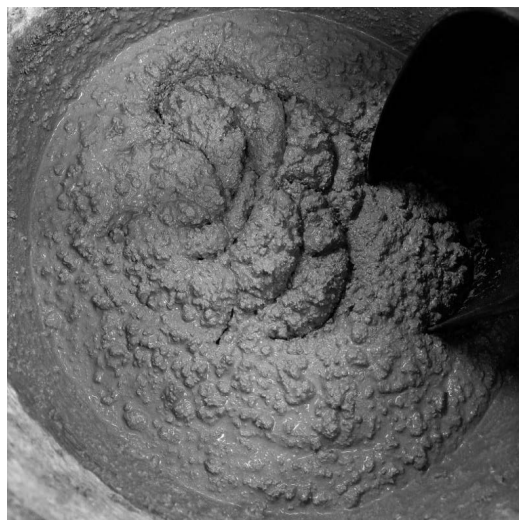
Figure 2. Grain size distribution of aggregate K-II



PB1



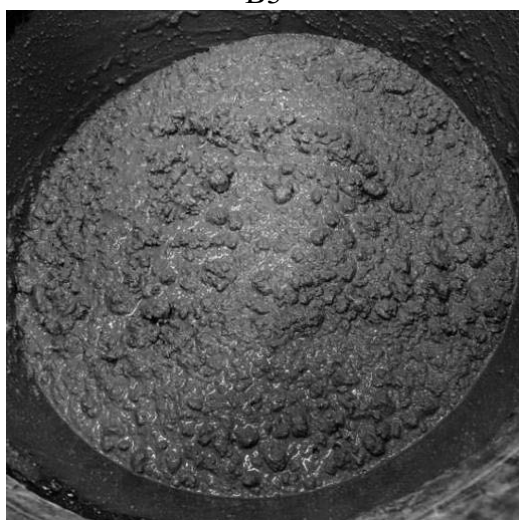
PB2



B3



M1

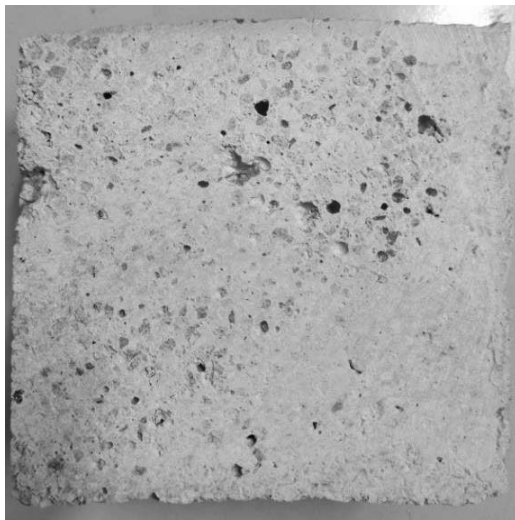


M2



M3

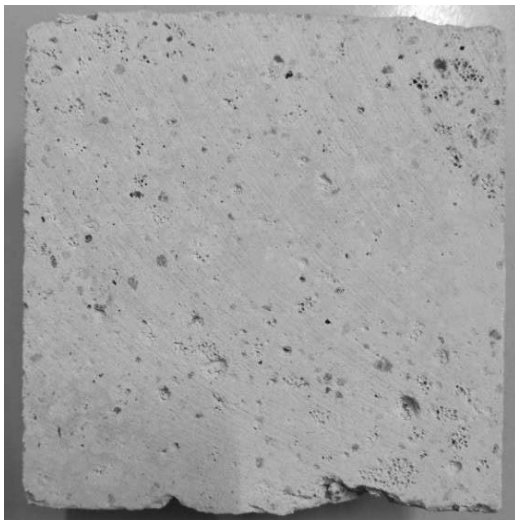
*Figure 3. Fresh concrete mixtures*



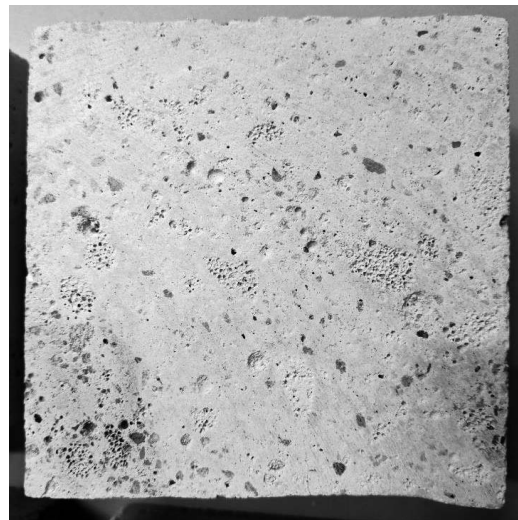
PB1



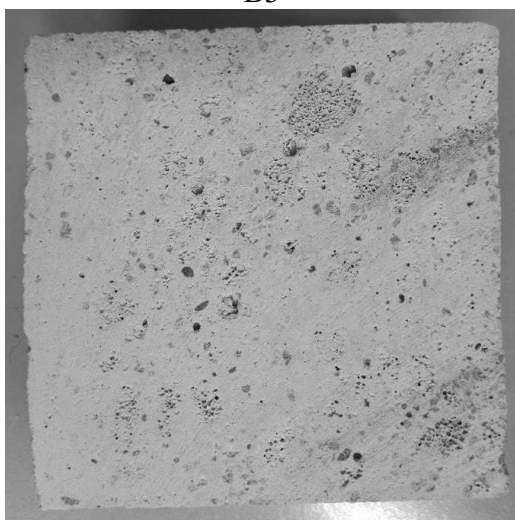
PB2



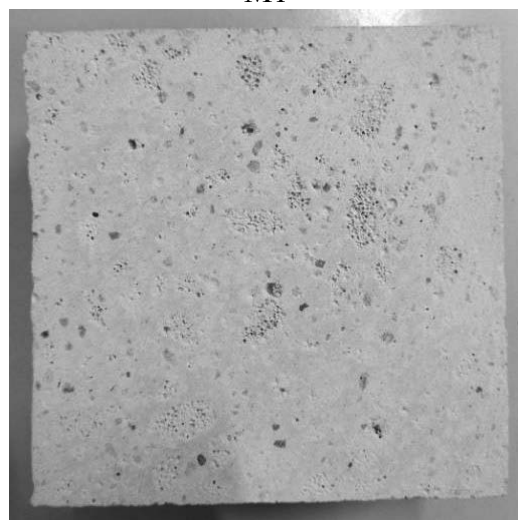
B3



M1



M2



M3

Figure 4. Cross-sections of hardened concrete mixtures with dimensions  $10 \times 10 \text{ cm}$

### 3. RESULTS WITH ANALYSIS

Table 2 lists the values of bulk density of reference samples without recycled aggregate and with recycled aggregate. It can be seen that samples B3, M1 and M3 had very similar densities, despite their different compositions. Sample M2 had a much lower density than sample M1, although it contained more water. Such results may be indicated by the different degree of water absorption of each of the aggregate fractions and the subsequent method of releasing water in the cement hydration reaction.

Table 2. The density of concrete cubes

Name of mixture	PB1	PB2	B3	M1	M2	M3
Density, kg/m <sup>3</sup>	987,7	695,9	896,1	901,0	814,7	904,0

Table 3 lists the compressive strength values calculated as the average of the tests of three samples with dimensions of 10 × 10 × 10 cm. The samples were subjected to a load of 0.5 MPa/s and did not show any failure shapes typical of concrete. After completing the test, the samples had no visible scratches or cracks, which may suggest good elasticity of the perlite and recycled ecological aggregates used. The compressive strength was between 6 MPa and 13 MPa in the case of samples with only K-I and between 6.5 MPa and 9.5 MPa in samples with a mixture of K-I and K-II aggregates. Figure 5 shows the relationship between the compressive strength and the density of the tested samples. The formation of the graphs is similar, but a clear relationship between density and strength cannot be assumed for the samples made.

Table 3. Average value of compressive strength of concrete cubes

Name of mixture	PB1	PB2	B3	M1	M2	M3
Average value. MPa	13,05	6,04	8,73	9,25	6,46	9,11

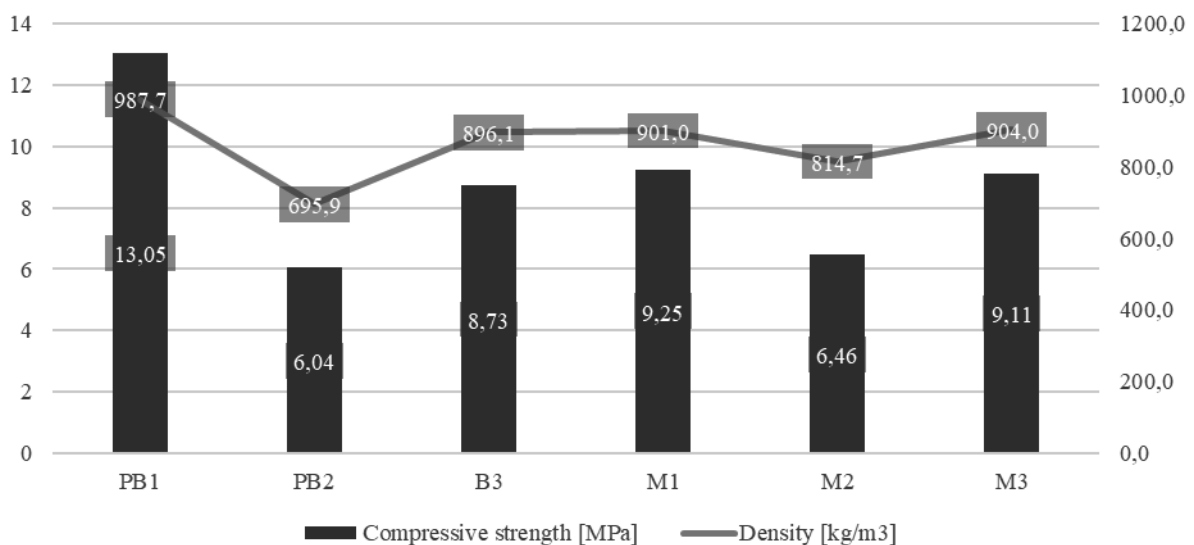


Figure 5. Relationship between compressive strength and density of concrete

Table 4 lists the water absorption values of appropriate concrete samples. It can be noticed that the high cement content in the PB1 sample halved its water absorption (26%) compared to other samples in which the water absorption is at a constant level of 44-52%. Figure 6 shows the relationship between water absorption and density. It can be noticed that in the case of samples with the addition of K-II aggregate and the same cement content (B3, M1, M2), there was a relationship that the higher the density, the lower the water absorption..

Table 4. The water absorption of concrete cubes

Name of mixture	PB1	PB2	B3	M1	M2	M3
Water absorption, %	26,4	47,9	50,4	44,3	51,1	46,0

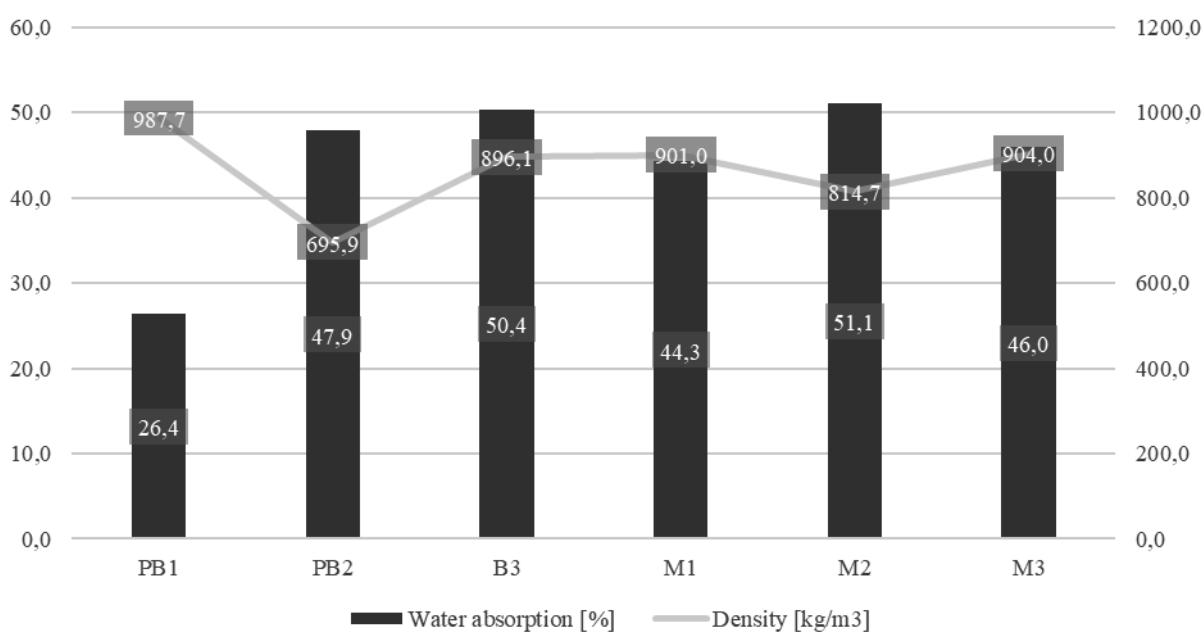


Figure 6. Relationship between water absorption and density of concrete

#### 4. SUMMARY AND CONCLUSIONS

The test results showed that reducing the mass content of K-II aggregate < 2 mm by 10% (in samples M1 and M2) reduced the compressive strength by 30%, which may be caused by a simultaneous increase in the w/c ratio (water-cement) and lower strength fine-grained aggregates from coarse-grained ones.

Increasing the amount of cement by 14% (in samples M2, M3) resulted in an increase in compressive strength by 40%. However, reducing the cement content by 50% in the initial samples (PB1, PB2) resulted in a 46% reduction in strength.

It can be concluded that the course of the relationship between compressive strength and density was compatible. Samples with the highest density had the highest strength, and samples with the lowest density had the lowest strength. Moreover, in the case of concretes with the same cement content and the addition of K-II aggregate, a relationship was obtained that the higher the density, the lower the water absorption.

Sample P2 had higher absorption than P1 because P2 contained more aggregate and less cement. The water absorption was higher in the case of cured samples with more free water, as seen in Figure 3. In the case of samples PB1, M1 and M3, no excess water was observed. It is logical that the more unbound water, the greater the porosity of the binder matrix. This results in a reduction in the strength value. As can be seen, it was the largest in the case of PB1, M1 and M3. Fresh PB2 and M2 mixtures had the most excess water and therefore had the lowest strength values after hardening.

## **BIBLIOGRAPHY**

1. Z. Jamróży. *Beton i jego technologie*. Wydawnictwo Naukowe PWN. Warszawa. 2015.
2. Ultra-Lightweight Concrete: Materials, Properties and Applications. *The Constructor* 2023. <https://theconstructor.org/concrete/ultra-lightweight-concrete-materials-properties-applications/566658/> (access date 03.05.2023).
3. B. Słomka-Słupik. T. Kruczek. N. Kocierz. *Betony lekkie z kruszywem z materiałów odpadowych W: Ochrona klimatu i środowiska. nowoczesna energetyka : wybrane zagadnienia / Werle Sebastian. Ferdyn-Grygierek Joanna (red.). Monografia / Politechnika Śląska. 2023. vol. 1006. Wydawnictwo Politechniki Śląskiej. s.135-150. ISBN 978-83-7880-929-6.*
4. A. Burkowicz. *Perlit ekspandowany – materiał termoizolacyjny mało znany w Polsce. Zeszyty Naukowe Instytutu Gospodarki Surowcami Mineralnymi i Energią PAN. nr 96. s.7-22. 2016.*
5. Sustainability Fact Sheet. Perlite Institute. 2023. <https://www.perlite.org/wp-content/uploads/2018/03/sustainability-factsheet-perlite.pdf> (access date 30.04.2023).
6. L. Domagała. *Konstrukcyjne lekkie betony kruszywowe. Monografia 462. Wyd. PK. 2014*
7. PN-B-06265:2018-10 *Beton. Wymagania, właściwości, produkcja i zgodność. Krajowe uzupełnienie PN-EN 206+A1:2016-12.*



17th-19th June 2024  
Gliwice, Poland

DEPARTMENT OF ENGINEERING MATERIALS AND BIOMATERIALS  
FACULTY OF MECHANICAL ENGINEERING  
SILESIA UNIVERSITY OF TECHNOLOGY

## INTERNATIONAL STUDENTS SCIENTIFIC CONFERENCE

### Flammability behavior of UV-curable varnishes for protection of wood-based substrates

Bartosz Kopyciński<sup>a,c</sup>, Sebastian Jurczyk<sup>a</sup>, Izabela Gajlewicz<sup>a</sup>, Alicja Duda<sup>b,c</sup>, Ewa Langer<sup>a</sup>

<sup>a</sup> Łukasiewicz Research Network – Institute for Engineering of Polymer Materials and Dyes, Toruń, Poland

<sup>a</sup> Łukasiewicz Research Network – Institute of Non-Ferrous Metals, Gliwice, Poland

<sup>c</sup> Doctoral School, Silesian University of Technology, Gliwice, Poland

email: bartosz.kopycinski@impib.lukasiewicz.gov.pl

**Abstract:** Ecological coating solutions for substrate protection against the destructive effects of fire are constantly sought in the wood and furniture industry. Hardly flammable, water-free, UV-curable coating compositions dedicated to wood and wood-based substrates have been developed. Based on the mixture of aliphatic urethane acrylate with modified polyester resin or phosphorus-containing difunctional acrylated oligomer, recipes containing pentaerythritol and ammonium polyphosphate – an environmentally friendly, halogen-free system of flame retardants were prepared. The characteristics of selected physicochemical properties of compositions with variable proportions of flame retardants (15, 30, and 45 wt%) were prepared. Thermal analysis was performed using thermogravimetry and cone calorimetry. The hardness by the method of pendulum damping and the water contact angle were determined. It has been shown that the addition of flame retardants increases the thermal stability of varnishes, increasing the decomposition temperature by up to 40°C, and improving their overall thermal characteristics during combustion. An increase in the hardness of the coatings by approximately 20-30 s, depending on the variant, and a hydrophobic effect of flame retardants were also observed, as the wetting angle of the composition increased by up to 37°.

**Keywords:** UV-curable varnishes, flame retardants, wood protection, coatings

## 1. INTRODUCTION

Despite the growing awareness of fire protection, over 135000 fires in residential and industrial buildings were registered in Poland only in 2022 [1]. This increases the need to develop new coating solutions, especially with a more environmentally friendly profile. These efforts include, among others, resignation from the use of halogen-based flame retardants, which, when heated, can decompose into the toxic dioxins that can accumulate in the human body, and formulation of varnishes without the use of organic solvents or water [2,3].

Light-curing varnishes are an interesting alternative to the traditional coating solutions. Free of volatile organic compounds, quick-drying, constituted in compact devices, perfectly fit into the concept of the so-called "Green Chemistry". The high solids content of the UV formulas allows the application of thin coatings, which, depending on their intended purpose, can be applied to a wide variety of surfaces. Their attractiveness is also reflected in the maximum efficiency of the application process, resulting directly from the waste-free nature of this technology [4,5].

In industrial practice, mainly coating compositions based on halogen or phosphorus flame retardants of organic origin are widespread. Most of all, compounds rich in chlorine and bromine remain in use [6]. Inorganic materials such as metal oxides and hydroxides are also employed [7]. On the other hand, the flame retardants found on a laboratory scale are carbon materials, both in micro and nanometric form (including carbon foams, carbon nanotubes, graphene and its oxide), often subjected to additional functionalization [8].

Despite the high application potential, the literature does not provide many examples of research devoted to the constitution of light-curing polymer coatings with increased fire resistance. The classically used intumescent coatings are based on melamine and pentaerythritol and ammonium polyphosphate, for which fire protection has been confirmed [9]. This article presents an approach involving the application of the above compounds as flame retardants for UV-curable polymer matrix based on the mixture of aliphatic urethane acrylate with modified polyester resin or phosphorus-containing difunctional acrylated oligomer. Based on commercially available materials, recipes for flame-retardant coating compositions hardened by UV radiation have been developed, dedicated to wooden and wood-based substrates, containing 15, 30, and 45 wt% of flame retardants on a liquid formula. Formulations with satisfactory compatibility of the raw materials used and stable during storage were obtained. It has been shown that applying such coatings to wooden and wood-based substrates not only contributes to the improvement of their thermal characteristics, i.e. an increase in the decomposition temperature or reduction of harmfulness during the combustion process, but also to an increase in the hardness of the coatings and the degree of their hydrophobicity.

## 2. EXPERIMENTAL

### 2.1. Materials

On the basis of commercially available materials, stable formulations of the coating compositions with satisfactory compatibility of the raw materials used have been developed. Varnishes based on two polymer matrices – then described as G and R respectively – were prepared. The first type of matrix was the mixture of aliphatic urethane acrylate (GENOMER\* 4269/M22, Rahn) with modified polyester resin (GENOMER\* 6050/TM, Rahn). The second was phosphorus-containing difunctional acrylated oligomer (RAYLOK® 1722, Allnex). Selected properties of oligomers are presented in Table 1. For the cross-linking of developed varnish formulas, Norrish type I photoinitiators belonging to the group of aromatic ketones have been used. The prepared systems also contain acrylic monomers, including nanosilica dispersion, and auxiliary agents such as polymerization inhibitor and adhesion promoter. Ammonium polyphosphate (Exolit® AP 422, Clariant) and pentaerythritol (Charmor™ PM15, Perstorp) together in the amount of 15, 30, and 45 wt% on total formulation were used as flame retardants.



Table 1. Chosen properties of used oligomers

<b>Commercial name</b>	GENOMER* 4269/M22	RAYLOK 1722
<b>Manufacturer</b>	RAHN	Allnex
<b>Chemical description</b>	Aliphatic urethane acrylate in 30% isobornyl acrylate	Phosphorus-containing difunctional acrylated oligomer
<b>Functionality</b>	2	2
<b>Color Index</b>	≤2 Gardner	2,5 Gardner
<b>Viscosity</b>	40000÷60000 mPa·s (25°C)	7100 mPa·s (60°C)
<b>Density, 20°C</b>	1.1 g/cm <sup>3</sup>	1.1 g/cm <sup>3</sup>

## 2.2. Preparation of varnishes

The first stage of preparing the varnishes was to prepare a paste consisting of flame retardants distributed in a mixture of acrylic monomers and a dispersion of nanosilica in the acrylic monomer. In the second step, all other varnish components were added, including oligomers, photoinitiators, and auxiliaries. To obtain the mentioned coating compositions, typical equipment used in the paint and varnish industry is used, i.e. an attritor-type mill and a high-speed agitator equipped with a tub. Ready mixtures are applied to a dry and loosely bound wood or wood-based substrate by airless spray or brush. The coating compositions need to be cured with UV radiation, which, when using 100 W/cm UV lamps, corresponds to an exposure time of preferably 30 s. The scheme of the preparation of varnishes is shown in Figure 1.

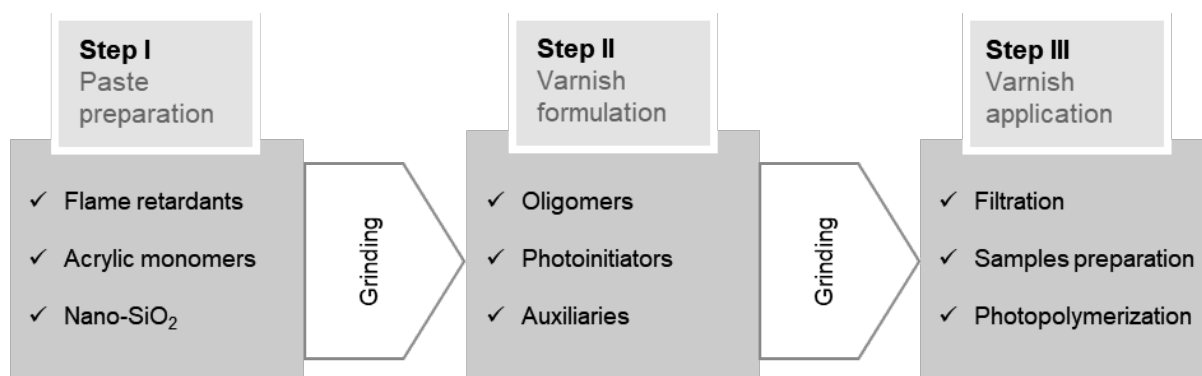


Figure 1. Stages of the varnishes preparation

## 2.3. Thermogravimetric analysis

The thermal parameters of the cross-linked varnishes were determined using the Mettler Toledo TGA/SDTA 851e analyzer in accordance with the standard ISO 11358-1 Plastics – Thermogravimetry (TG) of polymers - Part 1: General principles. Samples weighing 9÷15 mg were placed into 70 µl Al<sub>2</sub>O<sub>3</sub> crucibles and heated from room temperature to 800°C at a rate of 10°C/min in a stream of nitrogen set at a rate of 60 mL/min. Mettler Toledo StarSystem SW 15.00 software was used to analyze the obtained data. The following parameters were calculated:

5% decomposition temperature ( $T_{5\%}$ ), maximum decomposition temperature ( $T_{\max}$ ) and the presence of residual material as a wt%.

#### **2.4. Cone calorimetry**

The fire characteristics of tested varnishes were done using a Fire Testing Technology cone calorimeter (CC) according to the standard ISO 5660-1: Reaction-to-fire tests – Heat release, smoke production, and mass loss rate – Part 1: Heat release rate (cone calorimeter method) and smoke production rate (dynamic measurement). Horizontally positioned samples with dimensions of 100x100x4 mm were tested at a heat exposure of 50 kW/m<sup>2</sup> with a spark igniter as a source of the fire. The thermokinetic properties of the tested samples, such as time to ignition (TTI), flameout, total heat release (THR), total smoke release (TSR), total smoke production (TSP), fire growth rate index (FIGRA), heat release rate (HRR), and heat of combustion (HOC) were determined.

#### **2.5. Hardness**

The hardness of the polymerized varnishes was determined using a universal hardness tester TQC Sheen SP0500 equipped with Persoz pendulum in accordance with the standard ISO 1522. Then, according to standard PN-79/C-81530, the relative hardness being a percent of glass constant (430 s) was calculated. Coatings applied to the surface of the glass plate with a thickness of approx. 30 μm were tested. The pendulum damping time was measured in 5 different places on the sample.

#### **2.6. Contact angle measurement**

The ability of the UV-cured coatings to be physically repelled or attracted by water molecules was determined by measuring the wettability with a Krüss DSA 100 goniometer calorimeter in accordance with the standard ISO 19403. Drops of deionized water with a surface tension of 72.8 mJ/m<sup>2</sup> and of a volume of approx. 2 μl were deposited on the surface of a glass plate covered with a layer of varnish with a thickness of approx. 30 μm. The contact angles (CA) at the phase boundary were recorded in 5 replications per sample.

### **3. RESULTS AND DISCUSSION**

#### **3.1. Thermal analysis**

The abovementioned flame retardant system has the ability to create a sacrificial carbon layer that swells as a result of the thermal decomposition of polyphosphoric acid and ammonia salts to phosphoric acid and its further reaction with crystalline polyhydroxyl alcohol, which is a carbon source [10]. The addition of the abovementioned system of combustion inhibitors into the polymer matrix contributes to the increase in the thermal stability of cross-linked coatings and the shift of their decomposition temperature to higher values. The results of the TG and CC analysis are presented in Tables 2 and 3 and Figures 2-4.

Table 2. Results of TG analysis for the varnishes

Sample	T <sub>5%</sub> [°C]	T <sub>max_1</sub> [°C]	T <sub>max_2</sub> [°C]	Residue [wt%]
G	202.00	296.40	428.78	13.38
G15	217.81	294.66	359.01	25.30
G30	225.76	295.11	343.60	31.18
G45	227.20	294.65	340.77	35.92
R	203.78	263.69	405.51	13.16
R15	217.41	277.91	330.49	26.44
R30	230.93	284.37	334.58	35.98
R45	244.23	287.97	342.27	40.06

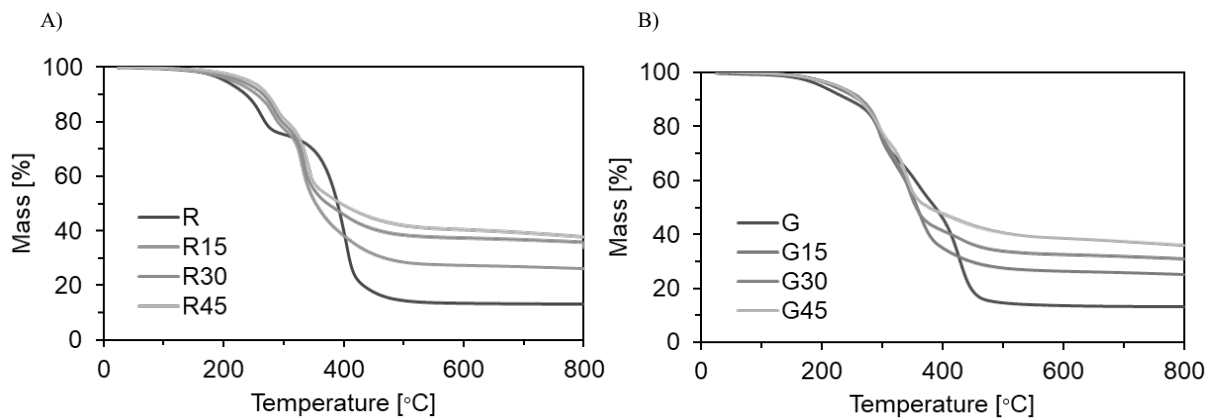


Figure 2. TG charts for the varnishes – series of R (A) and G (B) samples

It has been shown that the addition of flame retardants into the polymer matrix contributes to the increase in the thermal stability of varnishes. Thus, with an antipyrène content of 45%, a reduction in mass loss of almost 23 and 27% is observed compared to the unmodified G and R bases, respectively. In correlation with the increasing contents of flame retardants, the decomposition temperature T<sub>5%</sub> also increases the most intensively, i.e. by 25 and 40°C, for the G45 and R45 samples.

Table 3. Results of CC analysis for the varnishes

Sample	TTI [s]	THR [MJ/m <sup>2</sup> ]	TSR [m <sup>2</sup> /m <sup>2</sup> ]	TSP [m <sup>2</sup> ]	FIGRA [kW/m <sup>2</sup> s]	HRR <sub>avg</sub> [kW/m <sup>2</sup> ]	HRR <sub>max t</sub> [s]	HOC <sub>avg</sub> [MJ/kg]
G	22	74.9	2273.0	20.1	6.60	211.75	98	19.85
G15	23	52.8	2053.9	18.2	4.42	140.00	90	16.06
G30	23	64.0	1718.9	15.2	5.28	94.96	38	17.48
G45	25	46.7	1105.9	9.8	3.96	74.07	40	15.28

R	21	55.0	3037.6	26.9	5.04	170.56	87	14.78
R15	20	50.5	2277.6	20.1	7.79	164.24	57	15.66
R30	21	66.0	2513.7	22.2	6.69	136.15	45	16.13
R45	30	68.2	2291.9	20.3	5.12	129.02	57	16.36

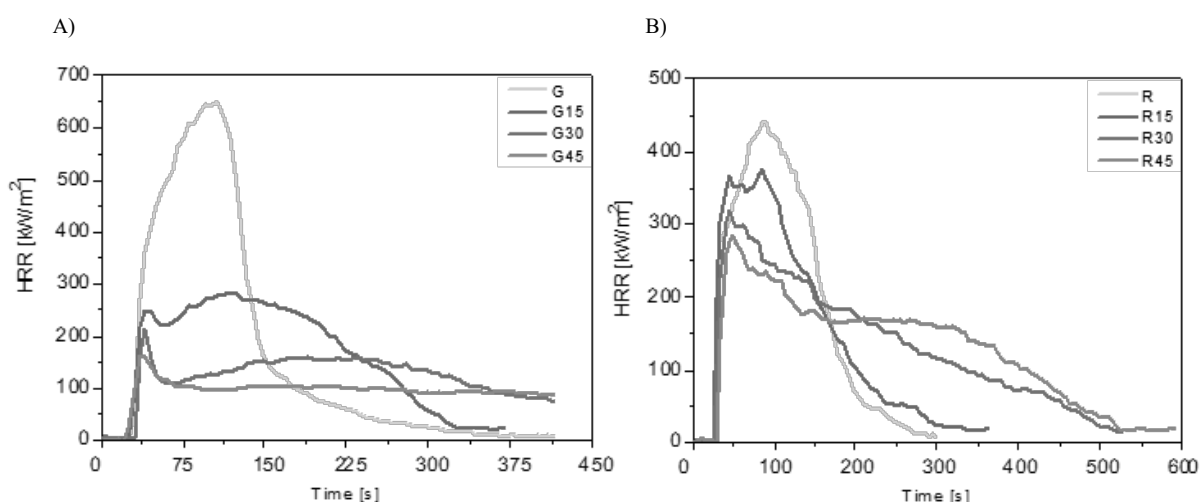


Figure 3. HRR charts for the varnishes – series of R (A) and G (B) samples

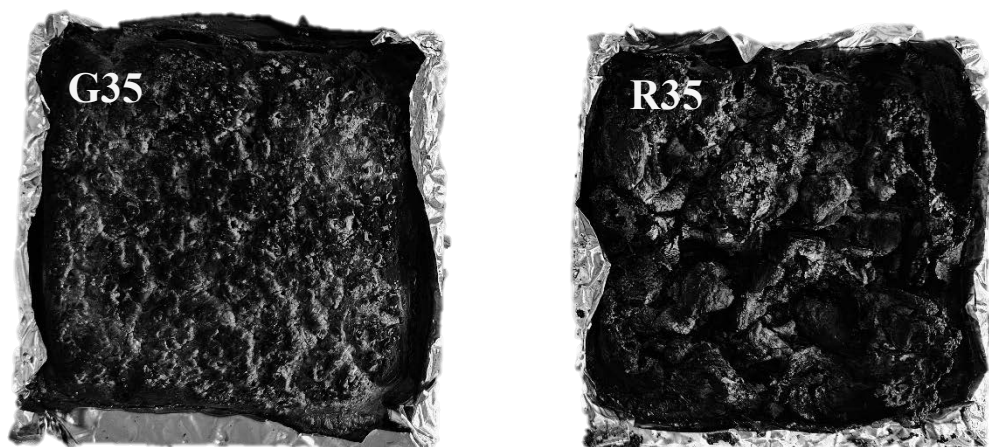


Figure 4. Carbonized samples after CC testing

The CC test allowed for the assessment of the behavior of the developed compositions under ignition and combustion conditions. A general improvement in the thermal degradation parameters of varnishes was observed. First of all, the time required for ignition (TTI) has been extended and the amount of smoke emitted (TSR, TSP) and heat release rate (HRR) have been reduced. Similar results were observed when various types of flame retardants were added into a whole range of polymeric materials, including paints and varnishes [11]. However, the recorded

changes for all prepared variants are not always correlated with the amount of flame retardants used.

The shape of the samples subjected to CC analysis, visible in Figure 4, indicates that they have been completely charred. Visible bulges on their surface create a carbon barrier layer that protects or delays the thermal degradation of the substrate. The resulting chars are in a foamed form, which is especially visible in the case of R series samples and is identical to the mechanism of creating a protective layer by the flame retardants used when exposed to high temperatures.

Table 4. Results of hardness and CA measurements for the varnishes

Sample	Hardness [s]	Relative hardness	CA [°]
G	109.70 [±0.82]	0.255	66.39 [±1.01]
G15	138.10 [±1.67]	0.321	76.80 [±0.53]
G30	142.00 [±0.86]	0.330	74.34 [±1.72]
G45	70.87 [±1.51]	0.165	75.67 [±1.26]
R	57.83 [±0.78]	0.134	59.82 [±0.39]
R15	83.80 [±1.41]	0.195	57.03 [±0.84]
R30	95.73 [±1.59]	0.223	60.21 [±1.67]
R45	93.27 [±0.45]	0.217	60.06 [±0.83]

It was shown that at 15 and 30 wt% the addition of flame retardants increases the damping time of the pendulum by 28 and 32 s, and 25 and 37 s for compositions G and R, respectively. The introduction of antipyrène with a share of 45 wt% into the system results in a sharp decrease in the hardness of the G45 composition by 38 s. For the R45 sample, the hardness was higher by 35 s relative to the warp, however, lower by 2 s than for sample R30. Similarly, all the abovementioned dependencies were observed for results expressed as % of the glass constant value. Interestingly, the wettability test showed the hydrophobic effect of flame retardants on the polymer matrices used. For the G series samples, an increase in CA was observed, amounting to approximately 10, 7, and 9° for samples G15, G30, and G45, respectively. In the case of the R series samples, the recorded increase in CA was much more pronounced, i.e. 25, 37, and 35°, similarly for samples R15, R30, and R45.

#### 4. CONCLUSION

Selected properties of UV-curable varnishes dedicated to wood and wood-based substrates were developed and characterized. It was confirmed that the pentaerythritol-ammonium polyphosphate flame retardant system, also in light-curing systems, allows a significant reduction of the flammability of varnish coatings. It is foreseen that the use of the abovementioned varnish may contribute to both increasing the safety of use and extending the lifetime of the covered wooden and wood-based elements. The application of flame-retardant coating compositions that are the subject of this work includes coating substrates in the form of hewn, planed or planed pine, larch and oak wood as well as wood-based composite boards such as MDF and OSB

intended for structural elements, especially roof trusses and panels and wall cladding. The selected compositions can be a highly useful and environmentally friendly choice for fire protection coatings. It is expected that the implementation of the developed solutions may contribute to both the increase in operational safety and the extension of the service life of wooden and wood-based elements exposed to high temperature and flame.

## BIBLIOGRAPHY

1. <https://www.gov.pl/web/kppsp-nowy-dwor-mazowiecki/statystyczne-podsumowanie-interwencji-strazakow-w-2022-roku> [access: 12.04.24]
2. C. D. Papaspyrides, P. Kiliaris (ed.), polymer green flame retardants – Chapter 4: Environmental drivers for replacement of halogenated flame retardants, Elsevier, 2014.
3. C. Ling, R. Zhou, Y. Xiang, J. Fang, X. Meng, Q. Ren, C. Wang, Solvent-free flexible epoxy intumescent fire-retardant coatings, *Journal of Coatings Technology and Research* (2024).
4. V. Shukla, M. Bajpai, D. K. Singh, M. Singh, R. Shukla, Review of basic chemistry of UV-curing technology, *Pigment & Resin Technology*, 272-279 (2004) 33(5).
5. B. Kopyciński, E. Langer, UV-curable coatings – environment-friendly solution for sustainable protection of metal substrates, *Ochrona przed Korozją* 160-169 (2023) 66(6).
6. I. Veen, J. Boer, Phosphorus flame retardants: Properties, production, environmental occurrence, toxicity and analysis, *Chemosphere* 1119-1153 (2012) 88(10).
7. A. A. Sertsova, M. Y. Koroleva, E. V. Yurtov, O. B. Pravednikova, O. S. Dutikova, L. S. Gal'braikh, Fire-resistant polymer nanocomposites based on metal oxides and hydroxides, *Nanotechnologies and Nanomaterials* 772–777 (2010) 44.
8. X. Wang, E. N. Kalali, J. T. Wan, D. Y. Wang, Carbon-family materials for flame retardant polymeric materials, *Progress in Polymer Science* 22-46 (2017) 69.
9. A. Andersson, S. Lundmark, F. H. J. Maurer, Evaluation and characterization of ammoniumpolyphosphate–pentaerythritol-based systems for intumescent coatings, *Journal of Applied Polymer Science* 748-753 (2007) 104(2).
10. M. Maqsood, G. Seide, Investigation of the flammability and thermal stability of halogen-free intumescent system in biopolymer composites containing biobased carbonization agent and mechanism of their char formation, *Polymers* (2019) 11(48).
11. B. Jurkowski, H. Rydarowski (ed.), *Materiały polimerowe o obniżonej palności*, Katedra Wydawnictwo Naukowe, 2012.



17th-19th June 2024  
Gliwice, Poland

DEPARTMENT OF ENGINEERING MATERIALS AND BIOMATERIALS  
FACULTY OF MECHANICAL ENGINEERING  
SILESIA UNIVERSITY OF TECHNOLOGY

## INTERNATIONAL STUDENTS SCIENTIFIC CONFERENCE

### Steel hardness

Mateusz Kozłowski<sup>a</sup>, Maja Kubacka<sup>a</sup>, Julia Popis<sup>b</sup>, Sabina Lesz<sup>b</sup>

<sup>a</sup>Upper-Secondary Schools of Communications in Gliwice

<sup>b</sup> Silesian University of Technology, Faculty of Mechanical Engineering, Department of Engineering Materials and Biomaterials, email: sabina.lesz@polsl.pl

**Abstract:** The article presents the results of hardness measurements of steel with varying carbon content and in different technological conditions. Based on the obtained results, an increase in hardness was observed as a function of the carbon content in the steel. The technological state has a significant impact on the achieved hardness of the steel.

### 1. INTRODUCTION

Hardness is the resistance of given materials to mechanical overloads and plastic deformations resulting from the mechanical pressing of another material (indenter) into the tested surface. The indenter is usually a steel ball, cone, or pyramid. As a result of hardness measurements and concentrated forces acting on the surface of the tested material, surface deformation, crushing or scratching occur. The hardness of a material depends on its properties, i.e. ductility, stiffness, plasticity, deformability, viscosity, and mechanical strength. Macroscopic hardness is characterized by strong intermolecular bonds, but the behavior of solid materials under the influence of force is complex, therefore there are various methods of measuring hardness [1,2]. We distinguish static and dynamic hardness measurement methods. Static methods, i.e. Brinell (HBS, HBW) [3], Rockwell (HRA, HRB, HRC, HRD, HRE, HRF, HRG, HRH, HRK, HRN, HRT) [4], and Vickers (HV) [5], are determined depending on the value of the loading force indenter and the amount of permanent deformation caused by this force. Depending on the hardness of the tested material and its thickness, an appropriate measurement method is selected. The occurrence of plastic deformations is the result of stresses in the material that exceed the elastic limits. These methods are used in the fields of engineering and metallurgy. Dynamic methods, i.e. the Shore method and the Poldi hammer, involve the impact of an indenter on the tested surface and measuring the height of the "rebound" of a hammer with a diamond tip dropped onto the material from a specific height. In

these hardness tests under dynamic load, the induced resistance of the material characterizes its elastic or plastic properties [6,7].

Below listed methods are not the only ones, but they are mainly used. Each of them has a different characteristic, different requirements, as well as advantages and disadvantages:

- **Rockwell hardness test**

It involves indenting the indenter into the tested material (Fig. 1). The test result is determined based on the measurement of the permanent increase in indentation depth after unloading. The indenter is in the form of a diamond cone, or a ball made of sintered carbides. In the Rockwell hardness measurement method, various hardness scales are used (e.g., A, B, C). Each scale has its corresponding indenter with specified geometry and materials to ensure appropriate measurement conditions. The dimensions of this indenter are standardized: for the cone, it has a vertex angle of 120° and a vertex radius of 0.2 mm, while for the balls, they have diameters of 1.5875 mm or 3.175 mm.

Advantages of this method are:

- Speed and ease of measurement.
- Simple handling of the hardness tester.
- Relatively small indentations.
- Applicability in hard products and certain hardened layers.

Disadvantages of this method are:

- Necessary correct, perpendicular positioning of the sample relative to the indenter.
- Inability to measure on thin products and thin carburized or nitrided layers.
- Clean, even, and smooth sample surface.
- Difficulty in selecting the measurement method, cumbersome comparison of measurement scales of different methods [7,8].

In this method, the indenter is gradually immersed into the material in two stages. The preload  $F_0$  is preliminary and only induces elastic deformation. It is only the application of the main load  $F_1$  that causes permanent deformation. The permanent increase in indentation depth  $e'$  is measured after unloading the main load  $F_1$  while maintaining the preload  $F_0$ . It is expressed in units of permanent deformation equal to 0.002 mm according to the following equation:

$$e = \frac{e'}{0,002}$$

For harder materials, there is a smaller indentation depth of the indenter, and for softer materials, a greater one. Therefore, the final hardness value is determined by the constant difference  $K$  and the permanent increase in indentation depth  $e$ :

$$HR = K - \frac{e'}{0,002}$$

Where:

- $K=100$  - constant for measurements using a cone.
- $K=130$  - constant for measurements using a ball.



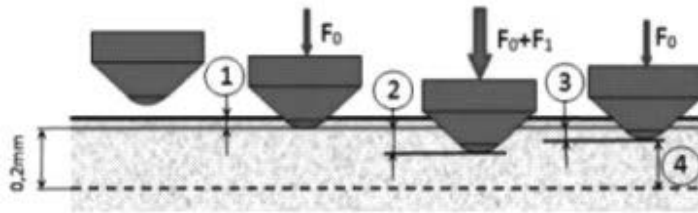


Fig. 1. Rockwell hardness measurement scheme

The table showing the applied indenters, loads, and methods of expressing hardness in the respective scales is presented in Table 1.

Table 1. Normal Rockwell Scales [4]

Indenter type	Load [N]			Scale designation	Hardness designation	Rockwell hardness test
	Initial $F_0$	Main $F_1$	Overall $F = F_0 + F_1$			
Diamond cone	98	1373	1471	C	HRC	$HRC = 100 - \frac{e'}{0,002}$
	98	490	588	A	HRA	$HRA = 100 - \frac{e'}{0,002}$
Steel ball $\frac{1}{16}$ "	98	883	982	B	HRB	$HRB = 130 - \frac{e'}{0,002}$
	98	490	588	F	HRF	$HRF = 130 - \frac{e'}{0,002}$

#### • Brinell hardness test

It involves determining the hardness based on the measurement of the diameter of the indentation formed after removing the load. The indenter, which is typically a steel ball with a smooth surface, is used to apply pressure to the surface of the tested material. The indenters used have a specified diameter: 1mm, 2.5mm, 5mm, 10mm.

Advantages of this method are:

- The ability to apply relatively large loads.
- The ability to conduct tests on surfaces situated not perfectly perpendicular to the direction of the indenter.
- The ability to analyze any deformations, which may indicate existing stresses in the material.

Disadvantages of this method are:

- Inability to conduct measurements on thin materials and the labor-intensive nature of the entire process.
- Difficulty in optically reading the indentation diameter, which is heavily influenced by the operator's skills.
- Surface preparation is required, without which the results often become unreliable because their variation depending on the indentation's location is significant.

- For measurements on cylindrical surfaces, preparation of a flat area on the surface is required [4,6].

The value of the applied load is selected based on the provided equation:

$$F = 9.803K \cdot D^2$$

K is a coefficient characterizing the tested material and taking certain values: 30, 10, 5, 2.5, or 1 (Table 2). The value of the coefficient K should be selected depending on the anticipated hardness value of the tested material so that the resulting impression diameter  $d$  falls within the range of  $0.25D < d < 0.5D$ . The applied values of the load depending on the diameter of the ball  $D$  and the coefficient  $K$  are presented in Table 3.

Table 2. Values of the load coefficient  $K$  for selected materials [3]

Recommended K value	HB hardness	Tested material
30	96 ÷ 600	Steels, cast irons with hardness greater than 140HB, copper and nickel alloys with hardness greater than 190HB.
10	32 ÷ 200	Cast iron with hardness less than 140HB, copper, nickel, and their alloys with hardness 32 ÷ 200HB, and aluminum alloys with hardness greater than 80HB.
5	16 ÷ 100	Copper and its alloys with hardness less than 40HB, aluminum and its alloys with hardness 35 ÷ 80HB, bearing alloys with hardness greater than 20HB, magnesium, zinc, and their alloys.
2.5	8 ÷ 50	Aluminum and its alloys with a hardness less than 35HB, bearing alloys with a hardness less than 20HB.
1	20 ÷ 32	Tin, lead, bearing alloys, and other metals and their alloys with a hardness less than 20HB.

Table 3. Loading forces for various measurement conditions [3]

Coefficient K	The value of force $F$ [N] depending on the diameter of the ball $D$ [mm]				
	10	5	2.5	2	1
30	29420	7355	1840	1176	294
10	9800	2450	613	392	98
5	4900	1225	306.5	196	49
2.5	2450	613	153.2	98	24.5
1	980	245	61	39.2	9.8

- **Vickers hardness test**

It involves indenting the surface under examination with a specified force using a diamond penetrator (Fig. 2). Hardness is determined by measuring the diagonals of the resulting square indentation. The penetrator used in this method is a regular tetrahedral diamond. The included angle of the penetrator apex is  $136^\circ$ . The standard specifies hardness measurement for diagonal lengths ranging from 0.020 mm to 1.400 mm [5,6].

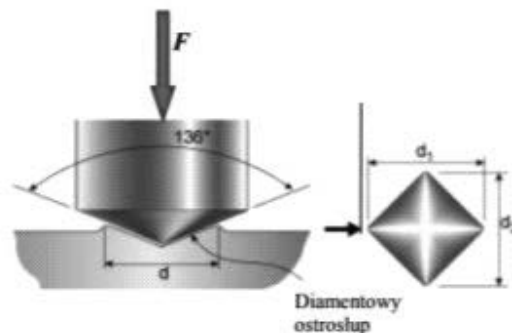


Fig. 2. Vickers hardness measurement scheme

The advantages of this method are:

- The universality resulting from the ability to use a single penetrator for every type of material.
- The widest measurement scale among commonly used testing methods.
- Low invasiveness of indentations on the sample surface.
- High measurement accuracy and relatively low uncertainty.
- The hardness measurement result is independent of the applied load during the test.
- speed and ease of measurement; very simple operation of the hardness tester.
- Direct reading without the need for tables.

Disadvantages of this method are:

- Low measurement efficiency compared to Rockwell's.
- The possibility of conducting the test depends on the roughness of the material.
- Difficulty applying the method to coarse-grained and non-uniform materials.
- Significant influence of incorrect object positioning on measurement results.
- Significant influence of contamination on the lifting screw and bases of the object table, as well as the shape of the product on measurement results.
- Inability to measure the hardness of very thin objects and thin carburized, nitride layers, etc.
- Inability to maintain high measurement accuracy due to unfavorable metrological conditions (many mechanical linkages).
- A significant number of hardness scales and difficult comparisons between them, as well as with the results of other methods [9,10].

The hardness of steel mainly depends on:

- Carbon content
- Technological condition

The mechanical properties primarily depend on the carbon content. Carbon strengthens the steel and improves its strength properties such as  $R_e$ ,  $R_m$ , and HB, while reducing the steel's ductility ( $A$ ,  $Z$ ,  $KC$ ). Hardness shows a continuous increase with increasing carbon content. This is due to the continuous decrease in the soft phase content - ferrite, and an increase in the amount of the harder phase - pearlite, as the carbon content rises [9].

The hardness of steel is determined by its chemical composition. There are many types of steel with different properties, including hardness. The percentage of carbon determines how hard the steel will be. A higher carbon content allows for the production of steel with a higher degree of hardness. Carbon, as one of the two primary components of steel, determines its hardness and its usability. Hardening increases the hardness of steel, allowing the production of material with very high strength and hardness, suitable for making tools, for example [7,11].

## 2. MATERIALS AND METHODS

The research material was ARMCO Pure Iron (max. 0.010 wt % C) and steel with varying carbon concentrations, namely: 0.10, 0.15, 0.20, 0.30, 0.45, 0.55, 0.90 wt% C.

The samples for testing also included C45 steel in different technological states. The chemical composition of the samples is presented in Table 4.

Table 4. Chemical composition of C45 steel

Symbol classification	Element concentration [wt%]								
	C	Si	Mn	Cr	Ni	Mo	Cu	S	P
C45	0.45	0.10	0.50	max	max	max	max	max	max
	÷	÷	÷	÷	÷	÷	÷	÷	÷
	0.50	0.40	0.80	0.30	0.30	0.10	0.30	0.04	0.04

Hardness tests were performed using the Brinell, Rockwell, and Vickers methods by standards [3-5]. A load of 500 gf was applied.

## 3. RESEARCH RESULTS

The results of the hardness measurements using the Brinell method for ARMCO Pure Iron (~0 wt % C) and steel with varying carbon concentrations are presented in Figure 3.

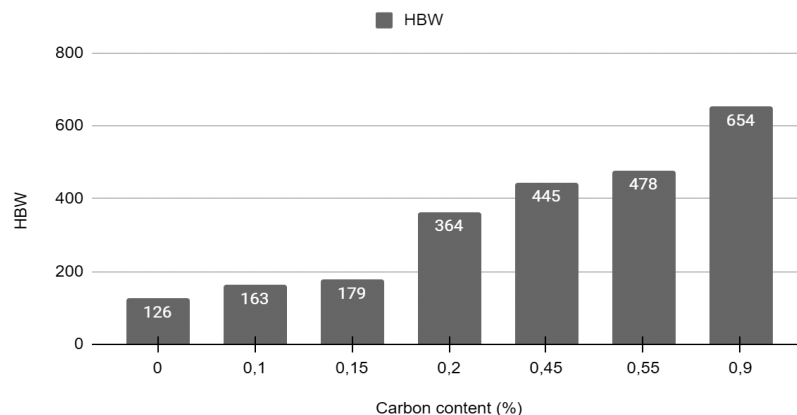


Fig. 3. Brinell hardness in function of carbon concentration

The results of the hardness measurements using the Vickers method for C45 steel in the as-delivered state, after normalization, as well as after hardening are presented in Figures 4, 5, and 6, respectively.

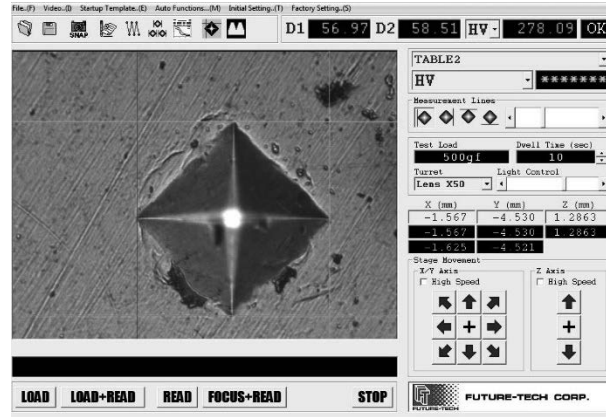


Fig. 4. The examples of data of Vickers hardness presented within the FT – ARS9000 software

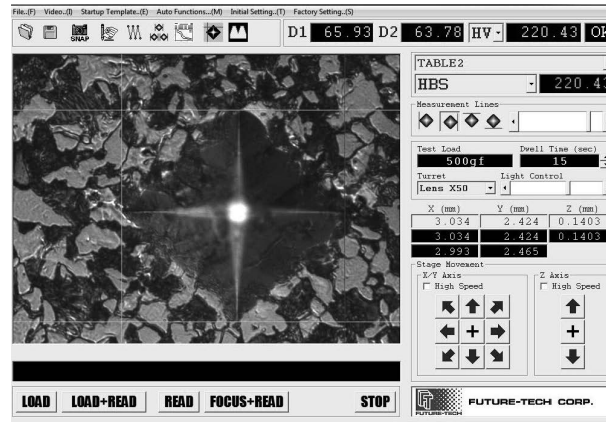


Fig. 5. The examples of data of Vickers hardness presented within the FT – ARS9000 software

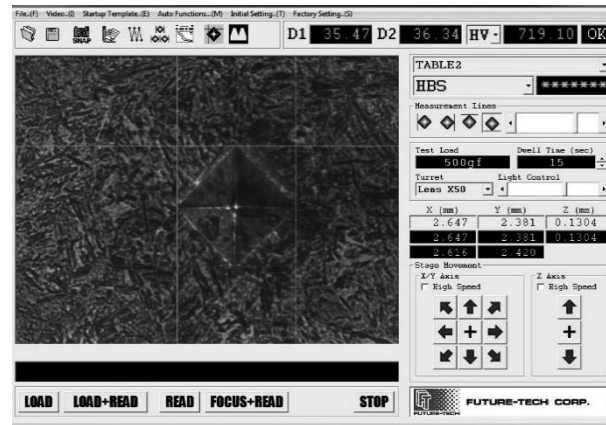


Fig. 6. The examples of data of Vickers hardness presented within the FT – ARS9000 software

#### 4. CONCLUSIONS

Based on the conducted research, the following conclusions can be drawn: the hardness of steel is determined by its chemical composition, including carbon as the primary component of steel.

- Among the hardness measurement methods, static measurements are most commonly used due to their accuracy.
- The hardness of steel increases with increasing carbon content.
- Observing the behavior of steel in various technological states confirms the assumption that its hardness depends on the processing it has undergone.

#### ACKNOWLEDGMENTS

The work was created as a result of a project carried out with secondary school pupils as a part of the Excellence Initiative - Research University program (3rd competition), Silesian University of Technology.

#### BIBLIOGRAPHY

1. Encyklopedia Popularna PWN, Wydawnictwo Naukowe PWN, Warszawa, 1996.
2. A. Di Gianfrancesco, Alloy 263, Elsevier 571–599 (2017), DOI: 10.1016/b978-0-08-100552-1.00017-8, ISBN 978-0-08-100552-1.
3. EN ISO 6506-1:2014-12. Metallic materials – Brinell hardness test.
4. EN ISO 6508-1:2016-10 Metale – Metallic materials – Rockwellhardness test
5. EN ISO 6507-1:2024-04. Metallic materials – Vickers hardness test
6. E. Broitman, Indentation Hardness Measurements at Macro-, Micro-, and Nanoscale: A Critical Overview, Tribology Letters 65, 1 (2016) DOI: 10.1007/s11249-016-0805-5.
7. J. Marciniak (red.): Ćwiczenia laboratoryjne z metaloznawstwa, Politechnika Śląska, 2001.
8. D. Szewieczek (red.), Ćwiczenia laboratoryjne z obróbki cieplnej stopów metali, Politechnika Śląska, 1994.
9. Ł. Cieślak (red.), Ćwiczenia laboratoryjne z metaloznawstwa, Część II, Wpływ składu chemicznego i zabiegów technologicznych na strukturę i własności stopów, Politechnika Śląska, Gliwice, 1983.
10. M. Blicharski, Inżynieria Materiałowa, Wydawnictwo WNT, Warszawa 2017.
11. Strona internetowa: <https://www.mtmstal.sk/?view=article&id=60:od-czego-zalezy-twardosc-stali&catid=21>



17th-19th June 2024  
Gliwice, Poland

DEPARTMENT OF ENGINEERING MATERIALS AND BIOMATERIALS  
FACULTY OF MECHANICAL ENGINEERING  
SILESIA UNIVERSITY OF TECHNOLOGY

## INTERNATIONAL STUDENTS SCIENTIFIC CONFERENCE

### Design of wrist orthosis made by 3d printing technique using reverse engineering methods

Mariusz Król<sup>a</sup>, Szymon Jędrzejewski<sup>b</sup>, Daniel Tatar<sup>c</sup>, Adam Woszczak<sup>d</sup>, Branislav Hadzima<sup>e</sup>

<sup>a</sup> Silesian University of Technology, Faculty of Mechanical Engineering, Department of Engineering Materials and Biomaterials, e-mail: mariusz.krol@polsl.pl,

<sup>b</sup> Student of Engineering and Materials Technologies, e-mail: szymjed659@student.polsl.pl

<sup>c</sup> Student of Engineering and Materials Technologies, e-mail: danitat271@student.polsl.pl,

<sup>d</sup> Student of Engineering and Materials Technologies, e-mail: adamwos244@student.polsl.pl

<sup>e</sup> Research Centre UNIZA, University of Zilina, Univerzita 8215/1, 010 26 Zilina, Slovakia

**Abstract:** The design and production of personalized orthoses are intended to help patients with various mobility issues. Orthoses are used to stabilize, relieve pressure, correct deformities, and support limb function. With the help of modern technology, it is now possible to create orthoses that are customized to meet the individual needs of each patient.

This study presents the outcomes of using scanning and 3D printing techniques, such as Fused Filament Fabrication, to create a personalized stabilizing orthosis.

**Keywords:** personalized stabilizing orthoses, healthcare, 3d scanning, additive manufacturing, modeling, topology optimization, lightweight structures

## 1. INTRODUCTION

Thousands of children, due to conditions such as cerebral palsy or spinal muscular atrophy, require the constant use of corrective orthoses. Another several thousand children were born with a congenital disability in one or both limbs and should use orthoses for proper development. Unfortunately, at present, professional orthoses cost several thousand zlotys. One waits for them for several weeks. After a year or even less, you must replace them with a new model. Parents can afford to replace orthoses or prostheses so often. Nowadays, orthoses are mainly produced manually. The automated system planned for development will make it possible to create an openwork orthosis for fractures or dislocations of the wrist. The system designed in this way will be implemented, and thanks to the research, it will be possible to help and make life more comfortable for many patients [1-4].

Injuries accompany people in everyday life. Mostly, they are harmless injuries to soft tissue (bruises, contusions), but sometimes bone damage occurs. Treatment methods for such injuries can be divided into operative and non-operative, among which the most popular method used, primarily for fractures or dislocations, is plastering. During the healing process, wearing a fibreglass dressing and plaster can be a smelly, itchy effort that is bothersome and

uncomfortable, all because the injury is entirely internal. Other methods of bracing are thermoplastic bandages and orthoses, which are designed to limit movement in a joint or to immobilize it completely. An orthosis is a type of brace for a joint that resembles, in effect, a plaster cover applied by a doctor. Unlike a plaster, however, it is not uncomfortable and allows the skin to breathe.

The application of reverse engineering, i.e. 3D scanning, as a method of obtaining geometry will make it possible to create a spatial model of a human body section without using expensive equipment. This model can then be used to design orthoses or other components that closely match the body's shape [5-8].

The proposed project involves developing design principles and knowledge of the possibility of manufacturing personalized orthoses based on non-contact 3D scanning and production using 3D printing technology. Using 3D scanning technology combined with Fused Deposition Modeling (FDM) 3D printing, the exoskeleton orthosis can provide a fully ventilated structure for treating broken bones (Figure 1).

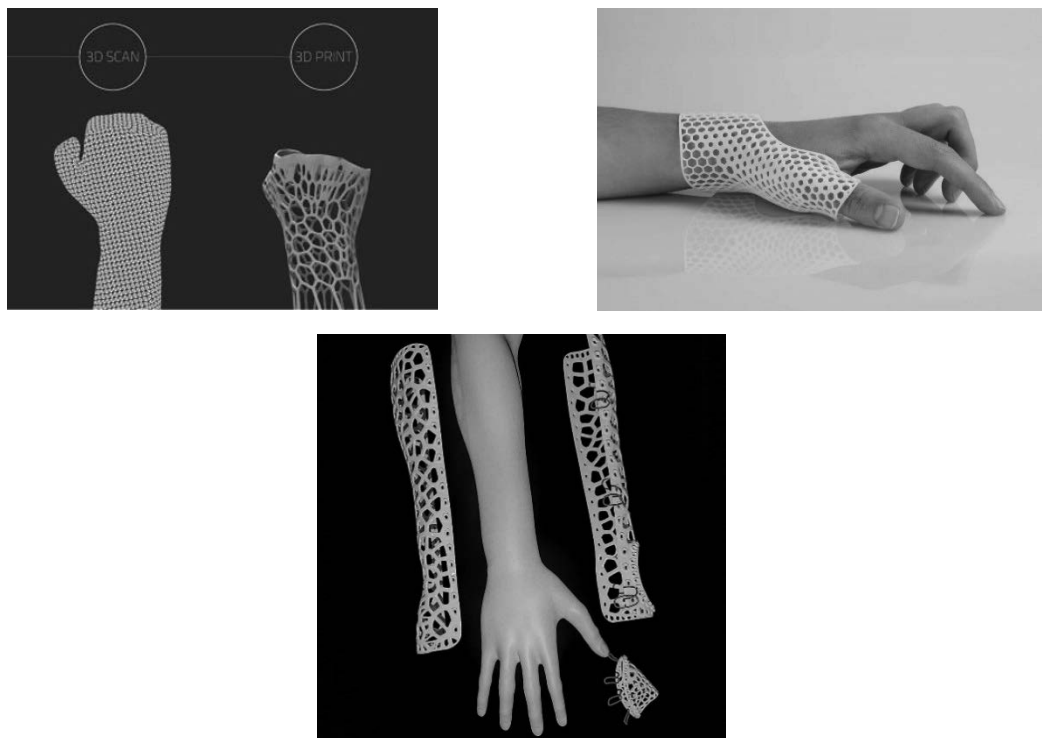


*Figure 1. Visualization of selected stages of project implementation*

Due to the need to design the orthosis with anatomical features in mind, it is necessary to acquire a limb model. For this purpose, a 3D scanner will be used. This is a frequently used solution in the medical industry since each product is different and must be tailored individually and precisely to a particular customer. When creating an orthosis, it is essential not only that it performs its function but also that it fits the person's body perfectly, provides comfort, and has aesthetic qualities. These elements are necessary for even the best orthosis to be used by the patient, as it will not give him a sufficient sense of comfort and fit to his body. The limb model obtained in this way will be optimized in terms of fit (so that it does not exert pressure) and the size of the holes to create an openwork structure that reduces the weight of the finished product.



Next, we will utilize the FDM technique to 3D print the designed orthotic structure. This method offers several key advantages, including the production of an ultralight, recyclable, and notably, shower-friendly orthotic.

At the initial stage of the project, PLA is planned to be used as a starting material, the most widely used thermoplastic in 3D printing. This material is biodegradable and very easy to process (low processing temperature), which makes it commonly used in incremental manufacturing techniques. Furthermore, such a filament can be transparent or, with a minimum of inputs, appear in any colour. Undoubtedly, a great advantage of PLA is its ease of processing, which allows its wide range of applications and doping with numerous additives such as ceramics or metal particles.

## 2. AIM OF THE RESEARCH

The project aimed to develop personalized wrist-stabilizing orthoses produced using the FDM 3D printing technique. The first step to creating the orthosis was to scan the potential patient's wrist with a non-contact 3D scanner. Digital processing uses tools that automatically clean the scanned model, refine the mesh, and adjust coordinates and contours. The project's next stage was to create a CAD model of the orthosis and optimize the topology to reduce the weight of the finished product by giving it an openwork structure. Thanks to the wrist scan, it was possible to perfectly match the internal shape of the orthosis to the patient's anatomy. A fully functional wrist orthosis will be created at a low cost through the correct selection of materials for the orthosis and the use of the incremental 3d printing technique FFF model. The design of a wrist orthosis was developed using reverse engineering methods and 3D printing techniques during the project. This project used an EinScan Pro HD scanner and Makerbot Method X 3d printer.

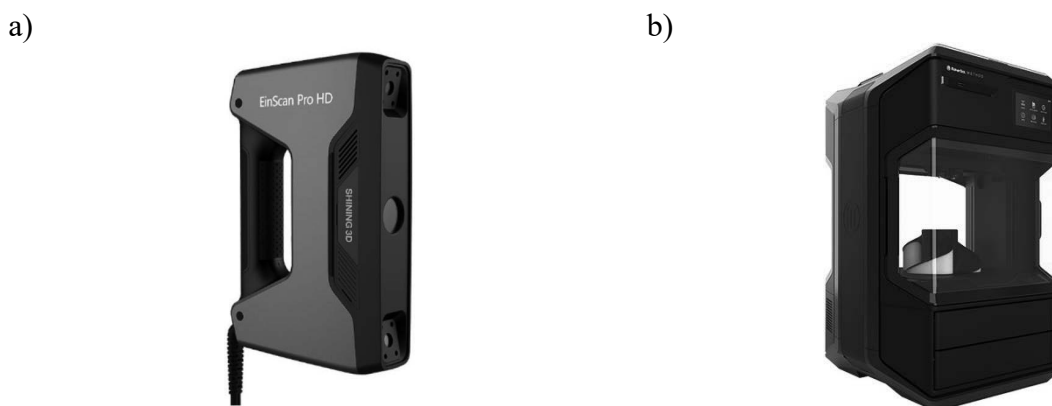
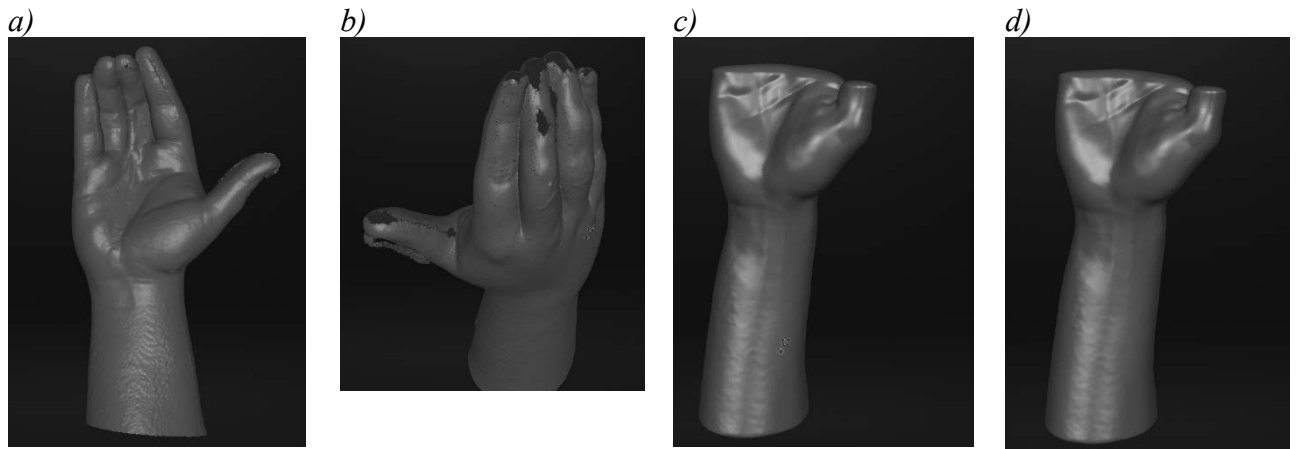


Figure 2. Used equipment in the project: a) scanner EinScan Pro HD and 3d printer b) Makerbot Method X

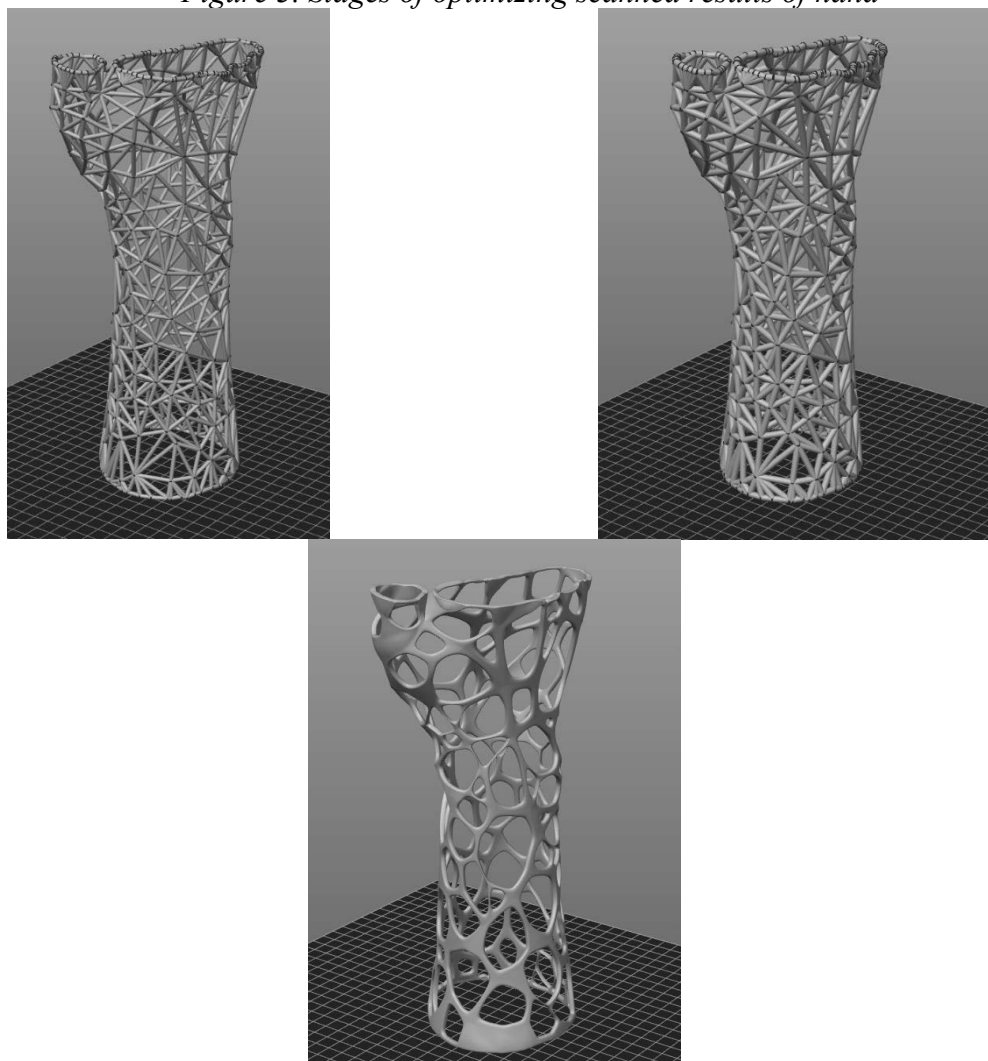
## 3. RESULTS AND DISCUSSION

Figure 3 presents the stages of scanning the potential patient's hand and postprocessing of the scanned hand. In the first step of the analysis of the results, the model was closed (watertight model) due to the difficulties in obtaining scans of several surfaces, or the scanner could not reach parts of the model. Auto hole filling as a curvature preset was used to watertight the model. Moreover, postprocessing reduced scanned points from 225,000 to

180,000. The next step was the meshing procedure of the model and simplification of the polygons from 180 000 to 95 000, which ultimately resulted in the stl model taking up less space on the hard disk.



*Figure 3. Stages of optimizing scanned results of hand*



*Figure 4. Results of cellular structure of the model mesh*

Figure 4 is presenting the stages of preparing 3d model to the orthosis in mesh structure. The last stage of the project was manufacturing the scanned and designed orthosis using a FFF printing machine. An ABS filament was utilized in the 3d printing technique to manufacture a final personalized orthosis (Figure 5).

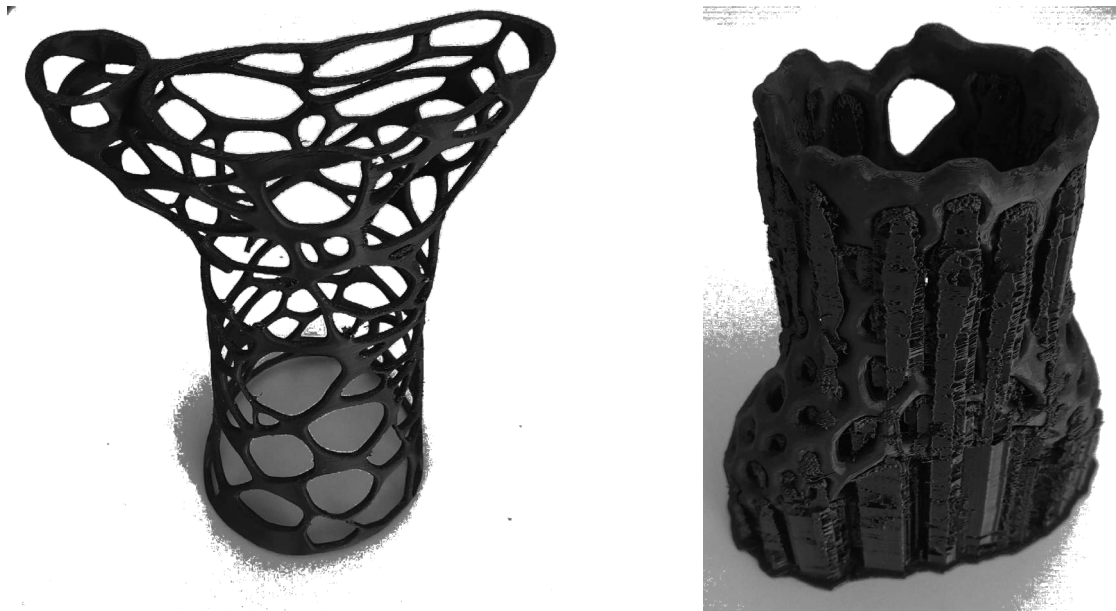


*Figure 5. Printed personalized orthosis*

#### **4. CONCLUSIONS**

Personalised orthoses are a key component in treating many orthopaedic and neurological conditions, enabling patients to improve their quality of life and function daily. Thanks to technological advances, increasingly advanced and practical solutions can be created, tailored to each patient's needs.

The application of reverse engineering, particularly 3D scanning, as a method of obtaining geometry, offers a level of precision that was previously unattainable. This technology allows us to easily create a spatial model of a section of the human body without the need for expensive equipment. This model can then be used to design an orthosis or other elements that perfectly fit the body's shape, such as a properly contoured chair back or jewellery components.

#### **ACKNOWLEDGEMENT**

The present study was produced as part of the activities of the Student Research Group "GYROID" operating at the Department of Engineering and Biomedical Materials at the Faculty of Mechanical Engineering, Silesian University of Technology in Gliwice.

The publication is result of cooperation within the Visegrad Scholarship Program 2023/2024.



## LITERATURE

1. Górski F., Zawadzki P., Wichniarek R., Kuczko W., Słupińska S., Żukowska M. , 2022, Automated Design and Rapid Manufacturing of Low-Cost Customized Upper Limb Prostheses, *J. Phys.: Conf. Ser.* 2198 012040
2. Żukowska M., Jezińska R., Górski F., Kuczko W., Wichniarek R., Banaszewski J., Buczkowska-Andruszko A., 2022, Methodology of the Rapid Manufacturing of an Individualized Anatomical Model of the Tongue with a Tumor for the Preparation of an Organ Reconstruction Operation, In: Gorski, F., Rychlik, M., Păcurar, R. (eds) *Advances in Manufacturing III. MANUFACTURING 2022. Lecture Notes in Mechanical Engineering.* Springer, Cham, pp. 45-58
3. Sośniak K., Biela D., Szalaty D. [i in.], Study of selected properties of PLA used in 3D printing *Journal of Achievements of Materials and Manufacturing Engineering*, 2023, vol. 116, nr 2, s.72-79. DOI:10.5604/01.3001.0053.4035
4. Sochaj S., Tobolik K., Kania Aneta [i in.], Metody wytwarzania ortez dla sportowców z urazami kończyn W: *TalentDetector2023\_Summer* : International Students Scientific Conference, Brenna, Poland, 26th June 2023 / Bonek Mirosław (red.), *Prace Katedry Materiałów Inżynierskich i Biomedycznych*, 2023, Gliwice, Politechnika Śląska, s.613-616, ISBN 978-83-65138-38-5
5. Kuczko W., Hamrol A., Wichniarek R., Górski F., Rogalewicz M., 2021, Mechanical properties and geometric accuracy of angle-shaped parts manufactured using the FFF method, *Bulletin of the Polish Academy of Sciences: Technical Sciences*, 69(3)
6. Górski F., Suszek E., Wichniarek R., Kuczko W., Żukowska M., Rapid Manufacturing of Individualized Prosthetic Sockets, *Adv. Sci. Technol. Res. J.* 2020; 14(1):42–49
7. Banaszewski J., Pabiszczak M., Pastusiak T., Buczkowska A., Kuczko W., Wichniarek R., Górski F., 3D printed models in mandibular reconstruction with bony free flaps, *J Mater Sci: Mater Med* (2018) 29: 23.
8. <https://www.bankier.pl/wiadomosc/Polscy-inzynierowie-szykuja-tanie-ortezy-i-protezy-z-druku-3D-8378264.html>



17th-19th June 2024  
Gliwice, Poland

DEPARTMENT OF ENGINEERING MATERIALS AND BIOMATERIALS  
FACULTY OF MECHANICAL ENGINEERING  
SILESIA UNIVERSITY OF TECHNOLOGY

## INTERNATIONAL STUDENTS SCIENTIFIC CONFERENCE

### Proecological aspects of laser cutting of metals and their alloys

Mateusz Król<sup>b</sup>, Jakub Kukuczka<sup>b</sup>, Anna Woźniak<sup>a</sup>, Mirosław Bonek<sup>a</sup>, Wojciech Pakieła<sup>a</sup>

<sup>a</sup> Silesian University of Technology, Faculty of Mechanical Engineering, Department of Engineering Materials and Biomaterials

email: [anna.wozniak@polsl.pl](mailto:anna.wozniak@polsl.pl); [miroslaw.bonek@polsl.pl](mailto:miroslaw.bonek@polsl.pl); [wojciech.pakiela@polsl.pl](mailto:wojciech.pakiela@polsl.pl).

<sup>b</sup> the 5th Andrzej Struga Secondary School with Bilingual Departments in Gliwice, e-mail: [mati.kroll7@gmail.com](mailto:mati.kroll7@gmail.com); [kuba1912.jk@gmail.com](mailto:kuba1912.jk@gmail.com)

**Abstract:** The dynamic technological development, especially in the automotive and aviation sectors, forces the search for increasingly advanced technologies for shaping engine components, suspensions, bodywork, etc. The construction of several completely different vehicles on one technological line, made of different elements and materials, forces automated and universal processing stations. Using tools in the form of punching dies involves significant downtime in production, as it is necessary to retool and reconfigure the machining centres. The noise that accompanies processing is also important. In addition, there are also aspects related to transport, the production of cutting dies made of high-quality steel, their heat treatment, and final disposal. Their operation itself also requires the use of cooling agents and lubricants. Each stage is associated with huge energy losses and thus translates into environmental pollution. Energy losses on heat are also very high when milling or cutting, so aggressive cooling agents are also required. Turning or milling produces a lot of waste in the form of chips, so larger batches must be ordered because processing allowances must be added. The use of water cutting for metals with poor corrosion resistance may cause major problems with the element's strength in later use. Moreover, such a process consumes large amounts of water, which is quite difficult to recycle afterwards because of the various elements contained in the metals.

Plasma torches introduce large amounts of heat into the processed details and do not ensure precise cutting. The noise emitted is also important to the environment. Recently, laser stations that allow cutting, welding, and surface treatment of almost all metal materials have become very popular. Such devices have a much lower environmental impact than other classic mechanical methods. Moreover, the laser beam allows you to cut almost any shape with very high precision, and conversion to another production takes less than a dozen or so minutes. This is usually associated with the need to reprogram the robot. For these reasons, using laser methods to shape body elements, engines, exhaust systems, suspension, etc., is among the most ecological. The process itself does not require additional cooling agents, and the losses are minimised to almost zero.

**Keywords:** metal, laser treatment, ecology, preservation of natural environment, laser cutting,

## 1. INTRODUCTION

Environmental pollution is responsible for almost half of all deaths worldwide. This is influenced by pollution from smoke, air, land, and water. The increase in public awareness forces us to look for alternative, much more eco-friendly techniques in producing and shaping devices and machines .

Shaping geometry, including cutting elements needed in industry, is always associated with huge losses and pollution generating. The most common and harmful waste includes metal shavings mixed with the abrasive of grinding wheels, oils, and other cooling liquids, and excessive water consumption. Also, often down-played, noise is harmful not only to humans but also to animals. Noise pollution can be defined as excessive exposure to sounds and noises above 65 decibels (dB), the threshold set by the World Health Organisation (WHO). Any sound above 75 dB is considered harmful to the hearing, while the pain threshold starts around 120 dB. According to the World Health Organisation (WHO), after smog, noise is the second most important environmental cause of poor health among Europeans. EEA research shows that noise pollution is responsible for 16.6 thousand deaths per year. premature deaths in EU countries.

In the first step, let us define what cutting means. We can define cutting as the separation of two pieces of solid material from each other. Cutting techniques can be divided into "cold" and "hot". Depending on the type of material, its dimensions and the required accuracy, they can be divided into classic cutting with grinding wheels, e.g. corundum, cutting on machine tools, e.g. using an electric welder or gas burner and laser cutting, using photon energy to evaporate/melt the material being cut[1, 2, 5].

This publication focuses on laser cutting methods as an ecological technique that reduces chemicals, process residues, and noise.

## 2. THE IDEA OF LASER CUTTING

We can therefore ask ourselves what laser cutting is and how it is done. Laser cutting is a technique that allows cutting metal and nonmetal materials of various thicknesses. The basis is a laser beam that is generated at the source, formed, and guided to the optics and head. The material melts or vaporises when a focused beam of photons hits the cut, or p. Some of the material in the form of small drops of liquid metal is blown out using a shielding gas, for example nitrogen, argon, or helium [6–8].

Therefore, in the first step, it is necessary to generate a beam (Fig. 1). Regarding the stand in question, we are dealing with a fiber laser, so we will focus on this source. The basic component of the IPG fiber laser is an active optical fiber. Typical fibre core diameters range from a few microns to hundreds of microns and lengths from metres to many kilometres. The fiber length to diameter ratio contributes to many of the unique characteristics of fiber lasers. Glass fiber is a classic waveguide. When the condition of total internal reflection of



*Fig. 1 IPG YLS - 4000 laser source.*

light is met, light propagates inside the optical fibre with negligible radiation losses. While a passive fiber is used for transport, active fibers introduce amplification by passing the pump light through a rare-earth-doped fiber core [9]. The laser is enclosed in a metal housing. To transport light, passive optical fiber is most often used, allowing the beam to be transported up to 50 m. This is very convenient because the source remains safe and the light can be transported straight to the machining centre. Fiber optics with a diameter of 100 to 1000  $\mu\text{m}$  are used for transport. Then the light beam goes to the head optics system (Fig. 2). There are at least two lenses in the head. The first is the collimator lens. It is a lens that focusses light. The second is a focussing lens that allows you to change the size of the laser spot. This combination allows the beam power density to be increased many times. This procedure also allows the use of one source for both cutting and welding or surface treatment of various materials with different thermophysical properties. Laser cutting is the most precise and popular technique for thermal separation of materials. It allows the processing of various types of materials, including metal materials such as steel and alloys of non-ferrous metals. The laser copes perfectly with materials such as stainless steel, aluminium, and carbon steel [10, 11]. The ability to cut details from sheet metal with dimensions often exceeding several square metres is also important. For cutting, depending on the application, lasers with powers ranging from several milliwatts to 15 kW are used. The cutting speed can reach 350 m/min, and the acceleration during movement exceeds  $50 \text{ m/s}^2$ . [6, 12]

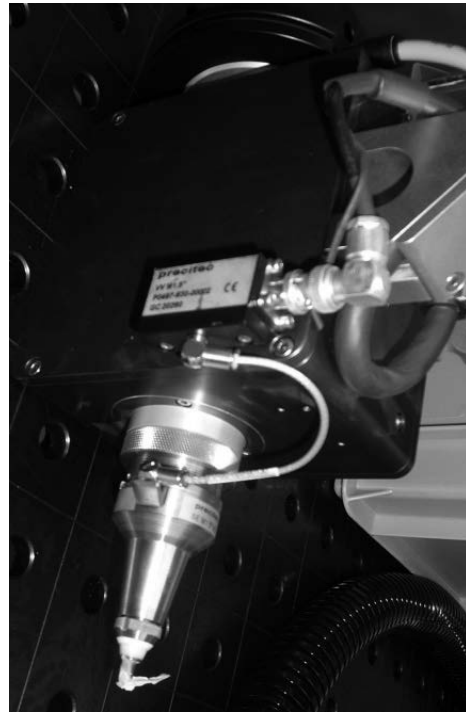


Fig. 2. laser cutting head

### 3. PRO-ECOLOGICAL ADVANTAGES OF LASER CUTTING

As already mentioned in the Introduction, metal cutting is the process of separating material. Classic cutting techniques have a relatively large negative impact on the natural environment. The harmful effects include, among others, emissions of used cooling lubricants, greases and oils, energy consumption, and cutting by-products in the form of chips, dust, and noise. High-pressure abrasive water jet cutting technology emits less pollutants than traditional machining (grinding, milling), but there is still the issue of the need to dispose of contaminated water with abrasive and cutting by-products. Cutting techniques with plasma torches, welders, abrasive discs, and machine tools emit many chemical and post-process pollutants [13–15].

Automation of the production process is an essential element of a modern enterprise. Thanks to the use of robotic stations, operators and other employees are not exposed to dangers related to the operation of the devices. Combining two manipulators or a manipulator and a robotic welding table allows the processing of almost all elements (Fig. 3). Moreover, using a manipulator allows almost immediately switching production to a completely different product shape. It all comes down to entering the programme into the controller. In the case of conventional cutting, for example, using dies, this is basically impossible. Thanks to automation,

even a person with physical disabilities can make a difference in society by carrying out tasks related to, e.g. programming. Also, isolating the operator from the environment significantly reduces the risk to his health. However, it should be emphasised that in the case of laser cutting, the noise level is significantly lower than in the case of, for example, a plasma torch or cutting with grinding wheels.



Fig. 3. Automated station for cutting welding and laser processing.

#### 4. SUMMARY

Therefore, it can be undoubtedly stated that cutting metals and their alloys is a safe and environmentally friendly technique. The use of photon beams for processing emits much less pollution than similar methods. A significant reduction in waste and, thus, a reduction in the amount of material used for processing positively contributes to improving the climate. In addition, aspects such as eliminating the need to use dangerous cooling agents and thus eliminating the need to dispose of them, eliminating smoke and dust, and reducing noise mean that this technology is increasingly used in industry.

#### ACKNOWLEDGEMENTS

The work was created as a result of a project carried out with secondary school students as part of project-oriented education - PBL, as part of the Excellence Initiative - Research University, Silesian University of Technology program.

#### BIBLIOGRAPHY

1. Anenberg, Susan Casper, J. Jason West, Arlene M. Fiore, Daniel A. Jaffe, Michael J. Prather, Daniel Bergmann, Kees Cuvelier, et al. 2009. Intercontinental Impacts of Ozone Pollution on Human Mortality. *Environmental Science & Technology* 43. American Chemical Society: 6482–6487. <https://doi.org/10.1021/es900518z>.
2. Huss, Anke, Adrian Spoerri, Matthias Egger, Martin Röösli, and for the Swiss National Cohort Study Group. 2010. Aircraft Noise, Air Pollution, and Mortality From Myocardial Infarction. *Epidemiology* 21: 829. <https://doi.org/10.1097/EDE.0b013e3181f4e634>.



3. Krolczyk, G. M., R. W. Maruda, J. B. Krolczyk, S. Wojciechowski, M. Mia, P. Nieslony, and G. Budzik. 2019. Ecological trends in machining as a key factor in sustainable production – A review. *Journal of Cleaner Production* 218: 601–615. <https://doi.org/10.1016/j.jclepro.2019.02.017>.
4. Darabant, András, Prem Bahadur Rai, Christina Lynn Staudhammer, and Tshewang Dorji. 2016. Designing and Evaluating Bamboo Harvesting Methods for Local Needs: Integrating Local Ecological Knowledge and Science. *Environmental Management* 58: 312–322. <https://doi.org/10.1007/s00267-016-0702-6>.
5. Road traffic noise, air pollution components and cardiovascu... : Noise and Health. 2024. [https://journals.lww.com/nohe/fulltext/2013/15670/road\\_traffic\\_noise,\\_air\\_pollution\\_components\\_and.3.aspx](https://journals.lww.com/nohe/fulltext/2013/15670/road_traffic_noise,_air_pollution_components_and.3.aspx). Accessed May 21.
6. Shin, Jae Sung, Ki-Hee Song, Seong Y. Oh, and Seung-Kyu Park. 2024. Laser cutting studies on 10–60 mm thick stainless steels with a short focus head for nuclear decommissioning. *Optics & Laser Technology* 169: 110121. <https://doi.org/10.1016/j.optlastec.2023.110121>.
7. Fu, Zhuorui, Ning Zhao, and Lei Luo. Digital twin-enhanced laser cutting production system design and operation. *International Journal of Computer Integrated Manufacturing*. Taylor & Francis: 1–27. <https://doi.org/10.1080/0951192X.2024.2328041>.
8. Liao, Wenling, Guorong Wang, Lin Zhong, Yinan Chen, and Jie Wang. 2024. Feasibility analysis and cutting process research on laser cutting medium-thick 20CrNiMo steel plates using a high-power fiber laser without assisted blowing. *Journal of Manufacturing Processes* 111: 130–138. <https://doi.org/10.1016/j.jmapro.2024.01.020>.
9. Jak jest zbudowany laser włóknowy – Fiber Laser Days. 2024. <https://fiberlaserdays.pl/swiatlowod-diody-budowa-laser/>. Accessed May 21.
10. Chandrasekaran, Balasubramanian, Rajkumar Kaliyamoorthy, Anandasimhan Murugavel, Gokul Vinayagam, Ehasanulla NoorMohammed, and Syed Hidayathullah Karimullah. 2024. Fiber Laser Cutting of AISI 431 Martensitic Stainless Steel: An Experimental Investigation. *Engineering Proceedings* 61. Multidisciplinary Digital Publishing Institute: 38. <https://doi.org/10.3390/engproc2024061038>.
11. Rohman, Muhamad Nur, Jeng-Rong Ho, Chin-Te Lin, Pi-Cheng Tung, and Chih-Kuang Lin. 2024. Predicting and Enhancing the Multiple Output Qualities in Curved Laser Cutting of Thin Electrical Steel Sheets Using an Artificial Intelligence Approach. *Mathematics* 12. Multidisciplinary Digital Publishing Institute: 937. <https://doi.org/10.3390/math12070937>.
12. Ghozali, Rizki Ghani, and Muttaqin Rahmat Pangaribawa. 2024. Analysis of the Effect of Cutting Motion Speed in CNC Laser Cutting on Roughness and Accuracy. *Engineering Proceedings* 63. Multidisciplinary Digital Publishing Institute: 10. <https://doi.org/10.3390/engproc2024063010>.
13. Wang, Le, Caixu Yue, Xianli Liu, Ming Li, Yongshi Xu, and Steven Y. Liang. 2024. Conventional and micro scale finite element modeling for metal cutting process: A review. *Chinese Journal of Aeronautics* 37: 199–232. <https://doi.org/10.1016/j.cja.2023.03.004>.
14. Elsharaky, E. A., M. R. Mishrif, A. S. El-Tabey, and Amira E. El-Tabey. 2024. Performance of new synthesized emulsifiers in ecofriendly metal cutting fluid formulations. *Scientific Reports* 14. Nature Publishing Group: 5299. <https://doi.org/10.1038/s41598-024-54636-2>.
15. Liu, Yuekai, Tianyang Wang, and Fulei Chu. 2024. Hybrid machine condition monitoring based on interpretable dual tree methods using Wasserstein metrics. *Expert Systems with Applications* 235: 121104. <https://doi.org/10.1016/j.eswa.2023.121104>.



17th-19th June 2024  
Gliwice, Poland

DEPARTMENT OF ENGINEERING MATERIALS AND BIOMATERIALS  
FACULTY OF MECHANICAL ENGINEERING  
SILESIA UNIVERSITY OF TECHNOLOGY

## INTERNATIONAL STUDENTS SCIENTIFIC CONFERENCE

### **Analysis of the possibilities of using BMS technology in network analysis – on the example of the Nazca environment**

Kacper Krysiak <sup>a</sup>, Bartosz Nikiel <sup>a</sup>, Kamil Oleksy <sup>a</sup>, Szymon Szeja <sup>a</sup>, Mirosław Bonek <sup>b</sup>

<sup>a</sup> Student of Silesian University of Technology, Faculty of Electrical Engineering, email: kacpkry923@student.polsl.pl

<sup>b</sup> Silesian University of Technology, Faculty of Mechanical Engineering, Department of Engineering Materials and Biomaterials

**Abstract:** The implementation of BMS (Building Management System) technology within the Nazca environment was proposed to analyze its potential as a network analyzer for electricity management. This would facilitate the rapid transmission of information packets from the network analyzer and energy meter to any internet-enabled device. The Operator Station was utilized as a tool for real-time monitoring of electrical network parameters, energy consumption analysis, visualization of parameter values in waveform formats, event logging, and providing a user-friendly interface. The project employed a hardware platform available on an industrial computer at the Laboratory of Intelligent Building and Industrial Infrastructure at the Department of Mechatronics, Faculty of Electrical Engineering, Silesian University of Technology. This platform includes TRB 135 current transformers, a Countis E34 energy meter, a DIRIS A-10 parameter recorder, and a USB-RS485 TH converter. By integrating these components into the low-voltage switchgear, the programming segment responsible for the user interface was developed, and new functionalities were added. The entire system was integrated within the Nazca environment, enabling efficient energy management. On the programming platform, views and logic were created in the operator station and configurator, facilitating the development of an automation system. Configurations included an astronomical clock, network parameter analyzer, energy reading, cost analysis, and event logging.

**Keywords:** Application, Configurator, Logic, Measurement, Parameters, Registry, Analyzer.

## 1. INTRODUCTION

A network parameter analyzer is a device commonly used in industrial sectors. It allows for the measurement of parameters such as voltage, current, frequency, active power, reactive power, and power factor, enabling diagnostics and optimization of electrical processes [1]. Analyzing these parameters makes it possible to monitor disturbances, short circuits, overloads, and inappropriate voltage levels. The analyzer facilitates fault diagnosis, prevents power loss, ensures the safety of users of electrical installations, and protects equipment. It also allows for the visualization of measured data, which aids in planning the expansion and modernization of

electrical networks and speeds up related decision-making processes. Retaining measurement data from the network analyzer also helps identify areas where energy can be saved and efficiency improved, positively impacting cost reduction. In recent years, many commercial network analyzers have emerged.

Among the leading manufacturers of network parameter analyzers are Siemens, Schneider Electric, and Lumer. The analyzers from these manufacturers are dedicated devices designed for industrial, private, and scientific purposes. Siemens is one of the largest companies in the world specializing in technology and industrial automation.

## **1. OBJECTIVE, ASSUMPTIONS, AND FINAL OUTCOME**

### **1.1. Objective**

The objective of this work is to modify the existing graphical user interface of the management system at the Laboratory of Intelligent Building and Industrial Infrastructure in the Department of Mechatronics, Faculty of Electrical Engineering, Silesian University of Technology. The modification includes adding a module for visualization, processing, and analysis of electrical installation parameters, along with cost analysis.

### **1.2. Assumptions**

The work was based on the following assumptions:

- Utilization of the existing hardware infrastructure in the laboratory.
- Use of the Nazca programming environment, which is fully available for programming purposes.

### **1.3. Final Outcome**

The final outcome of the work involved adding modules to the existing graphical user interface responsible for:

- Real-time monitoring of electrical network parameters.
- Monitoring of electrical energy consumption along with cost analysis for a selected energy distributor, enabling significant cost reductions.
- The ability to observe selected network parameters on graphs depending on the day, week, and month.
- An event log that informs about the current power factor for reactive power compensation, errors in data packet transmission from the analyzer and energy meter, and proper internet connection.
- A user-friendly interface.

## **2. HARDWARE PLATFORM**

The project utilized the building and industrial infrastructure of the laboratory, along with a license for the Nazca programming environment. Figure 1 presents a graphical connection diagram of the Hardware Platform.

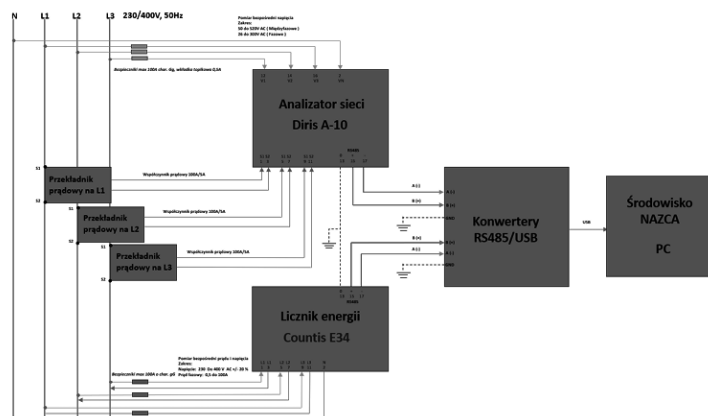


Figure 1. Diagram of the hardware platform.

### 3. PROGRAMMING PLATFORM

#### 3.1. Launch

After configuring the hardware platform, the next step was to create the automation system in the Nazca environment, which consists of three applications launched from the Launcher. The Launcher allows for the configuration of databases, connection to the Localhost server (i.e., the industrial computer hosting the Nazca environment), and Microsoft SQL (the database) where the project is stored.

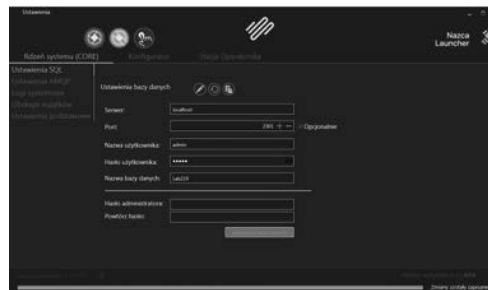


Figure 2. View of the attached Launcher.

Before launching the applications, a new SQL database was created in Microsoft Management Studio for storing, importing, and exporting data. A user account with a login and password was set up, resulting in the creation of both production and configuration databases. Additionally, MongoDB was used in the project to store variable values for display on graphs. Database configuration was not included within the scope of this project. Next, the user account was logged into across three tabs corresponding to the three applications. To simplify the process, the option to copy configuration settings to other applications was used, which is particularly useful if the settings, passwords, and logins are identical across applications. The first step was to launch the System Core application, commonly known as Purple Nazca. This application ensures correct connections to the databases for software licensing, current astronomical time, and services responsible for node status and the operation of components such as Messaging Big Data, Logic, and the MongoDB server, ensuring the proper functioning of the entire platform.



Figure 3. View of the enabled System Core application.

The next application is the Configurator, also known as Green Nazca. This application is used to create logic from nodes that enable the measurement of relevant parameters from the Analyzer and Energy Meter registers, among many other functions. To use this application, a login is required. In the bottom left corner, the correctness of the data connection and the operation of the topology can be observed. Connection to the DB Local host database occurs upon login.

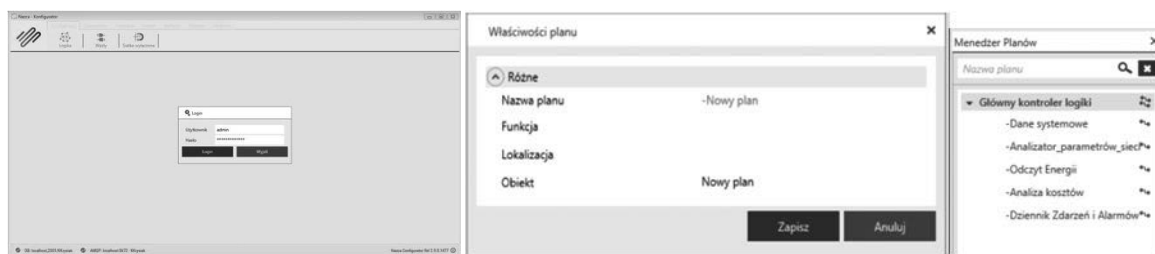


Figure 4. Login view in the Configurator and Creating a new plan and the view of the created plan group.

### 3.2. Network Parameters Analyzer

In the "Network Parameters Analyzer" section, the logic for displaying energy measurements and current parameters was developed. This involved creating a logic to read:

- Phase voltages and voltage harmonic distortion factors for each phase.
- Interphase voltages and voltage harmonic distortion factors.
- Phase currents and current harmonic distortion factors for each phase.
- Frequency.
- Energy consumption in the laboratory room over the entire day, previous day, week, previous week, month, and previous month.
- Daily, weekly, and monthly energy costs in the laboratory room.

To measure these parameters, the Modbus Master Node was utilized, enabling communication with measurement devices on the hardware platform via the RS485 communication module using the Modbus protocol.

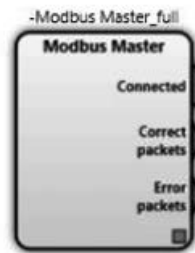


Figure 5. Modbus Master.

The node was configured to retrieve information from any device. For the node to function correctly and receive information packets from devices, the following steps were necessary:

1. Select the appropriate operating mode: In this case, the devices communicate using Modbus RTU, an interface type that encodes data in binary. Each data byte is encoded as a single communication byte.
2. Create a proper configuration file path: The configuration file, a CSV, stores device addresses, functions, and addresses in the Modbus protocol. A shared configuration file was chosen for both the network analyzer and energy meter to retrieve information from a single node universally.
3. Select the appropriate COM port: COM port 12 was used to identify the serial port on the Modbus bus, enabling data exchange between the computer and the Modbus-compatible device.
4. Set the transmission speed: Set to 9600 bits/sec, the most commonly used speed in communication modules.
5. Set the stop bits: Chose 2 stop bits for communication stability, allowing the receiver to distinguish the end of one data packet from the start of the next.

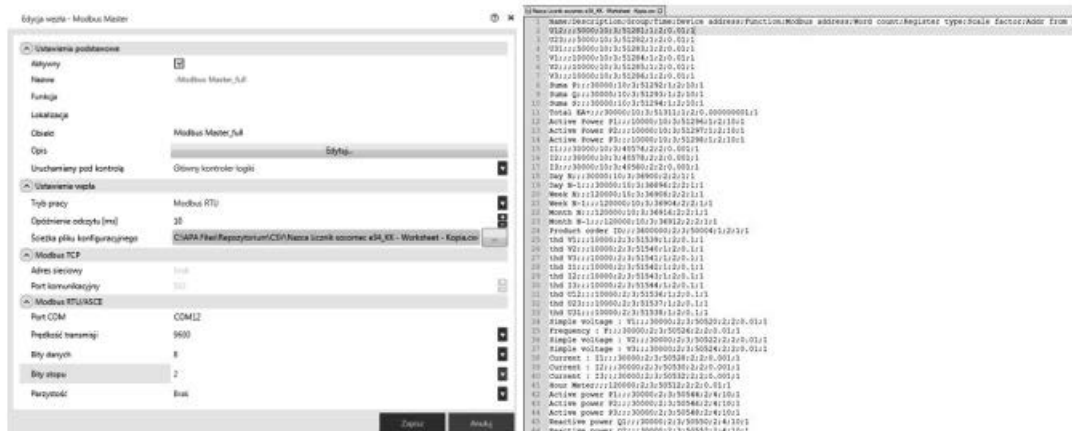


Figure 6. Editing a correctly configured Modbus Master node and file view Configuration.

When the steps are correctly executed, you can create the logic to verify all the current values ("data quanta") of the mentioned parameters and their types over the respective links and at the nodes' inputs and outputs. By right-clicking on the plan and using the Diagnostics option, the logic was checked for proper execution. The current value of the first phase current was displayed at the OUT output of the variable, as described. The logic for all variables scheduled for reading was performed in an identical way.

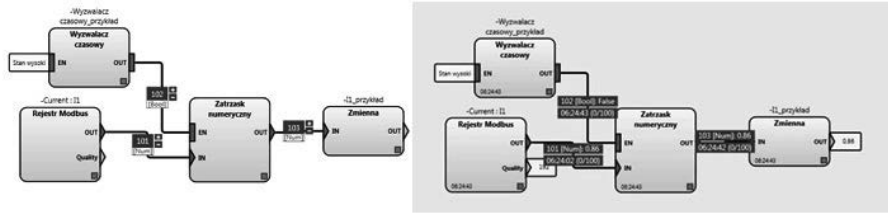


Figure 7. View of correct logic execution with Diagnostics.

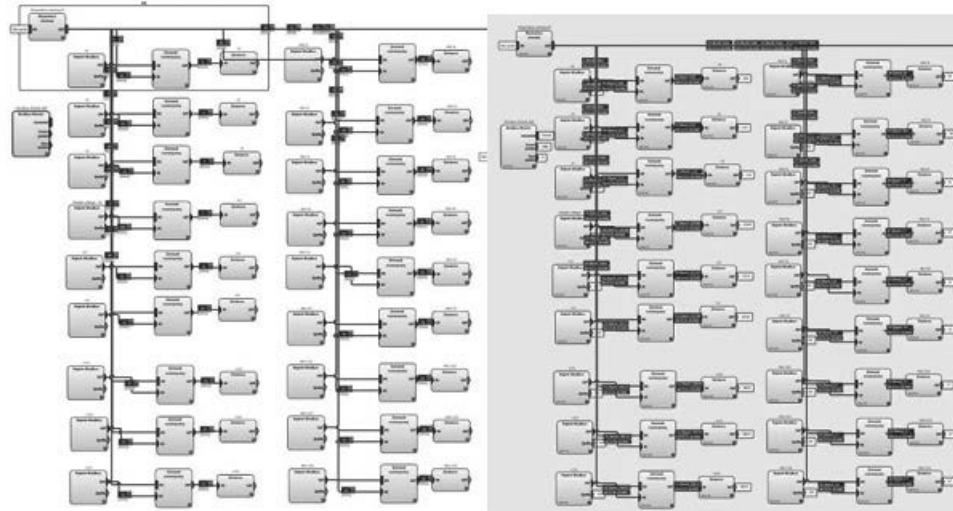


Figure 8. Sample Full logic view for currents, voltages, phase-to-phase voltages and their harmonic coefficients along with their diagnostics.

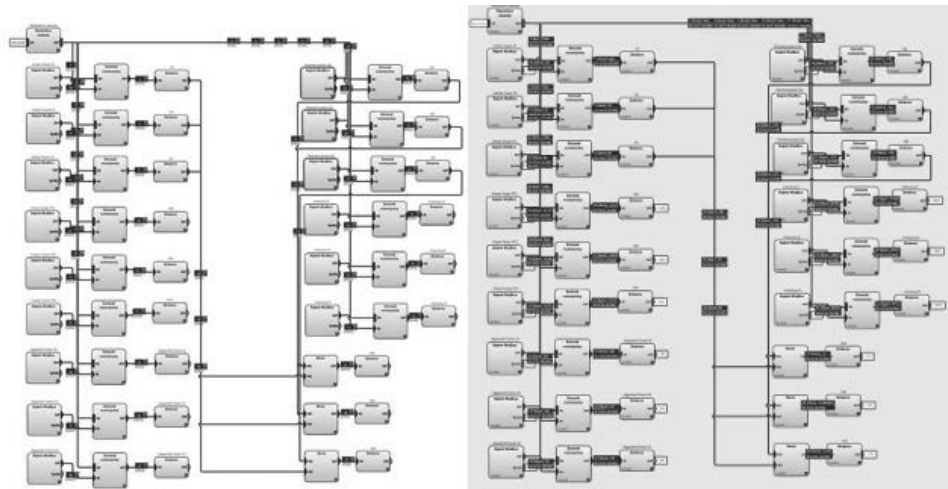


Figure 9. Sample View of the logic checking the energy consumption limit with Diagnostics.

#### 4. THE OPERATOR STATION

The Operator Station is the final application in the Nazca environment, responsible for visualizing process operations and diagnostic readings from the configurator. After launching and logging into the application, it allows you to select "View Configuration" for creating process visualizations.

The next step was configuring the views and template to create a user-friendly operator station interface. Configuration started with the template by double-clicking on the canvas. To create the appropriate interface, widgets were used, which can be found under the "Widgets" option in the "Views" menu in the upper left corner of the application. Selecting "Widgets" displays the widget palette.

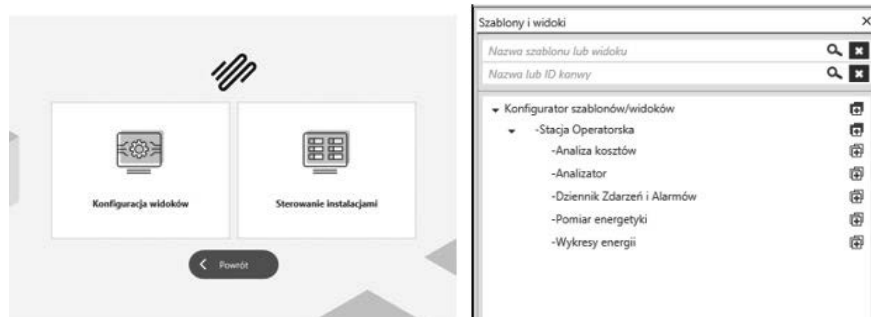


Figure 10. View of selection options in the Operator Station application and the created template with views.

#### 4.1. View Configuration

To create a user-friendly operator station interface, views and templates were configured using widgets found in the "Widgets" option in the "Views" menu.

1. Label Widget: Used for descriptions and titles, configured by setting display style, icon, and font. Label example: "Network Parameter Analyzer."
2. Date-Time Widget: Displayed current time by linking it to the Astronomical Clock node via the "Node Manager." The "Current DateTime ISO8601" pin was selected for accurate time display.
3. Date Display: Another Date-Time widget was used to show the current date.
4. View Widget: Enabled switching between different views created in the Template. Configured to display target views with appropriate descriptions and styles. Used five times with different descriptions.

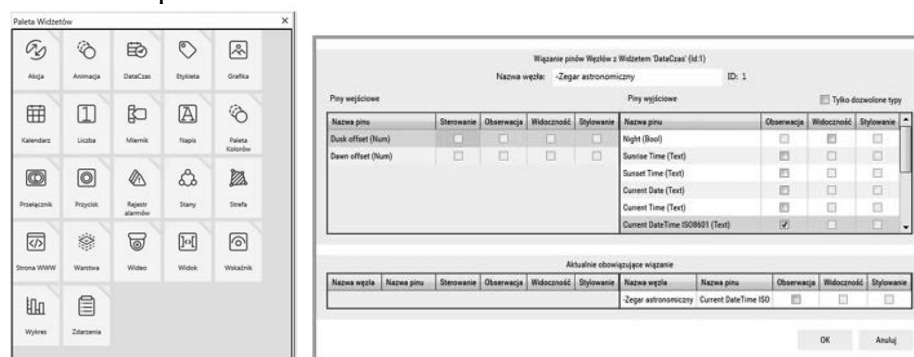


Figure 11. View Palette and Label Properties.

After designing the template, we started designing the rest of the views. Starting with Cost Analysis view. Initially, Label widgets were used for descriptive purposes and the Graphics widget to aesthetically improve the visualization of the applied widgets.





Figure. 12. Real view of all operator panel templates.

**5. CONCLUSIONS**

This project involved diagnosing, optimizing electrical processes, and monitoring for undesirable events in the electrical network. The developed Electrical Network Analysis enables real-time parameter readings, energy cost analysis, and visualization of selected parameters on graphs. Event Log Update; Modified to report reactive power compensation limits and monitor Modbus device connections. Cost Management Designed to improve cost management and compare costs among different energy providers. Due to time constraints, long-term data visualization wasn't achieved as the Operator Station was only activated in the final project phase, resulting in missing data from previous weeks and months. Future development possibilities include: Creating a mobile app. Analyzing current asymmetry. Developing electrical load prediction, Adding a Push node for notifications, alerts, and alarms via mobile messages.

**ACKNOWLEDGEMENTS**

The publication was created within the framework of the joint Slovak-Polish project International Visegrad Fund's V4 Generation Mobility Mini-Grant No 12410044 as a result of

cooperation between the Association of Alumni of the Silesian University of Technology, Gliwice, Poland and the University of Žilina, Slovakia.

The project is co-financed by the Governments of Czechia, Hungary, Poland and Slovakia through Visegrad Grants from the International Visegrad Fund. The mission of the fund is to advance ideas for sustainable regional cooperation in Central Europe.



## **BIBLIOGRAPHY**

[1] Analizatory parametrów typu N10 i P10 S Marcinkowski 2002 rok

[2] Analiza parametrów sieci wewnątrzzakładowej przy wykorzystaniu systemu BMS i PME Kołodziej K. Wydział Elektrotechniki i Automatyki; Politechnika Gdańska rok 2018.



17th-19th June 2024  
Gliwice, Poland

DEPARTMENT OF ENGINEERING MATERIALS AND BIOMATERIALS  
FACULTY OF MECHANICAL ENGINEERING  
SILESIA UNIVERSITY OF TECHNOLOGY

## INTERNATIONAL STUDENTS SCIENTIFIC CONFERENCE

### Stal nierdzewna do zastosowań w sztućcach

Natalia Łonczek<sup>a</sup>, Agata Majnusz<sup>a</sup>, Miłosz Kuźniak<sup>a</sup>, Barbara Grzegorzczak<sup>b</sup>

<sup>a</sup> Uczniowie Zespołu Szkół Łączności w Gliwicach

<sup>b</sup> Politechnika Śląska, Wydział Mechaniczny Technologiczny, Katedra Materiałów Inżynierskich i Biomedycznych,  
email: barbara.grzegorzczak@polsl.pl

**Streszczenie:** Sztućce to narzędzia używane do spożywania posiłków, które są integralną częścią kultury kulinarnej od tysiącleci. Najczęściej sztućce wykonane są ze stali nierdzewnej – materiału odpornego na uszkodzenia, zarysowania i rdzewienie. Choć stalowe sztućce są jednymi z najbardziej popularnych na rynku, to jednak jakość zestawu może się różnić. Aby określić odporność na korozję wybranych stali użytych do produkcji sztućców w praktycznych środowiskach zastosowań, przeprowadzono badania korozyjne przy użyciu komory solnej. Czas badania wyniósł 96h, ośrodkiem agresywnym był 5% roztwór NaCl. Spektrometrem iskrowym określono skład chemiczny badanych łyżeczek. Przy pomocy mikroskopu świetlnego określono strukturę stali. Twardość zmierzono metodą Vickersa. Stale zawierające od 16 do 18 % chromu oraz 10 i 8 % niklu nie wykazały oznak korozji. Na powierzchni stali zawierającej ok 12,5% chromu po ok. 48h pojawiły się czerwone produkty korozji.

**Abstract:** Cutlery is a dining tool that has been an integral part of culinary culture for millennia. Most often, cutlery is made of stainless steel - a material that is resistant to damage, scratches and rust. Stainless steel is safe for food contact and is usually dishwasher safe. Although steel cutlery is one of the most popular on the market, the quality of the set may vary. To determine the corrosion resistance of selected cutlery steels in practical application environments, corrosion tests were carried out using a salt spray chamber. The test time was 96 hours, the aggressive medium was a 5% NaCl solution. The chemical composition of the tested teaspoons was determined using a spark spectrometer. The structure of the steel was determined using a light microscope. Hardness was measured using the Vickers method. Steels containing 16 to 18% of chromium and 10 and 8% of nickel showed no signs of corrosion. Red rust appeared on the surface of steel containing approximately 12.5% chromium after approximately 48 hours.

**Keywords:** materials, cutlery, stainless steel, corrosion, structure.

### 1. WSTĘP

Sztućce to narzędzia wykorzystywane do spożywania posiłków. Podstawowe elementy zestawu sztućców to nóż, widelec i łyżka, choć istnieje wiele innych rodzajów dostosowanych

do różnych potrzeb kulinarnych, takich jak łyżeczka do herbaty, nóż do steków, widelczyk do ciasta czy łyżka do sałaty. Historia sztucców sięga starożytności. Pierwsze narzędzia przypominające współczesne noże były używane już przez naszych przodków z epoki kamienia. Noże były początkowo narzędziami do polowania i obróbki jedzenia. W starożytnym Rzymie i Grecji używano również łyżek wykonanych z kości, drewna lub metali. Widły, które później przekształciły się w widelce, były początkowo używane w rolnictwie [1] [2]. Współczesne sztucce są zazwyczaj wykonane ze stali nierdzewnej, która jest trwała, odporna na korozję i łatwa w utrzymaniu. Dla bardziej eleganckich zestawów używa się srebra lub posrebrzanych metali. W ostatnich latach, w odpowiedzi na rosnące świadomość ekologiczną, popularne stały się sztucce z materiałów biodegradowalnych, takich jak bambus czy drewno [3] [4].

Korozja metali to proces chemiczny lub elektrochemiczny, w wyniku którego metale ulegają degradacji pod wpływem czynników środowiskowych, takich jak wilgoć, tlen, kwasy i sole. Najczęstszą formą korozji stali jest rdzewienie żelaza, podczas którego metal reaguje z tlenem i wilgocią, tworząc tlenki żelaza, czyli rdzę. Dlatego gładkość i czystość powierzchni są kluczowymi czynnikami wpływającymi na odporność korozyjną [5]. Nawet niewielkie nierówności mogą stanowić punkty, w których zaczyna się proces korozji. Pierwszym widocznym objawem korozji ogólnej stali jest zazwyczaj matowienie jej powierzchni. Korozja może prowadzić do osłabienia strukturalnego metali, co zagraża bezpieczeństwu konstrukcji i wymaga kosztownych napraw [6].

Stal nierdzewna to wspólna nazwa dla dużej rodziny gatunków stali jakościowych, które ze względu na zawartość chromu, wynoszącą przynajmniej 11%, są odporne na niszczenie pod wpływem chemicznej lub elektrochemicznej reakcji z otaczającym środowiskiem. W skład stali nierdzewnej mogą wchodzić również inne pierwiastki, takie jak nikiel, molibden, mangan, oraz węgiel, które poprawiają jej wytrzymałość, twardość i elastyczność. Zawarty w stali chrom reaguje z tlenem z powietrza, tworząc na jej powierzchni niewidoczną warstwę tlenku chromu, która chroni stal przed korozją. Ta warstwa ochronna, jeśli zostanie uszkodzona mechanicznie lub przez chemikalia, samoczynnie się odbudowuje po ponownym kontakcie z tlenem, nawet w środowisku ubogim w tlen, takim jak woda. Wyższa zawartość chromu w stali zwiększa jej odporność na korozję, a dodatek molibdenu dodatkowo ją wzmacnia. Nikiel natomiast jest dodawany, aby uzyskać strukturę austenityczną stali, co ułatwia jej obróbkę plastyczną na zimno i spawanie [7] [8] [9].

Twardość i odporność na korozję to najważniejsze cechy jakościowe sztucców [10]. Sztucce najczęściej wykonuje się z następujących stali: Stal 18/10 - jest to najpopularniejszy rodzaj stali nierdzewnej używany do produkcji wysokiej jakości sztucców. Zawiera 18% chromu i 10% niklu, co zapewnia jej doskonałą odporność na korozję i nadaje połysk. Stal 18/0 - ten rodzaj stali zawiera 18% chromu i nie zawiera niklu. Jest mniej kosztowny i mniej odporny na korozję niż stal 18/10, ale nadal jest często stosowany w produkcji sztucców. Stal 13/0: zawiera 13% chromu i jest używana głównie do produkcji noży, ponieważ jest twardsza i bardziej odporna na ścieranie, co jest kluczowe dla zachowania ostrości ostrza. Mimo licznych zalet, produkcja stali nierdzewnej wiąże się z wyzwaniem ekologicznymi, takimi jak emisja dwutlenku węgla i zużycie energii. Przyszłość produkcji sztucców ze stali nierdzewnej może więc zmierzać w kierunku bardziej zrównoważonych i ekologicznych metod wytwarzania oraz poszukiwania alternatywnych, przyjaznych środowisku materiałów. Stal nierdzewna pozostaje jednak materiałem pierwszego wyboru dla sztucców ze względu na swoje unikalne właściwości, które łączą trwałość, estetykę i praktyczność, co czyni ją niezastąpionym elementem w kuchniach na całym świecie [11] [12].

Celem pracy było określenie odporności na korozję wybranych stali użytych do produkcji sztućców w praktycznych środowiskach zastosowań.

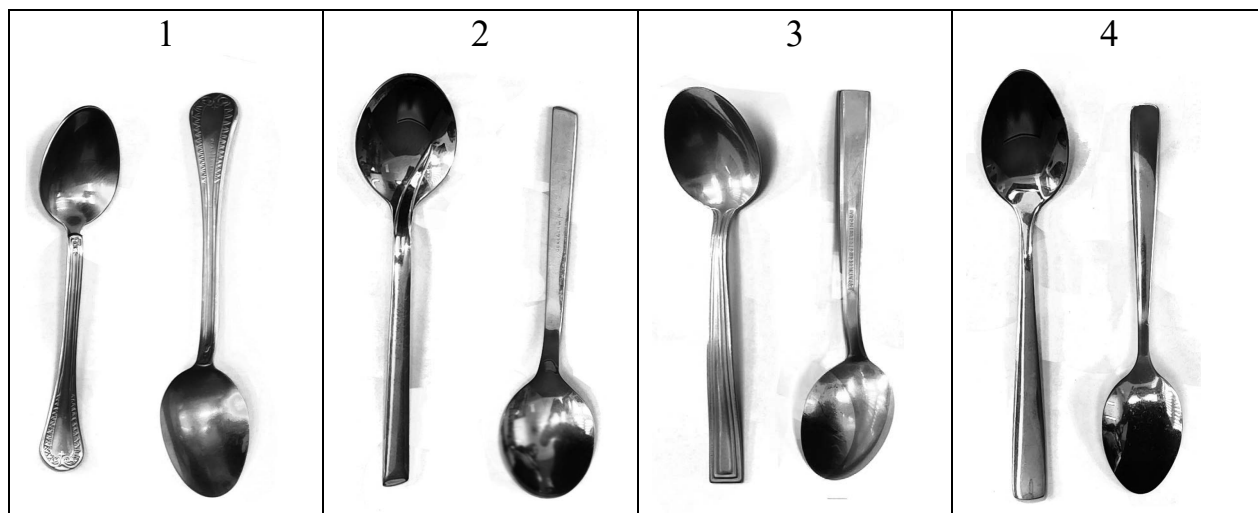
## 2. MATERIAŁ DO BADAŃ I METODY BADAWCZE

Do badań wykorzystano cztery losowo zakupione łyżeczki. Łyżeczki nr 1 i 2 posiadały grawer 18/10, łyżeczka nr 3 miała wygrawerowane Stainless Steel, natomiast łyżeczka nr 4 nie posiadała żadnego graweru (rys.1).

Przy pomocy spektrometru iskrowego Artus 8 Ultimate (OES) firmy ARUN Technology określono skład chemiczny badanych łyżeczek. Otrzymane składy chemiczne przedstawiono w tabeli 1.

Testy korozyjne przeprowadzono w komorze solnej CCip450 firmy Ascott w temperaturze 35°C w warunkach 100%wilgotności. Analizowany materiał poddany został działaniu 5% solanki (NaCl), rozpylonej w komorze w postaci mgły solnej. Eksperymenty przeprowadzono w oparciu o ISO 9227:2012 w czasie 96h. Wpływ czasu środowiska korozyjnego na stale z których wykonano łyżeczki sprawdzano co 24h. Przed przystąpieniem do badań korozyjnych łyżeczki trzykrotnie zważono na wadze analitycznej. Komorę do badań korozyjnych wraz z umieszczonymi w niej łyżeczkami przedstawiono na rys. 2. Po upływie całego założonego czasu wyciągnięte z komory łyżeczki sfotografowano oraz ponownie trzykrotnie zważono na wadze analitycznej.

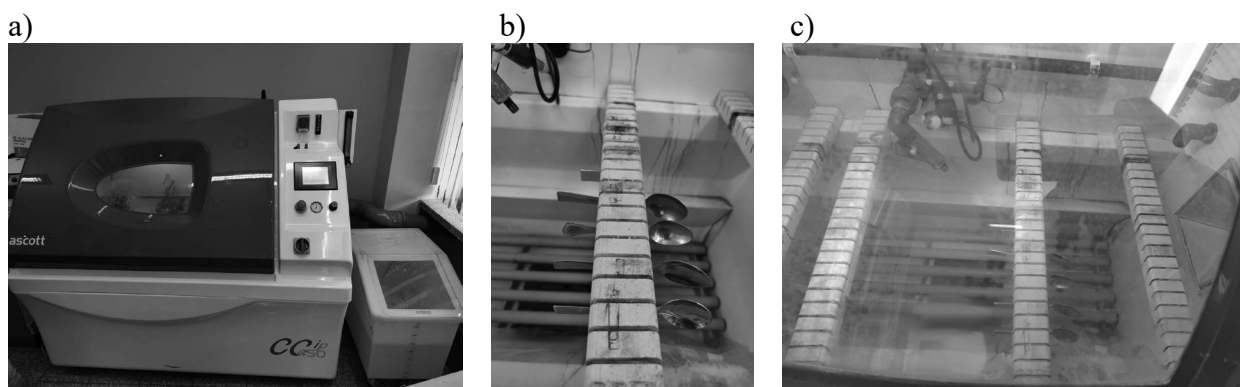
Obserwacje metalograficzne mikrostruktury łyżeczek wykonano po standardowej procedurze przygotowania złądów obejmującej cięcie, szlifowanie, polerowanie i trawienie w wodzie królewskiej w czasie 2-30s. Obserwacje wykonano na mikroskopie świetlnym firmy Zeiss przy powiększeniach 200x i 500x. Pomiary twardości na złądach metalograficznych zrealizowano metodą Vickersa, zgodnie z normą PN-EN ISO 6507, na mikrotwardościomierzu FM700 przy obciążeniu 4,9N.



Rys. 1. Łyżeczki użyte do badań

Tabela 1. Skład chemiczny badanych stali

		Nr łyżeczki/próbki			
		1	2	3	4
Skład chemiczny %	C	0.0334	0.0374	0.516	0.213
	Si	0.383	0.378	0.25	0.363
	Mn	1.32	1.56	0.199	0.32
	P	0.0201	0.0269	0.0195	0.0212
	S	0.00231	0.00235	0.0001	0.0001
	Cr	18.2	18.1	15.9	12.5
	N	0.099	0.121	0.0687	0.0634
	Mg	0.0020	0.00434	0.0001	0.0001
	Al	0.00291	0.00181	0.00167	0.0001
	Ti	0.0034	0.0024	0.00214	0.00245
	V	0.0554	0.0538	0.107	0.0554
	Co	0.125	0.126	0.0291	0.0195
	Ni	9.87	7.82	0.371	0.105
	Cu	0.441	0.436	0.269	0.0614
	Zn	0.0211	0.0326	0.0285	0.022
	Mo	0.199	0.209	0.0314	0.0113
	W	0.021	0.0476	0.0279	0.0181
Fe	rest.	rest.	rest.	rest.	



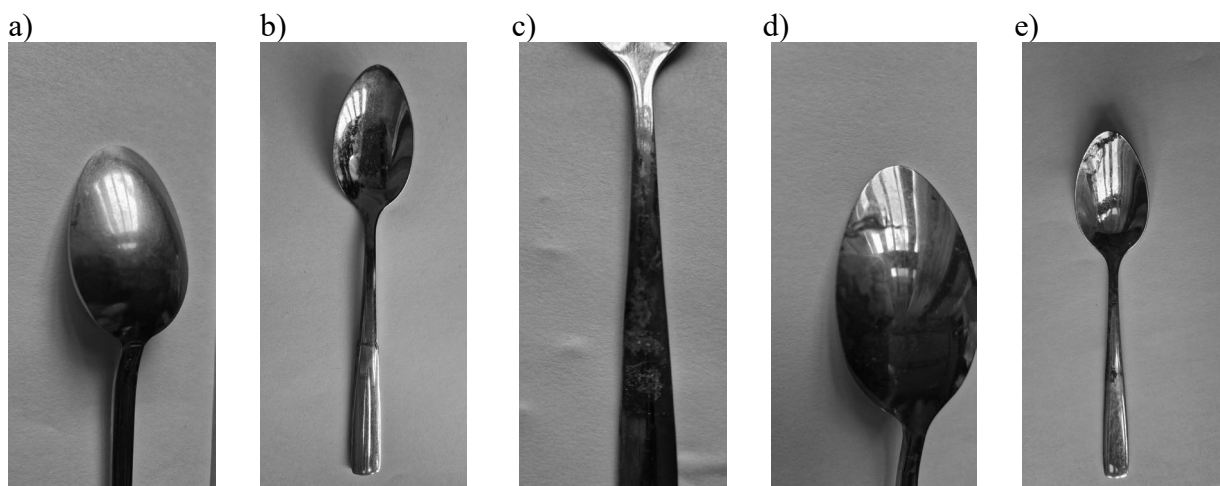
Rys. 2. Komora do badań korozyjnych a), unieszczenie łyżeczek w czasie testu b) c);

### 3. WYNIKI BADAŃ I ICH OMÓWIENIE

Badania w komorze solnej pozwoliły ocenić odporność korozyjną stali z których wykonano łyżeczki. Wpływ czasu środowiska korozyjnego na powierzchnie łyżeczek oraz ich masę przedstawiono w tabeli 2 oraz na rys. 3. Pierwsze zmiany korozyjne zauważono na części chwytowej łyżeczki nr 4 po 48 h. Charakteryzowały się one nieregularnym kształtem i różną głębokością wżerów. Zmiany korozyjne powiększały się wraz z upływem czasu badania. Po 78 h czerwone produkty korozji widoczne były także na tylnej stronie miseczki, a po 96h zmiany pojawiły się również na przedniej stronie miseczki łyżeczki nr 4. Po 96h niewielką zmianę korozyjną zauważono również na miseczce łyżeczki nr 3. Największy przyrost masy łyżeczek po teście korozyjnym wykazała łyżeczka nr 4. Przepuszczalnie niedostateczna ilość chromu w składzie chemicznym stali łyżeczki nr 4 była przyczyną obniżonej odporności korozyjnej.

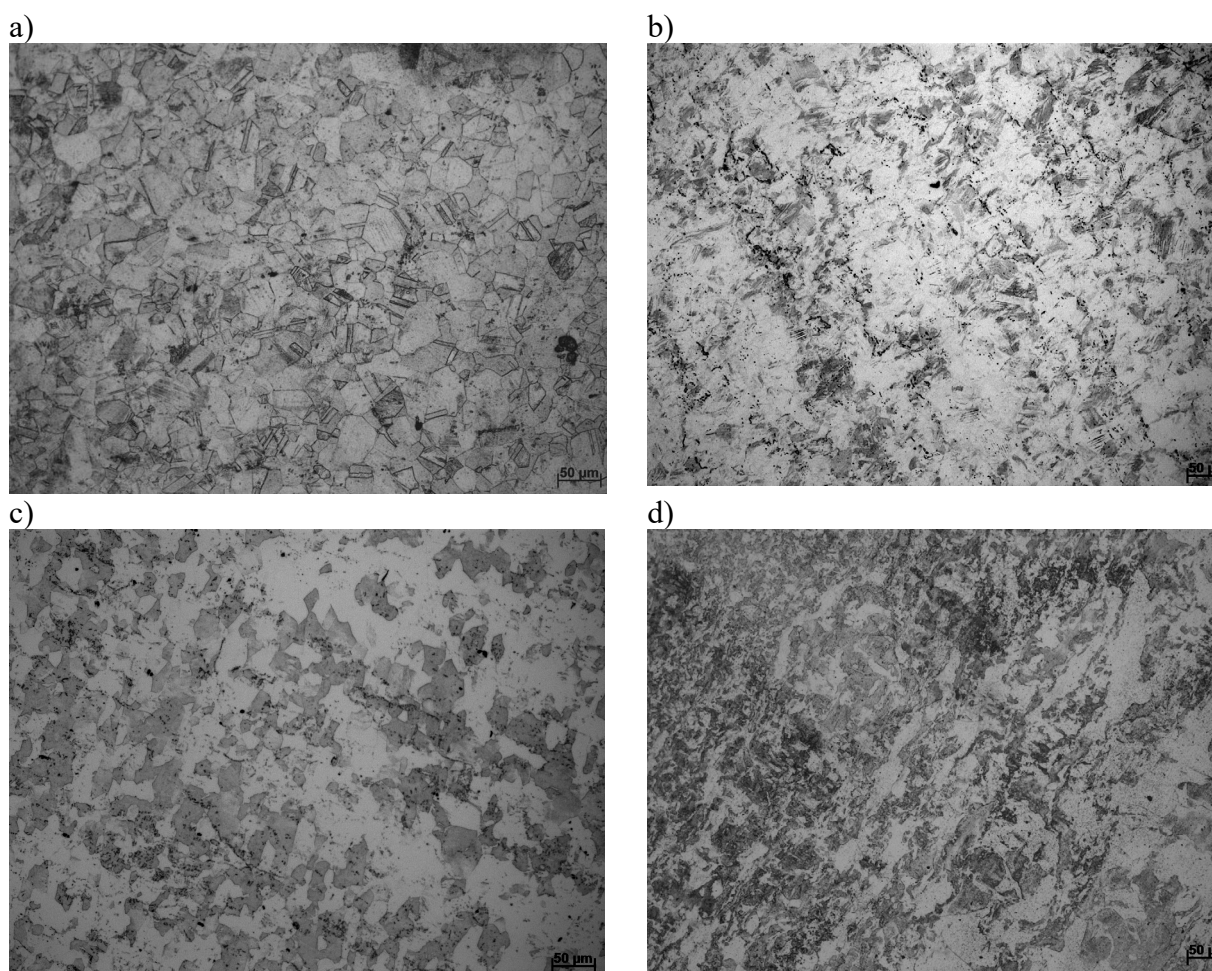
Tabela 2. Wyniki badań korozyjnych

Nr łyżeczki	Zmiany korozyjne na powierzchni łyżeczek				Masa łyżeczek, średnia z 3 pomiarów (g)			
	24h	48h	72h	96h	0 h	96h	różnica (g)	różnica %
1	brak	brak	brak	brak	17,7370	17,7373	+3	0,0016
2	brak	brak	brak	brak	12,8368	12,8370	+2	0,0015
3	brak	brak	brak	czerwone produkty korozji na miseczce	18,2645	18,2651	+6	0,0032
4	brak	czerwone produkty korozji na części chwytowej łyżeczki	czerwone produkty korozji w części miseczki i na części chwytowej łyżeczki	czerwone produkty korozji w części miseczki i na części chwytowej łyżeczki	19,5305	19,5322	+17	0,0087



Rys. 3. Zmiany powierzchni łyżeczek: łyżeczka nr 3 po 96h a), łyżeczka nr 4: po 48h b), po 72h c), po 95h d), e)

Obserwacje metalograficzne struktury wykonane na zglądach przygotowanych z łyżeczek przedstawiono na rys. 4 i rys. 5. Analiza metalograficzna pozwoliła zidentyfikować struktury w części miseczki i części chwytowej łyżeczek. łyżeczki nr 1 i 2 wykazują strukturę austenityczną, natomiast łyżeczki nr 3 i 4 strukturę ferrytyczną. W części miseczkowej łyżeczek nr 2, 3 i 4 fazy, odpowiednio austenitu i ferrytu, wykazują cechy odkształcenia, co jest spowodowane prawdopodobnie procesem tłoczenia. Ponadto w strukturze części chwytowej łyżeczki nr 4 widoczna jest zróżnicowana wielkość ziarn ferrytu co świadczy o częściowej rekrytalizacji. W części struktur, na granicach ziarn widoczne są prawdopodobnie węgliki i wtrącenia niemetaliczne. Struktura austenityczna łyżeczek 1 i 2 jest zgodna dla zbadanego składu chemicznego, 18% Cr oraz 8-10% Ni zapewniły stabilność tej fazy. Brak Ni w składzie w stalach łyżeczek nr 3 i 4 przy obecności Cr ok. 13-16 % jest powodem utworzenia struktury ferrytu stopowego.



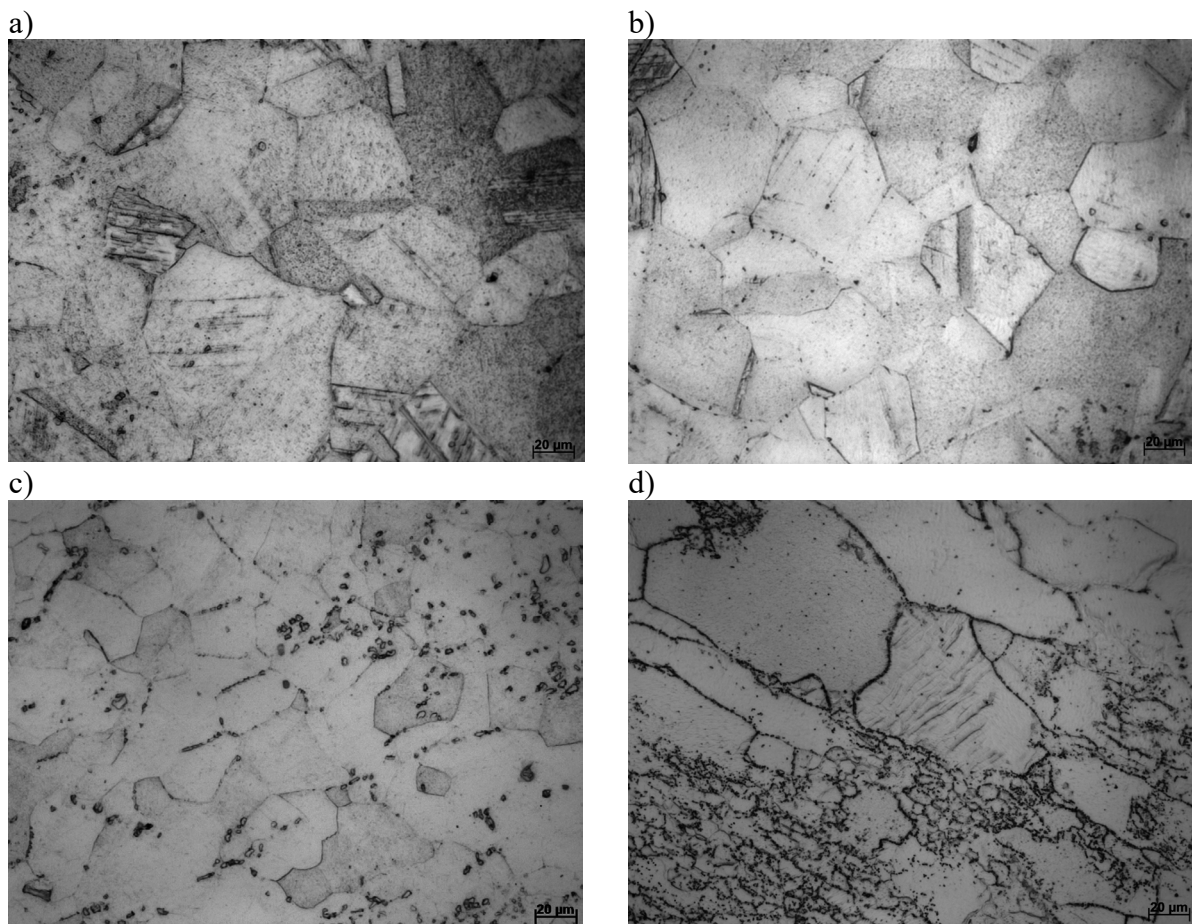
Rys. 4. Struktura miseczek łyżeczek: nr 1 a), nr 2 b), nr 3 c), nr 4 d), pow. 200x

Pomiary twardości wykonane na zglądach metalograficznych wykonanych z łyżeczek przedstawiono w tabeli nr 3. Wszystkie cztery łyżeczki wykazały wyższą twardość w miseczkach w porównaniu z częścią chwytową. Nawyższą twardością charakteryzowała się miseczka łyżeczki nr 2, co jest zgodne z uzyskany obrazem struktury odkształconego austenitu. Najniższą twardością charakteryzowała się część chwytowa łyżeczki nr 3.

Tabela 3. Wyniki pomiarów twardości

Nr pomiaru	Twardość łyżeczek HV <sub>5</sub>							
	Łyżeczka nr 1		Łyżeczka nr 2		Łyżeczka nr 3		Łyżeczka nr 4	
	obszar miseczki	część chwytowa	obszar miseczki	część chwytowa	obszar miseczki	część chwytowa	obszar miseczki	część chwytowa
1	250	232	358	264	254	196	260	244
2	240	227	364	248	242	197	280	253
3	248	228	353	240	259	189	268	242
4	250	220	365	250	256	188	265	265
5	245	230	354	245	260	197	267	250
Wartość średnia	246	227	358	249	254	193	268	250





Rys. 5. Struktura części chwytowej łyżeczek: nr 1 a), nr 2 b), nr 3 c), nr 4 d), pow. 500x

#### 4. WNIOSKI

Wykonane badania oraz analiza uzyskanych wyników pozwoliła na sformułowanie następujących wniosków:

1. Najwyższą odpornością korozyjną w 5% roztworze NaCl charakteryzowały się łyżeczki nr 1 o składzie chemicznym ok. 18% Cr i ok. 10 % Ni oraz łyżeczka nr 2 o składzie chemicznym ok. 18% Cr i ok. 8 % Ni
2. Zawartość Cr poniżej 13% w składzie chemicznym stali łyżeczki nr 4 nie zapewniła odpowiedniej ochrony przed działaniem 5% roztworu NaCl. Na powierzchni łyżeczki po ok. 48h pojawiły się czerwone produkty korozji.
3. Struktury badanych stali odpowiadają typowej strukturze stali nierdzewnych. Stale 18/10 i 18/8 charakteryzują się strukturą austenityczną natomiast stale zawierające ok. 13-16% Cr wykazują strukturę ferrytu stopowego.
4. Najwyższą twardością charakteryzowała się struktura austenitu odkształconego będąca w części miseczki łyżeczki nr 2.
5. Stal nierdzewna jest jednym z najlepszych materiałów, które można wybrać do produkcji sztućców. Jest trwała, łatwa w utrzymaniu i estetyczna, co sprawia, że jest popularnym wyborem w większości domów i restauracji.

## LITERATURA

1. K. Pągowska, A. O. Sujecka, and B. Zgodzińska-Wojciechowska, *Bon appétit: zabytkowe sztuce, ich historia, kształty i przeznaczenie: katalog wystawy z kolekcji prywatnej 16 XII 2016 - 17 IX 2017*, Muzeum Pomorza Środkowego w Słupsku. Słupsk: Muzeum Pomorza Środkowego, 2016.
2. R. Bobrow, *Dawne sztuce*. Warszawa: Pagina, 1998.
3. J. Xie, L. Guo, C. Zhu, H. Teng, F. Xing, G. Luo, H. Zhao, X. Wei, and H. Dong, "Tribocorrosion behavior of martensitic stainless cutlery steel in pressed Shanghai Bok Choy," *Corrosion Science*, vol. 228, pp. 111807, Mar. 2024.
4. A. Gupta, G. Singh, P. Ghosh, K. Arora, and S. Sharma, "Development of biodegradable tableware from novel combination of paddy straw and pine needles: A potential alternative against plastic cutlery," *Journal of Environmental Chemical Engineering*, vol. 11, no. 6, pp. 111310, Dec. 2023.
5. S. Zor, M. Soncu, and L. Çapan, "Corrosion behavior of G-X CrNiMoNb 18-10 austenitic stainless steel in acidic solutions," *Journal of Alloys and Compounds*, vol. 480, no. 2, pp. 885–888, Jul. 2009.
6. L. L. Shreir, "1.1 - Basic Concepts of Corrosion," in *Corrosion (Third Edition)*, L. L. Shreir, R. A. Jarman, and G. T. Burstein, Eds. Oxford: Butterworth-Heinemann, 1994, pp. 1:3-1:15.
7. L. Gardner, "Stability and design of stainless steel structures – Review and outlook," *Thin-Walled Structures*, vol. 141, pp. 208–216, Aug. 2019.
8. Y. Liang, T. Manninen, O. Zhao, F. Walport, and L. Gardner, "Elevated temperature material properties of a new high-chromium austenitic stainless steel," *Journal of Constructional Steel Research*, vol. 152, pp. 261–273, Jan. 2019.
9. D. T. Llewellyn and R. C. Hudd, "4 - Stainless steels," in *Steels (Third Edition)*, D. T. Llewellyn and R. C. Hudd, Eds. Oxford: Butterworth-Heinemann, 1998, pp. 291–379.
10. P. Rosemann, T. Müller, M. Babutzka, and A. Heyn, "Qualitätsbewertung von Schneidwaren durch Kurzzeit-Korrosionsprüfung," *HTM Journal of Heat Treatment and Materials*, vol. 68, no. 5, pp. 224–235, Oct. 2013.
11. K. Notomi, T. Shioura, "New stainless steel for cutlery applications," *Metal Powder Report*, vol. 53, no. 10, pp. 34, Oct. 1998.
12. P. J. Hidalgo, "Pitting corrosion of martensitic cutlery steels," *Surface Technology*, vol. 10, no. 3, pp. 193–208, Mar. 1980.



17th-19th June 2024  
Gliwice, Poland

DEPARTMENT OF ENGINEERING MATERIALS AND BIOMATERIALS  
FACULTY OF MECHANICAL ENGINEERING  
SILESIA UNIVERSITY OF TECHNOLOGY

## INTERNATIONAL STUDENTS SCIENTIFIC CONFERENCE

### The microstructure and properties of the nitrified layer with a compound zone after laser modification

Anna Mękarska<sup>a</sup>, Karolina Rogalewska<sup>b</sup>

<sup>a</sup> Poznan University of Technology, Faculty of Engineering Materials and Technical Physics, Department of Material Engineering, email: [anna.mekarska@student.put.poznan.pl](mailto:anna.mekarska@student.put.poznan.pl)

<sup>b</sup> Silesian University of Technology, Faculty of Mechanical Engineering, Department of Engineering Materials and Biomaterials, email: [kr313886@student.polsl.pl](mailto:kr313886@student.polsl.pl)

**Abstract:** Based on the literature it has been found that controlled gas nitriding is a process where control of the nitriding potential helps to make a layer with selected phase composition during the shortest time of process. It was noticed that laser heat treatment has positive impact on the properties of diffusion layers. Samples were made of 42CrMo4 of steel, on which controlled gas nitriding was carried out. Next were selected the parameters of the laser heat treatment, which made way to create the simple laser tracks with re-melting and without re-melting. The influence of laser processing parameters on the microstructure, chemical composition and dimensions of single laser paths was studied. Microhardness test enabled to compare impact of the laser treatment parameters on the hardness of the produced layers. Simultaneously, the hardness of the layers with and without laser heat treatment was compared.

**Keywords:** gas nitriding, compound zone, laser heat treatment, microstructure, hardness

## 1. INTRODUCTION

Nitriding is a thermochemical treatment process involving the diffusive saturation of metal alloys in a nitrogen-rich environment. This treatment aims to enhance the surface properties of materials by increasing hardness, corrosion resistance, and wear resistance. [1] Nitriding is typically the final stage of heat treatment after quenching and high temperature tempering, to avoid dimensional changes in finished parts.[2] Nitrogen atoms then diffuse into the material and occupy interstitial spaces.[3] The nitrogen atoms create interstitial solutions with iron, resulting in a nitrified layer called the compound zone (white layer). Compound zone consists of  $\epsilon$  nitrides -  $\text{Fe}_{2.3}\text{N}$  hexagonal close-packed structure and  $\gamma'$  nitrides -  $\text{Fe}_4\text{N}$  face-centered cubic structure. Below the compound zone is the diffusion zone made of  $\alpha$  ferritic iron saturated with nitrogen with body-centered cubic structure. [4]

Controlled gas nitriding enables complete control over the kinetics of growth and phase composition of the layer. The process involves using the maximum nitrogen potential within a given time. During the process, the nitrogen potential is decreased to limit the thickness of the  $\epsilon$  and  $\gamma'$  nitride zones without extending the process time. Changes in nitrogen potential lead to

changes in the microstructure of the produced layer [5]. Laser treatment can be applied to various heat treatment operations to create hybrid layers. It is used for surface modification due to its rapid heat generation and high processing speed. Laser heat treatment is one of the most promising methods for obtaining layers of suitable thickness with high wear and fatigue resistance [6]. In a very short time, the laser beam heats the iron-based substrate layer above the austenitizing temperature, followed by rapid cooling, which leads to hardening and the formation of a martensitic structure [7]. A key feature of the method is the rapid heating and cooling, which allows the formation of a very fine microstructure that improves the hardness and wear resistance of the laser-treated element. The processing parameters are selected to avoid melting the nitrided layer. [8, 9]

## 2. METODS AND MATERIAL

The samples were made of 42CrMo4 (40HM) which is low – alloy, medium carbon steel. The chemical composition of 42CrMo4 (tab. 1) was designed to facilitate heat treatment process (quenching and high-temperature tempering). Mostly used in machine and vehicles production, elements such as gears, shafts, axles, bolts, and piston rods. [10]

Table 1. Chemical composition of 42CrMo4 [11]

Material	C	Cr	Mn	Si	Mo	Ni	V	W	S,P	Fe
42CrMo4	0,38 - 0,45	0,9 - 1,2	0,4 - 0,7	0,17 - 0,37	0,15 - 0,25	Max 0,3	Max 0,05	Max 0,2	Max 0,035	rest

The first step included preparing disks with diameters of 25.4 mm and thicknesses of 6 mm. The next step involved quenching in oil from 860°C and tempering at a temperature of 600°C with a holding time of 2 hours. Afterwards, samples were subjected to a surface nitriding process. Saturation of the surface layer was obtained by regulating the nitriding potential at 580°C for the first sample and at 570°C within 5 hours in a nitriding atmosphere. Additionally, the disks were lasered using a TRUDIODE 3006 with a nominal power of 3 kW. Each laser path was marked while maintaining a distance between each path to ensure that none of the paths were treated twice. This process resulted in 11 paths, 5 on one side and 6 on the other side of the disk. Each path had a different parameter (tab. 2) such as laser power magnitude (P) and beam diameter (d) but the same laser velocity (2.88 m/min).

Table 2 Assigned laser properties to path number

Path number	1	2	3	4	5	6	7	8	9	10	11
<b>P [W]</b>	530	560	680	440	470	500	530	560	590	620	650
<b>d [mm]</b>	2	2	1,5	1,5	1,5	1,5	1,5	1,5	1,5	1,5	1,5

The finished sample was subjected to further observation: microstructure analysis, measurements of the depth and width of laser paths, and hardness profile. The structure of the fabricated coatings was analyzed a light optical microscope LAB-40 by OPTA-TECH. The photos taken by the LAB-40 were also used for measuring the depth and width of the heat-affected zone (HAZ) and the remelted zone, if present. The microhardness test was conducted on the cross sections of 5 laser paths (1, 2, 3, and 7) using a Buehler Micromet II. The Vickers method was applied with a force of 0.05 kG (0.49 N) for 15 seconds. The hardness profile was

created perpendicularly to the surface until the characteristic microstructure of heat-treated 42CrMo4 steel was reached.

### 3. RESULTS

#### 3.1. Microstructure analysis

Steel 42CrMo4 in its delivery condition exhibits a pearlitic-ferritic structure following normalizing and softening annealing. A sample of this steel was subjected to heat treatment, resulting in a mixture of fine cementite precipitates within a ferrite matrix. Subsequently, the prepared steel underwent thermo-chemical treatment through controlled gas nitriding with a progressively decreasing nitrogen potential. Figure 1 illustrates the distinct zones formed on the steel after nitrogen saturation.

In Figure 2, the heat-affected zone (HAZ) stands out against the dark diffusion zone. The HAZ is relatively small, indicating that the additional energy imparted during laser processing did not significantly alter the material's structure. However, when the laser beam power was increased by 30 W (Figure 3), the HAZ expanded, cover a deeper and wider area towards the core of the sample.

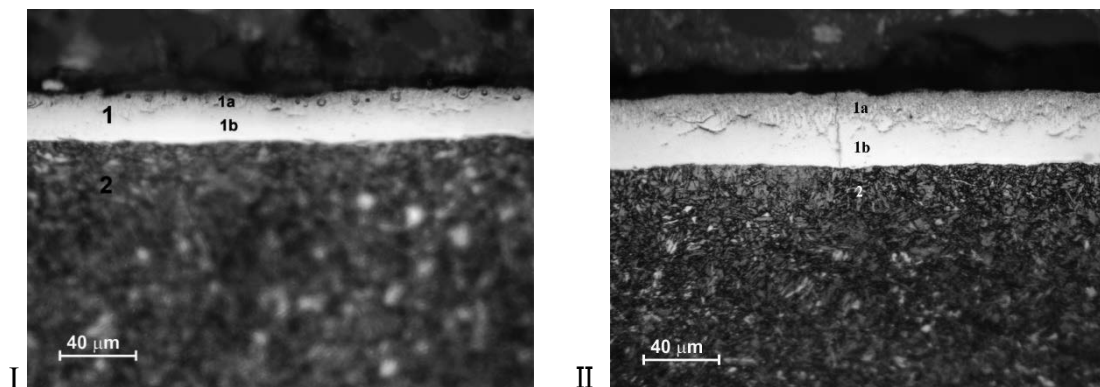


Fig. 1 The comparison of the microstructure of nitriding layer of Sample I and II: 1a – nitride  $\epsilon$  zone; 1b – nitride  $\epsilon + \gamma'$  zone; 2 – diffusion zone.

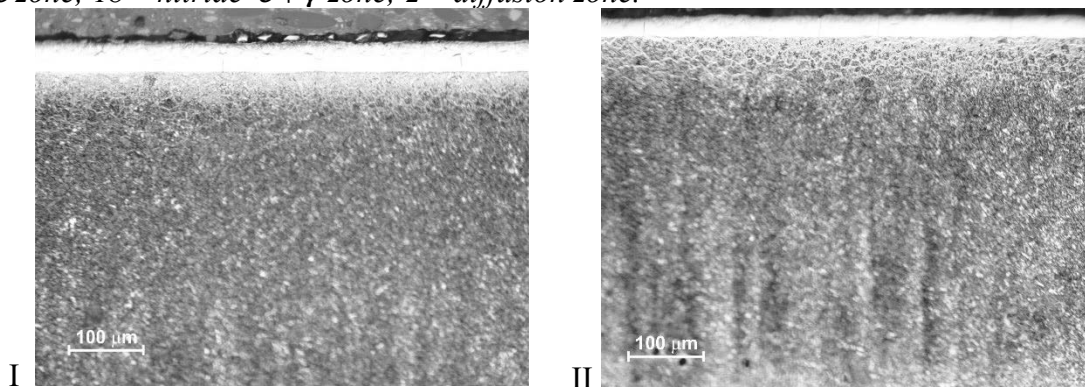


Fig. 2 The comparison of the microstructure of nitriding and laser treated sample I and II: path number 1 ( $d = 2 \text{ mm}$ ,  $P = 530 \text{ W}$ )

The reduction of the laser beam diameter to 1.5 mm (fig. 4 i 5), increased the heat-affected zone and a morphology of the compound zone. The white layer was melted and its appearance significantly altered, and the remelted zone was visibly deeper than the original nitride layer.

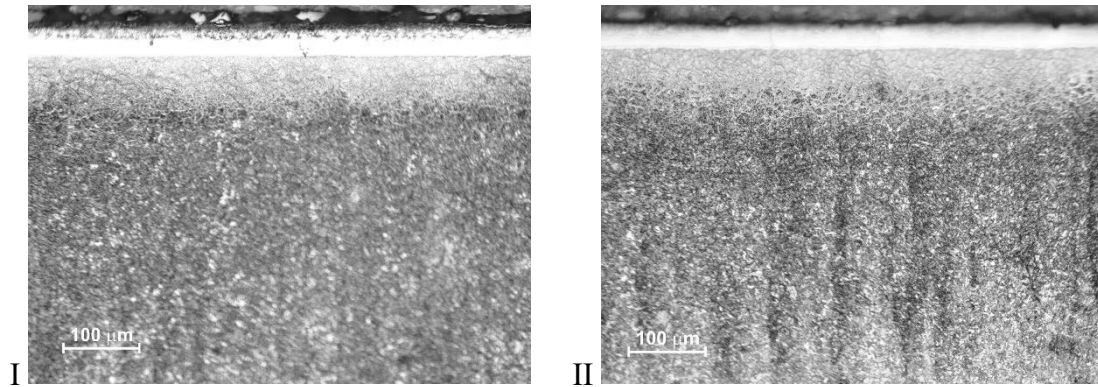


Fig. 3 The comparison of the microstructure of nitriding and laser treated sample I and II of path number 2 ( $d = 2 \text{ mm}$ ,  $P = 560 \text{ W}$ )

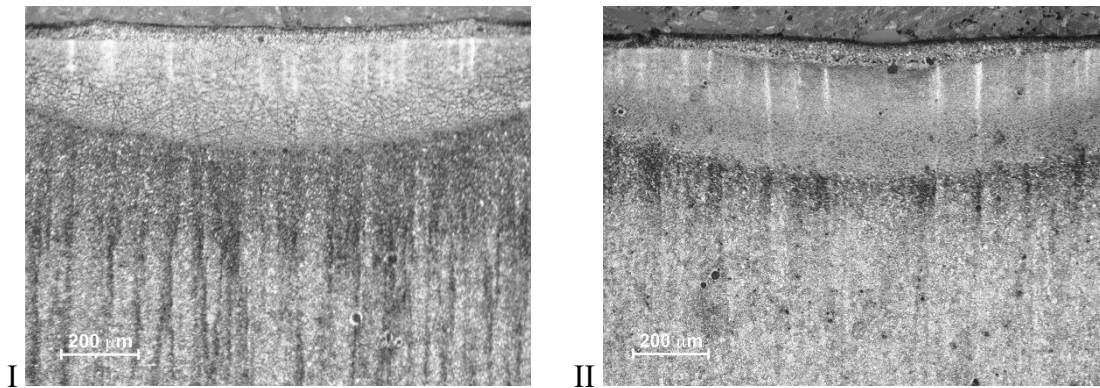


Fig. 4 The comparison of the microstructure of nitriding and laser treated sample I and II of path number 7 ( $d = 1,5 \text{ mm}$ ,  $P = 530 \text{ W}$ )

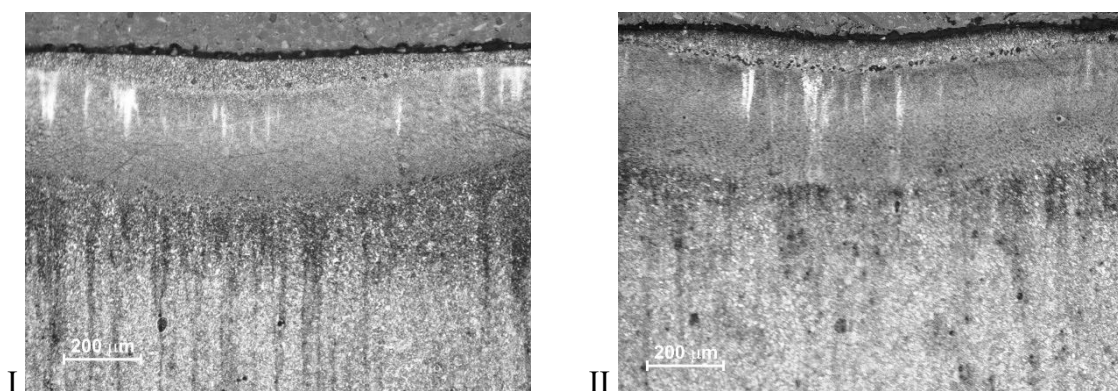


Fig. 5 The comparison of the microstructure of nitriding and laser treated sample I and II of path number 3 ( $d = 1,5 \text{ mm}$ ,  $P = 680 \text{ W}$ )

As the laser beam power increased, the HAZ expanded, even resulting porosity at the boundary between the HAZ and the diffusion zone. This is likely due to uncontrolled nitrogen evaporation during the surface layer processing. Given the rapid changes, the gas produced by evaporation could not escape from the treated area, leaving pores inside the material.

### 3.2. Microhardness testing

Microhardness graphs show the hardness gradient through the cross section of example laser paths on the nitrided surface. The chosen paths were obtained using 530 W and 680 W with  $d=1.5$ , and two paths  $d=2$  mm. Additionally, one more test was conducted in the area between two laser paths (Fig. 6), where the laser treatment did not alter the achieved nitriding layer in either of the samples. The profile was created from the white layer, through the diffusion zone, to the core. Figure 5 represents a comparison between two samples before laser treatment. The first value, around 900 HV0.05 in sample I, results from the porosity of the  $\epsilon$  nitride layer in the compound layer. The value distributions are similar in both cases. The highest results occur in the white layer, as expected, and gradually decrease to the value of the core microstructure-quenched and tempered low-carbon steel.

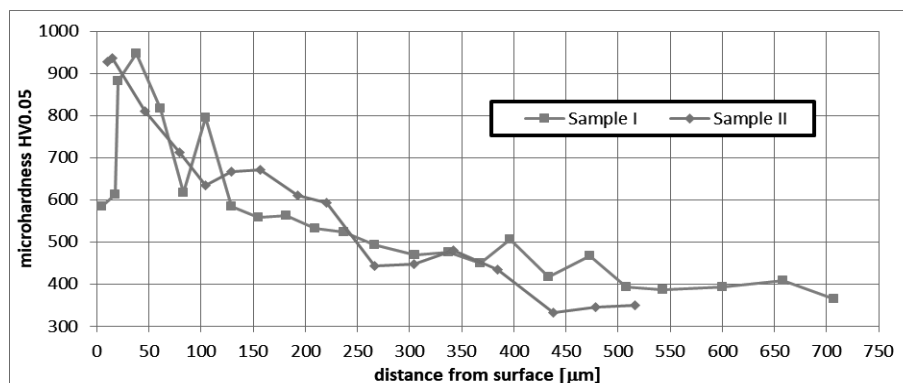


Fig. 6 Microhardness results comparison of Sample I and II of nitriding 42CrMo4 steel without laser treatment

Figures 7 and 8 represent the first two paths with a beam diameter of 2 mm, where remelting of the white layer compound does not appear. The surface layer increased compared to Figure 6, indicating less porosity of the  $\epsilon$  nitride phase. The distribution of hardness after the compound zone is also higher than in Figure 6, reflecting the effects of the heat treatment in the diffusion zone. The profile results continually decrease down to the core, remaining comparable.

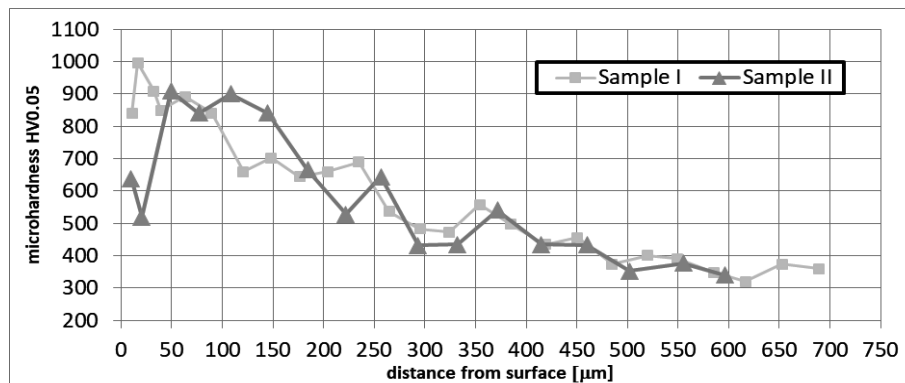


Fig. 6 Microhardness results comparison of Sample I and II of nitriding 42CrMo4 steel with laser treatment without remelt of compound zone ( $P=530$  W;  $d=2$  mm)

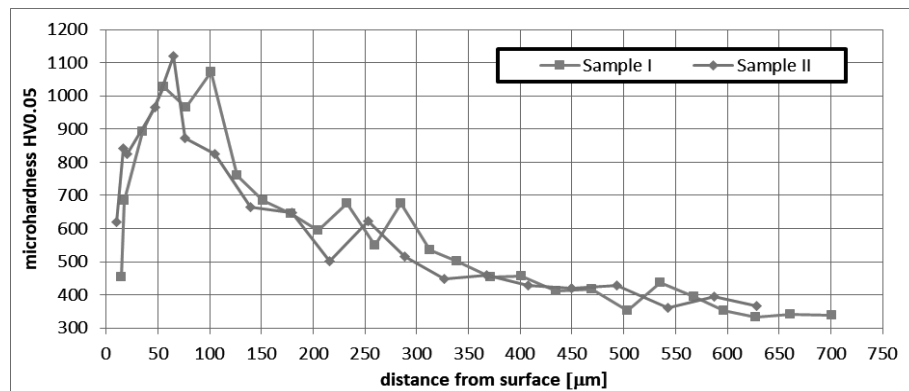


Fig. 7 Comparison of Sample I and II of nitriding 42CrMo4 steel with laser treatment without remelt of compound zone ( $P=560\text{ W}$ ;  $d=2\text{ mm}$ )

Paths with visible remelted compound zones of  $\epsilon$  and  $\epsilon + \gamma$  nitride exhibit lower values of microhardness than non-remelted ones, but noticeably higher values in the diffusion zone. The fact that the nitrided zone after laser treatment demonstrates lower hardness than the surface without any laser treatment may be due to the evaporation of nitride from the white layer. The diffusion zone, however, indicates high hardness results because of the martensite structure that appeared throughout the HAZ.

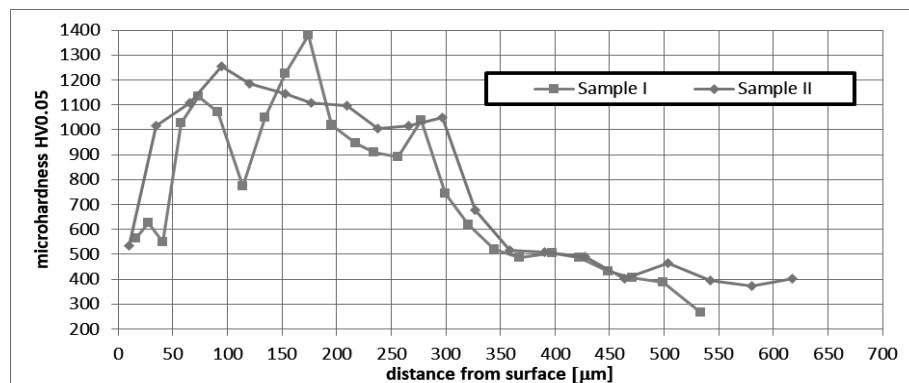


Fig. 8 Comparison of Sample I and II of nitriding 42CrMo4 steel with laser treatment with remelt of compound zone ( $P=530\text{ W}$ ;  $d=1,5\text{ mm}$ )

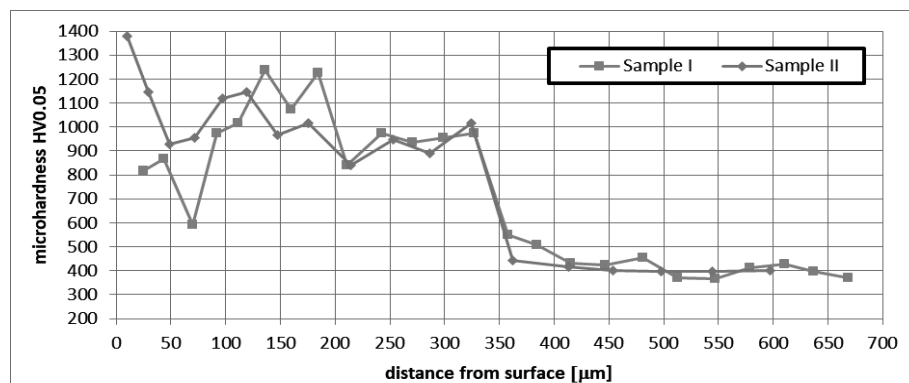


Fig. 9 Comparison of Sample I and II of nitriding 42CrMo4 steel with laser treatment with remelt of compound zone ( $P=680\text{ W}$ ;  $d=1,5\text{ mm}$ )



### 3.3. Measure analysis of zones formed after laser processing

The following graphs show the results of the measurements for each of the 11 prepared paths. Nine with laser beam diameter equal 1,5 mm and two with half millimetre wider beam. The dimensions of the heat-affected zone were presented for all paths produced with (fig.12) and without melting because the heat-affected zone appeared in every case of laser processing. The influence of beam diameter on the width and depth of the heat-affected zone is also clearly noticeable (Fig. 10 and 11). Paths produced by laser processing with a 2 mm beam diameter result in much smaller depths and widths of the paths compared to paths with a diameter smaller by 0.5 mm. The heat-affected zone is narrower and does not penetrate as deeply into the sample.

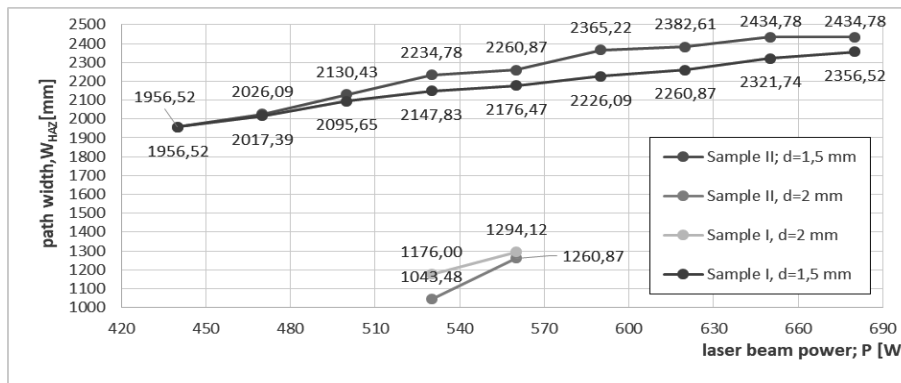


Figure 10. The dependence of HAZ width on laser beam power in Sample I and II

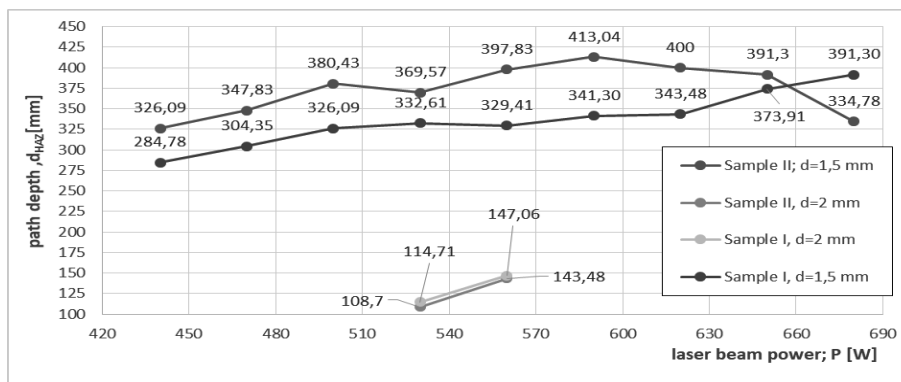


Figure 11. The dependence of HAZ depth on laser beam power in Sample I and II

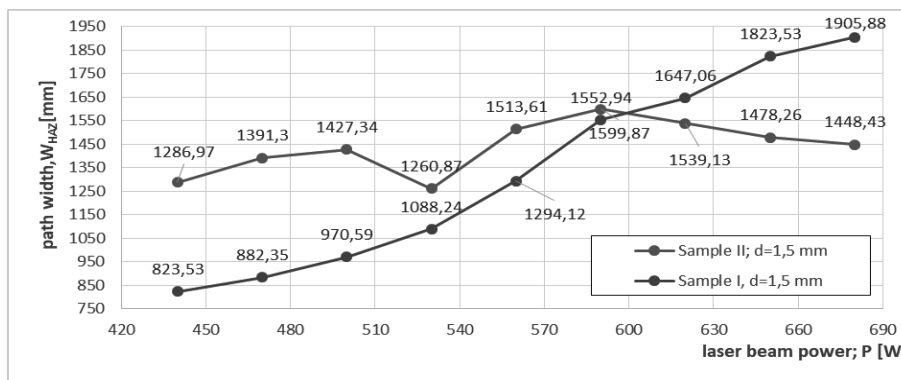


Figure 12. The dependence of RZ width on laser beam power in Sample I and II

There is a visible trend towards increasing the width of the paths with increasing laser beam power. There is a clear stabilization of the paths width within the range of 500 to 620 W beam power. The width of the melted zone then varies slightly, indicating that at these power values, not enough energy is supplied to cause a significant change in the width of the zone. The same trend persists for the depth (fig.13 ) of the melted zone.

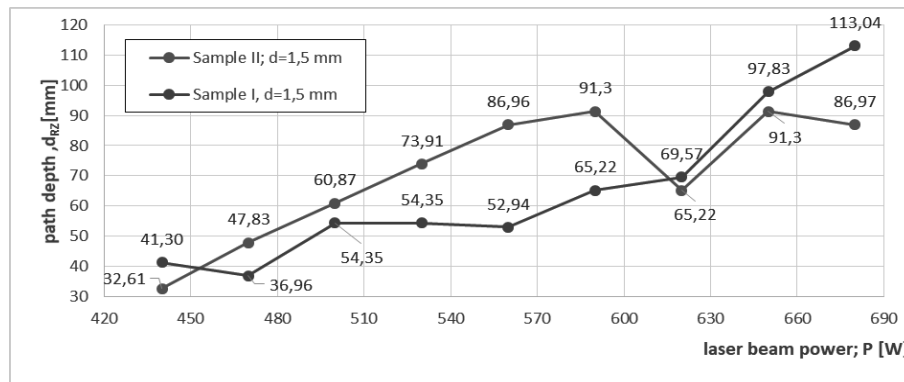


Figure 13. The dependence of RZ depth on laser beam power in Sample I and II

#### 4. SUMMARY AND CONCLUSIONS

Modification by laser heat treatment was proposed in order to change the microstructure and to improve properties of gas-nitrided layer produced on 42CrMo4 steel. LHT was carried out with and without re-melting. Based on the conducted research, the following conclusions can be drawn:

- As a result of the laser modification, it is possible to produce hybrid layers that are both nitrided and laser heat-treated, with and without melting.
- The microstructure of the obtained laser path after nitriding is influenced by the following laser processing parameters: beam power, beam diameter, and scanning speed.
- To obtain a path without melting, the process requires the use of a lower beam power density. In the conducted modifications, a path without melting was produced with a larger laser beam diameter.
- Laser paths with a smaller beam diameter had a larger heat-affected zone, which increased with the increasing laser beam power.
- The microstructure of the nitrided layer after laser modification for the path with melting consisted of a melted zone with coarse needle-like martensite, a heat-affected zone with fine needle-like martensite, and a diffusion zone (nitrided sorbite with  $\gamma'$  precipitates). For the path without melting, the microstructure included a zone with  $\epsilon + (\epsilon + \gamma')$  compounds, a heat-affected zone with martensite, and a diffusion zone with nitrided sorbite and  $\gamma'$  precipitates.
- The produced nitrided layers after laser modification are characterized by increased hardness compared to the layer after controlled gas nitriding.
- Near the surface, the hardness after laser modification was reduced. This could have been caused by poorer heat dissipation or the evaporation of some nitrogen at the surface (in the case of paths with melting).

## ACKNOWLEDGEMENTS

The publication was created within the framework of the joint Slovak-Polish project International Visegrad Fund's V4 Generation Mobility Mini-Grant No 12410044 as a result of cooperation between the Association of Alumni of the Silesian University of Technology, Gliwice, Poland and the University of Žilina, Slovakia.

The project is co-financed by the Governments of Czechia, Hungary, Poland and Slovakia through Visegrad Grants from the International Visegrad Fund. The mission of the fund is to advance ideas for sustainable regional cooperation in Central Europe.



## BIBLIOGRAPHY

1. Burakowski T., Wierzchoń T., Inżynieria powierzchni metali, Wydawnictwo Naukowo-Techniczne, Warszawa, 1995,
2. Dobrzański L., Podstawy nauki o materiałach i metaloznawstwo, Wydawnictwo Naukowo-Techniczne, Warszawa, 2002,
3. K. Przybyłowicz, Metaloznawstwo, Wydawnictwo Naukowo-Techniczne, Warszawa, 1999
4. An Introduction to Nitriding w: *Pye, D.S. Practical Nitriding and Ferritic Nitrocarburizing*, ASM International, 2003,
5. D. Panfil, M. Kulka, P. Wach, J. Michalski, D. Przystacki, Nanomechanical properties of iron nitrides produced on 42CrMo4 steel by controlled gas nitriding and laser heat treatment, *Journal of Alloys and Compounds* 706 (2017) 63-75.
6. M.F. Yan, Y.X. Wang, X.T. Chen, L.X. Guo, C.S. Zhang, Y. You, B. Bai, L. Chen, Z. Long, R.W. Li, Laser quenching of plasma nitrided 30CrMnSiA steel, *Materials and Design* 58 (2014) 154-160.
7. E. Colombini, R. Sola, G. Parigi, P. Veronesi, G. Poli, Laser Quenching of Ionic Nitrided Steel: Effect of Process Parameters on Microstructure and Optimization, *Metalurgical and Materials Transactions A* 45A (2014) 5562-5573.
8. Małdziński L.: Termodynamiczne, kinetyczne i technologiczne aspekty wytwarzania warstwy azotowanej na żelazie i stalach w procesach azotowania gazowego. Wydawnictwo Politechniki Poznańskiej, Seria Rozprawy Nr373, Poznań, 2002,
9. Monson T., Zheng B., Zhou Y., Lavernia E., Pearce C., Atcitty S.  $\gamma'$ -Fe<sub>4</sub>N, a new soft magnetic material for inductors and motors University of California, Irvine, 2016
10. Çalık, A., and O. Dokuzlar, and N., Uçar. "The effect of heat treatment on mechanical properties of 42CrMo4 steel". *Journal of Achievements in Materials and Manufacturing Engineering* 98, 1 (2020): 5-10.
11. PN-EN 10083-3:2008, Stale do ulepszania cieplnego -- Część 3: Warunki techniczne dostawy stali stopowych



17th-19th June 2024  
Gliwice, Poland

DEPARTMENT OF ENGINEERING MATERIALS AND BIOMATERIALS  
FACULTY OF MECHANICAL ENGINEERING  
SILESIA UNIVERSITY OF TECHNOLOGY

## INTERNATIONAL STUDENTS SCIENTIFIC CONFERENCE

### Deburring Tool Design for Copper Wire Drawing

Cemal Meran<sup>1</sup>, Cihan Atik<sup>2</sup>, Batuhan Gölcük<sup>2</sup>, Atike Oskay<sup>2</sup>, Orhan Akyuz<sup>3</sup>, Gizem Ordu<sup>3</sup>

<sup>1</sup>Prof. Dr., Pamukkale University, Faculty of Engineering, Department of Mechanical Engineering, Denizli, Turkey, cmeran@pau.edu.tr

<sup>2</sup>Student, Pamukkale University, Faculty of Engineering, Department of Mechanical Engineering, Denizli, Turkey

<sup>3</sup>Er-Bakir Electrolytic Copper Product Co., Denizli, Turkey

**Abstract:** In the process of drawing copper wire, cold welding must be performed in order not to stop production during the change of the spools. The cold welding process creates burrs on the copper wire. In addition, Nickel and Tin can be electrolytically plated on copper wires for different purposes. The aim of this study is to simply remove the burr in the drawing of uncoated bare copper wires without a significant change in wire diameter. In coated wires, it is to remove the burr easily in the same way in a minimum area without reducing the coating thickness. Within the scope of the study, a hand tool that allows easy chip removal for copper wire drawing has been designed without deteriorating the surface quality.

**Keywords:** copper wire, cold welding, burr.

### 1. INTRODUCTION

Cold pressure welding is a form of solid form welding and is unique because it is performed at ambient temperature. It is very difficult to produce a perfect cold welding process. This is due to the oxide layers that form on the metal in atmospheric conditions, surface irregularities, surface contamination and many more effects. Cold welding only works if there are no contaminants between the two surfaces pressed together. Also, the flatter and smoother the surface, the easier and smoother the weld will be. There are also limitations on the types of metals that can be joined by cold welding. Cold pressure welding is limited to non-ferrous materials or, at best, to soft iron with no carbon content. Most non-ferrous metals are suitable for cold welding. Wires can be welded on their own or with plain copper. Coated wires, such as tin-plated copper, silver and nickel-plated wires, can also be welded by themselves or with plain copper.

Cold welding process was used in this study and burrs were formed on the surface, **Figure 1**. The burrs formed on the surface were removed using a tool, but then surface roughness and shifts in the diameter of the wire were detected and the wire lost its aesthetic appearance at the cold welding point. The occurrence of such problems caused the process to slow down. With

the design produced, it was aimed to prevent the slowing down of these processes and at the same time to minimize the problems on the wire.

## 2. ELIMINATION OF BURR PROBLEM

There are many deburring methods for the burrs that can appear after cold welding; the oldest and simplest method of deburring is done by hand using a file, sandpaper or in some cases a leather strip. Its main advantage is that it can be adapted to the part and even to your physical location, for example between a workshop and a construction site. You can achieve a fine, high-quality finish by doing it manually, but it depends on the part and is very, very time-consuming. Other methods are deburring with machines and grinding machines, electrochemical methods and thermal deburring methods. Mechanical deburring refers to a range of machining methods that include various operations such as grinding, roller, etc. Basically, it covers any process in which a fast-moving abrasive wheel, abrasive belt or cutting tool removes burrs and smooths edges. In electrochemical deburring, the area where the burrs are located is immersed or washed in a fluid electrolyte. It is then electrically connected to a cathode. With careful control of operating voltages and currents, the "peaks" of the chips slowly dissolve until they are at the same height as the surrounding material. This can be thought of as the opposite of electroplating. Thermal deburring, on the other hand, is a very unique process. its most important advantage is that it can remove burrs from hard-to-reach areas such as holes and pockets. Wherever fuel gas can enter, it removes the burrs from the part by essentially vaporizing them before they reach the point where they can conduct heat into the body of the part. It encounters part size constraints based on firing chamber dimensions. Thermal deburring also leaves a residue on the parts that must be cleaned up afterwards.

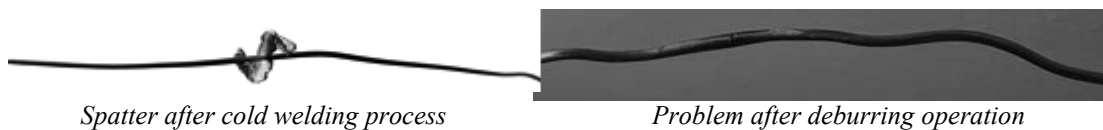


Figure 1: The traditional process of deburring

The burr formation in traditional cold wire drawing process was shown in **Figure 1**. This burr was removed manually using a file. The removal of the burr was successful, but structural deterioration and the copper wire lost its aesthetic appearance.

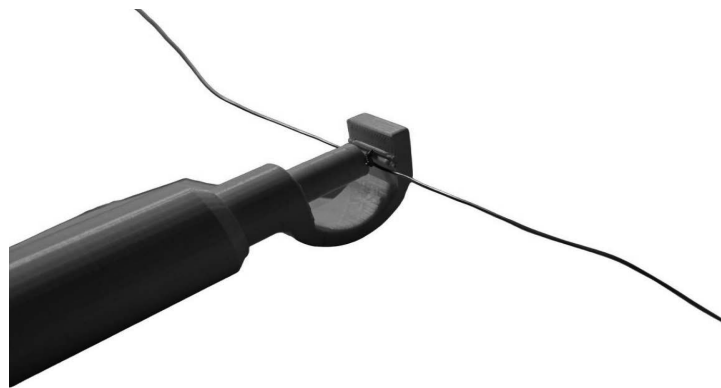
The burrs that appeared after the cold welding process were first removed as much as possible with an auxiliary apparatus, and then a file was used to remove the entire burr.



Figure 2: The solid view of tool and its application

At the place where this study was developed, it was observed that one of the most important reasons for the abrasion and deterioration of the aesthetic appearance of copper wire is hitting it with a hard tool such as a file. It was concluded that removing the burrs on the copper wire without impact would minimize these damages and the process of designing a tool that would not be hit by the person removing this burr was initiated.

A tool with rollers in the bearing system was developed and tested. It was concluded that the rollers in this tool did not hold the wire in **Figure 2** due to the small wire diameter and were insufficient for this process. This design was also tested on the burred copper wire in **Figure 3** and it was found that the roller bearing system was not sufficient for this design, but it was also found that the tool did not damage the copper wire. Inspired by these results, it was decided to develop a tool design without impact.



*Figure 3: Copper wire with burrs on the tool*

In our new design, a tool with a circular bearing was designed. The purpose of this is both to keep the copper wire in the bearing and to facilitate machining. After obtaining sample samples and the maximum diameter of the copper wire, a bearing was designed to be 0.1 mm more than the maximum diameter. In this way, even if the diameter of the copper wire changed, the tool we designed was suitable for all diameters.

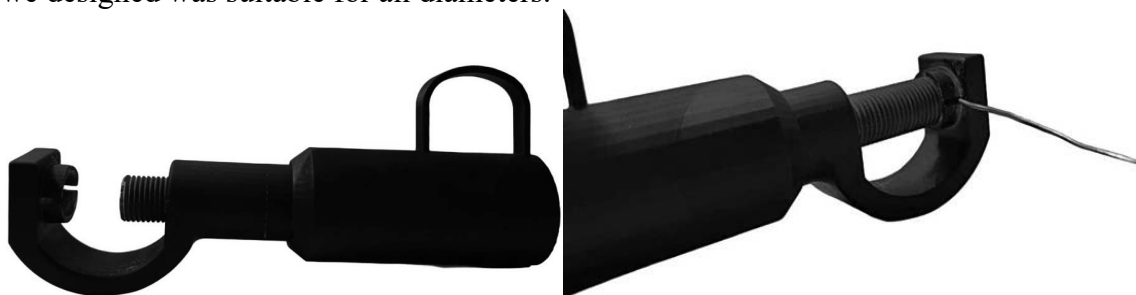


*Figure 4: New deburring tool design and deburring*

The design uses micrometre logic, allowing most people working in the field to easily understand the working principle of the tool. Split pin, holder, bearing, grinding bit, rear body, body, shaft, cylinder was used in the design given in Figure 4. Each of these parts was designed with minimum cost and materials were selected with great care to ensure long life. In the design, it was aimed to be small, to be easily portable in the working area and to easily solve the problem in areas with burr problems, and this purpose was achieved. The parts used in the

design can be easily installed and removed, and in case of a possible malfunction, the problem can be easily eliminated. Although it is known that this design will be successful in theory, observations were made by putting this design into practice with the help of a 3D printer. By making experiments with the samples taken from the company and our design, it was seen concretely that the design worked.

Since the tool designed within the scope of this study was produced in plastic in the 3D printer, the company started material research to produce the material from a metal material, taking into account that there may be situations where it cannot provide surface pressure.

### 3. DESIGN AND ASSEMBLY

The material EN AW-5083 (AlMg4,5Mn0,7) was found suitable for the part based on the easy portability of the part and the structural properties material. This aluminium alloy have good resistance to stress corrosion cracking. They are not suitable for welding or brazing because they are too soft, but they can be cold worked without losing their strength and hardness. 5083 aluminium alloy is a lightweight, low strength aluminium with good corrosion resistance, and contains magnesium. Split pins are used to allow other parts to be connected. The pin is inserted into a hole and then bent or pressed so that the slotted area fits against the edge of the pin hole. This ensures that the pin does not dislodge and the connection remains secure. Grinding allows precise dimensions to be obtained on workpieces. In hardened materials, grinding can also be used to get rid of hardened surfaces. It is a method used to smooth hard surfaces and get rid of hard surfaces. The shaft, which is responsible for transmitting the motion, is fitted inside the cylinder. The final version of the tool was given **Figure 5**.



*Figure 5: Final version of the tool design*

**Figure 6** shows how the copper wire should be inserted into the burr tool and how our tool will compress the part after insertion. The burr formed after cold welding will settle on our tool and when the tool is manually rotated around the wire, the burr will be removed and when the process is finished, our tool will easily come off the wire because it is similar to the micrometer logic. The practicality of this process will provide continuity in the field for the company working with this tool and at the same time will lighten the workload of the worker during the deburring process.

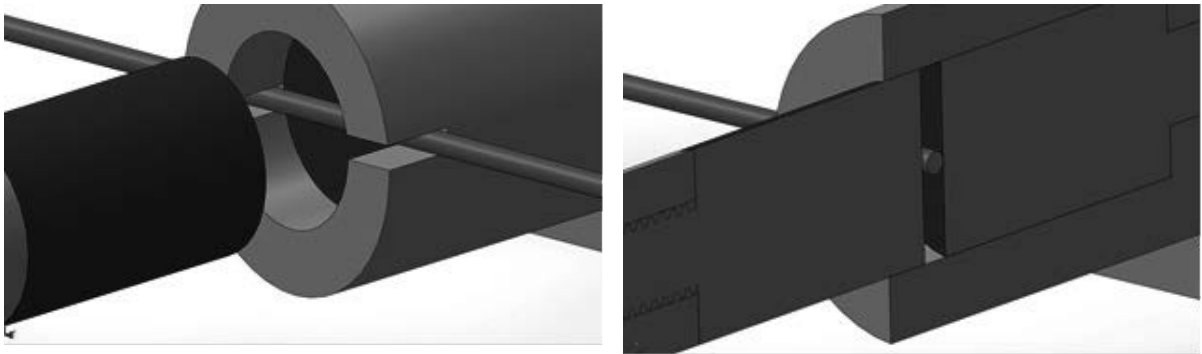


Figure 6: Inserting the copper wire into the deburring tool

In the process of finalizing the tool, the dimensions of the material were taken into account for easy handling in the work area. Since deburring is not an easy process, the connections between the parts were adjusted to be strong. The tool also needed to be easy to manufacture, so the body was secured with two bolts during assembly to make the tool both durable and easy to manufacture.

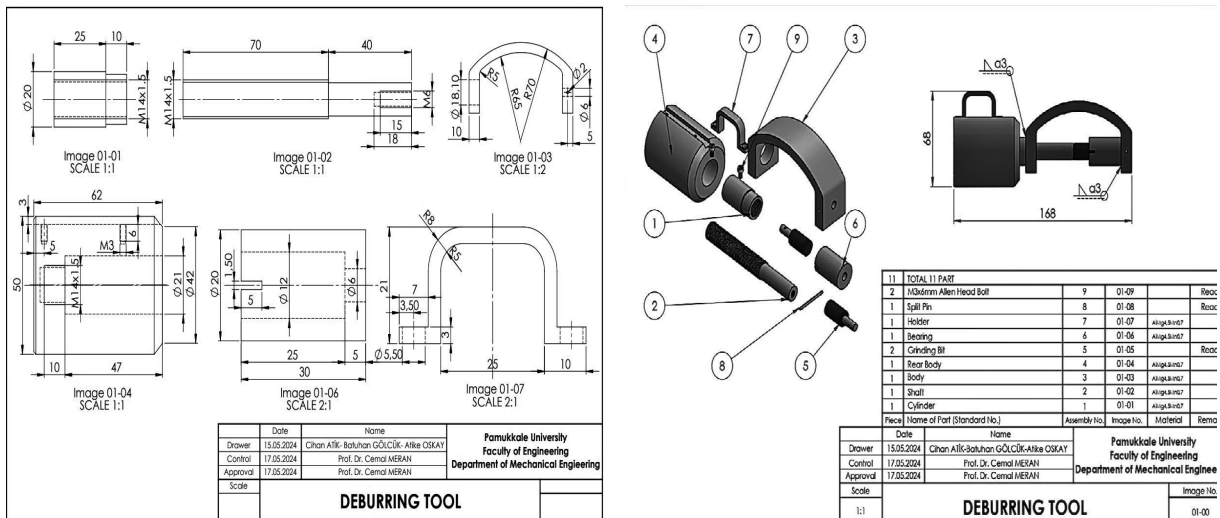


Figure 7: Sub-assembly parts and final version of the deburring tool

This ensured that it would remain intact when any force was applied to the tool by the worker. The other parts were connected to each other with split pins. Since the burr on the copper wire is compressed with the tool whose dimensions are given in the assembly drawing, the burr will be removed without damaging the wire geometry and surface by manually rotating the tool around the copper wire, **Figure 7**.

**BIBLIOGRAPHY**

1. Chicago Pneumatic, Kaynak ve Yüzey İşlemleri, 2024.
2. Pressure Welding Machines, Soğuk Kaynak İçin Uygun Metaller, 2024.
3. Aydınlar Makina Metal, EN AW-5083 Alüminyum Alaşımı: Özellikleri ve Kullanım Alanları, 2024.





17th-19th June 2024  
Gliwice, Poland

DEPARTMENT OF ENGINEERING MATERIALS AND BIOMATERIALS  
FACULTY OF MECHANICAL ENGINEERING  
SILESIA UNIVERSITY OF TECHNOLOGY

## INTERNATIONAL STUDENTS SCIENTIFIC CONFERENCE

### Investigation of Changes in Mechanical Properties of Nickel Plated Copper Wires at Drawing Stages

Cemal Meran<sup>1</sup>, Recep Tufan Celik<sup>2</sup>, Emre Guzel<sup>2</sup>, Arda Sengul<sup>2</sup>, Orhan Akyuz<sup>3</sup>, Ismail Kiyici<sup>3</sup>

<sup>1</sup>Prof.Dr., Pamukkale University, Faculty of Engineering, Department of Mechanical Engineering, Denizli, Turkey, cmeran@pau.edu.tr

<sup>2</sup>Student, Pamukkale University, Faculty of Engineering, Department of Mechanical Engineering, Denizli, Turkey

<sup>3</sup>Er-Bakir Electrolytic Copper Product Co., Denizli, Turkey

**Abstract:** The article examines the effect of wire drawing on the mechanical properties of nickel-coated copper wire. In the studies, a single series was passed through 13 dies, with samples taken after each die. For each sample, reduction, hardness (Vickers), single wire elongation, single wire strength, breaking load, and yield strength values were observed. The relationship between these parameters was interpreted at specific die angles for these samples.

**Keywords:** Wire, wire drawing die, elongation, breaking, copper wire, nickel-coated, yield strength

#### 1. INTRODUCTION

Wire drawing is a cold plastic deformation process in which the diameter of a rod or wire is reduced and its length is increased by pulling the workpiece through a calibrated hole in a conical die [1]. In this process, the wire is passed through drawing die to achieve size reduction. However, the size reduction achievable without the wire breaking is limited by the drawing force the wire can withstand [2]. The mechanical properties of the material may not be stable during the drawing of the wire, highlighting the importance of controlling hardness, yield strength, and tensile strength during the drawing process. To prevent breakage, the drawing process is typically completed as a multi-pass process, where a series of dies gradually reduce the cross-section while applying the desired yield strength [3]. The drawing test also demonstrates the wire material's resistance to necking and fracture. The micro mechanisms of plastic flow involve crystallographic slip through dislocation movement. In this process, the crystal structures and grain size of the material are rearranged. The optimum die angle for wire drawing is assumed to be achieved when the plastic deformation distribution is uniform across the wire diameter. Proper parameter control throughout the process can increase productivity, extend die life, and reduce wire breakages. Parameter control also defines properties such as good torsional strength, tensile strength, and fracture resistance of the wire [4]. Experiments and models have shown that tensile strength increases as the reduction (deformation) ratio

increases and decreases in the opposite case. A high reduction ratio leads to maximum tensile strength, as predicted by Cem (2012) and Narayanan et al. (2010). The larger the diameter, the higher the breaking load (force) required to break it, and vice versa [5,6].

## 2. WIRE DRAWING DIE

One of the most important elements in this study is the drawing die, which has a conical inner structure. A wire with a thick cross-sectional area passes through this structure and is reduced by a certain ratio. Drawing dies must be manufactured according to standards suitable for the process in which they will be used. Wire drawing dies can be produced in desired diameters. They are generally made from tungsten carbide-cobalt material due to its hardened properties, such as hardness, density, and strength [7].

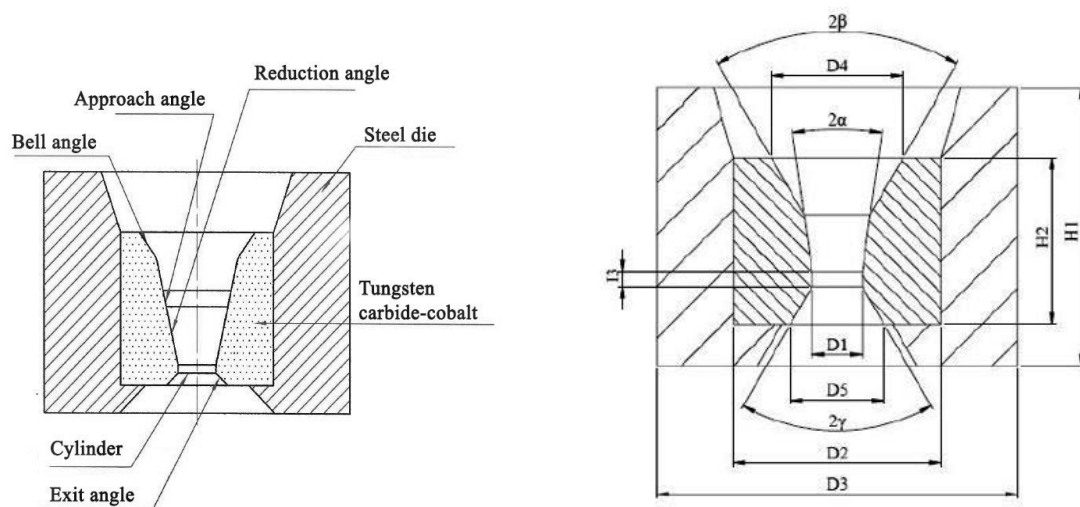


Figure 1: The angles and sections of wire drawing die

- Bell angle: ensures the wire enters the die in a straight line [8].
- Approach angle: ensures the soap flow is directed towards the die angle section. To prevent wire damage, there should be no sharp edges at the entry point [9].
- Reduction angle: The wire diameter reduction process and the compression of the soap onto the outer surface of the wire occur here. The efficiency of any die depends on the accuracy of this section's design and the precision of surface processing [10]. One of the most important factors in selecting the die angle is the "Contact Point." Depending on the reduction given in the die, the wire should contact the die wall in the middle of the die angle section (or as close to the middle as possible). This ensures the formation of the necessary pressure for adequate soap flow and deforms the wire over as wide a surface area as possible.
- Clutch angle: performs the final inspection of the drawn wire's diameter. The purpose of this is to ensure the roundness, accuracy, and surface quality of the wire [10].
- Exit angle: This section has a conical shape, and its function is to reinforce the exit side of the die and remove excess lubricant. Additionally, it helps keep the deforming part of the wire aligned with the center of the die [11].

### 3. MATERIAL AND METHOD

The multi-pass wire drawing machine depicted in the figure consists of 20 spools where the wire is wound and 13 dies used for wire shaping. While it is not possible to completely eliminate unwanted conditions such as wear, burrs, and friction that may occur during shaping with lubricating chemicals, the aim is to reduce them. The chemical properties of the nickel-coated copper wire used in the system are provided in **Table 1**.

*Table 1: Chemical composition nickel-coated copper wire substrate*

Material	Cu	As	Bi, Te, P	Fe	Pb, Cd, Co, Cr, Mn, Zn	S	Sb, Se	Ag
Unit	%	ppm	ppm	ppm	ppm	ppm	ppm	ppm
Value	99,99	<0,3	<0,5	<1,8	<0,1	<1,7	<0,6	<8,6

A multi-pass wire drawing machine is used to perform tests involving industrial conditions and to measure drawing force, **Figure 2**. The reason for this is that the drawn wire must have sufficient resistance and cross-section to withstand the drawing force without breaking. Additionally, the tested copper wires are gradually reduced to desired angles at a specific reduction ratio. The effect of reduction ratio and reduction cone angle parameters on the material will be examined in this study. For other process parameters, such as wire damage, material cost, and time-consuming experiments, it is more complex.

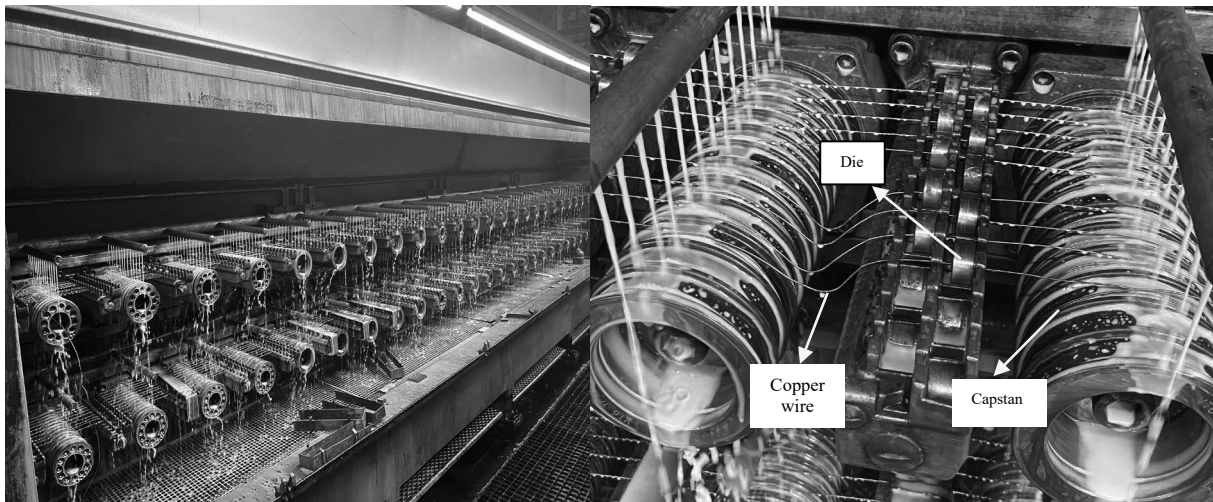


*Figure 2. Multipass drawing machine and principal equipment*

In this study, the multi-pass wire drawing machine Niehoff MMH121 was used. Samples were taken at each pass of the wire from 1.20 diameter to 0.3 diameter. The collected wires were prepared for metallographic examination using standard techniques for tensile testing. For hardness tests, a liquid mixture was poured to prepare cold bakelite (**Fig. 3a**). After cooling, the bakelite was mechanically polished with appropriate sandpaper (**Fig. 3b**). Vickers (HV 0.01) hardness measurements were taken (**Fig. 3c**).

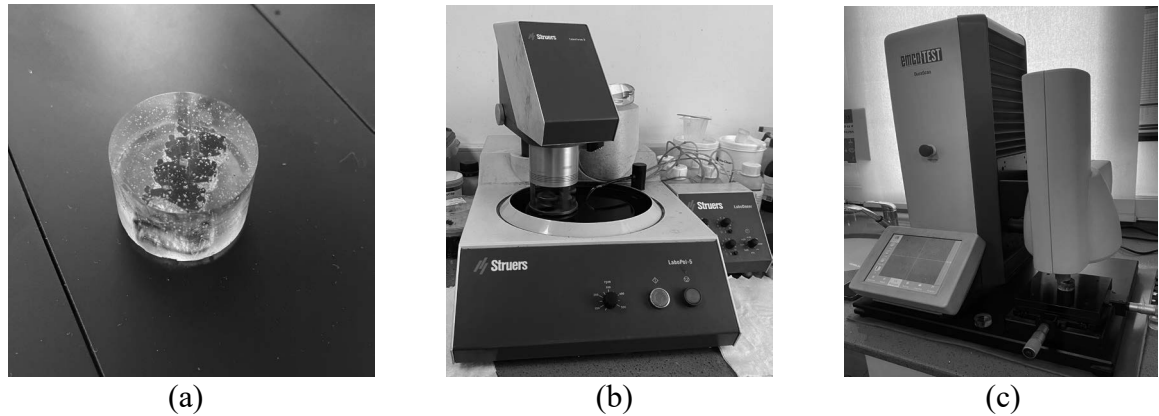


Figure 3: Steps of analysis - (a) Bakelite (b) Sanding and polishing (c) Hardness tester

After measuring the hardness of the first and last samples, their microscopic images were taken following the procedures shown in **Figure 3**. The entry and exit diameters were examined at scales of 500  $\mu\text{m}$ , as shown in **Figure 4**.

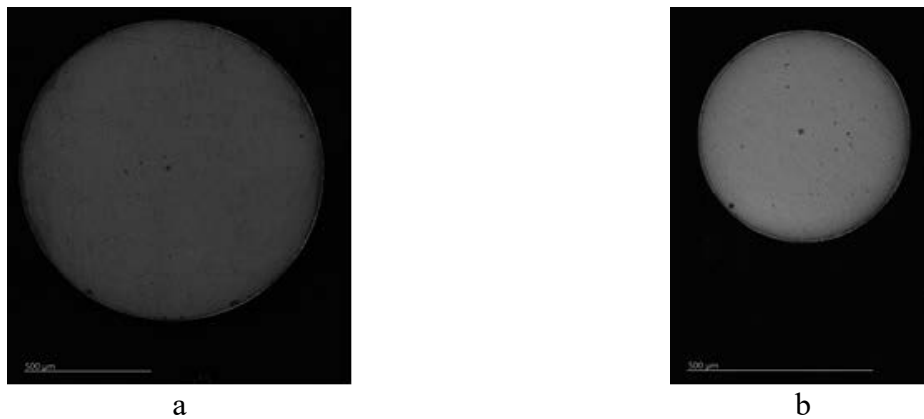


Figure 4: Coating thickness on 2 different diameter – (a)  $d: 1,20 \text{ mm}$  , (b)  $d: 0,574 \text{ mm}$

Table 2: Mechanical properties of the Nickel-coated copper wire after every drawing step.

No	Diameter (mm)	Coating thickness ( $\mu\text{m}$ )	Hardness (HV0.01)	Elongation (%)	Tensile strength (MPa)	Breaking load (N)	Yield strength (MPa)	Reduction ratio(%)
1	1,206	10,50	87	26,6	272	311,0	188	0
2	1,138	9,74	102	1,7	325	331,0	282	13,85
3	1,012	8,14	112	1,2	382	308,0	312	28,22
4	0,906	7,55	110	0,8	406	261,5	381	42,72
5	0,808	6,93	119	0,6	429	220,0	412	54,28
6	0,722	5,66	125	0,5	447	183,0	428	63,51
7	0,643	5,31	125	0,6	457	148,4	438	70,88
8	0,574	4,78	127	0,7	469	121,4	459	76,76
9	0,517	4,57	133	0,3	466	99,6	458	81,34
10	0,463	4,25	119	1,1	480	80,8	466	85,03
11	0,413	3,22	119	0,3	484	64,8	479	87,99
12	0,372	2,91	110	0,2	488	53,9	484	90,36
13	0,333	2,96	127	0,1	493	43,0	490	92,26
14	0,300	2,07	119	0,4	501	35,4	499	93,79

The diameter of the nickel plated wire after each drawing pass, and the resulting hardness, elongation, tensile strength, yield limit and sectional reducing ratio are given in **Table 2**.

#### 4. RESULTS AND DISCUSSION

In micro Vickers hardness measurement, cold deformation process will result in densification of the material's crystal structure. As a result of this phenomenon, hardness will increase. As hardness increases, the wire will become more brittle, and the possibility of shaping will decrease, **Figure 5a**.

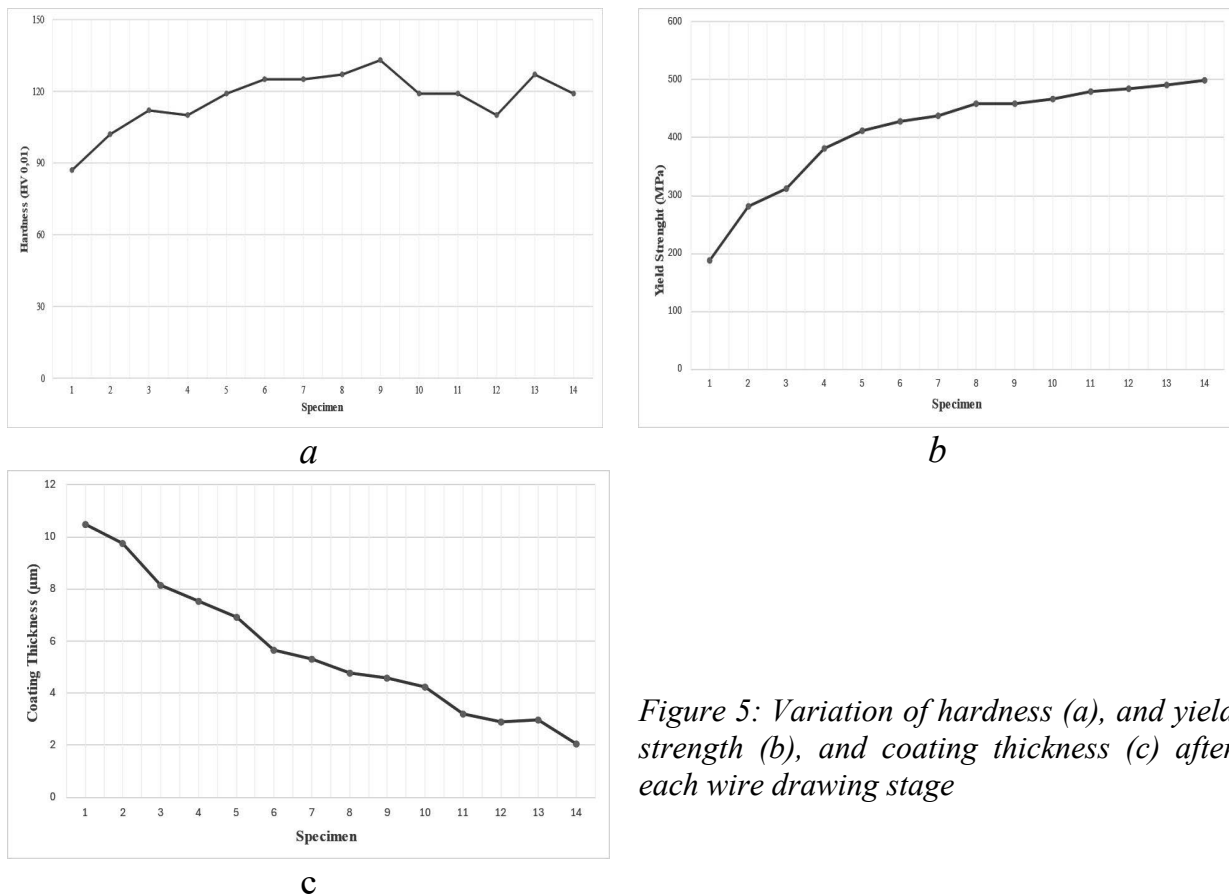


*Figure 5: Variation of hardness (a), and yield strength (b), and coating thickness (c) after each wire drawing stage*

As the diameter decreases, the yield strength will increase. This is because the defects in the material decrease and more grain boundaries are formed. The reduction in diameter at each die pass indicates that the material can withstand higher stresses. Similarly, an increase in the number of grain boundaries enhances resistance to deformation and withstands higher stress values, **Figure 5b**. It is seen that the nickel coating thickness decreases after each drawing. Nickel coating thickness, which was 10.5 micrometres at the beginning, decreased to 2.07 micrometres at the last stage of wire drawing, **Figure 5c**. As the sample sequence increases linearly (indicating a decrease in diameter), the coating thickness also decreases. The friction and heat generated during the passage through the drawing dies contribute to the reduction in the nickel coating thickness. As a result, just as the diameter decreases with each drawing die passage, the coating thickness also decreases in correlation with the diameter.

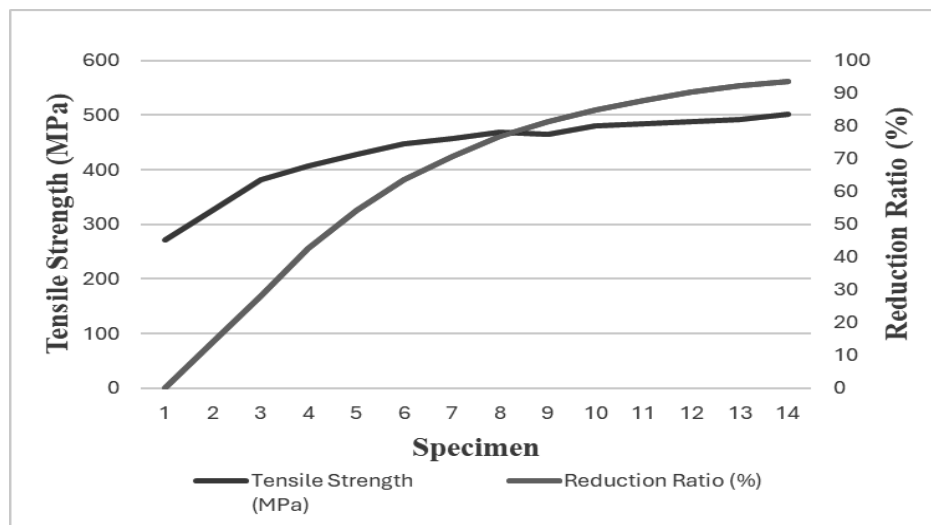


Figure 6: The effect of tensile strength on reduction ratio

The effect of tensile strength on reduction ratio of the experimental result is as shown in **Figure 6**. It is seen that increase in reduction ratio (deformation) leads to increase in tensile strength and vice-versa. The tensile strength is slightly directly proportional to reduction ratio. High reduction ratio causes maximum tensile strength. It is also seen that there is sporadic increase in tensile strength from 493 to 501 MPa when the reduction ratios increase from 92,26 to 93,79 %.

## 5. CONCLUSION

The wire drawing process of nickel-coated copper has been investigated using an experimental approach. The reduction angle in the die was considered as an average, and the reduction ratio was calculated based on the entry and exit angles. The effects of friction forces on the die-wire surface were neglected. In a continuous wire drawing setup, it has been observed that the reduction in diameter between dies significantly affects the material's tensile strength, hardness, breaking load, elongation, coating thickness, and yield strength. The elongation graph was not analyzed because the high difference between the first and second specimens indicates the beginning of the process, and thereafter, the change was minimal, so it was considered approximately constant. It has been observed that the cross-sectional reduction between passes is a maximum of 15%. Such a low reduction in a single pass eliminates lubrication issues. A lower cross-sectional reduction is a positive factor for surface quality. It has been observed that as the diameter decreases, the percentage of cross-sectional reduction also decreases. This indicates that as the wire gets thinner, the grain structure becomes finer and the increase in strength makes the material more resistant to breaking. In our study, it has been observed that the breaking load decreases while the tensile strength increases. Typically, a decrease in breaking load negatively affects the material. When processing the material, it is necessary to consider both factors together and balance them according to performance criteria, which may require setting certain limitations. The values in the study have generally been interpreted as resulting from internal structural changes occurring in the reduced wire cross-section. Consequently, by optimizing the wire drawing process to achieve the desired mechanical

properties, production efficiency can be improved and costs reduced, aiming for overall savings.

## BIBLIOGRAPHY

1. Ductility and Formability of Metals 2023, p. 365-376
2. J. G. Wistreich (1958) THE FUNDAMENTALS OF WIRE DRAWING, Metallurgical Reviews, 3:1, 97-142
3. Celentano DJ et al., 2009. Simulation and experimental validation of multiple-step wire drawing processes. Finite Elements in Analysis and Design 2009, 45, p. 163.
4. Shemanski, R.M. (1999):"Wiredrawing by computer simulation", Wire Journal International, 32(4):166-183.
5. Cem, S. C., (2012): "A study on influence of some process parameters on cold drawing of ferrous wires", department of Mechanical Engineering, Faculty of Engineering and Architecture, Trakya University, 22180 Edirne, Turkey
6. Narayanan, K.R., Sridhar, I., Subbiah, S. (2010):"Effect of cold work on the mechanical response of drawn ultra-fine gold wire". Computational materials science, 49 (1), S119 – S125
7. Ünseren, M, 2006: Tel Çekme Matrisleri Üzerine Bir Araştırma, Isparta, Türkiye
8. Özer, Ö., Yurci, M., 1997. Tel Çekme İşleminde Matris Açılarının Optimizasyonu ve Sapmaların Belirlenmesi. DTÜ Makine Fakültesi 1. Makine Mühendisliği Kongresi, 4-6 Haziran 1997, İstanbul.
9. Çapan, L., 1989. Metallerde Plastik Şekil Verme Usulleri, Çağlayan Kitabevi, 363 s, İstanbul Teknik Üniversitesi, İstanbul.
10. Koner, S., 1992. Tungsten Carbide Wire Drawing Dies, Wire Industry, 350-356
11. Dove, A., Moritz, J., Smigel, W., 1980. Steel Wire Handbook, 372 s, U.S.A.



17th-19th June 2024  
Gliwice, Poland

DEPARTMENT OF ENGINEERING MATERIALS AND BIOMATERIALS  
FACULTY OF MECHANICAL ENGINEERING  
SILESIA UNIVERSITY OF TECHNOLOGY

## INTERNATIONAL STUDENTS SCIENTIFIC CONFERENCE

### Investigation of the Effect of Silicon Dioxide Nanoparticle on Carbon and Basalt Composites

Cemal Meran<sup>1</sup>, Batuhan Şenkaya<sup>2</sup>

<sup>1</sup>Prof.Dr., Pamukkale University, Faculty of Engineering, Department of Mechanical Engineering, Denizli, Turkey, cmeran@pau.edu.tr

<sup>2</sup>M.Sc. Student, Pamukkale University, Faculty of Engineering, Department of Mechanical Engineering, Denizli, Turkey

**Abstract:** Increasing the strength of composites by using fabric reinforcement alongside nanoparticles is common. However, the effect of nanoparticles can vary with the changing fabric structure. This has become a topic that needs to be investigated. In the study, 200 g/m<sup>2</sup> and 245 g/m<sup>2</sup> plain carbon fabrics, and 200 g/m<sup>2</sup> plain basalt fabrics were used as reinforcements. SiO<sub>2</sub> nanoparticles were chosen as the nanoparticle additive, and composite parts were made using the vacuum infusion method. Tensile, three-point flexural, and Izod impact tests were conducted to present the test results regarding the relationship of SiO<sub>2</sub> nanoparticles with these fabric structures.

**Keywords:** carbon fabric, basalt fabric, silicon dioxide nanoparticle, vacuum infusion, composites

#### 1. INTRODUCTION

The most important reasons for the increasingly mandatory use of composite materials are their high strength/density ratio, corrosion resistance, and the ability to be manufactured in desired geometries due to advanced production methods. For these reasons, composite materials provide solutions for many sectors such as aerospace, energy, industrial products, maritime, defense industry, automotive, construction, and medical. Various methods are used to improve the mechanical properties obtained from composite materials. Some of these methods include agents and nanoparticles used in the matrix material. Nanoparticles added to the resin create a better interface between the matrix material and the reinforcement elements. This enhances the mechanical properties of the composite. However, the formation of a good interface depends on a homogeneous nanoparticle-additive resin and its relationship with the fabric construction. Liu et al. (2022) tested the effect of SiO<sub>2</sub> nanoparticles on 300 g/m<sup>2</sup> basalt fabric reinforced composites. Tensile strengths of the basalt composites were measured at 404.12 MPa for the control sample (without SiO<sub>2</sub> addition), 543.42 MPa for 0.5% SiO<sub>2</sub> addition, 618.22 MPa for 1% SiO<sub>2</sub> addition, and 493.23 MPa for 1.5% SiO<sub>2</sub> addition. The highest tensile strength was observed at 1% SiO<sub>2</sub> addition, and it was found that further increase in the SiO<sub>2</sub> ratio led to a



decrease in tensile strength [1]. Divya and Suresha (2021) investigated mechanical properties of SiO<sub>2</sub>/epoxy matrix carbon composites made from 3K fibers plain fabric. Tensile strength of the specimens prepared 0%, 0.5%, 1.5% and 3% SiO<sub>2</sub> was 518.28 MPa, 531.45 MPa, 560.55 MPa, and 590.15 MPa, respectively [2].

The aim of this study is to fabricate composites using carbon and basalt fabrics, which are among the most important reinforcement materials in composites, with resin systems and determine their mechanical properties with the addition of SiO<sub>2</sub>. However, the increasing production of carbon fiber poses a threat to the environment. As seen in **Table 1** and **Table 2**, the energy consumption and global warming indices associated with its production are also high.

*Table 1. Energy consumption in the production of some materials*

Material	Energy consumption (MJ/kg)	Reference
Carbon fiber	183-286	[3]
Basalt fiber	18	[4]
Glass fiber	54.7	[5]

*Table 2. Global warming potential of the production of some materials*

Material	Warming potential (kg CO <sub>2</sub> /kg)	Reference
Carbon fiber	31	[6]
Basalt fiber	0.98	[7]
Glass fiber	2.64	[8]

Four high-performance fibers used in composites stand out, and their mechanical properties are shown in **Table 3**. The mechanical properties of basalt fiber being close to those of carbon fiber, and at the same time, being more environmentally friendly, demonstrate how important its use is.

*Table 3. Mechanical properties of some reinforcement fibers [9]*

Properties	Basalt	S2-Glass	Aramid	Carbon
Density (g/cm <sup>3</sup> )	2.63-2.8	2.54	1.45	1.78
Filament diameter (μm)	6-21	6-21	5-15	5-15
Tensile strength (GPa)	3-4.8	4.02-4.65	2.9-3.45	3.5-6
Modulus (GPa)	93-110	83-97	70-140	230-600
Elongation at break (%)	3.1-6	5.3	2.8-3.6	1.5-2

## 2. WOVEN FABRIC REINFORCED COMPOSITES

Woven fabrics are the most commonly used reinforcement types in composite material production. Three basic patterns shown in **Figure 1** can be produced with the woven fabric production method. These are plain, twill, and satin patterns. Other patterns are derivatives of these patterns.

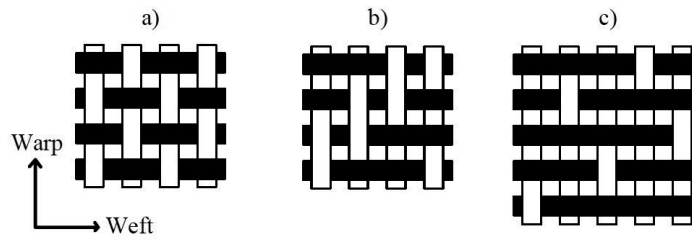


Figure 1. Basic woven patterns a) Plain, b) Twill, c) Satin

The properties of fabric constructions, can lead to variations in the mechanical properties of composites. The parameters of fabric construction are given in **Table 4**.

Table 4. Parameters of fabric construction [10]

Properties	Description
Fiber material	The main material of the fabric.
Yarn count	The weight of a specific length of yarn or filament.
Thread count	The number of warp and weft yarns per unit length in the fabric.
Pattern	The weave pattern of the fabric.
Fabric areal weight	The weight of the fabric. Its unit is generally g/m <sup>2</sup> .

Increasing the thread count in fabrics with the same yarn count and pattern leads to an increase in the crimp ratio and fabric areal weight. In fabrics with a high thread count, yarns tend to crimp more over a certain length of the fabric, making it more difficult to linearly accommodate the tensile load. Therefore, composites made from fabrics with a high thread count exhibit lower tensile strength. Increased crimping of yarns increases the contact surface area, thereby increasing the flexural strength. These crimp zones also have an impact-damping effect, so the impact resistance of the composites also increases.

### 3. MATERIAL AND METHODS

The 200 g/m<sup>2</sup> carbon fabric is made with DowAksa AKSACA™ A-38 3K fibers and 245 g/m<sup>2</sup> carbon fabric is made with Mitsubishi Chemical PYROFIL™ TR30S3L 3K fibers by Spinteks Tekstil İnşaat San. ve Tic. A.Ş. The 200 g/m<sup>2</sup> basalt fabric is manufactured by Zhejiang GBF Basalt Fiber Co., Ltd. from 100 tex fibers. The visual and technical specifications of fabrics are shown in **Figure 2** and **Table 5**.

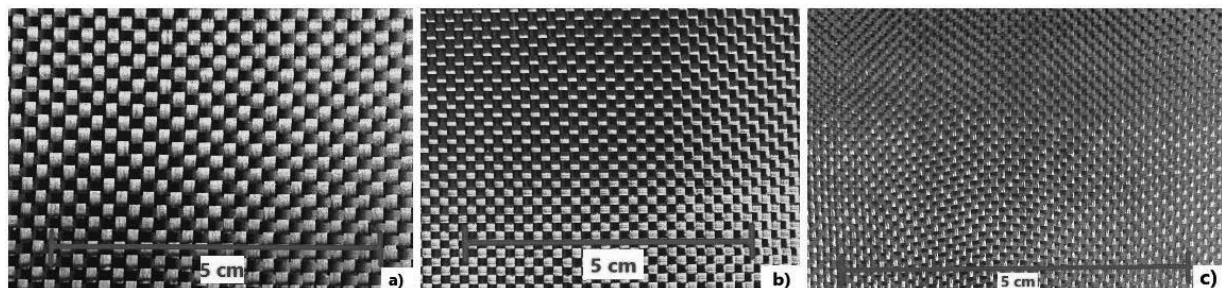


Figure 2. Reinforcement fabrics a) 200 g/m<sup>2</sup> carbon, b) 245 g/m<sup>2</sup> carbon, c) 200 g/m<sup>2</sup> basalt

Table 5. The properties of reinforcement fabrics

Properties	200 g/m <sup>2</sup> Carbon Fabric	245 g/m <sup>2</sup> Carbon Fabric	200 g/m <sup>2</sup> Basalt Fabric
Density (g/cm <sup>3</sup> )	1.78	1.79	2.60-2.63
Filament diameter (μm)	7	7	13
Yarn count (tex, g/km)	200 ± 5% (3K)	200 ± 5% (3K)	100 ± 5%
Thread count weft (cm <sup>-1</sup> )	5 ± 5%	6 ± 5%	10 ± 5%
Thread count warp (cm <sup>-1</sup> )	5 ± 5%	6 ± 5%	10 ± 5%
Fabric areal weight (g/m <sup>2</sup> )	200 ± 5%	245 ± 5%	200 ± 5%
Pattern	Plain	Plain	Plain
Tensile strength (MPa)	3800 ± 5%	4120 ± 5%	3100 ± 5%
E-Modulus (GPa)	240 ± 5%	235 ± 5%	88-92

The epoxy resin used is HEXION EPIKOTE™ Resin MGS® LR635 and the hardener is HEXION EPIKURE™ Curing Agent MGS® LH637. Mixtures with a ratio of 100 g LR635 / 28 g LH637 were prepared. The average particle size of the SiO<sub>2</sub> nanoparticle used is 13-22 nm and the specific surface area is 165-195 m<sup>2</sup>/g. Specimen codes assigned to the specimen based on the type of fabric, fabric areal weight, and SiO<sub>2</sub> ratio data. Codes are shown in **Table 6**.

Table 6. The specimen codes of composites

Specimen	Fabric Areal Weight (g/m <sup>2</sup> )		Fabric Type		SiO <sub>2</sub> Ratio (%)		
	200	245	Carbon	Basalt	0	1	2
200CF0	✓	-	✓	-	✓	-	-
200CF1	✓	-	✓	-	-	✓	-
200CF2	✓	-	✓	-	-	-	✓
245CF0	-	✓	✓	-	✓	-	-
245CF1	-	✓	✓	-	-	✓	-
245CF2	-	✓	✓	-	-	-	✓
200BF0	✓	-	-	✓	✓	-	-
200BF1	✓	-	-	✓	-	✓	-
200BF2	✓	-	-	✓	-	-	✓

The SiO<sub>2</sub> ratios are the ratios of the total weight of the epoxy resin and hardener used in the fabrication of composite parts. The removal of gases formed during the mixing process are crucial. The preparation process of the resin with SiO<sub>2</sub> additives is shown in **Figure 3**. After that, composite parts were produced using the vacuum infusion method. The system was kept at room temperature for 3 days for the resin to cure, and composite parts were obtained as shown in **Figure 4**. In order to reach the ultimate strength of the composite parts, a post-cure process was carried out at 80°C for 8 h. These steps were repeated for each composite plate production.

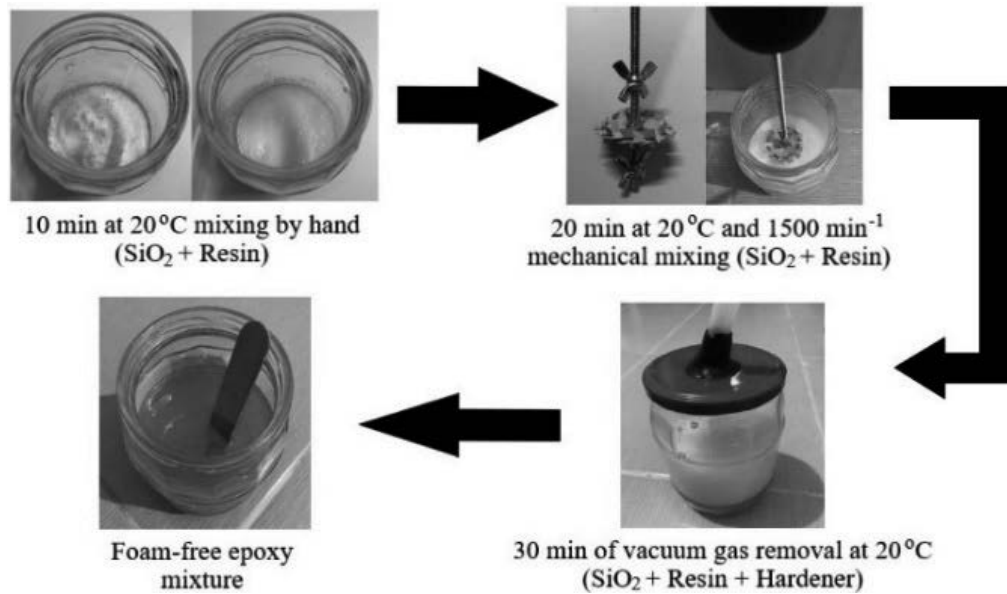


Figure 3. Preparation process of  $\text{SiO}_2$  modified epoxy

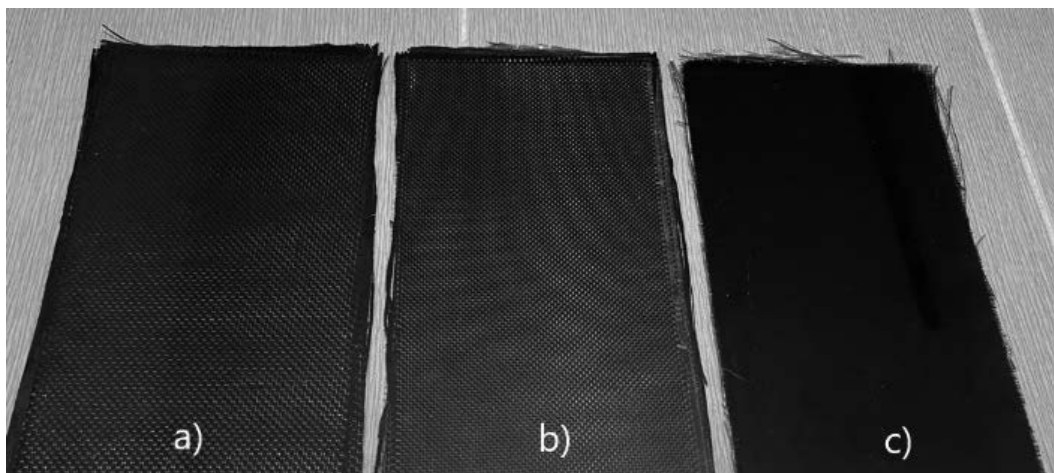


Figure 4. The composites a) 200CF, b) 245CF, c) 200BF

The composite plates were cut to the dimensions specified in the relevant standards using a water jet at a pressure of 1800 bar. Afterwards, Tensile tests were conducted according to ASTM D3039 standard. Specimen dimensions are 2.5x25x250 mm. Tensile tests were performed at a speed of 2 mm/min at room temperature [11].

Three-point flexural tests were conducted according to ASTM D790 standard. The specimen dimensions are 3.2x12.7x127 mm. Flexural tests were performed at a speed of 2 mm/min with a span length of 32 times the thickness at room temperature [12].

Izod impact tests were conducted according to ASTM D256 standard. Specimen dimensions are 3.2x12.7x63.5 mm. Impact tests were performed at room temperature with an angle of  $150^\circ$  and a capacity of 15 J [13].

#### 4. RESULTS AND DISCUSSION

The results of the tensile, flexural, and Izod impact tests conducted on the composite specimens are given in **Table 7**. Overall, the tensile and flexural strengths of carbon composites were higher than those of basalt composites, while the impact resistance of basalt composites was higher than that of carbon composites.

*Table 7. Tensile, flexural strength and impact resistance of composites*

Specimens	Tensile Strength (MPa)	Flexural Strength (MPa)	Impact Resistance (kJ/m <sup>2</sup> )
200CF0	760	579	62
200CF1	862	657	80
200CF2	949	732	78
245CF0	722	620	66
245CF1	749	614	74
245CF2	689	691	75
200BF0	355	235	101
200BF1	356	207	103
200BF2	353	252	100

When examining the without SiO<sub>2</sub> carbon composites 200CF0 and 245CF0, a decrease in tensile strength was observed as the fabric areal weight increased. Regarding tensile strength, a consistent increase effect was observed only in the SiO<sub>2</sub> additive specimens of the 200CF, while a consistent effect was not observed in the 245CF and 200BF. This situation is shown in **Figure 5**.

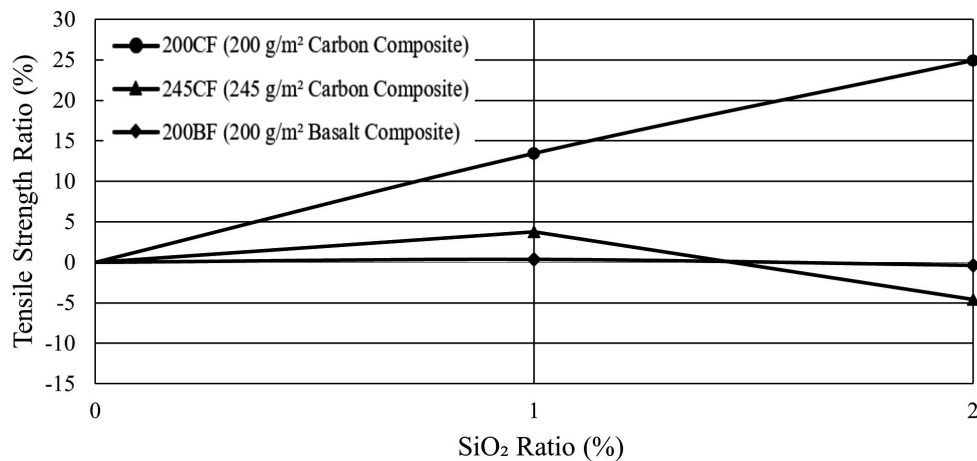


*Figure 5. The effect of SiO<sub>2</sub> nanoparticles on tensile strength*

In without SiO<sub>2</sub> carbon composites 200CF0 and 245CF0, an increase in fabric areal weight resulted in an increase in flexural strength. Regarding flexural strengths, a consistent increase effect was observed only in the SiO<sub>2</sub> additive 200CF specimens, while a consistent effect was not observed in the 245CF and 200BF. This situation is shown in **Figure 6**.

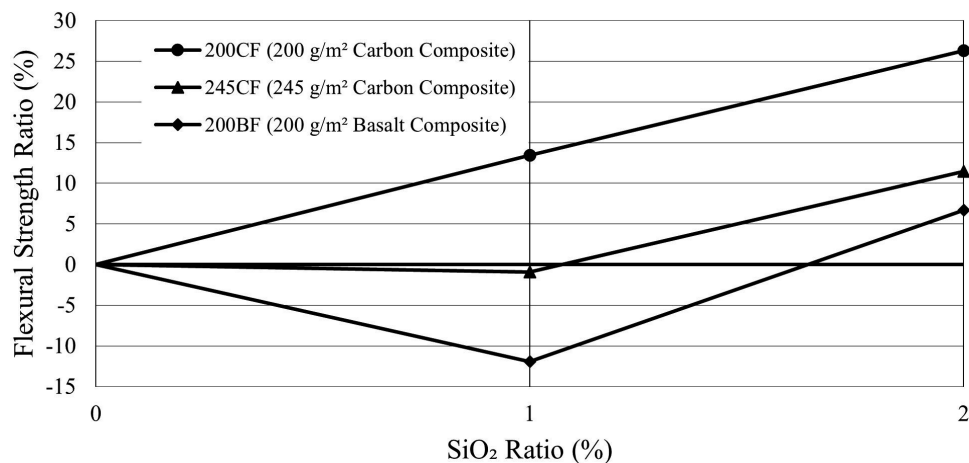


Figure 6. The effect of SiO<sub>2</sub> nanoparticles on flexural strength

The impact resistance of 200CF composites with 1% and 2% SiO<sub>2</sub> additives are almost the same. It is the same like for 245CF composites. The impact resistance of 200BF composites is almost the same for all SiO<sub>2</sub> additive ratios, and the effect of SiO<sub>2</sub> nanoparticles was not observed. This situation is shown in Figure 7.

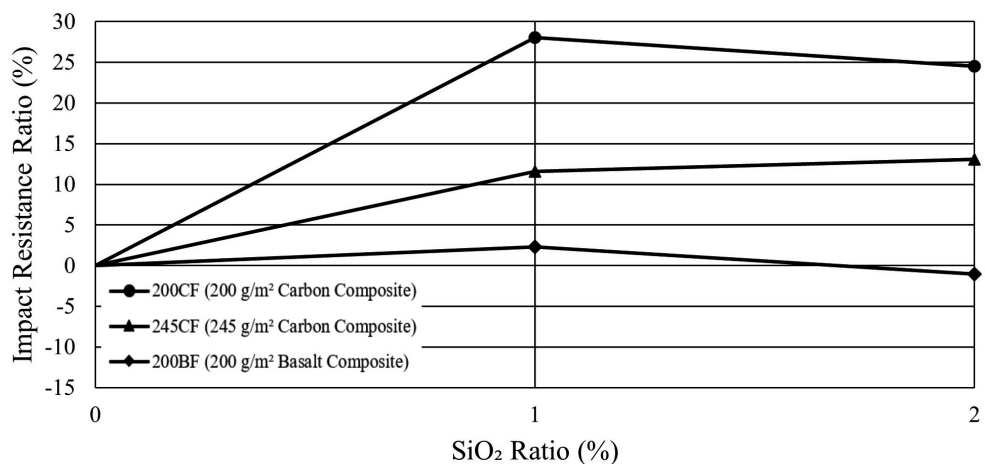


Figure 7. The effect of SiO<sub>2</sub> nanoparticles on impact resistance

#### 4. CONCLUSION

As the fabric areal weight increased in carbon composites, the tensile strength decreased while the flexural strength and impact resistance increased. This is because the 245 g/m<sup>2</sup> carbon fabric has more thread count than 200 g/m<sup>2</sup> carbon fabric.

The reason why the effect of SiO<sub>2</sub> nanoparticles is observed best in 200 g/m<sup>2</sup> carbon fabric reinforced composites in terms of flexural and tensile strength is that SiO<sub>2</sub> forms better interfaces in this fabric due to the vacuum infusion method. In other words, the structure of the

200 g/m<sup>2</sup> carbon fabric is more suitable for forming better interfaces with SiO<sub>2</sub> nanoparticles. Due to the denser structure of the 245 g/m<sup>2</sup> carbon fabric and the more porous structure of the 200 g/m<sup>2</sup> basalt fabric, good interfaces could not be formed with SiO<sub>2</sub> nanoparticles. Therefore, no significant changes were observed in tensile and flexural strengths.

In 200 g/m<sup>2</sup> carbon fabric composites, 1% SiO<sub>2</sub> addition was sufficient to increase the impact resistance. There was no significant increase in impact resistance with a 2% addition. Although the interfaces of 245 g/m<sup>2</sup> carbon fabric composites were not optimal, the presence of irregular SiO<sub>2</sub> was sufficient to increase impact resistance. No significant changes were observed in 200 g/m<sup>2</sup> basalt fabric due to its porous structure.

## REFERENCES

1. H. Liu, Y. Sun, Y. Yu, M. Zhang, L. Li, L. Ma, Effect of nano-SiO<sub>2</sub> modification on mechanical and insulation properties of basalt fiber reinforced composites., *Polymers*, 14, 2022, 3353.
2. G.S. Divya, B. Suresha, Impact of nano-silicon dioxide on mechanical properties of carbon fabric reinforced epoxy composites, *Materials Today: Proceeding*, 2021.
3. T. Suzuki, J. Takahashi, Prediction of energy intensity of carbon fiber reinforced plastics for mass-produced passenger car, *The 9<sup>th</sup> Japan International SAMPE Symposium*, 2005, 9-14.
4. P. Fazio, Basalt fiber: From earth an ancient material for innovative and modern application, *Energia Ambientee Innovazione*, 3, 2011, 89-96.
5. J. Diener, U. Siehler, Ökologischer vergleich von NMT- und GMT-bauteilen, *Die Angewandte Makromolekulare Chemie*, 272, 1999, 1-4.
6. S. Das, Life cycle assessment of carbon fiber-reinforced polymer composites, *Int. J. Life Cycle Assess.*, 16, 2011, 268-282.
7. K. Azrague, M.K. Wiik, L.I. Alneas, R.D. Schlanbusch, B. Johannesson, Life cycle assessment as a tool for resource optimisation of continuous basalt fibre production in Iceland, *Engineering Conferences International (ECI) Life Cycle Assessment and Other Assessment Tools for Waste Management and Resource Optimization*, 2016.
8. A. Le Duigou, P. Davies, C. Baley, Environmental impact analysis of the production of flax fibres to be used as composite material reinforcement, *Journal of Biobased Materials and Bioenergy*, Vol 5., 2011, 153-165.
9. H. Jamshaid, R. Mishra, A green material from rock: basalt fiber – a review, *The Journal of The Textile Institute*, 107(7), 2015, 923-937.
10. K. Y. Kim, L. Ye, Interlaminar fracture properties of weft-knitted/woven fabric interply hybrid composite materials, *Journal of Materials Science*, 47, 2012, 7280-7290.
11. ASTM D3039/D3039M-14, Standard Test Method for Tensile Properties of Polymer Matrix Composite Materials, West Conshohocken: ASTM International, 2017.
12. ASTM D790-17, Standard Test Methods for Flexural Properties of Unreinforced and Reinforced Plastics and Electrical Insulating Materials, West Conshohocken: ASTM International, 2017.
13. ASTM D256-23e1, Standard Test Methods for Determining the Izod Pendulum Impact Resistance of Plastics, West Conshohocken: ASTM International, 2023.



17th-19th June 2024  
Gliwice, Poland

DEPARTMENT OF ENGINEERING MATERIALS AND BIOMATERIALS  
FACULTY OF MECHANICAL ENGINEERING  
SILESIA UNIVERSITY OF TECHNOLOGY

## INTERNATIONAL STUDENTS SCIENTIFIC CONFERENCE

### Aplikácia DLC povlakov na valivé ložiská

Matúš Murín<sup>a</sup>, Martin Vicen<sup>a</sup>, Mirosław Bonek<sup>b</sup>

<sup>a</sup> Žilinská univerzita v Žiline, Strojnícka fakulta, Katedra materiálového inžinierstva, Univerzitná 8215/1, 010 26 Žilina, Slovak Republic

email: murin2@stud.uniza.sk martin.vicen@fstroj.uniza.sk

<sup>b</sup> Silesian University of Technology, Faculty of Mechanical Engineering, Department of Engineering Materials and Biomaterials, Gliwice, Poland

**Abstrakt:** Táto práca sa zaoberá analýzou DLC povlakov a ich aplikáciou v oblasti valivých ložísk. Popísané sú ocele, ktoré sa používajú na výrobu valivých ložísk, vznik, štruktúra a metódy vytvárania DLC povlakov a na záver ich využitie u valivých ložísk.

**Abstract:** The thesis focuses on analysis of DLC coatings and their application in the field of rolling bearings. The steels that are used for the production of rolling bearings, the origin, structure and methods of creating DLC coatings are described, and finally their use in rolling bearings.

**Kľúčové slová:** ocele na valivé ložiská, DLC povlaky, trenie, PVD

### 1. ÚVOD

Neustále sa zvyšujúce nároky na ekológiu a ekonomiku prevádzky, vyžadujú aj väčšie požiadavky na životnosť a odolnosť strojných súčastí a zariadení. Postupom času sa však ukazuje, že vytvárať neustále nové materiály, ktoré by mohli spĺňať tieto predpoklady, nie je jedinou cestou vývoja. V mnohých aplikáciách je kľúčový práve povrch súčastí a s jeho úpravou tak môžu materiály získať výnimočné vlastnosti a zachovať si nízku cenu. Jednou z možností, ako vyhovieť týmto požiadavkám, je použitie tvrdých a oteruvzdorných povlakov.

Dnes sa na vytváranie povlakov čoraz viac využívajú nové technológie povlakovania metódami PVD a CVD. Jedny z najrozšírenejších povlakov, vytvárané prevažne metódou PVD, sú povlaky DLC (Diamond-Like-Carbon). DLC povlaky sa stále viac používajú pre zníženie trenia a predĺženia životnosti vysoko namáhaných súčastí, vďaka svojim vynikajúcim tribologickým vlastnostiam. Vykazujú taktiež vysokú tvrdosť, odolnosť voči korózii a nachádzajú uplatnenie aj v medicíne, ako biomateriály.

Medzi jedny z najdôležitejších strojných súčastí nepochybne patria valivé ložiská. Nachádzajú sa takmer v každom zariadení, kde sa vyskytujú pohyblivé komponenty a podliehajú neustálemu procesu inovácie. Často sa na povrch valivých ložísk deponujú práve



povlaky DLC, ktoré výrazne predlžujú ich životnosť a zvyšujú ich odolnosť hlavne voči únavovému opotrebeniu.

## 2. OCELE NA VALIVÉ LOŽISKÁ

Medzi základné požadované vlastnosti, ktoré by mali vykazovať ložiskové materiály patrí napr. vysoká tvrdosť a pevnosť, vysoký stupeň čistoty chemického zloženia, alebo vysoká medza únavy pri kontaktnom namáhaní v mieste valivého vztyku. Hlavný dôraz sa však kladie na odolnosť voči opotrebeniu, keďže v bežných aplikáciách sú ložiskové materiály vystavené nepretržitému pohybu a kontaktu s inými komponentami zvyčajne pod veľkým tlakom. V súčasnosti bezpochyby tvoria prevažnú časť celkovej produkcie výroby ložísk na svete práve ložiská vyrobené z ocele. Ocele, ktoré sa používajú na výrobu ložísk patria do skupiny ocelí na menovité použitie, čo je špeciálna skupina konštrukčných ušľachtilých zliatinových ocelí. Sú to ocele, ktoré boli špeciálne vyvinuté na výrobu konkrétnych konštrukčných častí. Z tejto skupiny ocelí boli na výrobu ložísk vyvinuté ocele, ktoré nazývame ocele na valivé ložiská. Ocele na valivé ložiská sú zaradené medzi konštrukčné ocele, no ich chemické zloženie (tab. 1) a tak aj ich vlastnosti sú viac príbuzné nástrojovým oceliam. Sú to nadeutektoidné ocele legované 1,5% chrómom s obsahom uhlíka okolo 1% [1].

Tab.1 . Chemické zloženie vybraných ocelí na valivé ložiská

Table 1. Chemical composition of selected rolling bearing steels

Označenie	Chemické zloženie [%]					
	C	Mn	Si	Cr	Mo	Iné
14 209	0,9 -1,10	0,9 -1,20	0,35 - 0,65	1,30 -1,65	-	Ni max 0,30 Cu max 0,25
14109	1,10	0,50	0,35	1,30 - 1,65	-	Ni max 0,30 Cu max 0,25
100Cr6	1,10	0,45	0,35	1,35 - 1-65	-	-
100CrMo7	1,05	0,45	0,40	1,65 - 1,95	0,20 - 0,40	-

Jednou z najdôležitejších častí spracovania ložiskových ocelí je tepelné spracovanie. Tepelné spracovanie u ložiskových ocelí pozostáva zo žihania na mätko, čoho cieľom je dosiahnutie čo najmenšej tvrdosti a tým čo najlepšiu obrábatelnosť. Ďalej nasleduje samotná výroba ložiskových komponentov, ktoré sa ďalej tepelne spracovávajú kalením a nízkoteplotným popúšťaním na dosiahnutie požadovaných mechanických vlastností. Potom môže nasledovať povrchová úprava ložiskových komponentov, kde jednou z možností môže byť práve nanášanie rôznych povlakov [1].

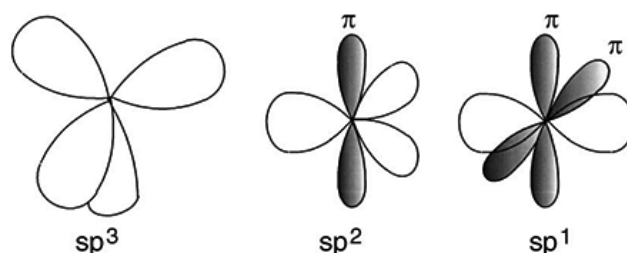
## 3. DLC POVLAKY

Väčšina degradačných mechanizmov vzniká na povrchu komponentov a z povrchu sa šíri ďalej do materiálu. Jednou z najúčinnějších možností zníženia účinnosti degradačných mechanizmov je ošetrovanie povrchu kvalitnými nátermi alebo povlakmi. V dnešnej dobe sa v priemysle čoraz viac využívajú nové technológie nanášania povlakov metódami PVD (Physical-Vapor-Deposition) a CVD (Chemical-Vapor-Deposition), ktoré umožňujú vytváranie širokého spektra tenkých povlakov. Medzi veľké množstvo povlakov vytvorených metódou

PVD, patrí aj väčšina DLC povlakov (Diamond-Like-Carbon). Skratka DLC v preklade môže znamenať „diamantu podobné vrstvy“, kedy sa na povrch súčiastok deponujú tenké vrstvy povlakov tvorené rôznymi štruktúrami uhlíka. Povlaky DLC vykazujú vysokú tvrdosť, sú chemicky inertné, majú veľmi nízky koeficient trenia, čiže majú vynikajúce tribologické vlastnosti, vysokú životnosť a s tým spojenú vysokú odolnosť voči opotrebeniu, vysokú korozivzdornosť a dajú sa deponovať aj na nekovové materiály [2,3].

### 3.1. Štruktúra DLC povlakov

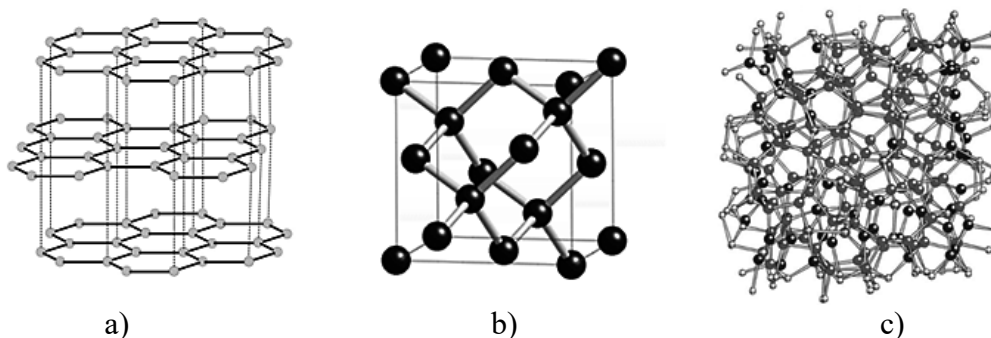
Pri charakterizácii tenkých vrstiev DLC povlakov je dôležité si uvedomiť, že sú tvorené amorfnou štruktúrou, čo znamená, že častice týchto vrstiev sú nepravidelne usporiadané. Amorfná štruktúra DLC povlakov je tvorená vodíkom a rôznymi štruktúrami uhlíka v určitom pomere. Uhlík je základom obrovského množstva rôznych štruktúr, ktorých výsledné vlastnosti závisia od druhu väzieb medzi atómami uhlíka. Väzby medzi atómami uhlíka môžu byť diamantového typu alebo grafitického typu. S typom väzby úzko súvisí hybridizácia atómu uhlíka, čiže usporiadanie orbitálov jednotlivých valenčných elektrónov. Atóm uhlíka obsahuje štyri valenčné elektróny a môže sa vyskytovať celkom v troch hybridizáciách a to v takzvanej  $sp^3$  hybridizácii,  $sp^2$  hybridizácii a  $sp^1$  hybridizácii, ktoré sú zobrazené na obr. 1. V prípade  $sp^3$  hybridizácie smeruje každý orbitál valenčného elektrónu do vrcholu pravidelného štvorstenu a vytvára s ďalším atómom pevnú  $\sigma$  väzbu. Atómy uhlíka v  $sp^3$  hybridizácii tvoria kryštalovú štruktúru diamantu. Hybridizácia  $sp^2$  je typická pre grafit, kedy pevnú  $\sigma$  väzbu medzi atómami tvoria len tri valenčné elektróny, ktorých orbitály smerujú do vrcholov rovnostranného trojuholníka. Posledný valenčný elektrón leží v p-orbitáli, ktorý sa nachádza nad a pod rovinou tvorenou  $sp^2$  orbitálmi a vytvára slabšiu  $\pi$  väzbu. V hybridizácii  $sp^1$  ležia dva valenčné elektróny v p-orbitáloch a ďalšie dva v sp-orbitáloch [2,3,6]



Obr. 1 Zobrazenie orbitálov valenčných elektrónov pre  $sp^3$ ,  $sp^2$  a  $sp^1$  hybridizáciu atómu uhlíka  
Figure 1. Showing the valence electron orbitals for  $sp^3$ ,  $sp^2$  and  $sp^1$  hybridization of a carbon atom

Diamant je najpevnejší a najtvrdší prírodný materiál a jeho extrémne fyzikálne vlastnosti vychádzajú zo silnej  $\sigma$  väzby medzi jednotlivými atómami. Usporiadaná diamantová kubická štruktúra sa vyznačuje najhustejším atómovým usporiadaním a jeho vysokú tvrdosť vytvárajú atómy uhlíka v  $sp^3$  hybridizácii. Grafit je tvorený jednotlivými vrstvami uhlíka so silnou  $\sigma$  väzbou, kde medzi jednotlivými vrstvami pôsobí slabá Van der Waalsova väzba. Takéto rovinné usporiadanie spôsobuje  $sp^2$  hybridizácia atómu uhlíka a práve absencia  $sp^3$  väzieb v grafitě ho radí medzi najmäkšie známe materiály. V DLC povlakoch je dôležitý práve podiel viazaných atómov uhlíka v  $sp^3$  hybridizácii, ktorý je kľúčový pre vytvorenie vlastností podobných diamantu. Rozdiel medzi diamantom a DLC povlakom je v usporiadaní. DLC

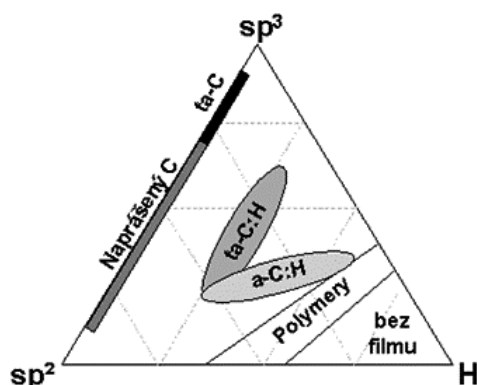
vrstvy dosahujú vlastnosti podobné diamantu, ale jedná sa o neusporiadanú (amorfnú) štruktúru. Na obr. 2 môžeme vidieť rozdiel medzi amorfnou štruktúrou DLC povlaku a usporiadanými štruktúrami diamantu a grafitu. Výslednú štruktúru DLC povlaku vytvárajú atómy uhlíka v rôznych hybridizáciách [2,3].



Obr. 2 Porovnanie štruktúry grafitu (a), diamantu (b) a amorfnej uhlíkovej štruktúry DLC povlaku (c)

Figure 2. Comparison of the structure of graphite (a), diamond (b) and amorphous carbon structure of DLC coating (c)

Ako už bolo spomenuté, amorfná štruktúra DLC povlakov je zložená z grafitického uhlíka, z diamantového uhlíka a z vodíka v určitom pomere v závislosti na danom procese. Hlavným parametrom, od ktorého sa odvíjajú vlastnosti vrstiev DLC povlakov, je podiel  $sp^3$  a  $sp^2$  uhlíkových väzieb, čiže pomer grafitickej a diamantovej štruktúry. Práve kvôli širokému spektru DLC vrstiev s rôznym zastúpením pomeru uhlíkových väzieb a vodíka sa vytvorilo základné delenie DLC vrstiev. Veľké množstvo metód prípravy DLC vrstiev využíva ako vstupný zdroj uhl'ovodíky a vo výslednej vrstve sú zakomponované aj atómy vodíka. Takto vzniklo základné rozdelenie vrstiev DLC povlakov, ktoré môžeme vidieť na obr. 3. Obr. 3 zobrazuje ternárny fázový diagram DLC vrstiev, ktorý sa obvykle používa pre znázornenie širokého spektra zloženia DLC povlakov. Tento obrázok predstavuje hlavné možné skupiny pre DLC vrstvy, v rozdelení podľa obsahu vodíka a podľa väzby uhlíkových atómov. Bod  $sp^2$  odpovedá grafitovému typu väzby atómov a bod  $sp^3$  potom odpovedá diamantovému typu väzieb medzi atómami uhlíka [3,6].



Obr. 3 Ternárny fázový diagram DLC povlakov

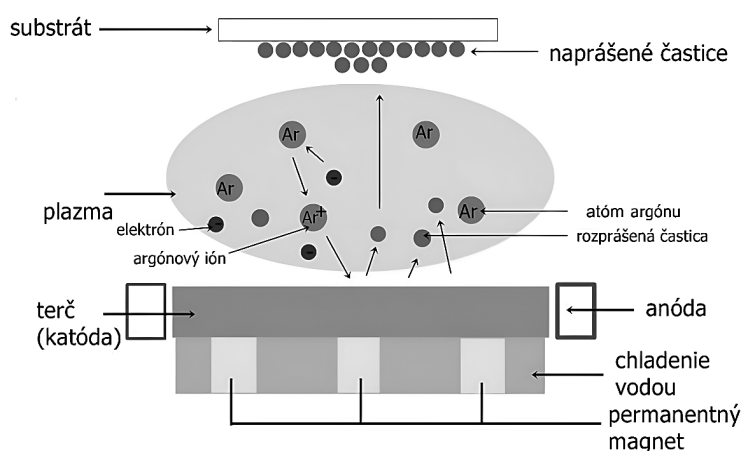
Figure 3. Ternary phase diagram of DLC coatings

V ľavej spodnej časti diagramu sa vyskytuje skupina neusporiadaných grafitických materiálov od čistého grafitu až po naprášený uhlík s vysokým podielom  $sp^2$  väzieb. Pravú spodnú časť charakterizujú uhl'ovodíkové polyméry, ktoré tvoria určitú hranicu, za ktorou sa dané atómy vyskytujú len v molekulárnej forme. Základné rozdelenie DLC vrstiev je teda nasledovné:

- **ta-C** bezvodíkové amorfné vrstvy s vysokým obsahom  $sp^3$  väzieb (takmer 90%). Majú najväčšiu podobnosť diamantu. Majú vysokú tvrdosť a veľký modul pružnosti.
- **ta-C:H** vrstvy s obsahom vodíka (25%-30%) s vysokým obsahom  $sp^3$  väzieb (cca 70%).
- **a-C:H** vrstvy s vysokým obsahom vodíka (40%-60%). Môžu obsahovať aj 70%  $sp^3$  väzieb, avšak nie len medzi atómami uhlíka, ale aj medzi atómami uhlíka a vodíka [3]

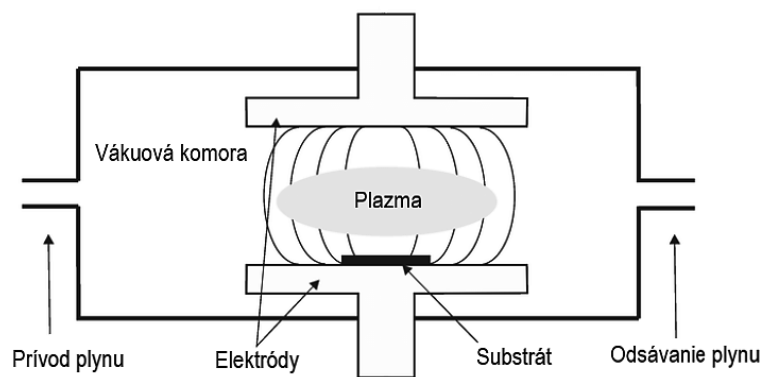
### 3.2. Metódy vytvárania DLC povlakov

Samotné metódy deponovania rôznych tenkých povlakov môžeme rozdeliť na dva základné druhy a to na metódy PVD (Physical-Vapor-Deposition) a CVD (Chemical-Vapor-Deposition). Pri metódach deponovania PVD dochádza k fyzikálnej depozícii vrstvy z plynnej fázy a pri metódach CVD dochádza k chemickej depozícii vrstvy z plynnej fázy. Na deponovanie DLC povlakov sa využívajú rôzne metódy v závislosti od druhu DLC povlaku. DLC povlaky využívané v praxi sa delia na už spomínané dva základné druhy a to bezvodíkové DLC povlaky (ta-C) a hydrogénové DLC povlaky (ta-C:H, a-C:H). Prvá skupina DLC povlakov sa zvyčajne nanáša metódou PVD s využitím uhlíkovej plazmy. V prípade hydrogénových DLC povlakov sa tieto bežne získavajú pomocou plazmového nanášania chemických pár a uhl'ovodíkových plynov, čiže metódou CVD.. Väčšina procesov, na ktorých je založená depozícia DLC vrstiev je fyzikálnej povahy (PVD), pretože na vytváranie väzieb  $sp^3$  majú hlavný vplyv ióny uhlíka. PVD procesy na nanášanie tenkých vrstiev DLC zahŕňajú napríklad nanášanie iónovým lúčom (IB), nanášanie katódovým oblúkom (CVA), ale najčastejším industriálnym depozičným procesom DLC vrstiev je magnetronové naprašovanie pomocou rozprašovania uhlíkoveho terča v Ar atmosfére (Obr. 4). Princíp spočíva v rozprašovaní uhlíkoveho terča v Ar plazme, kedy je povrch substrátu „bombardovaný“ atómami uhlíka. Na obr. 4 môžeme vidieť, že magnety sú umiestnené za terčom, aby spôsobili špirálový pohyb elektrónov a zväčšili dĺžku ich dráhy, a tým zvýšili stupeň ionizácie plazmy, ktorá „bombarduje“ povrch súčiastky iónmi uhlíka [2,3,6].



Obr. 4 Princíp magnetronového naprašovania  
Figure 4. Principle of magnetron sputtering

Chemická plazmová depozícia z pár (PACVD - Plasma Assisted Chemical Vapour Deposition) PACVD metóda deponovania DLC povlakov (Obr. 5) je vlastne CVD metóda povlakovania s tým, že sa celý proces zefektívňuje použitím plazmy. Základným princípom CVD metódy je, že tenká deponovaná vrstva sa na povrchu substrátu vytvára v dôsledku chemických procesov medzi chemickými zlúčeninami, ktoré sú v plynnom stave privedené k substrátu pri vyšších teplotách okolo 1000°C. Takýto plazmou aktivovaný CVD proces umožňuje zníženie teploty potrebnej pre vznik vrstvy na povrchu substrátu na približne 500°C. Pri tejto metóde sa používajú len prekurzory obsahujúce uhlík v plynnom stave, ako je napríklad acetylén. Ten je privedený v plynnom stave k povrchu substrátu, kedy vysoko energetické častice plazmy predávajú časť svojej energie jeho molekulám. Týmto spôsobom je získaná dostatočná energia potrebná pre priebeh chemickej reakcie vedúcej k depozícii povrchovej vrstvy. Využitie plazmy namiesto vysokej teploty, ako zdroja energie pre iniciáciu chemickej reakcie, prináša mnoho výhod. V prvom rade depozícia prebieha pri nižšej teplote a umožňuje rovnomerné nanášanie vrstvy aj v dutinách súčiastok bez nutnosti ich rotácie. Povlaky vytvorené metódou PACVD dosahujú hrúbku 2-3  $\mu\text{m}$  a obsahujú približne 70 % väzieb  $\text{sp}^3$  čo zabezpečuje ich vysokú tvrdosť [2,3,6].



Obr. 5 Schéma PACVD depozície  
Figure 5. Scheme of PACVD deposition

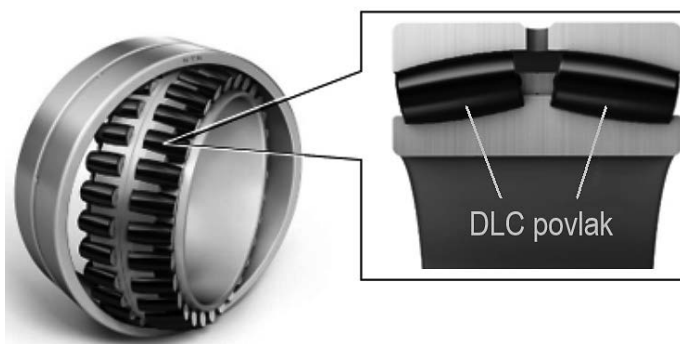
#### 4. APLIKÁCIA DLC POVLAČOV NA VALIVÉ LOŽISKÁ

Tendenciou vývoja valivých ložísk je zvyšovanie ich kvality, pričom sa veľký dôraz kladie na znižovanie strát energie trením a s tým súvisiacu životnosť ložísk. Vzhľadom na to, že najnamáhavejšia časť ložiska je jeho povrch, vývoj sa sústreďuje hlavne naň. Aby sme vlastnosti ložísk ešte zlepšili, začali sa na valivé ložiská deponovať rôzne nátery a povlaky, ktoré disponujú ďaleko lepšími tribologickými vlastnosťami ako základný materiál ložiska. Jedny z najpoužívanejších povlakov, ktoré sa deponujú na valivé ložiská sú práve povlaky DLC. Ich tvrdý povrch s veľmi nízkou drsnosťou prispieva k potlačeniu oteru a iným prejavom opotrebovania, a teda k podstatnému predĺženiu životnosti ložiska. Spojením odolnosti a pevnosti bežnej ložiskovej ocele s výnimočne nízkym trením a vysokou tvrdosťou povlakov DLC vznikne ložisko, ktoré sa vyznačuje vysokou tvrdosťou povrchu s nízkym koeficientom trenia. Typické hodnoty tvrdosti DLC povlakov deponovaných na ložiskových oceliach sa rádovo pohybujú okolo 1200 HV, zatiaľ čo tvrdosť bežnej ložiskovej ocele je 650 až 850 HV. Avšak aby nedochádzalo k opotrebovaniu, samotná tvrdosť povrchu nestačí, preto je tiež dôležitou

vlastnosťou koeficient trenia. Koeficient trenia valivých ložísk opatrených DLC povlakom závisí od prostredia, v ktorom budú pracovať, nakoľko povlakom môžu byť opatrené buď všetky súčasti ložiska, ako na obr. 6, alebo len valivé telieska ložiska (obr. 7). Je zrejmé, že najnižšie hodnoty koeficientu trenia sa dosiahnu u valivých ložísk, ktorých všetky funkčné plochy sú ošetrené DLC povlakom[4,5].

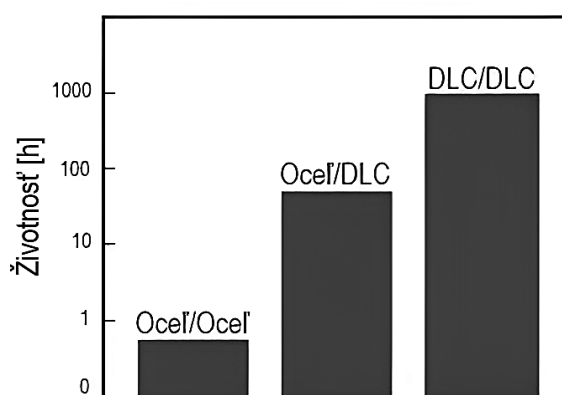


Obr. 6 Valivé ložisko s DLC povlakom  
Figure 6. Rolling bearing with DLC coating



Obr.7 Valivé telieska s DLC povlakom  
Figure 7. Rolling elements with DLC coating

Túto teóriu znižovania koeficientu trenia a predĺženia životnosti valivého ložiska pri ošetrení DLC povlakom všetkých súčastí ložiska, potvrdzuje aj výskum medzinárodnej spoločnosti SKF, ktorá je zameraná na výrobu a vývoj valivých ložísk. Autori Hultman a Sjöström (1998) vo svojom vedeckom článku pre spoločnosť SKF uvádzajú graf (Obr. 8), ktorý porovnáva životnosť jednotlivých trecích dvojíc vzhľadom na to, či ich povrchy boli alebo neboli ošetrené DLC povlakom [5].



Obr.8 Porovnanie životnosti trecích dvojíc vzhľadom na použitie DLC povlaku  
Figure 8. Comparison of the service life of friction pairs with regard to the use of DLC coating

Doteraz sa valivé ložiská ošetrené DLC povlakom prevažne používali v zariadeniach, ako sú kompresory a hydraulické motory. V týchto zariadeniach DLC povlak úspešne prispieva k ochrane proti poškodeniu ložísk takzvaným „rozmazaním“, čo je druh poškodenia ložiska, ktorý vzniká pri valcovom kontakte, keď sa rozdelí olejový film medzi valivými telieskami a ložiskovým krúžkom. Podobným problémom sa zaoberala vo svojom vývoji valivých ložísk

ďalšia spoločnosť s názvom NTN Corporation. Táto spoločnosť využila DLC povlaky na ošetrovanie valivých teliesok ložísk pre hlavný hriadeľ veternej turbíny. Pre ložiská hlavného hriadeľa veternej turbíny sa používajú súdkové telieska, ktoré pracujú pri extrémne nízkych prevádzkových rýchlostiach a pri vysokom kontaktnom zaťažení v dôsledku veľkej hmotnosti komponentov. Tieto ložiská majú problém s opotrebovaním povrchu obežnej dráhy, kde dochádza k jeho odlupovaniu a praskaniu. Spoločnosť NTN uvádza, že odolnosť ložísk ošetrovaných DLC povlakom výrazne stúpla, dokonca aj pri tak náročných prevádzkových podmienkach. Výskum a vývoj v tejto oblasti postupuje veľmi rýchlo a neustále sa objavujú nové koncepcie a nové typy DLC povlakov, ktoré majú stále širšie uplatnenie práve aj u valivých ložísk [4,5]

## 5. ZÁVER

Cieľom tejto práce bolo opísať súčasný stav poznatkov o DLC povlakoch, ich štruktúre, metódach vytvárania a ich využívaní v technickej praxi na povlakovanie valivých ložísk. Na základe tejto teoretickej analýzy môžeme tvrdiť, že DLC povlaky môžu efektívne zvyšovať povrchovú tvrdosť komponentov, ich odolnosť voči opotrebeniu a znížiť trenie v mnohých aplikáciách. Využitie DLC povlakov na valivé ložiská taktiež vykazuje výrazné zlepšenie ich odolnosti voči opotrebeniu, zníženie trenia a nárast životnosti. Na záver možno konštatovať, že DLC povlaky predstavujú sľubný nástroj na optimalizáciu funkčnosti valivých ložísk a mnohých iných strojných súčastí, kde dochádza k treniu.

## POĎAKOVANIE

Príspevok vznikol v rámci riešenia spoločného slovensko-poľského projektu International Visegrad Fund's V4 Generation Mobility Mini-Grant No 12410044 ako výsledok spolupráce medzi Politechnikou Slaskou (Poľsko) a Žilinskou univerzitou v Žiline a projektov KEGA č. 004ŽU-4/2023 a KEGA č.009ŽU-4/2023.



## LITERATÚRA

1. KONEČNÁ, R., TILLOVÁ, E., VAŠKO, A., MARKOVIČOVÁ, L. 2020. Materiály II Návod na cvičenia. Žilinská univerzita v Žiline/EDIS-vydavateľstvo ŽU, 2020, 26 s., ISBN 978-80-554-1708-0
2. ROBERTSON, J. Diamond-like amorphous carbon. In Materials Science and Engineering: R: Reports, vol 37, 2002. ISSN 0927-796X. DOI: [https://doi.org/10.1016/S0927-796X\(02\)00005-0](https://doi.org/10.1016/S0927-796X(02)00005-0)
3. KROKER, M. 2016. Vývoj průmyslové technologie přípravy diamantu podobných vrstev. Bakalárska práca. Masarykova univerzita 2016. 1-5s.
4. ŠKOVIERA, J. 2017. Návrh systému pro testování valivých ložisek s proměnnými parametry mazání. Diplomová práca. Vysoké učení technické v Brně 2017. 1s.

5. Hard coating for heavy bearing duty [Online]. Anna Hultman a Hans Sjöström 1998 [cit. 2023.22.02] Dostupné na internete: <https://evolution.skf.com/hard-coating-for-heavy-bearing-duty/>
6. AINSWORTH, S., UHURE, N. 2007. Diamond like carbon coatings for tribology: Production techniques, characterisation methods and applications. *International Materials Reviews*. 52. 153-174. DOI: 10.1179/174328007X160272





17th-19th June 2024  
Gliwice, Poland

DEPARTMENT OF ENGINEERING MATERIALS AND BIOMATERIALS  
FACULTY OF MECHANICAL ENGINEERING  
SILESIA UNIVERSITY OF TECHNOLOGY

## INTERNATIONAL STUDENTS SCIENTIFIC CONFERENCE

### **Identification and assessment of the employee's mental load at a selected production workplace**

Klaudia Niedziela<sup>a</sup>, Monika Spilka<sup>b</sup>

<sup>a</sup> Student, Silesian University of Technology, Faculty of Mechanical Engineering, Department of Engineering Materials and Biomaterials

<sup>b</sup> Silesian University of Technology, Faculty of Mechanical Engineering, Department of Engineering Materials and Biomaterials  
email: monika.spilka@polsl.pl

**Abstract:** The article concerns the work ergonomics at the injection molding machine operator workplace. The characteristics of the analyzed workplace and activities performed were presented. The mental loads to which an employee is exposed was also identified and assessed. It was found that the work of a plastic injection molding machine operator is not complicated, but it is quite demanding on a person's mental capacity.

**Keywords:** ergonomics, workplace, injection molding machine operator, mental load

### **1. INTRODUCTION**

Working in a production environment is characterized by a high level of risk resulting from the need to come into contact with machines and devices, as well as being among harmful substances. The application of principles related to occupational health and safety and work ergonomics provides employees to perform tasks in a safe and comfortable conditions.

Work ergonomics is a scientific field whose scope of research includes a system consisting of a person, a technical object and the work environment. The measures taken within the framework of work ergonomics consist of designing and adapting the workplace and the activities performed on it to human capabilities, so that the work at a given position can be performed in the most effective manner possible [1,2]. The goal of work ergonomics is to eliminate burdensome working conditions, such as, among others: forced body position, manual handling of elements, monotony of performed activities, mental load, working environment conditions [3,4].

A plastic injection molding machine operator is exposed to threats not only from the machines, but also from the specifics of the activities performed, so the workplace should be ergonomically designed and adapted to human capabilities.

## 2. CHARACTERISTICS OF THE PLASTIC INJECTION MOLDING MACHINE OPERATOR WORKPLACE

The plastic injection molding machine operator workplace is located in an enclosed production hall. The main components of the workplace are: an injection molding machine, a robot, a conveyor belt and a worker. The operator's tasks include taking the product from the conveyor belt, visually assessing the quality, removing any excess material created during the injection process with a knife (also called deburring), and then placing it in a container according to the instructions. After filling the container with finished products, the operator closes it, marks them with a special card containing the product data, and then puts the container on a trolley, which is collected by a logistician at a specified time.

At the workplace, the operator has a touch screen with software at his disposal, where he can enter the number of well-made pieces and the number of defects. It is also possible to view machine parameters on the screen and report a failure or need for help. The height of the conveyor belt and the method of removing molded parts from it are designed in such a way that the operator does not have to bend down or lift his hands.

## 3. IDENTIFICATION AND ASSESSMENT OF THE EMPLOYEE'S MENTAL LOAD AT THE WORKPLACE

Identification of mental load at the workplace consists of two stages: identification of the employee's information load and determination of the monotony load. The assessment of each category involves of assigning a point score on a five-point scale, where 1 means the lowest value and 5 means the highest value. The information load category (Table 1) consists of the following aspects: frequency of information inflow, information variability, information uncertainty, information complexity, information inaccuracy, information validity, and time stress. Each of them is evaluated in three stages of work execution: receiving information, which can be understood as the input data received by the employee, decision-making, which is the process of transforming input data, and performing activities, which means receiving output data.

Table 1. Identification of information load [5]

Stage	Receiving information	Decision-making	Performed activities
<b>Feature of information:</b>			
frequency of information inflow	2	1	3
variability of information	1	1	1
uncertainty of information	1	1	1
complexity of information	1	2	1
inaccuracy of information	1	1	1
validity of information	3	2	3
time stress	1	4	3
Total:	10	12	13
<b>Total score: 35 points</b>			

At the beginning of the working day, the injection molding machine operator learns information about the number of the machine it will be operating and the type of product that is being produced in a given series. When starting the machine, operator works at it for the entire shift, so he is not load with the frequency of information flow, its variability, uncertainty or

complexity, so these features were evaluated with lower values. The injection process is a short operation, that lasts several dozen seconds, therefore, when taking the product and assessing its quality, the operator works under time pressure, and his decision to consider product as correctly performed has consequences related to the execution of the order and subsequent customer satisfaction. For this reason, the importance of information and time stress were rated with higher values.

The information load can be rated as low, medium, high or very high. The reception of information at the tested workplace was rated with a total of 10 points, decision-making with 12, and performance of activities with 13. The total score was 35 points, therefore, according to the point assessment presented in Table 2, the information load at the injection molding machine operator's workplace can be described as medium.

Table 2. Assessment of information load [5]

Point rating	Verbal assessment
1 – 30 points	low load
31 – 70 points	medium load
71 – 90 points	high load
91 – 105 points	very high load

When evaluating the load of monotony, which generates mental fatigue in a person, the following aspects should be taken into account: uniformity of the work process, uniformity of the environmental conditions, great ease of work, that does not involve the intellect, and the need for constant tension of attention. The scores assigned to the above aspects are presented in Table 3. In this category, the assigned scores are significantly higher because the work at the plastic injection molding machine operator workplace is carried out in uniform ambient conditions and the process itself. The operator does not change the position or rearm the machine for another product. The activities performed in this position are not difficult and are repeated in a specific cycle, which does not cause in excessive intellectual involvement.

Table 3. Identification of monotony load [5]

A component of monotony:	Points
uniformity of the work process	4
uniformity of the environmental conditions	5
difficulty degree of the work and the need to engage the intellect	4
focusing attention on the activities performed	3
<b>Total:</b>	<b>16</b>

As in the case of information load, work monotony can be assessed as a load: low, medium, high or very high (Table 4). The identification of the monotony load allows the conclusion that the plastic injection molding machine operator is largely loaded by work monotony.

Table 4. Workload assessment [5]

Point rating	Verbal assessment
1 – 5 points	low load
6 – 12 points	medium load
13 – 17 points	high load
18 – 20 points	very high load

The determination of information and monotony loads allows for the summary determination of mental effort, as shown in Table 5.

Table 5. Summary assessment of mental effort [5]

Type of load:	Points
information load	35
monotonny load	16
<b>Total load</b>	<b>51</b>

Mental load is defined as low, medium, high or very high (Table 6). The analysis showed that the total mental effort was 51 points, that is, the work of an injection molding machine operator carries the risk of medium mental strain. When making this analysis, it can be concluded that the information load is more demanding than the monotony load, which may mean that a physical worker struggles with less mental effort than a mental worker, even though his work may seem monotonous and tedious.

Table 6. Interpretation of mental exertion assessment results [5]

Point rating	Verbal assessment
1 – 35 points	low load
36 – 82 points	medium load
83 – 107 points	high load
108 – 125 points	very high load

#### 4. SUMMARY

Work ergonomics is an inherent field of occupational health and safety, although not everyone is aware of its essence. Many companies focus mainly on reducing the level of risk generated by the machines in the workplace, and do not pay attention to analyzing the activities performed at the workplace and the way they are carried out. The development of ergonomic methods and tools allows for the assessment and adaptation of each work station to the person, regardless of whether it is office work or physical work.

Working as a plastic injection molding machine operator is not a complicated, but it is quite demanding on a person's mental capabilities. The injection molding machine operator is not a decision-making workplace, so the information load is not high, although the pace of the process and the specific nature of the work causes a significant loads on the employee due to the monotony of work. The process and working conditions are monotonous, which may cause the operator to become lost in thought and lack of focus on the tasks being performed.

#### BIBLIOGRAPHY

1. M. Błaszczok, Ergonomia bezpiecznej i higienicznej pracy, Wydawnictwo Politechniki Śląskiej, Gliwice, 2018.
2. M. Wojsznis, Ergonomia - ocena stanowisk pracy, Wydawnictwo Politechniki Poznańskiej, Poznań, 2018.
3. A. Zawada-Tomkiewicz, B. Storch, BHP i ergonomia dla inżynierów: projektowanie ergonomiczne procesów pracy i stanowiska roboczego, Wydawnictwo Uczelniane Politechniki Koszalińskiej, Koszalin, 2017.
4. M. Konarska, Ergonomia w dyrektywach i normach, Bezpieczeństwo pracy 1 (2007) 6-9.
5. K. Lachowicz, Badanie i ocena obciążenia i zagrożeń wynikających z warunków pracy w zawodzie pielęgniarki, Bezpieczeństwo. Teoria i praktyka 4 (2018) 239-253.



17th-19th June 2024  
Gliwice, Poland

DEPARTMENT OF ENGINEERING MATERIALS AND BIOMATERIALS  
FACULTY OF MECHANICAL ENGINEERING  
SILESIA UNIVERSITY OF TECHNOLOGY

## INTERNATIONAL STUDENTS SCIENTIFIC CONFERENCE

### Microprocessor color recognition and replication system

Bartosz Nikiel<sup>a</sup>, Mirosław Bonek<sup>b</sup>

<sup>a</sup> Student of Silesian University of Technology, Faculty of Electrical Engineering

<sup>b</sup> Silesian University of Technology, Faculty of Mechanical Engineering, Department of Engineering Materials and Biomaterials

**Abstract:** The aim of the thesis was to devise a device which recognises colours and to prepare HTML website depicting the read colour together with its detailed description. The first part of the thesis is dedicated to the choice of the appropriate elements necessary to generate the device. The latter part concentrates on its working principle and calibration. The last part of the thesis describes the operation of the complete device along with HTML website.

**Keywords:** microcontroller, HTML page, RGB components, replication

#### 1. INTRODUCTION

The main idea of the project was to help people with visual impairments or colorblindness. For this purpose a simple device has been created to facilitate colour recognition. The created device used the reception frequency of the basic RGB (red, blue, green) colours. Then, based on each of the read changes, it returned the appropriate colour in the database and displayed its name on our website or application.

#### 2. PURPOSE AND SCOPE OF WORK

The aim of the project was to develop a prototype of a device for replicating colours and displaying the corresponding names on an HTML page. An HTML page uses RGB components and uses them to name the colours received by the designed device.

##### 2.1 The Diagram of the device's structure and operation

The Illustrative diagram of the project intended to show its operation

##### 2.2 Elements used for the construction

The basis of the project was the ESP-32 microcontroller. It was chosen because of its small size, a built-in WiFi and Bluetooth modules. Thanks to these modules we could communicate

directly with the website. An additional feature is its easy programming. We can use ready-made libraries that significantly speed up its programming.

Another necessary element was a colour sensor. The choice fell on the TSC3200 sensor, whose advantage is high accuracy and repeatability of measurements, and it is compatible with ESP-32.

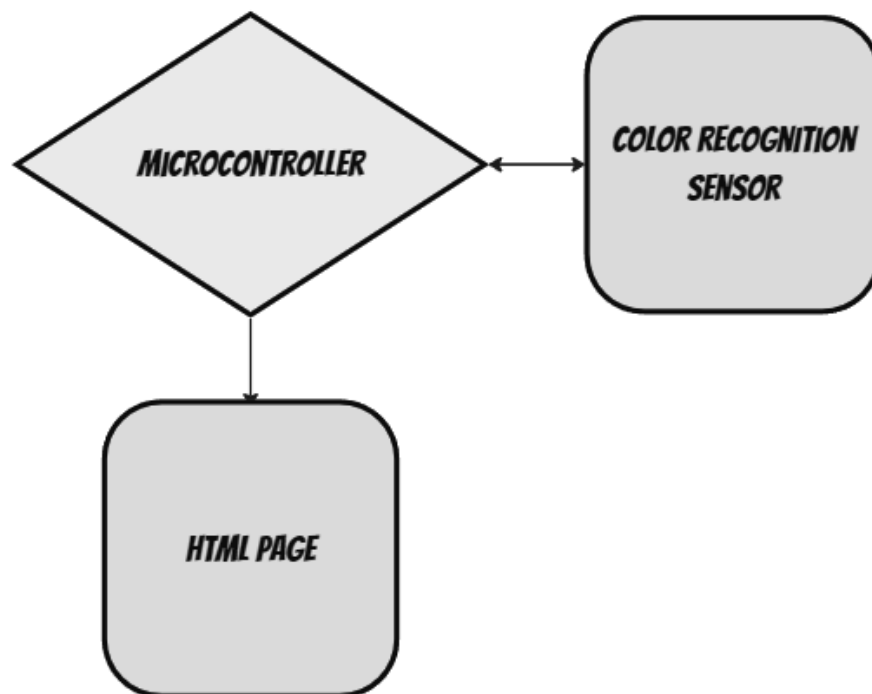


Figure 1. Schematic diagram of the designed device

### 2.3 Operating principle of the colour recognition device

After connecting to the power supply, the device automatically generates a link to the website. The link changes depending on the Wi-Fi network it uses because it is generated by the built-in Wi-Fi module located in the ESP32 microcontroller.

The second task of the device is to read RGB components through the TCS3200 sensor. After the sensor reads the individual components, they are sent to a previously generated HTML page, where they are replicated. Thanks to the built-in colour table, the website updates the colour read by the sensor and automatically displays its name.

The data automatically refreshes every second.

### 2.4 Principle of the Html page

The website allows you to enable reading data from the ESP32. This is done by pressing the “Start Interval” button. When the button is activated, the website starts downloading data from the microprocessor at a frequency of 1HZ. The downloaded RGB components are replicated and displayed along with the signature of the current colour. If necessary, it is possible adjust the data frequency, which can affect the accuracy of the reading. The page downloads data until the “Stop Interval” button is pressed.

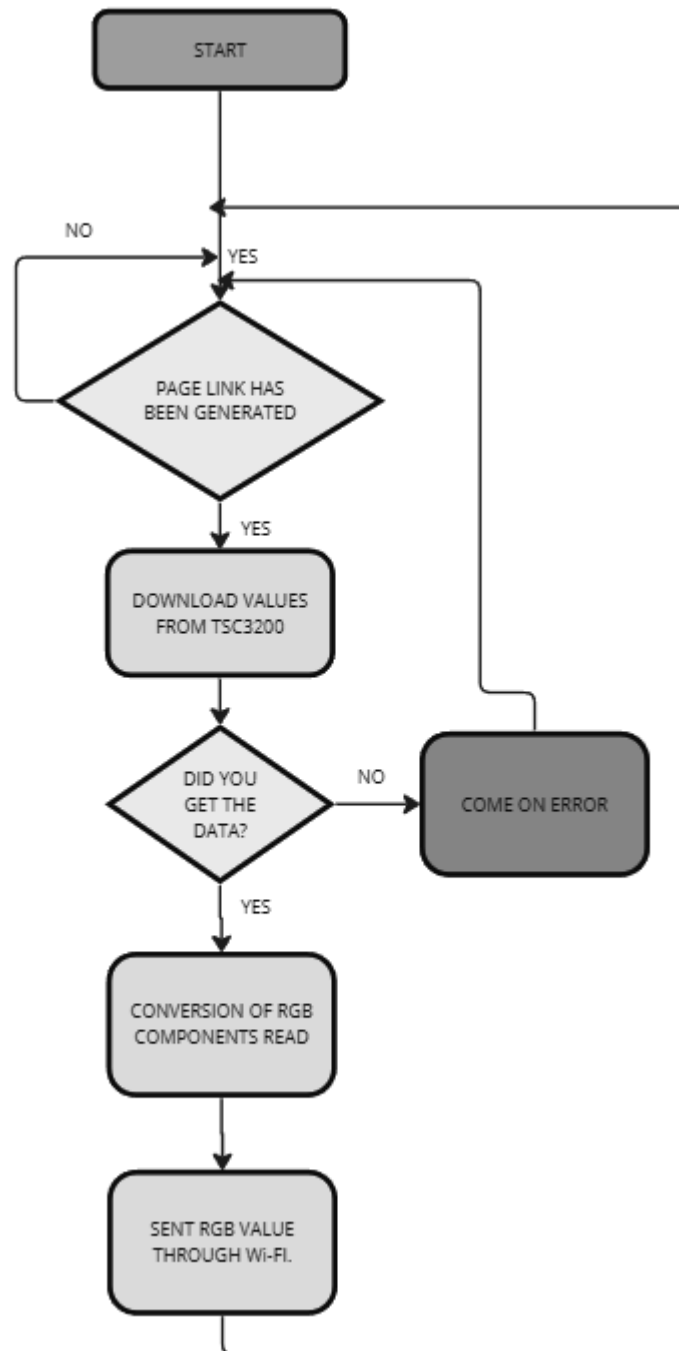


Figure 2. Block diagram of the operation of the microprocessor together with the sensor.

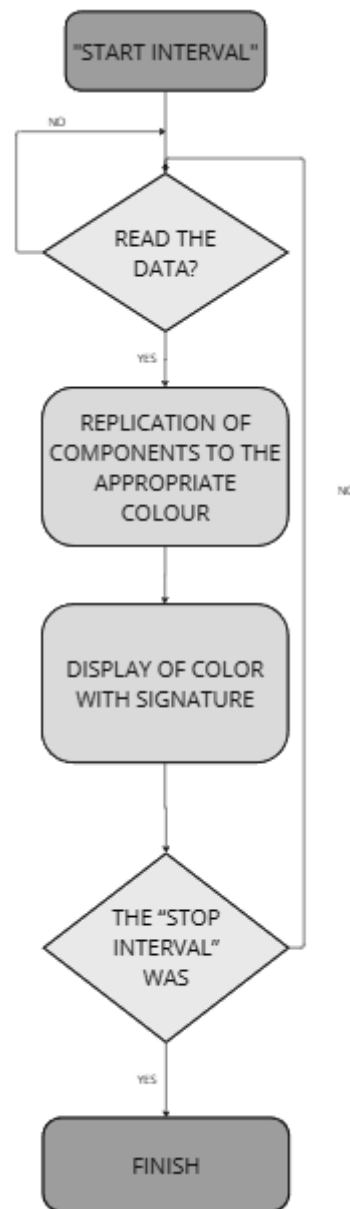


Figure 3. A block diagram of how an HTML page works.

## 2.5 Device calibration

After creating the code in the Arduino IDE program, the most difficult task was to calibrate the colour sense. The TCS3200 sensor provides frequency responses, depending on the intensity of light. Therefore, for each of the basic RGB colours, there is a created frequency map.



```
redFrequency = pulseIn(sensorOut, LOW);
redFrequency = map(redFrequency, 25, 350, 255, 0);
```

Figure 4. Example map for red colors.

```
R = 186 G = 83 B = 87
R = 186 G = 84 B = 87
R = 185 G = 83 B = 84
R = 185 G = 83 B = 86
R = 186 G = 84 B = 86
R = 186 G = 84 B = 85
R = 186 G = 80 B = 86
R = 185 G = 82 B = 86
```

Figure 5. Data read from the “Serial Monitor” - after applying red after calibration.



Figure 6. Reading from the color chart. [3]

The LEDs mounted on the TSC3200 sensor turn out to be the biggest problem during calibration. The light generated by them was too large. What is more, attempts to change the colour and intensity of the light using tapes in different colours or other materials ended unsuccessfully. Reducing the supply voltage of the LEDs was the only solution for proper effects of the device. As a result, the sensor works with greater precision.

### 3. CONCLUSIONS

While working on the project, I was able to develop my programming skills in the Arduino IDE and physically construct the device according to the previously established assumptions. As a result, I was able to observe the problems associated with creating my own project from scratch. The biggest problem was calibrating the device correctly, because after each change it was necessary to perform a series of tests and compare their results. The final result proved to

be satisfactory, though. In addition, you can still develop the designed device. One possibility for development is to create a housing, for example, on a 3D printer, which would ensure the mobility of the device. It is also possible to expand the circuit such as an LCD display, which could automatically display the colour being read. In such case, it would be possible to perform a regression of the colour base and display only basic colours, so as to provide the user with a more comfortable experience using the device.

## ACKNOWLEDGEMENTS

The publication was created within the framework of the joint Slovak-Polish project International Visegrad Fund's V4 Generation Mobility Mini-Grant No 12410044 as a result of cooperation between the Association of Alumni of the Silesian University of Technology, Gliwice, Poland and the University of Žilina, Slovakia.

The project is co-financed by the Governments of Czechia, Hungary, Poland and Slovakia through Visegrad Grants from the International Visegrad Fund. The mission of the fund is to advance ideas for sustainable regional cooperation in Central Europe.



## BIBLIOGRAPHY

1. <https://botland.com.pl/plytki-zgodne-z-arduino-dfrobot/9153-dfrobot-firebeetle-esp32-iot-wifi-bluetooth-6959420912155.html>
2. [https://botland.com.pl/czujniki-swiatla-i-koloru/4932-czujnik-koloru-przetwornik-swiatlo-czestotliwosc-tcs3200-waveshare-9520-5904422374211.html?cd=20567593583&ad=&kd=&gad\\_source=1&gclid=CjwKCAiA9ourBhAVEiwA3L5RFkixB7GFaF8kl0t5FDbNJ\\_KfoFcekKsKwc8D76wP93\\_NXEnvBNoqZxoCxa8QAvD\\_BwE](https://botland.com.pl/czujniki-swiatla-i-koloru/4932-czujnik-koloru-przetwornik-swiatlo-czestotliwosc-tcs3200-waveshare-9520-5904422374211.html?cd=20567593583&ad=&kd=&gad_source=1&gclid=CjwKCAiA9ourBhAVEiwA3L5RFkixB7GFaF8kl0t5FDbNJ_KfoFcekKsKwc8D76wP93_NXEnvBNoqZxoCxa8QAvD_BwE)
3. [https://www.rapidtables.org/pl/web/color/RGB\\_Color.html](https://www.rapidtables.org/pl/web/color/RGB_Color.html)
4. M. Banzi, przekł. M. Chaniewska. Wprowadzenie do Arduino”, wyd. 2, APNPromise, 2014.
5. S. Monk, przekł. A. Mizerska, K. Matuk, Arduino dla początkujących: Kolejnykrok, wyd. 2, Wydawnictwo Helion, 2021.
6. S. Monk, przekł. K. Matuk, Arduino dla początkujących: Podstawy i szkice, wyd. 2, Wydawnictwo Helion, 2019.



17th-19th June 2024  
Gliwice, Poland

DEPARTMENT OF ENGINEERING MATERIALS AND BIOMATERIALS  
FACULTY OF MECHANICAL ENGINEERING  
SILESIA UNIVERSITY OF TECHNOLOGY

## INTERNATIONAL STUDENTS SCIENTIFIC CONFERENCE

### The resistance to abrasive wear of internal oesophagus prosthesis

Agnieszka J. Nowak

Silesian University of Technology, Faculty of Mechanical Engineering Technology, Scientific and Didactic Laboratory of Nanotechnology and Materials Technology, Faculty of Mechanical Engineering Technology, Silesian University of Technology,  
e-mail: [agnieszka.j.nowak@polsl.pl](mailto:agnieszka.j.nowak@polsl.pl)

**Abstract:** In the work, methodology of abrasive wear investigations of oesophageal prosthesis, made of long-fiber composite material based on medical silicon, internal surface is presented. The measurements have been done using equipment designed and made in Division of Materials Processing Technology, Management and Computer Techniques in Materials Science of Institute of Engineering Materials and Biomaterials. The volume of obtained samples mass loss have been determined from approximate calculations of wear trace to simple geometrical figure mapping this loss, and then the volume of this figure have been calculated. The main aim of the work is investigation of abrasive wear resistance of evaluated oesophageal prosthesis internal layer, considering its long-term exploitation possibility and extreme option of food consumed by patient after implementation.

**Keywords:** composite material, long-fiber, medical silicon, the resistance to abrasive wear

### 1. INTRODUCTION

In case of damage or dysfunction of the oesophagus caused by disease, chemical burn or mechanical trauma, it is necessary to replace it with some substitute. Currently, the most common cause of this type of dysfunction is cancer - oesophageal cancer. In Poland and around the world, depending on the advancement of this disease, stents (to expand the narrowed oesophagus), natural "prostheses" (the patient's vital tissues are used - e.g. the stomach) and so-called extracorporeal probes (used to reconstruct defects in the digestive system) are used interchangeably. In the case of removal of a significant part of the digestive system, i.e. resection of the oesophagus or stomach and duodenum). Just as in the first and second cases, the patient can take food in a "normal" way, in the third case, the position of intake and the consistency of nutrients are strictly defined. Having this type of probe is associated with:

With additional health complications, limited patient mobility, significant discomfort, and social exclusion. The solution to this problem is a synthetic, fully biocompatible oesophageal prosthesis that meets the features and functions of the natural human oesophagus [4-7, 9-10].

From a mechanical point of view, the human oesophagus can be compared to a tube that transports food contents to the stomach using wormlike movements (muscle contraction). The

direction of food movement is controlled by the so-called sphincters that prevent the regurgitation of ingested food. Due to the lack of real possibilities of reproducing the worm's movements in an artificial oesophagus, particular emphasis should be placed on its structure and internal surface to facilitate the free movement of food towards the stomach using its appropriate consistency and gravity [10].

However, in the case of long-term food intake with incorrect consistency, tribological damage (related to the friction process) of the inner layer of the prosthesis may occur. In this case, abrasive wear is closely related to separating material particles due to micro-cutting, scratching or furrowing with hard food particles. The scale of resistance to abrasive wear is determined by the strength of the friction areas of the surface layers and the mechanism of their interaction. In the case of a prosthesis and its future use, any damage to the surface mentioned above, which may lead to loss of its tightness, may have disastrous consequences for the implanted patient [1-4, 8, 11-13].

The primary focus of this study is to meticulously examine the resistance to abrasive wear of the inner layer of the developed oesophageal prosthesis. This investigation is crucial as it takes into account the potential for long-term use and the extreme food options, such as unchewed nut particles, that patients may consume after implantation.

## 2. SIMULATION TECHNIQUES IN INJECTION MOLDING

The following composite material components were used to make the intracorporeal oesophageal prosthesis:

- medical silicone MDX4-4159 from Dow Corning was used as the matrix material, consisting of 50% silicone and co-soluble ingredients: white spirit and isopropanol (iPA) with a concentration of 70% and 30%, respectively (Table 1);
- para-aramid fibre type 2200 1610 produced by DuPont with properties listed in Table 2 was used as reinforcement; the fibre was used in the continuous form (roving).

Tab. 2. Physical properties of medical silicone MDX4-4159 from Dow Corning

PHYSICAL PROPERTIES				
Boiling point/range [°C]	Flash-point [°C]	Relative density [g/cm <sup>3</sup> ]	Viscosity [cSt]	Appearance: character, color, smell
> 82	13,3 (closed crucible Pensky-Martens)	0,865	132 (in temperature 25°C)	liquid, straw, solvent
Chemical characteristics of the substance: <i>Aminofunctional silicosan</i>				

Tab. 2. Properties para-aramid fibre type 2200 1610 produced by DuPont

PROPERTIES OF PARA-ARAMID FIBER					
Type fibers	Density [g/cm <sup>3</sup> ]	Young's modulus [GPa]	Tensile strength [MPa]	Elongation at break [%]	Temperature decomposition [°C]
2200	1,44	105	3053	2,70	490
Shrinkage in warm air (15 min. at 190°C) => 0.1 [%]*					
Heat resistance (48h at 200°C) => 90 [%]*					

The following references describe the construction and individual stages of manufacturing an intracorporeal oesophageal prosthesis [3-6].

### 3. METHODOLOGY AND RESEARCH

Due to the future use of the material in question, it was decided to test the resistance to abrasive wear of the inner layer of the esophageal prosthesis on a device designed and manufactured at the Department of Material Process Technology and Computer Techniques in Materials Science of the Institute of Engineering and Biomedical Materials (Fig. 1). Due to the nature and type of use (i.e. moving food content under the influence of gravity) in the oesophageal prosthesis, roughness testing of polymeric materials using the Schopper or Graselli apparatus was not taken into account due to the type of abrasive factor. Introduction to the above. Suspension systems imitating food would not be possible. The test stand used in the research is intended to test the abrasion resistance of various engineering materials and coatings. The research method is based on the fact that in the presence or absence of abrasive, the process of rubbing the sample from the tested material and the counter-sample is activated. The tests were performed in the metal-composite material system; the counter-sample, in this case, was a steel ball with a diameter of 8.7 mm. Tests for a series of samples were performed while maintaining the same operating conditions, i.e. sliding speed  $v$  and load  $F$ .

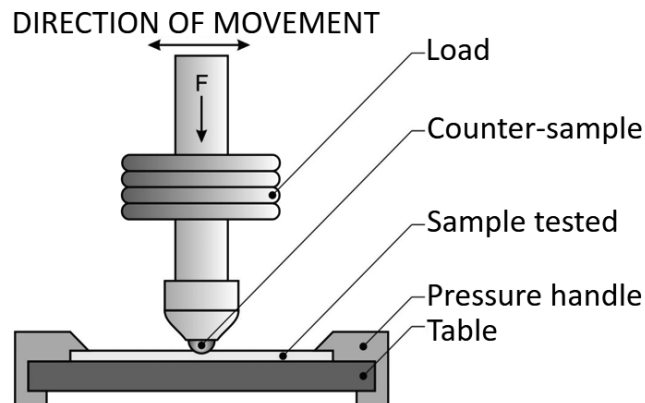


Fig. 1. Diagram of the equipment for abrasive wear resistance testing

The minimum pressure and number of cycles were determined based on preliminary tests. The samples were placed on a specially prepared table, which ensured their stable mounting during the test. The tests were performed with a constant number of cycles of 30,000 (1 cycle = 10mm) and at a load of 2 and 10 N with and without adding an abrasive suspension, simulating the food taken by the patient. The samples before and after the abrasion test were cleaned with compressed air to remove any contaminants from the abrasion process, and then the length and width of abrasion marks were measured on a Stereo Discovery.V12 stereoscopic microscope from Zeiss using the Leica-Qwin computer image analysis system at 20x magnification. The volume of the sample mass loss was determined based on calculations approximating the wipe trace to the simplest possible geometric figure reflecting this loss (Fig. 2). Then the volume of this figure was calculated using the following equations:

$$P_{WYT} = P_{WYC} - P_T \quad (1)$$

where:

$P_{WYT}$  – abrasion cross-sectional area,

$P_{WYC}$  – pole wycinka koła,

$P_T$  – area of a triangle.

$$V_{WYT} = P_{WYT}l \quad (2)$$

where:

$V_{WYT}$  – wipe volume,

$l$  – length of abrasion.

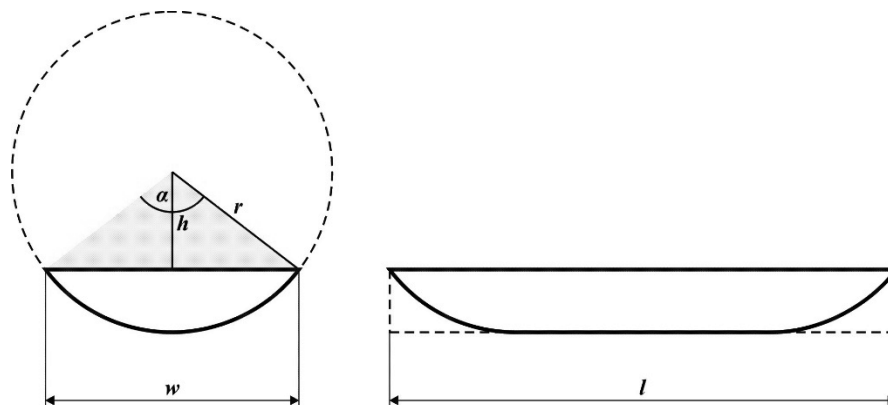


Fig. 2. The approximation of wear track to a simple geometric figure used in the work

CAD software (CATIA by CADSOL Design Polska) was used to verify the approximation method, which enabled precise determination of the mass loss. A wear trace model was created for each case, and its volume was determined in the program (Fig. 3). The abrasion profiles necessary for the calculations were determined on the LSM 5 EXCITER confocal microscope from Zeiss at 5x magnification. Sample surface scanning was performed using a diode laser

with a wavelength of 405nm and a power of 25 mW using an anti-interference filter transmitting radiation with a 405/488nm wavelength.

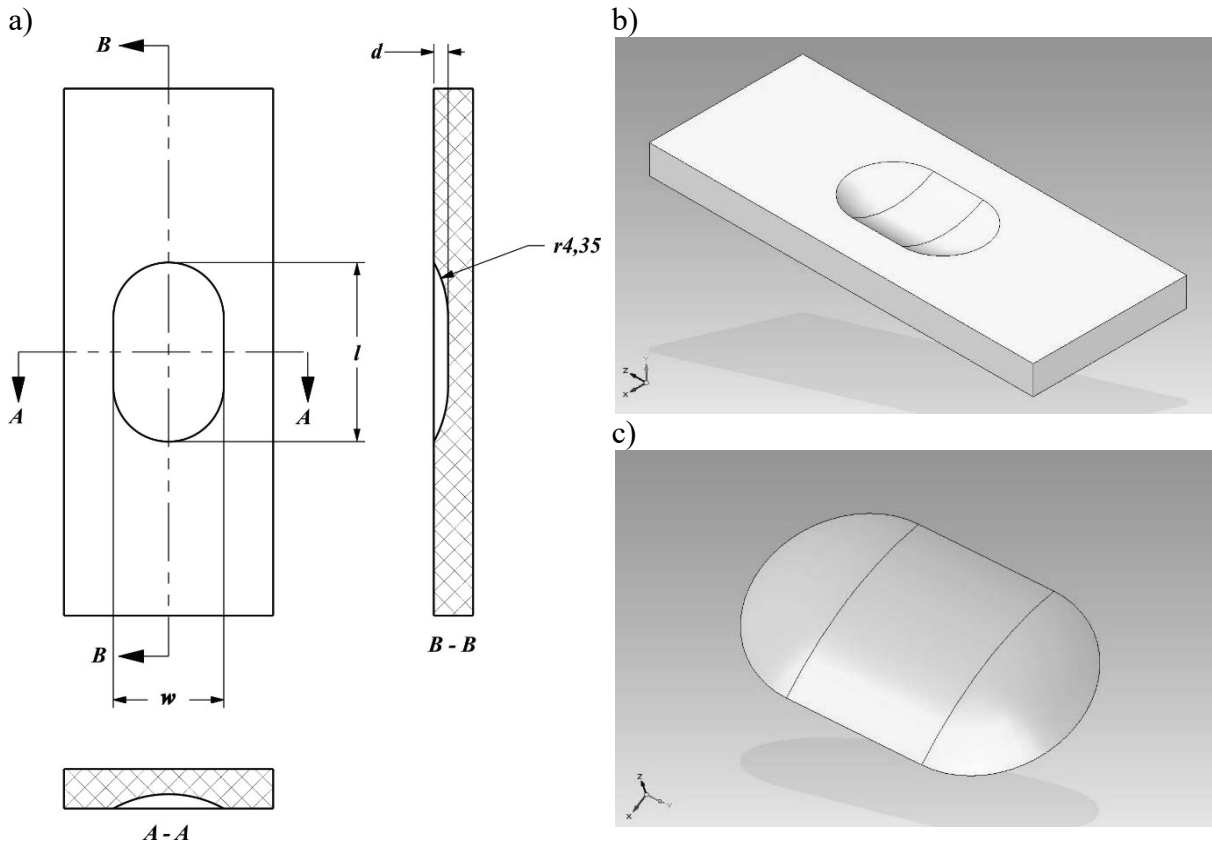


Fig. 3. An example of a wear track samples model made in CAD program after the wear resistance test: a) size; b) the model; c) weight loss

#### 4. THE RESULTS

The results of testing the resistance to abrasive wear of the internal surface of the intracorporeal oesophageal prosthesis are presented in Table 3. However, exemplary fragments of abrasion traces of samples and their profiles were created while testing the resistance to abrasive wear of the devices mentioned above. The prostheses are shown in Figures 4 and 5. The photos were taken from the top of the wear marks, and the depth was measured from the edge to the centre of the wear marks. All abrasion traces were characterized by a form similar to the one assumed in the calculations; small deviations were limited only to slight edge irregularities visible in the photos related to the so-called tearing out fragments of material rather than rubbing it evenly. Based on the results obtained, it was found that under a load of 2N, the tested material did not undergo any damage visible on the stereological microscope (no trace of abrasion). This is most likely related to the elastic deformation occurring almost immediately with the occurrence of stress and the subsequent highly elastic and plastic deformations of a relaxing nature of the matrix material during the test, which do not lead to significant surface damage for a given number of cycles. An increase in the number of cycles or an increase in temperature would damage the matrix material due to creep and not exceeding the yield point.

Tab. 3 Volumetric weight loss of samples after abrasion test of the inner layer of oesophageal prostheses

Load type	Abrasion volume [mm <sup>3</sup> ]	Median	Quarterly range	Min.	Max.
2N + suspension	0,017	0,0150	0,0014	0,0120	0,0170
	0,012				
	0,015				
	0,015				
	0,016				
	0,013				
10N	2,244	3,1820	0,3965	2,2440	3,6580
	3,239				
	3,244				
	3,125				
	3,658				
	2,461				
10N + suspension	6,377	5,5980	0,6514	4,6610	6,9190
	5,531				
	5,665				
	4,661				
	6,919				
	4,801				

However, introducing an additive as an abrasive suspension imitating a possible (extreme) form of food consumed by the patient initiated an increasing effect of weight loss of the sample ( $0.0169 \pm 0.0028 \text{ mm}^3$ ) through its mechanical damage. Changing the load to 10N increases the mass loss for samples without abrasive suspension to  $4.0531 \pm 1.0362 \text{ mm}^3$  and with suspension to  $8.0671 \pm 1.9587 \text{ mm}^3$ . In the case of samples without abrasive suspension, sample failure occurred after approximately 20,000 cycles. However, introducing an additional abrasive agent led to sample damage after approximately 10,000 cycles. The probabilities are listed in Table 4, considering the assumed significance of the study, i.e.  $\alpha = 0.05$ .

Tab. 4. Comparison of load variants; multiple comparison of mean ranks for all pairs performed using a post-hoc test,  $\alpha = 0.05$ 

Rodzaj obciążenia - parowanie		Prawdopodobieństwo, p
2N + zawiesina	10N	< 0,0050
10N + zawiesina	2N + zawiesina	< 0,0050
10N	10N + zawiesina	< 0,0051



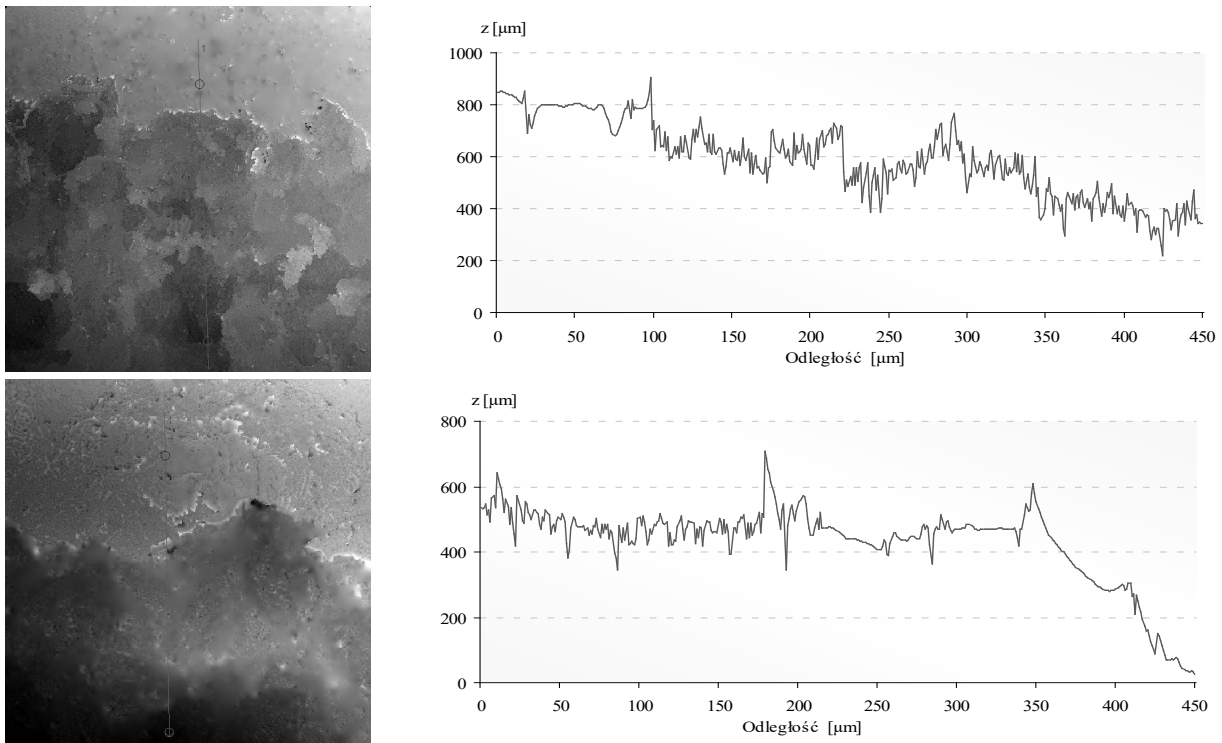


Fig. 4. Representative images and profiles of wear track samples after abrasion resistance testing with a load of 10N

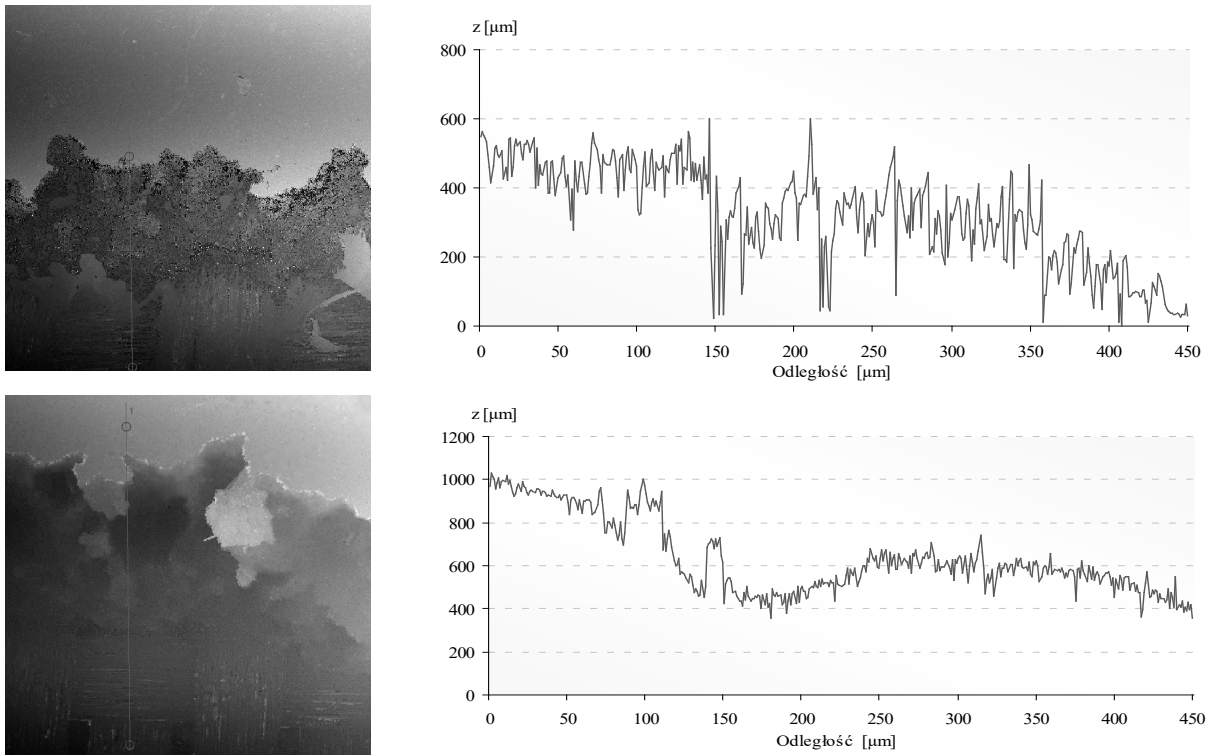


Fig. 5. Representative images and profiles of wear track samples after abrasion resistance testing with a load of 10N, and the addition of a suspension

## 5. SUMMARY

The resistance to abrasive wear of the internal surface of the prosthesis prototypes made of composite material allowed us to determine whether it may be damaged when the patient shift takes the food contents. The resistance to abrasive wear of the intracorporeal oesophageal prosthesis, and thus of the developed composite material, indicates that this surface cannot be damaged during natural and proper use. It was established that this surface's abrasion process can only begin due to its mechanical or chemical damage. Taking foods with a so-called "mushy" consistency or solid foods recommended by the medical community, washed down with large amounts of fluids, should not initiate the process of abrasive wear of the prosthesis, leading to its destruction. This is undoubtedly related with the plasticity of the matrix used (medical silicone), which upon contact with more challenging elements and food particles, it will deform elastically and plastically, avoiding thus starting the material used to crumble.

## BIBLIOGRAPHY

1. Bieliński D.M., Ostaszewska U., Jagielski J.: Application of ion bombardment to modify tribological properties of elastomers, *Polimery* 59 (5) 2014 416-422
2. Broniewski T. i in: Test methods and assessment of the properties of plastics. WNT Warszawa 2000
3. Capanidis D.: Selected aspects of the methodology of tribological investigations of polymer materials. *Archives of Civil and Mechanical Engineering*, 2007 vol. 7 no. 4, 39-55
4. Dobrzański L.A., Nowak A.J., Błażejowski W., Rybczyński R., The concept of an intracorporeal esophageal prosthesis using long-fiber reinforcement, *Structural Polymers and Composites*, Collective work edited by Gabriel Wróbel; Olsztyn 2011, 141-150
5. Dobrzański L.A., Nowak A.J., Błażejowski W., Rybczyński R.: The concept of preparation of oesophageal prosthesis based on long-fiber composite material, *Journal of Achievements In Materiale and Manufacturing Engineering* 2011, 46 (1) 18-24
6. Dobrzański L.A., Pusz A., Nowak A.J., Górnjak M.: Constructional model of internal oesophageal prosthesis, *Archives of Materials Science and Engineering* 2010, 42(2) 69-76
7. Dobrzański L.A., Pusz A., Nowak A.J.: Intracorporeal implants, *Composite materials* 2012,1
8. Dobrzański L.A., Nowak A.J.: Tests of resistance to abrasive wear of the internal surface of the esophageal prosthesis, *Contemporary Achievements in Mechanics, Manufacturing and Materials Science*, 2011 39
9. Kordek A.H.: *Oncology: a textbook for students and doctors*, Medical Press, Gdańska 2024
10. Krawczyk M.: *Cancers of the gastrointestinal tract*, Medical Publishing House PZWL, Warszawa 2001
11. Kwiatkowski K., Michalski P.: Tribological properties of urethane elastomers - comparison of two methods for assessing abrasive wear, *Elastomers* 20 (1) 2016 18-25
12. Siciński M., Bieliński D., Grams J.: Tribo Chemical modification of the surface layer against a sample of a magnesium alloy of 31 cooperating with an elastomer containing sulfur and chlorine, *Tribology* 2-2009 225-232
13. Wieleba W.: The mechanism of tribological wear of thermoplastic materials, *Archives of Civil and Mechanical Engineering*, 2007 vol. 7 no. 4, 185-199



17th-19th June 2024  
Gliwice, Poland

DEPARTMENT OF ENGINEERING MATERIALS AND BIOMATERIALS  
FACULTY OF MECHANICAL ENGINEERING  
SILESIAAN UNIVERSITY OF TECHNOLOGY

## INTERNATIONAL STUDENTS SCIENTIFIC CONFERENCE

### Polymer composite materials

Anna Nowak<sup>a</sup>, Anna Włodarczyk-Fligier<sup>b</sup>

<sup>a</sup> Silesian University of Technology, Faculty of Mechanical Engineering, Department of Engineering and Biomedical Materials, student of Engineering and Materials Technologies  
email: annanow044@student.polsl.pl

<sup>b</sup> Silesian University of Technology, Faculty of Mechanical Engineering, Department of Engineering Materials and Biomaterials, email: anna.wlodarczyk@polsl.pl

**Abstract:** The article describes selected properties of polymer composite materials reinforced with nut shell meal. In recent years, interest in these materials has increased, which has resulted in an increase in their demand on the European and global markets. Due to the wide range of applications of these materials, their development and improvement of their properties is still ongoing. The article presents a comparison of the results of selected studies of polymer composites reinforced with shell meal of different nuts of the same fraction and the same % share.

**Keywords:** polymer composites, polymer matrix, natural fillers.

### 1. INTRODUCTION

Wood-polymer composites, abbreviated as WPC (Wood Plastic Composites), are a group of innovative materials, consisting mainly of biodegradable materials. Thanks to the use of biodegradable polymers, a fully biodegradable composite can be obtained. Wood compares favorably with other available inorganic fillers, such as glass fibers or talc, because it is inexpensive, readily available, and causes less wear and tear on machines in plastics processing equipment. Hazelnut shells and walnut shells can also be used as fillers in plastic composites, due to their cellulosic structure. Nut shells contribute to the improvement of the mechanical properties of the finished material. The possibility of using ground nut shells, both hazelnut and walnut, has its ecological and environmentally friendly use, primarily because it is a waste material generated during production in the food sector.

The nut shell consists of sclerychema in the form of fibers (steroids). It is a plant-strengthening tissue that is characterized by considerable hardness and stiffness. Sclerichem fibers are characterized by a rather irregular, elongated shape, with tips overlapping each other. The use of hazelnut or walnut shells as a filler contributes to the reduction of water absorption from the environment, and thus the improvement of mechanical properties [1-4].

### 1.1. Research methodology

The tested composite materials with a polypropylene PP Moplen HP400R matrix, reinforced with a meal of ground walnut or hazelnut shells, with a fraction of 315-443  $\mu\text{m}$  and a share of 30%. The determination of the samples is shown in the Table 1.

*Table 1. Designations of polymer composite materials with a polypropylene matrix*

Type of control network	Percentage of nut shell meal [%],	Type of filler	Designation
Polipropylen PP Moplen HP400R	0	lack	PP
Polipropylen PP Moplen HP400R	30	walnut shell meal	WPCW
Polipropylen PP Moplen HP400R	30	hazelnut shell meal	WPCL

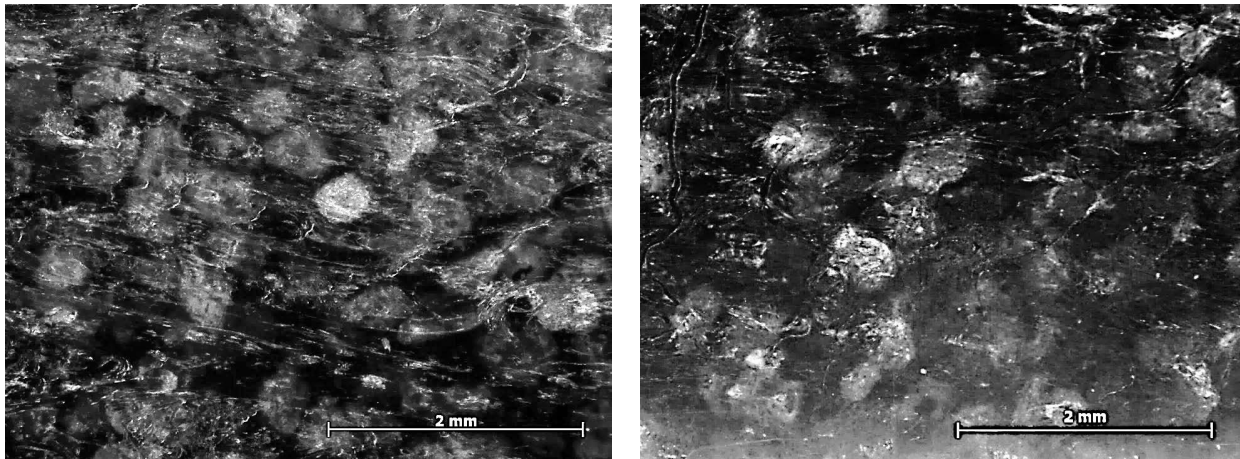
On samples of a composite material with a polypropylene matrix, filled with walnut shell meal (WPCW) and hazelnut (WPCL) shell, microscopic observations of the surface were made. Microscopic observations were aimed at determining the size, density and shape of filler grains in samples filled with meal. The surface evaluation of the polymer composite materials was carried out using the ZEISS SteREO Discovery.V12 stereoscopic microscope, at magnifications of 30x.

Tests of static tensile testing of the manufactured composites were carried out on a universal testing machine by Zwick/Roell Z020, in accordance with the PN-EN ISO 527-1:1998 standard [5]. A test speed of 5 mm/min was used to carry out the test, and the test was carried out at room temperature.

The hardness test of polymer composite materials was carried out on the Zwick 3106 hardness tester, according to the PN-EN ISO 2039-1 standard [6]. The test was performed using the ball method, at room temperature, at a load of 358 N.

### 1.2. Discussion of research results

On the surface of the tested samples of polymer composites reinforced with both hazelnut and walnut shell meal, surface heterogeneity was observed (Figure 1). The grains of the filler meal have a slightly spherical form, there are mainly grains of irregular shape. A more regular distribution of grains was observed in the case of the shape filled with hazelnut shell meal than in the case of the shape filled with walnut shell meal. Locally, areas of lower intensity and accumulation of filler grains can be observed. The irregular shape of the filler grains contributes to better filling of voids by the matrix. This results in a tighter connection between the filler and the die used.



a)

b)

Figure 1. Moulded part made of polymer composite material, 30% filled with walnut meal: a) hazelnut, b) walnut, at 30x magnification

Table 2. Tensile strength results of polymer composite materials

Materials	Tensile strength [MPa]					Average value	Standard deviation	
	Measurement number	1	2	3	4			5
WPCL		20,58	20,19	20,73	20,19	20,58	20,45	0,22
WPCW		21,85	21,65	20,53	20,73	20,87	21,13	0,52

Table 3. Results of hardness measurements of polymer composite materials

Materials	Hardness [HB]					Average value	Standard deviation	
	Measurement number	1	2	3	4			5
PP		52,16	59,39	61,46	64,1	52,63	57,95	4,78
WPCL		71,70	72,49	71,72	72,97	72,11	72,20	0,48
WPCW		69,11	66,56	70,38	67,70	70,38	68,83	1,50

The results of the static tensile test measurements (Table 2) show that the use of a hazelnut shell meal filler has a slightly worse effect on the strength results obtained compared to the walnut shell meal filler used. On the basis of the results of the research, it can also be observed that a higher value of the standard deviation was observed for the fittings filled with walnut meal.

The hardness results obtained during the test are summarized in Table 3. The average hardness of the WPCW composite fitting, filled with hazelnut shell meal, was the highest. Samples without filler have a much lower hardness than those filled with powder.

## 2. CONCLUSION

Differences in the surface structure of the WPCW and WPCW samples were observed. This is influenced by the different size and shape of the grains of the filler used. The irregularity of the flour grains has an impact on the uneven surface of the tested materials. The injection method of the produced samples has an effect on the uneven distribution of filler grains in the matrix. Microscopic observations of the surfaces show that a slightly more regular distribution of grains occurs in samples filled with hazelnut shell meal than in the case of samples filled with walnut shell meal.

The tests of the static tensile test showed that the use of hazelnut shell meal filler in polymer composites has a slightly worse effect on the strength results obtained compared to the walnut shell meal filler used.

The type of filler used in composite materials has an impact on the resulting hardness of the composite. The average hardness value of the WPCW composite sample, filled with hazelnut shell meal, was the highest and differed from the WPCW sample by a hardness of 3.37 HB. The samples of the matrix itself have a much lower hardness than those filled with meal.

## BIBLIOGRAPHY

1. A. Włodarczyk-Fligier, M. Polok-Rubiniec, Studies of resistance of PP/natural filler polymer composites to decomposition caused by fungi, *Materials* 14 (2021) 1-18
2. H. Zhou, Recycling end-of-life WPC products into ultra-high-filled, high-performance wood fiber/polyethylene composites: a sustainable strategy for clean and cyclic processing in the WPC industry, *Journal of Materials Research and Technology* 18 (2022) 1-14
3. H. Demirel, I. Kartal, A. Yildirim, K. Büyükkaya, The utilisability of ground hazelnut shell as filler in polypropylene composites, *Acta Phys. Pol. A* 134 (2018) 254-256
4. A. Włodarczyk-Fligier, M. Polok-Rubiniec: Kompozyty polimerowe wzmocnione mączką z łupin orzechów jako alternatywa dla wytworów z drewna, W: Międzynarodowa konferencja naukowa *Material Technologies in Silesia'2022*, 12-15 czerwca 2022, Wisła / Bonek Mirosław (red.), Politechnika Śląska, (2022) 209-210
5. PN-EN ISO 527-1:1998 standard, Tworzywa sztuczne. Oznaczanie właściwości mechanicznych przy statycznym rozciąganiu. Zasady ogólne
6. PN-EN ISO 2039-1 standard, Tworzywa sztuczne. Oznaczanie twardości. Część 1: Metoda wciskania kulki



17th-19th June 2024  
Gliwice, Poland

DEPARTMENT OF ENGINEERING MATERIALS AND BIOMATERIALS  
FACULTY OF MECHANICAL ENGINEERING  
SILESIA UNIVERSITY OF TECHNOLOGY

## INTERNATIONAL STUDENTS SCIENTIFIC CONFERENCE

### The impact of cerium oxide nanoparticle addition on the morphology of electrospun PVP nanofibers used in the medical industry

Antonina Olszewska <sup>a</sup>, Wiktoria Wanczura <sup>a</sup>, Wiktor Matysiak <sup>b</sup>

<sup>a</sup> Student of the Silesian University of Technology, Faculty of Mechanical Engineering, Department of Engineering Materials and Biomaterials

email: antools020@student.polsl.pl, wiktwan199@student.polsl.pl

<sup>b</sup> Silesian University of Technology, Faculty of Mechanical Engineering, Laboratory of Nanotechnology and Materials Technology Scientific and Didactic

email: wiktor.matysiak@polsl.pl

**Abstract:** This study explores the electrospinning process to produce PVP/CeO<sub>2</sub> nanofibers using solutions with varying CeO<sub>2</sub> concentrations. A comprehensive literature review was conducted, emphasizing topics relevant to nanotechnology, nanomaterials, and production methods. The analysis primarily focused on the potential medical applications of the fibers. Scanning electron microscopy (SEM) was employed to examine the fibers' morphology, while EDS testing confirmed their chemical composition, revealing the presence of CeO<sub>2</sub>.

**Keywords:** Nanotechnology, nanofibers, electrospinning, polyvinylpyrrolidone, cerium oxide

## 1. INTRODUCTION

Contemporary materials engineering is an area of intensive research and innovation, with applications in fields like medicine. This thesis focuses on manufacturing nanofibers from poly(N-vinyl-2-pyrrolidone) (PVP) with cerium oxide (CeO<sub>2</sub>) and analyzing their potential medical applications. Research on these nanomaterials opens new avenues for advanced medical products, such as dressings, drug carriers, and implants, enhancing the effectiveness and safety of therapies.

Nanotechnology is increasingly applied in modern medicine, with a promising future. Its development relies on integrating proven solutions and introducing innovations, benefiting both clinical research and treatment effectiveness. The dynamic growth of this field expands medical intervention possibilities, potentially revolutionizing disease treatment. Continued implementation of nanotechnological solutions is expected to further improve medical methods and healthcare.

The first part of the article reviews scientific literature, forming the foundation for this research. The analysis identified key aspects, knowledge gaps, and areas for further study. Parameters for the electrospinning process and solutions were selected to create effective nanofibers. The final stage examined nanofiber properties for potential medical applications.

This integrated approach aims to bring new perspectives to nanofiber manufacturing for medical use.

## **2. MATERIAL AND METHODS**

### **2.1. Electrospinning**

Electrospinning is one of the most common and efficient methods for producing nanofibers. There are two approaches to electrospinning: from a polymer solution and from a molten polymer. The entire process takes place in a device that consists of a reservoir for the polymer solution in the form of a syringe with a nozzle, a collector often covered with aluminum foil, two electrodes, and a constant-current high-voltage power source [1].

High voltage occurring during the electrospinning process excites an electric charge in the polymer solution, leading to the formation of a Taylor cone from the droplet released from the nozzle, which is directed towards the collector. During this process, the solvent used to prepare the solution evaporates, so after successful "spinning," dry fibers are found on the aluminum foil spread on the collector. The direction of the stream is not random. The area near the collector exhibits a lower potential. Therefore, it is possible to position the collector in a different orientation, not only perpendicular to the nozzle [1].

The morphology of the nanofibers produced by electrospinning is directly influenced by the parameters of the polymer solution used in this process. The viscosity of the polymer used in the solution plays a crucial role in this context. [1].

### **2.2. Characteristics of Polyvinylpyrrolidone**

One of the commonly used polymers in nanotechnology, particularly in the production of nanofibers via electrospinning, is polyvinylpyrrolidone (PVP). It is a product of the polymerization of vinylpyrrolidone [5]. It is also known as polyvidone or povidone. PVP has a carbon chain containing polar amide groups and non-polar ethylene groups [5,6]. This structure allows the polymer to bind with surfactants, which is crucial because surfactants reduce the surface tension of the spinning solution [1,5].

A significant characteristic of povidone, regarding its medical application, is its biocompatibility, biodegradability, and chemical stability [6,7]. When administered orally, it is completely excreted from the body without being metabolized. This property means that administering it in ways other than orally can lead to accumulation in the body [6].

### **2.3. Characteristics of CeO<sub>2</sub>**

Among metal and metal oxide particles, the most well-known and widely used in medicine are gold, silver, and zinc oxide. These particles exhibit remarkable antibacterial and anti-inflammatory properties. However, some of their properties can significantly disrupt the functioning of healthy cells by compromising cell membrane integrity [9].

Currently, there is significant interest in the application of cerium oxide nanoparticles. These particles display excellent anti-inflammatory, antibacterial, and antioxidant properties [8,9]. The most common application of cerium oxide nanoparticles is in polishing smooth surfaces, such as glass [9].

Nonetheless, cerium oxide exhibits phenomenal properties that could be utilized in the medical field. The antioxidant properties of cerium oxide have garnered significant attention, particularly in the context of tissue engineering and wound healing [8,9]. The antioxidant



mechanism of cerium oxide nanoparticles largely depends on their size. The significant antioxidant activity of cerium oxide allows it to capture free radicals, thereby reducing oxidative stress [9,10]. By mitigating the production of reactive oxygen species, cerium oxide can help reduce inflammation and tissue damage [10].

### 3. RESULTS

#### 3.1. Aim and Scope of the Research

The aim of the conducted research was to produce PVP/CeO<sub>2</sub> nanofibers using the electrospinning method from a polymer solution. Spinning solutions were prepared, and electrospinning parameters were selected based on available literature. The produced nanofibers were examined using a scanning electron microscope (SEM), and an EDS spectrum was generated to control the chemical composition of the fibers.

#### 3.2. Course of studies

The materials used to prepare the spinning solution were: pure PVP from Sigma Aldrich, with a molecular weight of 1,300,000 g/mol, 98.8% ethanol with a molecular weight of 46.07 g/mol from Chempur and cerium oxide particles from Sigma Aldrich with a molecular weight of 172.11 g/mol.

Four solutions were prepared: a 10% solution of pure PVP with ethanol, a 10% solution of PVP with the addition of 5% CeO<sub>2</sub>, a 10% solution of PVP with the addition of 10% CeO<sub>2</sub>, and a 10% solution of PVP with the addition of 15% CeO<sub>2</sub>. The concentrations of the solutions were determined based on the literature [1,3,4]. The weight distribution of the concentrations is presented in Table 1.

Table 1. Weight ratio of solution components

	Pure PVP 10%	PVP+ CeO <sub>2</sub> 5%	PVP+ CeO <sub>2</sub> 10%	PVP+ CeO <sub>2</sub> 15%
Ethanol	15, 8 g	15,8 g	15,8 g	15,8 g
PVP	1,75 g	1,66 g	1,575 g	1,488 g
CeO <sub>2</sub>	-----	0,0875 g	0,175 g	0,262 g

All dry ingredients were weighed on an analytical balance, and ethanol was measured using a pipette. The ingredients were placed in vials and mixed on a magnetic stirrer for 45 minutes at room temperature. Additionally, solutions containing CeO<sub>2</sub> were subjected to sonication. This process aimed to break up the cerium oxide particles, preventing the accumulation of agglomerates on the produced fibers. The sonication lasted 10 minutes for each solution, with an ultrasonic power of 15W.

Then, for the control sample, which was a solution of pure PVP in ethanol, spinning parameters were adjusted. Unfortunately, the selected parameters did not allow to achieve the intended effect. During the process, electrospaying phenomenon occurred, which prevented fiber formation.

Due to the situation that arose, namely the inability to conduct a stable process, it was decided to significantly change the parameters (Table 2). Since the research plan assumed the

observation of fiber morphology produced from solutions with different concentrations of nanoparticles, the parameters of the electrospinning process remained constant in all cases.

*Table 2. Changed electrospinning parameters for all solution*

	Voltage	Distance from the collector	Flow rate
PVP 10%	11 kV	15 cm	0,5 ml/h
PVP + CeO <sub>2</sub> 5%	11 kV	15 cm	0,5 ml/h
PVP + CeO <sub>2</sub> 10%	11 kV	15 cm	0,5 ml/h
PVP + CeO <sub>2</sub> 15%	11 kV	15 cm	0,5 ml/h

In the case of the control sample from the pure PVP solution, the electrospinning process occurred; however, it was interrupted by solution droplet formation. Samples from the solution with the addition of CeO<sub>2</sub> successfully underwent the electrospinning process. The addition of CeO<sub>2</sub> increased the viscosity of the solution, thereby stabilizing it. After initiating the process, as per the assumptions, a Taylor cone formed, from which several fiber bundles emanated.

### 3.3. Study results

The nanofiber structure studies were conducted using a scanning electron microscope (SEM), utilizing the BSE (Backscattered Electron) spectrum. The applied spectrum is significantly more sensitive to chemical composition compared to the SE (Secondary Electron) spectrum. Therefore, it was used for the examination of samples. Using the scanning electron microscope, EDS (Energy Dispersive Spectroscopy) spectra were also obtained for each sample. This allowed for the determination of the chemical composition of the nanofibers and, consequently, the verification of the presence of cerium oxide particles used in the solutions.

Subsequently, the microscope images were processed with software that enabled the measurement of the diameters of the produced fibers. Each sample was measured one hundred times to ensure the most accurate assessment of the diameters and to potentially average the results.

The first sample subjected to microscopic examination was the control sample made of pure PVP. Imaging revealed the presence of beads in the nanofiber structure (Fig. 1). Additionally, contaminants were also present on the fiber surfaces (Fig. 1). This could indicate that the PVP used to prepare the spinning solution was contaminated.

As mentioned earlier, the electrospinning process with the pure PVP solution was unstable. Polymer condensation occurred during fiber formation. The initiator of this phenomenon and the accompanying presence of beads could have been the low viscosity of the solution [1]. However, despite all the anomalies present in the produced fibers and the process, regular nanofibers were successfully produced (Fig. 2).

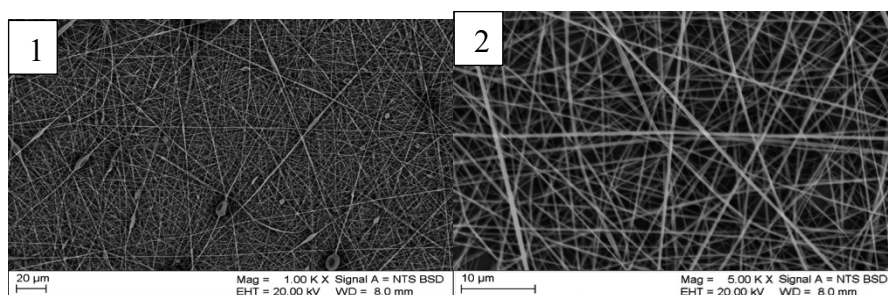


Figure 1. SEM image of the control sample made of pure PVP, magnification 1000x.

Figure 2. SEM image of the control sample made of pure PVP, magnification 5000x.

The results of the fiber diameter measurements showed that the average value for the examined area was 138.45 nm. The smallest observed value was 40 nm, and the largest was 266 nm. A summary of all observation results along with their frequency is presented in the chart.

The examination of the PVP sample with a 5% content of CeO<sub>2</sub> also revealed the presence of beads. In this case, the beads took on a spindle-like shape (Fig. 3). This could indicate that the viscosity of the solution affected the stretching of the nanofibers. An increase in the solution's viscosity increases its resistance to stretching, but on the other hand, it is one of the factors determining the production of uniform nanofibers [1]. The solution, or rather its viscosity, created resistance during stretching, simultaneously transforming the beads into uniform fibers. This likely explains the spindle-like shape of the beads.

Similar to the PVP sample, contaminants were observed, likely resulting from the contamination of one of the components. Additionally, the presence of CeO<sub>2</sub> agglomerates was confirmed based on the images. Nonetheless, the produced fibers are uniform (Fig. 4).

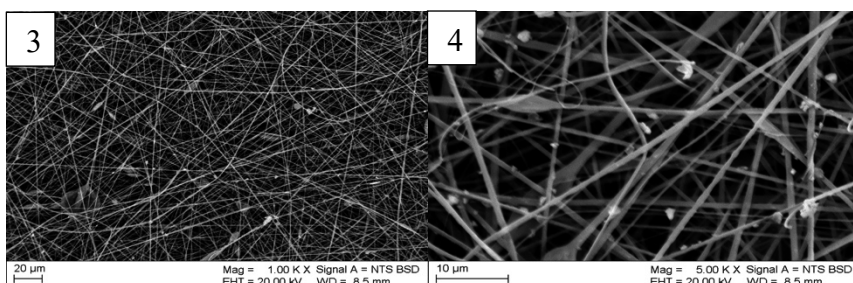


Figure 3. SEM image of the PVP/CeO<sub>2</sub> 5% sample, magnification 1000x.

Figure 4. SEM image of the PVP/CeO<sub>2</sub> 5% sample, magnification 5000x.

By examining the diameter of the nanofibers in the sample, an average value of 162.81 nm was obtained from the measurements. The highest value reached 286 nm, while the lowest was 64 nm. A summary of the sample measurements is presented in the chart.

The solution with a 10% concentration of CeO<sub>2</sub> allowed for the production of thinner nanofibers. This could have been caused by the increased conductivity of the solution, which made it stretch better during spinning. Uniform fibers with spindles containing cerium particles were still observed (Fig. 5). Contaminants were also present on the surface of the fibers. Their presence could have resulted from the contamination of the PVP powder. One of the probable reasons could have been electrospinning, although during the spinning of fibers from the solution with cerium oxide particles, this phenomenon was not observed.

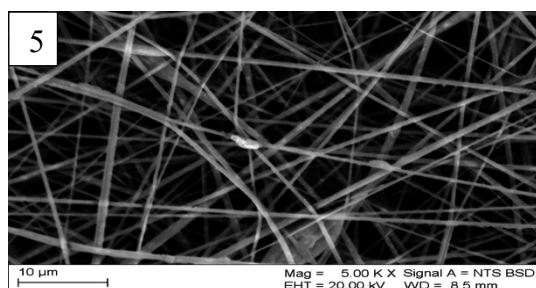


Figure 5. SEM image of the PVP/CeO<sub>2</sub> 10% sample, magnification

The average value for the measured sample was 129.24 nm. Additionally, an extremely low diameter nanofiber measuring 26 nm was observed. The widest nanofiber examined in this sample had a diameter of 238 nm. A summary of the sample measurements is presented in the chart.

In the structure of the sample, the presence of uniform fibers, fibers with beads, and associated cerium particle agglomerates was observed. In the images (Figs. 6), distinct bright spots were also observed, clearly indicating the presence of cerium oxide.

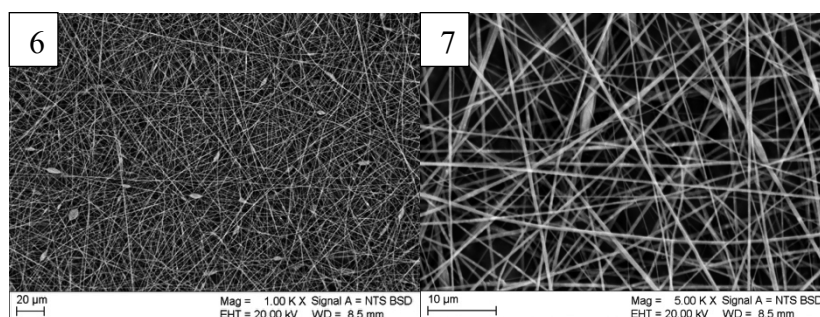


Figure 6. SEM image of the PVP/CeO<sub>2</sub> 15% sample, magnification 1000x.

Figure 7. SEM image of the PVP/CeO<sub>2</sub> 15% sample, magnification 5000x.

The analysis conducted with the scanning electron microscope using energy dispersive spectroscopy revealed the chemical composition of the tested samples. In the case of the sample from the pure PVP solution, the presence of elements characteristic of this solution was observed (Fig. 8).

The EDS spectrum confirmed the presence of cerium oxide for samples with its percentage share (Figs. 9, 10, 11). Depending on the concentration of CeO<sub>2</sub> in the solution, the peaks in the spectrum correspondingly reflected the actual presence of cerium oxide and other accompanying elements.

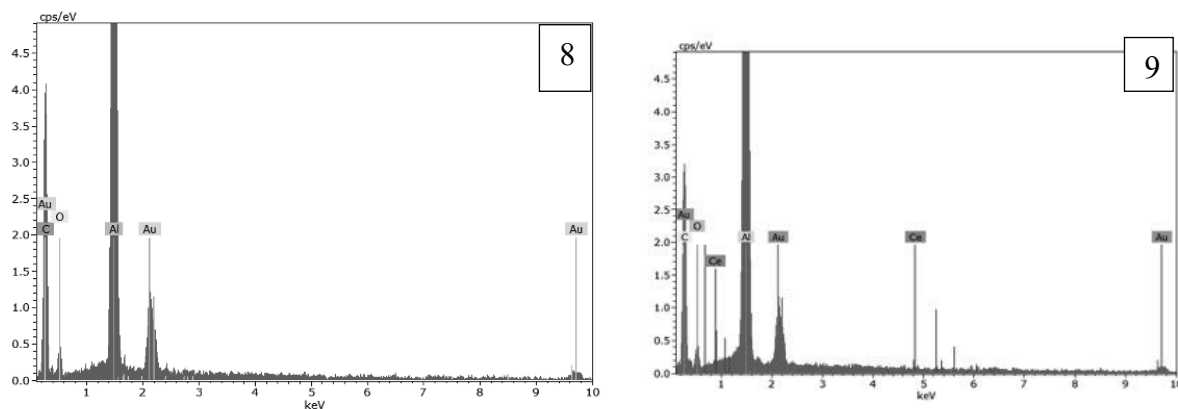


Figure 8. EDS spectrum of fibers from pure PVP.

Figure 9. EDS spectrum of PVP/CeO2 5%.

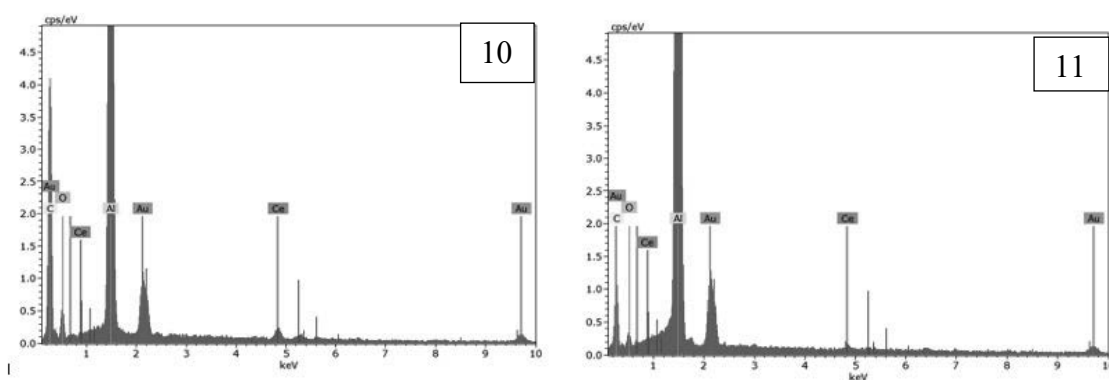


Figure 10. EDS spectrum of PVP/CeO2 10%.

Figure 11. EDS spectrum of PVP/CeO2 15%.

#### 4. SUMMARY AND CONCLUSIONS

In the constantly evolving medical industry, nanotechnology is playing an increasingly significant role, revolutionizing areas of treatment and diagnostics. Nanomaterials, with their precise structure and unique properties, open up new possibilities in medicine. Examples of such materials, like polyvinylpyrrolidone and cerium oxide, demonstrate potential for therapeutic and diagnostic applications.

Research into generating nanofibers using electrospinning from PVP/CeO<sub>2</sub> solutions has confirmed the ability to produce uniform fibers, despite observations of beads and contaminants. While these defects may be seen as process errors, they also open up new opportunities, such as controlled drug delivery.

Continued research into the electrospinning process and technology refinement holds the potential for even more precise and effective solutions in medical nanotechnology. In vitro studies on live cells are a key step in translating nanofiber technology into clinical practice, opening doors to new therapeutic strategies and manipulation of biological processes at the cellular level.

The development of electrospinning technology becomes a powerful tool in the hands of researchers and specialists in medical nanotechnology, promising a revolution in healthcare through the introduction of innovative therapeutic and diagnostic solutions.

Analyzing the conducted research leads to the following conclusions:

- To achieve uniform nanofibers, it is crucial to maintain an appropriately high viscosity of the solution.
- High viscosity contributes to the stability of the nanofiber structure during the electrospinning process.
- The proper ratio between voltage and flow rate of the spinning solution is crucial for obtaining optimal nanofiber structure.
- Balancing these parameters contributes to controlled nanofiber production.
- Prolonged sonication is necessary to prevent the presence of nanoparticle agglomerates on the fiber surface. Sonication aids in evenly dispersing nanoparticles in the solution, improving the uniformity of the nanofiber structure.
- To ensure complete solvent evaporation and avoid potential fiber agglomeration, maintaining an appropriate distance between the nozzle and the collector is essential. Precisely adjusting this distance allows for controlling the evaporation process and shaping the nanofiber structure.

## ACKNOWLEDGEMENTS

The publication was created within the framework of the joint Slovak-Polish project International Visegrad Fund's V4 Generation Mobility Mini-Grant No 12410044 as a result of cooperation between the Association of Alumni of the Silesian University of Technology, Gliwice, Poland and the University of Žilina, Slovakia.

The project is co-financed by the Governments of Czechia, Hungary, Poland and Slovakia through Visegrad Grants from the International Visegrad Fund. The mission of the fund is to advance ideas for sustainable regional cooperation in Central Europe.



## BIBLIOGRAPHY

1. K. Kurzydłowski i M. Lewansowska, *Nanomateriały inżynierskie konstrukcyjne i funkcjonalne*, Warszawa: Wydawnictwo Naukowe PWN, 2010.
2. G. Michalak, K. Głuszek, E. Piktel, P. Deptuła, I. Puszkarcz, K. Niemrowicz i R. Bucki, „Polimeric nanoparticles - a novel solution for delivery of antibacterial agents,” *Studia Medyczne*, tom 32/1, pp. 56-59, 2016.
3. A. Socha i A. Błażewicz, „Badania mikroskopowe włókien polilaktydu otrzymanych techniką elektroprzędzenia jako materiałów na komórkowe dla inżynierii tkankowej,” *Inżynieria Biomateriałów*, tom 115, pp. 12-17, 2012.
4. A. Pinabresi i F. C. Callioglu, „Electrospinning of PVP Nanofibers Optimization with Taguchi Experimental Design,” *Suleyman Demirel University Faculty of Arts and Science*

Jurnal of Science, tom 17, nr 2, pp. 478-495, 2022.

5. M. W. Sułek, W. Sas, T. Wasilewski, A. Bąk i U. Żak , „Wpływ rodzaju i stężenia poliwinylpyrrolidonów na wybrane charakterystyki tribologiczne ich wodnych roztworów,” *Tribologia*, tom 3, pp. 129-141, 2011.
6. M. Teodorescu i M. Berca , „Poly(vinylpyrrolidone) - A Versatile Polymer for Biomedical and Beyond Medical Application,” *Polymers - Plastics Technology and Engineering*, tom 54, pp. 923-943, 22 January 2016.
7. M. Q. Khan, D. Kharaghani, N. Nishat i T. Ishikawa, „The development of nanofibers tubes based on nanocomposites of polyvinylpyrrolidone incorporated gold nanoparticles as scaffolds for neuroscience application in axons,” *Textile Research Journal*, tom 00, pp. 1-8, 2018.
8. H. A. Raczej , R. Thakore, R. Singh, D. Jhala, S. Singh i R. Vasita, „Antioxidative Study of Cerium Oxide Nanoparticle Functionalized PCL-Gelatine Electrospun Fibers for Wound Healing,” *Bioactive Materials*, pp. 201-210, 2 October 2017.
9. C. Sandoval, C. Reyes, P. Rosas, K. Godoy, V. Souza-Mello i J. Farias, „Effectiveness of Cerium Oxide Nanoparticles in Non-Alcoholic Fatty Liver Disease Evolution Using In Vivo and In Vitro Studies: A Systematic Review,” *MDPI*, pp. 1-22, 29 October 2023.
10. M. A. Dar, R. Gul, P. Karuppiah i N. A. Al-Dhabi, „Antybakteryjna Aktywność Nanoparticel Tlenku Ceru przeciwko Uciekającym Patogenom,” *MDPI*, pp. 1-10, 26 January 2022.



17th-19th June 2024  
Gliwice, Poland

DEPARTMENT OF ENGINEERING MATERIALS AND BIOMATERIALS  
FACULTY OF MECHANICAL ENGINEERING  
SILESIA UNIVERSITY OF TECHNOLOGY

## INTERNATIONAL STUDENTS SCIENTIFIC CONFERENCE

### Modern 3D Printing Technologies in Space Industry

Emil Pająk<sup>a</sup>, Błażej Tomiczek<sup>b</sup>

<sup>a</sup> Student, High School No. 5 with Bilingual Units in Gliwice

email: emilpajak.edu@gmail.com

<sup>b</sup> Politechnika Śląska, Wydział Mechaniczny Technologiczny, Laboratorium Naukowo-Dydaktyczne Nanotechnologii i Technologii Materiałowych,

email: blazej.tomiczek@polsl.pl

**Abstract:** The purpose of this paper is to present an overview of how additive manufacturing technologies are currently applied in the space industry and what possible uses they might have in the future.

**Keywords:** space, 3D printing, additive manufacturing, ISS, 'Space Fabric'

## 1. INTRODUCTION

Currently, the 3D printing industry is developing quite dynamically. Year by year, additive manufacturing finds applications in new fields. Nowadays, it is possible to print with a wide variety of materials, including polymers, metals, ceramics, concrete, and even organic tissues. The main advantage of 3D printing is the fact that it is an additive method. This allows for the creation of various complex geometries without significant difficulty, which would be impossible to achieve with traditional subtractive methods. As a result, houses [1], a rocket [2], a satellite [3], parts of human organs [4], small implants [5], and even food [6] have already been printed. Scientists are convinced that in the near future, 3D printing will play a significant role in many fields, especially in the space industry.

## 2. METHODS OF 3D PRINTING

While printing a structure designed in CAD software, it is important to consider which 3D printing method to choose. The choice usually depends on the material we want the element to be composed of, the size of the creating structure, the desired precision, and the budget that is going to be devoted to printing. Below there is a brief description of two most common ones, the relatively cheap FDM and precise SLM.

### 2.1. Fused Deposition Modelling (FDM)

Fused Deposition Modelling (FDM), also known as Fused Filament Fabrication (FFF) [8], involves creating a model from a material in the form of a wire, called filament, by extruding it.



The extruder is responsible for controlling the amount and speed of material delivered to the nozzle, where it is then heated and melted. The nozzle moves in three-dimensional space, applying the material layer by layer to gradually build the model.

This method is most commonly used while printing from polymers. However, it also allows for the manufacturing of metal and ceramic elements. To achieve this, a special filament is used, which is a mixture of metallic (or ceramic) powder with a polymer binder. In this case after the printing finishes, the model is heat-processed to remove contaminants from its structure. During this process, the polymer binder changes its state to gas and escapes due to the porosity of the structure.

## **2.2. Selective Laser Melting (SLM)**

Selective Laser Melting (SLM), also known as Direct Metal Laser Sintering (DMLS) is an additive technology using a laser to melt and combine metallic powders, which were previously spread and smoothed as a thin layer. It allows for creation of precise and tough structures from alloys of steel, titanium, aluminium and even noble elements. It has already been used in medicine to fabricate dental implants made of alloys specially adapted for biological applications [5], in the space industry for printing rocket engine components [10] and for prototyping [10].

## **2.3. Others methods**

There are a lot of various and unique methods of 3D printing, usually designed for a given, specific purpose. Among others, there is bioprinting 3D [11] making it possible to print with cells and fabricate tissues, but also one can use concrete to create buildings with nontrivial geometries [12].

# **3. APPLICATIONS OF 3D PRINTING IN SPACE INDUSTRY**

## **3.1. Creation of elements directly in space**

The International Space Station (ISS) for the last 25 years has been a home for more than 270 astronauts [13]. Up to this day, problems connected with supply of necessary materials or equipment are solved by sending about 3 tons of parts there each year. Nowadays, about 13 tones are stored on the station and 17 tones are ready on Earth to be sent if necessary.

Solution this might work well for an object orbiting about 400 km above the surface of our planet, but resupplying a mission located on the Moon, Mars or heading in outer space would be very difficult [14]. That is why, the possibility of manufacturing needed elements in place and immediately is crucial in further development of space technologies. Moreover, this new solution would also allow for designing necessary parts at a base on Earth and sending ready-to-print files to the station or a ship without any time delay or financial expenses on organising the resupply mission.

In 2014 a FFF 3D printer was installed on the ISS allowing for fabrication of polymer elements. Already it has been used to create a wrench, aerial parts, a part for the oxygen generating system and many more. Furthermore, after testing the samples printed on the station and comparing them with the ones fabricated on the ground, no significant difference has been detected between objects printed in microgravity and in ordinary conditions.

For the last few years the number of 3D printers on the ISS has been constantly increasing. In 2018 the “Refabricator” was launched to the space station [20], which is able to create its

own filament from unnecessary, previously printed, polymer tools or elements. Moreover, this device allows to transform plastic bags and food packaging into filament. This solution not only reduces the amount of waste that would have to be kept on a station, but also allows recycling, unneeded in the moment, made from polymers objects. Furthermore in 2024 on the ISS a first printer was sent, which was able to print from metal. It works due to the use of a wire made from a type of stainless-steel, which is being melted by a laser [22].

### **3.2. 3D printing food**

It has already been demonstrated that 3D printing might also solve the problem of access to diverse food in space. The ability to create animal tissues would broaden the possible meals containing fresh meat, enriching the astronauts' diet. In 2019, the Israeli company Aleph Farms showed that with use of cow stem cells, it is possible to print a steak which after baking, fully resembled ordinary meat in terms of structure, taste and consistency. Moreover, a printer Bioprinting Solutions' 3D used to fabricate this steak was designed to be also able to print in microgravity conditions.

Lastly, an Italian startup, Novameat, developed a method of printing fully vegan meat [23], which does not require animal stem cells, but is based on a mixture of plant-based ingredients. The printed products were also fully resembling ordinary products features.

### **3.3. 3D printing parts of rocket engines**

Another field, where 3D printing is commonly used is industry connected with creating complicated and atypical parts of rocket engines. In 2013 Elon Musk published on Twitter an image of printer EOS 3D, during fabrication of the SuperDraco rocket chamber [15]. A possibility of creating strong and complex structures has been spotted also by a Spanish company Pangea, which after embracing 3D printing technologies increased the efficiency of its engines by 15% in comparison to ones produced by conventional means [6]. Moreover, in recent years this technology has been used to create a Terran R rocket with its engine Aeon R and a satellite [16]. Even, sent on Mars in 2020, Perseverance rover took 11 3D printed parts or tools on the Red Planet.

### **3.4. Future possible applications**

3D printing will play an important role during the colonisation of the Moon or other celestial objects. Not only would it facilitate building structures in human unfriendly environments, but it is also much easier to launch a spaceship with a 3D printer and compact packed filament, than to transport large, fabricated on Earth elements [17, 18]. Furthermore, scientists are now trying to develop a method of filament production, which will use materials found on a given celestial object, mostly focusing on a lunar regolith.

The possibility of 3D printing a space base or a part of it, in the future, is increasing from year to year. In 2015, NASA started a competition for a 3D-printed space habitat and in 2019 awarded the winners [21].

## **4. POSSIBILITY OF PRINTING COMPLICATED STRUCTURES**

### **4.1. Designed by NASA 'Space Fabric'**

Additive technologies, such as 3D printing, allows for creation of structures, which might not be fabricated by any other means. It has been shown by NASA with a design of 'Space

Fabric'. This structure resembles a mediaeval chainmail, allowing the elements building it for a free movement.

Primarily the 'Space Fabric' was designed as a protective layer for an astronaut's suits or spaceships to save them from the impact of quick moving cosmic powder. Furthermore, it could also be used to cover the legs of a lander from below and thermally isolate if the mission would happen on icy celestial bodies, which in the Solar System might be a moon of Jupiter – Europa.

#### 4.2. Understanding the model

Thanks to a cooperation with the Silesian University of Technology during the first edition of research projects implemented with secondary school pupils under the Excellence Initiative - Research University, our team, inspired by 'Space Fabric', decided to print similar structures [24] to better understand how they precisely work. Models [24] shown on *Figures 1-2* have been printed from a PLA using a FDM printer, however the model on a *Figure 3* was created from a stainless steel using method SLM.

#### 4.3. Creation of a new design.

After the investigation of designs downloaded from the Internet a completely new model was created in the Inventor Pro software (fig. 4) and printed on a Prusa printer (fig. 5-6).

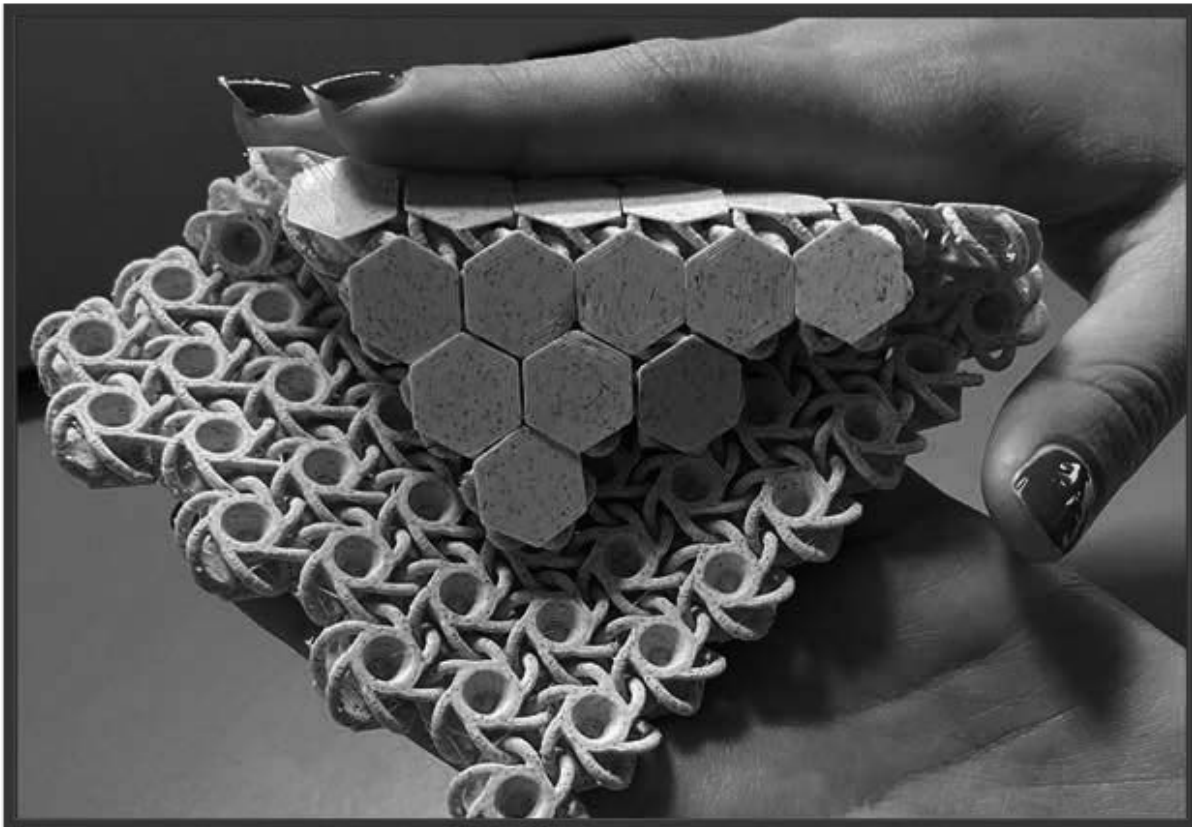


*Figure 1. Model printed from PLA*

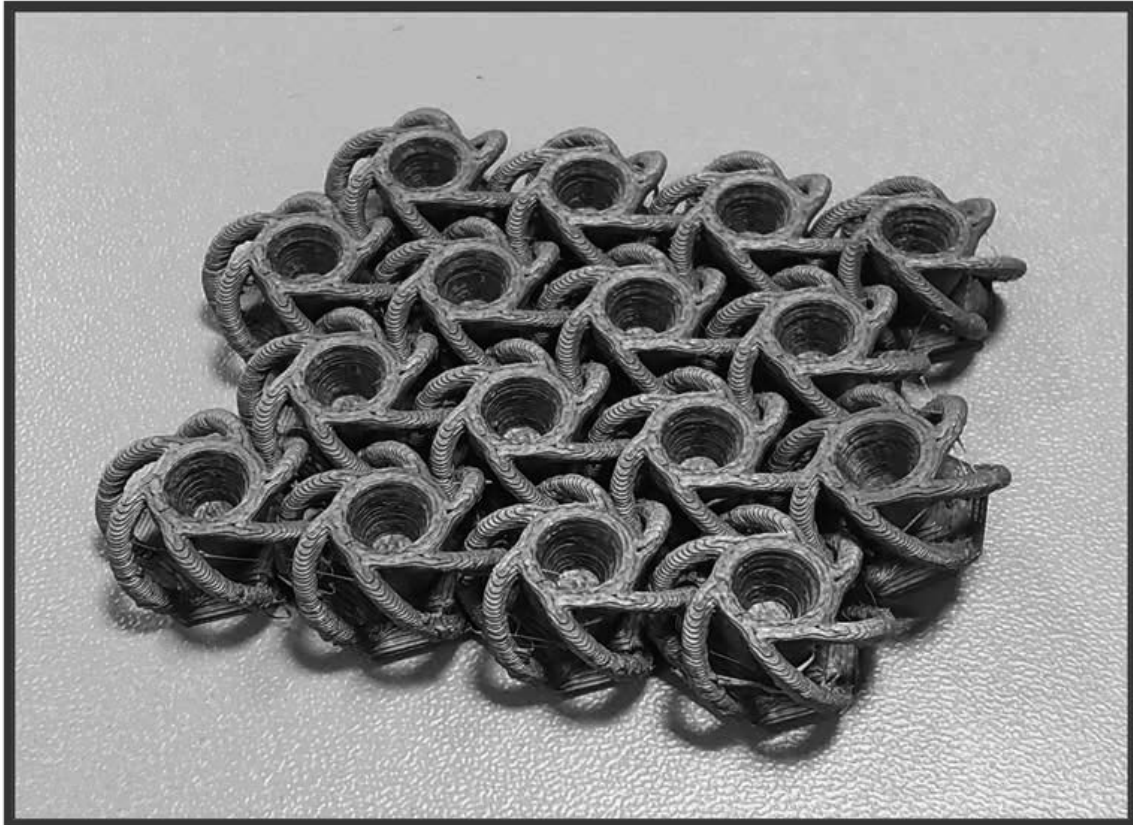


Figure 2. Model printed from PLA

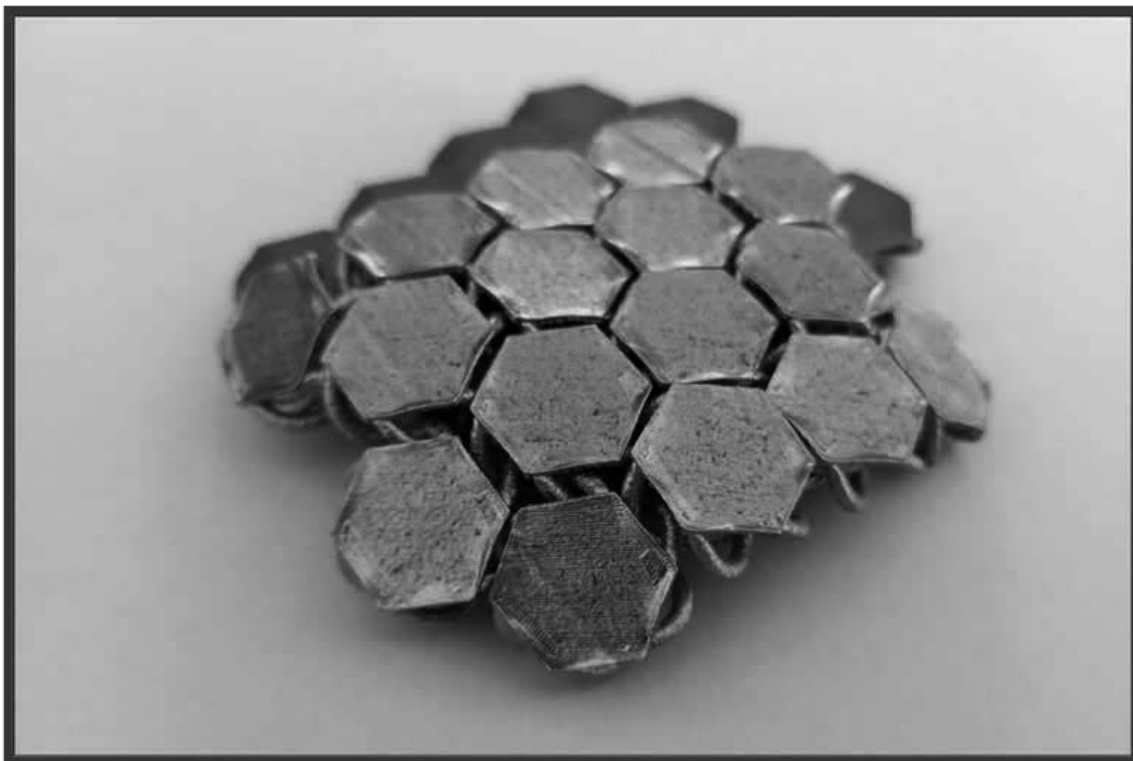


Figure 3. Model printed from stainless-steel

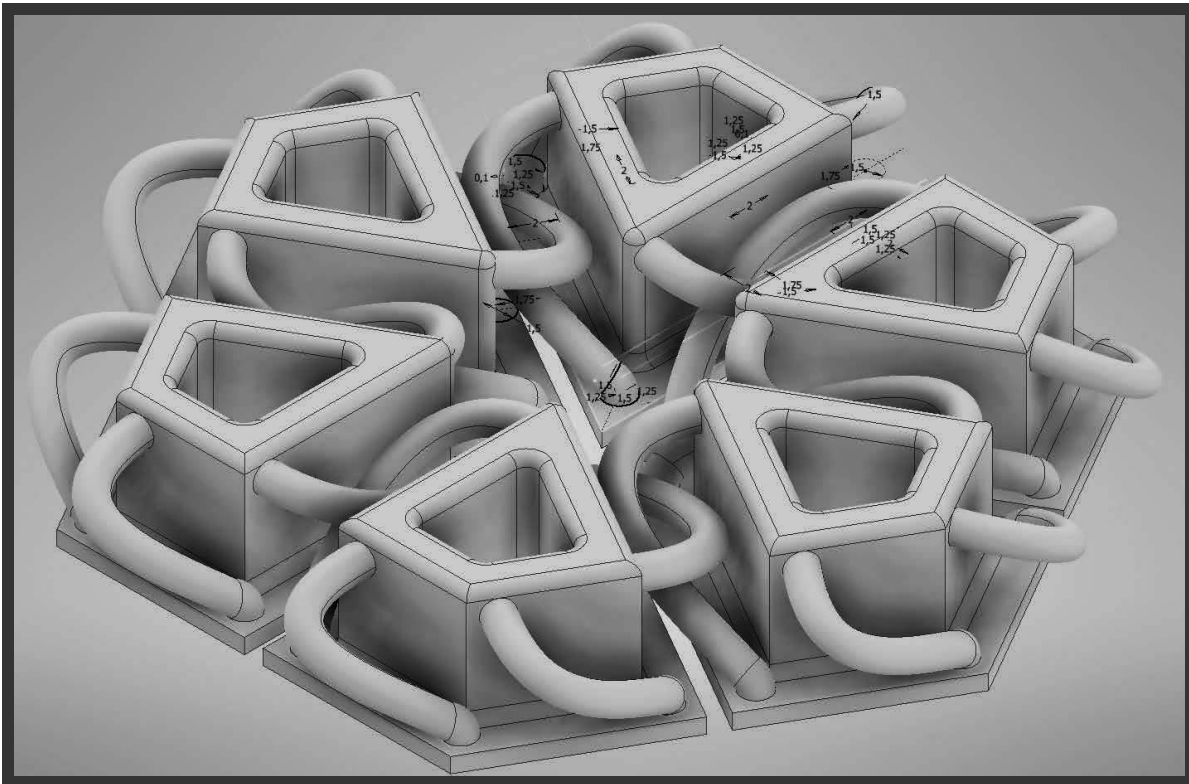


Figure 4. Designed CAD model of a structure

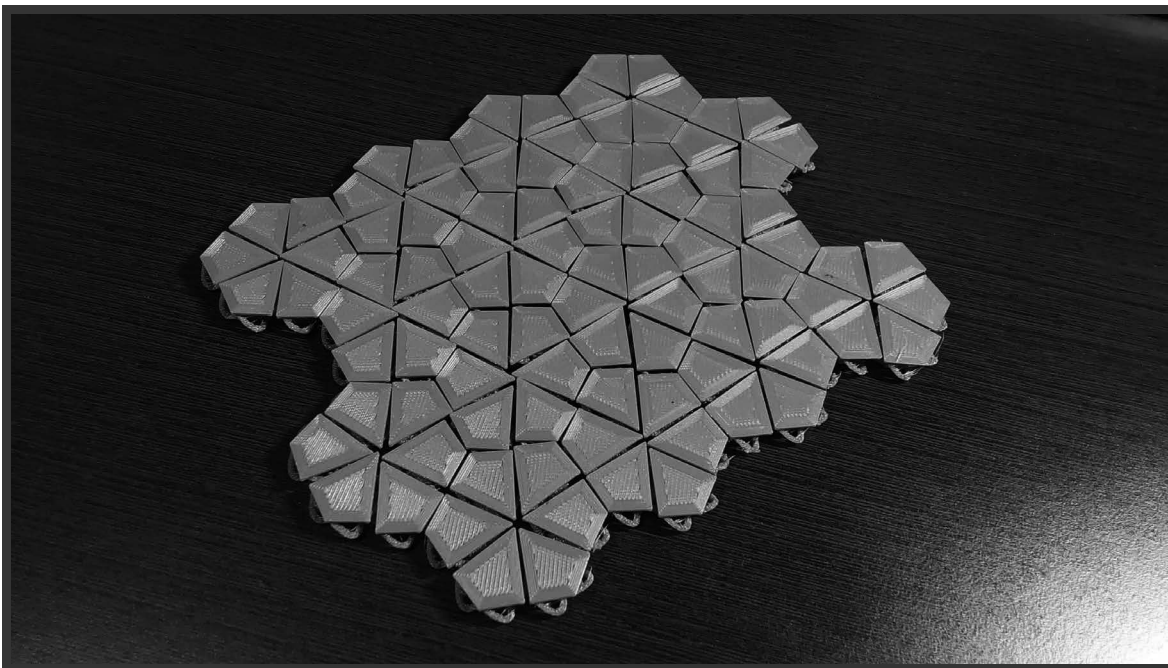


Figure 5. Designed model printed from PLA, view from top

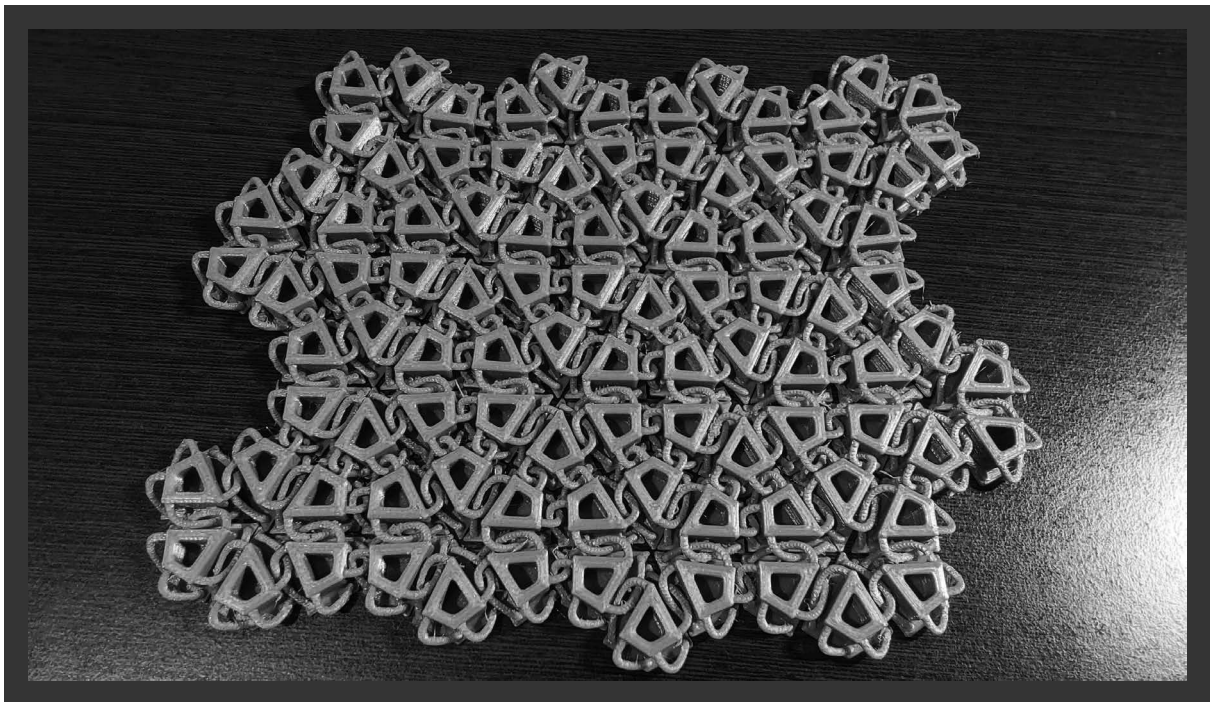


Figure 6. Designed model printed from PLA, view from bottom

## BIBLIOGRAPHY

- [1] Nitika Choraria “Step into the future – 3D-printed houses are here and in high demand” 28.12.2022 Available: <https://designwanted.com/3d-printed-houses/>
- [2] Nancy Smith Kilkenny “3D Printed Rocket Launched Using Innovative NASA Alloy” 02.05.2023 Available: <https://www.nasa.gov/centers-and-facilities/marshall/3d-printed-rocket-launched-using-innovative-nasa-alloy/>
- [3] Madeleine Prior, “Fleet Space Has Developed Fully 3D Printed Satellites” 03.01.2022, Available: <https://www.3dnatives.com/en/fleet-space-has-developed-fully-3d-printed-satellites-030120214/>
- [4] Jennifer Lewis, “3D Bioprinting of Living Tissues”, Available: <https://wyss.harvard.edu/technology/3d-bioprinting/>
- [5] Carlota V., “3D-Printed Medical Implants: Discover Some of the Most Innovative Projects” 01.10.2021, Available: <https://www.3dnatives.com/en/best-3d-printed-implants-230720195/>
- [6] Jamie D., “What Are the Applications for 3D Printing in Space?”, 27.01.2022 Available: <https://www.3dnatives.com/en/top-10-3d-printing-space/>
- [7] Paweł Ślusarczyk, <https://3dwpraktyce.pl/rodzaje-technologie-druku-3d/>
- [8] [https://en.wikipedia.org/wiki/Fused\\_filament\\_fabrication](https://en.wikipedia.org/wiki/Fused_filament_fabrication)
- [9] Kinga Skrzek „Druk 3D w technologii SLM z użyciem stali, stopów, a nawet złota i srebra” 16.04.2020, Available: <https://przemyslprzyszlosci.gov.pl/specjalistyczny-druk-3d-w-technologie-slm-z-uzyciem-stali-stopow-a-nawet-zlota-i-srebra/>
- [10] [https://en.wikipedia.org/wiki/Selective\\_laser\\_melting](https://en.wikipedia.org/wiki/Selective_laser_melting)
- [11] <https://biolife4d.com/science-and-technology/>

- [12] José Tomás Franco “Round Houses of Raw Earth: 3D Printing Sustainable Homes in 200 Hours” 18.02.2021 Available: <https://www.archdaily.com/956854/round-houses-of-raw-earth-3d-printing-sustainable-homes-in-200-hours>
- [13] <https://www.nasa.gov/international-space-station/>
- [14] Melissa Gaskill “Solving the Challenges of Long Duration Space Flight with 3D Printing” 16.12.2019 Available: <https://www.nasa.gov/missions/station/solving-the-challenges-of-long-duration-space-flight-with-3d-printing/>
- [15] <https://en.wikipedia.org/wiki/SuperDraco>
- [16] Madeleine Prior “Fleet Space Has Developed Fully 3D Printed Satellites” 03.01.2022 Available: <https://www.3dnatives.com/en/fleet-space-has-developed-fully-3d-printed-satellites-030120214/>
- [17] “Podbój kosmosu z pomocą drukarek 3D” 17.06.2020, Available: <https://kosmonauta.net/2020/06/podboj-kosmosu-z-pomoca-drukarek-3d/>
- [18] Madeleine Prior “Using 3D Printing to Conquer Outer Space” 21.04.2022 Available: <https://www.3dnatives.com/en/using-3d-printing-to-conquer-outer-space-210420226/>
- [19] Elizabeth Landau “'Space Fabric' Links Fashion and Engineering” 18.04.2017 Available: <https://www.jpl.nasa.gov/news/space-fabric-links-fashion-and-engineering>
- [20] NASA “Full Circle: NASA to Demonstrate Refabricator to Recycle, Reuse, Repeat” 28.08.2017 Available: <https://www.nasa.gov/missions/station/full-circle-nasa-to-demonstrate-refabricator-to-recycle-reuse-repeat/>
- [21] NASA “3D-Printed Habitat Challenge News” Available: <https://www.nasa.gov/prizes-challenges-and-crowdsourcing/centennial-challenges/3d-printed-habitat-challenge/>
- [22] ESA “ESA launches first metal 3D printer to ISS” 31.01.2024 Available: [https://www.esa.int/Science\\_Exploration/Human\\_and\\_Robotic\\_Exploration/ESA\\_launches\\_first\\_metal\\_3D\\_printer\\_to\\_ISS](https://www.esa.int/Science_Exploration/Human_and_Robotic_Exploration/ESA_launches_first_metal_3D_printer_to_ISS)
- [23] <https://en.wikipedia.org/wiki/Novameat>
- [24] Halling Slimta “Nasa chainmail (4x4, 8x8, 12x16 and 32x34)” 15.05.2022 <https://www.printables.com/pl/model/205674-nasa-chainmail-4x4-8x8-12x16-and-32x34>



17th-19th June 2024  
Gliwice, Poland

DEPARTMENT OF ENGINEERING MATERIALS AND BIOMATERIALS  
FACULTY OF MECHANICAL ENGINEERING  
SILESIA UNIVERSITY OF TECHNOLOGY

## INTERNATIONAL STUDENTS SCIENTIFIC CONFERENCE

### Schlieren Optics: Unveiling the Invisible

Emil Pająk<sup>a</sup>, Alicja Jankiewicz<sup>a</sup>, Błażej Tomiczek<sup>b</sup>

<sup>a</sup> Student, High School No. 5 with Bilingual Units in Gliwice

email: emilpajak.edu@gmail.com, alicja.jankiewicz@op.pl

<sup>b</sup> Politechnika Śląska, Wydział Mechaniczny Technologiczny, Laboratorium Naukowo-Dydaktyczne Nanotechnologii i Technologii Materiałowych,

email: blazej.tomiczek@polsl.pl

**Abstract:** The purpose of this project was to create a well-functioning Schlieren Imaging system using basic everyday objects. It allowed the differences in air pressure and density to be visualised due to the changes of the refractive index. Multiple tests were performed confirming predictions about air flow around many daily life items.

**Keywords:** Schlieren optics, Schlieren Imaging, air currents, refractive index, homemade experiment

## 1. INTRODUCTION

### 1.1. Necessary Equipment

To conduct the experiment a spherical concave mirror was used. In this case it was the D160F1300 mirror, which can be commonly found in astronomical telescopes. To capture the desired effect camera Canon EOS 800D with 75-300 lens on a tripod was sufficient. A point light source was also needed. Here it was obtained by covering a 10000 lumen bike lamp with a sheet of aluminium foil having a hole about 1 mm in diameter. Important element of the system was a colour filter allowing to differentiate light rays [3, 11]. It was produced by taping together 2 thin coloured transparent foils taken from red-blue 3D glasses. It is possible to achieve a similar effect with help of a sharp razor blade [2], but here better results were obtained without it. Moreover, a stable table was required and a place with possibly low surrounding vibrations.

### 1.2. How the system works

The reason Schlieren setup works is the phenomenon of light refraction [1-6, 8-12]. A light ray travelling through different media changes its path depending on whether it passes through more or less dense surroundings. This effect is a consequence of various optical media having distinct refractive indices. Moreover, these little differences in light paths are sufficient to be detected using a homemade system.



In the homogeneous medium when a beam of light is emitted from a point-like source it spreads hitting the whole surface of the mirror, reflects back and focuses in one point (with a size about the same as a hole in an aluminium foil). However, if the medium is inhomogeneous the area of focus is still close to point-like but is fractionally larger. It is caused by different refractive indices of the media the light has travelled through and the fact that not necessarily whole light, which came to the same precise point, derived from the same part of a point-like light source. Meaning that it is possible to visualise these differences by either blocking a portion of the light using a razor blade (fig. 1), then dimmer and lighter spots appear (fig. 2b) or by marking one half of the light with one colour and the other half with another colour, then the light passing through the more dense medium will appear mostly in the first colour and the less dense in the second (fig. 2c).

Furthermore, to amplify the results during setting up the system or the demonstration of this phenomenon it is advised to compare objects having large differences in density or temperature. Nevertheless, on a well prepared and adjusted set-up it is possible to visualise even slight variations as it will be demonstrated below.

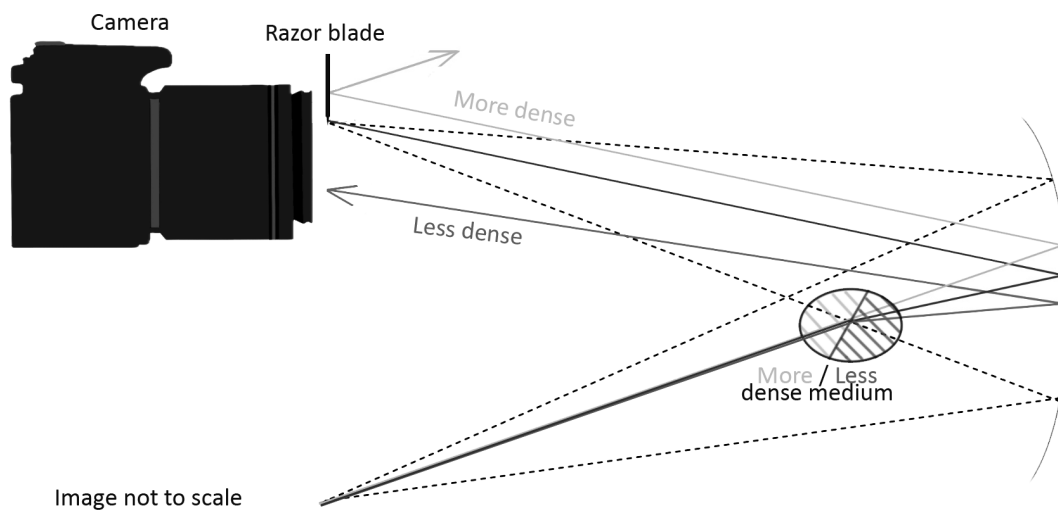


Figure 1. Refraction of light passing through more or less dense medium

## 2. SETTING UP THE SYSTEM

### 2.1. Mirror, light source and camera placement

The whole system should be aligned in one plane [2, 3, 11, 12], it is recommended to choose the horizontal plane for easier adjustments, but vertical or diagonal planes are also possible. Mirror should be placed on a stable surface pointing to the open space. Correct placement of the light source depends on the used mirror, because it should be located in front of the reflective surface with a distance about double the focal length of the mirror, so that the light beam after bouncing off the mirror focuses with a close proximity to the light source [1-3]. It is important to reduce astigmatism of the system and to position the light source in a way that an angle between the light source and the focus point of the light is minimal [1]. Larger angles will result with the reflected image and the one seen by a camera not overlapping perfectly, creating an illusion of seeing objects doubled. In some cases correcting it by moving

a light source might be complicated, that is why sometimes rotating a mirror for a fraction of an angle might be an easier solution.

To check if the light source is set properly it is sufficient to darken the room and move a sheet of paper along the path of reflected light up to a point when the lightened area is the smallest - it will be the focus point [1].

To capture the correct image a camera on a tripod should be placed a little further away from the mirror than the focus point. Moreover, it should be positioned in a way that on a camera display the whole surface of the mirror is illuminating (fig. 2a). This effect will appear even if the point-like light source is relatively small. However, if on the camera display only the crescent of the mirror is illuminating, it is advised to change the angle between camera lens and a plane in which everything should be aligned.

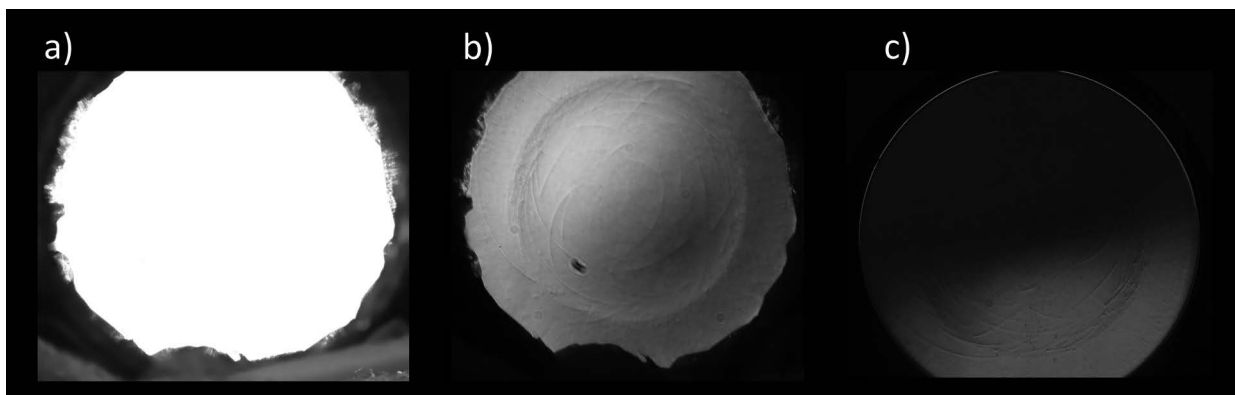


Figure 2. Photos of a) illuminating mirror, b) mirror with proper alignment of a razor blade, c) mirror with proper alignment of a colour filter

## 2.2. Aligning the razor blade or colour filter

Important aspect of the whole system is a proper alignment of an object responsible for blocking or marking the part of the passing light. No matter which technique is used, the edge of a razor blade or the connection line of the colour filter should be precisely located in a focus point and accurately divide the point-like area into two halves [1-3]. Due to the necessity of exact positioning, it is recommended to use a stable laboratory stand or other rigid object. Here, the filter was attached to a metal stand with a neodymium magnet, which made the alignment easier.

During the adjustment, it is recommended to constantly control the camera display and to continue adjusting up to a point when on a camera screen imperfections of a mirror are visible - in a case of using a razor blade (fig. 2b) or both halves of image have different colours - in the case of using a filter (fig. 2c).

## 2.3. Placing items in front of the mirror

Generally items should be placed as close to the surface of a mirror as possible and it should be considered while designing a mirror case or a mirror holder. Here the 4-piece casing (fig. 3a) was designed in 3D using the Inventor Pro software and then 3D printed from PLA on a Prusa printer.

Moreover, worth pondering is also the fact what objects or phenomena are going to be observed using the particular set-up and whether it requires extra space in front of a mirror. Here during the demonstration of the Coandă effect the mirror had to be located on the edge to fully achieve the desired effect (fig. 3b).

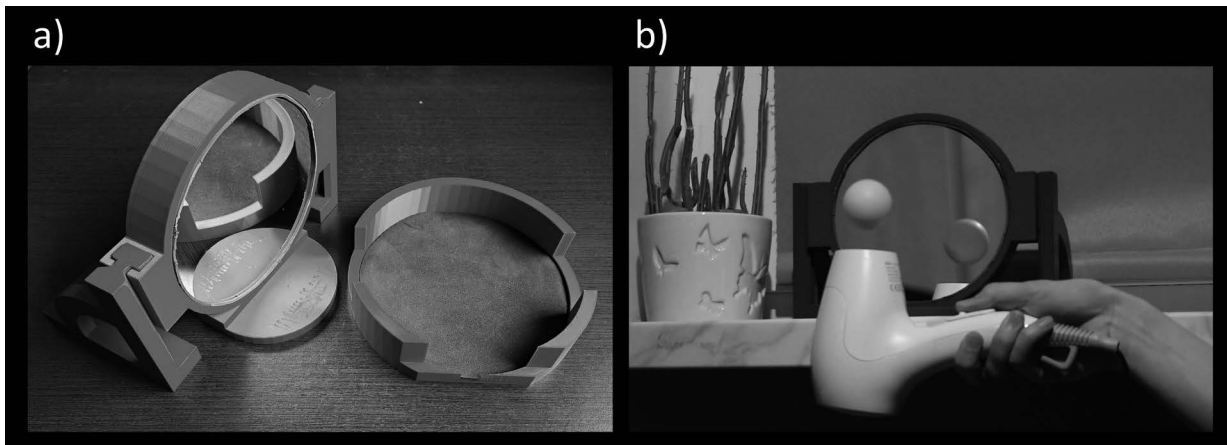


Figure 3. a) Photo of a D160F1300 concave mirror in a 3D printed case next to the protective cover, b) Photo taken during the demonstration of the Coandă effect

#### 2.4. Reducing disturbing factors

Due to high sensibility of the whole system a lot of factors might disturb the experiments. The most common one (for setups not placed on vibration damping tables) are vibrations caused by walking next to the camera tripod or other components of the system. It is recommended to stand back from a set-up after placing the examined object in front of the mirror and control the camera from a distance if possible. However, while demonstrating an effect requiring presence of a person close to the mirror it is advised to sit still next to it and reduce all unnecessary vibrations.

Another common disturbing factor might be a heat-releasing object located in the space between the camera and the mirror or in close proximity to the system. Especially trammelling are hot air streams produced by cooling fans removing heat from the equipment. Moreover, the presence of a person close to the system also affects the experiment, because the human body temperature is higher than an average room temperature (fig. 4).

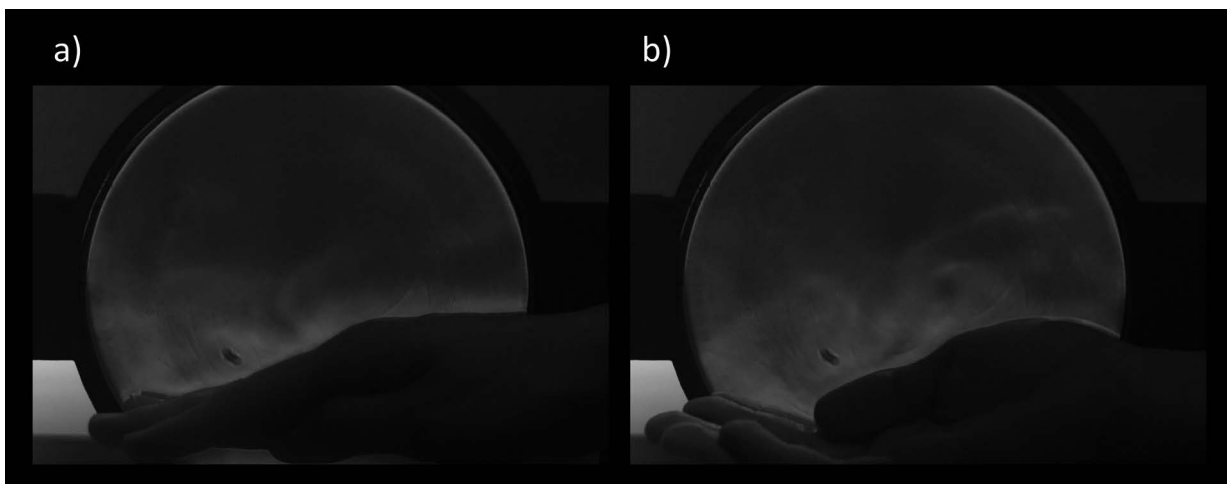


Figure 4. Heat rising from a human hand captured using Schlieren set-up

### 3. EXPERIMENTS WITH TEMPERATURE AND DENSITY

The properly aligned system allows to visualise a difference in temperature, due to the fact that hot air is less dense than the cold one. The desired effect can be achieved with the help of a lighted candle (fig. 5a). To enrich a demonstration and get an effect portrayed on a *Figure 5b* a vacuum cleaner might be used to bend the stream of rising hot air and gases (fig. 5c). It is also possible to see the heat generated during striking a match (fig. 6a) and heat rising from a hot soldering iron (fig. 6b-c), warmed up frying pan (fig. 7a) or a stream of hot air (fig. 7b) produced by a hot air welder (fig. 7c). However not only warm, rising up, air can be visualised. By placing objects cooler than surrounding it is also feasible to demonstrate the subsiding cold air (fig. 8).

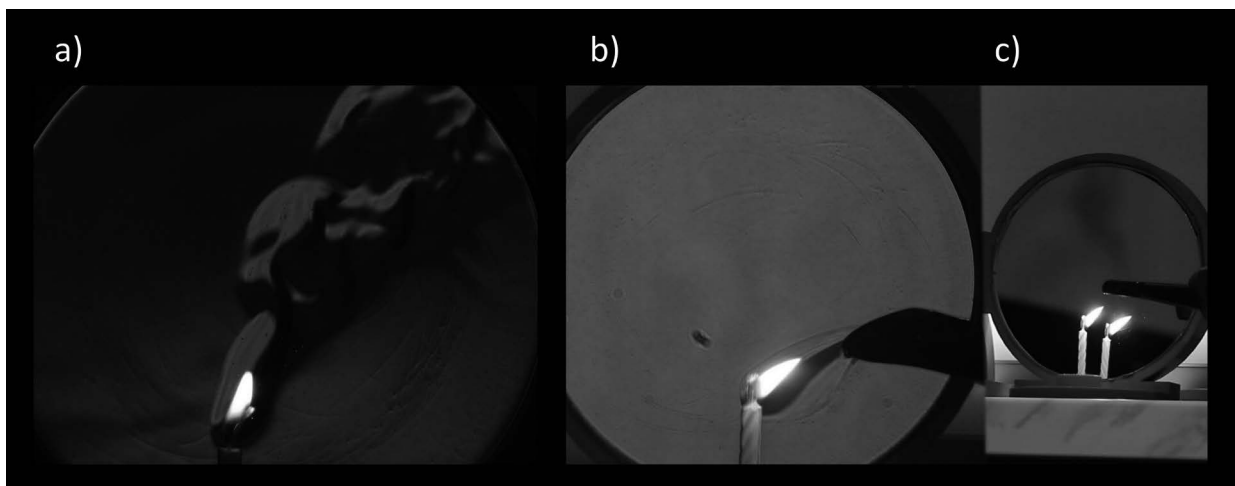


Figure 5. Schlieren image of a) a lighted candle and the mixture of hot air and gases rising from it, b) the rising stream of gases from candle bended with a vacuum cleaner, c) Photo taken during conducting this experiment from a different angle.

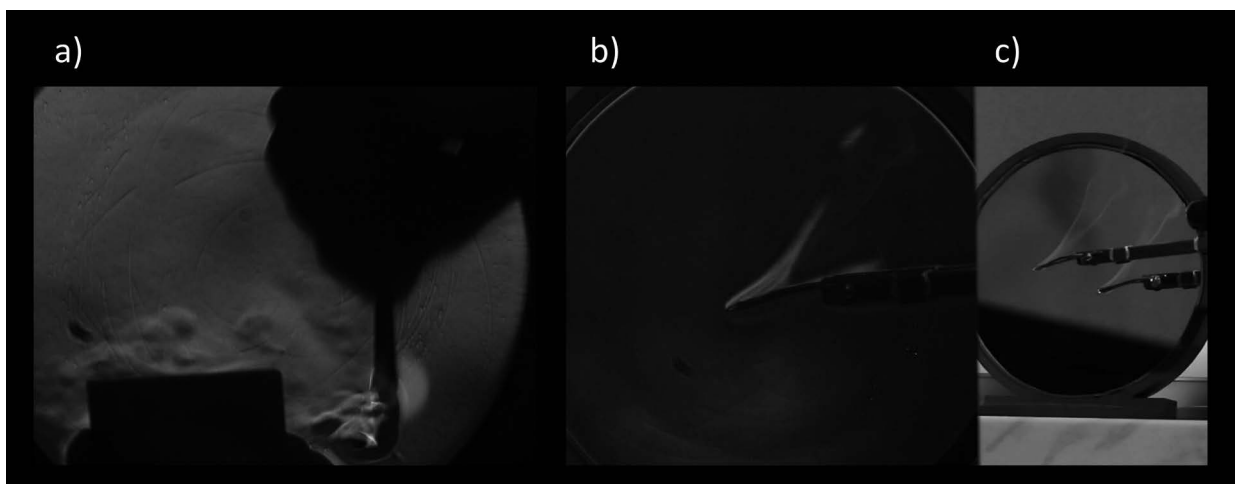


Figure 6. a) Schlieren image of a) a match that is being struck, b) a hot soldering iron, c) Photo of the soldering iron taken from different angle

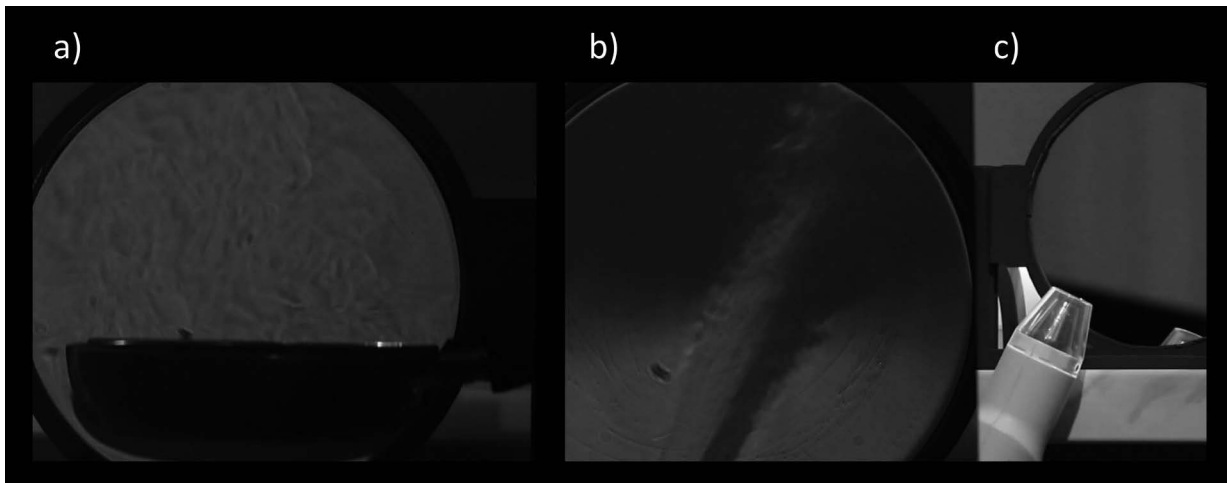


Figure 7. Schlieren image of a) a warmed up frying pan, b) a stream of hot air produced by a hot air welder, c) Photo of a hot air welder

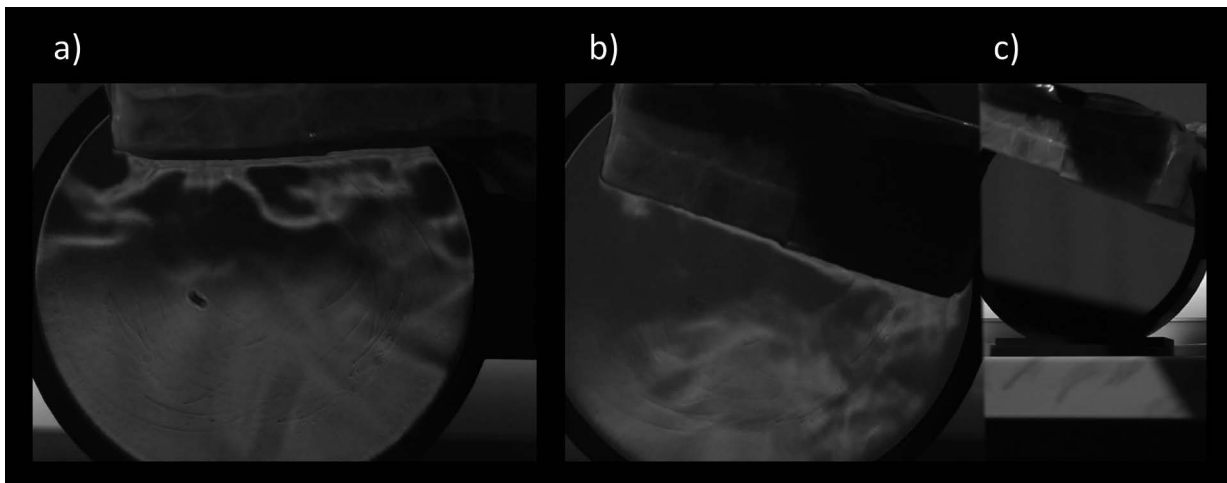


Figure 8. a-b) Schlieren images of an object having temperature close to  $-10^{\circ}\text{C}$ , c) Photo taken from a different angle of the object shown in b)

Moreover, the density difference might not only be caused by the variation in temperature. It is equally achievable to visualise gas leakage or a carbon dioxide flow. In *Figure 9b-c*) a gas from a lighter was used, whereas *Figure 9a* presents a cloud of  $\text{CO}_2$  caused by squishing the bottle of sparkling water. The carbon dioxide used here primarily originated from a decomposition of a carbonic acid added to sparkling water after shaking the bottle, but it could be replaced by any other transparent fumes having different than surrounding density.

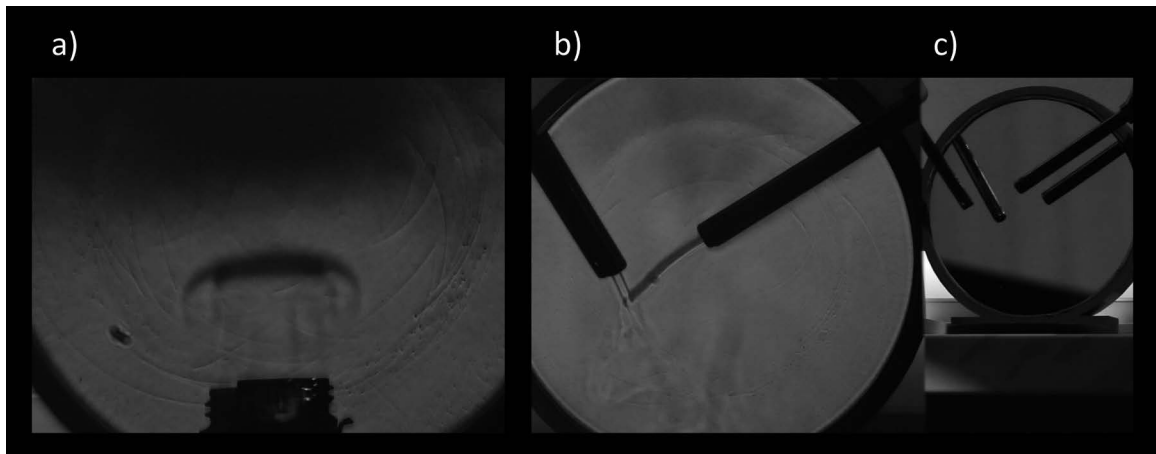


Figure 9. Schlieren image of a) a cloud of carbon dioxide escaping the sparkling water bottle after squishing it, b) a stream of gas coming from a lighter, c) Photo of the situation shown in b) from a different angle

#### 4. EXPERIMENTS WITH PRESSURE

##### 4.1. The Coandă effect

The Coandă effect is a phenomenon playing an important role in aviation, especially in the process of designing rotors and wings. Nevertheless, it is also responsible for a ping pong ball not escaping the air stream produced by a hair dryer (fig. 3b). Effect this can be easily explained using the Schlieren setup [14]. Accelerated air, upon encountering a ping pong ball in its path, flows around it, compressing on the windward side and creating higher pressure regions there, which result in a creation of a force allowing the ball to float and overcome the gravity. However, air after flowing around the ball, drags the molecules located on the leeward side, creating there a region of lower pressure. Due to the fact that surrounding air has higher pressure than a leeward side a net force appears acting on a moving air stream, bending it towards the region behind the ball and stabilising the ball in place [14].

Here, during the visualisation, a hot air was used to amplify the effect. In *Figure 10a* presented is the ball floating on a horizontal air stream, whereas *Figure 10b* portrays how the pressure regions shift after tilting the air stream by an angle of about 30 degrees.

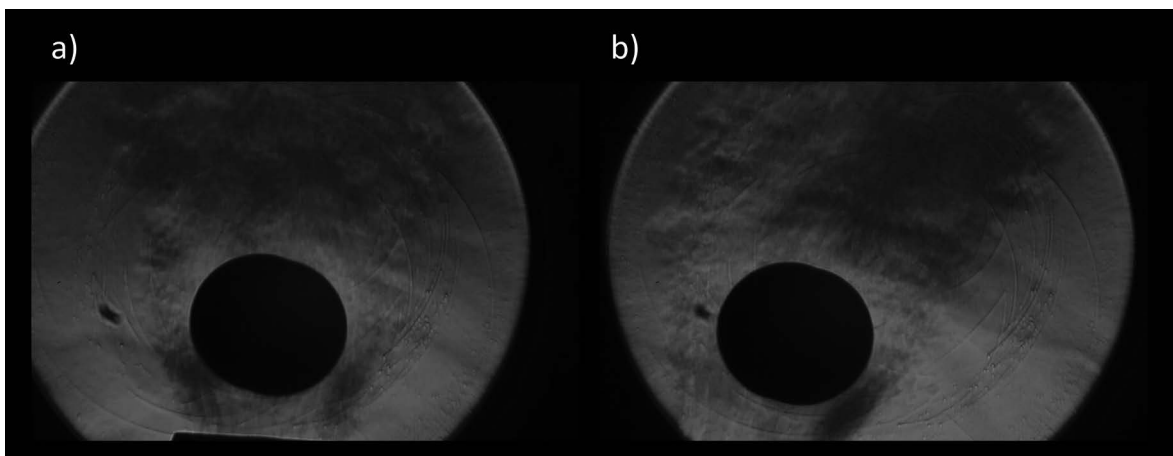


Figure 10. Schlieren image of a ping pong ball floating on a a) horizontal, b) diagonal stream of air

## 5. CONCLUSIONS

As demonstrated it is feasible to create a working Schlieren Imaging system even in home conditions. However, results are mostly limited by the quality of the camera lens, parameters of the concave mirror and the stability of the whole system.

## ACKNOWLEDGEMENTS

We would like to thank the Scientific and Didactic Laboratory of Nanotechnology and Material Technologies for allowing us to print the mirror case on a Prusa 3D printer, assistant professor Błażej Tomiczek, physics teacher Dagmara Czerwińska-Wróbel for content-related supervision and friend Wiktoria Łowczycka for helping us with creation of illustrations and assisting us during conducting the experiments.

## BIBLIOGRAPHY

1. Bryan Rolfe (2015) “Schlieren Imaging: How to See Air Flow!” [online] Available: <https://www.instructables.com/Schlieren-Imaging-How-to-see-air-flow/>
2. Veritasium (2017) “How To See Air Currents” [online] Available: <https://www.youtube.com/watch?v=4tgOyU34D44>
3. Veritasium (2017) “Schlieren Imaging in Color!” [online] Available: <https://www.youtube.com/watch?v=K7pQsR8WFS0>
4. Harvard Natural Sciences Lecture Demonstrations (2018) “Visualizing Ultrasound with Schlieren Optics Part I” [online] Available: <https://www.youtube.com/watch?v=MBPh410Gnes>
5. Harvard Natural Sciences Lecture Demonstrations (2018) “Visualizing Ultrasound with Schlieren Optics Part II” [online] Available: <https://www.youtube.com/watch?v=VrgyKFBPQW4>
6. Harvard Natural Sciences Lecture Demonstrations (2018) “Visualizing Ultrasound with Schlieren Optics Part III” [online] Available: <https://www.youtube.com/watch?v=doxD0lwEblg>
7. Harvard Natural Sciences Lecture Demonstrations (2017) “Acoustic Standing Waves and the Levitation of Small Objects” [online] Available: <https://www.youtube.com/watch?v=XpNbyfxxkWE>
8. UNSW Canberra (2020) “Schlieren Imaging Systems” [online] Available: <https://www.youtube.com/watch?v=JonG86KrxCMo>
9. JoshTheEngineer (2015) “How To: Build Your Own Schlieren Setup” [online] Available: <https://www.youtube.com/watch?v=IZ0bYi9UFv8>
10. Nexus (2021) “How to See Air! | DIY Schlieren Imaging (Part 1)” [online] Available: [https://www.youtube.com/watch?v=rbiF\\_qNm-Bg](https://www.youtube.com/watch?v=rbiF_qNm-Bg)
11. MIT Professional Education (2019) “Schlieren System Demonstration at MIT” [online] Available: <https://www.youtube.com/watch?v=alCXGoSJSXM>
12. Antoni Cepel (2016) “Schlieren Optics / Photography UAM Poznań” [online] Available: <https://youtu.be/QpP4qM8wcNM>
13. Wikipedia “Schlieren photography” [online] Available: [https://en.wikipedia.org/wiki/Schlieren\\_photography](https://en.wikipedia.org/wiki/Schlieren_photography)
14. Harvard Natural Sciences Lecture Demonstrations (2017) “Coanda Effect” [online] Available: <https://www.youtube.com/watch?v=NvzXKZJ7ZU>



17th-19th June 2024  
Gliwice, Poland

DEPARTMENT OF ENGINEERING MATERIALS AND BIOMATERIALS  
FACULTY OF MECHANICAL ENGINEERING  
SILESIA UNIVERSITY OF TECHNOLOGY

## INTERNATIONAL STUDENTS SCIENTIFIC CONFERENCE

### 3D Printing Applications in Manufacturing

Patryk Pająk <sup>a</sup>, Mateusz Zapiór <sup>a</sup>, Michał Ledwoń <sup>a</sup>, Magdalena Szindler <sup>b</sup>, Mirosław Bonek <sup>b</sup>

<sup>a</sup> Silesian University of Technology, Faculty of Mechanical Engineering, Student of Student of Engineering Production and Management, Gliwice,

<sup>b</sup> Silesian University of Technology, Faculty of Mechanical Engineering, Department of Engineering Materials and Biomaterials

**Abstract:** 3D printing has the potential to revolutionize the industry by shortening production time, minimizing material and energy consumption, and reducing costs and environmental impact. It allows you to create parts with complex geometry, which is difficult and expensive in traditional methods. This technology is used in jewelry, medicine, aviation and automotive, enabling the production of personalized implants, spare parts and light components. Despite its numerous advantages, 3D printing faces limitations related to speed, size and materials, especially ceramics and metals. Future trends include process automation, hybrid production technologies, and the development of new materials, including biomaterials and nanomaterials.

**Keywords:** 3D printing, manufacturing, thermoplastics

### 1. INTRODUCTION

Hence, with the ability for a 3D printer to use a variety of materials to fabricate products made of substances like nylon, polycarbonate, ABS, PLA, or different types of metal or ceramics, 3D printing is expected to impact nearly every business, making nearly everything. However, a downsized version of some of the printers is probably necessary to print small parts in customer premises. Three-dimensional or 3D printing has the potential to be a revolutionary tool for manufacturing. It can significantly reduce design to product lead time and minimize materials and energy use while reducing costs and environmental impacts. However, it is not a simple solution to all manufacturing needs and has technical, economic, and intellectual property risks not found in traditional mass manufacturing processes. One of the technological advancements which resulted in a profound impact on the industrial world is 3D printing. By layering on material, 3D printing is a quick prototyping technique that turns digital design data into tangible 3D objects. This is a cutting-edge technology that manufacturers are beginning to adopt because it makes it possible to quickly turn inexpensive computer drawings into tangible items. There have been several significant advances in 3D printing technology in recent years. It is now not only possible to make a wide variety of very useful products using 3D printing methods, but it is also practical to use a wide number of materials including plastics, metals, and ceramics. [1] [2]



## 2. BENEFITS OF 3D PRINTING IN MANUFACTURING

Companies around the world are just beginning to encounter the substantial potential offered by additive manufacturing. With traditional manufacturing processes, the amount of work done prior to commencing the production process is significant and includes activities such as sourcing materials, detailing specifications, finding and purchasing equipment, placing and receiving orders, and scheduling time and equipment for production. However, these steps are compressed, and in many cases eliminated through the use of 3D printing.

Interestingly, traditional manufacturing processes generally call for costs that are directly proportional to the number of parts produced, a factor that 3D printing, with the exception of the durability or longevity of the 3D printing machine, does not experience. It is important to recognize that 3D printing can also help to reduce the weight of products that need to be transported by reducing the number of components required to fabricate the final product. The application of 3D printing technology can assist with the development of an impressive range of new products that generate less material waste at the end of a useful life. When used in this manner, the minimal amount of toxic substance is released as waste.

Another significant advantage of 3D printing is its ability to fabricate parts with complex geometry. In the traditional manufacturing system, the parts with complex geometric designs are very expensive, difficult to produce, time-consuming, not cost-effective, and require a number of tools, molds, and processes. These disadvantages are insignificant when 3D printing processes are used to realize and produce the final product. This process encourages us to produce less expensive complex components and commercial products. Furthermore, 3D printing technology is capable of generating parts that are lighter and have less material waste on the production finish. This will minimize the weight of large structures that require some form of transport and minimize their negative impact on the environment. When 3D printing techniques are used with biodegradable materials, the reduction of heavy parts becomes more significant. [3] [4]

### 2.1. Cost reduction and time efficiency

Companies involved in manufacturing can gain great benefits from the use of additive manufacturing technologies (e.g. 3D printing). At the level of an individual company, the benefits of using 3D printing are: cost reduction (primarily through the removal of tooling), time efficiency, improved quality of products, and customization of products.

With respect to the monetary savings on cost reduction, often overlooked are the costs associated with the different segments of the manufacturing process, especially with large systems that involve a number of steps for manufacturing or fabrication. These costs are not only related to traditional manufacturing processes but also relate to other activities in the process, such as outsourcing the production of parts and the management of these operations.

When the production tasks are carried out directly within the company, production flexibility can reduce the costs, namely the costs related to holding some kinds of resources for a longer time. On the other hand, a company that uses 3D printing has very limited capital equipment investments, relying mainly on design software and 3D printing equipment. [5] [6]

### **3. KEY INDUSTRIES UTILIZING 3D PRINTING**

The jewelry industry was one of the first to use 3D printing, changing the way small and intricate elements are produced. Using the lost-wax casting technique, jewelers create detailed models using resin printing, which significantly reduces mold production time. This technology enables the creation of complex pieces that would otherwise require precise hand work, making it groundbreaking for jewelry production. The 3DP technology is particularly useful in the early concept design and direct investment casting stage for functional testing and design validation, allowing the production of physical objects for visual-based concept testing. This allows the manufacturer to quickly produce several different concepts and select the materials before the actual production of jewelry parts. A parallel emerging area is medical and dental 3D printing applications, providing personalized and customized fabrication. 3D printable materials like titanium, aluminium, steel, and precious metals together with biomaterials are used for producing patient-specific implants and other medical parts. The potential time saving and cost reduction are the reasons that prompted aviation service providers, aircraft part manufacturers, and independent repair and overhaul service providers to adopt Additive Manufacturing (AM) processes, such as 3DP, to produce aircraft parts. Plastic, metal, and composite 3D printed parts are widely used as retrofit parts due to the ability to produce parts with similar strength as the original part. In the recent phase, 3DP has shifted to printing complex repair or substantially modified parts. The printing of spaceship parts adds unique design freedoms utilized by 3D printed materials that have weight-saving advantages. This will surely consolidate 3D printing into an essential part of spacecraft fabrication. Growth of 3D printed parts applications in the automotive domain is anticipated due to the availability of architectural customization, design freedom, and mass customization capabilities in design and production. It is used for rapid development, reducing manufacturing time, and expedited introduction to the market. [7]

### **4. CHALLENGES AND LIMITATIONS OF 3D PRINTING IN MANUFACTURING**

It is anticipated that as 3D printing technology develops, more materials and items will be able to be 3D printed. The things that can be made using the 3D printing manufacturing technique are still limited, though. The speed and size limitation are obvious challenges. And while it is possible to use 3D printing to create very complex yet delicate structures, 3D printing also creates regions under compression, which generates a force towards their surroundings once they are printed. This makes it challenging to use 3D printing to create customized and deployable parts. Coupling issues are significant with multiple materials. For example, unfused material might also interfere with the fabrication process, affecting the design of some products. Therefore, the selection of compatible materials is significant as it can determine the success of the fabrication in a continuous process. Another limitation is in the compositional design and shaping of the architecture for cellular materials, with the risk of fabricating materials that are unexpectedly vulnerable due to an unanticipated stress enhancement under real-life loading conditions. In particular, entangled and nearly inextensible voxel networks typically occur unwanted in other areas of the space, such as in thin or printed in air features. The necessity of adding over footholds to the structures will lead to redundancies, which will add to the challenges of the load carrying mechanisms in the design. With all of these challenges, it is also problematic to employ topology optimization. Finally, let us notice that the zero thickness assemblies, such as point, line, or plane contacts in bundle-like, shell-like, or

crystalline structures, might also appear in the arbitrary scoped numerical simulations. What is the magnitude of such inaccuracies in the simulation of mechanics of materials? [8] [9]

#### 4.1. Material limitations

While offering a novel yet prominent approach to conventional manufacturing methodologies, 3D printing almost evades time-consuming and costly waste reduction processes. At the same time, it also puts forward critical obstacles in the implementation process of a 3D printer for immediate product fabrication. One of the primary obstacles is 3D printing's material limitations. Conventional 3D printers are capable of accepting materials such as thermoplastics, but the requirement can extend up to ferrous and non-ferrous metals. However, the mainstream of 3D printers utilizes and feeds thermoplastic filaments or uses digitally or electronically controlled inkjet nozzles to deposit droplets of photo-curable liquid resins layer by layer on a platform to fabricate three-dimensional products.

Using other materials, especially ceramics and metals, remains a stumbling block highly impairing the effective function of 3D printers. Most of the reasons can be traced back to ceramics' nature and metallic properties, such as rising to and solidifying from high-temperature conditions that are needed. These high requirements demand an optimal solution that remains elusive, which has hampered the rapid increase in pristine and ongoing 3D printer provision, and more notably, the optimization quality path. The scenario is so critical that it almost hindered the actual industrial applications. An exception of a commercially available 3D metal printer is by the company ExOne. The aforementioned material requirements have created many complications, such as the cost-value trade-off, connectivity assurance, forming gigantic porous spaces, precision integrity and reliability, and throughput speed. These consequences often entangle the numerous elemental metals within a single alloying family [8-9].

### 5. FUTURE TRENDS AND INNOVATIONS IN 3D PRINTING

Although 3D printing has matured as an additive technology, it continues to be developed in some surprising ways. As the number and extent of 3D printed products grow, more scalable factory solutions are being developed. This includes machine automation to streamline factory work processes, as well as increasingly efficient job planning and 3D file optimization methods. The technology is also expanding beyond plastic and metal materials. An exciting area of development in 3D printing is biotechnology. Applications of 3D printing required for life sciences have unique needs compared to those for manufacturing. A variety of organic materials must be used in 3D bio-printer or assembly applications in order to cater to a myriad of tissues that may be printed.

Increasing interest is seen in the combination of 3D printing with other engineering processes to enable end-use products. With the growing scope of products that incorporate 3D elements being manufactured by processes apart from 3D printing, studying hybrid manufacturing processes of this nature is essential. This benefits industries that need short lead times and low minimum production numbers. Combining the best of 3D printing with various finishing processes, it becomes possible now to deliver finely detailed end-use products that no one would suspect had close to three-quarters of their components 3D printed. And the complexities

supported by hybrid adaptability may also allow easy incorporation of sensors and semiconductor chips with the lowest cost and skill labor requirements. [10] [11]

### 5.1. Advancements in materials and processes

The origins of 3D printing as a prototyping tool to predict designs have ventured to the current state in which 3D printing has become widely recognized as the fabrication process during the design phase. This development has created an enabling environment that has attracted advancements in materials and improvements in the processing aspects such as the development of larger scale 3D printers (Z axis), higher resolution (XY axes) and the potential for more materials (resin, powder, plastics, metal). There are also developments such as the use of high-resolution stereolithography (SLA) for dental applications and the development of application-oriented materials. The use of 3D printed models as investment cast patterns, the print-in-place mechanical actuators and the tabletop selective laser sintering (SLS) are some examples in this regard. Furthermore, 3D printing is heading to be the future of plastic electronics and flexible organic light-emitting diodes.

The ability to handle bio-ink combined with the advantages of self-assembly fabrication has led to a niche in 3D bioprinters. Research has also been conducted on the use of integrated ink of multi-cells for the development of multi-cellular networks and relative bio-inks. The electronic, optical and magnetic fields have also shown potential in handling bio-inks for previously impossible patterning on substrate surfaces with complex geometries. In the use of 3D printing in the fabrication of wearable technology, many research lines are focused on developing inks that have flexibility and stretchability and the idea of fabricating electronic devices directly on stretchable materials (epidermal-stretchable electronic-device). The implantation of soft robotics and microfluidics as well as the responsive nanomaterials and the concept of assisted 3D printing (A3DP) are discussed in this section. [10] [11]

## BIBLIOGRAPHY

1. <https://monroeengineering.com/blog/5-benefits-of-3d-printing-in-manufacturing/>
2. <https://www.hubs.com/knowledge-base/advantages-3d-printing/>
3. <https://www.raise3d.com/academy/3d-printing-advantages/>
4. <https://shoplogix.com/3d-printing-in-manufacturing-ultimate-guide/>
5. <https://blog.grabcad.com/blog/2022/06/08/aerospace-industry-using-3d-printing-2022/>
6. <https://formlabs.com/asia/blog/3d-printed-jewelry/>
7. <https://bmf3d.com/blog/3d-printing-industry-challenges/>
8. <https://www.mdpi.com/2073-4360/15/11/2519>
9. <https://www.mdpi.com/2076-3417/13/19/10957>
10. <https://3dprintingindustry.com/news/the-future-of-3d-printing-2024-the-3d-printing-industry-executive-survey-228135/>
11. <https://www.3dsystems.com/blog/2024/2024-02/2024-3d-printing-trends-and-predictions>



17th-19th June 2024  
Gliwice, Poland

DEPARTMENT OF ENGINEERING MATERIALS AND BIOMATERIALS  
FACULTY OF MECHANICAL ENGINEERING  
SILESIA UNIVERSITY OF TECHNOLOGY

## INTERNATIONAL STUDENTS SCIENTIFIC CONFERENCE

### **Analysis of the structure and thickness of the nitrided layer in 1.2343 steel depending on the furnace used for thermochemical treatment**

Mateusz Paluch<sup>a</sup>, Szymon Jędrzejewski<sup>a</sup>, Janusz Mazurkiewicz<sup>b</sup>

<sup>a</sup> Silesian University of Technology, Faculty of Mechanical Engineering, Student of Engineering and Materials Technologies, Gliwice

<sup>b</sup> Silesian University of Technology, Faculty of Mechanical Engineering, Department of Engineering Materials and Biomaterials

**Abstract:** The research analyzed the structure, hardness, and thickness of the nitrided layer in two batches of 1.2343 steel samples subjected to gas nitriding in two different industrial furnaces with significantly varying technological efficiencies. These nitriding processes displayed substantial differences in performance and effectiveness for various workpieces. The study aimed to assess the impact of each furnace on the properties and thickness of the nitrided layers, providing an objective evaluation of the processing quality and potential reasons for variations in layer thickness. The investigation included light microscopy and Vickers microhardness tests to examine the structure and mechanical properties of the nitrided layer. The results revealed notable differences in hardness distribution of the nitrided samples, depending on the furnace used. The results confirmed clear differences in the thickness of the nitrided layer for the two heat-chemical treatment furnaces used. It was determined that the reason for this is the different design of the nitrogen distribution system in the two analyzed furnaces, which translates into such strong differences in the thickness of the nitrided layer.

**Keywords:** Nitriding, Steel 1.2343, structure of nitrided layers, hardness of nitrided layers, thickness of nitrided layer, chemical composition profile of nitrided layer

## **1. INTRODUCTION**

### **1.1. Characteristics of nitriding technology**

Nitriding has long been a key thermochemical treatment process, dominating surface modification technology. The process is most often applied to low-alloy steels, but is also used for titanium, aluminum and molybdenum. Nitriding is the final technological step, requiring no additional heat treatment, as is the case, for example, with carburizing, after which hardening is necessary. As a result of nitriding, the surface of the component gains hardness, wear resistance, better corrosion resistance and fatigue life [1]. In the context of the nitriding process, both the thickness of the layer and its cohesion with the substrate are important, as they are crucial to the physical properties of the component. The nitride layer, due to its chemical stability, improves

corrosion resistance. However, when the nitride concentration is too high, the layer can become porous and brittle, often leading to peeling away from the substrate. Such a condition can result in damage to precision wear parts or contamination of products by the peeling layer. This undesirable phenomenon requires special attention [2].

**Advantages of nitriding [3]:**

- Can treat a wide variety of steels and non-ferrous metals.
- Carried out at a much lower temperature than the alternative treatment by carburizing, which reduces energy consumption.
- The lower temperature minimizes the risk of distortion.
- No additional heat treatment is required after nitriding.
- High hardness of the nitride layer.
- Improved surface corrosion properties.

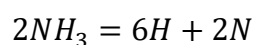
**Disadvantages of nitriding [3]:**

- The layer obtained is thin, despite the long duration of the process.
- The nitride layer, due to its high hardness, can crack and splinter.
- Relatively high price.

**1.2. Gas nitriding technology**

This work deals with problems in gas nitriding technology. The gas nitriding process is a popular and effective method of improving surface properties, increasing their wear resistance, hardness and fatigue strength by forming hard nitrides on the surface of the component. The process is widely used in machinery subjected to intensive loads, where high surface hardness and wear and fatigue resistance are key. In the case of gas nitriding, the basic reaction is the catalytic decomposition of ammonia, leading to the formation of mono-atomic nitrogen [4].

This reaction occurs at temperatures above 270°C according to the following equation [4]:



Ammonia must be supplied to the furnace continuously so that the dissociation reaction can take place without interruption. Due to the instability of the mono-atomic nitrogen necessary for gas nitriding and its propensity to form N<sub>2</sub> molecules, dissociation must take place directly in the furnace [4].

Depending on the length of the process, gas nitriding is divided into [5]:

- long-term over tens of hours for highly loaded machinery and exposed to frictional wear,
- short-term ones carried out for a few to several hours.

**1.3. Steels subjected to the nitriding process**

Nitriding is applied to various types of steels, including carbon steels, low-alloy steels, tool steels, stainless steels and cast irons. To achieve optimal properties after nitriding, specially designed steels with specific chemical compositions are used. These steels contain nitride-forming elements such as Al, Cr, Mn, Mo and V. It is important to limit the carbon content to

0.5%, because most of the nitrogen-creating elements form stable carbides, which limits their combination with nitrogen. In particular, steels with Al additions, forming AlN nitrides, achieve high surface hardness. However, Al additions, usually in the 1% range, can cause embrittlement of the steel [3].

Nitriding is also used for maraging steels, which have a very low carbon content, usually less than 0.03%, and are strengthened by precipitation of intermetallic compounds at a temperature of about 480 °C. The purpose of nitriding maraging steels is to increase their wear resistance. Since the temperature of conventional gas nitriding exceeds the aging temperatures of maraging steels, plasma nitriding is more suitable [6-7].

## 2. MATERIAL AND RESEARCH METHODOLOGY

Structure and properties of 1.2343 steel is a type of tool steel designed specifically for high-temperature service, making it an ideal material for applications where strength is required to be maintained under intense loading and elevated temperatures. intense loading and elevated temperatures. Because of these properties, the 1.2343 steel finds its use in a wide variety of industries, covering the automotive, aerospace and machine tool sectors as a material for making molds for die casting aluminum, zinc or magnesium alloys, pressing tubes, copper alloy rods and light metals. In addition, it performs well as a material in tool presses for shaping tubes and rods from copper and other light metals, meeting the needs for strength and resistance to harsh working conditions. 1.2343 steel is also used as a material for plastic forming inserts, particularly where very low surface roughness is required [8].

The classification shows 1.2343 steel as a tool alloy steel with the addition of chromium, molybdenum and vanadium. Due to its good ductility, good thermal conductivity this material is widely used in industry. In addition, it is distinguished by its resistance to tempering during operation and cracking at high temperatures, which translates into its durability and ability to maintain mechanical properties even under harsh operating conditions [8]. It is also characterized by good mechanical properties, including high hardness. 1.2343 steel is distinguished by good machinability, thanks to which processes such as drilling or milling are carried out without difficulty. An additional advantage is its low susceptibility to cracking. This set of characteristics makes it durable and safe for use [8]. The chemical composition of the analysed steel presented in Table 1.

*Table. 1 Chemical composition of 1.2343 steel according to EN ISO 4957:2018-09 [9]*

Chemical element	C	Si	Mn	P	S	Cr	Mo	V
Element mass concentration [%]	0,33-0,41	0,80-1,2	0,25-0,5	<0,03	<0,03	4,80-5,5	1,1-1,5	0,3-0,5

The base for the samples was a hardened rod with a diameter of 25.8mm, which was successively cut into slices with a thickness of 5mm. In this way, 6 samples were prepared with the shape and dimensions shown in Figure 1. A photo of the samples before thermochemical treatment is shown in Figure 2. Before the nitriding process, it was necessary to properly preparation of the samples by washing, degreasing and drying them.

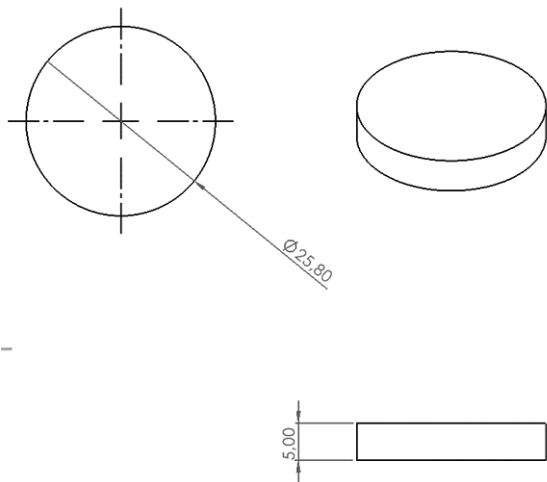


Figure 1. Shape and dimensions of the test specimen

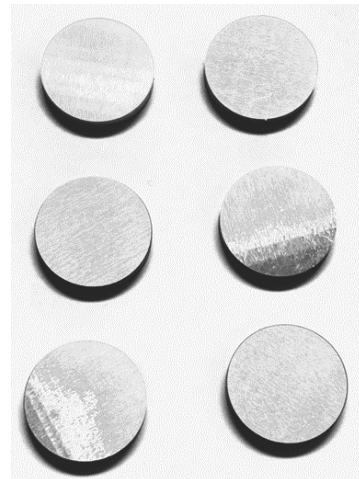


Figure 2. Prepared samples before the nitriding process

The same nitriding processes were carried out in both furnaces 1 and 2 under an atmosphere of dissociated ammonia. The total time of the thermo-chemical treatment process was almost 20 hours, while the nitriding process itself was carried out in two stages, differing in time-temperature parameters. The first stage at a temperature of 480° took about 30 minutes, while the second stage at 530° took about 3.5 hours. The total nitriding time was about 4 hours. Both furnaces used the same source of ammonia, and other process parameters such as temperature and heating times, nitriding and cooling were similar. The thermo-chemical treatment of the samples was carried out in Elterma Pegat 100.200-650-25-ZF (furnace number 1) and Remix PNF-07/1600 (furnace number 2) furnaces. Both furnaces are retort furnaces with the same volume. The working space inside the retort of both units is  $\Phi 1000\text{mm}$  by 2000mm. Apart from the dimensions, they are also similar in design and gasification arrangement.

The prepared samples, due to the need to study the cross-section of the layer, were subjected to metallographic specimen preparation methods. This process is necessary in order to evaluate the hardness distribution and cross-section of the structure, and thus the thickness of the nitrided layer, during further work. The first step was to cut four specimens on a precision cutting saw. The inlaying process was carried out so that each of the two specimens obtained contained two different specimens, nitrided in the same furnace. The next step was to carry out the grinding and polishing process. The grinding of the samples was carried out using sandpaper discs of decreasing abrasive gradation. The final step in the preparation of the deposits was polishing, using a synthetic disc and a diamond slurry with a particle size of 1  $\mu\text{m}$ .

Microhardness tests were carried out on metallographic specimens. In the first step, microhardness distribution was measured using the Vickers method with a load of 0.98 N (100 g) on samples marked z3 and d3



Figure 3. Future-Tech ARS-9000 microhardness tester



(sample d3 from furnace number 1 and sample z3 from furnace number 2). Three series of measurements were carried out for each sample, with each series consisting of 15 impressions taken at 15  $\mu\text{m}$  intervals. The test was repeated three times at randomly selected locations. After reading the dimensions of the impressions obtained, the average hardness of the substrate material on the cross-section of the samples was determined. The structure was studied using a Zeiss Axioobserver light microscope. Samples were digested in 3% nital reagent.

### 3. TEST RESULTS

Analyzing the obtained results of hardness measurements, it is possible to identify several significant discrepancies in the properties of the tested samples. In sample d3 it was found, that the maximum hardness obtained in the surface layer is about 1049HV<sub>0.1</sub> (tab. 2).

This layer has a thickness of up to 50 $\mu\text{m}$ . After exceeding 50 $\mu\text{m}$  from the surface, the hardness decreases reaching at a distance of 70 $\mu\text{m}$  from the surface to a value of about 700HV<sub>0.1</sub> (fig.4, 5) At a distance of above 70 $\mu\text{m}$ , the hardness stabilizes at less than 500HV<sub>0.1</sub>. The zone of increased hardness in this sample has a thickness of up to about 70 $\mu\text{m}$

In the case of sample z3 (fig. 6, 7), the very first measurement, taken at a depth of just 10 $\mu\text{m}$ , shows a significantly lower hardness value compared to the corresponding measurement performed on sample d3. The maximum hardness in sample z3 is only 875 HV<sub>0.1</sub>, which, at a distance value of 30 $\mu\text{m}$ , decreased to only 600HV<sub>0.1</sub>. Thus, one can confidently conclude that the furnace 2 treatment yields significantly lower maximum hardness of the nitrided layer and a layer with a significantly lower thickness. In the base (non-nitrided) zone of the samples, the hardnesses are comparable and oscillate between 400-420HV<sub>0.1</sub>.

Table 2. Results of microhardness test

Distance of imprint from surface [ $\mu\text{m}$ ]	Sample d3	Sample z3
	Average of measurements [HV <sub>0.1</sub> ]	
10	1049	875
30	1040	599
50	978	482
70	696	466
90	489	433
110	465	417
130	458	399
150	429	409
170	424	407
190	423	412
210	416	398
230	410	411
250	422	403
270	411	413
290	417	408

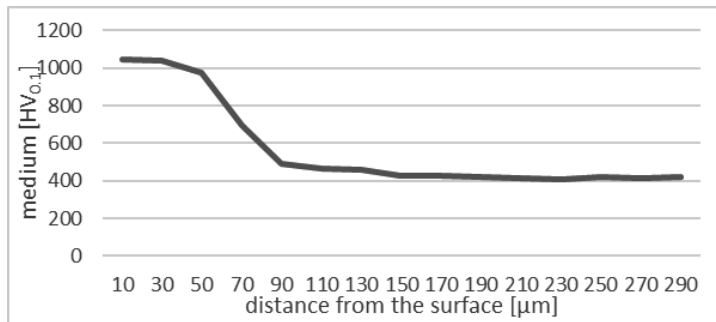


Figure 4. Graph of average hardness  $HV_{0.1}$  in sample d3

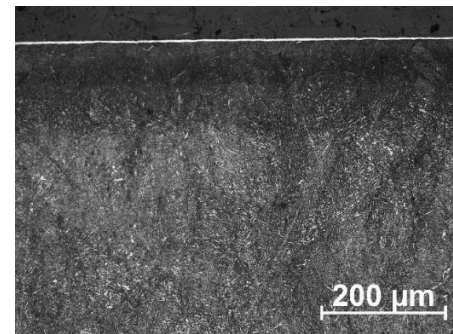


Figure 5. Structure samples d3  
LM 200x

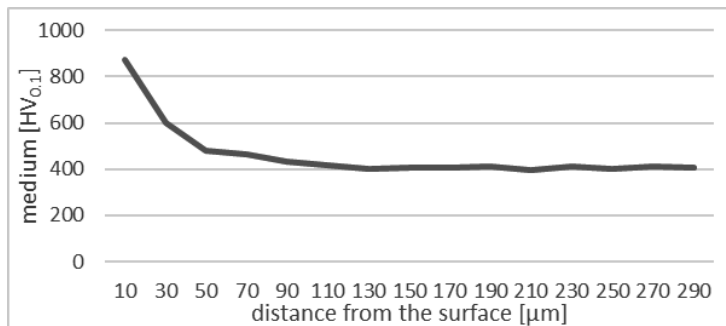


Figure 6. Graph of average hardness  $HV_{0.1}$  in sample z3

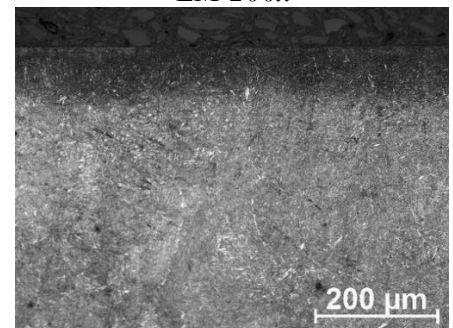


Figure 7. Structure samples d3  
LM 200x

In the context of the research carried out into the nitriding of WCL steel specimens, a key issue became the observed variation in the structure of the nitrided layer depending on the thermochemical treatment furnace used. This subtle but important variation was of interest because of the potential impact on the mechanical and chemical properties of the resulting layers. It is noteworthy that understanding and controlling the structure of the nitrided layer can open the door to new perspectives in improving nitriding processes. Identification of factors influencing differences in structure will not only allow optimisation of the nitriding conditions, but also precise adjustment of the process parameters to the intended technological goals. Research into the effects of different nitriding process conditions on the microstructure of steel not only allows a better understanding of the mechanisms of the process, but also opens the door to new possibilities for improving nitrided materials. The ability to control the structure can translate into improvements in mechanical properties, wear resistance or corrosion properties. In conclusion, this research is a step towards increasing the efficiency of nitriding processes, which may find practical applications in various areas of the metallurgical industry.

## 4. CONCLUSION

### 4.1 Variation in Diffusion Zone Thickness:

- Microhardness analysis has established that there is a clear variation in the thickness of the diffusion zone of the nitrided layer depending on the furnace used. The diffusion zone is a key factor affecting the mechanical properties of nitrided steel. In furnace number 1, diffusion is far more efficient than in furnace number 2. It has not been possible to determine at this stage what causes such differences, but they have been confirmed in scientific studies.

#### 4.2 Changes in Hardness Profiles:

- The study showed significant differences in the changes in the hardness profile depending on the distance from the surface of the sample. These differences are directly related to the type of furnace used for the nitriding process, suggesting that furnace conditions have a significant impact on the final hardness of the layer. There must be an unfavourable decomposition of the nitriding atmosphere in furnace No. 2, which contributes to the disruption of the nitriding process.
- The microhardness analysis determined the nitriding depths for both furnaces and indicated a strong variation in the variation of the hardness profile as a function of the distance from the sample surface for both furnaces analysed. The measured thickness of the nitrided layer could be a key factor influencing the mechanical properties of the resulting nitrided layers.
- The results of the chemical composition analysis of the nitrided layer micro-areas provided valuable information on the distribution of nitrogen and other elements. Precise control of the chemical composition is becoming a key aspect in tailoring the layers for specific applications.
- Phase analysis using an X-ray diffractometer showed that the volume proportion of nitrogen phases for samples treated in furnace No. 1 is below the method's detection level. For samples treated in furnace No. 2, the presence of nitride phases in their structure was confirmed.

#### ACKNOWLEDGEMENTS

The publication was created within the framework of the joint Slovak-Polish project International Visegrad Fund's V4 Generation Mobility Mini-Grant No 12410044 as a result of cooperation between the Association of Alumni of the Silesian University of Technology, Gliwice, Poland and the University of Žilina, Slovakia.

The project is co-financed by the Governments of Czechia, Hungary, Poland and Slovakia through Visegrad Grants from the International Visegrad Fund. The mission of the fund is to advance ideas for sustainable regional cooperation in Central Europe.



#### BIBLIOGRAPHY

- [1] T. Burakowski, T. Wierzchoń, Inżynieria powierzchni metali, WNT, Warszawa 1995
- [2] K. Przybyłowicz, Metaloznawstwo, WNT, 2007
- [3] J. Borowski, J. Wendland, A. Laurentowska, H. Jurczak, Struktura przypowierzchniowa matryc do wyciskania profili aluminiowych, Obróbka Plastyczna Metali 24.1:5-14, 2013
- [4] T. Malkiewicz, Metaloznawstwo stopów żelaza, PWN, Warszawa-Kraków, 1971
- [5] S. Głowacki, A. Majchrzak, W. Majchrzak, Wpływ proporcji składników atmosfery azotującej na strukturę warstwy azotowanej jonowo. Obróbka Plastyczna Metali, 16(2), 15- 22, 2005
- [6] M. Blicharski, Inżynieria materiałowa - Stal, WNT, Warszawa, 2004

- [7] W. A. Rakowski, M. Kot, S. Zimowski, T. Wierzchoń, Właściwości warstw azotowanych jarzeniowo, wytworzonych na stali 316L. Problemy Eksploatacji, (3), 107-115, 2006
- [8] M. Korecki, M. Bazel, M. Sut, P. Kula, E. Wołowicz, Nawęglanie i azotowanie próżniowe dysz wtrysku paliwa wykonanych ze stali WCL (H11), Piece Przemysłowe i Kotły 3, 2014
- [9] PN-EN ISO 4957:2018-09 - Stale narzędziowe



17th-19th June 2024  
Gliwice, Poland

DEPARTMENT OF ENGINEERING MATERIALS AND BIOMATERIALS  
FACULTY OF MECHANICAL ENGINEERING  
SILESIA UNIVERSITY OF TECHNOLOGY

## INTERNATIONAL STUDENTS SCIENTIFIC CONFERENCE

### Influence of sintering time on the composition and properties of sinters obtained from elemental powder mixture of refractory metals

Krzysztof Pęczak<sup>a, b</sup>, Piotr Tomczyk<sup>a</sup>, Alicja Duda<sup>a, b</sup>, Monika Czerny<sup>a</sup>

<sup>a</sup>Łukasiewicz Research Network – Institute of Non-Ferrous Metals, Sowińskiego 5 St., 44-100, Gliwice, Poland

<sup>b</sup> Doctoral School, Silesian University of Technology, Akademicka 2A St., 44-100, Gliwice, Poland, email: krzysztof.pecak@imn.lukasiewicz.gov.pl

**Abstract:** High Entropy Alloys have gained significant attention from scientists in recent years. One of the most often used method of their preparation is mechanical alloying, a process that is often lengthy and leads to contamination of the alloy. This article explores whether increased sintering time could help with achieving homogenous chemical composition in the fabricated material. A mixture of refractory metal powders has been prepared and sintered with varying holding times using Spark Plasma Sintering method. The phase composition, hardness, and density of obtained sinters have been investigated. Results show, that while there are noticeable changes in the properties of the obtained sintered samples, they cannot be simply attributed to better alloying of the material. The use of finer powders and higher sintering temperatures are proposed as possible solutions for achieving the intended effect of homogenisation.

**Keywords:** High Entropy Alloys, Spark Plasma Sintering, Refractory Metals, Multi-Principal Metal Alloys, Complex Concentrated Alloys

#### 1. INTRODUCTION

High Entropy Alloys (HEAs), also known as complex concentrated alloys (CCAs) and multi-principal element alloys (MPEAs), have been introduced into the wider scientific community in 2004 [1]. There are a few definitions of this group of alloys. HEAs can be defined as containing at least 5 principal elements, each constituting 5 to 35 atomic percent of the alloy [1] or having configurational entropy of at least  $1.5R$  ( $R$  – gas constant) [2]. Some other definitions require the alloys to be equiatomic or only consisting of a single solid solution phase [1, 2]. In the light of those differing definitions the most sensible appears to be the one based on configurational entropy, as it is applicable to any alloy composition and any fabrication state (as cast, sintered, quenched etc.). Configurational entropy can be calculated as follows [1]:

$$\Delta S_{conf} = -R \sum_{i=1}^n X_i \ln X_i$$

where  $R$  – gas constant,  $X_i$  – atomic concentration of  $i$  element.

A distinct group of HEAs introduced in 2010 by Senkov et al. are Refractory HEAs (RHEAs) [3]. They were originally introduced as a way to achieve high temperature strength, as compositions investigated in aforementioned work reached an ultimate strength of over 400MPa [4], which is one of the, if not the highest achieved by a metal alloy. Since then many other compositions were proposed, usually with higher emphasis on reduced density at the expense of overall melting point and strength at elevated temperature. Most RHEAs suffer from low room temperature ductility and low oxidation resistance, improvement of which are objectives of many recent studies published in this area [5].

HEAs are often prepared using mechanical alloying (MA), vacuum arc melting or Additive Manufacturing [6]. When it comes to MA, its advantages are the possibility of preparation of materials from elements which widely differ in their melting point and the homogenous mixing of the elements. Disadvantage of this method is that it is often very time costly (even hundreds of hours of milling time per batch) and can result in contamination of the alloy with the material of milling balls and vials [7]. MA is still a convenient method, especially for RHEAs. Refractory elements are often produced in the form of powders that can be readily processed by MA, as their high melting point bars them from large scale melting production routes.

In this work, sintering holding time extension to promote better mixing of elements and shorten required milling times is investigated. The experiments were done with the use of a simple mix of elemental powders. Properties of the constituent elemental powders and sintered samples were investigated.

## 2. EXPERIMENTAL

### 2.1 Materials

Elemental powders obtained from KAMB Import-Export (Poland) were used to prepare the powder mix. Particle size distribution and apparent density of the powders as measured by laser diffraction and gas pycnometry are presented in Table 1. Powder mixture was prepared by mixing in a bottle mixer for 8h.

Table 1. Physical properties of the powders used in mixture preparation.

Powder	$d_{10}$ , $\mu\text{m}$	$d_{50}$ , $\mu\text{m}$	$d_{90}$ , $\mu\text{m}$	Median, $\mu\text{m}$	Mode, $\mu\text{m}$	Apparent density, $\text{g}/\text{cm}^3$
Mo	5.417	19.303	53.397	19.3	21.2	10.0829±0.0101
Nb	6.301	21.732	54.94	21.72	22.39	8.5325±0.0053
Re	4.169	17.668	48.782	17.66	20.63	20.7414±0.0424
Ta	4.501	15.227	40.414	15.22	20.07	16.5513±0.0117
W	1.845	5.241	13.001	5.24	5.71	18.8708±0.0298

The targeted material composition is characterized by a high configurational entropy of 1,61R (assuming complete mixing after sintering) as calculated from equation 1.

## 2.2. Methods

- Apparent density (AD)

AD was measured by the gas pycnometry method using the Micromeritics AccuPyc 1340 II pycnometer. Measurements were performed at room temperature in a sample chamber with a volume of 10 cm<sup>3</sup> and helium as an inert gas. Results for density were obtained for 50-cycle repetitions preceded by 30 measuring cell purges.

- Powder size distribution (PSD)

Powder size distribution was investigated using laser diffraction method. Analysette 22 apparatus (FRITSCH GmbH, Germany) has been used for the measurements. Fraunhofer diffraction equation was used to determine particle size. PSD was measured 3 times on the same sample introduced into measuring chamber.

- X-ray powder diffraction (XRD)

Qualitative phase analysis was carried out on powders and sintered samples using diffractograms recorded with an XRD7 diffractometer made by Seifert-FPM. Characteristic X-ray radiation of Cu K $\alpha$  and nickel filter were used for the investigation. Analysis was carried out in the 2 $\theta$  range 10°÷100°. Identification of the phases was done using Seifert and Match! software, basing the results on the ICDD PDF-4+ catalogue from 2023.

- Sintering

Sintering was done with the use of HP D5 Spark Plasma Sintering by FCT Systeme GmbH. All samples were sintered with the same parameters and regime (Table 2), excluding holding time, which was varied from 5 to 60 minutes. Sintering has been done in medium vacuum of 60 to 100Pa. Due to temperature control being based on pyrometer readings and hence the lowest detectable temperature being 400°C, first stage of heating was performed at constant power of 2,5kW. After reaching the temperature of 450°C further heating was conducted with the speed mentioned in the Table 2 below. Due to previous experiences with sintering materials containing tantalum and niobium, hexagonal boron nitride suspension was sprayed on the walls of the graphite inserts to prevent direct contact of the powder with graphite, as it leads to significant carburization of the material. Sintering temperature was chosen based on previous experiences with sintering individual elemental powders Mo, W and Re, in which case 1600°C was suitable for obtaining sinters of over 97% density.

Table2. Sintering parameters.

Sintering pressure, MPa	Heating rate, °C/min	Sintering temperature, °C	Die and punches material	Powder facing material
35	25	1600	Graphite	Hexagonal boron nitride

- Metallographic samples preparation

Sintered samples were sandblasted to remove leftover hBN and graphite that adhered to the sample surfaces. Afterwards, samples were ground on MetaServ 250 grinder-polisher (Buehler, Germany) with the use of diamond grinding disks (MD Piano, Buehler) with gradations of 80, 220, 500, 1200 and 2000. Ground samples were polished with the use of microdiamond suspensions (Pureon GmbH, Germany) deposited on microfiber cloths, wherein the average

particle size was 9 $\mu\text{m}$  and 3 $\mu\text{m}$  consecutively. Samples were dried in air for 2 hours in ED 23 laboratory drier (BINDER GmbH, Germany), to remove moisture retained in the pores.

- Electron probe microanalyzer (EPMA)

JXA 8230 electron microprobe (JEOL, Japan) was used to perform micrographic and chemical composition investigations. Voltage of 15kV and EDS detector was used to prepare elemental distribution maps.

- Hardness measurements

Hardness of the samples was measured using a standard hardness tester equipped with a spheroconical diamond indenter at a load of 150kG (HRC scale). 7 measurements were taken, extremes on both sides were discarded, and the average was calculated from the remaining 5 values.

- Sinter density (SD)

SD was measured with the Archimedes method. The procedure was conducted according to PN-EN ISO 2738:2001 (ISO 2738:1999) Sintered metal materials, excluding hardmetals — Permeable sintered metal materials — Determination of density, oil content and open porosity.

### 3. RESULTS AND DISCUSSION

Figure 1 shows XRD results for powder mix and sintered samples. As the powder was simply mixed and not milled, peaks from constituent elements are clearly visible. Of note is the fact, that pairs W-Mo and Ta-Nb were marked together, as their structures are almost identical. Results show, that even though the phase composition of the sintered samples differ greatly from the powder mix, there is no significant difference between samples held at sintering temperature for different times. 5 phases were detected in the samples:  $\text{Nb}_{0.6}\text{Re}_{0.4}$ ,  $\text{Ta}_2\text{C}$ , NbO, W/Mo and Re. While the  $\text{Nb}_{0.6}\text{Re}_{0.4}$  was chosen as the best match for the most intensive observed peaks it is important to note that due to the similarity in their structures refractory metals form many isostructural phases. Hence, the actual phase is most likely composed not only of Nb and Re, but also of W, Mo and Ta as well.

Even though measures were taken to avoid carburization of the material,  $\text{Ta}_2\text{C}$ -type phase was detected. Additionally, minor amount of NbO was also present in the sintered samples.



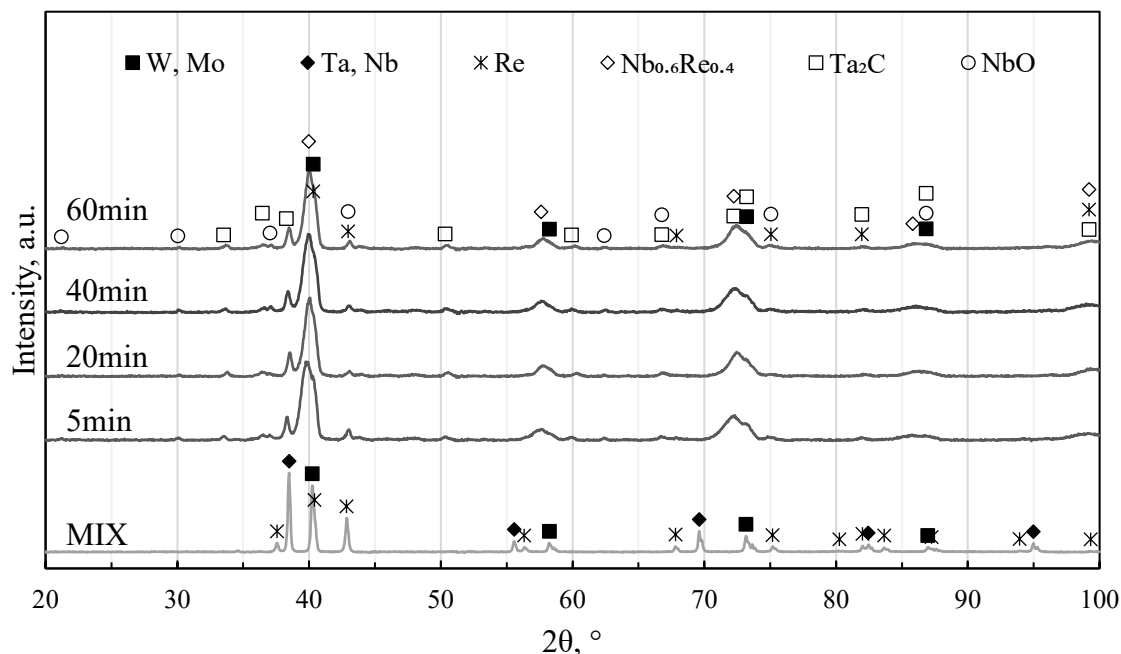


Figure 1. XRD of powder mix and samples sintered with varying holding time.

The results obtained with XRD were confirmed with EPMA. As can be seen in Figure 2, even with holding time of 60 minutes there is clear separation between constituent elements. The apparent co-occurrence of Ta-W-Re and Nb-Mo is mainly due to the similarity in atomic mass. Based on apparent brightness, 4 different regions were observed in all sintered samples. Point EDS analysis revealed, that very dark spots contained Nb, Ta as well as O and/or C. Dark spots consisted of more than 90 at.% Mo with minor Nb, Ta or W additions. Bright regions were determined as areas rich in W, Nb and Ta also being present. Very bright areas contained Re with minor additions of Ta and Nb. Results for sample 40min are presented in Figure 3.

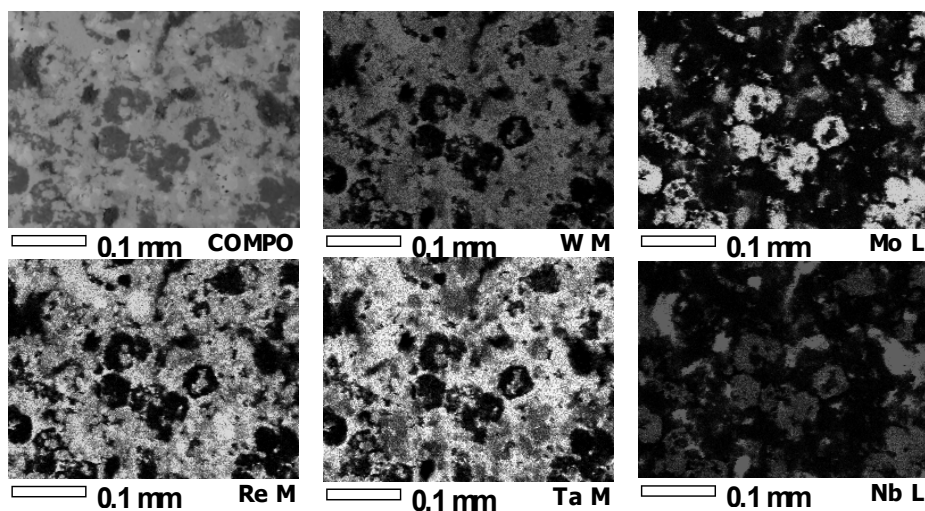


Figure 2. Elemental distribution maps of the sample held at 1600°C for 60 minutes.

At.%	Mo	Nb	Re	Ta	W	O
1	n/a	57.67	n/a	n/a	n/a	42.33
2	94.24	n/a	n/a	5.76	n/a	n/a
3	n/a	11.19	n/a	17.12	71.69	n/a
4	n/a	n/a	100	n/a	n/a	n/a
5	n/a	n/a	100	n/a	n/a	n/a
6	15.79	24.95	22.89	19.85	16.51	n/a

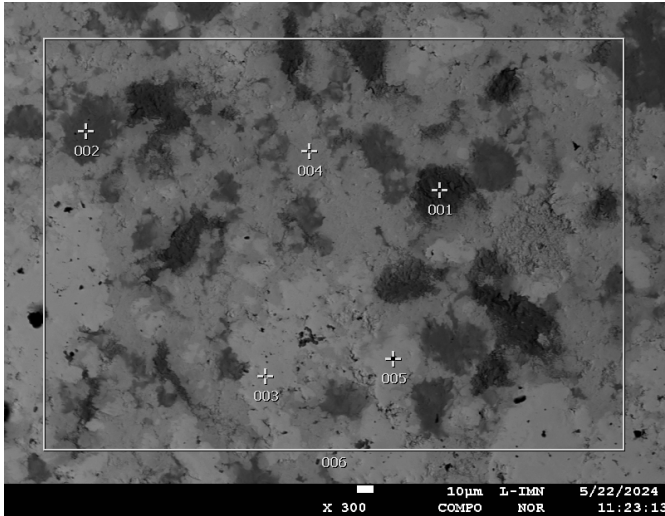


Figure 3. BSE micrograph with marked points/areas of EDS analysis.

As mentioned, density of the sintered samples was measured. Compared with theoretical density ( $15.16\text{g/cm}^3$ ), the density is relatively low and does not exceed 84% (Table 3). However, as XRD and EPMA investigations revealed, chemical composition of the samples differs from the target, as oxides and carbides are present in the material in unknown quantities. Hence, the actual density of a fully compacted material should be lower than theoretical value calculated from the rule of mixtures for a pure alloy.

Rockwell hardness values cannot be simply correlated with density of the samples. Highest hardness value was achieved for sample held in  $1600^\circ\text{C}$  for 40 minutes – 22,2 HRC.

Table3. Density, open porosity, relative density and Rockwell hardness of sintered samples.

Holding time, min	Density, $\text{g/cm}^3$	Open porosity, %	$\rho/\rho_t$ , %	HRC
5	12.29	11.7	81.07	18.0
20	12.66	10.07	83.51	17.7
40	12.6	10.67	83.11	22.2
60	12.69	9.68	83.71	21.0

#### 4. CONCLUSION

For the investigated material, phase composition and chemical homogeneity do not significantly change with the increase of holding time. Hardness did not correlate with achieved density of the sample and was the highest for sample held for 40 minutes at the sintering

temperature (22.2 HRC). Highest achieved density was 83.71% of the theoretical value, which was much lower than anticipated from previous experiments involving individual constituent metals. Medium vacuum did not prevent oxidation of niobium and tantalum, which were elements with the highest propensity for oxygen adsorption used in the mix. Also, significant amount of a carbide phase with a structure based on Ta<sub>2</sub>C was detected. This would indicate, that while hexagonal boron nitride coating on the graphite inserts can help avoid carburization, it does not always fully prevent it. Whether carburization and oxidation occurs only in close proximity to the surface of the samples or in fact in the whole volume will be a topic of further investigations.

While the desired effect of homogenisation was not achieved, further investigations with the use of finer powders, preferably with sizes in the submicron or nanometre range, could yield better results. Such materials are much easier to prepare than a fully mechanically alloyed powder. Additionally, higher sintering temperature could be employed, to promote faster diffusion. Both of those approaches will be investigated in further work.

## BIBLIOGRAPHY

1. B.S. Murty, J.W. Yeh, S. Ranganathan, High Entropy Alloys, Butterworth-Heinemann, 2014.
2. D.B. Miracle, J.D. Miller, O.N. Senkov, C. Woodward, M.D. Uchic, J. Tiley, Exploration and Development of High Entropy Alloys for Structural Applications. *Entropy*, 2014; 16(1):494-525, <https://doi.org/10.3390/e16010494>
3. O.N. Senkov, G.B. Wilks, D.B. Miracle, C.P. Chuang, P.K. Liaw, Refractory high-entropy alloys, *Intermetallics*, Volume 18, Issue 9, 2010, Pages 1758-1765, ISSN 0966-9795, <https://doi.org/10.1016/j.intermet.2010.05.014>.
4. O.N. Senkov, G.B. Wilks, J.M. Scott, D.B. Miracle, Mechanical properties of Nb<sub>25</sub>Mo<sub>25</sub>Ta<sub>25</sub>W<sub>25</sub> and V<sub>20</sub>Nb<sub>20</sub>Mo<sub>20</sub>Ta<sub>20</sub>W<sub>20</sub> refractory high entropy alloys, *Intermetallics*, Volume 19, Issue 5, 2011, Pages 698-706, ISSN 0966-9795, <https://doi.org/10.1016/j.intermet.2011.01.004>.
5. D.B. Miracle, O.N. Senkov, A critical review of high entropy alloys and related concepts, *Acta Materialia*, Volume 122, 2017, Pages 448-511, ISSN 1359-6454, <https://doi.org/10.1016/j.actamat.2016.08.081>.
6. Bingqing Chen, Longchao Zhuo, Latest progress on refractory high entropy alloys: Composition, fabrication, post processing, performance, simulation and prospect, *International Journal of Refractory Metals and Hard Materials*, Volume 110, 2023, 105993, ISSN 0263-4368, <https://doi.org/10.1016/j.ijrmhm.2022.105993>.
7. C. Suryanarayana, Mechanical alloying and milling, *Progress in Materials Science*, Volume 46, Issues 1–2, 2001, Pages 1-184, ISSN 0079-6425, [https://doi.org/10.1016/S0079-6425\(99\)00010-9](https://doi.org/10.1016/S0079-6425(99)00010-9).



17th-19th June 2024  
Gliwice, Poland

DEPARTMENT OF ENGINEERING MATERIALS AND BIOMATERIALS  
FACULTY OF MECHANICAL ENGINEERING  
SILESIA UNIVERSITY OF TECHNOLOGY

## INTERNATIONAL STUDENTS SCIENTIFIC CONFERENCE

### Using laser and 3D printing in fashion

Michał Pietruszka <sup>a</sup>, Olaf Sobek <sup>a</sup>, Magdalena Szindler <sup>b</sup>, Mirosław Bonek <sup>b</sup>

<sup>a</sup> Silesian University of Technology, Faculty of Mechanical Engineering, Student of Engineering Production and Management, Gliwice

<sup>b</sup> Silesian University of Technology, Faculty of Mechanical Engineering, Department of Engineering Materials and Biomaterials

**Abstract:** The use of laser and 3D printing in fashion focuses on the innovative ways in which advanced technologies such as 3D printing and lasers are being used in the fashion industry. It discusses how fashion designers are using these technologies to create unique and bespoke garments, accessories and jewellery. Examples of the use of 3D printing to create custom garments, such as decorative accents and details, and the use of lasers to cut fabrics into precise patterns and shapes are presented. It also highlights the impact these cutting-edge technologies are having on the development of fashion, enabling designers to be more creative, produce faster and take a more personalised and environmentally friendly approach to the design and creation of clothing and accessories.

**Keywords:** 3D printing in fashion, laser cutting, fashion, design

### 1. INTRODUCTION

Fashion has always reflected creativity, innovation and technological progress. In recent years, these three elements have come together in a unique way thanks to two groundbreaking technologies: 3D printing and laser cutting. Both methods have revolutionised the design and production processes of clothing and accessories, opening up entirely new possibilities for designers and consumers.

### 2. THE USE OF LASER CUTTING IN FASHION

Laser fabric cutting uses lasers to cut the fabric into the desired shapes. A very thin laser beam is focused on the surface of the fabric, which significantly increases the temperature and causes evaporation, enabling precise cutting. CO2 lasers are most commonly used here. Unlike traditional knife cutting, the laser beam does not blunt and does not require sharpening.

Laser cutters are very efficient in many ways. Firstly, the main advantage of laser cutters is their speed. The laser cutting process is much faster than traditional cutting methods, allowing for high-volume production in a short period of time[3]. Laser cutting machines are safer,

easier to maintain and can last longer. Integration with computer technology enables products to be produced according to computer designs. Laser cutting is faster and easier to use.

Laser cutting machines are ideal for cutting a wide variety of materials, such as textile fabrics, composites, leather and moulded materials. They allow you to work with a wide range of fabrics, making them increasingly popular in the garment and textile industry. Advantages of using lasers include:

1. ability to cut, engrave and perforate in a single process
2. high cutting quality without mechanical wear
3. no need to clamp the material
4. clean cut edges
5. simple process thanks to computer-aided design
6. extremely precise contour cutting
7. fast working speed
8. contact-free technology
9. no chip formation, reducing waste and costs

### **3. USE OF LASER IN GARMENT MANUFACTURING**

1. Fabric cutting: laser cutting allows precise cutting of fabrics without the need for a blade, eliminating the risk of damaging the material.
2. engraving and marking: the laser can be used to engrave or mark designs, logos or labels on fabrics and garments, adding a personal touch to products.
3. Perforation: The laser can punch or perforate into fabrics, creating unique patterns or effects.
4. Detail creation: Laser cutting allows the precise cutting of intricate details, e.g. pockets, holes, improving the quality and appearance of garments.

### **4. USE OF LASER IN THE PRODUCTION OF CLOTHING ACCESSORIES**

1. Logo engraving on metal cufflinks: The laser can precisely engrave company logos or individual designs on metal cufflinks, adding an exclusive look.
2. Cutting leather for decorative handbag details: The laser can cut intricate patterns and details from natural or synthetic leather, which can then be used as decorations on handbags, wallets or key rings.
- 3 Making perforations on leather straps: The laser can precisely produce evenly spaced perforations on leather straps, creating a striking pattern or allowing the length of the strap to be adjusted.
4. Brand name branding on metal belt buckles: The laser can permanently mark a brand name or logo on metal belt buckles, creating elegant and personalised accessories.
5. Felt cutting on caps: The laser can cut precise patterns from felt, which can then be applied to hats as original decorations, adding character and style.
6. Engraving wooden buttons: The laser can engrave individual designs, symbols or lettering onto wooden buttons, giving them a unique look and feel.

## **5. 3D PRINTING IN FASHION**

3D printing in fashion clothing is revolutionising the way garments are designed and manufactured. The technology allows designers to create custom, unique patterns and textures that are difficult to achieve with traditional tailoring methods. Furthermore, 3D printing in fashion enables customization by providing customers with clothing suited to their specific proportions[7]. Using 3D printing, it is possible to create garment elements such as embellishments, buttons or even entire pieces of clothing that are lightweight, durable and perfectly tailored to individual customer needs and tastes. In addition, 3D printing allows for a variety of materials to be used in the production of garments, opening the way for experimentation with new textures and structures.

## **6. 3D PRINTING OF CLOTHING:**

1. Personalisation: 3D printing enables the personalisation of clothing, accessories and jewellery, allowing customers to create items perfectly tailored to their individual preferences and dimensions.
2. Innovative design: This technology opens the door to creating innovative designs and shapes that are difficult or impossible to achieve with traditional manufacturing methods.
3. Speed of production: 3D printing enables rapid production of prototypes and small batches of products, reducing the time it takes to bring new designs to market.
4. Diverse materials: With 3D printing, it is possible to experiment with different materials, from plastic to metal, allowing the creation of garments and accessories with different properties and textures.
5. Sustainable manufacturing: 3D printing can contribute to more sustainable production, as it minimises material waste and reduces energy consumption compared to traditional manufacturing methods.

## **7. 3D PRINTING OF ACCESSORIES**

3D printing in fashion accessories such as bracelets provides an innovative approach to the design and production of these pieces. Instead of traditional handmade methods, 3D printing allows bracelets to be precisely created from a variety of materials, such as plastic, metal or even ceramic, according to a chosen pattern or design. One of the biggest advantages of 3D printing in accessory manufacturing is the possibility of personalisation. Customers can choose from ready-made designs or have a bracelet created exactly according to their preferences. These can include unique designs, initials or even dedicated designs[6].

This opens up a world of possibilities for creating intricate filigree, interlocking patterns, and geometric shapes that were previously difficult to achieve by hand [2]. Additionally, with 3D printing, accessories can be produced quickly and with fewer materials, which can be more eco-friendly and cost-effective. As a result, 3D printing is revolutionising fashion accessories, enabling the design and creation of unique, personalised and innovative bracelets and other accessories that express customers' individuality and style.

## 8. INNOVATIVE IDEAS FOR USING 3D PRINTING AND LASER CUTTING IN FASHION (EXAMPLES)



Picture 1 - photo of 3D printed sole[1]

## 9. SHOE SOLES

Shoe soles are an innovative solution that is revolutionising the footwear industry by offering new possibilities in terms of design, personalisation and functionality. The technology allows soles to be created layer by layer using materials such as elastomers, plastics or composites. Such soles can be used in sports, orthopaedic footwear or on fashion catwalks.

The advantages of such soles are:

- the possibility of personalisation and customisation
- creation of complex structures
- speed of prototyping
- sustainability



Picture 2 – laser cut dress [4]

## 10. FINISHING AND DETAILING

Laser cutting is becoming increasingly popular in fashion. It can be used to cut custom designs on leather or other materials used to make shoes, skirts, T-shirts etc. allowing original details to be created.

The main benefits associated with the use of laser cutting in fashion [5]:

1. High Speed and Productivity
2. Complex and Creative Designs
3. Rapid Prototyping
4. Customization and On-demand Production
5. Streamlined Production
6. Faster, Cleaner, and More Adaptable

## 11. SUMMARY

In recent years, the fashion industry has seen a rapid increase in the use of advanced technologies such as 3D printing and laser cutting. These innovative tools allow designers to create unique, precise and often previously impossible patterns and textures. 3D printing makes it possible to produce customised pieces with minimal material consumption, reducing environmental impact. Laser cutting of fabrics, on the other hand, ensures high precision and allows experimentation with different patterns and textures. These technologies not only expand the creative possibilities for designers, but also contribute to the growth of sustainable production in the fashion industry. As technology continues to advance, we can expect to see more innovations that will further develop this field.



**BIBLIOGRAPHY**

1. [1] <https://3don.pl/druk3d/newsy/4159/drukarki-3d-stworza-buty-adidasa> [access:27.05.2024]
2. [2] IN3DTEC <https://www.in3dtec.com/the-application-of-3d-printing-in-fashion/> [access:27.05.2024]
3. [3] Xometry <https://www.xometry.com/resources/sheet/laser-cutting-in-textile-industry/> [access:27.05.2024]
4. [4] Laserowe wycinanie tkanin <https://lasertrade.pl/laserowe-wycinanie- tkanin> [access:27.05.2024]
5. [5] Leather Laser Engraving & Cutting: A Comprehensive Guide <https://www.thunderlaser.ca/leather-laser-cutting/> [access:27.05.2024]
6. [6] How 3D Printing Allows for Customizable Consumer Goods <https://www.3dnatives.com/en/consumer-goods-3d-printing-08022023/> [access:27.05.2024]
7. [7] 3D Printing Fashion Accessories (and the Industry) <https://www.elegoo.com/blogs/3d-printing-projects/3d-printing-in-fashion#chapter5> [access:27.05.2024]



17th-19th June 2024  
Gliwice, Poland

DEPARTMENT OF ENGINEERING MATERIALS AND BIOMATERIALS  
FACULTY OF MECHANICAL ENGINEERING  
SILESIA UNIVERSITY OF TECHNOLOGY

## INTERNATIONAL STUDENTS SCIENTIFIC CONFERENCE

### Computer simulation of hip joint loading

Jakub Polis<sup>a</sup>, Jakub Bicz<sup>a</sup>, Zuzanna Buchaj<sup>b</sup>, Rafał Szymik<sup>c</sup>, Zuzanna Zielińska<sup>c</sup>, Mateusz Szojda<sup>d</sup>, Agata Śliwa<sup>e</sup>, Marek Sroka<sup>e</sup>, Amadeusz Dziwis<sup>e</sup>, Wojciech Mikołajko<sup>e</sup>

<sup>a</sup> Student of Silesian University of Technology, Faculty of Mechanical Engineering  
email: jakupol064@student.polsl.pl; jakubic839@student.polsl.pl

<sup>b</sup> Student of Silesian University of Technology, Faculty of Biomedical Engineering  
email: zb301191@student.polsl.pl

<sup>c</sup> Student of Silesian University of Technology, Faculty of Materials Engineering  
e-mail: zz304779@student.polsl.pl; rs301942@student.polsl.pl

<sup>d</sup> Student of the Academic High School of the Silesian University of Technology in Gliwice  
email: matiszozjda@icloud.com

<sup>e</sup> Silesian University of Technology, Faculty of Mechanical Engineering, Department of Engineering Materials and Biomaterials

email: agata.sliwa@polsl.pl; marek.sroka@polsl.pl; amadeusz.dziwis@polsl.pl; wojciech.mikolajko@polsl.pl

**Abstract:** This paper presents an FEM analysis of the distribution of stresses, displacements and deformations caused by a specific force on a hip replacement, depending on the material used – which was a Ti-6Al-4V alloy and high-density polyethylene (PE-HD). The analysis was carried out using SOLIDWORKS software. The areas of highest stress and displacement were determined, as well as the value of the critical force at which deformation of the component occurs.

**Keywords:** hip endoprosthesis, FEM analysis, stresses, deformations.

### 1. INTRODUCTION

The hip joint is one of the most stressed joints in the human body. It is characterised by a complex and fragile structure, that has to function under extreme and constantly stressed conditions. The performance of the hip joint is due to the combination of articular cartilage and connective (load-bearing) tissues surrounding the articulated joint with nutrient fluid (synovial fluid) released in the articulated area. In a pair of normal articulated joints, wear and tear occurs in rare cases, because the presence of synovial fluid and cartilage – that provide proper lubrication between the articulating surfaces. When this cartilage becomes damaged or infected due to arthritis, further damage occurs due to reduced joint function. In a normal synovial joint, there is an articular cartilage ependyma and synovial fluid flowing between them, making movements easy to perform; but when someone is struggling with osteoarthritis or rheumatoid

arthritis, performing the simplest of movements can be downright impossible. Osteoarthritis is an age-related condition in which the cartilage ependyma wears away, causing bone friction – which results in pain. Rheumatoid arthritis, on the other hand, is an age-independent condition, in which the patient struggles with swelling of the cartilage ependyma, followed by bone erosion, ligament damage – resulting in restricted movement for the patient. Therefore, in both cases, it is necessary to remove the patient's hip joint and replace it with a hip joint endoprosthesis. The hip endoprosthesis implantation procedure is one of the most commonly performed orthopedic procedures in the world – and it can significantly improve patient's quality of life [1, 2].

Implant placement always results in an inflammatory response and increased blood supply to the tissues around the implant, as evidenced by their redness. Along with the blood, leukocytes are supplied, which are responsible for the body's response to the foreign body that is the implant – among them monocytic cells, which transform into macrophages at the inflamed site. As a result of their activity, fibroblasts are also activated – which in turn produce collagen, contributing to the formation of a fibrous, collagenous capsule around the implant insulating it from the surrounding tissues. The thickness of the fibrous capsule increases with prolonged phagocytic activity of macrophages and is also an indicator of the biocompatibility of the implant. A significant thickness of the fibrous capsule, together with prolonged inflammation, is indicative for poor implant biocompatibility. The formation of a fibrous capsule of considerable thickness prevents proper osseointegration of the implant, which can lead to implant loosening [3, 4, 5].

The use of metals as implant materials is also linked to the problem of corrosion in the aggressive environment found inside the human body. This is due to the nature of the body fluids, which contain, among other things, chlorine, sodium, potassium, calcium and magnesium ions – as well as phosphates and proteins. The intensity of the corrosion phenomena is further influenced by the constant, relatively high temperature prevailing inside the body – as well as the stresses and tribological conditions under which the implant operates. Under normal conditions, body fluids have a pH level of around 7.4 – however, when there is inflammation, they can become acidic in surroundings of the implant – reaching a pH level of 3-4. All these characteristics make the living organism a very demanding environment, which not every material can withstand [3, 4].

As a result of corrosion processes, metal ions are released from the surface of the implants, which accumulate in the tissues surrounding the implant – and in other soft tissues, such as the liver. This can result in allergic reactions or, in extreme cases, metallosis, which manifests itself in the death of tissues surrounding the implant. In addition, some of the elements in the metal alloys used have toxic and carcinogenic effects [3].

## 2. MATERIALS AND METHODOLOGY

The analysed component of a hip endoprosthesis is a head, neck assembly with an angle of 135° and a stem. Two models of the endoprosthesis are presented, made of Ti-6Al-4V alloy and high density polyethylene, respectively. The main consideration is that the endoprosthesis should be able to carry a load of 2.300 N without losing its integrity. In addition, the material used should be biologically safe for the patient.

### 3. SELECTION OF MATERIALS

One of the most promising metallic biomaterials are titanium alloys. Taking into account their structure, titanium alloys can be divided into single-phase  $\alpha$  alloys, alloys with a dual-phase  $\alpha+\beta$  structure and single-phase  $\beta$  alloys. For the manufacture of implants used in orthopedics, alloys with an  $\alpha+\beta$  and  $\beta$  structure are used, due to the insufficient strength properties of  $\alpha$  alloys. Titanium alloys with a dual-phase structure include the Ti-6Al-4V alloy used in the simulation. These materials can be successfully used to produce long-term implants due to their high corrosion resistance, biocompatibility and good fatigue resistance. The factor contributing to the high biocompatibility of titanium alloys is ability to formation of passive oxide layer on their surface. Formation of the passive layer occurs immediately after exposure of the material to oxygen – it reaches a thickness of 2÷5 nm in one second and increases over time, eventually reaching a thickness of 6÷10 nm [1, 3, 6].

The use of titanium for the manufacture of long-lasting implants is also favoured by its unique – in comparison to other metallic biomaterials – ability to form a bond with bone. As mentioned, a fibrous, collagenous envelope is formed around the implant as a result of the body's defence response. When stainless steel or Co-Cr-Mo alloys are used as the implant material, the resulting thick layer of fibrous tissue prevents proper osseointegration of the implant, which can lead to implant loosening. In contrast, for titanium alloys, the encapsulation is minimal – and the implant shows the ability to integrate with the surrounding bone tissue. The mechanism of bonding to bone tissue is multistage – it is assumed that, at first, a layer of titanates (such as  $\text{NaTiO}_3$ ) is being formed on the surface of the implant through ion exchange, which are then replaced by carbonated hydroxyapatite (hydroxyapatite in which some of the phosphate ions are replaced by carbonate ions) through further reactions. Then, collagen fibres penetrate the carbonated hydroxyapatite layer, forming a connection between the implant and the bone tissue. Various techniques are used to modify the surface of titanium alloy implants to improve implant osseointegration. One of these is the application of hydroxyapatite coating – deposited using plasma spraying or physical vapour deposition methods – such as pulsed laser deposition (PLD) method. It has been demonstrated that osseointegration is also favored by a developed implant surface – hence, various methods are used to increase the contact surface, such as acid etching and sandblasting [3, 5, 6].

Table 1. Chemical composition of Ti-6Al-4V alloy [7]

Chemical element	Min [%]	Max [%]
V	3.5	4.5
Al	5.5	6.75
Fe	-	0.3
O	-	0.2
C	-	0.08
N	-	0.05
H	-	0.015
Y	-	0.005
Ti	Balance*	

\* The percentage of titanium is determined by difference and does not need to be determined or certified.

Table 2. Selected mechanical and physical properties of Ti-6Al-4V alloy

Elasticity modulus [N/m <sup>2</sup> ]	1.048003*10 <sup>18</sup>
Poisson's ratio	0.31
Shear stress ratio [N/m <sup>2</sup> ]	4.102381*10 <sup>17</sup>
Specific mass [kg/m <sup>3</sup> ]	4428.784
Ultimate tensile strength [N/m <sup>2</sup> ]	1.05*10 <sup>9</sup>
Yield strenght [N/m <sup>2</sup> ]	8.273709*10 <sup>8</sup>
Thermal expansion coefficient [K]	9*10 <sup>-6</sup>
Thermal conductivity coefficient [W/(m*K)]	586.04
Specific heat [J/(kg*K)]	586.04

High-density polyethylene (PE-HD) is the one of the cheapest and most widely used variety of polyethylene. It is characterized by a crystallinity of 60-80%. Compared to other polymeric materials, it has a high specific strength and good ultimate tensile strength. Polyethylene has a high level of biocompatibility, but can be degraded in body fluid environment – leading to a deterioration of mechanical properties. Another limitation is its low melting point and tendency to deform under high temperature and pressure – making it impossible to be sterilized by conventional methods [8, 9].

Biomedical applications mainly use high-density polyethylene and ultra-high molecular weight polyethylene (UHMWPE). High-density polyethylene is commonly used as an implant material for plastic and reconstructive surgery. A variety of UHMWPE is commonly used to manufacture hip replacement acetabular cups. This has been attributed to the fact that the combination of a polyethylene acetabulum with a metal or ceramic endoprosthesis head provides relatively low friction resistance, as well as relatively good wear resistance [8, 10].

Table 3. Selected mechanical and physical properties of PE-HD

Elasticity modulus [N/m <sup>2</sup> ]	1,07*10 <sup>9</sup>
Poisson's ratio	0.4101
Shear stress ratio [N/m <sup>2</sup> ]	3.772*10 <sup>8</sup>
Specific mass [kg/m <sup>3</sup> ]	952
Ultimate tensile strength [N/m <sup>2</sup> ]	2.21*10 <sup>7</sup>
Heat transfer coefficient [W/(m*K)]	0.461
Specific heat [J/(kg*K)]	1796

#### 4. CAD GEOMETRIC MODEL

A model of the hip endoprosthesis was made using SOLIDWORKS to carry out strength analysis by means of computer simulation. The designed hip endoprosthesis model is shown in Figure 1a.

#### 5. BOUNDARY CONDITIONS

The loading and boundary conditions used are in accordance with ASTM F2996-13 and ISO 7206 4:2010(E) [11]. The following boundary conditions were adopted in the computer simulation:

- A finite element mesh was superimposed on the hip endoprosthesis model (Figure 1b),
- A force of 2.300 N was applied, the value of which is derived from ASTM F2996-13 and ISO 7206-4:2010(E) (Figure 1c),
- The location of force application and immobilisation geometry of the hip endoprosthesis model are shown in Figure 1c.

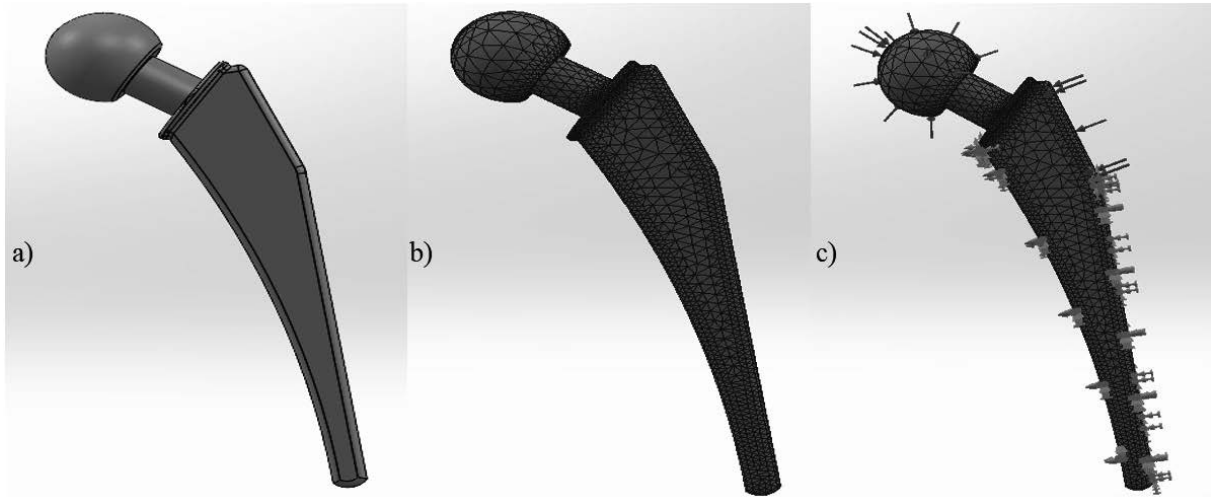


Figure 1. CAD model of hip endoprosthesis (a); with superimposed finite element mesh (b); with superimposed finite element mesh, visible direction of forces and immobilised endoprosthesis geometry (c)

## 6. ANALYSIS OF RESULTS

### 6.1 Results of numerical stress analysis

The analysis was based on the Huber-Mises hypothesis. After loading the component, stress diagrams were obtained, the values of which are expressed in MPa. Figure 2 shows the distribution of stresses developed during the given loading.

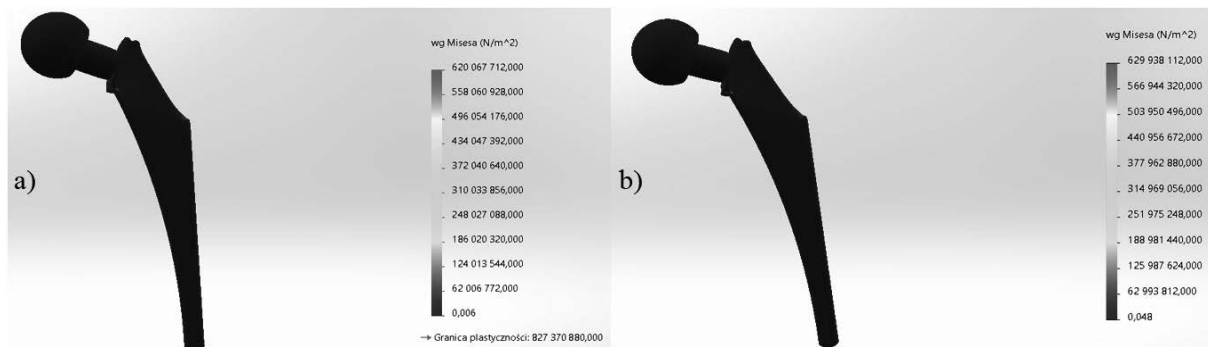


Figure 2. Huber-Mises stress reduction distribution for Ti-6Al-4V alloy (a) and PE-HD (b)

### 6.2 Results of the numerical analysis of displacements

The purpose of the subsequent computer simulation carried out was to determine the magnitude of the displacement under a given force and to generate displacement diagrams of the structure,

which are shown in Figure 3. As a result of the load, the geometric dimensions of our model can change. The largest displacement in each material analysed occurred at the head surface of the endoprosthesis.

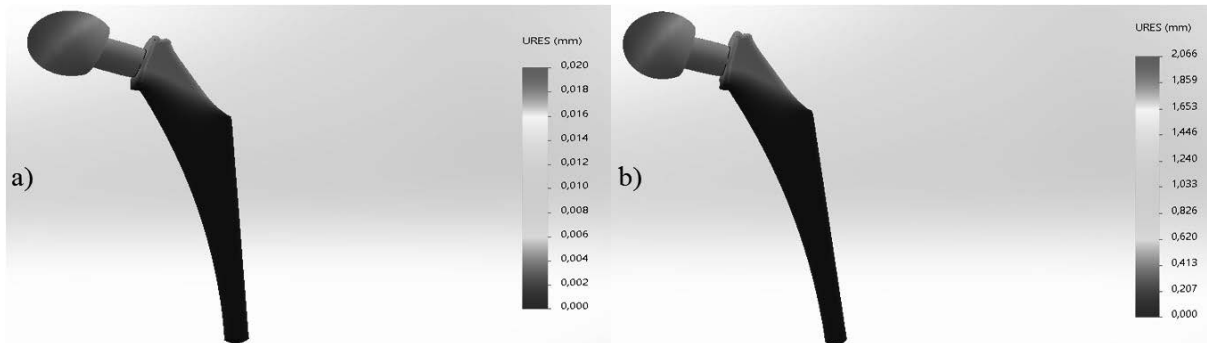


Figure 3. Displacement distribution for Ti-6Al-4V alloy (a) and PE-HD (b)

### 6.3 Results of numerical analysis of equivalent deformation

The last simulation carried out was to determine the critical force causing the deformation. Figure 4 shows the equivalent deformation represented by the largest force required to deform the axis.

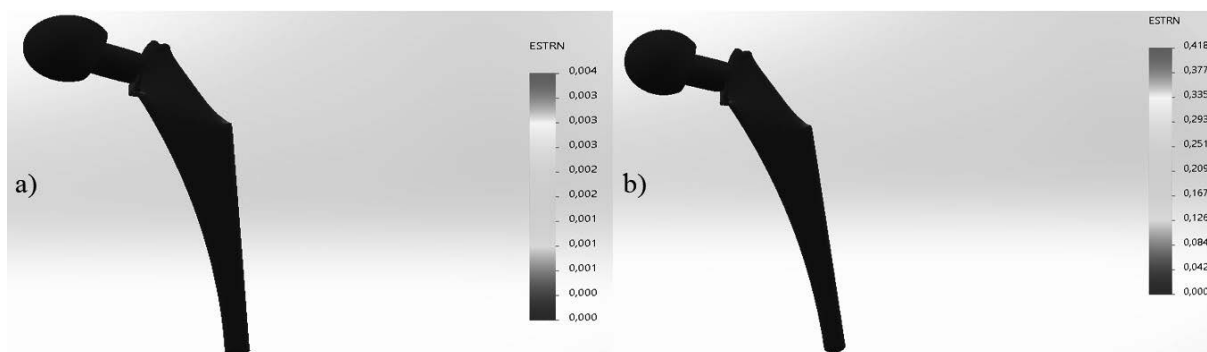


Figure 4. Equivalent deformation for Ti-6Al-4V alloy (a) and PE-HD (b)

The overall results of the simulations performed are shown in Table 4.

Table 4. Summary of overall results from computer simulations carried out

Material used	Maximum stress value [MPa]	Maximum displacement [mm]	Maximum deformation value
Ti-6Al-4V alloy	620.067	0.020	0.004
PE-HD	629.938	2.066	0.418

## 7. CONCLUSION

The results of the strength analysis indicate that, of the materials analysed, Ti-6Al-4V alloy is the most suitable material for use in hip endoprostheses. This is because it showed negligible displacement and deformation values, even when subjected to significant loading, at stresses

similar to those of the polymeric material PE-HD. In the case of PE-HD, when a significant force is applied, there is a significant deformation of the material – which can significantly reduce the functionality of the implant and pose a potential danger to the user. The deformation in this case is due to the limited mechanical properties of the polymer materials. However, advanced work is underway to implement this group of materials as replacements for components made of other engineering materials – including metal alloys.

The highest stresses were obtained when PE-HD was used. However, it is worth noting that the difference between the materials analysed is insignificant – amount only 9 MPa.

Larger displacement was recorded for the model made of high-density polyethylene – the displacement value is more than 100 times that of the alloy Ti-6Al-4V.

For the use of PE-HD as the implant material, the highest strain was also obtained – while the strain value recorded for the alloy Ti-6Al-4V, is more than 100 times lower.

## BIBLIOGRAPHY

1. Shekhawat D., Singh A., Patnaik, A., Tribo-behaviour of biomaterials for hip arthroplasty. *Materials Today: Proceedings*, 2021.
2. T. Ahlroos, Effect of lubricant on the wear of prosthetic joint materials, *Acta Polytechnica Scandinavica, Mechanical Engineering Series*, 2001.
3. Świczko-Żurek B., *Biomateriały*, Wyd. Politechniki Gdańskiej, Gdańsk, 2009.
4. Chen Q., Thouas G. A., *Metallic implant biomaterials. Materials Science and Engineering: R: Reports*, 87, 2015, p.1–57.
5. Manmeet Kaur, K. Singh, Review on titanium and titanium based alloys as biomaterials for orthopaedic applications, *Materials Science and Engineering: C*, volume 102, 2019, p.844-862.
6. Dobrzański L.A., *Podstawy nauki o materiałach i metaloznastwo*, Wydawnictwo Naukowo-Techniczne, Warszawa, 2002.
7. <http://bqw.csstgc.com.cn/userfiles/04d50d7598c54325a4f12f868710a407/files/teckSolution/2019/11/Standard%20Specification%20for%20Wrought%20Titanium-6Aluminum-4Vanadium%20Alloy%20for%20Surgical%20Implant%20> – dostęp 19.05.2024 r.
8. Paxton N. C., Allenby, M. C. Lewis, P. M., Woodruff M. A., *Biomedical applications of polyethylene*, *European Polymer Journal*, 2019.
9. <https://www.plastech.pl/plastechopedia/HDPE-PE-HD-98> – data dostępu 19.05.2024 r.
10. Gierzyńska-Dolna M., Wiśniewska-Weinert H., Adamus J., Tribologiczne i materiałowe uwarunkowania stosowania endoprotez stawowych, *Tribologia* 1, 2009, p.47-62.
11. Chethan K. N., Shyamasunder Bhat N., Zuber M., Satish Shenoy B., Finite element analysis of hip implant with varying in taper neck lengths under static loading conditions, *Computer Methods and Programs in Biomedicine*, 2021.





17th-19th June 2024  
Gliwice, Poland

DEPARTMENT OF ENGINEERING MATERIALS AND BIOMATERIALS  
FACULTY OF MECHANICAL ENGINEERING  
SILESIA UNIVERSITY OF TECHNOLOGY

## INTERNATIONAL STUDENTS SCIENTIFIC CONFERENCE

### Computer simulation of crankshaft loading

Jakub Polis<sup>a</sup>, Jakub Bicz<sup>a</sup>, Agata Śliwa<sup>b</sup>

<sup>a</sup> Student of Silesian University of Technology, Faculty of Mechanical Engineering  
email: jakupol064@student.polsl.pl; jakubic839@student.polsl.pl

<sup>b</sup> Silesian University of Technology, Faculty of Mechanical Engineering, Department of Engineering Materials and Biomaterials  
email: agata.sliwa@polsl.pl

**Abstract:** This paper presents an FEM analysis of the distribution of stresses, displacements and deformations resulting from the application of a specific pressure value to the crankshaft, depending on the material used – which were C17000 beryllium bronze, aluminium alloy AA6061 T6 and titanium alloy Ti-6Al-4V. The analysis was carried out using SOLIDWORKS software. The locations with the highest stress and displacement values were determined, as well as the value of the critical force at which deformation of the component occurs.

**Keywords:** aluminium alloy, beryllium bronze, crankshaft, deformations, displacements, FEM analysis, material selection, stresses, titanium alloy.

### 1. INTRODUCTION

Crankshaft is one of the key components of internal combustion engine. Using crankshaft, reciprocate motion of pistons is being converted into rotational motion. Obtained torque is being transmitted via flywheel to clutch, propelling also part of auxiliary devices of engine – like pumps, compressors and generators [1, 2].

In crankshaft structure, main journals and crankpins can be distinguished – which are being connected by the crank webs. Main journals are being positioned on one axis, allowing to bear the in crankcase. Crankpins in turn, allow to embed the connecting rod bearings. In order to properly weighting of crankshaft, counterweights are being used [1, 2].

Most commonly crankshafts are made from forged steel or cast iron. For heavy loads, much more expensive alloy steels are used, e.g. chrome-manganese, chrome-nickel and chrome-nickel-molybdenum. In a few cases of traction engines, cast shafts made of cast steel and perlitic malleable or ductile iron are encountered. Previously, carbon steels are used, or steels containing minor addition of sulphur – in order to improve machinability. However, for high strength applications sulphur content cannot be higher than 0.12%. After machining, crankshafts are subjected to quenching with subsequent tempering. More recently, micro-alloyed steels containing vanadium are being commonly used. Forged or cast crankshafts are used, less often assembled [2, 3].

In order to obtain a hardened surface, the crankshaft is subjected to a flame or induction hardening process. The hardness obtained is 50-60 HRC for carbon steel and the thickness of the hardened layer is 2-4mm [3].

The observed increase in engine power ratings obtained from 1dm<sup>3</sup> of displacement is realized as a result of an increase in average useful pressure and an increase in rated speeds. For these reasons, the crankshaft should provide adequate stiffness, which depends on the dimensions of the shaft. Therefore, the crankshafts of modern automotive internal combustion engines are arranged between each cylinder [4].

## 2. MATERIALS AND METHODOLOGY

The analysed component is a monolithic crankshaft of four-cylinder combustion engine. Three models of the crankshaft are presented, made of C17000 beryllium bronze, AA6061 T6 and Ti-6Al-4V alloy, respectively. The main assumption is that the crankshaft should be able to withstand pressures of 40 MPa without loss of integrity.

## 3. SELECTION OF MATERIALS

As it was mentioned earlier, as crankshaft materials, C17000 beryllium bronze, AA6061 T6 and Ti-6Al-4V alloy were used. Selected mechanical properties of these materials are summarized in Table 1.

Table 1. Selected mechanical and physical properties of materials used in simulation.

Material Property	C17000 beryllium bronze	AA6061 T6 alloy	Ti6-Al-4V alloy
Elasticity modulus [N/m <sup>2</sup> ]	1.15*10 <sup>11</sup>	6.9*10 <sup>10</sup>	1.048003*10 <sup>11</sup>
Poisson's ratio	0.3	0,33	0,31
Shear stress ratio [N/m <sup>2</sup> ]	5*10 <sup>10</sup>	2.6*10 <sup>10</sup>	4.102381*10 <sup>10</sup>
Specific mass [kg/m <sup>3</sup> ]	8260	2700	4428.784
Ultimate tensile strength [N/m <sup>2</sup> ]	4.83*10 <sup>8</sup>	3.1*10 <sup>8</sup>	1.05*10 <sup>9</sup>
Yield strenght [N/m <sup>2</sup> ]	2.21*10 <sup>8</sup>	2.75*10 <sup>8</sup>	8.27*10 <sup>8</sup>
Thermal expansion coefficient [K]	1.67*10 <sup>-5</sup>	2.4*10 <sup>-5</sup>	9*10 <sup>-6</sup>
Thermal conductivity coefficient [W/(m*K)]	118	166.9	6.7
Specific heat [J/(kg*K)]	-	896	586.04

### C17000 beryllium bronze

Beryllium copper alloys, described also as beryllium bronzes, containing between 0.4 and 2.0% of Be. Beryllium bronzes exhibit good conductivity, corrosion resistance and non-sparking characteristics. Furthermore, these alloys distinguishes with the highest strength properties among the copper-based alloys – achieved after appropriate heat treatment. Beryllium bronzes are susceptible to precipitation hardening, as the solubility of beryllium in copper decreases from 2.7% at 870°C to 0.2% at ambient conditions. These alloys can be divided into two categories – simple, composed only of copper and beryllium and complex, containing also additional alloying elements, such as manganese, iron, cobalt, nickel or titanium. Addition of alloying elements, such as cobalt or nickel contribute to more effective response to precipitation hardening. In effect, complex beryllium bronzes exhibit significantly higher strength properties, which translate into their wider usage [5-8].

Heat treatment of beryllium bronzes includes solution annealing with soaking at 720 - 760°C and quenching to obtain a supersaturated state. Subsequently, aging at 300 - 400°C is conducted. Microstructure obtained as result of the treatment is comprised of metastable  $\gamma'$  and  $\gamma''$  phase precipitates, uniformly dispersed in  $\alpha$  solid solution. Precipitates cause hindering of dislocation motion, contributing to increase in strength properties. After precipitation hardening, tensile strength of these alloys can reach 1300 - 1400 MPa. Beryllium bronzes are being used for bearings, springs, tools, and structural components of aircrafts – which is due to their high strength and good fatigue resistance. Furthermore, due to high electrical conductivity, their applications include also electrical components – such as electrical contacts [5-7]. In simulation C17000 beryllium bronze was used – their chemical composition was presented in Table 2.

Table 2. Chemical composition of C17000 beryllium bronze [9]

Element	Min [%]	Max [%]
Be	1,6	1.85
Al	-	0.20
Si	-	0.20
Co + Ni	0.20	-
Co + Ni + Fe	-	0.60
Cu	99.5	-

### Ti-6Al-4V alloy

Titanium is the ninth most abundant element on Earth, belonging to group of transitional metals. It exhibits two allotropic varieties –  $Ti\alpha$ , crystallizing in hexagonal close packed structure, which occurs under 882.5°C and  $Ti\beta$  existing in temperatures above that value. Titanium alloys exhibit exceptional properties, such as excellent resistance to corrosion and high specific strength – 1.5 time higher than steels. Furthermore, titanium alloys maintain high strength in high temperatures. It is possible to obtaining alloys with single-phase  $\alpha$ , dual-phase  $\alpha + \beta$  and single-phase  $\beta$  alloys. In order to stabilize the  $\beta$  phase alloying elements contributing to decrease of the transus temperature are being used, called  $\beta$  stabilizers. Examples of such additions are, among others, V, Mo, Cr and Fe [10 - 12].

The  $\alpha + \beta$  alloys exhibit 10 – 50% volume content of  $\beta$  phase in ambient conditions. These alloys can be subjected to precipitation hardening – consisting of solution treatment

and aging, leading to significant enhancement of mechanical properties. In effect of appropriate heat treatment, their strength can be enhanced by 20 - 30% [10].

Ti-6Al-4V alloy, used in simulation is one of the most commonly used titanium alloys, accounting nearly 60% of annual titanium alloys production. As it belongs to  $\alpha + \beta$  alloys, it is possible to increase their strength by heat treatment [13]. Chemical composition of Ti-6Al-4V alloy is summarized in Table 3.

Table 4. Chemical composition of Ti-6Al-4V alloy [14]

Element	Min [%]	Max [%]
Al	5.5	6.75
V	3.5	4,5
Fe	-	0.3
O	-	0.2
C	-	0.08
N	-	0.05
H	-	0.0125
Y	-	0.005
Ti	Balance*	

\* The percentage of titanium is determined by difference and does not need to be determined or certified.

#### AA6061 T6

Aluminium alloys due to their lightweight, sufficient mechanical properties and resistance to atmospheric corrosion are popularly used in wide variety of applications. Aluminium alloys usually exhibit good resistance to corrosion – which is connected with their chemical activity. Under exposition to corrosive environment, dense  $Al_2O_3$  layer is being forming on their surface, preventing it from further oxidation. Mechanical properties of aluminium can be significantly enhanced by addition of alloying elements and heat treatment. Most important alloying elements in aluminium alloys are zinc, magnesium, copper and silicon [15, 16].

Table 3. Chemical composition of AA6061 T6 [17]

Pierwiastek	Min [%]	Max [%]
Mg	0.80	1.20
Si	0.40	0.80
Cu	0.15	0.40
Cr	0.04	0.35
Fe	-	0.70
Zn	-	0.25
Mn	-	0.15
Ti	-	0.15
Al	Balance*	

\* The percentage of aluminium is determined by difference and does not need to be determined or certified.

According to their susceptibility to precipitation hardening, aluminium alloys can be divided into heat-treatable or non-heat-treatable alloys. The 6061 aluminium alloy belongs to the group of heat treatable wrought aluminium alloys. Main alloying elements of this alloy are magnesium and silicon. As other alloys of 6XXX class, it exhibit good capability to hot forming – extruding, forging and rolling. These alloys show good weldability and excellent susceptibility to anodizing. [15, 16].

#### 4. CAD GEOMETRIC MODEL

A model of the crankshaft was made using SOLIDWORKS to carry out strength analysis by means of computer simulation. The designed crankshaft model is shown in Figure 1a.

#### 5. BOUNDARY CONDITIONS

The following boundary conditions were adopted in the computer simulation:

- A finite element mesh was superimposed on the crankshaft model (Figure 1b),
- A pressure of 40 MPa was applied on the of crankshaft (Figure 1c),
- The location of pressure application and immobilisation geometry of the crankshaft model are shown in Figure 1c.

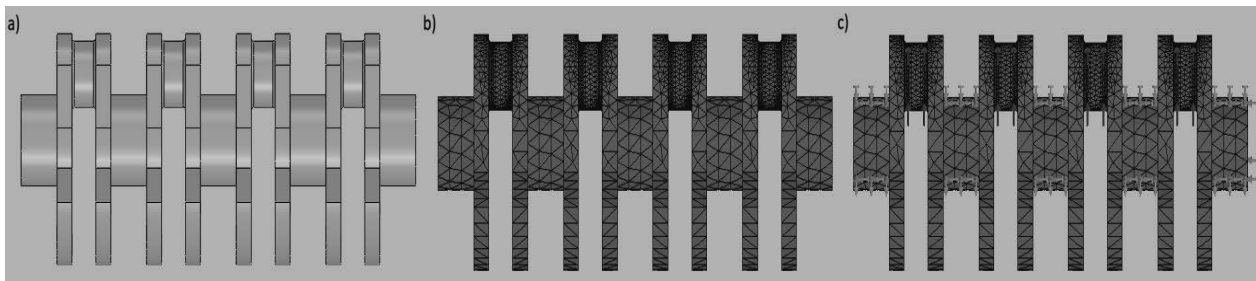


Figure 1. CAD model of the crankshaft (a); with finite element mesh superimposed (b); with finite element mesh superimposed, force direction visible and geometry immobilized (c)

#### 6. ANALYSIS OF RESULTS

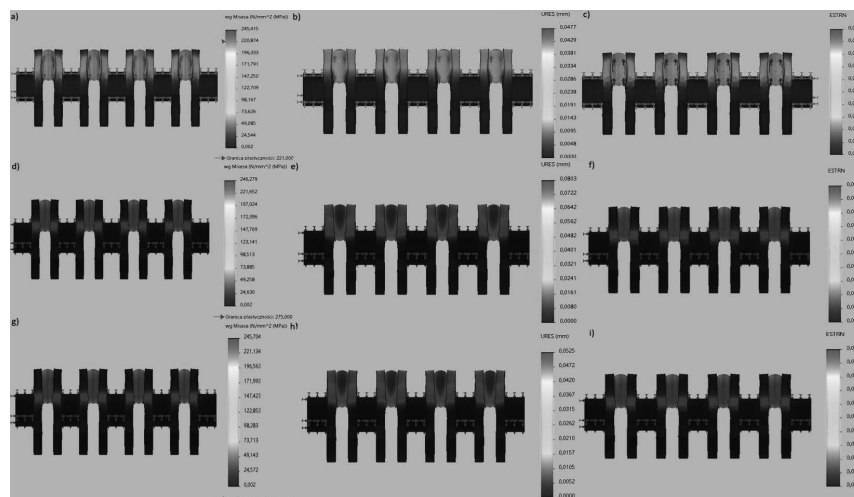


Figure 2. Huber-Mises reduced stress distribution for C17000 beryllium bronze (a); aluminium alloy AA6061 T6 (d); and Ti-6Al-4V alloy (g). Displacement distribution for C17000 beryllium bronze (b); AA6061 T6 (e); and Ti-6Al-4V alloy (h). Equivalent deformation for C17000 beryllium bronze (c); AA6061 T6 (f); and Ti-6Al-4V alloy (i).

The overall results of the simulations performed are shown in Table 4.

Table 4. Summary of overall results from computer simulations carried out

Material used	Maximum stress value [MPa]	Maximum displacement [mm]	Maximum deformation value
C17000 beryllium bronze	245.415	0.0477	0.002
AA6061 T6 alloy	246.279	0.0803	0.003
Ti-6Al-4V alloy	245.704	0.0525	0.002

## 6. CONCLUSION

The results of the strength analysis indicate that, of the materials analysed, C17000 beryllium bronze is the most suitable material for use as crankshaft material. This is because it showed negligible displacement and deformation values. However, it is worth noting, that values of displacements and deformations obtained for C17000 beryllium bronze and Ti-6Al-4V alloy exhibited minor differences. Higher stresses were obtained in case of aluminium alloy – albeit showing negligible difference when compared to those obtained for titanium alloy and beryllium bronze. The largest displacement was noticed for the model made of AA6061 T6 – the displacement value is nearly 70% higher than in case of C17000 beryllium bronze. For the use of AA6061 T6 as the crankshaft material, the highest deformation was also obtained – 1.5 times higher than value recorded for the C17000 beryllium bronze.

## BIBLIOGRAPHY

1. L. Witek, R. Woś, Analiza wytrzymałościowa wału korbowego silnika tłokowego, *Autobusey* 12, 2017, str.1415-1418.
2. H. Yamagata, The crankshaft, *The Science and Technology of Materials in Automotive Engines*, 2005, p.165–206.
3. S. Andrzejewski, *Poradnik inżyniera mechanika Tom II zagadnienia konstrukcyjne*, Wydawnictwo Naukowo-Techniczne, Warszawa 1969.
4. J. Caban, L. Gardyński, R. Wrona, Badania uszkodzeń wałów korbowych w trakcyjnych silnikach o zapłonie samoczynnym, *Zeszyty Naukowe/Wyższa Szkoła Oficerska Wojsk Lądowych im. gen. T. Kościuszki* 3. 2013, 77-87.
5. W. Zhang, Z. Zhao, J. Fang, P. He, Z. Chao, D. Gong, L. Jiang, Evolution and strengthening mechanism of metastable precipitates in Cu-2.0 wt% Be alloy, *Journal of Alloys and Compounds* 857, 2021, 157601.
6. J. Cao, Ch. Li, Y. Sun, B. Wu, H. Tang, X. Shen, K. Song, Y. Zhou, Ch. Cui, Study on the effect of heat treatment on the microstructure and properties of C17300 beryllium copper alloy microwires, *Journal of Materials Research and Technology* 25, 2023, p.6578-6592.
7. A. K. Bhargava, M. K. Banerjee, *Heat-Treating Copper and Nickel Alloys*. Comprehensive Materials Finishing, 2017, p. 398–420.
8. <https://www.avivametals.com/collections/beryllium-copper> - dostęp dnia: 20.05.2024 rok.

9. <https://www.lksteelpipe.com/uns-c17000-beryllium-copper-alloys> - dostęp dnia: 20.05.2024 rok.
10. Dobrzański L.A., Podstawy nauki o materiałach i metaloznawstwo, Wydawnictwo Naukowo-Techniczne, Warszawa, 2002.
11. F. H. Froes, Titanium: Alloying. Reference Module in Materials Science and Materials Engineering, 2016.
12. P. Pushpa, S.M. D., C. Aratib, Classification and applications of titanium and its alloys, Materials Today: Proceedings 54, 2022, P.537–542.
13. C. Wang, N. Xu, G. Zhang, G. Xu, F. Xing, Effect of heat treatment on microstructures and properties of vacuum laser welding Ti–6Al–4V titanium alloy, Journal of Materials Research and Technology 30, 2024, p.6309–6320.
14. [https://emetal.eu/tytan/tytan\\_grade\\_5\\_R56400\\_Ti-6Al-4V\\_3.7165/](https://emetal.eu/tytan/tytan_grade_5_R56400_Ti-6Al-4V_3.7165/) - dostęp dnia: 20.05.2024 rok.
15. E. A. Starke, H. M. M. A. Rashed, Alloys: Aluminum, Reference Module in Materials Science and Materials Engineering, 2017.
16. C. Vargel, 6XXX series alloys, Corrosion of Aluminium, 2020, 485–495.
17. <https://www.jfkgroup.pl/wyroby-hutnicze/aluminium/aluminium-6061/> - dostęp dnia: 20.05.2024 rok.



17th-19th June 2024  
Gliwice, Poland

DEPARTMENT OF ENGINEERING MATERIALS AND BIOMATERIALS  
FACULTY OF MECHANICAL ENGINEERING  
SILESIA UNIVERSITY OF TECHNOLOGY

## INTERNATIONAL STUDENTS SCIENTIFIC CONFERENCE

### Computer simulation of gear wheel loading

Jakub Polis<sup>a</sup>, Jakub Bicz<sup>a</sup>, Agata Śliwa<sup>b</sup>

<sup>a</sup> Student of Silesian University of Technology, Faculty of Mechanical Engineering  
email: jakupol064@student.polsl.pl; jakubic839@student.polsl.pl

<sup>b</sup> Silesian University of Technology, Faculty of Mechanical Engineering, Department of Engineering Materials and Biomaterials  
email: agata.sliwa@polsl.pl

**Abstract:** This paper presents an FEM analysis of the distribution of stresses, displacements and deformations resulting from the application of a specific force on a gear wheel, depending on the material used - which were Ti-3Al-8V 6Cr-4Mo-4Zr (SS) alloy, AISI 316 stainless steel and AC41A cast zinc alloy. The analysis was carried out using SOLIDWORKS software. The locations with the highest stress and displacement values and the value of the critical force at which the component deforms were determined.

### 1. INTRODUCTION

Gears are the most commonly used machine components and are a key part of most mechanical drive systems. It is assumed that gears were invented by Greek mechanics from Alexandria in the 3rd century BC. From Greek times until the Industrial Revolution, there were no significant developments in gears. Modern gears with an involute profile were developed in the late 19th and early 20th century. Prior to this, the development of gears was mainly limited by low production capacity - it was almost impossible to produce gears with an involute profile. Evolute gears are widely used today. Nowadays, research on gears focuses on the optimisation of the tooth profile with a special focus on the frontal gearing ratio [1, 2].

The front toothing coefficient  $\varepsilon_\alpha$  is determined for equivalent normal cylindrical wheels in a section passing through the centre of the toothing width. As a result, it can serve as an indicator of gear quality independently of the design method of the primarily toothed toothing. It allows the circular-arc, epicycloid and involute toothing to be compared and contrasted with each other [3].

The involute outline has the following advantages [4]:

- the tooth can be made resting on a toothed tool with rectilinear contours, which facilitates accurate tool making,
- the orbital method of gear manufacturing used in these cases is cheap and has a high degree of accuracy,
- a change in the distance of the axes (parallel shift of the axes) does not affect the magnitude of the ratio and therefore does not induce dynamic forces,



- wheels with the same pitch can be mated in any pair, regardless of the number of teeth in each wheel,
- corrected teeth can be made with the same tool,
- the direction of the interdental force does not change during operation, as the mesh line is a straight line, which has a major impact on the nature of the gearbox operation.

The main disadvantage of an involute outer gear is the relatively high pressures that occur between the teeth due to the fact that the teeth are in convex contact [4].

Due to the varying operating conditions, gear wheels should be characterised by both high mechanical strength, abrasion resistance and high hardness of the surface layer. For this reason, gear wheels are often subjected to surface treatments that enable varying properties to be achieved across the cross-section of the material [5, 6].

One of the more commonly used surface treatments for gears is carburising. The carburising process consists of saturating the surface layer of the material with carbon to a certain depth (0.3-2,5 mm) with subsequent hardening. This produces a hardened surface (59-63 HRC) with increased resistance to abrasive wear while maintaining a flexible core capable of carrying loads [6, 7].

The dominant group of materials used for gears are metals and their alloys. However, research is currently underway to implement polymeric materials as an alternative group of materials to those commonly used today. The advantage of polymeric materials over other engineering materials is their relatively low price. However, polymeric materials have poor mechanical strength and thermal resistance compared to metals. For this reason, polymer materials that would replace metal gears are reinforced with other materials such as glass fibres [2, 8].

A currently promising polymer in research that could replace metallic materials is polycaprolactam - PA-6. The trade name for polycaprolactam given by the DuPont company is nylon 6. By reinforcing the PA-6 polymer with glass fibres, its mechanical strength, thermal resistance and, compared to metallic materials, its quieter operation and lower weight are significantly increased. However, current research shows that components made of nylon 6 can absorb moisture, which can directly affect premature gear wear [8, 9].

## 2. MATERIALS AND METHODOLOGY

The analysed component of a gear wheel is its teeth. Three gear wheel models made of Ti-3Al-8V-6Cr-4Mo-4Zr (SS) alloy, AISI 316 stainless steel and cast AC41A alloy are presented. The main objective is to transfer a load of 600 N through the teeth without loss of integrity.

## 3. SELECTION OF MATERIALS

As mentioned above, the gear model was made from Ti-3Al-8V-6Cr-4Mo-4Zr alloy, AISI 316 stainless steel and cast AC41A alloy. These materials are inherently linearly isotropic and do not show any variation in properties. Selected mechanical and physical properties of all three materials are shown in Table 1. Table 2, Table 3 and Table 4 show the chemical composition of Ti-3Al-8V-6Cr-4Mo-4Zr alloy, AISI 316 stainless steel and AC41A alloy, respectively.

Table 1. Selected mechanical and physical properties of the materials from which the gear model was made.

Material	Ti-3Al-8V-6Cr-4Mo-4Zr	AISI 316	AC41A
Property			
Spring rate [N/m <sup>2</sup> ]	1,04*10 <sup>11</sup>	1,93*10 <sup>11</sup>	8,5*10 <sup>10</sup>
Poisson's ratio	0,33	0,3	0,3
Shear stress ratio [N/m <sup>2</sup> ]	4*10 <sup>10</sup>	-	-
Specific mass [kg/m <sup>3</sup> ]	4820	8000	6700
Tensile strength [N/m <sup>2</sup> ]	1,22*10 <sup>9</sup>	5,5*10 <sup>8</sup>	3,3*10 <sup>8</sup>
Compressive strength [N/m <sup>2</sup> ]	1,09*10 <sup>9</sup>	-	6*10 <sup>8</sup>
Yield stress [N/m <sup>2</sup> ]	1,034214*10 <sup>9</sup>	1,378951*10 <sup>8</sup>	-
Thermal expansion coefficient [K]	8*10 <sup>-6</sup>	1,6*10 <sup>-5</sup>	2,74*10 <sup>-5</sup>
Thermal conductivity coefficient [W/(m*K)]	6,2	16,3	108,9
Specific heat [J/(kg*K)]	515	500	420

Table 2. Chemical composition of Ti-3Al-8V-6Cr-4Mo-4Zr alloy [10].

Chemical element	Min [%]	Max [%]
V	7,5	8,5
Cr	5,5	6,5
Zr	3,5	4,5
Mo	3,5	4,5
Al	3	4
Fe	-	0,30
O	-	0,12
C	-	0,050
N	-	0,030
H	-	0,020
Ti	Balance*	

\* The percentage of titanium is determined by difference and does not need to be determined or certified.

Table 3. Chemical composition of AISI 316 steel [11].

Pierwiastek	Min [%]	Max [%]
Cr	16,5	18,5
Ni	10	13
Mo	2	2,5
Mn	-	2
Si	-	1
C	-	0,07
P	-	0,045
S	-	0,015
N	-	0,11
Al	Balance*	

\* The percentage of aluminium content is determined by difference and does not need to be determined or certified.

Table 4. Chemical composition of alloy AC41A [12].

Pierwiastek	Min [%]	Max [%]
Al	3,5	4,3
Cu	0,75	1,25
Fe	-	0,10
Mg	0,030	0,080
Pb	-	0,0050
Cd	-	0,0040
Sn	-	0,0030
Zn	Balance*	

\* The percentage of zinc is determined by difference and does not need to be determined or certified.

#### 4. CAD GEOMETRIC MODEL

To carry out the strength analysis using computer simulation, a model of the gear wheel was made using SOLIDWORKS. The designed gear wheel model is shown in Figure 1a.

#### 5. BOUNDARY CONDITIONS

The following boundary conditions were assumed in the computer simulation:

- A finite element mesh was superimposed on the gear wheel model (Figure 1b),
- A force of 600 N was applied to the upper surface of all 30 teeth (Figure 1c),
- The location of force application and the immobilisation of the gear model geometry are shown in Figure 1c.

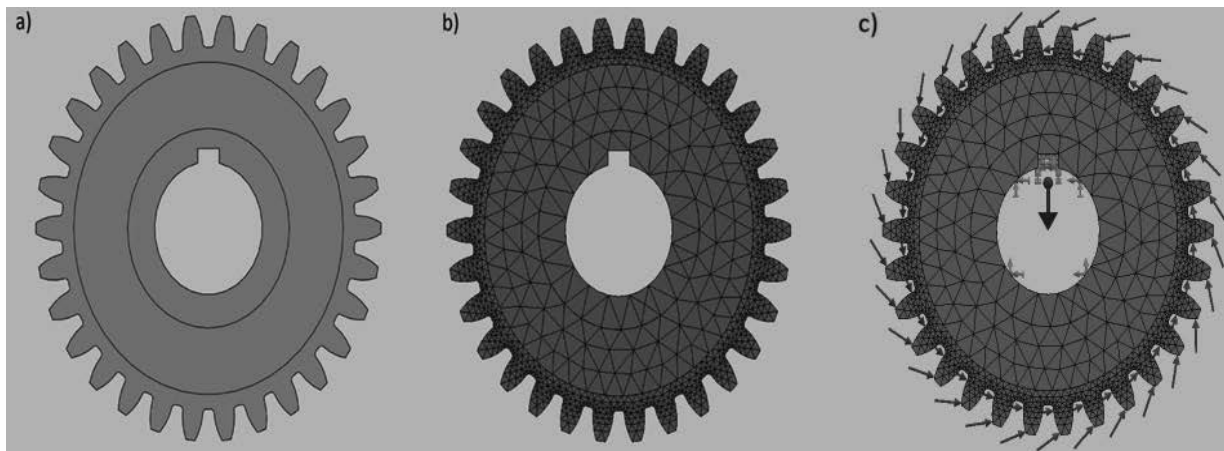


Figure 1. CAD model of gear wheel (a); with finite element mesh superimposed (b); with finite element mesh superimposed, force direction visible and geometry immobilized (c)

## 6. ANALYSIS OF RESULTS

### 6.1 Results of numerical stress analysis

The analysis was based on the Huber-Mises hypothesis. After loading the component, stress diagrams were obtained, the values of which are expressed in MPa. Figure 2 shows the distribution of stresses developed during the given loading.

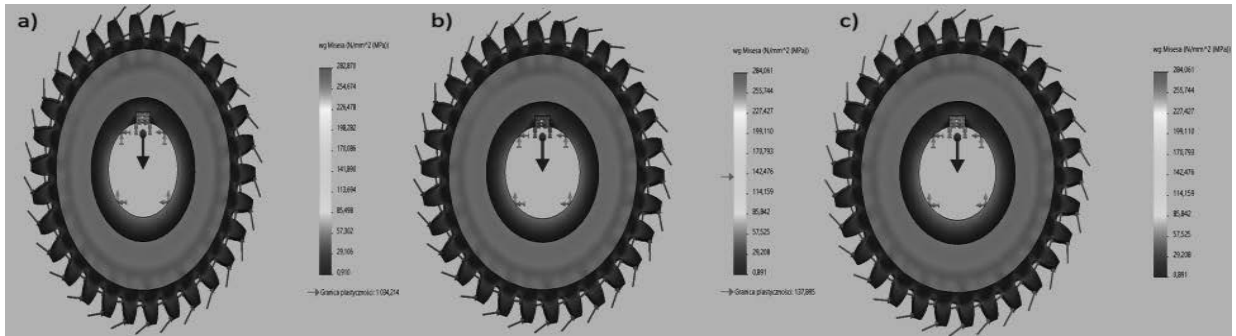


Figure 2. Huber-Mises reduced stress distribution for Ti-3Al-8V-6Cr-4Mo-4Zr alloy (a); AISI 316 steel (b); and AC41A alloy (c)

### 6.2 Results of the numerical analysis of displacements

The purpose of the subsequent computer simulation carried out was to determine the magnitude of the displacement under a given force and generate displacement diagrams of the structure, which are shown in Figure 3.

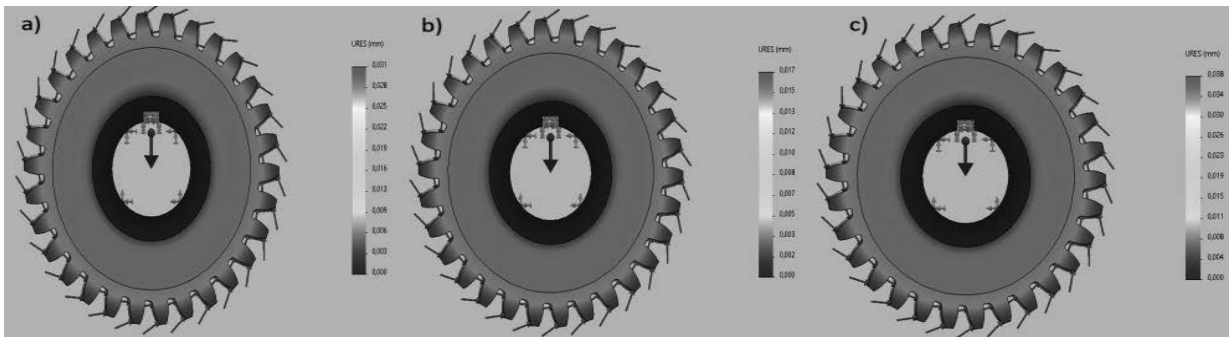


Figure 3. Displacement distributions for Ti-3Al-8V-6Cr-4Mo-4Zr alloy (a); AISI 316 steel (b); and AC41A alloy (c)

### 6.3 Results of numerical analysis of equivalent deformation

The last simulation carried out was to determine the critical force causing the deformation. Figure 4 shows the equivalent deformation represented by the largest force required to deform the axis.

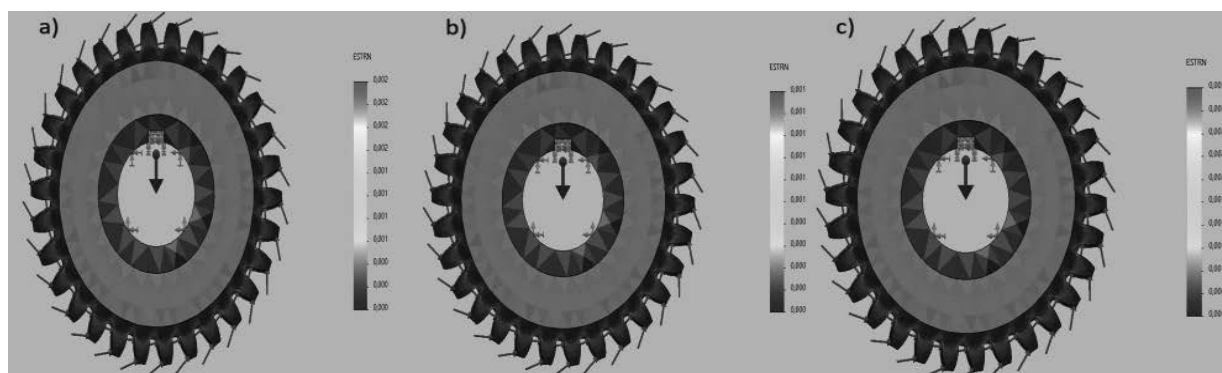


Figure 4. Equivalent deformation for Ti-3Al-8V-6Cr-4Mo-4Zr alloy (a); AISI 316 steel (b); and AC41A alloy (c)

The overall results of the simulations performed are shown in Table 5.

Table 5. Summary of overall results from computer simulations carried out

Material used	Maximum stress value [MPa]	Maximum displacement [mm]	Maximum deformation value
Ti-3Al-8V-6Cr-4Mo-4Zr alloy	282,870	0,031	0,002
AISI 316 steel	284,061	0,017	0,001
Alloy AC41A	284,061	0,038	0,003

## 7 CONCLUSION

The results of the strength analysis obtained indicate that, of the materials analysed, AISI 316 stainless steel is the most suitable material for use in the gear wheel. This material showed, even when subjected to significant loading, negligible displacement and deformation values - with stresses higher than Ti-3Al-8V-6Cr-4Mo-4Zr alloy and identical to AC41 alloy.

The highest stresses were obtained when using AISI 316 steel and AC41A alloy. It is worth noting, however, that the difference between these two materials and the Ti-3Al-8V-6Cr-4Mo-4Zr alloy is negligible - only 1.19 MPa.

The largest displacement was recorded for the model made from the AC41A alloy - the displacement value is 0.07 mm higher than for the Ti-3Al-8V-6Cr-4Mo-4Zr alloy. And by 0.014 mm compared to AISI 316 steel.

For the use of AC41A alloy as a gear wheel, the highest strain was also obtained - the strain value recorded for Ti-3Al-8V-6Cr-4Mo-4Zr alloy is more than twice as low. In contrast, it is three times less for AISI 316 steel.

Based on the results obtained from the strength analysis, it can be concluded that, due to the marginal differences in the obtained values discussed above, each of the three materials can be successfully used as a gear material.

**BIBLIOGRAPHY**

1. A.J. Muminovic, M. Colic, E. Mesic, I. Saric, Innovative design of spur gear tooth with infill structure, *Bulletin of the Polish Academy of Sciences, Technical Sciences* 68(3) (2020) 477-483.
2. S. Choudhury, P. Patnaik, Design and numerical analysis of spur gear using SolidWorks simulation technique, *Materials Today: Proceedings*, 2020
3. R. Kuryjański, Wskaźniki zazębienia krzywoliniowych przekładni stożkowych jako podstawowy wyznacznik poprawności konstrukcji przekładni, *Mechanik*, 89(12) (2016) 1876-1878.
4. S. Andrzejewski, *Poradnik inżyniera mechanika Tom II zagadnienia konstrukcyjne*, Wydawnictwo Naukowo-Techniczne, Warszawa 1969.
5. C. Zhang, F. Chen, Z. Huang, M. Jia, G. Chen, G., Y. Ye, L. Yaojun, W. Liu, B. Chen, Q. Shen, L. Zhang, E.J. Lavernia, Additive manufacturing of functionally graded materials: A review. *Materials Science and Engineering, A* 764 (2019) 138209.
6. M. Vamshi, S.K. Singh, N. Sateesh, D.S. Nagaraju, R. Subbiah, A review on influence of carburizing on ferritic stainless steel, *Materials Today: Proceedings*, 26 (2020) 937-943.
7. O. Kärki, *Small Spur Gear Manufacturing Study*, Metropolia University of Applied Sciences, (2021).
8. S. Senthilvelan, R. Gnanamoorthy, Effect of rotational speed on the performance of unreinforced and glass fiber reinforced Nylon 6 spur gears, *Materials & Design*, 28(3) (2007) 765–772.
9. Snowberg D, IACMI Project 4.2: Thermoplastic Composite Development for Wind Turbine Blades, Final Technical Report PA16-0349-4.2-01, (2021).
10. [https://emetal.eu/tytan/tytan\\_grade\\_19\\_R58640\\_Ti-3Al-8V-6Cr-4Mo-4Zr/](https://emetal.eu/tytan/tytan_grade_19_R58640_Ti-3Al-8V-6Cr-4Mo-4Zr/) - data dostępu 19.05.2024 r.
11. <https://virgamet.pl/00h17n14m2-1-4404-1-4401-aisi-316-316l-tp316-tp316l-stal-nierdzewna> - data dostępu 19.05.2024 r.
12. <https://www.matweb.com/search/datasheet.aspx?matguid=9e4cc640b315418eb49d473e5d697ba2&ckck=1> – data dostępu 19.05.2024 r.



17th-19th June 2024  
Gliwice, Poland

DEPARTMENT OF ENGINEERING MATERIALS AND BIOMATERIALS  
FACULTY OF MECHANICAL ENGINEERING  
SILESIA UNIVERSITY OF TECHNOLOGY

## INTERNATIONAL STUDENTS SCIENTIFIC CONFERENCE

### Brain-Computer-Interface Numeric Keyboard Designs

Maja Rudnicka<sup>a</sup>, Michał Lasak<sup>a</sup>, Igor Puchala<sup>a</sup>, Piotr Bartosz<sup>b</sup>, Dominik Bereta<sup>b</sup>,  
Dariusz Myszor<sup>f</sup>

<sup>a</sup>Silesian University of Technology, Faculty of Automatic Control, Electronics and Computer Science, SKN SpaceCoffee

<sup>b</sup>Silesian University of Technology, Faculty of Automatic Control, Electronics and Computer Science, SKN vFly

<sup>c</sup>Silesian University of Technology, Faculty of Automatic Control, Electronics and Computer Science, Department of Algorithmics and Software, email: maja.rudnicka@alogliwice.polsl.pl

**Abstract:** This article presents projects of various Brain-Computer-Interface (BCI) numeric keyboard interfaces that were created in the Unity Engine.

**Keywords:** brain-computer Interface, neural, brain activity

## 1. INTRODUCTION

This paper delves into the development of different types of Brain-Computer-Interface (BCI) numeric keyboard interfaces designed for entering numbers, crafted within the Unity engine. Electroencephalography (EEG) is a non-invasive method used to monitor brain activity by detecting voltage fluctuations that arise predominantly from the synchronous activity of neurons in the brain. These fluctuations are typically observed within a frequency range of 1 to 30 Hz. [1]. Various effects stemming from brain activity, including slow cortical potentials (SCP), stimulus-induced synchronization and desynchronization, steady-state evoked potentials (SSEP), and the P300 wave, can be harnessed to regulate diverse processes effectively [2, 3].

In this study, the employment of electroencephalography (EEG) capitalizes particularly on steady-state evoked potentials (SSEP), with a specific focus on steady-state visual evoked potentials (SSVEP). These potentials, elicited by stimuli of specific frequencies, exhibit rapid response times, rendering them invaluable for BCI applications. This technology holds significant promise, especially in aiding individuals with disabilities for rehabilitation and communication purposes.

## 2. DESIGNS

The Designs were implemented in the Unity Engine, seven different layouts were created. An important aspect is the limitation to 10 different buttons (actions) on a single screen that can be

interpreted by the applied BCI device (NextMind). The buttons work through SSVEP [4], they have assigned a different type of NextMind active asset. NextMind assets interpretation is based on different patterns and blinking frequencies. Looking at a specific button creates a specific signal in brain that the EEG can read. That allows to determine which button is chosen by the user.

### 2.1 First design

The first design features a standard numerical keyboard layout, but it omits the “0”, which reduces the number of possible combinations. A potential solution is to implement a method for inputting zeros, such as using the “enter” key to advance to the next number with zero as the default (Fig. 1).

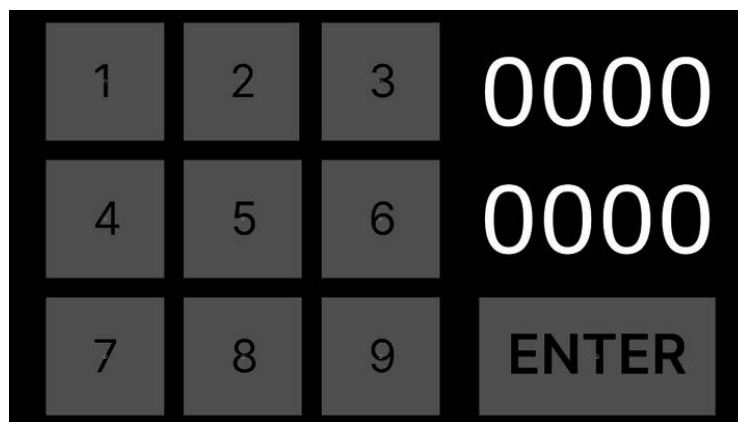


Figure 1. First Design of a BCI numerical keyboard

### 2.2 Second design

The second design accommodates more characters, though it may operate slower than other designs. It allows for future expansion to include more buttons, as none of the menus exceed the ten-button limit. This design comprises one main menu (Fig. 2) and multiple submenus (Figs. 3-4).

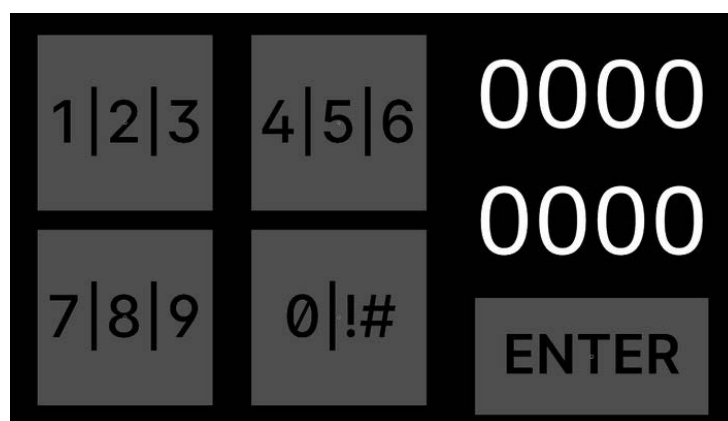


Figure 2. Second Design of a BCI numerical keyboard, in the main menu



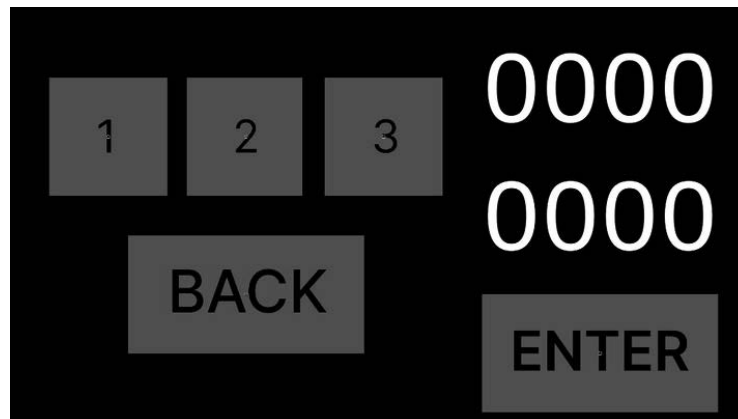


Figure 3. Second Design of a BCI numerical keyboard, in the first menu

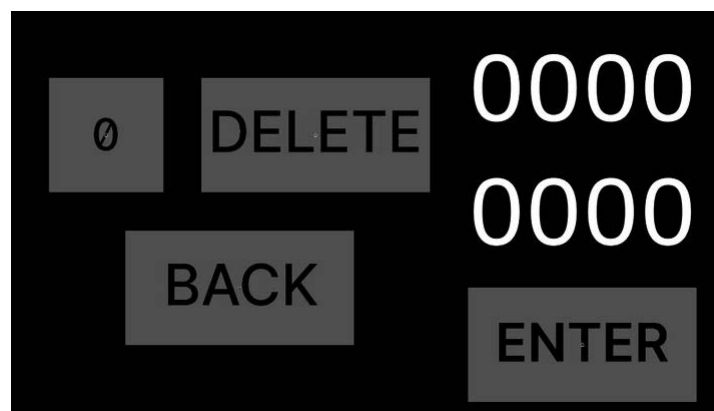


Figure 4. Second Design of a BCI numerical keyboard, in the last menu

### 2.3 Third design

The third design merges elements from the first two, utilizing menus similar to the second design but maintaining a familiar layout similar to the phone keyboard approach to the alphanumeric characters. While it lacks some of the second design's features, its familiar layout may be advantageous during testing (Figs. 5-6).

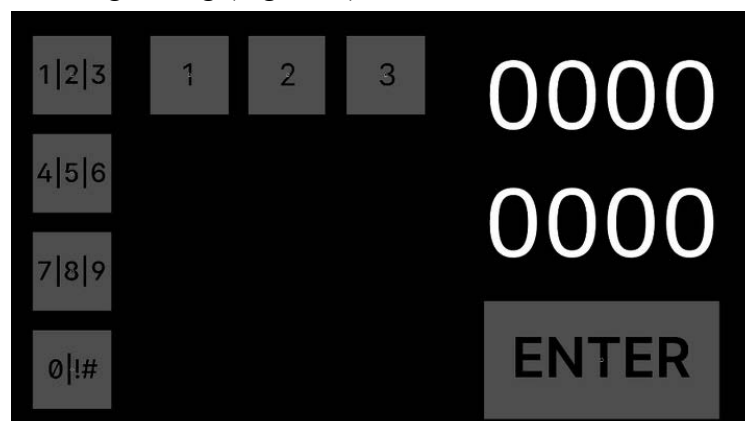


Figure 5. Third Design of a BCI numerical keyboard, with the first menu open

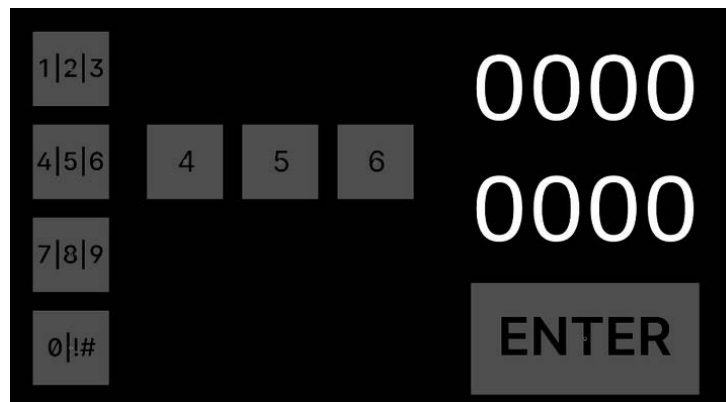


Figure 6. Third Design of a BCI numerical keyboard, with the second menu open

#### 2.4 Fourth design

The fourth design is a simplified version of the second, with only two menus. Although it offers less flexibility for future improvements, it retains some potential for enhancements. It consists of a main menu (Fig. 7) and two submenus (Fig. 8).

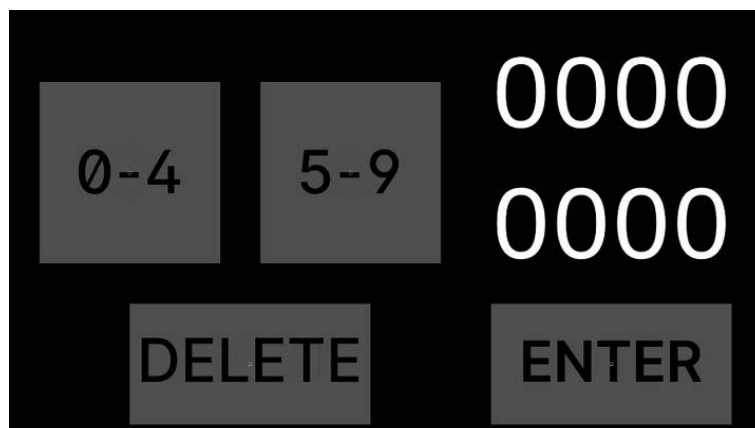


Figure 7. Fourth Design of a BCI numerical keyboard, with the main menu open

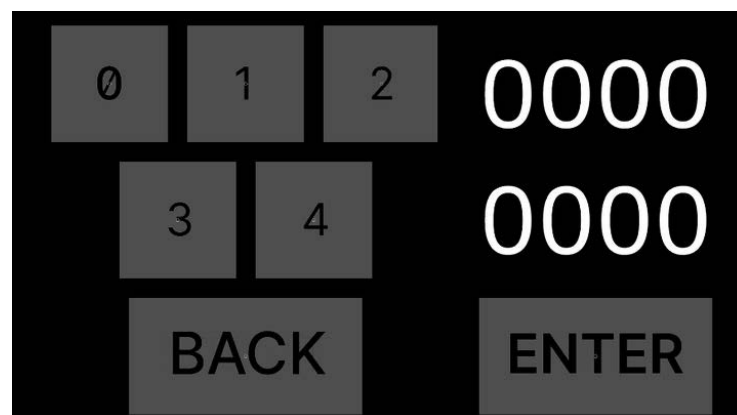


Figure 8. Fourth Design of a BCI numerical keyboard, with the first sub-menu open

### 2.5 Fifth design

The fifth design is based on the first one but includes zeros instead of an enter key. This introduces a challenge in number selection, as there is no confirmation that entered number is correct (Enter key).

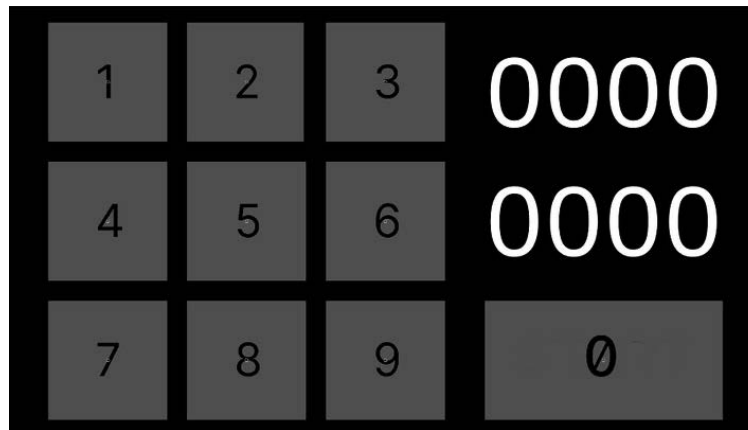


Figure 9. Fifth Design of a BCI numerical keyboard

### 2.6 Sixth design

The sixth design is a variant of the fourth, featuring two circular menus. This more intuitive layout, however, offers even less flexibility with additional buttons, nearing the 10-button limit.

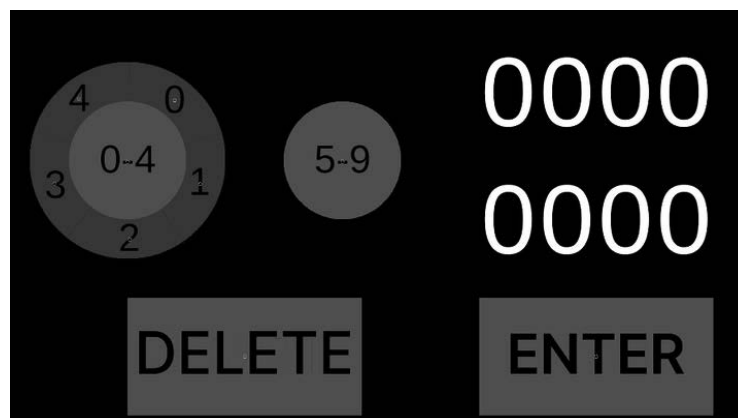


Figure 10. Sixth Design of a BCI numerical keyboard, with the first part expanded

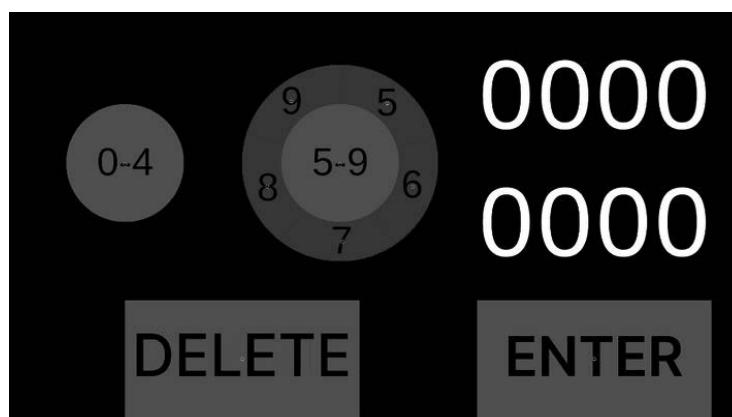


Figure 11. Sixth Design of a BCI numerical keyboard, with the second part expanded

### 2.7 Seventh design

The Seventh Design is similar to the Fifth Design. It has a different layout, that could be more effective and intuitive.

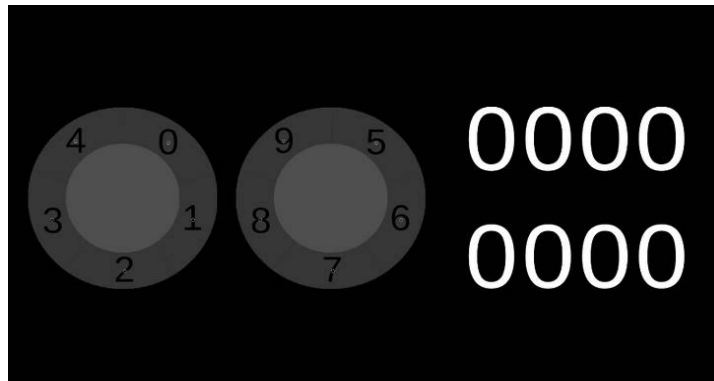


Figure 12. Seventh Design of a BCI numerical keyboard

## 3. FUTURE FURTHER DEVELOPMENTS

The next step of the development process is to test all of the designs and choose the best ones to extend them further. A few possible further developments include extending the BCI to include more combinations and buttons, that is especially likely if the keyboards based on menus and submenus prove effective. Another way of development is a more personalized interface, customizable by the user, that would allow for the best effectiveness, but would require better calibration and would be less objective in tests.

## 4. CONCLUSION

Various designs of Brain-Computer-Interface (BCI) numeric keyboard interfaces were developed within the Unity Engine, leveraging electroencephalography (EEG) technology, particularly steady-state evoked potentials (SSEP). Each design offers unique features and trade-offs, ranging from simplicity to flexibility. The future of this technology lies in rigorous testing to identify the most effective designs for further refinement. These developments hold promise for improving accessibility and communication for individuals with disabilities, marking a significant step forward in BCI technology.

## BIBLIOGRAPHY

1. H.J. Craig, Electroencephalography: basic principles, clinical applications, and related fields. *Neurology* 67.11 (2006): 2092-2092.
2. Xing, X., Wang, Y., Pei, W., Guo, X., Liu, Z., Wang, F., ... & Chen, H. (2018). A high-speed SSVEP-based BCI using dry EEG electrodes. *Scientific reports*, 8(1), 14708.
3. Zhichuan Tang, Xinyang Wang, Jiayi Wu, Yaqin Ping, Xiaogang Guo, and Zhixuan Cui. 2022. A BCI painting system using a hybrid control approach based on SSVEP and P300. *Comput. Biol. Med.* 150, C (Nov 2022)

4. Nguyen, Trung-Hau, and Wan-Young Chung. "A single-channel SSVEP-based BCI speller using deep learning." *IEEE Access* 7 (2018): 1752-1763.
5. D. Mattia, L. Astolfi, J. Toppi, M. Petti, F. Pichiorri i F. Cincotti, Interfacing brain and computer in neurorehabilitation, 4th International Winter Conference on Brain-Computer Interface (BCI), Yongpyong, 2016.



17th-19th June 2024  
Gliwice, Poland

DEPARTMENT OF ENGINEERING MATERIALS AND BIOMATERIALS  
FACULTY OF MECHANICAL ENGINEERING  
SILESIA UNIVERSITY OF TECHNOLOGY

## INTERNATIONAL STUDENTS SCIENTIFIC CONFERENCE

### Wireless communication between a flight simulation and its controllers

Maja Rudnicka<sup>a</sup>, Michał Lasak<sup>a</sup>, Igor Puchala<sup>a</sup>, Piotr Bartosz<sup>b</sup>, Dominik Bereta<sup>b</sup>, Dariusz Myszor<sup>c</sup>, Maria Ochman<sup>b</sup>, Jakub Wiczorek<sup>b</sup>

<sup>a</sup>Silesian University of Technology, Faculty of Automatic Control, Electronics and Computer Science, SKN SpaceCoffee

<sup>b</sup>Silesian University of Technology, Faculty of Automatic Control, Electronics and Computer Science, SKN vFly

<sup>c</sup>Silesian University of Technology, Faculty of Automatic Control, Electronics and Computer Science, Department of Algorithmics and Software  
email: maja.rudnicka@alogliwice.polsl.pl

**Abstract:** This article presents the results of research conducted to evaluate potential methods for achieving error-free and wireless communication between a device running flight simulation software and its controllers. The issues that the research sought to address are not uncommon, yet the proposed solutions often entail significant costs or present implementation challenges. Therefore, an inexpensive and straightforward solution was sought.

**Keywords:** wireless, connection, flight simulation, yoke system, controller

### 1. INTRODUCTION

Flight simulation technology (Fig.1) has witnessed remarkable advancements in recent years, offering unparalleled realism and immersion to enthusiasts and professionals alike. Central to the efficacy of these simulations is the seamless interaction between users and control interfaces. It is often difficult to imagine that completely wireless communication between flight simulation controls, such as pedals and yoke, and the simulation itself would be necessary. However, with the development of the simulator situated on the moving platform (Fig. 2), the issue became evident.



Figure 1. Flight simulation software

The purpose of the research is to identify a straightforward approach to establishing a wireless connection between the two devices, utilizing pre-built, publicly available, plug-and-play versions of both the software and the controllers. The objective is to identify a solution that is both straightforward to implement and highly accurate.



Figure 2. The platform on which the simulator is situated.

## 2. INITIAL VERSION

Upon initial examination, it was hypothesized that a regular network connection could be established between a compact computing device, such as the Raspberry Pi (Fig. 3), connected to the flight simulation controllers, and a computer running the simulation software.



Figure 3. Raspberry Pi - a potential candidate for utilization as the transceiver in the aforementioned solution.

Although the solution appears straightforward, it is, in fact, quite complex [1, 2]. The majority of publicly available flight simulation controllers are connected via the Universal Serial Bus (USB). In fact there exists a simple method for wireless data transmission from the controllers. However, it is challenging to persuade a computer to interpret the received data as if it were acquired from the USB protocol [8]. Furthermore, we attempted to develop software that would be capable of receiving data from the aforementioned controllers.

The initial investigation involved the utilization of an external network adapter in conjunction with the Raspberry Pi Zero board. Our approach led to the conclusion that the development of self-designed software would be necessary, as existing pre-made software did not meet our expectations. The design and implementation of error-free, long-lasting, and robust software is a challenging endeavour. Furthermore, the challenge is compounded by the fact that the solution must be developed for a constantly evolving environment of flight simulation and virtual reality [9, 10].

### 3. ESTABLISHED SOLUTION

While still considering the implementation of the aforementioned software to correctly interpret controllers' data, we encounter another solution. Upon initial examination, the endeavour appeared to be a formidable challenge. However, upon closer examination, it became evident that the implementation process was relatively straightforward. The solution employs a flight simulation controller set comprising a yoke and pedals in conjunction with a regular wireless gaming console controller. The utilization of pre-built devices in this solution necessitates the disassembly of both components in order to reestablish the analog connections of the printed



circuit boards (PCBs) of both devices, thereby enabling the gaming pad to function as a transceiver in a ready-made solution [7]. By affixing the console controller to the yoke system, a robust and secure connection can be established. Furthermore, this configuration obviates the issue of interpreting acquired data as the USB protocol data in subsequent stages of the simulation, as the simulation software can receive data directly from the gaming pad.



*Figure 4. Xbox controller - a potential candidate for utilization as the transceiver in the aforementioned solution.*

The implementation of this solution is relatively straightforward. The integration of a regular wireless gaming pad with the flight simulator controllers set is a key aspect of this solution. The internal wired outputs of the controllers set would be connected to the gamepad PCB, thereby enabling wireless connection. It is indeed possible due to the already existing remote connection integrated into a gaming controller [12]. Subsequently, the gamepad's receiver can be directly connected to the simulation computer, allowing the utilization of data acquired from the pad's internal PCB within the simulation software. This is possible because these types of gamepads are already supported as input devices for the majority of available flight simulators. Moreover, the aforementioned solution is likely to be highly durable due to the limited number of alterations currently being implemented in flight simulation controllers. The prevailing focus of current developments is on enhancing the simulation itself.

The final design would function as a single device capable of wirelessly controlling any currently available simulation software. Given the utilization of professional flight simulation equipment (Fig. 5), the solution can be used to train future pilots in a revolutionary and highly immersive manner [13].



*Figure 5 Practical training conducted on the flight simulator*

#### **4. CONCLUSION**

In conclusion, investigations conducted to establish error-free and wireless communication between flight simulation software and its controllers have yielded a solution that combines simplicity, durability, and effectiveness. Although the achieved results necessitate the utilization of a self-made device for the remote control of the flight simulator, the solution is relatively simple in its implementation and can be readily reproduced if necessary.

#### **BIBLIOGRAPHY**

1. Sohn, J. M., Baek, S. H., & Huh, J. D. (2008, September). Design issues towards a high performance wireless USB device. In 2008 IEEE International Conference on Ultra-Wideband (Vol. 3, pp. 109-112). IEEE.
2. Bit, A., Orehek, M., & Zia, W. (2010, September). Comparative analysis of Bluetooth 3.0 with UWB and Certified Wireless-USB protocols. In 2010 IEEE International Conference on Ultra-Wideband (Vol. 2, pp. 1-4). IEEE.
3. Ng, T. S., & Ng, T. S. (2018). Flight Simulator Systems. *Flight Systems and Control: A Practical Approach*, 43-53.
4. Cameron, B., Rajae, H., Jung, B., & Langlois, R. G. (2016, May). Development and implementation of cost-effective flight simulator technologies. In *International Conference of Control, Dynamic Systems, and Robotics* (No. 126, p. DOI).
5. Vujović, V., & Maksimović, M. (2014, May). Raspberry Pi as a Wireless Sensor node: Performances and constraints. In 2014 37th international convention on information and communication technology, electronics and microelectronics (MIPRO) (pp. 1013-1018). IEEE.

6. Vitsas, P. A. (2016). Commercial simulator applications in flight test training. *Journal of Aerospace Engineering*, 29(4), 04016002.
7. Wagner, M., Avdic, D., & Heß, P. (2016, July). Gamepad Control for Industrial Robots. In *Proceedings of the 13th International Conference on Informatics in Control, Automation and Robotics* (pp. 368-373).
8. Dawoud, D. S., & Dawoud, P. (2022). *Serial communication protocols and standards*. River Publishers.
9. Muñoz-Saavedra, L., Miró-Amarante, L., & Domínguez-Morales, M. (2020). Augmented and virtual reality evolution and future tendency. *Applied sciences*, 10(1), 322.
10. Kenwright, B. (2019). Virtual reality: Where have we been? where are we now? and where are we going?.
11. van der Linden, J., van der Heijde, F., & van Remundt, K. (2021). Bluetooth Ultrasimple Gamepad: Design of a wireless cooperative gaming device.
12. Thorpe, A., Ma, M., & Oikonomou, A. (2011, July). History and alternative game input methods. In *2011 16th International Conference on Computer Games (CGAMES)* (pp. 76-93). IEEE.
13. Caro, P. W. (1973). Aircraft simulators and pilot training. *Human Factors*, 15(6), 502-509.



17th-19th June 2024  
Gliwice, Poland

DEPARTMENT OF ENGINEERING MATERIALS AND BIOMATERIALS  
FACULTY OF MECHANICAL ENGINEERING  
SILESIA UNIVERSITY OF TECHNOLOGY

## INTERNATIONAL STUDENTS SCIENTIFIC CONFERENCE

### Sample collection and containment system for a compact planetary exploration rover

Maja Rudnicka<sup>a</sup>, Michał Lasak<sup>a</sup>, Igor Puchała<sup>a</sup>, Piotr Bartosz<sup>b</sup>, Dominik Bereta<sup>b</sup>,  
Dariusz Myszor<sup>c</sup>

<sup>a</sup>Silesian University of Technology, Faculty of Automatic Control, Electronics and Computer Science, SKN SpaceCoffee

<sup>b</sup>Silesian University of Technology, Faculty of Automatic Control, Electronics and Computer Science, SKN vFly

<sup>c</sup>Silesian University of Technology, Faculty of Automatic Control, Electronics and Computer Science, Department of Algorithmics and Software  
email: maja.rudnicka@alogliwice.polsl.pl

**Abstract:** The purpose of this research is to develop an exploration rover for use in Earth and Martian-like environments, which requires the development of a sample collection system for soil, rock and atmosphere. Along with that system, a corresponding sample containment method has to be developed, in order to preserve the materials which are being brought back. A rover with a drilling module and a compartment container part, holding the total capacity of 5 isolated samples, was designed and implemented. A weighing module for immediate post-collection sample test was added, as well as pH, temperature and humidity sensors for the soil. For atmosphere examination, sensors of pressure, temperature, humidity and CO<sub>2</sub> concentration were employed, with plans of future development and new sensory modules addition.

**Keywords:** space, exploration, rover, sample collection, drilling

## 1. INTRODUCTION

In light of a growing interest in interplanetary exploration and conquest, the number of projects researching and developing probing rovers and sondes is at its height. Sample-based research of foreign environments is the objective of, among others, NASA's 2020 Perseverance rover mission [1] and ESA's ExoMars programme [2]. A future perspective of the construction of such vehicles is space colonization, targeting carefully and suitably chosen areas for scientific and utilitarian bases, which will be made possible due to appropriate environmental examination.

The project of the rover under development presents an advantageous approach to further use, since it is a low-cost (under 2000 EUR), low-mass (under 18 kg) solution for an exploratory rover design. Its dimensions are under 600x500x500mm. The mentioned simplicity allows for the control of multiple similar vehicles at once and makes them more reliable than complex

missions, which can be doomed by a single-point failure. This approach focuses on enabling free exploration of vast terrain by multiple smaller rovers.

A concept of such a mission could involve a main non-mobile lander—a science laboratory which could be even more advanced than NASA’s Perseverance, with a fleet of tens of rovers and drones of various sizes preparing and bringing samples to the main laboratory.

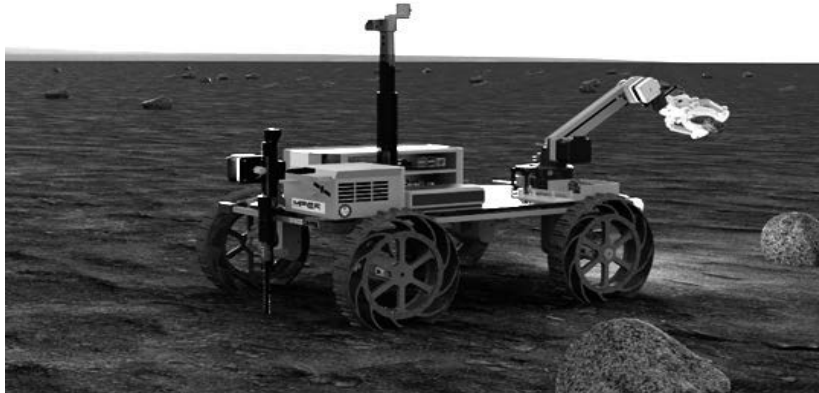


*Figure 1. MPER rover render on Mars, including the modules: Drill (leftmost), Manipulator (rightmost) and Chassis. A movable camera and antenna module are visible in the middle.*

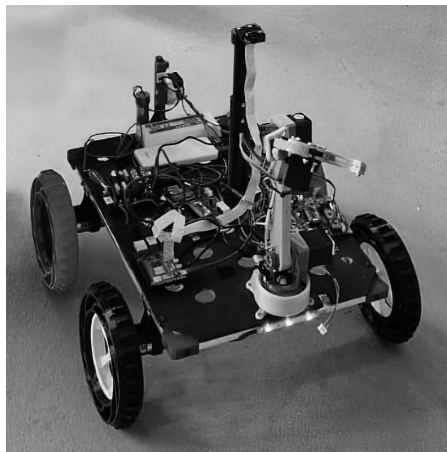


*Figure 2. MPER rover prototype during testing of remote control and video transmission*

## **2. COMPONENTS AND FUNCTIONALITY OF THE DRILLING SYSTEM**

The prototype of an exploration rover (Fig. 1, Fig. 2) is equipped with a three-part system of sample collection through drilling and gripper manipulation. It is an effective and secure tool for conducting research on gathered resources, allowing for instant preservation and containment of a sample, after an initial study of its parameters. The complexity of the task is conquered by the Manipulator, Drill and Sample Containment modules. On top of the more basically needed parts, the rover is accommodated to uneven and rugged planetary surface areas thanks to its 4-wheel drive with a shock absorption system, which grants it an agility of movement to gather specimens in hard-to-reach or obstructed places.

## 2.1 Manipulator

The rover arm, with its manipulator and gripper, were designed and constructed with the goal of optimal sample collection (Fig. 3). The 4-degrees-of-freedom, 5-articulated manipulator enables the rover to pick up materials from surfaces around it, and carry them over to its platform, which is equipped with a weight for a primary determination of a sample's parameters.

The Robotic Arm, of which the manipulator constitutes the main part, is lightweight, with 4DOF, utilizing 3 stepper and 2 servo motors for precise movement navigation. Its maximal pickup capacity stands at 0.5 kg, with a planned expansion to 1 kg.

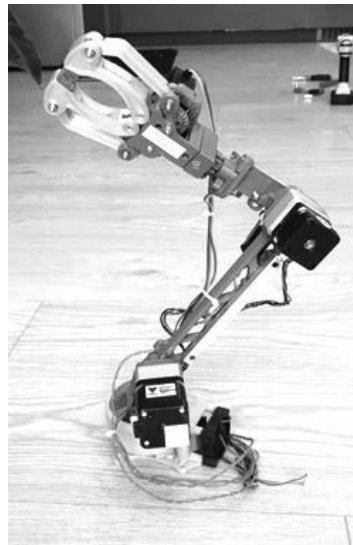


*Figure 3. Rover arm prototype, made with COTS electronic components and custom 3D printed mechanical parts.*

In the ongoing project, special attention has been given to the development of the manipulator's gears, designed to enhance the torque output of the motors. This design incorporates a combination of two gear types—planetary and cycloidal reduction gears, which are considered standard solutions in this context. The resulting component is a stepped-planetary gear (distinct from compound gears), achieving a significant reduction ratio of 40:1 within a compact 40x40x20 mm package. This gear system is entirely 3D-printed and has been successfully tested to withstand torques up to 23 Nm when fabricated using PETG material. We anticipate even higher torque capacities when utilizing Nylon for printing.

The manipulator prototype has been assembled and finished for use. The prepared version relies on stepper motors and servomechanisms.

## 2.2 Drilling and Sampling system

The Drill is a module responsible for soil-samples collection. The design depth of a drill is up to 20cm under the surface. The newest design of the system includes a stepper motor moving a carriage across a V-slot rail, with an endstop at the top. The stepper motor's torque is increased using the custom-made stepped-planetary gearbox described above.

The drill has a diameter of 16mm and a length of 320mm, and rotates in a drill guide, allowing the sample to be carried upwards toward the sample container system. The guide is split into

two parts - fixed and moving. The fixed part provides mechanical support and acts as a linear bearing, while the moving part is attached to the carriage and has a tight fit with the drill bit, allowing the soil samples to travel upwards, as shown in Fig. 4.

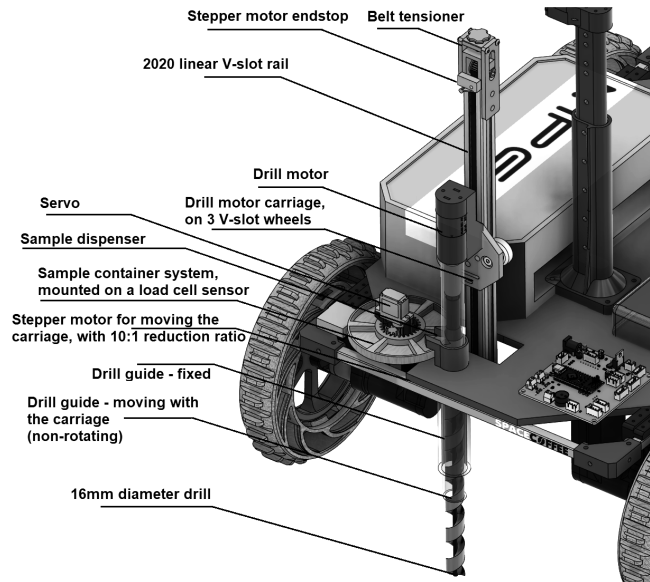


Figure 4. Drilling and sampling system design, with major components highlighted.

One of the design goals was to minimize the number of motors and mechanical joints needed for the whole system. One stepper motor, one DC motor for drill rotation and one small servo for sample container rotation bring the complexity to absolute minimum, while maintaining good capability.

Assembly and tests of the new design, shown in Fig. 4 and Fig. 5., in simulated foreign planetary conditions are the next step of the Drilling Module's development.

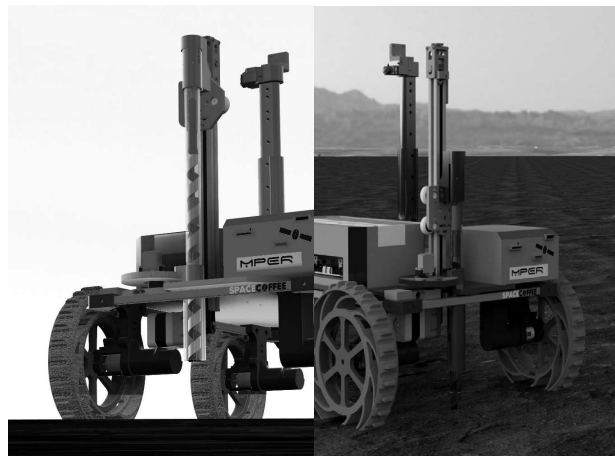


Figure 5. Renders of the drilling system in the stowed (left) and deployed position (right). Note the guide, one part of it extending with the motor (attached to the gantry). This allows the travel of the drilled sample upwards.

### 2.3 Sample Containment

Sample containment is conducted through a combination of three elements: the Manipulator and two Containers—first located in the front part of the platform, second in the rear. Using the manipulator, specimens can be transported and preserved in the prepared containers, with regard to their particular fragility and assuring previous sterilization of the containment.

The rear container has five compartments for soil samples from the drill bit. It is capable of weighing the samples with  $\pm 0.5$  g precision using a single load cell sensor. The individual samples can be weighed by measuring the change in the total weight of the module.

The samples can be emptied and filled remotely as necessary, and the revolver-style container system is controlled by a single servo motor. The front cargo compartment, within the reach of the robot arm, also includes an ionizing radiation sensor and a weight sensor. It's suitable for storing rocks or other items picked up by the rover, including basic tools that can be used by the Manipulator.

### 2.4 System operation and control

All compounds of the system for sample collection and storage are driven by an independent microcontroller, which only receives and sends data to the main controller (Raspberry Pi). The data is sent in custom CAN-like frames format, but over a UART bus. These frames contain control sums and are transmitted every 100 ms. The control isn't achieved by sending single commands, but rather by a set of flags, indicating the desired state of the rover. This way, missing single or multiple frames won't impact the rover extensively, only delaying the sent command. Acknowledgement flags are also used, and transmitted in every frame until the command is executed and the request stops. The user interface can be accessed by browser on any PC or mobile device, allowing intuitive control of the vehicle (Fig. 6).

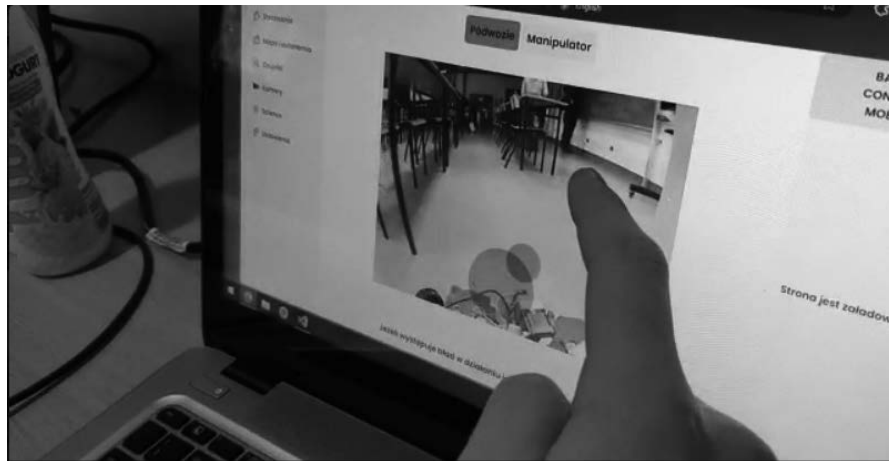


*Figure 6. User Interface of MPER rover - can be accessed in a browser and provides virtual joystick control of all functions of the rover.*



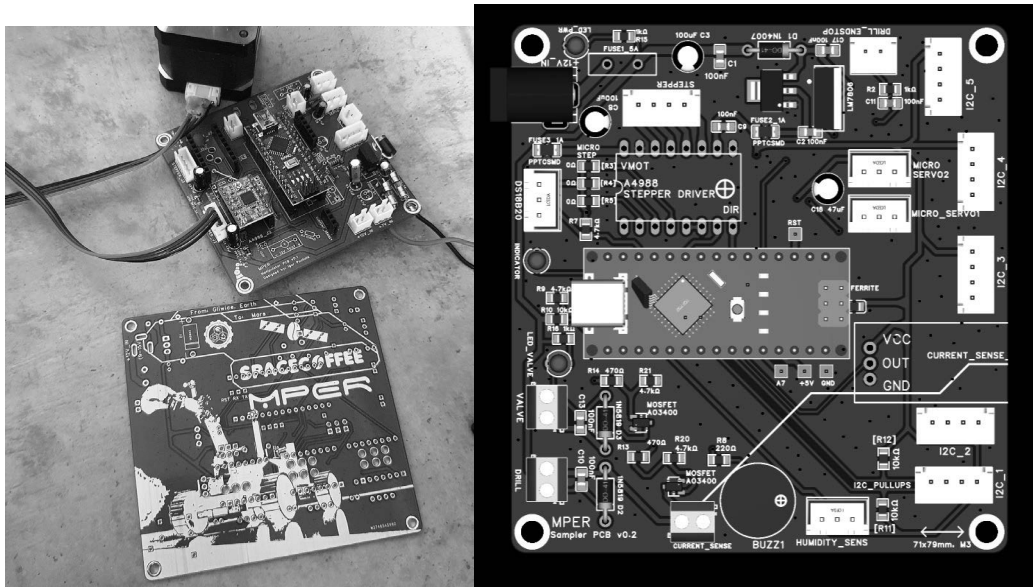


Figure 7. One of four custom PCBs designed for the rover's electronic components (left). Render of the PCB for the Sampling system (right)

## 2.4 Environmental sensors

A collection of sensors was deployed for separate examinations of the atmosphere and soil of extraterrestrial planet conditions measurement.

To analyse the atmospheric factors, an Arduino Nano-based system of pressure, temperature, humidity and CO<sub>2</sub> sensors was completed. An NC DN15 electrovalve collects the general sample, which is tested by the set of components: a BME688 humidity, temperature and pressure sensor, a DFRobot SEN0377 gas recognition sensor (CO<sub>2</sub>), a Geiger counter, and an ionizing radiation sensor, which, mounted next to the front cargo compartment, can be used to measure background radiation and solar storms, and also detect radioactivity of objects picked up by the rover. The examination of factors related to soil conditions will be possible due to the use of humidity and temperature probes, consecutively: MTK339 and DFRobotKIT 0021.

All of the above-listed devices are needed among the modules devoted to assessing the elements of a planet's nature, evaluating its habitability and, for example, crop harvest ability. Measurements prepared during the study of the sample are transmitted from the sensory modules through a UART bus to the Raspberry Pi 5-based main computer. The noted values are then sent to the ground base for the conduct of further research (Fig. 7).

## 3. FUTURE DEVELOPMENTS

Work is being done to improve the rover in all aspects. For the manipulator, there is a need to enhance the range and torque capability of this module so that it can easily perform various tasks. To achieve more dexterity, there is a plan to add one more degree of freedom - wrist angle. This will allow the manipulator to be equipped with an inverse kinematics algorithm and absolute positioning. When the design is finalized, there's a plan to release the manipulator's documentation as an open-source project. The arm can serve a wide range of interactions with the environment, functioning as a low-cost educational Cobot.

Under consideration are also upgrades and developments of the sample retrieval system, with the objective of optimising specimen-gathering methods for more secure storage and isolation of samples [9, 10]. A larger, stationary version of the developed drill module is also considered, which can be used for Earth research or fitted on a larger rover. A depth of up to 1 meter is expected to be achievable. An important addition to the work is a UV radiation sensor, which is part of the environmental sampling module.

A highly promising solution is the use of solar panels as part of the Power supply module, an approach adopted by various already-existing exploration rover projects [12, 13, 14]. However, the idea is not as straightforward in execution as in vehicles and devices operating on Earth—the distance and position of other planets in regards to the Sun, proper solar cell selection and consideration of an energy storage system for contingency or highest demand situations. A design of a collapsible solar array, for preserving the rover's mobility and stability when not charging, is possible.

#### 4. CONCLUSIONS

In this paper, the main capabilities of a proposed Sample Collection and Containment System have been summarized. This proposal is a simple and effective solution to the challenge of surface sample retrieval and transport.

The testing performed so far provides a confirmation of the effectiveness of drilling and sample collection down to 20 cm when mounted on the designed small-scale rover. The design of the sampling and drilling system can be scaled up appropriately for larger rovers.

Further tests are now planned to enhance the rover's system capabilities of detecting substances and materials of higher interest, in view of the space colonization objective, as well as Earth surface research.

#### BIBLIOGRAPHY

1. Moeller, R.C., Jandura, L., Rosette, K. et al. "The Sampling and Caching Subsystem (SCS) for the Scientific Exploration of Jezero Crater by the Mars 2020 Perseverance Rover." *Space Sci Rev* 217, 5 (2021). <https://doi.org/10.1007/s11214-020-00783-7>
2. Vago, J., Witasse, O., Svedhem, H. et al. "ESA ExoMars program: The next step in exploring Mars." *Sol Syst Res* 49, 518–528 (2015). Vago, J., Witasse, O., Svedhem, H. et al. *ESA ExoMars program: The next step in exploring Mars. Sol Syst Res* 49, 518–528 (2015). DOI: <https://doi.org/10.1134/S0038094615070199>
3. Sverrisson, A.I., Laxdal, B., Urbonas, I., Foley, J.T. (2024). "Design of Bio-inspired Gripper Arm for Mars Sample Retrieval." In: Puik, E., Cochran, D.S., Foley, J.T., Foith-Förster, P. (eds) *Proceedings of the 15th International Conference on Axiomatic Design 2023. ICAD 2023. Lecture Notes in Networks and Systems*, vol 849. Springer, Cham. DOI: [https://doi.org/10.1007/978-3-031-49920-3\\_10](https://doi.org/10.1007/978-3-031-49920-3_10)
4. Gromov, V. (1999). "Physical and Mechanical Properties of Lunar and Planetary Soils." In: Ehrenfreund, P., Krafft, C., Kochan, H., Pirronello, V. (eds) *Laboratory Astrophysics and Space Research. Astrophysics and Space Science Library*, vol 236. Springer, Dordrecht. DOI: [https://doi.org/10.1007/978-94-011-4728-6\\_5](https://doi.org/10.1007/978-94-011-4728-6_5)

5. Parnell J., Cullen D., Sims M. R., Bowden S., Cockell C. S., Court R., Ehrenfreund P., Gaubert F., Grant W., Parro V., Rohmer M., Sephton M., Stan-Lotter H., Steele A., Toporski J., and Vago J.. "Searching for life on mars: Selection of molecular targets for ESA's Aurora ExoMars mission." *Astrobiology*, 7(4):578–604, 2007. PMID: 177230. DOI: <https://doi.org/10.1089/ast.2006.0110>
6. Magnani, Piergiovanni, et al. "The drill and sampling system for the exomars rover." *International Symposium on Artificial Intelligence, Robotics and Automation in Space (i-SAIRAS)*. 2010.
7. Thangeda P. and Ornik M., "Adaptive Sampling Site Selection for Robotic Exploration in Unknown Environments," 2022 IEEE/RSJ International Conference on Intelligent Robots and Systems (IROS), Kyoto, Japan, 2022, pp. 4120-4125. DOI: 10.1109/IROS47612.2022.9982113.
8. Younse P. et al., "Sample acquisition and caching using detachable scoops for mars sample return," 2009 IEEE Aerospace conference, Big Sky, MT, USA, 2009, pp. 1-12, DOI: 10.1109/AERO.2009.4839312.
9. Fantoni G., Capiferri S., and Tilli J.. "Method for supporting the selection of robot grippers." *Procedia CIRP*, 21:330–335, 2014. 24th CIRP Design Conference.
10. Vago JL, et. al.. "Habitability on Early Mars and the Search for Biosignatures with the ExoMars Rover." *Astrobiology*. 2017 Jul 1;17(6-7):471-510. DOI: 10.1089/ast.2016.1533. PMID: 31067287; PMCID: PMC5685153.
11. Ravi kiran Bollineni, Sidharth S. Menon, and Ganesha Udupa. "Design of rover and robotic arm." *Materials Today: Proceedings*, 24:1340–1347, 2020. International Conference on Advances in Materials and Manufacturing Applications, IConAMMA 2018, 16th -18th August, 2018, India.
12. Michaud, Stéphane, et al. "SOLERO: Solar powered exploration rover." *Proc. of The 7. ESA Workshop on Advanced Space Technologies for Robotics and Automation (ASTRA)*. ETH-Zürich, 2002.
13. P. M. Stella, R. C. Ewell and J. J. Hoskin, "Design and performance of the MER (Mars Exploration Rovers) solar arrays," *Conference Record of the Thirty-first IEEE Photovoltaic Specialists Conference, 2005.*, Lake Buena Vista, FL, USA, 2005, pp. 626-630, doi: 10.1109/PVSC.2005.1488209.
14. Ochotorena, Michaela, et al. "Solar Solution for Mini-Rover." (2022).



17th-19th June 2024  
Gliwice, Poland

DEPARTMENT OF ENGINEERING MATERIALS AND BIOMATERIALS  
FACULTY OF MECHANICAL ENGINEERING  
SILESIA UNIVERSITY OF TECHNOLOGY

## INTERNATIONAL STUDENTS SCIENTIFIC CONFERENCE

### **Advanced Surface Engineering and characterization Techniques for Enhancing and Understanding Charge Injection Processes in Metal/Organic Interfaces of Optoelectronic Devices**

Sakineh Akbari Nia <sup>a</sup>, Mirosław Bonek <sup>b</sup>

<sup>a</sup> Silesian University of Technology, Institute of Physics – CSE, Gliwice, Poland,  
mail: sakbari@polsl.pl

<sup>b</sup> Silesian University of Technology, Faculty of Mechanical Engineering, Department of Engineering Materials and Biomaterials, Gliwice, Poland

**Abstract:** Advanced surface engineering plays an essential role in increasing the performance and efficiency of optoelectronic devices, such as light-emitting diodes, solar cells, photodetectors, and transistors. These devices heavily rely on the interaction between light and semiconductor materials at their surfaces. Key aspects of advanced surface engineering include surface passivation, texturing, surface Plasmon resonance (SPR), functionalization, coatings, and cleaning. In this concise review, we aim to provide insights into advanced surface engineering techniques and surface characterization techniques crucial for performing and understanding charge injection processes at metal/organic interfaces, a significant research area in the field of optoelectronic devices.

**Keywords:** Metal/organic interfaces, surface engineering, characterization, charge injection

#### **1. INTRODUCTION**

In recent decades, optoelectronic devices and their evaluation have become one of the most widespread technologies, from smartphone displays to solar energy harvesting systems[1]. After inventing a device, increasing the performance and efficiency of the device is becoming an important issue. About optoelectronic devices, the performance can be increased not only by the properties of the semiconductor materials[2], [3] but also by the engineering of their surfaces, and consequently the interfaces[2], [4]; because, surface defects, dangling bonds, and other imperfections can hinder the interaction between light and semiconductor materials processes, leading to decrease in converting photons into electrical current or vice versa and consequently reduced device performance and efficiency[5]. In the structure of the optoelectronic devices, there will be several interfaces, as shown in Figure 1, playing an important role in light absorption, emission, and charge transport processes. As it has been shown in Figure 1, to convert a surface into an interface, it is necessary to add a new layer on top of a deposited layer[6]. Therefore, the strict control of surface properties including surface adsorbates and contaminations is crucial. In this review, we aim to seek advanced surface

engineering for optoelectronic devices. We especially are going to focus on surface characterization technologies to provide valuable insights into the optimization of optoelectronic device performance and pave the way for future advancements in this rapidly evolving field.

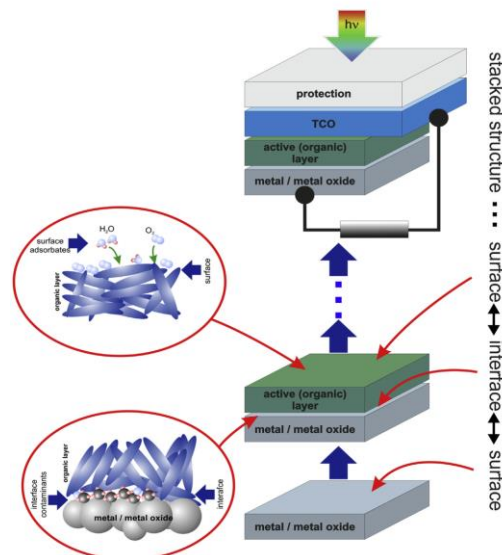


Figure 1. Schematic diagram of a multilayer photovoltaic cell[6]

## 2. ADVANCED METHODS AND TECHNOLOGY FOR SURFACE ENGINEERING AND SURFACE CHARACTERIZATION

To address the challenges mentioned in the introduction section, advanced surface engineering techniques (ASETs) have emerged as key strategies for enhancing the performance of optoelectronic devices. ASETs include a wide range of approaches such as surface cleaning, passivation, Plasmon resonance, coatings, and functionalization. Mainly, ASETs aim to minimize non-radiative recombination and losses. In other words, applying ASETs results in improved light absorption and extraction, and mitigate degradation mechanisms[7], [8].

To evaluate the electronic, chemical, and structural properties of the surfaces and interfaces in the fabricated optoelectronic devices, surface characterization techniques (SCTs) play a fundamental role. By providing insights into surface morphology, chemical composition, and electronic structure, these techniques facilitate a deeper understanding of surface-engineering strategies and their impact on device performance[9], [10].

In continuation, some of the most commonly used ASETs, as mentioned above, are briefly described. Also, we provide an overview of key surface characterization techniques commonly employed in the study of optoelectronic devices.

### 2.1. ASETs

Among the ASETs, surface cleaning is the easiest and most necessary to prepare the surface and provide a better interface. Surface cleaning strategy can remove surface residues, contaminants, and native oxides[11]. Therefore, this method can provide a uniform surface and effectively increase the performance of the fabricated optoelectronic devices. Ultraviolet ozone cleaning[12], plasma tuning[13], [14], and solvent cleaning[15] are utilized to gain a clean and uniform surface.

The performance of the optoelectronic devices can be degraded by dangling bonds and surface defects due to non-radiative recombination centers' introduction or surface recombination. As surface passivator methods, chemical passivation, plasma-enhanced chemical vapor deposition, and atomic layer deposition are utilized. These methods can diminish surface recombination centers and increase device performance and efficiency[16], [17].

Light-matter interaction as a main process inside the optoelectronic devices is manipulated by surface Plasmon resonance at the nanoscale. Therefore, depositing metallic nanoparticles or Nanofilms on the surface can enhance light emission, transmission, or absorption by coupling with surface Plasmon[8].

Besides, to protect the surface of the optoelectronic devices against environmental degradation, a thin layer, such as passivation layers, anti-reflection coatings, and encapsulation layers, should be deposited. This thin film coating process can improve charge carrier injection and extraction[18].

Organic and inorganic materials are usually used as surface functionalization materials to modify the surface properties to tune the optical properties, electronic structure, and charge transport properties of optoelectronic devices. Organic/inorganic surface modifiers[19], self-assembled monolayers[20], and surface ligands[21] are usually utilized for surface functionalization.

## **2.2. SCTs**

After modification, the modified surfaces and interfaces need to be characterized by appropriate techniques surface characterization techniques, for probing different aspects of surface properties, with a diverse helpful array of techniques. Atomic force microscopy (AFM), scanning electron microscopy (SEM), scanning tunneling microscope (STM), ultraviolet photoelectron spectroscopy (UPS), and X-ray photoelectron spectroscopy (XPS) are the most famous and important SCTs. These methods can provide us an insight into the effectiveness of the strategies applied for surface engineering; so that, with a combination application of SCTs, we can obtain comprehensive information about the surface morphology, electronic structure, and chemical composition, thereby guiding the development and optimization of optoelectronic devices.

## **3. CHARGE INJECTION PROCESSES IN METAL/ORGANIC INTERFACES OF OPTOELECTRONIC DEVICES**

To increase the performance of optoelectronic devices, charge injection at the interface between metal electrodes and organic semiconductors has an undeniable role. Therefore, focusing on the parameters affecting the injection current is essential. Charge transport in organic materials is based on the site-to-site hopping method because organic materials are van der Waals solids and have highly localized electron states[22].

To evaluate a tunable charge injection barrier at the metal/organic interface, XPS and UPS methods have commonly been applicable[23]. After emitting X-ray photons at a sample and causing the emission of photoelectrons from the surface, by measuring the kinetic energies of these photoelectrons, XPS and UPS can determine the elemental composition and chemical bonding states present on the surface of a material[23].

Charge injection at metal/organic interfaces in optoelectronic devices is influenced by several parameters playing a crucial role in determining device performance and efficiency. In continuation, the most important factors affecting charge injection in metal/organic interfaces will be concisely explained.

### 3.1 Charge Injection Processes in Metal/Organic Interfaces of Optoelectronic Devices

#### 3.1.1. Work function

Work function is the minimum energy required to remove an electron from a solid to a point just outside its surface. Materials with different work functions can induce charge transfer across their interface. The energy level alignment between the metal electrode and the organic semiconductor is critical for efficient charge injection because, in a typical organic semiconductor, there are no intrinsic charge carriers and all charges must be injected from electrode-organic interfaces; so that, a favorable alignment minimizes the energy barrier for charge carrier injection from the metal into the organic material. Therefore, the electronic structure or the energy level of this structure determines the performance of these devices. As the metal is the main injector, the work function of the metal has a crucial role in the barrier height in this interface[24]. This parameter can be easily evaluated by UPS measurements and Kelvin probe measurements (KPM). Figure 2 demonstrates the schematic energy-level diagram of different organic optoelectronic devices (where parts a, b, c, and d show two-layered OLED, two-layered OPV, one-layer p-OFET, and one-layer OFET, respectively). The movement of charge carriers has been shown by the green arrows. Charge injection barriers have been shown by  $\Delta h$  and  $\Delta e$ , respectively for hole and electron injection barriers.

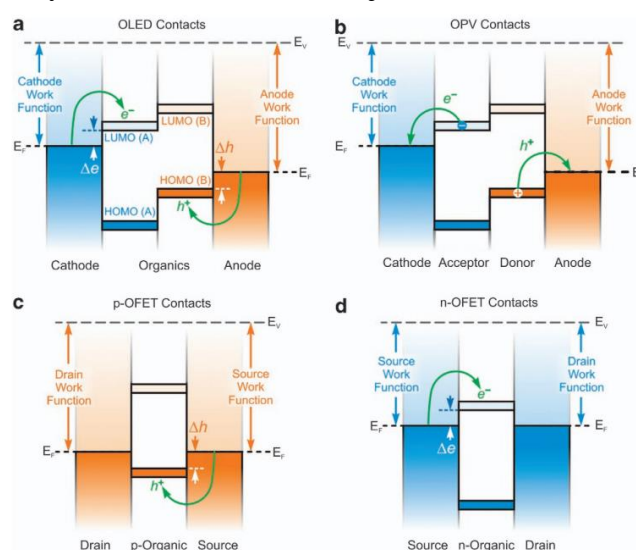


Figure 2. Schematic energy-level diagram for different organic optoelectronic devices[24]

#### 3.1.2. Morphology, Roughness, and Surface Modification

Furthermore, the charge injection processes in the metal/organic interface can significantly be affected by the morphology and roughness of the interface. When the interface is smoother and includes an intimate contact between the metallic electrode and the organic semiconductor, it can facilitate efficient charge transfer. In this research area of advanced interface engineering, we also can discuss surface treatment technologies such as surface modification, interfacial layers, or self-assembled monolayers that can modify the energy levels and interfacial

properties, improving charge injection and reducing interface barriers. Analysis such as AFM, SEM, and TEM are used to consider the topology and morphology of the layer to evaluate the changes. Morphology, roughness, and surface modification by utilizing atmospheric argon plasma have been considered to increase the charge injection in the fabrication process of the MEH-PPV-based light-emitting diodes[13], [25].

### 3.1.3. Contact Resistance

The resistance at the metal/organic interface impacts charge injection efficiency, and it can be managed by advanced surface engineering methods. Sangmoo Choi et al. considered a method to reduce the contact resistance in organic field-effect transistors[26]. Based on the correlation between the work function of the source and drain electrodes and the contact resistance, they reported a remarkable decrease in contact resistance attributed to the reduction of vertical bulk resistance in contacts of the organic field-effect transistors. Lower contact resistance leads to more efficient charge transfer and reduced voltage losses. Contact resistance is mainly measured by the transfer line method (TLM) and the four-probe technique which is more reliable[27]. Figure 3 demonstrates the Width-normalized contact resistance as a function of the work function values of electrodes[26].

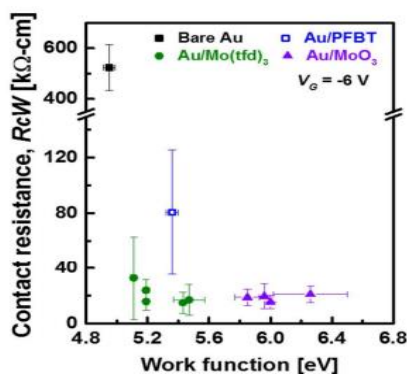


Figure 3. Width-normalized contact resistance as a function of work function values of electrodes[26]

### 3.1.4. Material Properties and Energy Level Offset

Choosing the organic semiconductor and metal electrode materials, wisely, can effectively impact charge injection. Materials with suitable electronic properties, such as high carrier mobility and appropriate energy levels, are preferred for efficient charge injection. The offset of the energy level between the highest occupied molecular orbital (HOMO) or lowest unoccupied molecular orbital (LUMO) of the organic semiconductor and the Fermi level of the metal electrode, as a potential barrier, influences charge injection. A suitable energy level alignment provides an efficient injection of electrons or holes[28]. The most useful characterization methods here are XPS and UPS.

### 3.1.5. Interface Dipoles

When materials come into contact, electrons redistribute to equalize the electrochemical potential. This redistribution results in a net charge separation at the interface, creating a dipole moment. Differences in electronegativity or work function between the metal and organic materials are the origin of forming interface dipoles. Also, the arrangement of atoms and chemical bonds at the interface can contribute to dipole formation. The presence of surface



dipoles can significantly influence charge injection by modifying the energy barrier for carrier transfer[7], [12].

Advanced surface engineering techniques such as surface modification, interfacial engineering, and selection of appropriate materials can be employed to tailor surface dipoles and optimize device functionality. Also to consider the effect of the applied surface engineering methods, the advanced characterization method such as XPS and UPS is essential.

### **3.1.6. Temperature and Environmental Effects**

This factor should be noticed before fabricating all optoelectronic devices; because these devices mainly are used in different temperatures and environmental situations. Especially, solar cells which are installed directly under the influence of the focused sunlight. Also, this factor can be counted as an advantage; so that, temperature variations and environmental conditions can influence charge injection by affecting the molecular packing, interface properties, and energy level alignment at the metal/organic interface. Therefore, during the fabrication process, the annealing process, and the other helpful surface engineering methods can be considered to gain the best interface properties[22], [29].

### **3.1.7. Device Architecture**

The device structure and configuration, including the layer thicknesses, interfacial layers, and electrode geometry, influence charge injection efficiency by affecting the electric field distribution and charge transport pathways[28].

### **3.1.8. Device Processing Techniques**

Fabrication methods, such as thermal evaporation, chemical vapor deposition, or spin coating can affect the morphology and quality of the metal/organic interface, thereby impacting charge injection properties[22], [29].

## **4. CONCLUSION**

In conclusion, to enhance the efficiency and performance of optoelectronic devices by optimizing charge injection processes at metal/organic interfaces, ASETs play an important role. Here, we tried to provide a comprehensive review of the most applicable ASETs including surface cleaning, passivation, surface Plasmon resonance, coatings, and functionalization. Also, it has been highlighted that the mentioned technologies mainly lead to improving light absorption and extraction, minimizing non-radiative recombination and losses, and mitigating degradation mechanisms. Furthermore, the importance of SCTs (such as AFM, SEM, STM, UPS, and XPS) to understanding surface morphology, chemical composition, and electronic structure is undeniable. The SCTs offer valuable insights into the effectiveness of surface engineering strategies and their impact on device performance.

The discussion on charge injection processes at metal/organic interfaces underscored the critical parameters influencing device efficiency. Understanding and optimizing the parameters are imperative for realizing the full potential of organic optoelectronic devices. By addressing the challenges associated with surface defects, dangling bonds, and interface imperfections, we can push the boundaries to improve device efficiency, reliability, and scalability.

## ACKNOWLEDGEMENTS

The publication was created within the framework of the joint Slovak-Polish project International Visegrad Fund's V4 Generation Mobility Mini-Grant No 12410044 as a result of cooperation between the Association of Alumni of the Silesian University of Technology, Gliwice, Poland and the University of Žilina, Slovakia.

The project is co-financed by the Governments of Czechia, Hungary, Poland and Slovakia through Visegrad Grants from the International Visegrad Fund. The mission of the fund is to advance ideas for sustainable regional cooperation in Central Europe.



## BIBLIOGRAPHY

1. C. Zheng, C. Bi, F. Huang, D. Binks, and J. Tian, "Stable and strong emission CsPbBr<sub>3</sub> quantum dots by surface engineering for high-performance optoelectronic films," *ACS Appl. Mater. Interfaces*, vol. 11, no. 28, pp. 25410–25416, 2019.
2. C. Liang *et al.*, "Boosting the optoelectronic performance by regulating exciton behaviors in a porous semiconductive metal–organic framework," *J. Am. Chem. Soc.*, vol. 144, no. 5, pp. 2189–2196, 2022.
3. K. Zhou *et al.*, "Single-crystal metal-organic frameworks for electronic and optoelectronic devices," *Cell Reports Phys. Sci.*, vol. 4, no. 11, 2023.
4. Y. C. Choi, J. Lee, J. J. Ng, and C. R. Kagan, "Surface Engineering of Metal and Semiconductor Nanocrystal Assemblies and Their Optical and Electronic Devices," *Acc. Chem. Res.*, pp. 7493–7501, 2023.
5. B. Nath *et al.*, "Understanding the Heterointerfaces in Perovskite Solar Cells via Hole Selective Layer Surface Functionalization," *Adv. Mater.*, p. 2307547, 2023.
6. L. Grządziel and M. Krzywiecki, "Chapter 8 - Interface and surface properties of oxide–organic hybrid nanostructures: From charge transfer to degradation effects," in *Nanostructured Thin Films*, vol. 14, M. Benelmekki and A. B. T.-F. of N. Erbe, Eds. Elsevier, 2019, pp. 215–256. doi: <https://doi.org/10.1016/B978-0-08-102572-7.00008-8>.
7. M. Ramezani, Z. Mohd Ripin, T. Pasang, and C.-P. Jiang, "Surface engineering of metals: techniques, characterizations and applications," *Metals (Basel)*, vol. 13, no. 7, p. 1299, 2023.
8. A. Zada *et al.*, "Surface plasmonic-assisted photocatalysis and optoelectronic devices with noble metal nanocrystals: design, synthesis, and applications," *Adv. Funct. Mater.*, vol. 30, no. 7, p. 1906744, 2020.
9. and A. E. Maciej Krzywiecki, Lucyna Grzadziel, Adnan Sarfraz, Danish Iqbal, Anna Sz wajcac, "No TZinc oxide as a defect-dominated material in thin films for photovoltaic applications – experimental determination of defect levels, quantification of composition, and construction of band diagramitle," *Phys. Chem. Chem. Phys.*, vol. 17, pp. 10004–10013, 2015.
10. R. M. Hewlett and M. A. McLachlan, "Surface structure modification of ZnO and the impact on electronic properties," *Adv. Mater.*, vol. 28, no. 20, pp. 3893–3921, 2016.
11. T. Dey and D. Naughton, "Cleaning and anti-reflective (AR) hydrophobic coating of glass surface: a review from materials science perspective," *J. Sol-Gel Sci. Technol.*, vol. 77, pp. 1–27, 2016.

12. M. Kim *et al.*, “Work function tuning of directly grown graphene via ultraviolet–ozone treatment for electrode application in organic photovoltaic devices,” *Surfaces and Interfaces*, vol. 41, p. 103228, 2023.
13. S. Akbari Nia, Y. S. Jalili, and A. Salar Elahi, “Application of argon atmospheric cold plasma for indium tin oxide (ITO) based diodes,” *AIP Adv.*, vol. 7, no. 9, p. 95210, 2017.
14. S. Molamohammadi, S. A. Nia, and Y. S. Jalili, “Improvement of inverted structure organic solar cells by Ar plasma treatment on P3HT: PC61BM active layer,” *Sustain. Energy Technol. Assessments*, vol. 34, pp. 43–48, 2019.
15. D. G. Purdie, N. M. Pugno, T. Taniguchi, K. Watanabe, A. C. Ferrari, and A. Lombardo, “Cleaning interfaces in layered materials heterostructures,” *Nat. Commun.*, vol. 9, no. 1, p. 5387, 2018.
16. X.-J. She *et al.*, “A solvent-based surface cleaning and passivation technique for suppressing ionic defects in high-mobility perovskite field-effect transistors,” *Nat. Electron.*, vol. 3, no. 11, pp. 694–703, 2020.
17. T.-Y. Seong and H. Amano, “Surface passivation of light emitting diodes: From nano-size to conventional mesa-etched devices,” *Surfaces and Interfaces*, vol. 21, p. 100765,
18. C. Ji *et al.*, “Recent applications of antireflection coatings in solar cells,” in *Photonics*, 2022, vol. 9, no. 12, p. 906.
19. S. H. Mir, L. A. Nagahara, T. Thundat, P. Mokarian-Tabari, H. Furukawa, and A. Khosla, “Organic-inorganic hybrid functional materials: An integrated platform for applied technologies,” *J. Electrochem. Soc.*, vol. 165, no. 8, pp. B3137–B3156, 2018.
20. S. Casalini, C. A. Bortolotti, F. Leonardi, and F. Biscarini, “Self-assembled monolayers in organic electronics,” *Chem. Soc. Rev.*, vol. 46, no. 1, pp. 40–71, 2017.
21. T. Han, S. Tan, J. Xue, L. Meng, J. Lee, and Y. Yang, “Interface and defect engineering for metal halide perovskite optoelectronic devices,” *Adv. Mater.*, vol. 31, no. 47, p. 1803515, 2019.
22. J. C. Scott, “Metal–organic interface and charge injection in organic electronic devices,” *J. Vac. Sci. Technol. A Vacuum, Surfaces, Film.*, vol. 21, no. 3, pp. 521–531, 2003.
23. Z. Xu, S. Li, L. Ma, G. Li, G. Yang, and Y. Yang, “A photoelectron spectroscopy study of tunable charge injection barrier between metal/organic interface,” *Appl. Phys. Lett.*, vol. 93, no. 2, 2008.
24. M. T. Greiner and Z.-H. Lu, “Thin-film metal oxides in organic semiconductor devices: their electronic structures, work functions and interfaces,” *NPG Asia Mater.*, vol. 5, no. 7, pp. e55–e55, 2013.
25. S. Akbari Nia, S. Mohammadi, and Y. Seyed Jalili, “Comparison of simulated and experimental data for optimized OLEDs,” *Opt. Quantum Electron.*, vol. 54, no. 4, pp. 1–15, 2022.
26. S. Choi *et al.*, “A study on reducing contact resistance in solution-processed organic field-effect transistors,” *ACS Appl. Mater. Interfaces*, vol. 8, no. 37, pp. 24744–24752, 2016.
27. G. Horowitz, “Interface modification for tuning the contact resistance of metal/organic semiconductor junctions,” *Open Appl. Phys. J.*, vol. 4, no. 1, 2011.
28. P. Li and Z.-H. Lu, “Interface Engineering in Organic Electronics: Energy-Level Alignment and Charge Transport,” *Small Sci.*, vol. 1, no. 1, p. 2000015, 2021.
29. M. Fahlman, S. Fabiano, V. Gueskine, D. Simon, M. Berggren, and X. Crispin, “Interfaces in organic electronics,” *Nat. Rev. Mater.*, vol. 4, no. 10, pp. 627–650, 2019.



17th-19th June 2024  
Gliwice, Poland

DEPARTMENT OF ENGINEERING MATERIALS AND BIOMATERIALS  
FACULTY OF MECHANICAL ENGINEERING  
SILESIA UNIVERSITY OF TECHNOLOGY

## INTERNATIONAL STUDENTS SCIENTIFIC CONFERENCE

### The micro-laser texturing process of stainless steel

Jan Sędlak<sup>a</sup>, Jakub Gawek<sup>a</sup>, Wojciech Pakieła<sup>b</sup>, Mirosław Bonek<sup>b</sup>, Anna Woźniak<sup>c</sup>

<sup>a</sup> V Liceum Ogólnokształcące z Oddziałami Dwujęzycznymi im. Andrzeja Struga

<sup>b</sup> Silesian University of Technology, 18a Konarskiego Str., 41-100 Gliwice, Poland, Department of Engineering Materials and Biomaterials, Faculty of Mechanical Engineering

<sup>c</sup> Silesian University of Technology, 18a Konarskiego Str., 41-100 Gliwice, Poland, Faculty of Mechanical Engineering, Materials Research Laboratory  
email: jachojachojacho@gmail.com, jakub.gawek@gmail.com

**Abstract:** Modern surface engineering, especially using laser beams, offers precise modification of material structures and properties through cutting, alloying, melting, ablation, welding, and engraving. Key parameters such as laser power, exposure time, and shielding gas type are crucial for optimal results. In our research, we used a picosecond laser for texturing, creating microgrooves and honeycomb patterns. The resulting textures demonstrated high quality with excellent dimensional and shape accuracy, closely matching the design specifications. The use of lasers in production enhances product competitiveness by providing advanced repeatability, efficiency, and automation capabilities, underscoring their transformative impact on modern manufacturing and material science.

**Keywords:** 316L stainless steel, laser texturing, picosecond lasers

## 1. INTRODUCTION

Modern surface engineering is relentlessly advancing, seeking innovative tools for the precise modification of material structures and properties. The use of laser beams as a precise engineering instrument is one of the most popular methods in recent years. A laser beam, characterized by its concentrated, high-intensity light, can interact with materials through various mechanisms, including melting, evaporation, ablation, and structural modification. This technology unlocks new possibilities across diverse fields such as manufacturing, micromechanics, medicine, and numerous other technological domains. By manipulating critical parameters - such as laser power, scanning speed, and the type of shielding gas, leads to achieving highly economical, precise, and efficient operations. The automation of laser processes in production settings further amplifies product competitiveness in the market, owing to enhanced repeatability and exceptional efficiency. As a result, laser-based surface engineering stands out as a transformative approach, propelling advancements in modern technology and material science [1].

Laser ablation is a highly precise and versatile technique used in various scientific and industrial applications. It involves the removal of material from a solid surface by irradiating it with a laser beam. The process begins when the laser energy is absorbed by the material, causing rapid heating, melting, and vaporization of the surface layers. The high-energy laser radiation weakens the atomic bonds, resulting in the ejection of atoms or clusters of atoms from the surface. One of the key advantages of laser ablation is its ability to precisely control the amount of material removed, which allows for the creation of intricate patterns and structures with high dimensional accuracy. The process parameters, such as laser wavelength, pulse duration, intensity, and scanning speed, can be finely tuned to achieve the desired results. This level of control makes laser ablation suitable for a wide range of applications, from microelectronics and medical device manufacturing to art restoration and material science research. Laser ablation can be used to modify the surface properties of materials, such as improving their hardness, wear resistance, or biocompatibility. Additionally, it is a clean and efficient process, as it typically produces minimal waste and can be performed in various environments, including air, vacuum, or under protective gases. The technique's ability to create precise and complex structures, coupled with its adaptability and efficiency, underscores its importance in modern technology and material engineering [2].

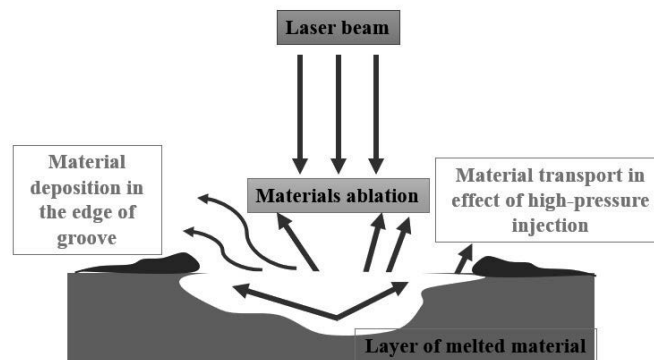


Figure 1. Scheme of laser ablation process.

Picosecond lasers, which emit pulses lasting one trillionth of a second (10<sup>-12</sup> seconds), are renowned for their precision and minimal thermal damage [3]. These ultra-short pulses allow for high peak power and non-linear material interactions, enabling precise ablation and modification with minimal heat diffusion. This makes picosecond lasers ideal for applications in microelectronics, medical devices, and delicate material processing [4-7].

## 2. MATERIAL AND METHODS

### 2.1 Material

Austenitic stainless steel 316L, the substrate material, was subjected to laser texturing process. Table 1 shows the chemical composition of stainless steel used.

Table 1. Chemical composition of 316L stainless steel.

Element, wt. (%)											
Cr	Ni	Mo	C	Si	Mn	Nb	P	S	N	Cu	Fe
19.00-21.00	10.00-11.00	2.00-3.00	≤0.03	≤1.00	≤12.00	0.25-0.80	≤0.04	≤0.03	≤0.10	≤0.25	rest

## 2.2 Methods

The surface texturing process was conducted using an A-355 picosecond laser system (Oxford Lasers Ltd) (Figure 2). This system features a 335 nm wavelength, diode-pumped solid-state picosecond laser capable of generating pulse durations of 5-10 ps with an energy of 120  $\mu\text{J}$  at a pulse frequency of 400 Hz. The average laser power utilized was 24 mW. The picosecond laser ensures effective ablation, where high-energy laser radiation weakens the atomic bonds (Fig. 1a), causing atoms to evaporate layer by layer. All samples underwent texturing under identical conditions at room temperature ( $T = 22.5 \pm 1^\circ\text{C}$ , humidity  $53 \pm 1\%$ ), with a jet of air used to remove debris produced during the process.



Parameter	[unit]
Laser	Picosecond laser system
Wave length	335 nm
Power	18 mW
Pulse frequency	1 – 400 Hz
Pulse time	5-10 ps (6 ps)
$M^2$	<1.2
Laser beam diameter	1,5 mm
Beam divergence	$\sim 0.65$ mrad

Figure 2. A-355 picosecond laser system and machine parameters (specification).

The laser patterning strategy was developed using Cimita software (Oxford Lasers, Didcot, UK), integrated into the micromachining system. Two texture laser pattern was selected: (I) groove layout that formed a truss pattern with a groove spacing of 150  $\mu\text{m}$  (Figure 3a), (II) the tightly arranged regular hexagonal honeycomb pattern with the side length of 290  $\mu\text{m}$  (Figure 3b). The laser beam was precisely focused on the sample surface to achieve a diameter of 30  $\mu\text{m}$  (Figure 2). Laser texturing parameter conditions were defined and given in Table 2.

Table 2. Laser-texturing process parameters.

Name	N, Number of the passes of the laser beam	Laser scan speed (mm/s)	Frequency (Hz)	Laser Power (mW)	Beam width ( $\mu\text{m}$ )	Beam quality factor $M^2$
S1	6	1	400	28	30	<1.2
S2	8	1				

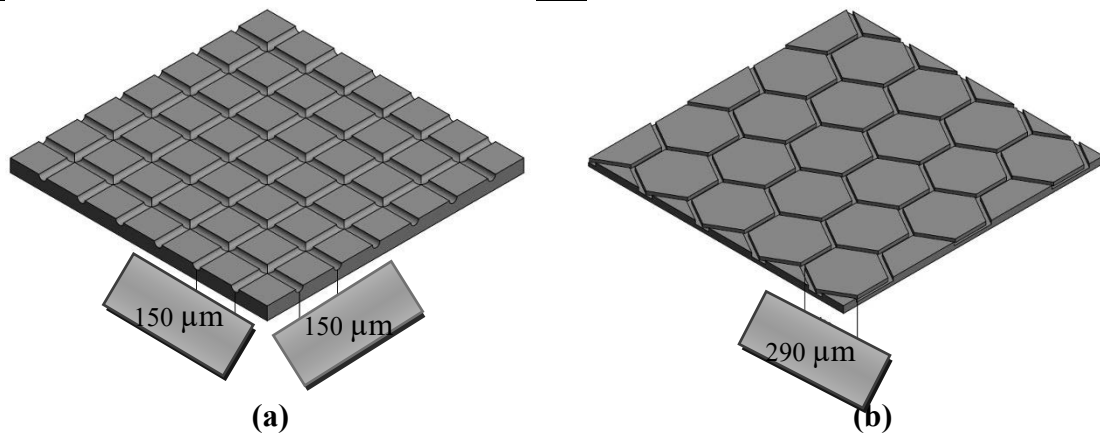


Figure 3. Selected laser pattern (a) S1 samples group, and (b) S2 samples group.

The view of the Cimita software with pointed main process parameters during the process was presented in Figure 4.

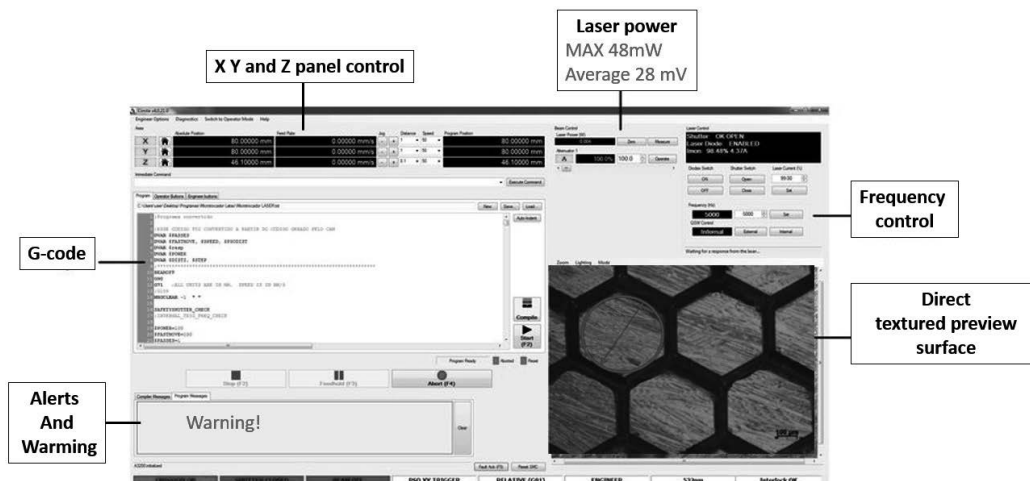


Figure 4. Cimita panel control.

Next sample was placed into microtexturing machine and the process was started (Figure 5).

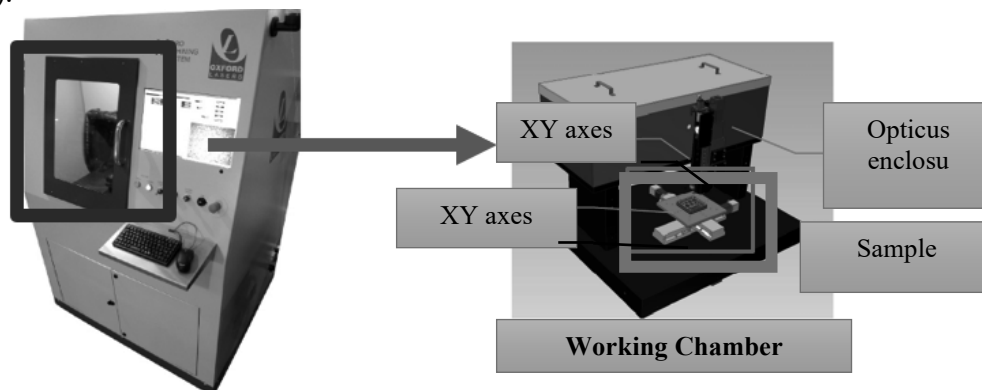


Figure 5. Positioning samples in the working chamber.

To surface topography examination the digital 3D microscope DVM6 (Leica Microsystems, Wetzlar, Ger-many) was used.

### 3. RESULTS

Laser-textured processes were carried out on both groups of samples. The results of samples after laser texturing process surface observation in the form of 2D and 3D view were presented in Figure 6 and 7, respectively. Laser-textured processes were carried out on both groups of samples. The dimples created had a consistent diameter that closely matched the design specifications. Figure 6 a-b, and 7a demonstrates that the dimensions of the truss and honeycomb patterns produced were in line with the planned design. For the S1 sample group, the grooves were regularly spaced and uniform, with an average spacing of  $248 \pm 3 \mu\text{m}$ , which aligned well with the designed laser texture pattern. In the S2 sample group, each hexagon was approximately  $290 \mu\text{m}$  in size (Figure 6 c-d and 7b). Microscopic analysis indicated that the

grooves displayed typical laser-induced surface features, created by the interaction between the laser beam and the sample surface.

The surfaces textured through laser ablation were characterized by continuous grooves with irregular, explosively evaporated bottoms (Figure 6). In the S1 and S2 sample groups, this process resulted in areas with varying colours, a consequence of different oxide films forming on the treated surfaces. The texturing was performed without the use of a protective atmosphere.

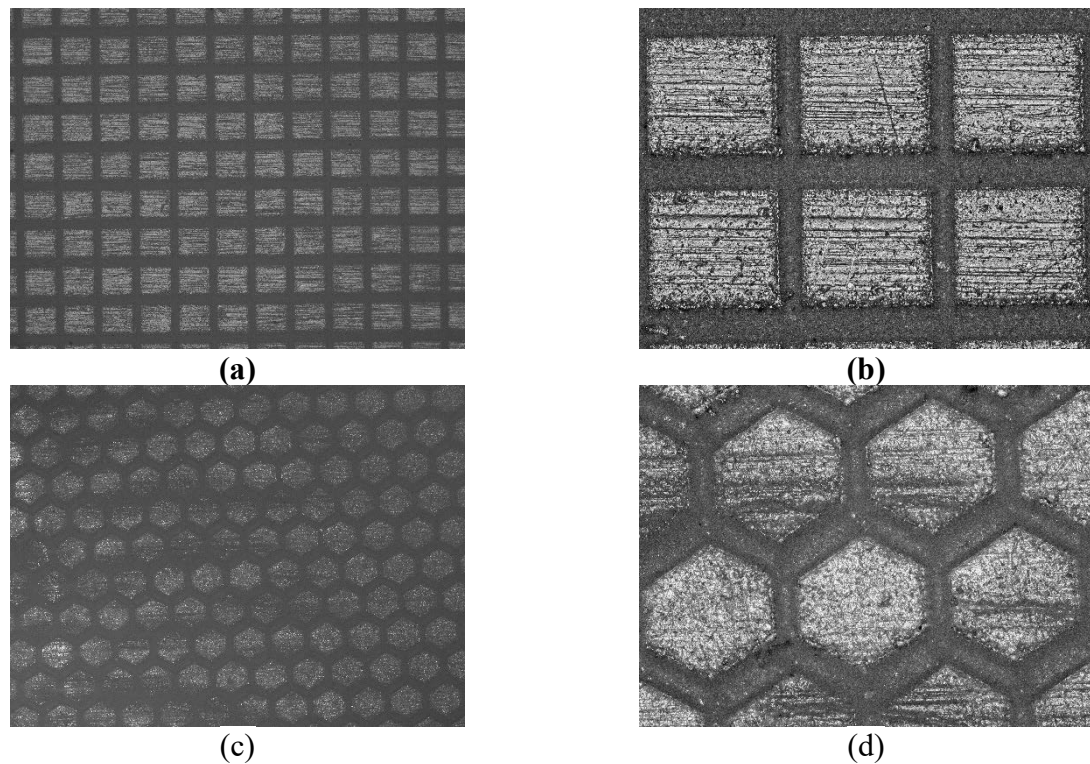


Figure 5. 2D view of samples surface topography: (a) and (b) microgroove texture pattern, (c) and (d) hexagonal honeycomb texture pattern.

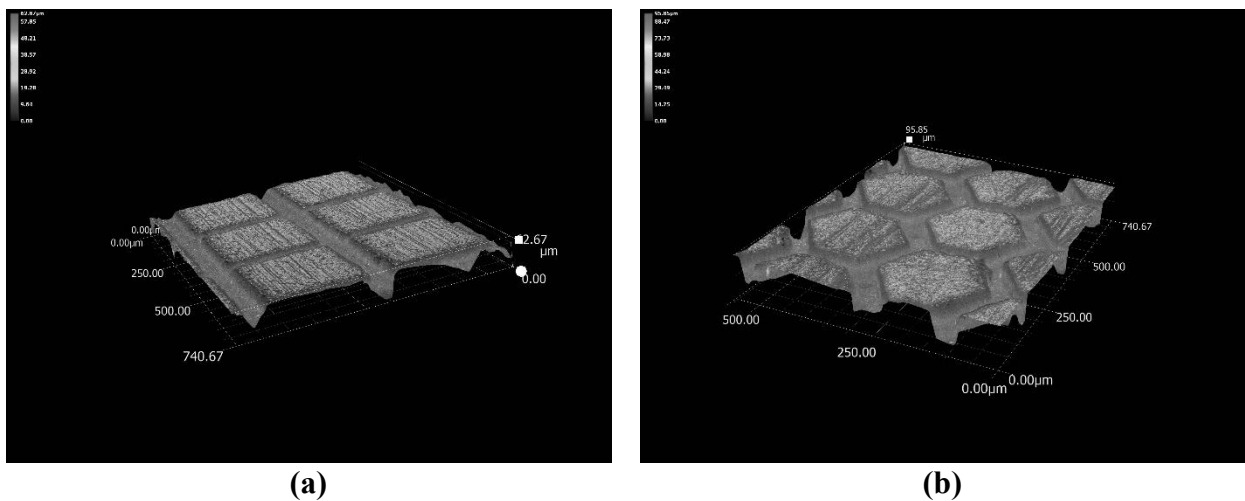


Figure 6. 3D view of samples surface topography: (a) microgroove texture pattern, and (b) hexagonal honeycomb texture pattern.



#### 4. CONCLUSION

Laser-based technologies exemplify their versatility through a wide range of applications. Surface treatment, in particular, is crucial as it enables the modification of material structures and the alteration of their properties. Our research has demonstrated that laser micro-texturing systems can produce surface structures with high dimensional accuracy, closely matching the designed shapes. This precision underscores the effectiveness of laser technology in achieving intricate and accurate patterns on material surfaces.

#### ACKNOWLEDGEMENTS

The work was created as a result of a project carried out with secondary school students as part of project-oriented education - PBL, as part of the Excellence Initiative - Research University, Silesian University of Technology program.

#### BIBLIOGRAPHY

- [1] A. Woźniak, M. Adamiak, G. Chladek, M. Bonek, W. Walke, O. Bialas, The Influence of Hybrid Surface Modification on the Selected Properties of CP Titanium Grade II Manufactured by Selective Laser Melting, *Materials* (Basel). 13 (2020) 2829. <https://doi.org/10.3390/ma13122829>.
- [2] Y. Cai, X. Luo, M. Maclean, Y. Qin, M. Duxbury, F. Ding, A single-step fabrication approach for development of antimicrobial surfaces, *J. Mater. Process. Technol.* 271 (2019) 249–260. <https://doi.org/10.1016/j.jmatprotec.2019.04.012>.
- [3] A. Grabowski, T. Florian, J. Wiczorek, M. Adamiak, Structuring of the Ti6Al4V alloy surface by pulsed laser remelting, *Appl. Surf. Sci.* 535 (2021) 147618. <https://doi.org/10.1016/j.apsusc.2020.147618>.
- [4] [https://esab.com/pl/eur\\_pl/esab-university/blogs/what-is-laser-welding-and-how-does-the-technique-work/](https://esab.com/pl/eur_pl/esab-university/blogs/what-is-laser-welding-and-how-does-the-technique-work/)
- [5] <https://www.drukarniasrem.pl/blog/przebieg-i-zastosowanie-grawerowania-laserowego>
- [6] <https://procestechnologiczny.com.pl/teksturowanie-laserowe-gfms-laser-p/>



17th-19th June 2024  
Gliwice, Poland

DEPARTMENT OF ENGINEERING MATERIALS AND BIOMATERIALS  
FACULTY OF MECHANICAL ENGINEERING  
SILESIA UNIVERSITY OF TECHNOLOGY

## INTERNATIONAL STUDENTS SCIENTIFIC CONFERENCE

### **Wykorzystanie termowizji w kontroli przebiegu laserowej obróbki powierzchniowej**

Tymoteusz Setnik <sup>a</sup>, Jan Płocica <sup>a</sup>, Mirosław Bonek <sup>b</sup>

<sup>a</sup> Uczeń V Liceum Ogólnokształcące z Oddziałami Dwujęzycznymi im. Andrzeja Struga w Gliwicach, email: rozer0902@gmail.com

<sup>b</sup> Politechnika Śląska, Wydział Mechaniczny Technologiczny, Katedra Materiałów Inżynierskich i Biomedycznych

#### **WPROWADZENIE**

Termowizja, zwana też termografią, stała się techniką powszechnie stosowaną nie tylko w przemyśle, energetyce czy budownictwie. Z powodzeniem wykorzystywana jest przez personel medyczny, służby leśne, wojsko czy policję. W dobie pandemii sprawdziła się przy masowej kontroli temperatury ludzi wchodzących na lotniska czy do centrów handlowych i pozwalała „wyłapać” osoby gorączkujące, a więc potencjalnie chore, które mogły przyczynić się do rozpowszechniania patogenów. Technologia na tyle spowszechniała, że bez problemu można nabyć nawet nakładki termowizyjne na smartfony czy telefony fabrycznie wyposażone w kamery termowizyjne. Kamera termowizyjna rejestruje promieniowanie podczerwone emitowane przez obiekt i przetwarza je na obraz widzialny przedstawiający rozkład temperatury. Detektor wewnątrz kamery odbiera światło podczerwone i przetwarza je na sygnał elektryczny proporcjonalny do temperatury obiektu. Elektronika aparatu przekształca te sygnały w obrazy termowizyjne, w których różne kolory odpowiadają różnym temperaturom. Kamery te są kalibrowane w celu zapewnienia dokładności pomiaru, a wyniki można wizualizować i analizować na ekranie kamery lub komputera.

Termowizja jest obecnie najpopularniejszą metodą bezkontaktowego obrazowania i rejestrowania rozkładu temperatury na badanych obiektach, przy wykorzystaniu detekcji promieniowania podczerwonego, oznaczanego też jako IR, od ang. infrared, która nie powoduje zmian w środowisku badanym. Początek termowizji datuje się na 1800 r., kiedy to w trakcie poszukiwań filtra optycznego, który mógłby ograniczać jaskrawość obrazu słońca w teleskopie astronom sir William Herschel przypadkowo odkrył promieniowanie podczerwone. W 1803 r. Saussure i Pictet potwierdzili, że promieniowanie podczerwone może być odbijane, rozszczepiane, załamywane i transmitowane, dokładnie w taki sam sposób, jak promieniowanie widzialne.

W połowie XX w., w wyniku intensywnych prac związanych z wojskowym wykorzystaniem techniki podczerwieni, zbudowano pierwsze kamery podczerwone, a w latach 60. pojawiły się pierwsze urządzenia termowizyjne do zastosowań cywilnych. Kamera termowizyjna, nazywana też kamerą termalną lub termowizorem to urządzenie do rejestracji i wizualizacji rozkładu

temperatury na powierzchniach obiektów czyli odwzorowania obrazu termalnego obserwowanych obiektów.

## 1. ZASTOSOWANIE TECHNIK TERMOWIZYJNYCH

Każdej barwie wyświetlanego na ekranie kamery termowizyjnej termogramu odpowiada ściśle określona, zarejestrowana temperatura. Z reguły barwami jasnymi oznacza się powierzchnie o wysokiej temperaturze, natomiast kolorami ciemniejszymi powierzchnie o temperaturze niższej. Ponadto współczesne kamery termowizyjne umożliwiają precyzyjne określenie temperatury w wybranym miejscu. Co więcej, istnieje też możliwość porównania termogramów wykonanych w różnym czasie lub na różnych obiektach, dzięki czemu łatwo zaobserwować tendencje i różnice, dzięki określeniu zmian temperatury na powierzchni badanego obiektu. Możliwa jest też analiza termogramów polegająca na wykreślaniu izoterm, określaniu rozkładu temperatury wzdłuż dowolnego profilu lub obiektu, tworzenie i wyświetlanie histogramów czy też podawanie uśrednionej wartości temperatury. Zastosowanie technik termowizyjnych w sterowaniu laserową obróbką powierzchni ma ogromne znaczenie, ponieważ umożliwia bezdotykowy pomiar temperatury powierzchni obrabianej próbki.

Procesy laserowej obróbki powierzchni, takie jak spawanie, cięcie i wykańczanie, generują wysokie temperatury, które mają kluczowe znaczenie dla wydajności i jakości procesu.

Monitoring temperatury: Technologia termowizyjna pozwala na ciągłe monitorowanie temperatury na powierzchni obrabianej próbki.

Umożliwia to operatorom śledzenie zmian temperatury i dostosowywanie parametrów obróbki w czasie rzeczywistym, pomagając w utrzymaniu odpowiednich warunków obróbki.

Identyfikacja obszarów problematycznych: Termowizja pozwala również na identyfikację obszarów narażonych na ryzyko nadmiernego nagrzania lub niepożądanych efektów termicznych.

Umożliwia to operatorom szybką reakcję i uniknięcie szkód materialnych.

Ocena efektywności procesu: Analizując dane obrazu termowizyjnego, możesz ocenić postęp procesu obróbki.

Na ich podstawie można ocenić równomierność rozkładu temperatury na powierzchni obrabianej próbki oraz zidentyfikować obszary, w których mogą pojawić się defekty i nieregularności.

Kontrola jakości: Termowizja może być również wykorzystana do kontroli jakości produkowanych części.

Analiza obrazów termicznych może wykryć defekty, takie jak słabe połączenia lub niespójności temperaturowe, które mogą wskazywać na niedoskonałości procesu obróbki.

## 2. ZASTOSOWANIA KAMERY TERMOWIZYJNEJ PRZY RÓŻNYCH TECHNOLOGIACH LASEROWYCH

Pomiar temperatury przy wykorzystaniu termowizji polega na zmierzeniu natężenia promieniowania, które jest emitowane przez wszystkie ciała o temperaturze wyższej od zera bezwzględnego (0 K, czyli  $-273,15\text{ }^{\circ}\text{C}$ ). Następnie wykorzystując prawo Plancka i znając

zakres spektralny, w jakim obserwuje się promieniowanie cieplne, można wyznaczyć temperaturę na powierzchni ciała emitującego promieniowanie.

Długość fali promieniowania cieplnego mieści się w granicach od 760 nm do 1 mm. Jest ono wykrywane i mierzone przez urządzenia termowizyjne dwoma sposobami. Z pierwszym mamy do czynienia wówczas, gdy detektor pochłania całkowicie promieniowanie podczerwone o każdej długości fali; z drugim, gdy detektor reaguje jedynie na promieniowanie o ściśle określonej długości fali. Następnie detektor, a w zasadzie matryca detektorów kamery termowizyjnej, bo inaczej mielibyśmy do czynienia z pomiarem punktowym, tak jak w pirometrze, zamienia energię promieniowania podczerwonego na sygnał elektryczny. Sygnał ten jest dalej przetwarzany przez elektronikę kamery i oprogramowanie wewnętrzne i zamieniany na wspomniany obraz, czyli widziany na ekranie kamery termogram.

We współczesnych kamerach termowizyjnych najczęściej wykorzystuje się pasmo średniej podczerwieni, czyli długości fal od ok. 0,9  $\mu\text{m}$  do 14  $\mu\text{m}$ . Dzięki temu można rejestrować promieniowanie cieplne o temperaturze z zakresu od około  $-50\text{ }^{\circ}\text{C}$  do około  $+2000\text{ }^{\circ}\text{C}$ . Ze względu na koszty związane z wytworzeniem tak szeroko-temperaturowej matrycy i tak naprawdę braku potrzeby pomiaru w tak szerokim przedziale temperatury, większość dostępnych na rynku kamer ma jednak ten przedział pomiarowy ograniczony do zakresu od  $-20\text{ }^{\circ}\text{C}$  do  $+250\text{ }^{\circ}\text{C}$ . Rzadziej zdarzają się modele pozwalające na pomiary temperatury w przedziale od  $-20\text{ }^{\circ}\text{C}$  do  $+650\text{ }^{\circ}\text{C}$  czy modele mierzące w zakresie od  $-40/-50\text{ }^{\circ}\text{C}$  do  $+1600/1700\text{ }^{\circ}\text{C}$ , a nawet dochodzące do górnej granicy  $+2000\text{ }^{\circ}\text{C}$ . Warto też podkreślić, że w pomiarach termowizyjnych obserwowane obiekty nie muszą być oświetlane zewnętrznym źródłem promieniowania podczerwonego.

Termowizja sprawdza się podczas kontroli stanu technicznego instalacji cieplnych i różnego rodzaju zbiorników. Technologia ta doskonale nadaje się też do przeprowadzenia kontroli kotłów grzewczych i pieców używanych w hutnictwie, odlewnictwie czy hartowaniu metali. W ten sposób można nie tylko sprawdzić stan techniczny urządzeń, które w normalnych warunkach pracują w wysokiej temperaturze, ale również skontrolować równomierność nagrzania lub przetopienia wsadu. Tę ostatnią czynność, można przeprowadzić za pośrednictwem specjalnych okienek inspekcyjnych pieca.

Podczas pomiarów wysokotemperaturowych szczególną uwagę zwraca się na diagnozowanie niewłaściwej pracy wymienników ciepła w piecach oraz na monitorowanie temperatury zewnętrznych powierzchni kadzi odlewniczych, w których transportowana jest roztopiona stal. Na termogramach ważne jest dostrzeżenie gorących punktów, świadczących o uszkodzeniach wewnętrznej, ogniotrwałej powłoki kadzi lub nadmiernym zużyciu obudowy. Trzeba jednak pamiętać, że w tak ekstremalnie gorącym środowisku istnieje wiele czynników wpływających na możliwość błędnej interpretacji termogramu. Chodzi tu przede wszystkim o zakłócenia rejestrowanego obrazu spowodowane przez spaliny, płomienie, żużel czy popiół. Z tego względu stosuje się kamery mające możliwość filtrowania określonych długości fal, dzięki czemu zmniejsza się niepożądany wpływ na rejestrowany obraz warunków otoczenia.

W obróbce laserowej obrazowanie termiczne można stosować na różnych etapach produkcji w celu poprawy jakości, wydajności i bezpieczeństwa procesu.

Poniżej znajdują się przykłady etapów produkcji, w których wykorzystywane są obrazy termowizyjne.

**Cięcie laserem:** Podczas cięcia laserem termowizja może monitorować temperaturę materiału w czasie rzeczywistym.

Optymalizuje to parametry cięcia, takie jak moc lasera i prędkość cięcia, aby uzyskać czyste krawędzie i zminimalizować odkształcenia termiczne.

Obrazowanie termowizyjne może również wykryć anomalie, takie jak nierównomierne nagrzewanie, które może prowadzić do błędów cięcia.

**Spawanie laserowe:** Technologia termowizyjna służy do monitorowania temperatur podczas spawania laserowego. Jest to ważne, aby uzyskać wysoką jakość spoin. Termowizja pozwala kontrolować rozkład ciepła i zapobiegać przegrzaniu materiałów, które może prowadzić do pęknięć i deformacji.

Pozwala to również na precyzyjną regulację parametrów spawania, takich jak moc lasera i czas naświetlania.

**Utwardzanie laserowe:** Utwardzanie laserowe wykorzystuje technologię termowizyjną do monitorowania i kontrolowania temperatury powierzchni materiału.

Pozwala to na równomierne ogrzewanie i chłodzenie, co jest ważne dla uzyskania pożądanych właściwości mechanicznych materiału, takich jak twardość i wytrzymałość.

Obrazy termowizyjne mogą również pomóc w wykryciu niejednorodności termicznych, które mogą prowadzić do defektów w strukturze materiału.

**Napawanie laserowe:** Podczas napawania laserowego technologia termowizyjna monitoruje temperaturę nałożonej warstwy materiału, dzięki czemu możliwa jest kontrola procesu napawania w czasie rzeczywistym.

Dzięki temu nowa warstwa dobrze przylega do podłoża i minimalizuje ryzyko powstania defektów w postaci porowatości i pęknięć.

**Mikroobróbka laserowa:** W mikroobróbce laserowej, gdzie precyzja ma kluczowe znaczenie, techniki termowizyjne umożliwiają monitorowanie temperatury bardzo małych obszarów. Zapobiega to przegrzaniu i uszkodzeniu wrażliwych konstrukcji oraz optymalizuje parametry procesu, aby osiągnąć najwyższą precyzję i jakość obróbki.

**Spawanie Laserowe:** Technologia termowizyjna podczas spawania laserowego pozwala na monitorowanie rozkładu temperatury na powierzchni spawanych elementów. Pozwala to na precyzyjną kontrolę procesu spawania. Jest to szczególnie ważne przy łączeniu cienkich materiałów lub elementów o różnych właściwościach termicznych.

Termowizja w obróbce laserowej jest cennym narzędziem pozwalającym na precyzyjne monitorowanie i kontrolę temperatury oraz osiągnięcie wysokiej jakości, precyzji i wydajności procesu produkcyjnego.

## PODSUMOWANIE

Najważniejszymi zaletami pomiarów termograficznych jest brak inwazyjności i możliwość pomiaru rozkładu temperatury na badanym obiekcie, a nie tylko punktowy pomiar w jednym jego miejscu. Dzięki temu możliwe jest wykonywanie pomiarów temperatury w przemyśle, bez ingerencji w proces technologiczny

Procesy takie jak spawanie i cięcie generują wysokie temperatury, które mają kluczowe znaczenie dla jakości i wydajności.

Obrazowanie termowizyjne umożliwia monitorowanie temperatury, identyfikację obszarów problematycznych, ocenę wydajności procesu i kontrolę jakości.

Można go stosować na różnych etapach produkcji, takich jak cięcie laserowe, spawanie laserowe i hartowanie laserowe, pomagając poprawić jakość, wydajność i bezpieczeństwo procesu produkcyjnego.

## **PODZIĘKOWANIE**

Praca powstała w wyniku realizacji projektu realizowanego z uczniami szkoły ponadpodstawowej w ramach kształcenia zorientowanego projektowo - PBL, w ramach programu Inicjatywa Doskonałości – Uczelnia Badawcza, Politechnika Śląska.

## **BIBLIOGRAFIA**

[1] [https://www.dipol.com.pl/kamery\\_termowizyjne\\_w\\_monitoringu\\_bib750.htm](https://www.dipol.com.pl/kamery_termowizyjne_w_monitoringu_bib750.htm)

[2] <https://www.europro.com.pl/jak-dziala-kamera-termowizyjna/>

Inne użyte linki:

- <https://pl.wikipedia.org/wiki/Termowizor>

- <https://www.fluke.com/pl-pl/nauka/blog/termografia/jak-dzialaja-kamery-termowizyjne>

- <https://automatykaonline.pl/Artykuly/Pomiary/Termowizja-i-jej-zastosowanie>



17th-19th June 2024  
Gliwice, Poland

DEPARTMENT OF ENGINEERING MATERIALS AND BIOMATERIALS  
FACULTY OF MECHANICAL ENGINEERING  
SILESIA UNIVERSITY OF TECHNOLOGY

## INTERNATIONAL STUDENTS SCIENTIFIC CONFERENCE

### Computer simulation of the mechanical properties of the piston of a passenger car internal combustion engine

Agata Śliwa<sup>a</sup>, Martin Kusy<sup>b</sup>

<sup>a</sup> Silesian University of Technology, Faculty of Mechanical Engineering, Department of Engineering Materials and Biomaterials, email: [agata.sliwa@polsl.pl](mailto:agata.sliwa@polsl.pl)

<sup>b</sup> Institute of materials, Faculty of Materials Science and Technology in Trnava, Slovak University of Technology in Bratislava, email: [martin.kusy@stuba.sk](mailto:martin.kusy@stuba.sk)

**Abstract:** The aim of this was to perform computer simulation of stresses and displacements of different piston construction of a passenger car engine under the influence of a given pressure. As a part of work, three models of pistons with different piston head were compared: piston with deep bowl, piston with deep bowl and cooling galleries, piston with flat bowl. In addition, for the simulation made models of pin, connecting rod and the surface corresponding to the cylinder block. A numerical analysis of stresses and displacement was performed using the finite element method in the SolidWorks program and performed comparative analysis of them.

**Keywords:** internal combustion engine piston, pin, connecting rod, SolidWorks, FEM, stresses.

#### 1. INTRODUCTION

The piston of an internal combustion engine is a key element in the engine's operation. Its main task is to transfer the energy generated by the combustion of the fuel-air mixture to the connecting rod and then to the crankshaft.

As part of the engine, the piston is subjected to many tasks and serious requirements that are directly dependent on the use of the piston [2].

- a typical internal combustion engine piston consists of four elements [1]:
- a piston crown
- rings
- piston hubs
- engine jacket

An important element in piston design is currently ensuring adequate cooling. The most common solutions are the use of a spray jet or the use of cooling channels inside the piston, between a piston crown and the piston rings.

There are different types of engine pistons, depending on their purpose. Figures 1 and 2 below show several types of internal combustion engine pistons.

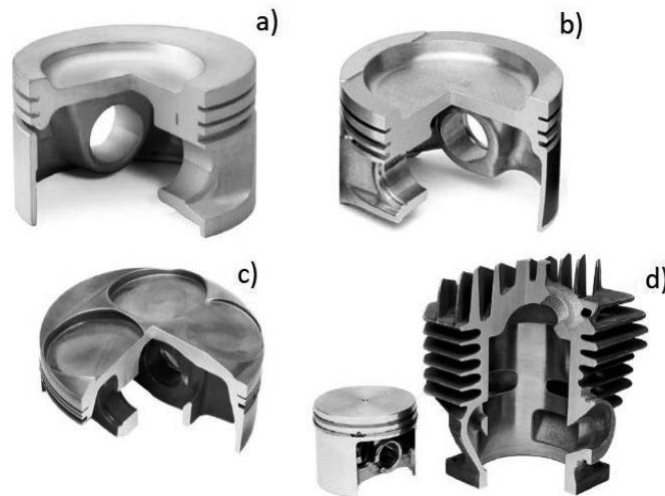


Fig. 1. Photos of petrol engine pistons: a) controlled-expansion piston, b) box-type piston, c) piston used in Formula 1, d) two-stroke engine piston [1]

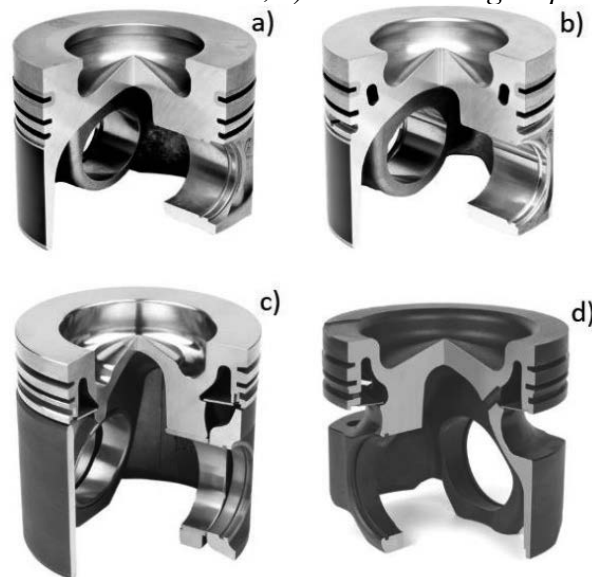


Fig. 2. Pictures of diesel engine pistons: a) piston without cooling galleries, b) piston with cooling galleries, c) FERROTHERM piston, d) MONOTHERM piston [1]

## 2. MATERIAL

To perform the computer simulation, it was decided that the material of the diesel engine piston would be an aluminum-silicon alloy 4032, which is used in the production of pistons. Information on the chemical composition is presented in Table 1, while the material properties are summarized in Table 2

Table 1. Chemical composition of 4032 alloy [4]

Chemical composition						
Si	Fe	Cu	Mg	Cr	Ni	Al
11-13,5%	1%	0,5-1,3%	0,8-1,3%	0,1%	0,5-1,3%	the rest



Table 2. Properties of 4032 alloy [4]

Material properties				
The Young module MPa	Poisson coefficient	Density g/cm <sup>3</sup>	Plasticity boundary MPa	Shear stress coefficient MPS
79000	0.34	0.268	315	26000

Additionally, the same aluminum alloy was used for a cover imitating a cylinder. The other materials used in the simulation are aluminum bronze CuAl1Fe3Mn2 for the piston pin and GJS 700-2 ductile iron for the connecting rod.

### 3. MODELS USED IN COMPUTER SIMULATION

Three models of diesel combustion engine pistons were made. Each model differed in the type of piston crown. These were pistons with a deep combustion chamber, a deep combustion chamber with cooling channels and a shallow combustion chamber.

Figure 3 shows a cross-sectional view of individual piston models. Additionally, models of the piston pin, connecting rod and cover imitating the cylinder block were made, which are shown in Figures 4-6. Figure 7 shows an isometric view of the assemblies for all three pistons.

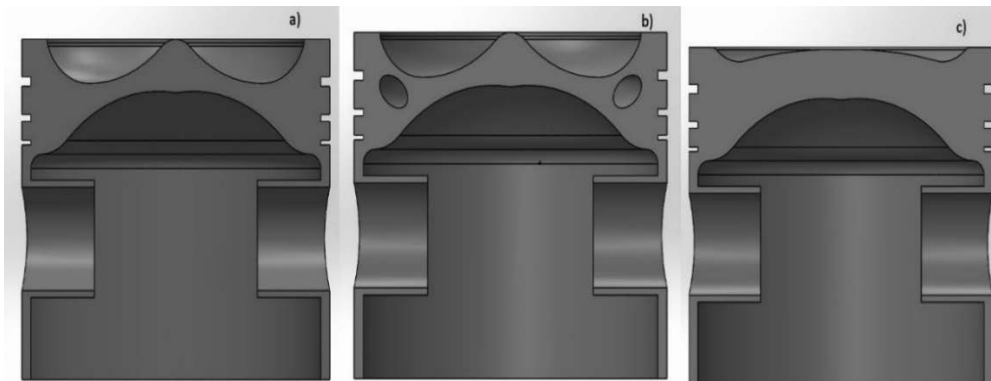
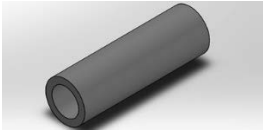


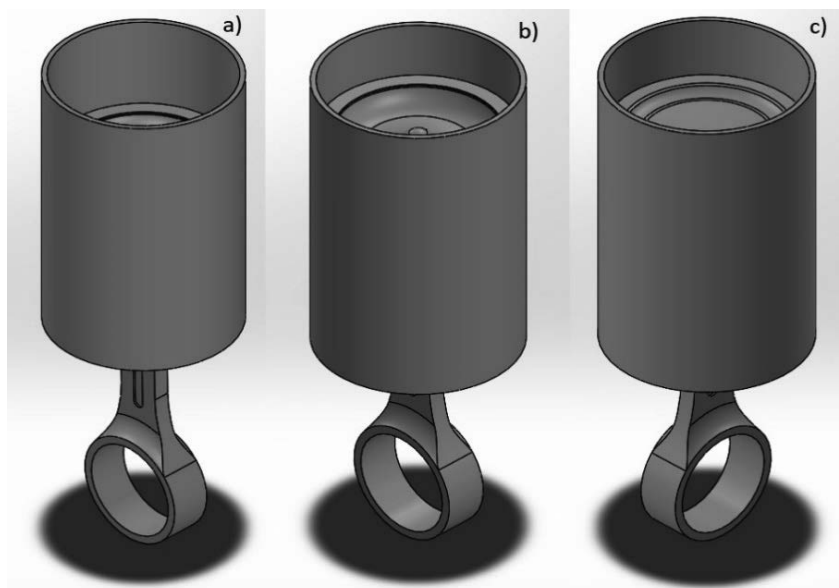


Fig. 3. Cross-section view of piston models: a) deep bowl, b) deep bowl with cooling galleries, c) flat bowl

		
<p><i>Fig. 4. Piston pin model in isometric view</i></p>	<p><i>Fig. 5. Conrod model in isometric view</i></p>	<p><i>Fig. 6. Model of cover imitating cylinder block in isometric view</i></p>



*Fig. 7. Isometric view of assemblies for the following pistons: a) deep bowl, b) deep bowl with cooling galleries, c) flat bowl*

#### 4. SIMULATION

The first step in preparing for the simulation was for the assemblies to be permanently fixed, using stationary geometry, on the surface of the cover imitating a cylinder and in the inner part of the connecting rod head, as shown in the drawing

The next stage was to apply an appropriate load on the piston crown. In accordance with the data contained in the literature, it was decided to set a pressure of 24 MPa, which is the highest value to which a diesel engine piston can be subjected, according to the data contained in the literature. Figure 9 shows the pressure applied to each of the diesel engine piston assemblies. The last stage was to apply a finite element mesh, which is shown in Figure 10.



Fig. 8. View of places with fixed translation: a) model with deep bowl, b) model with deep bowl with cooling galleries, c) model with flat bowl

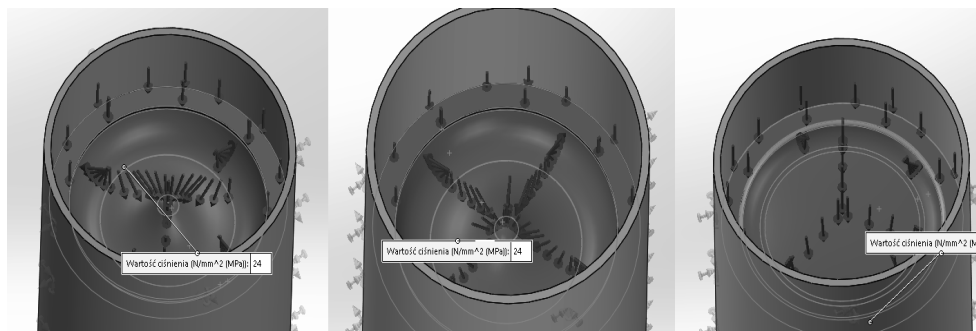


Fig. 9. View of place where external load was applied. a) model with deep bowl, b) model with deep bowl with cooling galleries, c) model with flat bowl

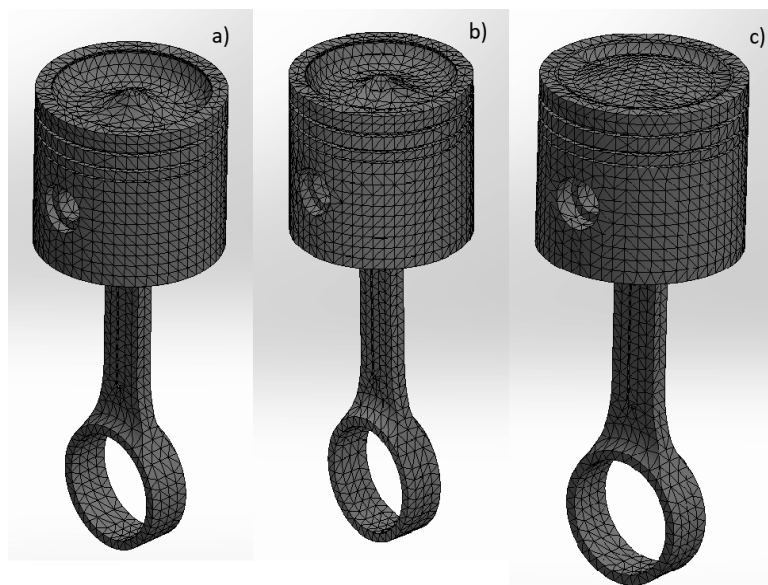


Fig. 10. Geometric of piston models with finite element mesh a) model with deep bowl, b) model with deep bowl with cooling galleries, c) model with flat bowl

#### 4. RESULTS OF COMPUTER SIMULATION

Figures 11, 12 and 13 show the distribution of von Mises stress in the analyzed internal combustion engine piston assemblies in isometric, cross-sectional and top view.

In all models, the highest stress values are concentrated in the center of the piston crown, and in the case of pistons with a deep combustion chamber, they occur especially in places where the piston crown is the least thick.

It was observed that the stresses are higher when cooling channels are used and that there is a greater accumulation of stresses in the cooling channels themselves.

In the case of the model with a shallow combustion chamber, which is also the model with the thickest piston crown, the lowest stress values were observed. Moreover, it was noticed that due to the greater thickness, there are almost no stresses in the piston crown part.

The distribution of displacements is presented in Figures 14, 15 and 16, it can be concluded that their value depends on the thickness of the piston crown, which is why the piston with a shallow chamber has the lowest displacement values, while the pistons with a deep chamber recorded a higher displacement value, but the displacement values do not exceed 0.11mm.

It is also worth indicate the small impact of the presence of cooling channels on the maximum displacement value.

An important aspect is also the mass of the piston models made, which allow for an additional opportunity to compare the obtained simulation results. An increase in stresses and displacements is visible as the mass of the completed model decreases. However, it should be taken into consideration that each of the presented piston types has a different purpose.

For example, pistons with a deep chamber will be used when higher engine power is needed, and cooling channels are used in cases of very high thermal loads. This means that mass cannot be a decisive factor, because the shape of the piston also influences the individual simulation values.

The collective results of the simulation of stress, displacement and mass of the completed piston models are presented in Table 3.

Table 3. Summary results of computer simulation.

Piston model	Obtained property values for individual models		
	Maximum stresses [MPa]	Maximum displacements [mm]	Mass [g]
With a deep combustion chamber	185,674	0,103	322
With a deep combustion chamber and cooling channels	203,554	0,107	302
With a shallow combustion chamber	95,612	0,050	379

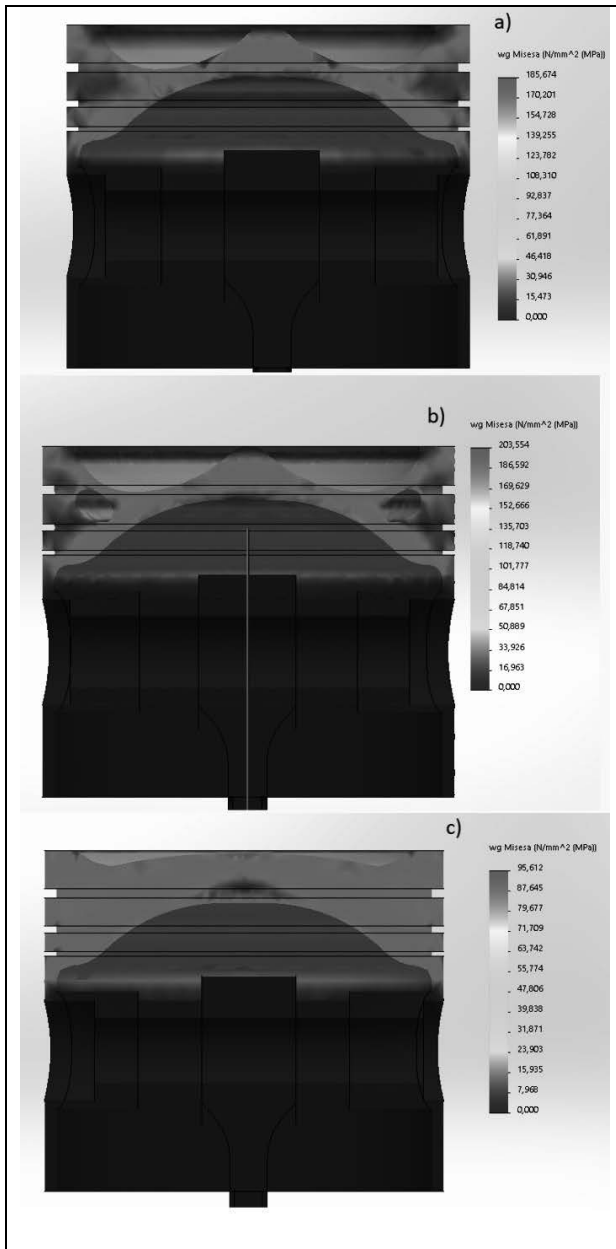


Fig. 11. Cross-section view of stresses



Fig. 12. Isometric view of the stress distribution

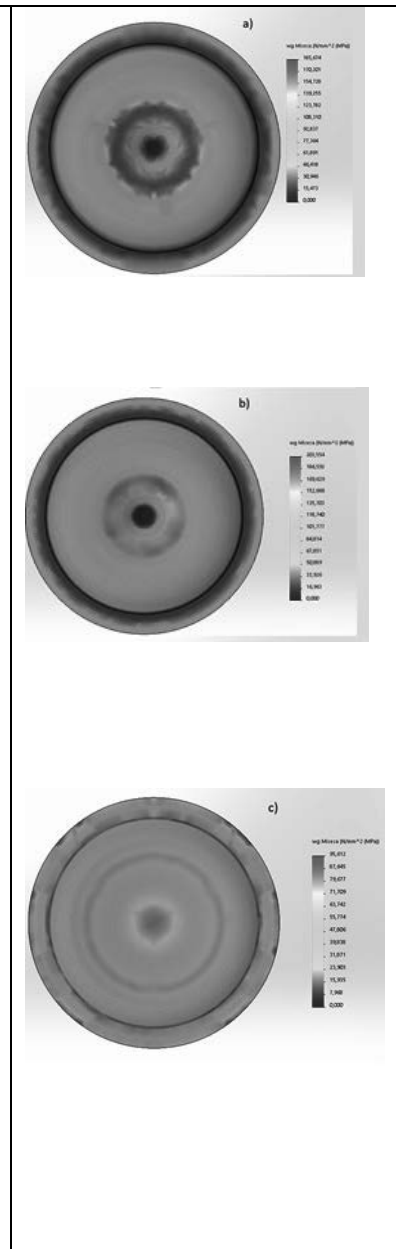


Fig. 13. Top view of the stress distribution

a) model with deep bowl, b) model with deep bowl with cooling galleries, c) model with flat bowl

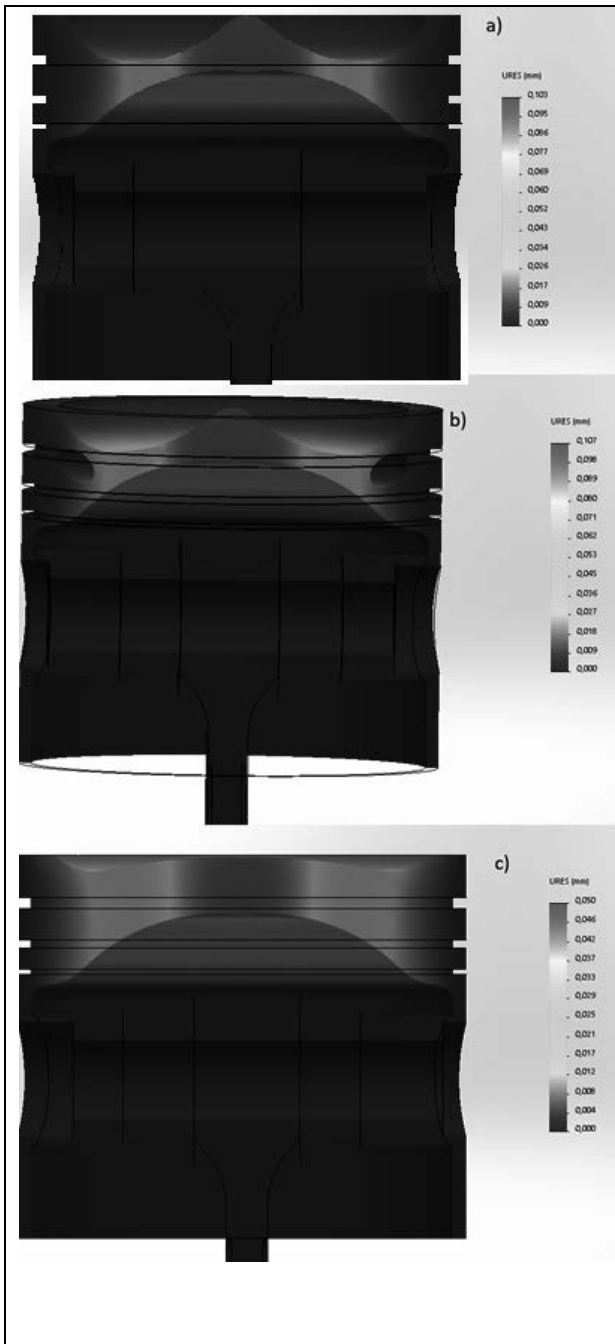


Fig. 14. Cross-section view of displacement



Fig. 15. Isometric view of the displacement distribution

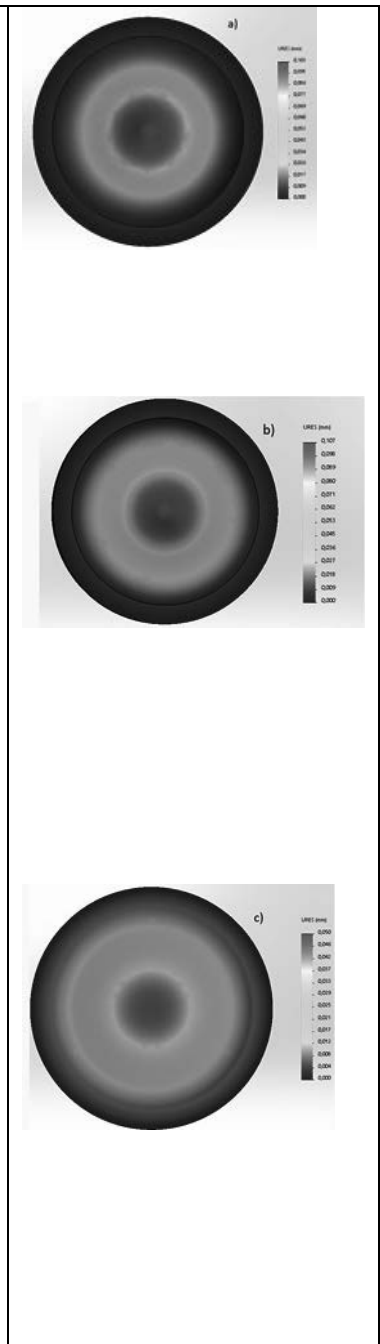


Fig. 16. Top view of the displacement distribution

a) model with deep bowl, b) model with deep bowl with cooling galleries, c) model with flat bowl

## 5. CONCLUSIONS

- The computer simulation of the properties of the pistons of a passenger car's internal combustion engine allowed for obtaining the stress distribution occurring in them. Taking into account the conditions in which individual pistons operate, it should be remembered that their high value in the case of a piston with cooling channels is compensated due to better cooling conditions.
- The lowest stress value was recorded for the piston with a shallow combustion chamber. However, focusing on the efficiency aspect, in the case of a combustion engine with good efficiency without the need to create additional cooling systems, the best solution is a piston with a deep combustion chamber without cooling channels.
- Numerical analysis showed that the differences between the displacement values for all three pistons are small and can be considered insignificant in the context of their operation; it is worth noting the marginal impact of adding cooling channels on the increase in their values. When comparing shallow and deep chamber pistons, the displacement value depends only on the thickness of the piston crown.

## ACKNOWLEDGEMENTS

The publication is result of cooperation within the Visegrad Scholarship Program 2023/2024.

- Visegrad Fund

## LITERATURE

1. MAHLE GmbH Pistons and engine testing, 2016, Springer Vieweg
2. G. Genta, L. Morello, F. Cavallino The Motor Car, 2014, Springer
3. F. van Basshuysen, R. Schäfer, Internal Combustion Engine Handbook - Basics, Components, Systems, and Perspectives, 2016, SAE
4. Norma PN-EN 573-3:2019-12



17th-19th June 2024  
Gliwice, Poland

DEPARTMENT OF ENGINEERING MATERIALS AND BIOMATERIALS  
FACULTY OF MECHANICAL ENGINEERING  
SILESIA UNIVERSITY OF TECHNOLOGY

## INTERNATIONAL STUDENTS SCIENTIFIC CONFERENCE

### Thin films of PNDI(2HD)2T conductive polymer for use in photovoltaics

Michał Sładek<sup>a</sup>, Patryk Radek<sup>a</sup>, Jarosław Tłołka<sup>a</sup>, Magdalena Monika Szindler<sup>b</sup>,  
Marek Szindler<sup>c</sup>, Grzegorz Nowak<sup>de</sup>

<sup>a</sup> Student of Silesian University of Technology, Faculty of Electrical Engineering, Akademicka 3, 44-100 Gliwice

<sup>b</sup> Silesian University of Technology, Faculty of Mechanical Engineering, Department of Engineering Materials and Biomaterials, Gliwice, Poland

<sup>c</sup> Silesian University of Technology, Faculty of Mechanical Engineering, Didactic Laboratory of Nanotechnology and Material Technologies, Gliwice, Poland

<sup>d</sup> Łukasiewicz Research Network – Krakow Institute of Technology, Centre of Biomedical Engineering, Zabrze, Poland

<sup>e</sup> Silesian University of Technology, Faculty of Biomedical Engineering, Department of Biomaterials and Medical Devices Engineering, Zabrze, Poland

**Abstract:** Electrically conductive polymeric materials are an attractive direction for research and development in the field of electronics and photovoltaics. The article presents the results of research on Thin films of PNDI(2HD)2T conductive polymer deposited using the spin coating technique. The surface morphologies, optical and electrical properties of the tested polymer were examined.

**Keywords:** Thin film, Spin coating, Conductive polymers

## 1. INTRODUCTION

A special group of polymers are conductive polymers, which have the ability to conduct electricity. They can be obtained by: chemical synthesis, biocatalyzed chemical synthesis, electrochemically, photochemically and by solid state reaction [1-3]. The advantage of these materials is their ease of processing, mainly due to dispersion. The doping of polymers allows them to maintain high electrical conductivity, which is close to that of metals [4]. These polymers are used in many areas of technology. The simplest example of application is in devices that everyone owns i.e. cell phones and portable computers. In electronics in the broadest sense, they are used in field-effect transistors, light-emitting diodes, photovoltaic cells, organic lasers and sensors, among others. Their use in this field makes it possible to obtain electronic circuits that operate much faster and consume much less energy than traditional circuits. Such circuits will be lightweight, cheap and flexible [3-5].

We distinguish a division into 3 groups when considering how polymers conduct electricity:

- conjugated polymers,



- polyelectrolytes,
- conductive polymers by redox pathway.

Conductive polymers have the ability to modify electrical properties with electrons that can be introduced or removed from the system. In inorganic semiconductors, doping of electron-poor or electron-rich elements is used, while in conducting polymers, oxidation of polymer macromolecules or partial reduction is carried out, leading to the formation of ion radicals. Depending on the doping method used, a distinction is made between p-doping (oxidation) and n-doping (reduction). In general, p-doping is used more often, since conducting polymers in the reduced state are prone to react with atmospheric oxygen, which consequently leads to their degradation [4-6].

Polymer cells, also known as solar cells, are used to convert solar energy into electricity. They are used to generate electricity in a greener and more sustainable way than traditional energy sources. Polymer cells, unlike other types of solar cells, use polymers as the active layer that converts solar energy into electricity. These polymers are cheaper and easier to manufacture than the materials used in other types of solar cells, such as silicon or tellurium. Polymer cells are also more flexible and can be produced in a variety of shapes and sizes, making them more versatile for practical applications. Among the parameters that characterize polymer cells are efficiency values, fill factor, open circuit voltage and short circuit current. The values of these parameters depend on the type and chemical structure of the polymer, as well as the production and operating conditions of the cells [5, 6].

These cells are created by applying thin layers of polymers to a substrate, which is usually made of transparent plastic or glass. The polymer layer contains dopants that enable the conversion of solar energy into electricity. The manufacturing process of polymer cells is more flexible and less expensive than the production of other types of solar cells, making them more attractive to industry. The advantages of these cells include a lower production cost, ease of manufacturing, flexibility, the ability to produce them in different shapes and sizes, and a lower environmental impact compared to other types of solar cells. The cells also have their disadvantages such as lower solar-to-electricity conversion efficiency compared to other types of solar cells, lower durability and weather resistance, and lower thermal stability [5-7].

PNDI(2HD)2T, also known as P(NDI2HD-T2), is a copolymer of naphthalene and bithionaphthalene, which is used as a polymer acceptor in high-efficiency all-polymer solar cells. The values of HOMO (Highest Occupied Molecular Orbital) -5.80 eV and LUMO (Lowest Unoccupied Molecular Orbital) is -3.82 eV. It has a higher level of crystal behavior. This translates into excellent charge transport between the polymer's donor and acceptor materials. This results in increased efficiency [6, 7].

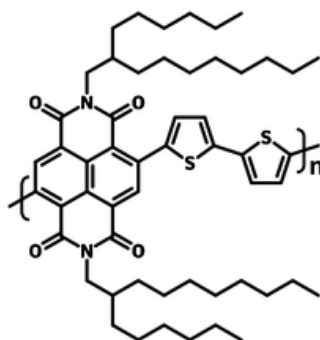


Fig. 1 Chemical structure of PNDI(2HD)2T [7]

## 2. MATERIALS AND METHODS

To prepare thin films from the PNDI(2HD)2T polymer, a preliminary preparation step was necessary. Chlorobenzene was chosen as the solvent for this process. The compound, obtained from Ossila, was dissolved at a concentration of 10 mg of the polymer per 1 ml of solution. The solutions were centrifuged at 3000 rpm. The 2D and 3D topographic images of  $2 \times 2 \mu\text{m}$  were taken using a Park Systems XE-100 atomic force microscope (AFM). Root mean square (Rq), roughness and average coefficient values (Ra) were determined using XEI software. UV/VIS spectroscopy analysis was performed and wavelength dependence of absorbance was obtained. The resistivity and conductivity of the deposited polymer layer were measured using four-point probe equipment (Ossila, United Kingdom). In this method, the sheet resistance was determined with the probes linearly arranged at equal intervals. The measurement involves applying current through the two outer probes, which induces a voltage change between the two inner probes.

## 3. RESULTS

Topographic images were captured on a  $2 \times 2 \mu\text{m}$  surface using AFM (Fig. 2). The images reveal that the clusters of atoms are densely packed, forming a planar structure. The amplitude of the disparity for PNDI(2HD)2T polymer ranges from  $-2.5\text{nm}$  to  $2.5\text{nm}$  (Fig. 3). The PNDI(2HD)2T polymer exhibits surface roughness, with Rq and Ra values of  $1.04 \text{ nm}$  and  $0.82 \text{ nm}$ , respectively.

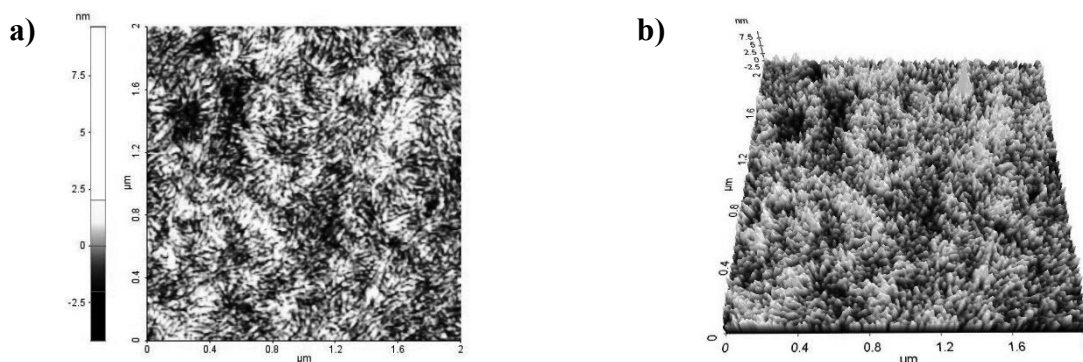


Figure 2. The 2D and 3D AFM images (a, b) of the surface topography PNDI(2HD)2T

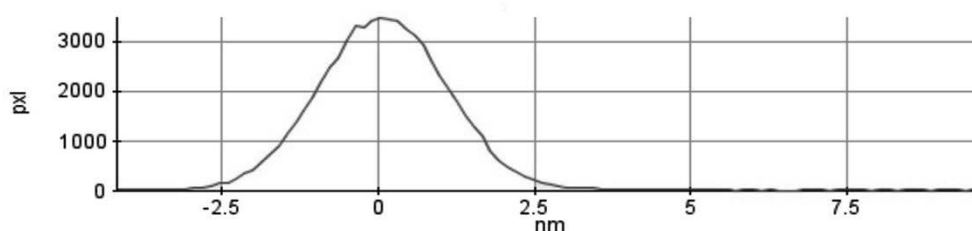


Figure 3. The histogram of the inequality of the PNDI(2HD)2T

The PNDI(2HD)2T thin film has three absorption maxima of 250, 390 and 690 nm, respectively. The first one corresponds to 2HD, while the second and third ones correspond to PNDI.

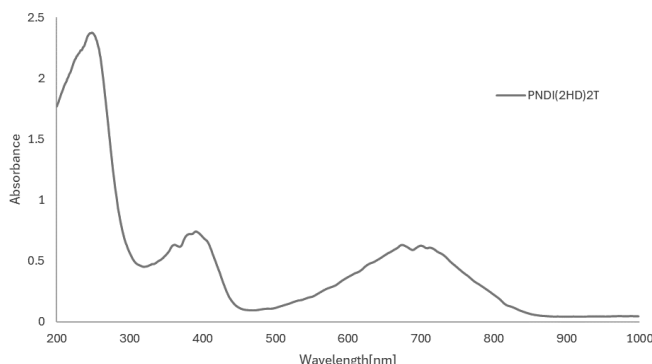


Figure 3. Characterization of the wavelength dependence of absorbance (UV/VIS)

The surface resistance of the deposited polymer thin film was measured (Table 1). Based on these measurements, the resistivity and conductivity of the deposited polymer thin films and their blend were calculated.

Table 1. Summary of electrical properties of the PNDI(2HD)2T sample

No	Sheet Resistance [ $\Omega/\square$ ]	Resistivity [ $k\Omega \cdot m$ ]	Conductivity [ $\mu S/cm$ ]
PNDI(2HD)2T	$1.59 \times 10^{10}$	15.87	0.63

#### 4. CONCLUSIONS

The obtained results allow us to conclude that it is possible to dissolve the PNDI(2HD)2T polymer in chlorobenzene and obtain even, continuous thin films using the spin coating method. Thin films of PNDI(2HD)2T polymer are characterized by a sheet resistance of  $1.59 \times 10^{10}$  and a conductivity of  $0.63 [\mu S/cm]$

#### BIBLIOGRAPHY

1. Czerwiński W., Kaczmarek H., Kędziera D., Kowalonek J., Nowaczyk J., Olewnik E., Przewodzące i fotoczułe materiały polimerowe, UMK Toruń, 2012, 2
2. Tapan K. Das, Prusty S., Review on Conducting Polymers and Their Applications, PolymerPlastics Technology and Engineering, 51 (2012), nr 14, 1487
3. Lelek-Borkowska U., Podstawy chemii polimerów, Akademia Górniczo-Hutnicza im. St. Staszica w Krakowie, 2021
4. Bokwa M., Wierzbicka B., Tański T., Wiśniowski M., Polimery przewodzące i ich zastosowanie, PSKN, 42 (2015)
5. Nezakati T., Seifalian A., Tan A., Seifalian A. M., Conductive Polymers: Opportunities and Challenges in Biomedical Applications, Chem. Rev., 118 (2018), 6766-6843
6. Oskay W., Barrett R, Make: The Annotated Build-It-Yourself Science Laboratory, O'Reilly, 2016
7. Ossila Limited, PNDI(2HD)2T DataSheet, <https://www.ossila.com>



17th-19th June 2024  
Gliwice, Poland

DEPARTMENT OF ENGINEERING MATERIALS AND BIOMATERIALS  
FACULTY OF MECHANICAL ENGINEERING  
SILESIA UNIVERSITY OF TECHNOLOGY

## INTERNATIONAL STUDENTS SCIENTIFIC CONFERENCE

### **Description of the process of preparing ceramic bas-reliefs cast from slips using 3D scanning and printing and making plaster molds**

Barbara Słomka-Słupik<sup>1</sup>, Marek Kremzer<sup>2</sup>, Wojciech Zieliński<sup>3</sup>, Julia Franosz<sup>1</sup>, Anna Słupik<sup>4</sup>,  
Władysława Buriak<sup>3</sup>, Daniel Kostyra<sup>3</sup>

<sup>1</sup>Silesian University of Technology, Faculty of Civil Engineering

<sup>2</sup>Silesian University of Technology, Faculty of Mechanical Engineering

<sup>3</sup>Building and Ceramic School Complex, Gliwice

<sup>4</sup>Academic Secondary School of the Silesian University of Technology, Gliwice

**Abstract:** This article represents a didactic study that presents a method of making a duplicate of an actual product (architectural detail) or a designed product in two ways. The given activity diagram was developed during project classes from the PBL-IDUB series, 10th edition, in the winter semester of the academic year 2023/2024 at the Silesian University of Technology. The work concerned the preparation of plaster molds and then the use of ceramic slip casting to create bas-reliefs. Plaster molds were prepared by pouring plaster over ready-made products or bas-reliefs printed from designed 3D objects. Ceramic coatings resulting from firing may represent as duplicate of open products, original bas-reliefs, or sculptures

**Keywords:** clay, ceramics, 3D printing, plaster molds, architectural details

## 1. INTRODUCTION

Making reproductions of ceramic objects can be done on an industrial or retail scale.. The target ceramic object - a copy, can be made using ready-made plaster molds (industrial scale) and ceramic slip casting. It can also be designed in graphic programs and printed with a 3D printer by extruding a paste, which can be clay with appropriate rheological properties. To copy a real object, you need to prepare a plaster mold. We make a mold from a suspension (powdered plaster + water). The plaster suspension should be poured into the object of interest previously coated with a release agent. You can make one-piece molds (open objects like bowls) or multi-piece forms (closed objects like sculptures, statuettes) connected with special locks/clasps. If we do not care about the smoothness of the object and we have a printer for printing using the extruding paste method, we can scan the object, save the scan in STL format, and after processing, transfer it to a program called a "slicer" to prepare the graphics appropriately for a 3D printer. The following additive manufacturing conditions should be optimized: printing speed, layer height, fill share and pattern, and thickener feed rate.

Preparing plaster molds, you should know that dedicated ceramic plaster is used for this purpose, which can be purchased in ceramic shops. Plaster molds are used to form the element

by extracting water from the ceramic cast mass and should not be thinner than 2 cm. Typically, multi-element forms connected by locks/clasps are available on the market. After gluing with tape or fastening with rubber bands (so that the form parts do not separate), the mold is all filled with ceramic pour mass. It is prepared poured clay. The net result is a jug, vase, figurine, or other full-size object. To prepare the open, one-piece molds used in this work, the object should be poured with plaster from the outside. The initial stage of learning the technique of making plaster molds began with an easier method. Thanks to it, you can obtain open objects such as dishes in the final stage. Making multi-piece forms with locks requires more proficiency. After making and drying the plaster mold, need to prepare the ceramic cast mass. The purchased cast mass may be in the form of a powder or a thick suspension. This powder should be mixed with water and a fluidizing agent (after dissolving in water), according to the recommendations of the cast mass manufacturer. The consistency of the ceramic pour mass should resemble that of cream and must not contain clumps. After mixing manually or mechanically (with a slow-speed mixer), it can be poured into the plaster mold, filling the hole (creating a convex meniscus. The gypsum/plaster (form) begins to absorb water from the cast mass, no chemical reactions occur as a result, it is water chemically unbound in the plaster mass. Then wait a few minutes until a layer of compacted cast mass, a few millimeters thick, forms on the walls of the plaster mold. The thicker our product is, the longer you have to wait before pouring the excess cast mass. After casting, and pouring the cast mass from the plaster mold, we leave the mold with a dense layer of clay to dry. The clay coating should shrink and detach from the plaster mold.. Then, using a knife, you can gently cut off the unnecessary overfilled parts from the proper shape of the coating or shell, which after firing in a ceramic kiln will become a finished object. However, before this happens, it must be dried, bisque fired, glazed, and fired again at the right temperature. The temperature range for firing clay and glaze is indicated on the packaging by the manufacturer. You can also apply the glaze to a dried product and fire it only once, although, in the case of thin-walled products, this may be dangerous because the glaze suspension is applied to an element that has no mechanical strength and is susceptible to softening under the influence of liquid.

## 2. PROCESS DESCRIPTION

As part of PBL X-IDUB entitled: "Designing and printing molds, in particular from plaster, to produce architectural details from ceramic cast masses" (winter semester of the academic year 2023/2024) work was carried out in the order listed in the points (below). Both original preparation paths presented in Fig. 1 were used. The goal was to immortalize the ceramic sculpture of a horse's head by scanning it. Then, the objects were divided into 2 parts in a 3D printing program and printed, and the prints were poured with plaster. Further work consisted of forming coatings with poured masses and creating ceramic products from them.

1. scanning a model made of clay and processing it in a graphics program
2. printing a copy of the model in a 3D printer using FDM technology
3. making a plaster mold/form
4. preparation of the coating from the ceramic cast mass
5. firing and glazing of the product

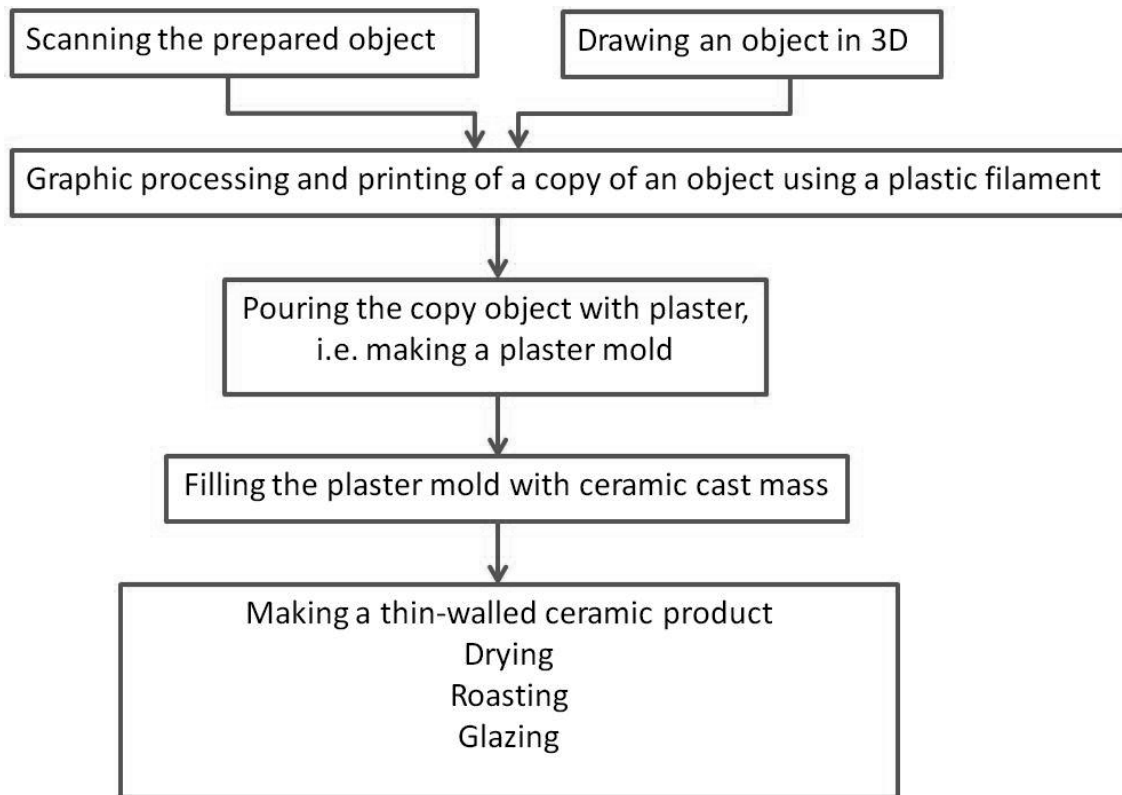


Figure 1. Diagram of the planned work

**Ad.1.** The horse's head sculpture was made of red clay by Zuzanna Kasieczko from the Academic Secondary School of the Silesian University of Technology as part of participation in PBL VII - IDUB entitled: "Basics of ceramics technology for building materials, including circular economy - part 3: Making ornaments using the 3D printing method" in the summer semester of the academic year 2021/2022. This project first won the competition announced in December 2021 by SKN Build Green. The competition concerned the design of the "Na Stajnie" ornament. The model of a horse's head made of clay - (Fig. 1) was dried, first in room conditions for 3 days, and then in a dryer at 105 °C for a week. After evaporation of free water and initial shrinkage, the model was fired in a ceramic furnace at 950 °C. For scanning, the sculpture was left unglazed so that the surface would be matte, otherwise the object would have to be covered with a special coating. The Shining3D EinScan Pro HD optical 3D scanner was used, which is part of the equipment of the Department of Engineering and Biomedical Materials of the Faculty of Mechanical Engineering at the Silesian University of Technology. The scanned object was placed on a turntable (Fig. 2). The image was reconstructed in the scanner software based on 36 frames. Surface texture was not recorded.

**Ad.2.** The scan of the model, after being prepared in the program and saved in STL format, had to be made up for printing. To finally assemble the ceramic object from two halves (required when using cast mass), a scan of the horse's head was cut with a vertical plane (Fig. 3) and printed in 2 parts constituting negatives for making plaster molds (Fig. 4). The BCN3D Sigma D25 printer was used for printing using PLA filament. The printing speed was 45 mm/s, the nozzle temperature was set to 210°C, and the table temperature was set to 60°C.

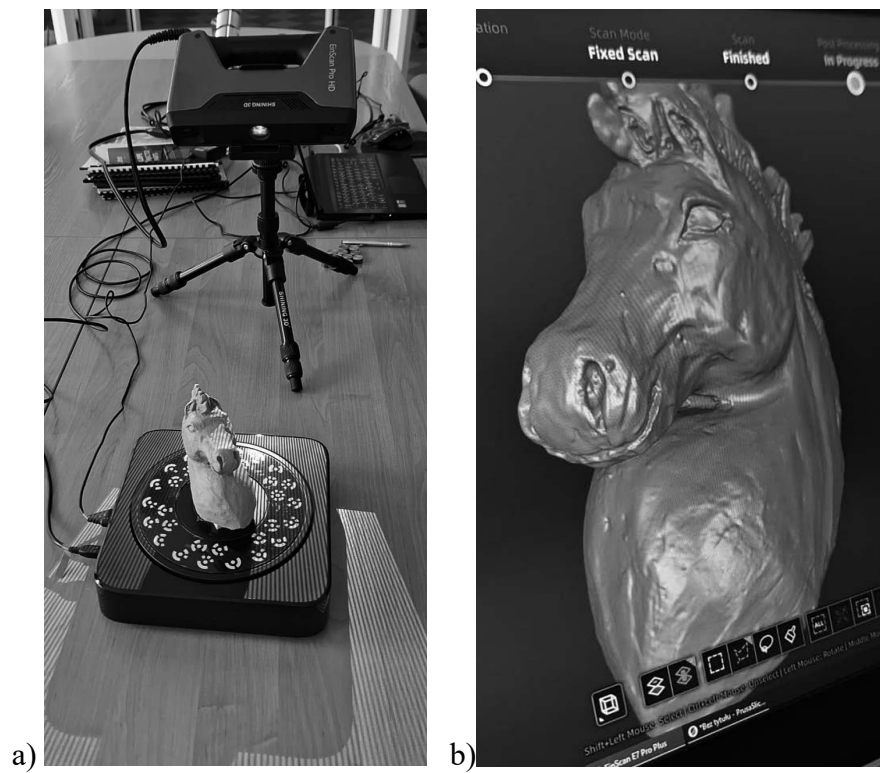


Figure 2. Scanning a ceramic sculpture: a) working scanner, b) processing in a specialized program

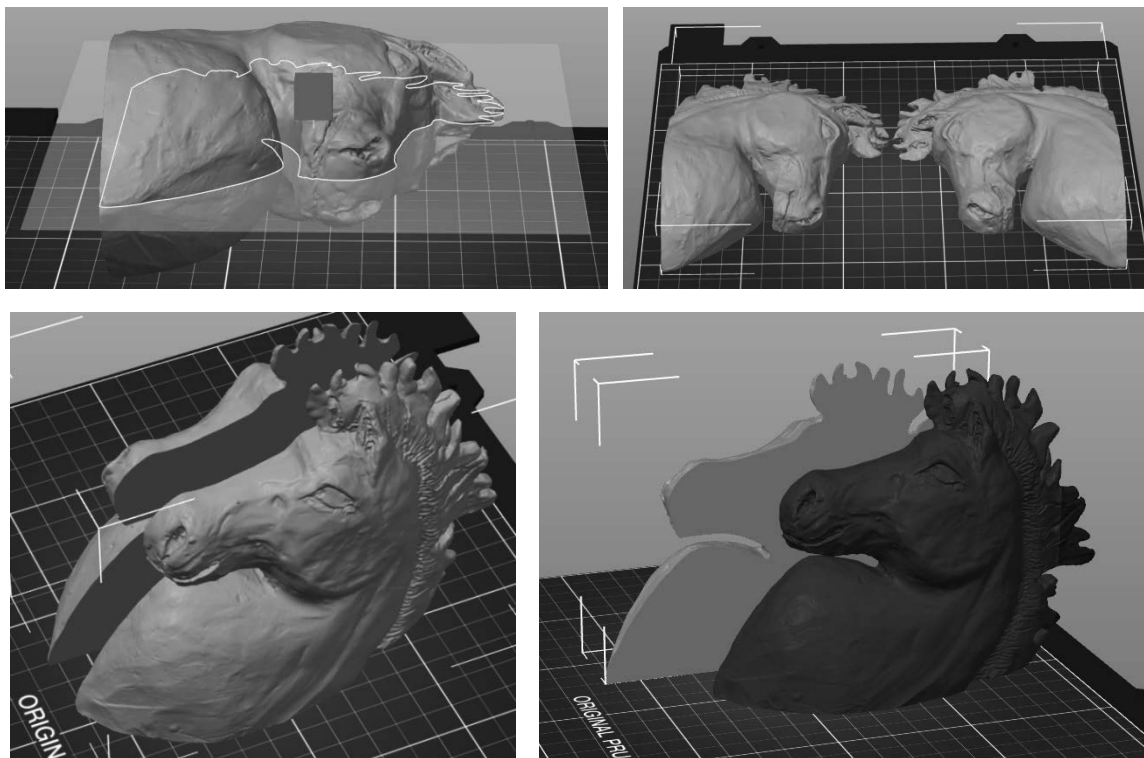


Figure 3. Results of working with a 3D printer program. Preparation of the scan for printing.



Figure 4. Printed halves of a sculpture

**Ad.3.** Preparing the plaster mold consisted of placing the printed element in a container and applying a release agent to it (Fig. 5a). In addition to the method presented above, the element that we want to duplicate can be designed in a graphics program, e.g. AutoCAD, and after saving as STL, printed as a bas-relief. It can also be a ready-made product, such as a ceramic bowl.

The plaster suspension was made from commercial molding plaster in the form of powder, mixed with water in a mass ratio of 1:2 (water: plaster), and poured into a container with a negative (Fig. 5b). After the plaster hardened (Fig. 5c), the negative (horse's head) was separated after about 2 hours. The plaster mold was dried because, as already indicated, its task is to absorb water from the cast mass (clay).

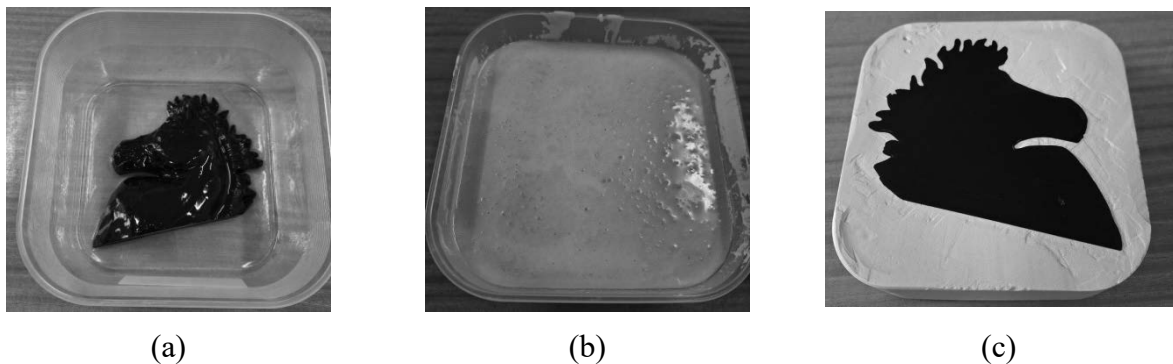


Figure 5. Consecutive stages of preparing a plaster mold for ceramic casting

**Ad.4.** Preparing the shell from a ceramic cast mass consisted of pouring the mass into a plaster mold so that the hole was all filled and the mirror remained convex. This is necessary because the hardened plaster absorbs water and the volume of the slurry decreases in the hole. After about 30 minutes, the layer of clay adhering to the mold became thick, the thickness of this layer was 3 mm. The mold was tilted to allow the pouring mass to flow back into the container for further use. The coating of thickened ceramic slip adhered to the plaster mold dried and shrank over time until it was ready for removal. The shell-like coating was dried in a closed, heated room and then transferred to drying in a dryer at 105°C.



**Ad.5.** The cast was dried at room conditions, then in a dryer at 105 °C, and placed in a ceramic kiln for bisque firing at 900 °C. The glaze was then applied and fired again at 1050°C.

### 3. SUMMARY AND CONCLUSIONS

The activities presented above will be scientifically developed towards printing plaster molds, not casting them. For this purpose, we intend to add agents to the plaster that increase its plasticity and delay hardening, and then we will check whether the concentrated mass absorbs water (from the ceramic cast mass).

If the scanner head is positioned above the object during scanning, the lower planes will not be reflected in a real way, this is where a discontinuity occurs. Therefore, the lower planes should be filled in the program "manually" or using the functions proposed by the program cooperating with the scanner. However, to fully reflect the sculpture, it is possible to additionally scan from a different angle and combine taken scans.

### BIBLIOGRAPHY

1. Jastrzębska, M. Kostecki, A.R. Olszyna, Tworzywa ceramiczne, Oficyna Wydawnicza Politechniki Warszawskiej, Warszawa, 2014.
2. D. G. Cuevas, G. Pugliese, Advanced 3D Printing with Grasshopper, Clay and FDM, Independently published, 2020.
3. Steve Mattison, Podrecznik ceramika, Arkady, Warszawa, 2023.
4. J. Atkin, tł. K. Wojciechowski, Podstawy ceramiki: wszystko, co trzeba wiedzieć, by zacząć tworzyć piękną ceramikę, Arkady, Warszawa 2007.
5. S. Gabrysiak, M. Kocur, M. Poloczek, A. Sadkowska, M. Kremzer, B. Słomka-Słupik, Ceramika budowlana jako element GOZ, W: TalentDetector2022\_Winter: Międzynarodowa Studencka Konferencja Naukowa, Gliwice, styczeń, 2022. T. 1 / Bonek Mirosław (red.), Prace Katedry Materiałów Inżynierskich i Biomedycznych, ISBN 978-83-65138-30-9, s.215-222, Politechnika Śląska, Gliwice, 2022.



17th-19th June 2024  
Gliwice, Poland

DEPARTMENT OF ENGINEERING MATERIALS AND BIOMATERIALS  
FACULTY OF MECHANICAL ENGINEERING  
SILESIA UNIVERSITY OF TECHNOLOGY

## INTERNATIONAL STUDENTS SCIENTIFIC CONFERENCE

### **Analysis of corrosion changes in geopolymer binders. Carbonation**

Barbara Słomka-Słupik<sup>a</sup>, Paulina Wiśniewska

<sup>a</sup> Silesian University of Technology, Faculty Civil Engineering, Department of Building Structures  
email: barbara.slomka-slupik@polsl.pl

#### **Abstract:**

Despite the fact that carbonation of concrete is considered a negative effect of corrosion processes, the article describes the advantage of carbonation of geopolymer binders. Six mixtures of geopolymer binder pastes were made. Each of them were immersed in 23% NH<sub>4</sub>Cl water solution to check the durability of binders and compare with not corroded. The solution simulated highly aggressive industrial waters. The conclusion of the study is that geopolymers are binders that are easily carbonated in corrosive environment and therefore can contribute to the decarbonization of the environment.

**Keywords:** construction geopolymers, carbonation, decarbonization, ammonium chloride, corrosion

### **1. INTRODUCTION**

In the case of cement-based concrete, carbonation is defined as the formation of carbonates, in particular CaCO<sub>3</sub>, as a result of the reaction of bicarbonate ions with calcium cations present in the pore fluid. In short, it is a reaction between calcium hydroxide and atmospheric CO<sub>2</sub> [1-4].

Minelli et al. in article “*Geopolymers as solid adsorbent for CO<sub>2</sub> capture*” confirmed the absorption of CO<sub>2</sub> by the geopolymer matrix“ [5]. Geopolymer materials, a new class of alkali-activated minerals, have been prepared in order to investigate the adsorptive performances of CO<sub>2</sub> [5]. The analysis of the gas adsorption properties showed a quite good capacity for CO<sub>2</sub> in the geopolymer hardened specimens, pointing out the significant ability in the selective capture of CO<sub>2</sub> of these geopolymers. However, why do we need such research and what impact does it have? From research conducted by John L. Provis et al. [6], we know that carbonation of cements through uptake of CO<sub>2</sub> from the atmosphere causes a decrease in the alkalinity of concrete, so not only absorption, but also reactions are going between CO<sub>2</sub> and geopolymeric matrix. Carbonation leads to changes in the chemical and mechanical properties of standard concrete, and when is natural going, it is a long-term process, lowers pH of pore solution, as well. In this work we used acidifying environment in form of NH<sub>4</sub>Cl water solution, and it was not strictly carbonation. In case of cement concrete NH<sub>4</sub>Cl water solution causes

decalcification of matrix, and we wanted to check how it would work with geopolymer matrix [3,4].

## 2. MATERIALS AND METHODS

The composition of binder mixtures is presented in table 1. It was selected that the aluminum to silicon ratio allowed the creation of a multi-component geopolymer binder. Fig 1 shows the ingredients before mixing and ready-made hardened mixtures formed in the form of slurry bars 4×4×16 cm. Table 2 shows the method of testing mixtures over time. 2 weeks after forming, the bars were still damp and did not show much cohesion, 2 even were cracked, so they were all placed in a dryer where they stayed at 105°C for 14 days. The compressive strength of the halves was then tested. The other halves were left and, after 2 months of curing, placed in a water immersion of ammonium chloride in natural, outdoor conditions.

Table 1. Composition of dry components of binder mixtures, in %mas.

Name of mixture / Components	CEM Al-Ca	GGBFS	GK-0	GK-1	PVG	PLB	SOL	PWR	NSH <sub>5</sub>	NaOH
B1	30	30	15		5		5		5	10
B2	30	30		15	5			5	5	10
B3	30	30	15		5			5	5	10
C1	30	30	15		5	5			5	10
C2	30	30		15	5	5			5	10
C3	30	30		15	5		5		5	10

\*CEM Al-Ca – clay-lime cement

\*GGBFS – ground granulated blast furnace slag

\*GK-0 – kaolin clay

\*GK-1 – metakaolin

\*PVG – glass from photovoltaic panels

\*PLB – biomass ash

\*SOL – ground autoclaved cellular concrete

\*PWR – black ash with a large amount of unburned coal

\*NSH<sub>5</sub> and NaOH – alkaline activators

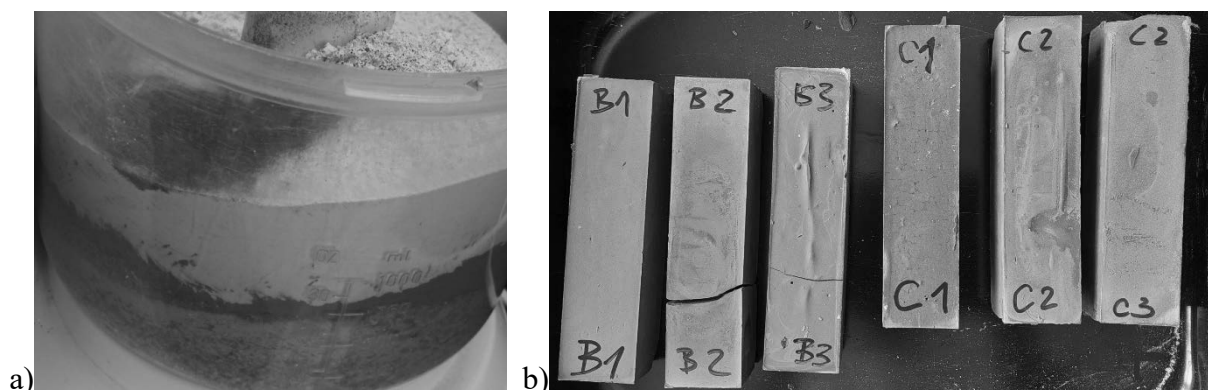


Figure 1. Dry powdered ingredients (B2 mixture) in the mixer (a) and hardened paste bars (b)

NH<sub>4</sub>Cl is aggressive towards cement samples because it causes strong decalcification of the cement matrix, its dissolution and an increase in porosity [4]. This salt was selected to assess its aggressiveness towards the geopolymer matrix. Non-corroded and corroded samples were compared in terms of strength and changes in phase composition. The phase composition was examined by X-ray diffraction (XRD).

Table 2. Research schedule

Actions	Date	Time after preparation, months
Preparation	V - 2022	0
Demoulding and drying	VI - 2022	0,5
Strength testing of non-corroded samples	VI - 2022	1
Immersion in brine	VII - 2022	2
Removal from brine and strength testing of corroded samples	X - 2023	18
XRD examination	XI - 2023	19

### 3. RESULTS WITH ANALYSIS

After 28 days of hardening, the strength of the beams of binders not subjected to brine immersion was tested (Figure 2). Subsequent compressive strength tests were carried out after 19 months, including 16 months of immersion in brine. The chart below compares these values (Figure 2). As could be expected, samples that were exposed to brine causing strong decalcification under changing temperature conditions: from -5°C to 30°C were characterized by lower strength. However, it was not less than 50% of the strength value of non-corroded samples. It can therefore be assumed that despite the difficult corrosion conditions, further hardening of the binder matrix occurred to some extent. Opposite results were obtained by non-corroded samples B2 and B3, in which "greasy" PWR ash was used; as it is known, fats significantly reduce strength. However, the uncalcined GK-0 kaolin clay in B3 probably did the job just fine. This relationship can be explored further.

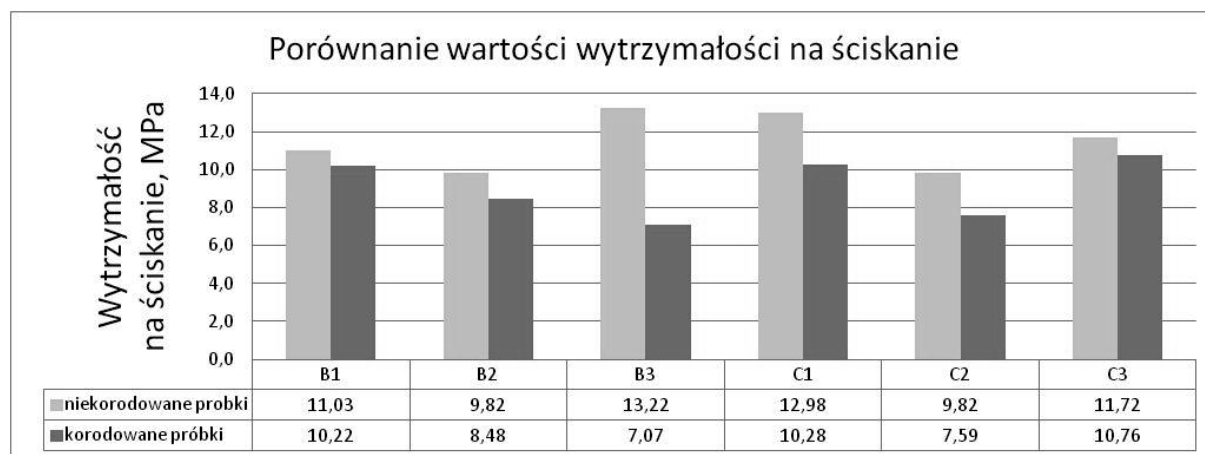


Figure 2. Compressive strength values of corroded and non-corroded specimens

Figures 3 and 4 show the results of phase composition tests, for example for a binder called B1. The remaining amounts of calcite were determined in the same way - using XRD spectra.

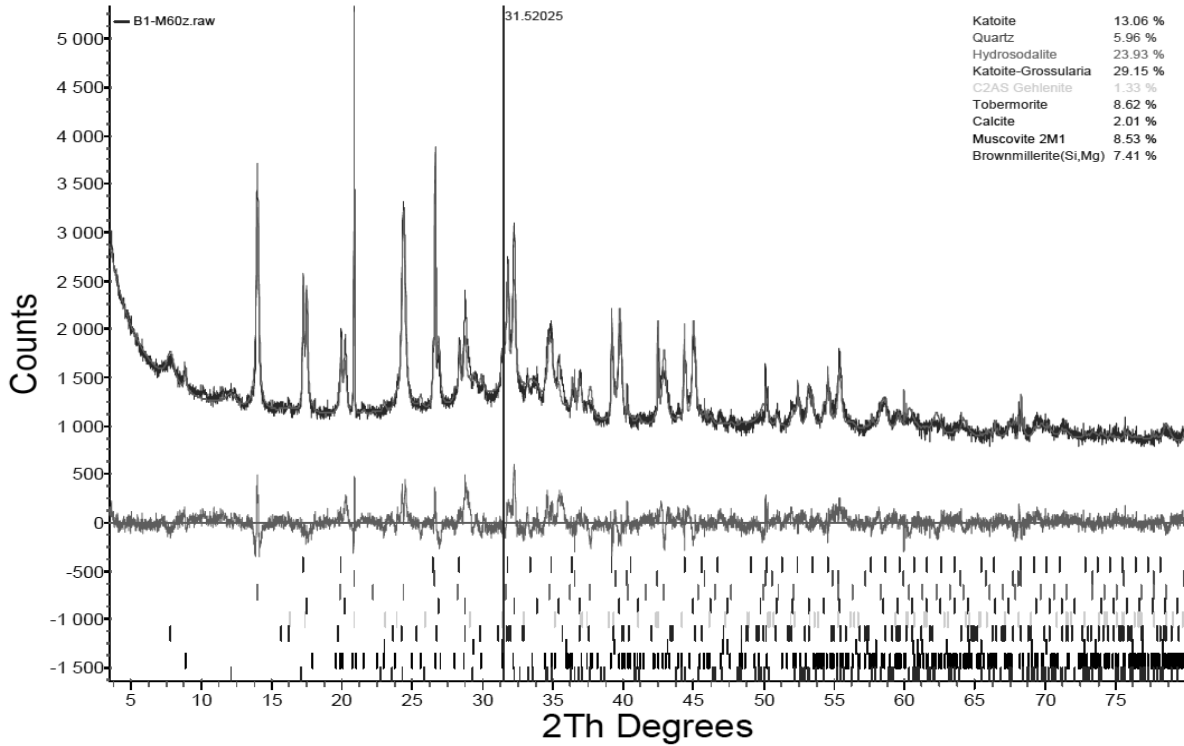


Figure 3. XRD pattern of B1.0 specimen

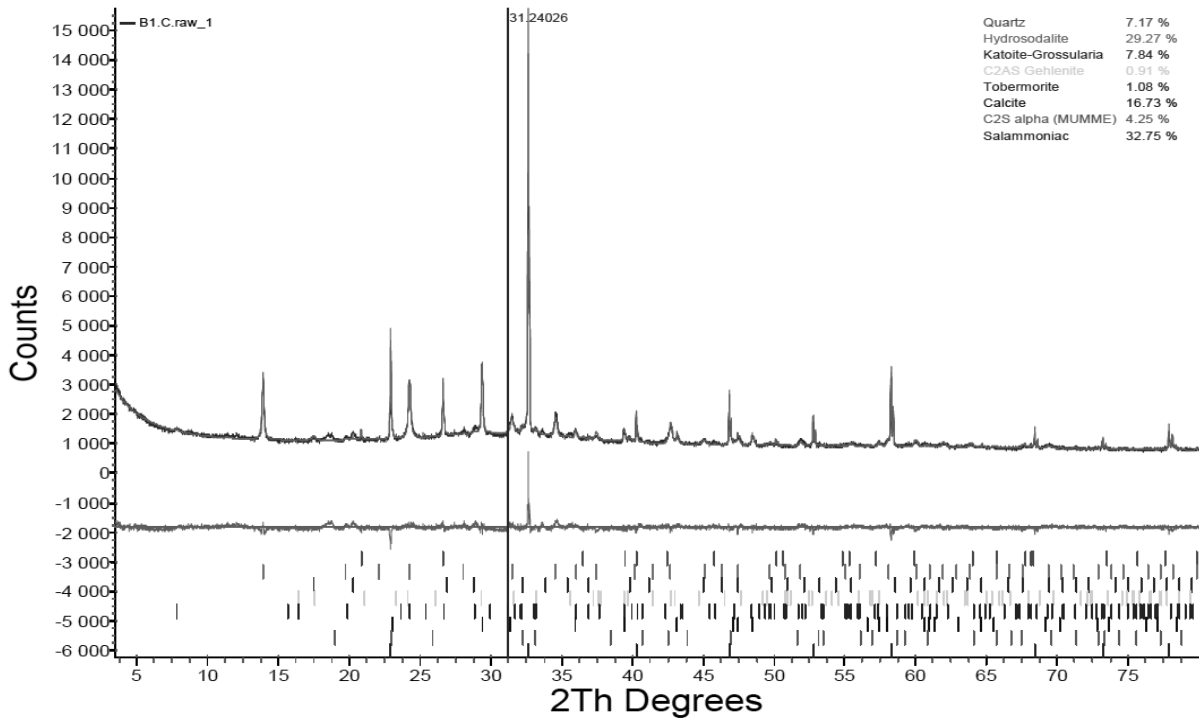


Figure 4. XRD pattern of B1.C specimen

As can be seen, the content of individual phases in the corroded sample significantly changed quantitatively and even qualitatively. The influence of brine resulted in a significant increase in the content of the amorphous phase, which is occupied by the dissolved phases. Calcium aluminates (Katoite, Grossular and Brownmillerite) and tobermorite have dissolved and decalcified. Calcium silicate was probably formed from dissolved tobermorite. Additional amounts of calcium carbonate were produced from the released calcium ions, even though the container in which the immersion took place was closed. A large part of the phase composition is also occupied by the ammonium chloride salt itself. Crystallization of the new phases could seal the matrix and thus improve the strength of the samples.

Table 3. Phases content in exemplary specimens

Name	Formula	B1.0	B1.C
Muskovite	$\text{KAl}_2(\text{AlSi}_3)\text{O}_{10}(\text{F,OH})_2$	6,06	
Brownmillerite	$\text{Ca}_2(\text{Al,Fe})_2\text{O}_5$	5,26	
Katoit	$\text{Ca}_3\text{Al}_2(\text{OH})_{12}$	9,27	
Grossular	$\text{Ca}_3\text{Al}_2(\text{SiO}_4)_3$	20,70	3,77
Quartz	$\text{SiO}_2$	4,23	3,44
Hydrosodalite	$\text{Na}_8[\text{Cl}_2(\text{AlSiO}_4)_6]$	16,99	14,06
Gelenite	$\text{Ca}_2\text{Al}[(\text{Al,Si})_2\text{O}_7]$	0,94	0,44
Tobermorite	$\text{Ca}_5\text{Si}_6\text{O}_{16}(\text{OH})_2 \cdot 4\text{H}_2\text{O}$	6,12	0,52
Calcite	$\text{CaCO}_3$	1,43	8,04
$\alpha$ -Belite	$\text{Ca}_2\text{SiO}_4$		2,04
Ammonium chloride	$\text{NH}_4\text{Cl}$		15,73
Amorphous phase	-	29	52

Calcium carbonates may also be present in the amorphous phase, but this cannot be demonstrated using the XRD method because it is only used to study crystalline phases. Samples stored in containers, not exposed to direct contact with air, and tested after 19 months were carbonated to some extent, whether corroded or not. Geopolymer binders have an affinity for atmospheric  $\text{CO}_2$ , and if they contain large amounts of calcium, calcite is formed. The most calcite was formed in the corroded sample B1 and non-corroded sample B2.

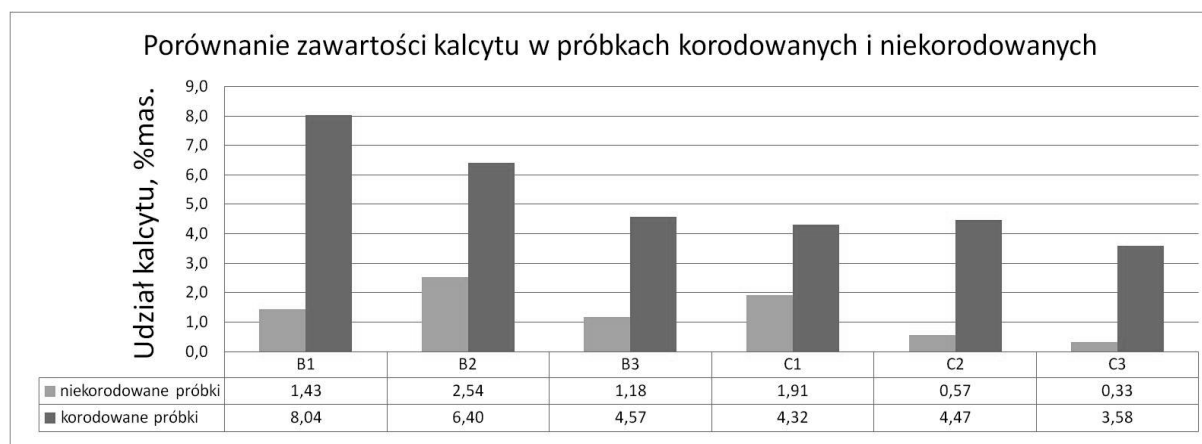


Figure 5. Percentage amount of calcite in corroded and non-corroded specimens

#### 4. SUMMARY AND CONCLUSIONS

Geopolymer binders with the composition presented in this work have an affinity for atmospheric carbon dioxide, despite the fact that they were in an aqueous solution, in a covered container. This affinity increases if the matrix is additionally exposed to decalcifying brine, imitating industrial sewage. The geopolymer used was high in calcium, hence the formation of calcite, while traditional geopolymer binders, alkali-activated aluminosilicates, are also believed to contribute to decarbonization due to their porous structure. The decrease in strength after such a long immersion time in brine was insignificant. It can be safely concluded that geopolymer binders, even with high calcium content, should be tested in contact with very aggressive environments, because they show quite decent properties.

#### BIBLIOGRAPHY

1. B. Słomka-Słupik, P. Wiśniewska, W. Bargieł, Multicomponent low initial molar ratio of  $\text{SiO}_2/\text{Al}_2\text{O}_3$  geopolymer mortars: pilot research, *Materials* (2022) 1-20.
2. B. Słomka-Słupik, P. Wiśniewska, W. Bargieł, Influence of ground PV glass addition on selected properties of geopolymer mortars, in: *Global challenges for a sustainable society. EURECA-PRO. The European university for responsible consumption and production / Benítez-Andrades José Alberto [i in.] (red.)*, Springer Proceedings in Earth and Environmental Sciences, 2023, Cham, Springer, s.343-350, ISBN 978-3-031-25839-8.
3. B. Słomka-Słupik, P. Wiśniewska, Resistance of geopolymers to chemical aggression. Literature study, *Ochrona przed Korozją* 65, 12 (2022).
4. B. Słomka-Słupik, The concrete degradation caused by ammonium chloride present in coke wastewater, in: *Recent Advances in Environmental Science from the Euro-Mediterranean and Surrounding Regions (2nd Edition) : Proceedings of 2nd Euro-Mediterranean Conference for Environmental Integration (EMCEI-2), Tunisia, 2019 / Ksibi M. [et all.] (red.)*, Environmental Science and Engineering, 2021, Springer, s.493-497, ISBN 978-3-030-51209-5. DOI:10.1007/978-3-030-51210-1\_78.
5. M. Minelli, V. Medri, E. Papa, F. Miccio, E. Landi, F. Doghieri, Geopolymers as solid adsorbent for  $\text{CO}_2$  capture, *Chemical Engineering Science* 148 (2016) 267-274.
6. J.L. Provis, A. Palomo, C. Shi, Advances in understanding alkali-activated materials, *Cement and Concrete Research* 78, Part A (2015) 110-125.



17th-19th June 2024  
Gliwice, Poland

DEPARTMENT OF ENGINEERING MATERIALS AND BIOMATERIALS  
FACULTY OF MECHANICAL ENGINEERING  
SILESIA UNIVERSITY OF TECHNOLOGY

## INTERNATIONAL STUDENTS SCIENTIFIC CONFERENCE

### Deep Convolutional GAN for realistic sky image generation

Katarzyna Słowiak<sup>a</sup>, Dariusz Myszor<sup>b</sup>

<sup>a</sup> Silesian University of Technology, Virtual Flying Student Research Club

<sup>b</sup> Silesian University of Technology, Faculty of Automatic Control, Electronics and Computer Science, Department of Algorithmics and Software

**Abstract:** The article focuses on advancing a Deep Convolutional GAN (DCGAN), to achieve higher resolution outputs without compromising visual fidelity or the stability of the training process.

**Keywords:** deep learning, artificial neural networks

#### 1. INTRODUCTION

GAN (Generative Adversarial Network), is a type of generative neural network used to create images based on existing data [1]. The concept revolves around the simultaneous training of two complimentary networks, a generator and a discriminator, that compete in a min-max game. They depend on each other as the generator aims to fool the discriminator by creating data that is difficult to distinguish from real data, while the discriminator evaluates whether the data provided looks realistic or not.

The model was later improved with the creation of DCGAN, a Deep Convolutional Generative Adversarial Network [2], which has been developed from the original GAN concept and has made significant improvements. DCGAN differs from the basic GAN primarily through the use of convolution layers in both generator and discriminator. The original GAN used a unidirectional neural network for both networks, focusing on fully connected layers, which posed a difficulty with learning images of high complexity.

The goal is to develop a DCGAN that allows the generation of higher-resolution images without losing the quality and fidelity of generated data or destabilizing the training process. To achieve this, modifications are introduced to a simple network capable of generating images with a resolution of 64px [3] to achieve an end result of 512px. The network is trained on a dataset of 14,400 varying photos of the sky, taken in varying environmental conditions.



## 2. ENVIRONMENT CONFIGURATION

### 1.1. Requirements

The project was written using PyTorch, an open-source Python library for machine learning. It includes built-in support for hardware (in this case GPUs -Graphics Processing Units), and is optimized for performance. GPUs are indispensable for network training, as they enable simultaneous processing of many mathematical operations, offering significantly higher performance than traditional CPUs. The project was trained on a machine with a 24GB VRAM (Nvidia RTX 3090) graphics card to achieve the highest performance.

## 3. NETWORK STRUCTURE

Data transfer between layers in DCGAN is based on convolution operations for the discriminator or transposed convolution (deconvolution) operations for the generator. Data movement occurs by passing the signal through successive layers, and the network parameters are adjusted by the ADAM optimization algorithm.

### 3.1. Generator

The DCGAN generator starts with a random noise vector, which is passed through hidden layers, each of which consists of transposed convolutional layers, also known as deconvolution layers. While gradually increasing the dimensions of the generated data, each layer adds more details according to the trained features [4]. After each of these layers, batch normalization is applied, which brings their output values into the expected range, i.e., normalizes them. This is done to ensure that the values processed by the network do not become too large or too small, which could negatively affect the training process. The ReLU activation function is applied. The last layer of the network uses the Tanh activation function, which normalizes the output values (range between 0 and 1). This is an operation typically performed in image generation tasks, since many graphical datasets are normalized to this range.

### 3.2 Discriminator

As with the generator, the discriminator uses convolution layers for feature extraction, but in this case, they are standard convolutions. Convolution layers process the input data, looking for features that allow for the distinction between real and artificially generated data. In this type of layer, it is possible to set the convolution filter offset parameter (stride) by more than one cell, which has the effect of gradually reducing the resolution of the tensors on which the network operates while extracting feature information. As with the generator network, each convolutional layer is followed by a BatchNorm2d layer, which normalizes the outputs of the previous layer. Each such layer is then followed by a Leaky ReLU activation function. Finally, nn.Sigmoid is the last activation function applied to the output of the last convolution layer. It normalizes the discriminator output to the range [0, 1], representing the probability that the image is true (1) or false (0).

### 3. METHODOLOGY

The initial stages of the network's development focused on increasing the resolution of the processed data gradually. The efficiency of image generation and the stability of the training process are influenced by the network structure and the parameters responsible for the training process (ex. learning rate, among others). Selecting the right parameter values for a specific network is an empirical process, where experimentation is required to find the optimal parameters for a particular problem and model architecture. In this setup, each increase in the network's capacity may cause a disruption of this balance and require re-adjustments.

After each increase of the network's dimensionality, the goal was to ensure that designed network structure could generate high-quality samples that did not result in the generation of any unwanted artifacts, and that its training would converge, before moving on to the next step of iteratively increasing the end resolution of generated images. Such expansion can be achieved with an increase in network depth by adding an additional set of layers.

The target result of correct training of a neural network is minimizing the value of the loss function. In most cases, at the very beginning, the achieved loss values are relatively high, because the weights in the network are initiated randomly. As training progresses, a gradual decrease in the value of the function should be observable, until both the generator and discriminator converge to the equilibrium, in which the generator generates data that is indistinguishable from the real data, and the discriminator has 50% uncertainty about whether the data is true or false.

#### 3.1. Most common issues

GANs may yield outputs of subpar quality, characterized by distortions, inconsistencies, and lack of coherence. One of the most prevalent issues observed during the development of higher-resolution models was the occurrence of checkerboard artifacts [5], where generated images exhibit grid-like patterns, detracting from their fidelity and realism. Such issues typically stem from the way convolutional operations within the network operate, necessitating specialized techniques to mitigate their presence and ensure smooth image generation.

Another common limitation is the lack of diversity in the generated data, where the network produces outputs that lack variation and fail to adequately capture the underlying data distribution. This limitation can hinder the network's ability to generalize effectively across different data instances, undermining its utility in diverse applications.

Alongside challenges related to artifact mitigation, GAN training is subject to inherent instabilities, characterized by oscillations and fluctuations in the learning dynamics of the generator and discriminator networks. Training failure may arise when one constituent network dominates the adversarial process, resulting in an imbalance that impedes mutual learning. This imbalance can hinder the network's ability to converge. Furthermore, the training may encounter the issue of lack of convergence, wherein the optimization process fails to reach a stable equilibrium state. This phenomenon can manifest as persistent fluctuations in the training loss functions or a failure to achieve consistent improvement in the generated outputs.

### 3.2. Strategies for improvement

The developed 512px model consists of 8 sets of convoluted layers for the discriminator and 7 for the generator, along with respective activation functions and batch. Each of base networks consists of 5 sets of convolution layers, the value was increased in order to accommodate for the complexity of higher-resolution data. Additionally, the generator network includes an inception module in place of one of its layers.

The Inception module [6] is a block that allows the network to capture features using different filter sizes in parallel (e.g., 1x1, 3x3, 5x5). The module is built by combining several convolutional layers of different kernel sizes (which determine the size of the applied filter), which are then concatenated in the output. Smaller filter sizes (such as 1x1 and 3x3), are effective, respectively, in processing fine details in the input image, which can include small textures, edges or patterns, and medium shapes. While the 5x5 and larger filters are used to detect large-scale features and patterns. This allows for simultaneous analysis and processing of image context and elements on a local and global scale.

Both networks use dropout, which is a normalization technique commonly used in neural network training. Dropout and its probability of occurrence are set for specific layers of the network and are designed to zero out, or deactivate, a random set of neurons for each packet of data processed during the training process. This hinders the network from becoming overly dependent on specific neurons, to prevent focusing on a limited number of features and patterns trained by the most influential neurons, instead of using their entire available set. In this model, dropout was set in two layers of the discriminator and two layers of the generator, with a triggering probability of 0.5.

As for the training parameters, this setup involves establishing schedules for adjusting the learning rates (the degree of change in the coefficients of a neural network) of two optimizers during the training of neural networks. The schedules are determined by specified milestones, representing key epochs in the training process. At these milestones, the learning rates are decreased by a predetermined amount. This reduction is calculated as a fraction of the current learning rate, derived from the difference between the initial learning rate and the desired drop. The resulting decay factor is then applied to the optimizers' learning rates at the respective milestones, facilitating a gradual decrease in learning rates over the course of training. This ensures that once the network has learned the initial patterns, it fine-tunes its adjustments to focus on higher-level features.

### 3.3. Network development

The initial tests of the base 64px resolution network reveal satisfactory image quality with minor blurring. Transitioning to 128px sustains similar image quality; however, training exhibits diminished stability and prolonged convergence times. Further tests on increased resolutions are detailed in the accompanying tables. Noteworthy, contrary to classical problems (such as classification or semantic segmentation) in which the quality of the network can be described by coefficients e.g., accuracy, in case of GAN visual inspection is needed in order to grade the quality of obtained results.

Table 1. Developments of the model during training of the model after increase to 256px

Change	Training stability	Generated samples issues
No changes to the base network structure, with a recommended learning rate of 0.0002 [2]	Discriminator overpowers the generator, training gets stuck at the very beginning and fails to converge	N/A
Halve the learning rate of the discriminator	Training takes a long time to show any effects, is unstable, convergence is poor	Blurry, heavy checkerboard, unnatural patterns and symmetry, lack of variety, muted colours
Introduce dropout to the discriminator	Training starts normally and is stabilized, but convergence is poor	Blurry, less prominent checkerboard, unnatural symmetry, lack of variety, muted colours
Increase the learning rate of discriminator back to the original value while keeping dropout	Training is further stabilized, but even if convergent, the loss heavily fluctuates	Slightly blurry, low variety, unnatural symmetry, muted colours
Introduce dropout to the generator	Similar to previous	Muted colours, unnatural symmetry

Table 2. Developments of the model during training of the model after increase to 512px

Change	Training stability	Generated samples issues
Increase of network depth without any changes to the structure or parameters	Training converges at first, gradually unconverging halfway through the training	Heavy checkerboard artifacts, muted colours
Add two blurring layers to the generator to refine the output and stop the generation of artifacts	Similar to previous	Muted colours, heavy distortions reminiscent of spilled paint
Remove one of two blurring layers from the generator	Lower loss fluctuations, but similar issues with convergence	Slight checkerboard artifacts, occasional symmetry
Adaptive learning rate for both networks	Better convergence	Slight checkerboard, excessive sharpness
Increase of learning rate reducing factor	Good convergence and lowered loss fluctuations	Blurry
Introduce the inception module to the generator network	Higher loss fluctuation but even more stable convergence	No prominent issues

#### 4. SUMMARY

The final results of the research work carried out on the optimization of the network structure led to the expected result. The generated images were enlarged to a resolution of 512px while constantly maintaining their clarity and readability.

Initially designed for 64px resolution, the network had additional convolution layers incorporated to increase its capacity. Adding these layers, without fine-tuning, for the 256px and higher resolution tasks destabilized the training process, undermining the delicate balance required when augmenting network complexity. For generating images at 256x256 resolution, the changes that worked best involved introducing dropout regularization to both the discriminator and generator networks while keeping the learning rates at their original value. This combination helped stabilize the training process, albeit with loss fluctuations.

Further increasing network depth to allow for 512x512 resolution without structural or parameter change led to issues like very prominent checkerboard artifacts and convergence issues. The addition of blurring layers improved artifact reduction but failed to fully address all distortions. Notably, the introduction of adaptive learning rates significantly improved convergence, offering a promising solution to stabilize training dynamics whenever it started unconverging. However, despite this improvement, the model still exhibited slight checkerboard artifacts and excessive sharpness, indicating the need for further fine-tuning. Ultimately, introducing the inception module to the generator network led to higher loss fluctuations but stable convergence and good-quality sample generation, with no prominent issues reported. This suggests that for higher resolutions, incorporating more complex modules like the inception module can help enhance stability and quality.

While the higher resolution promises greater detail and fidelity in generated samples, it also amplifies the complexity of training, demanding more computational power and longer training times. To upscale the resolution beyond 512px, the network would require a different approach, for example, lowering the resolution of generated images upscaling them by another neural network.



Figure 1. Example of 512x512 px images generated by the trained network.

## **BIBLIOGRAPHY**

1. Ian J. Goodfellow, Jean Pouget-Abadie, Mehdi Mirza, Bing Xu, David Warde-Farley, Sherjil Ozair, Aaron Courville, Yoshua Bengio. Generative Adversarial Networks. *Advances in neural information processing systems*, 2014
2. Alec Radford, Luke Metz, Soumith Chintala. Unsupervised Representation Learning with Deep Convolutional Generative Adversarial Networks. arXiv preprint arXiv:1511.06434, 2015
3. Nathan Inkawhich. [https://pytorch.org/tutorials/beginner/dcgan\\_faces\\_tutorial.html](https://pytorch.org/tutorials/beginner/dcgan_faces_tutorial.html)
4. Vincent Dumoulin, Francesco Visin. A guide to convolution arithmetic for deep learning. arXiv preprint arXiv:1603.07285, 2016
5. Augustus Odena, Vincent Dumoulin, Chris Olah. Deconvolution and Checkerboard Artifacts. *Distill*, 2016.
6. Christian Szegedy, Wei Liu, Yangqing Jia, Pierre Sermanet, Scott Reed, Dragomir Anguelov, Dumitru Erhan, Vincent Vanhoucke, Andrew Rabinovich. Going Deeper with Convolutions. *Proceedings of the IEEE conference on computer vision and pattern recognition*, 2014



17th-19th June 2024  
Gliwice, Poland

DEPARTMENT OF ENGINEERING MATERIALS AND BIOMATERIALS  
FACULTY OF MECHANICAL ENGINEERING  
SILESIA UNIVERSITY OF TECHNOLOGY

## INTERNATIONAL STUDENTS SCIENTIFIC CONFERENCE

### Interactive diagram of transformations of subcooled austenite

Tomasz Sokoła, Łukasz Soja, Marek Romanowski, Rafał Honysz<sup>a</sup>

<sup>a</sup> Silesian University of Technology, Faculty of Mechanical Engineering, Department of Engineering Materials and Biomaterials  
email: rafal.honysz@polsl.pl

**Abstract:** This work describes an interactive diagram illustrating the transformation of subcooled austenite. The simulation aims to familiarize the user with basic information about steel and demonstrate changes in the structure and properties of various types of steel cooled at different speeds. Thanks to the features available in the presentation, users can independently create visualizations and familiarize themselves with the fundamental parameters of the process.

**Keywords:** Computer Materials Science, Continuous Cooling Transformation (CCT), Time Temperature Transformation (TTT), Simulation, Virtual Reality.

### 1. INTRODUCTION

The transformation of austenite into specific structures significantly depends on the cooling rate and temperatures of these transformations. These factors, in turn, have a significant impact on the functional properties of products after heat treatment. Understanding the critical temperatures for specific steel grades is essential, but it is not sufficient information for establishing heat treatment parameters. Comprehensive data on the relationship between structure and hardness, based on heat treatment parameters such as temperature and time, are presented in kinetic phase transformation diagrams. These types of diagrams have been developed in two versions:

- CCT - Continuous Cooling Transformation is used for isothermal transformations
- TTT - Time Temperature Transformation diagrams illustrate transformations that occur during continuous cooling,

The influence of time on phase transformations is much weaker than that of temperature. Therefore, a logarithmic scale was adopted in the time diagrams to ensure good readability across a wide range of very short and long times. In CCT/TTT plots, isotherms represent temperatures at A<sub>3</sub>, A<sub>cm</sub>, M<sub>s</sub>, and M<sub>r</sub>. The curves between the A<sub>1</sub> and M<sub>s</sub> isotherms indicate the onset and completion of diffusion changes.

The behavior of austenite in isothermal conditions below A<sub>1</sub> is illustrated by curves plotted in the "amount of transformed austenite - logarithm of time" system. These curves

illustrate the progress of the transformation of subcooled austenite at a constant temperature. By plotting the initial and final points of the transformation of subcooled austenite on a shared diagram and connecting them with a solid line, the curves illustrate the beginning and end of the transformation process of subcooled austenite. This method produces a diagram illustrating the transformation of subcooled austenite under continuous cooling transformation isothermal conditions.

Due to the nature of the ongoing changes, the CCT/TTT diagrams have the following ranges:

- the temperature range varies from A1 temperature to the minimum durability temperature of austenite (550-600°C), during which the pearlitic transformation occurs.
- the temperature range extends from the minimum durability temperature of austenite to the Ms temperature, at which the bainitic transformation takes place.
- the range between Ms and Mf within which the martensitic transformation occurs.

From CCT/TTT diagrams it is possible to determine the time at which the phase transformation of subcooled austenite begins and ends. They also allow for reading the temperature range of the lowest durability of austenite, thus determining the necessary cooling rate. This helps prevent pearlitic transformation and leads to obtaining bainitic or martensitic structures. The line running from the austenitization temperature tangentially to the transformation onset curve at the point of the lowest durability of subcooled austenite represents the critical cooling rate. On CCT/TTT diagrams. For steels with hypoeutectoid or hypereutectoid carbon content, an additional line above the curve indicates the beginning of austenite transformation, marking the separation of ferrite or cementite from austenite, respectively.

## 2. INTERACTIVE DIAGRAM

After initiating the presentation and closing the presentation title window, the steel selection window appears, allowing users to choose the type of steel for which they want to create a virtual graph. We can choose from several types of unalloyed, structural, special, and other steels. After making the selection, the user navigates to the main window as shown in Figure 1. The largest section of the diagram is occupied by an empty field of the Time-Temperature-Transformation (TTT) diagram, illustrating the steel temperature in relation to time, with additional sections indicating the corresponding transformations. The temperature axis indicates the range within which the steel will be cooled at the beginning of graph plotting. At the bottom left of the screen, there is information about the selected steel grade and its chemical composition. On the right side, there are buttons that can be used to select the cooling speed. There are three speeds to choose from: critical, normal, and slow. Pressing one of the buttons will draw a line on the graph representing the selected cooling speed. It will also display information about the resulting steel structure and the hardness obtained (in HV).

Once the user has finished drawing the graph, he can repeat the process for a different cooling rate. There is a RESET button in the lower right corner. Pressing it at any time will return you to the beginning of the presentation. Example diagrams for C45 steel are presented in Figure 2.

All works, graphics, text information, and animations were created using Adobe Animate.



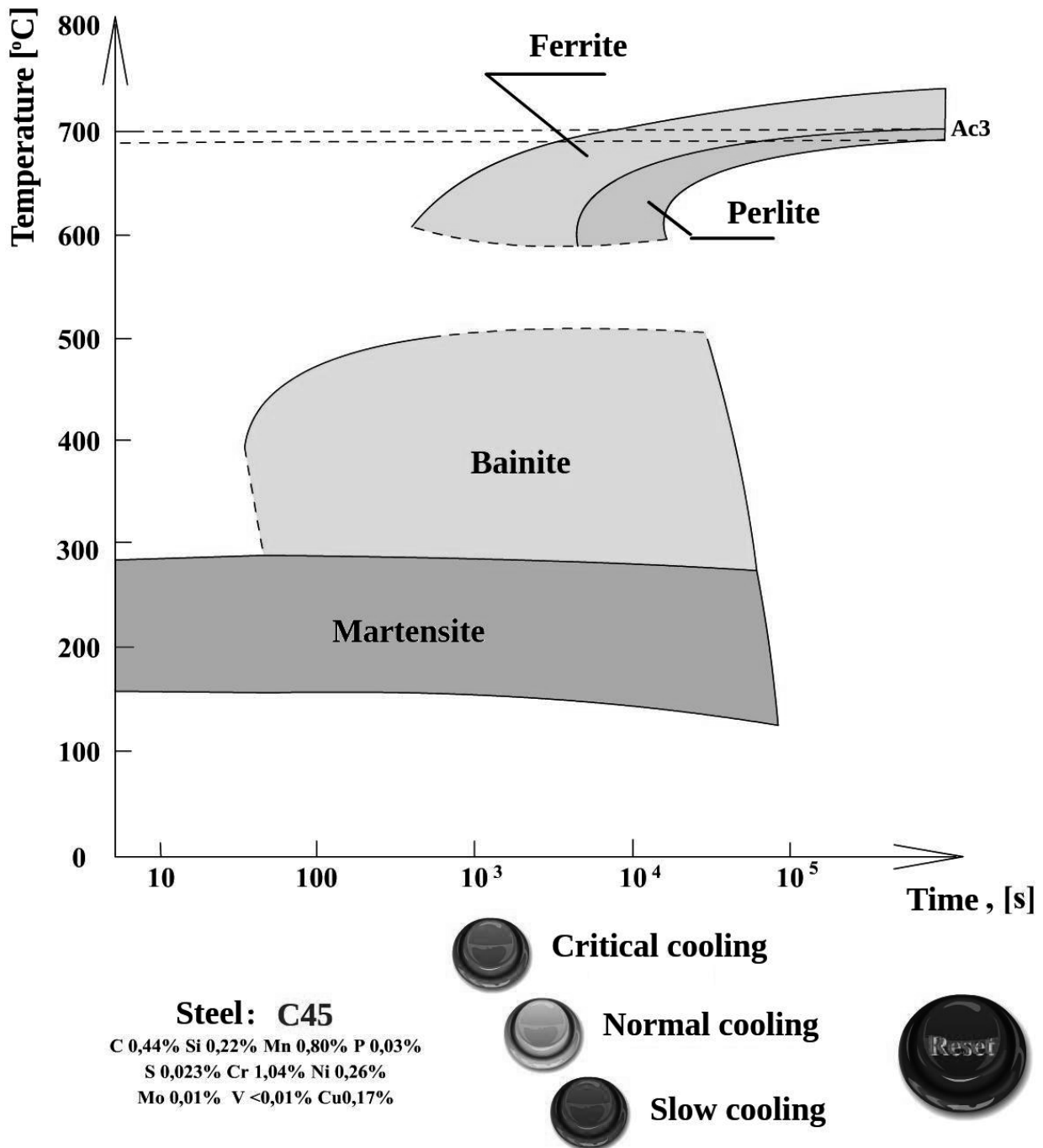


Figure 1. Presentation main window.

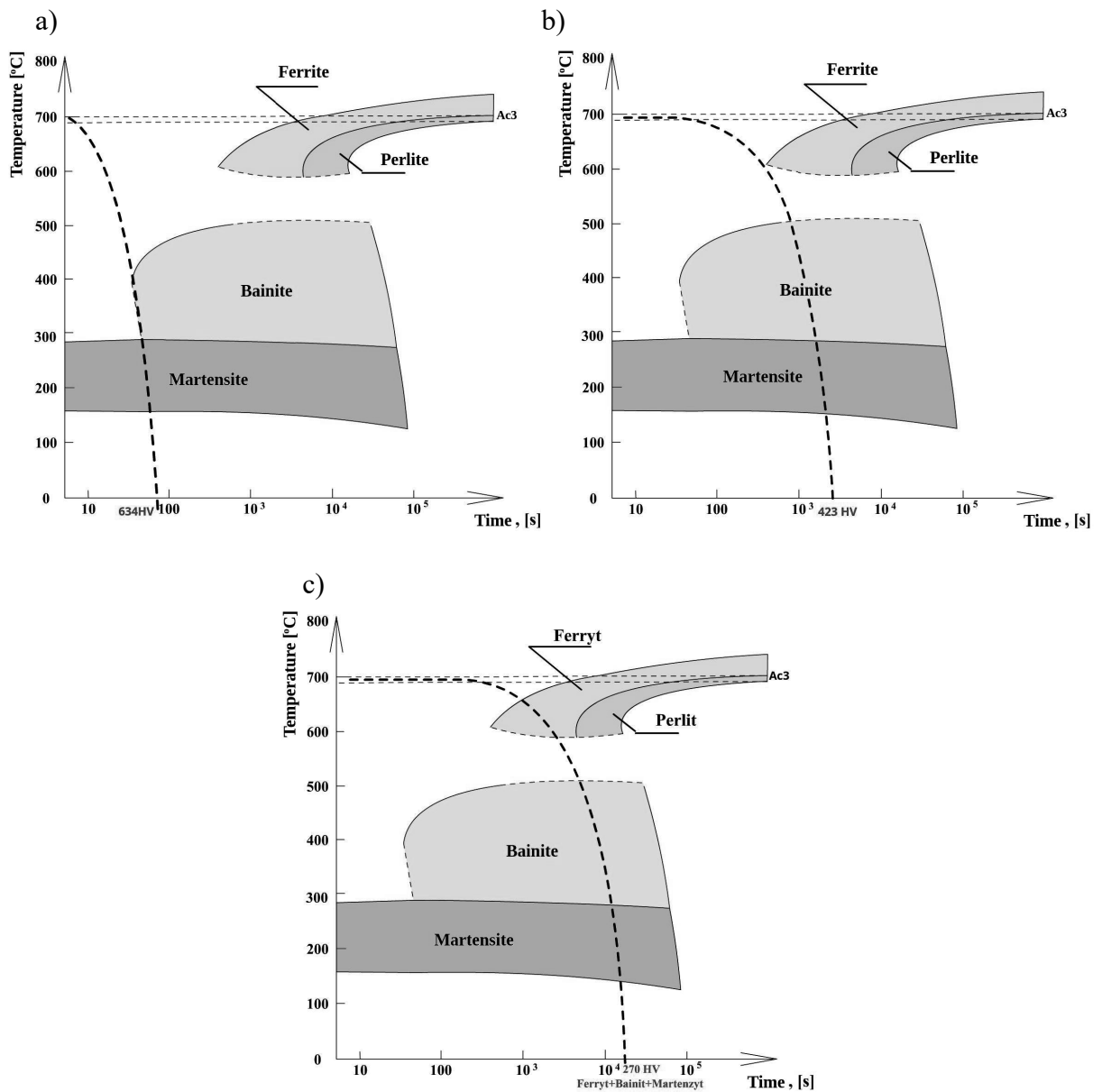


Figure 2. Examples of graphs obtained for C45 steel for a) critical, b) normal and c) slow cooling speed

### 3. SUMMARY

The presentation made for our topic is only an instructional and illustrative form. Its purpose is to graphically familiarize the user with the process of martensite transformation depending on the selected cooling speed. However, due to the simplifications adopted, it is not suitable for performing serious engineering calculations or for other non-educational applications.

**BIBLIOGRAPHY**

1. L. A. Dobrzański, Podstawy nauki o materiałach i metaloznawstwo: materiały inżynierskie z podstawami projektowania materiałowego, Wydawnictwo Naukowo-Techniczne WNT 2006.
2. R. Honysz, L. A. Dobrzański, Virtual laboratory methodology in scientific researches and education, Journal of Achievements in Materials and Manufacturing Engineering, 84/2, (2017), 76-84.
3. J. Adamczyk, Inżynieria materiałów metalowych, Cz.1 i 2, Wydawnictwo Politechniki Śląskiej, 2004
4. L. A. Dobrzański, J. Trzaska, Zastosowanie sieci neuronowych do prognozowania wykresów CTPc, II Krajowa Konferencja "Nowe materiały - nowe technologie w przemyśle okrętowym i maszynowym", Międzyzdroje 7-10 września 2003.
5. M. Morawiec, A. Kozłowska, A. Grajcar, M. Król, Konstrukcja wykresów CTP dla stali konstrukcyjnych, Laboratoria, Aparatura, Badania 1/2019.
6. J Trzaska, LA Dobrzański, Modelling of CCT diagrams for engineering and constructional steels, Journal of Materials Processing Technology 192, 504-510.
7. <https://www.stalnierzewna.com/pytania-do-eksperta/pytanie/wykresy-ctpc/>
8. <http://inzynier-jakosci.blogspot.com/2015/02/wykres-ctp-i-ctpc-czas-temperatura.html>
9. <https://www.adobe.com/pl/products/animate.html>



17th-19th June 2024  
Gliwice, Poland

DEPARTMENT OF ENGINEERING MATERIALS AND BIOMATERIALS  
FACULTY OF MECHANICAL ENGINEERING  
SILESIA UNIVERSITY OF TECHNOLOGY

## INTERNATIONAL STUDENTS SCIENTIFIC CONFERENCE

### **Enhancing Osteointegration of Dental and Orthopedic Implants Through Advanced Surface Engineering Techniques**

Maryam Soleimani<sup>a</sup>

<sup>a</sup> Silesian University of Technology, Faculty of Mechanical Engineering, Department of Engineering Materials and Biomaterials  
email: maryam.soleimani@polsl.pl

**Abstract:** Biomedical alloys play a crucial role in orthopedic applications, with titanium and its alloys being extensively utilized due to their outstanding mechanical properties and biocompatibility. However, their inherent drawbacks, such as biological inertness and limited antibacterial properties, hinder further advancements. Hence, the surface properties of titanium are pivotal in the implantation process, determining implant success. This review aims to comprehensively describe surface modification techniques for titanium implants with orthopedic and dental usage.

**Keywords:** biomaterials, bone regeneration, implants, surface modification

#### **1. INTRODUCTION**

Implantable biomaterials are widely used in orthopedics and dentistry, however, they often fail due to loosening, osteolysis, and infections [1]. When osteointegration in the bone-implant area diminishes, the risk of bacterial colonization will increase, leading to biofilm formation and subsequent infection [2]. Surface modifications can be tailored to improve the interaction between biomaterials and biological systems, reducing the risk of adverse reactions, and promoting integration with host tissues [3], functionalized surfaces to resist fouling by biomolecules and microbial adhesion, thereby reducing the risk of infections and biofilm formation on medical implants and devices [4]. One of the best choices for modifying dental and orthopedic implants is coating by utilizing alternative methods, such as laser-based fabrication, electrophoretic deposition, electrochemical deposition, magnetron sputtering, and biomimetic deposition, which are also being actively studied [5]. There are several methods to enhance osteointegration by coating the biomaterials to reduce the side effects of infections. Also, TiO<sub>2</sub> coatings, as well as methods for achieving antibacterial properties [6]. The TiO<sub>2</sub> coating was widely used in pure Ti, Ti6Al4V, and TiNbSn [7–10]. Because of the prosperity of new processing technologies, a considerable number of advanced surface-modification methods have emerged in recent years, such as friction stir processing (FSP), laser surface modification, and MAO. These methods offer new solutions to obtain better surface properties of Ti and Ti alloys. These newly emerged methods can also be classified into mechanical methods, physical

methods, and chemical methods. Additionally, biochemical and drug-load technologies become useful surface-modification methods to improve the bioactivity and bio functionality of Ti and Ti alloys for meeting clinical requirements currently. Detailed information about these advanced surface-modification methods is presented as follows [11]. This study will briefly consider the different surface engineering methods for improving the rejection of the implant caused by infections and biofilms.

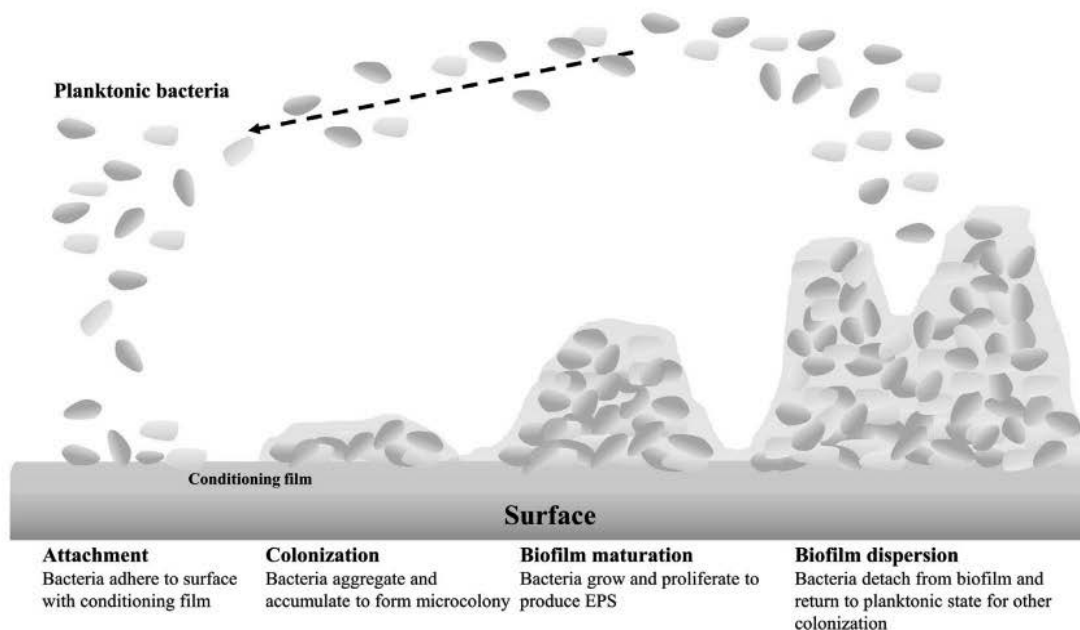


Fig1. Schematic representation of biofilm formation [5]

## 2. TiO<sub>2</sub>-RELATED COATING METHODS

The favorable biological performance of titanium alloys largely stems from the natural formation of a titanium dioxide (TiO<sub>2</sub>) layer on the surface. This layer acts as an outstanding bioactive ceramic, particularly well-suited for orthopedic applications. naturally constructed naturally constructed TiO<sub>2</sub> layer is relatively thin with an approximate thickness of 1–4 nm, which is inefficient in tuning the bio inertness of the titanium substrate; thus, limits their potential in promising osteogenesis and osteointegration [12]. Recent studies have focused on intentionally coating titanium alloys with titanium dioxide (TiO<sub>2</sub>) through various surface oxidation techniques and direct coating methods to enhance bioactivity. Similar to calcium phosphate (CaP) coatings, bioactive elements like magnesium (Mg) and strontium (Sr) ions can be incorporated into TiO<sub>2</sub> coatings to improve osteoinduction and osteoconduction. Thermal atmospheric oxidation is one method for forming an oxide layer on metallic implants, resulting in different surface compositions depending on the oxidizing atmosphere. In the air, a rutile bioactive phase (TiO<sub>2</sub>) is deposited, while under a pure oxygen atmosphere, titanium monoxide (TiO) forms in addition to TiO<sub>2</sub>. Different atmospheric treatments do not significantly affect surface topography, but air-treated surfaces exhibit higher hydrophilicity and are more efficient in apatite formation, cell attachment, and proliferation compared to pure oxygen-treated surfaces. Thermal oxidized Ti6Al4V implants also enhance bone-implant contact (BIC) and accelerate osteointegration due to TiO<sub>2</sub> deposition. Micro-arc oxidation (MAO) is an

electrochemical surface treatment that can produce porous TiO<sub>2</sub> coatings on implants, with characteristics adjustable by electrolyte composition and process parameters. Incorporating bioactive elements like calcium phosphate (CaP) into MAO coatings enhances osteointegration.

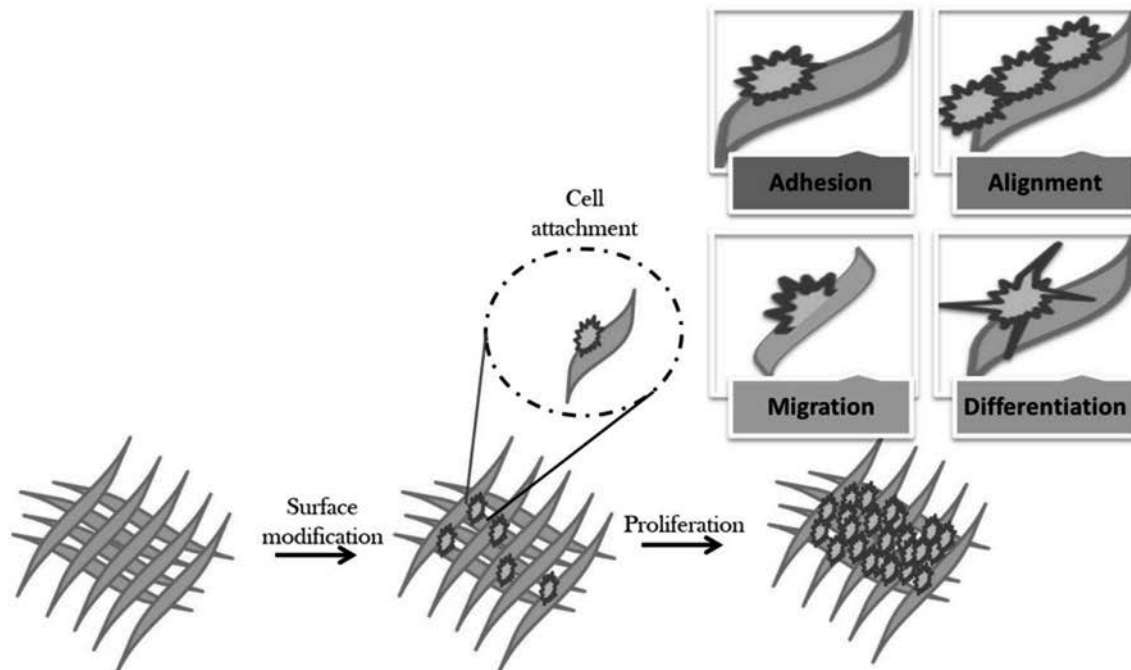


Fig 2. Schematic representation of cellular responses of surface-modified biomaterials [13]

Recent studies have focused on intentionally coating titanium alloys with titanium dioxide (TiO<sub>2</sub>) through various surface oxidation techniques and direct coating methods to enhance bioactivity. Similar to calcium phosphate (CaP) coatings, bioactive elements like magnesium (Mg) and strontium (Sr) ions can be incorporated into TiO<sub>2</sub> coatings to improve osteoinduction and osteoconduction. Thermal atmospheric oxidation is one method for forming an oxide layer on metallic implants, resulting in different surface compositions depending on the oxidizing atmosphere. In the air, a rutile bioactive phase (TiO<sub>2</sub>) is deposited, while under a pure oxygen atmosphere, titanium monoxide (TiO) forms in addition to TiO<sub>2</sub>. Different atmospheric treatments do not significantly affect surface topography, but air-treated surfaces exhibit higher hydrophilicity and are more efficient in apatite formation, cell attachment, and proliferation compared to pure oxygen-treated surfaces. Thermal oxidized Ti6Al4V implants also enhance bone-implant contact (BIC) and accelerate osteointegration due to TiO<sub>2</sub> deposition. Micro-arc oxidation (MAO) is an electrochemical surface treatment that can produce porous TiO<sub>2</sub> coatings on implants, with characteristics adjustable by electrolyte composition and process parameters. Incorporating bioactive elements like calcium phosphate (CaP) into MAO coatings enhances osteointegration.

It's widely recognized that materials with ultrafine-grained structures, featuring grain sizes in the submicron or nanometer range, often demonstrate improved mechanical properties, corrosion resistance, and biocompatibility compared to their coarser-grained counterparts. These ultrafine-grained materials are typically achieved through severe plastic deformation techniques. Consequently, several methods involving severe plastic deformation have been developed to create ultrafine-grained surface-modified layers on titanium and its alloys. This

section focuses on two advanced mechanical methods: friction stir processing (FSP) and surface mechanical attrition treatment (SMAT).

Friction Stir Processing (FSP) is a surface modification technique adapted from friction stir welding. It utilizes a stir tool, consisting of a shoulder and a pin, to induce severe plastic deformation on the surface of materials in a milling machine. Heat generated by friction weakens the material, allowing the stir tool to move along a predetermined path, resulting in an ultrafine-grained surface-modified layer through severe plastic deformation and dynamic recrystallization. The width and depth of this layer depend on the stir tool's shape and processing parameters. FSP-treated materials exhibit higher hardness and improved wear resistance due to refinement strengthening. Additionally, their corrosion resistance is enhanced under optimized parameters. The ultrafine-grained structure of FSP-treated materials also enhances bioactivity, making them suitable for biomedical applications. FSP can also create composite layers by incorporating functional particles into pre-punched holes, offering antibacterial properties with controlled particle content.

Laser beams, known for their high coherence and directionality, are widely utilized in surface modification processes for various metals. In laser-related methods, a defocused laser beam serves as a heat source to melt materials on the surface of workpieces, which can include the workpiece surfaces themselves, additional powder placed on the surfaces, or synchronous feeding of powder/wires. These methods encompass laser surface remelting, laser surface alloying, and laser cladding. Laser surface remelting involves melting the surface of workpieces with an energetic laser beam, resulting in a thin surface layer that solidifies immediately. This process can create a fine martensite structure and a TiO<sub>2</sub> layer on the surface, enhancing hardness, wear resistance, and corrosion resistance. Laser surface alloying uses additives that react with the melt pool to produce alloyed layers, such as TiN, which significantly improves wear resistance. Laser cladding involves melting pre-placed or synchronous feeding powder/wires to form coatings on the surface of metals, providing advantages like high homogeneity and deposition rate. Various materials, including metals, ceramics, and cermets, can be used as cladding materials to enhance hardness, wear resistance, and corrosion resistance. However, challenges such as cracks in cladding coatings and low bond strength in ceramic coatings with substrates still need to be addressed, often requiring optimized processing parameters and buffer interlayers. Overall, laser surface treatment methods offer versatile options for creating surface-modified layers applicable in diverse environments, from aerospace applications to biomedical fields.

During Physical Vapor Deposition (PVD), single or multiple source materials are evaporated or sputtered in a high vacuum environment. The resulting atoms, molecules, or ions are then transferred to the surface of a substrate, initiating the nucleation and growth of a thin film. Although categorized as a physical method, some reactions with the material's surface may occur to facilitate film growth. PVD-processed films boast high density and strong adhesion to the substrate, typically falling into three categories: evaporation plating, ion plating, and sputtering. Evaporation plating involves a thermal-assisted phase transformation in source materials, with deposition rates typically ranging from 10 to 25,000 nm per minute. Various metals and compounds can be used as source materials, with some forming compound films on the substrate surface. Ion plating utilizes energetic particles to bombard the substrate surface and deposit films, typically achieving similar deposition rates as evaporation plating. Films synthesized through ion plating include TiN, TiC, TiCN, and others, enhancing wear resistance for applications such as cutting and forming operations. However, the significant difference in

hardness between films and substrates can lead to potential delamination and cracks, which may be mitigated through diffusive treatment or bias voltage adjustment [14].

Sputtering, compared to evaporation plating and ion plating, typically has a lower deposition rate ranging from 25 to 1000 nm per minute. It involves ejecting species from a condensed matter source using energetic projectile particles, making it suitable for depositing ceramics and refractory metals with high melting points. Sputtering offers versatility and flexibility and is often used in combination with plasma deposition techniques. Various sputtering methods have been utilized to prepare thin films on titanium and its alloys, improving wear resistance, corrosion resistance, biocompatibility, and bioactivity. Film properties can be tailored by adjusting chemical compositions, such as incorporating copper or silicon to enhance tribological properties and hardness, respectively. Biomedical applications include the development of antimicrobial films and the growth of hydroxyapatite (HA) films to improve biocompatibility. Multilayered HA/Ti films synthesized via RF magnetron-assisted sputtering show promise in overcoming delamination issues after implantation, with wide atomic intermixed zones contributing to enhanced adhesion strength [15]. Micro-arc oxidation (MAO), also known as anodic spark oxidation or plasma electrolytic oxidation, is a method that evolved from anodic oxidation. It involves synthesizing ceramic coatings on various metals like Ti, Al, Zr, and Mg. During MAO, the sample serves as the anode and is immersed in an aqueous solution with a high voltage, typically above 150 V for Ti and its alloys. This process leads to sparking on the surface, resulting in porous coatings with high hardness, wear resistance, and adhesion. MAO is extensively used in biomedical applications to enhance the biocompatibility of Ti and its alloys. The chemical composition, morphology, and microstructure of MAO-produced coatings are heavily influenced by parameters like alloy compositions, electrolyte, temperature, time, voltage, duty cycle, and current density. The choice of electrolyte is crucial, with NaOH/KOH commonly used as the base electrolyte. Additives like phosphate, fluoride, silicate, sodium salt, and calcium salt are often incorporated to tailor the properties of the coatings. Fluoride-containing electrolytes, for example, induce the formation of fluoridated hydroxyapatite (HA) in the coatings, enhancing bone response and interface adhesion. MAO has promising applications not only in biomedical fields but also in electronics and environmental protection industries due to the dielectric properties and photocatalytic performance of the TiO<sub>2</sub> produced in the coatings. However, challenges such as low processing rate, high energy cost, and non-uniform coating thickness in complex geometries need to be addressed. Future developments in MAO technology may involve optimizing energy utilization, understanding the discharge and film growth models better, and combining MAO with other methods like heat treatment and electrophoresis to enhance the performance of Ti and its alloys for broader applications [16,17].

### **3. SUMMARY**

This review explores various methods for modifying the surfaces of titanium (Ti) and its alloys to enhance their mechanical, corrosion, and biological properties. Despite their impressive attributes like high strength, corrosion resistance, and biocompatibility, Ti and its alloys encounter surface-related issues during service. Consequently, surface modifications are applied to synthesize protective or biologically modified layers, ensuring their longevity and reliability in diverse environments. Traditionally, surface modification methods are categorized into mechanical, physical, chemical, and biochemical techniques, including sandblasting,



thermal spraying, alkali treatment, and glow discharge plasma treatment. However, these conventional methods have limitations in improving surface properties or adapting to different workpiece geometries. Thus, advanced methods like friction stir processing (FSP), surface mechanical attrition treatment (SMAT), laser surface modification, micro-arc oxidation (MAO), and physical vapor deposition (PVD), among others, have emerged in recent decades, enhancing the performance and applications of Ti and its alloys. While these methods greatly enhance Ti and its alloys' properties, further research is necessary to meet increasingly stringent surface requirements. Advancing surface modification technologies requires a deep understanding of the underlying mechanisms. Moreover, combining different surface modification techniques (e.g., plasma spray-PVD) or using one method as pretreatment before another may become more prevalent. Additionally, the development of new high-performance coating materials is crucial. Hence, integrating various high-performance surface modification technologies may become the norm for Ti and its alloys (as well as other metals), aiming for superior performance and broader applications.

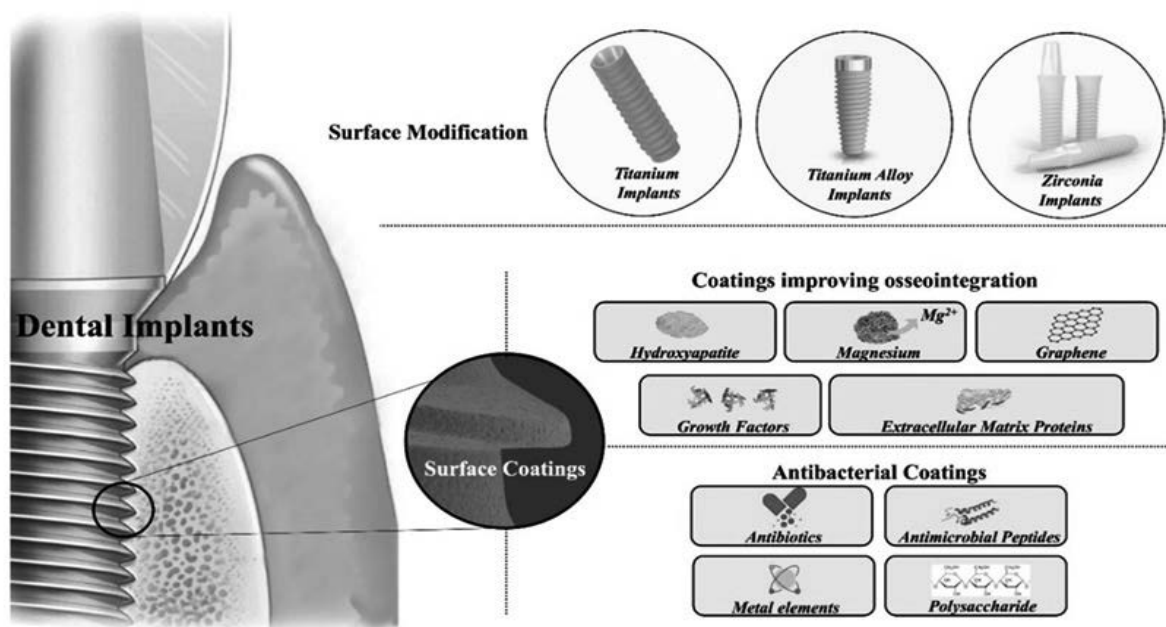


Fig 3. A schematic illustration of Surface Modifies and Functional Coating of Dental Implants [18].

## BIBLIOGRAPHY

1. Kurtz, S.; Mowat, F.; Ong, K.; Chan, N.; Lau, E.; Halpern, M. Prevalence of Primary and Revision Total Hip and Knee Arthroplasty in the United States from 1990 through 2002. *J. Bone Joint Surg. Am.* 2005, 87 (7), 1487–1497.
2. Hu, C.; Ashok, D.; Nisbet, D. R.; Gautam, V. Bioinspired Surface Modification of Orthopedic Implants for Bone Tissue Engineering. *Biomaterials* 2019, 219.
3. Vladkova, T. G. Go To 6.8.4 Cell Function Analysis Page. *Surf. Eng. Polym. Biomater.* 2013.

4. Eldeeb, A. E.; Salah, S.; Elkasabgy, N. A. Biomaterials for Tissue Engineering Applications and Current Updates in the Field: A Comprehensive Review. *AAPS PharmSciTech* 2022, 23 (7), 3.
5. Liu, Z.; Liu, X.; Ramakrishna, S. Surface Engineering of Biomaterials in Orthopedic and Dental Implants: Strategies to Improve Osteointegration, Bacteriostatic and Bactericidal Activities. *Biotechnol. J.* 2021, 16 (7), 2000116.
6. Tian, L.; Zhang, Z.; Tian, B.; Zhang, X.; Wang, N. Study on Antibacterial Properties and Cytocompatibility of EPL Coated 3D Printed PCL/HA Composite Scaffolds. *RSC Adv.* 2020, 10 (8), 4805–4816.
7. Alipour, S.; Nour, S.; Attari, S. M.; Mohajeri, M.; Kianersi, S.; Taromian, F.; Khalkhali, M.; Aninwene, G. E.; Tayebi, L. A Review on in Vitro/in Vivo Response of Additively Manufactured Ti–6Al–4V Alloy. *J. Mater. Chem. B* 2022, 10 (46), 9479–9534.
8. Azari, R.; Rezaie, H. R.; Khavandi, A. Investigation of Functionally Graded HA-TiO<sub>2</sub> Coating on Ti–6Al–4V Substrate Fabricated by Sol-Gel Method. *Ceram. Int.* 2019, 45 (14), 17545–17555.
9. Tepla, T.; Pleshakov, E.; Sieniawski, J.; Bohun, L. Causes of Degradation of Titanium Dental Implants. *Ukr. J. Mech. Eng. Mater. Sci.* 2022, 8 (4), 31–40.
10. Sung, J.; Shin, M.; Deshmukh, P. R.; Hyun, H. S.; Sohn, Y.; Shin, W. G. Preparation of Ultrathin TiO<sub>2</sub> Coating on Boron Particles by Thermal Chemical Vapor Deposition and Their Oxidation-Resistance Performance. *J. Alloys Compd.* 2018, 767, 924–931.
11. Kumar, S.; Kumar, R. Recent Advances in Design and Fabrication of Wear Resistant Materials and Coatings: Surface Modification Techniques. <https://services.igi-global.com/resolvedoi/resolve.aspx?doi=10.4018/978-1-7998-9683-8.ch005> 1AD, 87–117.
12. Yang, T. Sen; Huang, M. S.; Wang, M. S.; Lin, M. H.; Tsai, M. Y.; Wang Wang, P. Y. Effect of Electrical Discharging on Formation of Nanoporous Biocompatible Layer on Ti-6Al-4V Alloys. *Implant Dent.* 2013, 22 (4), 374–379.
13. Sultana, A.; Zare, M.; Luo, H.; Ramakrishna, S. Surface Engineering Strategies to Enhance the in Situ Performance of Medical Devices Including Atomic Scale Engineering. *Int. J. Mol. Sci.* 2021, 22 (21).
14. Barhoumi, N.; Khlifi, K.; Attia-Essaies, S. Mechanical and Bioactive Properties of PVD TiO<sub>2</sub> Coating Modified PEEK for Biomedical Applications. *J. Mech. Behav. Biomed. Mater.* 2023, 144, 105935.
15. Han, X.; Ma, J.; Tian, A.; Wang, Y.; Li, Y.; Dong, B.; Tong, X.; Ma, X. Surface Modification Techniques of Titanium and Titanium Alloys for Biomedical Orthopaedics Applications: A Review. *Colloids Surfaces B Biointerfaces* 2023, 227, 113339.
16. Wang, R.; Ni, S.; Ma, L.; Li, M. Porous Construction and Surface Modification of Titanium-Based Materials for Osteogenesis: A Review. *Front. Bioeng. Biotechnol.* 2022, 10.
17. Ma, Y.; Wu, P.; Mei, J.; Yu, Z.; Yang, J.; He, Y.; Li, H.; Lv, C.; Ren, S.; Xu, J.; Cai, Z.; Chu, P. K. Effects of Micro-Arc Oxidation Surface Treatment on the Corrosion Resistance of Ti-6Al-4V Electron-Beam-Welded Joints. *Met.* 2023, Vol. 13, Page 1161 2023, 13 (7), 1161.
18. Dong, H.; Liu, H.; Zhou, N.; Li, Q.; Yang, G.; Chen, L.; Mou, Y. Surface Modified Techniques and Emerging Functional Coating of Dental Implants. *Coatings* 2020, Vol. 10, Page 1012 2020, 10 (11), 1012.



17th-19th June 2024  
Gliwice, Poland

DEPARTMENT OF ENGINEERING MATERIALS AND BIOMATERIALS  
FACULTY OF MECHANICAL ENGINEERING  
SILESIA UNIVERSITY OF TECHNOLOGY

## INTERNATIONAL STUDENTS SCIENTIFIC CONFERENCE

### Process mapping on a selected example

Magdalena Stanik<sup>a</sup>, Aneta Kania<sup>b</sup>

<sup>a</sup> Student of Production Engineering and Management at the Faculty of Mechanical Engineering at the Silesian University of Technology

email: magdsta103@student.polsl.pl

<sup>b</sup> Silesian University of Technology, Faculty of Mechanical Engineering, Department of Engineering Materials and Biomaterials

email: aneta.kania@polsl.pl

**Abstract:** The article presents the methods and techniques of process mapping and the characteristics of a process-oriented organization. The research showed that a process map is an effective tool for introducing improvements and solving problems, what was presented on the example of a selected company.

**Keywords:** process mapping, flowchart, SIPOC, problem identification and solving.

### 1. INTRODUCTION

Adopting process management is considered the first step to process and business improvements. The improvement process helps companies constantly adapt to changing environmental conditions and allows them to efficiently use opportunities [1]. The undeniable advantages of process organization include a better description of the organization's operations, the ability to influence the organization's efficiency, increasing employee involvement by increasing their influence on the company's operations. What is more, the process approach has a positive impact on cost reduction and flexibility of the business [2]. Process analyzes allow not only to create profits for the company, but also to identify sources of losses.

Process management is a great approach for solving problems. Furthermore, it is a good alternative for searching for new solutions and opportunities in the company. By focusing on processes and improvement in accordance with the Kaizen philosophy, the company is able to achieve large profits and savings.

There are three main elements that are the basis for implementing a project of process management. These are: processes, people and technology. People are distinguished as the most important element, while technology is a supporting factor. In order to effectively implement process management, leadership concepts such as change, risk and strategic management should also be taken into account.

The implementation of a process management system in organizations includes the following stages [3]:

- Development of a process model, including defining the process architecture and goals and principles of process management and their connection with the strategy.
- Process design and implementation.
- Monitoring and evaluation of processes, supervision of their implementation.
- Improving the process model and processes.

## 2. TECHNIQUES AND METHODOLOGY OF PROCESS MAPPING

The best way to visualize a process is to develop a process map. It is a graphical presentation of the process. This presents the set of processes/operations and their interconnections. Development of process maps allows for easier analysis of the process in terms of quality and efficiency. Basically, there are two approaches to creating process maps: block and value chain.

Value Stream Mapping (VSM) is a visual representation of the flow of the value stream in a company. The basic assumption of VSM is to develop a state map of the current process, which presents all information flows and dependencies of a given process [4].

Process diagram is also called a flowchart, algorithm, or linkage flowchart. This tool has no limits on applications, it can be used in production processes, services and administration. Depending on the needs and the goals an enterprise aims to achieve. Flowcharts can be a carrier of various information. This tool uses standard symbols representing different types of activities or tasks [5]. The diagram may show the route taken by an invoice, the flow of production components, stages of the sales process or product service process. It should vary in level of detail depending on the needs.

A method of documenting processes derived from Six Sigma tools is a SIPOC matrix. The input assumption is that each process can be documented through the following elements [6]:

- SUPPLIER – supplier of input resources to the process,
- INPUT – input resources,
- PROCESS – the way in which input is transformed into output,
- OUTPUT – process result,
- CUSTOMER – recipient of process results.

The matrix can be extended by two more elements: resources and legal regulations [6].

## 3. APPLICATION OF FLOWCHART AND SIPOC METHOD IN THE SELECTED PROCESS

The studies include an analysis of the process of installing pipe connectors, implemented in one of the international companies, selection of an interdisciplinary team and defining improvement actions. The review of process documentation allowed identification of management areas that did not have documented processes. The corrective actions taken partially solved the problem, but they focused on reducing the effects rather than solving the problem.

The process team was built using the SIPOC diagram. Thanks to the diagram, all functional units involved in the process were specified. The diagram was created to identify employees and functional units involved in the process (Fig. 1). According to the methodology, mapping started from the end, i.e. from defining customers. The results of the process were then

collected. Employees from the field were asked to define this process, i.e. the standard procedure for organizing the installation, in several steps. Finally, based on the previous steps, input suppliers to the process were defined.

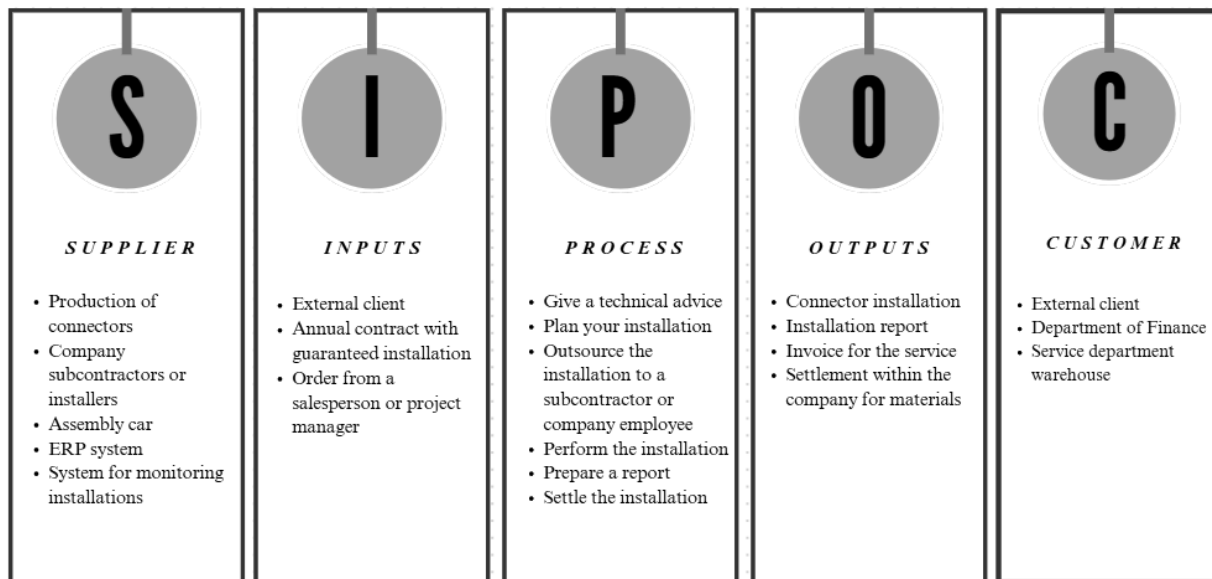


Figure 1. SIPOC diagram of the connector installation process.

As a result of a brief analysis of the process, it was determined that the interdisciplinary process team should consist of:

- people planning the installation and providing technical advice,
- decision makers, service department managers,
- the finance department and the person responsible for service settlements.

In the next stage, a flowchart was developed. The map presents the general flow of the process. The input to the process is a request for installation, and the process ends with the completed installation, for which the customer receives an invoice.

Analysis of the process documented in the form of a flowchart allowed the identification of potential threats and their places of occurrence. These include:

1. Lack of each service quote and customer acceptance of the terms of the obligation.
2. Failure to clearly document pricing conditions.
3. Manual editing of subcontractor reports to company standards.
4. Lack of smooth information about changes in the number of installations.

Taking into account the identified irregularities, a 'to be' process was proposed (Fig. 2). In this way, activities were significantly automated by full use of the EMS program functions. The new process was based on the installation order in the ERP system. The installation order is now placed at the beginning of the process. Thanks to the process management through the SAP installation order, at each stage of the process it is possible to verify open orders and their value, as well as eliminate unnecessary verification steps. The 'to be' process has gained financial transparency.





17th-19th June 2024  
Gliwice, Poland

DEPARTMENT OF ENGINEERING MATERIALS AND BIOMATERIALS  
FACULTY OF MECHANICAL ENGINEERING  
SILESIA UNIVERSITY OF TECHNOLOGY

## INTERNATIONAL STUDENTS SCIENTIFIC CONFERENCE

### **Methodology for EEG signal comparison in virtual and real-life flight scenarios**

Michał Sujkowski <sup>a</sup>, Dariusz Myszor <sup>b</sup>, Piotr Bartosz <sup>a</sup>, Jakub Sarno <sup>a</sup>, Wojciech Cofalik <sup>a</sup>, Patryk Mondry <sup>a</sup>

<sup>a</sup> Silesian University of Technology, Student Scientific Circle of Virtual Flying.

<sup>b</sup> Silesian University of Technology, Faculty of Automatic Control, Electronics and Computer Science, Department of Algorithmics and Software.

**Abstract:** The description of the methodology applied in order to compare the data acquired in real-life and simulated plane flights.

**Keywords:** flight simulator, EEG

### **1. INTRODUCTION**

Brain-Computer interfaces are characterized by growing popularity. It is caused by many factors such as abundance of various relatively cheap BCI interfaces such as Emotiv[1], KT88-2400[2], OpenBCI[3], NeurSky [4], etc. as well as development of AI models which can improved interpretation of EEG signals [5] (e.g. EEGNet [6], Long Short-Term Memory (LSTM) etc.).

The application of Brain-Computer Interface (BCI) systems extends to various domains, including aviation environments. However, acquiring electroencephalogram (EEG) signals during actual flight operations presents significant challenges and costs. The high expense arises from the comprehensive costs associated with flight operations, such as fuel, aircraft maintenance, and airfield fees. Moreover, the confined space of a cockpit complicates the setup and deployment of BCI systems. In small aircraft, such as the Cessna, the pilot's movement is severely restricted, making it difficult to experiment with and optimize various hardware configurations.

Testing BCI systems in a flight simulator can significantly streamline the process. Operating a flight simulator for an hour is considerably less expensive than an equivalent duration in an actual aircraft. The spatial constraints are alleviated as the pilot is accessible from outside the cockpit, greatly facilitating the headset mounting process. However, discrepancies between real aircraft and simulators may result in data variations. The objective of this article is to describe the methodology employed to acquire EEG signals in both real aircraft and flight simulators, with the aim of comparing their characteristics.

## 2. HOLDING PROCEDURE

Holding is a precisely defined aviation maneuver primarily utilized by pilots of passenger aircraft when it is necessary to delay the execution of a specified procedure, such as an approach to landing, or to await improved weather conditions.

The holding procedure is one of the most challenging maneuvers for studying pilots to master, yet it is highly repeatable. Pilots typically learn to execute this procedure during professional training after obtaining of a Private Pilot License (PPL). Proficiency in this procedure usually requires between several dozen to approximately 100 hours of practice.

Performing the holding procedure is initiated by a clear instruction from the air traffic controller and can be executed in two ways:

- According to the standard procedure for a given area published on the navigational chart.
- Through providing by the controller the so-called FLIRT
  - Fix: The location where the procedure is to be performed.
  - Level: The altitude at which the procedure is to be performed.
  - Inbound Track: The direction in which the procedure should be executed.
  - Right/Left: The direction of turns in the holding pattern.
  - Time: The duration of the outbound leg.

Controllers typically strive to facilitate the pilot's execution of the procedure by providing the current position, course, and altitude whenever possible.

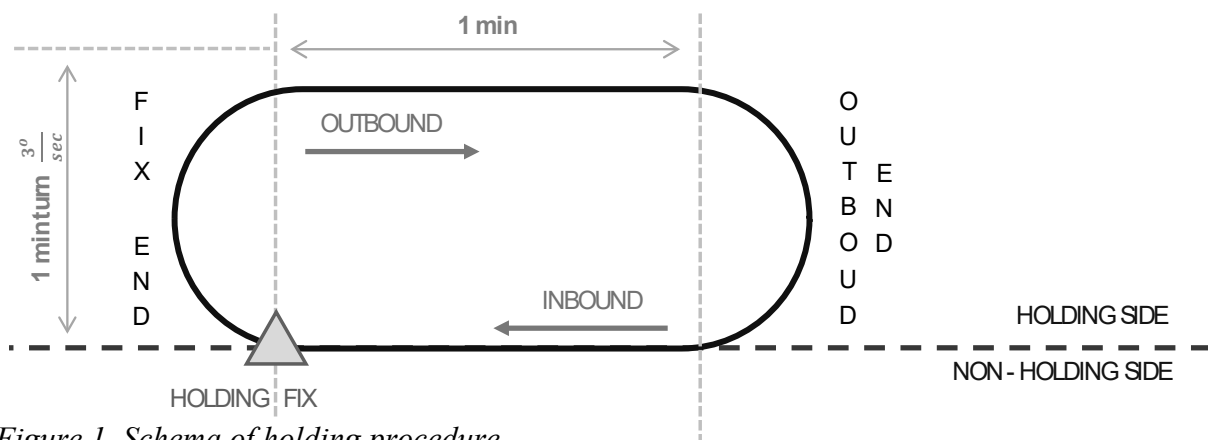


Figure 1. Schema of holding procedure

For example:

- SP-ABC, Kamień Radio, hold over MAPIK at 3000 ft altitude, inbound track 270 degrees, right turns, outbound time 1 min
- [wind, for example, is 110 degrees at 15 knots]
- The pilot, upon receiving the instruction, must calculate the "entry type" and wind correction angles (WCE)



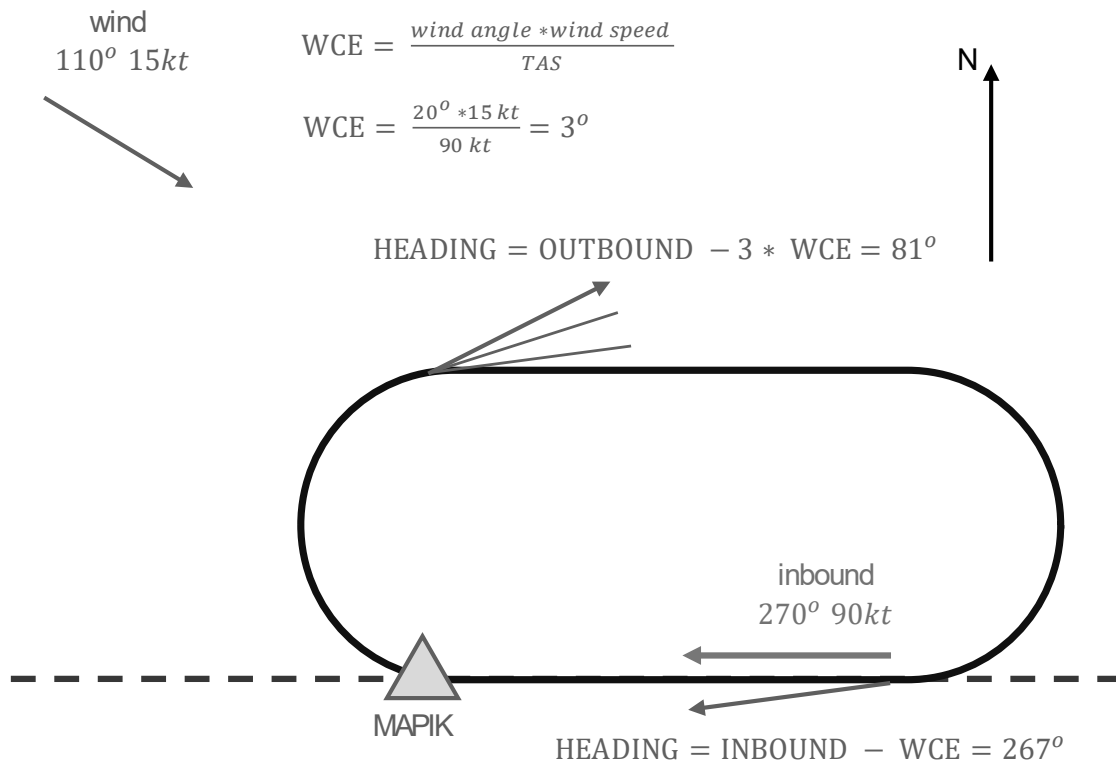


Figure 2. Schema of holding procedure execution

For the holding procedure, there are three different entry procedures depending on the direction of the "inbound track" and the current flight direction of the aircraft. These different procedures are necessary because the aircraft has limitations related to minimum flight speed, and the pilot cannot change the flight direction over a short distance. Appropriate entry procedures also ensure greater passenger comfort due to the limitation of the turn rate, usually at 3 degrees per second.

Depending on the orientation of the aircraft's longitudinal axis relative to the "inbound track," the following procedures are distinguished:

- Direct Entry – entering the holding pattern directly after passing the designated point.
- Parallel Entry – entering the holding pattern by flying over the point, then flying parallel to the "inbound leg," and making a turn to intercept the inbound course. After passing the point, the aircraft begins the holding procedure.
- Teardrop Entry – entering the holding pattern by flying over the point with a 30-degree offset from the course used in the Parallel Entry. Upon reaching the endpoint of the "outbound leg," the aircraft makes a turn in the assigned holding direction and continues towards the designated FIX point.

A graphical visualization of the types of holding entries is shown in Fig. 3.

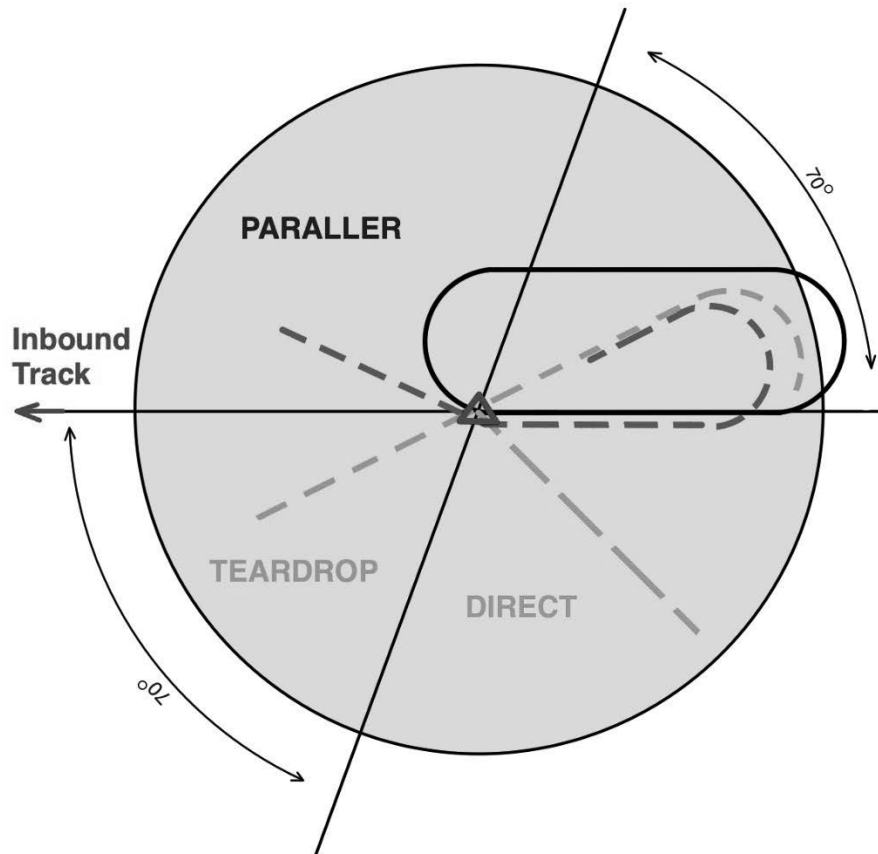


Figure 3. Types of holding entries

### 3. METHODOLOGY DESCRIPTION

For both real flights and simulated flights, the pilot will respectively perform a holding procedure (entry and one full holding procedure with parameters set by the "controller"). A command with instructions for the next procedure will be given each time when performing the "outbound leg". Such a task will require the pilot to perform repetitive calculations, corrections and pilot activities. After each instruction received, the pilot should clearly notify the person operating the EEG collection software when he has calculated the type of input and the necessary wind corrections, and provide the calculated values. This information will facilitate subsequent analysis of EEG results

Implemented software for EEG data collection allows to facilitate the data acquisition phase. It is responsible for registering of :

- The values given to the pilot, along with the time of their issuance
- The pilot's information regarding the conducted assessments/calculations
- The initiation of the holding entry procedure.
- The start and end of each turn (fix end, outbound end).

### 3. SUMMARY

The article focuses on the methodology for EEG signal acquisition during real and simulated flights. Undertaken approach allows to perform set of repetitive tasks thus facilitates significantly comparison of the data acquired in various conditions.

### BIBLIOGRAPHY

1. Binias, B., Myszor, D., Palus, H., & Cyran, K. A. (2020). Prediction of pilot's reaction time based on EEG signals. *Frontiers in neuroinformatics*, 14, 6.T. Suntola, J. Anlson, U.S. Patent 4,058.430, 1977.
2. Khan, H. A., Ul Ain, R., Kamboh, A. M., Butt, H. T., Shafait, S., Alamgir, W., ... & Shafait, F. (2022). The NMT scalp EEG dataset: an open-source annotated dataset of healthy and pathological EEG recordings for predictive modeling. *Frontiers in neuroscience*, 15, 755817.
3. Cardona-Álvarez, Y. N., Álvarez-Meza, A. M., Cárdenas-Peña, D. A., Castaño-Duque, G. A., & Castellanos-Dominguez, G. (2023). A novel OpenBCI framework for EEG-based neurophysiological experiments. *Sensors*, 23(7), 3763.
4. Sabio, J., Williams, N. S., McArthur, G. M., & Badcock, N. A. (2024). A scoping review on the use of consumer-grade EEG devices for research. *Plos one*, 19(3), e0291186.
5. Schirrneister, R. T., Springenberg, J. T., Fiederer, L. D. J., Glasstetter, M., Eggensperger, K., Tangermann, M., ... & Ball, T. (2017). Deep learning with convolutional neural networks for EEG decoding and visualization. *Human brain mapping*, 38(11), 5391-5420.
6. Lawhern, V. J., Solon, A. J., Waytowich, N. R., Gordon, S. M., Hung, C. P., & Lance, B. J. (2018). EEGNet: a compact convolutional neural network for EEG-based brain-computer interfaces. *Journal of neural engineering*, 15(5), 056013.



17th-19th June 2024  
Gliwice, Poland

DEPARTMENT OF ENGINEERING MATERIALS AND BIOMATERIALS  
FACULTY OF MECHANICAL ENGINEERING  
SILESIA UNIVERSITY OF TECHNOLOGY

## INTERNATIONAL STUDENTS SCIENTIFIC CONFERENCE

### Development of an active vibration protection system

Tornike Tetunashvili, Amkoladze Khatuni, Givi Sanadze

Georgian Technical University, Faculty of Transport Systems and Mechanical Engineering,  
Department of Mechanical Engineering and Technology  
email: tetunashvilitornike@gmail.com

Supervisors:

Amkoladze Khatuni, Associate professor, PhD., k.amkoladze@gtu.ge

Givi Sanadze, Associate professor, PhD., sanadzegivi05@gtu.ge

**Abstract:** Active vibration protection devices are effective means of protecting humans from low-frequency vibration effects. The qualitative indicators of the functioning of such systems largely depend on the dynamic characteristics of the position-closed electrohydraulic and hydraulic servo drives used in these devices with additional control elements, which, in turn, is linked to the development of new progressive structural and design schemes and the optimization selection of parameters of the developed systems. In this work, a diagram of a vibration protection device with an original servo drive is proposed, and research has been carried out aimed at constructing a mathematical model of the dynamics.

**Keywords:** vibration, protection device, servo drive, active system, control valve.

### 1. INTRODUCTION

Active vibration protection systems based on the use of electrohydraulic and hydromechanical servo drives have become widespread. And the improvement of the dynamic performance of servo drives and vibration protection systems in general is largely linked to the problems of stability, sensitivity and speed of the mentioned drives.

### 2. MAIN PART

Improving the dynamic properties of these servo drives can be achieved by increasing the stability at small openings of the control valves. For this purpose, a drive circuit with a nonlinear control law, consisting of two four-slot valves and additional hydraulic lines with chokes connected in series to them, can be used in the structure of the hydraulic part. Another approach to solving this problem is a hydraulic circuit with a correction circuit in the form of hydraulic resistance and a piston with elastic return, which provides the necessary damping at small openings of the control spool [2].

A schematic diagram of an active electro-hydraulic vibration protection system with deviation control, which includes the named correction device circuit in the hydraulic part of the system is shown in Fig. 1.

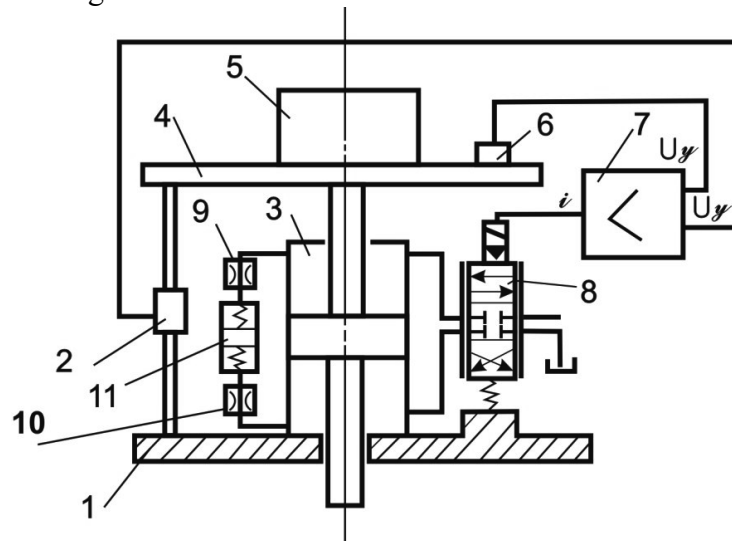


Fig. 1. Schematic diagram of the electro-hydraulic system

It contains a hydraulic cylinder 3 mounted on the base 1, an electro-hydraulic amplifier-converter 8, an electric amplifier-adder 7, an accelerometer 6 mounted on the frame 4, a position sensor 2, as well as elements of the correction device: a piston 11, throttles 9, 10 and springs 12. All these elements are connected to the executive hydraulic cylinder 3 through additional hydraulic lines. A vibration protection object 5 is placed on the frame 4.

The equation for the dynamics of the hydraulic part of an electrohydraulic servo system with four-slot valves with zero initial valve opening is described by the differential equation:

$$m\ddot{x} + h\dot{x} + k_r x = k_r F(P_n; P_1 \varepsilon) - K_F \dot{x}_1, \quad (1)$$

where

$$K_F = k_r \frac{F_1}{F};$$

$F(P_n; P_1 \varepsilon)$  – nonlinear dependence determined by the flow characteristic of a four-slot control valve;

$F$  and  $F_1$  – according to the area of the working surfaces of the hydraulic cylinder pistons 3 and 11;

$k_r$  – reduced rigidity coefficient of the hydraulic system;

$m$  – the mass of the moving parts of the device, reduced to the piston of the hydraulic cylinder 3;

$h$  – viscous damping coefficient;

$p$  – pressure drop in hydraulic cylinder 3;

$\varepsilon$  – current opening of the control valve;

$P_n$  – pressure supplied to the system;

$\dot{x}_1$  – piston coordinate of cylinder 11;

$x$  – coordinate of the hydraulic cylinder piston 3.

The nonlinear dependence  $F(P_n; P_1 \varepsilon)$  can be represented in linearized form.

$$F(P_n; p; \varepsilon) \approx K_{v\varepsilon}\varepsilon - K_{vp}p; \quad (2)$$

Where

$$K_{v\varepsilon} = \frac{k_{Q\varepsilon}}{F};$$

$$K_{vp} = \frac{k_{Qp}}{F}$$

and expressions  $K_{Q\varepsilon}$  and  $K_{Qp}$  taken from.

To determine the functional relationship between the coordinates  $x(t)$  and  $x_{\square}(t)$ , we write the equilibrium equation of the forces applied to the piston 11 of the corrective devices

$$F_1(P - 2p_{\theta p}) = m_k \ddot{x}_1 + h_k \dot{x}_1 + k_{sp} x_1, \quad (3)$$

Given the expressions:

$$P = m\ddot{x} + h\dot{x} + |P_{df}| \text{sign}\dot{x}$$

and

$$p_{\theta p} = k_{\theta p} \dot{x}_1,$$

get

$$m_k \ddot{x}_1 + (2k_{\theta p} + k_k) \dot{x}_1 + k_{sp} x_1 = m\ddot{x} + h\dot{x} + |P_{df}| \text{sign}\dot{x}. \quad (4)$$

Here:  $m_k$  – the mass of moving parts reduced to the piston rod of the hydraulic cylinder 11;

$k_{sp}$  – spring hardness;

$k_{th}$  – throttle flow coefficient 9 and 10;

$k_k$  – viscous friction coefficient;

$P_{df}$  – dry friction force reduced to the piston of hydraulic cylinder 3;

$P_{th}$  – pressure drop across the throttle.

Neglecting values  $m_k$  and  $h_k$ ,  $h$  and also by the force of dry friction, dependence (4) can be written in the form:

$$(T_k s + 1)x_1(s) = K_m S^2 \cdot x(s), \quad (5)$$

where

$$T_k = \frac{2k_{th}}{k_{sp}};$$

$$K_m = \frac{m}{k_{sp}};$$

$s$  – Laplace operator.

Using the linearized form of equation (1) in the form

$$(ms^3 + hs^2 + k_r s)x(s) = k_r k_{v\varepsilon} \varepsilon - k_r k_{vp} (B_2 s^2 + B_1 s)x(s) - K_F s x_1(s), \quad (6)$$

Taking into account dependence, the equation for the dynamics of the hydraulic part of the system takes the form:

$$A_4 s^4 + A_3 s^3 + A_2 s^2 + A_1 s)x(s) = k_r K_{v\varepsilon} (T_k s + 1) \varepsilon(s),$$

Where

$$A_4 = m T_k;$$

$$A_3 = m + a_2 T_k + K_m k_r K_{v\varepsilon};$$

$$A_2 = a_2 + T_k a_k; \quad a_2 = h; \quad a_1 = k_r.$$

### 3. CONCLUSION

Based on the research carried out, the main patterns were identified and a mathematical model of the dynamics of the proposed vibration protection device with an original diagram of the hydraulic part of the servo drive was built.

### BIBLIOGRAPHY

1. Mchedlishvili T.F., Diasamidze R.A., Amkoladze Kh.M., Diasamidze A.A. on issue of active vibroprotective system's development. "Transport and mashinbuilding".
2. Diasamidze R.A. Overseer of marine ship propulsion systems and anti-vibration devices Dynamic modeling and research. GTU. 2014.



17th-19th June 2024  
Gliwice-Szczyrk, Poland

DEPARTMENT OF ENGINEERING MATERIALS AND BIOMATERIALS  
FACULTY OF MECHANICAL ENGINEERING  
SILESIA UNIVERSITY OF TECHNOLOGY

## INTERNATIONAL STUDENTS SCIENTIFIC CONFERENCE

### **Optimization of the electrospinning process of PVP nanofibers used in the production of dressings**

Wiktoria Wanczura<sup>a</sup>, Antonina Olszewska<sup>a</sup>, Wiktor Matysiak<sup>b</sup>

<sup>a</sup> Student of the Silesian University of Technology, Faculty of Mechanical Engineering, Department of Engineering Materials and Biomaterials

email: wiktwan199@student.polsl.pl, antools020@student.polsl.pl

<sup>b</sup> Silesian University of Technology, Scientific and Educational Laboratory of Nanotechnologies and Material Technologies, email: wiktoria.matysiak@polsl.pl

**Abstract:** In this work, research was carried out to determine the optimal voltage conditions for the electrospinning process of nanofibers with a 10% solution of polyvinylpyrrolidone in ethanol. Nanofibers produced in this way are ultimately intended to be used in the production of medical dressings. These tests consisted of the electrospinning process itself, and then examining the morphology of the obtained fibers using a scanning electron microscope (SEM) with an EDS attachment to confirm the chemical composition of the tested sample. The nanofibers were also measured in a dedicated program. Based on all the information obtained during the above activities, the optimal voltage range was identified for the remaining constant parameters of the environment, process and solution.

**Keywords:** materials, nanotechnology, nanomaterials, nanofibers, polyvinylpyrrolidone, electrospinning, voltage

## **1. INTRODUCTION**

### **1.1. Nanomaterials and Nanotechnology**

The term nanotechnology is associated primarily with the lack of precision and unambiguity in its definition, which is justified by the wide range of issues it covers and the fact that it is currently at the stage where it is dynamically developed, improved, and updated. It all started in 1959 at the California Institute of Technology (Caltech) during the annual meeting of the American Physical Society, where a lecture was given by an outstanding physicist, Richard P. Feynman. His lecture entitled "There's Plenty of Room at the Bottom" was the first mention of a concept that focused on the conscious creation and use of processes or technological means that were aimed at miniaturization. The possibility of manipulating atoms using them as building particles for new nanostructures was considered [1]. Eventually, many scientists became interested in the topic of nanotechnology and two concepts were developed that talk about two different possibilities for the synthesis of nanostructures - the "bottom-up" and "top-down" methods. The first one, bottom-up, involves the creation of nanostructures from the bottom up,



atom by atom, molecule by molecule, which are on the nano scale (from 1 nm to 100 nm). The second method, which is top-down, involves grinding solid material to obtain nanoscale particles. This method often leads to various defects in the crystal lattice. [2,3] Currently, Richard P. Feynman's lecture is considered the beginning of the nanotechnology paradigm. The time that has passed since this famous speech has allowed nanotechnology to have a wide impact on many aspects of human life.

In accordance with the European Commission Recommendation (2022/C 229/01) of 10 June 2022 on the definition of nanomaterial, the definition has been updated as follows: "Nanomaterial means a natural, incidental or manufactured material consisting of particles in a solid state, which occur either alone or as identifiable component particles in aggregates or agglomerates, and where at least 50% of such particles in the number size distribution meet at least one of the following conditions: at least one external dimension of the particle is in the range 1-100 nm; the particle has an elongated shape, such as a rod, fiber, or tube, where two dimensions; the outer dimensions are less than 1 nm and the second dimension is greater than 100 nm; the particle has the shape of a plate, where one external dimension is less than 1 nm, and the remaining dimensions are greater than 100 nm. [4]

## 1.2. Electrospinning

Electrospinning is of great interest because it can be used to spin nanofibers from a wide variety of materials. The basic electrospinning equipment consists of four main elements: a syringe with a syringe pump, a nozzle, a collector, and a high-voltage power supply [5]. The electrospinning process, its course and effects depend on many parameters, forming three main groups. These are the parameters of the prepared spinning solution, the parameters of the electrospinning process itself and the parameters of the environment in which the electrospinning process takes place.

## 2. MATERIAL AND METHODOLOGY

To prepare the spinning solution, polymer powder was used - polyvinylpyrrolidone from Sigma Aldrich, with an average molecular weight of 1,300,000, and ethyl alcohol EtOH from Chempur with a purity of 99.8% and an average density of 0.780 g/cm<sup>3</sup>. The mass of both components of the solution needed to obtain a 10% solution of PVP in EtOH was calculated. Calculations showed that 15.6g of ethyl alcohol would be needed, and the required mass of PVP was 1.73g. The required values were measured using an analytical balance. Then the solution was stirred for 30 minutes on a magnetic stirrer. The solution prepared in this way was applied to the feeder of the Flow Nanotechnology Solutions Electrospinner 2.2 D-500 device. The parameters used in electrospinning of PVP nanofibers: flow rate – 0,5 ml/h; distance of the nozzle from the collector – 15 cm; solution concentration – 10 %; and voltage – 7,5 kV, 10 kV, 12,5 kV, 15 kV, 17,5 kV, 20 kV. Six electrospinning processes of polyvinylpyrrolidone nanofibers were carried out using the obtained solution. Additionally, the samples were plated with gold. The coating was applied using a Bal-Tec SCD 050 Sputter Coater. The penultimate stage was to examine the morphology of the spun PVP nanofibers using a SEM Zeiss EVO/MA10 scanning electron microscope in the BSE (backscattered electrons) mode. The chemical composition of the samples was confirmed using the EDS device. The last activity that was performed was to perform one hundred measurements observed using a fiber microscope on each sample in the Makroaufmassprogramm program.

### 3. RESULTS

Electrospinning was performed in 6 consecutive processes. PVP nanofibers were produced on an aluminum foil base placed on a collector. The process took place at room temperature. The fibers were produced for approximately 15-20 minutes.

The first electrospinning process of PVP nanofibers with an applied voltage of 7.5 kV (of which 5 kV - voltage applied to the nozzle, 2.5 kV - voltage applied to the collector) did not demonstrate stability. Due to the instability of the process caused by too low voltage, the polymer solution sometimes dripped from the nozzle, as shown in Fig. 1 a).

The second electrospinning process was performed with a voltage of 10 kV (of which 7.5 kV - voltage applied to the nozzle, 2.5 kV - voltage applied to the collector). The process was still unstable, although slightly more stable than at 7.5 kV. Also, as in the previous process, solution dripping from the nozzle could be observed, electrospaying also appeared, visible in Fig. 1 b) in the form of tiny dots.

The third electrospinning process was carried out with a voltage of 12.5 kV (of which 10 kV - voltage applied to the nozzle, 2.5 kV - voltage at the collector). The process stabilized and no dripping or electrospaying occurred. The fibers were produced correctly and are shown in Fig. 1 c).

The fourth electrospinning process was carried out with a voltage of 15 kV (of which 12.5 kV - voltage applied to the nozzle, 2.5 kV - voltage at the collector). After an initial lack of stabilization, the process stabilized after a few minutes. No dripping or electrospay occurred. The fibers were produced correctly using the multibeam. A view of the fibers produced in this process is shown in Fig. 1 d).

The fifth electrospinning process was carried out with a voltage of 17.5 kV (of which 15 kV - voltage applied to the nozzle, 2.5 kV - voltage at the collector). There was no dripping, but electrospaying occurred, and, as in the previous process, a multi-beam appeared. However, the process was not stable and sometimes had a pulsating character. A view of the fibers produced in this process is shown in Fig. e).

The sixth and last electrospinning process was carried out with a voltage of 20 kV (of which 17.5 kV - voltage applied to the nozzle, 2.5 kV - voltage at the collector). A similar process pattern was observed as in the previous one - no dripping, electrospaying and unstable, pulsating nature of the beam generation and the beam in the form of a multi-beam. The fibers are shown in Fig. f).

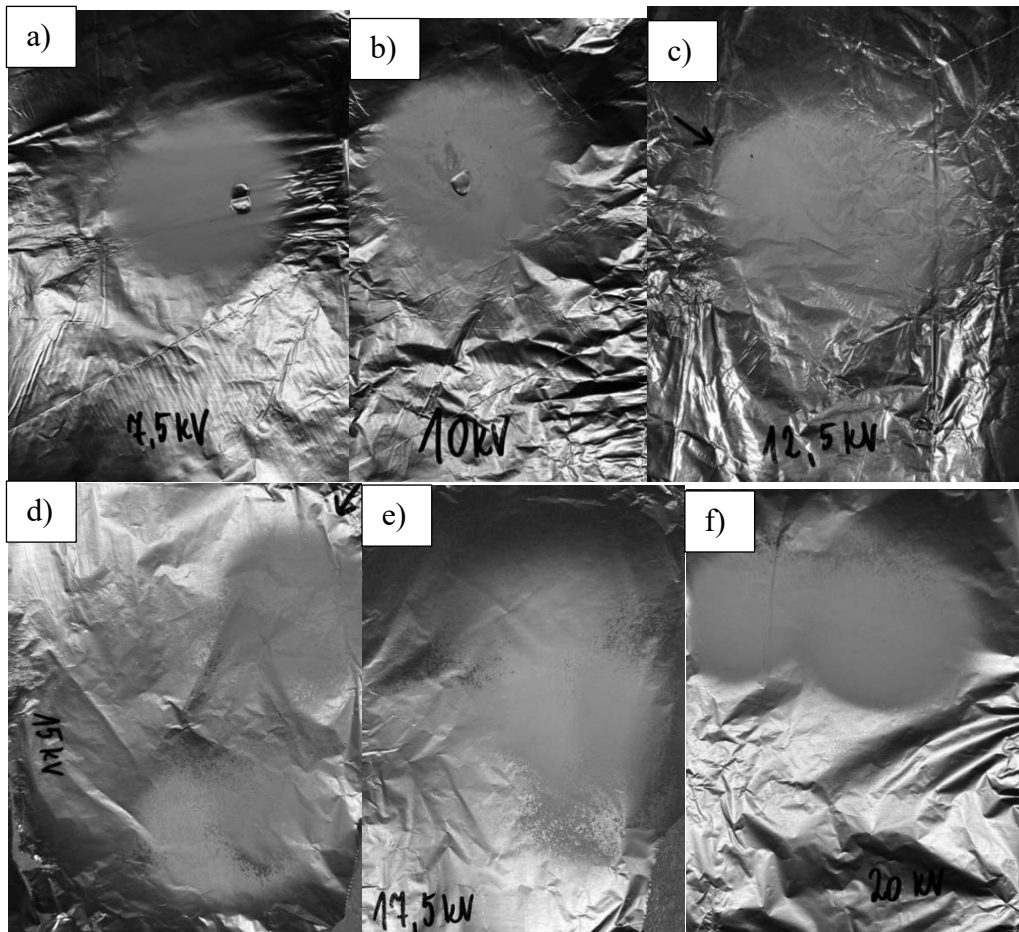


Figure. 1. View of PVP fibers produced by electrospinning with voltage: a) 7,5 kV; b) 10 kV; c) 12,5 kV; d) 15 kV; e) 17,5 kV; f) 20 kV.

Fig. 2 shows a patch of fibers removed from the aluminum foil acting as a support. These are fibers produced during the last process where the applied voltage reached 20 kV. Observing this patch of fibers even on a macro scale, we can suspect that fibers were successfully produced.



Figure. 2. PVP fibers produced in the electrospinning process.

First, the morphology of nanofibers produced from a 10% PVP/EtOH spinning solution was analyzed on a sample electrospun at a voltage of 7.5 kV. The analysis showed that beads were visible between the fibers, caused by the low voltage value. In addition, structural defects are visible. Local contamination can also be noticed. Fig. 3 a) and 3 b) show photos from the SEM microscope, magnified 1000 and 5000 times respectively. Measurements of fiber diameters one hundred times showed that the smallest diameter value of the measured fibers was 41 nm and the largest diameter was 491 nm. The average value of the observed nanofibers was 149nm.

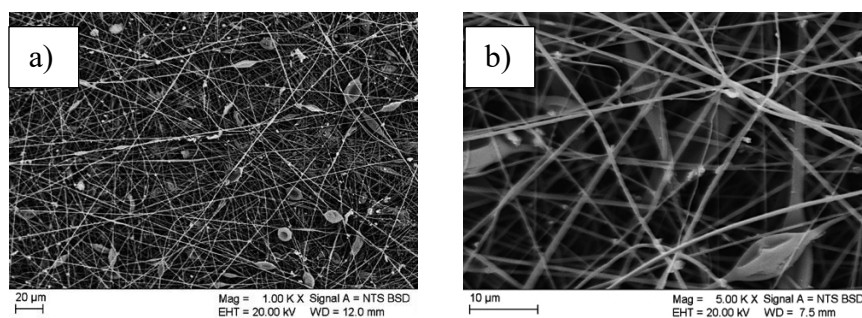


Figure. 3 SEM image of the morphology of 10% PVP/EtOH fibers produced at approximately 7.5 kV: a) x1000; 3 b) x5000

Then, the morphology of the nanofibers produced during the electrospinning process with a voltage of 10 kV was analyzed. The analysis again showed visible beads between the fibers, but increasing the tension resulted in their elongation. Beads of this shape are called spindle beads. There are fewer structural defects than in the previous case. Local contamination can again be noticed. Fig. 4 a) and 4 b) show photos from the SEM microscope, magnified 1000 and 5000 times respectively. Measurements of fiber diameters one hundred times showed that the smallest diameter value of the measured fibers was 16 nm and the largest diameter was 289 nm.

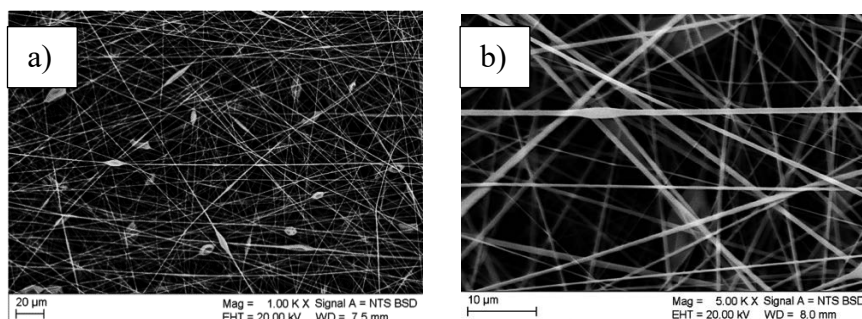


Figure. 4 SEM image of the morphology of 10% PVP/EtOH fibers produced at approximately 10 kV: a) x1000; 3 b) x5000

The next sample subjected to morphology analysis was a sample whose fibers were spun at a voltage of 12.5 kV. Observing the photos of the fiber morphology taken on a scanning electron microscope, you can notice slightly more impurities than in the previous photos. The fibers have almost no structural defects. Single spindle-shaped beads appear. Figures 5 a) and 5 b) show photos from the SEM microscope, magnified 1000 and 5000 times respectively. Measurements of fiber diameters one hundred times showed that the smallest diameter value of the measured fibers was 30 nm, and the largest diameter was 166 nm. The average value of the observed nanofibers was 90 nm.

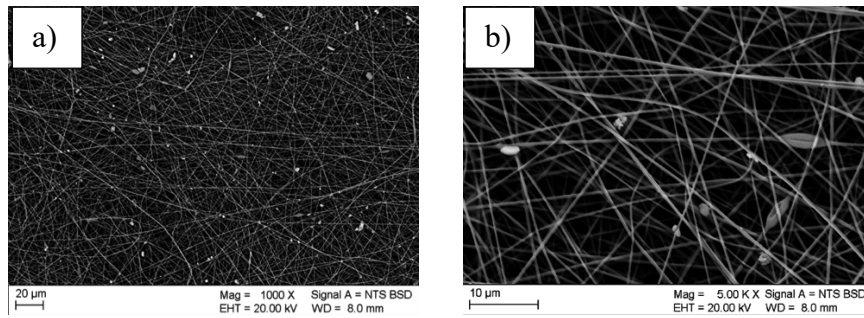


Figure. 5 SEM image of the morphology of 10% PVP/EtOH fibers produced at approximately 12,5 kV: a) x1000; 3 b) x5000

The fourth analysis was the analysis of a sample spun under voltage conditions of 15 kV. The morphology of the fibers indicates that they are the most regular fibers obtained from the spinning solution used. There are no structural defects and no beads appeared this time. Only single impurities in the form of white dots can be observed. Fig. 6 a) and 6 b) show photos from the SEM microscope, magnified 1000 and 5000 times respectively. When measuring the fiber diameters one hundred times, it was shown that the smallest diameter of the measured fibers was 31 nm and the largest diameter was 234 nm. The average value of the observed nanofibers was 105 nm.

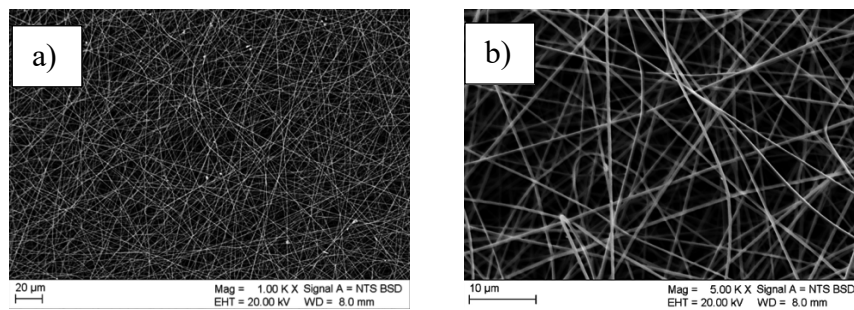


Figure. 6 SEM image of the morphology of 10% PVP/EtOH fibers produced at approximately 15 kV: a) x1000; 3 b) x5000

The next analysis concerned the morphology of nanofibers produced by electrospinning at a voltage of 17.5 kV. During the analysis, the beads reappeared. Reappearing structural defects and impurities are noticeable, most likely the result of electrospinning. Fig. 7 a) and 7 b) show photos from the SEM microscope, magnified 1000 and 5000 times respectively. Measurements of fiber diameters showed two extreme values, the smallest diameter value of the measured fibers was 15 nm and the largest diameter was 448 nm. The average value of the observed nanofibers was 108 nm.

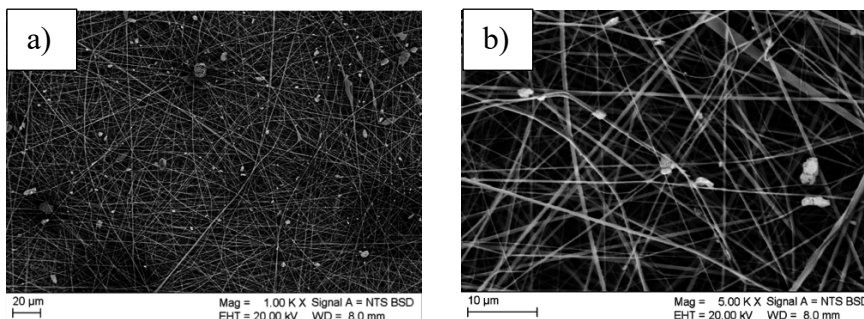


Figure. 7 SEM image of the morphology of 10% PVP/EtOH fibers produced at approximately 17,5 kV: a) x1000; 3 b) x5000

The last analysis performed was the analysis of PVP nanofibers produced at a voltage of 20 kV. The analysis did not reveal the presence of beads, but numerous structural defects and contamination are visible, which are probably to some extent caused by electrospinning. Figures 8 a) and 8 b) show photos from the SEM microscope, magnified 1000 and 5000 times respectively. As in all previous analyses, fiber diameter measurements were also performed one hundred times, which showed that the smallest diameter value of the measured fibers was 33 nm and the largest diameter was 212 nm. The average value of the observed nanofibers was 109 nm.

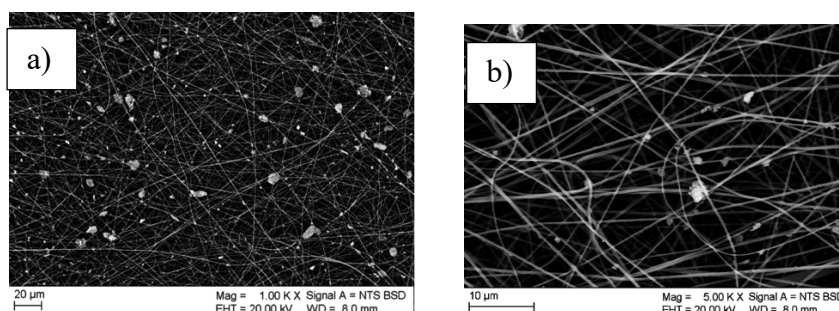


Figure 8 SEM image of the morphology of 10% PVP/EtOH fibers produced at approximately 20 kV: a) x1000; b) x5000

The chemical composition was also analyzed by energy dispersive spectroscopy using an EDS device, which clearly confirmed the presence of elements characteristic of polyvinylpyrrolidone. The EDS spectrum is shown in Fig. 9.

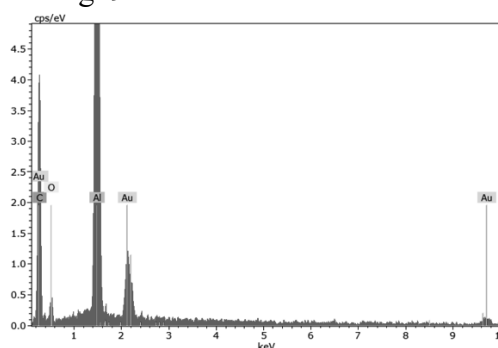


Figure 9 EDS spectrum of the obtained 10% PVP/EtOH fibers.

#### 4. CONCLUSIONS

Polymer materials reduced to the nanometer scale have a chance to revolutionize the world, including in the field of producing nanofiber dressings. Polyvinylpyrrolidone nanofibers turn out to be a very good candidate, characterized by significant biocompatibility, absorbency and, above all, the ability to transport other substances. Due to the fact that nanotechnology is a young issue, the optimization of processes involving it is still being pursued. The same is the case with electrospinning of polyvinylpyrrolidone nanofibers. The impurities that were visible on most of the produced nanofibers when observed on the SEM microscope could have appeared for three reasons. Firstly, they could be the result of the electrospinning process - then the contaminants would turn out to be agglomerates of the sprayed polymer. Secondly, they could have gotten there as a result of contamination of the polymer powder with foreign particles. And thirdly, they could also appear there due to contaminated elements of the electrospinning machine after

previous processes. The beads that appeared in the microstructure of nanofibers spun at voltages of 7.5 kV, 10 kV, 12.5 kV, 17.5 kV and 20 kV are not perceived as defects, they are often even a desired effect. In the form of such beads, therapeutic active substances are trapped in nanofibers, which are later released by hitting the target site directly. The average diameter of PVP nanofibers was for a voltage of 7.5 kV - 149 nm, for 10 kV - 134 nm, for 12.5 kV - 90 nm, for 15 kV - 105 nm, for 17.5 kV - 108 and for 20 kV - 109nm. The greater the tension, the smaller the diameter of the fibers. However, the prohibitive voltage value for a 10% solution concentration turns out to be 12.5 kV. Once this voltage value is exceeded, the fiber diameter begins to increase again. When increasing the tension, the % concentration of the spinning solution should also be increased to still keep the fiber diameters as small as possible. The most accurate voltage for the flow parameters used for electrospinning, the distance of the nozzle from the collector, and the concentration of the spinning solution turn out to be 12.5 kV and 15 kV. If the goal is to keep the fiber diameters as small as possible, then a voltage of 12.5 kV should be used. However, if we care about microstructures fibers that are most free from any defects and most regular, then it should be applied a voltage of 15 kV.

## ACKNOWLEDGEMENTS

The publication was created within the framework of the joint Slovak-Polish project International Visegrad Fund's V4 Generation Mobility Mini-Grant No 12410044 as a result of cooperation between the Association of Alumni of the Silesian University of Technology, Gliwice, Poland and the University of Žilina, Slovakia.

The project is co-financed by the Governments of Czechia, Hungary, Poland and Slovakia through Visegrad Grants from the International Visegrad Fund. The mission of the fund is to advance ideas for sustainable regional cooperation in Central Europe.



## BIBLIOGRAPHY

1. W. Matysiak, Wytwarzanie i analiza własności wieloskładnikowych nanowłókien kompozytowych zawierających polimery przewodzące i nanocząstki tlenków metali ziem rzadkich, Gliwice: Wydawnictwo Politechniki Śląskiej, 2023.
2. S. Bayda, M. Adeel, T. Tuccinardi, M. Cordani i F. Rizzolio, „The History of Nanoscience and Nanotechnology: From Chemical-Physical Applications to Nanomedicine,” *Molecules*, tom 25, nr 112, 2020.
3. A. Krzepińko, A. Świącilo i K. Matyszczuk, Wpływ nanocząstek na bakterie i grzyby, Lublin: Wydawnictwo Uniwersytetu Przyrodniczego w Lublinie, 2022.
4. Komisja Europejska, „Zalecenie Komisji z dnia 10 czerwca 2022 r. dotyczące definicji nanomateriału (Tekst mający znaczenie dla EOG),” *Dziennik Urzędowy Unii Europejskiej*, tom (2022/C 229/01), 2022.
5. G. R. Williams, B. T. Raimi-Abraham i C. J. Luo, „Electrospinning Fundamentals,” w *Nanofibres in Drug Delivery*, UCL Press, 2018.



17th-19th June 2024  
Gliwice, Poland

DEPARTMENT OF ENGINEERING MATERIALS AND BIOMATERIALS  
FACULTY OF MECHANICAL ENGINEERING  
SILESIA UNIVERSITY OF TECHNOLOGY

## INTERNATIONAL STUDENTS SCIENTIFIC CONFERENCE

### Corrosion mapping with the use of ultrasonic testing

Edyta Wójtowicz <sup>a</sup>, Santina Topolska <sup>b</sup>, Andrzej Wójtowicz <sup>c</sup>

<sup>a</sup> Member of the Student Scientific Circle of Corrosion Process Chemistry and General Chemistry "KORNIKUS", edytawojtowicz321@gmail.com

<sup>b</sup> Silesian University of Technology, Faculty of Mechanical Engineering, Department of Welding, santina.topolska@polsl.pl

<sup>c</sup> Sieć Badawcza Łukasiewicz – Górnośląski Instytut Technologiczny, andrzej.wojtowicz@git.lukasiewicz.gov.pl

**Abstract:** The article deals with corrosion mapping using ultrasonic testing. Spot thickness measurements make it possible to detect corrosion cavities on components with relatively small component thicknesses. The method helps avoid dangerous failures of operating equipment

**Keywords:** korozja, mapy korozyjne, badanie nieniszczące, badania ultradźwiękowe, eksploatacja

### 1. INTRODUCTION

An increasingly common problem facing modern industry is damage caused by corrosive phenomena. Currently, many facilities, built in the second half of the last century, undergoing major renovations show a significant percentage of corroded elements. The costs associated with the replacement or repair of damaged elements have made builders, designers, investors and contractors aware of the scale of the problem, which is the processes of corrosion damage. This has contributed to the development of methods for protecting structures against corrosion, as well as diagnostic methods for detecting corrosion foci as early as possible and determining the location of their occurrence.

Recently, non-destructive testing has become increasingly important in the field of corrosion diagnostics, as it makes it possible to inspect components without cutting out a section of the installation. Nowadays, ultrasonic and radiographic methods are gaining wide industrial use, which, with different testing techniques and procedures, make it possible to diagnose various parameters of corrosion foci. The key factors influencing the choice of method are the thickness of the material, the presence of protective coatings or insulation. The industrial sectors that most often require this type of diagnostics are the power, petrochemical and offshore industries [1 ÷ 5].



## 2. SAMPLE PREPARATION

The test object was a sheet of S235 steel with dimensions of 150x210 mm and a thickness of 5mm, corresponding to the initial state of corrosion grade B, subjected to blasting. Blasting was carried out with sharp-edged shot (G) to a substrate preparation grade corresponding to the BSa2½ standard according to PN EN ISO 8501-1. The surface development after blasting corresponded to the fine-grain profile according to EN ISO 8503-2 and also the lowest according to the standard. The sample immediately after blasting was placed in a salt chamber, where an environment conducive to the rapid development of corrosion processes was maintained, with a 5% NaCl solution as the working medium - sprayed in the form of an inert salt spray (NSS). The sample was subjected to destruction twice, each time for 360h [6 ÷ 8]. Figure 1 shows the sample after the first 360h, and Figure 2 after 720h in the salt chamber. Between sessions in the chamber, the upper part of the sample was purposely cleaned of corrosion products, as shown in Figure 3. The rear part of the sample was purposely protected against corrosion so that ultrasonic testing, which requires relatively low roughness on the side of the introduced wave, could be carried out.



Figure 1. Sample after 360h in salt chamber



Figure 2. Sample after 720h in salt chamber



Figure 3. Sample cleaning between sessions in the chamber

## 3. CORROSION MAPPING

In order to create a map of corrosion cavities, it was decided to use the UT-PA, or Phased Array ultrasonic testing technique, which uses multi-transducer heads. The chosen test method allows multiple thickness measurements to be taken at a resolution specified by the software.

### 3.1. Test stand

The Olympus OmniScan SX defectoscope, which has the ability to generate a beam from up to 16 transducers, was used for the test. For the test, a 3.5L64-NW1 multi-transducer head was used along with a SNW1-0L-AQ25 wedge (Fig. 4). Technical data of the apparatus used is shown in Table 1.



Figure 4. The 3.5L64-NW1 head used in the study, along with the SNW1-0L-AQ25 wedge

Table 1. Technical data of the used apparatus

Type of device	Olympus, OmniScan SX
Module Phased Array	OMNISX-PA1664PR
Software version	MXU - 4.4R5

Prior to the start of ultrasonic testing using the Phased Array technique, a stand was prepared in accordance with Figure 5. The system consisted of an encoder, a metal frame along which the magnetic wheels of the entire set were guided. The aforementioned auxiliary instruments were intended to ensure the repeatability and staticness of the measurements performed. The test recording data are shown in Table 2.

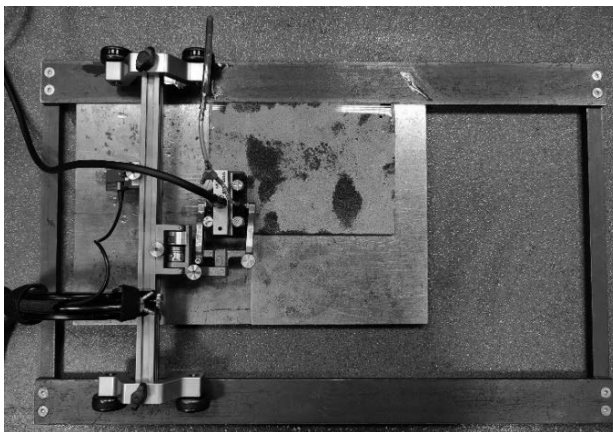


Figure 5. Test stand

Table 2. Parameters for recording the test

Scan length, [mm]	200
Scan resolution, [mm]	1,0
Maximum scanning speed, [mm/s]	60
Encoder separation, [step/mm]	12
Encoder type	quadrature

### 3.2. Test parameters

In the ultrasonic testing method, many parameters are responsible for obtaining the correct test result. Table 3 shows the most important parameters, and Figure 6 shows how to record the test with a defectoscope.

Table 3. The most important parameters of UT examination by PA technique

Beam delay, $\mu\text{s}$	32,0
Voltage, V	40
Reinforcement, dB	29,96
Mode	PE
Scope (halfway), mm	19,44
Wave type	Elongated
Maximum acquisition speed	60
Speed of sound in the material, m/s	5890
Frequency of digitization, MHz	100
Pulse width, ns	142,5
A-scan time resolution, ns	30
Resolution, mm	1,0
Focal length, mm	50
Beam configuration	Linear for $0^\circ$
Gate	A,B
Threshold, %	15%
Sync	Impulse
Peak selection	Max peak

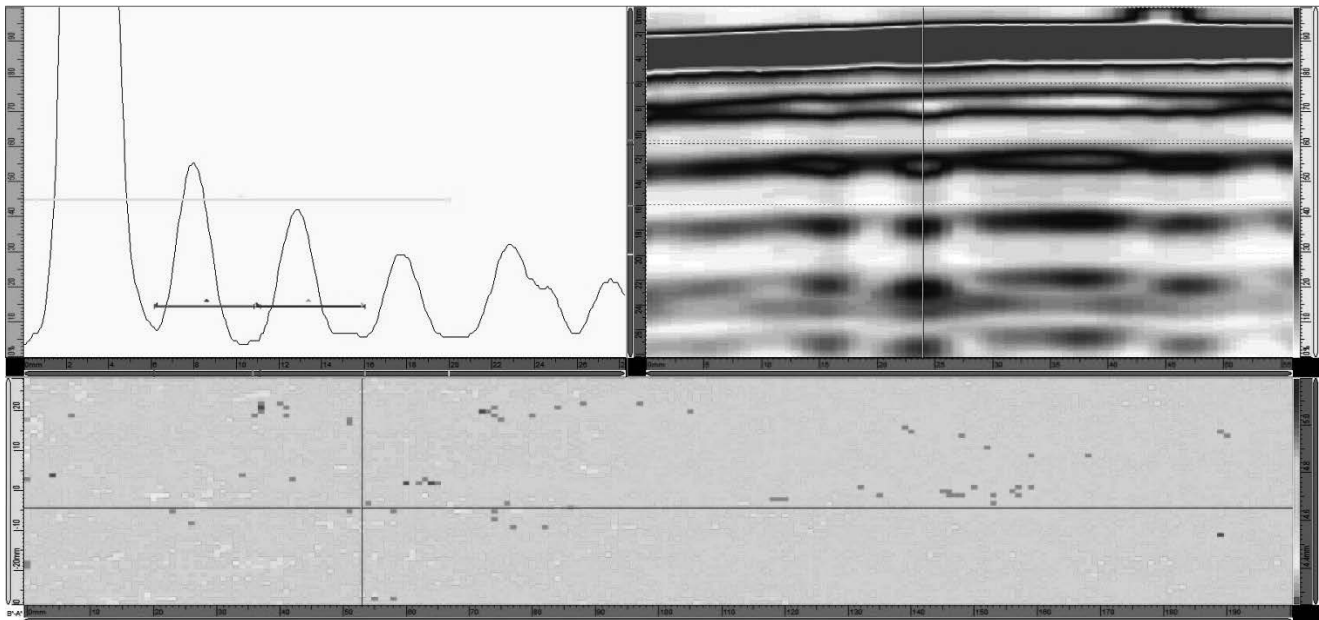


Figure 6. The result of the test from the defectoscope

#### 4. RESEARCH RESULTS

Thickness measurements were made based on a preset range of 4.25 to 5.20 mm. This is illustrated by the color scale in Figure 6. Figure 7 shows a map of the thickness measurements of the sample before placement in the chamber, and Figure 8 after 720h of exposure. The numerical values of the selected points are shown in Table 4, while the calculated corrosion loss values are presented in Table 5.

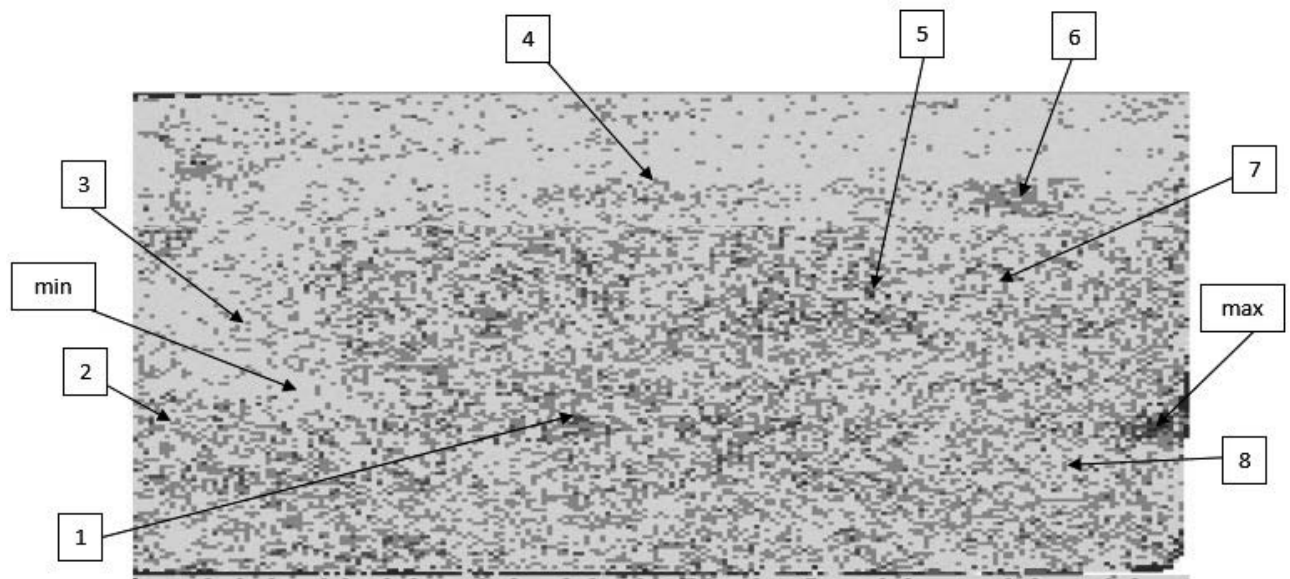


Figure 7. Sample scanned before being placed in the salt chamber - Sample used as a reference point for testing

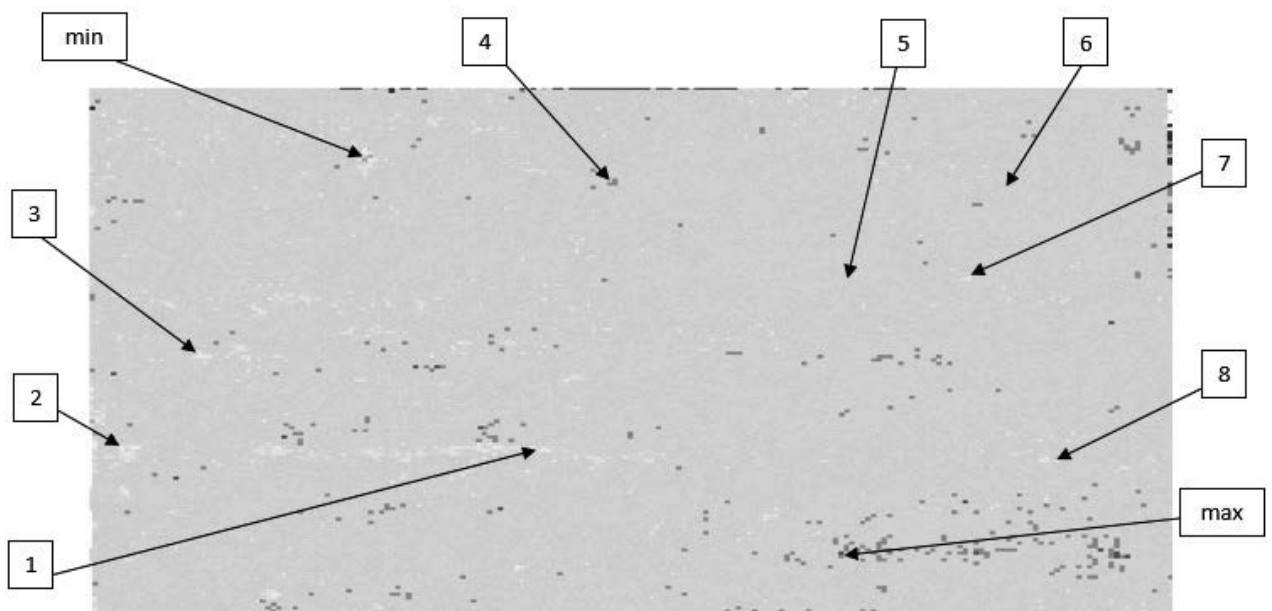


Figure 8. Sample scanned after 720 hours of detention in the salt chamber

Table 4. Spot thickness measurements before and after the salt chamber

	max thickness [mm]		min thickness [mm]	
<b>Before the salt chamber</b>	5,11		4,71	
<b>After the salt chamber</b>	4,99		4,32	
Measurement point number	Thickness of the element before the salt chamber [mm]	Thickness of the element after 360h in the salt chamber [mm]	Thickness of the element after 720h in the salt chamber [mm]	
1	5,04	4,85	4,41	
2	4,84	4,68	4,40	
3	4,92	4,86	4,42	
4	4,89	4,86	4,84	
5	5,05	4,84	4,62	
6	4,95	4,83	4,67	
7	4,83	4,65	4,56	
8	4,94	4,79	4,52	

Table 5. Corrosion defect diagnosed by UT PA test

Measurement point number	Thickness difference [mm]	Cavity [%]
1	0,63	12,50
2	0,44	9,09
3	0,50	10,16
4	0,05	1,02
5	0,43	8,51
6	0,28	5,66
7	0,27	5,59
8	0,42	8,50

## 5. SUMMARY AND CONCLUSIONS

In the case of the examined object, the corrosion loss ranged from 1.02% to 12.5%, which corresponds to losses of 0.05mm to 0.63mm. The detected corrosion foci are within a within a small dimensional range, which demonstrates the degree of difficulty in diagnosing components of relatively small thickness. The technological capabilities of the test method

presented above make it possible, by changing the parameters, to adapt to small changes in thickness on the surface of the sample.

Analyzing Figure 8, it can be concluded that cleaning the sample after 360h of exposure from corrosion products, contributed little to the acceleration of the corrosion process. In the corrosion map, the left side corresponds to the cleaned part and the right side to the untreated part. However, the observed changes are insignificant, and to confirm this hypothesis it would be necessary to extend the scope of the study in the future.

In conclusion, ultrasonic testing makes it possible to determine the degree of corrosion damage very precisely. In addition, the Phased Array technique allows recording the test performed. However, it has limitations regarding, among other things, the thickness of the tested material, the shape of curved elements such as a pipe, the possibility of testing elements covered with insulation or a layer of paint. The aforementioned limitations set future directions for the development and evaluation of techniques for the diagnosis of corrosion phenomena.

## BIBLIOGRAPHY

1. Baszkiewicz J., Kamiński M., „Korozja materiałów”, Oficyna Wydawnicza Politechniki Warszawskiej, Warszawa 2006
2. Lewińska-Romicka A., „Badania nieniszczące, Podstawy defektoskopii”, Wydawnictwo Naukowo – Techniczne, Warszawa 2011
3. Czerwiński J. (red), „Ochrona przed korozją – poradnik”, Wydawnictwa Komunikacji i Łączności, Warszawa 1986
4. <https://www.energodiagnostyka.pl/badania-nieniszczace/badania-ultradzwieowe-phased-array-utpa.html>, dostęp: 10.02.23r.
5. <https://www.ndt24.pl/pl/badania-ultradzwiekowe/mapowanie-korozji-oraz-pomiar-gruboscitechnika-ultradzwiekowa-zastosowaniem-rejestracji-ciaglej>, dostęp: 10.02.23r.
6. Polski Komitet Normalizacyjny, Norma PN EN ISO 8501-1:2008, Przygotowanie podłoży stalowych przed nakładaniem farb i podobnych produktów – Wzrokowa ocena czystości powierzchni – Część 1: Stopnie skorodowania i stopnie przygotowania niepokrytych podłoży stalowych oraz podłoży stalowych po całkowitym usunięciu wcześniej nałożonych powłok
7. Polski Komitet Normalizacyjny, Norma PN-EN ISO 8503-2:2012, Przygotowanie podłoży stalowych przed nakładaniem farb i podobnych produktów – Charakterystyki chropowatości powierzchni podłoży stalowych po obróbce strumieniowo-ściernej – Część 2: Metoda stopniowania profilu powierzchni stalowych po obróbce strumieniowo-ściernej – Sposób postępowania z użyciem wzorca
8. Polski Komitet Normalizacyjny, Norma PN EN ISO 9227:2023, „Badania korozyjne w sztucznych atmosferach – Badania w rozpylonej solance”



17th-19th June 2024  
Gliwice, Poland

DEPARTMENT OF ENGINEERING MATERIALS AND BIOMATERIALS  
FACULTY OF MECHANICAL ENGINEERING  
SILESIA UNIVERSITY OF TECHNOLOGY

## INTERNATIONAL STUDENTS SCIENTIFIC CONFERENCE

### **Modelling and Simulation of gyroid structure-based bone scaffold using TiZrNb titanium alloy for bone scaffold; state-of-the-art and evaluation of deformation**

Sichale Worku Fita <sup>a</sup>, Mirosław Bonek <sup>b</sup>, Sebastian Sławski <sup>c</sup>, Anna Woźniak <sup>d</sup>

<sup>a</sup> Silesian University of Technology, Faculty of Mechanical Engineering, Department of Engineering Materials and Biomaterials, email: sichale.fita@gmail.com

<sup>b</sup> Silesian University of Technology, Faculty of Mechanical Engineering, Department of Engineering Materials and Biomaterials

<sup>c</sup> Silesian University of Technology, Faculty of Mechanical Engineering, Department of Theoretical and Applied Mechanics

<sup>d</sup> Silesian University of Technology, Faculty of Mechanical Engineering, Department of Engineering Materials and Biomaterials

**Abstract:** Gyroid structures are a class of triply periodic minimum surfaces whose special architectural and mechanical characteristics have drawn much interest in their possible use as bone scaffolds. This study aims to use advanced computational approaches to describe and simulate the deformation behavior of bone scaffolds made from the biocompatible TiZrNb titanium alloy. The gyroid geometry is generated and enhanced using computer-aided design (CAD) tools and Finite element analysis (FEA) is used to investigate the deformation properties of the gyroid scaffold under different loads.

**Keywords:** Gyroid structure, simulation, bone scaffold, FEA

## 1. INTRODUCTION

The bone structure within the human body is a naturally occurring composite material that is sensitive to fracture due to impact stress and high loads. The density and strength of human bones decrease differently with age according to gender, making them susceptible to fracture. As shown in Figure 1(a) below. To solve this problem, the development of biomaterial-based scaffolds for bone tissue engineering has revolutionized regenerative medicine. Bone scaffolds are essential components in bone tissue engineering, providing a structural framework for cell growth and tissue regeneration.

A wide range of biomaterials are used in the manufacturing of bone scaffolds, including synthetic biomaterials, metallic materials, and biomaterials derived from nature[1]. The selection of the best material or composite for bone regeneration is a matter of careful consideration. Thus, researchers are actively investigating various materials to enhance the specific biomechanical properties that are deemed essential from their perspective.

Among those various materials, titanium and its alloys have emerged as top contenders owing to their favourable mechanical properties and biocompatibility. Different techniques have been investigated for the modification of titanium alloys used in bone tissue engineering. These techniques include altering alloy compositions, transforming surface structures, making three-dimensional (3D) structural changes, applying coatings, and using surface functionalization technologies[2].

The role of porosity and design in titanium-based scaffolds is of greatest significance in the context of bone regeneration and the success of implants. Porosity, which refers to the proportion of the structure that lacks solidity, is commonly observed to be approximately 65% in conventional porous scaffolds. Stamp et al. recommend a porosity greater than 65% in medical implants[3].

One of the present challenges encountered in the field of 3D printing is to achieve an appropriate balance between mechanical properties, porosity, interconnectivity, and pore size. In this paper, we will see the application of mathematical modelling and computer simulation to the improvement of mechanical properties, and our future work will be the improvement of porosity and design of titanium-based scaffolds with meticulous attention to enhance biocompatibility, mechanical characteristics, and overall efficacy in the context of bone regeneration and implant technology.

## **2. MATERIAL AND METHODS**

### **2.1 Material**

Titanium (Ti) is a commonly used material that possesses several remarkable characteristics, including high strength, lightweight nature, robust flexibility, resistance to corrosion, and favourable biocompatibility[4]. However, titanium has several disadvantages. Including higher Young's modulus compared to normal bone, having a limited capacity to promote osteogenesis, which affects bone regeneration and integration, and wearing titanium debris might trigger local biological responses.

Since 1940, starting from Bothe et al.[22] Pure titanium was used until 1982 when Ti6Al4V was used to produce an artificial joint prosthesis and provided a new idea for using a novel titanium alloy[5]. Today's researchers recommend pure Titanium and Ti alloys of TiZrNb and TiAlV.

Different types of TiZrNb alloys have been investigated to produce bone scaffolds. The powder metallurgy process was used to create porous Ti35Zr28Nb scaffolds, which consisted of a single  $\beta$  phase. These scaffolds had porosity ranging from 50% to 65% and pore diameters between 230 and 430  $\mu\text{m}$ . This indicates that they have promising applications in the field of hard-tissue engineering[6].

### **2.2 Methods**

To see Constitutive Behavior Modeling and Scaffold Design, It is recommended that the ideal design of a scaffold, i.e. its microarchitecture, has elements such as high porosity, appropriate connectivity of pore structures, and a sufficient specific surface area to facilitate cell attachment, segregation of new matrix, and proliferation[7]. The lattice-based scaffold microstructural characteristics of several families were studied by Egan et al. Those families



are cubic and octahedron. The results showed that each family may have a suitable application based on its distinct characteristics. L. Zhao et al. designed five porous titanium bone tissue scaffolds, diamond, gyroid, orthogonal, truss, and cube. From these, the design of the diamond (d) and gyroid(g) porous structure can effectively improve the distortion and specific surface area of the connected pore channel[8].

The gyroid and diamond bone scaffold constructs display differences in their mechanical properties and ability to regenerate bone. Gyroid structures show improved compressive strength due to their ability to limit stress distribution, hence promoting superior bone growth in critical-sized defects when compared to grid structures[9]. On the other hand, diamond structures show high stiffness and osseointegration characteristics that approach cortical bone, hence minimizing the likelihood of scaffold failure[10]. Additionally, the gyroid design shows higher porosity and permeability, which promotes increased bone formation and ingrowth compared to diamond structures[11]. Although both substances mimic bone qualities effectively, gyroid scaffolds are more effective in facilitating bone regeneration in vivo due to their distinctive structural characteristics[12]. In this Article, a 2mm single part of a gyroid is drawn in Solid Work 2023@student version from Silesian University as investigated in figure 1(b) below, and for Analysis, a gyroid with 4,2,2 mm dimensions is used by STEL file format in ANSYS @2024, Student version, Silesian University.

Simulation techniques offer a cost-effective and efficient means to predict the behavior of these scaffolds under different loading conditions, aiding in the design process and optimization of scaffold architectures. Advanced methodologies are employed in simulation procedures for bone scaffolds composed of titanium-based materials, to optimize their design and characteristics to facilitate better bone regeneration[13].

FEA, which is finite element analysis, has been used at the macroscopic level to investigate the solid mechanical properties of the scaffold. At this scale, the literature puts forward finite element analysis (FEA) models.

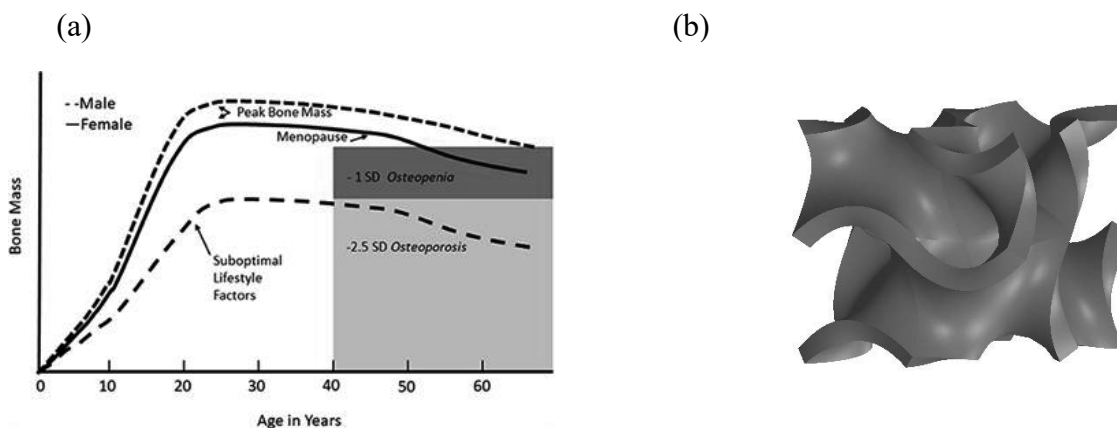


Figure 1(a) Decreasing strength of human bone with age and gender issues. (b) a single part of gyroid

### 3. MIAN ASSUMPTIONS AND PARAMETERS

#### 3.1 Main assumptions

While using ANSYS, a software for finite element analysis, specific assumptions are commonly established to simplify the simulation process and guarantee accurate and practical

findings when evaluating bone scaffolds. The assumptions can be classified into material attributes, boundary conditions, and geometric factors. Based on this, the scaffold material is considered to be homogenous, indicating that its characteristics remain similar throughout the entire material, isotropic, meaning that its mechanical properties are uniform in all directions, exhibits linear elasticity, meaning that stress is directly proportional to strain as long as it remains within the material's elastic limit, and material properties are considered to be constant across time, neglecting any viscoelastic or time-dependent deformation behaviours.

The geometry of the scaffold and the natural bone around it is commonly simplified to decrease computational complexity, under the assumption that this simplification does not substantially impact the correctness of the outcomes. The fixed boundary conditions in the model represent the immovable parts that mimic the physical limits seen in the real biological environment. Loads are applied in a controlled manner, usually under static loading conditions to neglect dynamic effects such as impact forces. It is assumed that once the scaffold and the bone come into contact, there is no relative motion between them. This means they move together as a single unit when external forces are applied.

### 3.2 Parameters

The elastic modulus of TiZrNb alloys is dependent upon their specific composition and method of production employed. An example of this is a TiZrNb medium entropy alloy (MEA) that showed an elastic modulus of  $72 \pm 3$  GPa, a value similar to that of human bone[14].

Obtaining a precise value for Poisson's ratio in titanium alloys is challenging because of anisotropy, which causes slight variations in both elastic and shear moduli. Consequently, the calculated Poisson's ratio for the annealed ASTM Grade sheet can range from 0.287 to 0.391. However, the widely acknowledged numerical representation for economically pure titanium is 0.36, while the corresponding number for ASTM Grade 5 is 0.31. The density of TiZrNb alloys ranges from  $4.99 \text{ g/cm}^3$  to  $6.12 \text{ g/cm}^3$ , depending on the specific alloy composition and processing method. Khanaki et al. show that high-density scaffolds have higher compressive strengths[15]. So we have decided to take high density with medium porosity for this research, i.e.  $6.12 \text{ g/cm}^3$ .

Based on those assumptions and material properties, we analysed The deformation of the scaffold under loading. Using the technique of finite element analysis allows the prediction of stress and deformation patterns inside the scaffold structure[16], the effect of fixed support on mechanical properties, and deformational behavior under different Force(load) applications.

The mechanical properties of bone regeneration scaffolds are crucial for implant success, especially with load-bearing bone defects[17]. The key mechanical parameters that must be included are the stiffness of the scaffold, measured by its compressive moduli, which falls within the range of 50-1500 MPa, with an average value of approximately 194 MPa, closely resembles the properties of human trabecular bone[18]. The second parameter is the scaffold's maximal stress tolerance before failure is within the 1-30 MPa range, with an average value of approximately 3.55 MPa. These compressive strengths make the scaffold acceptable for replicating the characteristics of trabecular bone[19]. To reach this criterion in this Article, we used three forces, 9.81N, 50 N, and 100N of force are assumed to be applied in the opposite direction of fixed support.

### 4. RESULTS AND DISCUSSION

For structural integrity and functionality, mesh convergence plays a crucial role in the design of bone scaffolds. Several research has investigated the utilization of various mesh arrangements to improve both mechanical qualities and biological activity[20] [21]. For example, the integration of 3D-printed polymer or ceramic-based meshes into mineralized collagen scaffolds has demonstrated enhanced mechanical capabilities and promoted the formation of new bone tissue[22]. In addition, the fabricating of 2D meshes and 3D cylindrical composite scaffolds that have varying fiber orientation and mechanical properties in different regions has shown the capability to induce cell responses that are specific to each location and can conform to different shapes[23]. We used an element size of 0.1mm for analysis results shown in Figure 2 (a) below. Based on the different and small force application on one side of the model by fixing the opposite part, we got slightly different but crucial total deformation behavior as shown in Figure 2( b-d) below.

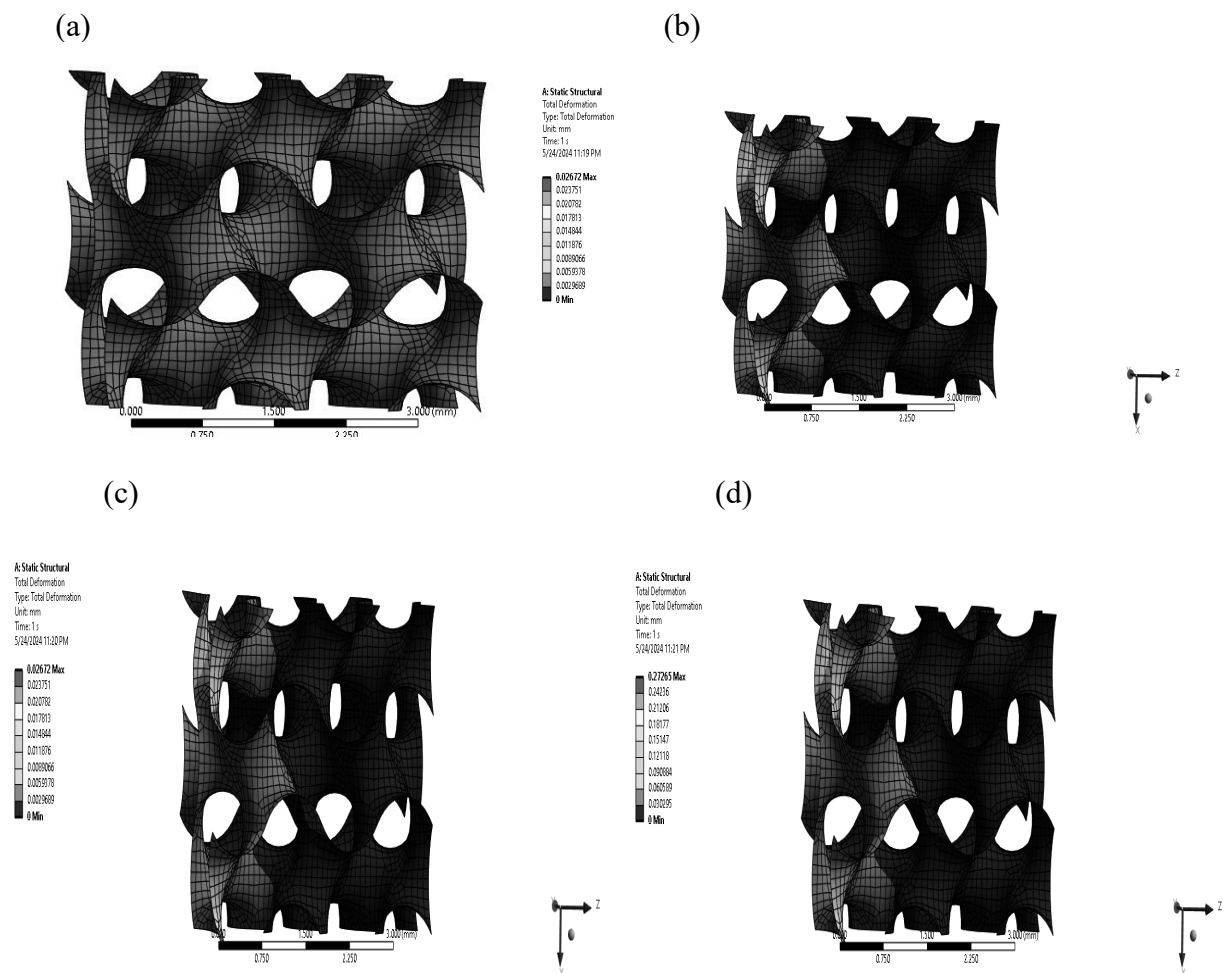
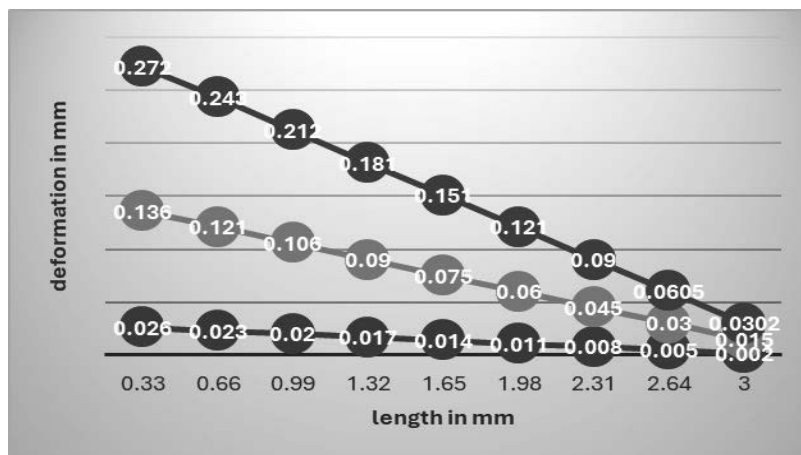


Figure 2(a) mesh generated by ANSYS (b) deformation under force of 9.8N (c) deformation under force of 50N (d) deformation under force of 100N



Blue: 9.8N, Red: 50N, Green: 100N

Figure 3. Relation between deformation and elongation;

The relation between deformation and application of force is directly proportional, while deformation and length (size of material) on which the material is compressed due to the application of Force are inverse, i.e. as force increases the length of our material decreases and the material passes under deformation leading to breakage of the material, which is the reverse of our investigation. From the above chart, analyzed during a small application of force we have a small deformation length and a small change in the size of our material. As the force increases the deformational length increases and the size of the material decreases i.e. results with compressional behavior.

Additionally, the direction of deformation is from the direction of force to fixed support, which is higher at the bottom of the part, which is inversely related to less deformation from the fixed support side. Generally, the deformation range we got from this analysis is not as high as other bio-ceramic materials which improves the importance of titanium alloy for bone scaffold application.

## 5. CONCLUSION

Using the TiZrNb titanium alloy, the modelling and simulation of bone scaffolds based on the gyroid structure show great potential in the field of bone tissue engineering and regenerative medicine. Through the utilization of advanced computational methods, such as finite element analysis (FEA) we may acquire valuable knowledge on the mechanical properties and deformation patterns of these complex scaffolds when they are subjected to different loads. deformational behavior of shell elements is investigated in this article, and investigating stress parameters, and porosity based on the application of thickness, Compressive strength, and application of coating will be the future work.

## ACKNOWLEDGEMENTS

The publication was created within the framework of the joint Slovak-Polish project International Visegrad Fund's V4 Generation Mobility Mini-Grant No 12410044 as a result of cooperation between the Association of Alumni of the Silesian University of Technology, Gliwice, Poland and the University of Žilina, Slovakia.

The project is co-financed by the Governments of Czechia, Hungary, Poland and Slovakia through Visegrad Grants from the International Visegrad Fund. The mission of the fund is to advance ideas for sustainable regional cooperation in Central Europe.



## BIBLIOGRAPHY

- [1] M. W. published, "Boeing begins fueling Starliner capsule ahead of 1st astronaut launch," Space.com. Accessed: Mar. 20, 2024. [Online]. Available: <https://www.space.com/boeing-begins-fueling-starliner-first-astronaut-launch>
- [2] H. Chen, Q. Han, C. Wang, Y. Liu, B. Chen, and J. Wang, "Porous Scaffold Design for Additive Manufacturing in Orthopedics: A Review," *Front. Bioeng. Biotechnol.*, vol. 8, p. 609, Jun. 2020, doi: 10.3389/fbioe.2020.00609.
- [3] D. Martinez-Marquez, Y. Delmar, S. Sun, and R. A. Stewart, "Exploring Macroporosity of Additively Manufactured Titanium Metamaterials for Bone Regeneration with Quality by Design: A Systematic Literature Review," *Materials*, vol. 13, no. 21, p. 4794, Oct. 2020, doi: 10.3390/ma13214794.
- [4] M. Geetha, A. K. Singh, R. Asokamani, and A. K. Gogia, "Ti-based biomaterials, the ultimate choice for orthopedic implants – A review," *Prog. Mater. Sci.*, vol. 54, no. 3, pp. 397–425, May 2009, doi: 10.1016/j.pmatsci.2008.06.004.
- [5] A. Blanquer *et al.*, "Cytocompatibility assessment of Ti-Zr-Pd-Si-(Nb) alloys with low Young's modulus, increased hardness, and enhanced osteoblast differentiation for biomedical applications," *J. Biomed. Mater. Res. B Appl. Biomater.*, vol. 106, no. 2, pp. 834–842, 2018, doi: 10.1002/jbm.b.33892.
- [6] "Fabrication and properties of newly developed Ti<sub>35</sub>Zr<sub>28</sub>Nb scaffolds fabricated by powder metallurgy for bone-tissue engineering," *J. Mater. Res. Technol.*, vol. 8, no. 5, pp. 3696–3704, Sep. 2019, doi: 10.1016/J.JMRT.2019.06.021.
- [7] D. W. Hutmacher, "Scaffolds in tissue engineering bone and cartilage," *Biomaterials*, vol. 21, no. 24, pp. 2529–2543, Dec. 2000, doi: 10.1016/S0142-9612(00)00121-6.
- [8] L. Zhao *et al.*, "Bionic design and 3D printing of porous titanium alloy scaffolds for bone tissue repair," *Compos. Part B Eng.*, vol. 162, pp. 154–161, Apr. 2019, doi: 10.1016/j.compositesb.2018.10.094.
- [9] "Triply Periodic Minimal Surface-Based Scaffolds for Bone Tissue Engineering: A Mechanical, *In Vitro* and *In Vivo* Study," *Tissue Eng. Part A*, Jun. 2023, doi: 10.1089/ten.tea.2023.0033.
- [10] "Mechanical Characterisation and Numerical Modelling of TPMS-Based Gyroid and Diamond Ti6Al4V Scaffolds for Bone Implants: An Integrated Approach for Translational Consideration," *Bioengineering*, vol. 9, no. 10, pp. 504–504, Sep. 2022, doi: 10.3390/bioengineering9100504.
- [11] "Superiority of Triply Periodic Minimal Surface Gyroid Structure to Strut-Based Grid Structure in Both Strength and Bone Regeneration.," *ACS Appl. Mater. Interfaces*, Jul. 2023, doi: 10.1021/acsami.3c06263.

- [12] “On the Morphological Deviation in Additive Manufacturing of Porous Ti6Al4V Scaffold: A Design Consideration,” *Materials*, vol. 15, no. 14, pp. 4729–4729, Jul. 2022, doi: 10.3390/ma15144729.
- [13] W. Zuo, L. Yu, J. Lin, Y. Yang, and Q. Fei, “Properties improvement of titanium alloys scaffolds in bone tissue engineering: a literature review,” *Ann. Transl. Med.*, vol. 9, no. 15, p. 1259, Aug. 2021, doi: 10.21037/atm-20-8175.
- [14] “Achieving high strength and low elastic modulus in interstitial biomedical Ti–Nb–Zr–O alloys through compositional optimization,” *Mater. Sci. Eng. -Struct. Mater. Prop. Microstruct. Process.*, vol. 839, pp. 142833–142833, Feb. 2022, doi: 10.1016/j.msea.2022.142833.
- [15] “Fabrication and properties of newly developed Ti35Zr28Nb scaffolds fabricated by powder metallurgy for bone-tissue engineering,” *J. Mater. Res. Technol.*, vol. 8, no. 5, pp. 3696–3704, Sep. 2019, doi: 10.1016/J.JMRT.2019.06.021.
- [16] M. Amini, A. Reisinger, and D. H. Pahr, “Influence of processing parameters on mechanical properties of a 3D-printed trabecular bone microstructure,” *J. Biomed. Mater. Res. B Appl. Biomater.*, vol. 108, no. 1, pp. 38–47, Jan. 2020, doi: 10.1002/jbm.b.34363.
- [17] L. Polo-Corrales, M. Latorre-Esteves, and J. E. Ramirez-Vick, “Scaffold Design for Bone Regeneration,” *J. Nanosci. Nanotechnol.*, vol. 14, no. 1, pp. 15–56, Jan. 2014.
- [18] Y. Hou, W. Wang, and P. Bártolo, “Investigating the Effect of Carbon Nanomaterials Reinforcing Poly( $\epsilon$ -Caprolactone) Printed Scaffolds for Bone Repair Applications,” *Int. J. Bioprinting*, vol. 6, no. 2, p. 266, Apr. 2020, doi: 10.18063/ijb.v6i2.266.
- [19] K. Zhou, F. A. Azaman, Z. Cao, M. Brennan Fournet, and D. M. Devine, “Bone Tissue Engineering Scaffold Optimisation through Modification of Chitosan/Ceramic Composition,” *Macromol*, vol. 3, no. 2, Art. no. 2, Jun. 2023, doi: 10.3390/macromol3020021.
- [20] “Inclusion of a 3D-printed Hyperelastic bone mesh improves mechanical and osteogenic performance of a mineralized collagen scaffold,” *bioRxiv*, Aug. 2020, doi: 10.1101/2020.06.26.171835.
- [21] “A curve-shaped flexible mesh cage for treatment of large segmental bone defects - a finite element analysis,” *Biomed. Tech.*, vol. 57, pp. 825–828, Sep. 2012, doi: 10.1515/BMT-2012-4468.
- [22] *Bone defect filling scaffold structure*, (Jun. 15, 2018). Accessed: Apr. 29, 2024. [Online Video]. Available: <https://typeset.io/papers/bone-defect-filling-scaffold-structure-1ddsfnbm58>
- [23] “In situ functionalization of wet-spun fibre meshes for bone tissue engineering,” *J. Tissue Eng. Regen. Med.*, vol. 5, no. 2, pp. 104–111, Feb. 2011, doi: 10.1002/TERM.294.



17th-19th June 2024  
Gliwice, Poland

DEPARTMENT OF ENGINEERING MATERIALS AND BIOMATERIALS  
FACULTY OF MECHANICAL ENGINEERING  
SILESIA UNIVERSITY OF TECHNOLOGY

## INTERNATIONAL STUDENTS SCIENTIFIC CONFERENCE

### **Strategic Site Selection for the Expansion of the University of Prishtina's Faculty of Mechanical Engineering laboratory: Developing a Production Center for Research and Education**

Samet Xhemajli<sup>a</sup>, Besart Berisha<sup>b</sup>, Afrim Gjelaj<sup>b</sup>

<sup>a</sup> University of Applied Sciences, Faculty of Mechanical Engineering, Department of Industrial Engineering, email: samet.xhemajli@student.fh-kiel.de

<sup>b</sup> University of Prishtina, Faculty of Mechanical Engineering, Department of Manufacturing and Industrial Engineering with Management, email: besart.berisha@uni-pr.edu

<sup>b</sup> University of Prishtina, Faculty of Mechanical Engineering, Department of Manufacturing and Industrial Engineering with Management, email: afrim.gjelaj@uni-pr.edu

**Abstract:** In this paper, we have analysed the possibility of expanding the laboratory of mechanical Engineering at the University of Prishtina. The current laboratory faces limitations in fitting all the necessary equipment, particularly manufacturing machines. Therefore, the objective is to expand and select a new location to establish a center for production, international research, and education. We assess three different locations through various decision-making analyses, including SWOT analysis, analysis of hard and soft factors, utility analysis, and pair comparison analysis. The results of our analyses are very interesting for the Faculty of Mechanical Engineering and other experts in the field, as they provide important insights and a systematic approach for decision-making regarding relocation or expansion efforts.

**Keywords:** Location Analysis, Strategic Planning, Decision-Making Criteria, SWOT analysis

## 1. INTRODUCTION

Relocating or analysing a new location can be challenging, especially for research or educational purposes, which carry significant responsibility. This process is complex due to the influence of many factors such as land, labor, machinery, transport, and capital. To simplify the analysis, we will classify these factors as hard and soft in this paper.

A poor location can severely harm any business and eventually lead to bankruptcy. Fixing a bad location decision is especially hard and expensive for large plants. Therefore, it's crucial to be very careful when choosing a location. A bad location results in higher costs, marketing difficulties, transportation problems, employee dissatisfaction, and lower quality [3].

When considering location options, expanding the existing facility is often less costly than other alternatives. While on the other hand moving to a new location includes the cost of

relocating from the existing site. However, doing nothing fails to uncover potential benefits, that's why in order to increase the potential we need to either expand or relocate [2].

The goal of this paper is to analyse the current space and new space for laboratories of FME, regarding the necessary equipment for Press brake, manufacturing, and other devices using multiple analyses.

## **2. LITERATURE REVIEW**

Sun-Weng Huang, James J.H. Liou, William Tang, and Gwo-Hshiong Tzeng (2020) discussed a critical issue for the firms who need to relocate in order to reduce their risk. Recognizing that traditional models often overlook the complex relationships between decision-making criteria, the authors propose a new hybrid multiple criteria decision-making (MCDM) model.

This model integrates the Decision Making Trial and Evaluation Laboratory-based Analytic Network Process (DANP) for subjective weighting and the entropy method for objective weighting, allowing for both subjective opinions and objective data. Using a case study of an electronics manufacturing firm with a global supply chain, the authors show how the model works in practice. The findings suggest that this approach helps companies find the best relocation strategies, supporting their sustainable development in a changing global environment [1].

In his work, Haider Basil (2010), focuses his attention to the strategic significance of facility location decisions within a firm's supply chain management. He highlights that facility location has enduring implications and must align with the firm's overarching strategy to ensure long-term success. By strategically choosing facility locations, firms can save time, turning these efficiencies into financial benefits for their customers. This approach not only increases customer satisfaction but also contributes to the firm's competitive advantage in the marketplace [2].

Suman Gothwal and Rajeev Saha in their paper of 2015 explore the complexities involved in selecting a plant location, a decision characterized by its multi-person and multi-criteria nature, in their study at YMCA University of Science and Technology. Recognizing that similar strategic decisions are not easily adaptable and can result in long term impacts, they focus on detailed planning.

## **3. METHODS OF RESEARCH**

In this paper, we examined two distinct locations within the campus of FME, ensuring that each underwent a SWOT analysis. We considered both soft and hard factors, as well as comparisons between them.

SWOT Analysis is a tool used by organizations to plan and manage strategies. It looks at both the organization itself and the world outside, helping to understand strengths, weaknesses, opportunities, and threats. This helps in making smart decisions for the future [4].

Hard factors encompass crucial and technical considerations in selecting a location, such as infrastructure, energy sources, climate, proximity to research/academic institutions, and available space [5].



Soft factors are non-technical aspects that affect decision-making, such as social life, quality of services, education, and the work environment. They're based on personal experiences and perceptions rather than numbers or technical details [6].

Utility analysis is a method for evaluating decisions in complex situations. It's used for personal, economic, operational, or technical choices. The goal is to compare different options and make the best decision [7].

#### 4. RESULTS AND DISCUSSIONS

One of the locations we considered for expanding the laboratory is right next to the Faculty of Mechanical Engineering. This proximity would save costs and allow for resource sharing between the laboratory and the faculty.

The potential location is shown in the figure below: the building of technical faculties is marked with number 1, and the laboratories with number 2. The green rectangle indicates the possible site for constructing the laboratory (research center) with the exact coordinates: 42°38'52.9"N 21°09'58.6"E.



Figure 1. Possible location for expansion of the laboratory. Source: Google Maps

We'll explain why we recommend this location using the analyses we mentioned earlier.

As mentioned before, for an easier analyse we have classified the factors to analyse in 2 groups, hard and soft factors. First we will describe some of the hard factors which we took into account and which were positive for our possible location.

- **Infrastructure and Traffic:** Our chosen location for laboratory expansion boasts favourable considerations, especially regarding infrastructure and traffic accessibility. Positioned within proximity are key facilities, including the bus station at 2.8 kilometers, University Clinical Center of Kosovo at 800 meters. Additionally, the Prishtina Airport is conveniently situated 18 kilometers away, enhancing connectivity for travel and logistics. Notably, the regular urban traffic lines 1 and 4 directly serve our

location, providing convenient transportation options for students, faculty, and visitors commuting from different areas within the city.

- **Source of energy:** Our location is good because we can easily get energy from Prishtina's power grid. Kosovo is also starting to use more solar power, which is good for the environment. Being in the city means we probably won't have many problems with power cuts. This makes our location a good choice for expanding the laboratory.
- **Space availability:** The location is limited but enough for the current needs of the laboratory/research center. We have identified a suitable area for our operations, demarcated by **green lines**, which measures approximately **625** square meters. This area provides enough space not only for our production, research and educational purposes. Besides this, the area marked by **red lines** adjacent to our primary location measures approximately **2500** square meters, and we plan to use it for future expansion purposes. Its geographic location aligns well with our requirements, making it an ideal choice for expanding our operations when the time is right.

Table 1. SWOT analysis for the possible location for expansion of the laboratory

SWOT Analysis			
Strength	Weakness	Opportunity	Threat
<ul style="list-style-type: none"> <li>- Proximity to the FME allows for easy collaboration and resource sharing</li> <li>- Cost savings due to shared infrastructure and facilities</li> <li>- Accessed to a skilled workforce from the university</li> </ul>	<ul style="list-style-type: none"> <li>- Limited space for expansion within the university campus</li> <li>- Dependence on university regulations and processes for decision-making</li> </ul>	<ul style="list-style-type: none"> <li>- Enhanced research capabilities through collaboration with faculty members.</li> <li>- Potential for joint research projects and funding opportunities.</li> <li>- Improved visibility and reputation for both the laboratory and the Faculty of Mechanical Engineering</li> <li>- Involving students in practical work</li> </ul>	<ul style="list-style-type: none"> <li>- Regulatory hurdles and bureaucratic processes within the university administration</li> </ul>

As for the soft factors we have taken into considerations these 3 main characteristics: social life, basic services and professional environment. These factors are necessary to take into account for the researches who want to work on the laboratory, permanent employees or even the people who want to visit it. In the table below are shown the opportunities for each of the soft factor.

To continue with, we conducted a thorough analysis comparing various factors and potential for future expansion. Our analysis was conducted using a utility analysis approach which is a valuation method with which solution alternatives can be judged and compared after looking at several different goal criteria. It is suitable judging both individual factors and solution alternatives. It also permits the consideration of aspects which are not quantifiable or such criteria which are quantifiable, although they cannot be converted to cash value straight away (what is often the case in location planning).

First, we have determined the evaluation points and their meaning such as below.

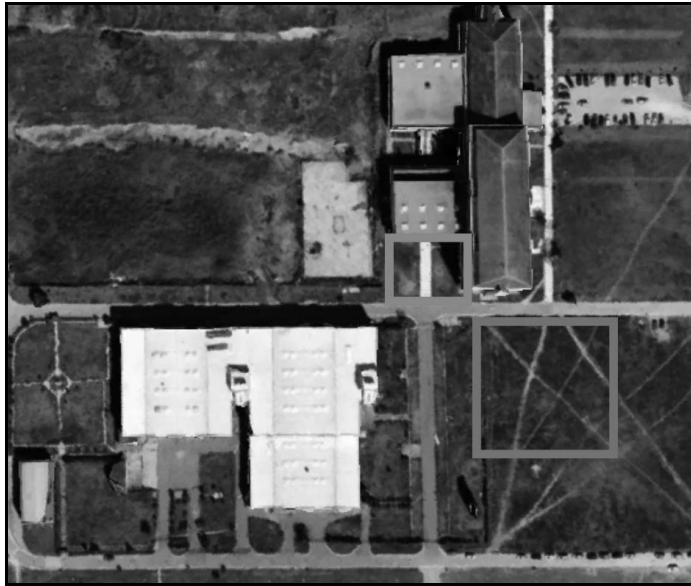


Figure 2. The area of current planning and future expansion possibility. Source: Google Maps

Table 2. Soft factors and the opportunities

Soft factors	Opportunities
<b>Social Life</b>	<ul style="list-style-type: none"> <li>- Sports and green spaces</li> <li>- Security</li> <li>- Cultural events, fairs and festivals</li> <li>- Diversity</li> </ul>
<b>Basic Services</b>	<ul style="list-style-type: none"> <li>- Transportation</li> <li>- Housing and utilities</li> <li>- Healthcare</li> </ul>
<b>Professional Environment</b>	<ul style="list-style-type: none"> <li>- Research and Innovation</li> <li>- Internationalization</li> <li>- Job opportunities</li> <li>- Training and Development</li> </ul>

Evaluation	Meaning
1	bad
2	not sufficient
3	okay
4	good
5	perfect

Figure 3. Evaluation points and their meaning

Then we have listed the factors which we have considered important to take into account and we have given them a weight percentage according to their significance. Each factor's importance is reflected in its weight percentage, ensuring a balanced and comprehensive evaluation process. Following this, for each location, we have provided our evaluation scores.

The main factors we focused on are zoning, cost factors, legal concerns, and utilities availability, elaborated below

1. Zoning: which dictates that how the land can be used and if it is permitted, including the possibility of expansion.
2. Cost factors: which includes the land acquisition costs, construction costs, movement of machines, manpower costs etc.
3. Legal concerns: checking for any existing legal restrictions or covenants that might limit development
4. Utilities availability: which includes water supply, electricity, waste management, internet and all the costs related to these.

By assigning scores to each factor based on the above criteria and then applying the weight percentages, we can determine the overall suitability of each location, as shown below:

	Weighting	Location 1 (Green)		Location 2 (Red)	
		Evaluation	Weighted	Evaluation	Weighted
<b>Zoning</b>	25%	3	0.75	4	1
<b>Cost factors</b>	25%	4	1	3	0.75
<b>Legal concerns</b>	25%	4	1	3	0.75
<b>Utilities availability</b>	25%	5	1.25	3	0.75
	<b>100%</b>	<b>16</b>	<b>4</b>	<b>13</b>	<b>3.25</b>

Figure 4. Utility analysis for both locations

## 5. CONCLUSION

Based on the analysis of space and other parameters, we can conclude that this space could fulfil the some of our requirements regrading of the Press brake machines and other manufacturing machine tools.

Where, as analysis of decision making, swot analysis and other method of analysis we can propose some idea for new space/facilities to have the best solution of research and education.

Considering this analysis, we can conclude that the location marked in green is a better opportunity for us to expand our laboratory by keeping the cost lower, and the red-marked location can be considered as a potential location for expansion in the future.

## BIBLIOGRAPHY

1. Huang S., Liou J., Tang W., Tzeng W., (2020), "Location Selection of a Manufacturing Facility from the Perspective of Supply Chain Sustainability", *symmetry*. pp. 2-5,
2. Basil H., (2010) "Location Planning", Researchgate

3. Gothwal S., Saha R., (2015), “Plant location selection of a manufacturing industry using analytic hierarchy process approach”, *Int. J. Services and Operations Management*, Vol. 22, No. 2
4. Gurel E., Tat M., (2017), “SWOT Analysis: A Theoretical Review”, *The Journal of International Social Research*, Vol. 10, Issue: 51
5. <https://my-business-location.com/en/glossary/hard-location-factors>
6. <https://my-business-location.com/en/glossary#Soft%20location%20factors>
7. FFE (2020). What is Utility Analysis [online] Available at:<https://www.ffe.de/en/publications/what-is-a-utility-analysis/>



17th-19th June 2024  
Gliwice, Poland

DEPARTMENT OF ENGINEERING MATERIALS AND BIOMATERIALS  
FACULTY OF MECHANICAL ENGINEERING  
SILESIA UNIVERSITY OF TECHNOLOGY

## INTERNATIONAL STUDENTS SCIENTIFIC CONFERENCE

### **UWB objects positioning system with the ability to change the ranging method dynamically**

Tomasz Zawadzki<sup>a</sup>, Krzysztof Paszek<sup>b</sup>

<sup>a</sup> Silesian University of Technology, Faculty of Automatic Control, Electronics and Computer Science, Computer Science Student

<sup>b</sup> Silesian University of Technology, Faculty of Automatic Control, Electronics and Computer Science, Department of Telecommunications and Teleinformatics  
email: Krzysztof.Paszek@polsl.pl

**Abstract:** The article describes the UWB (ultra-wideband) positioning system that allows determining positions using TWR (two-way ranging) and TDoA (time difference of arrival) ranging methods. The proposed system allows to change positioning method wirelessly by one of the nodes in the UWB network. A frame format changing the ranging method and a method for correcting timestamps taking into account clock drift are proposed.

**Keywords:** UWB, positioning, TWR, TDoA

### **1. INTRODUCTION**

The UWB system is increasingly used in positioning systems [1]. Ranging methods such as TWR and TDoA (and their modifications) are the most commonly used methods in UWB-based positioning systems [2-4]. The first one involves measuring the ToF (time of flight) of a signal between two UWB nodes in the network, which allows determining the distance between them (based on the speed of electromagnetic wave propagation). This method does not need time synchronisation between nodes to work. In turn, TDoA is based on the difference in the time of arrival of a signal (frame) to different receivers from a single node (usually tag) in the network. The position in this method is calculated based on time differences. This technique requires time synchronisation between stationary nodes in the network. Both methods are widely used in various areas, such as indoor navigation, e.g. Pozyx [4], and device discovery, e.g. Apple AirTag [6]. It becomes important to dynamically adapt the method of determining position to changing environmental conditions. The ability to change the ranging method while the system is running allows to use the advantages of both techniques, depending on specific system requirements and environment. The TWR method becomes a better choice when the user's priority is accuracy. Still, it does not work in large networks due to the number of messages exchanged during a single positioning process. In turn, TDoA allows to determine the position after sending only one message, but the accuracy depends on the accuracy of time synchronisation between nodes.

Available solutions on the market use a single method of ranging at a given time, and changing the technique requires manually reconfiguring each node.

The system described in this article allows the user to change the ranging method online, and the new configuration is propagated wirelessly in the network (via a special type of message). The article also presents the methods of clock synchronisation and drift correction.

## 2. POSITIONING

The method of exchanging frames using TWR and TDoA techniques is different. The prepared system uses a modification of the TWR method, namely asynchronous double-sided two-way ranging (ADS-TWR). When using this technique, ToF is determined based on the exchange of three frames (their timestamps): poll, response, and final (see Figure 1). Often, positioning systems (this is the case in the proposed one) also use a report frame, which does not affect the calculated distance but only acts as a medium of the calculated distance. Distances to at least three anchors must be determined to calculate the 2D position in the trilateration [7].

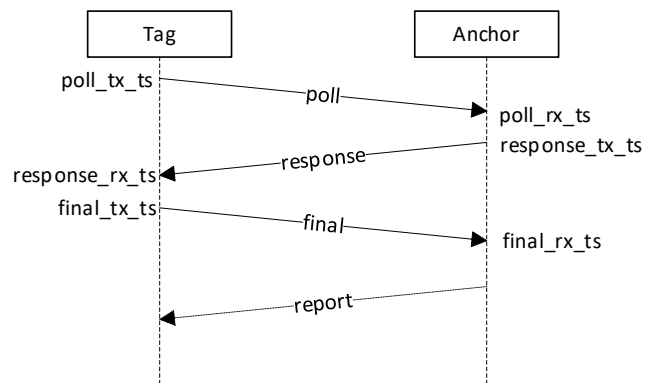


Figure 1. TWR frames exchange

However, in the TDoA method, only one blink frame is used to determine the position, which is broadcast to all reference nodes. The position is determined based on the difference in the reference nodes' time of receipt of this message.

### 2.1. System description

The positioning system test stand consisted of four Makerfabs ESP32 DW3000 modules. Three are reference points (anchors) and one is a tag. The tag is connected to the computer via a USB port, while the other nodes are only connected to the power supply.

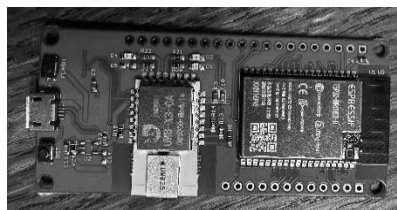


Figure 2. Makerfabs ESP32 DW3000 module

The created application (see Figure 3) controls the positioning process (initialise ranging method and receive data on distances and signal strength) and visualises the system (anchors and tags positions).

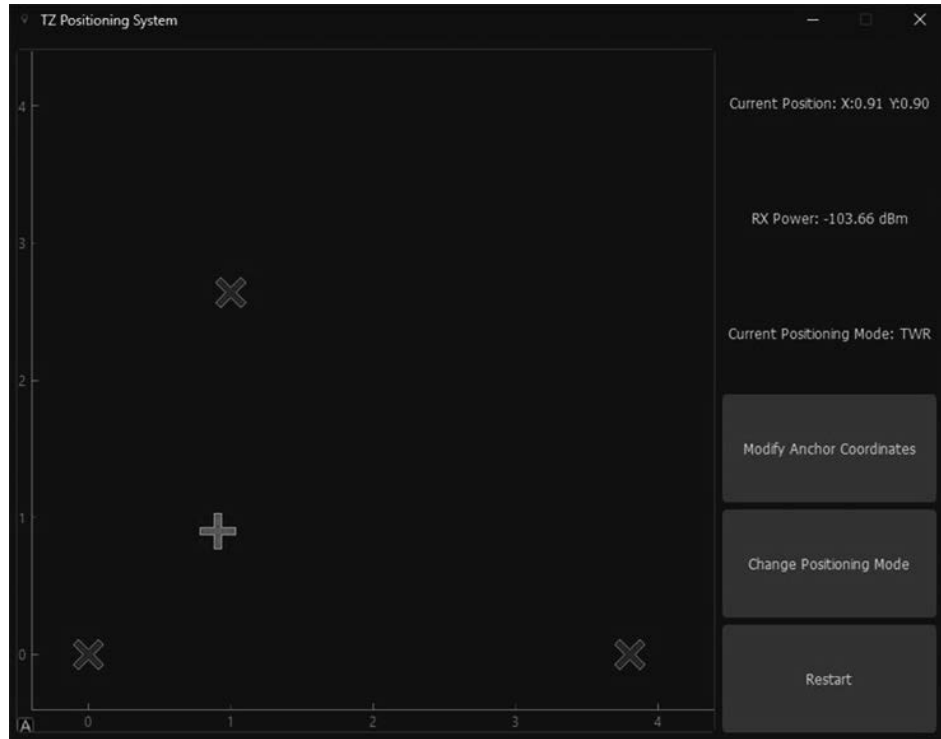


Figure 3. Positioning system user interface

The basic structure of the positioning system (addresses and anchor coordinates) is predefined in the tag firmware. However, anchor coordinates can be modified, or a new node can be added while the system runs.

## 2.2. Positioning method change

A switch frame is used to change the dimensioning method dynamically. Position determination is assumed in 2D, so the addresses and coordinates of three anchors (which participate in position determination in the TDoA method) are included in a single broadcast frame. Once the frame is received, each anchor decodes it, and the distances between them are calculated. Next, the slave anchors wait for a synchronisation frame from the coordinating anchor.

## 3. CLOCK SYNCHRONISATION

In positioning systems that use the TDoA method, one of the main challenges is synchronising the time between nodes. The proposed system for clock synchronisation used the one-way ranging (OWR) method. The modified method involves broadcasting a single sync frame containing the transmission timestamp (this is possible because the system schedules the time for



sending the message) of the frame by the coordinating anchor (see Figure 4), which is 8 bytes long (UWB modules use a 64-bit time register). Once the distance between the anchors is known, the ToF can be calculated, which allows to determine the expected timestamp on the receiver. Calculating the offset between the clocks using the received start of transmission timestamp (from the coordinating anchor) and the timestamp of receiptment (1) is possible. This offset is then used to adjust the time the blink frame was received, allowing to determine the time differences used for positioning accurately.

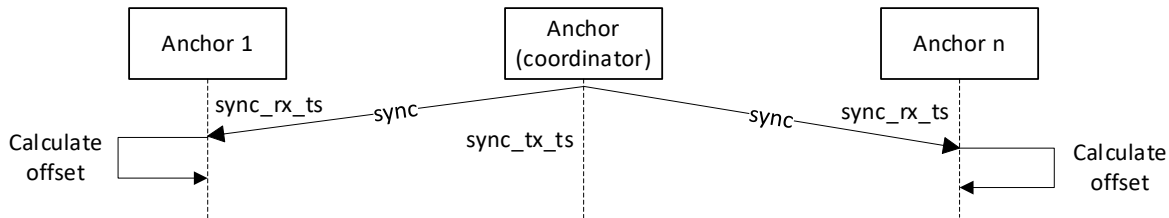


Figure 4. Node clocks synchronisation

$$ts_{offset} = ToF + sync_{tx_{ts}} - sync_{rx_{ts}} \tag{1}$$

where:  $ts_{offset}$  – offset between clocks,  $ToF$  – time of flight calculated from knowing distance and speed of electromagnetic wave,  $sync_{tx_{ts}}$  – time of sending sync frame,  $sync_{rx_{ts}}$  – time of receiving sync frame.

The counter register has a limited length (64 bits, 15.65 ps/LSb), so after a specific time, it starts counting from the beginning, as shown in Figure 5.

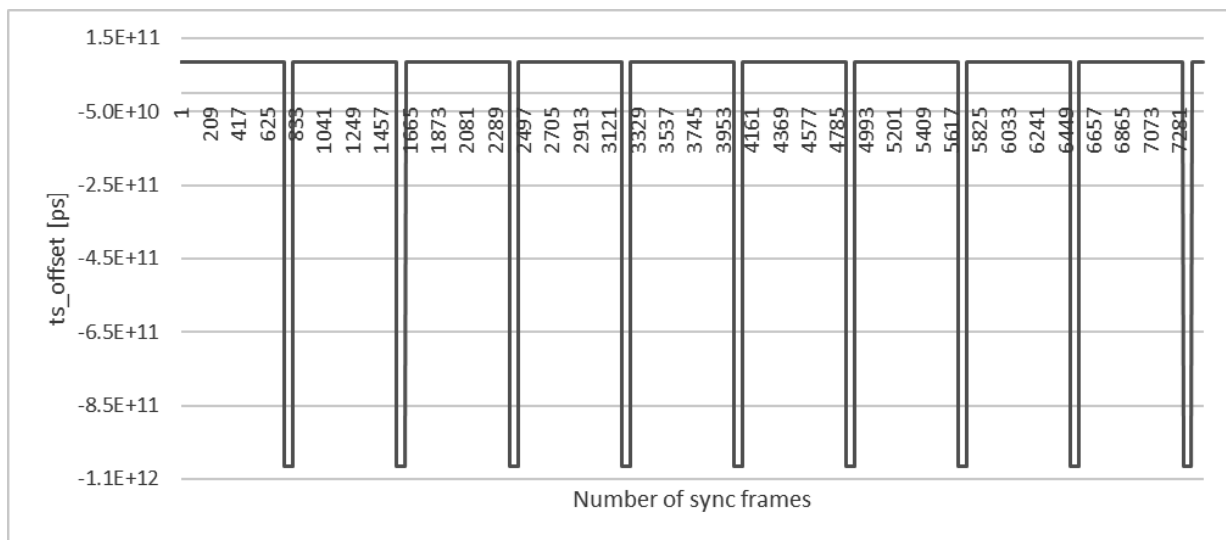


Figure 5. Example offset value between two anchors

Unfortunately, the offset between two selected nodes within a full counter cycle is not constant (see Figure 6). Therefore, to minimise the desynchronisation between the synchronisation and ranging processes, it was decided to model drift changes each time before ranging. As the change in the offset value is linear, a linear approximation of the offset was performed based on the last four synchronisation measurements.

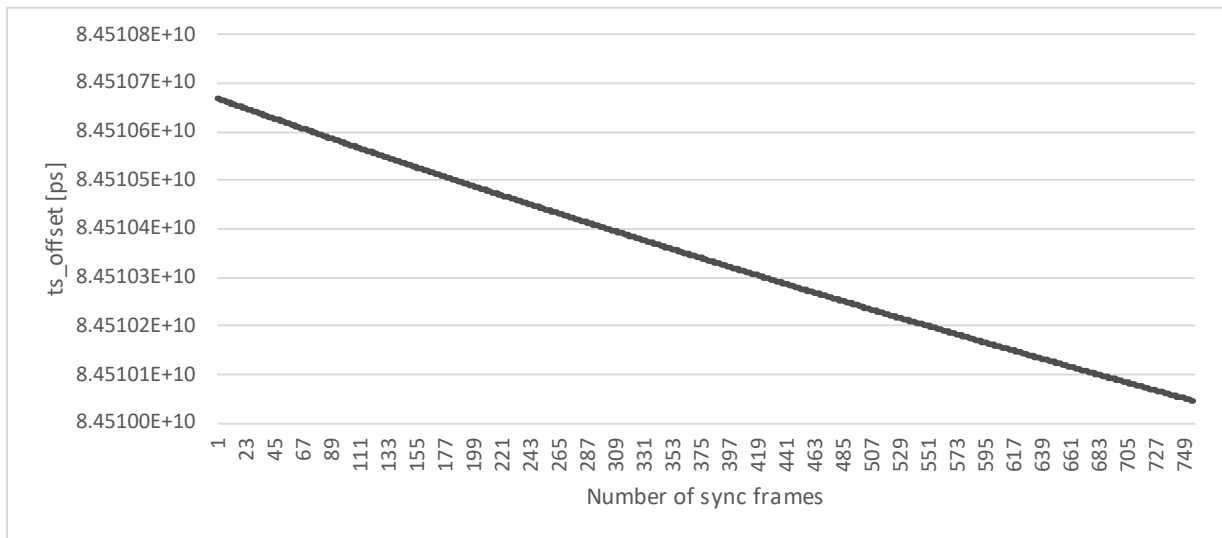


Figure 6. Example offset value between two anchors – one clock cycle

### 3.1. Synchronisation results

Due to the short transmission times of UWB frames, a small error in the determined time results in a significant error in the determined distances and next positions. When determining the position (using the TDoA ranging method) without approximation, the RMSE of the determined position was up to 500 m. After the proposed linear approximation was performed, the positioning error decreased to approximately 1 m. For comparison, positions were determined using the TWR method for the same conditions and an RMSE of less than 20 cm was obtained. Even though the accuracy of the determined position is higher for TWR, the frequency of receiving the position is many times lower compared to TDoA, which is important when positioning many objects at the same time (1 positioning message for TDoA, 9 messages (3 frames to three nodes)).

## 4. CONCLUSION

The article presents a system that allows to change the dimensioning method while the system is running. The tests indicate that the proposed method of node synchronisation and the approximation of the offset change allows reducing the positioning error to approximately 1 m (using TDoA). The system still requires improvement, but the results show that the work is going in the right direction and will continue.

## BIBLIOGRAPHY

1. D. Grzechca, K. Tokarz, K. Paszek, K. Hanzel, Wyzwania stojące przed miastami przyszłości. Inteligentne miasta i mobilność przyszłości / Sierpiński Grzegorz (red.), Inicjatywa Doskonałości - Uczelnia Badawcza, 2021.
2. K. A. Horváth, G. Ill and Á. Milánkovich, Passive extended double-sided two-way ranging algorithm for UWB positioning, 2017 Ninth International Conference on Ubiquitous and Future Networks (ICUFN), Milan, Italy, 2017.

3. Y. Weng, W. Xiao, L. Xie, Total Least Squares Method for Robust Source Localization in Sensor Networks Using TDOA Measurements, *International Journal of Distributed Sensor Networks*, 7(1):172902, 2011.
4. K. Hanzel, K. Paszek, D. Grzechca, The influence of the data packet size on positioning parameters of UWB system for the purpose of tagging smart city infrastructure, *Bull. Pol. Acad. Sci. Tech. Sci.*, t. 68, 2020.
5. Pozyx, <https://www.pozyx.io/products/hardware/hardware-anchors>
6. Apple AirTag, <https://www.apple.com/pl/airtag/>



17th-19th June 2024  
Gliwice, Poland

DEPARTMENT OF ENGINEERING MATERIALS AND BIOMATERIALS  
FACULTY OF MECHANICAL ENGINEERING  
SILESIA UNIVERSITY OF TECHNOLOGY

## INTERNATIONAL STUDENTS SCIENTIFIC CONFERENCE

### Laser technology in the production of silicon solar cells (part I)

Dominik Żebrowski<sup>a</sup>, Olaf Humeniuk<sup>a</sup>, Mikołaj Guzek<sup>a</sup>, Małgorzata Musztyfaga-Staszuk<sup>b</sup>, Aleksandra Drygała<sup>c</sup>, Krzysztof Wiśniewski<sup>d</sup>, Marcin Staszuk<sup>c</sup>

<sup>a</sup> Pupil, Complex of Communication Schools, Warszawska 35, 44-100 Gliwice, Poland

<sup>b</sup> Silesian University of Technology, Faculty of Mechanical Engineering, Welding Department, Konarskiego 18a, 44-100 Gliwice, Poland

<sup>c</sup> Silesian University of Technology, Department of Engineering Materials and Biomaterials, Konarskiego 18a, 44-100 Gliwice, Poland

email: malgorzata.musztyfaga@polsl.pl

<sup>d</sup> Łukasiewicz Research Network – Institute of Non Ferrous Metals, Centre of Advanced Material Technologies

**Abstract:** The study aims to compare the microstructural properties and the electrical obtained results of crystalline silicon solar cells. The work compared two techniques, i.e. classic and modern, for producing front metallization of solar cells. The work presented in the paper is an extension of the ongoing project entitled "*Classical and modern technologies in the production of silicon photovoltaic cells (part II)*".

**Keywords:** crystalline silicon solar cells, front electrode, electrical parameters, screen printing, selective laser sintering

### 1. INTRODUCTION

Crystalline silicon photovoltaic cells are divided into monocrystalline and polycrystalline. Monocrystalline cells differ from polycrystalline cells in that the silicon used for their production is one grain, a mono-crystal, while the production of polycrystalline cells uses silicon that consists of many grains, a poly-crystal [1]. Monocrystalline cells are more efficient than polycrystalline cells. They reflect less light due to their relatively flat surface. However, their efficiency can be increased. For example, when immersed in some potassium bases, pyramids form on their surface. This further reduces the amount of reflected light [1].

The front electrode, namely its shape and size, is a compromise between electrical and optical losses (Fig. 1) resulting from its covering. The power losses of a photovoltaic cell are influenced, among others, by the resistance of the metal-semiconductor contact, which depends on the composition of the conductive paste or powder mixer from which the electrode was made and on the conditions of its production [2].

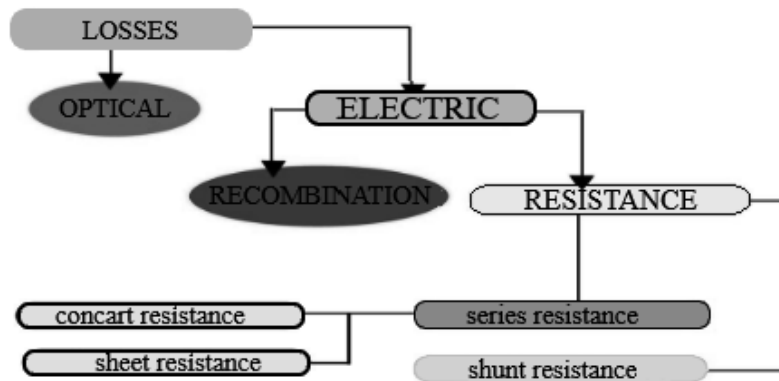


Fig. 1. Classification of solar cell losses [2]

One aspect of photovoltaic cell production is the metallization operation, which has a direct impact on the efficiency of converting sunlight into electricity. When comparing classic and modern production methods, one can notice the advantages and disadvantages of these solutions. The work focused on two methods (classic and modern) of producing front metallization of a silicon solar cell [3].

The cheapest and most frequently used method is screen printing (Fig. 2a). The front electrode is printed in the form of thin fingers connected by a collecting electrode in a way that guarantees high efficiency in reaching solar radiation to the connector area. If a template is used, printing is simple (Fig. 2b). A template with a given shape is applied directly to a specific substrate and, for example, printed paste is pushed through the holes in the pattern using a squeegee. After removing the template, a printed pattern is created on the surface [4].

Using a modern method of selective laser sintering (Fig. 2c.), which involves high-temperature consolidation of buried powder, which is transformed into a solid material by the action of the laser, a high quality of manufactured elements is obtained, both in terms of cleanliness and accuracy, compared to elements obtained using conventional methods [ 5].

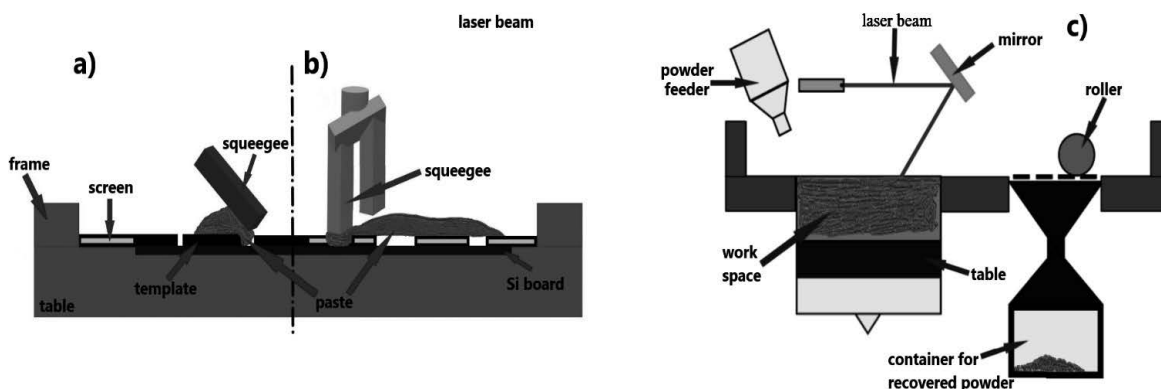


Fig. 2. Scheme of applying metallization using the conventional method - screen printing using a) a screen. b) template and unconventional c) selective laser sintering [2, 3,5]

## 2. MATERIAL

Table 1 presents the monocrystalline silicon material parameters applied to produce the solar cells examined in this paper. The front electrode was deposited from commercial silver paste PV19B and experimentally prepared silver (nano-paste) paste using screen-printing method and next to co-fired at 920°C in a belt furnace (sample 1) and selective laser sintering in an Eosint M 250 Xtended device with laser beam feed rate 55 mm/s and laser beam 100 W (sample 2).

Table 1. Crystalline silicon parameters

Conductivity	type p
Dopant	bor
Wafer thickness	330 ± 10 μm
Surface area	5 cm x 5 cm
Resistivity	~1 Ω·cm

## 3. METHODOLOGY

Two devices for sintering/melting conductive pastes were used during the investigations:

- the conveyor IR furnace. It was equipped with tungsten filament lamps, heating both the top and bottom of the conveyor, where the conveyor belt feed rate was 200 cm/min).
- the Eosint M 250 Xtended device. The device had the following technical data: laser beam feed rate - max. 3.0 m/s, laser beam output power - 270 W, laser beam diameter - 300 μm, wavelength -10640 nm, shielding gas – nitrogen.

The following investigations were performed in this paper:

- The topography and cross-section of front contacts using:
  - Zeiss Supra 35 scanning electron microscope (SEM) using secondary electron detection with accelerating voltage in the range 5÷20 kV.
  - atomic force microscope (Park Systems XE 100) in the non-contact mode,
  - Leica DVM6 digital optical microscope.
- Microchemical analysis of front chosen contacts using the scanning electron microscope equipped with an energy dispersive X-ray (EDS) spectrometer.
- Electrical measurements of chosen parts of solar cells using:
  - a measuring station equipped with a Corescan device. It was designed by SunLab. During the investigation was applied Core scan (Contact Resistance Scan) mode to determine among others: contact resistance  $R_c$ , specific contact resistance  $\rho_c$ ,
  - a measuring station equipped with a test stand (patent number P.398223). The contact resistance  $R_c$  and specific contact resistance  $\rho_c$  of front contact solar cell using the Transmission Line Model (TLM) method onto measuring position was determined.
  - a measuring station equipped with a Sherescan device. It was designed also by SunLab. During the investigation, sheet resistance settings were used to determine sheet resistance.

## 4. RESULTS

### 4.1. Electrical properties

The results of the electrical properties measurements of the investigated samples obtained by applying a Sherescan device are summarized in Table 2 and Figure 3.

Table 2. Parameters of sheet resistance of the emitter diffusion layer of monocrystalline wafer

Sample number	Device applied	Sheet resistance, $\Omega/\square$				
		Average	Standard Deviation	Median	Maximum	Minimum
1	Conveyor IR furnace	46.5	2.4	47.3	48.9	42.6
2	Eosint M 250 Xtended	49.7	1.1	50.1	50.8	48.0

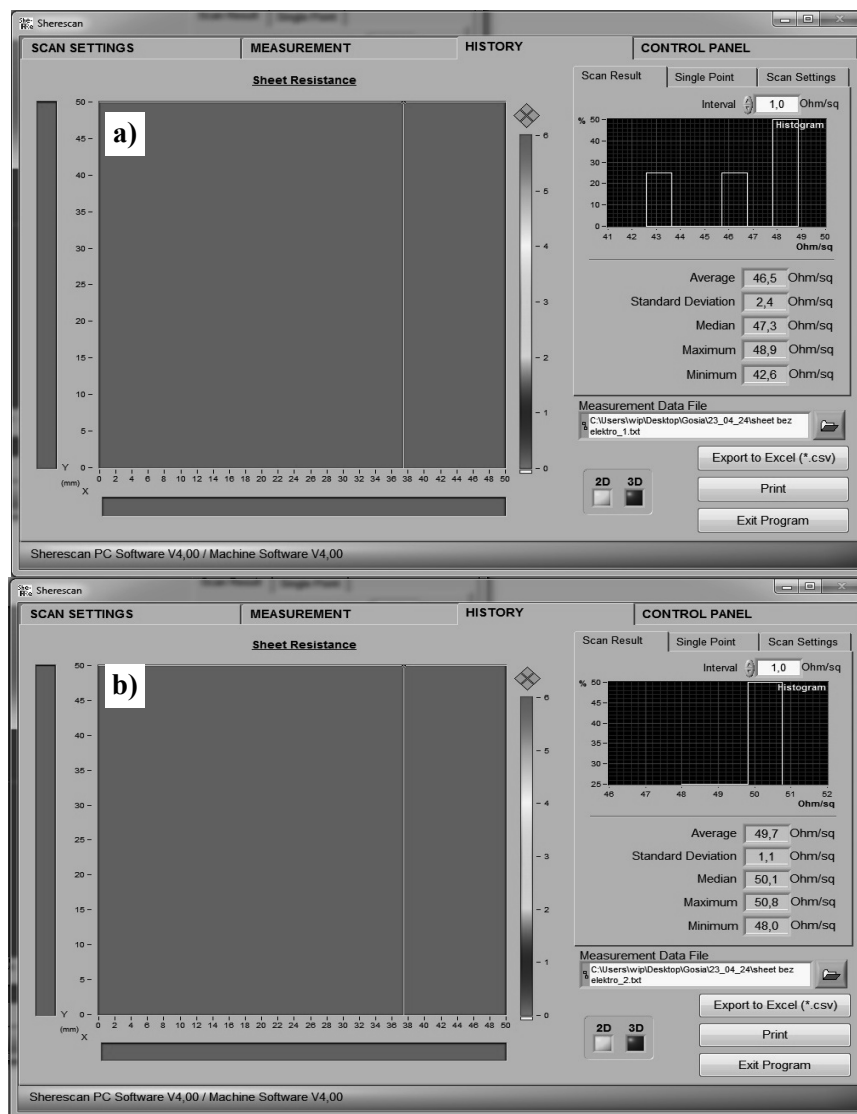


Fig. 3. View of the sheet resistance measurement result: a) sample 1, b) sample 2

In table 3 are summarized the results of the electrical properties measurements of the investigated samples obtained applying a Corescan device (\*) using the Potential Differences (PD) method (Fig. 4) and test stand with patent number P.398223 using transmission line model (TLM) method (\*\*).

Table 3. Parameters of contact resistance and resistivity between the emitter and the front metallization grid of solar cell, where:  $V$  – voltage,  $R_c$  – contact resistance,  $\rho_c$  – resistivity,  $J$  – current density,  $I$  – obtained from a solar cell

Sample number	Device applied	PD			
		$J$ , mA/cm <sup>2</sup>	$R_p$	$R_c$ , $\Omega$ cm	$\rho_c$ , m $\Omega$ cm <sup>2</sup>
1	Conveyor IR furnace *	30	47	3.1	31
		TLM method			
		$I$ , mA	$R_p$ , $\Omega/\square$	$R_c$ , $\Omega$ cm	$\rho_c$ , m $\Omega$ cm <sup>2</sup>
2	Eosint M 250 Xtended **	30	50	1.3	188

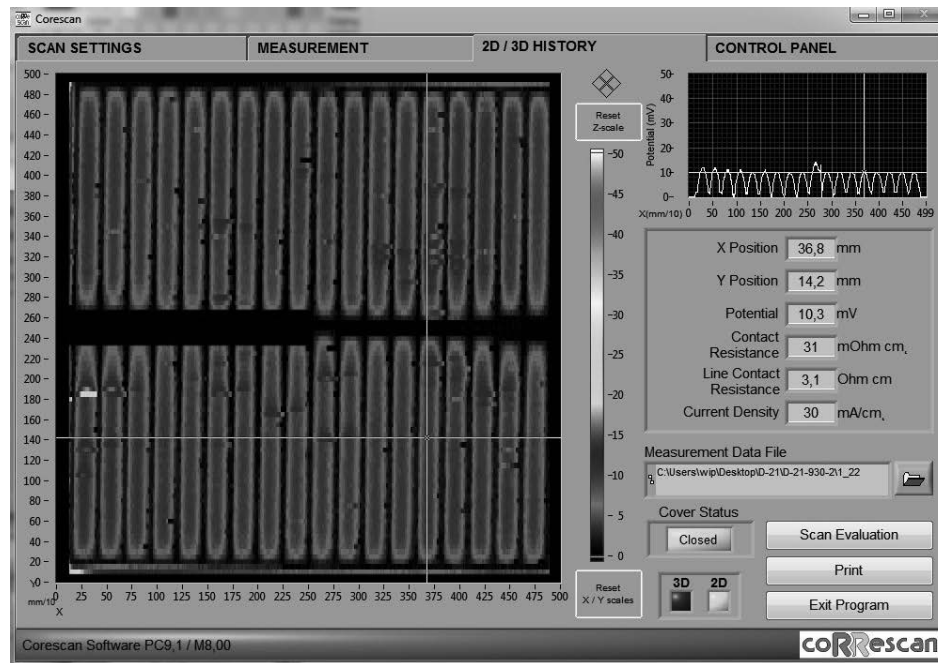


Fig. 4. View of the electrical parameters ( $R_c$ ,  $\rho_c$ ) measurement results sample 1

## 4.2. Microstructural properties

Surface observations in a scanning electron microscope of the front electrode deposited from both silver paste using screen printing method and next to co-fired in a belt furnace and selective laser sintering on the monocrystalline silicon surface of solar cells are shown in Figure 5.



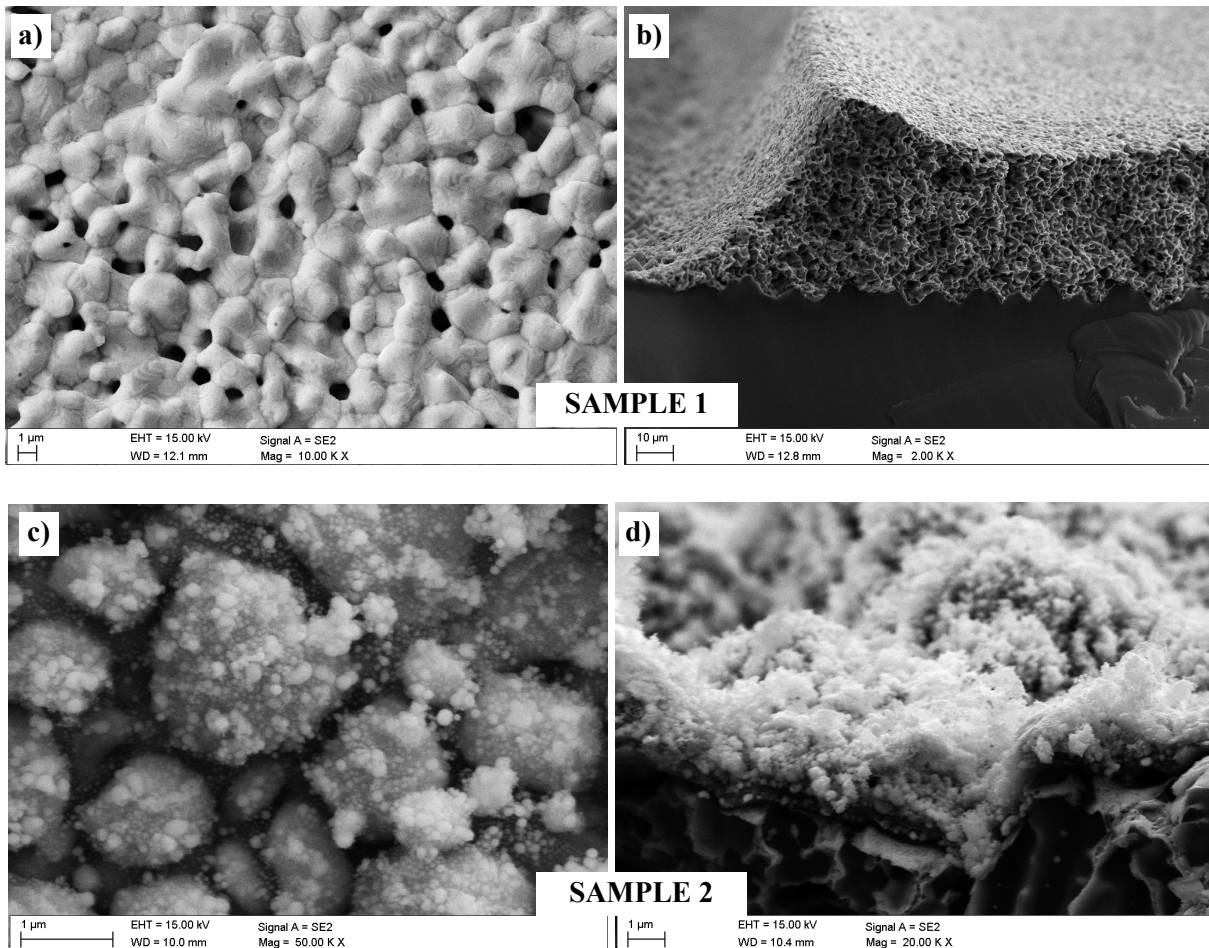


Figure 5. Topography (a, c) and cross-section (b, d) of the front electrode made from commercial paste (sample 1) and experimental paste (sample 2) (SEM)

The topography observations in the scanning electron microscopy show that the morphology of a front electrode deposited from paste PV 145 and co-fired in the furnace shows a porous structure (Fig. 5a). In the case of the morphology a front electrode deposited from experimental paste and selective laser sintered shows high heterogeneity, which is related to the presence of numerous agglomerates in the shape of silver balls of varying sizes from several to several dozen micrometers (fig. 5c).

Based on the fractographic investigations, it was found that front electrodes manufactured from commercial and experimental paste demonstrated continuous connection (Fig. 5b,d).

Microscopic observations with chemical composition analysis confirm the presence of elements suitable for the substrate (element Si) with deposited layers and the front electrode (mainly the element Ag) of solar cells (Figures 6 and 7).

Figure 8 presents topography observations in the optical microscopy of samples. Using this microscope, the finger width of investigated samples was measured. In the case of sample 1, the busbar was 2 mm, and the collecting path was 0.12 mm. In the case of sample 2, one test path was 1 mm long and 2 mm wide.

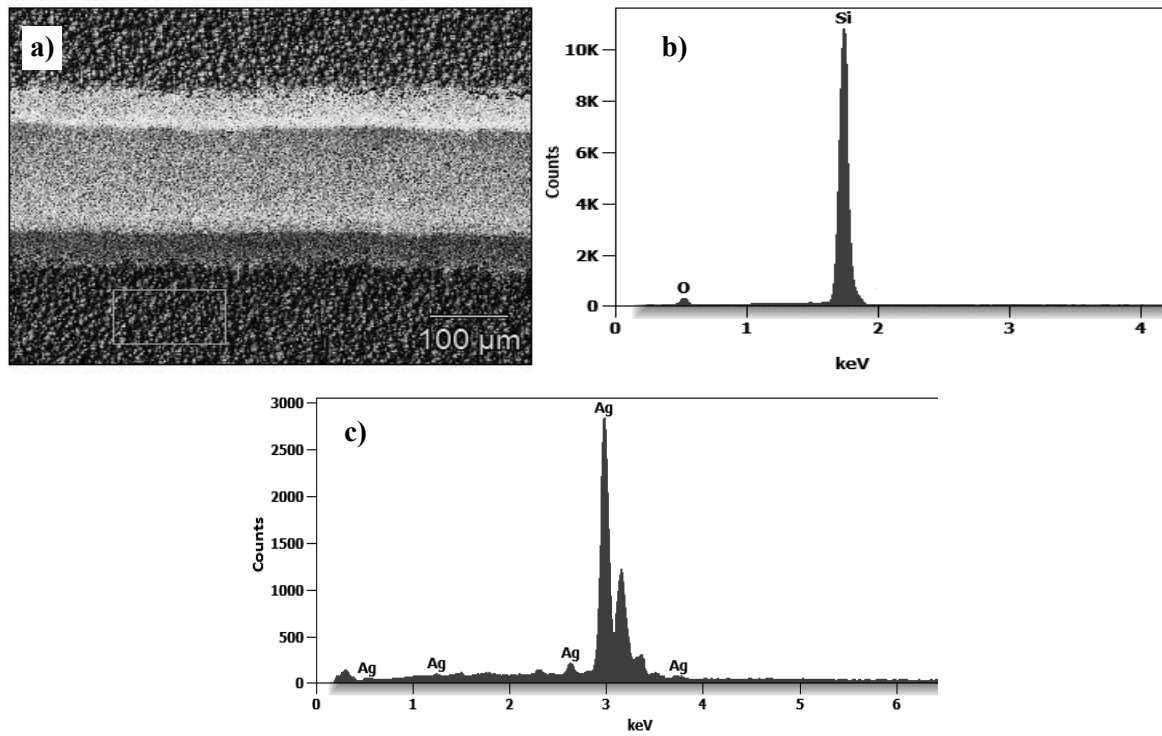


Figure 6. a) Topography of a sample 2 and EDS microanalysis from the area: b)1 (silicon with deposited layers) c) 2 (front electrode)

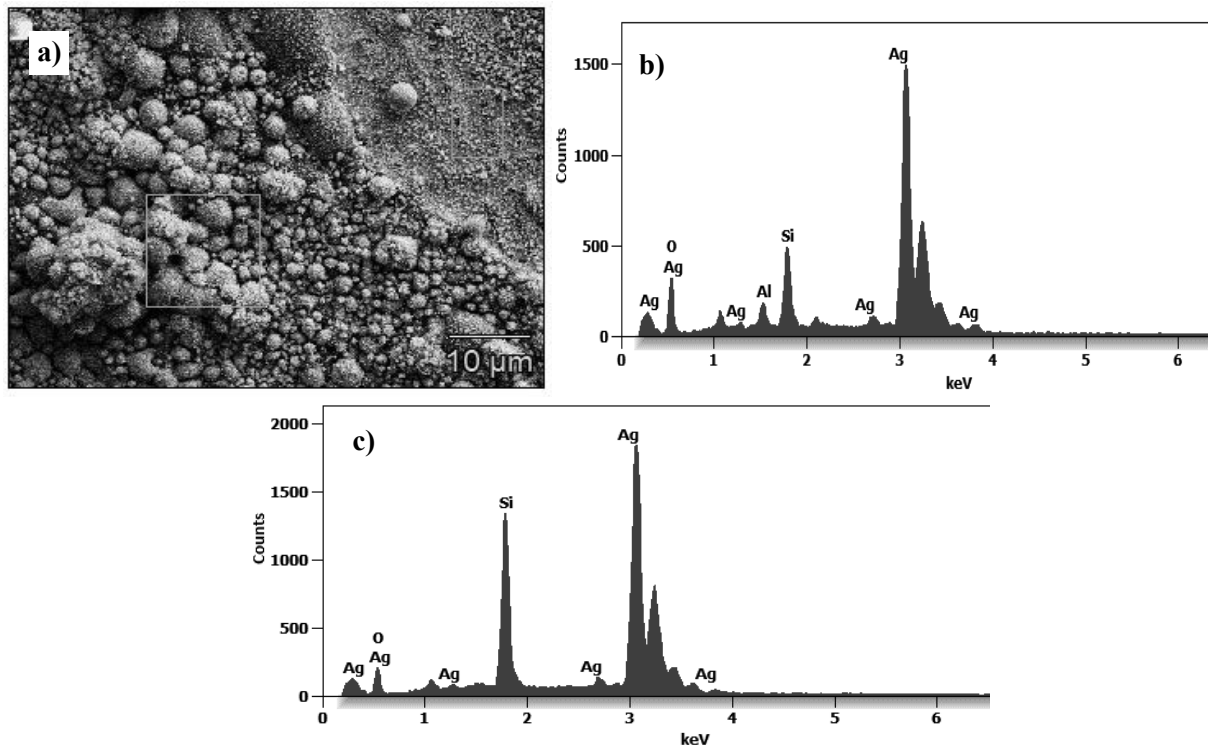


Figure 7. a) Topography of a sample 1 and EDS microanalysis from the area: b)1 (silicon with deposited layers) c) 2 (front electrode)

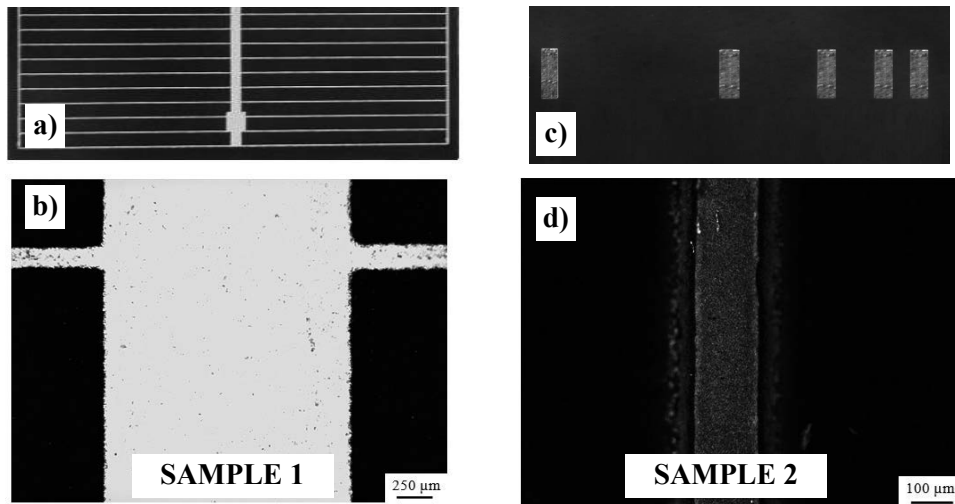


Fig. 8. Electrical contacts: a, b) collecting front electrode, c, d) test front electrode of a monocrystalline solar cell

## 5. RESULTS

It was found in the study results, that laser micro-treatment of the front metallization of solar cells made from monocrystalline silicon, including selective laser sintering to its surface using CO<sub>2</sub> laser improves the quality by minimization of the connection resistance of the front electrode with the surface. In the case of a sample made using this technique, the smaller resistance value of the connection zone electrode with the substrate was obtained, but a higher resistivity value, therefore fewer experiments should be performed to improve this parameter that affects the conversion of photovoltaic cells. Comparable samples showed different structures based on topography investigations. Fractographic investigations showed that front electrodes manufactured from commercial and experimental paste presented similar continuous connections. Chemical composition analysis confirmed the presence of elements suitable for the deposited layers and the front electrode.

## BIBLIOGRAPHY

1. M. Macek, A. Drygała, Ogólna charakterystyka krzemowych ogniw fotowoltaicznych. PSKN zeszyt nr 2/2010, Gliwice 2010.
2. M. Musztyfaga-Staszuk, Nowe kompozyty na bazie miedzi w zastosowaniu do wytwarzania krzemowych ogniw fotowoltaicznych, vol. 778, 2019, Pol. Śląska, 161 s., ISBN 978-83-7880-626-4
3. Musztyfaga M., Mikroobróbka laserowa elementów krzemowych ogniw fotowoltaicznych, Praca doktorska niepublikowana, Biblioteka Główna Politechniki Śląskiej, Gliwice, 2011.
4. M. Prokopiuk vel Prokopowicz, A. Tomiczek, A. Drygała, Screen-printing deposition of electrodes and its firing, PSKN zeszyt nr 30/2014, Gliwice 2014.
5. R. Podstawski, A. Achteлик-Franczak, Technologia selektywnego spiekania laserowego – możliwości wykorzystania w przemyśle w organicznej elektronice, Rozprawa doktorska, Polska Akademia Nauk, Warszawa, 2011.



17th-19th June 2024  
Gliwice, Poland

DEPARTMENT OF ENGINEERING MATERIALS AND BIOMATERIALS  
FACULTY OF MECHANICAL ENGINEERING  
SILESIA UNIVERSITY OF TECHNOLOGY

## INTERNATIONAL STUDENTS SCIENTIFIC CONFERENCE

### **Leveraging the CARLA Simulator for Realistic Image Generation to Train and Evaluate AI Methods for Autonomous Vehicles**

Michał Zieliński<sup>a</sup>, Dariusz Myszor<sup>b</sup>, Marcin Paszkuta<sup>c</sup>, Tomasz Kukuczka<sup>d</sup>, Eryk Szmyt<sup>a</sup>, Daniel Sobieraj<sup>a</sup>, Kacper Matys<sup>a</sup>, Michał Wieczorek<sup>a</sup>, Paweł Michalski<sup>f</sup>, Krzysztof Pawełczyk<sup>g</sup>, Michał Polończyk<sup>g</sup>

<sup>a</sup> Silesian University of Technology, Faculty of Automatic Control, Electronics and Computer Science, Virtual Flying Student Research Club

<sup>b</sup> Silesian University of Technology, Faculty of Automatic Control, Electronics And Computer Science, Department of Algorithmics and Software

<sup>c</sup> Silesian University of Technology, Faculty of Automatic Control, Electronics And Computer Science, Department of Graphics, Computer Vision and Digital Systems

<sup>d</sup> Silesian University of Technology, Faculty of Automatic Control, Electronics And Computer Science, Department of Graphics, Department of Cybernetics, Nanotechnology and Data Processing

<sup>e</sup> Silesian University of Technology, Virtual Flying Student Research Club

<sup>f</sup> Opole University of Technology, Department of Informatics

<sup>g</sup> Autonomos Systems Sp. z o. o.

**Abstract:** This article presents Carla simulator, focusing on its capabilities and provide a simple example of its application

**Keywords:** computer graphics, unreal engine, autonomous vehicles, autonomous driving

## **1. INTRODUCTION**

With the dynamic advancement of artificial intelligence, autonomous technologies are becoming an increasingly realistic vision, aiming to revolutionize many aspects of life. Among them, autonomous vehicles are of particular interest[1], promising to improve road safety and efficiency. However, the development of this technology is accompanied by many challenges that require appropriate tools and solutions.

One of the key challenges is ensuring the safety of autonomous systems. Autonomous vehicles must be able to navigate roads safely and predictably, considering the complex and dynamic road environment in which various road users such as pedestrians, cyclists, and other motor vehicles operate[2]. Additionally, autonomous systems must be resilient to unforeseen events and failures to ensure the safety of passengers and other road users.

To achieve spatial awareness, an autonomous system requires various sensors, such as LiDARs and cameras. LiDAR provides information about the distance to surrounding components of the vehicle. However, these devices are expensive and generate sparse point clouds. The resolution of the data degrades with increasing distance from the sensor, meaning smaller objects are only detected when they are closer.

A potential solution to this limitation is the use of a set of synchronized heterogeneous cameras paired with a properly trained deep neural network. Cameras are less expensive than LiDARs and can determine the distance to objects in the environment for each pixel in the captured image. However, this approach necessitates a substantial amount of data to train and evaluate the deep neural network models responsible for converting images into depth maps.

Simulators offer significant advantages in this context. The in-silico data generation process substantially reduces both the time and cost associated with data acquisition, facilitating the efficient training and testing of these models.

CARLA[3] is an open-source simulator developed to address these problems. With CARLA, we can create a virtual environment based on the Unreal Engine 4 platform where we can easily generate the data from various sensor as well as train or validate various autonomous navigation systems. The list of CARLA functionalities includes:

- **Sensor systems:** Users have a wide range of possible sensors to be used by the agent. In addition to classics such as RGB cameras or lidar distance sensors, it also includes, for example, depth cameras, dynamic vision sensors (DVS), optical flow, and many more.
- **Traffic management system:** In addition to our target agent, users can create an entire traffic system containing components such as intersections with or without traffic lights, other vehicles, and pedestrians. Compatibility with OpenDrive allows for the creation of comprehensive systems.
- **API:** The entire simulation operates on a server-based API through which users can control aspects of the virtual environment or acquire necessary data.
- **ROS compatibility:** Compatibility with ROS enables seamless transfer of code between simulation and real-world implementation.

## 2. ENVIRONMENT PREPARATION

We can start working with Carla in two ways. The first is by downloading the compiled version from GitHub repository. This version should work out-of-the-box, containing all the basic components allowing for quick setup.

The second option is to build the project from source. This option gives us much more flexibility. In addition to being able to customize the source code to our needs, we also gain access to the Unreal editor, which provides us with many tools for editing maps or adding new assets.

The first step is to prepare a special version of the Unreal Engine. The creators of Carla have prepared their own fork introducing the necessary changes for simulation to work. For licensing reasons, the user must first obtain access the source code of the original version<sup>1</sup>.

The next step is to build the CARLA itself. This step consists of the following actions:

- Downloading the built-in asset collection
- (Optional) Compiling the library for the Python language. This allows avoiding potential version conflicts between the one installed from an external repository (e.g., PyPi) and the compiled version of the server
- Compiling the server (Project and Plugin)

After the first launch, we should receive the Unreal editor window (Figure 2). If everything has gone smoothly, the project should be available for quick launch via the *uproject* file or through the dedicated Epic Games launcher.



Figure 1 Unreal Engine Editor with one of Carla's built-in maps

Access to the project files allows us to seamlessly add additional assets through the built-in marketplace or external sources. While environmental elements should not pose a problem, adding items that require control during simulation (such as vehicle models) necessitates proper integration with CARLA's blueprints. Detailed instructions on how to achieve this, such as incorporating a new vehicle, are available in the project documentation.<sup>2</sup>

<sup>1</sup> <https://dev.epicgames.com/documentation/en-us/unreal-engine/downloading-unreal-engine-source-code>

<sup>2</sup> [https://carla.readthedocs.io/en/latest/custom\\_assets\\_tutorials/](https://carla.readthedocs.io/en/latest/custom_assets_tutorials/)

### 3. SIMULATION EXAMPLE USECASE

CARLA's simulation operates on a server-based architecture, with communication facilitated through a dedicated API. Integration with code is streamlined using a specialized Python library. In this example, we will perform the following operations:

- Establish a connection with the simulation server
- Create a controllable car
- Add two sensors to the created vehicle (RGB camera and segmentation)
- Run the built-in primitive autopilot moving between random points on the map
- Start capturing data from sensors at a frequency of 25 measurements per second
- Additionally: set the simulation conditions to a wet sunset

The example above was created with the aim of obtaining a dataset for semantic segmentation task.

```
: import carla
import random
from queue import Queue
from queue import Empty

: #Establishing connection to Carla server instance
client = carla.Client('localhost', 2000)
client.set_timeout(15)
world = client.get_world()
```

Figure 2 Importing libraries and establishing the connection to the Carla server

After importing the necessary libraries, the first step is to establish a connection with the server. Once this is done, we can obtain a reference to the world object, which represents our simulation.

```
: #Set weather to designated preset
world.set_weather(carla.WeatherParameters.WetSunset)
```

Figure 3 Setting up the weather

A wet sunset is one of the ready-made weather types built into Carla. If necessary, the user can define their own weather type<sup>3</sup>. After selecting the appropriate object, we pass it to the simulation.

---

<sup>3</sup> [https://carla.readthedocs.io/en/latest/tuto\\_M\\_custom\\_weather\\_landscape/#bp\\_weather](https://carla.readthedocs.io/en/latest/tuto_M_custom_weather_landscape/#bp_weather)

```
: def spawn_vehicle(world):
    # Get the map's spawn points
    spawn_points = world.get_map().get_spawn_points()
    #Acquire list of valid vehicle objects
    vehicle_blueprints = world.get_blueprint_library().filter('*vehicle*')
    #Spawning random vehicle in random spawn point
    vehicle=world.try_spawn_actor(random.choice(vehicle_blueprints), random.choice(spawn_points))
    #Enabling autopilot
    vehicle.set_autopilot(True)
    return vehicle
ego_vehicle=spawn_vehicle(world)
```

Figure 4 Creating a vehicle with autopilot enabled

Most controllable objects in Carla operate based on a schema library. This allows us to easily select a random vehicle. The vehicle will appear at one of the predefined points on our map. Additionally, we set an autopilot for it.

```
#Sensors will be placed in local space of vehicle with given offset
camera_init_trans = carla.Transform(carla.Location(z=1.5))

# Create cameras through a blueprint that defines its properties
sensor_rgb = world.get_blueprint_library().find('sensor.camera.rgb')
sensor_seg = world.get_blueprint_library().find('sensor.camera.semantic_segmentation')

# Spawn the sensors and attach it to our vehicle
camera_rgb = world.spawn_actor(sensor_rgb, camera_init_trans, attach_to=ego_vehicle)
camera_seg = world.spawn_actor(sensor_seg, camera_init_trans, attach_to=ego_vehicle)
```

Figure 5 Creating target sensors

The next step is to create our two sensors: RGB and segmentation. During the creation of the actor, we inform the simulation that they are attached to our previously defined vehicle (Figure 6).

```
: #Enable synchronous mode
settings = world.get_settings()
settings.fixed_delta_seconds = (1/25)
settings.synchronous_mode = True
world.apply_settings(settings)
#Create queue for sensors
sensor_queue = Queue()
```

Figure 6 Enabling synchronous mode

Due to our example's use case, captured images from cameras must be perfectly matched; even a slight deviation in time can make the data unsuitable. To solve this problem, we run the simulation in synchronous mode (Figure 7). At the time of data acquisition, our simulation will be frozen in time, allowing for precise matching of sensor data.



```

def sensor_callback(sensor_data, sensor_queue, sensor_name):
    # Do stuff with the sensor_data data like save it to disk
    # Then you just need to add to the queue
    directory="demo/"
    if sensor_name=="seg":
        sensor_data.save_to_disk(directory+sensor_name+"_%06d.png" % sensor_data.frame, carla.ColorConverter.CityScapesPalett
    else:
        sensor_data.save_to_disk(directory+sensor_name+"_%06d.png" % sensor_data.frame)

    sensor_queue.put((sensor_data.frame, sensor_name))

camera_rgb.listen(lambda data: sensor_callback(data, sensor_queue, "rgb"))
camera_seg.listen(lambda data: sensor_callback(data, sensor_queue, "seg"))

sensor_list=[
    camera_rgb,
    camera_seg
]

```

Figure 7 Defining and registering sensor callback

The next step is to define the callback for our sensors. This is a function responsible for processing data from the sensors. In our case, it is sufficient to define the logic for saving images to disk and informing the higher process about the completion of this operation (Figure 8).

```

: for i in range(500):
    # Advance the simulation and wait for the data.
    world.tick()
    try:
        for _ in range(len(sensor_list)):
            s_frame = sensor_queue.get(True, 10.0)
            # print(" Frame: %d Sensor: %s" % (s_frame[0], s_frame[1]))
    except Empty:
        print("Some of the sensor information is missing")

```

Figure 8 Main loop

In the final stage, we define the main data generation loop. The simulation is resumed every 1/25 of a second (i.e., until the next sensor acquisition moment), and then the data is saved to disk. Thanks to the queue system, if there are problems with the sensor, the simulation can continue to operate (Figure 9).



Figure 9 Frame-by-frame comparison of segmentation and RGB sensors

After running the entire code, we obtained 500 pairs of RGB images and segmentation masks (Figure 10). According to Carla's documentation, 13 classes are distinguished (12 types of objects and 'others' class). Detailed information about color mapping can be found in the project documentation<sup>4</sup>.

#### 4. SUMMARY

Carla is a powerful tool for engineers working on autonomous vehicles. Our example shows that with just a few lines of code, we can start generating vast and diverse datasets that can be used for training or evaluating autonomous control. Additionally, because it is a virtual environment, it allows for starting work without the need for high initial costs; a regular computer with a modern graphics card should be sufficient.

#### 6. ACKNOWLEDGEMENTS

The publication/paper was based on the results of the project no. POIR.01.01.01-00-0123/20 co-financed by the European Union under the European Regional Development Fund - Smart Growth program 2014-2020.



#### BIBLIOGRAPHY

1. Arwa E. Abulwafa, A Survey of Deep Learning Algorithms and its Applications, Nile Journal of Communication & Computer Science, 2022
2. Hong Wang, Wenbo Shao, Chen Sun, Kai Yang, Dongpu Cao, Jun Li, A Survey on an Emerging Safety Challenge for Autonomous Vehicles: Safety of the Intended Functionality, Science Direct Engineering, 2024
4. Alexey Dosovitskiy , German Ros, Felipe Codevilla, Antonio Lopez, and Vladlen Koltun, CARLA: An Open Urban Driving Simulator, Proceedings of the 1st Annual Conference on Robot Learning, 2017

---

<sup>4</sup> [https://carla.readthedocs.io/en/0.8.4/cameras\\_and\\_sensors/#camera-semantic-segmentation](https://carla.readthedocs.io/en/0.8.4/cameras_and_sensors/#camera-semantic-segmentation)



17th-19th June 2024  
Gliwice, Poland

DEPARTMENT OF ENGINEERING MATERIALS AND BIOMATERIALS  
FACULTY OF MECHANICAL ENGINEERING  
SILESIA UNIVERSITY OF TECHNOLOGY

## INTERNATIONAL STUDENTS SCIENTIFIC CONFERENCE

### **Development of LMD surfacing technology and evaluation of the properties of surface layers produced on components of oil and gas extraction tools**

Julia Żuławska <sup>a</sup>, Michał Wnętrzak <sup>a</sup>, Mateusz Dziergas <sup>a</sup>, Bartosz Siedlaczek <sup>a</sup>,  
Artur Czupryński <sup>a</sup>

<sup>a</sup> Silesian University of Technology, Faculty of Mechanical Engineering, Department of Welding Engineering, email: artur.czuprynski@polsl.pl

**Abstract:** This article delves into a comprehensive study focusing on the structural and mechanical attributes of pioneering surface layers applied to oil and gas extraction tool components. These layers are engineered to withstand harsh conditions characterized by intense metal-mineral abrasive wear. Employing a multi-batch technique, the layers were meticulously deposited onto a low-alloy ASTM 4715 structural steel sheet through Laser Metal Deposition (LMD) utilizing a high-power fiber laser. Four distinct matrix powders were considered for surfacing: nickel-chromium with 60% ceramic reinforcement in the form of crushed tungsten carbide (WC), iron, nickel with 65% ceramic tungsten carbide reinforcement, and nickel with 60% ceramic tungsten carbide reinforcement. The study rigorously evaluates the impact of powder material variation on the wear resistance of the composite coating. Structural analyses of the coatings were conducted employing penetrant testing (PT), optical microscopy and scanning electron microscopy (SEM). Mechanical properties were assessed through hardness measurements, metal-mineral abrasion resistance testing, and abrasion area profile analysis. The findings from laboratory experiments establish a clear correlation between the hardness of the surfaced layers and their resistance to metal-mineral abrasion. Notably, the presence of tungsten carbide particles in the powder used during the surfacing process demonstrates a significant enhancement in abrasion resistance.

**Keywords:** Laser Metal Deposition, cladding, tungsten carbide, abrasive wear

## **1. INTRODUCTION**

Given the global shift towards sustainability, there is a growing demand not just for more efficient materials but also for remanufacturing worn-out components. Surface treatments, especially those employing Laser Metal Deposition (LMD) technology, have emerged as highly effective solutions. By hardening surface layers, technical components gain enhanced durability, leading to substantial cost savings for industries. LMD technology, increasingly popular

in recent years, offers exceptional load resistance through simultaneous laser quenching during layer formation [1]. This process alters surface structure, resulting in layers resistant to

corrosion and abrasive wear. LMD is particularly favored for remanufacturing worn machine parts due to its cost-effectiveness compared to purchasing new components. This is crucial for critical components, where failure can cause prolonged production downtimes and significant financial losses. Moreover, LMD is preferred when replacement parts are not readily available or need to be custom-made [2]. These advantages position LMD as a promising method for repairing machine parts, notably in sectors like oil and gas.

Laser surfacing involves creating a weldable layer on the parent material by melting filler metal along with the substrate's surface layer [3]. Depending on the method, the parent material's percentage in the weld deposit can be substantial [4]. This process rejuvenates damaged components by applying a wear-resistant layer with enhanced properties. Laser deposition ensures precise replication of tool geometry at a relatively low cost and high speed. LMD laser powder deposition stands out as one of the most advanced welding technologies. It entails melting the parent material while supplying energy through laser beam absorption [5]. Simultaneously, powder acts as additive material, forming a metallurgical bond when blown into the liquid metal pool under pressure. Shielding gases like Ar or CO<sub>2</sub> are commonly used in the process. This process yields layers with high purity, minimal mixing of materials, excellent mechanical properties, and no surface cracks [6].

The purpose of the study was to determine the effect of the choice of the chemical composition of the powder used in the laser surfacing process on the structure and wear resistance of coatings composed of composite powders. A novelty in the presented results is the development

of a comparison of the effect of reinforcement of a matrix consisting of a composite containing superhard phases in the form of ceramic particles of finely ground WC on the wear of machine components used in conditions of special tribological wear hazard depending on the matrix material and the percentage of carbide content. Our findings demonstrate the feasibility of producing laser-deposited composite coatings utilizing a ceramic reinforcing phase system alongside a nickel and nickel-chromium matrix. These coatings exhibit microstructural characteristics and abrasive properties ideally suited for safeguarding the working surfaces of drills utilized within the petrochemical industry. Presently, the utilization of laser surfacing for the working surfaces of drill bits remains absent from production environments. Traditionally, these components undergo wear protection via oxyacetylene welding, employing a composite stick with a powder core.

The adoption of Laser Metal Deposition (LMD) surfacing technology in lieu of the previously employed gas surfacing technique within this industrial context stands to enhance surface layer quality by mitigating nonconformities, weld stresses and strains, as well as minimizing the proportion of base metal dilution in the weld. Moreover, it facilitates the attainment of the requisite weld chemical composition in the initial layer, thereby enhancing production efficiency through automation and robotization of the surfacing process [7]. This advancement also enables shorter finishing times for the clad surface, further streamlining production processes.

## **2. MATERIALS AND METHODS**

### **2.1. Laser Processing**

The laser powder surfacing process utilized the LMD technique, featuring direct composite powder feeding into the weld pool. This operation was conducted on a robotic platform

equipped with an advanced surfacing system incorporating a YLS-4000 ytterbium fiber laser system (IPG Photonics Corporation, Oxford, MA, USA). The laser system emitted light at a wavelength of  $\lambda=1070$  nm with a maximum power output of 4000 W. The setup was mounted on a REIS RV30-26 six-axis robot (Reis Robotics, Obernburg am Main, Germany), as shown in Figure 1.



Figure 1. View of robotic LMD surfacing station used for sample surfacing

At a working distance of 26 mm from the nozzle tip, the laser spot diameter measured 5 mm, with energy distribution in the TEM01\* beam. Coaxial powder injection was facilitated using carrier gas and shielding gas – specifically Argon 5.0 (99.999%). Cladding operations were conducted with carrier gas (Ar) flow rate set at 4 l/min and shielding gas (Ar) at 10 l/min.

Table 1. Sample surfacing process parameters

Type of powder	NiCr + 60%WC	Fe	Ni + 65%WC	Ni + 60%WC
Powder gradation [ $\mu\text{m}$ ]	45 - 125	43 - 180	53 - 150	53 - 150
Powder output [g/min]	24	20	23	24
Laser power [W]	1250	1400	1150	1200

Test samples, measuring  $75 \times 25.5 \times 9.5$  mm, were welded without substrate preheating. The properties of the padding layers formed in examined LMD process are shown in Table 2.

Table 2. Properties of formed cladding layers

Type of powder	NiCr + 60%WC	Fe	Ni + 65%WC	Ni + 60%WC
Surfacing mass [g]	32	24	32	30
Surfacing thickness [mm]	2,2	2,4	2,0	2,2
Sample surfacing time [min]	1,9	1,9	2	1,9
Amount of material consumed [g]	45,6	38	46	45,6

The surfacing parameters for the composite coatings (detailed in Table 1) were meticulously chosen to ensure uniform powder distribution across the liquid metal in the weld pool. Key criteria included maintaining a depth of fusion less than 2 mm, a layer height below 5 mm, and a base metal dilution percentage less than 5% for each sample. The process involved applying a single layer, with a surfacing speed of 5 mm/s. The distance between stitches was maintained at 2.4 mm. The base material used was ASTM 4715.

## **2.2. Methodology of Research**

To evaluate the integrity of the surfacing welds and ascertain the incidence of cracks across the surfacing layers at various metallic powders, non-destructive testing methods such as visual inspection and penetration testing (PT) were employed. Structural and mechanical properties were further elucidated through the analysis of macro- and microscopic metallographic tests using optical and scanning electron microscopy, along with hardness measurements and evaluations of metal – mineral abrasive wear resistance.

## **3. RESULTS AND DISCUSSION**

### **3.1. Non-Destructive Testing Results**

Non-destructive testing of laser-deposited composite layers of powder containing NiCr + 60%WC, Fe, Ni + 65%WC and Ni + 60%WC on an ASTM 4715 low-alloy structural steel substrate allowed the type, location and size of surface imperfections to be determined. Before testing, the samples were carefully cleaned with a remover. A penetrant-reactive developer was applied to the thus prepared surface to reveal discontinuities in the structure. MR's penetrant test system was used for the test to detect surface cracks according to EN ISO 3452: fluorescent red penetrant MR 68 NF, remover MR 79 in accordance with AMS 2644 - class 2 and white developer MR 70. The results of penetration testing of surface coatings with the specified matrixes are shown in Figure 2.

In terms of craftsmanship, the coatings exhibited a high degree of uniformity in the outer surface plane. The utilization of Fe matrix powder led to a complete absence of cracks on the resulting weld surface (Figure 2b). Conversely, employing NiCr matrix powder with WC ceramic reinforcement resulted in the formation of a single transverse crack, spanning more than a half of the width of the coating (Figure 2a). The elimination of Cr from the chemical composition of the surfacing material, notably increased the occurrence of transverse cracks (Figure 2c-d). Cracks emerged during the cooling phase due to disparate thermal expansion coefficients between the base material and the surfacing weld material.

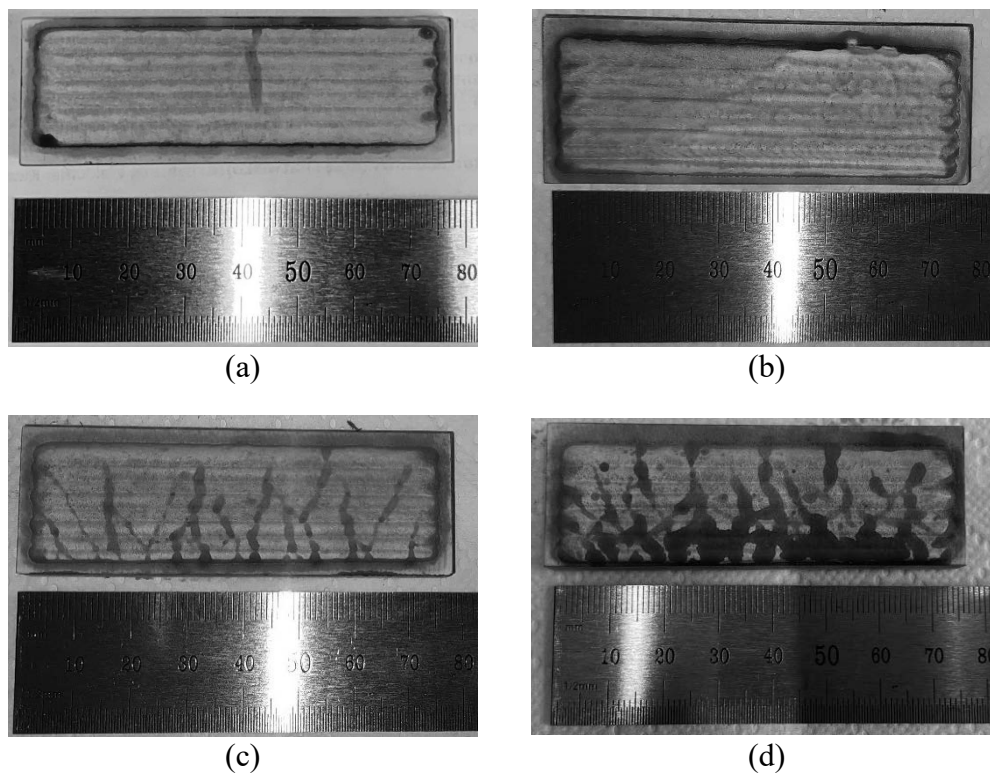
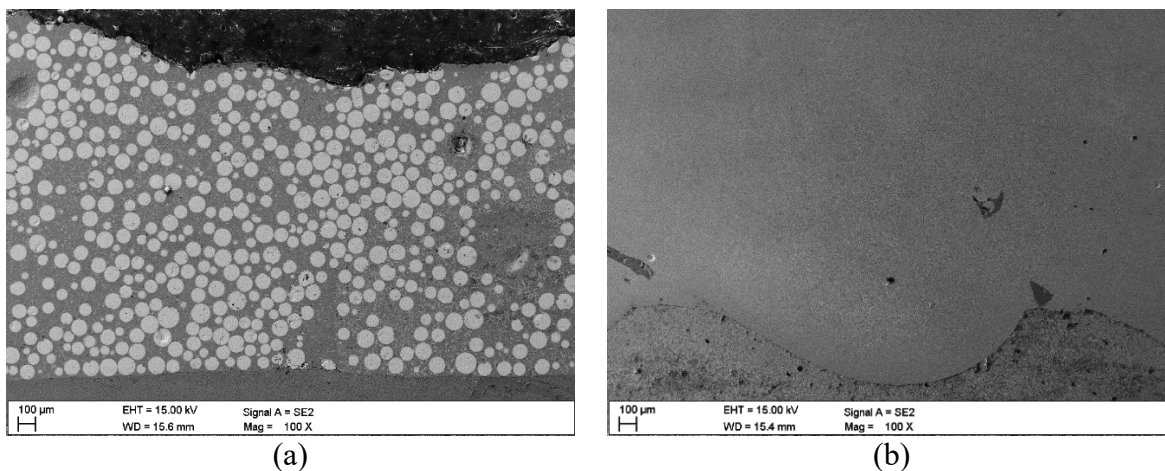


Figure 2. View of the composite laser-coated surface after penetration tests (PT): a) NiCr + 60%WC sample, b) Fe sample, c) Ni + 65%WC sample, d) Ni + 60%WC sample

### 3.2. Metallographic Test Results

The microscopic metallographic analysis of composite coatings facilitated the determination of the matrix structure, type, distribution, and dimensions of the ceramic reinforcement. Image acquisition utilized both secondary electron and backscattered electron detectors, with the latter offering clearer chemical contrast and superior image quality. A detailed structural examination of regions containing carbide reinforcement particles, was employed by a transmission electron microscope (TEM). Illustrative results of the microscopic observations are depicted in Figure 3.



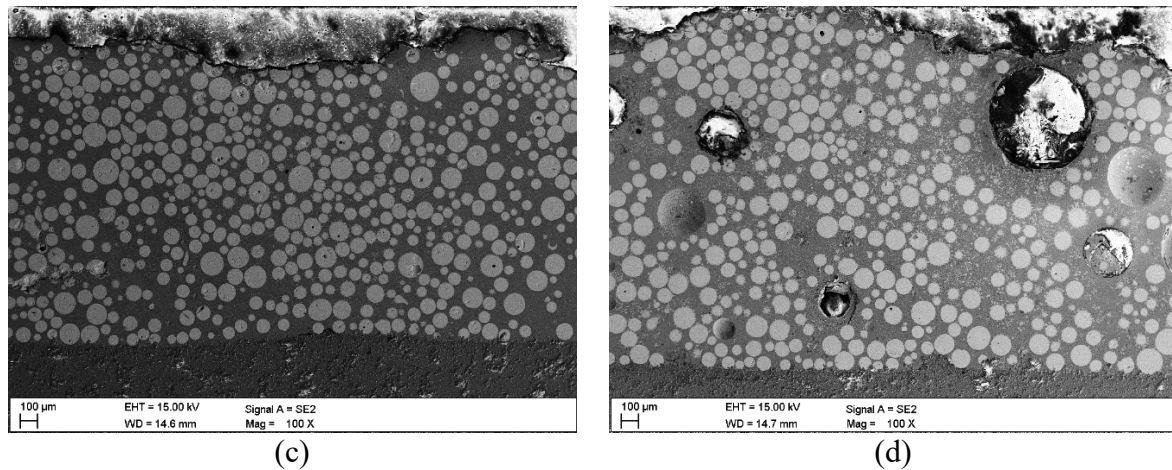


Figure 3. Example of metallographic SEM test results: a) NiCr + 60%WC sample, b) Fe sample, c) Ni + 65%WC sample, d) Ni + 60%WC sample

### 3.3. Hardness Measurements' Test Results

Hardness measurements for both the outer surface and the cross-section of the coating are detailed respectively in Table 3 and Table 4.

Table 3. Rockwell outer surface hardness measurements of coatings laser-welded with examined composite powders on ASTM 4715 low-alloy structural steel

Sample designation	Hardness of the surface layers (HRC)					Average hardness of the tested samples
	Measurement point number					
	1	2	3	4	5	
NiCr + 60%WC	76	77	76	72	79	76
Fe	62	64	63	59	59	61,4
Ni + 65%WC	84	83	82	83	82	82,8
Ni + 60%WC	78	69	79	71	79	75,2

Table 4. Vickers cross-sectional hardness measurements coatings laser-welded with examined composite powders on ASTM 4715 low-alloy structural steel

Sample designation	Cross-sectional hardness* (HV 0.5)									
	Measurement point number									
	1	2	3	4	5	6	7	8	9	10
NiCr + 60%WC	723	795	543	618	649	612	588	591	550	280
Fe	554	535	464	447	441	420	466	377	425	303
Ni + 65%WC	909	761	911	715	860	556	341	306	192	198
Ni + 60%WC	739	757	683	794	731	677	290	274	206	202

\*Owing to the diversity of results stemming from the arrangement of measurement points, the study did not ascertain the average hardness of the cross-section.



### 3.4. Abrasive Wear Test Results

The metal-mineral abrasion resistance test was conducted utilizing a specialized tribological wear test rig following ASTM G 65-00 - Procedure A guidelines. Specimens of appropriate dimensions, featuring a linear abrasion surface, were subjected to specialized sand A.F.S. Testing Sand 50-70, falling between the test surfaces and the friction wheel. The test involved 6,000 rotations at an intensity of 335 g/min.

The analysis of results of the tribological wear resistance test reveals a significant advantage in tribological resistance for samples treated with nickel matrix powders augmented with tungsten carbide, exhibiting nearly three times the resistance compared to those treated with iron matrix powder. This underscores the efficacy of incorporating hard carbide particles to prolong the lifespan of machine components. Notably, samples treated with WC-containing powders exhibit a consistently shallow abrasive wear profile, in stark contrast to the pronounced wear profile observed in samples treated with iron matrix powder. The observations of the samples post the metal-mineral abrasion test are consolidated in Figure 4.

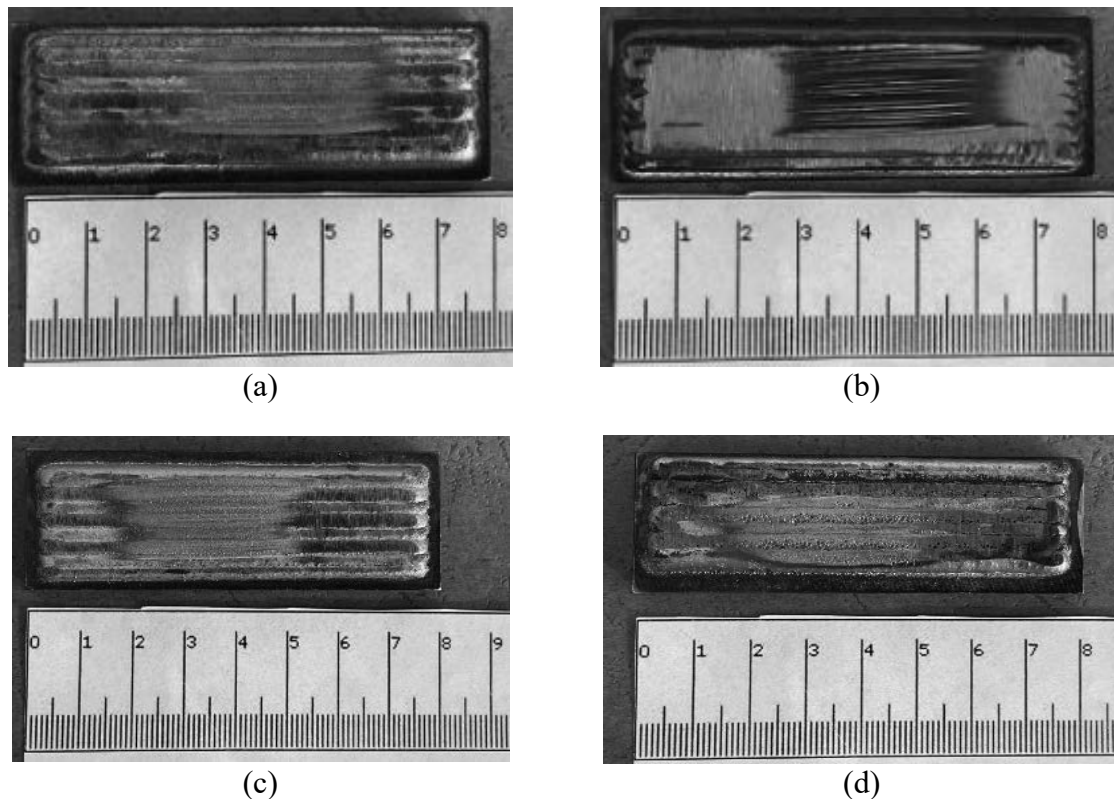


Figure 4. Summary of surface views of specimens after metal – mineral abrasive wear testing: a) NiCr + 60%WC sample, b) Fe sample, c) Ni + 65%WC sample, d) Ni + 60%WC sample

A comparison of the volumetric losses of the considered samples is shown in Figure 5.

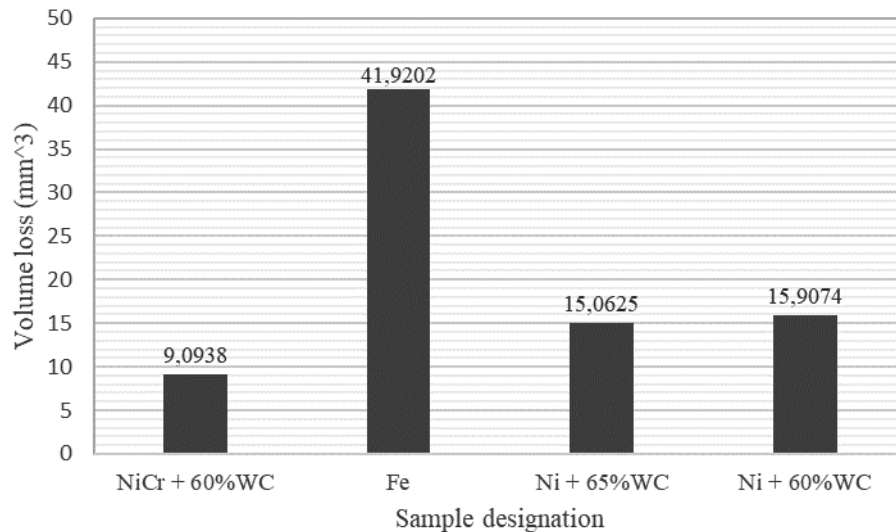


Figure 5. Summary of volumetric loss of test specimens after abrasive wear testing in accordance with ASTM procedure G 65-00

#### 4. CONCLUSIONS

The objective of this research was to assess how the chemical composition of the powder utilized as an additive material in the LMD surfacing process affects the surface properties of ASTM 4715 low-alloy steel. The investigation encompassed evaluating the fracture susceptibility of the coatings, discerning variances in metallographic structures, and appraising the metal-mineral wear resistance of samples treated with powders comprising NiCr + 60%WC, Fe, Ni + 65%WC, and Ni + 60%WC matrixes. The findings underscored that hardness is not solely contingent on the grain size within the material's structure but also hinges on its chemical composition, inclusive of supplementary elements such as tungsten carbides. Notably, specimens featuring these carbides exhibited a marked enhancement in abrasion wear resistance. Analysis of the experimental outcomes leads to the inference that the specific chemical composition of the metallic phases, coupled with the type, quantity, and particle size of the hard phase within the composite powders, facilitate precise dosing and reproducibility, alongside seamless remelting through laser powder deposition systems. The robust deposition and even distribution of the hard phase, manifested as WC particles within the alloy matrix, effectively impeded abrasive agents.

Employing laser powder deposition, with direct powder feed into the weld pool, notably enhances the abrasive wear resistance of metal-mineral components in oil and gas extraction tools, as well as machine parts subjected to abrasive wear across various key industries. Transitioning from conventional gaseous surfacing to LMD surfacing in industrial applications can enhance surfaced layer quality by minimizing non-conformities, weld stresses and strains, and base metal dilution. Moreover, it facilitates achieving the requisite chemical composition in the surfacing surface from the initial layer, thereby bolstering production efficiency through process automation and robotization, and reducing the surfacing finishing time.

**FUNDING:** The research was conducted thanks to the co-financing of project-oriented education – PBL edition. X, as part of the Excellence Initiative – Research University program

## **BIBLIOGRAPHY**

1. Thijs, L., Verhaeghe, F., Craeghs, T., Van Humbeeck, J., & Kruth, J. P. (2010). A study of the microstructural evolution during selective laser melting of Ti–6Al–4V. *Acta Materialia*, 58(9), 3303-3312.
2. Wang, F., Williams, S., & Colegrove, P. (2014). A review of laser deposition technologies for additive manufacturing and their potential applications in hard coatings. *Surface and Coatings Technology*, 261, 98-106.
3. Tlili, B., Ayadi, K., Matsumoto, M., & El Mansori, M. (2018). Numerical analysis of temperature distribution and residual stress induced by laser metal deposition. *The International Journal of Advanced Manufacturing Technology*, 94(9-12), 3275-3285.
4. Tan, W., Kar, A., & Yao, H. (2020). Corrosion behavior of laser metal deposited Ti-6Al-4V and Inconel 718 alloys. *Journal of Manufacturing Processes*, 56, 181-189.
5. Paul, C. P., Ganesh, P., & Sundararajan, G. (2021). Microstructure and wear performance of laser deposited WC-Ni coatings on 304 stainless steel. *Wear*, 474-475, 203712.
6. Sun, S., & Brandt, M. (2019). Laser surface cladding: Process, materials, and future perspectives. *Journal of Laser Applications*, 31(2), 022401.
7. Kruth, J. P., Levy, G., Klocke, F., & Childs, T. H. C. (2007). Consolidation phenomena in laser and powder-bed based layered manufacturing. *CIRP Annals*, 56(2), 730-759.



17th-19th June 2024  
Gliwice, Poland

DEPARTMENT OF ENGINEERING MATERIALS AND BIOMATERIALS  
FACULTY OF MECHANICAL ENGINEERING  
SILESIA UNIVERSITY OF TECHNOLOGY

## INTERNATIONAL STUDENTS SCIENTIFIC CONFERENCE

### Modeling of a screw extruder 3D printer

Oleh Polishchuk<sup>a</sup>, Andrii Polishchuk<sup>b</sup>, Volodymyr Misiats<sup>c</sup>, Svitlana Lisevych<sup>d</sup>,  
Mirosław Bonek<sup>e</sup>

<sup>a</sup> Khmelnytskyi National University, Faculty of Engineering, Transport and Architecture, Khmelnytskyi, Ukraine email: opolishchuk71@gmail.com.

<sup>b</sup> Khmelnytskyi National University, Faculty of Engineering, Transport and Architecture, Khmelnytskyi, Ukraine email: andrepol215@gmail.com .

<sup>c</sup> Khmelnytskyi National University, Faculty of Engineering, Transport and Architecture, Khmelnytskyi, Ukraine email: vladimirmisiats@gmail.com.

<sup>d</sup> Khmelnytskyi National University, Faculty of Engineering, Transport and Architecture, Khmelnytskyi, Ukraine email: lisevichsv@gmail.com.

<sup>e</sup> Silesian University of Technology, Faculty of mechanical and technological, Gliwice, Poland, email: mirosław.bonek@polsl.pl

**Abstract:** In this article, the process of moving polymer material in the screw extruder of a 3D printer, which uses granules or crushed polymer waste as raw materials, is chosen as the object of mathematical modeling. It is noted that the modeling of screw extruders is an extremely relevant task, as it is an important tool for optimizing production processes in the polymer industry and other industries where they are used. It allows you to study and optimize the processes taking place inside the material cylinder in detail. It is noted that the modeling of screw extruders for 3D printers, which use granules or shredded plastic waste, is a key factor in supporting innovation, in increasing production efficiency, improving product quality, and developing new technological solutions in various industries. It was noted that during the movement of the material along the channel of the extruder screw, several of its states continuously change from a solid at the entrance of the channel to a viscous liquid at the exit. In the feed zone, the polymer is in solid form and moves along the material cylinder due to friction. A physical model was used in the simulation, in which compacted polymer particles do not move relative to each other during movement through the channel. This is due to the fact that the internal friction forces in the polymer greatly outweigh the friction of the polymer on the steel, and the particles move as a single elastic compressible medium due to the balance of dry friction between the cylinder wall and the screw. The geometrical parameters of the extruder in the feed zone are shown. A diagram of the expanded extruder channel for calculating productivity is given. To determine the productivity of the extruder feed zone, a diagram of the movement of material in it was drawn up. A mathematical model of productivity was obtained depending on the diameter of the screw, the frequency of rotation, the depth of the screw channel, the angle of elevation of the screw line of the screw cutting. The pressure in the extruder channel was calculated. A scheme for calculating the forces acting on the material in the feeding zone is given. A formula was obtained for determining the pressure in the

material loading zone from the hopper, which connects the characteristics of the polymer material and the geometric parameters of the loading hopper.

**Keywords:** 3D printer, screw extruder, modeling; polymer material; loading area; bunker; productivity; pressure

## 1. INTRODUCTION

Modeling of screw extruders is an extremely relevant task, as it is an important tool for optimizing production processes in the polymer industry and other industries where they are used. It allows you to study and optimize the processes occurring inside the material cylinder in detail. This includes temperature distribution, flow rate, pressure and mixing quality. Optimizing these parameters can significantly improve the quality of the final product and increase product yield. Modeling helps to avoid long and expensive experimental studies. Instead of numerous physical tests, a series of simulations can be conducted, which significantly shortens the development time of new products and processes. By enabling a detailed analysis of the processes inside the material cylinder of the extruder, simulation helps in identifying and eliminating potential problems that can affect the quality of the final product. It opens the way for innovation by allowing experimentation with new polymer materials, screw designs and process parameters without actually producing prototypes. Optimizing processes through analytical research can help reduce production waste and energy consumption, which is an important aspect of global environmental conservation efforts.

Modeling a 3D printer screw extruder using pellets or shredded plastic waste is also very relevant today. Using shredded plastic waste for 3D printing plays an important role in solving the problem of plastic waste. In this way, it helps to understand how different types of recycled plastic behave during printing, which is key to improving the quality of the final products. Using pellets or shredded waste instead of traditional filaments for 3D printing can be significantly cheaper. Therefore, analytical research will help optimize processes for effective use of these materials.

Screw extruders make it possible to print a wider range of materials, including those that have a high viscosity or are composite. Modeling these processes opens up new opportunities for personalized and innovative printed products and allows designers and engineers to experiment with different process parameters, leading to new and more efficient 3D printing technologies.

Considering these aspects, the modeling of screw extruders for 3D printers that use pellets or shredded plastic waste is a key factor in supporting innovation, in increasing production efficiency, improving product quality and developing new technological solutions in various industries.

## 2. OBJECT AND RESEARCH METHODS

The object of research is the processes occurring during the passage of the polymer in the screw extruder of the 3D printer, which uses granules or crushed plastic waste as raw materials. The method of system analysis was used to solve the problems. Experimental research is based on the main provisions of the scientific method, including theoretical analysis, study of material

properties, analysis of working characteristics, which allows to optimize the technological process and increase the efficiency of using 3D printing.

### 3. SETTING OBJECTIVES

The goal is to develop and analyze a model of a screw extruder for a 3D printer that uses pellets or shredded polymer waste as raw materials. The main focus will be on determining the key performance parameters of the extruder, namely the performance of the screw extruder in the polymer loading zone and the resulting pressure. This will provide a better understanding of the extrusion process during 3D printing and assess the impact of different types of raw materials on print efficiency and quality.

### 4. RESULTS AND THEIR DISCUSSION

During the movement of the material along the channel of the extruder screw, several of its states continuously change from a solid at the entrance of the channel to a viscous liquid at the exit [1, 2, 3]. At the same time, this channel is traditionally divided into three functional zones [2, 3]: nutrition (I), melting (II) and homogenization (III) (Fig. 1).

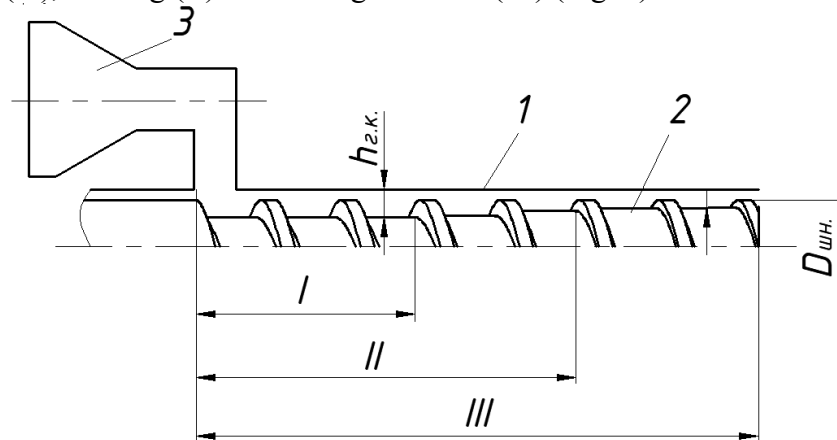


Fig. 1. Scheme of a single-screw extruder: 1 – material cylinder; 2 – screw; 3 – loading hopper; I, II, III - functional zones of the auger;  $h_{e.k.}$  – depth of the screw channel (cutting depth);  $D_{un.}$  - screw diameter

In the supply zone, the polymer is in solid form and moves along the material cylinder 1 (Fig. 1) due to friction. Usually, the screw channel is filled with polymer, where the granules are compacted due to dry friction against the walls of cylinder 1 and screw 2, which leads to an increase in pressure. At the same time, the air remaining between the granules is released through the loading hole 3. In the places of friction, heat appears, which requires cooling (air, water, etc.) to prevent premature melting of the polymer. In the absence or inefficiency of cooling, the polymer begins to melt and is pushed back into the loading hopper, disrupting the process of feeding the extruder.

The polymer in the feed zone retains its solid form. During the movement of plastic through the working channel, it is compacted, heated, and the pressure increases due to friction between the surfaces of the screw and the cylinder. Many theoretical studies of the extrusion process [1–

8] are based on a physical model in which compacted polymer particles do not move relative to each other during movement through the channel. This is due to the fact that the internal friction forces in the polymer greatly outweigh the friction of the polymer on the steel, and the particles move as a single elastic compressed medium due to the dry friction balance between the cylinder wall 1 and the screw 2.

The geometric parameters of the extruder in the feed zone are presented in Fig. 2.

In the feed area of the extruder, the depth of the screw channel is much smaller than the diameter of the hole in the material cylinder. This feature allows you to reproduce the screw channel unfolded on a plane. To simplify the visualization of the interaction between the screw channel, the material cylinder and the material, imagine this as inverse relative motion: the screw channel remains static (not moving), while the surface of the cylinder moves in a direction  $l$  with a certain speed  $V_c$  (Fig. 3).

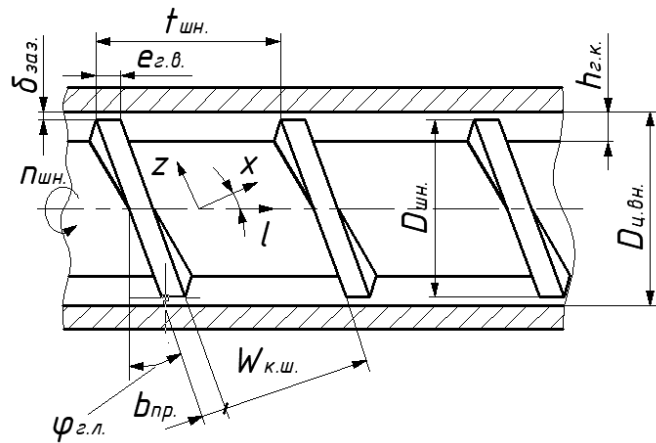


Fig. 2. Geometrical parameters of the extruder in the feed zone:  $D_{ц.вн.}$  - the inner diameter of the material cylinder;  $t_{шн.}$  - screw cutting step;  $e_{з.б.}$  - the width of the crest of the turn;  $\delta_{заяз.}$  - the size of the gap between the auger crest and the inner wall of the material cylinder;  $\varphi_{з.л.}$  - the angle of elevation of the helical cutting line of the auger;  $W_{к.ш.}$  - the width of the screw channel in the direction normal to the wall;  $b_{пр.}$  - span width

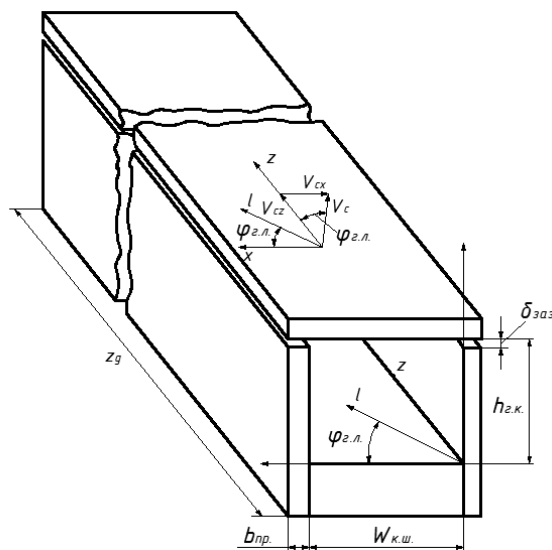


Fig. 3. Scheme of the expanded channel of the extruder for calculating productivity

In the further calculations, it is assumed that the gap  $\delta_{3a3}$  between the inner wall of the material cylinder 1 (Fig. 1) and the screw 2 is insignificant and, in further calculations, it can be neglected.

Then:

$$V_c = \pi \cdot D_{un.} \cdot n_{un.} \tag{1}$$

where  $n_{un.}$  is the rotation frequency of the screw.

Velocity projections  $V_c$  on the  $x$  and axis  $z$  are determined by the following expressions:

$$V_{cx} = \pi \cdot D_{un.} \cdot n_{un.} \cdot \sin(\varphi_{z.l.});$$

$$V_{cz} = \pi \cdot D_{un.} \cdot n_{un.} \cdot \cos(\varphi_{z.l.}). \tag{2}$$

The relation of the coordinate of movement in the direction  $z$  and in the direction  $x$  (along the axis of rotation of the screw in the direction  $l$ ) is determined by the equation:

$$z = \frac{x}{\sin(\varphi_{z.l.})} = \frac{l}{\sin(\varphi_{z.l.})}. \tag{3}$$

Determining the productivity of the extruder feed zone.

Consider the movement of material in the feed zone of the extruder using the scheme presented in Fig. 4. The screw channel (Fig. 4) moves at a speed  $V_c$  of Point A defines the initial position of the material element.

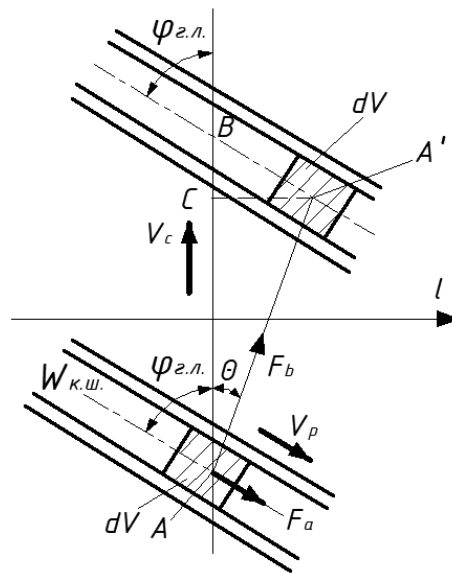


Fig. 4. Scheme of movement of material in the feeding zone of the extruder

Over time,  $t_{p.m.}$  the screw channel will move along with the material to segment  $AB$ . The movement of the material occurs due to the action of frictional forces arising on the surfaces of its contact with the screw channel. The point  $A$  will shift relative to the surface of the cylinder by the segment  $AA'$ , and relative to the surface of the screw channel – by the segment  $BA'$ .



Then you can express the speed  $V_p$  as the ratio of the path of movement of the material and the time of this movement:

$$V_p = \frac{BA'}{t_{p.m.}}. \quad (4)$$

The time of moving the material can be represented by the relation:

$$t_{p.m.} = \frac{AB}{V_c}, \quad (5)$$

where  $V_c$  is the speed determined by formula (1).

According to the trigonometric relations for triangles  $CBA'$  and  $CAA'$ , taking into account (5), we will rewrite equation (4) in the form:

$$V_p = \frac{V_c}{\cos(\varphi_{z.l.}) + \sin(\varphi_{z.l.}) \cdot \operatorname{ctg}(\theta)}. \quad (6)$$

We will use the expression for the sine of the sum of two angles and the tangent and rewrite equation (6) in the form:

$$V_p = V_c \frac{\sin(\theta)}{\sin(\theta + \varphi_{z.l.})}. \quad (7)$$

We express the productivity in the feed zone as the product of the speed  $V_p$  and the cross-sectional area of the screw channel:

$$Q_{\text{extm.}} = W_{\text{к.ш.}} \cdot h_{z.к.} \cdot V_p, \quad (8)$$

From the diagram in fig. 2 we get:

$$W_{\text{к.ш.}} = \left( \frac{t_{\text{шн.}}}{\lambda_{3\text{ax.}}} - b_{\text{np.}} \right) \cdot \cos(\varphi_{z.l.}). \quad (9)$$

where  $\lambda_{3\text{ax.}}$  is the number of auger cutting operations.

Taking into account (7) and (9), we rewrite (8) in the form:

$$Q_{\text{exc.}} = \pi \cdot D_{\text{шн.}} \cdot n_{\text{шн.}} \cdot h_{z.к.} \cdot \left( \frac{t_{\text{шн.}}}{\lambda_{3\text{ax.}}} - b_{\text{np.}} \right) \cdot \frac{\sin(\theta) \cdot \cos(\varphi_{z.l.})}{\sin(\theta + \varphi_{z.l.})}. \quad (10)$$

With constant movement of the material, the condition of equilibrium of the acting forces will be fulfilled:

$$F_a = F_b \cdot \cos(\theta + \varphi_{z.l.}). \quad (11)$$

We will analyze the movement of material in the feed zone of the extruder. We present equation (11) in the form:

$$\cos(\theta + \varphi_{z.l.}) = A_b, \quad (12)$$

where  $A_b = \frac{F_a}{F_b}$ .

It follows from equation (12) that with a known value,  $A_b$  the material transport angle can be found  $\theta$  and the extruder performance can be calculated from expression (10).

The value  $A_b$  can only be less than one, because the cosine of any angle does not exceed one. Equality  $A_b=1$  is possible under the condition  $F_a = F_b$ . At the same time  $\theta + \varphi_{z.l.} = 0$ , what is possible if  $\theta = -\varphi_{z.l.}$ .

It is clear that under this condition, the plug of material does not move in the direction of exit from the channel, but rotates together with the auger in a circle. That is, material movement is possible under the condition:

$$F_a < F_b. \tag{13}$$

The limiting case will be provided  $F_a = 0$  and  $F_b = 0$ , which is possible if  $\theta + \varphi_{z.n.} = 90^\circ$ . In this case, the extruder works with maximum productivity.

An increase in the angle of the helical line of the auger leads to a decrease in productivity. In most cases, the condition is accepted for extruders  $t_{un.} = D_{un.}$ . Then we get:

$$\varphi_{z.n.} = \arctg\left(\frac{1}{\pi}\right),$$

From  $\varphi_{z.n.} = 17,657^\circ$

Calculation of pressure in the extruder channel.

Let's select an element of the volume of material in the channel of the extruder screw by length  $dz$  and consider the forces acting on it. The scheme for calculating the forces acting on the material in the feeding zone is shown in Fig. 5.

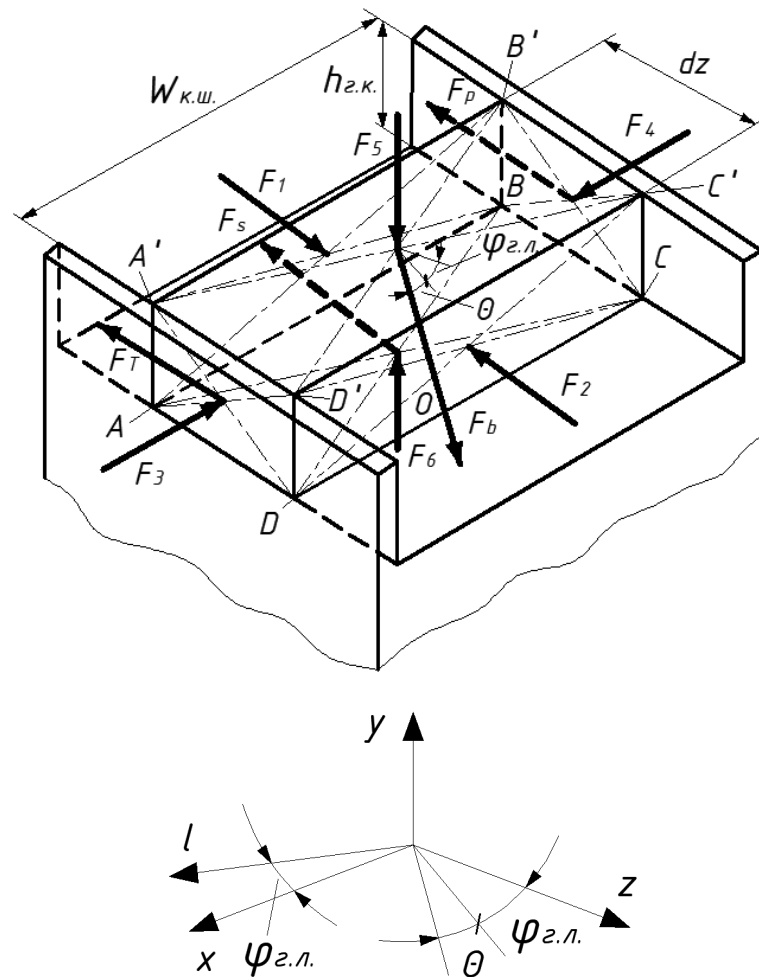


Fig. 5. Scheme for calculating the forces acting on the material in the feed zone

The force  $F_b$  is the frictional force acting on the material in contact with the surface of the

opening of the material cylinder. This force causes the material to move along the helical channel of the auger. The force  $F_b$  is proportional to the pressure in the material and is directed at an angle  $\theta$  to the plane perpendicular to the screw axis:

$$F_b = f_b \cdot P_y \cdot W_{\kappa.u.} \cdot dz, \quad (14)$$

where  $f_b$  is the coefficient of friction of the polymer material on the surface of the opening of the material cylinder;  $P_y$  - pressure in the material in the direction of the axis  $y$ .

The non-isotropy of granules or powder of a polymer material can be expressed using the coefficient:

$$K_y = \frac{P_y}{P_z}, \quad (15)$$

where  $P_z$  is the pressure in the material in the direction of the axis  $z$ .

Considering (15), we rewrite (14) in the form:

$$F_b = f_b \cdot K_y \cdot P_z \cdot W_{\kappa.u.} \cdot dz, \quad (16)$$

Similarly, the equation for the friction force  $F_s$  acting between the material and the surface of the screw core:

$$F_b = f_s \cdot K_y \cdot P_z \cdot W_{\kappa.u.} \cdot dz. \quad (17)$$

Forces  $F_1$  and  $F_2$  are reactions from the sides of the rejected material on the selected element  $dz$ . Expressions for  $F_1$  and  $F_2$  have the form:

$$F_1 = P_z \cdot h_{z.k.} \cdot W_{\kappa.u.}; \quad F_2 = (P_z + dP_z) \cdot (h_{z.k.} - A_k \cdot dz) \cdot W_{\kappa.u.}, \quad (18)$$

where  $A_k$  is the parameter that determines the taper of the screw core;

$$A_k = \frac{(h_{z.k.1} - h_{z.k.2})}{Z_g}, \quad (19)$$

where  $h_{z.k.1}$ ,  $h_{z.k.2}$  - the depth of the screw channel at the beginning and at the end of the feed zone;  $Z_g$  - the length of the channel of the feed zone of the screw in the direction of the axis  $z$ .

Normal forces act on the sides of the walls of the screw channel  $F_3$  and  $F_4$ :

$$F_3 = K_{xT} \cdot P_z \cdot h_{z.k.} \cdot dz; \quad F_4 = K_{xp} \cdot P_z \cdot h_{z.k.} \cdot dz, \quad (20)$$

where  $K_{xT}$ ,  $K_{xp}$  are coefficients characterizing the anisotropy of the pressure field along the axis  $x$  in relation to the pressure along the axis  $z$ .

By analogy with (15), we write:

$$K_{xT} = \frac{P_{xT}}{P_z}; \quad K_{xp} = \frac{P_{xp}}{P_z}, \quad (21)$$

where  $P_{xT}$ ,  $P_{xp}$  - pressure in the direction of the axis  $x$  near the front and rear walls of the screw channel.

Normal forces act on the material element from the front and back walls of the screw channel  $F_5$  and  $F_6$ :

$$F_5 = F_6 = K_y \cdot P_z \cdot W_{\kappa.u.} \cdot dz. \quad (22)$$

Also on the material element from the front and back walls of the screw channel act friction forces  $F_T$  and  $F_p$ :

$$F_T = K_{xT} \cdot P_z \cdot h_{z,k} \cdot f_s \cdot dz; F_p = K_{xp} \cdot P_z \cdot h_{z,k} \cdot f_s \cdot dz, \quad (23)$$

Under the condition of steady motion of the material, the vector sum of all forces acting on it must be zero. Therefore, the sum of the projections of the acting forces on the coordinate axis is also zero.

The equation for the sum of the projections of all forces on the axis  $z$  has the form:

$$F_1 - F_2 - F_T - F_p - F_s + F_b \cdot \cos(\theta + \varphi_{z,l}) = 0. \quad (24)$$

Let us assume that  $dP_z \cdot h_{z,k} \cdot W_{k,u} \gg dP_z \cdot A_k \cdot W_{k,u} \cdot dz$ , then the expression for determining the force  $F_2$  will take the form:

$$F_2 = P_z \cdot (h_{z,k} - A_k \cdot dz) \cdot W_{k,u} + dP_z \cdot h_{z,k} \cdot W_{k,u}. \quad (25)$$

Substitute the corresponding formulas for all forces into equation (25) and divide all terms by the product  $h_{z,k} \cdot W_{k,u} \cdot dz$ , we get:

$$\frac{dP_z}{dz} - P_z \cdot AF = 0, \quad (26)$$

$$\text{where } AF = \frac{K_y \cdot W_{k,u} \cdot [f_b \cdot \cos(\theta + \varphi_{z,l}) - f_s] - h_{z,k} \cdot f_s \cdot (K_{xT} + K_{xp}) + A_k \cdot W_{k,u}}{h_{z,k} \cdot W_{k,u}} \quad (27)$$

The solution of the differential equation (26) under the initial conditions  $P_z = P_1$  at  $z = 0$ , has the form:

$$P_z = P_{3.3} \cdot \exp(AF \cdot z). \quad (28)$$

where  $P_{3.3}$  is the pressure in the material loading zone from the hopper.

The pressure in the material loading zone from the hopper can be determined by the formula [8]:

$$P_{3.3} = \left( \frac{h_{\sigma,1}}{h_{\sigma,0}} \right)^{b_\phi} \cdot P_{k,y} + \frac{\rho_{h,z} \cdot g \cdot h_{\sigma,1}}{b_\phi - 1} \cdot \left[ 1 - \left( \frac{h_{\sigma,1}}{h_{\sigma,0}} \right)^{b_\phi - 1} \right], \quad (29)$$

where  $\rho_{h,z}$  is the bulk density of the material;  $g$  - Acceleration of gravity;  $b_\phi$  - coefficient that takes into account the shape of the bunker and the properties of the material;  $P_{k,y}$  - the pressure generated at the entrance to the conical part of the hopper due to the available material in the cylindrical part.

To determine the pressure,  $P_{k,y}$ , you can use the formula [8]:

$$P_{k,y} = \frac{\rho_{h,z} \cdot g \cdot D_\delta}{4 \cdot f_\omega \cdot K_\delta} \cdot \left[ 1 - \exp\left( \frac{4 \cdot f_\omega \cdot K_\delta \cdot h_{\sigma,2}}{D_\delta} \right) \right], \quad (30)$$

where  $K_\delta$  is the coefficient of lateral compression of the material;  $f_\omega$  - coefficient of friction on the hopper wall.

Values  $h_{\sigma,0}$ ,  $h_{\sigma,1}$ ,  $h_{\sigma,2}$ ,  $D_\delta$  - geometric parameters of the bunker, which are presented in Fig. 5.

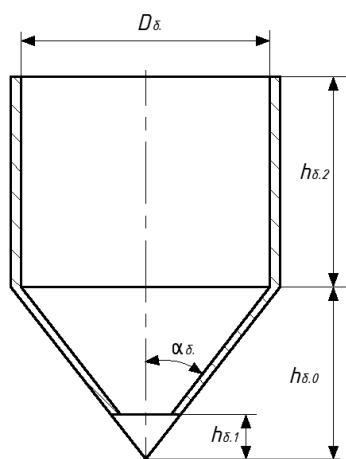


Fig. 5. Geometric parameters of the bunker

Substituting formula (30) into (29), we obtain:

$$P_{3.3.} = \left( \frac{h_{\delta,1}}{h_{\delta,0}} \right)^{b_{\phi}} \cdot \frac{\rho_{u.z.} \cdot g \cdot D_{\delta}}{4 \cdot f_{\omega} \cdot K_{\delta}} \cdot \left[ 1 - \exp \left( - \frac{4 \cdot f_{\omega} \cdot K_{\delta} \cdot h_{\delta,2}}{D_{\delta}} \right) \right] + \frac{\rho_{u.z.} \cdot g \cdot h_{\delta,1}}{b_{\phi} - 1} \cdot \left[ 1 - \left( \frac{h_{\delta,1}}{h_{\delta,0}} \right)^{b_{\phi} - 1} \right]. \quad (31)$$

Power consumed in the power zone.

The power in the feed zone is spent on overcoming the frictional forces between the polymer and the surface of the channel. The expression for determining power in the general case:

$$N_{3.3.} = \sum_i (\Delta N_{bi} + \Delta N_{si}), \quad (32)$$

where  $\Delta N_{bi}$ ,  $\Delta N_{si}$  - the power spent along the length  $\Delta z$  to overcome the frictional forces, respectively, on the surface of the cylinder and the screw;

$$\Delta N_{bi} = V_p \cdot P_{zi} \cdot f_{bi} \cdot W_{\kappa.u.} \cdot \Delta z, \quad (33)$$

$$\Delta N_{si} = V_p \cdot P_{zi} \cdot f_{si} \cdot (W_{\kappa.u.} + 2 \cdot h_{z.\kappa.}) \cdot \Delta z. \quad (34)$$

## 5. CONCLUSIONS

In the article, the development and analysis of the screw extruder model of the 3D printer, which uses granules or crushed polymer waste as raw materials, is carried out. The determination of the key parameters of the extruder, in particular the productivity and pressure in the material cylinder at the stage of loading the polymer, was carried out. In the course of the research, a mathematical model was created that describes the performance of the screw extruder depending on the main parameters, such as the diameter of the screw, its rotation frequency, the depth of the screw channel and the angle of elevation of the screw cutting line, etc. The formula for determining the pressure in the material loading zone from the hopper effectively links the physical and geometric characteristics of the polymer material with the parameters of the loading hopper, which is key to optimizing the extrusion process. The simulation results indicate the possibility of optimizing the design of the screw extruder to increase the productivity of the device and the quality of 3D printing from secondary raw materials. They pave the way for further research, including determining the power of the electric motor to drive the extruder screw and will help improve the efficiency of using different types of recycled materials in screw extruders for 3D printing.

**BIBLIOGRAPHY**

1. Vytvytskyi V.M. Simulation of the process of feeding a worm extruder with polymer raw materials: monograph / V.M. Vytvytskyi, I.O. Mikulonok. - K.: NTUU «KPI», 2021. - 136 c.
2. Tadmor Z, Klein I. Engineering Principles of Plasticizing Extrusion. - New York: Van Nostrand Reinhold, 1970. - 479 p.
3. Mikulonok I.O., Radchenko L.B. Processing of secondary raw materials by extrusion. - K.: NTUU «KPI», 2006. - 184 p.
4. Mikulonok I.O. Equipment and processing processes of thermoplastic materials using secondary raw materials: monograph. - K.: IVC «Polytechnic Publishing House», 2009. - 265 p.
5. Radchenko L.B. Processing of thermoplastics by the extrusion method: Science. manual - K.: IZMN, 1999. - 220 p.
6. Misiats V.P. Mathematical modeling of the material movement process in an extruder-shredder with a channel of a variable profile under non-isothermal conditions / KNUTD Bulletin. 2006. № 2. - P.42-49.
7. Misiats V.P. Analytical studies of the operation of a screw device for pressing coffee / V.P. Misiats, T.I. Kulik, O.S. Polishchuk, S.P. Lisevych // Bulletin of the Khmelnytskyi National University. Technical sciences. 2018. - № 2. - P.64-70.
8. Kuzyaev IM Modeling of extrusion and extruders during polymer processing: monograph. In 2 parts / IM Kuzyaev, VA Sviderskyi, AD Petukhov. - K.: NTUU " KPI " " Polytechnic ", 2016. - 412